



Proceedings of the International Symposium of Mechanism and Machine Science, 2010
AzCIFTtoMM – Izmir Institute of Technology
5-8 October 2010, Izmir, TURKEY

AzC IFTtoMM
International Symposium of
Mechanism and Machine Science

Proceedings

5-8 October 2010
Izmir-Turkey



Proceedings of the International Symposium of Mechanism and Machine Science, 2010
AzCIFTtoMM – Izmir Institute of Technology
5-8 October 2010, Izmir, TURKEY



Preface

AzCIFTtoMM 2010 - International Symposium of Mechanism and Machine Science (ISMMS) has taken place in Izmir Institute of Technology, Izmir, Turkey, on 5-8 October 2010. The aim of the symposium is to gather scientists, scholars, students and producers with interest in the general area of the mechanism and machine science.

The symposium is organized by Azerbaijan Committee of International Federation of for the Theory of Mechanisms and Machines (Prof. Dr. Sc. Rasim Alizade), Azerbaijan National Aviation Academy (Academician, Prof. Dr. Sc. Arif Pashayev) and Izmir Institute of Technology (Prof. Dr. Zafer İlken).

Symposium Themes:

The International Symposium is one of the largest conferences that will cover the general areas of the theory and practice of mechanisms and machines. The programs cover sections of relevance to MMS, Mechanism and Machine Science, namely;

- Structural Synthesis and Kinetic Architecture, **SsKa**
- Linkages, Cams, Gearing and Transmissions, **LcGt**
- Control Systems, **Cs**
- Mechanisms of Flying and Space Machinery, **MfSm**
- Mechatronics, **Mc**
- Robotics, **Rb**
- Dynamics and Vibrations of Machinery, **DvM**
- Computational Kinematic Synthesis and Analysis, **CkSa**
- Nanotechnology and Micro: Manipulators, Robots, Mechanisms, **NtMm**



Symposium Chairs

Prof. Dr. Sc. Rasim Alizade - Azerbaijan Committee of International Federation for the Promotion of MMS
Prof. Dr. Sc. Arif Pashayev - National Aviation Academy, Azerbaijan
Prof. Dr. Zafer İlken - Izmir Institute of Technology

Scientific Committee

Rasim Alizade	Turkey	Kostas Terzidis	USA
Arif Pashayev	Azerbaijan	Zhong You	Great Britain
B. Zafer İlken	Turkey	Yan Chen	Singapore
Bernard Roth	USA	Eres Söylemez	Turkey
Karl Wohlhart	Austria	Abdulkadir Erden	Turkey
V.S. Siromyathikov	Russia	Kemal Özgören	Turkey
Ayaz Abdullayev	Azerbaijan	Bülent Yardımoğlu	Turkey
Alishir Alifov	Russia	Serhan Özdemir	Turkey
Adalat Samedov	Azerbaijan	Can Dede	Turkey
Nazim Mirnasiri	Australia	Salih Okur	Turkey
Dan Zhang	Canada	Özgür Kilit	Turkey
Ramiz A. Sadigov	Azerbaijan	Koray Korkmaz	Turkey
Charis Gantes	Greece		
Simon Guest	Great Britain		

Local Organizing Committee

Metin Tanoğlu	Koray Korkmaz
Bülent Yardımoğlu	Erkin Gezgin
Serhan Özdemir	Yenal Akgün
Can Dede	E. Selahattin Umdu

Symposium Coordinators

Erkin Gezgin, Yenal Akgün, Can Dede

Proceeding Book Editing & Posters

Erkin Gezgin, Yenal Akgün



Table of Contents

Key Lectures	09
Structural Synthesis of Robot Manipulators Rasim ALIZADE	11
Revisiting a Noble Structural Modification Method for Linear and Nonlinear Dynamic Reanalysis of Machinery H. Nevzat ÖZGÜVEN	33
BioMimetic/BioInspired Robots and Mechatronics Engineering Design Abdülkadir ERDEN	45
Kinematic Analysis of Spatial Mechanical Systems with a Systematic Approach to Describe Joint Kinematics M. Kemal ÖZGÖREN	55
Session 1: Structural Synthesis and Kinetic Architecture (SsKa) Linkages, Cams, Gearing and Transmissions (LcGt)	71
Research of Velocity and Acceleration of Suspension Point of New Constructive Decision of a Mechanical Drive for Sucker-Rod Pumps Ali NAJAFOV, Ayaz ABDULLAYEV, Yusif YAGUBALIYEV	73
Structural Synthesis of Multiloop Manipulators with General Constraint One Rasim ALIZADE, Özgün SELVI, Erkin GEZGIN	78
Multifunctional 7R Linkages Karl WOHLHART	85
Survey of Rigid Body Motions In Space and Subspaces by Using Method of Intersections Erkin GEZGIN	92
Structural Synthesis of Novel Parallel Manipulators Fatih Cemal CAN, Erkin GEZGIN	96
Design of Foldable Shelter Peilin TIAN, Yan CHEN	102
A Method for Kinetic Tessellation with Planar Mechanisms Aylin GAZI, Koray KORKMAZ	107
A Novel Spatial Scissor-hinge Structural Mechanism for Transformable Roofs Yenal AKGÜN, Koray KORKMAZ, Werner SOBEK, Charis GANTES	116
Design of Novel Mechanism Based on Bennett Linkage for Architectural Application Koray KORKMAZ, Yenal AKGÜN, Feray MADEN	123



Designing a Bricard Linkage Module to Stabilize Unstable Space Frames Melodi Simay ACAR, Koray KORKMAZ	130
Obtaining New Linkages from Jitterbug-Like Polyhedral Linkages Gökhan KIPER, Eres SÖYLEMEZ	137
Session 2: Control Systems (Cs)	145
Mechanisms of Flying and Space Machinery (MfSm)	
<hr/>	
Structure of a Complex Diagnosis System for Aviation Engines Arif. PASHAYEV, Ramiz SADIQOV, Parviz ABDULLAYEV, Ajdar SADIQOV, Azer MIRZOYEV	147
Vibration Control of Rail Vehicle Body Using Parameters Adaptive PID Muzaffer METIN, Rahmi GÜÇLÜ, Fatih DUMAN	155
An Electro-Hydraulic Spherical Manipulator, Dynamic Modelling and Simulation: A Case Study Mehmet TOPALBEKIROGLU, L.Canan DÜLGER, Ali KIREÇCI	162
Neural Network-based Nonlinear Control Design for Twin Rotor MIMO Systems Alper BAYRAK, Mohammad SALAH, Nitendra NATH, Enver TATLICIOGLU	172
Adaptive Identification of Tire Cornering Stiffness and Vehicle Center of Gravity Alper BAYRAK, Enver TATLICIOGLU, Michael L. MCINTYRE	179
State Space Smoothing through Singular Value Decomposition (SVD) Hakkı Erhan SEVİL, Serhan ÖZDEMİR, Tunç BILGINCAN	184
Moving sliding Mode Control of a DC Motor Driven Four-Bar Mechanism Alper Kadir TANYILDIZI, Orhan ÇAKAR	190
Space Vector Modeling and Control of a Three Pole Magnetic Bearing Barış Oğuz GÜRSES, Aysun BALTACI, Mutlu BOZTEPE, Mehmet SARIKANAT	198
Vibration Control of Beams Via electromagnetic Fields Barış Oğuz GÜRSES, Aysun BALTACI, Mutlu BOZTEPE, Mehmet SARIKANAT	204
Numerical Modelling of Protection of Gas Turbine Blades from Influence of igh Temperature A. PASHAYEV, R. SADIQOV, A. SAMADOV, R. MAMMADOV	209
Single and Multi Objective Genetic Algorithm Optimizations of the Laminated Composites Used in Satellite Structures Levent AYDIN, H. Seçil ARTEM	219
The Influence of the Spring Rate on the Dynamics of the Special Centrifugal Regulator Jafar AGALAROV, Vugar JAVADOV	227
Fault Detection and Isolation using Redundant Sensors for a Wind Turbine with Doubly-Fed Induction Generator (DFIG) Hakki Erhan SEVİL	232



Session 3: Mechatronics (Mc)	239
Robotics (Rb)	
<hr/>	
Dexterity of a Welding Industrial Robot Karl GOTLIH, Tomaz VUHERER	241
Design Kinematic Solution and Control of a 3-PUU Translational Parallel Manipulator Erol UYAR, Lyutvi Yusein YUMER, İsmet ATEŞ	246
Morphology of a Single Actuator Tetrapod Walking Spider Robot Servet SOYGUDER, Hasan ALLI	254
Gaits and Trajectory Planning with Optimal Hip-Mass Positioning strategies for 4-DoF Parallelogram Bipedal Robot Nazim Mir NASIRI, Hudyjaya Siswoyo JO	259
Integration of the Hybrid-Structure Haptic Interface: HIPHAD v1.0 Tunç BILGINCAN, Erkin GEZGIN, Can DEDE	267
Navigation of a Hydraulically Actuated Mobile Robot Using Stereo Vision Ali KILIÇ, Sadettin KAPUCU	285
Decoding Process and Characterization Studies of a 2D Laser Scanning Range Finder Gökhan BAYAR, A. Buğra KOKU, E. İlhan KONUKSEVEN	295
Design and Control of an Inserting Mechanism for PP (Polypropylene) and PE (Polyethylene) Sacks Gökhan BAKIR, L. Canan DÜLGER	300
Multiaxis Three Dimensional (3D) Circular Weaving: Concept to Prototype Design Methodology and Preliminary Investigation of Feasibility of Weaving Method Kadir BILISIK	308
Robust Optimal Design of a Micro Series Elastic Actuator (uSEA) Ozan TOKATLI, Volkan PATOGLU	318
Design and Multi-criteria Optimization of a Haptic Interface Aykut Cihan SATICI, Ahmet Mehmet ERGIN, Volkan PATOGLU	328
Kinematic Analysis of the Cam Lever Mechanisms of the Cotton Cleaning Machines Fazil VELIYEV, Mazakhir FARZALIEV	337
Session 4: Dynamics and Vibrations of Machinery (DvM)	341
Computational Kinematic Synthesis and Analysis (CkSa)	
<hr/>	
Dynamics and stability of Large Turbine Generators Jan DUPAL, Tomas KURUC	343
An adaptive Tuned Vibration Absorber Using a String Mass System with Quasi-zero Stiffness String Tension Adjustment Mechanism Mustafa Ali ACAR, Çetin YILMAZ	349



Vibration Characteristics of a Vertical Roller Mill Engin H. ÇOPUR, Metin U. SALAMCI, Tuncay KARAÇAY, Emine TOKA	355
Vibrations of Crank Slider Mechanism with Multi Cracks and Micromechanisms' Side Effects Vedat KARADAG	361
The Free Vibration of Symmetrically Laminated Conical Shells with Freely Supported Edges A.H. SOFIYEV, E. SCHNACK, A. Deniz, M. AVCAR	372
About Some Methods of Calculation Nonlinear Oscillations in Machines A. A. ALIFOV	378
On Function Generation of Watt I Mechanisms for Finger Design Qiong SHEN, Kevin RUSSELL, Raj S. SODHI	383
A New Geometric Algorithm for Workspace Analysis in Planar 3-RRR Manipulator Özgür KILIT, Sedat SAVAS	389
A New Geometric Algorithm for Direct Position Analysis of Planar 3-RRR Manipulator" Özgür KILIT	396
Interactive Least Squares Synthesis of a Watt I Six Bar Path Generator Andrew B. KIKIN, Anton A. KIKIN	403
An Experimental Evaluation of Earthquake Effects on Mechanism Operation Marco CECCARELLI, Özgün SELVI	408
Session 5: Dynamics and Vibrations of Machinery (DvM) Nanotechnology and Micro: Manipulators, Robots, Mechanisms (NtMm)	417
The Influence of the Vibration Frequency on the Torsion Stiffness of the Driving Coupling I. KHALILOV	419
The Dynamics of Actuators of the Technological Machines in the Textile Industry Mazakhir FARZALIEV, Elman DJAFAROV	425
The Photoelectric Properties In₂O₃-SiO₂-Si-M Structures A.Z. BADALOV, B.A. YUSIFOV, Sh. H. ZEYNALOVA	429
Process of Growth and Self Organization on of Nanofragment on TlGaSe₂ Vicinal Surfaces A.M.PASHAEV, B.Y.TAGIYEV, F.K.ALESKEROV, K.Sh.KAHRAMANOV	434



Proceedings of the International Symposium of Mechanism and Machine Science, 2010
AzCIFTtoMM – Izmir Institute of Technology
5-8 October 2010, Izmir, TURKEY

Key Lectures:



Proceedings of the International Symposium of Mechanism and Machine Science, 2010
AzCIFTtoMM – Izmir Institute of Technology
5-8 October 2010, Izmir, TURKEY

Structural Synthesis of Robot Manipulators

Rasim ALİZADE^{1*}

^{1*}Izmir Institute of Technology
 Department of Mechanical Engineering
rasimalizade@iyte.edu.tr

Abstract

Structural synthesis theory was developed by using screw theory. As a mathematical tool, screw theory can represent the displacement, velocity, forces and torques in three dimensional spaces. Displacement of one, two and three screws are described. The transformation unit vector matrix equation and the transformation unit screw matrix equation were investigated. Structural design of RRRS mechanism with general constraint one regarding angular and linear conditions are introduced. New structural formulations for independent loops, for the platform motion and the mobility of robot manipulators with variable general constraint are presented.

Also new structural formulas of mobility of parallel Cartesian and Euclidean platform robot manipulators are presented. At the end a novel universal mobility formulations are presented in terms of screw theory.

Keywords: Screw theory, transformation displacement equation, platform motion, structural formula, independent loops.

1. Screw Theory

Screw theory is mostly used in the structural analysis, structural-kinematic synthesis, kinematic analysis and synthesis and in the dynamics, where screw can represent the displacements, velocities, forces and torques in three dimensional space by using dual form including both rotational and translational components.

1.1. Introduction to Screws

The displacement of a rigid body (Fig.1) is described as unit vector $s=[l, m, n]^T$ and moment $u=[P+\mu l, Q+\mu m, R+\mu n]^T$ with respect to origin of reference coordinate system and to the rotation axis on the pitch μ distance. Unit vector s and moment u can be introduced as dual vector that is called a screw with the six independent components

$$\mathcal{S}=s+\omega u \quad (1.1)$$

where ω is the Clifford's operator ($\omega^2=0$)

Six independent components (l, m, P, Q, R, μ) describe the displacement of screw as follow

$$\mathcal{S}=\begin{bmatrix} s \\ r \times s + \mu s \end{bmatrix} \quad (1.2)$$

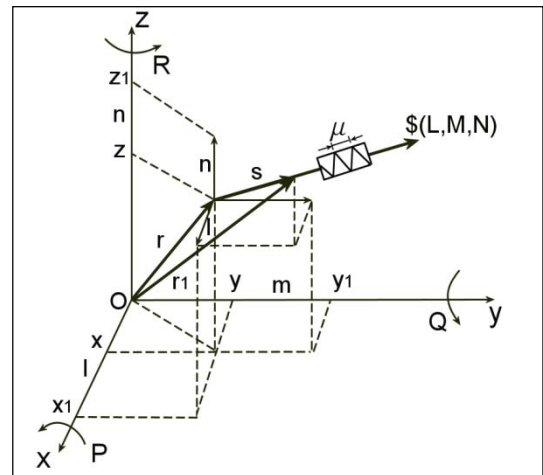


Fig.1. Displacement of screw

As shown in Eq.s(1.1) and (1.2) the moment u of the screw \mathcal{S} is

$$u=r \times s + \mu s \quad (1.3)$$

Multiplying left and right sides of Eq.(1.3) to the unit vector s gives the pitch distance μ , as:

$$s \cdot u = (r \times s) \cdot s + \mu s \cdot s \text{ or } \mu = \frac{s \cdot u}{s \cdot s} \quad (1.4)$$

If the screw is lack of pitch μ that is also called zero screw, it forms a line that can be described as particular line of the screw axis.

$$\$(s, r \times s) \quad (1.5)$$

Each screw axis Eq.(1.5) can be introduced as screw with three dual coordinates $\$(\tilde{L}, \tilde{M}, \tilde{N})$ where

$$\tilde{L}=l+\omega P, \quad \tilde{M}=m+\omega Q, \quad \tilde{N}=n+\omega R \quad (1.6)$$

So, parameters (l, m, n, P, Q, R) are the Plücker coordinates of screw axis.

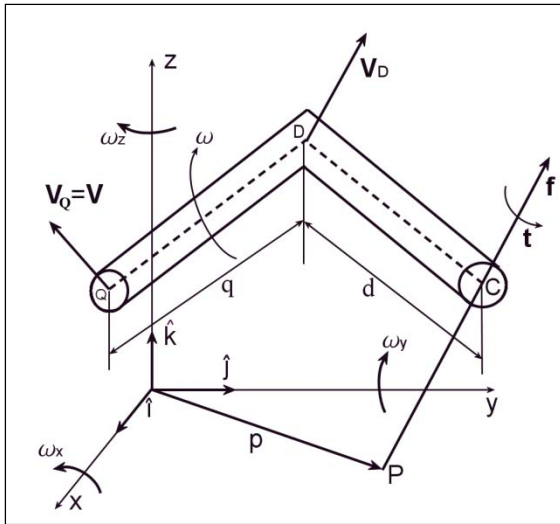


Fig. 2. Rigid body assembled into a twist and wrench

The angular velocity ω and linear velocity \mathbf{V} of a moving rigid body (Fig.2) are three dimensional vectors that can be assembled into two vectors called a twist. So, the twist, T , of a rigid body, which is the velocity of one point of the body and the angular velocity of the body, can be introduced as a vector.

$$T = \begin{bmatrix} \omega \\ \mathbf{V} + \mathbf{q} \times \omega \end{bmatrix} \quad (1.7)$$

Similarly, the resultant force $\mathbf{f} = [f_x, f_y, f_z]^T$ and a resultant moment

$\mathbf{t} + \mathbf{p} \times \mathbf{f} = [t_x + \mathbf{p}_x \times f_x, t_y + \mathbf{p}_y \times f_y, t_z + \mathbf{p}_z \times f_z]^T$ acting at a point on the rigid body can be assembled into another vector system called wrench. Thus, the wrench \mathbf{W} of a rigid body can be represented as a vector:

$$\mathbf{W} = \begin{bmatrix} \mathbf{f} \\ \mathbf{t} + \mathbf{p} \times \mathbf{f} \end{bmatrix} \quad (1.8)$$

The mathematics of these vector pairs (dual vectors Eq.s (1.2), (1.7) and (1.8)) are known as screw theory and dual vector algebra.

1.2. Motor Screw

Screw $\$(s, \mathbf{u})$, that may be a displacement of a rigid body, or a twist, or a wrench is a line $L = [s, r \times s]^T$ called axis of the screw. Before defining the motor screw, sliding vectors should be discussed. Sliding vector can be described as a vector with known length, direction, position and zero pitch $\mu=0$. Consider that arbitrary number of sliding vectors in space is given as $\{s_i\}_1^n$.

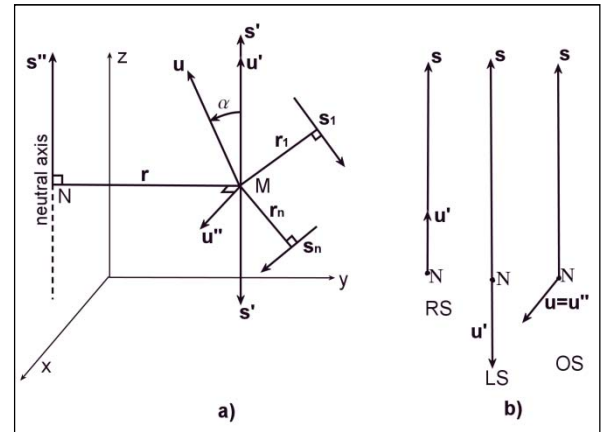


Fig. 3. Motor Screw

As shown in Fig.3 the resultant vector of sliding vectors in space will be the main vector $\mathbf{s} = \sum_{i=1}^n s_i$ while the main moment with respect to an arbitrary point, M in space will be $\mathbf{u}_M = \sum_{i=1}^n (\mathbf{r}_i \times s_i)$. Changing the arbitrary point to a new one N , the main moment will become

$$\mathbf{u}_N = \sum_{i=1}^n (\mathbf{r} + \mathbf{r}_i) \times s_i = \mathbf{u}_M + \mathbf{r} \times \mathbf{s}, \quad \text{where } \mathbf{r} = \overline{NM}.$$

The system of main vector and main moment is called motor screw.

In the general case the main vector \mathbf{s} and main moment \mathbf{u} are placed to an arbitrary point M and form some angle α (Fig.3). The main moment \mathbf{u} can be assembled into two component vectors $\mathbf{u} = (\mathbf{u}', \mathbf{u}'')$, where $\mathbf{u}' // \mathbf{s}$ and $\mathbf{u}'' \perp \mathbf{s}$. If the moments are said to be taken from some arbitrary point N than $\mathbf{u}'' = \mathbf{r} \times \mathbf{s}$, where \mathbf{r} is the shortest distance from point N to the main vector \mathbf{s} . In order to find \mathbf{r} in terms of the main vector and main moment following algebraic procedure can be introduced as,



$$\mathbf{r} = \frac{\mathbf{u}''}{\mathbf{s}} = \frac{\mathbf{u} \sin(\alpha)}{\mathbf{s}} = \frac{\mathbf{s} \cdot \mathbf{u} \sin(\alpha)}{\mathbf{s} \cdot \mathbf{s}} = \frac{\mathbf{s} \times \mathbf{u}}{\mathbf{s} \cdot \mathbf{s}} \quad (1.9)$$

The Plücker coordinates of this line (neutral axis $MN=r$) can be described as $\mathbf{L}=(\mathbf{s}, \mathbf{r} \times \mathbf{s})$ and form a particular type of screw that we call a Plücker vector. Notice that the two vectors that make up a Plücker vector are orthogonal.

1.3. Derivation

Collinear conditions are executed or all points located on line parallel to \mathbf{s} , and passing through the point N. This line is called main axis of screw of the system of sliding vectors, main vector and main moment. If \mathbf{s} and \mathbf{u}' are directed to the same direction that screw is called right screw. If \mathbf{s} and \mathbf{u}' are directed in opposite directions that screw is called left screw. If \mathbf{s} and \mathbf{u}'' are orthogonal vectors that screw is called zero screw. Two vectors \mathbf{u}' and \mathbf{s} is interconnected by the ratio $|\mathbf{u}'|=\mu|\mathbf{s}|$, where parameter μ is the pitch of screw. The magnitude at the pitch is defined by multiplying left and right sides by $|\mathbf{s}|$, as $|\mathbf{s}||\mathbf{u}'|=\mu|\mathbf{s}||\mathbf{s}|$ or $|\mathbf{s}||\mathbf{u}''|\cos(\alpha)=\mu|\mathbf{s}||\mathbf{s}|$ or $\mathbf{s} \cdot \mathbf{u}''=\mu|\mathbf{s}||\mathbf{s}|$ or $\mu = \frac{\mathbf{s} \cdot \mathbf{u}''}{|\mathbf{s}| \cdot |\mathbf{s}|}$

- Screw pitch μ is the ratio at magnitude of the component of \mathbf{u} in the direction \mathbf{s} to the magnitude of \mathbf{s}
- If the parameter of screw $\mu=0$, then the screw is equivalent to the vector \mathbf{s} and is called zero screw.
- If the vector $\mathbf{s}=0$, that screw equivalent to the moment vector \mathbf{u} and is called degenerated screw.
- Any sliding vector is equivalent to zero vector.
- Any free vector is equivalent to degenerated screw.
- A screw is written in terms of the Plücker coordinates of its axis as $\mathcal{S}=[\mathbf{s}, \mu\mathbf{s}+\mathbf{r} \times \mathbf{s}]^T$
- A line of the axis of the screw in terms of the Plücker coordinates are defined as $\mathcal{S}=[\mathbf{s}, \mathbf{r} \times \mathbf{s}]^T$, where $\mathbf{s}=[l, m, n]^T$, $\mathbf{u}=[P, Q, R]^T$, $\mathbf{r}=[x, y, z]^T$
- Two conditions $\mathbf{s} \cdot \mathbf{s}=1$ and $\mathbf{s} \cdot \mathbf{u}=0$ gives that four Plücker coordinates of line are independent

2. Displacement of One, Two and Three Screws in Space

2.1. Displacement of Unit Screw in Space

The moment of unit screw with respect to origin of reference coordinate system is

$$\mathbf{u} = \mathbf{r} \times \mathbf{s} \quad (2.1)$$

where $\mathbf{r}=[x, y, z]^T$ is the radius-vector of any point of unit screw and $\mathbf{u}=[P, Q, R]^T$ is the moment.

Eq. (2.1) can be describe in matrix form as

$$\begin{bmatrix} P \\ Q \\ R \end{bmatrix} = \begin{bmatrix} 0 & n & -m \\ -n & 0 & l \\ m & -l & 0 \end{bmatrix} \begin{bmatrix} x \\ y \\ z \end{bmatrix} \quad (2.2)$$

Eq (2.2) is the equation of unit screw axis in space, so $\mathcal{S}^2=1+\omega \cdot 0$, or with respect to Eq.s(1.6) in dual coordinate form yields:

$$\tilde{L}^2 + \tilde{M}^2 + \tilde{N}^2 = 1 + \omega \cdot 0 \quad (2.3)$$

where

$$\tilde{L}^2 = l^2 + 2\omega lP, \quad \tilde{M}^2 = m^2 + 2\omega mQ, \quad \tilde{N}^2 = n^2 + \omega nR \quad (2.4)$$

Using Eq.s(2.3) and (2.4) gives.

$$l^2 + m^2 + n^2 + 2\omega(lP + Qm + Rn) = 1 + \omega \cdot 0 \quad (2.5)$$

Equation (2.5) can be introduce in the vector form

$$\mathbf{s} \cdot \mathbf{s} + 2\omega \mathbf{s} \cdot \mathbf{u} = 1 + \omega \cdot 0 \quad \text{or} \quad \mathbf{s} \cdot \mathbf{s} = 1 \quad \text{and} \quad \mathbf{s} \cdot \mathbf{u} = 0 \quad (2.6)$$

The system of Eq.s (2.6) describe that from six Plücker coordinates just four parameters are independent:

- Plücker coordinates are dependent
- Axis of unit screw is described by unit vector $\mathbf{s}=[l, m, n]^T$ and moment of unit vector $\mathbf{u}=[P, Q, R]^T$

2.2. Displacement of Two Screws in Space

The displacement of a rigid body in space can be introduced by two arbitrary attached unit screws \mathcal{S}_1 and \mathcal{S}_2 (Fig.4) with the following equations:

$$\begin{aligned} \tilde{L}_1^2 + \tilde{M}_1^2 + \tilde{N}_1^2 &= 1 + \omega \cdot 0, & \tilde{L}_2^2 + \tilde{M}_2^2 + \tilde{N}_2^2 &= 1 + \omega \cdot 0, \\ \tilde{L}_1 \tilde{L}_2 + \tilde{M}_1 \tilde{M}_2 + \tilde{N}_1 \tilde{N}_2 &= \cos(\tilde{A}) \end{aligned} \quad (2.7)$$

where $\tilde{A}=\alpha+\omega \cdot a$, α -twist angle between axes of two screws, a - short distance between screw axes, $\cos(\tilde{A})=\cos(\alpha)-\omega \cdot a \sin(\alpha)$

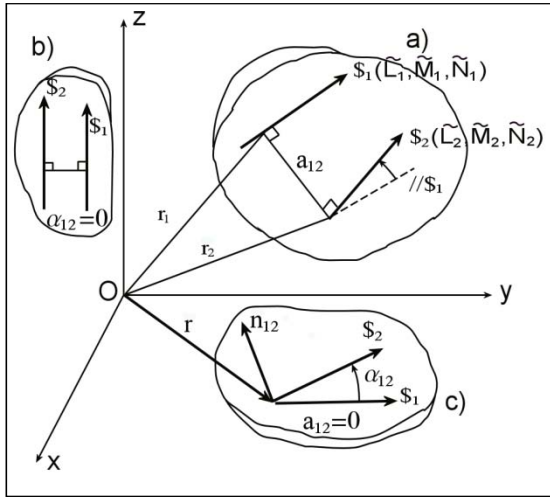


Fig. 4. Displacement of rigid body

Eqs.(2.7) can be introduce as:

$$\begin{aligned} l_1^2 + m_1^2 + n_1^2 + 2\omega(l_1 P_1 + m_1 Q_1 + n_1 R_1) &= 1 + \omega \cdot 0 \\ l_2^2 + m_2^2 + n_2^2 + 2\omega(l_2 P_2 + m_2 Q_2 + n_2 R_2) &= 1 + \omega \cdot 0 \\ l_1 l_2 + m_1 m_2 + n_1 n_2 + \omega(l_2 P_1 + l_1 P_2 + m_2 Q_1 + m_1 Q_2 \\ + n_1 R_2 + n_2 R_1) &= \text{Cos}(\alpha_{12}) - \omega a_{12} \text{Sin}(\alpha_{12}) \end{aligned} \quad (2.8)$$

Eq.(2.8) gives following six equations

$$\begin{aligned} s_1 \cdot s_1 &= 1, s_1 \cdot u_1 = 0, s_2 \cdot s_2 = 1, s_2 \cdot u_2 = 0 \\ s_1 \cdot s_2 &= \text{Cos}(\alpha_{12}), s_2 \cdot u_1 + s_1 \cdot u_2 = -a_{12} \text{Sin}(\alpha_{12}) \end{aligned} \quad (2.9)$$

The last equation in (2.9) is called mutual moment of two screws s_1 and s_2 . Mutual moment equals to zero when

- $\alpha_{12} = 0$, the axes of s_1 and s_2 are parallel (Fig. 4b)
- $a_{12} = 0$, the axes of s_1 and s_2 are intersecting (Fig. 4c)

We have six equation (2.9) that means from 12 Plücker parameters just six parameters are independent.

Let's consider the components of moments u_1 and u_2 of the two screws s_1 and s_2 that are arbitrary directed in a rigid body (Fig.4a). If given $r_i = [x_i, y_i, z_i]^T$,

$s_1 = [l_1, m_1, n_1]^T, r_2 = [x_2, y_2, z_2]^T, s_2 = [l_2, m_2, n_2]^T$, that Eq.(2.2) gives the displacement of a rigid body as:

$$\begin{aligned} \begin{bmatrix} P_1 \\ Q_1 \\ R_1 \end{bmatrix} &= \begin{bmatrix} 0 & n_1 & -m_1 \\ -n_1 & 0 & l_1 \\ m_1 & -l_1 & 0 \end{bmatrix} \begin{bmatrix} x_1 \\ y_1 \\ z_1 \end{bmatrix}, \begin{bmatrix} P_2 \\ Q_2 \\ R_2 \end{bmatrix} = \begin{bmatrix} 0 & n_2 & -m_2 \\ -n_2 & 0 & l_2 \\ m_2 & -l_2 & 0 \end{bmatrix} \begin{bmatrix} x_2 \\ y_2 \\ z_2 \end{bmatrix} \text{ or} \\ \begin{bmatrix} P_1 \\ Q_1 \\ R_1 \end{bmatrix} &= \begin{bmatrix} 0 & z_1 & -y_1 \\ -z_1 & 0 & x_1 \\ y_1 & -x_1 & 0 \end{bmatrix} \begin{bmatrix} l_1 \\ m_1 \\ n_1 \end{bmatrix}, \begin{bmatrix} P_2 \\ Q_2 \\ R_2 \end{bmatrix} = \begin{bmatrix} 0 & z_2 & -y_2 \\ -z_2 & 0 & x_2 \\ y_2 & -x_2 & 0 \end{bmatrix} \begin{bmatrix} l_2 \\ m_2 \\ n_2 \end{bmatrix} \end{aligned} \quad (2.10)$$

The position and orientation of the rigid body (Fig.4a) for the general case yields:

$$\begin{aligned} \begin{bmatrix} x_1 \\ y_1 \\ z_1 \end{bmatrix} &= \begin{bmatrix} 0 & n_1 & -m_1 \\ -n_1 & 0 & l_1 \\ m_1 & -l_1 & 0 \end{bmatrix}^{-1} \begin{bmatrix} P_1 \\ Q_1 \\ R_1 \end{bmatrix}, \begin{bmatrix} x_2 \\ y_2 \\ z_2 \end{bmatrix} = \begin{bmatrix} 0 & n_2 & -m_2 \\ -n_2 & 0 & l_2 \\ m_2 & -l_2 & 0 \end{bmatrix}^{-1} \begin{bmatrix} P_2 \\ Q_2 \\ R_2 \end{bmatrix} \text{ and} \\ \begin{bmatrix} l_1 \\ m_1 \\ n_1 \end{bmatrix} &= \begin{bmatrix} 0 & z_1 & -y_1 \\ -z_1 & 0 & x_1 \\ y_1 & -x_1 & 0 \end{bmatrix}^{-1} \begin{bmatrix} P_1 \\ Q_1 \\ R_1 \end{bmatrix}, \begin{bmatrix} l_2 \\ m_2 \\ n_2 \end{bmatrix} = \begin{bmatrix} 0 & z_2 & -y_2 \\ -z_2 & 0 & x_2 \\ y_2 & -x_2 & 0 \end{bmatrix}^{-1} \begin{bmatrix} P_2 \\ Q_2 \\ R_2 \end{bmatrix}, \end{aligned} \quad (2.11)$$

Controlling Eqs(2.9-2.11) the displacement (position and orientation) of the rigid body are described by six independent and six dependent parameters of the two arbitrary located unit screws with respect to the additional Eq.s (2.9)

- Considering two unit screws s_1 and s_2 (Fig.4b) that are parallel in space ($\alpha_{12} = 0, l = l_1 = l_2, m = m_1 = m_2, n = n_1 = n_2$) the number of additional Eq.s(2.9) yields:

$$\begin{aligned} l^2 + m^2 + n^2 &= 1 \\ lP_1 + mQ_1 + nR_1 &= 0 \\ lP_2 + mQ_2 + nR_2 &= 0 \end{aligned} \quad (2.12)$$

So the displacement of the rigid body are defined by the given parameters of two parallel unit screws (s, r_1, r_2):

$$\begin{aligned} \begin{bmatrix} P_1 \\ Q_1 \\ R_1 \end{bmatrix} &= \begin{bmatrix} 0 & n & -m \\ -n & 0 & l \\ m & -l & 0 \end{bmatrix} \begin{bmatrix} x_1 \\ y_1 \\ z_1 \end{bmatrix}, \begin{bmatrix} P_2 \\ Q_2 \\ R_2 \end{bmatrix} = \begin{bmatrix} 0 & n & -m \\ -n & 0 & l \\ m & -l & 0 \end{bmatrix} \begin{bmatrix} x_2 \\ y_2 \\ z_2 \end{bmatrix}, \text{ or} \\ \begin{bmatrix} P_1 \\ Q_1 \\ R_1 \end{bmatrix} &= \begin{bmatrix} 0 & -z_1 & y_1 \\ z_1 & 0 & -x_1 \\ -y_1 & x_1 & 0 \end{bmatrix} \begin{bmatrix} l \\ m \\ n \end{bmatrix}, \begin{bmatrix} P_2 \\ Q_2 \\ R_2 \end{bmatrix} = \begin{bmatrix} 0 & -z_2 & y_2 \\ z_2 & 0 & -x_2 \\ -y_2 & x_2 & 0 \end{bmatrix} \begin{bmatrix} l \\ m \\ n \end{bmatrix}, \end{aligned} \quad (2.13)$$

The position and orientation of the rigid body with two parallel unit screws gives:

$$\begin{aligned} \begin{bmatrix} x_1 \\ y_1 \\ z_1 \end{bmatrix} &= \begin{bmatrix} 0 & n & -m \\ -n & 0 & l \\ m & -l & 0 \end{bmatrix}^{-1} \begin{bmatrix} P_1 \\ Q_1 \\ R_1 \end{bmatrix}, \begin{bmatrix} x_2 \\ y_2 \\ z_2 \end{bmatrix} = \begin{bmatrix} 0 & n & -m \\ -n & 0 & l \\ m & -l & 0 \end{bmatrix}^{-1} \begin{bmatrix} P_2 \\ Q_2 \\ R_2 \end{bmatrix} \\ \begin{bmatrix} l \\ m \\ n \end{bmatrix} &= \begin{bmatrix} 0 & -z_1 & y_1 \\ z_1 & 0 & -x_1 \\ -y_1 & x_1 & 0 \end{bmatrix}^{-1} \begin{bmatrix} P_1 \\ Q_1 \\ R_1 \end{bmatrix} \end{aligned} \quad (2.14)$$

The position and orientation of the rigid body with respect to the given two parallel unit screws (Eqs(2.12-2.14)) are defined by six independent and three dependent parameters respect to Eq.s(2.12).

- In the case when two unit screws s_1 and s_2 (Fig.4c)



are intersected in space ($a_{i2} = 0, x=x_1=x_2, y=y_1=y_2, z=z_1=z_2$) the displacement of the rigid body can be described by six independent and three dependent parameters s, r, r_2 bearing in mind the three additional conditions $s_1 \cdot s_1 = 1, s_2 \cdot s_2 = 1, s_1 \cdot s_2 = \cos(\alpha_{12})$:

$$\begin{bmatrix} P_1 \\ Q_1 \\ R_1 \end{bmatrix} = \begin{bmatrix} 0 & n_1 & -m_1 \\ -n_1 & 0 & l_1 \\ m_1 & -l_1 & 0 \end{bmatrix} \begin{bmatrix} x \\ y \\ z \end{bmatrix}, \quad \begin{bmatrix} P_2 \\ Q_2 \\ R_2 \end{bmatrix} = \begin{bmatrix} 0 & n_2 & -m_2 \\ -n_2 & 0 & l_2 \\ m_2 & -l_2 & 0 \end{bmatrix} \begin{bmatrix} x \\ y \\ z \end{bmatrix} \quad (2.15)$$

In order to find the position of the rigid body $r(x,y,z)$, sufficient equation groups from displacement Eq.s(2.15) can be used, such as $[P_2 \ Q_1 \ R_1]^T, [P_1 \ Q_2 \ R_1]^T$ and $[P_1 \ Q_1 \ R_2]^T$. After solving the mentioned equation groups the three coordinates of the position of the rigid body can be introduced as,

$$\begin{aligned} x &= (m_2 Q_1 + n_2 R_1 + l_1 P_2) l_{12}^{-1} & x &= (l_1 Q_2 - l_2 Q_1) m_{12}^{-1} \\ y &= (m_1 P_2 - m_2 P_1) l_{12}^{-1} & y &= (l_2 P_1 + m_1 Q_2 + n_2 R_1) m_{12}^{-1} \\ z &= (n_1 P_2 + n_2 P_1) l_{12}^{-1} & z &= (n_1 Q_2 - n_2 Q_1) m_{12}^{-1} \\ x &= (l_1 R_2 - l_2 R_1) n_{12}^{-1} & l_{12} &= \begin{vmatrix} m_1 & n_1 \\ m_2 & n_2 \end{vmatrix}, m_{12} = \begin{vmatrix} n_1 & l_1 \\ n_2 & l_2 \end{vmatrix} \\ y &= (m_1 R_2 - m_2 R_1) n_{12}^{-1} & n_{12} &= \begin{vmatrix} l_1 & m_1 \\ l_2 & m_2 \end{vmatrix} \\ z &= (l_2 P_1 + m_2 Q_1 + n_1 R_2) m_{12}^{-1} \end{aligned} \quad (2.16)$$

where in Eq.s(2.16) l_{12}, m_{12}, n_{12} are the projections of normal vector $s_1 \times s_2 = n_{12}$ onto axes of system coordinates.

2.3. Displacement of Three Screws in Space

Let's consider three unit screws in space $\$, \$_j$ and $\$_k$ (Fig.5). In order to form the algorithm to find the dual coordinates of the third screw $\$_k(\tilde{L}_k, \tilde{M}_k, \tilde{N}_k)$ with respect to the known dual coordinates of unit screws $\$_i(\tilde{L}_i, \tilde{M}_i, \tilde{N}_i)$ and $\$_j(\tilde{L}_j, \tilde{M}_j, \tilde{N}_j)$ that is directed along the short distance between $\$_i$ and $\$_k$.

It is clear from Fig.5 that two unit screw pairs $\$, \$_j$ and $\$, \$_k$ are orthogonal unit screws $\alpha_{ij} = \alpha_{jk} = \pi/2, a_{ij} = a_{jk} = 0$. So, the position and orientation of unit screw $\$_k$, with respect to $\$_i$ can be described by two independent parameters a_{ik} and α_{ik} .

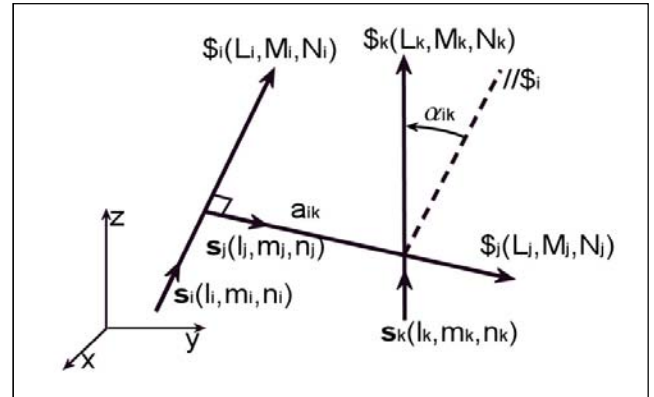


Fig.5 Displacement of three screws in space

Firstly we have to consider the task for the system of unit vectors s as the real path of unit screw $\$$. We have to describe the orientation of any rigid body $\$_k$ by given coordinates of unit vectors $\$_j$ and $\$_i$.

2.4. Transformation Unit Vector Matrix Equation.

The transformation unit vector equations are described by link ($a_j = a_{ik}, \alpha_j = \alpha_{ik}$) and kinematic pair ($d_j = a_{ik}, \theta_j = \alpha_{ik}$) parameters (Fig.6). Note that transformation unit vectors are the unit vectors, where their directions are intersected by one another in series. The unit vector equations are derived to find the direction of the third unit vector s_k with respect to any reference frame by given the directions of two unit vectors s_i and s_j in the same reference frame.

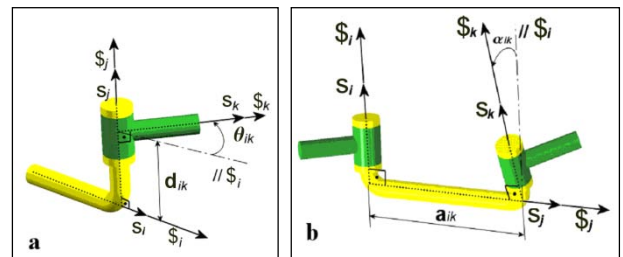


Fig.6. Joint and link parameters

As shown in Fig.6 three independent unit vectors $s_i(l_i, m_i, n_i)$, $s_j(l_j, m_j, n_j)$ and $s_k(l_k, m_k, n_k)$ describe the joint and link parameters. Note that, for revolute pair parameters α_{ik} is variable while a_{ik} is constant, on the other hand for prismatic pair, while parameters α_{ik} is constant a_{ik} is variable (Fig.6a)

First we will describe the vector equations of the three



unit vectors as

$$\mathbf{s}_i \times \mathbf{s}_k = \mathbf{s}_j \sin(\alpha_{ik}), \mathbf{s}_i \cdot \mathbf{s}_k = \cos(\alpha_{ik}), \mathbf{s}_j \cdot \mathbf{s}_k = 0 \quad (2.17)$$

The first Eq.(2.17) can be introduced in matrix form:

$$\begin{bmatrix} l_j \\ m_j \\ n_j \end{bmatrix} \sin(\alpha_{ik}) = \begin{bmatrix} 0 & -n_i & m_i \\ n_i & 0 & -l_i \\ -m_i & l_i & 0 \end{bmatrix} \begin{bmatrix} l_k \\ m_k \\ n_k \end{bmatrix} \text{ or } \mathbf{s}_j \sin(\alpha_{ik}) = \mathbf{A} \mathbf{s}_k \quad (2.18)$$

If both sides of the Eq.(2.18) are multiplied by \mathbf{s}_j^T , the result will be :

$$\mathbf{s}_j^T \mathbf{s}_j \sin(\alpha_{ik}) = \mathbf{s}_j^T \mathbf{A} \mathbf{s}_k \text{ or } \sin(\alpha_{ik}) = \mathbf{s}_{ij} \cdot \mathbf{s}_k \quad (2.19)$$

where $\mathbf{s}_j^T \mathbf{s}_j = 1$, $\mathbf{s}_{ij} = \mathbf{s}_j^T \mathbf{A}$, $\mathbf{s}_{ij} = [l_{ij}, m_{ij}, n_{ij}]^T$ and

$$l_{ij} = \begin{vmatrix} m_i & n_i \\ m_j & n_j \end{vmatrix}, m_{ij} = \begin{vmatrix} n_i & l_i \\ n_j & l_j \end{vmatrix}, n_{ij} = \begin{vmatrix} l_i & m_i \\ l_j & m_j \end{vmatrix}$$

Using Eq.(2.19), the system of Eq.(2.17) can be written in the following form,

$$\mathbf{s}_{ij} \cdot \mathbf{s}_k = \sin(\alpha_{ik}), \mathbf{s}_i \cdot \mathbf{s}_k = \cos(\alpha_{ik}), \mathbf{s}_j \cdot \mathbf{s}_k = 0 \quad (2.20)$$

Solution of the system of Eq.s(2.20) gives the transformation unit vector matrix equation as:

$$\begin{bmatrix} l_k \\ m_k \\ n_k \end{bmatrix} = \begin{bmatrix} l_i & l_{ij} & l_j \\ m_i & m_{ij} & m_j \\ n_i & n_{ij} & n_j \end{bmatrix} \begin{bmatrix} \cos(\alpha_{ik}) \\ \sin(\alpha_{ik}) \\ 0 \end{bmatrix} \text{ or } \mathbf{s}_k = \mathbf{B}_{3 \times 3} \mathbf{a}_{3 \times 1} \quad (2.21)$$

Transformation unit vector matrix Eq.(2.21) can be used to describe an orientation of a rigid body with respect to the reference frame. The orientation of one unit vector of any rigid body with respect to the previous frames can be presented by using Eq.(2.20) in another matrix form as follow:

$$\begin{bmatrix} l_k \\ m_k \\ n_k \end{bmatrix} = \begin{bmatrix} C\alpha_{ik} & S\alpha_{ik} & 0 & 0 & 0 & 0 \\ 0 & 0 & C\alpha_{ik} & S\alpha_{ik} & 0 & 0 \\ 0 & 0 & 0 & 0 & C\alpha_{ik} & S\alpha_{ik} \end{bmatrix} \begin{bmatrix} l_i \\ l_{ij} \\ m_i \\ m_{ij} \\ n_i \\ n_{ij} \end{bmatrix} \text{ or} \quad (2.22)$$

$$\mathbf{s}_k = \mathbf{C}_{3 \times 6} \mathbf{e}_{6 \times 1}$$

So we have two form of transformation unit vector matrices Eqs.(2.21) and (2.22). So, orientation of rigid body can be described by two unit vectors $\mathbf{s}_j, \mathbf{s}_k$ and the

conditions $\mathbf{s}_j \cdot \mathbf{s}_k = \cos(\alpha_{ik}), \mathbf{s}_j \cdot \mathbf{s}_j = 1, \mathbf{s}_k \cdot \mathbf{s}_k = 1$.

2.5. Design of Novel Overconstrained RRRS Linkage with Linear and Angular Constraints.

In the path of a new design of the current design, linear and angular constraints have been created by using transformation unit vector approach for creating loop closure equation for the new RRRS linkage shown in Fig.7 The hinges 1,2, and 3 with arbitrary directions $\mathbf{s}_2, \mathbf{s}_4$ and \mathbf{s}_6 are described by joint parameters $\{\alpha_{13}, \alpha_{13}\}, \{\alpha_{35}, \alpha_{35}\}$ and $\{\alpha_{57}, \alpha_{57}\}$, so that remaining link parameters will be $\{\alpha_{24}, \alpha_{24}\}, \{\alpha_{46}, \alpha_{46}\}$ and a_{68} .

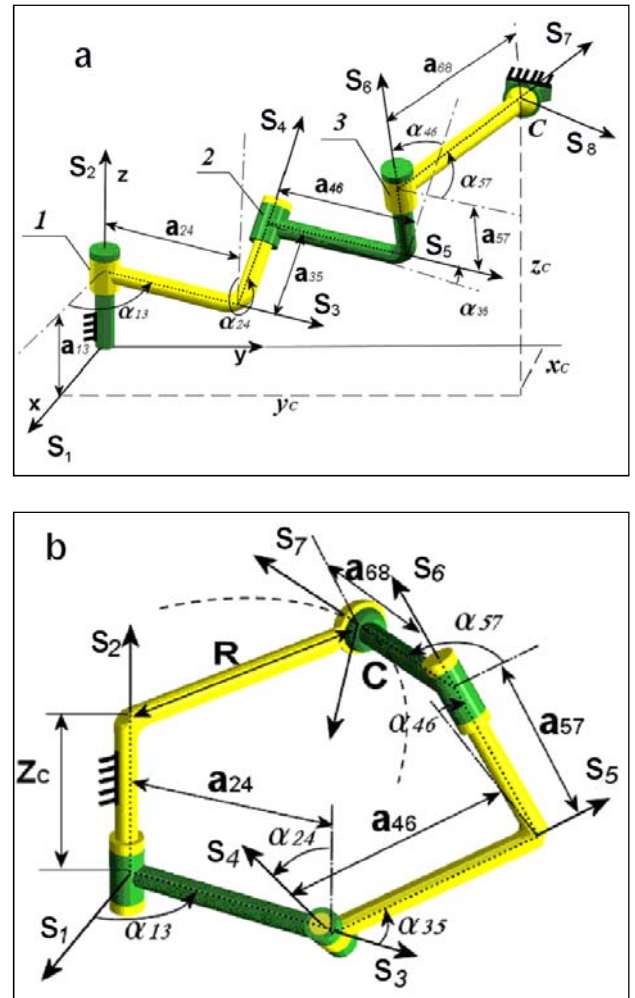


Fig.7. Novel overconstraint RRRS linkage

Note that, the spherical joint S and the first revolute joint



are connected to the fixed frame, parameters α_{13} , α_{35} and α_{57} are variable and remaining parameters are constant. As shown in Fig.7a the vector loop closure equation for the mentioned overconstrained mechanism can be written as follows:

$$\sum_{i=2}^7 \mathbf{s}_i \mathbf{a}_{i-1,i+1} = \mathbf{r}_C \quad (2.23)$$

where; $\mathbf{r}_C = [x_C, y_C, z_C]^T$, $\mathbf{s}_i = [l_i, m_i, n_i]^T$

The vector $\{\mathbf{s}_i\}_3^7$ can be calculated by using transformation unit vector matrix Eq.(2.21) or Eq.(2.22) with given vectors $\mathbf{s}_1 = [1, 0, 0]^T$ and $\mathbf{s}_2 = [0, 0, 1]^T$ as below.

$$\begin{bmatrix} l_3 \\ m_3 \\ n_3 \end{bmatrix} = \begin{bmatrix} C_{13} \\ S_{13} \\ 0 \end{bmatrix}, \begin{bmatrix} l_4 \\ m_4 \\ n_4 \end{bmatrix} = \begin{bmatrix} S_{13}S_{24} \\ -C_{13}S_{24} \\ C_{24} \end{bmatrix}, \begin{bmatrix} l_5 \\ m_5 \\ n_5 \end{bmatrix} = \begin{bmatrix} C_{13}C_{35} - C_{24}S_{13}S_{35} \\ S_{13}C_{35} + C_{24}C_{13}S_{35} \\ S_{24}S_{35} \end{bmatrix} \\ \begin{bmatrix} l_6 \\ m_6 \\ n_6 \end{bmatrix} = \begin{bmatrix} C_{46}S_{13}S_{24} + (C_{24}S_{13}C_{35} + C_{13}S_{35})S_{46} \\ S_{35}S_{13}S_{46} - (C_{24}S_{46}C_{35} + C_{46}S_{24})C_{13} \\ C_{24}C_{46} - C_{35}S_{24}S_{46} \end{bmatrix} \quad (2.24) \\ \begin{bmatrix} l_7 \\ m_7 \\ n_7 \end{bmatrix} = \begin{bmatrix} C_{13}(C_{35}C_{57} - C_{46}S_{35}S_{57}) - S_{13}(-S_{24}S_{46}S_{57} + C_{24}(C_{57}S_{35} + C_{35}C_{46}S_{57})) \\ C_{57}(C_{35}S_{13} + C_{13}C_{24}S_{35}) + S_{57}(-C_{46}S_{13}S_{35} + C_{13}(C_{35}C_{46}C_{24} - S_{24}S_{46})) \\ C_{57}S_{24}S_{35} + S_{57}(C_{35}S_{24}C_{46} + C_{24}S_{46}) \end{bmatrix}$$

where C_{ik} and S_{ik} represent the cosine and sine of the angle α_{ik} respectively.

Substitution of the elements of the unit vector values from Eq.s(2.24) into Eq(2.23) yields,

$$\begin{aligned} a_{57}C_{46} + a_{68}S_{46}S_{57} &= pC_{24} + K_1S_{24} - a_{35} \\ (a_{46} + a_{68}C_{57})S_{35} - (a_{57}S_{46} - a_{68}C_{46}S_{57})C_{35} &= pS_{24} - K_1C_{24} \\ (a_{46} + a_{68}C_{57})C_{35} + (a_{57}S_{46} - a_{68}C_{46}S_{57})S_{35} &= K_2 - a_{24} \end{aligned} \quad (2.25)$$

where,

$$p = z_C - a_{13}, \quad K_1 = x_C S_{13} - y_C C_{13}, \quad K_2 = y_C S_{13} + x_C C_{13}$$

We may consider S_{ik} and C_{ik} as two independent variables and add following trigonometric identities as supplementary equations of constraint,

$$S_{35}^2 + C_{35}^2 = 1, \quad S_{57}^2 + C_{57}^2 = 1, \quad K_1^2 + K_2^2 = x_C^2 + y_C^2 \quad (2.26)$$

The problem is to eliminate the following variable parameters α_{13} , α_{35} and α_{57} .

After summing the squares of Eq.s(2.25) by taking into account Eq.s(2.26), we obtain the following equation.

$$2a_{46}a_{68}C_{57} = x_C^2 + y_C^2 + p^2 + a_{24}^2 + a_{35}^2 - a_{46}^2 - a_{57}^2 - a_{68}^2 - 2pa_{35}C_{24} - 2K_1a_{35}S_{24} - 2K_2a_{24} \quad (2.27)$$

So, we have eliminated unknowns S_{35} and C_{35} (unknown variable parameter α_{35}). Now, the combination of Eq.(2.27) and the first equation of system Eq.(2.25) gives two equations respect to two unknowns α_{57} and α_{13} :

$$2a_{46}a_{68}C_{57} = p_1 - 2K_1a_{35}S_{24} - 2K_2a_{24} \quad (2.28)$$

$$a_{68}S_{46}S_{57} = q + K_1S_{24}$$

where, $p_1 = x_C^2 + y_C^2 + p^2 + a_{24}^2 + a_{35}^2 - a_{46}^2 - a_{57}^2 - a_{68}^2 - 2pa_{35}C_{24}$
 $q = pC_{24} - a_{57}C_{46} - a_{35}$

Now we have to eliminate variable parameter α_{57} . Multiplying the first equation by S_{46} and the second equation by $2a_{46}$ (Eq.s(2.28)) and summing the squares of both equations we can reach the following overconstraint equation with respect to the variable parameter α_{13} :

$$4a_{46}^2a_{68}^2S_{46}^2 = 4a_{46}^2(q + K_1S_{24})^2 + S_{46}^2(p_1 - 2K_1a_{35}S_{24} - 2K_2a_{24})^2 \quad (2.29)$$

Arranging the overconstraint Eq.(2.29), the following polynomial equation can be constructed as,

$$A K_1^2 + BK_1 + CK_2 + DK_1K_2 + E = 0 \quad (2.30)$$

where,

$$A = 4a_{46}^2S_{24}^2 + 4a_{35}^2S_{24}^2S_{46}^2 - 4a_{24}^2S_{46}^2,$$

$$B = 8qa_{46}^2S_{24} - 4p_1a_{35}S_{24}S_{46}^2, \quad C = -4p_1a_{24}S_{46}^2,$$

$$D = 8a_{24}a_{35}S_{24}S_{46}^2$$

$$E = 4q^2a_{46}^2 + p_1^2S_{46}^2 - 4a_{46}^2a_{68}^2S_{46}^2 + 4(x_C^2 + y_C^2)a_{24}^2S_{46}^2$$

$$K_1 = x_C S_{13} - y_C C_{13}, \quad K_2 = x_C C_{13} + y_C S_{13}$$

In the case of mobile mechanism, the functions $K_1 = f(\alpha_{13})$ and $K_2 = f(\alpha_{13})$ are not constant thus coefficients of the polynomial Eq.(2.30) must be equal to zero ($A=B=C=D=E=0$)

So, the condition of mobility one of the structural group RRRS will be the following mathematical expressions

$$D=0 \Rightarrow a_{35}=0, \quad C=0 \Rightarrow p_1=0, \quad B=0 \Rightarrow pC_{24} = a_{57}C_{46}, \quad (2.31)$$

$$A=0 \Rightarrow a_{46}S_{24} = a_{24}S_{46}, \quad E=0 \Rightarrow a_{24}^2(x_C^2 + y_C^2) = a_{46}^2a_{68}^2$$

Using the expression of parameters p , p_1 and q in Eq.(2.31) we can illustrate the following five constraint equations for kinematic parameters of RRRS mechanism



$$\begin{aligned} a_{35} &= 0, a_{46} = a_{24} S_{46} S_{24}^{-1}, z_c = a_{13} + a_{56} C_{46} C_{24}^{-1} \\ x_c^2 + y_c^2 &= -(z_c - a_{13})^2 - a_{24}^2 + a_{46}^2 + a_{57}^2 + a_{68}^2 \\ x_c^2 + y_c^2 &= a_{68}^2 a_{46}^2 a_{24}^{-1} = a_{68}^2 S_{46}^2 S_{24}^{-1} \end{aligned} \quad (2.32)$$

Substituting the value of a_{46} and $z_c - a_{13}$ to the fourth equation of system Eq.s(2.32) yields:

$$a_{68}^2 (S_{46}^2 S_{24}^{-2} - 1) + a_{57}^2 C_{46}^2 C_{24}^{-2} - a_{24}^2 S_{46}^2 S_{24}^{-2} + a_{24}^2 - a_{57}^2 = 0 \quad (2.33)$$

After some identical transformation of Eq.(2.33) we can get the value of parameter $a_{68} = (a_{24}^2 + a_{57}^2 \tan^2(\alpha_{24}))^{0.5}$

As a result we will get the following linear and angular conditions for the overconstraint mechanism RRRS with mobility $M=1$ (Fig.7b)

$$\begin{aligned} a_{35} &= 0, a_{46} = a_{24} S_{46} S_{24}^{-1}, a_{68} = (a_{24}^2 + a_{57}^2 \tan^2(\alpha_{24}))^{0.5} \\ z_c &= a_{13} + a_{57} C_{46} C_{24}^{-1}, x_c + y_c = a_{46}^2 a_{68}^2 a_{24}^{-2} \end{aligned} \quad (2.34)$$

The system of Eq.s(2.34) are equation of circle in space with the center $(0,0,z_c)$ and radius $r = a_{46}^2 a_{68}^2 a_{24}^{-2}$. So for mechanism RRRS with mobility $M=1$ the Eq.s(2.31) gives us the linear and angular constraints as $a_{35}, a_{46}, a_{68}, \alpha_{24}, \alpha_{46}$ and the coordinates of spherical joint.

Example: let $\alpha_{24}, \alpha_{46} = 45^\circ$ and $a_{13} = 0$ then we obtain spatial RRRS mechanism with one input link (Fig.7b) with linear and angular constraint.

$$a_{35} = 0, a_{13} = 0, a_{46} = a_{24}, a_{68} = (a_{24}^2 + a_{57}^2)^{0.5}, z_c = a_{57}, r = a_{68}$$

2.6. Transformation unit screw matrix equation.

Using the transferring principle of Kotelnikov-Shtudi which state that all formulas of vector algebra can be used in screw algebra formulations if and only if the values should be interpreted in dual form. In Eq.s(2.21) and (2.22) the unit screw $\$_k$ with respect to the known dual coordinates of unit screw $\$_i$ and $\$_j$, can be represented as $\$_k(\tilde{L}_k, \tilde{M}_k, \tilde{N}_k)$, $\$_i(\tilde{L}_i, \tilde{M}_i, \tilde{N}_i)$, $\$_j(\tilde{L}_j, \tilde{M}_j, \tilde{N}_j)$. Also the angles between the unit screws $\$_i$ and $\$_k$ in the form as $A_{ik} = \alpha_{ik} + \omega a_{ik}$ where, α_{ik} is the angle between the screw axes and a_{ik} is the short distance between corresponding screw axes (Fig6b) respectively. If the trigonometric operations are to be carried out in the dual angle, following formulas should be used.

$$\begin{aligned} \sin(A_{ik}) &= \sin(\alpha_{ik}) + \omega a_{ik} \cos(\alpha_{ik}) \\ \cos(A_{ik}) &= \cos(\alpha_{ik}) - \omega a_{ik} \sin(\alpha_{ik}) \end{aligned} \quad (2.35)$$

So, Eq.s(2.21) and (2.22) can be indicated in dual form as.

$$\begin{bmatrix} \tilde{L}_k \\ \tilde{M}_k \\ \tilde{N}_k \end{bmatrix} = \begin{bmatrix} \tilde{L}_i & \tilde{L}_{ij} & \tilde{L}_j \\ \tilde{M}_i & \tilde{M}_{ij} & \tilde{M}_j \\ \tilde{N}_i & \tilde{N}_{ij} & \tilde{N}_j \end{bmatrix} \begin{bmatrix} \cos(A_{ik}) \\ \sin(A_{ik}) \\ 0 \end{bmatrix} \text{ or} \\ \$_k = \tilde{B}\tilde{A} \quad (2.36)$$

and

$$\begin{bmatrix} \tilde{L}_k \\ \tilde{M}_k \\ \tilde{N}_k \end{bmatrix} = \begin{bmatrix} CA_{ik} & SA_{ik} & 0 & 0 & 0 & 0 \\ 0 & 0 & CA_{ik} & SA_{ik} & 0 & 0 \\ 0 & 0 & 0 & 0 & CA_{ik} & SA_{ik} \end{bmatrix} \begin{bmatrix} \tilde{L}_i \\ \tilde{L}_{ij} \\ \tilde{M}_i \\ \tilde{M}_{ij} \\ \tilde{N}_i \\ \tilde{N}_{ij} \end{bmatrix} \text{ or} \\ \$_k = \tilde{C}\tilde{E} \quad (2.37)$$

where

$$\begin{aligned} \begin{bmatrix} \tilde{L}_k \\ \tilde{M}_k \\ \tilde{N}_k \end{bmatrix} &= \begin{bmatrix} l_k \\ m_k \\ n_k \end{bmatrix} + \omega \begin{bmatrix} P_k \\ Q_k \\ R_k \end{bmatrix}, \begin{bmatrix} \tilde{L}_i \\ \tilde{M}_i \\ \tilde{N}_i \end{bmatrix} = \begin{bmatrix} l_i \\ m_i \\ n_i \end{bmatrix} + \omega \begin{bmatrix} P_i \\ Q_i \\ R_i \end{bmatrix}, \\ \begin{bmatrix} \tilde{L}_j \\ \tilde{M}_j \\ \tilde{N}_j \end{bmatrix} &= \begin{bmatrix} l_j \\ m_j \\ n_j \end{bmatrix} + \omega \begin{bmatrix} P_j \\ Q_j \\ R_j \end{bmatrix}, \tilde{L}_{ij} = \begin{vmatrix} \tilde{N}_i & \tilde{M}_i \\ \tilde{N}_j & \tilde{M}_j \end{vmatrix}, \tilde{M}_{ij} = \begin{vmatrix} \tilde{L}_i & \tilde{N}_i \\ \tilde{L}_j & \tilde{N}_j \end{vmatrix}, \\ \tilde{N}_{ij} &= \begin{vmatrix} \tilde{M}_i & \tilde{L}_i \\ \tilde{M}_j & \tilde{L}_j \end{vmatrix}, P_{ij} = \begin{vmatrix} n_i & Q_i \\ n_j & Q_j \end{vmatrix} - \begin{vmatrix} m_i & R_i \\ m_j & R_j \end{vmatrix}, Q_{ij} = \begin{vmatrix} l_i & R_i \\ l_j & R_j \end{vmatrix} - \begin{vmatrix} n_i & P_i \\ n_j & P_j \end{vmatrix}, \\ R_{ij} &= \begin{vmatrix} m_i & P_i \\ m_j & P_j \end{vmatrix} - \begin{vmatrix} l_i & Q_i \\ l_j & Q_j \end{vmatrix}. \end{aligned}$$

Using the rules of screw algebra Eq.s(2.35) and (2.37) after some arrangements in the elements, the transformation unit screw matrix equations with real Plücker coordinates can be represented as follows respectively:

$$\$_k = \tilde{B}\tilde{a} \quad (2.38)$$

where $\$_k = [l_k, m_k, n_k, P_k, Q_k, R_k]^T$
 $\tilde{a}_k = [\cos(\alpha_{ik}), \sin(\alpha_{ik}), -a_{ik} \sin(\alpha_{ik}), a_{ik} \cos(\alpha_{ik}), 0, 0]^T$

$$\tilde{B} = \begin{bmatrix} l_i & l_{ij} & 0 & 0 & 0 & 0 \\ m_i & m_{ij} & 0 & 0 & 0 & 0 \\ n_i & n_{ij} & 0 & 0 & 0 & 0 \\ P_i & P_{ij} & l_i & l_{ij} & 0 & 0 \\ Q_i & Q_{ij} & m_i & m_{ij} & 0 & 0 \\ R_i & R_{ij} & n_i & n_{ij} & 0 & 0 \end{bmatrix} \text{ and} \\ \$_k = \tilde{C}\tilde{E} \quad (2.39)$$

where

$$\tilde{E} = [l_i, l_{ij}, m_i, m_{ij}, n_i, n_{ij}, P_i, P_{ij}, Q_i, Q_{ij}, R_i, R_{ij}]$$



$$\tilde{C} = \begin{bmatrix} C\alpha_{ik} & S\alpha_{ik} & 0 & 0 & 0 & 0 & 0 & 0 & 0 & 0 & 0 & 0 \\ 0 & 0 & C\alpha_{ik} & S\alpha_{ik} & 0 & 0 & 0 & 0 & 0 & 0 & 0 & 0 \\ 0 & 0 & 0 & 0 & C\alpha_{ik} & S\alpha_{ik} & 0 & 0 & 0 & 0 & 0 & 0 \\ -a_{ik}S\alpha_{ik} & a_{ik}C\alpha_{ik} & 0 & 0 & 0 & 0 & C\alpha_{ik} & S\alpha_{ik} & 0 & 0 & 0 & 0 \\ 0 & 0 & -a_{ik}S\alpha_{ik} & a_{ik}C\alpha_{ik} & 0 & 0 & 0 & 0 & C\alpha_{ik} & S\alpha_{ik} & 0 & 0 \\ 0 & 0 & 0 & 0 & -a_{ik}S\alpha_{ik} & a_{ik}C\alpha_{ik} & 0 & 0 & 0 & 0 & C\alpha_{ik} & S\alpha_{ik} \end{bmatrix}$$

As it is shown above each unit screw is determined by six Plücker coordinates, and only four of them are independent as $\mathbf{s} \bullet \mathbf{s} = 1$ and $\mathbf{s} \bullet \mathbf{u} = 0$. So that the displacement of the rigid body in space can be defined by using six independent parameters as $l_k, m_k, P_k, Q_k, a_{ik}, \alpha_{ik}$ or other combinations with respect to the transformation unit screw matrix Eq.s (2.38) and (2.39).

3. General Constraint of Active Motion of a Rigid Body.

If all the joints in a robot- manipulator are described by unit screws we will create a screw system $\{\$ _j\}_1^n$. The general constraint d of a mechanical system is taken to be the difference between six and the dimension of active motion (λ) of an unpaired link of the mechanism in the space (spatial, subspaces: plane, cylindrical, spherical and others) in which the mechanism is assumed to operate. The dimension of active motion of rigid body λ is the number of independent, scalar loop-closure equations associated with i th independent loop. The total number of independent, scalar, displacement variables is determined by the rank of the coefficient matrix of the differential loop-closure equations. In the general case this is equal to the total number of screws permitted at each joint.

The dimension of active motion of a rigid body λ is equal to the rank of matrix of the screw system and the mutual moments is not zero:

$$\$_j \circ \$_i = -(\mu_j + \mu_i) \cos(\alpha_{ji}) - r_{ji} \sin(\alpha_{ji}) \quad (3.1)$$

$j=1,2,\dots,n$ and $i=1,2,\dots,6$

Let $A = \begin{bmatrix} a_{11} & \dots & a_{16} \\ \vdots & \ddots & \vdots \\ a_{n1} & \dots & a_{n6} \end{bmatrix}$ is matrix of Eq.(3.1) with n row

and 6 column. The rank of matrix A is called the maximum number λ , that there is the sub matrix M of order λ in matrix A .

- Matrix $A = \begin{bmatrix} 0 & \dots & 0 \\ \vdots & \ddots & \vdots \\ 0 & \dots & 0 \end{bmatrix}$ with zero elements has rank $\lambda=0$

-Matrix $A = \begin{bmatrix} l_1 & m_1 & \dots & 0 \\ l_2 & m_2 & \dots & \vdots \\ \vdots & \vdots & \ddots & \vdots \\ 0 & \dots & 0 & 0 \end{bmatrix}$ has rank $\lambda=1$ if elements of

two any row and two any column are proportional.

The maximum number $\lambda=6$ is equal to the maximum number of independent parameters of screw $\$ = [l, m, P, Q, R, \mu]^T$. So, the maximum number of linear independent row of matrix equal to the maximum number of linear independent column. If rank of matrix equal to λ , there should be a minor with $\det M \neq 0$.

The standard base of the screw system with $\lambda=6$ is $3\$ _0 3\$ _\infty$ that describe three translational and three rotational active motions with respect to xyz axis respectively. Another example about basis of screw system with $\lambda=5$ are $3\$ _0 2\$ _\infty$ and $2\$ _0 3\$ _\infty$ that describe three translational and two rotational or two translational and three rotational active motion of an unpaired link of the mechanism in subspace with respect to xyz axis respectively. But, if there are screws in the screw system whose mutual moments equal to zero that means there exists linear dependent screws.

Then, the general constraint is the difference between the dimension of active motion of a rigid body in space and the rank of screw system:

$$d=6-\lambda \text{ or } \lambda=6-d \quad (3.2)$$

So, the term "general constraint" of a mechanism refers to the difference between the degree of freedom of a link moving freely in space and the dimension of active motion of subspace in which the link is actually move, (Eq 3.2).

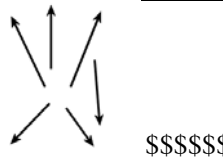
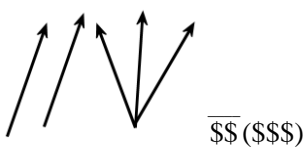
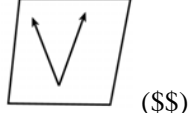
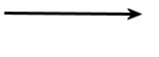
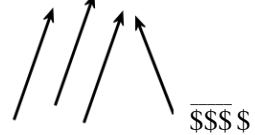
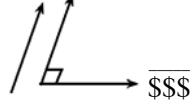
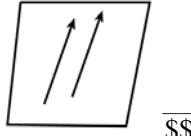
4. Operation on Screw Systems

4.1. Sub Screw Systems

Sub screw systems of an $\$_n$ screw system are linear combination of λ basis screw systems:
 $0 \leq \lambda \leq 6$, λ is the dimension of active motion



Table 4.1. Geometry of basis of screw systems

λ	Basis of screw system	Geometry and simple structural group bonding by sub screw system	Comments
6	$3\$_{\infty}3\$_0$		If the directions of all $\$$ screws are linear dependent of basis $3\$_{\infty}3\$_0$.
Case 1			
5	$2\$_{\infty}3\$_0$		If the directions of all screws $\$$ parallel to the plane $2\$_{\infty}$ or belong to the $3\$_0$ system.
4	$1\$_{\infty}3\$_0$		If the all screws $\$$ belong to the $1\$_{\infty}3\$_0$ system respectively.
3	$3\$_0$		If the directions of all screws $\$_0$ intersect at a common point and noncoplanar.
2	$2\$_0$		If the directions of all $\$_0$ screws intersect at a common point and are coplanar.
1	$1\$_0$		If the directions of all screws $\$_0$ are directed along the same line.
Case 2			
5	$3\$_{\infty}2\$_0$		If the directions of all screws $\$$ are parallel to the line on the plane or directed to the center.
4	$3\$_{\infty}1\$_0$		If all screw system $\$$ are linear dependent of the basis $3\$_{\infty}1\$_0$ screw system.
3	$3\$_{\infty}$		If all screw system $\$$ are parallel to the orthogonal basis screw system $3\$_{\infty}$.
2	$2\$_{\infty}$		If the directions of all the $\$_{\infty}$ are parallel to same plane.
1	$\$_{\infty}$		If all the screws $\$_{\infty}$ are directed along the same direction



4.2. Linear Combination of Two Screw Systems

Linear combination of the two basis screw systems (the order of the new screw system is less or equal to the sum of the orders of the screw systems)

Table 4.2 Linear combination of basis screw systems

λ	Linear combination of screw system	Screw diagrams	Comments
1	A $1\$_0$ screw system $1\$_0 + 1\$_0 \Rightarrow 1\$_0$		If the directions of the $\$_0$ within the $1\$_0$ system are on the one line.
2	A $2\$_\infty$ screw system $2\$_\infty + 1\$_\infty \Rightarrow 2\$_\infty$		IF the directions of the $\$_\infty$ within the $1\$_\infty$ and the $\$_\infty$ within the $2\$_\infty$ system is parallel to the same plane.
3	A $3\$_\infty$ screw system $2\$_\infty + 1\$_\infty \Rightarrow 3\$_\infty$		IF the directions of the $\$_\infty$ within the $1\$_\infty$ system is not parallel to the directions of all $\$_\infty$ within the $2\$_\infty$ system.
4	A $3\$_0 1\$_\infty$ screw system $3\$_0 + 1\$_\infty 1\$_0 \Rightarrow 3\$_0 1\$_\infty$		If the directions of the $\$_\infty$ and $\$_0$ within the $1\$_0 1\$_\infty$ system are consistent to the direction of all $\$_0$ within the $\$'_{02}$ of the $3\$_0$ system.
5	A $3\$_0 2\$_\infty$ screw system $3\$_0 + 2\$_\infty \Rightarrow 3\$_0 2\$_\infty$		If the directions of $\$_\infty$ within the plane $2\$_\infty$ is parallel to one of the plane of all $\$_0$ within the $3\$_0$ system.
6	A $3\$_0 3\$_\infty$ screw system $3\$_0 + 3\$_\infty \Rightarrow 3\$_0 3\$_\infty$		If the directions of all $\$_0$ within the $3\$_0$ system and all the $\$_\infty$ within the $3\$_\infty$ system are equal to the sum of the order of the screw system.



4.3. Reciprocal Screws

A) Two screws $\$1$ and $\$2$ are called reciprocal if their mutual moment equal to zero $\$1 \circ \$2 = 0$. The screw operator “ \circ ” is defined as the reciprocal product of two screws.

Usually the mutual moment of two screws are

$$\$1 \circ \$2 = [\Pi \$1]^T \$2 = -r_1 \sin(\alpha) \quad (4.1)$$

$$\text{where } \Pi = \begin{bmatrix} O & I_3 \\ I_3 & O \end{bmatrix}_{6 \times 6}, I_3 = \begin{bmatrix} 1 & 0 & 0 \\ 0 & 1 & 0 \\ 0 & 0 & 1 \end{bmatrix}_{3 \times 3}, O = \begin{bmatrix} 0 & 0 & 0 \\ 0 & 0 & 0 \\ 0 & 0 & 0 \end{bmatrix}_{3 \times 3}$$

$$\$1 = [l_1, m_1, n_1, P_1 + \mu_1 l_1, Q_1 + \mu_1 m_1, R_1 + \mu_1 n_1]^T$$

$$\$2 = [l_2, m_2, n_2, P_2 + \mu_2 l_2, Q_2 + \mu_2 m_2, R_2 + \mu_2 n_2]^T$$

Using Eq.(4.1) the mutual moment of $\$1$ and $\$2$ screws yields

$$l_2 P_1 + m_2 Q_1 + n_2 R_1 + l_1 P_2 + m_1 Q_2 + n_1 R_2 = -(\mu_1 + \mu_2) \cos(\alpha_{12}) - r_{12} \sin(\alpha_{12}) \quad (4.2)$$

where r_{12} is the offset distance along the common perpendicular leading from screw $\$1$ to screw $\$2$; α_{12} is the angle between the axes of $\$1$ and $\$2$, measured from $\$1$ to $\$2$ about the common perpendicular according to the right-hand rule; μ_1 and μ_2 are pitch of the screw.

The reciprocity equation of two screws $\$1$ and $\$2$ comes from Eq.(4.2)

$$l_2 P_1 + m_2 Q_1 + n_2 R_1 + l_1 P_2 + m_1 Q_2 + n_1 R_2 = 0 \quad (4.3)$$

The reciprocity condition can be derived as:

No constraint if μ_1 and μ_2 are ∞

$\cos(\alpha_{12})=0, \alpha_{12}=90^\circ, \alpha_{12}=270^\circ$ if μ_1 or μ_2 is ∞

$-(\mu_1 + \mu_2) \cos(\alpha_{12}) - r_{12} \sin(\alpha_{12})=0$ if μ_1 and μ_2 are both finite

The reciprocity conditions of two screws gives:

- $2\$_\infty$ are always reciprocal to each other $\overline{\$ \$}$ (parallel to each other)

- A $1\$_\infty$ is reciprocal to a $1\$_0$ if and only if their axes are perpendicular to each other $\$ \perp \$$

- $2\$_0$ are reciprocal to each other if and only if their axes are coplanar ($\overline{\$ \$}$)

B) Two screws $\$1$ and $\$2$ are said to be reciprocal if the virtual work of a wrench $\$1 = \mathbf{W}$ acting on a twist $\$2 = \mathbf{T}$ is zero.

The work done by a wrench $\mathbf{W} = [\mathbf{F}, \mathbf{p} \times \mathbf{F} + \boldsymbol{\tau}]^T$ as it moves through a twist $\mathbf{T} = [\boldsymbol{\omega}, \mathbf{V} + \mathbf{q} \times \boldsymbol{\omega}]^T$ over a virtual time period δt is given by

$$\delta A = \mathbf{W}^T (\Pi \mathbf{T}) \delta t = [\mathbf{F}, \mathbf{p} \times \mathbf{F} + \boldsymbol{\tau}]^T \begin{bmatrix} O & I \\ I & O \end{bmatrix} \begin{bmatrix} \boldsymbol{\omega} \\ \mathbf{V} + \mathbf{q} \times \boldsymbol{\omega} \end{bmatrix} \delta t \text{ or}$$

$$\delta A = [\mathbf{F}, \mathbf{p} \times \mathbf{F} + \boldsymbol{\tau}] \begin{bmatrix} \mathbf{V} + \mathbf{q} \times \boldsymbol{\omega} \\ \boldsymbol{\omega} \end{bmatrix} \delta t = [\mathbf{F} \mathbf{V} + \boldsymbol{\tau} (\boldsymbol{\omega} - (\mathbf{p} - \mathbf{q}) (\boldsymbol{\omega} \times \mathbf{F}))] \delta t$$

The reciprocity conditions of two screws \mathbf{T} and \mathbf{W} is received if the virtual work δA of a wrench acting on a twist is zero,

$$\mathbf{F} \mathbf{V} + \boldsymbol{\tau} (\boldsymbol{\omega} - (\mathbf{p} - \mathbf{q}) (\boldsymbol{\omega} \times \mathbf{F})) = 0 \quad (4.4)$$

C) Reciprocal screw system. The reciprocal screw system of a given screw system can be obtained by using the reciprocity condition of screws.

-The reciprocal system of the $2\$_0$ system is still the $2\$_0$ screw system. The $\{\$0_1, \$0_2\}$ is the basis of screw system and the $\{\$0_1^r, \$0_2^r\}$ is reciprocal basis of the reciprocal system.

-The reciprocal system of a $3\$_0$ screw system is still a $3\$_0$ screw system. $3\$_0$ screw system is represented by a basis $\{\$0_1, \$0_2, \$0_3\}$ and its reciprocal screw system which is also a $3\$_0$ system is represented by a basis $\{\$0_1^r, \$0_2^r, \$0_3^r\}$.

-The reciprocal system of the $3\$_\infty$ system is still the $3\$_\infty$ system. the basis of $3\$_\infty$ system is $\{\$_\infty 1, \$_\infty 2, \$_\infty 3\}$ and the basis of reciprocal systems of $3\$_\infty$ system are $\{\$_{\infty 1}^r, \$_{\infty 2}^r, \$_{\infty 3}^r\}, \{\$_{\infty 1}^r, \$_{\infty 2}^r, \$_{\infty 3}^r\}$.

-The reciprocal system of the $2\$_\infty 1\$_0$ system is still $2\$_\infty 1\$_0$ system is represented by a basis $\{\$_\infty 1, \$_\infty 2, \$0\}$ and its reciprocal systems are represented by a bases $\{\$_{\infty 1}^r, \$_{\infty 2}^r, \$0^r\}$ and $\{\$_{\infty 1}^r, \$_{\infty 2}^r, \$0^r\}$.

-The mixed reciprocal system of the $3\$_\infty 3\$_0$, and $2\$_\infty 3\$_0$, and $3\$_0$, and $2\$_\infty 1\$_0$ screw system is still the mixed $3\$_\infty 3\$_0$, $2\$_\infty 3\$_0$, $3\$_0$ and $2\$_\infty 1\$_0$ screw system.

Screw system $\$0$ and $\$_\infty$ is represented by a basis $\{\$0_1, \$0_2, \$0_3, \$_\infty 1, \$_\infty 2, \$_\infty 3\}$ and its reciprocal system which is also a $3\$_0$ and $3\$_\infty$ is represented by a basis $\{\$0_1^r, \$0_2^r, \$0_3^r, \$_\infty 1^r, \$_\infty 2^r, \$_\infty 3^r\}$. The reciprocal system of the $2\$_\infty 3\$_0$ is represented by a basis $\{\$0_1^r, \$0_2^r, \$0_3^r, \$_\infty 1^r, \$_\infty 2^r\}$. The same way reciprocal system of a $3\$_0$ system is described by a basis $\{\$0_1^r, \$0_2^r, \$0_3^r\}$. So the last reciprocal basis is $\{\$_{\infty 1}^r, \$_{\infty 2}^r, \$0^r\}$. As shown, the mixed reciprocal system has the mixed reciprocal basis of screw system.



5. Structural Synthesis of Robot Manipulators

Structural synthesis of robot manipulators is one of the main branches of the fundamental Mechanism and Machine Science. The investigation on structural synthesis of mechanisms is generally studied as geometrical and kinematic structural synthesis. The geometrical structural synthesis focuses on,

- Further development mobility theory of Mechanisms and motions of platforms.
- Creating simple overconstraint structural groups.
- Linking simple structural groups with variable general constraint.
- Creating new parallel Cartesian robot- manipulators.
- Creating new Euclidean platform robot-manipulators with variable general constraints
- Computer-aided structural synthesis.

The kinematic structural synthesis concentrates on,

- Kinematic structural synthesis and identifying angular and linear conditions for overconstraint mechanisms.
- Rearranging the leg configurations of parallel manipulators in such a way that it will be easier to carry out the kinematic task.
- Generation of the branches and legs of parallel manipulators by describing the axis of kinematic pairs and lines, also joint and link construction, parameters.

5.1. Structural Formula - The number of independent loops

Consider a parallel manipulator including mobile platforms B , total number of connections c (that is sum of numbers of legs c_l , hinges c_h , and branches c_b) of the manipulator respectively.

By definition it follows that:

$$c = c_b + c_l + c_h \quad (5.1)$$

Assume that each leg or hinge, or branch in the manipulator consist of only one link and the total number of moving links would be:

$$n = B + c_b + c_l + c_h \quad (5.2)$$

The total number of joints would be:

$$j = j_p + c_l + c_h \quad (5.3)$$

Euler's formula to find the member of independent loops in a closed kinematic chain is stated as follows:

$$L = j - n \quad (5.4)$$

where L is the number of independent loops, j is the number of joints and n is the number of moving links in the mechanism.

Substituting Eq.s(5.2) and (5.3) in (5.4) we get the new formula that gives the number of independent loops as:

$$L = j_p - B - c_b \quad (5.5)$$

Since a leg is connected to only one joint on a mobile platform and a branch is connected to two joints on different mobile platforms, the total number of joints on the mobile platforms in a parallel manipulator can be described as:

$$j_p = 2c_b + c_l + c_h \quad (5.6)$$

Using Eq.(5.1) in Eq.(5.6) gives:

$$j_p = c + c_b \quad (5.7)$$

Substituting Eq.(5.7) into Eq.(5.5) we obtain another form of the number of independent loops in a closed kinematic chain (Table 5.1):

$$L = c - B \quad (5.8)$$

All branches, legs and hinges of the manipulators create independent loops as $L_b = c_b - B + 1$, $L_l = c_l - 1$ and $L_h = c_h$ respectively.

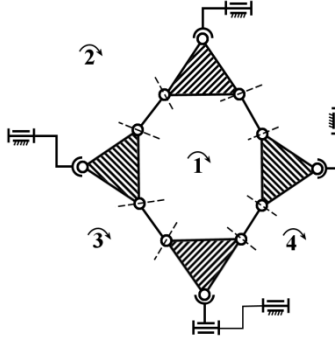
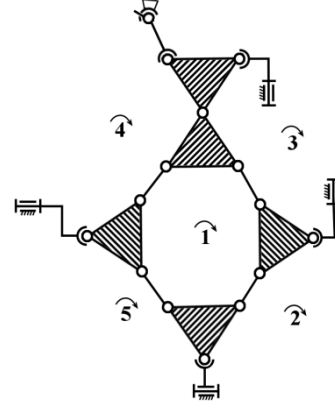
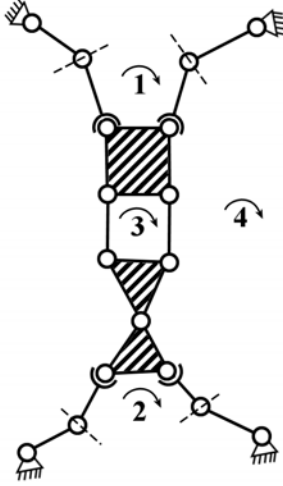
The number of independent loops in a closed kinematic chain of robot manipulators can be introduced as:

$$L = L_b + L_l + L_h = c_b + c_l + c_h - B = c - B \quad (5.9)$$

Using Eq.s (5.1-5.9) we can formulate the following definitions

- Total number of connection chains is the sum of the number of branches, legs and hinges.
- Number of independent loops in closed branches' kinematic chains is the difference of the number of branches and platforms plus one.
- Number of independent loops in closed legs' kinematic chains is one less of the number of legs.
- Two platforms that are connected by a hinge will create independent loops in a closed kinematic chain is the difference of the number of the connection chains and platforms.

Table 5.1 Number of independent loops

N	Equations	Diagrams	Comments
1	$L = j_b - B - c_b$ Rasim Alizade 1988	 <p style="text-align: center;">$j_b = 12, B = 4, c_b = 4, L = 4$</p>	<p>L is the number of independent loops j_b is the total number of joints on the mobile platforms B is the number of mobile platforms c_b is the total number of branches between mobile platforms</p>
2	$L = c - B$ $c = c_b + c_l + c_h$ $c_l = j_p - 2c_b - c_h$ RRasim Alizade Çağdaş Bayram 2004	 <p style="text-align: center;">$c_b = 4, c_l = 5, c_h = 1, c = 10, B = 5, L =$</p>	<p>c is the total number of connection chains c_l is the total number of legs, connecting mobile platform to ground c_h is the number of hinges connecting two mobile platforms</p>
3	$L = L_b + L_l + L_h$ $L_b = c_b - B + 1$ $L_l = c_l - 1$ $L_h = c_h$ Rasim Alizade Çağdaş Bayram Erkin Gezgin 2007	 <p style="text-align: center;">$L_b = 1, L_l = 2, L_h = 1, L = 4$</p>	<p>L_b is the number of independent branches loops as the difference of the number of branches and platforms plus one L_l is the number of independent leg loops as one less of the number of legs L_h is the number of hinge independent loops that created by a hinge of two moving platforms</p>



5.2. Structural Formula – The Motion of Platform of a Robot Manipulator

Euclidean space geometry introduces that any three vectors that are not on the same plane define a space \mathbf{R}^3 with dimension $D=3$, also any two non-zero independent vectors define a plane \mathbf{R}^2 with dimensions $d=2$, and in the end one vector define a line \mathbf{R}^1 passing through origin of coordinate system with dimension $d=1$.

5.2.1 Motion in Euclidean Planes

In order to obtain Euclidean plane motion in the design, legs of manipulators are selected as dyads RR, RP, PR and PP chains. Note that the end point of each dyad is connected to the platform by universal (U), spherical (S) or spherical torus pairs (S_1). Position of the end point of each dyad with respect to the fixed reference frame

defines the curve of one point of the platform in reference Euclidean plane. The motion of the platform can be defined by minimum three independent curves of three platform points moving on three Euclidean reference planes

It is clear that freely moving platform in three dimensional space has six degrees of freedom. This DoF is related to the displacement (position and orientation) of the platform in space with respect to the reference frame $f_p = \lambda$. Two moving platform can be connected by hinge

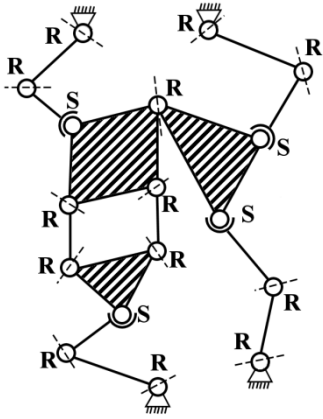
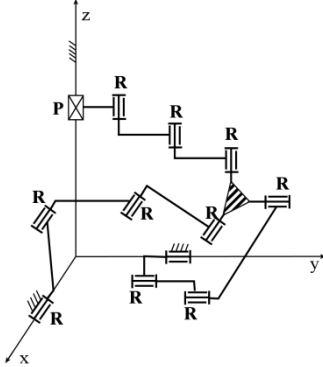
joint j_h or by branch loop with mobility $\sum_{L_b}^{c_b} (f_{L_b} - \lambda_{L_b})$.

DoF of moving kinematic chains will be $f_p = \lambda + j_h$ or

$f_p = \lambda + \sum_{L_b}^{c_b} (f_{L_b} - \lambda_{L_b})$. Three and more platforms can

be jointed by hinges and branches with DoF of platform kinematic chain as

Table 5.2 Motion of general platform of a robot manipulator

N	Equations	Diagrams	Commentary
1	$m = (\lambda + c_l) + j_h + \sum_{L_b=1}^n (f_{L_b} - \lambda_{L_b}) + \sum_{l=1}^{c_l} (d_l - D)$ <p>Rasim Alizade, Fatih Cemal Can, Erkin Gezgin, 2008</p>		<p>m- general formula of motion of platforms D is the number of dimensions of vectors in space \mathbf{R}^3 ($D=3$). d_l is the number of dimensions of vectors of the legs ($d_l=2$ for plane \mathbf{R}^2, $d_l=1$ for axis \mathbf{R}^1) $c_l = 4, \lambda=6, j_h=1, f_{L_b}=4, \lambda_{L_b}=3,$ $d_l=(1, 1, 1, 1), D=3, m=4$</p>
2	$m_p = (\lambda + 3) + \sum_{l=1}^{c_l} (d_l - D)$ <p>Rasim Alizade, Çağdaş Bayram, Erkin Gezgin, 2006</p>		<p>m_p - motion of general moving platform in Cartesian system. $\lambda=3, d_l=(1, 1, 2), D=3, m_p=1$</p>



$$f_p = \lambda + j_h + \sum_{L_b=1}^{c_b} (f_{L_b} - \lambda_{L_b}) \quad (5.10)$$

The motion of one platform on the parallel robot manipulators can be described by

$$m = \lambda + c_l + \sum_{l=1}^{c_l} (d_l - D) \quad (5.11)$$

Also the motion of two or more serial platforms can be formulated as,

$$m = \lambda + c_l + j_h + \sum_{l=1}^{c_l} (d_l - D) \quad (5.12)$$

The general formula of motion of platforms that are created by branch-loops and hinges can be given in the following form.

$$m = (\lambda + c_l) + j_h + \sum_{L_b=1}^n (f_{L_b} - \lambda_{L_b}) + \sum_{l=1}^{c_l} (d_l - D) \quad (5.13)$$

Using the structural formula, Eq(5.10) we can calculate the DoF of serial or parallel joint platforms in space, while Eq.s(5.11-5.13) can be used to describe the motion of platforms related to them.

Example: Design a serial Euclidean robot manipulator with $c_l=4, \lambda=6, n=1, \lambda_{L_b}=3, f_{L_b}=4$ and $j_h=1$, Find the motion of platforms (Table 5.2).

The motion of platforms can be calculated by using Eq.(5.13) as:

$$m = (6+4) + 1 + (4-3) + (1-3) + (1-3) + (1-3) + (1-3) = 4$$

5.2.2 Motion in Cartesian Planes

If the platform moves in Cartesian system coordinates simple structural groups will be constructed in the orthogonal planes separately. Simple structural groups can be connected to the general moving platforms and the actuators are positioned in the orthogonal Cartesian planes. Each actuators will moved (or rotated if it is possible) around the orthogonal Cartesian coordinate system.

Let the structural groups of three legs $c_l = 3$ are placed in three orthogonal planes with dimension of active motion as λ . The general moving platform and the actuators, positioned along orthogonal axis, are connected

by simple structural groups with general constraint parameters $\lambda_i=3,4,5,6$. Each simple structural group creates the legs and introduces the plane or line with two or one dimensions, so the total number of leg dimensions are $\sum_{i=1}^{c_l} (d_i - D)$. Thus, the motion of the general moving platform in Cartesian orthogonal system will be in the following form:

$$m_p = (\lambda + 3) + \sum_{l=1}^{c_l} (d_l - D) \quad (5.14)$$

Example: Let us design the motion of general platform of Cartesian manipulator PRR-[RRR]-2RRR. The three simple structural groups are selected from the subspace $\lambda=3$, one linear actuator moving along z- axis, and for symmetry two links rotating around x and y axes((Table 5.2). The motion of the general moving platform can be calculated by using Eq.(5.14) as $\lambda=3, d_l=(1,1,2), D=3, C_l=3, m_p=(3+3)+(1-3)+(1-3)+(1-3)=1$. The result by moving platform has translational motions along z-axis

5.3. Structural Formula –Mobility Equation of Mechanisms

A. Definition of mobility: in any position of a mechanical system the mobility is the difference between the numbers of independent displacement variables and the number of independent differential constraint equations. Let's consider a mechanism with interconnected rigid links. The displacement variables are associated with the relative motion between paired links. The mechanical system has a certain number of independent loops. The constraint equations are the equations of loop closure of the independent loops.

The mobility equation applies to mechanisms without exception is

$$M = \sum_{i=1}^e m_i - \sum_{K=1}^L \lambda_K \quad (5.15)$$

where M =mobility of mechanism, m_i = the relative displacements at a joint; e =total number of independent displacement variables; L =number of independent loops of mechanism, λ_K = number of independent loop-closure equations.

When the displacement variables are in 1:1 correspondence with DoF of relative motion at joints

$\sum_{i=1}^e m_i = \sum_{i=1}^j f_i$ the Eq.(5.15) becomes



$$M = \sum_{i=1}^j f_i - \sum_{K=1}^L \lambda_K \quad (5.16)$$

This case occurs in many kinematic chains with mixed $\lambda_k (2,3,4,5,6)$, If the number of independent loop-closure equations identical in each independent loop then the Eq.(5.15) becomes

$$M = \sum_{i=1}^e m_i - \lambda L \quad (5.17)$$

Combining Eq.s(5.16) and (5.17) we have the mobility equation of general kinematic chains:

$$M = \sum_{i=1}^j f_i - \lambda L \quad (5.18)$$

The above equations show that basically the mobility number is not associated with the motion of a link, but with the constraint of an independent loop. We summarize the conclusions in the following theorems.

Theorem 1: The constraint number, λ is a characteristic of an independent loop of a mechanism. It is equal to the number of independent, differential loop-closure equations for the loop.

Theorem 2: The total number of independent displacement variables is determined by the rank of the coefficient matrix of the differential loop-closure equations.

In the general case constraint number is equal to DoF of the space within which the mechanism operates. The result of this investigation is illustrated in $N=1$, Table 5.3

Example: As shown in $N=1$, Table 5.3, we have chosen a riveting machine. There are 7 links and 8 joints, giving two independent loops. Loop 7-6-5-4 has plane motion with active dimension $\lambda=3$. In loop 4-5-3-1-2 the motion of link 1 is spatial, but the loop-closure equation does not involve the rotation of links 2 and 3 about the screw axis of link 1. It involves the variable distance between the axes of joints (2,4) and (3,5), and their loop is planar, hence $\lambda=3$.

In counting displacement variables in this loop, we count the variable distance between joints (2,4) and (3,5) as a displacement variable. This gives $\sum m_i = 7$.

$$\text{Therefore, we have } M = \sum_{i=1}^7 m_i - \sum_{K=1}^2 \lambda_K = 7 - 6 = 1$$

B. In this section, a structural formula that is the function of number of branches, platforms, joints on the mobile platforms and the sum of DoF of kinematic pairs for a parallel manipulator will be described.

A platform is an n -pair link where $n \geq 2$. A parallel manipulator has at least one mobile platform. A mobile platform is connected to the frame via kinematic chains that are generally referred as legs. In the case of a manipulator having more than one mobile platform, these mobile platforms can be connected to each other by hinges and by kinematic chains which we will refer as branches. A leg, hinge or a branch is a serial kinematic chain.

Substituting Eq.(5.5) in Eq.(5.18) and added parameters q and j_p we get:

$$M = \sum_{i=1}^j f_i - \lambda(j_B - B - c_p) + q - j_p \quad (5.19)$$

Likewise, substituting Eq.(5.8) in Eq.(5.18) we get:

$$M = \sum_{i=1}^j f_i - \lambda(c - B) + q - j_p \quad (5.20)$$

where q is the number of excessive links, j_p is the number of passive joints.

Two examples have been done in $N=2$, Table 5.3 and in $N=3$, Table 5.3.

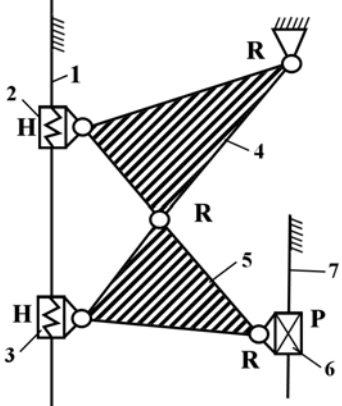
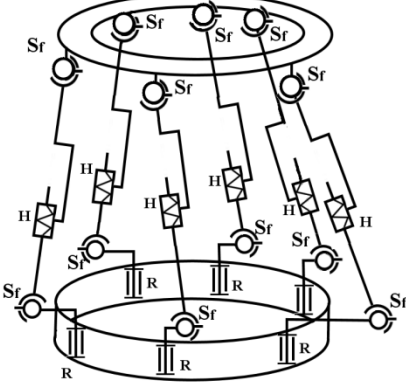
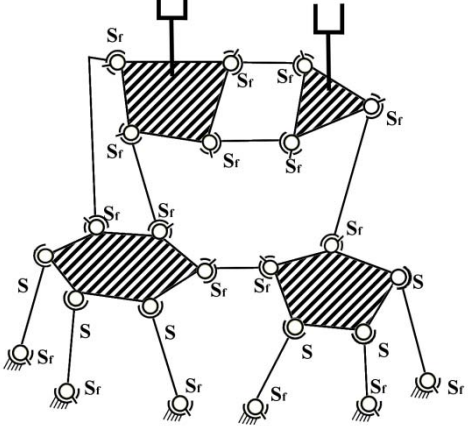
C. An important class of robotic mechanical system consist of parallel platform manipulators, serial platform manipulators, multiple serial chains and hybrid robotic mechanical system. One or more grippers can be connected to one or several platforms. That system will describe one or more gripper robotic system. All platform robotic mechanical systems constructed from the actuators and kinematic chains consist of one or more platforms, legs, branches and hinges.

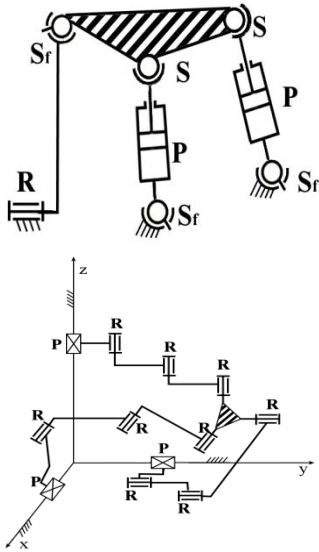
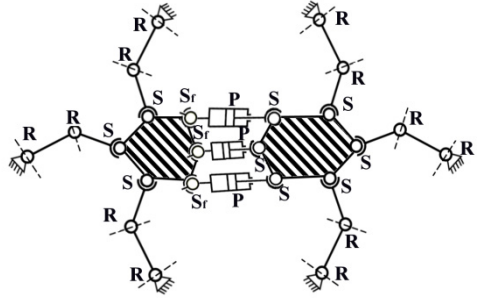
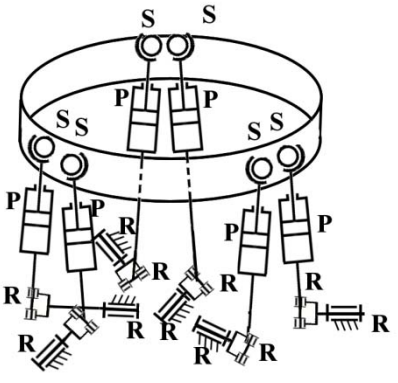
Using structural formula Eq.(5.19), we can describe the mobility loop equation in the following form

$$M = \lambda B + \sum_{i=1}^c (f_i - \lambda) + q - j_p \quad (5.21)$$

where $\lambda B = M_B$ is the sum of mobilities of all platforms in the unconstrained space or subspace; $\sum_{i=1}^c (f_i - \lambda) = M_c$ is the sum of constraints imposed by the legs, branches and hinges.

Table 5.3. Mobility Equations

N	Equations	Diagrams	Comments
1	<p>a) $M = \sum_{i=1}^e m_i - \sum_{K=1}^L \lambda_K$</p> <p>b) $M = \sum_{i=1}^j f_i - \sum_{K=1}^L \lambda_K$</p> <p>c) $M = \sum_{i=1}^e m_i - \lambda L$</p> <p>d) $M = \sum_{i=1}^j f_i - \lambda L$</p> <p>F.Freudenstein R.I.Alizade 1975</p>	 <p>$\sum m_i = 7, \sum \lambda_K = 6, M=1, L=2, \lambda=3$</p>	<p>a) and b) are mobility Eq.s for mechanisms that contain independent loops with variable general constraint</p> <p>c) and d) are mobility Eq.s with constant general constraint. λ_K is dimension of active motion of a rigid body in loop.</p> <p>m_i is the relative displacements of the joint</p> <p>f_i is corresponding 1:1 with DoF in joints.</p>
2	<p>a) $M = \sum_{i=1}^e m_i - \lambda(j_B - B - c_b) + q - j_p$</p> <p>b) $M = \sum_{i=1}^j f_i - \lambda(j_B - B - c_b) + q - j_p$</p> <p>c) $\sum_{i=1}^j f_i = \lambda(j_B - B - c_b)$</p> <p>R.I.Alizade 1988</p>	 <p>$\lambda=6, B=1, c_b = 0, j_B = 6, \sum f_i = 36, M = 6$</p>	<p>a) and b) are mobility Eq.s. in space with dimension of motion λ,</p> <p>B is number of mobile platforms,</p> <p>j_b is the total number of joints on the mobile platforms,</p> <p>c_b is the total number of branches between mobile platforms,</p> <p>q is the number of excessive links,</p> <p>j_p is the number of passive joints,</p> <p>c) is Eq. for simple structural groups ($\lambda=6,5,4,3,2$)</p>
3	<p>a) $M = \sum_{i=1}^j f_i - \lambda(c - B)$</p> <p>b) $\sum_{i=1}^j f_i = \lambda(c - B)$</p> <p>$c = c_l + c_b$</p> <p>$c_l = j_b - 2c_b$</p> <p>Rasim Alizade Çağdaş Bayram 2003</p>	 <p>$\lambda=6, c=12, B=4, \sum f_i = 54, M = 6$</p>	<p>a) is mobility Eq. of mechanism</p> <p>b) is Eq. for simple structural group</p> <p>λ is the DoF of space where the mechanism operate.</p> <p>c is the sum of legs c_l and branches c_b</p>

<p>4</p> <p>a) $M=(B-c)\lambda+\sum_{i=1}^j f_i+q-j_p$ b) $M=\lambda B+\sum_{i=1}^c (f_i-\lambda_i)+q-j_p$ c) $(\lambda+3)+\sum_{i=1}^{c_i} (f_i-\lambda_i)+\sum_{i=1}^{d_i} (d_i-D)$ d) $\sum_{i=1}^{c_i+c_p} f_{ci}=\lambda(c_i+c_h-B)$, $\lambda=3,6$ e) $\lambda+3+\sum_{i=1}^{d_i} (d_i-D)=0$ $\sum_{i=1}^{c_i} (f_i-\lambda_i)=0$ Rasim Alizade Çağdaş Bayram Erkin Gezgin 2005</p>	 <p>$\lambda=6$, $c=3$, $B=1$, $q=j_p=0$, $\sum f_i=15$, $M=3$ $m_p=3$, $\lambda=3$, $d_i=(2,2,2)$, $\lambda_i=(4,4,4)$, $f_i=(4,4,4)$, $M=3$</p>	<p>a) is mobility Eq. for robotic system., b) is mobility loop equation. c) is mobility loop Eq. for parallel Cartesian platform manipulators with variable general dimension constraint of motion, d) equation of simple structural group for robotic system ($M=0$, $\lambda=3,6$), e) are the formulas of simple Cartesian orthogonal structural group.</p>
<p>5</p> <p>a) $M=\lambda+j_h+\sum_{i=1}^n (f_{L_i}-\lambda_{L_i})+\sum_{i=1}^{c_i} (f_i-\lambda_i)+q-j_p$ b) $M=\lambda B+\sum_{i=1}^c (f_i-\lambda_i)$ c) $M=\lambda+j_h+\sum_{i=1}^{c_i} (f_i-\lambda_i)$ d) $M=\lambda+\sum_{i=1}^{c_i} (f_{L_i}-\lambda_{L_i})+\sum_{i=1}^{c_i} (f_i-\lambda_i)$ Rasim Alizade Fatih C. Can Erkin Gezgin 2008</p>	 <p>$\lambda=6$, $\lambda_{L_B}=6$, $\lambda_i=6$, $c_i=6$, $c_i f_i=30$ $c_i \lambda_i=36$, $j_h=q=j_p=0$, $\sum f_{L_B}=18$</p>	<p>a) The general structural formula of serial- parallel Euclidean robot manipulators with variable general constraint. b) Mobility formula for parallel robot manipulators c) Mobility formula of serial platform robot manipulators d) Mobility formula of the parallel robot manipulators with variable general constraint</p>
<p>6</p> <p>a) $\\$_i=f-\tilde{s}+T+1$ b) $M=\sum_{i=1}^j (\\$_i-2)-\sum_{K=1}^L \lambda_K+\tilde{s}+q-j_p$ c) $M=\sum_{i=1}^j (\\$_i-2)-\sum_{K=1}^L \lambda_K+\tilde{s}-T_2-2T_3$ Rasim Alizade Erkin Gezgin 2010</p>	 <p>$\\$_p=3$, $\\$_R=3$, $\\$_S=5$, $2j=48$, $\sum \\$_i=84$ $\sum \lambda_K=30$, $S=T_2=T_3=0$, $M=6$</p>	<p>$\\$_i$ is number of screws of the kinematic pair a) Number of screws of kinematic pairs b) General mobility screw Eq. for the mechanism and manipulators with lower kinematic pairs. $\sum \\$_i$ represents the total number of screws. \tilde{s} is the number of screws with variable pitch. T stands for the type number of the kinematic pair (surface $T_1=1$, $T_2=2$, $T_3=3$) c) Mobility screw Eq. for mechanisms lower and higher kinematic pairs; $2j$ are number of element of joints</p>



Each leg, branch and hinge separately introduces an insufficient ($f_i - \lambda < 0$), sufficient ($f_i - \lambda = 0$), or a redundant ($f_i - \lambda > 0$) kinematic chain. Sum of DoF of all platforms and the degrees of constraint that is imposed by kinematic chains describe the mobility of serial platform and parallel platform manipulators, Eq.(5.21)

Mobility loop equation Eq.(5.21) for robotic systems could be described as follows.

$$M = (B - c)\lambda + \sum_{i=1}^c f_i + q - j_p \quad (5.22)$$

where $\lambda = 2, 3, 4, 5, 6$

Application of Eqs.(5.21) and (5.22) to the platform robotic system is illustrated as an example in $N=4$, Table 5.3. Now our problem is to describe a new structural formula for platform manipulators which operate in Cartesian space or subspace and the legs consist from simple structural groups and actuators operate in orthogonal planes.

Let the number of independent parameters describing the structural groups of three legs $c_l = 3$ are placed in three orthogonal planes is λ . The general moving platform and the actuators, positioned along orthogonal axis, are connected by simple structural groups with general constraint parameters $\lambda_l = 3, 4, 5, 6$. The mobility of legs at the general moving platform in Cartesian orthogonal system will be in the following form.

$$M_l = \sum_{l=1}^{c_l} (f_l - \lambda_l) + q - j_p \quad (5.23)$$

where λ_l is the general leg constraint, f_l is DoF of leg kinematic pairs.

The mobility of parallel Cartesian platform robot manipulators consists of the motion of the general moving platform m_p and the mobility of legs M_l moving in orthogonal planes:

$$M = m_p + M_l \quad (5.24)$$

Combining the Eqs.(5.14) and (5.23) we can describe the new structural formula of mobility loop-legs equations as follows ($N=4$, Table 5.3)

$$M = (\lambda + 3) + \sum_{l=1}^{c_l} (f_l - \lambda_l) + \sum_{l=1}^{c_l} (d_l - D) + q - j_p \quad (5.25)$$

Example: Let us design parallel Cartesian platform

manipulator, where the motion of the general moving platform has translational motions P_z .

For the orthogonal robot manipulator we will take three simple structural groups RRR from the subspace $\lambda=3$, one linear actuator moving along Z- axis and for symmetry two links rotating around x and y axes ($N=4$, Table 5.3). In each orthogonal plane, simple structural groups will be connected to the general moving platform actuator and two rotating links. Using mobility Eq.(5.25) we can calculate the mobility of the type PRR-(RRR)-2RRR parallel orthogonal robot manipulator as: $q = j_p = 0, \lambda = 3, \lambda_l = (3, 3, 4), d_l = (1, 1, 2), \sum f_l = 12, M = 3$. By using Eq.s(5.14) and (5.23) the motion of the general moving platform and the mobility of legs will be $m_p = 1$ and $M_l = 2$ respectively.

D. It is clear that the entire legs of the serial platform manipulators are connected to the moving serial platforms and to the ground, mobility of the kinematic chains of the legs can be defined as,

$$M_l = \sum_{l=1}^{c_l} (f_l - \lambda_l) \quad (5.26)$$

where $\sum_{l=1}^{c_l} f_l$ is the total DoF of all the kinematic pairs on the legs c_l , and λ_l is the general constraint of each leg ($\lambda_l = 2, \dots, 6$).

If the number of hinges between the platforms is more than one, DoF of the serial moving platforms can be calculated as

$$f_{SP} = \lambda + j_h \quad (5.27)$$

The combination of Eq.s(5.26) and(5.27) results in the general structural formula of serial platform robot manipulator as

$$M = \lambda + j_h + \sum_{l=1}^{c_l} (f_l - \lambda_l) \quad (5.28)$$

If the number of moving platforms is unity ($j_h = 0$), Eq.(5.28) will be reduced to the structural formula of parallel manipulators as

$$M = \lambda + \sum_{l=1}^{c_l} (f_l - \lambda_l) \quad (5.29)$$

If several number of platforms are connected by



several branch-loops with variable general constraints, total DoF of parallel moving platforms can be calculated as,

$$f_{PP} = \lambda + \sum_{L_B=1}^n (f_{L_B} - \lambda_{L_B}) \quad (5.30)$$

where n is the number of branch-loops, λ_l is the number of independent, loop closure equations. Associated with each independent branch-loop, $\sum_{L=1}^n f_L$ is the total DoF of kinematic pairs on the branch-loops.

The general mobility formula of the parallel robot manipulators can be generated by using the combination of Eq.s(5.26) and (5.30), as

$$M = \lambda + \sum_{L_B=1}^n (f_{L_B} - \lambda_{L_B}) + \sum_{l=1}^{c_l} (f_l - \lambda_l) \quad (5.31)$$

Also, by combining Eq.s(5.10) and (5.26) and added parameters q and j_p , the general structural formula of serial- parallel Euclidean robot manipulators with variable general constraints that include several hinges, legs and branch-loops can be defined as,

$$M = \lambda + j_h + \sum_{L_B=1}^n (f_{L_B} - \lambda_{L_B}) + \sum_{l=1}^{c_l} (f_l - \lambda_l) + q - j_p \quad (5.32)$$

The mobility equations for Euclidean platform robot manipulators with diagrams and commentary are illustrated in $N=5$, Table 5.3.

Example: Design a parallel Euclidean robot manipulator with $c_l=6, \lambda_l=6, n=2, \lambda_{L_B}=6, \lambda=6, j_p=q=j_h=0$. The kinematic pairs of branch loops and legs are described by kinematic diagram in $N=5$, Table 5.3. Find the mobility and the motion of platforms of parallel Euclidean robot manipulator.

By using Eq.(5.32), the mobility can be calculated as, $M=6+0+(12-6)+(6-6)+6(5-6)+0-0=6$. By using Eq.(5.13), the motion of the platforms will be $m_p=(6+6)+0+(18-12)+6(1-3)=6$

E. At the end of this chapter a novel universal mobility formulation for both kinematic pairs and robot manipulators are presented in terms of screw theory. From this point of view, the total number of screws that represent the types of kinematic pairs can be introduced as

$$\$ = f - \tilde{s} + T + 1 \quad (5.33)$$

where, f represents DoF of the kinematic pair; \tilde{s} is the number of screws with variable pitch (screw with variable pitch describe independent translation motion along kinematic pair contact axis.); T is the contact origin for the type number of the kinematic pair (the contact geometry between two attached links can be a surface -Type 1, a line- Type 2, or a point- Type 3, so $T_1=1, T_2=2, \text{ and } T_3=3$)

Example: Let's consider the revolute joint R, prismatic joint P and spherical joint S. the revolute pair can be represented by DoF $f=1$ and it has not got any screws with variable pitch $\tilde{s}=0$. Being as a kinematic pair. Type 1, its total number of screws can be calculated by using Eq. (5.33) as, $\$R=1-0+1+1=3$. The same way for prismatic pair $\$P=1-0+1+1=3$, and for spherical joint $\$S=3+0+1+1=5$.

Having learned the idea of screw number of kinematic pairs by the help of transformation screw matrix equations, the subject can be extended by applying the mobility of mechanism and robot manipulators with lower kinematic pairs- Type 1. The formula can be introduced as,

$$M = \sum_{i=1}^j (\$i - 2) - \sum_{K=1}^L \lambda_K + \tilde{s} + q - j_p \quad (5.34)$$

where, $\$i$ is the number of screws in i th joint; j is the number of joint; $2j$ is the number of elements of all kinematic pairs; λ_K is the dimension of active motion in independent loop L ; \tilde{s} is the number of screw with variable pitch; q is the number of excessive links; j_p is number of passive joints..

The general mobility screw equation Eq. (5.34) can be extended by applying it to the mechanisms and manipulators with lower and higher kinematic pairs as follow ($q=j_p=0$):

$$M = \sum_{i=1}^j (\$i - 2) - \sum_{K=1}^L \lambda_K + \tilde{s} - T_2 - 2T_3 \quad (5.35)$$

The mobility screw Eq.s (5.34) and (5.35) for mechanisms and manipulators with diagrams and commentary are illustrated in $N=6$, Table 5.4.

Example: Checking the number of screws from above



example we have $\$R = 3$, $\$P = 3$ and $\$S = 3$. There is 12 revolute pairs, 6 prismatic pairs and 6 spherical pair on the 6 legs, that are connected to the moving platform with the frame ($N=6$), Table 5.4

Total number of joints with screw $\$ = 3$ is equal to 18, and with screw $\$ = 5$ equal to 6. The number of elements constructed by kinematic pairs are $2j=48$. The number of independent loop $L=5$ and dimension of active motion $\lambda=6$. Parameters are $\tilde{s}=q=j_p=0$. Using mobility screw Eq.(5.34), the number of actuators of the parallel spatial 6RRPS manipulator can be calculated as,
 $M=(18 \cdot 3 - 18 \cdot 2) + (6 \cdot 5 - 6 \cdot 2) - 5 \cdot 6 = 6$

Note:

The axis of two revolute pairs adjusted to frame and legs are perpendicular to each other and $R-R \Rightarrow U$ gives universal joint, thus our parallel manipulator RRPS is identical with 6UPS manipulator.

As the presented investigation related with the author's references [1-11] shows the development of robotic systems, it is clear that there will be more advanced future studies by the help of rapidly evolving new theoretical methods and technology.

References

[1]. F. Freudenstein, R. Alizade, *On the degree of freedom of mechanisms with variable general constraint*, IV. World

- IFTOMM Congress, pages 51-56, England, 1975.
- [2]. R.I. Alizade, E.T. Hajiyev, G.N. Sandor, *Type synthesis of spatial mechanisms on the basis of spatial single loop structural groups*, Mechanism and Machine Theory 20 (2), pages 95-101, 1985.
- [3]. R.I. Alizade, *On the DoF of kinematic chains*, Az.PI., pages 3-14, Baku, 1988
- [4]. R.I. Alizade, *Investigation of linkage mechanisms with lower pairs from point of view of its structure and classification*, Az.PI., pages 111-127, Baku, 1988.
- [5]. R.I. Alizade, *Physical substance and geometrical interpretation of variable constraint parameters of universal structural formula*, Az.PI., pages 3-12, Baku, 1991.
- [6]. R.I. Alizade, *Modular method of kinematic analysis and synthesis of spatial linkage mechanisms*, Dr. Tech. Sc. Dissertation, page 395, Kaz.St.Un., Almata, 1992.
- [7]. R. Alizade, Ç. Bayram, *Structural synthesis of parallel manipulators*, Mechanism and Machine Theory 39(8), pages 857-870, 2004.
- [8]. R. Alizade, Ç. Bayram, E. Gezgin, *Structural synthesis of serial platform manipulators*, Mechanism and Machine Theory 42(5), pages 580-599, 2007.
- [9]. R.I. Alizade, F.C Can, E. Gezgin, O. Selvi, *Structural synthesis of new parallel and serial platform manipulators*, 12 th IFTOMM World Congress, pages 18-27, France, 2007.
- [10]. R.I. Alizade, F.C Can, E. Gezgin, *Structural synthesis of Euclidean platform robot manipulators with variable general constraints*, Mechanism and Machine Theory 43(11), pages 1431-1449, 2008.
- [11]. R.I. Alizade, O. Selvi, E. Gezgin, *Structural design of parallel manipulators with general constraint one*, Mechanism and Machine Theory, 45(1), pages 1-14, 2010.



Revisiting a Noble Structural Modification Method for Linear and Nonlinear Dynamic Reanalysis of Machinery

H. Nevzat ÖZGÜVEN

Mechanical Engineering Department
Middle East Technical University, Ankara, Turkey
ozguven@metu.edu.tr

Abstract

In this paper, the structural modification method developed by the author more than two decades ago is revisited. The method is used to calculate the frequency response functions of a modified system from those of the original system and the system matrices of the modifying part. Modification can also be in the form of coupling another system to the original one. After summarizing the theory, various applications of the method used in different recent research areas, ranging from machine tool dynamics to vibro-acoustics and from distributed structural modifications to non-linear dynamic coupling, are presented in this paper. The method is most advantageous when the degree of freedom of the system is very large and modifications are local. Therefore, it is very suitable for structural dynamics problems, as well as for any machine dynamic problem where large ordered finite element models are employed. An example from machine dynamics application is also given in the paper.

Keywords: Structural modification, dynamic reanalysis, forward modification, structural coupling, nonlinear dynamic coupling

1. Introduction

Dynamic reanalysis, also known as forward structural modification is the term used for the incorporation of the response or modal data of an existing mechanical system with the information representing structural modification, in order to predict the dynamic behavior of the modified system. Reanalysis is usually employed in design stage for vibration optimization, and is very useful especially when dynamic models with high number of degrees of freedom, such as finite element models, are used. Various dynamic reanalysis methods have been developed.

The matrix inversion method proposed in an earlier study for finding receptances of locally damped structures from undamped counterparts [1] has been combined with an efficient recursive solution algorithm

[2] in order to avoid matrix inversion. The method later has been generalized for dynamic reanalysis when there is a modification in the mass, stiffness and/or damping of the original system [3]. In this method, the Frequency Response Functions (FRFs) of a modified system are calculated from those of the original system and the mass, stiffness and damping matrices representing the modifications in the system. The method has been extended in the same work for modifications which require additional degrees of freedom (DOF), which means coupling a sub-system to the original system. There are various other methods addressing structural modification problems; however, in the methods proposed by Özgüven [1-3] the major part of the computations is limited to the modified coordinates, which makes the methods favorable for systems with large DOF with local modifications. The method is very efficient in such applications, as it is required to invert only a matrix of the size equal to the number of DOF related with modified coordinates, which can even be avoided by using the recursive formulation presented in [2]. Furthermore, as the formulation is based on FRFs, in addition to the modified coordinates only the coordinates at which a force is applied and/or response is required are to be kept in the formulation. The rest of the coordinates may be eliminated from the matrices in the formulation without deteriorating the accuracy of the results.

In order to avoid matrix inversion, Şanlıtürk [4] has started with the same matrix inversion formulation and combined it with Sherman-Morrison formula [5]. However, this method is restricted to structural modification problems where there are no additional degrees of freedom. Köksal et al. [6] extended the Successive Matrix Inversion (SMI) method of Bae et al. [7] for reanalysis of static systems, to dynamic reanalysis of structures. The basic starting equation is again the same as the one presented in [3], but power series expansion is used in that work in order to avoid matrix



inversion. In a recent work of Köksal et al. [8], three structural reanalysis methods ([3], [4] and [6]) are compared with each other from computational efficiency point of view, and it is concluded that the structural modification method developed by Özgüven [3] is the most efficient one among the three methods studied. This method has also the advantage of being suitable for structural modifications with additional degrees of freedom (for structural coupling problems).

The method has been used by the author and his research group in structural and machine dynamics research in several different fields, such as geared rotor dynamics [9], turbine blade vibrations [10], machine tool dynamics [11-13], part dynamics for machining stability analysis [14, 15] and vibro-acoustic analysis [16, 17]. It also served as a starting point in developing new methods in various different areas, such as non-linear structural dynamics [18-21], finite element model updating [22, 23] and identification of structural non-linearity [24, 25]. The method can also directly be used in compensating the mass loading effect of accelerometers on measured vibration response [26]. Quite recently, the method has also been successfully used and extended by Hang et al. [27-29] to predict the effect of distributed structural modifications with additional DOF. A review of structural modification methods can also be found in recent papers of Hang et al. [27-29].

In this paper, after the presentation of the resultant equations of the structural modification method developed earlier [1, 3], various applications of the method to structural and machine dynamic problems will be given, and thus versatility of the method will be demonstrated. Although dynamic reanalysis methods are very advantageous and therefore are mostly used for structural dynamic problems (as DOF is very large), in several machine dynamics problems where finite element models are employed, reanalysis methods may be equally advantageous and reduce computational effort considerably. Examples for such an application will also be given in this paper.

2. Theory

2.1 Structural Modifications without Increasing Degree of Freedom

In this section, the theory of the structural modification method (dynamic reanalysis method) developed in [3], based on the general approach proposed in earlier studies [1, 2] for harmonic response of non-proportionally damped systems is summarized.

Frequency response functions (FRFs) of a dynamic system expressed in the form of a receptance matrix $[\alpha]$ can be written as

$$[\alpha] = \left[[K] - \omega^2 [M] + i\omega [C] + i[H] \right]^{-1} \quad (1)$$

Here, $[K]$, $[M]$, $[C]$ and $[H]$ are stiffness, mass, viscous damping and structural damping matrices, respectively. Similarly, the receptance matrix of the same system when it is structurally modified can be expressed as

$$[\gamma] = \left[[K] + [\Delta K] - \omega^2 [M] + [\Delta M] + i\omega [C] + [\Delta C] + i[H] + [\Delta H] \right]^{-1} \quad (2)$$

where $[\Delta K]$, $[\Delta M]$, $[\Delta C]$ and $[\Delta H]$ are the matrices representing modifications in stiffness, mass, viscous damping and structural damping matrices, respectively. By using equations (1) and (2), after some simple matrix operations, the receptance matrix of the modified system can be expressed in terms of that of the original system and the dynamic stiffness matrix representing structural modifications, as follows:

$$[\gamma] = \left[[I] + [\alpha][D] \right]^{-1} [\alpha] \quad (3)$$

where $[D]$ is expressed as

$$[D] = \left[[\Delta K] - \omega^2 [\Delta M] + i\omega [\Delta C] + i[\Delta H] \right] \quad (4)$$

Generally the modification is not on all coordinates, but on limited number of coordinates, and in many practical applications the modification is local. Then, by partitioning the system matrices such that the dynamic stiffness matrix representing structural modifications can be written as

$$[D] = \begin{bmatrix} [D_{11}] & [0] \\ [0] & [0] \end{bmatrix} \quad (5)$$

where the subscript 1 represents the coordinates on which modification is applied and subscript 2 denotes the remaining coordinates, the receptances of the modified system can be expressed, after some matrix manipulations [3], in terms of their counterparts in the original system as follows:

$$[\gamma_{11}] = \left[[I] + [\alpha_{11}][D_{11}] \right]^{-1} [\alpha_{11}] \quad (6)$$

$$[\gamma_{12}]^T = [\gamma_{21}] = [\alpha_{21}][[I] - [D_{11}][\gamma_{11}]] \quad (7)$$



$$[\gamma_{22}] = [\alpha_{22}] - [\alpha_{21}][D_{11}][\gamma_{12}] \quad (8)$$

As can be seen from the above equations, in order to calculate the dynamic behavior of a modified system from that of the original system, it is sufficient to invert a matrix of order equal to the number of degrees of freedom on which modifications are applied, regardless of the total DOF of the system. This method is extremely useful when there is a local modification on a large system. Moreover, the efficient recursive solution algorithm developed for damping modifications [2] can easily be used in order to avoid matrix inversion (for instance see [21]).

2.2 Structural Modifications Increasing Degree of Freedom – Coupling Analysis

The equations derived in the previous section are for a system where the modifications do not add new degrees of freedom to the system. However, when the modification is in the form of coupling another system to the original system, then there will be additional degrees of freedom in the modified system. The derivation of the receptance matrix of the modified system in that case from that of the original system is given in [3]. Here, only the resultant equations are presented for completeness:

$$\begin{bmatrix} \gamma_{ba} \\ \gamma_{ca} \end{bmatrix} = \begin{bmatrix} [I] & [0] \\ [0] & [0] \end{bmatrix} + \begin{bmatrix} \alpha_{bb} & [0] \\ [0] & [I] \end{bmatrix} \cdot [D]^{-1} \begin{bmatrix} \alpha_{ba} \\ [0] \end{bmatrix} \quad (9)$$

$$\begin{bmatrix} \gamma^{bb} & \gamma^{bc} \\ \gamma^{ab} & \gamma^{ac} \end{bmatrix} = \begin{bmatrix} [I] & [0] \\ [0] & [0] \end{bmatrix} + \begin{bmatrix} \alpha^{bb} & [0] \\ [0] & [I] \end{bmatrix} \cdot [D]^{-1} \begin{bmatrix} \alpha^{bb} & [0] \\ [0] & [I] \end{bmatrix} \quad (10)$$

$$\gamma^{aa} = \alpha^{aa} - \begin{bmatrix} \alpha^{ab} \\ [0] \end{bmatrix} [D]^{-1} \begin{bmatrix} \gamma^{ba} \\ \gamma^{ca} \end{bmatrix} \quad (11)$$

$$\begin{bmatrix} \gamma^{ab} \\ \gamma^{ac} \end{bmatrix} = \begin{bmatrix} \alpha^{ab} \\ [0] \end{bmatrix} \left[[I] - [D] \begin{bmatrix} \gamma^{bb} & \gamma^{bc} \\ \gamma^{cb} & \gamma^{cc} \end{bmatrix} \right]^{-1} \quad (12)$$

Here; superscript *a* represents DOFs which correspond to the original system only, superscript *b* represents DOFs corresponding to the nodes common to the original and modifying systems (i.e., DOFs corresponding to connection points), and superscript *c* represents DOFs that belong to modifying structure only.

The formulations for both reanalysis cases reduce the computational effort drastically when large structural

systems modeled by using finite elements (FE) are analyzed for local modifications, especially when similar analyses are to be repeated several times in a design stage for various modification alternatives. It has also been demonstrated [8] that the structural modification (dynamic reanalysis) method presented in section 2.1 is faster than similar methods which use FRF data of the original structure and the modification matrices for predicting the FRFs of a modified structure. As can be seen from the derivation, the method mathematically gives exact results. However, for large ordered systems, the receptances of the original system are calculated by using modal analysis, not from equation (1) and therefore although the calculated receptances are very accurate, they are not “exact”. The effect of modal truncation made in calculating the receptances of the original structure on the accuracy of the method is also studied [30] and it is observed that the performance of the method increases when the number of modes included in the computation of the receptances of the original structure is increased.

The method has successfully been used for structures with distributed modifications [30], and the performance of both formulations have also been investigated by applying them to a real scaled aircraft test structure with and without additional DOFs [30, 8], and very good agreements are observed between predicted and measured results.

2.3 Harmonic Response of Non-linear Multi Degree of Freedom Systems by Using Structural Modification Approach, and Dynamic Reanalysis in Non-linear Systems

It can be shown that when there are non-linear elements in a multi degree of freedom (MDOF) system, the pseudo receptance matrix $[\theta]$ of the non-linear system can be written as

$$[\theta] = [-\omega^2 \cdot [M] + i \cdot \omega \cdot [C] + i \cdot [H] + [K] + [\Delta]]^{-1} \quad (13)$$

where $[\Delta]$ is response level dependent, the so called ‘non-linearity matrix’, which has first been introduced by Budak and Özgüven [18-20] and then was expressed more generally for any type of non-linearity by using describing functions by Tanrikulu et al. [21]. It can easily be seen from equation (13) that, the analysis of the non-linear system can be regarded as the reanalysis of the linear counterpart with a modification in the system expressed as an equivalent dynamic stiffness matrix $[\Delta]$ which is response level dependant. Then, the formulations given in previous sections can easily be

adopted here by replacing $[D]$ with $[\Delta]$ in equation (3). Thus the pseudo receptance matrix can be calculated from receptance matrix of the linear counterpart of the non-linear system $[\alpha]$ and nonlinearity matrix $[\Delta]$ by using equation (13). However, as the system is non-linear, the pseudo receptance matrix will also be response level dependant. Therefore, it will be necessary to use an iterative solution procedure. This approach is basically the application of the harmonic balance method and describing functions to non-linear MDOF systems. Similar approaches later became a common and standard procedure and used by several researchers. In these studies, however, harmonic balance method and describing function approach are directly used. The formulation given by equations (6)-(8), on the other hand, reduce the computational effort considerably when the total DOF of the system is large and the non-linearity is local.

Moreover, equations (9)-(12) and equations (6)-(8) can also be used for non-linear structural modifications with and without additional DOFs, respectively, by replacing $[D_{11}]$ by $[\Delta_{11}]$. If modification includes both linear and non-linear elements, then $[D]$ takes the form

$$[D] = [[\Delta K] - \omega^2 [\Delta M] + i\omega [\Delta C] + i[\Delta H] + [\Delta]] \quad (14)$$

and it is response level dependant. For local non-linearity in a system without additional DOF, equations (6)-(8), and for non-linear coupling (or non-linear modifications with additional degrees of freedom) equations (9)-(12) can be used defining $[D]$ as given in equation (14). Then solution is obtained by employing an iterative solution procedure.

3. Applications

The reanalysis method has been used in several different structural dynamic analysis problems in various fields, such as turbine blade vibrations [10], part dynamics for machining stability analysis [14, 15] and vibro-acoustic analysis [16, 17], as well as in machine dynamics research in different fields, such as geared rotor dynamics [9] and machine tool dynamics [11-13]. Moreover, the method served as a starting point in developing new methods in different areas, such as finite element model updating [22, 23] and identification of structural non-linearity [24, 25]. The method was also directly used in compensating the mass loading effect of accelerometers on vibration measurements of light structures [26]. In this section, examples from some of the different application areas will be presented to demonstrate the versatile applications of the method. Finally, an application on machine dynamics will be

given.

3.1 Machine Tool Dynamics

In machine tools, regenerative chatter which is self-excited vibration of the tool that results in unstable cutting process, can be predicted and eliminated if the stability lobe diagram of the spindle-holder-tool assembly is known. The stability lobe diagram can be obtained if the dynamics of the tool tip (in receptance form) is known. In the analytical model developed for predicting the tool point FRF (which relates the harmonic displacement and force at tool tip) of spindle-holder-tool assembly (shown in Figure 1), the structural modification method is successfully used [11, 12]. By using the method suggested the effects of bearing dynamics on the tool point FRF which determines the stability regions are studied [13]. In the analytical model, FRF coupling is used in dynamic modeling of tool-holder-shaft system, and the dynamics of bearings are included via the structural modification method. If a finite element (FE) model were used for the tool-holder-shaft system, the advantage of employing the structural modification method would be more pronounced. In such an application, the structural modification method used makes it possible to calculate the tool tip FRF for different values of bearing stiffness, by first making the dynamic analysis of the whole assembly without bearing dynamics only once, and then using it with different bearing properties. Such an approach reduces the computational effort and time considerably and therefore is very suitable to be used in design stages to study the effects of bearing properties on the dynamics of the system.

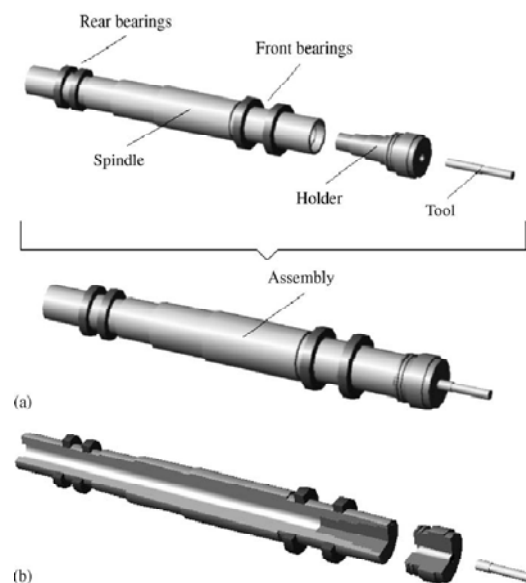




Fig. 1. Spindle-holder-tool assembly.

Figure 2 shows the tool point FRFs for three different sets of bearing stiffness for the system analyzed in [13]. It is observed from the figure that the bearing stiffness values have a considerable effect on the first two modes of the shaft-holder-tool system which correspond to the rigid body modes of the system, and they have almost no effect on the other modes. Figure 3 and Figure 4 show the effects of front and rear bearing stiffness, respectively, on the tool point FRF. Thus it is possible to study the effect of each bearing's dynamics on the stability regions of the cutting process.

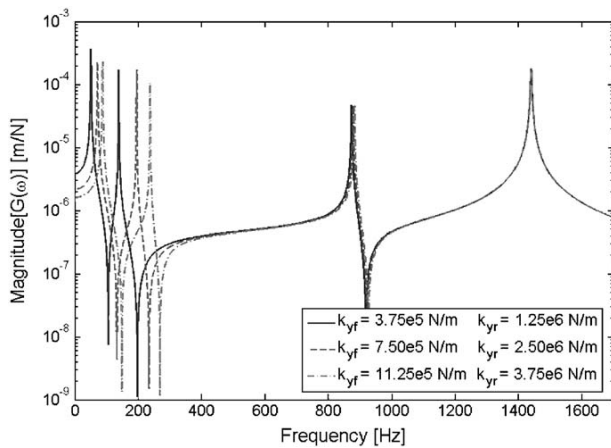


Fig. 2. Tool point FRFs.

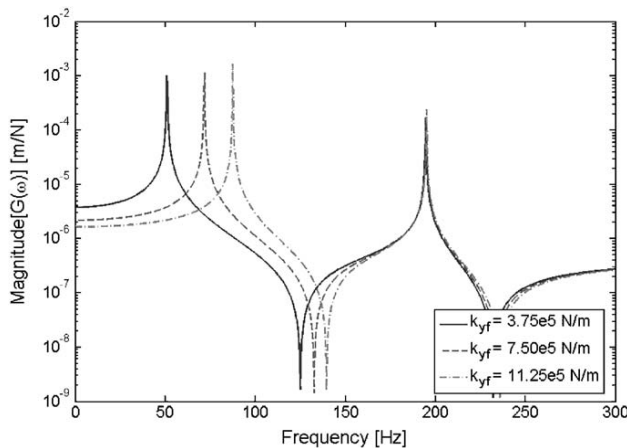


Fig. 3. Effect of front bearing stiffness on tool point FRF.

3.2 Part Dynamics for Machining Stability Analysis

An interesting example of a very effective use of the

structural modification method is the study of workpiece dynamics on chatter stability regions. Although in general tool point FRF, which determines stability regions in chatter analysis, is calculated considering the machine tool dynamics only, for a flexible workpiece the contribution coming from the part dynamics may be equally important, and even more in some cases. Then FRFs of the part must be known at all stages of the machining cycle. In such cases, the general practice is to determine part dynamics prior to and after machining and use it in stability analyses. However, this would not be an accurate analysis since at each stage of manufacturing the part dynamics will vary continuously because of changing part geometry.

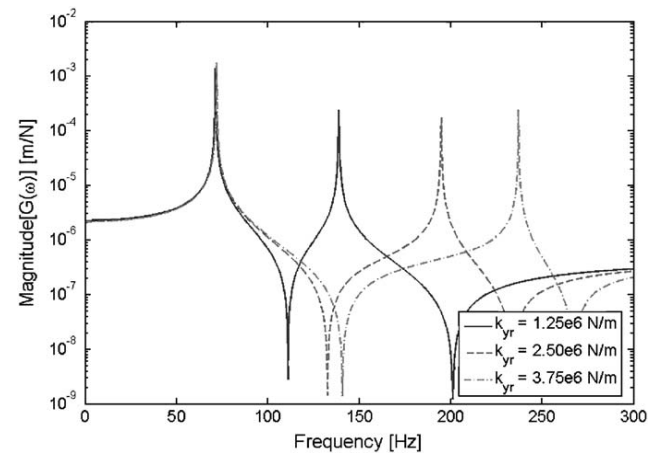


Fig. 4. Effect of rear bearing stiffness on tool point FRF.

In a very recent study [14, 15] an analytical procedure is developed to predict workpiece dynamics in a complete machining cycle in order to obtain FRFs required for stability analysis, by employing the structural modification method presented above. The mass removed by machining is considered as a structural modification in determining the FRFs at different stages of the process. By using the predicted FRFs in chatter stability analyses, the effects of part dynamics on stability are studied, which made it possible to compare different cutting strategies for increased chatter-free material removal rates considering part dynamics.

As a numerical example, one of the case studies of [15] is given here. A plate of Al 7075 alloy is to be machined along its thickness in order to reduce the thickness from 9.5 mm to 3 mm. The geometry for the unmachined plate is shown in Fig. 5. The material properties, dimensions and other details are given in reference [15]. The effect of the decreased part thickness on the FRF of the part at the cutting point location is shown in Fig. 6. The coding convention used to indicate

the position of machining, i.e., tool position, is such that steps A-1-1-1, A-2-1-1, and A-3-1-1 correspond to the machining of the first elements of the first steps of the first, second and third layers, respectively. As can be seen from Fig. 6, the magnitudes of the FRFs increase as the thickness of the plate is reduced, and consequently the stability regions change as depicted in Figure 7 (for the tools and cutting conditions described in [15]). The upper parts of the curves represent unstable region. It can be clearly seen that as the thickness is reduced the stable depth of cut decreases considerably which increases the machining time. The method developed in [15] makes it possible to compare the machining time of different production strategies. For instance, 6 different machining strategies compared in [15] showed that for the same radial depth of cuts, step removal strategies require much less time than the layer removal strategies, and in the case study given, the machining time for the most productive strategy was found to be just 25% of the worst strategy.

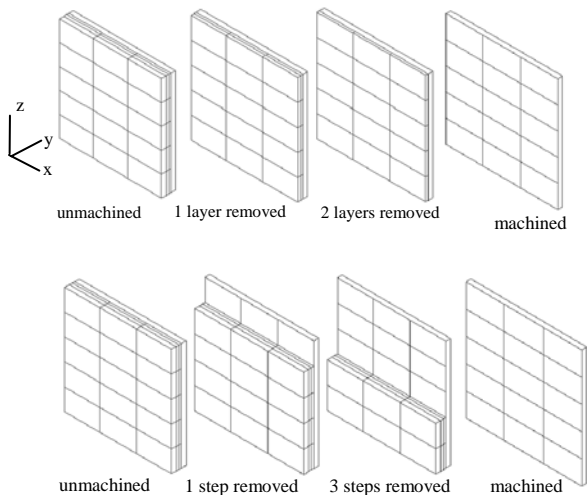


Fig. 5. Stages of layer (upper) and step removal (lower) processes.

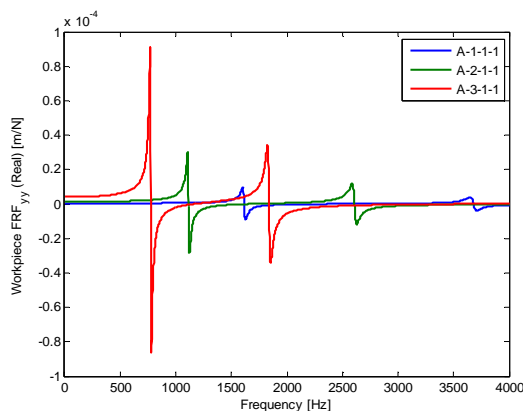


Fig. 6. Workpiece FRF for the steps A-1-1-1, A-2-1-1, and A-3-1-1

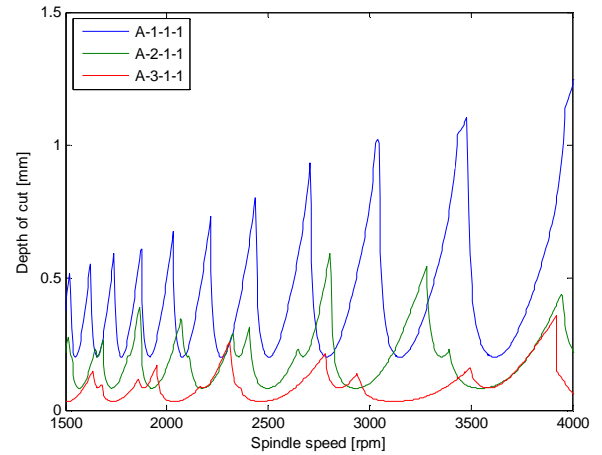


Fig. 7. Stability limits for the steps A-1-1-1, A-2-1-1, and A-3-1-1

3.3 Distributed Modifications

The structural modification method can be applied to structures with distributed modifications by considering the modifying structure as a subsystem coupled to the original system. Then coupling analysis formulation is to be used. The application of the method to a real structure with distributed modifications is given in [30] where the performance of the method is investigated by applying it to a scaled aircraft model. Modifications are taken in the form of beams attached under the wings acting as stiffeners increasing flexural rigidity. The receptances calculated by using the structural modification method are compared with those obtained from the finite element analysis of the modified structure as a whole, as well as with the measured ones. For the verification of the method for distributed modifications, simpler structures are analyzed and the FRFs calculated with the structural modification method are compared with those obtained from the FE analysis of the modified structure. A perfect match is observed as expected, since the method yields exact FRFs when exact values of the FRFs of the original structure are used. It is observed in these case studies that the accuracy of the predictions strongly depends on the accuracy of the FRFs used for the original structure, so that using higher number of the modes in the computation of the FRFs of the original system increases the accuracy of the predicted responses for modified structures.

For the application of the method to a real system, the scaled aircraft model used by the Group for Aeronautical Research and Technology in Europe



(GARTEUR SM-AG19) is employed (Fig. 8). The FE model of the modified system is shown in Fig. 9. The FRFs of the original and the modified structure at the tip point of the wing are given in Fig. 10. Then the FRF of the modified system obtained by using the structural modification method is compared with the experimentally measured one in the same figure. The modal damping of the structure is taken as 0.032. From the good agreement observed between the calculated and experimentally measured FRFs for the modified system, it is concluded that the structural reanalysis method proposed can successfully and efficiently be used for structures with distributed modifications. The discrepancy around the third mode is attributed to the slight differences between the theoretical and experimental FRFs of the original structure [30].



Fig. 8. Scaled aircraft model used (GARTEUR SM-AG19)

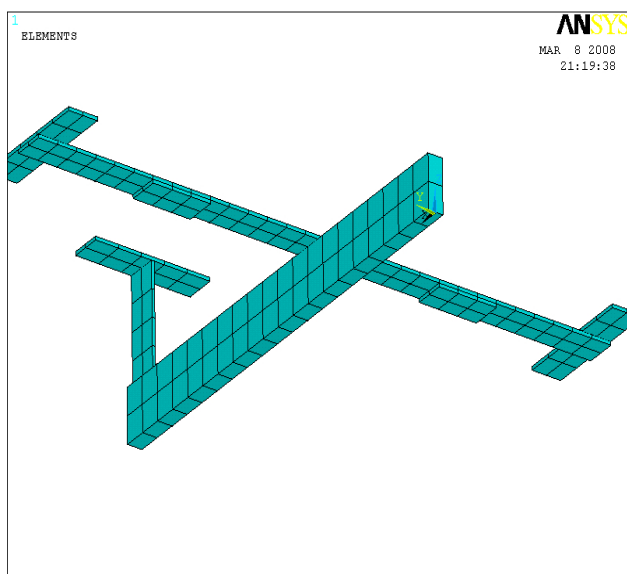


Fig. 9. FE model of the modified scaled aircraft.

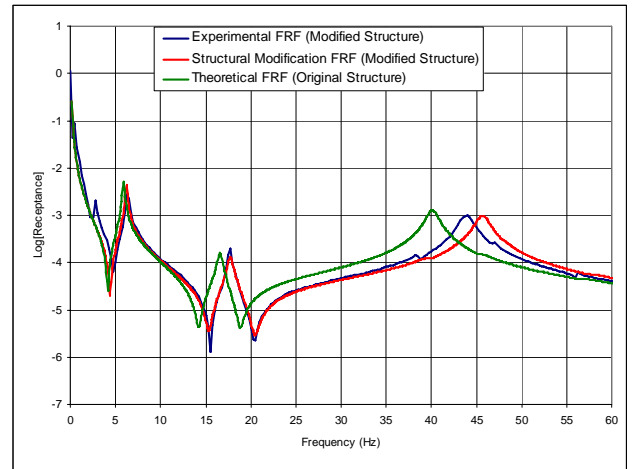


Fig. 10. Measured and calculated FRFs at the wing tip.

3.4 Vibro-Acoustic Response of Enclosed Spaces

In a recent work, the structural modification technique is integrated with a vibro-acoustic model of a simple box like structure as an introductory work for studying the effects of stiffeners added to panels to decrease low frequency noise (booming noise) inside vehicles [17]. Analysis of vibro-acoustic behaviour is carried out by calculating frequency response functions of the structure using Finite Element Method and predicting sound pressure level (SPL) inside the cabin by employing Boundary Element Method. Structural design of the vibrating panels can be modified by adding stiffeners to improve the acoustic field inside the cabin. Then, the dynamic analysis of the structure should be repeated after every structural modification, which is a time consuming process if the whole system is reanalyzed, and can be a real burden when numerous different configurations, geometries and sizes are to be considered in a design stage. However, the structural modification method is found to be very efficient to investigate the effects of various structural modifications on acoustic pressure inside the closed space.

As an example application, a box-like structure (1200 mm x 1400 mm x 3600 mm) with a more flexible panel at the middle is analyzed: First the calculated responses obtained by using the structural modification method are verified, and then various different stiffener applications are studied [17]. FRFs of the mid point on the panel with and without stiffener application are given in Fig. 11 as an example. The stiffener used is a steel strip (1400 mm x 30 mm) with a thickness of 5 mm and placed to the middle of the plate. The effect of stiffener on the SPL at a specified location is shown in Fig. 12.

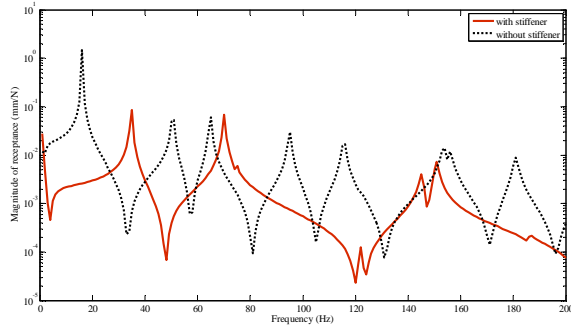


Fig. 11. The effect of stiffener on transverse FRFs.

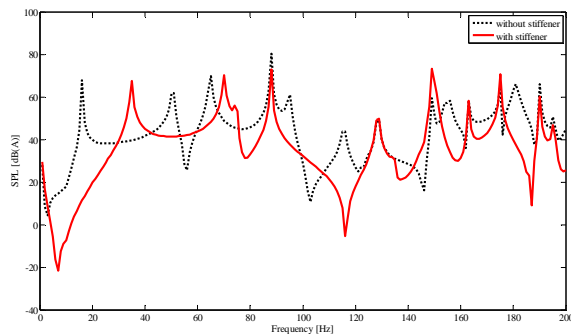


Fig. 12. The effect of stiffener on sound pressure level.

3.5 Non-linear Structural Modification

The structural modification method can also be used for non-linear modifications. Once the non-linear forces in a system is expressed as a response level dependant non-linearity matrix $[\Delta]$ multiplied by displacement vector, then the modification method can easily be adopted by treating non-linearity matrix as an equivalent dynamic stiffness matrix, as discussed in section 2.3. When the system is non-linear, the pseudo receptance matrix calculated from equation (13) will be response level dependent, and the solution will require an iterative procedure. As an example application a cantilever beam welded to a smaller beam on elastic supports having cubic stiffness properties (with cubic stiffness constant of 2×10^{12} N/m³) is considered (Fig. 13) [31]. The properties of the original and modifying beams are given in Table 1. Material damping with a loss factor of 0.12% is assumed in the calculations.

Frequency responses of the modified beam at the point where the force of 1000 N is applied are shown in Figures 14-16 around the first three modes, respectively.

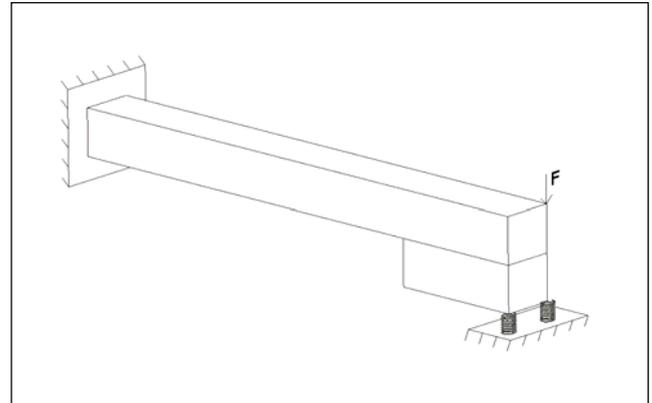


Fig. 13. Cantilever beam welded to another beam on non-linear supports.

Table 1. Properties of the beams.

	Original Beam	Modifying Beam
Young's Modulus	200 GPa	200 GPa
Poisson's Ratio	0.3	0.3
Density	7850 kg/m ³	7850 kg/m ³
Cross Section	100 x 100 mm ²	100 x 100 mm ²
Length	1000 mm	250 mm

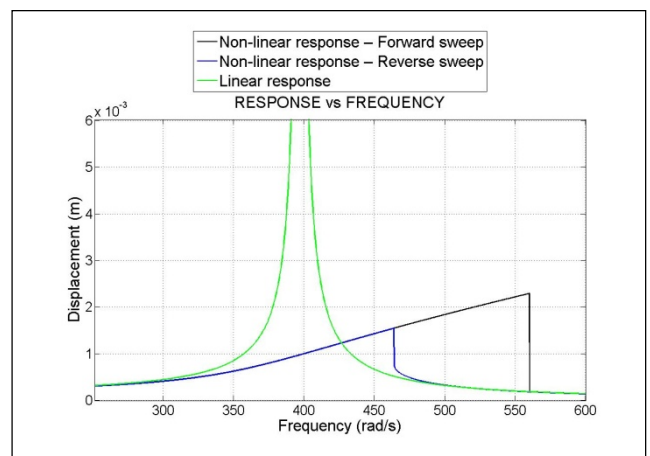


Fig. 14. Frequency response around first mode.

The frequency responses calculated by using the modification method proposed are verified by the

response predictions obtained from the analysis of the whole system by using harmonic balance method. In an ongoing research a software program is being developed which is compatible with a standard FE program so that non-linear modification problems of real structures with large DOFs can be solved.

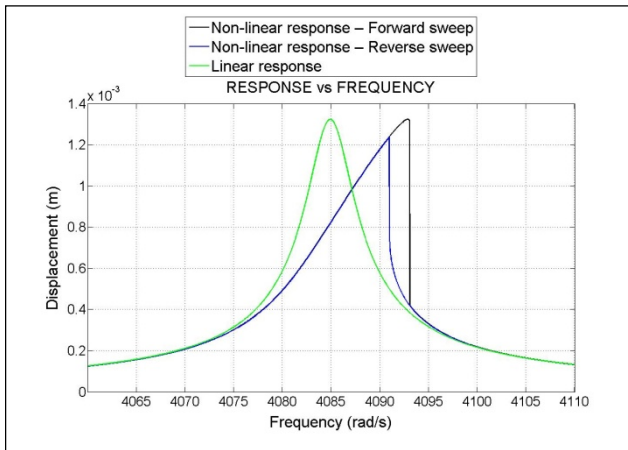


Fig. 15. Frequency response around second mode.

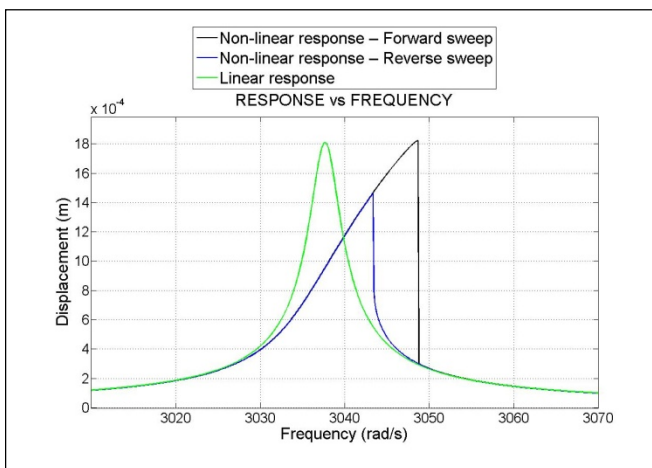


Fig. 16. Frequency response around third mode.

3.6 Effects of Bearing Stiffness on Rotor Dynamics

As last two examples, the use of the structural modification method in machine dynamic analysis is given. Let us first consider the stepped shaft on two bearings as shown in Fig. 17. The shaft is modeled with finite elements, whereas discrete models are used for the

bearings (each bearing is represented by 2x2 stiffness and damping matrices). In order to study dynamic response of the shaft on different sets of bearings in a design problem, the complete system needs to be analyzed each time with the selected bearing properties. However, this may require considerable computational effort when the system has large number of degrees of freedom and the effects of several different sets of bearings have to be studied. Instead, the FE dynamic analysis of the shaft with free end conditions can be made only once, and the results can be coupled with bearing dynamics by using the modification method. This approach has also the advantage of making computations only for the required coordinates. Then, the order of the matrices used in equations will be determined by the number of coordinates where the response is calculated and/or forcing is applied, and also by the number of coordinates related with modifications. Furthermore, the order of the matrix to be inverted in the computations is equal to only the DOFs related with modifications, which is 4 in this simple example application, although the total degree of freedom of the shaft is 30 000. Then, once the related FRFs are calculated for the free-free shaft by using FE analysis, the response of the system with various different sets of bearings can be obtained by making computations with very small size matrices, irrespective of the total DOF of the FE model employed which can be much higher depending on the complexity of the shaft geometry and the mesh sizes used.

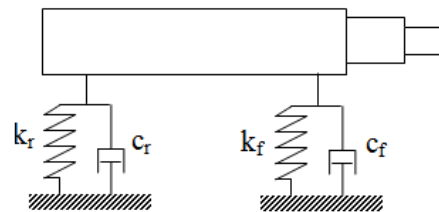


Fig. 17. An elastic shaft on elastic bearings.

Fig. 18 shows the frequency responses at the tip point of the shaft at the RHS, for a unit harmonic force at the same point for free-free end conditions as well as for two different sets of bearing stiffness values. As expected, bearing dynamics affect only the first two modes of the system without changing the response at elastic modes of the shaft notably. Fig. 19 shows the zoomed responses at these two modes. With this very fast analysis method, the dynamics of the system with many different bearings can be studied in a design problem. The effect of any



other element on the shaft (for instance a disk) can be studied in a similar manner.

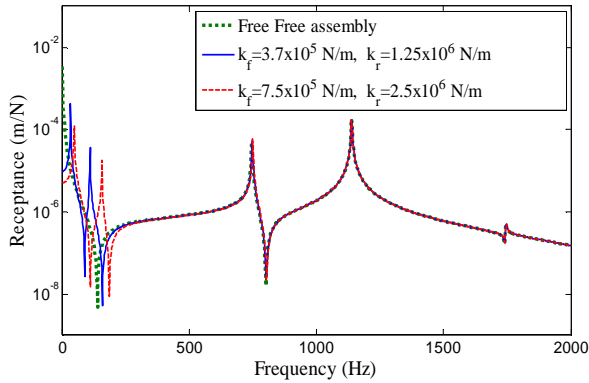


Fig. 18. FRFs for the shaft with different bearing stiffnesses (k_f , k_r : Front and rear bearing stiffness).

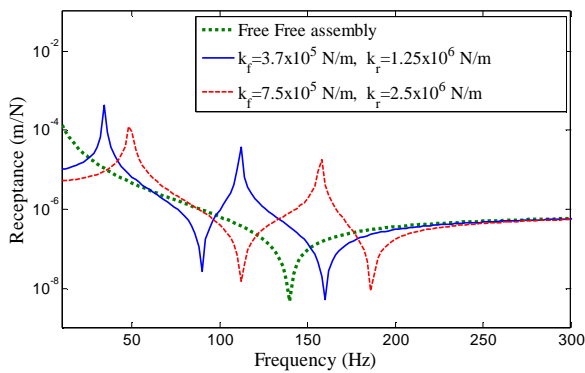


Fig. 19. Zoomed FRFs for the shaft with different bearing stiffnesses.

When the masses of the bearings are required to be included into the analysis, the modifications will introduce additional DOFs, which will make it necessary to use the equations given in section 2.2 rather than those in section 2.1. Such an example is given below.

Consider the shaft-bearing system shown in Fig. 20, where the bearings carrying the shaft are modelled as spring-mass systems in three directions. In order to study the effect of bearing dynamics on the dynamic response of the shaft, first the FRFs of the shaft with free-free end conditions are obtained by using FE analysis, and then the effects of different sets of bearings on the harmonic response of the shaft-bearing assembly are studied by employing the modification method. Three different sets of stiffness values are used for each bearing, and two sets of analyses are carried out, in each set keeping one bearing properties fixed and changing the other.

As in the previous case, it is observed that the bearing properties affect only the first two rigid body modes, without changing the flexible modes notably. Fig. 21 and 22 show the effect of left and right bearings, respectively, on shaft dynamics. In this example case, left bearing flexibility affects mainly the first rigid body mode, while the right bearing flexibility has a major effect on the second rigid body mode.

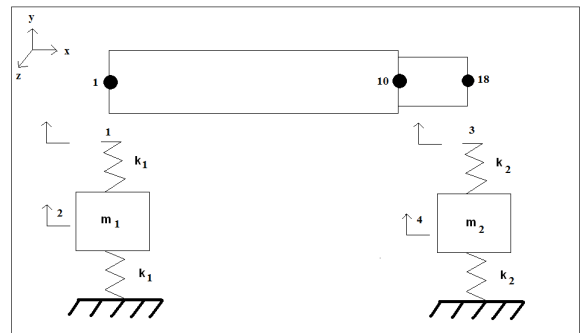


Fig. 20. An elastic shaft on elastic bearings – masses of bearings are included.

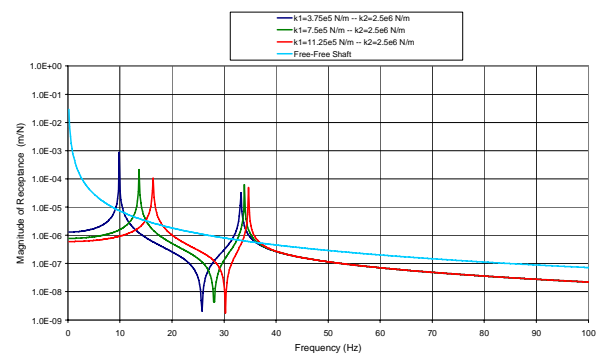


Fig. 21. Effect of stiffness of the left bearing on direct point FRF of node 10.

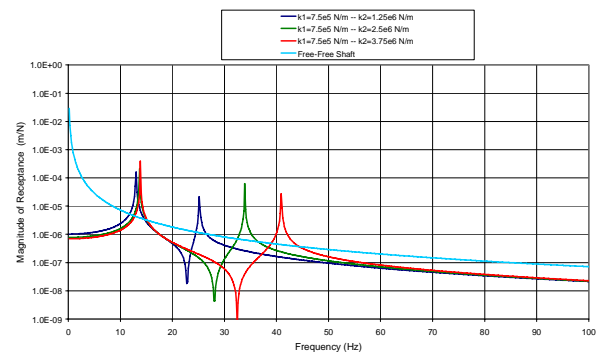


Fig. 22. Effect of stiffness of the right bearing on direct point FRF of node 10.



4. Conclusions

In this paper, a noble structural modification method developed by the author two decades ago [3], based on his earlier study for calculating receptances of non-proportionally damped systems from their undamped counterparts [1], is revisited. The method has been successfully used in structural and machine dynamics research in several different fields, ranging from geared rotor dynamics to turbine blade vibrations, and from machine tool dynamics to vibro-acoustic analysis. In this paper, examples from some of the recent applications are presented.

In the method suggested, the dynamic behavior of a modified system, (expressed in terms of FRFs) is calculated from that of the original system and modifying system matrices. The method can be used for modifications which result in additional degrees of freedom, which means coupling a sub-system to an original system. This formulation makes it possible to apply the method for continuous modifications as well. As the formulation is based on FRFs, it is sufficient to keep only the coordinates at which a force is applied and/or response is required, in addition to the modified coordinates, by eliminating the rest of the coordinates from the matrices in the formulation. Although, theoretically, the method can also be used with experimentally measured FRFs of the original system, in structural dynamic problems, due to the difficulty in measuring FRFs corresponding to rotational DOFs, it is more appropriate to use the method in theoretical analyses.

In this method a matrix inversion is required; however the order of the matrix to be inverted is equal to the number of degrees of freedom on which modifications are applied, regardless of the total DOF of the system. Therefore, the method is extremely advantageous when the total DOF is high, but the modification is local. In such cases the computational effort is drastically reduced, especially when similar analyses are to be repeated several times in a design stage for various modification alternatives. Furthermore, when there is no additional DOF, in order to avoid matrix inversion the method can also be used with the efficient recursive solution algorithm developed for damping modifications [2].

The case studies presented in this paper are from recent applications of the method in several different research areas, and they show the versatility of the method. The method has also served as a starting point for research in several other areas, which is beyond the scope of this paper, and therefore only references to some of the related papers are given here.

Acknowledgement

The works of my present and former students whose papers are cited here are gratefully acknowledged. The author also thanks to O. Özşahin, G. Canbaloglu and T. Kalaycıoğlu for additional numerical examples prepared.

References

- [12]. Özgüven, H. N., "Determination of Receptances of Locally Damped Structures", Proceedings of the Second International Conference on Recent Advances in Structural Dynamics, v.2, pp.887-892, Southampton, England, April 9-13, 1984.
- [13]. Özgüven, H. N., "A New Method for Harmonic Response of Non-proportionally Damped Structures Using Undamped Modal Data", Journal of Sound and Vibration, v.117, n.2, pp.313-328, September 1987.
- [14]. Özgüven, H. N., "Structural Modifications Using Frequency Response Functions", Mechanical Systems and Signal Processing, v.4, n.1, pp.53-63, 1990.
- [15]. Sherman, J. and Morrison W. J., "Adjustment of an Inverse Matrix Corresponding to Changes in the Elements of a Given Column or a Given Row of the Original Matrix", Ann. Math. Statist., v.20, pp. 621, 1949.
- [16]. Şanlıtürk, K. Y., "An Efficient Method for Linear and Nonlinear Structural Modifications", Proceedings of ESDA2002: 6th Biennial Conference on Engineering Systems Design and Analysis, ESDA2002/APM-028, Istanbul, Turkey, July, 2002.
- [17]. Köksal, S., Cömert, M.D. and Özgüven, H. N., "Reanalysis of Dynamic Structures Using Successive Matrix Inversion Method", Proceedings of the 24th International Modal Analysis Conference, St. Louis, Missouri, January 30 - February 2, 2006.
- [18]. Bae, H., Grandhi, R. V. and Canfield, R. A., "Successive Matrix Inversion Method for Reanalysis of Engineering Structural Systems", AIAA Journal, v.42, n.8, pp.1529-1535, 2004.
- [19]. Köksal, S., Cömert, M. D. and Özgüven, H. N., "Comparison and Application of Reanalysis Methods", Proceedings of the 25th International Modal Analysis Conference, Orlando, Florida, 19-22 February 2007.
- [20]. Maliha, R., Doğruer, C. U. and Özgüven, H. N., "Nonlinear Dynamic Modeling of Gear-Shaft-Disk-Bearing Systems Using Finite Elements and Describing Functions", ASME Journal of Mechanical Design, v.126, n.3, pp.528-534, 2004.
- [21]. Çiğeroğlu, E. and Özgüven, H. N., "Non-linear Vibration Analysis of Bladed Disks with Dry Friction Dampers", Journal of Sound and Vibration, v. 295, pp. 1028-1043, 2006.
- [22]. Ertürk, A., Özgüven, H.N. and Budak, E., "Analytical Modeling of Spindle-Tool Dynamics on Machine Tools Using Timoshenko Beam Model and Receptance Coupling for the Prediction of Tool Point FRF", International Journal of Machine Tools and Manufacture, v. 46, n. 15, pp. 1901-1912, 2006.
- [23]. Budak, E., Ertürk, A. and Özgüven, H. N., "A Modelling Approach for Analysis and Improvement of Spindle-Holder-Tool Assembly Dynamics", CIRP Annals, v.55, n.1, pp. 369-372, 2006.
- [24]. Ertürk, A., Özgüven, H. N. and Budak, E., "Effect Analysis of Bearing and Interface Dynamics on Tool Point FRF for Chatter Stability in Machine Tools by using a New Analytical Model for Spindle-Tool Assemblies", International Journal of Machine Tools and Manufacture, v. 47, n.1, pp. 23-32, 2007.
- [25]. Atlar, S., Budak, E. and Özgüven, H. N., "Modeling Part Dynamics and Chatter Stability in Machining Considering Material Removal", Proceedings of 1st International Conference on Process Machine Interactions, pp. 61-72, Hannover, Germany,



- September 3-4, 2008.
- [26]. Alan, S., Budak, E. and Özgüven, H. N., “Analytical Prediction of Part Dynamics for Machining Stability Analysis”, *International Journal of Automation Technology* (special issue on Modeling and Simulation of Cutting Process), v. 4, n. 3, 2010.
- [27]. Başdoğan, İ., Canbaloglu, G., Kamci, G. and Özgüven, H. N., “A Structural Modification Methodology Adapted to a Vibro-Acoustic Model to Improve the Interior Noise”, *EURONOISE 2009*, Edinburgh, October 26-28, 2009.
- [28]. Demirkan, Ö., Başdoğan, İ., Özgüven, H. N. and Çalışkan, M., “Prediction of Vibro-Acoustic Response of Enclosed Spaces by Using Structural Modification Techniques”, *Proceedings of the 24th ISMA International Conference on Noise and Vibration Engineering*, Leuven, Belgium, September 20-22, 2010.
- [29]. Budak, E. and Özgüven, H. N., “A Dynamic Analysis Method for Harmonically Excited Nonlinear Structures”, *Structural Vibration and Acoustics*, ASME, DE-Vol, 18-3, pp.23-29, 1989.
- [30]. Budak, E. and Özgüven, H. N., “A Method for Harmonic Response of Structures with Symmetrical Nonlinearities”, *Proceedings of the 15th International Seminar on Modal Analysis and Structural Dynamics*, v.2, pp. 901-915, Leuven, Belgium, September 17-21, 1990.
- [31]. Budak, E. and Özgüven, H. N. “Iterative Receptance Method for Determining Harmonic Response of Structures with Symmetrical Non-Linearities”, *Mechanical Systems and Processing*, v.7, n.1, pp. 75-87, January 1993.
- [32]. Tanrikulu, Ö., Kuran, B., Özgüven, H. N. and Imregün, M., “Forced Harmonic Response Analysis of Nonlinear Structures Using Describing Functions”, *AIAA Journal*, v.31, n.7, pp. 1313-1320, July 1993.
- [33]. Kozak, M. T., Cömert, M. D. and Özgüven, H. N., “A Model Updating Routine Based on the Minimization of a New Frequency Response Based Index for Error Localization”, *Proceedings of the 25th International Modal Analysis Conference*, Orlando, Florida, February 19-22, 2007.
- [34]. Kozak, M., Öztürk, M. and Özgüven, H. N., “A Method in Model Updating Using Miscorrelation Index Sensitivity”, *Mechanical Systems and Signal Processing*, v.23, pp. 1747-1758, 2009.
- [35]. Özer, M. B. and Özgüven, H. N., “A New Method for Localization and Identification of Non-Linearities in Structures”, *Proceedings of ESDA 2002: 6th Biennial Conference on Engineering Systems Design and Analysis*, ASME, İstanbul, Turkey, July 8-11, 2002.
- [36]. Özer M. B., Özgüven H. N. and Royston, T. J., “Identification of Structural Non-linearities Using Describing Functions and the Sherman-Morrison Method”, *Mechanical Systems and Signal Processing*, v.23, n.1, pp. 30-44, 2009.
- [37]. Özşahin, O., Özgüven, H. N. and Budak, E., “Analysis and Compensation of Mass Loading of Accelerometers on Tool Point FRF Measurements for Chatter Predictions”, *International Journal of Machine Tools and Manufacture*, v. 50, n. 6, pp. 585-589, 2010.
- [38]. Hang, H., Shankar, K. and Lai, J. C. S., “Prediction of the Effects on Dynamic Response due to Distributed Structural Modification with Additional Degrees of Freedom”, *Mechanical Systems and Signal Processing*, v. 22, pp. 1809–1825, 2008.
- [39]. Hang, H., Shankar, K. and Lai, J. C. S., “Effects of Distributed Structural Dynamic Modification with Reduced Degrees of freedom”, *Mechanical Systems and Signal Processing*, v.23, pp. 2154-2177, 2009.
- [40]. Hang, H., Shankar, K. and Lai, J. C. S., “Effects of Distributed Structural Dynamic Modification with Additional Degrees of Freedom on 3D Structure”, *Mechanical Systems and Signal Processing*, v. 24, pp. 1349-1368, 2010.
- [41]. Canbaloglu, G. and Özgüven, H. N., “Structural Modifications with Additional DOF - Applications to Real Structures”, *Proceedings of the 27th International Modal Analysis Conference*, Orlando, Florida, February 4-7, 2009.
- [42]. Kalaycıoğlu, T. and Özgüven, H. N., “Harmonic Response of Large Engineering Structures with Nonlinear Modifications”, (under preparation).



BioMimetic/BioInspired Robots and Mechatronics Engineering Design

Abdülkadir ERDEN^{1*}

^{1*}Department of Mechatronics Engineering
Atılım University, Ankara, Turkey
aerden@atilim.edu.tr

Abstract

It is well known that there are many amazing studies for using inherit advantages of biological systems to solve engineering problems and improve design performances. Although these approaches are often ad hoc and they rely mostly on the experience of the designer personally, available knowledge and facilities of the current engineering environment, existing approaches are highly valuable efforts toward further studies on the development of a systematic and formal methodology for biomimetic/biologically inspired (bioinspired) engineering design. Various research works at the Atılım University on bioinspired design methodology, behavioral modeling of biological systems and robots, and bioinspired design at senior level student projects are presented in the paper.

Keywords: Biomimetic/bioinspired design, behavioral modeling, mechatronics engineering design, bio-robots.

1. Introduction

Engineering is defined as an *activity of overcoming difficulties for practical applications of concepts that are proved to be true theoretically*. Engineering activities include mental activities, paperwork, human power and machine power. **Engineering design** is a decision-making engineering activity against true physical, economical and social limitations to develop materials, products or processes that satisfy a human need. It is more than a combination of *engineering* and *design*. It is a phenomenon with a blend of complex concepts and activities, so that both comfort and problems of the humankind are closely related to the availability of natural sources, and by using the human creativity. It is the heart of technology generation, and it is a process that develops human comfort and human problems out of human imagination.

Design activity is strikingly different from the well-known scientific work. The basic motivation behind the scientific activity is the intellectual curiosity of the scientist, whereas design is initiated by the recognition

and identification of a need. The scientist works in an environment in which time and money are not the primary factors, whereas design activity is constrained with a number of factors including time, finance and other resources. The scientist seeks peer recognition of his work, whereas the output of design activity is always subject to wide spread acceptance by relevant part of society.

The most striking **nature of design** problem is that it is *open-ended* and *ill-structured*. Contrary to scientific problems, there are usually many acceptable alternative solutions to a stated design problem. Although none of these solutions can be claimed to be correct in strict scientific sense, only one of the feasible solutions emerges as the best one or simply as the preferred design. Furthermore, design problems cannot normally be solved by routine application of mathematical equations in a structured way (*design computations*). Instead, the design process is of *iterative nature*, that is; the only way to improve design is through time taking iterations. Design activity needs the acquisition of a broad database, and the solution to design builds on several decisions that have to be taken at various levels of design work (*cumulative nature of design*). More striking is the fact that a technical solution may not be sufficient alone, issues like cost, safety, aesthetics, market preferences, standards and codes cannot be ignored and may emerge as overwhelming factors in the final design. The engineering design is always subject to physical, economic, social and political constraints.

As microprocessor applications are introduced in product development, overall and integrated design approach benefitted the synergy of integration in mechanical, electrical and computer technology into a simple product. **Mechatronics** is considered in its broader sense as the name given to the special philosophy behind the design and development of the microprocessor-based products. The reflection of mechatronics philosophy on the design methodology of these products is defined as the **mechatronic design** or **mechatronics engineering design**.



There are various definitions about the mechatronics in the literature. One of the important definitions states that mechatronics is the synergistic integration of mechanical engineering with electronics and intelligent computer control in the design and manufacture of products and processes [1-3]. Mechatronics is also defined as an interdisciplinary field of engineering science, which characterizes the interconnections between mechanical engineering, electrical engineering and computer science such that these interconnections are the basis for an "intelligent" behavior of a machine [4]. The common features of mechatronics extracted from these definitions are mainly the application of computer-based digital control techniques, through various interfaces of different complexity to achieve efficient mechanical functions.

Mechatronics is mainly a product-oriented approach and mechatronic philosophy should be applied carefully particularly in the conceptual design phase of the product development. This is because the functional and geometric integration of **mechatronic organs** is performed mostly during conceptual design. A special methodology of mechatronic design is necessary because of the following reasons;

1. Designers with different engineering background in a design team experience difficulty to describe and discuss their approaches at the conceptual stage, without going into the details. These efforts result in time loss in product development, increase cost, blur the focus point of the design and therefore; an inefficient working environment.

2. Engineering creativity require availability of all the design information together with possible solution principles. However, usually few designers are involved in the creative stage of the design; hence many alternatives are omitted because of the missing concepts, weak and narrow knowledgebase and/or poor communication among the team members.

3. Technologically, it is difficult to divide the design activities into mechanical, electronics and software parts, and interfaces between the three areas require special knowledge outside these engineering branches.

4. Overall design evaluation and verification are difficult until a very late stage of the project. Hence, redundant design, or functionally oversafe designs are very common.

In addition to the above items, the need for a special design methodology for functional description and conceptual design arises from the fact that a design methodology, which handles total aspects of mechanics, electronics and software combination, is missing. Buur states [2] that **design methodologies** of different fields are not sufficient for mechatronic design because:

1. Machine design methodology has no means of abstractly describing the logical relations between

functions (i.e. when, in which sequence and under which conditions the functions must be performed) since these relations are built in a complex way into the physical structure of the machine.

2. Electronic design methodology is mainly based on the analysis of 2-D structures. There are neither tools nor traditions for formulating alternative concept ideas.

3. Software design methodology is not capable of bridging the gap between abstract functional descriptions, physical effects and spatial relations, since such effects and relations do not exist in the software domain.

Some other researchers also agree that a careful application of mechatronic design methodology in the conceptual design stage is the key issue to be successful in the development of mechatronic products [5].

There are many diverging views on the nature of design. One is that design is experiential in nature. This is rather traditional view and it is based on the belief that creativity cannot be taught, and should not be interfered with. Accordingly, designing would be the only way to learn design. The modern view, however, emphasizes the need for a more scientific approach to the design activity. The basic argument underlying this model is that design is a cognitive activity and its study must be through experiential learning within the framework of a cognitive process [6].

Engineering design is a unique activity where a physical design artifact is created from an abstract need after human imagination. Although the methodology is dependent on the particular design need, all of the engineering design activities have some common engineering features. They are;

- 1- Engineering design is densely **creative** at the beginning, and significance of creativity decreases towards the end of the process,

- 2- Engineering design is **iterative** during the whole design process both at macro scale and at element scale,

- 3- Engineering design is **methodological (productive)** towards the end of the design process.

There are many published work on these topics, however it is beyond the scope and aim of this paper. Mechatronics engineering design is not an exception and it has all of the features listed above. Furthermore; robots, products of mechatronics engineering design, are normally inspired from or mimicking of human, animals, insects etc. Biological systems are studied closely by the mechatronics engineering and many successful engineering applications are originated from design ideas of biological systems. It is always highly challenging for mechatronics engineers to study biological systems to extract design hints.



2. Engineering and Design in Nature

It is well known that the “Nature is the world’s foremost designer with billions of years of experience and boasting the most extensive laboratory available, it conducts research in every branch of engineering and science” [7, 8]. The evolution process creates highly effective and power efficient biological mechanisms. The nature is the most important source of engineering materials, processes, methods, structures, tools, devices, mechanisms, systems etc. through inspiration to foster engineering creativity and innovation.

One of design criteria of design in nature is the minimum energy consumption with maximum functional performance. Additionally; other criteria like efficiency, functionality, precision, self-repair, and durability [9] are considered. Structural and functional perfection of the biological systems are achieved through evolution, the nature is an experimental platform of science and engineering. The idea of inspiration and/or imitating of natural systems have initiated bio-mimetic and/or bio-inspired design for engineering designers. Although the nature has always served as a model with their superior features, such as metabolism, adaptability, self maintenance (autonomy), self repair, growth, replicability, evolution etc [10], transfer of knowledge between engineering and biology domains, and even understanding of each other domain is difficult and not very successful. An immediate difficulty is observed to transfer knowledge from biology domain to engineering domain and to transfer requirements from engineering domain to biology domain. It is an essential requirement to develop mutually strong relations between two domains. There are many attempts to develop and use databases to transfer knowledge, they are useful to develop advanced tools towards better bioinspired engineering tools.

3. Biomimetic and/or Bioinspired Design Process

A biological inspiration process called as “**Biomimetic**” or “**Bioinspired**” aims to develop creative and novel artificial products in engineering domain via inspiring ideas from structures, materials, processes, and functions in biology domain. Developing of a systematic biomimetic/bioinspired design (**BID**) is challenging for engineers for many reasons, such as; low cost, high efficiency, and high reliability. Many case studies are available in literature. There are mainly two design approaches based on the starting point of the design. One of them is the “**problem-based design**” approach in which the design starts with an engineering problem and the other is the “**solution-based design**” approach which starts by selecting of a biological system.

BID includes both engineering features and scientific features in a well balanced medium with optimum solutions. You may refer to Eroğlu’s paper for further information. [11]. Some examples of implementation for both approaches are summarized in *Table 1*.

Problem-Based BID Process (PB_BID) is enhanced by the opportunity to look into biological systems with a focused engineering problem and context to see “what they do” and then to transform the useful forms, processes, and systems within the design context [12, 13]. This approach suggests that a design starts with a problem definition in engineering domain. The problem is decomposed into its elements such as functions, forms, behaviors, and structures using top-down approach. Then, investigation and selection of a biological system should be started in such a way that matching components can be found for any of the decomposition elements at any level. After matching, implementation of the biological systems into the engineering systems should be started.

Most of the published studies utilize only one biological system to meet maximum number of the elements for decomposition of the engineering problem. Then, for the elements that cannot match with the selected biological system, conventional artificial elements on the required system elements are added. For example; if a bee is selected for a mobile navigation problem used on a terrain surface, the designer add a conventional caterpillar wheel system on the navigation system for terrain surface which is independent from the locomotion mechanism of the bee. This is one of the weakest point and need to be studied further in detail. There should be no limit on the number and variety of bioinspired ideas for a unique and simple engineering problem.

Solution-Based BID Process (SB-BID) is characterized if a designer starts his/her work by focusing on a specific biological system without any engineering problem in his/her mind and attempts to mimic the behavior of this system in the engineering domain and it is emerged in practice [14, 15]. This is a typical process in developing completely new materials and devices [16].

In solution-based design approach, design starts with a selected biological system as a first step. This selection from the biological systems is based on an idea. For example; if the designer seeks a jumping mechanism, he/she can select grasshoppers into a clump of the rabbit, kangaroo, and like biological systems. As a second step, the designer should decompose the selected biological system to elements, such as, behaviors, functions, structures like problem-based design decomposition. Then, these elements are implemented into the engineering domain. Finally, the design should be evaluated. Each of the study with solution-based design



approach in the literature is only work on individual biological systems. The methodological problem in this approach that should be studied further is the selection

criteria and methodology in selecting the initial (starting) biological system.

Table 1: Some examples for problem-based design and solution-based design for BID

BID Approach	BID Case Study	Phenomenon in Nature	Engineering Application
Problem-Based Design	Flying studies of Leonardo da Vinci [17].	Birds wings	Flying machine designs (Flying)
	Flying studies of Hezarfen Ahmet Çelebi [18]	Eagle wings	Artificial eagle wings (Flying)
	A smart cloth [16].	Pinecones	A smart cloth (Textile)
	An armor [7].	Hard-shell body of turtles	An armor (Textile and Defense Industry)
	Big Dog, developed by Boston Dynamics Company [19].	A dog	Animal-like robot (big dog) (Robotics and Defense Industry)
	Eiffel's tower	Trabecular struts in the head of the human femur or the taper of a tulip stem.	A tower (Architecture)
	The roof of the Crystal Palace	Types of leaf such as beech or hornbeam	A palace (Architecture)
	A bionic car [16, 17].	The shape of the boxfish	A car (Automotive)
Solution-Based Design	Velcro [20]	Burrs	Velcro (hook and loop) (Textile)
	Gecko of University of Manchester [21].	the natural hairs covering the soles of gecko's feet	A new type of adhesive (Tribology and Robotic)

4. A BID Design Methodology Based on Hybrid Systems

Survey on the design approaches reveals that individual biological systems are used to inspire for each of problem-based and solution-based approaches. The use of a biological system for an engineering problem may decrease creativity, fidelity, and novelty. To increase the creativity and novelty all engineering elements burrowed from engineering problem can be matched with biological elements of decomposition from different biological systems in the problem-based approach. Similarly, in the solution-based design approach, different elements from

multiple biological systems can be combined to provide an artificial system. Hence, an inspired novel hybrid system that includes more than one biological system should be developed. These hybrid systems may be constructed by using a new SB-BID methodology as shown in Figure 1.

In this methodology, there are two main approaches; *reverse engineering* and *direct engineering*. Reverse engineering part is based on reverse engineering principles in biological domain and starts with multiple biological systems. The problem to be studied here is the scope of multiple biological systems. Direct engineering is based on known engineering design principles that start

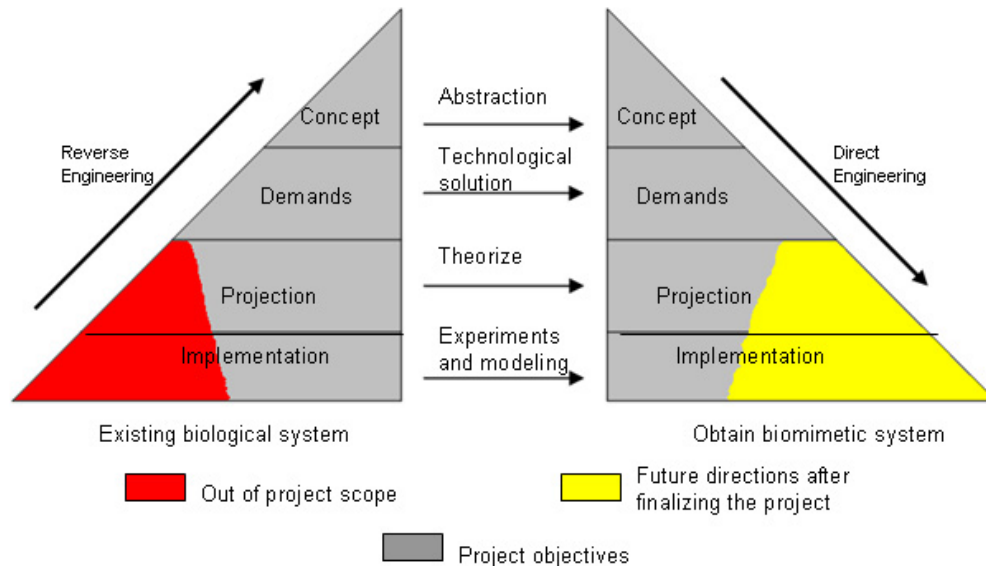


Figure 1 A BID methodology suggested by Atılım University and Craiova University in a joint TÜBİTAK project (2010-2012)

with a conceptualization phase to develop an artificial system or artificial systems. Although reverse engineering is based on biological domain and direct engineering is based on engineering domain, both have similar four phases; implementation, projection, demands, and concept. There are cross links between reverse engineering and direct engineering for each phase which constructs bridges between engineering and biological domains. This bridging may be unidirectional as it is illustrated in the figure for solution based BID. There may be many cases where bridging is required in both direction frequently all thru the design activities.

This model recalls one of the operational models for the design process that describes the design activities into two phases [22]:

- a. **Divergent Phase:** Recognition and definition of the problem search for alternative solutions.
- b. **Convergent Phase:** Feasibility study, selecting one from alternatives (decision-making), specification of the solution.

Further study is required on the model.

5. Modeling and Simulation of Bioinspired Design

Design process models aim at reflecting the methodology and characteristics of the engineering design process and propose strategies for the designers about how to proceed in the design procedure. One of the most important models in the engineering design process in this category is the systematic approach [23] in which the flow of work during the design process is divided into four main steps as follows;

1. **Clarification of the task** (collection of information about the requirements and about the constraints),
2. **Conceptual design** (establishment of functional structures, the search for suitable solution principles and their combinations into concept variants/design alternatives),
3. **Embodiment design** (development of layouts and forms for the concepts, evaluation of them, determination of a preliminary layout, optimization, definite layout, determination of production procedures),
4. **Detail design** (finalization of design).

Similarly, Product development process has four main phases;

1. Feasibility phase
2. Preliminary design phase
3. Detail design phase
4. Planning (Design review) phase

Both models can be modified for BID methodology in seven steps:

1. Survey in biology domain
2. Adoption of knowledge from biology domain into engineering domain
3. Iterative (biology and engineering domains) conceptual design
4. Desktop design on engineering domain for behavioral design
5. Desktop tests for behavioral design performance
6. Packaging-Integration of the desktop design into biomimetic/bioinspired system/robot

7. Iterative tests (biology and engineering domains) for the final design

The model has been tested four years in Atılım University senior level bioinspired design projects and

early results are highly promising to develop successful bioinspired robots. Further systematic results will be available in future. A picture of these bioinspired robots is given in *Figure 2*.

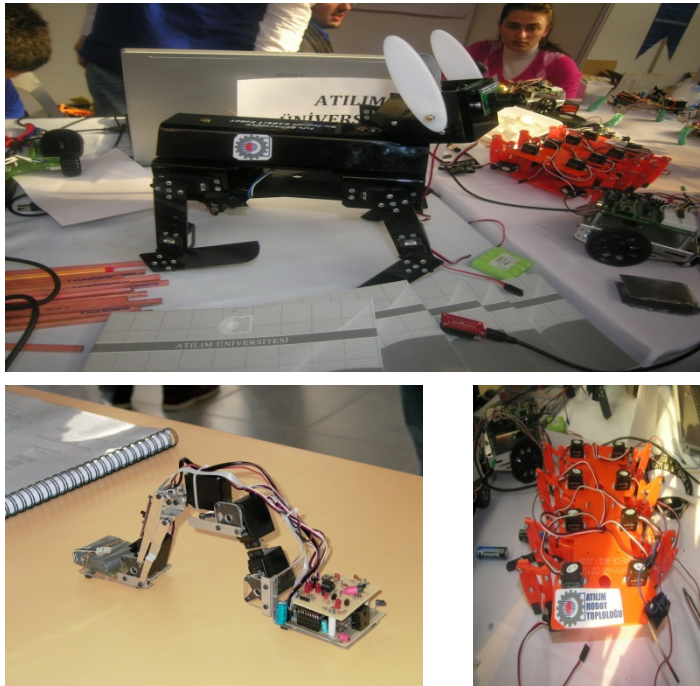


Figure 2: Examples of bio-inspired robots a senior level mechatronics engineering capstone design projects courses.

One of the key features of the 7-step design process model is the behavioral modeling and simulation of the biological systems and the engineering systems before the completion of the engineering design. Behavioral models are particularly important for top-down design of multidisciplinary products such as mechatronic systems. During the conceptual design of such systems, intended “operational behavior” of the artifact is described without any physical realization. As design stages become more concrete, operational behavior can be refined so as to represent well defined mathematical descriptions of corresponding physical behaviors.

Conceptual design is an early stage of product development process and involves high degree of uncertainty at an abstract level [24]. A significant problem during conceptual design is to develop and simulate an artifact’s intended behavior to perform an overall function without developing its physical model. Thus designers need virtual prototypes based on behavioral models that reduce the design time at conceptual design stage. These models use operational-logical descriptions, which are based on the decomposition of a process into sub-processes [25]. From engineering design perspective, operational-logical descriptions are considered to be based

on the decomposition of an overall function into sub-functions and these descriptions are used to develop a model for the corresponding behavior of a design artifact at conceptual level.

The need for virtual prototypes resulted in related scientific research and one of the important approaches for developing virtual prototypes is to use behavioral models [26, 27]. Behavioral models for simulation are virtual prototypes that represent artifact behaviors rather than artifacts and they are typically based on operational-logical descriptions, algebraic descriptions or algorithms as stated in the extensive survey on the approaches for artifact-behavior simulation for conceptual design. In this survey, possible artifact behaviors are classified as a subdivision according to the common areas of physics such as mechanical behavior, acoustic behavior, optical behavior, etc. The effects of these behaviors can be observed as flows and transformations of energy and matter. Information exchange can also be simulated as an observable physical effect because it is based on signals encoded as energy or matter. However, as it is shown in the survey, certain simulation approaches disregard the physical background of information exchange. They operate on the interpretation of physical effects as



information. It is for that reason that *interpreted physical behavior* is distinguished as a special type of behavior alongside *observed physical behavior*.

Behavioral models and their software implementations [28-31] allow designers to represent concept variants and to analyze, compare and evaluate their possible behavior at an early design stage. There exist successful high level behavioral modeling and simulation tools developed for computational design support. Among these, Schemebuilder represents designs as schemes structured based on the Function/Means tree approach and simulations of these designs are performed by the help of a partially bond graph based ontology [32, 33]. Schemebuilder utilizes the facilities of Dymola which has been developed for modeling and simulation of the *dynamic behavior* of complex engineering systems. MathModelica [34] is another integrated development environment for advanced system modeling and simulation. These tools are based on an object-oriented modeling language Modelica [35], which is designed for *component-oriented modeling of complex physical systems*.

These tools and modeling languages compare designs based on performance evaluations. Since engineering systems are conceptualized as flows of energy, material and information [23]. Performance evaluations related with such systems require mathematical descriptions of these flows through the artifact. These flows become mathematically identifiable at concrete levels of the design process. However, at the most abstract level of the conceptual design phase, evaluation of performance is very difficult. Therefore in order to contribute the modeling and simulation of designs at this level, we initiated a research work to develop a Petri Net based model for simulating the behavior of concept variants in which information flow through any design artifact was modeled for concept design [36].

Information flow should be integrated with material and energy flows in a unified model for complete simulation of the behavior of design artifacts at the conceptual design phase. Modeling of the energy and material flow is treated as modeling the “operational behavior” of the design artifact. Combining logical behavior and operational behavior of an artifact in a unique modeling framework forms a bridge from symbolic reasoning in conceptual design to a formal one encountered in the embodiment and detailed design phases. In addition, modeling and integration of energy,

material and information flows allows the designer to analyze the interactions between various functions of the system under conceptual design and to determine any deadlocks related with the three flows for the operation of the system. Thus, necessary changes can be done during an early design phase to prevent any deadlock. Further research was initiated such that the ultimate objective is to develop a formal model for the operational behavior of a design artifact via integration of material, energy and information flow. We started with a demonstrative case study a model for representing the intended operational behavior of a nonexistent educational robot, a rabbit robot, is presented for conceptual design. The operational behavior of the robot is defined as composed of states and state transitions independent of any physical embodiment. Discrete Event System Specification (DEVS) and Petri Net formalism are used for the model. This representational model is the first step towards the development of a virtual prototype for the operational behavior of an educational robot.

6. Case Studies

Representation of the operational behavior of a non-existent design artifact requires formal modeling for qualitative simulation. An educational robot is considered as a hybrid system with continuous and discrete behaviors. A widely used formalism for modeling such systems is DEVS (Discrete Event System Specification) formalism [37]. It is used to create system models in which the discrete-event behavior is modeled using a Finite State Machine (FSM) called DEVS diagram and the continuous behavior is modeled algebraically using dedicated differential equations [25]. Since the present study concerns an artifact’s behavior at the conceptual design level, the model is developed only for the discrete-event behavior keeping the modeling of continuous behavior to further studies. The discrete-event behavior is represented by using DEVS formalism together with Petri Nets. This type of qualitative modeling allows designers to simulate the intended behavior of a non-existent artifact using the mathematical constructs of Petri Nets such as reachability and liveness (deadlock free operation) at conceptual design level. Petri Net model and initial marking representing initial state of rabbit robot is given in Figure 3. Further details can be found in Z. Erden’s paper [38].

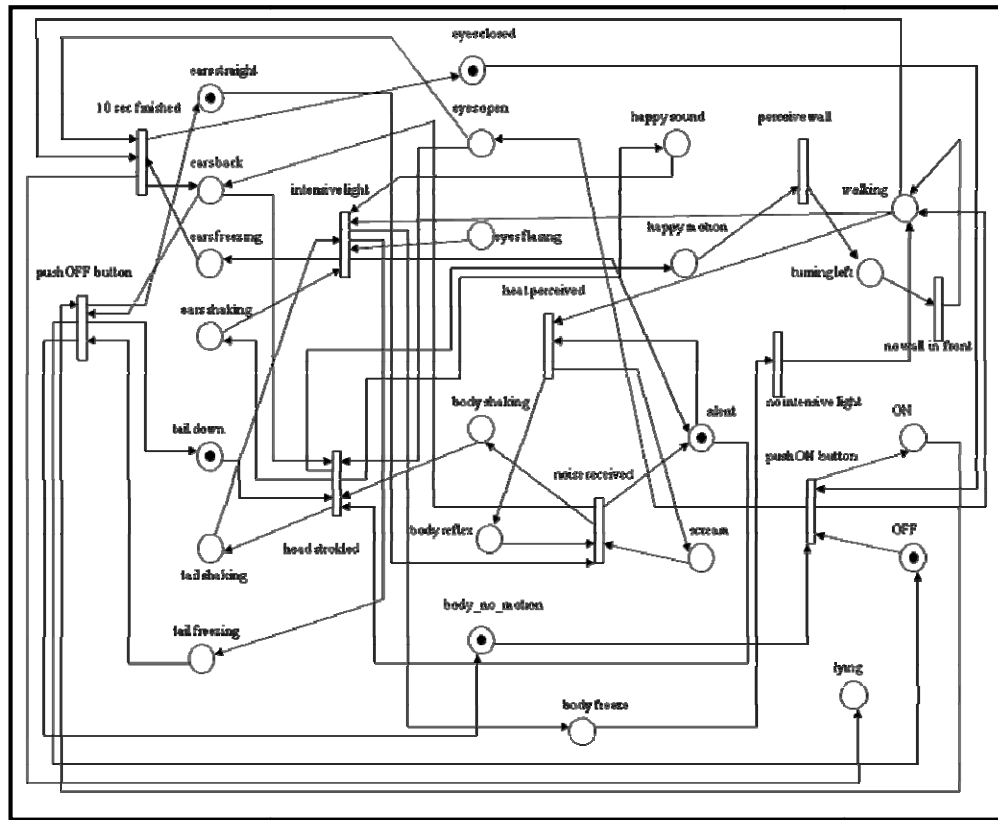


Figure 3: Petri Net model of a rabbit robot at initial state.

7. Conclusion

Biomimetic/bioinspired design (BID) is one of the most promising engineering design methodologies to foster engineering creativity and innovation. Many fine works and some case studies are available as challenging in many respects. Advances on the BID methodology may improve engineering design activities, by;

1. increasing variety of available technology on engineering domain,
2. reducing cost of the engineering products,
3. designing power/energy efficient and more reliable systems,
4. increasing human comfort,

5. developing environment friendly design (green design).

Any BID methodology may be decomposed into seven steps. Experimental work support that these steps improve efficiency of the design process in a systematic way with relatively low cost and shorter time. Behavioral modeling of bio-robots, hybrid bio-inspired robots are believed to be the main the key features of BID process to improve design quality and foster innovation.

Acknowledgement

Contributions of Dr. Zühal Erden and Aylin Konez Eroğlu are gratefully acknowledged in authoring the manuscript.



References

- [1]. C. Fraser, J. Milne, *Integrated Electrical and Electronic Engineering for Mechanical Engineers*, McGraw-Hill Book Co. 1994.
- [2]. J. Buur, *A Theoretical Approach to Mechatronic Design*, Inst. Engineering Design, IK Publ. 90.74 A, Tech. Univ. Denmark, 1990.
- [3]. J. Buur, *Mechatronics Design Methodology*, NATO ASI Workshop on the Advancements and Applications of Mechatronics Design in Textile Engineering, 1992.
- [4]. S. Schweitzer, *Advancements in Technology and its Impact on the Future Developments of Mechatronics Concept*, NATO ASI Workshop on the Advancements and Applications of Mechatronics Design in Textile Engineering, 1992.
- [5]. Bracewell and Sharpe, *The Use of Bond Graph Reasoning for Function-Means Analysis and Scheme Generation in an Integrated Interdisciplinary Design System*, Proc. Joint Hungarian-British International Mechatronics Conference, pp. 595-600, 1994.
- [6]. C.L. Dym, *Engineering Design: A Synthesis of views*, New York, Cambridge University Press, 1994.
- [7]. Y. Bar-Cohen, *Biomimetics: Biologically Inspired Technologies*, Taylor and Francis, 2006.
- [8]. Y. Bar-Cohen, *Biomimetics-using nature to inspire human innovation*, *Bioinspiration and Biomimetics*, vol. 1, no. 1, pp. 1-12, 2006.
- [9]. V. Giurgiutiu, A.M.E., Bayoumi G. Nall, *Mechatronics and Smart Structures: Emerging Engineering Disciplines for the third millennium*, *Mechatronics* 12 pp. 169-181, 2002.
- [10]. Y. Bar-Cohen, *Biologically Inspired Intelligent Robotics Using Artificial Muscles*, *Industrial Robots*, Emerald Publisher, Vol. 30, No. 4, pp. 331-337, 2003.
- [11]. A.K. Eroğlu, Z. Erden, A. Erden, *Towards Development Of A New Biomimetic/Bioinspired Design Methodology*, Proceedings The 14th International Conference on Machine Design and Production, TRNC, 2010.
- [12]. Anon, *The Natural Edge Project Engineering Sustainable Solutions Program*, "Unit 3 - Biomimicry/Green Chemistry; Lecture 9: Biomimicry - Design Inspired by Nature", 2008.
- [13]. V. Vakili, L.H. Shu, *Towards biomimetic concept generation*, ASME 2001 Design Engineering Technical Conferences Design Theory and Methodology (DETC'01), Pittsburgh, Pennsylvania, September 9-12, 2001.
- [14]. J.O. Wilson, *A Systematic Approach to Bio-Inspired Conceptual Design*, PhD. Thesis, Georgia Institute of Technology, Mechanical Engineering, 2008.
- [15]. M. Helms, S.S. Vattam, A.K. Goel, *Biologically inspired design: process and products*, *Design Studies*, vol. 30 No. 5 pp. 606-622, 2009.
- [16]. Anon, *Biomimetics: strategies for product design inspired by nature- a mission to the Netherlands and Germany*, Report of a DTI Global Watch Mission, 2007.
- [17]. J.F.V. Vincent, O.A. Bogatyreva, N.R. Bogatyrev, A. Bowyer, A.K. Pahl, *Biomimetics: its practice and theory*, *J R Soc Interface*, August 22; vol. 3(9), pp. 471-482, 2006.
- [18]. A. Terzioğlu, *The first attempts of Flight, Automatic Machines, Submarines and Rocket Technology in Turkish History*, Foundation for Science Technology and Civilisation, FSTC. 2007
- [19]. M. Raibert, K. Blankespoor, G. Nelson, R. Playter, R., and the BigDog Team, *BigDog, the Rough-Terrain Quadruped Robot*, Proceedings of the 17th World Congress The International Federation of Automatic Control Seoul, Korea, July 6-11, pp. 10822-10825, 2008.
- [20]. J.O. Wilson, and D. Rosen, *The effects of biological examples in idea generation*, *Design Studies*, vol. 31, no. 2, pp. 169-186, 2010.
- [21]. P. Hawken, *Innovation inspired by nature: Biomimicry*, *Industrial Ecology, ECOS*, Feb-Mar, pp. 27-29, 2006.
- [22]. W. Lewis, A. Samuel, *Fundamentals of Engineering Design*, Prentice Hall Inc., 1989.
- [23]. G.Pahl, and W. Beitz, *Engineering Design-A Systematic Approach*, The Design Council, London, UK., 1988.
- [24]. S.F. Qin, R. Harrison, A.A. West, I.N. Jordanov, and D.K. Wright, *A Framework of Web-Based Conceptual Design*, *Computers in Industry* (50), pp.153-164, 2003.
- [25]. W. Frederick van der Vegte, *A Survey of Artifact-Simulation Approaches from the Perspective of Application to Use Processes of Consumer Durables*, Proceedings of TMCE 2006, pp.617-632, 2006.
- [26]. M. M. Andreasen, *Modelling-The Language of the Designer*, *Journal of Engineering Design*, 5(2), 103-115, 1994.
- [27]. I. Horvath, *A Treatise on Order in Engineering Design Research*, *Research in Engineering Design*, 15, 155-181. 2004.
- [28]. S. Szykman, J. W. Racz and R. D. Sriram, *The Representation of Function in Computer-Based Design*, Proceedings of the 1999 ASME Design Engineering Technical Conferences, Las Vegas, Nevada, 1999.
- [29]. J. D. Summers, N. Vargas-Hernandez, Z. Zhao, J.J. Shah, and Z. Lacroix, *Comparative Study of Representation Structures for Modelling Function and Behaviour of Mechanical Devices*, Proceedings of DETC 2001: Computers in Engineering, Pittsburgh, PA., 2001.
- [30]. W. Y. Zhang, S. B. Tor and G. A. Britton, *A Graph and Matrix Representation Scheme for Functional Design of Mechanical Products*, *Int. J. Adv. Manuf. Technology*, 2004.
- [31]. G. Mocko, R. Malak, C. Paredis, and R. Peak, *A Knowledge Repository for Behavioural Models in Engineering Design*, In 24th



Computers and Information Science in Engineering Conference,
Salt Lake City, Utah, 2004.

- [32]. R. H. Bracewell and J. E. E. Sharpe, *Functional Descriptions Used in Computer Support for Qualitative Scheme Generation – Schemebuilder*, AI EDAM Journal - Special Issue: Representing Functionality in Design, 10(4), 333-346, 1996.
- [33]. D. A. Bradley, R. H. Bracewell and R. V. Chaplin, , “[Engineering Design and Mechatronics - The Schemebuilder Project](#)”, Research in Engineering Design, Vol. 4, No.4, pp.241-248, 1993.
- [34]. P. Fritzson, J. Gunnarsson and M. Jirstrand, *MathModelica-An Extensible Modelling and Simulation Environment with Integrated Graphics and Literate Programming*, Second International Modelica Conference, Germany, 2002.
- [35]. H. Elmqvist, S. E. Mattsson and M. Otter, *Modelica-A Language for Physical System Modelling, Visualization and Interaction*, IEEE Symposium on Computer-Aided Control System Design (CACSD '99), Hawaii, USA, 1999.
- [36]. Z. Erden, A. Erden and A.M. Erkmen, *A Petri Net Approach to Behavioral Simulation of Design Artifacts with Application to Mechatronic Design*, Research in Engineering Design, 14, pp.34-46, 2003.
- [37]. B. P. Ziegler, *DEVS representation of dynamic systems: Event-based intelligent control*, Proceeding of the IEEE 77, No. 1, 72-80, 1989.
- [38]. Z. Erden, *Representation of the Operational Behaviour of an Educational Robot at Conceptual Design Using Petri Nets*, Proceedings of 10th Biennial Conference on Engineering Systems Design and Analysis, ESDA2010, Istanbul, Turkey, 2010.



Kinematic Analysis of Spatial Mechanical Systems with a Systematic Approach to Describe Joint Kinematics

M. Kemal ÖZGÖREN

Mechanical Engineering Department
Middle East Technical University
06531 Ankara, Turkey
ozgoren@metu.edu.tr

Abstract

Considering a spatial mechanical system containing links with multiple joints, a systematic approach is introduced in order to describe the kinematic features of the joints in a convenient way. As an example, this approach is demonstrated on a parallel manipulator with six degrees of freedom and three legs. Afterwards, the kinematic analysis of the same manipulator is carried out both in the inverse and forward senses. The inverse kinematic solution is obtained analytically and the forward kinematic solution is obtained semi-analytically in such a way that the number of scalar equations to be solved numerically is reduced from twelve to three. During the solutions, the manipulation of the matrix expressions is facilitated by using the algebraic features of the rotation matrices in exponential form.

Keywords: Spatial Mechanisms, Parallel Manipulators, Inverse Kinematics, Forward Kinematics, Analytical Methods.

1. Introduction

For the spatial mechanical systems, the traditional systematic approach for the kinematic description of the joints is the Denavit-Hartenberg (D-H) convention [1]. However, the D-H convention has been introduced only for the single-axis joints, i.e. for the revolute, prismatic, screw, and cylindrical joints. Of course, it can be extended to the multi-axis joints by modelling them as if they are decomposed into a number of single-axis joints [2], [3]. However, this practice necessitates introducing extra virtual links between the hypothetical single-axis joints that replace the actual decomposed joints. Consequently, the complexity of the system increases. For example, if a spherical joint is replaced with three revolute joints, then two extra virtual links must be inserted next to the actual links connected by the spherical joint. Moreover, the D-H convention dictates the orientations of the link frames and the locations of their origins on the joint axes. Thus, there remains no

freedom for the analyst to assign the link frames independently of the joint axes. This lack of freedom may be considered as a drawback especially for a multi-joint link that takes place in a general mechanical system with several closed kinematic chains.

In the first part of this paper, the lack of freedom in assigning the link frames is eliminated by introducing an alternative systematic approach for the kinematic description of the joints. A preliminary version of this approach was introduced and used in Reference [4]. This approach also allows the multi-axis joints to be treated as they are without requiring any decomposition and extra virtual links.

In the second part of this paper, the joint description approach introduced in the first part is applied to a spatial parallel manipulator with six degrees of freedom and three legs. The legs are connected to the fixed and moving platforms with universal and spherical joints, respectively. The two pieces of each leg are interconnected with prismatic joints. The actuators of the manipulator command the displacements of the prismatic joints and the rotations about the fixed axes of the universal joints. Afterwards, the kinematic analysis of the same manipulator is carried out both in the inverse and forward senses. The inverse kinematic solution is obtained in a completely analytical way for both the actuated and unactuated joint variables. The forward kinematic solution for the location and orientation of the moving platform and the unactuated joint variables is obtained semi-analytically in such a way that the number of scalar equations to be solved numerically is reduced from twelve to three. Owing to the analytical nature of the solutions, the multiple and singular configurations of the manipulator are readily identified. During the solution procedures, the manipulation of the matrix expressions is facilitated by using the algebraic features of the rotation matrices in exponential form [4], [5].

2. Description of a Mechanical System

2.1. Description of the Link and Joint Frames

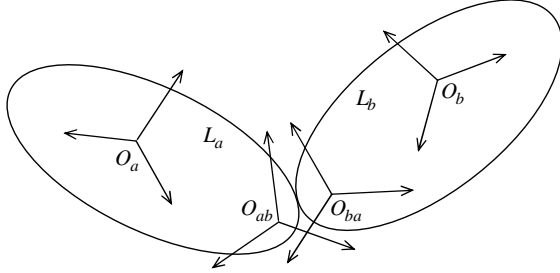


Fig. 1. Two Connected Links of a Mechanical System

Consider a spatial mechanical system that consists of several links such as L_a , L_b , L_c , etc. Two connected links of such a system is depicted in Fig. 1. The links are assumed to be rigid. The joint between L_a and L_b is denoted as J_{ab} or J_{ba} . On each of the links, e.g. L_a , there are attached several reference frames such as F_a , F_{ab} , F_{ac} , ..., F_{ap} . Here, F_a is the *link frame* and the others (F_{ab} , F_{ac} , ..., F_{ap}) are the *joint frames*. All these frames are assumed to be *orthogonal* and *right handed*. The joint frame F_{ab} on L_a and its companion F_{ba} on L_b are arranged in such a way that the relative displacement between the kinematic elements that form the joint J_{ab} is expressed in the simplest possible way. The origins of the frames F_a and F_{ab} are O_a and O_{ab} . Their unit basis vector triads are denoted as

$$\{\vec{\mathbf{u}}_1^{(a)}, \vec{\mathbf{u}}_2^{(a)}, \vec{\mathbf{u}}_3^{(a)}\} \text{ and } \{\vec{\mathbf{u}}_1^{(ab)}, \vec{\mathbf{u}}_2^{(ab)}, \vec{\mathbf{u}}_3^{(ab)}\}$$

Considering the two connected links in Fig. 1, the position (location and orientation) of L_b with respect to L_a can be expressed as described below.

a) Orientation Equation

$$\mathbf{C}^{(a,b)} = \mathbf{C}^{(a,ab)} \mathbf{C}^{(ab,ba)} \mathbf{C}^{(ba,b)} \quad (2.1)$$

Concerning Eq. (2.1), as a general symbol, $\mathbf{C}^{(p,q)}$ denotes the *orientation matrix* of a frame F_q with respect to another frame F_p . It also denotes the *component transformation matrix* from F_q to F_p . In Eq.

(2.1), $\mathbf{C}^{(a,ab)}$ and $\mathbf{C}^{(ba,b)}$ are constant matrices, whereas $\mathbf{C}^{(ab,ba)}$ is a variable matrix being a function of the variable or variables of the joint J_{ab} . The details of $\mathbf{C}^{(ab,ba)}$ will be taken up later in Section 3, which is about joint descriptions.

b) Location Equation

The vector equation that expresses the location of O_b with respect to O_a is

$$\vec{\mathbf{r}}_{a,b} = \vec{\mathbf{r}}_{a,ab} + \vec{\mathbf{r}}_{ab,ba} + \vec{\mathbf{r}}_{ba,b} \quad (2.2)$$

Concerning Eq. (2.2), as a general symbol, $\vec{\mathbf{r}}_{p,q}$ denotes the *location vector* directed from the origin O_p of a frame F_p to the origin O_q of another frame F_q . As expressed in F_a , the matrix equation corresponding to Eq. (2.2) is written as

$$\mathbf{r}_{a,b}^{(a)} = \mathbf{r}_{a,ab}^{(a)} + \mathbf{r}_{ab,ba}^{(a)} + \mathbf{r}_{ba,b}^{(a)} \quad (2.3)$$

Concerning Eq. (2.3), considering a vector $\vec{\mathbf{r}}$, $\mathbf{r}^{(a)}$ is the *column matrix* that consists of the components of $\vec{\mathbf{r}}$ in a frame F_a . In other words, $\mathbf{r}^{(a)}$ is the matrix representation of $\vec{\mathbf{r}}$ in F_a . That is,

$$\vec{\mathbf{r}} = \sum_{k=1}^3 r_k^{(a)} \vec{\mathbf{u}}_k^{(a)} \Rightarrow \mathbf{r}^{(a)} = \begin{bmatrix} r_1^{(a)} \\ r_2^{(a)} \\ r_3^{(a)} \end{bmatrix} \quad (2.4)$$

The matrix representation of $\vec{\mathbf{r}}$ in F_a can be denoted compactly as

$$\mathbf{r}^{(a)} = \{\vec{\mathbf{r}}\}_{F_a} \quad (2.5)$$

Note that $\vec{\mathbf{r}}_{a,ab}$ and $\vec{\mathbf{r}}_{ba,b}$ appear to be constant in F_a and F_b , respectively. Moreover, $\vec{\mathbf{r}}_{ab,ba}$ is expressed most simply in F_{ab} (or F_{ba}). Therefore, Eq. (2.3) can be written more expressively as

$$\mathbf{r}_{a,b}^{(a)} = \mathbf{r}_{a,ab}^{(a)} + \mathbf{C}^{(a,ab)} \mathbf{r}_{ab,ba}^{(ab)} + \mathbf{C}^{(a,b)} \mathbf{r}_{ba,b}^{(b)} \quad (2.6)$$

In Eq. (2.6), $\mathbf{r}_{a,ab}^{(a)}$ and $\mathbf{r}_{ba,b}^{(b)}$ are constant, whereas $\mathbf{r}_{ab,ba}^{(ab)}$ is variable being a function of the variable or variables of the joint J_{ab} . The details of $\mathbf{r}_{ab,ba}^{(ab)}$ will also be taken up later in Section 3.

2.2. Assignment of the Joint Frames

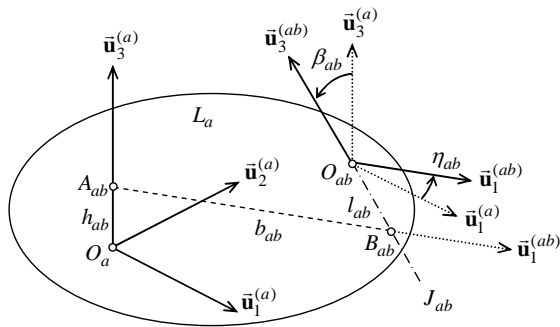


Fig. 2. Joint Frame Assignment

Here, the joint frame F_{ab} is assigned systematically by using a method, which is a similar but extended version of the Denavit-Hartenberg (D-H) method. It involves *five* parameters differently from the *four* parameters of the D-H method. The parameters of the assignment are shown in Fig. 2. The assignment procedure is as described below.

The link frame F_a with the basis vector triad $\{\bar{\mathbf{u}}_1^{(a)}, \bar{\mathbf{u}}_2^{(a)}, \bar{\mathbf{u}}_3^{(a)}\}$ is attached to link L_a in some convenient way. The *main axis* of the kinematic element of link L_a that belongs to joint J_{ab} is represented by the unit vector $\bar{\mathbf{u}}_3^{(ab)}$. The *common normal* is determined between the axes along $\bar{\mathbf{u}}_3^{(a)}$ and $\bar{\mathbf{u}}_3^{(ab)}$ or a convenient common normal is selected if there are many of them. The unit vector $\bar{\mathbf{u}}_1^{(ab)}$ is assigned to the common normal being oriented from $\bar{\mathbf{u}}_3^{(a)}$ to $\bar{\mathbf{u}}_3^{(ab)}$. The intersection points of the common normal with the axes along $\bar{\mathbf{u}}_3^{(a)}$ and $\bar{\mathbf{u}}_3^{(ab)}$ are labeled as A_{ab} and B_{ab} , respectively. A_{ab} and B_{ab} are defined as the *auxiliary points*. The origin O_{ab} of the joint frame F_{ab} is also located on the main axis of J_{ab} . The location and orientation of F_{ab} with respect to F_a is described by means of the following five parameters.

1. First Offset Distance along $\bar{\mathbf{u}}_3^{(a)}$:

$$h_{ab} = O_a A_{ab} \quad (2.7)$$

2. Second Offset Distance along $\bar{\mathbf{u}}_3^{(ab)}$:

$$l_{ab} = B_{ab} O_{ab} \quad (2.8)$$

3. Separation Distance along $\bar{\mathbf{u}}_1^{(ab)}$:

$$b_{ab} = A_{ab} O_{ab} \quad (2.9)$$

4. Turn Angle about $\bar{\mathbf{u}}_3^{(a)}$:

$$\eta_{ab} = \angle[\bar{\mathbf{u}}_1^{(a)} \rightarrow \bar{\mathbf{u}}_1^{(ab)}] \quad (2.10)$$

5. Twist Angle about $\bar{\mathbf{u}}_1^{(ab)}$:

$$\beta_{ab} = \angle[\bar{\mathbf{u}}_3^{(a)} \rightarrow \bar{\mathbf{u}}_3^{(ab)}] \quad (2.11)$$

By using these parameters, the constant orientation and location matrices $\mathbf{C}^{(a,ab)}$ and $\mathbf{r}_{a,ab}^{(a)}$ are expressed as follows.

$$\mathbf{C}^{(a,ab)} = e^{\bar{\mathbf{u}}_3 \eta_{ab}} e^{\bar{\mathbf{u}}_1 \beta_{ab}} \quad (2.12)$$

$$\begin{aligned} \mathbf{r}_{a,ab}^{(a)} &= h_{ab} \mathbf{u}_3^{(a/a)} + b_{ab} \mathbf{u}_1^{(ab/a)} + l_{ab} \mathbf{u}_3^{(ab/a)} \\ &= h_{ab} \mathbf{u}_3^{(a/a)} + \mathbf{C}^{(a,ab)} [b_{ab} \mathbf{u}_1^{(ab/ab)} + l_{ab} \mathbf{u}_3^{(ab/ab)}] \end{aligned}$$

This equation can be simplified as shown below.

$$\begin{aligned} \mathbf{r}_{a,ab}^{(a)} &= h_{ab} \mathbf{u}_3 + e^{\bar{\mathbf{u}}_3 \eta_{ab}} e^{\bar{\mathbf{u}}_1 \beta_{ab}} (b_{ab} \mathbf{u}_1 + l_{ab} \mathbf{u}_3) \\ &= h_{ab} \mathbf{u}_3 + b_{ab} e^{\bar{\mathbf{u}}_3 \eta_{ab}} \mathbf{u}_1 + l_{ab} e^{\bar{\mathbf{u}}_3 \eta_{ab}} e^{\bar{\mathbf{u}}_1 \beta_{ab}} \mathbf{u}_3 \end{aligned} \quad (2.13)$$

Eq. (2.13) can also be written as follows by expanding the matrix products on the right hand side.

$$\begin{aligned} \mathbf{r}_{a,ab}^{(a)} &= \mathbf{u}_1 (b_{ab} \cos \eta_{ab} + l_{ab} \sin \eta_{ab} \sin \beta_{ab}) + \\ &+ \mathbf{u}_2 (b_{ab} \sin \eta_{ab} - l_{ab} \cos \eta_{ab} \sin \beta_{ab}) + \\ &+ \mathbf{u}_3 (h_{ab} + l_{ab} \cos \beta_{ab}) \end{aligned} \quad (2.14)$$



Eqs. (2.12) to (2.14) contain the following definitions.

- a) The matrix representations of the basis vectors of one frame in another frame:

$$\mathbf{u}_k^{(b/a)} = \{\bar{\mathbf{u}}_k^{(b)}\}_{F_a}; \quad k = 1, 2, 3 \quad (2.15)$$

- b) The basic column matrices:

$$\mathbf{u}_1 = \begin{bmatrix} 1 \\ 0 \\ 0 \end{bmatrix}, \quad \mathbf{u}_2 = \begin{bmatrix} 0 \\ 1 \\ 0 \end{bmatrix}, \quad \mathbf{u}_3 = \begin{bmatrix} 0 \\ 0 \\ 1 \end{bmatrix} \quad (2.16)$$

Note that, for $k = 1, 2, 3$,

$$\mathbf{u}_k^{(a/a)} = \mathbf{u}_k^{(b/b)} = \mathbf{u}_k^{(c/c)} = \dots = \mathbf{u}_k \quad (2.17)$$

- c) The angle-axis description of a rotation matrix:

$$\begin{aligned} \mathbf{C}^{(p,q)} &= e^{\tilde{\mathbf{n}}^{(p)}\theta} \\ &\equiv \mathbf{I} + \tilde{\mathbf{n}}^{(p)} \sin \theta + [\tilde{\mathbf{n}}^{(p)}]^2 (1 - \cos \theta) \\ &\equiv \mathbf{I} \cos \theta + \tilde{\mathbf{n}}^{(p)} \sin \theta + \mathbf{n}^{(p)} \mathbf{n}^{(p)\tau} (1 - \cos \theta) \end{aligned} \quad (2.18)$$

The matrix expressed in Eq. (2.18) represents the following rotation.

$$F_p \xrightarrow{\text{rot}(\tilde{\mathbf{n}}, \theta)} F_q$$

Here, $\tilde{\mathbf{n}}$ is the unit vector along the axis of rotation and $\mathbf{n}^{(p)}$ is the matrix representation of $\tilde{\mathbf{n}}$ in F_p .

Note that if $\tilde{\mathbf{n}}$ happens to be one of the basis vectors of F_p , i.e. if $\tilde{\mathbf{n}} = \bar{\mathbf{u}}_k^{(p)}$ for $k = 1, 2$, or 3 , then $\mathbf{n}^{(p)} = \mathbf{u}_k^{(p/p)} = \mathbf{u}_k$. As for $\tilde{\mathbf{n}}^{(p)}$, it is the skew symmetric *cross-product matrix* corresponding to $\mathbf{n}^{(p)}$. It functions on a column matrix $\mathbf{r}^{(p)}$ so that $\tilde{\mathbf{n}}^{(p)} \mathbf{r}^{(p)} \equiv \mathbf{n}^{(p)} \times \mathbf{r}^{(p)}$. It is generated as shown below.

$$\mathbf{n}^{(p)} = \begin{bmatrix} n_1 \\ n_2 \\ n_3 \end{bmatrix} \Rightarrow \tilde{\mathbf{n}}^{(p)} = \begin{bmatrix} 0 & -n_3 & n_2 \\ n_3 & 0 & -n_1 \\ -n_2 & n_1 & 0 \end{bmatrix} \quad (2.19)$$

For the other constant position matrices in Eqs. (2.1) and (2.6), the following relationships can be written.

$$\mathbf{C}^{(ba,b)} = [\mathbf{C}^{(b,ba)}]^\tau \quad \text{and} \quad \mathbf{r}_{ba,b}^{(b)} = -\mathbf{r}_{b,ba}^{(b)} \quad (2.20)$$

So, they are obtained by expressing $\mathbf{C}^{(b,ba)}$ and $\mathbf{r}_{b,ba}^{(b)}$ similarly as above. That is,

$$\mathbf{C}^{(b,ba)} = e^{\tilde{\mathbf{u}}_3 \eta_{ba}} e^{\tilde{\mathbf{u}}_1 \beta_{ba}} \quad (2.21)$$

$$\mathbf{r}_{b,ba}^{(b)} = h_{ba} \mathbf{u}_3 + b_{ba} e^{\tilde{\mathbf{u}}_3 \eta_{ba}} \mathbf{u}_1 + l_{ba} e^{\tilde{\mathbf{u}}_3 \eta_{ba}} e^{\tilde{\mathbf{u}}_1 \beta_{ba}} \mathbf{u}_3 \quad (2.22)$$

On the other hand, the variable orientation and location matrices $\mathbf{C}^{(ab,ba)}$ and $\mathbf{r}_{ab,ba}^{(ab)}$ are expressed as described in Section 3.

2.3. Special Cases of Joint Frame Assignment

a) Case with Parallel Axes

In this case, $\tilde{\mathbf{u}}_3^{(ab)} // \tilde{\mathbf{u}}_3^{(a)}$, $\beta_{ab} = 0$, and there are infinitely many common normals. So, the common normal passing through O_{ab} can be selected as the most convenient one. For this common normal, $l_{ab} = 0$. Thus, Eqs. (2.12) to (2.14) reduce to the following ones.

$$\mathbf{C}^{(a,ab)} = e^{\tilde{\mathbf{u}}_3 \eta_{ab}} \quad (2.23)$$

$$\begin{aligned} \mathbf{r}_{a,ab}^{(a)} &= h_{ab} \mathbf{u}_3 + b_{ab} e^{\tilde{\mathbf{u}}_3 \eta_{ab}} \mathbf{u}_1 \\ &= \mathbf{u}_1 (b_{ab} \cos \eta_{ab}) + \mathbf{u}_2 (b_{ab} \sin \eta_{ab}) + \mathbf{u}_3 h_{ab} \end{aligned} \quad (2.24)$$

b) Case with Intersecting Axes

In this case, the three points A_{ab} , B_{ab} , and O_{ab} become coincident. Then, although the common normal is determined uniquely, the sense of $\tilde{\mathbf{u}}_1^{(ab)}$ acquires two options. These options can be represented by a sign variable $\sigma_{ab} = \pm 1$ so that $\beta_{ab} = \sigma_{ab} |\beta_{ab}|$. As a possible option, σ_{ab} can be selected so that η_{ab} comes out as an acute angle. Another feature of this case is that $b_{ab} = l_{ab} = 0$. Thus, Eqs. (2.12) to (2.14) reduce this time further to the following ones.



$$\mathbf{C}^{(a,ab)} = e^{\bar{\mathbf{u}}_3 \eta_{ab}} e^{\bar{\mathbf{u}}_1 \beta_{ab}} \quad (2.25)$$

$$\mathbf{r}_{a,ab}^{(a)} = h_{ab} \mathbf{u}_3 \quad (2.26)$$

c) Case with Coincident Axes

In this very special but not very uncommon case, it becomes possible to orient the common normal arbitrarily. Then, it is normally oriented so that $\eta_{ab} = 0$. Thus, Eqs. (2.12) to (2.14) simplify even further to the following ones.

$$\mathbf{C}^{(a,ab)} = \mathbf{I} \quad (2.27)$$

$$\mathbf{r}_{a,ab}^{(a)} = h_{ab} \mathbf{u}_3 \quad (2.28)$$

3. Joint Descriptions

3.1. Single-Axis Joints

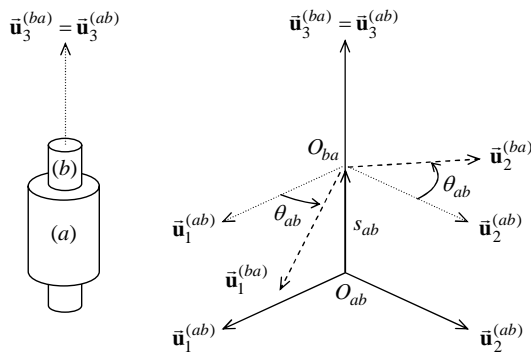


Fig. 3. A Single-Axis Joint

A single-axis joint with the frames F_{ab} and F_{ba} is shown in Fig. 3. Without a significant loss of generality, the joint axis is aligned with $\bar{\mathbf{u}}_3^{(ba)} = \bar{\mathbf{u}}_3^{(ab)}$. In such a joint, the relative displacement between the kinematic elements is characterized by two joint variables. One of them is the angular displacement θ_{ab} , which indicates the relative rotation of F_{ba} with respect to F_{ab} . The other variable is the linear displacement s_{ab} , from O_{ab} to O_{ba} , which indicates the relative translation of F_{ba} with respect to F_{ab} .

There are four kinds of single-axis joints. They are known as cylindrical, screw, revolute, and prismatic joints. Their kinematic details are described below.

a) Cylindrical Joints

In a cylindrical joint, s_{ab} and θ_{ab} are independent variables. Therefore, the degree of freedom of a cylindrical joint is two.

b) Screw or Helical Joints

In a screw joint, s_{ab} and θ_{ab} are related to each other. Therefore, the degree of freedom of a screw joint is one. The relationship between s_{ab} and θ_{ab} is expressed as follows.

$$s_{ab} = d_{ab} + \lambda_{ab} \theta_{ab} \quad (3.1)$$

In Eq. (3.1), d_{ab} (initial offset) and λ_{ab} (pitch or lead) are constant parameters.

c) Revolute Joints

In a revolute joint, θ_{ab} is variable but $s_{ab} = d_{ab}$ is constant. Therefore, the degree of freedom of a revolute joint is one.

d) Prismatic Joints

In a prismatic joint, s_{ab} is variable but $\theta_{ab} = \delta_{ab}$ is constant. Therefore, the degree of freedom of a prismatic joint is one.

In a single-axis joint, the position of F_{ba} with respect to F_{ab} is expressed by the following equations.

a) Orientation Equation

$$\mathbf{C}^{(ab,ba)} = e^{\bar{\mathbf{u}}_3 \theta_{ab}} \quad (3.2)$$

b) Location Equation

The vector equation is

$$\bar{\mathbf{r}}_{ab,ba} = s_{ab} \bar{\mathbf{u}}_3^{(ab)} \quad (3.3)$$

In Eq. (3.3), $\bar{\mathbf{r}}_{ab,ba}$ is the location vector oriented from O_{ab} to O_{ba} . As expressed in F_{ab} , the corresponding matrix equation is

$$\mathbf{r}_{ab,ba}^{(ab)} = s_{ab} \mathbf{u}_3 \quad (3.4)$$

3.2. Spherical Joint

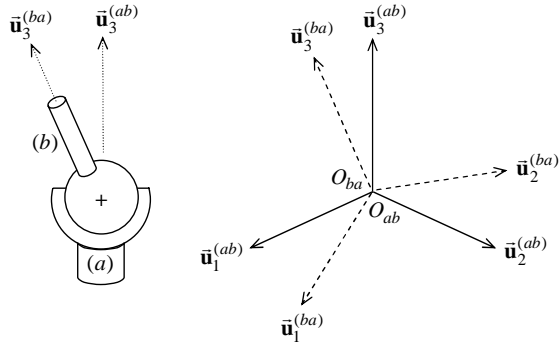


Figure 4. A Spherical Joint

A spherical joint is depicted in Fig. 4. The location equation is trivial, i.e.

$$\mathbf{r}_{ab,ba}^{(ab)} = \mathbf{0} \quad (3.5)$$

So, without any relative translation, the degree of freedom of a spherical joint is three. Therefore, the orientation equation is mostly written as follows in terms of three independent angular joint variables ϕ_{ab} , θ_{ab} , and ψ_{ab} , which are generally designated as Euler angles.

$$\mathbf{C}^{(ab,ba)} = e^{\tilde{\mathbf{n}}_1 \phi_{ab}} e^{\tilde{\mathbf{n}}_2 \theta_{ab}} e^{\tilde{\mathbf{n}}_3 \psi_{ab}} \quad (3.6)$$

In Eq. (3.6), \mathbf{n}_1 , \mathbf{n}_2 , and \mathbf{n}_3 are unit column matrices and they can be selected in any convenient way so long as $\mathbf{n}_2 \neq \mathbf{n}_1$ and $\mathbf{n}_2 \neq \mathbf{n}_3$. However, it is possible to have $\mathbf{n}_3 = \mathbf{n}_1$. Typical selections are given below forming the commonly used rotation sequences.

(i) 1-2-3 sequence ($\mathbf{n}_1 = \mathbf{u}_1$, $\mathbf{n}_2 = \mathbf{u}_2$, $\mathbf{n}_3 = \mathbf{u}_3$):

$$\mathbf{C}^{(ab,ba)} = e^{\tilde{\mathbf{u}}_1 \phi_{ab}} e^{\tilde{\mathbf{u}}_2 \theta_{ab}} e^{\tilde{\mathbf{u}}_3 \psi_{ab}}$$

(ii) 3-2-1 sequence ($\mathbf{n}_1 = \mathbf{u}_3$, $\mathbf{n}_2 = \mathbf{u}_2$, $\mathbf{n}_3 = \mathbf{u}_1$):

$$\mathbf{C}^{(ab,ba)} = e^{\tilde{\mathbf{u}}_3 \phi_{ab}} e^{\tilde{\mathbf{u}}_2 \theta_{ab}} e^{\tilde{\mathbf{u}}_1 \psi_{ab}}$$

(iii) 3-2-3 sequence ($\mathbf{n}_1 = \mathbf{u}_3$, $\mathbf{n}_2 = \mathbf{u}_2$, $\mathbf{n}_3 = \mathbf{u}_3$):

$$\mathbf{C}^{(ab,ba)} = e^{\tilde{\mathbf{u}}_3 \phi_{ab}} e^{\tilde{\mathbf{u}}_2 \theta_{ab}} e^{\tilde{\mathbf{u}}_3 \psi_{ab}}$$

(iv) 3-1-3 sequence ($\mathbf{n}_1 = \mathbf{u}_3$, $\mathbf{n}_2 = \mathbf{u}_1$, $\mathbf{n}_3 = \mathbf{u}_3$):

$$\mathbf{C}^{(ab,ba)} = e^{\tilde{\mathbf{u}}_3 \phi_{ab}} e^{\tilde{\mathbf{u}}_1 \theta_{ab}} e^{\tilde{\mathbf{u}}_3 \psi_{ab}}$$

In addition to the Euler angles, it is possible to express $\mathbf{C}^{(ab,ba)}$ by using other means as well. Two typical ones are mentioned below.

(i) Angle-Axis Representation with γ_{ab} and \mathbf{n}_{ab} :

In this representation, $\mathbf{n}_{ab}^T \mathbf{n}_{ab} = 1$ and

$$\begin{aligned} \mathbf{C}^{(ab,ba)} &= e^{\tilde{\mathbf{n}}_{ab} \gamma_{ab}} \\ &= \mathbf{I} + \tilde{\mathbf{n}}_{ab} \sin \gamma_{ab} + \tilde{\mathbf{n}}_{ab}^2 (1 - \cos \gamma_{ab}) \end{aligned} \quad (3.7)$$

(ii) Quaternion Representation with $\hat{\mathbf{q}}_{ab} = \lambda_{ab} + \boldsymbol{\mu}_{ab}$:

In this representation,

$$\lambda_{ab} = \cos(\gamma_{ab} / 2) \text{ and } \boldsymbol{\mu}_{ab} = \mathbf{n}_{ab} \sin(\gamma_{ab} / 2)$$

So, $\lambda_{ab}^2 + \boldsymbol{\mu}_{ab}^T \boldsymbol{\mu}_{ab} = 1$ and

$$\mathbf{C}^{(ab,ba)} = \mathbf{I} + 2\lambda_{ab} \tilde{\boldsymbol{\mu}}_{ab} + 2\tilde{\boldsymbol{\mu}}_{ab}^2 \quad (3.8)$$

3.3. Universal or Hooke Joint

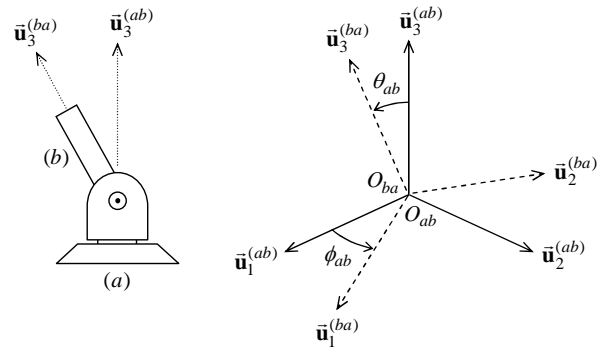


Fig. 5. A Universal Joint

A universal joint is actually a combination of two successive revolute joints with orthogonally intersecting axes as seen in Fig. 5. So, its degree of freedom is two. The relative displacement between the kinematic elements can be expressed in terms of two angles such as

ϕ_{ab} and θ_{ab} . Hence, the location and orientation equations can be written as follows.

$$\mathbf{r}_{ab,ba}^{(ab)} = \mathbf{0} \quad (3.9)$$

$$\mathbf{C}^{(ab,ba)} = e^{\tilde{\mathbf{u}}_3 \phi_{ab}} e^{\tilde{\mathbf{u}}_1 \theta_{ab}} \quad (3.10)$$

3.4. Plane-Contact Joint

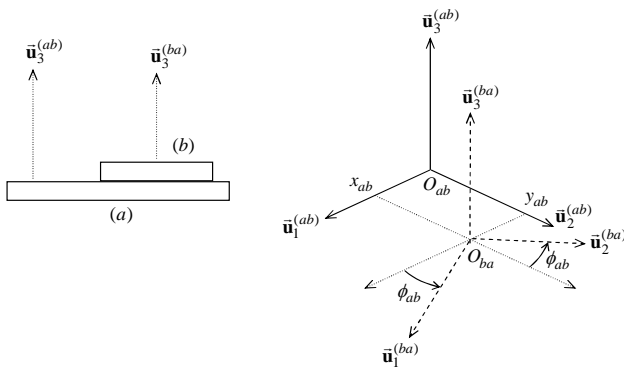


Fig. 6. A Plane-Contact Joint

In a plane-contact joint, the kinematic elements are in contact with each other on a planar surface as seen in Fig. 6. Therefore, the degree of freedom of such a joint is three. So, the relative displacement between the kinematic elements can be expressed in terms of three joint variables, which can be taken as the angle ϕ_{ab} about the third axis and the two coordinates x_{ab} and y_{ab} along the first and second axes. By using these joint variables, the location and orientation equations can be written as follows.

$$\mathbf{r}_{ab,ba}^{(ab)} = x_{ab} \mathbf{u}_1 + y_{ab} \mathbf{u}_2 \quad (3.11)$$

$$\mathbf{C}^{(ab,ba)} = e^{\tilde{\mathbf{u}}_3 \phi_{ab}} \quad (3.12)$$

3.5. Line-Contact Joint

In a line-contact joint, the kinematic elements are in contact with each other along a line as seen in Fig. 7. Therefore, the degree of freedom of such a joint is four. So, the relative displacement between the kinematic elements can be expressed in terms of four joint variables, which can be taken as the angles ϕ_{ab} and θ_{ab} about the third and first axes and the two coordinates x_{ab} and y_{ab} along the first and second axes. By using

these joint variables, the location and orientation equations can be written as follows.

$$\mathbf{r}_{ab,ba}^{(ab)} = x_{ab} \mathbf{u}_1 + y_{ab} \mathbf{u}_2 \quad (3.13)$$

$$\mathbf{C}^{(ab,ba)} = e^{\tilde{\mathbf{u}}_3 \phi_{ab}} e^{\tilde{\mathbf{u}}_1 \theta_{ab}} \quad (3.14)$$

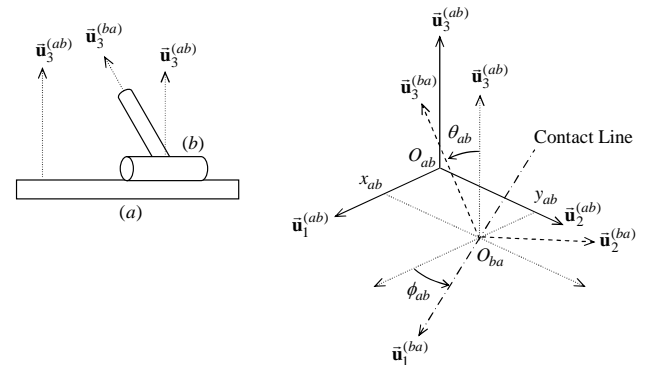


Fig. 7. A Line-Contact Joint

3.6. Point-Contact Joint

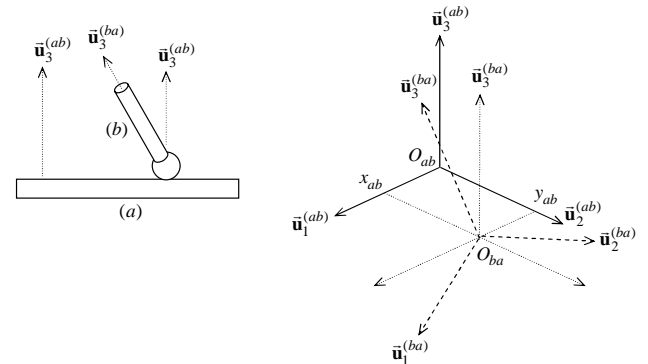


Fig. 8. A Point-Contact Joint

In a point-contact joint, the kinematic elements are in contact with each other at a point as seen in Fig. 8. Therefore, the degree of freedom of such a joint is five. So, the relative displacement between the kinematic elements can be expressed in terms of five joint variables, which can be taken as three angles such as ϕ_{ab} , θ_{ab} , and ψ_{ab} and the two coordinates x_{ab} and y_{ab} along the first and second axes. They lead to the following equations.

$$\mathbf{r}_{ab,ba}^{(ab)} = x_{ab} \mathbf{u}_1 + y_{ab} \mathbf{u}_2 \quad (3.15)$$

$$\mathbf{C}^{(ab,ba)} = e^{\tilde{\mathbf{u}}_1 \phi_{ab}} e^{\tilde{\mathbf{u}}_2 \theta_{ab}} e^{\tilde{\mathbf{u}}_3 \psi_{ab}} \quad (3.16)$$

or as another alternative,

$$\mathbf{C}^{(ab,ba)} = e^{\tilde{\mathbf{u}}_3 \phi_{ab}} e^{\tilde{\mathbf{u}}_2 \theta_{ab}} e^{\tilde{\mathbf{u}}_3 \psi_{ab}} \quad (3.17)$$

4. Example: A 6-DOF Parallel Manipulator

4.1. Description of the Manipulator

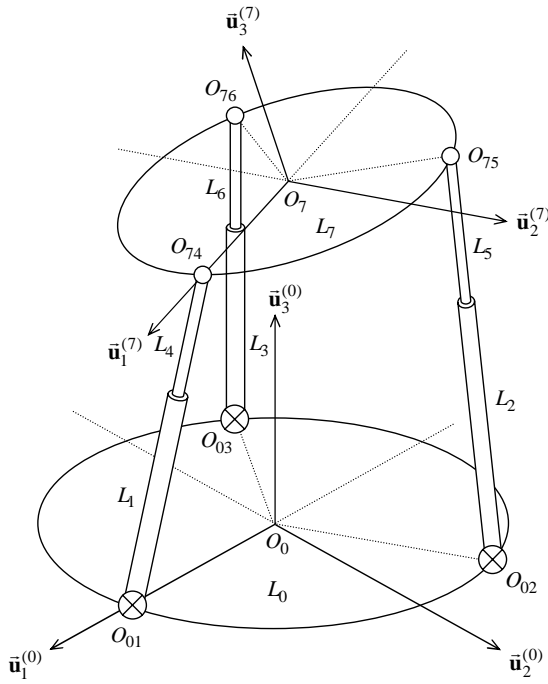


Fig. 9. A 6-DOF Parallel Manipulator

The parallel manipulator shown in Fig. 9 consists of two platforms L_0 and L_7 , which are connected by three identical legs. L_0 is fixed and the legs consist of the link pairs denoted as $\{L_1, L_4\}$, $\{L_2, L_5\}$, and $\{L_3, L_6\}$. The link pairs of the legs are connected by prismatic joints J_{14} , J_{25} , and J_{36} . The joints J_{01} , J_{02} , and J_{03} on the fixed platform are universal (denoted by \otimes symbols) and the joints J_{74} , J_{75} , and J_{76} on the moving platform are spherical (denoted by \circ symbols). The universal joints are symmetrically located about O_0 with $\eta_{01} = 0$, $\eta_{02} = 2\pi/3$, $\eta_{03} = -2\pi/3$, and $b_{01} = b_{02} = b_{03} = r_0$. Similarly, the spherical joints are symmetrically located about O_7 with $\eta_{74} = 0$, $\eta_{75} = 2\pi/3$, $\eta_{76} = -2\pi/3$, and $b_{74} = b_{75} = b_{76} = r_7$. The details of the first leg are shown in Fig. 10. The details of the other legs are similar. The controlled joint variables of the manipulator

are the first angles of the universal joints ($\phi_{01}, \phi_{02}, \phi_{03}$) and the lengths of the prismatic joints (s_{14}, s_{25}, s_{36}).

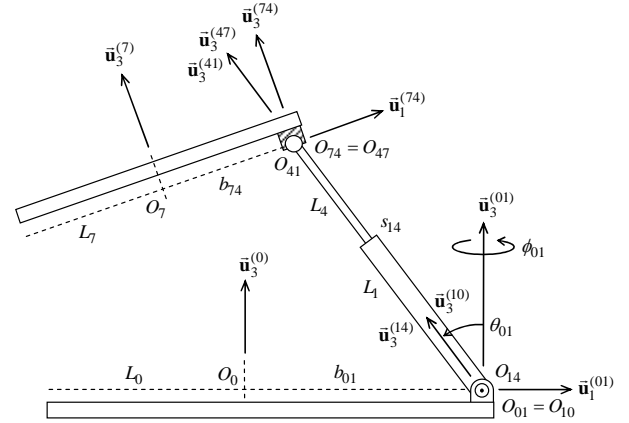


Fig. 10. Details of the First Leg

4.2. Kinematic Equations

Referring to Figs. 9 and 10, the following equations can be written in order to express the position of the moving platform (L_7) with respect to the fixed platform (L_0).

a) Orientation Equations

The orientation of the moving platform can be expressed with respect to the base frame in the following three ways.

$$\begin{aligned} \mathbf{C}^{(0,7)} &= \mathbf{C}^{(0,1)} \mathbf{C}^{(1,4)} \mathbf{C}^{(4,7)} \\ &= [\mathbf{C}^{(0,01)} \mathbf{C}^{(01,10)} \mathbf{C}^{(10,1)}] \cdot \\ &\quad \cdot [\mathbf{C}^{(1,14)} \mathbf{C}^{(14,41)} \mathbf{C}^{(41,4)}] \cdot \\ &\quad \cdot [\mathbf{C}^{(4,47)} \mathbf{C}^{(47,74)} \mathbf{C}^{(74,7)}] \end{aligned} \quad (4.1)$$

$$\begin{aligned} \mathbf{C}^{(0,7)} &= \mathbf{C}^{(0,2)} \mathbf{C}^{(2,5)} \mathbf{C}^{(5,7)} \\ &= [\mathbf{C}^{(0,02)} \mathbf{C}^{(02,20)} \mathbf{C}^{(20,2)}] \cdot \\ &\quad \cdot [\mathbf{C}^{(2,25)} \mathbf{C}^{(25,52)} \mathbf{C}^{(52,5)}] \cdot \\ &\quad \cdot [\mathbf{C}^{(5,57)} \mathbf{C}^{(57,75)} \mathbf{C}^{(75,7)}] \end{aligned} \quad (4.2)$$

$$\begin{aligned} \mathbf{C}^{(0,7)} &= \mathbf{C}^{(0,3)} \mathbf{C}^{(3,6)} \mathbf{C}^{(6,7)} \\ &= [\mathbf{C}^{(0,03)} \mathbf{C}^{(03,30)} \mathbf{C}^{(30,3)}] \cdot \\ &\quad \cdot [\mathbf{C}^{(3,36)} \mathbf{C}^{(36,63)} \mathbf{C}^{(63,6)}] \cdot \\ &\quad \cdot [\mathbf{C}^{(6,67)} \mathbf{C}^{(67,76)} \mathbf{C}^{(76,7)}] \end{aligned} \quad (4.3)$$



The joints J_{01} , J_{02} , and J_{03} are universal.
Therefore,

$$\left. \begin{aligned} \mathbf{C}^{(01,10)} &= e^{\tilde{\mathbf{u}}_3 \phi_{01}} e^{\tilde{\mathbf{u}}_1 \theta_{01}} \\ \mathbf{C}^{(02,20)} &= e^{\tilde{\mathbf{u}}_3 \phi_{02}} e^{\tilde{\mathbf{u}}_1 \theta_{02}} \\ \mathbf{C}^{(03,30)} &= e^{\tilde{\mathbf{u}}_3 \phi_{03}} e^{\tilde{\mathbf{u}}_1 \theta_{03}} \end{aligned} \right\} \quad (4.4)$$

The joints J_{14} , J_{25} , and J_{36} are prismatic.
Therefore,

$$\mathbf{C}^{(14,41)} = \mathbf{C}^{(25,52)} = \mathbf{C}^{(36,63)} = \mathbf{I} \quad (4.5)$$

The joints J_{47} , J_{57} , and J_{67} are spherical. Their kinematics can be completely and compactly characterized by the rotation matrices \mathbf{R}_4 , \mathbf{R}_5 , and \mathbf{R}_6 so that

$$\mathbf{C}^{(47,74)} = \mathbf{R}_4, \quad \mathbf{C}^{(57,75)} = \mathbf{R}_5, \quad \mathbf{C}^{(67,76)} = \mathbf{R}_6 \quad (4.6)$$

If the details are required, the matrices \mathbf{R}_4 , \mathbf{R}_5 , and \mathbf{R}_6 can be expressed in terms of the Euler angles of a desired sequence, such as 1-2-3, 3-2-3, etc.

Note that

$$\tilde{\mathbf{u}}_3^{(01)} // \tilde{\mathbf{u}}_3^{(02)} // \tilde{\mathbf{u}}_3^{(03)} // \tilde{\mathbf{u}}_3^{(0)}$$

and

$$\tilde{\mathbf{u}}_3^{(74)} // \tilde{\mathbf{u}}_3^{(75)} // \tilde{\mathbf{u}}_3^{(76)} // \tilde{\mathbf{u}}_3^{(7)}$$

Therefore, with the given values of the turn angles,

$$\left. \begin{aligned} \mathbf{C}^{(0,01)} &= e^{\tilde{\mathbf{u}}_3 \eta_{01}} = \mathbf{I} \\ \mathbf{C}^{(0,02)} &= e^{\tilde{\mathbf{u}}_3 \eta_{02}} = e^{\tilde{\mathbf{u}}_3 (2\pi/3)} \\ \mathbf{C}^{(0,03)} &= e^{\tilde{\mathbf{u}}_3 \eta_{03}} = e^{-\tilde{\mathbf{u}}_3 (2\pi/3)} \end{aligned} \right\} \quad (4.7)$$

$$\left. \begin{aligned} \mathbf{C}^{(7,74)} &= e^{\tilde{\mathbf{u}}_3 \eta_{74}} = \mathbf{I} \\ \mathbf{C}^{(7,75)} &= e^{\tilde{\mathbf{u}}_3 \eta_{75}} = e^{\tilde{\mathbf{u}}_3 (2\pi/3)} \\ \mathbf{C}^{(7,76)} &= e^{\tilde{\mathbf{u}}_3 \eta_{76}} = e^{-\tilde{\mathbf{u}}_3 (2\pi/3)} \end{aligned} \right\} \quad (4.8)$$

For the links connected by the prismatic joints, the joint frames can be taken to be coincident with the relevant link frames. That is,

$$\left. \begin{aligned} \mathbf{C}^{(1,10)} &= \mathbf{C}^{(2,20)} = \mathbf{C}^{(3,30)} = \mathbf{I} \\ \mathbf{C}^{(1,14)} &= \mathbf{C}^{(2,25)} = \mathbf{C}^{(3,36)} = \mathbf{I} \end{aligned} \right\} \quad (4.9)$$

$$\left. \begin{aligned} \mathbf{C}^{(4,47)} &= \mathbf{C}^{(5,57)} = \mathbf{C}^{(6,67)} = \mathbf{I} \\ \mathbf{C}^{(4,41)} &= \mathbf{C}^{(5,52)} = \mathbf{C}^{(6,63)} = \mathbf{I} \end{aligned} \right\} \quad (4.10)$$

Consequently, Eqs. (4.1) to (4.3) become

$$\mathbf{C}^{(0,7)} = e^{\tilde{\mathbf{u}}_3 \phi_{01}} e^{\tilde{\mathbf{u}}_1 \theta_{01}} \mathbf{R}_4 \quad (4.11)$$

$$\mathbf{C}^{(0,7)} = e^{\tilde{\mathbf{u}}_3 (2\pi/3)} e^{\tilde{\mathbf{u}}_3 \phi_{02}} e^{\tilde{\mathbf{u}}_1 \theta_{02}} \mathbf{R}_5 e^{-\tilde{\mathbf{u}}_3 (2\pi/3)} \quad (4.12)$$

$$\mathbf{C}^{(0,7)} = e^{-\tilde{\mathbf{u}}_3 (2\pi/3)} e^{\tilde{\mathbf{u}}_3 \phi_{03}} e^{\tilde{\mathbf{u}}_1 \theta_{03}} \mathbf{R}_6 e^{\tilde{\mathbf{u}}_3 (2\pi/3)} \quad (4.13)$$

b) Location Equations

The location vector of the origin O_7 can be expressed with respect to the base frame as follows through the first leg.

$$\begin{aligned} \mathbf{r}_{0,7}^{(0)} &= \mathbf{r}_{0,01}^{(0)} + \mathbf{r}_{01,47}^{(0)} + \mathbf{r}_{47,7}^{(0)} \\ &= r_0 \mathbf{u}_1^{(01/0)} + s_{14} \mathbf{u}_3^{(10/0)} - r_7 \mathbf{u}_1^{(74/0)} \end{aligned}$$

$$\mathbf{r}_{0,7}^{(0)} = r_0 \mathbf{C}^{(0,01)} \mathbf{u}_1 + s_{14} \mathbf{C}^{(0,10)} \mathbf{u}_3 - r_7 \mathbf{C}^{(0,74)} \mathbf{u}_1$$

$$\begin{aligned} \mathbf{r}_{0,7}^{(0)} &= r_0 \mathbf{C}^{(0,01)} \mathbf{u}_1 + s_{14} \mathbf{C}^{(0,01)} \mathbf{C}^{(01,10)} \mathbf{u}_3 - \\ &\quad - r_7 \mathbf{C}^{(0,7)} \mathbf{C}^{(7,74)} \mathbf{u}_1 \end{aligned} \quad (4.14)$$

The same location vector can be expressed through the other two legs similarly as follows.

$$\begin{aligned} \mathbf{r}_{0,7}^{(0)} &= r_0 \mathbf{C}^{(0,02)} \mathbf{u}_1 + s_{25} \mathbf{C}^{(0,02)} \mathbf{C}^{(02,20)} \mathbf{u}_3 - \\ &\quad - r_7 \mathbf{C}^{(0,7)} \mathbf{C}^{(7,75)} \mathbf{u}_1 \end{aligned} \quad (4.15)$$

$$\begin{aligned} \mathbf{r}_{0,7}^{(0)} &= r_0 \mathbf{C}^{(0,03)} \mathbf{u}_1 + s_{36} \mathbf{C}^{(0,03)} \mathbf{C}^{(03,30)} \mathbf{u}_3 - \\ &\quad - r_7 \mathbf{C}^{(0,7)} \mathbf{C}^{(7,76)} \mathbf{u}_1 \end{aligned} \quad (4.16)$$

When the relevant orientation matrices are substituted, Eqs. (4.14) to (4.16) take the following forms.

$$\mathbf{r}_{0,7}^{(0)} = r_0 \mathbf{u}_1 + e^{\tilde{\mathbf{u}}_3 \phi_{01}} e^{\tilde{\mathbf{u}}_1 \theta_{01}} (s_{14} \mathbf{u}_3 - r_7 \mathbf{R}_4 \mathbf{u}_1) \quad (4.17)$$



$$\begin{aligned} \mathbf{r}_{0,7}^{(0)} &= e^{\tilde{\mathbf{u}}_3(2\pi/3)} [r_0 \mathbf{u}_1 + \\ &+ e^{\tilde{\mathbf{u}}_3 \phi_{02}} e^{\tilde{\mathbf{u}}_1 \theta_{02}} (s_{25} \mathbf{u}_3 - r_7 \mathbf{R}_5 \mathbf{u}_1)] \end{aligned} \quad (4.18)$$

$$\begin{aligned} \mathbf{r}_{0,7}^{(0)} &= e^{-\tilde{\mathbf{u}}_3(2\pi/3)} [r_0 \mathbf{u}_1 + \\ &+ e^{\tilde{\mathbf{u}}_3 \phi_{03}} e^{\tilde{\mathbf{u}}_1 \theta_{03}} (s_{36} \mathbf{u}_3 - r_7 \mathbf{R}_6 \mathbf{u}_1)] \end{aligned} \quad (4.19)$$

4.3. Inverse Kinematics

The orientation of the moving platform and the location of its center are specified as \mathbf{C} and \mathbf{r} so that

$$\mathbf{C}^{(0,7)} = \mathbf{C} \quad \text{and} \quad \mathbf{r}_{0,7}^{(0)} = \mathbf{r} \quad (4.20)$$

It is desired to determine the corresponding joint variables.

To start the solution procedure, the location vectors of the spherical joint centers (O_{74}, O_{75}, O_{76}) can be expressed in terms of \mathbf{C} and \mathbf{r} as described below.

For the sake of notational convenience, let

$$\mathbf{r}_4 = \mathbf{r}_{0,74}^{(0)}, \quad \mathbf{r}_5 = \mathbf{r}_{0,75}^{(0)}, \quad \mathbf{r}_6 = \mathbf{r}_{0,76}^{(0)} \quad (4.21)$$

Then, for $k = 4, 5, 6$,

$$\mathbf{r}_k = \mathbf{r}_{0,7k}^{(0)} = \mathbf{r}_{0,7}^{(0)} + \mathbf{r}_{7,7k}^{(0)} = \mathbf{r}_{0,7}^{(0)} + \mathbf{C}^{(0,7)} \mathbf{r}_{7,7k}^{(7)} \quad (4.22)$$

Note that

$$\left. \begin{aligned} \mathbf{r}_{7,74}^{(7)} &= r_7 \mathbf{u}_1 \\ \mathbf{r}_{7,75}^{(7)} &= r_7 e^{\tilde{\mathbf{u}}_3(2\pi/3)} \mathbf{u}_1 \\ \mathbf{r}_{7,76}^{(7)} &= r_7 e^{-\tilde{\mathbf{u}}_3(2\pi/3)} \mathbf{u}_1 \end{aligned} \right\} \quad (4.23)$$

Hence,

$$\mathbf{r}_4 = \mathbf{r} + r_7 \mathbf{C} \mathbf{u}_1 \quad (4.24)$$

$$\mathbf{r}_5 = \mathbf{r} + r_7 \mathbf{C} e^{\tilde{\mathbf{u}}_3(2\pi/3)} \mathbf{u}_1 \quad (4.25)$$

$$\mathbf{r}_6 = \mathbf{r} + r_7 \mathbf{C} e^{-\tilde{\mathbf{u}}_3(2\pi/3)} \mathbf{u}_1 \quad (4.26)$$

On the other hand, similarly to Eqs. (4.17) to (4.19), the location vectors of the spherical joint centers can also be expressed in terms of the joint variables as follows.

$$\mathbf{r}_4 = r_0 \mathbf{u}_1 + s_{14} e^{\tilde{\mathbf{u}}_3 \phi_{01}} e^{\tilde{\mathbf{u}}_1 \theta_{01}} \mathbf{u}_3 \quad (4.27)$$

$$\mathbf{r}_5 = e^{\tilde{\mathbf{u}}_3(2\pi/3)} (r_0 \mathbf{u}_1 + s_{25} e^{\tilde{\mathbf{u}}_3 \phi_{02}} e^{\tilde{\mathbf{u}}_1 \theta_{02}} \mathbf{u}_3) \quad (4.28)$$

$$\mathbf{r}_6 = e^{-\tilde{\mathbf{u}}_3(2\pi/3)} (r_0 \mathbf{u}_1 + s_{36} e^{\tilde{\mathbf{u}}_3 \phi_{03}} e^{\tilde{\mathbf{u}}_1 \theta_{03}} \mathbf{u}_3) \quad (4.29)$$

Eqs. (4.27) to (4.29) can also be written as shown below.

$$s_{14} e^{\tilde{\mathbf{u}}_3 \phi_{01}} e^{\tilde{\mathbf{u}}_1 \theta_{01}} \mathbf{u}_3 = \mathbf{x}_4 = \mathbf{r}_4 - r_0 \mathbf{u}_1 \quad (4.30)$$

$$s_{25} e^{\tilde{\mathbf{u}}_3 \phi_{02}} e^{\tilde{\mathbf{u}}_1 \theta_{02}} \mathbf{u}_3 = \mathbf{x}_5 = e^{-\tilde{\mathbf{u}}_3(2\pi/3)} \mathbf{r}_5 - r_0 \mathbf{u}_1 \quad (4.31)$$

$$s_{36} e^{\tilde{\mathbf{u}}_3 \phi_{03}} e^{\tilde{\mathbf{u}}_1 \theta_{03}} \mathbf{u}_3 = \mathbf{x}_6 = e^{\tilde{\mathbf{u}}_3(2\pi/3)} \mathbf{r}_6 - r_0 \mathbf{u}_1 \quad (4.32)$$

Note that $\mathbf{x}_4, \mathbf{x}_5, \mathbf{x}_6$ are known in terms of $\mathbf{r}_4, \mathbf{r}_5, \mathbf{r}_6$ which are in turn known in terms of \mathbf{r} and \mathbf{C} . Hence, the joint variables belonging to the legs can be determined from Eqs. (4.30) to (4.32) as explained below.

When each side of Eq. (4.30) is premultiplied by its transpose, s_{14} is obtained easily as follows.

$$(s_{14} e^{\tilde{\mathbf{u}}_3 \phi_{01}} e^{\tilde{\mathbf{u}}_1 \theta_{01}} \mathbf{u}_3)^T (s_{14} e^{\tilde{\mathbf{u}}_3 \phi_{01}} e^{\tilde{\mathbf{u}}_1 \theta_{01}} \mathbf{u}_3) = \mathbf{x}_4^T \mathbf{x}_4$$

$$\begin{aligned} & s_{14}^2 (\mathbf{u}_3^T e^{-\tilde{\mathbf{u}}_1 \theta_{01}} e^{-\tilde{\mathbf{u}}_3 \phi_{01}} e^{\tilde{\mathbf{u}}_3 \phi_{01}} e^{\tilde{\mathbf{u}}_1 \theta_{01}} \mathbf{u}_3) \\ &= s_{14}^2 (\mathbf{u}_3^T \mathbf{u}_3) = s_{14}^2 = \mathbf{x}_4^T \mathbf{x}_4 \end{aligned}$$

Note that $s_{14} > 0$. So,

$$s_{14} = \sqrt{\mathbf{x}_4^T \mathbf{x}_4} \quad (4.33)$$

Similarly,

$$s_{25} = \sqrt{\mathbf{x}_5^T \mathbf{x}_5} \quad (4.34)$$

$$s_{36} = \sqrt{\mathbf{x}_6^T \mathbf{x}_6} \quad (4.35)$$

As the next step, Eqs. (4.30) to (4.32) can be written as shown below.



$$e^{\bar{\mathbf{u}}_3\phi_{01}} e^{\bar{\mathbf{u}}_1\theta_{01}} \mathbf{u}_3 = \mathbf{w}_4 = \mathbf{x}_4 / s_{14} \quad (4.30)$$

$$e^{\bar{\mathbf{u}}_3\phi_{02}} e^{\bar{\mathbf{u}}_1\theta_{02}} \mathbf{u}_3 = \mathbf{w}_5 = \mathbf{x}_5 / s_{25} \quad (4.31)$$

$$e^{\bar{\mathbf{u}}_3\phi_{03}} e^{\bar{\mathbf{u}}_1\theta_{03}} \mathbf{u}_3 = \mathbf{w}_6 = \mathbf{x}_6 / s_{36} \quad (4.32)$$

Note that \mathbf{w}_4 , \mathbf{w}_5 , and \mathbf{w}_6 are known at this stage and they represent the unit vectors along the legs of the manipulator. The product on the left hand side of Eq. (4.30) can be expanded as follows.

$$\begin{aligned} e^{\bar{\mathbf{u}}_3\phi_{01}} e^{\bar{\mathbf{u}}_1\theta_{01}} \mathbf{u}_3 &= e^{\bar{\mathbf{u}}_3\phi_{01}} (\mathbf{u}_3 \cos \theta_{01} - \mathbf{u}_2 \sin \theta_{01}) = \mathbf{w}_4 \\ e^{\bar{\mathbf{u}}_3\phi_{01}} \mathbf{u}_3 \cos \theta_{01} - e^{\bar{\mathbf{u}}_3\phi_{01}} \mathbf{u}_2 \sin \theta_{01} &= \mathbf{w}_4 \\ \mathbf{u}_3 \cos \theta_{01} - \mathbf{u}_2 \cos \phi_{01} \sin \theta_{01} + \\ &+ \mathbf{u}_1 \sin \phi_{01} \sin \theta_{01} = \mathbf{w}_4 \end{aligned} \quad (4.33)$$

Let $w_{4k} = \mathbf{u}_k^T \mathbf{w}_4$ for $k=1,2,3$. Then, Eq. (4.33) leads to the following scalar equations.

$$\cos \theta_{01} = w_{43} \quad (4.34)$$

$$\sin \phi_{01} \sin \theta_{01} = w_{41} \quad (4.35)$$

$$\cos \phi_{01} \sin \theta_{01} = -w_{42} \quad (4.36)$$

Eq. (4.34) implies that

$$\sin \theta_{01} = \sigma_1 \sqrt{1 - w_{43}^2} \quad \text{with } \sigma_1 = \pm 1 \quad (4.37)$$

Hence, θ_{01} is obtained with a sign ambiguity as

$$\theta_{01} = \text{atan}_2 \left(\sigma_1 \sqrt{1 - w_{43}^2}, w_{43} \right) \quad (4.38)$$

If $\sin \theta_{01} \neq 0$, or if $w_{43} \neq 1$, Eqs. (4.35) and (4.36) give sine and cosine of ϕ_{01} as

$$\left. \begin{aligned} \sin \phi_{01} &= \sigma_1 w_{41} / \sqrt{1 - w_{43}^2} \\ \cos \phi_{01} &= -\sigma_1 w_{42} / \sqrt{1 - w_{43}^2} \end{aligned} \right\} \quad (4.39)$$

Hence, ϕ_{01} is obtained without any additional sign ambiguity as

$$\phi_{01} = \text{atan}_2(\sigma_1 w_{41}, -\sigma_1 w_{42}) \quad (4.40)$$

Depending on σ_1 , Eqs. (4.38) and (4.40) imply that

$$\theta_{01}^{(-)} = -\theta_{01}^{(+)} \quad \text{and} \quad \phi_{01}^{(-)} = \phi_{01}^{(+)} \pm \pi$$

These relationships in turn imply that the pairs $\{\theta_{01}^{(+)}, \phi_{01}^{(+)}\}$ and $\{\theta_{01}^{(-)}, \phi_{01}^{(-)}\}$ give the same appearance to the first leg of the manipulator except an undiscernible axial flip. Therefore, it is possible to take $\sigma_1 = +1$ without any loss of generality.

On the other hand, if $\sin \theta_{01} = 0$, i.e. if $\theta_{01} = 0$, the first leg of the manipulator will be in its singular position. In this singular position, the first leg stands vertically up as implied by the following reduced forms of Eqs. (4.34) to (4.36).

$$w_{43} = \cos \theta_{01} = 1, \quad w_{42} = 0, \quad w_{41} = 0$$

These equations also show the fact that ϕ_{01} becomes indefinite in the singularity. In other words, when the first leg is vertically up, it can be spun freely by the actuator controlling ϕ_{01} .

The solution procedure described above for the first leg can be applied to the other legs as well. Thus, Eqs. (4.31) and (4.32) lead to the following solutions for the joint angles of the associated universal joints, provided that the legs are not in their singular positions. As discussed for the first leg, the sign variables are taken to be positive for the other legs too.

$$\theta_{02} = \text{atan}_2 \left(\sigma_2 \sqrt{1 - w_{53}^2}, w_{53} \right), \quad \sigma_2 = +1 \quad (4.41)$$

$$\theta_{03} = \text{atan}_2 \left(\sigma_3 \sqrt{1 - w_{63}^2}, w_{63} \right), \quad \sigma_3 = +1 \quad (4.42)$$

$$\phi_{02} = \text{atan}_2(\sigma_2 w_{51}, -\sigma_2 w_{52}) \quad (4.43)$$

$$\phi_{03} = \text{atan}_2(\sigma_3 w_{61}, -\sigma_3 w_{62}) \quad (4.44)$$

As for the rotation matrices associated with the spherical joints, they can be determined by writing the orientation equations, i.e. Eqs. (4.11) to (4.13), as follows.

$$\mathbf{R}_4 = e^{-\bar{\mathbf{u}}_1\theta_{01}} e^{-\bar{\mathbf{u}}_3\phi_{01}} \mathbf{C} \quad (4.45)$$



$$\mathbf{R}_5 = e^{-\tilde{\mathbf{u}}_1\theta_{02}} e^{-\tilde{\mathbf{u}}_3\phi_{02}} e^{-\tilde{\mathbf{u}}_3(2\pi/3)} \mathbf{C} e^{\tilde{\mathbf{u}}_3(2\pi/3)} \quad (4.46)$$

$$\mathbf{R}_6 = e^{-\tilde{\mathbf{u}}_1\theta_{03}} e^{-\tilde{\mathbf{u}}_3\phi_{03}} e^{\tilde{\mathbf{u}}_3(2\pi/3)} \mathbf{C} e^{-\tilde{\mathbf{u}}_3(2\pi/3)} \quad (4.47)$$

Suppose, \mathbf{C} is specified by specifying three Euler angles (α, β, γ) according to the 3-2-3 sequence. In other words,

$$\mathbf{C} = e^{\tilde{\mathbf{u}}_3\alpha} e^{\tilde{\mathbf{u}}_2\beta} e^{\tilde{\mathbf{u}}_3\gamma} \quad (4.48)$$

With the preceding expression of \mathbf{C} , Eqs. (4.45) to (4.47) can be written as

$$\mathbf{R}_4 = e^{-\tilde{\mathbf{u}}_1\theta_{01}} e^{\tilde{\mathbf{u}}_3(\alpha-\phi_{01})} e^{\tilde{\mathbf{u}}_2\beta} e^{\tilde{\mathbf{u}}_3\gamma} \quad (4.49)$$

$$\mathbf{R}_5 = e^{-\tilde{\mathbf{u}}_1\theta_{02}} e^{\tilde{\mathbf{u}}_3(\alpha-\phi_{02}-2\pi/3)} e^{\tilde{\mathbf{u}}_2\beta} e^{\tilde{\mathbf{u}}_3(\gamma+2\pi/3)} \quad (4.50)$$

$$\mathbf{R}_6 = e^{-\tilde{\mathbf{u}}_1\theta_{03}} e^{\tilde{\mathbf{u}}_3(\alpha-\phi_{03}+2\pi/3)} e^{\tilde{\mathbf{u}}_2\beta} e^{\tilde{\mathbf{u}}_3(\gamma-2\pi/3)} \quad (4.51)$$

4.4. Forward Kinematics

The values of the actuated joint variables $(\phi_{01}, \phi_{02}, \phi_{03}, s_{14}, s_{25}, s_{36})$ are specified. It is desired to determine the consequent position matrices (\mathbf{C} and \mathbf{r}) of the moving platform together with the twelve unspecified joint variables, which are $\theta_{01}, \theta_{02}, \theta_{03}$, and the nine Euler angles of the three spherical joints.

The solution procedure can be started by writing the orientation and location equations, i.e. Eqs. (4.11) to (4.13) and Eqs. (4.17) to (4.19), as shown below.

$$\mathbf{C} = e^{\tilde{\mathbf{u}}_3\phi_{01}} e^{\tilde{\mathbf{u}}_1\theta_{01}} \mathbf{R}_4 \quad (4.52)$$

$$\begin{aligned} e^{\tilde{\mathbf{u}}_3(2\pi/3)} e^{\tilde{\mathbf{u}}_3\phi_{02}} e^{\tilde{\mathbf{u}}_1\theta_{02}} \mathbf{R}_5 e^{-\tilde{\mathbf{u}}_3(2\pi/3)} \\ = e^{\tilde{\mathbf{u}}_3\phi_{01}} e^{\tilde{\mathbf{u}}_1\theta_{01}} \mathbf{R}_4 \end{aligned} \quad (4.53)$$

$$\begin{aligned} e^{-\tilde{\mathbf{u}}_3(2\pi/3)} e^{\tilde{\mathbf{u}}_3\phi_{03}} e^{\tilde{\mathbf{u}}_1\theta_{03}} \mathbf{R}_6 e^{\tilde{\mathbf{u}}_3(2\pi/3)} \\ = e^{\tilde{\mathbf{u}}_3\phi_{01}} e^{\tilde{\mathbf{u}}_1\theta_{01}} \mathbf{R}_4 \end{aligned} \quad (4.54)$$

$$\mathbf{r} = r_0 \mathbf{u}_1 + e^{\tilde{\mathbf{u}}_3\phi_{01}} e^{\tilde{\mathbf{u}}_1\theta_{01}} (s_{14} \mathbf{u}_3 - r_7 \mathbf{R}_4 \mathbf{u}_1) \quad (4.55)$$

$$\begin{aligned} e^{\tilde{\mathbf{u}}_3(2\pi/3)} [r_0 \mathbf{u}_1 + e^{\tilde{\mathbf{u}}_3\phi_{02}} e^{\tilde{\mathbf{u}}_1\theta_{02}} (s_{25} \mathbf{u}_3 - r_7 \mathbf{R}_5 \mathbf{u}_1)] \\ = r_0 \mathbf{u}_1 + e^{\tilde{\mathbf{u}}_3\phi_{01}} e^{\tilde{\mathbf{u}}_1\theta_{01}} (s_{14} \mathbf{u}_3 - r_7 \mathbf{R}_4 \mathbf{u}_1) \end{aligned} \quad (4.56)$$

$$\begin{aligned} e^{-\tilde{\mathbf{u}}_3(2\pi/3)} [r_0 \mathbf{u}_1 + e^{\tilde{\mathbf{u}}_3\phi_{03}} e^{\tilde{\mathbf{u}}_1\theta_{03}} (s_{36} \mathbf{u}_3 - r_7 \mathbf{R}_6 \mathbf{u}_1)] \\ = r_0 \mathbf{u}_1 + e^{\tilde{\mathbf{u}}_3\phi_{01}} e^{\tilde{\mathbf{u}}_1\theta_{01}} (s_{14} \mathbf{u}_3 - r_7 \mathbf{R}_4 \mathbf{u}_1) \end{aligned} \quad (4.57)$$

For the sake of brevity, let

$$\left. \begin{aligned} \phi'_{02} &= \phi_{02} - \phi_{01} + 2\pi/3 \\ \phi'_{03} &= \phi_{03} - \phi_{01} - 2\pi/3 \end{aligned} \right\} \quad (4.58)$$

Then, Eqs. (4.53) and (4.54) can be written further as

$$\mathbf{R}_5 = e^{-\tilde{\mathbf{u}}_1\theta_{02}} e^{-\tilde{\mathbf{u}}_3\phi'_{02}} e^{\tilde{\mathbf{u}}_1\theta_{01}} \mathbf{R}_4 e^{\tilde{\mathbf{u}}_3(2\pi/3)} \quad (4.59)$$

$$\mathbf{R}_6 = e^{-\tilde{\mathbf{u}}_1\theta_{03}} e^{-\tilde{\mathbf{u}}_3\phi'_{03}} e^{\tilde{\mathbf{u}}_1\theta_{01}} \mathbf{R}_4 e^{-\tilde{\mathbf{u}}_3(2\pi/3)} \quad (4.60)$$

When Eqs. (4.58) and (4.59) are substituted, Eqs. (4.56) and (4.57) take the following forms.

$$\begin{aligned} r_0 [e^{\tilde{\mathbf{u}}_3(2\pi/3)} - \mathbf{I}] \mathbf{u}_1 + s_{25} e^{\tilde{\mathbf{u}}_3(\phi_{02}+2\pi/3)} e^{\tilde{\mathbf{u}}_1\theta_{02}} \mathbf{u}_3 \\ = e^{\tilde{\mathbf{u}}_3\phi_{01}} e^{\tilde{\mathbf{u}}_1\theta_{01}} \{s_{14} \mathbf{u}_3 + r_7 \mathbf{R}_4 [e^{\tilde{\mathbf{u}}_3(2\pi/3)} - \mathbf{I}] \mathbf{u}_1\} \end{aligned} \quad (4.61)$$

$$\begin{aligned} r_0 [e^{-\tilde{\mathbf{u}}_3(2\pi/3)} - \mathbf{I}] \mathbf{u}_1 + s_{36} e^{\tilde{\mathbf{u}}_3(\phi_{03}-2\pi/3)} e^{\tilde{\mathbf{u}}_1\theta_{03}} \mathbf{u}_3 \\ = e^{\tilde{\mathbf{u}}_3\phi_{01}} e^{\tilde{\mathbf{u}}_1\theta_{01}} \{s_{14} \mathbf{u}_3 + r_7 \mathbf{R}_4 [e^{-\tilde{\mathbf{u}}_3(2\pi/3)} - \mathbf{I}] \mathbf{u}_1\} \end{aligned} \quad (4.62)$$

Note that

$$[e^{\tilde{\mathbf{u}}_3(2\pi/3)} - \mathbf{I}] \mathbf{u}_1 = -(\sqrt{3}/2)(\sqrt{3} \mathbf{u}_1 - \mathbf{u}_2)$$

and

$$[e^{-\tilde{\mathbf{u}}_3(2\pi/3)} - \mathbf{I}] \mathbf{u}_1 = -(\sqrt{3}/2)(\sqrt{3} \mathbf{u}_1 + \mathbf{u}_2)$$

With these expressions, Eqs. (4.61) and (4.62) can be manipulated into the following ones.



$$\begin{aligned} & s_{25}e^{-\bar{u}_1\theta_{01}}e^{\bar{u}_3\phi'_{02}}e^{\bar{u}_1\theta_{02}}\mathbf{u}_3 - \\ & -(\sqrt{3}/2)r_0e^{-\bar{u}_1\theta_{01}}e^{-\bar{u}_3\phi_{01}}(\sqrt{3}\mathbf{u}_1 - \mathbf{u}_2) \end{aligned} \quad (4.63)$$

$$= s_{14}\mathbf{u}_3 - (\sqrt{3}/2)r_7\mathbf{R}_4(\sqrt{3}\mathbf{u}_1 - \mathbf{u}_2)$$

$$\begin{aligned} & s_{36}e^{-\bar{u}_1\theta_{01}}e^{\bar{u}_3\phi'_{03}}e^{\bar{u}_1\theta_{03}}\mathbf{u}_3 - \\ & -(\sqrt{3}/2)r_0e^{-\bar{u}_1\theta_{01}}e^{-\bar{u}_3\phi_{01}}(\sqrt{3}\mathbf{u}_1 + \mathbf{u}_2) \end{aligned} \quad (4.64)$$

$$= s_{14}\mathbf{u}_3 - (\sqrt{3}/2)r_7\mathbf{R}_4(\sqrt{3}\mathbf{u}_1 + \mathbf{u}_2)$$

As additional definitions, let

$$\mathbf{p} = (\sqrt{3}/2)r_0e^{-\bar{u}_3\phi_{01}}(\sqrt{3}\mathbf{u}_1 - \mathbf{u}_2) \quad (4.65)$$

$$\mathbf{q} = (\sqrt{3}/2)r_0e^{-\bar{u}_3\phi_{01}}(\sqrt{3}\mathbf{u}_1 + \mathbf{u}_2) \quad (4.66)$$

$$\mathbf{f} = s_{25}e^{\bar{u}_3\phi'_{02}}e^{\bar{u}_1\theta_{02}}\mathbf{u}_3 - \mathbf{p} \quad (4.67)$$

$$\mathbf{g} = s_{36}e^{\bar{u}_3\phi'_{03}}e^{\bar{u}_1\theta_{03}}\mathbf{u}_3 - \mathbf{q} \quad (4.68)$$

$$\mathbf{y} = (3/2)r_7\mathbf{R}_4\mathbf{u}_1 \quad (4.69)$$

$$\mathbf{z} = (\sqrt{3}/2)r_7\mathbf{R}_4\mathbf{u}_2 \quad (4.70)$$

Then, Eqs. (4.63) and (4.64) can be written compactly as follows.

$$\begin{aligned} & e^{-\bar{u}_1\theta_{01}}(s_{25}e^{\bar{u}_3\phi'_{02}}e^{\bar{u}_1\theta_{02}}\mathbf{u}_3 - \mathbf{p}) \\ & = e^{-\bar{u}_1\theta_{01}}\mathbf{f} = s_{14}\mathbf{u}_3 - \mathbf{y} + \mathbf{z} \end{aligned} \quad (4.71)$$

$$\begin{aligned} & e^{-\bar{u}_1\theta_{01}}(s_{36}e^{\bar{u}_3\phi'_{03}}e^{\bar{u}_1\theta_{03}}\mathbf{u}_3 - \mathbf{q}) \\ & = e^{-\bar{u}_1\theta_{01}}\mathbf{g} = s_{14}\mathbf{u}_3 - \mathbf{y} - \mathbf{z} \end{aligned} \quad (4.72)$$

When Eqs. (4.71) and (4.72) are premultiplied sequentially by \mathbf{u}_1^T , \mathbf{u}_2^T , and \mathbf{u}_3^T , the following scalar equations are obtained.

$$s_{25} \sin \phi'_{02} \sin \theta_{02} = p_1 - y_1 + z_1 \quad (4.73)$$

$$s_{36} \sin \phi'_{03} \sin \theta_{03} = q_1 - y_1 - z_1 \quad (4.74)$$

$$f_2 \cos \theta_{01} + f_3 \sin \theta_{01} = -(y_2 - z_2) \quad (4.75)$$

$$f_3 \cos \theta_{01} - f_2 \sin \theta_{01} = s_{14} - y_3 + z_3 \quad (4.76)$$

$$g_2 \cos \theta_{01} + g_3 \sin \theta_{01} = -(y_2 + z_2) \quad (4.77)$$

$$g_3 \cos \theta_{01} - g_2 \sin \theta_{01} = s_{14} - y_3 - z_3 \quad (4.78)$$

Note that the components of \mathbf{y} and \mathbf{z} are functions of the three independent parameters of \mathbf{R}_4 , which can be taken as the Euler angles of the 3-2-3 sequence so that

$$\mathbf{R}_4 = e^{\bar{u}_3\phi_{47}}e^{\bar{u}_2\theta_{47}}e^{\bar{u}_3\psi_{47}} \quad (4.79)$$

With this in mind, Eqs. (4.73) and (4.74) can be solved for θ_{02} and θ_{03} as follows if $\sin \phi'_{02} \neq 0$ and $\sin \phi'_{03} \neq 0$.

$$\sin \theta_{02} = \zeta_{02} = \frac{p_1 - y_1 + z_1}{s_{25} \sin \phi'_{02}}$$

$$\cos \theta_{02} = \xi_{02} = \sigma_2 \sqrt{1 - \zeta_{02}^2}, \quad \sigma_2 = +1$$

$$\theta_{02} = \text{atan}_2(\zeta_{02}, \xi_{02}) \quad (4.80)$$



$$\begin{aligned}\sin \theta_{03} &= \zeta_{03} = \frac{q_1 - y_1 - z_1}{s_{36} \sin \phi'_{03}} \\ \cos \theta_{03} &= \xi_{03} = \sigma_3 \sqrt{1 - \zeta_{03}^2}, \quad \sigma_3 = +1 \\ \theta_{03} &= \text{atan}_2(\zeta_{03}, \xi_{03})\end{aligned}\quad (4.81)$$

Note that the sign variables σ_2 and σ_3 are both taken to be positive because the angles θ_{02} and θ_{03} can never be obtuse. On the other hand, the actuated joint angles $(\phi_{01}, \phi_{02}, \phi_{03})$ can be specified so that the singularity conditions, i.e. the equalities $\sin \phi'_{02} = 0$ and $\sin \phi'_{03} = 0$, are avoided.

With θ_{02} and θ_{03} as obtained above, the components of \mathbf{f} and \mathbf{g} also become known as functions of the Euler angles of \mathbf{R}_4 . Proceeding with the solution, θ_{01} can be obtained twice from Eqs. (4.75) and (4.76) and also from Eqs. (4.77) and (4.78) as follows.

$$\left. \begin{aligned}\cos \theta_{01} &= \xi'_{01} = \frac{(s_{14} - y_3 + z_3)f_3 - (y_2 - z_2)f_2}{f_2^2 + f_3^2} \\ \sin \theta_{01} &= \zeta'_{01} = -\frac{(s_{14} - y_3 + z_3)f_2 + (y_2 - z_2)f_3}{f_2^2 + f_3^2}\end{aligned}\right\} \\ \theta_{01} &= \text{atan}_2(\zeta'_{01}, \xi'_{01})\quad (4.82)$$

$$\left. \begin{aligned}\cos \theta_{01} &= \xi''_{01} = \frac{(s_{14} - y_3 - z_3)g_3 - (y_2 + z_2)g_2}{g_2^2 + g_3^2} \\ \sin \theta_{01} &= \zeta''_{01} = -\frac{(s_{14} - y_3 - z_3)g_2 + (y_2 + z_2)g_3}{g_2^2 + g_3^2}\end{aligned}\right\} \\ \theta_{01} &= \text{atan}_2(\zeta''_{01}, \xi''_{01})\quad (4.83)$$

The two solutions obtained above for θ_{01} must be the same. That is,

$$\text{atan}_2(\zeta'_{01}, \xi'_{01}) = \text{atan}_2(\zeta''_{01}, \xi''_{01})\quad (4.84)$$

Moreover, the consistency of the equation pairs used above necessitates that

$$f_2^2 + f_3^2 = (s_{14} - y_3 + z_3)^2 + (y_2 - z_2)^2\quad (4.85)$$

$$g_2^2 + g_3^2 = (s_{14} - y_3 - z_3)^2 + (y_2 + z_2)^2\quad (4.86)$$

Note that Eqs. (4.86), (4.85), and (4.84) contain only three unknowns, which are the Euler Angles $(\phi_{47}, \theta_{47}, \psi_{47})$ of \mathbf{R}_4 . However, these equations are highly nonlinear and they can only be solved by means of a suitable numerical method. After they are solved though, the other unspecified joint variables $(\theta_{02}, \theta_{03}, \theta_{01})$ become readily available as given by Eqs. (4.80), (4.81), and (4.82) or (4.83). Afterwards, Eqs. (4.59) and (4.60) give the rotation matrices \mathbf{R}_5 and \mathbf{R}_6 of the other spherical joints J_{57} and J_{67} . Hence, if desired, the associated Euler angles can be extracted from them. Finally, Eqs. (4.52) and (4.55) give the required position matrices \mathbf{C} and \mathbf{r} of the moving platform.

4. Conclusion

A systematic approach is introduced in order to describe the kinematic features of the joints utilized in spatial mechanical systems. This approach is especially convenient for the systems that contain several closed kinematic chains with multi-joint links. After explaining the basic features of the approach, the convenience in its application is demonstrated on a parallel manipulator with six degrees of freedom, which has three legs between its fixed and moving platforms. The legs are connected to the platforms with the universal-prismatic-spherical joint arrangements.

In the remaining part of the paper, the kinematic analysis of the same manipulator is carried out both in the inverse and forward senses. The inverse kinematic solution is obtained in a completely analytical way. The forward kinematic solution is obtained in a semi-analytical way such that the number of scalar equations to be solved numerically is reduced from twelve to three. During writing the kinematic equations, simplifying them, and carrying out the solution operations, the manipulation of the matrix expressions are facilitated to a large extent by using the algebraic features of the rotation matrices in exponential form. Owing to the analytical nature of the solutions, the multiple and singular configurations are readily identified as natural by-products. The sign variables (σ_1, σ_2 , etc), which are introduced to denote the multiple configurations, turn out to be very useful to keep track of them along the solution steps.



References

- [1] Denavit, J. and Hartenberg, R. S., 1955, "A Kinematic Notation for Lower-Pair Mechanisms Based on Matrices", *Journal of Applied Mechanics*, pp. 215-221.
- [2] Özgören, M. K., 1999, "Kinematic Analysis of Spatial Mechanisms using Exponential Rotation Matrices", *Proc. Tenth World Congress on the Theory of Machines and Mechanisms*, Oulu, Finland, pp. 711-716.
- [3] Soltani, Fariborz, 2005, "Kinematic Synthesis of Spatial Mechanisms using Algebra of Exponential Rotation Matrices", *M.S. Thesis* (Supervised by E. Söylemez and M. K. Özgören), Middle East Technical University, Ankara, Turkey.
- [4] Özgören, M. K., 2002, "Topological Analysis of 6-Joint Serial Manipulators and Their Inverse Kinematic Solutions", *Mechanism and Machine Theory*, 37, pp. 511-546.
- [5] Özgören, M. K., "Kinematic Analysis of Spatial Mechanical Systems Using Exponential Rotation Matrices", *Journal of Mechanical Design*, ASME, Vol. 129, November 2007, pp. 1144-1152.



Proceedings of the International Symposium of Mechanism and Machine Science, 2010
AzCIFTtoMM – Izmir Institute of Technology
5-8 October 2010, Izmir, TURKEY



Session 1:

Structural Synthesis and Kinetic Architecture (SsKa) Linkages, Cams, Gearing and Transmissions (LcGt)



Proceedings of the International Symposium of Mechanism and Machine Science, 2010
AzCIFTtoMM – Izmir Institute of Technology
5-8 October 2010, Izmir, TURKEY



Research of Velocity and Acceleration of Suspension Point of new Constructive Decision of a Mechanical Drive for Sucker-Rod Pumps

Ali NAJAFOV^{1*}, Ayaz ABDULLAYEV², Yusif YAGUBALIYEV³

^{1*} Institute for Machine Elements and Lifting-&-Shifting Machines
of Azerbaijan Technical University,
25 H. Cavid Ave, AZ-1073 Baku, Azerbaijan.
E-mail: ali.najafov@rohe.az

² Institute for Machine Elements and Lifting-&-Shifting Machines
of Azerbaijan Technical University

³ Institute of Technological Complexes and Special Techniques of Azerbaijan Technical University

Abstract

This paper compares the kinematics of transforming mechanism of common pumping unit and geared linkage transforming mechanism of new constructive decision of mechanical drive for sucker-rod pumps.

Keywords: Mechanical Drive for Sucker-rod Pump, Transforming Mechanisms Velocity, Acceleration, Bifurcation

1. Introduction

Implementation of pumping methods of oil recovery in oil industry has begun about a century ago. Steady increment of depths and transition to faster ways of production and exploitation of oil wells call for reconstruction of mechanisms used in oil industry and development of new constructive decisions of transforming mechanisms of mechanical drive for sucker-rod pumps, that ensure stability of wellhead rod's movement with the laws that are particularly close to harmonic laws, and also reduction of overall dimensions and increase of reliability level of mechanical drive for sucker-rod pumps.

With the introduction of bottom hole pumping in the oil industry it has been used four-bar linkage as a transforming mechanism whereas in the common beam-pumping units the rod's suspension point is situated on the continuation of arm in the opposite direction relative to rolling bearing [1,2]. In the uncommon beam-pumping units the four-bar linkage is moved from the end support bearing of the beam forward to the well. One of the main disadvantages of the modern mechanical drives for sucker-rod pumps – beam-pumping units is that by the long stroke of rod's suspension point besides the

increment of the overall dimensions of the pumping unit, the dimensions of the wellhead increase as well. It causes difficulties by the transportation, assembling and repair of the well. Using common beam with the arched horse head, it is formed chord arrow at any position of the mechanism. For the liquidation of the chord arrow the beam needs to execute compound motion in the direction of the beam's bar. In this case the beam's support has to have not the rigid attachment, but a joint, than enables translational motion. Under these circumstances it is required to use beam-pumping units with the floating beam having composite construction

In the known construction of the pumping unit the real law of variation of the way, velocity and acceleration of the rod's suspension point has relatively complex pattern that significantly differs from the simple harmonic one. The pumping unit [3] consists of double- or triple-reduction unit of classical execution that requires use of high power electric motors with extremely low frequencies of rotation and efficiency. This significantly increases the overall dimensions of the whole system and decreases the reliability.

Analysis and experience of exploitation of the operating schemes and constructions has revealed their following disadvantages:

- laws of variation of way, velocity and acceleration of the rod's suspension point of these mechanical systems don't fully ensure qualitative functioning of deep-well pumps;
 - high power electric motors with lower rotation frequency are used and this results in high energy consumption;
 - share part of V-belt drive and reduction gear unit in the rated(nominal) load distribution is ensured irrationally.
- On the assumption of the premises, the problem of increasing of technical level and performance figures of

mechanical drive for sucker-rod pumps sets before the researchers and constructors necessity to solve the problem to ensure best qualitative functioning of rod's suspension point of mechanical drive for sucker-rod pumps and lower energy consumption by saving their main performance figures

One of the demands to meet by the kinematic scheme of pumping unit is conservation of the same value of the average velocity of rod's suspension point by upward and downward motion, in other words time spent on upward and downward motion has to be the same.

Inobservance of this condition can lead to following problems:

1. $V_1 > V_2$ or ($t_1 < t_2$) is accompanied by the increase of dynamic load under the inertia of the rods and the liquid and hydraulic impact, which worsen the work of the pumping unit, this requires decrease of the static load and leads to underuse of the unit's capabilities.
2. $V_1 < V_2$ or ($t_1 > t_2$) is accompanied by the intensity increase of fluid weepage through the gaps between the plunger and pump cylinder.

Ensuring the symmetric pumping conditions, the above mentioned events take place only by average operating conditions. Moreover, this pumping condition is favorable for the operation of the mechanism as a whole, because the forces in the pieces of the mechanism have the same magnitude in both directions of motion or rod's suspension point, which also enables use of more cheaper asynchronous electric motors with higher frequencies of rotation and lower power.

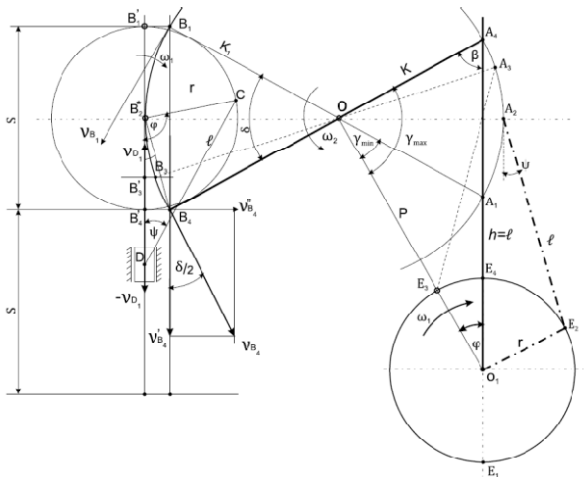


Fig1. Kinematic scheme of the common beam-pumping units

Figure 1 presents the kinematic scheme of the common beam-pumping units. On the extreme positions A_1 and A_2 the crank FE and connecting rod AE are

stretched into a straight line. By transfer of the tail half of beam from the position OA_1 to the position OA_2 the crank turns through angle φ_1 , and by the transfer from OA_2 position into OA_1 – through angle φ_2 .

Thus, by rotation of the crank with the constant angular velocity:

$$\varphi_1/\varphi_2 = t_1/t_2 = V_2/V_1 = k_i$$

where t_1 and t_2 is time spent for the turn of the crank through angles φ_1 и φ_2 ; V_2, V_1 – average speed of point A by passing from A_1 to A_2 position and backwards; k_i – velocity change coefficient of crank's motion.

In the construction of modern beam-pumping units the crank and the connecting rod on the both extreme positions lie on the straight line, that passes through the rotation center of the crank. And velocity change coefficient of crank's motion k_i equals to one 1, thus ensuring same velocity of rod's suspension point by the upward and downward motion. For the estimation of the way, velocity and acceleration of the rod's suspension point of the common beam-pumping units for any position of the crank the following equations can be used [1]:

$$S = k_i \delta = \frac{S_0}{2} \cdot \frac{1}{\arcsin \frac{r}{k}} \cdot \delta \quad (1)$$

$$V = \frac{\pi n}{30} \cdot \frac{S_0}{2} \cdot \frac{\frac{r}{k}}{\arcsin \frac{r}{k}} \cdot \frac{\sin \alpha}{\sin \beta} \quad (2)$$

$$a = \left(\frac{\pi n}{30} \right)^2 \cdot \frac{S_0}{2} \cdot \frac{\frac{r}{k}}{\arcsin \frac{r}{k}} \cdot \frac{p}{l} \cdot \frac{\cos \alpha \cdot \sin \gamma + \frac{r}{k} \sin \alpha \cdot \text{ctg} \beta \cdot \sin \varphi}{\sin^2 \beta} \quad (3)$$

Where $k=OA$ - is the length of the tail half of beam, $k_1=OB$ – length of the front half of the beam, r - crank's length, l - length of the connecting rod, n - rotation frequency of the crank, min^{-1} , S_0 - the maximum stroke length of rod's suspension point, φ – angle between the crank and the connecting rod, β - angle between the tail half of the beam k and the connecting rod, γ - angle between the tail half of the beam k and the pole p , δ -swinging angle of the beam.

However, the real displacement of the plunger of the deep-pump performed by the common pumping units, as a rule, does not correspond to the made demands. As a main cause for this are considered elastic deformations of the

bars and rods, that are formed as a result of impose of variable in magnitude loads, influence of the inertial forces of flowing liquid masses and pumping bars, which substantially depend also on significant difference between laws of variations of way, velocity and acceleration of rod's suspension point in common beam-pumping units and simple harmonic laws.

At the department Machine Elements of Azerbaijan Technical University has been developed, made and tested fundamentally new constructive decision of mechanical drive for sucker rod pumps [4], (fig. 2).

And the execution of the transforming mechanism as a slide-crank mechanism with the embedded planetary gear possessing the laws that are particularly close to the theoretic laws of variation of way, velocity and acceleration of rod's suspension point, and bifurcation enables to eliminate the beam in the present mechanical system, that has a relatively compound construction and leads to increase of the overall dimensions of the system.



Fig. 2. New constructive decision of the mechanical drive for sucker rod pumps.

This way friction losses in kinematic pairs decrease, and stroke of wellhead rod's bracket by oil extraction takes place in a wide range due to theoretically derived laws of motion of rod's suspension point respectively cosinusoid - for way, sinusoid - for velocity and cosinusoid - for acceleration with the amplitudes r , $r\omega$ and $r\omega^2$ of mechanical drive of well pumps. Fig.3 shows scheme of transforming mechanism of patented beamless pumping unit with the unique design of geared linkage mechanism.

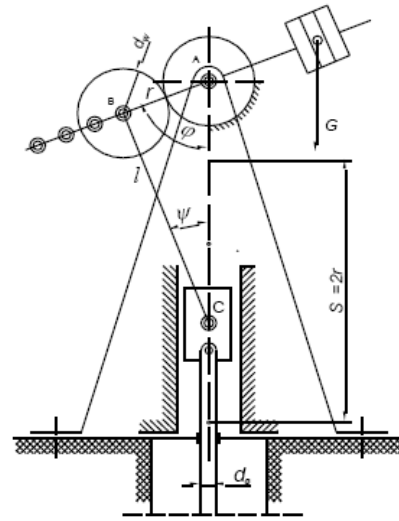


Fig. 3 Design diagram of geared linkage mechanism of new constructive decision of mechanical drive for sucker rod pumps

Compared with beam-pumping units the developed beamless pumping unit has more reliability and infallibility, because it lacks such weak links as swivel horsehead and its supporting nodes. The pumping unit equipped with the developed transforming geared linkage mechanism has better dynamic behavior because the crank rotates uniformly, there are not significant unbalanced masses and acting on the base horizontally directed alternating forces that are characteristic for beam-pumping units. Since the horsehead with the beam is replaced by the fixed base with the positioned guide gear wheel, better centering with the wellhead is ensured.

And the equation of displacement of wellhead rod's suspension point of new constructive decision of mechanical drive for sucker rod pumps can be found as difference between the sum of crank's and connecting rod's lengths and sum of lengths of their projection on the trajectory of last one [5]:

$$s_c = r \left[(1 - \cos\varphi) + \frac{1}{\lambda} (1 - \cos\psi) \right] \quad (4)$$

Now doubly differentiating the equation (4) it is not difficult to find analytical equations for the velocity and acceleration of rod's suspension point:

$$V_c = r \frac{\pi n}{30} \frac{\sin(\varphi + \psi)}{\cos\psi} \quad (5)$$

$$a_c = r \left(\frac{\pi n}{30} \right)^2 \left[\frac{\cos(\varphi + \psi)}{\cos\psi} + \lambda \frac{\cos^2\varphi}{\cos^3\psi} \right] \quad (6)$$



And parameters of the present mechanical system are rotation frequency n , length r , angle of rotation of crank φ and also dimensionless coefficient $\lambda = r/l$. On the assumption of premises by using (4), (5), (6) it has been made a numerical experiment, which results are presented on the figure 4 and 5.

Based on the drawn results it has been established that by using new constructive decision of the mechanical drive for sucker rod pumps deviations of real maximum speed and acceleration from maximum speed and acceleration of ideal harmonic motion depending on the value of parameter $\langle \lambda \rangle$ make (2... 7%). This circumstance denotes reasonability of the use of new constructive decision of mechanical drive for sucker rod pumps by oil recovery.

Comparing with the proposed construction of new constructive decision of mechanical drive for sucker rod pump in the common pumping units exists a problem of “bifurcation” – output of system from the dead points. The quantitative value of rod’s suspension point’s holding time at these positions (consequently plunger’s as well) of mechanism can be estimated using the following equations (pic.1):

$$t^* = \frac{[(\alpha \cdot k_1)^2 - S^2]^{\frac{1}{2}}}{2\omega_2 \cdot OB} \quad (7)$$

where: $\omega_2 = f(\omega_1)$; $B_2^* B_4 = 0,5\alpha \cdot k_1$; $B_2' B_4' = 0,5\alpha \cdot S$;

$$B_4^* B_4 = \left[(B_2^* B_4)^2 - (B_2' B_4')^2 \right]^{\frac{1}{2}} = 0,5 \left[(\alpha \cdot k_1)^2 - S^2 \right]^{\frac{1}{2}}$$

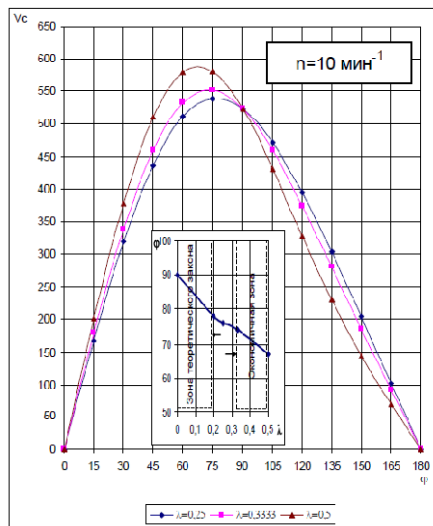


Fig. 4. Behavior pattern of of rod’s suspension point of new constructive decision of mechanical drive for sucker rod pumps depending on the crank’s rotation angle and dimensionless parameter λ

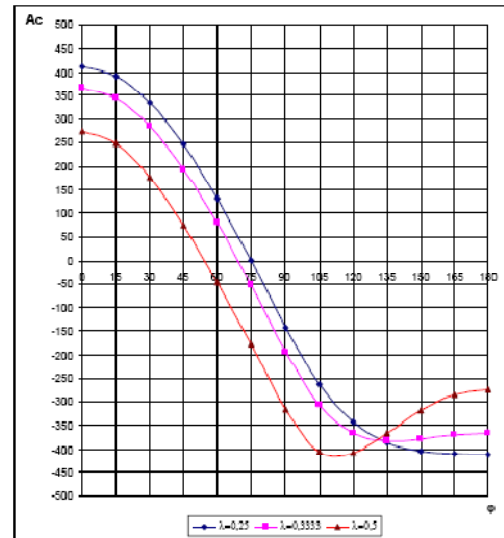


Fig. 5. Behavior pattern of acceleration of rod’s suspension point of new constructive decision of mechanical drive for sucker rod pumps depending on the crank’s rotation angle φ and dimensionless parameter λ .

Thereby, comparing with the proposed construction of the new construction decision of mechanical drive for sucker rod pumps, plunger of the deep-well pump of common pumping units is staying at the lower and upper dead points longer for the time t^* , that can lead to the anticipatory deterioration of pump’s plunger because of the ingress of big amount of sand into the cavity of pump’s cylinder or incomplete use of whole capacity of the cylinder because of the ingress of condensate gases and oil displacement.

Approaching of the laws of variation of way, velocity and acceleration of rod’s suspension point of new constructive decision of mechanical drive for sucker rod pumps to the harmonic laws decreases additional dynamic load caused by rods’ vibrations and also inertial loads on the rods, which undoubtedly will increase their durability [6].

2. Conclusion

All the aforesaid proves higher efficiency and reliability of the new construction of mechanical drive for sucker rod pumps compared with the common beam-pumping units.

References

- [43]. Aliverdzade K.S., *Technology and technique of oil and gas recovery*, Moscow, 1971.
- [44]. Molchanov G.V., Molchanov A.G. *Machines and equipment for oil and gas recovery. Manual*. Nedra Press, Moscow, 1984.
- [45]. Web, [http:// www.neftemash.ru / products/ 23/ index.htm](http://www.neftemash.ru/products/23/index.htm)



- [46]. Abdullayev A.I., Najafov A.M., Gasimov R.M., *Mechanical drive*
- [47]. *for sucker rod pumps*. Eurasian patent № 012103, F04B 47/02, Moscow, 28.08.2009
- [48]. Abdullayev A.I., Najafov A.M., *Analytical kinematics geared linkage mechanism of new constructive decision of mechanical drive for sucker rod pumps*, Azerbaijan Oil industry 4, pages 52-56, 2006.
- [49]. Abdullayev A.I., A.Albers, Najafov A.M., *Estimation of inertial load in new constructive decision of mechanical drive for sucker rod pumps*, Azerbaijan Oil Industry Baku 9, pages 46-49, 2006.



Structural Synthesis of Multi Loop Manipulators with General Constraint One

Rasim ALIZADE¹, Özgün SELVI¹, Erkin GEZGIN¹

¹ Mechanical Engineering Department
Izmir Institute of Technology, 35437 Izmir, Turkey

rasimalizade@iyte.edu.tr, ozgunselvi@iyte.edu.tr, erkingezgin@iyte.edu.tr

Abstract

This study is concentrated on one of the main areas of the fundamental mechanism and machine science as the structural synthesis of multi loop manipulators with general constraint one. The rigid body motions are defined to clarify the motions of the end effector in an overconstrained subspace. The multi-mobility loops with general constraint one are taken from the previous study of the same authors. Theory in the structural design of overconstrained multi loop manipulators is given and presented by several examples.

Keywords: Overconstrained Multi Loop Manipulators, Structural Synthesis, Mobility Equations, General Constraint One, Overconstrained Rigid Body Motions

1. Introduction

Study of structural synthesis on parallel manipulators is in a state of development during the last centuries. Due to this development many investigations on the subject are discussed in the area of mechanism and machine science.

Throughout the literature different methodologies are proposed for the structural design of parallel manipulators. Most apparent ones of these methods can be given as screw theory and group theory. In their researches Huang and Li [1-4] proposed a screw theory based method for the type synthesis of parallel manipulators. The proposed method can be summarized as finding constraints that are given to the end effector from limbs by using reciprocal screws. 3, 4, and 5 DoF non constrained and overconstrained manipulators are also revealed in these researches. Fang and Tsai [5-7] investigated 4 and 5 DoF parallel manipulators with identical limb structures and 3 DoF translational and rotational non constrained and overconstrained manipulators by using theory of reciprocal screws. Kong and Gosselin [8-11] proposed a way for the type synthesis of parallel manipulators that composed of screw theory and virtual chain approach. In their investigations many parallel manipulators with

different type of motions are introduced. Jin et. al. [12] examined the structural synthesis of parallel manipulators based on selective actuation by using screw algebra. The research resulted in 3 DoF spherical motions, 3 DoF translational motions, 3 DoF hybrid motion and 6 DoF spatial motions depending on the types of the actuation. Group theory can be given as another method that is used to define the displacement of rigid body. Herve and Sparacino [13] investigated the structural synthesis of parallel robots that generate translations by using the group theory. In this study the motion of the ends of the limbs is assigned to the same displacement groups and intersection of these subgroups result in the end effector motion as a main displacement group. In the research of Herve [14] the planar-spherical kinematic bond and its usage in structural synthesis of parallel manipulators is deeply investigated by using group theory. Angeles [15-16] implemented the group theory in to the structural synthesis of parallel manipulators. Π , Π^2 and Π^3 type joints are utilized for the type synthesis.

Another procedure related with the parallel manipulator synthesis problem is proposed by Meng et. al. [17], where the set of desired end effector motions is in the form of Lie sub groups or regular sub manifolds of SE (3). In the study of Gao et. al. [18], methodology in the design of parallel manipulators based on Plücker coordinates is proposed. The only investigation known to authors so far about structural synthesis of overconstrained parallel manipulators is done by Zhao et. al. [19] and Gogu [20]. An analytical method of using equivalent screw groups is proposed in the study of Zhao. 3RRC, 3CPR, 3UPU/SPS and 4UPU mechanisms are exposed. A method is proposed by Gogu for structural synthesis of 2 DoF parallel wrist manipulators with uncoupled motions by utilizing theory of linear transformations.

This study deals with the design of new multi loop manipulators with general constraint one by introducing



the procedure in the structural design of overconstrained multi loop manipulators.

2. Rigid Body Motions of the End Effector

The general constraint for a rigid body can be defined as the restrictions that are imposed by external elements. Similarly, for a manipulator, it is the restrictions applied by the geometrical conditions of the linkages and joints. The general constraint of a manipulator can be calculated from the difference of the maximum possible achievable motion of the end effector in general space and the maximum possible achievable free motion of any end effector in its subspace. The formulation for the general constraint of rigid body can be given as,

$$d = 6 - \lambda \quad (1)$$

where in Eq.(1) d stands for the general constraint of the system, λ is the space or subspace number and 6 is the general degrees of freedom in space.

It is clear that, in space any rigid body has six independent motions that consist of three translations and three rotations (PPRRR) with respect to the orthogonal Cartesian coordinate system. On the other hand, in the subspace with general constraint one, the rigid body can only reach two independent motions as three translations and two rotations (PPRR), or two translations and three rotations (PPRRR).

Before describing the rigid body motions in subspace $\lambda=5$ in detail, the related surfaces and their generators must be clearly defined. The spherical surface shown in table 1.1 can be generated by at least two intersecting revolute joints. As shown in table 1.2 planar surface can be generated by RR, RP or PP dyads, whose screw axes are parallel. Note that in planar surfaces, number of prismatic joints can not exceed two. The elliptic cylinder surface ECS can be generated by the combination of prismatic joint and revolute joint, whose screw axes are not parallel (table 1.3). The hyperbolic surface shown in table 1.4 can be generated by a RP dyad with arbitrary screw axes. The elliptic torus surface ETS presented in table 1.5 can be generated by two revolute joint dyads, whose axes are arbitrarily placed. Now the general constraint one or the subspace $\lambda=5$ can be prescribed with the relation of two rigid body surfaces that are defined in table 1. The rigid body motion PPP-RR is described by the motion of a planar surface with respect to a planar surface or a hyperbolic surface HS. PP-RRR motion can be described by the contact motion of a spherical surface or an elliptic torusoidal surface ETS on a planar surface. P-RRRR motion is shown by the respective motions of ECS on spherical surface, HS on spherical surface or HS on ETS. Finally RRRRR motion is described by the motions of a spherical surface on spherical surface or on

ETS and motion of ETS on ETS. Note that, although there are more than 3 rotational motions in some examples, the excessive ones can be represented by translational motions (table 2).

Table 1. Surfaces and Motion Generators

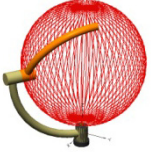
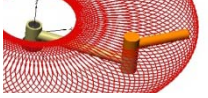
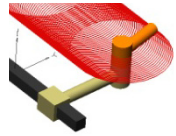
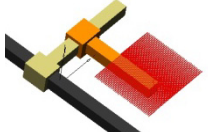
	Surface	Generators	
		Structural Bonding	Figure
1	 Spherical Surface	(RR)	
2	 Planar Surface	$\overline{\text{RR}}$	
		$\overline{\text{PR}}$	
		$\overline{\text{PP}}$	
3	 Elliptic Cylindrical Surface	PR	
4	 Hyperboloid Surface	RP	
5	 Elliptic Torusoidal surface	RR	



Table 2. Summary of Rigid Body Motions in Subspace $\lambda=5$

	Structure	Motion
1	Planar Surface-Planar Surface	PPP-RR
2	Hyperbolic Surface- Planar Surface	PPP-RR
3	Planar Surface- Spherical Surface	PP-RRR
4	ETS-Planar Surface	PP-RRR
5	ECS-spherical surface	P-RRRR
6	HS- Spherical Surface	P-RRRR
7	Hyperbolic Surface-ETS	P-RRRR
8	Spherical Surface- Spherical Surface	RRRRR
9	ETS-Spherical Surface	RRRRR
10	ETS-ETS	RRRRR

It should be noted that, all the structural motions mentioned in table 2 can be also generated or represented by one DoF mechanisms of general constraint one (table 3).

After the description of rigid body motions of the end effector in subspace $\lambda=5$, the procedure in the structural synthesis of multi loop manipulators can be given. As a definition, multi loop manipulator can be specified as a closed loop mechanism with an end-effector that is connected to the base by at least two independent loops and its actuators should be distributed to each leg. These manipulators have some advantages when compared with serial manipulators such as higher precision, robustness, stiffness and load carrying capacity. It is also obvious that multi loop manipulators should consist of multi mobility loops. As a result of this the structural bonding of multi mobility loops with general constraint one should be identified before explaining the structural design of multi loop manipulators. The method of creation of multi mobility loops with angular and linear-angular conditions can be found in the study of Alizade et al. [21]. In their study the structural bonding of multi-mobility loops are illustrated.

3. Structural Synthesis of Overconstrained Multi Loop Manipulators

In addition to the previous definition, multi loop manipulators can be referred as the manipulators that have more than two legs and consist of either one platform or many platforms that are connected by hinges or branches. During the structural synthesis of overconstrained multi loop manipulators, both legs and the loops of the manipulator should be considered and the general mobility formula for multi loop manipulators with variable general constraint should also be developed.

Definition 1: The total number of linear independent close loops L is defined as the difference $L = N - C - B$ [22], where B is the number of platforms, C is the number of connections between platforms and N is the number of joints on the platforms.

By using definition 1, the structural formula for the multi loop manipulators with variable general constraint can be introduced as

$$M = \sum m_i - \lambda(N - C - B) + q \quad (2)$$

where, m_i is the i^{th} independent displacement variable of manipulator associated with the relative displacements at a joint [23] and q is the number of excessive links. If the displacement variables exactly correspond with the DoF of relative motions at joints than the Eq. (2) will become

$$M = \sum_{i=1}^j f_i - \lambda(N - C - B) + q - j_p \quad (3)$$

Where, j is the total number of joints, f_i is the total DoF of the i^{th} joint, and j_p is the number of passive joints.

Using Eq. (3) the general structural formula for multi loop manipulators with variable general constraint one that are composed of only one DoF pairs with no passive joints or excessive links can be given as,

$$\sum_{i=1}^j f_i = j, \quad M = j - 5(N - C - B) \quad (4)$$

$$j = M + 5(N - C - B)$$

As the number of loops also equals to the $L = j - l + 1$ [24], the number of moving links $n = l - 1$ (l = number of total links of the manipulator including the ground link) for the related manipulators can be also described as follows.



$$j = L + l - 1 = L + n$$

$$n = j - N + C + B = \sum_{i=1}^j f_i - N + C + B \quad (5)$$

From this point, using Eq. (4) and Eq. (5) the general procedure of the structural synthesis of multi loop manipulators with general constraint one that are composed of only one DoF pairs with no passive joints or excessive links in subspace ($\lambda=5$) can be given after introducing another definition,

Definition 2: In order to construct a valid multi loop manipulator with general constraint one, the constraint conditions of the whole multi loop manipulator should be consistent with the constraint conditions of the selected first loop.

- Define the motion for the end effector of the multi loop manipulator.
- Decide the number of the platforms (B), the joints on the platforms (N), and the connections (C) with their types (hinges, branch loops or both).
- Select the motions of the platforms from table 2.
- Calculate the number of independent loops $L=N-C-B$.
- Determine the mobility (M) and calculate the number of one DoF joints from Eq (4).
- Calculate the number of moving links (n) by using Eq. (5).
- Select the subspace conditions [21] for the first loop.
- Add legs/loops to the first loop with same or different subspace conditions to fulfill definition 2.
- Choose the actuated joints.

Example 1: Let us design an overconstrained multi loop manipulator for a desired motion. Firstly an overconstrained manipulator with 3 DoF is decided to be designed where the end effector motion can be prescribed by two orientations along a circular arc. Number of platforms is decided as one ($B=1, C=0$) and the platform type is selected as triangular ($N=3$). In order to reach this configuration, total number of joints and independent loops that are needed can be calculated as $L = N - C - B = 3 - 0 - 1 = 2$ $\sum f_i = M + 5L = 3 + 5 \cdot 2 = 13$. Joints will be distributed to the legs as 4-4-5. The subspace condition of loop 1, which is formed by the legs 1 and 2 is selected for 3DoF as $(\text{$$$$})-\text{$$$}$ [21]. Then one leg is attached to the platform as shown in table 4 that will compose a loop that belongs to subspace $\lambda=5$

with leg 1. Note that leg 2 can also be selected. Finally all the actuated joints are selected as shown in Table 4. During the design of this manipulator if the distribution of joints on legs is selected as 3-5-5, another design can be introduced. For the loop that composed by legs 1 and 2 assembly condition is selected for 3DoF as $(\text{$$$})-\text{$$$$}$ [21]. And the second loop, which is formed by legs 2 and 3 has the condition of intersecting axes in 2 points (table 4). It can be seen clearly that leg 2 fits the conditions of each loop. The actuated joints and the construction of manipulator are also shown in Table 4.

Table 3. One Dof Generators of General Constrained One

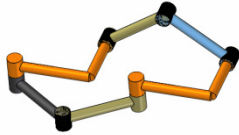
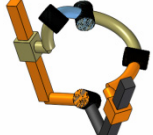
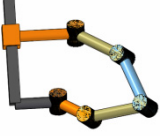
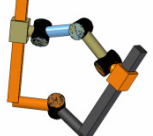
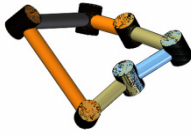
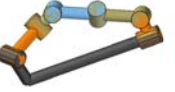
#	Structure		
1	 Planar Surface-Planar Surface	6	 HS- Spherical Surface
2	 Hyperbolic Surface-Planar Surface	7	 Hyperbolic Surface-ETS
3	 Planar Surface-Spherical Surface	8	 Spherical Surface-Spherical Surface
4	 ETS-Planar Surface	9	 ETS-Spherical Surface
5	 ECS-spherical surface	10	 ETS-ETS

Table 4. Steps for Constructing Overconstrained



Manipulators.

First loop	Added leg	Manipulator
a	b	c
d	e	f

Example 2: Let us design an overconstrained serial multi loop manipulator with 4 DoF. The manipulator is decided to have two triangular platforms that are hinged together ($N=6, B=2, C=1$). It is obvious that each platform should have at least two legs. The number of joints and the independent loops will be $L = N - C - B = 6 - 1 - 2 = 3$. $\sum f_i = M + 5L = 4 + 5 \cdot 3 = 19$. The joints could be distributed in a combination of 5-5+4-4 (Figure 1).

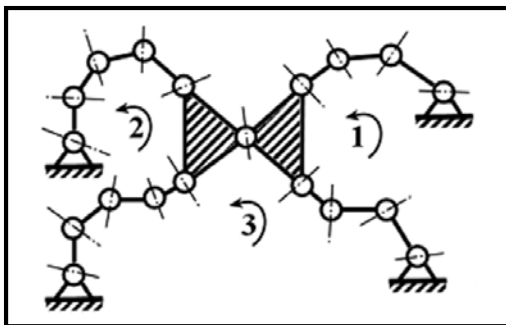


Fig. 1. Structure of Overconstrained Serial Multi Loop Manipulator.

For the combination 5-5+4-4 first loop is defined for 8 joints as $\overline{\text{$$$$}}-\text{(\$$$$)}$ [21]. Then second loop is constructed for 10 joints as $\overline{\text{$$$$}}-\text{(\$$$$\text{\$})}$ [21]. The platforms are connected with a hinge which also fits the conditions of subspace. Finally the actuated joints are selected as shown in Table 5.

Table 5. Construction Steps for Overconstrained Serial

Multi Loop Manipulator.

First loop	Manipulator
a	
Second loop	
	c
b	

Example 3: Let us design an overconstrained parallel multi loop manipulator with 4 DoF. The manipulator is decided to have two rectangular platforms that are connected by one branch loop from subspace $\lambda=3$ ($N=8, B=2, C=2$). The number of joints and the independent loops of the manipulator will be $L = N - C - B = 8 - 2 - 2 = 4$. As the manipulator consists of loops from variable subspaces, another general mobility equation for the manipulators with variable general constraint can be used [23], $\sum f_i = M + \sum \lambda_k = 4 + (5 + 5 + 5 + 3) = 22$. Note that as the number of general constraint of the branch loop is higher than the leg loops it is selected as the fourth independent loop. The joints are decided to be distributed to the legs and branch as seen in figure 2.

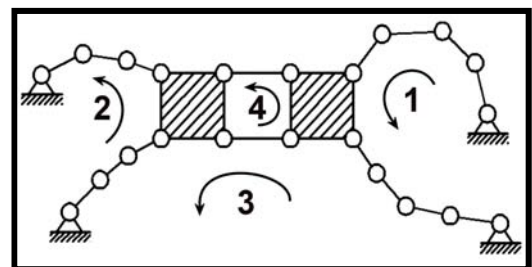


Fig. 2. Structure of Overconstrained Parallel Multi Loop Manipulator.

For the system in figure 2 the first loop is defined for 10 joints as $\overline{\text{(\$$$$\text{\$})}}-\text{(\$$$$)}$ [21]. Then second loop is constructed for 11 joints with respect to the $\overline{\text{(\$$$$\text{\$})}}-\text{(\$$$$\text{\$})}$ [21]. The platforms are connected with a branch loop which also fits the conditions of the subspace with general constraint one as $\overline{\text{(\$$$$\text{\$})}}$. Finally

the actuated joints are selected as grounds shown in figure 3.

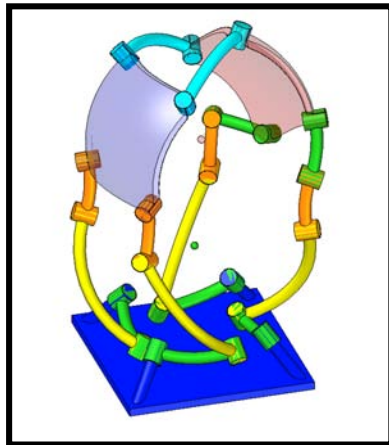


Fig. 3. Overconstrained Parallel Multi Loop Manipulator.

Example 4: Let us design an overconstrained serial-parallel multi loop manipulator with 5 DoF. The manipulator is decided to have two rectangular platforms and one triangular platform that are connected by one branch loop from subspace $\lambda=3$ and a hinge ($N=11, B=3, C=3$). The number of joints and independent loops of the manipulator will be $L = N - C - B = 11 - 3 - 3 = 5$, $\sum f_i = M + \sum \lambda_k = 5 + (5 + 5 + 5 + 5 + 3) = 28$. The joints are decided to be distributed to the legs and branch as seen in figure 4. Note that again as the number of general constraint of the branch loop is higher than the leg loops it is selected as the fourth independent loop.

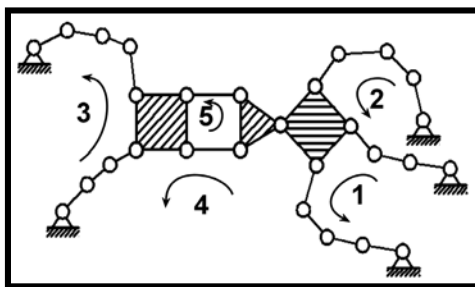


Fig. 4. Structure of Overconstrained Serial-Parallel Multi Loop Manipulator.

For the system in figure 4 the first loop is defined for 9 joints as $\overline{\text{$$$$$$-$$$}}$ [21]. Then second loop is constructed for 9 joints in the configuration of $\overline{\text{$$$$$$-$$$}}$ [21]. Then third loop is constructed for 9 joints as $\overline{\text{$$$$$$-$$$}}$ [21]. The platforms are connected

with a branch loop which also fits the conditions of the subspace of general constraint one as $\overline{\text{$$$$}}$ and a hinge. Finally the actuated joints are selected as grounds as shown in Figure 5.

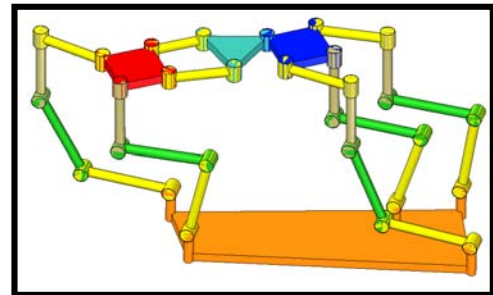


Fig. 5. Overconstrained Serial-Parallel Multi Loop Manipulator.

4. Conclusion

During this study, one of the fundamental area of the mechanism and machine science “structural synthesis” is applied and developed for the multi loop manipulators with general constraint one. After the rigid body motions of the end effector are clarified in an overconstrained subspace by the help of multi mobility loop tables from the previous study [21], a new procedure for the structural synthesis of multi loop manipulators are proposed. Several examples are given for both parallel platform, serial platform and serial-parallel platform manipulators with overconstraint one. Using this study and tables from the previous study of the same authors [21] any designer can develop multi loop manipulators with over constraint one with respect to the desired motion of the end effector, platform kinds and manipulator type.

References

- [1]. Z. Huang, Q.C. Li, General methodology for type synthesis of symmetrical lower-mobility parallel manipulators and several novel manipulators, The International Journal of Robotic Research Vol.21, No2, February (2002), pp. 131-145.
- [2]. Z. Huang, Q.C. Li, Type synthesis of 4-dof parallel manipulators, Proceedings of the 2003 IEEE International Conference on Robotics & Automation, Taipei, Taiwan, September 14-19 (2003), pp. 755-760
- [3]. Z. Huang, Q.C. Li, Type synthesis of 5-dof parallel manipulators, Proceedings of the 2003 IEEE International Conference on Robotics & Automation, Taipei, Taiwan, September 14-19 (2003), pp. 1203-1208
- [4]. Z. Huang, Q.C. Li, On the type synthesis of lower-mobility parallel manipulators, Proceedings of the workshop on Fundamental Issues and Future Research Directions for Parallel mechanisms and manipulators Quebec, Canada (2002), pp. 272-283.
- [5]. Y. Fang, L.W. Tsai, Structure synthesis of a class of 4-dof and 5-dof parallel manipulators with identical limb structures, The



- International Journal of Robotic Research, Vol.21, No. 9, September (2002), pp. 799-810.
- [6]. Y. Fang, L.W. Tsai, Analytical identification of limb structures for translational parallel manipulators, *Journal of Robotic Systems*, Vol. 21 No.5(2004), pp. 209-218
- [7]. Y. Fang, L.W. Tsai, Structure synthesis of a class of 3-dof rotational parallel manipulators, *IEEE Transactions on Robotics and Automation*, Vol.20, No.1, February (2004), pp. 117-121.
- [8]. X. Kong, C.M. Gosselin, Type synthesis of 3T1R 4-dof parallel manipulators based on screw theory, *IEEE Transactions on Robotics and Automation*, Vol.20, No.2, April (2004), pp. 181-190.
- [9]. X. Kong, C.M. Gosselin, Type synthesis of 4-dof SP-equivalent parallel manipulators: A virtual chain approach, *Mechanism and Machine Theory*, 41(2006), pp. 1306-1319.
- [10]. X. Kong, C.M. Gosselin, Generation of parallel manipulators with three translational degrees of freedom based on screw theory, *Proceedings of CCToMM Symposium on Mechanisms, Machines and Mechatronics*, Montreal, Canada (2001)
- [11]. X. Kong, C.M. Gosselin, Type synthesis of parallel mechanisms, Springer (2007)
- [12]. Y. Jin, I.M. Chen, G. Yang, Structure synthesis and singularity analysis of a parallel manipulator based on selective actuation, *Proceedings of the IEEE International Conference on Robotics and Automation*, 6 April-1 May (2004), pp. 4533-4538.
- [13]. J.M. Herve, F. Sparacino, Structural synthesis of parallel robots generating spatial translation, *Fifth International Conference on Advanced Robotics, 'Robots in Unstructured Environments'* (1991), pp. 808-813.
- [14]. J.M. Herve, The planar-spherical kinematic bond: Implementation in parallel mechanisms, (2003), Available from: <<http://www.parallemic.org/Reviews/review013.html>>.
- [15]. J. Angeles, The qualitative synthesis of parallel manipulators, *Proceedings of the workshop on Fundamental Issues and Future Research Directions for Parallel Mechanisms and Manipulators*, Quebec, Canada, October 3-4 (2002), pp.1-10
- [16]. J. Angeles, The degree of freedom of parallel robots: A group theoretic Approach, *Proceedings of the 2005 IEEE International Conference on Robotics and Automation*, Barcelona, Spain, April (2005), pp. 1005-1012
- [17]. J. Meng, G.F. Liu, Z. Li, A geometric theory for synthesis and analysis of sub-6 dof parallel manipulators, *Proceedings of the 2005 IEEE International Conference on Robotics and Automation*, Barcelona, Spain, April (2005), pp. 2938-2943
- [18]. F. Gao, W. Li, X. Zhao, Z. Jin, H. Zhao, New kinematic structures for 2-,3-,4-, and 5-dof parallel manipulator designs, *Mechanism and Machine Theory* 37 (2002), pp. 1395-1411.
- [19]. T.S. Zhao, J.S. Dai, Z. Huang, Geometric analysis of overconstrained parallel manipulators with three and four degrees of freedom, *JSME International Journal Series C*, Vol. 45, No. 3 (2002), pp.730-740.
- [20]. G. Gogu, Fully-isotropic over-constrained parallel wrists with two degrees of freedom, *Proceedings of the 2005 IEEE International Conference on Robotics and Automation*, Barcelona, Spain, April (2005), pp. 4014-4019
- [21]. R. Alizade, O. Selvi, E. Gezgin, Structural design of parallel manipulators with general constraint one, *Mech. Mach. Theory* 45-1 (2010), pp. 1-14.
- [22]. R. Alizade, C. Bayram, Structural synthesis of parallel manipulators, *Mech. Mach. Theory* 39 (2004), pp. 857-870.
- [23]. F. Freudenstein and R. Alizade, On the degree of freedom of mechanisms with variable general constraint, *IV World IFToMM Congress (1975)*, England, pp. 51-56.
- [24]. R. Courant, H. Robbins, I. Steward, 1996, *What is mathematics, Euler's formula*, NY, USA, 1752, pp 235-240.

Multifunctional 7R Linkages

Karl Wohlhart¹

¹ Graz University of Technology, Institute for Mechanics
A8010 Graz, Kopernikusgasse 24
wohlhart@tugraz.at

Abstract

In this paper we present the results of a study on the impact of an “insertion” of mobile over-constrained kinematic chains (such as the 6R Bricard chains, the Goldberg 5R chain or the Bennett 4R chain) into a closed kinematic chain with seven rotary joints (a 7R linkage), which in general is movable with one degree of freedom. Let us assume that in a certain position of a 7R linkage, six (or five, or four) of its rotor joint axes are chosen in such a way that, if rigidly connected, they would present an over-constrained but mobile 6R (5R, 4R) kinematic chain; in other words, by blocking the „remaining“ rotary joint (joints), the 7R linkage could alternatively move as a kinematic 6R (5R, 4R) chain. Then such a manipulated 7R linkage is evidently a multifunctional mechanism. Depending on the starting position any point on such a mechanism could describe two different paths in space which are either totally separated or intersect each other at one or more points. Of special interest is the case when the paths do not intersect but only touch each other at a point. At such a point the two paths smoothly bifurcate. In this paper the existence of such peculiar smooth bifurcations is demonstrated on a number of cases.

Keywords: Over-constrained spatial linkages, bifurcation, smooth bifurcation.

1. Introduction

A closed kinematic chain consisting of seven rigid bodies held together by seven rotary joints (R7) is theoretically finitely movable if body-interferences are excluded (or disregarded). The degree of mobility ranges from one to four, depending on the permanent relative positions of the joint axes or the mutual linear dependency of the joint axes. The topological Grübler-Kutzbach structure formula yields the lower limit for the general kinematic (one-loop) chain, and the upper limit for the planar or the spherical kinematic chain in which all joint-axes are permanently parallel or intersect one another at one point. If four or five or six adjacent joint axes are permanently parallel or meet at one common point, the degree of freedom of the kinematic chain becomes one, two, three, respectively. Now we assume that, in a special position a part of the seven joint-axes of

the 7R linkage shows, exactly the configuration of a mobile over-constrained linkage. We want to know how this fact effects the mobility of the 7R linkage: will it start moving like an over-constrained linkage and block the remaining rotary joints, or will it ignore this configuration and start to move on with seven active joints? Does the inclusion of an over-constrained linkage change the overall degree of freedom? In special cases the answer can be given immediately. Let us look at the 7R linkage shown in Fig. 1, in which four adjacent rotary joint axes are permanently held parallel, i.e. a 7R linkage in which a planar 4R linkage is inserted. By opening the joint k we get two open kinematic chains, a planar chain and a spatial one. The spatial chain has four degrees of freedom relative to the base, just sufficient to be mounted onto the planar chain with a rotary k joint, but only as a rigid chain. Therefore its three inner joints can never become active. Consequently, this special 7R linkage never moves as a genuine 7R linkage but only as a 4R linkage with one degree of freedom and each of its points can only move along one path. The same can be shown for a 7R linkage with four adjacent joint axes intersecting in one point.

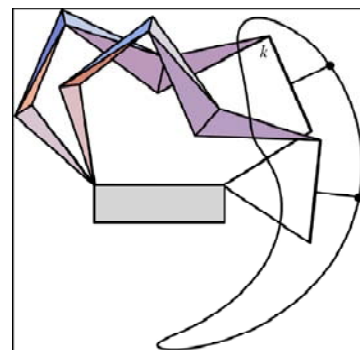


Fig. 1: Path of a point on a special R7 linkage with four permanent parallel adjacent joint axes

In the following it will be shown that in general the existence of an over-constrained linkage topology within the seven axes of a 7R linkage does not change its degree

of freedom, but there are then two possible paths for each linkage point. These two paths either intersect each other nowhere, or intersect at one or more points. The two path-tangents at an intersection point are in general different, but occasionally they are even identical. The intersection points are bifurcation points because at such positions the linkage moving into this position can continue to move differently. At a common bifurcation, i.e. if the path-tangents at this position are different, the linkage must be stopped to avoid infinite accelerations, But if the path-tangents are identical, the linkage can pass the bifurcation at full speed. We shall call this peculiar kind of bifurcation a smooth bifurcation. The main object of this paper is to identify several 7R linkages that permit common or smooth bifurcations and which are therewith multifunctional 7R mechanisms.

2. Planar 4R linkage within a 7R linkage

If the four axes of the implanted 4R linkage are not adjacent in series as shown in Figure 1, the behavior of the 7R linkage becomes essentially different: it can move either as a pseudo 4R linkage with three inactive joints or as a genuine 7R linkage with all seven joints active. Figure 2 shows such a special linkage together with the different paths one of its points can move along. Its Denavit-Hartenberg parameters [1] are collected in Table 1.

$a_1 = 100,$	$\alpha_1 = 0^\circ,$	$s_1 = 0,$
$a_2 = 25,$	$\alpha_2 = -40^\circ$	$s_2 = 0,$
$a_3 = 30,$	$\alpha_3 = 25^\circ.$	$s_3 = 0,$
$a_4 = 35,$	$\alpha_4 = 15^\circ,$	$s_4 = 0,$
$a_5 = 50,$	$\alpha_5 = 0^\circ,$	$s_5 = 0,$
$a_6 = 29.9$	$\alpha_6 = 20^\circ,$	$s_6 = 0,$
$a_7 = 50.1$	$\alpha_7 = -20^\circ,$	$s_7 = 0,$

Table 1: Denavit-Hartenberg parameters of a 7R linkage which includes a planar 4R linkage

The two paths intersect each other in two points as shown in Figure 3. At these points the linkage is in a position from which it can move on differently. Both points are bifurcation points but only one of them is a smooth bifurcation point. In the projection shown in Figure 3 the tangents on the two curves at both intersection points seem to be identical. But another projection of these curves (Figure 4) reveals that at only one intersection point the bifurcation is smooth, i.e. the path tangents coincide.

The intersection points divide each point-paths into

two parts. These parts can be combined to the six different closed curves shown in Figure 5.

Thus the 7R linkage which contains a 4R topology is a multifunctional linkage because in can be made to work in six different ways.

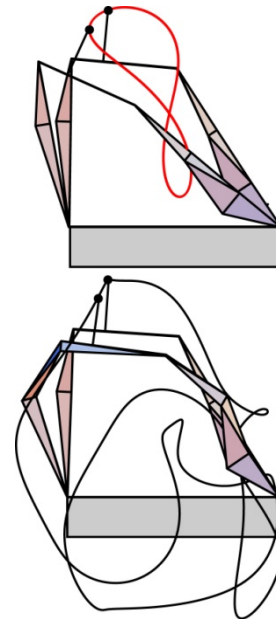


Fig. 2: Planar 4R linkage configuration within a 7R linkage

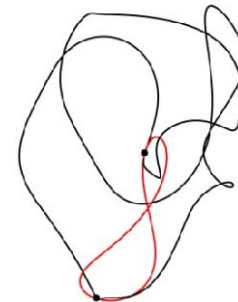


Fig. 3: The intersection points of the two paths

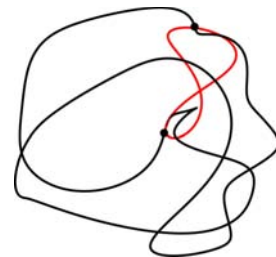


Fig. 4: Another projection of the two paths in Fig.3

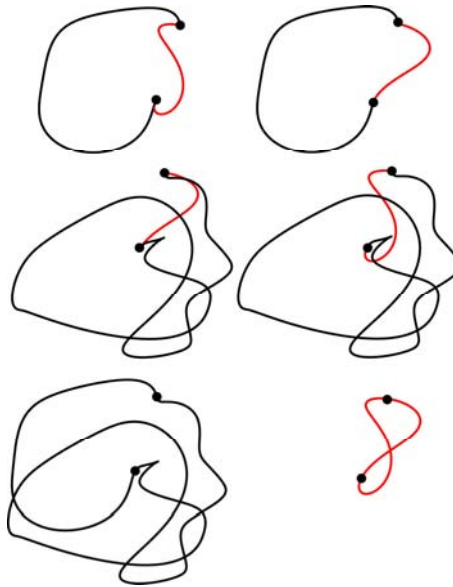


Fig.5. Six possible closed paths of the multifunctional 7R linkage

The intersection points are “stations” on the paths at which some manipulations are necessary in order to switch to another connected path. These manipulations consist in blocking or re-activating some joints or inverting the path direction.

3. Bennett R4 linkage within a 7R linkage

The system parameters of the 7R linkage shown in Table 2 are interconnected in such a way that it can be brought in a position in which a Bennett configuration [2] appears.

$a_1 = 50,$	$\alpha_1 = 20^\circ,$	$s_1 = 0,$
$a_2 = 35,$	$\alpha_2 = -16^\circ,$	$s_2 = 0,$
$a_3 = 25,$	$\alpha_3 = 11^\circ,$	$s_3 = 0,$
$a_4 = 33.969,$	$\alpha_4 = -35^\circ,$	$s_4 = 0,$
$a_5 = 50.$	$\alpha_5 = 20^\circ.$	$s_5 = 0.$
$a_6 = 45,$	$\alpha_6 = -20^\circ,$	$s_6 = 0,$
$a_7 = 48.969,$	$\alpha_7 = -20^\circ,$	$s_7 = 0.$

Table 2. Denavit-Hartenberg parameters of a 7R linkage containing a Bennett linkage

The conditions in Table 2 are the well-known Bennett conditions:

$$a_5 = a_1$$

$$\alpha_2 + \alpha_3 + \alpha_4 = \alpha_6 + \alpha_7,$$

$$a_2 + a_3 + a_4 = a_6 + a_7 = -a_1 \sin(\alpha_2 + \alpha_3 + \alpha_4) / \sin \alpha_1.$$

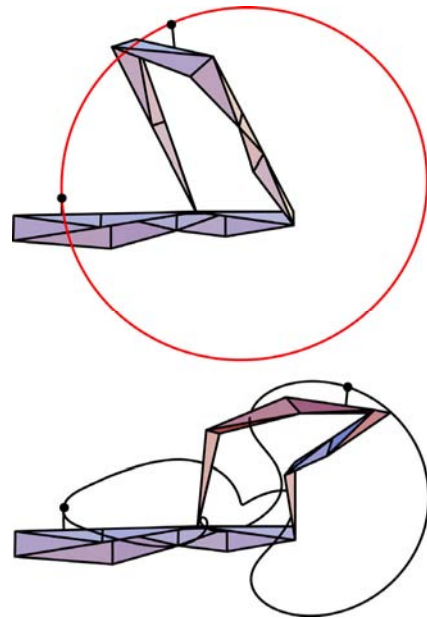


Fig.6. 4R Bennett configuration within a 7R linkage

This linkage can either move as a 4R Bennett linkage (with three joints blocked) or as a genuine 7R linkage with all joints active. The corresponding two paths of a point on the linkage intersect each other in two points, signaling the possibility of bifurcations at two “stations”. While the projection of the two paths shown in Figure 6 is misleading, Figure 7 reveals that there is no smooth bifurcation.

The points of intersections divide each path into two parts. By combining two parts we obtain (as in chapter 2) six closed paths this multifunctional 7R linkage can move along.

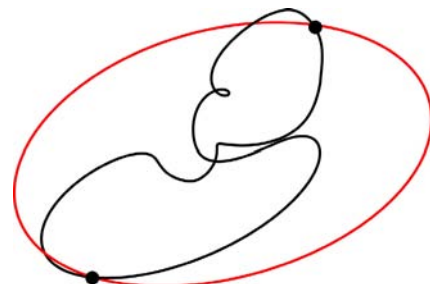


Fig.7. The points of intersection of the two possible paths

4. Orthogonal Bricard 6R linkage in a 7R linkage

If in a link of an orthogonal over-constrained Bricard 6R linkage [3,4] a rotor joint is implanted, a multifunctional 7R linkage is obtained.

$a_1 = 4.2,$	$\alpha_1 = 90^\circ,$	$s_1 = 0,$
$a_2 = 1.85,$	$\alpha_2 = -35^\circ,$	$s_2 = 0,$
$a_3 = 1.85,$	$\alpha_3 = -55^\circ,$	$s_3 = 0,$
$a_4 = 3,$	$\alpha_4 = 90^\circ,$	$s_4 = 0,$
$a_5 = 3.5,$	$\alpha_5 = -90^\circ,$	$s_5 = 0,$
$a_6 = 1.5,$	$\alpha_6 = 90^\circ,$	$s_6 = 0,$
$a_7 = 1.7175,$	$\alpha_7 = -90^\circ,$	$s_7 = 0.$

Table 3. Denavit-Hartenberg parameters of the R7 linkage containing an orthogonal Bricard 6R linkage

Table 3 gives the Denavit-Hartenberg parameters of this 7R linkage and it can be seen that the Bricard conditions for the orthogonal 6R linkage are fulfilled:

$$\alpha_2 + \alpha_3 = -90^\circ,$$

$$a_7 = \sqrt{(a_1^2 + a_4^2 + a_6^2) - ((a_2 + a_3)^2 + a_5^2)}.$$

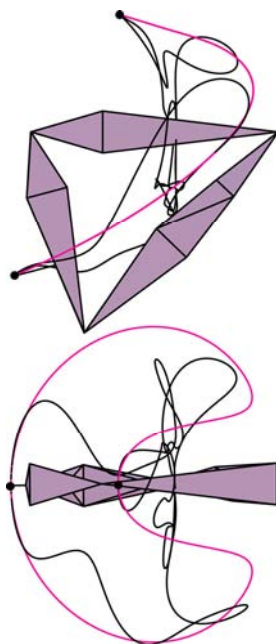


Fig.8: Orthogonal Bricard 6R linkage in a 7R linkage in the starting position together with the two possible paths

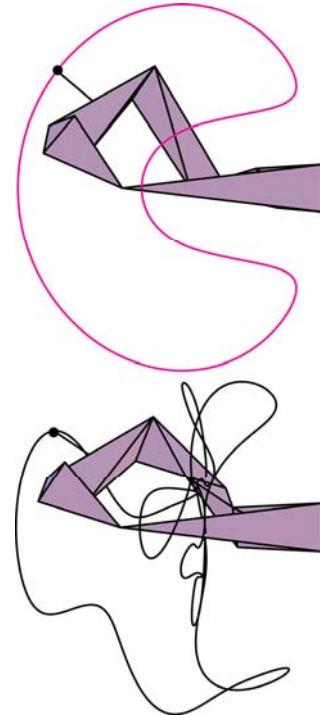


Fig.9. Multifunctional 7R linkage moved out of the starting position in two different ways

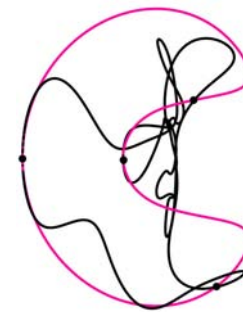


Fig.10: The four intersection points of the two paths

As Figure 10 shows, the two paths intersect at four points, whereby two of the intersections are smooth. The intersection points divide both paths into four parts.

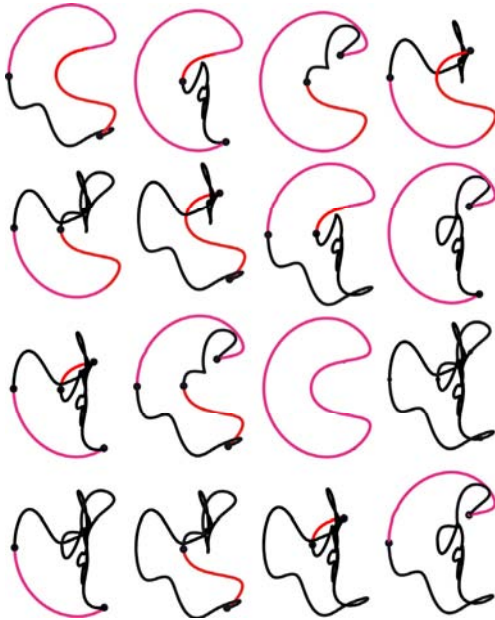


Fig.11: The 16 closed paths together with the “stations”

By combining these parts we find 16 closed paths leading through the four intersection points, which we call “stations” in which path directions have to be changed if the tangents of the successive paths are different (Fig.11).

5. Planesymmetric Bricard 6R in a 7R linkage

By adding a rotor joint into one of the six links of a planesymmetric Bricard 6R linkage [4] we again obtain a multifunctional 7R linkage.

Figure 12 shows this multifunctional 7R linkage in the position from which it can smoothly bifurcate (first picture) and the two different positions into which it can move (second and third pictures). Table 4 gives the corresponding Denavit-Hartenberg parameters.

$a_1 = 70,$	$\alpha_1 = -25^\circ,$	$s_1 = 0,$
$a_2 = 60,$	$\alpha_2 = -30^\circ,$	$s_2 = 30,$
$a_3 = 87.274,$	$\alpha_3 = 0,$	$s_3 = 0,$
$a_4 = 87.274,$	$\alpha_4 = 30.857^\circ,$	$s_4 = 0,$
$a_5 = 174.548,$	$\alpha_5 = -30.857^\circ$	$s_5 = -30$
$a_6 = 60,$	$\alpha_6 = 30^\circ,$	$s_6 = 0,$
$a_7 = 70,$	$\alpha_7 = 25^\circ,$	$s_7 = 0.$

Table 4. Denavit-Hartenberg parameters of the 7R linkage which contains a planesymmetric 6R linkage

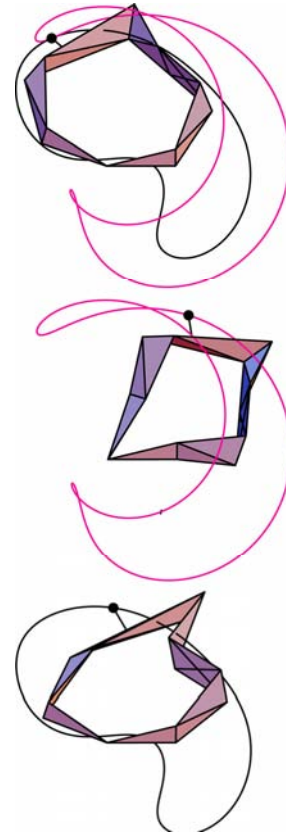


Fig.12. R7 linkage in the position from where it can smoothly bifurcate in two different ways, together with the corresponding two point-traces

Figure 13 shows two projections of the two possible paths of a point on this multifunctional linkage. It can be seen that the two paths contact each other at only one point where the path-tangents coincide.

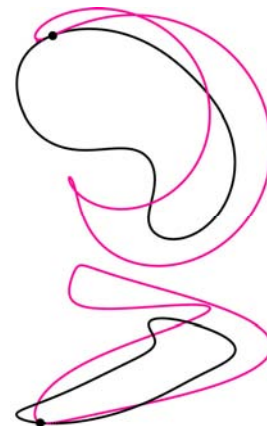


Fig.13. Two projections of the two paths of a point on the multifunctional 7R linkage

As there is only one (smooth) intersection point, the paths are not divided and therefore a point of this linkage can only describe two closed curves, in other words it is a bifunctional linkage.

6. Goldberg 5R linkage within a 7R linkage

By implanting rotor joints into two links of a Goldberg 5R linkage [5], a multifunctional 7R linkage is obtained. This linkage is shown in Figure 14. The first picture shows it in a position of bifurcation from which it can start to move in two different ways. The second and the third pictures show the linkage on these ways. Table 5 collects the Denavit-Hartenberg parameters of this linkage, which confirm the conditions a generalized Goldberg 5R linkage has to comply with [6]:

$$\begin{aligned}
 a_3 + a_4 &= a_7, & \alpha_3 + \alpha_4 &= \alpha_7, & a_5 &= a_6, \\
 a_6 &= \sin \alpha_6 a_7 / \sin \alpha_7, & s_2 &= s_7, & a_1 + a_2 &< 2a_5.
 \end{aligned}$$

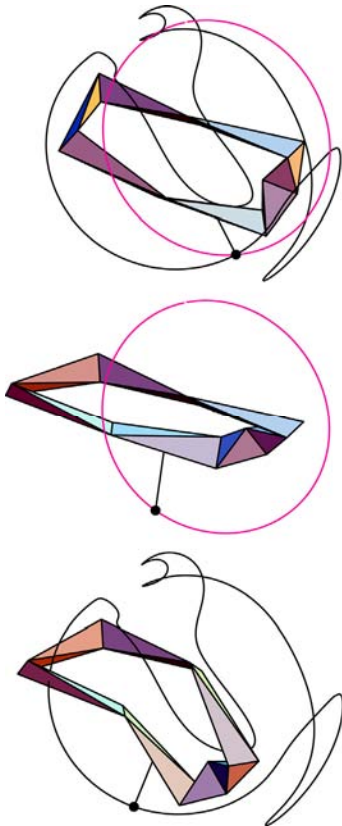


Fig.14. 7R linkage in the position where it can bifurcate in two different ways, together with the two corresponding traces of one of its points

$a_1 = 89.074,$	$\alpha_1 = 39.817^\circ,$	$s_1 = 0,$
$a_2 = 89.074,$	$\alpha_2 = 39.817^\circ,$	$s_2 = -8.48104,$
$a_3 = 40,$	$\alpha_3 = 72.5^\circ,$	$s_3 = 0,$
$a_4 = 40,$	$\alpha_4 = 72.5^\circ,$	$s_4 = 0,$
$a_5 = 89.653,$	$\alpha_5 = 40^\circ$	$s_5 = 0$
$a_6 = 89.653,$	$\alpha_6 = 40^\circ,$	$s_6 = 0,$
$a_7 = 80,$	$\alpha_7 = 145^\circ,$	$s_7 = -8.48104.$

Table 5. Denavit-Hartenberg parameters of the 7R linkage which contains a generalized Goldberg 5R linkage

As can be clearly seen from the projection of the two paths shown in Figure 15, the paths do not touch each other but intersect at two points. So the bifurcations are common bifurcations. The intersection points divide each path into two parts, and with the four parts six closed paths can be formed in the same way as in section 2.

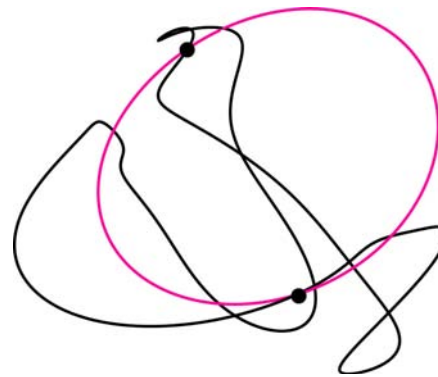


Fig.15. The two intersection points of the two paths a point of the 7R linkage traces in space

7. Conclusions

The formal insertion of a mobile over-constrained linkage with four, five or six axes into a 7R linkage results in a multifunctional linkage because it can bifurcate in a number of different ways, depending on the number of intersections (genuine or tangential) of the two basic point curves. An overview of all the known over-constrained linkages with less than seven rotary joints that can be used to synthesize a multifunctional linkage with seven rotor joints can be found in [7].



The first derivation of the 32nd degree polynomial displacement equation for the general 7R linkage was given by J. Duffy and C. Crane [8] in 1979. A direct way to determine for any input angle the corresponding six position angles of the 7R linkage is shown in the appendix. Therewith the position of any point on the 7R linkage can be found.

Acknowledgements

I want to thank Prof P. Dietmaier for providing me with the Mathematica software to draw the traces of the various points.

References

- [1]. J. Denavit, R.S.Hartenberg, *A kinematic notation for lower pair mechanisms based on matrices*, Journal of Applied Mechanics. 22, pages 215–221, 1955.
- [2]. G.T. Bennett, *The parallel motion of Sarrus and some allied mechanisms*, Philosophical Magazine, 6th Series 9 pages 803–810, 1905.
- [3]. R. Bricard, *Leçons de Cinématique*, Tome II Cinématique Appliquée, Gauthier–Villars, Paris. 1927.
- [4]. J.E. Baker, *An Analysis of the Bricard Linkages*, Mechanism and Machine Theory, 15 pages 219–233.1980.
- [5]. M. Goldberg, *New five-bar and six-bar linkages in three dimensions*. Transactions of the A.S.M.E. 65, pages 649–656, 1943.
- [6]. K.Wohlhart, *Merging two General Goldberg 5R Linkages to obtain a New 6R Space Mechanism*, Mechanism and Machine Theory 26 (7) pages 659–668, 1991.
- [7]. P. Dietmaier, *Einfach übergeschlossene Mechanismen mit Drehgelenken*, Habilitationsschrift TU-Graz 1995.
- [8]. J. Duffy, C.Crane, *A Displacement Analysis of the General Spatial 7-Link, 7R Mechanism*, Mechanism and Machine Theory 15 pages 153–169, 1980.

Appendix

With the vectors

$$\begin{aligned} N_0 &= \{0, 0, 1\}, \\ n_0 &= \{1, 0, 0\}, \\ p_0 &= \{0, 0, 0\}, \end{aligned}$$

$$\begin{aligned} N_1 &= \{-\sin \alpha_1 N_0 \times n_0 + \cos \alpha_1 N_0\}, \\ n_1 &= \{\cos \theta_1 n_0 + \sin \theta_1 N_1 \times n_0\}, \\ p_1 &= p_0 + a_1 n_0 + s_1 N_1, \end{aligned}$$

$$\begin{aligned} N_2 &= -\sin \alpha_2 N_1 \times n_1 + \cos \alpha_2 N_1, \\ n_2 &= \cos \theta_2 n_1 + \sin \theta_2 N_2 \times n_1, \\ p_2 &= p_1 + a_2 n_1 + s_2 N_2, \end{aligned}$$

$$\begin{aligned} N_3 &= -\sin \alpha_3 N_2 \times n_2 + \cos \alpha_3 N_2, \\ n_3 &= \cos \theta_3 n_2 + \sin \theta_3 N_3 \times n_2, \\ p_3 &= p_2 + a_3 n_2 + s_3 N_3, \end{aligned}$$

$$\begin{aligned} N_4 &= -\sin \alpha_4 N_3 \times n_3 + \cos \alpha_4 N_3, \\ n_4 &= \cos \theta_4 n_3 + \sin \theta_4 N_4 \times n_3, \\ p_4 &= p_3 + a_4 n_3 + s_4 N_4, \end{aligned}$$

$$\begin{aligned} n_6 &= \cos \theta_7 n_0 - \sin \theta_7 N_0 \times n_0, \\ N_6 &= \cos \alpha_7 N_0 + \sin \alpha_7 N_0 \times n_6, \\ p_6 &= p_0 - s_7 N_0 - a_7 n_6, \end{aligned}$$

$$\begin{aligned} n_5 &= \cos \theta_6 n_6 - \sin \theta_6 N_6 \times n_6, \\ N_5 &= \cos \alpha_6 N_6 + \sin \alpha_6 N_6 \times n_5, \\ p_5 &= p_6 - s_6 N_6 - a_6 n_5. \end{aligned}$$

$$\begin{aligned} nn_4 &= \cos \theta_5 n_5 - \sin \theta_5 N_5 \times n_5, \\ NN_4 &= \cos \alpha_5 N_5 + \sin \alpha_5 N_5 \times nn_4, \\ pp_4 &= p_5 - s_5 N_5 - a_5 nn_4. \end{aligned}$$

the following set of vector equations can be obtained which contains nine ordinary equations:

$$\begin{aligned} G_1 &= p_4 - pp_4 = 0, \\ G_2 &= n_4 - nn_4 = 0, \\ G_3 &= N_4 - NN_4 = 0. \end{aligned}$$

For a given full set of Denavit-Hartenberg parameters six of the nine equations are sufficient to determine for any value of the input position angle θ_1 the corresponding values of the angles $\theta_2, \theta_3, \theta_4, \theta_5, \theta_6, \theta_7$ via the FindRoot formula in Mathematica. If not all Denavit-Hartenberg parameter are known at the outset, the nine equations can be used to determine the lacking geometric parameters together with the position angles.



Survey of Rigid Body Motions in Space and Subspaces by Using Method of Intersections

Erkin GEZGİN^{1*}

^{1*} Mechanical Engineering Department
Izmir Institute of Technology, 35437 Izmir, Turkey
erkingezgin@iyte.edu.tr

Abstract

This study concentrates on the development of rigid body geometries by using method of intersections, where simple geometric shapes representing revolute (R) and prismatic (P) joint motions are intersected by means of desired space or subspace requirements to create specific rigid body geometries in predefined octahedral fixed frame. Using the methodical approach, space and subspace motions are clearly visualized by the help of resulting geometrical entities that have physical constraints with respect to the fixed working volume. Also, using the idea a new mechanism with variable general constraint one is created and illustrated along with its design procedure for further reference.

Keywords: Subspace, Method of Intersections, Rigid Body Motions, General Constraint.

1. Introduction

Investigation of rigid body motions in space and constrained subspaces is the fundamental tool for designing different new kinds of mechanisms in the area of mechanism and machine science. Although there are not so many studies that are solely concentrated on rigid body movements and subspaces, the idea is indirectly found in the works such as mechanism designs and mobility calculation criterions.

Zhao et al. [1] points out in the beginning of their study that, determination of the independent motions of the end effectors is the main problem in mechanism analysis. Müller [2] mentions in the part of his study about mobility criteria based on motion groups, where the main idea is to identify the group of rigid body motions. Herve [3] introduces the lie group of rigid body displacements as an important tool for mechanism design. Alizade et al. [4] presented the history of structural formulations, where space or subspace number λ was introduced in many works of different authors. Also in their papers [4-6], they proposed new mobility and end effector motion formulations by taking into account subspace of the platforms, leg loops, branch loops and legs. Using these formulations along with the design procedures, they

created different kinds of manipulators. Gogu [7] proposed a new mobility calculation formulation for parallel mechanisms with elementary legs. In his formulation, the independent motion parameters of the platform and the legs must be observed with respect to the fixed frame.

Throughout the works in the literature, it is apparent that, the visualization of the end effector motions and determination of the space or subspace number λ have vital importance. Multiple kinds of manipulators are designed or analyzed after these sequences are fulfilled. To make this process simpler, rigid body motions in space and subspaces should be understood clearly.

2. Rigid Body Motions

Starting from the clearest example, a rigid body with no general constraints ($d = 0$) has six independent motions in Cartesian space ($\lambda = 6$), three revolutions around and three translations along x , y and z axes (figure 1). These motions can be represented as $RRRPPP$, where R and P stand for revolute rotations and prismatic translations respectively. It is very important to note that, any rigid body whether in space or subspaces can not have more than three independent rotations or translations; due to the fact that, there exist only three independent directions in Cartesian space.

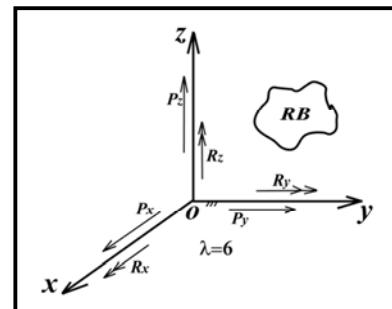
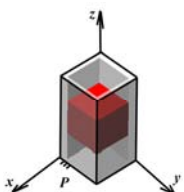
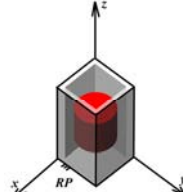
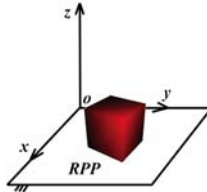
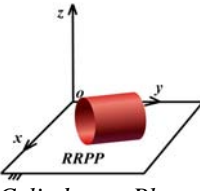
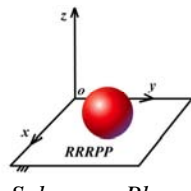
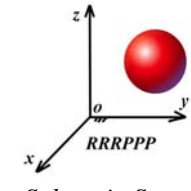


Fig. 1. Rigid Body Motions in Cartesian Space $\lambda = 6$



Table 1. Possible Independent Motion Configurations of Rigid Bodies in Subspaces

λ	1	2	3
Motions	R, P	RR, RP, PP	RRR, RRP RPP, PPP
Examples	 <i>Cube in Slot</i>	 <i>Cylinder in Slot</i>	 <i>Cube on Plane</i>
λ	4	5	6
Motions	$RRRP, RRPP$ $RPPP$	$RRRPP$ $RRPPP$	$RRRPPP$
Examples	 <i>Cylinder on Plane</i>	 <i>Sphere on Plane</i>	 <i>Sphere in Space</i>

Considering this rule, achievable independent motions of the rigid bodies in various subspaces can easily be tabulated. As it is seen in *table 1*, one example for a specific motion related with each of the subspace is given for different rigid body geometries and fixed frames. In the cases of examples, cube in a slot is simply a prismatic joint that have only one translational motion (P) along the z axis. If the cube is changed by a cylindrical rigid body, it gains additional capability to rotate (R) around the z axis keeping its translational motion, so that its subspace is increased by one. On the cube on plane case, without losing area of contact, the rigid body can rotate around the z axis and translate along the x, y axes ($RPP, \lambda = 3$). If the area of contact is changed with line of contact by using cylinder instead of a cube, the rigid body gains another rotation around x or y axis preserving its other motions ($RRPP, \lambda = 4$). Similarly if the cylinder is replaced by a sphere, its line of contact is transformed into a point of contact that means another rotational capability around x or y axis ($RRRPP, \lambda = 5$). Note that, if there is no contact constraint, $RRRPPP$ motion in $\lambda = 6$ is being reached.

Although representing rigid body motions like this way clears the subspace concept, it is difficult to find examples for all motion configurations that preserve one common analogy. As a result, this study contributes the

literature an easy approach that simplifies the visualization of rigid body motions in space or subspaces by introducing unique methodology called method of intersections.

3. Method of Intersections

Briefly, the idea behind the methodology is based on the construction of the octahedral fixed frame, which will be called “*moi space*” hereafter, and the intersections of the simple geometric shapes that carry the behaviors of the prismatic or revolute motions (*figure 2*).

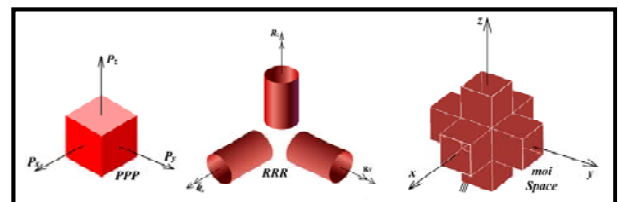


Fig. 2. Simple Geometric Rigid Bodies with Unique Motion Behaviors and moi Space

It can be easily seen from the figure that the selected cube element is just capable of exiting three translational motions along x, y and z axes unless any other constraints prevent it to do so. The other three unique cylinders represent three distinct rotational motions around the



Cartesian axis and the moi space is composed of three slots with square cross sections that are orthogonally combined. Assuming the sides of the cube, the height and the diameter of the cylinders and the side of the inner square cross section of the moi space slots are equal, the following procedure can be performed to visualize the rigid body motions in a specific subspace.

- Select the desired space or subspace number λ_i ($i = 1, 2, \dots, 6$).
- Select the motion configuration of the determined subspace from *table 1*.
- Intersect the geometrical representations of individual motions to end up with a unique geometrical shape.
- If there exist missing translational motions, remove a slot from moi space that is representing missing translational motion axis to create constrained moi space (Note that, if there are not any translational motions in the selected motion configuration, the constrained moi space will just transformed into a hollow cube).
- Put the resultant geometrical shape into moi or constrained moi space to identify the rigid body motion in determined space or subspace.

The idea can appear confusing; however, examples will clarify the subject.

Example 1: Consider that subspace $\lambda = 5$ is selected with the motion configuration $R_x R_y PPP$. After the intersection of the related simple geometrical shapes, the resultant rigid body is placed into the moi space (*figure 3*). Due to the fact that the rigid body has a square cross section on xy plane, its rotation around z axis is constrained as desired. On the other hand circular cross sections on xz and yz planes makes the rotations around x and y axes possible. Also note that all of the translations can be fulfilled thanks to the unconstrained moi space.

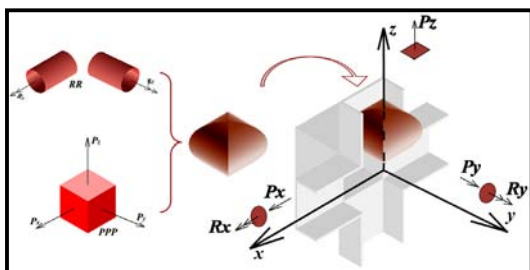


Fig. 3. Visualization of Rigid Body Motions $R_x R_y PPP$ in $\lambda = 5$ by Method of Intersections

Example 2: Consider that again subspace $\lambda = 5$ is

selected, but with different motion configuration $RRR P_x P_y$. As translation along the z axis is not included, z slot of the moi space is removed. After the intersection of the related simple geometrical shapes, the resultant rigid body is this time placed into the constrained moi space (*figure 4*). Due to the fact that the rigid body has circular cross sections on all planes, its rotations around x , y and z axes are possible.

However, removed z slot of the moi space constraints the z translation of the rigid body, while other translations are achievable.

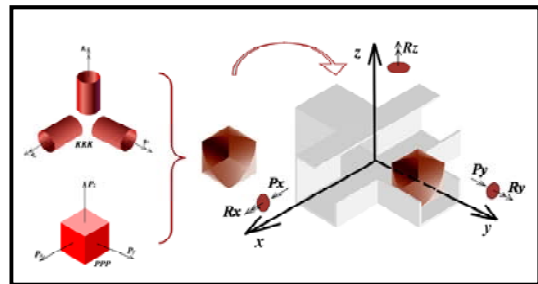


Fig. 4. Visualization of Rigid Body Motions $RRR P_x P_y$ in $\lambda = 5$ by Method of Intersections

Despite of being a useful tool for visualization of rigid body motions in space or subspaces, the methodology explained in this study can also be used for designing new mechanisms. In the light of *example 1*, two dyads are needed to represent two cylinders, where they should be assembled together and articulated in the Cartesian frames to end up with a $\lambda = 5$ mechanism. The dyads are selected as $P-R-R$ chains as they are sufficient for cylinder creation and assembled orthogonally, where prismatic joints are translated along the x and y axes. Finally a new $\lambda = 5$ mechanism with mobility $M = 1$ is created by using the idea behind method of intersections (*figure 5*).

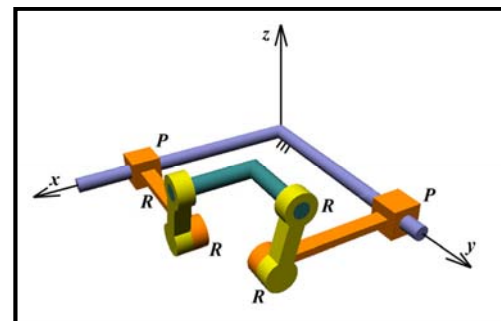


Fig. 5. $\lambda = 5$, $M = 1$ Mechanism by Method of Intersections

Note that by fixing another link instead of the one in the



figure, different motions of the end effector in $\lambda = 5$ can be achieved.

4. Conclusion

As mentioned earlier in the study, this investigation contributes the literature a unique methodology called method of intersections, where rigid body motions in space or subspaces are clearly visualized. All of the space and subspace motions can be described by using this method in a common analogy behind the given examples. Moreover the method is proved to be used for the creation of new mechanisms by introducing the design of $\lambda = 5$ mechanism with mobility $M = 1$.

References

- [1]. J. S. Zhao, J. Z. Feng, J. X. Dong, *Computation of the configuration degree of freedom of a spatial parallel mechanism by using reciprocal screw theory*, Mech. Mach. Theory 41 (2006) 1486-1504
- [2]. A. Müller, *Generic mobility of rigid body mechanisms*, Mech. Mach. Theory 44 (2009), 1240-1255
- [3]. J. M. Herve, *The Lie group of rigid body displacements, a fundamental tool for mechanism design*, Mech. Mach. Theory 34 (1999) 719-730
- [4]. R. Alizade, C. Bayram, E. Gezgin, *Structural synthesis of serial platform manipulators*, Mech. Mach. Theory 42 (2007) 580-599
- [5]. R. Alizade, F. C. Can, E. Gezgin, *Structural synthesis of Euclidean platform robot manipulators with variable general constraints*, Mech. Mach. Theory 43 (2008) 1431-1449
- [6]. R. Alizade, C. Bayram, *Structural synthesis of parallel manipulators*, Mech. Mach. Theory 39 (2004) 857-870
- [7]. G. Gogu, *Mobility of mechanisms: a critical review*, Mech. Mach. Theory 40 (2005) 1068-1097



Structural Synthesis of Novel Overconstrained Parallel Manipulators

Fatih Cemal CAN^{1*}, Erkin GEZGİN²

^{1*} Machine Education Department
Pamukkale University, Technical Education Faculty
Kınıklı Campus KINIKLI / DENİZLİ
fccan@pau.edu.tr

² Mechanical Engineering Department
İzmir Institute of Technology URLA/İZMİR

Abstract

This study represents structural synthesis of several novel parallel manipulators. Invention of single-loop RPRPR and RRRRR mechanisms enables us the idea of designing novel overconstrained parallel manipulators. These manipulators are constructed by using RP (revolute and prismatic are indicated by R and P, respectively) kinematic chain whose motion generates a hyperboloid. The platforms of some novel manipulators have three translational and one rotational motion in space due to the fact that RP chain makes the platforms be constrained. A novel 5 DoF parallel manipulator is constructed by using a planar branch between two platforms. Furthermore, a novel 4 DoF parallel manipulator including a spatial branch-loop is invented.

Keywords: structural synthesis, parallel manipulators, intersection of hyperboloids and spheres, Overconstrained mechanism, branch-loop.

1. Introduction

Structural synthesis always enables researches to find the new way and formulations when they design new structures. This new structures are essential for the development of simulators, medical devices, CNC milling machines, measurement devices and even retractable roof of some buildings.

If all translational and rotational motions in space are not needed for an application, the overconstrained manipulators are good choice. Overconstrained manipulators have an important role due to the fact that they require less kinematic pairs and motors. This is the reason of low cost and less manufacturing process.

The first step of overconstrained manipulators' synthesis is to design single-loop overconstrained mechanism. Then, the special geometric condition of the single-loop mechanism can be applied to the construction of multi-loop overconstrained parallel

manipulators' limbs [1, 2, 3].

The first single-loop 6R overconstrained mechanism was invented by Sarrus in 1853 [4]. In the light of this invention, a lot of overconstrained mechanisms have been proposed by researchers. Waldron emphasized that all 4 link overconstrained mechanisms with lower pairs are determined [5]. The 3 link overconstrained mechanisms are also invented because they are known as a special case of the 4 link ones. However, very few 5 link overconstrained mechanisms are found [5].

Mavroidis and Roth stated that most known overconstrained mechanism were invented by the researcher's geometric intuition rather than analytical mathematic methods [5]. In this study, 5 link overconstrained mechanisms are proposed by geometric intuition since the intersection of two 3D geometric shapes is used during the design. However, it is also possible to verify the proposed mechanisms by means of analytical method that is represented in their research of Mavrodís and Beddows [6].

Aim of the study is to show that the intersections of two identical 3D geometric shapes such as hyperboloids and spheres can be used to construct single-loop 5 link overconstrained mechanisms. Furthermore, novel parallel manipulators are invented by means of special geometric condition of these single-loop mechanisms.

2. Single-Loop RPRPR Kinematic Chain

A single loop RPRPR kinematic chain can be constructed by using idea of two hyperboloids' intersection. A hyperboloid is a ruled surface with its centre at the origin and its symmetric planes coinciding with the origin [7] (see Fig.1. (a)). The equation of the ruled hyperboloid is usually in the form

$$(x^2/a^2) + (y^2/b^2) - (z^2/c^2) - 1 = 0$$

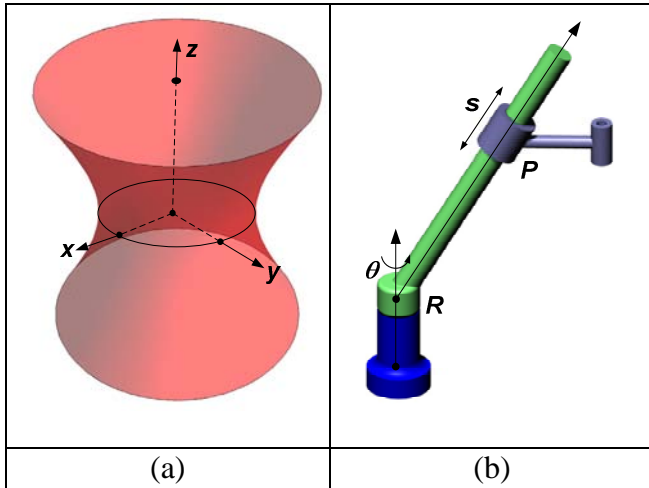


Fig. 1. (a) A ruled hyperboloid by generating equation
 (b) RP open kinematic chain

A hyperboloid can be represented by an open kinematic chain consisting of revolute and prismatic pairs [8]. It is similar to kinematic chain shown in Fig.1(b).

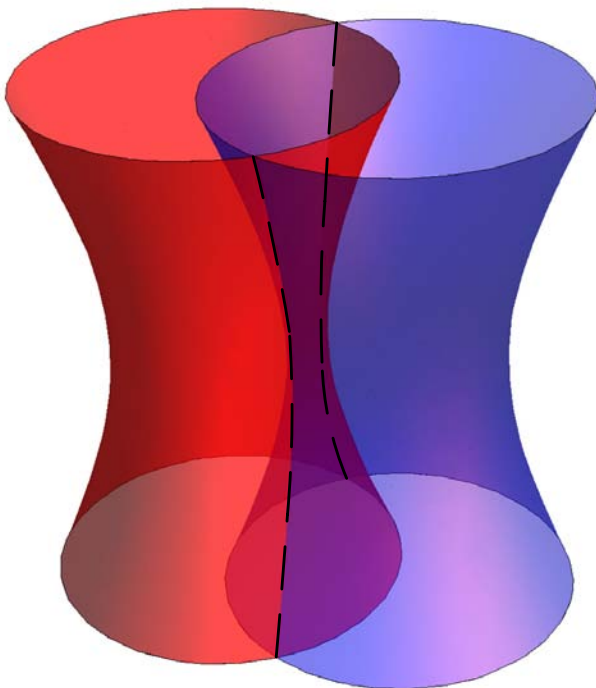
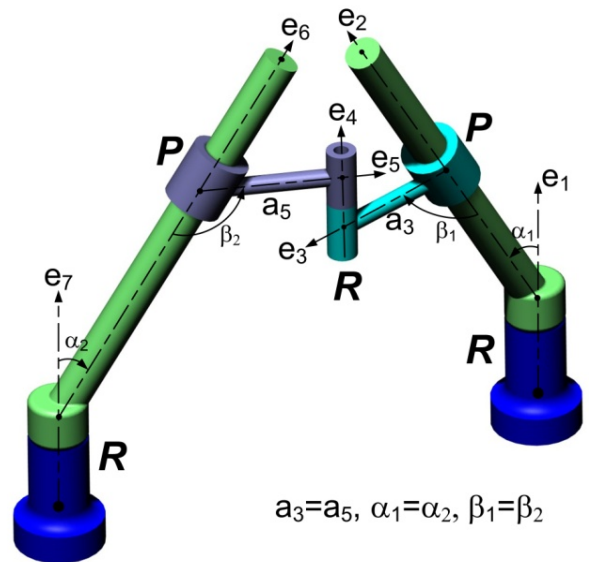


Fig. 2. Intersection of two hyperboloids

Intersection of two hyperboloids ends up with an arc

as shown in Fig.2. If we use two RP kinematic chains generating two intersected hyperboloids and we connect two RP kinematic chains by one revolute pair moving on the intersection arc, the RPRPR closed kinematic chain shown in Fig. 3 is constructed.



$$a_3=a_5, \alpha_1=\alpha_2, \beta_1=\beta_2$$

Fig.3. Single-loop RPRPR overconstrained mechanism

The RPRPR overconstrained mechanism shown in Fig.3 works due to linear dependence of lines and it has one degree of freedom. Therefore subspace of the kinematic chain is four. The system suits explanations in the section 11.6 linear dependence of lines in the book written by Hunt [7]. (Especially see the Fig. 11.6) The same system was preferred as a branch loop for a new advanced serial-parallel Euclidean platform robot manipulator. [9]

2. Single-Loop RRRRR Kinematic Chain

By using the idea of sphere-sphere intersection, RRRRR closed kinematic chain is able to be constructed. Intersection of two spheres is a circle whose center A lies on the line O_1O_2 in Fig.4.

Two revolute pairs whose axes are intersected at one point give spherical surface similar to Fig. 4 . By adding a revolute pair on the circle of intersection such a way that axis of revolute pair is aligned to center of circle, RRRRR closed kinematic chain is formed. Here, two twist angles α_1 and α_2 are equal when distances $|O_1A|$ and $|O_2A|$ are also equal. These are linear and angular constrains for the mechanism. Intersection circle can be named mirror plane of the mechanism.

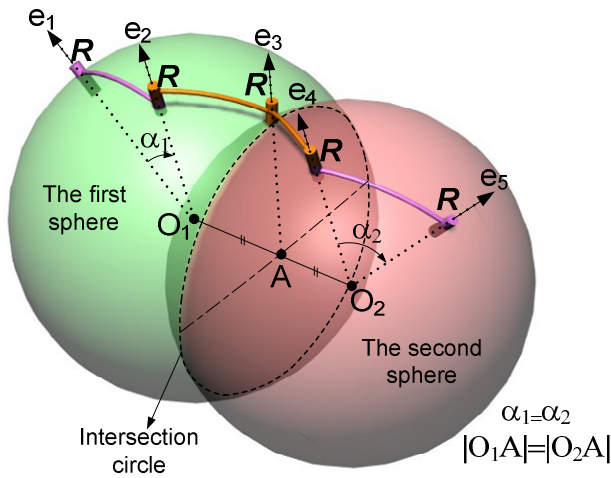


Fig. 4. Single-loop RRRRR overconstrained mechanism

3. Structural Synthesis a 4 DoF Parallel Manipulator

The manipulator is designed by using equation 3 in structural synthesis study of Euclidean platform robot manipulators [9]. This equation was written in the form

$$M = \lambda + j_h + \sum_{l=1}^{c_l} (f_l - \lambda_l) \quad (1)$$

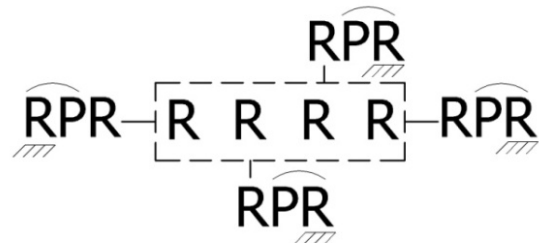
where λ is the number of independent parameters describing the positions and orientations of any rigid body

in space or subspaces, j_h is the number of hinges between platforms, $\sum_{l=1}^{c_l} f_l$ is the total DoF of all the kinematic pairs on the legs c_l , and λ_l is the general constraint of each

leg ($\lambda_l = 2, \dots, 6$).

Now, it is desired to create 4 DoF manipulator ($M=4$) with four legs ($c_l=4$). For one platform, j_h is set to be zero. The leg shown in Fig. 1 (b) constrains two rotational motions in space ($\lambda_l=4$). Therefore subspace of platform ($\lambda=4$) will also be four if these legs are used. By using Eq. (1), total DoF of kinematic pairs of the legs can be calculated as $\sum_{l=1}^{c_l} f_l = M + \sum_{l=1}^{c_l} \lambda_l - \lambda - j_h = 4 + 16 - 4 - 0 = 16$. Therefore, in the design of the manipulator, all leg will consist of four kinematic pairs $j_l = c_l^{-1} \sum_{l=1}^{c_l} f_l = 4$. Using exchangeability of kinematic pairs and RP kinematic chain similar to Fig. 1(b), the design of manipulator can be completed. So that, RPRR kinematic chain is selected for each leg of the manipulator.

Structural bonding of the manipulator can be represented as follows,



Three dimensional model of the designed manipulator is depicted in Fig. 5. Four revolute motors are connected to the ground to generate three translational and one rotational of the platform. Motion of the motors are defined as $\theta_1 = 10 \sin(5t) \text{ deg}$, $\theta_2 = 5 \sin(5t) \text{ deg}$, $\theta_3 = 5 \sin(3t) \text{ deg}$, $\theta_4 = 5 \sin(4t) \text{ deg}$. Here t is time and the motion of the manipulator is simulated for $0 \leq t \leq 5.12 \text{ s}$. Orientation and position of the platform are plotted in Fig. 6 and Fig. 7, respectively. Variation of one rotation is observed from orientation plot whereas all translations are varied in time. The motion of the platform can be described by adding translation about z to planar motion.

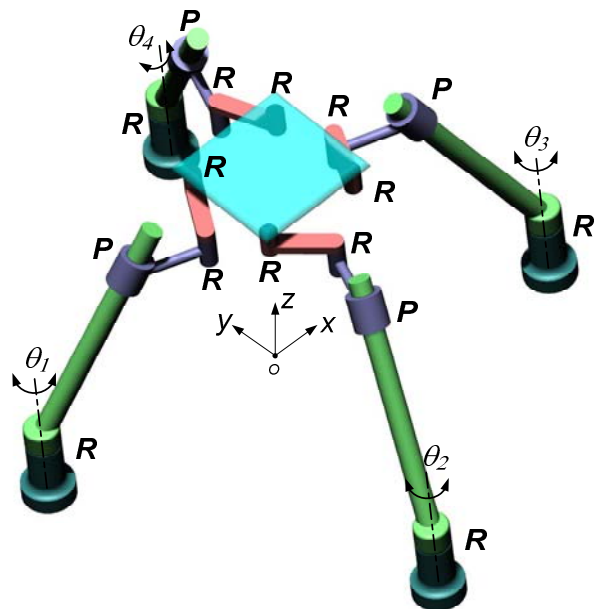


Fig. 5. 4 DoF Parallel Manipulator

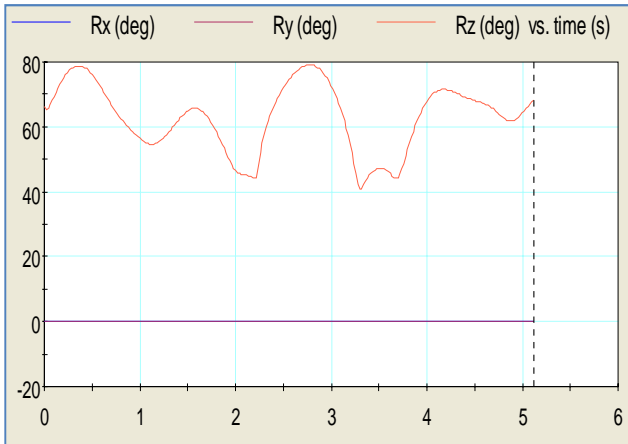


Fig. 6. Orientation of the platform

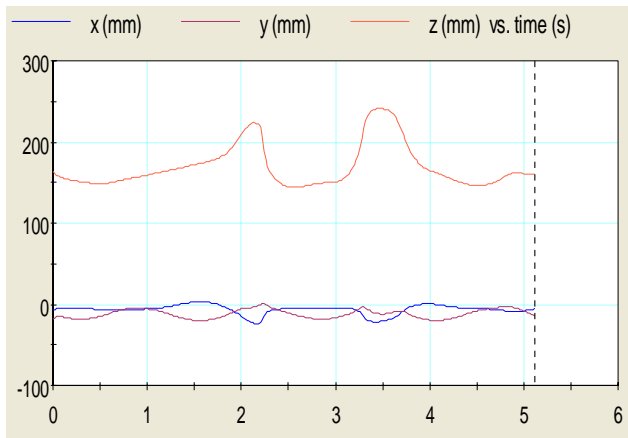


Fig. 7. Position of the platform

Similar motions including one rotation and three translations can be generated by the manipulator shown in Fig. 8. At the first glance, it can be considered that this manipulator is better than the designed one due to usage of less kinematic pairs. However, there are some distinctions between this manipulator and the designed one. For example, three revolute motors must be lifted by pneumatic cylinder for the manipulator in Fig. 8. But all revolute motors are connected to ground for the designed one. Another example is that platform weight is distributed to the four legs for the designed manipulator when three legs must carry the weight for the manipulator in Fig. 8.

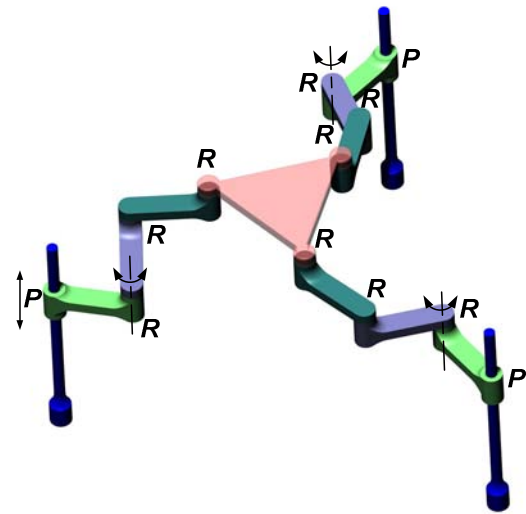


Fig. 8. 4 DoF 3 PRRR Parallel Manipulator

4. Structural Synthesis a Novel 5 DoF Parallel Manipulator that Includes a Planar Branch-Loop

The design of novel manipulator is proposed by means of equation 8 in structural synthesis of Euclidean platform robot manipulators [9]. The equation was written as follows,

$$M = \lambda + \sum_{l=1}^{c_l} (f_l - \lambda_l) + \sum_{L=1}^n (f_L - \lambda_L) \quad (2)$$

where n is the number of branch-loops, λ_l is the number of independent, scalar, loop-closure equations associated with each independent loop, $\sum_{L=1}^n f_L$ is the total DoF of kinematic pairs on the branch-loops.

Assume that platforms of a 5 DoF parallel manipulator ($M=5$) are connected to the ground by means of five similar legs in previous design ($c_l=5, \lambda_l=4$). It is desired to use a planar branch-loop ($n=1, \lambda_L=3$) between two platforms is configured in the same manner with kinematic chain in Fig. 9.

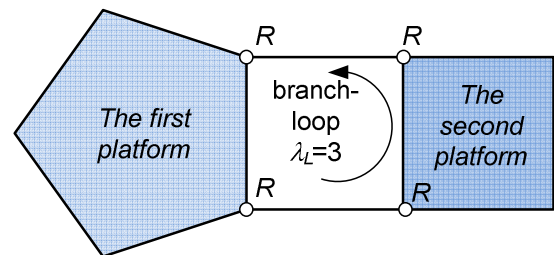
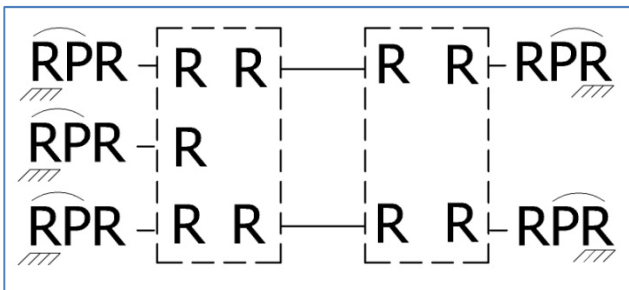


Fig. 9. Two platforms are connected by a planar loop



By substituting known parameters into Eq. (2), total DoF of kinematic pairs of the legs can be calculated as $\sum_{l=1}^{c_l} f_l = M + \sum_{l=1}^{c_l} \lambda_l - \lambda - \sum_{l=1}^n (f_L - \lambda_L) = 5 + 20 - 4 - 1 = 20$. Therefore, in the design of the manipulator, all leg will consist of four kinematic pairs $j_l = c_l^{-1} \sum_{l=1}^{c_l} f_l = 4$. Again, RPRR kinematic chain is selected for each leg of the manipulator.

Structural bonding of the manipulator can be illustrated as follows,



After drawing structural bonding, three dimensional model of the manipulator is created by means of Computer Aided Design programs. The designed manipulator is shown in Fig. 10. There are five motors that generate three translations and one orientation for both platforms of the manipulator.

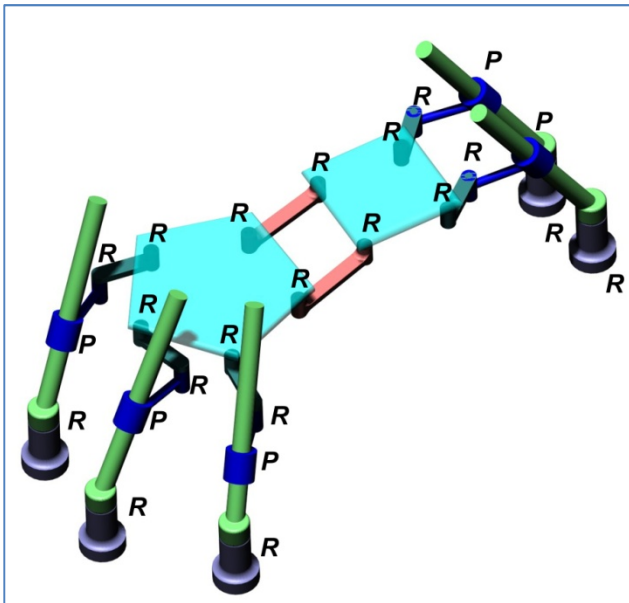


Fig. 10. Novel 5 DoF Parallel Manipulator that includes a planar branch loop.

5. Structural Synthesis a Novel 4 DoF Parallel Manipulator that Includes a Spatial Branch-Loop

The design of this manipulator is also accomplished by means of Eq. (2) that is used in previous example. The platforms of 4 DoF parallel manipulator ($M=4$) are connected to the ground by four similar legs in Fig.1 (b) ($c_l=4, \lambda_l=4$). In the design, two platforms will be connected a spatial branch-loop ($n=1, \lambda_L=6$) shown in Fig. 11.

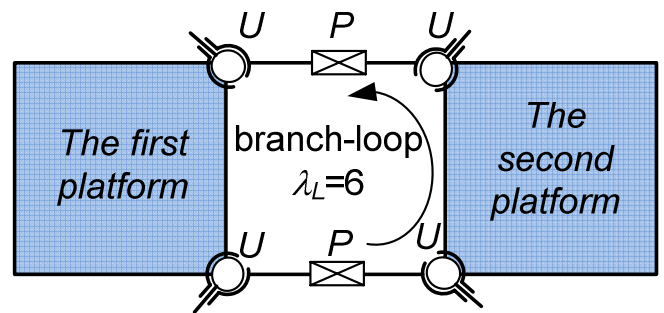
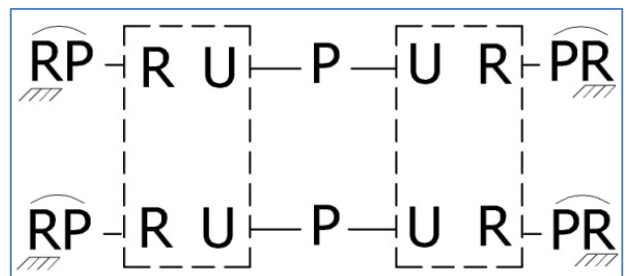


Fig. 11. Spatial branch-loop

Total DoF of kinematic pairs of the legs can be calculated as $\sum_{l=1}^{c_l} f_l = M + \sum_{l=1}^{c_l} \lambda_l - \lambda - \sum_{l=1}^n (f_L - \lambda_L) = 4 + 16 - 4 - 4 = 12$. Hence, all leg will consist of three kinematic pairs $j_l = c_l^{-1} \sum_{l=1}^{c_l} f_l = 3$.

By considering exchangeability of kinematic pair and special geometric conditions, RPR kinematic chain is preferred for each of the manipulator.

Structural bonding of the manipulator can be shown as follows,



The design of novel manipulator is completed by converting structural bonding to 3-D model shown in Fig. 12. The first platform of the manipulator has three translational and one rotational motion with respect to the second platform.

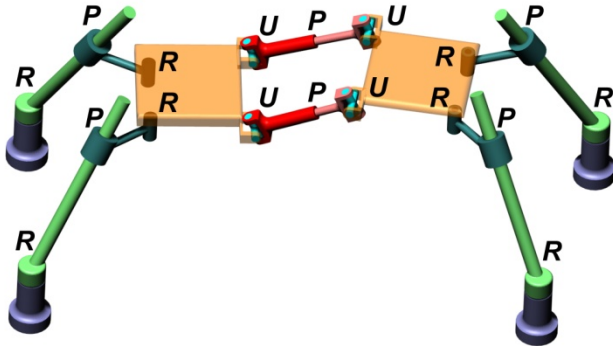


Fig.12. Novel 5 DoF Parallel Manipulator that includes a spatial branch loop.

6. Structural Analysis of a Novel 3 DoF Parallel Manipulator

The novel 3 DoF manipulator is depicted in Fig.13. This manipulator is different from the designed manipulators in previous sections due to the fact that its legs are different. Two legs of the manipulator are in same configuration (RPRR) when the remaining one is different (RRS). Two same legs are working in subspace four when the leg including spherical pair is working in space. The platform is also working in subspace four although one leg is in space. The reason of this is that platform motion is constrained by other two legs. By using Eq. (1), the DoF of the manipulator is calculated as,

$$M = \lambda + j_h + \sum_{l=1}^3 (f_l - \lambda_l)$$

$$M = 4 + 0 + (4 - 4) + (4 - 4) + (5 - 6) = 3$$

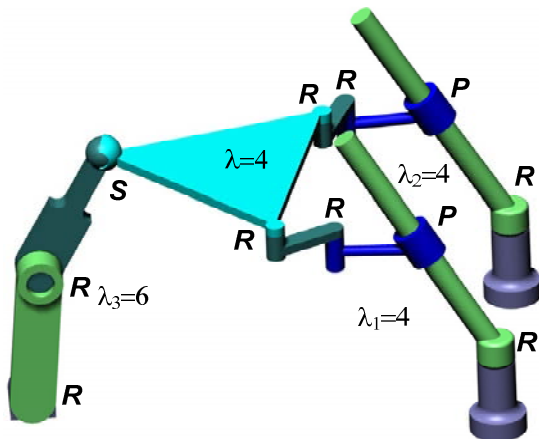


Fig. 13. Novel 3 DoF Parallel Manipulator

Conclusions

In this study, two overconstrained mechanisms are invented by means of intersection of two 3-D shapes such as hyperboloid and sphere. The special geometric conditions (linear and angular constraints) for these mechanisms play an important role for the design of novel parallel manipulators. The novel parallel manipulators are presented by using structural synthesis formulations proposed in a previous research [9]. In that research, Euclidean parallel manipulators are built by using legs in space (RRS, RRS, etc.). However, the presented work show that these formulations can also be used for the overconstrained parallel manipulators whose legs in subspace (RPRR). It is observed that these legs constraint the platform motion of the manipulator. Future work of this study:

- New overconstrained mechanism will be invented by using intersections of two cylinders, two torus d etc.
- New overconstrained parallel manipulator will be invented by using special geometric features of RRRRR single-loop overconstrained mechanism.
- Prototypes of novel manipulators will be prepared for industrial applications.

References

- [50]. Z. Huang & Q. C. Li, *General methodology for type synthesis of symmetrical lower-mobility parallel manipulators and several novel manipulators*, The International Journal of Robotics Research 21, pages 131-145, 2002.
- [51]. X. Kong & C. M. Gosselin, *Type synthesis of 4-DoF SP-equivalent parallel manipulators: A virtual chain approach*, Mechanism and Machine Theory 41, pages 1306-1319, 2006.
- [52]. R. Alizade, O. Selvi, E. Gezgin, *Structural design of parallel manipulators with general constraint one*, Mechanism and Machine Theory 45, pages 1-14, 2010.
- [53]. Web, http://en.wikipedia.org/wiki/Sarrus_linkage
- [54]. C. Mavroidis & B. Roth, *Analysis and synthesis of overconstrained mechanisms*, in Mechanism Synthesis and Analysis, Proceedings of the 1994 ASME Technical Conferences, Minneapolis, MI, September 1994, DE-70, edited by Pennock G., pages 115-133. (This paper won the Best Paper Award in the conference)
- [55]. C. Mavroidis & M. Beddows, *A spatial overconstrained mechanism that can be used in practical applications*, Proceedings of the 5th Applied Mechanisms and Robotics Conference, Cincinnati, OH, October 1997.
- [56]. K. H. Hunt, *Kinematic Geometry of Mechanisms*, Oxford University Press: Walton Street, Oxford, 1978.
- [57]. H.-J. Su & J. M. McCharty, *The synthesis of an RPS serial chain to reach a given set of task positions*, Mechanism and Machine Theory 40, pages 757-775, 2005.
- [58]. R. Alizade, F. C. Can, E. Gezgin, *Structural synthesis of Euclidean platform robot manipulators with variable general constraints*, Mechanism and Machine Theory 43, pages 1431-1449, 2008.

Design of a Foldable Shelter

Peilin TIAN¹, Yan CHEN^{1*}

* Corresponding Author
School of Mechanical & Aerospace Engineering
Nanyang Technological University
Singapore 639798
chenyan@ntu.edu.sg

Abstract

A family of foldable shelters have been designed. The frame of the shelter is an assembly of 5 Bennett linkages. In order to get a compact folding while keeping the large interior space for deployed shelter, the alternative form of the linkages has been used. The assembly has only one degree of mobility, which is used for the deployment and folding of the shelter. The shelter has only two kinds of components, the joints and bars. By changing the length of the bars, the size of the shelter can be modified easily, which makes the proposed design have wide applications.

Keywords: foldable shelter; Bennett linkage, alternative form, mobile assembly.

1. Introduction

Shelter is a structure providing privacy and protection from all sorts of dangers. Most of shelters are for temporary use, such as emergency housing for homeless people after natural disasters, medical centre in many emergent cases, and a number of military command or aid centres and storages. All of them request rapid set-up, easy transportation, light weight and robust structure. Therefore, the foldable shelters are more favorable comparing with the conversional assembling shelters. There are two major methods for the erection and folding of the shelters, the internal mobility and deformation of the shelter components. The first kind is either in large scale or in modular to integrate into different outlays, while the second is either inflated shelter or the deformable-truss one with extra covers, both of which are in relative smaller size. In this paper, we intend to propose a foldable shelter with only single internal mobility, whose size can be changed easily for different purposes.

The proposed shelter is based on Bennett linkage, 3D 4R over-constrained mechanism consisting of four rigid links connected by revolute hinges whose axes of rotation are neither parallel nor concurrent. see Fig. 1. If we define

the length and the twist as the shortest distance and skew angle between the axes of two adjacent revolute joints, the conditions for the linkage to have single degree of mobility are as follows [1-3].

(a) Two alternate links have the same length and the same twist, i.e.

$$a_{12} = a_{34} = a, \quad a_{23} = a_{41} = b$$

$$\alpha_{12} = \alpha_{34} = \alpha, \quad \alpha_{23} = \alpha_{41} = \beta$$

(b) Lengths and twists should satisfy the condition

$$\frac{\sin \alpha}{a} = \frac{\sin \beta}{b}$$

The closure equation of the linkage is

$$\theta_1 + \theta_3 = 2\pi \quad (1)$$

$$\theta_2 + \theta_4 = 2\pi \quad (2)$$

And set $\theta = \theta_1$ and $\varphi = \theta_2$, then

$$\tan \frac{\theta}{2} \tan \frac{\varphi}{2} = \frac{\sin \frac{1}{2}(\beta + \alpha)}{\sin \frac{1}{2}(\beta - \alpha)} \quad (3)$$

When the linkage are in the special equilateral case, $a = b$, then $\alpha + \beta = \pi$, and (3) becomes

$$\tan \frac{\theta}{2} \tan \frac{\varphi}{2} = \frac{1}{\cos \alpha} \quad (4)$$

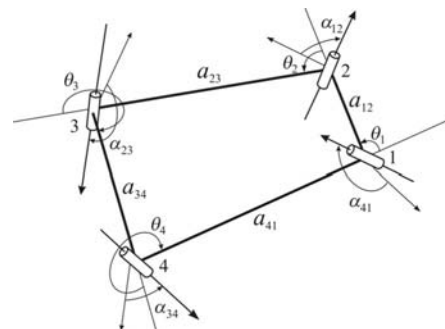


Fig. 1: Bennett linkage.

Chen and You [1, 2] have used Bennett linkage as basic element to form a family of mobile assemblies. When the construct element is equilateral Bennett linkage, the structure can be used as deployable shelters [3]. However, the patented deployable shelters can be folded only in one direction while the dimension in another direction increases as demonstrated in Fig. 2. Then the alternative form of Bennett linkage has been proposed [4, 5], which offers the most compact folding. In the proposed foldable shelter, the alternative form of Bennett linkage has been used as construct unit.



Fig. 2: The folding process of the mobile assembly of equilateral Bennett linkage.

The layout of the paper is as follows. Section 2 introduces alternative form of Bennett linkage. The detailed Shelter design is presented in Sections 3. The conclusions and discussion follow in Section 4.

2. The alternative from Bennett linkage

The mathematical representation of the Bennett linkage defines the length of the rigid links as the shortest distance between two adjacent axes. The links are always perpendicular to the axes at their ends, which we call the original form. In the alternative form, the axes of the revolute joints are extended and the joints are connected with the links that are not perpendicular to the joint axes. It has been found that by doing so, the Bennett linkage can be retracted to a bundle. Previous study [7, 8] has shown that the condition of existence of alternative forms of the linkage, which can achieve the most compact folding and maximum expansion so that the linkage can be used as basic building blocks for large deployable structures. And a simple method to build the Bennett linkage in its alternative form has been introduced and verified. Such example is shown in Fig. 3.



Fig. 3: The folding process of the alternative form of Bennett linkage.

Here we expand the alternative form to any spatial shape with four equilateral links rather than flat rhombus. In Fig. 4, the linkage is in such a shape that the angle between the plane formed by links 12 and 41 and the one

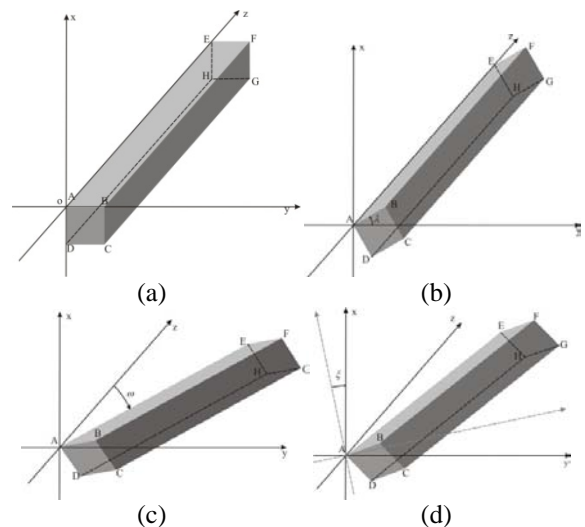
formed by links 23 and 34 is not restrict to π .



Fig. 4: The alternative form in the spatial quadrilateral.

Such linkage with square cross-section bar can be constructed by following steps.

1. Put the bar with cross-section as an $a \times a$ square and length as b along the z -axis in coordinate system as shown in Fig. 5(a);
2. Rotate the bar counterclockwise an angle λ about z -axis, see Fig. 5(b);
3. Rotate the bar clockwise an angle ω about x -axis, see Fig. 5(c);
4. Rotate the bar counterclockwise an angle ζ about z -axis, see Fig. 5(d);
5. Cut the bar at the near end with plane $z = 0$, which is the xoy plane passing point A, to get a parallelogram AJKL, and cut the bar at the far end with plane $y = b \cos \zeta \sin \omega$, which is the plane parallel to xoz plane passing point E to get a parallelogram EIUQ, see Figs. 5(e) and 5(f). the single bar in Fig. 5(f) is links 12 and 34 in Fig. 4, while the links 23 and 41 are the mirror images of the link 12; and
6. Connect such four links with four hinges located in the position marked by dark lines in Fig. 4 to form the alternative form.



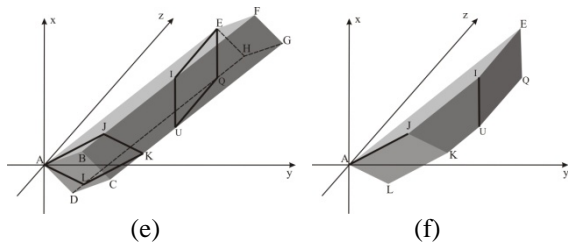


Fig. 5: A single link of the alternative form.

In such a way, the alternative form is still a spatial $4R$ linkage with single degree of mobility, which is in fact corresponding to an equilateral Bennett linkage. And at the deployed configuration, the angle between the plane formed by links 12 and 41 and the one formed by links 23 and 34 is equal to $\pi - 2\xi$. Meanwhile, this alternative form can be folded into a compact bundle as shown in Fig. 6.

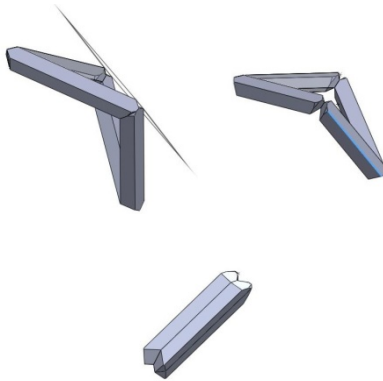


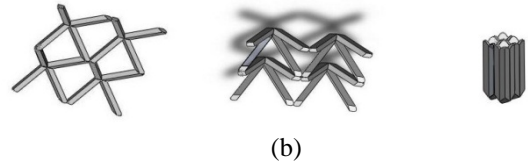
Fig. 6: The motion sequence of the alternative form from deployed to folded configuration.

3. Assembly of Bennett linkages for shelter design

A number of the same flat alternative forms can be connect into a mobile assembly with single degree of mobility as shown in Fig. 7(a) [8]. So with the same method, the spatial alternative form we have just derived can also form a mobile assembly following the plane tiling, which could be used as roof of certain buildings, see Fig. 7(b). However, here we explore the possibility to construct a shelter with four-side support.



(a)



(b)

Fig. 7: The motion sequence of the assemblies of the flat (a) and spatial (b) alternative forms from deployed to folded configuration.

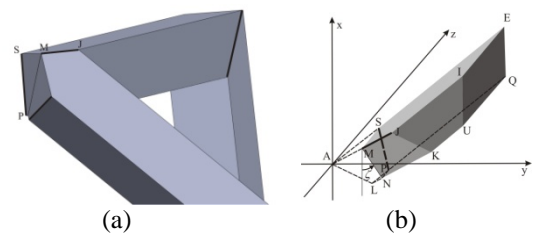
Firstly, a U-shape connection of two spatial alternative forms is constructed by cutting the joint 1 corner of the alternative form in Fig. 4 with the plane

$$x \tan \zeta + y = x_M \tan \zeta + y_M \quad (5)$$

where $M(x_M, y_M, z_M)$ is the middle point of edge AJ. So the cutting plane is formed by rotating xoz plane clockwise an angle ζ about z -axis and parallel moved to pass point M, see Fig. 8 (a) and (b). Then the edge SP will be the position of hinges, through which such two frames can be connected together. The four hinges in the top corner of the assembly (see Fig. 8 (c) and (d)) form another alternative form of Bennett linkage. Therefore, the whole assembly is still mobile with 1 DoF. In the front view of the assembly in Fig. 8(c), the two cutting angles should satisfy

$$\zeta = 2\xi \quad (6)$$

so that both sides are vertical.



(a)

(b)



(c)

(d)

Fig. 8: Connection of two alternative forms on left and right sides.

Secondly, the legs in the front and rear sides are added. Geometrically, the pair of legs should be similar as the left and right ones, i.e., they are vertically positioned. Kinetically, two additional bars added in the front or rear side should also form the alternative forms of Bennett

linkage with existing bars on the roof so that the whole assembly is kept in one DoF. Therefore, the additional two bars should put in the vertical plane if viewed from side-view of the U-shape frame we constructed earlier, see Fig. 9(a). Due to the symmetric characteristics of the spatial alternative frame, the hinge lines, which connect the additional two bars with the two bars on the roof in the front part to form the spatial alternative frame, should be generated by cutting the two bars on the roof by a plane angled $\pi/2 - \xi$ to the plane formed by two roof bars, see Fig. 9(a). Fig. 9(b) shows the details, in which line XY is the new hinge position. The same construction can be carried out in the rear side as well. Then two legs can be added as the transparent ones in Fig. 9(c).

Because the spatial alternative form applied here consists of four links in the same length, in order to make sure the front and rear legs in the same vertical length as two side legs, the top view of the assembly should be a square. The design parameters must satisfy the following conditions generally.

$$\tan \omega \cdot \sin 2\xi = 1 \quad (7)$$

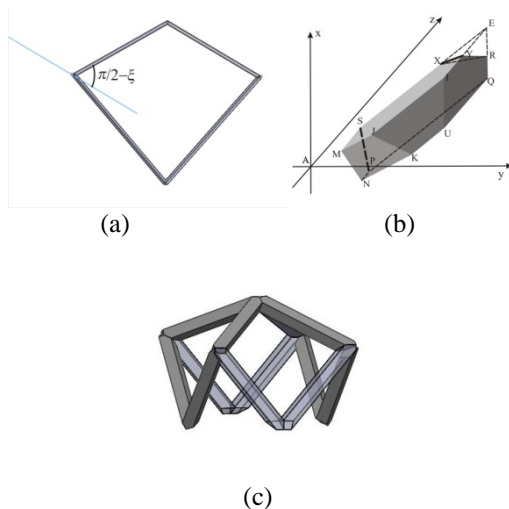


Fig. 9: Connection of two alternative forms in the front and rear sides

In such a way, a shelter frame has been constructed. There are totally five alternative forms of Bennett linkages, four in four sides of the shelter and a small one in top corner of the shelter. Two linkages on the left and right sides have the same twist, so do two linkages on the front and rear sides. The whole frame has only one degree of mobility, which makes it easy to control the deployment and folding process manually or automatically by certain actuation method. Fig. 10 shows the motion sequence of the shelter example with all the bars in the same cross

section and length. The design parameters are

$$\lambda = 45^\circ, \omega = 49.1^\circ, \\ \xi = 30^\circ, \text{ and } \zeta = 60^\circ.$$

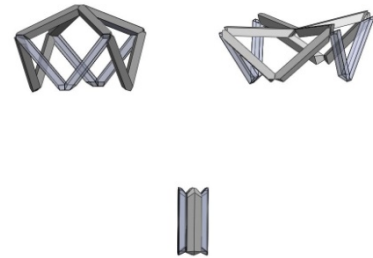


Fig. 10: The motion sequence of the shelter frame from deployed to folded configuration.

4. Conclusions and discussion

In this paper, we have designed a family of foldable shelter frames. It is in fact an assembly of the spatial alternative forms of Bennett linkages. The folding of the frame is achieved by the internal single degree of mobility, which makes the frame folded and deployed repeatedly without inducing any strain to the components.

The length of the bar and the size of the square cross section can be selected based on the application. The four angle design parameters, only λ and ξ are independent, while ω and ζ are constrained by $\zeta = 2\xi$ and $\tan \omega \cdot \sin 2\xi = 1$. λ is to decide the orientation of the bars and ξ is to decide the overall shape of the shelter frame. The selection of λ and ξ will affect not only the kinematic behavior of folding and deployment process but also the static behavior of frame serving as the shelter. Therefore, in the detailed design, these two parameters should be optimised carefully.

For a real product, the frame can be divided into two types of components, the joints and the bars in the same length as shown in Fig. 11. For the same set of joints, the dimension of the shelter can be modified linearly by assembling the joints to twelve bars in a different length. And the cover should be attached after the shelter is deployed.

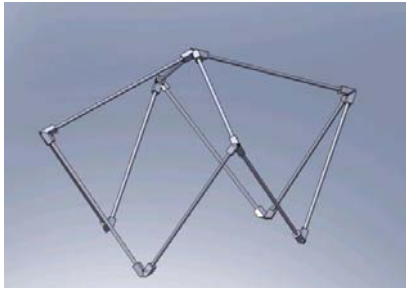


Fig. 11 A product design of the foldable shelter frame.

References

- [1]. G.T. Bennett, A new mechanism. *Engineering* 76, 777-778, 1903.
- [2]. G.T. Bennett, The skew isogram mechanism. In: *Proceedings of the London Mathematics Society*, 2nd Series 13, 151-173, 1914.
- [3]. J. E. Baker, The Bennett, Goldberg and Myard linkages---in perspective. *Mechanism and machinery Theory*, 14, 239-253, 1979.
- [4]. Y. Chen and Z. You, Mobile assemblies based on the Bennett linkage, *Proceedings of the Royal Society A (Mathematical, Physical and Engineering Sciences)*, 461, 1229 – 1245, 2005. (doi:10.1098/rspa.2004.1383)
- [5]. Y. Chen and Z. You, On mobile assemblies of Bennett linkages, *Proceedings of the Royal Society A (Mathematical, Physical and Engineering Sciences)*, (2008) 464, 1275-1283, 2008. (doi:10.1098/rspa.2007.0188)
- [6]. Y. Chen and Z. You, Deployable Structure, UK Priority Patent Application 0229599.6, 19 December 2002; US Patent Publication Number: US 2004/0120758 A1, 24 June 2004; International Publication Number: WO 2004/057134, 8 July 2004.
- [7]. Y. Chen and Z. You, Square deployable frame for space application: Part I: Theory, *Proceedings of the Institution of Mechanical Engineers, Part G, Journal of Aerospace Engineering*, 220(4), 347–354, 2006. (doi:10.1243/09544100JAERO68);
- [8]. Y. Chen and Z. You, Square deployable frame for space application: Part II: Realization, *Proceedings of the Institution of Mechanical Engineers, Part G: Journal of Aerospace Engineering*, 221(1), 37-45, 2007. (doi:10.1243/09544100JAERO100)



A Method for Kinetic Tessellation with Planar Mechanisms

Aylin GAZI^{1*}, Koray KORKMAZ¹

^{1*} Izmir Institute of Technology, Department of Architecture, Turkey
aylingazi@msn.com

Abstract

Designing the surface has been one of the major problems throughout the history in architecture. To achieve this goal, architects has benefited from the mathematics to reach beauty, stability or new construction methods. Mathematical tessellation technique has been usually used to design planar surfaces. Moreover, due to rapid change in social activities of modern society in XXth century, need of adaptation has appeared. This appearance has caused the rise of the concept of motion or kinetic architecture. The main purpose of this study is to develop a methodology to design kinetic planar surfaces with mathematical regular tessellation technique in the light of architectural, mechanical and mathematical interdisciplinary approach.

Keywords: Kinetic Tessellation, Periodic Tiling, Planar Surface, Duality

1. Introduction

The main purpose of this study is to develop a methodology to design kinetic planar surfaces with mathematical tessellation techniques in the light of architectural, mechanical and mathematical interdisciplinary approach.

Geometry plays a central role in both of the design of buildings and the analysis of these buildings with architectural and engineering aspects at the same time. Throughout the history, many architects and artist have benefited from some mathematical and geometrical knowledge such as golden ratio, fractal geometry and tessellation. Liapi [1] claims that complex and sophisticated knowledge and use of geometry underlines the conception, design and construction of the most significant achievement in the history of buildings. In the ancient times, proportioning systems were the most essential elements of visual order and aesthetics, thus architects and artist benefited from the golden ratio in their works. Moreover, in the XXth century, many architects such as Renzo Piona, and Santioga Calatrava have developed their designs by using the relationship between geometry and structure.

Tessellation is a kind of mathematical technique that has been the common method to cover plane without any gaps or overlaps. Due to this property of the technique, it has been usually used on the planar surfaces such as

facade of the buildings.

In today's life many buildings give negative impact to the economy and environment due to consuming much more natural and human resources. Meanwhile, because of the rapid change in the activities of modern society and the development in building technology, building parts are in need of change in terms of shape and form to adapt to different function and weather conditions to reach positive impact on the economy and environment. As a result, architecture has developed a new aspect that is called kinetic architecture. In the literature there aren't many studies which deal with the relationship between mathematic and kinetic architecture that may be used as the design of kinetic building parts.

Kinetic architecture is an interdisciplinary study between architecture and mechanism science. Kinetic aspect of the architecture mainly suggests a new concept of form with the kinetic parts that is capable of being transformable, deployable or foldable. Many researchers deal with a particular type of mechanisms. However, a method is necessary to construct a network with planar mechanisms for variable building surfaces.

During the design process of kinetic building parts, many questions might be a problem such as how many links should be used, what kind of joints and platform should be chosen and finally the mobility of the whole kinetic system. In the cases of these questions, architects need a method or a tool that is currently lacking in the literature when designing kinetic systems.

This investigation will focus on developing a methodology to design planar surfaces by using mathematical tessellation method by considering kinetic aspects. In the light of this aim, this study coherently addresses tessellation technique that fall within usage of tessellation on architecture and briefly presents tessellation technique with mathematical aspect.

2. Usage of Tessellation

Basically, tessellation means to cover a plane without any gaps or overlaps by considering some methods. Another term synonym with tessellation is tiling.

Tessellation is a kind of mathematical technique which is used in different fields, such as science, art and architecture (Figures 1-3).

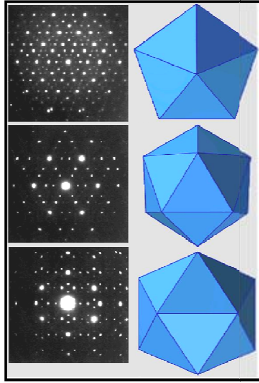


Fig. 1. Tessellation and x-ray Crystallography (Encyclopedia Britanica 1994)

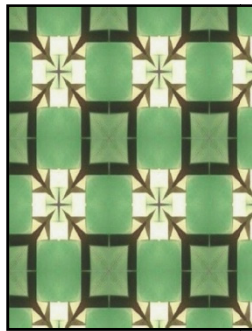


Fig. 2. Origami tessellation [2]



Fig. 3. A tessellation of surface in Alhambra [3]

2.1. Tessellation and Architecture

Tessellation technique is mainly governed by rules of geometric repetition, continuity and symmetry.

According to this strict adherence to conformity, a relatively simple motif may be used to produce an increasing pattern, which may continue on to infinity [4].

Architecture has been using the tessellation on the many different areas. When people began to build their houses and fortifications, they tried to fill space or plane. The first houses, churches and castles were built by broken stones which made up random tessellations. Later, arrangements of prismatic stones and bricks possessed a large regularity.



Fig. 4. Usage of the tessellation in ancient times, 1) Arabic, 2) Islamic and 3) Byzantine [5]

Islamic artisans have developed into a rich system of intricate ornamentation that followed the spread of Islamic culture into Africa, Europe, and Asia to adorn architectural surfaces with geometric patterns.

The Islamic world has a rich heritage of incorporating geometry in the construction of intricate designs that appear on architecture. Medieval Islamic artisans developed intricate geometric tiling to decorate their mosques, mausoleums, and shrines. The most well-known usage of the tessellation has been seen in the Alhambra at Granada

Islamic tessellation from the Alhambra falls into two major categories in a mathematical manner. These are Radial patterns (Finite Symmetry Groups) and periodic patterns (Infinite symmetry group). Radial tessellation (Figure 5) may have rotations about the central point with the total number of symmetries being finite. These types of patterns do not have any translations or glide reflections [6]. On the contrary to this, periodic tessellation contains translational symmetries in two independent directions that can be seen in figure 6 [4].



Fig. 5. Radial tiling from the Alhambra [4]



Fig. 6. Periodic tiling from the Alhambra [4]

3. Tessellation with Mathematical Aspect

Tessellation is usually represented by the number of sides of the polygons around any cross point in the clockwise or anti-clockwise order. For instance, (3^6) represents a tiling in which each of the points are surrounded by six triangles, 3 is the number of the sides of a triangle and superscript 6 is the number of triangles around the referred point (Figure 7).

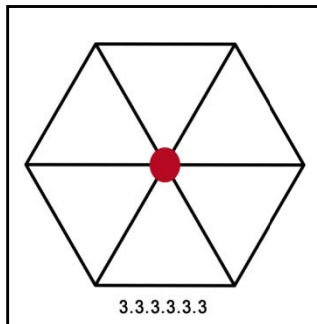


Fig. 7. 3^6 Tiling

Each tessellation is a closed topological disk whose boundary is a single simple closed curve. By this it is meant to be a curve whose ends join up to form “loop” and which has no crossing or branches. For most of tessellation considered here, such an intersection may be empty or may consist of a set of isolated points and arcs. In these cases the points will be called vertices of the tessellation and arcs will be called edges [7]. This work deals with the tessellation, which is formed by polygons. Polygons have vertices and edges, so it would be confusion to some terminology. Because of this reason, Grünbaum and Shephard have explained the differences between corners and vertices, sides and edges in the case of a polygonal tessellation on their book that the points A, B, C, D, E, F, G are corners but A, C, D, E, G are vertices of the tessellation, AB, BC, CE, EF, FG and GA are sides while AC, CD, DE, EG and GA are edge (Figure 8).

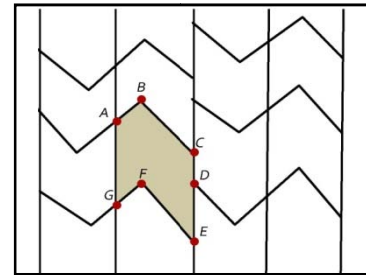


Fig. 8. The illustration of tessellation element [7]

Tessellations can be categorized by considering to regular polyhedra mainly regular and semi regular tessellation.

3.1. Regular Tessellation

Regular tessellation includes a fixed number of specific n-gon at every vertex. Kinsey and Moore claims that “Regular tessellation consists of repeated copies of a single regular polygon, meeting edge to edge so that every vertex has the same configuration.” [8]. There are three regular tessellation of the plane (Figure 9).

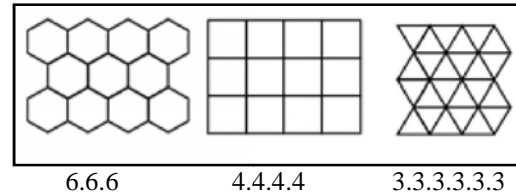


Fig. 9. Regular tessellation

3.2. Semi-Regular Tessellation

Two or more convex regular polygons such that the same polygons in the same order surround each polygon vertex are called semi regular tessellations, or sometimes Archimedean tessellations [9]. In plane, there are eight semi-regular tessellations (Figure 10).

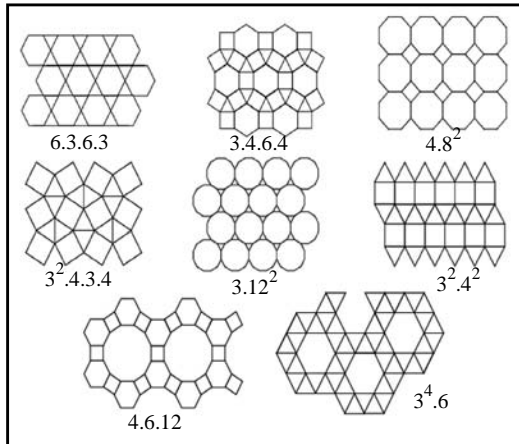


Fig. 10. Semi- Regular tessellation

3.3. Duality of the Tessellation

The dual of tessellation is formed by joining the center of each polygon as a vertex and joining the centers of all neighboring polygons. The number of sides remains the same. Moreover, Grünbaum and Shephard describe the dual tessellation on their book as, “two tilings are said to be dually situated to each other if they lie in the same plane, every vertex of one is an interior point of a tile of the other, every tile of one contains precisely one vertex of the other, and crosses, just one edge of the other”. Moreover, they claim that, tessellation and its dual are homomorphic to one of the two dually situated tessellations. Thus, any motion or change of scale affects each other [7].

The triangular and hexagonal tessellations are duals of each other, while the square tessellation is its own dual.

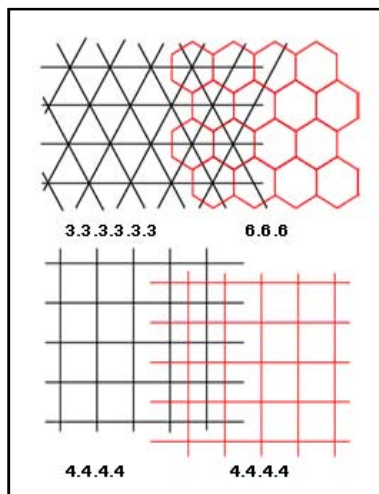


Fig. 11. Dual of regular tessellations

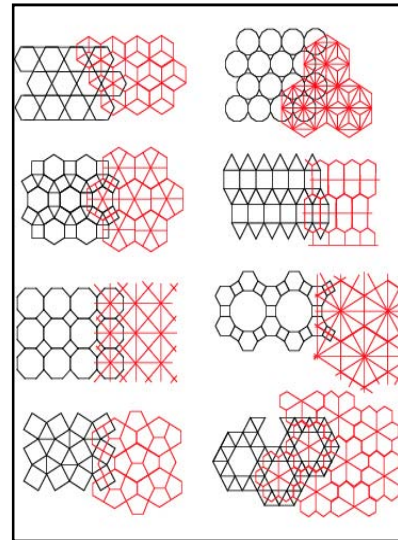


Fig. 12. Dual of semi- regular tessellations

4. Design of Kinetic Planar Surface with the Regular Tessellation

This section presents a method to design a kinetic planar surface by using the mathematical tessellation technique. Thus, in the first step, this study hands out the tessellation with regarding to their shape that is regular tessellation and semi regular tessellation with respect to the platform shape.

The investigation deals with the regular tessellation. The planar surface will be covered with regular platforms in order to reach kinetic regular tessellation. In this case, the most important point is, the planar mechanism reaches the regular tessellation on the first point of the motion and on the last point of the motion. In the light of this aim, developing a method, this paper tries to find an answer to the question of how a kinetic tessellation can be reached by using regular platforms.

4.1. Method of the Study

As mentioned before, the main problem is how a regular kinetic tessellation can be reached by using regular platforms. This problem will be approached by using a method based on duality of the tessellations. Moreover, this kinetic tessellation unit will be iterated according to periodic tiling.

Within the scope of this study, the main points requiring the realization of the method will be the decision of link type, platform type, and joint type to be used as well as their connection combinations to reach planar mechanism. Therefore, this method examines the kinetic tessellation in three steps successively building upon each

other.

The first step of the methodology aims to determine the type of the link with regular tessellation. The second step of the methodology is to determine the type of the platform by the help of the duality of the regular tessellation. Finally, the last step of the methodology will be the determination of the combination order of the platforms and the links.

4.2. Kinetic Square Tessellation

Square tessellation is one of the regular tessellations that can be defined as $\{4, 4\}$ (Figure 13).

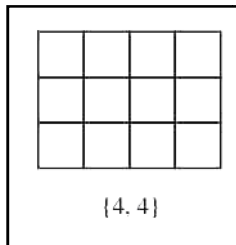


Fig. 13. Square tessellation

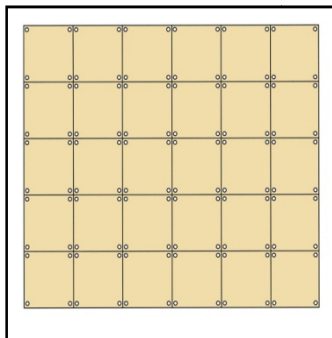


Fig. 14. Closed form of square tessellation

The first step of the methodology is to find the form of the first link by considering to regular square tessellation (Figure 14).

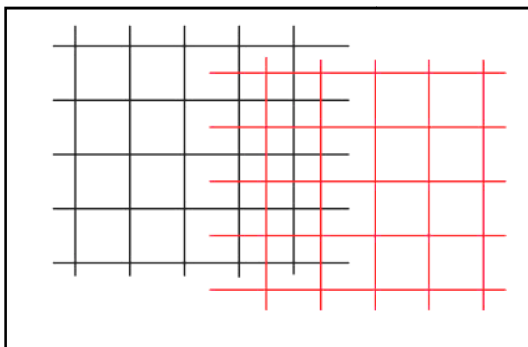


Fig. 15. Dual tessellation of the square tessellation

Black line shows the real part of the square tessellation while the red line shows the dual of the square tessellation. Those two tessellations give the desired information of the form of the platform and the link.

Form of the link is determined by the intersection of the real part of the square tessellation. In this step, determination of the vertices of the tessellation is an important point. The length of the links will be determined by pointing one vertex to the others around (Figure 16).

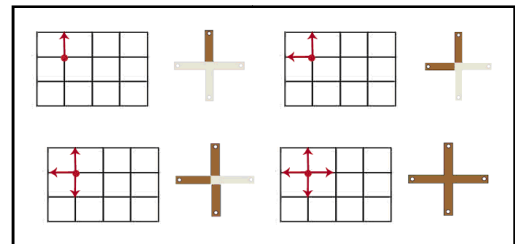


Fig. 16. Process of obtaining the form of the first link

In the second step dual of the tessellation provides the form of the platform of the mechanism. The dual of the square tessellation is its own dual that is formed by taking the center of each polygon as a vertex and joining the centers of adjacent polygons. In this step, the line is drawn successively by starting from the vertices point until the same vertices point is being reached (Figure 17).

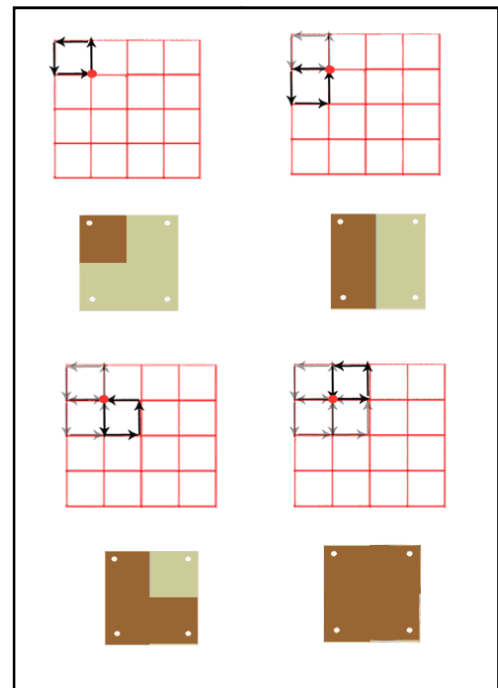


Fig. 17. Process of obtaining the form of the platform

The final step is determined the placement of the combination of link and platform. To achieve this aim we have to look at the intersection of the square tessellation and its dual. Firstly, platform of the mechanism will be placed to the point where the square tessellation and its dual intersect, and then the links of the mechanism will be added to that platform (Figure 18).

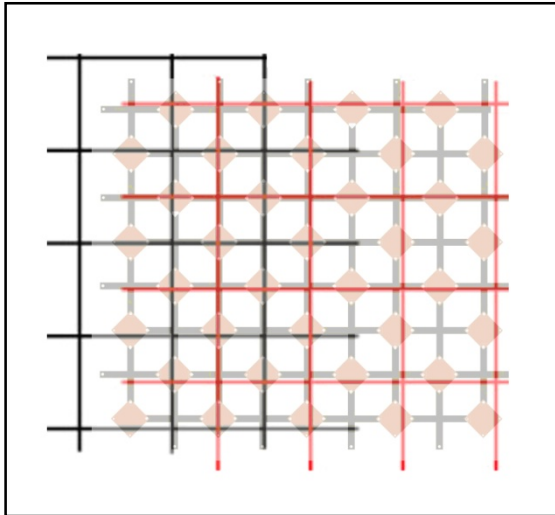


Fig. 18. Placement of the kinetic regular tessellation

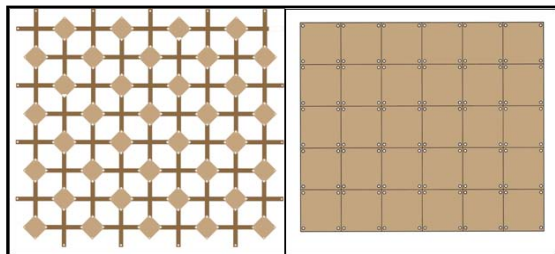


Fig. 19. Open and closed forms of the kinetic regular tessellation

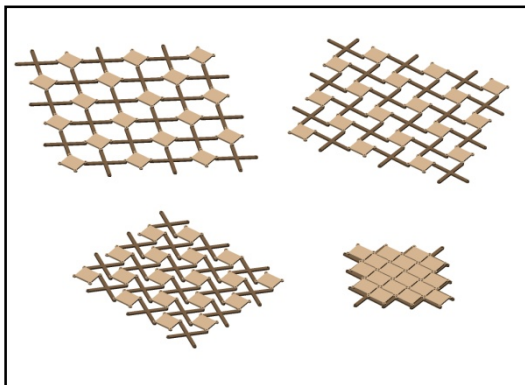


Fig. 20. Kinetic Square tessellation

This methodology can be applied to all of the regular tessellations. Figure 21 displays the process of obtaining the kinetic square tessellation and figure 23 displays the process of obtaining the kinetic hexagonal regular tessellation.

Due to triangle and hexagonal tessellation dual of each other, the process of triangular tessellation is near the hexagonal one. In this case, form of the first link is consisting of 6 legs and platform is triangle (Figure 24).

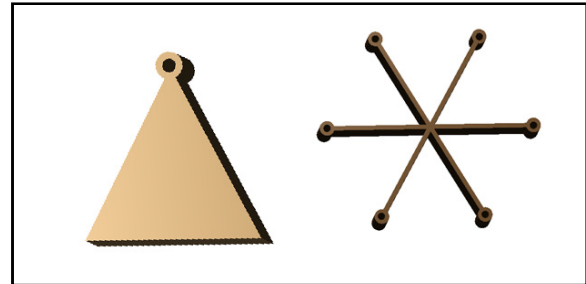


Fig. 24. Platform and link of triangle tessellation

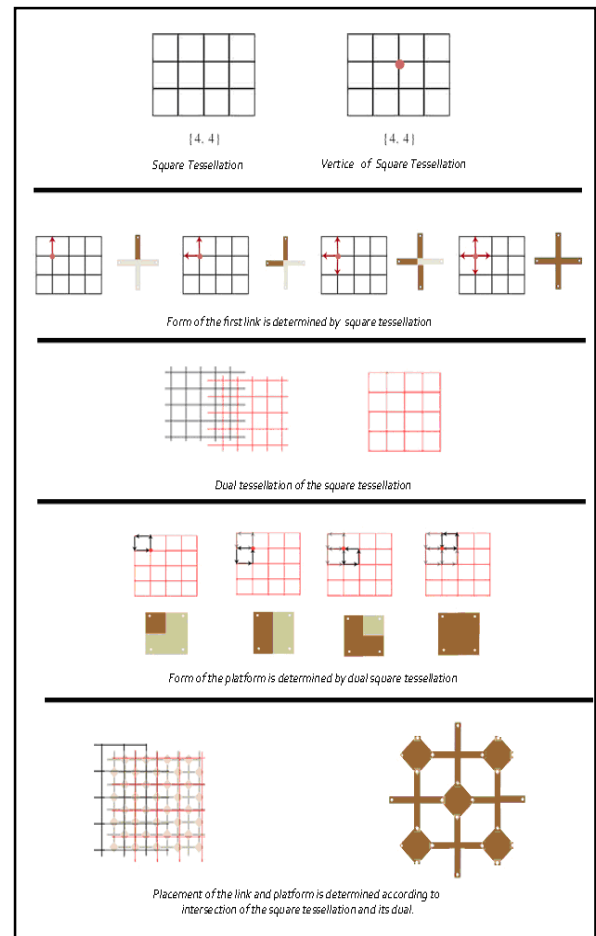


Fig. 21. Process of the obtaining kinetic square tessellation

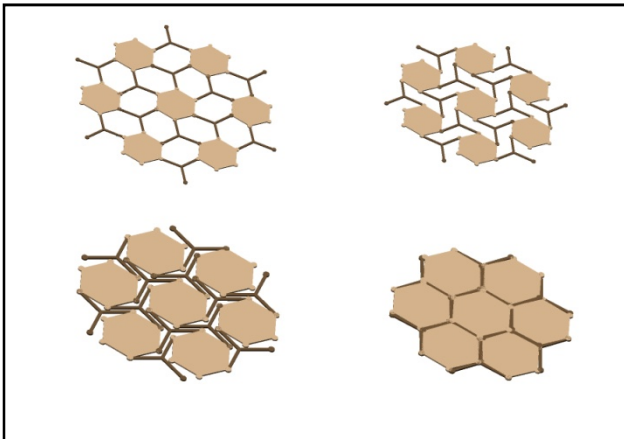


Fig. 22. Kinetic hexagonal tessellation

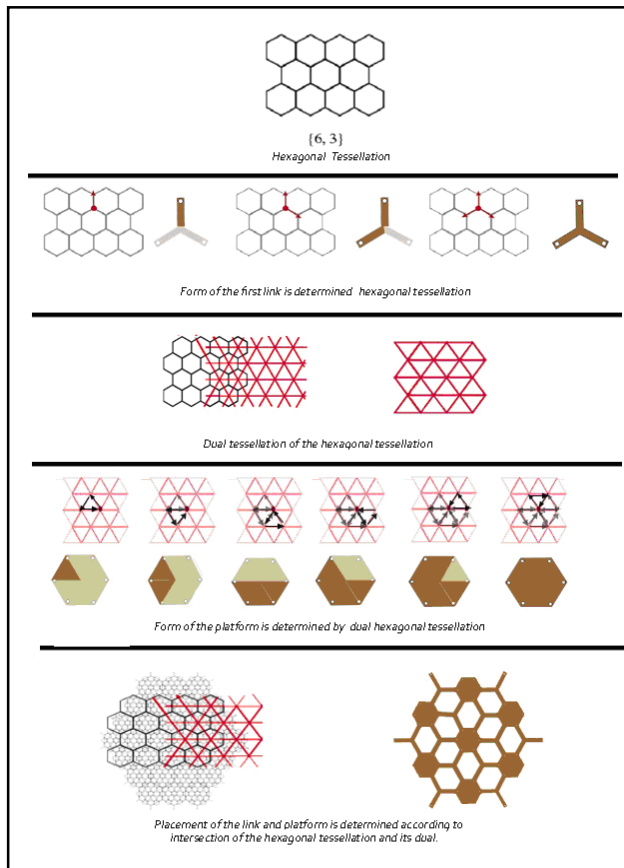


Fig. 23. Process of the obtaining hexagonal tessellation

4.3. Mobility of the Kinetic Regular Tessellation

After explaining method of the regular kinetic tessellation, now let's construct the mobility calculation algorithm of the kinetic regular tessellation by using two different mobility formulation (Equations 1-2) [10].

$$\sum f_i - \sum_{k=1}^L \lambda_k + q - J_p = M \quad (1)$$

According to Freudenstein - Alizade mobility criterion formulation, f_i is the degrees of freedom of i^{th} kinematic pair, λ_k is the space or subspace number of the k^{th} independent loop, L is the total number of independent loops, q is the number of excessive links and J_p is the number of passive joints.

$$\lambda(j-1) - \sum_{i=1}^{\lambda-1} (\lambda-i)P_i + q - J_p = M \quad (2)$$

According to Grübler mobility criterion formulation, j is the total number of links including ground link and P_i is the total number of joints with i^{th} degrees of freedom.

As the study deals with the planer cases ($\lambda = 3$), the equations will become;

$$P_1 - 3L + q - J_p = M$$

$$3(j-1) - 2P_1 + q - J_p = M$$

In order to start the process the smallest mobile element of the regular tessellation should be considered (Figure 25). As shown in table 1 if the equation variables are inserted to the formulations, the mobility of the smallest system will be calculated as unity ($M=1$).

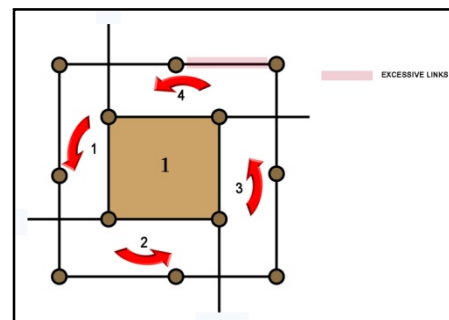


Fig. 25. The smallest mobile element of regular tessellation

Table 1. Equation variables of figure 22

L	j	J _p	q	P ₁
4	9	0	1	12

After calculating the mobility of the first module, let's iterate the system by sharing loops (Figure 26). As seen in figure, two modules are sharing one loop and the equation variables are shown in table 2.

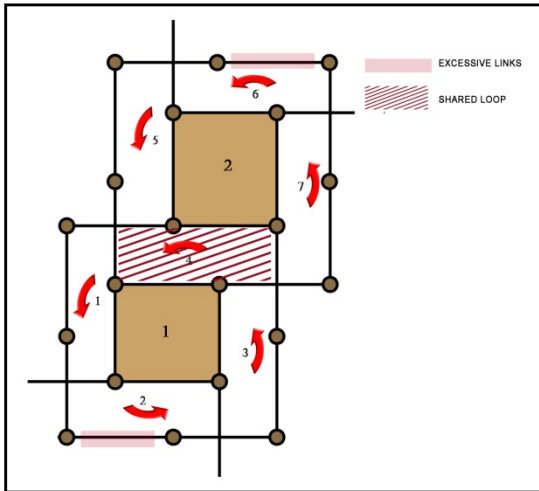


Fig. 26. The first iterated mobile regular tessellation modul

Table 2. Equation variables of figure 23

L	j	J_p	q	P_1
7	14	0	1+1	20

Note that each addition of module that shares only one loop will add one more excessive link to the system. If the mobility of the resulting system is to be calculated, it will be revealed again as unity ($M=1$). Now let's iterate the structure with one more module.

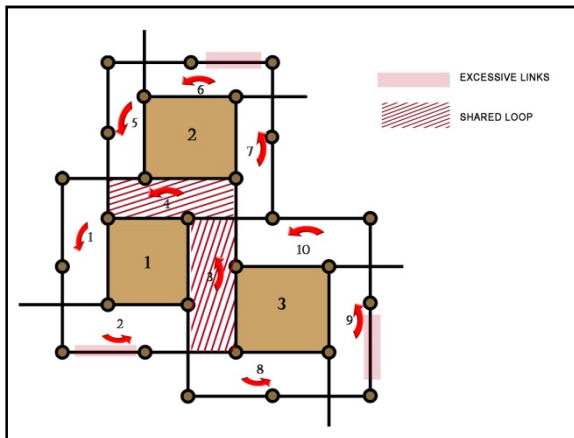


Fig. 27. The second iterated mobile regular tessellation module

Table 3. Equation variables of figure 24

L	j	J_p	q	P_1
10	19	0	2+1	28

Similar to the second iteration the third module (Figure 27) will add an additional excessive link to the system.

Using the parameters in table three the mobility of the resulting system will also revealed to be one ($M=1$).

After two identical iterations, let's carry out the most important one. This time the iterated module will share two loops with the previous system (Figure 28).

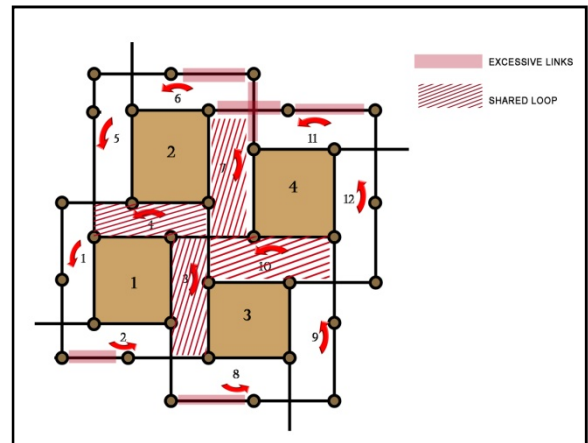


Fig. 28. The fourth iterated mobile regular tessellation module

Table 4. Equation variables of figure 25

L	j	J_p	q	P_1
12	20	0	4+1	32

Using the new variables of the system (Table 4), the mobility of the system will again be calculated as unity.

It should be again noted that, the most important point in the last iteration is the fact that sharing two loops with one additional module will add two more excessive links to the system instead of one. If the iteration procedure is combined, a new theorem can be introduced to the literature related with the mobility calculations of the regular tessellations.

Theorem: Number of redundant or excessive links is equal to the one plus the number of loops that will be shared during the whole iteration process.

5. Conclusions

This study firstly tries to develop an aspect to the methodology which considers the kinetic systems in the light of architectural, mechanical and mathematical interdisciplinary approach.

In order to achieve this aim, this investigation focuses on the mathematical tessellation technique. The area of this work has been restricted by the regular tessellations. It develops a methodology to reach kinetic planar surfaces by using regular tessellations and their duals. Moreover, this study demonstrates the mobility calculations of the created



mechanisms by using two different formulations. Both of the formulations proved that the mobility of the kinetic regular tessellation will always be one.

In conclusion, this study has therefore arrived at the conclusion that the relationship between mathematical knowledge, mechanism science and building parts deserves more serious consideration in kinetic architecture field. In the future, this investigation aims to apply this methodology to the existing eight semi regular tessellations.

6. Acknowledgements

I would like to express my sincere appreciation to Prof. Oktay PASHAEV and Prof. Rasim ALIZADE. Their extensive knowledge, vision and creative thinking have been the source of inspiration for me through this work. Also my special thanks to Erkin GEZGİN and Melodi Simay ACAR for their support and eternal friendship.

References

- [1]. K.Liapi. "Transformable Structures: Design Features And Preliminary Investigation". Journal of Architectural Engineering, Vol 13, (2001).
- [2]. Web, <http://www.math.lsu.edu/~verrill/origami/OriTesIns>
- [3]. Web, www.5cense.com/Granada_Seville.htm
- [4]. R. F. Tennant, A. Dhabi. "Islamic Tilings of the Alhambra Palace: Teaching the Beauty of Mathematics." Teachers, Learners, and Curriculum Journal Vol. 2. (2004).
- [5]. Web, <http://www2.spsu.edu/math/tile>
- [6]. R. F. Tennant, "Medieval Islamic Architecture, Quasicrystals, and Penrose and Girih Tiles: Questions from the Classroom. Proceedings" – Bridges Conference Leeuwarden, CHN University Netherlands, 24-28 July 2008.
- [7]. Grünbaum, B. and Shephard, G.C, Tilings and Patterns. W. H. Freeman and Company; New York, 1986.
- [8]. Kinsey, L. and Moore, Symmetry, Shape and Space. Key College Publishing; New York, 2002
- [9]. Web, <http://mathworld.wolfram.com/SemiregularTessellation.html>
- [10]. R. Alizade, C. Bayram, E. Gezgın. "Structural Synthesis of Serial Platform Manipulators." Mechanism and Machine Theory Vol 42 (2007).



A Novel Spatial Scissor-hinge Structural Mechanism for Transformable Roofs

Yenal AKGÜN^{1*}, Koray KORKMAZ¹, Werner SOBEK², Charis GANTES³

^{1*}Izmir Institute of Technology Department of Architecture
Gülbahçe Kampüsü 35430 Izmir, Turkey
yenalakgun@gmail.com

² Institute for Lightweight Structures and Conceptual Design (ILEK), University of Stuttgart, Germany

³ Department of Civil Engineering, National Technical University of Athens, Greece

Abstract

This paper introduces a novel scissor-hinge structural mechanism (SSM) which is designed as a transformable roof structure. Most of the current deployable SSMs have predefined open and closed body forms; and transformations occurs between these two forms by using one of the various transformation types such as sliding, deploying, and folding. However, the proposed SSM system can transform between rectilinear geometries and double-curved shapes without changing the size of the covered area. In order to achieve such kind of form flexibility, a new primary element called modified scissor-like element (M-SLE) has been developed. In the paper, first, main principles of current SSMs are summarized. Then, primary elements, geometric and kinematic principles of the proposed SSM have been explained. Finally, potential architectural uses of this novel structural mechanism are introduced.

Keywords: Kinetic Structures, Deployable Structures, Scissor-hinge Structures, Adaptive Structures

1. Introduction

In all periods of history, humans have tried to construct flexible buildings which are capable of adapting to ever-changing requirements and conditions. Kinetic architecture's primary objective is the design of adaptable building envelopes and spaces as the major components of the building using mechanical structures [1]. Recent developments in construction technology, robotics, architectural computing and material science have increased the interest for deployable and transformable structures. The reasons behind this interest relate to the growing need for functional flexibility, adaptability, sustainability and extended capabilities of structural performance.

Scissor-hinge structural mechanisms (SSMs) are one of the most common types of deployable structures. Since

1960s, many designers have studied to develop novel SSMs. Piñero, Escrig, Valcarcel and Hoberman are the important figures on the research of SSMs.

Piñero is the first researcher, who developed and used SSMs as portative covers. He designed reticulated single and double-layer domes and various foldable spatial grids with scissor systems [2]. Escrig and Valcarcel mainly focused on development of new spatial grids and patterns for deployable arches, geodesic domes and large scale umbrellas [3-7]. While developing these novel grids, they proposed several connection details, and connection elements for various patterns. After Piñero, Hoberman is the most important figure in the research area of deployable SSMs. Following the development of the angulated element, which is a variation of the simple SLE, he designed various deployable spatial SSMs like Iris Dome or Hoberman Sphere [8].

When all current deployable SSMs are examined, it can be seen that all of these structures have definite "deployed" and "contracted" body forms; and transformations occur between these two body forms. Moreover, all these examples change the size of their cover area during the transformation process. Thus, it can be claimed that existing deployable structures are not adequate to be used as permanent transformable coverings which can achieve multiple shapes without changing the size and boundaries of the covered area. Aiming to provide a solution to this, the primary objective of this study is to introduce a novel SSM which is designed as a roof structures, and has a wide range of form flexibility without changing the size of the covered area.

2. Main Principles of Current SSMs

To form the primary unit of an SSM, two bars are connected to each other at an intermediate point through a pivotal connection allowing them to rotate freely about an

axis perpendicular to their common plane but restraining all other degrees of freedom [9]. This scissor unit is called scissor-like element (SLE) (Figure 1). By the addition of some other intermediate elements, all planar and spatial SSMs arise from the concatenation of SLEs.

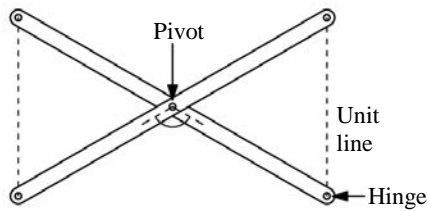


Fig. 1: Scissor-like element (SLE)

When straight bars are used as members, two different primary SLE unit type can be obtained according to the location of the pivot point: *translational* and *polar* units. Each unit types give rise to specific configurations with different deployment behavior and kinematic properties. First group is called translational scissor structures. The SSM which is composed of these units can only slide without any rotation. The main rule to meet this condition is that all unit lines should be parallel to each other (Figure 2a). Second group is called curvilinear scissor structures. For this group, the axes intersect and are rotated around their intersection points during deployment (Figure 2b). Both of these groups can only transform on one axis; so it is only possible to constitute contracted, deployed and some semi-deployed forms.

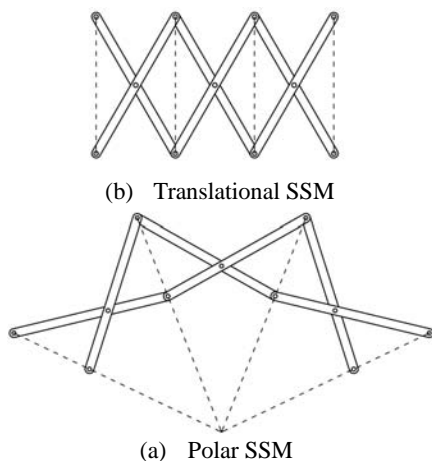


Fig. 2: Translational (a) and Polar (b) SSMs

One of the most important requirements of SSMs is that the configuration is able to be contracted in a compact shape. Figure 3 shows a basic scissor structure. According to this shape, it can be said that in the compact shape, the three units will have theoretically one dimension, and A_{i-1} ,

B_{i-1} , C_{i-1} , A_i , B_i , C_i , A_{i+1} , B_{i+1} , C_{i+1} will be co-linear. To meet this condition, the sum of the lengths of the bar segments on either side of an SLE, should be equal to the sum of the lengths of the corresponding bar segments of the adjacent SLEs [9-10]. When this rule is generalized:

$$a_{i-1} + b_{i-1} = a_i + b_i \quad (1)$$

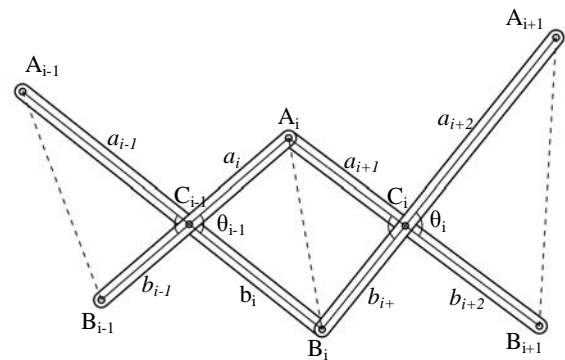


Fig. 3: SLE and Deployability Condition for SSMs

All common SSMs are $M=1$ structural mechanisms. This means, when a single SLE moves, all the other SLEs imitate this transformation as well. This property is valid not only for planar SLEs but also spatial scissor-like elements (S-SLEs). An S-SLE is graphically illustrated in Figure 4. The unit in this figure is fixed to the ground from the “element A”. When “element B” is slid through y axis, all the other elements adapt themselves to this movement. As a result of this movement, all distances between elements, and the size of the whole structures, change ($a_1 < a_2$, $b_1 < b_2$, $c_2 < c_1$).

Another deficiency of the common SSMs can be seen: When Figure 4 is investigated, it can be seen that these common examples are not suitable to cover a defined area as a permanent roof. This is because, when the structure transforms, the size of the covered area under it changes.

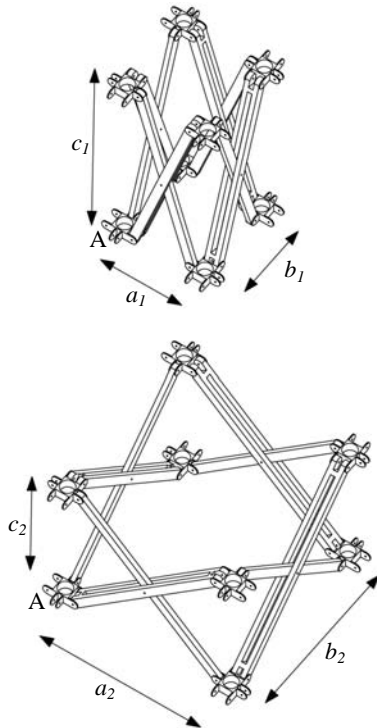


Fig. 4: Transformation of the unit of a common SSM

3. Primary Units of the Proposed Spatial SSM

In order to understand the logic of the proposed SSM and its transformation capability, first, the proposed primary units should be investigated. Proposed spatial SSM has three primary units: Spatial scissor-like element (S-SLE), Modified spatial scissor-like element (MS-SLE) and the Hybrid element which is a half MS-SLE (See Figure 5).

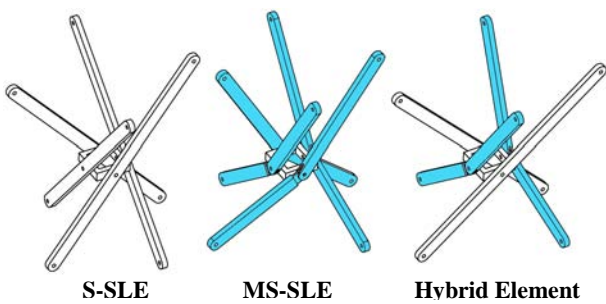


Fig. 5: Primary units of the proposed spatial SSM

All these primary units are based on the principles of Polar SSMs. Main difference of these units from the common spatial scissor units is the connection type of the struts. At common scissor units, struts are connected from the hinge points with an intermediate element. As it can be seen in Figure 4, when one member of the unit moves,

all the other members move as well. However, the units in Figure 5 have a different connection detail, and each strut can move individually. This individuality constitutes the main advantage of the proposed system.

4. Main Properties of the Proposed Spatial SSM

The proposed spatial SSM is generated by multiplication of the primary units in Figure 5. Emplacement of these primary units is illustrated in Figure 6. The SSM in Figure 6 has 25 S-SLEs, 4 MS-SLEs, 20 Hybrid Elements and eight special SLEs for the support points. The SSM is connected to the ground from eight points (A_1 to A_8). Span of the structure is 1400cm in both directions; and the lengths of the struts are 270 cm.

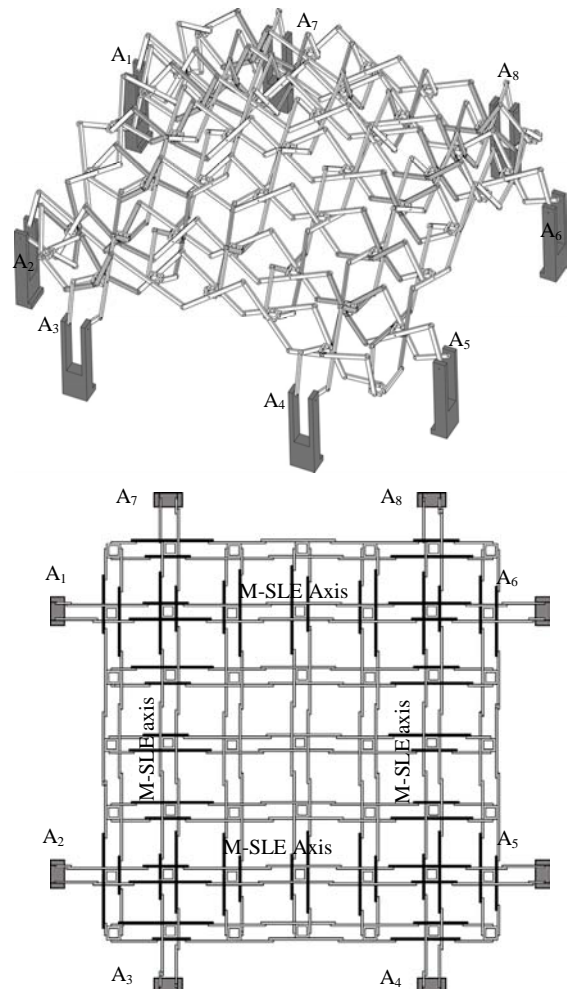


Fig. 6: Isometric and top view of the proposed SSM

5. Kinematic Analysis of the Proposed Spatial SSM

In order to understand the kinematic analysis of the system, first mobility of the system should be found. In this study, Freudenstein and Alizade formula [11] is used. According to this formula:

$$M = \sum_{i=1}^j f_i - \lambda L + q - j_p \quad (2)$$

where;

L = Number of closed loops in the system

M = Mobility

$$\sum_{i=1}^j f_i$$

= Sum of DoF all joints

λ = DoF of space where the mechanism operates

($\lambda=3$ for planar systems and $\lambda=6$ for spatial systems)

q = Number of over-constraint links

j_p = Passive mobilities in the joints

Kinematic analysis of the proposed spatial SSM is investigated in two phases: Analysis of a single unit (S-SLE) and analysis of the whole system.

5.1. Kinematic Analysis of a Single S-SLE

As it can be seen in Figure 5, all struts of the primary elements of the proposed SSM can move individually and rotate 360° unless they collide with the other struts. Mobility of this unit can be found as four by Alizade-Freudenstein formula.

Transformation capability of an S-SLE is directly related to the dimensions of intermediate element and the struts. An example to express the importance of these two factors can be seen in Figure 7. In this figure, it can be seen that when the intermediate element gets bigger, α and β angles which define the rotation of struts increase as well. This means, when $l_2 > l_1$, then $\alpha_2 > \alpha_1$; $\beta_2 > \beta_1$. From this example, it can be understood that the bigger intermediate elements increase the transformation capability of the unit. However, a bigger intermediate element increases the weight of the SLE and decreases the feasibility.

Another factor which affects the transformation capability of the S-SLE is the width (w) of the struts. When the length (w) increases, transformability range of the struts and of course α and β angles decreases.

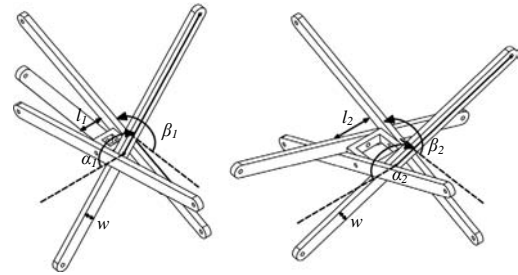


Fig. 7: Transformation limits of the S-SLE

An S-SLE can be thought as the combination of two perpendicular SLEs. These SLEs constitute individual planar systems, unless they collide with the perpendicular SLE. Shape limit of an S-SLE directly depends on the shape limit of one SLE. When a simple example of SLE as in Figure 8 is investigated experimentally, it can be observed that the angle θ_1 must be bigger than 180° , because when it is smaller than 180° , the whole system gives error. According to the result of this experimental study, the maximum and minimum limits of γ_1 and α_1 angles can be found as follows:

$$180^\circ \geq \theta_1 \geq 0^\circ \quad (3)$$

$$180^\circ \geq \alpha_1 \geq \cos^{-1}\left(\frac{b}{a}\right) \quad (4)$$

$$0^\circ \leq \frac{\gamma_1}{2} \leq \sin^{-1}\left(\frac{b}{a}\right) \quad (5)$$

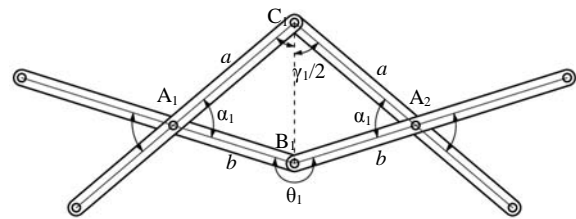


Fig. 8: Shape limit of SLE

5.2. Kinematic Analysis of the Whole System

Similar to the common deployable structures, additional actuators are needed to fix and transform the proposed spatial SSM. After the experimental studies with small prototypes, it was seen that these actuators should be utilized on the scissor axes which connect the support points (A_1 - A_6 , A_2 - A_5 , A_3 - A_8 , A_4 - A_7 axes). By this way, these four planar sub-structures become the main transformation elements of the whole structure. The other elements which are called as the “cover scissors” are secondary members and do not have a distinguishing role at form transformations. They only adapt themselves to

the actual positions of the main load bearing scissors (See Figure 9). At kinematic analysis of the proposed spatial SSM, transformation capability of the main scissors was investigated thoroughly; but the transformation of the cover scissors was not taken into consideration.

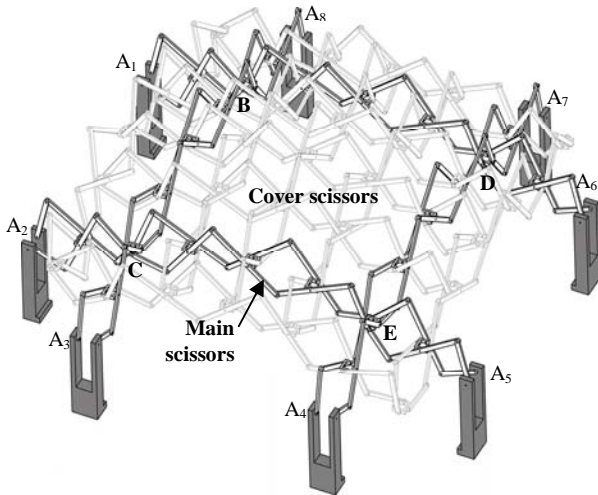


Fig. 9: Main and cover scissors of the proposed SSM

To find the number of additional actuators, mobility of the structure should be calculated. To facilitate this calculation, main scissors in Figure 9 were abstracted and presented in Figure 10. At this figure, it can be seen that; due to the use of revolute joints at connections of struts, all the subsystems (A_3CBA_8 , A_4EDA_7 , A_2CEA_5 and A_1BDA_6) cannot deviate from their planes, and can achieve only planar transformations. Besides, subsystems intersect at some certain points (B, C, D and E) which are called as “knots”. In order to keep the planes of the main axes, knots can only slide through (z) direction. This property is very important factor for the transformation capability of the proposed spatial structure.

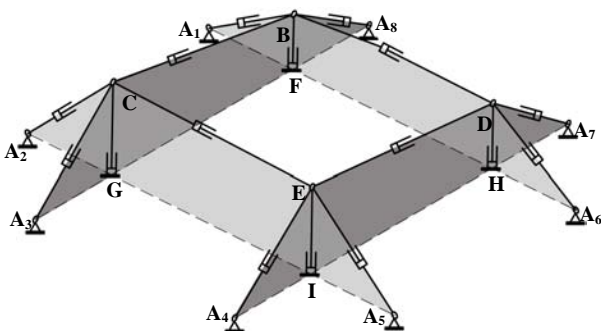


Fig. 10: Abstraction of the main scissors

When Freudenstein-Alizade Formula is applied to find the mobility, it is seen that the abstracted system in

the figure has 40 joints and 12 loops (such as A_3CG , A_3CEA_4 , A_4EI , etc.). All sub-systems are planar, so λ is equal to three. According to these variables, mobility of the system can be found as;

$$M = 40 - 12 \times 3 = 4$$

From the Figures 9 and 10, it can be seen that the main scissors of the proposed spatial SSM is composed of four identical perpendicular planar sub-systems. In this paper, kinematic analysis of the whole system was made with one of these planar sub-systems (The system between A_1 to A_6). The analysis was made according to Denavit-Hartenberg method, and the formulations were tested with a Microsoft Excel® based computer program.

When a rigid body transforms, it has four different kinds of rotation and transformation matrix: Rotation angle around z axis (T_z^ϕ), rotation around x axis (T_x^ω), shortest distance between the z axis (T_z^d), and shortest distance between x axis (T_x^a). All these four transformations can be shown with a matrix equation and the multiplication of these matrices give Denavit-Hartenberg general transformation matrix.

$${}^{n-1}T_n = T_z^\phi \times T_x^d \times T_z^a \times T_x^\omega \quad (6)$$

According to the aforementioned parameters, general Denavit-Hartenberg transformation matrix is written as;

$${}^{n-1}T_n = \begin{bmatrix} \cos\phi_n & -\sin\phi_n \cos\omega_n & \sin\phi_n \sin\omega_n & a_n \cos\phi_n \\ \sin\phi_n & \cos\phi_n \cos\omega_n & -\cos\phi_n \sin\omega_n & a_n \sin\phi_n \\ 0 & \sin\omega_n & \cos\omega_n & d_n \\ 0 & 0 & 0 & 1 \end{bmatrix} \quad (7)$$

When this transformation matrix is applied to the analyzed planar sub-system of the proposed SSM (A_1 - A_6), ω_n and d_n variables become 0, because the system is planar. Denavit-Hartenberg parameters of the sub-system A_1 to A_6 can be seen in Figure 11.

To apply Denavit-Hartenberg matrices to the system, the whole system was considered as two individual parts. First part includes the upper part which consists of the bars $|OA|$, $|AB|$, $|BC|$, $|CD|$, $|DE|$, etc; and second part includes the bars which consists of the bars $|OA'|$, $|A'B|$, $|BC'|$, $|C'D|$, $|DF|$, $|FE'|$, etc. These two individual systems intersect in the pivot points of each SLE (such as points B, D, F).

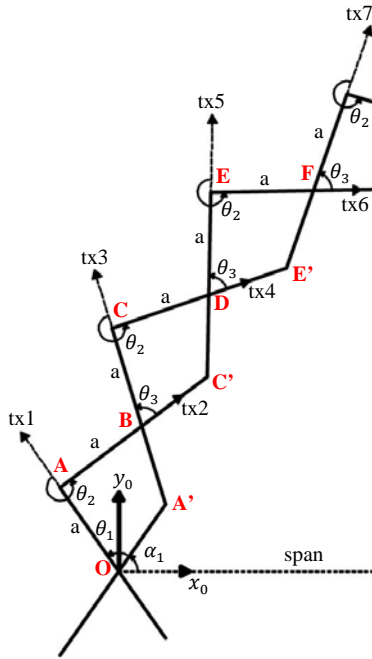


Fig. 11: Denavit-Hartenberg parameters of the planar scissor

By using Denavit-Hartenberg general transformation matrix, coordinates and rotation of a point according to the in Cartesian system can be found. This is possible with the multiplication of transformation matrices. For example, when the rotation and orientation of point A is needed, according to the upper system, the transformation matrix can be written as;

$${}^0A_1 = \begin{bmatrix} \cos(\theta_1 + \alpha_1) & -\sin(\theta_1 + \alpha_1) & 0 & a\cos(\theta_1 + \alpha_1) \\ \sin(\theta_1 + \alpha_1) & \cos(\theta_1 + \alpha_1) & 0 & a\sin(\theta_1 + \alpha_1) \\ 0 & \sin\alpha_1 & 1 & 0 \\ 0 & 0 & 0 & 1 \end{bmatrix} \quad (8)$$

In this multiplication, 0A_1 is the expression of transformation of the first strut according to x_0 Cartesian coordinate; $\theta_1 + \alpha_1$ is the rotation of tx1 bar axis to the x_0 Cartesian coordinate system; $a\cos(\theta_1 + \alpha_1)$ is the x component of the point A, and $a\sin(\theta_1 + \alpha_1)$ is the y component of point A. Moreover, when the coordinates and rotation of point F according to the O point is required, transformation matrices from point O to point F must be multiplied. This multiplication can be written as;

$${}^0A_6 = {}^0A_1 {}^1A_2 {}^2A_3 {}^3A_4 {}^4A_5 {}^5A_6 \quad (9)$$

For the upper side of the system, when the equations from tx1 to tx21 are calculated, system constitutes a

closed loop. Thus, the result of this transformation matrix comes to the point O. This means, at point O, the orientation is 0, and the rotation is 180. When the general form of the matrix is written;

$${}^0A_{21} = {}^0A_1 \dots {}^{20}A_{21} == \begin{bmatrix} -1 & 0 & 0 & 0 \\ 0 & -1 & 0 & 0 \\ 0 & 0 & 1 & 0 \\ 0 & 0 & 0 & 1 \end{bmatrix} \quad (10)$$

To verify the kinematic analysis based on Denavit-Hartenberg Method, a Microsoft Excel 2007® based program was prepared. This program is efficient to see the final shape of the main scissors according to the inputs. In this program, span of the whole structure, dimension of the elements, angles between the elements (θ_2 , θ_4) and location of the perpendicular axes which define the location of knots are the input variables. By spin buttons, users can vary input angles and lengths, According to the changes on these input variables, the graphic interface can update itself simultaneously. In addition, the system gives error for unavailable shapes or inconsistent input configurations. Thus, if the algorithm fails for an input configuration, it is understood that this shape is unavailable for those inputs. The interface of this program is given below in Figure 11. For further information about the kinematic analysis of the planar sub-scissors, please look at the article of the authors [12].

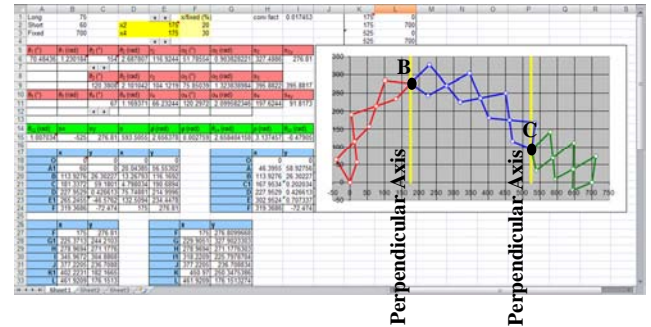


Fig. 11: Interface of the computer program for the proposed spatial SSM

6. Conclusions

This study has proposed a flexible and transformable SSM. This proposed SSM expands the transformation capability, adaptability and form flexibility of deployable structures. Until now, deployable structures have been only used as portative building components. However, after the model proposed in this study, deployable structures will also be used as permanent transformable building coverings.

As a hypothetical example, such a transformable SSM

can be used as roof of an exhibition hall. According to the activity and the necessities for the activities in that hall, the shape of the roof can be transformed by the users. This kind of a transformation offers great flexibility for spaces. As an example of functional need, the proposed scissor-hinge model can be used as a solar roof. It can be rotated according to the location of the sun and benefit from the sun more than the conventional solar panels. Scissor-hinge structures are conveniently used with control systems, so by using a few motors, these transformations can be performed easily. An example application of the proposed SSM as a roof structure, and its sample transformations can be seen in Figure 12.

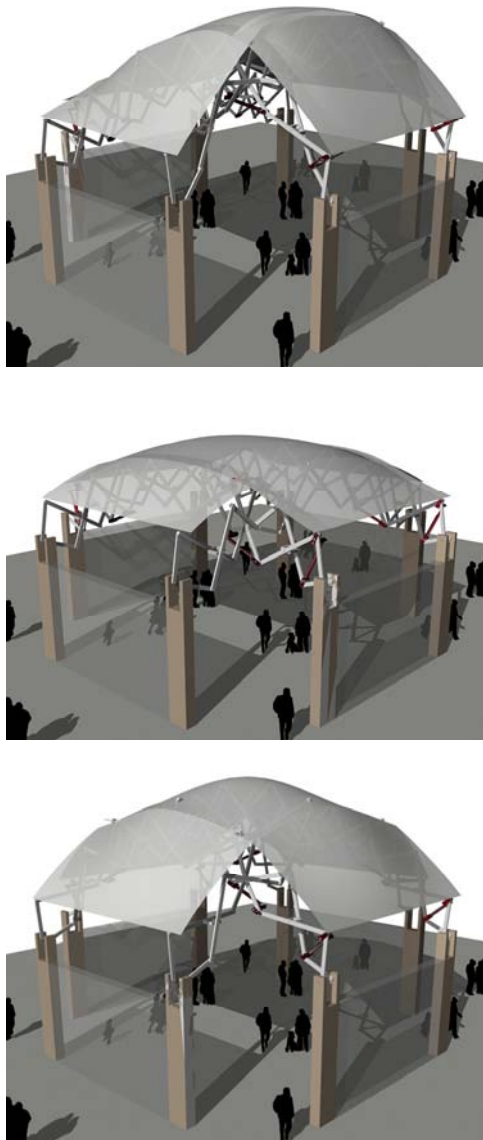


Fig. 12: Transformation of the proposed spatial SSM as a roof structure

References

- [1]. W. Zuk, & R. Clark, *Kinetic Architecture*. Van Nostrand Reinhold Press; New York, 1970.
- [2]. J. Chilton, *Space Grid Structures*, Architectural Press, Oxford, 2000.
- [3]. F. Escrig, J.P. Valcarcel, *Geometry of Expendable Space Structures*, International Journal of Space Structures, 1993; 8: pages 71-84.
- [4]. F. Escrig, *Expandable Space Frame Structures*. Proceeding of the 3rd International Conference on Space Structures, Guildford, UK: Elsevier Applied Science Publishers; pages 845-850, 1984.
- [5]. F. Escrig, *Expendable Space Structures*, Space Structures Journal, 2 (1): 79-91, 1985.
- [6]. F. Escrig, J.P. Valcarcel, *Curved Expandable Space Grids*, Proceedings of the International Conference on the Design and Construction of Non-Conventional Structures, London, England. Civil-Comp Press, pages 157-168, 1987.
- [7]. F. Escrig, J.P. Valcarcel, *Great Size Umbrellas with Expendable Bar Structures*, Proceedings of the 1st International Conference on Lightweight Structures in Architecture, Sydney, Australia; (1): pages 676-681, 1986.
- [8]. C. Hoberman, *Unfolding Architecture: An Object that is identically a Structure and a Mechanism*, Architectural Design, 63: pages 56-59, 1993.
- [9]. C. Gantes, *Deployable Structures: Analysis and Design*, WIT Press, Boston, 2001.
- [10]. T. Langbecker, *Kinematic Analysis of Deployable Scissor Structures*, International Journal of Space Structures, Vol. 14, No. 1, pages 1-15, 1999.
- [11]. F. Freudenstein, R. Alizade. *On the Degree of Freedom of Mechanisms with Variable General Constraint*, IV. World IFToMM Congress. England, pages 51-56, 1975.
- [12]. Y. Akgün, C. Gantes, K.E. Kalochairetis, G. Kiper, *A novel concept of convertible roofs with high transformability consisting of planar scissor-hinge structures*, Engineering Structures, In Press, Corrected Proof, Available online 9 June 2010, doi:10.1016/j.engstruct.2010.05.006



Design of Novel Mechanism based on Bennett Linkage for Architectural Applications

Koray KORKMAZ^{1*}, Yenal AKGÜN¹, Feray MADEN¹

^{1*}Izmir Institute of Technology Department of Architecture
Gülbahçe Kampüsü 35430 Izmir, Turkey
koraykorkmaz@iyte.edu.tr

Abstract

By the development of new materials and construction techniques, double curved geometries including hyperbolic paraboloids (hypars) have become a trend in contemporary architecture. However, most of the constructed architectural examples of the hypars are static and cannot offer any form variability. Bennett linkage is a spatial mechanism which can constitute deployable hypar, but it has many geometric limitations. In this paper, a novel mechanism is introduced which is derived from the basic design principles of Bennett linkage. By its distinctive connection details and the additional links, this novel mechanism has a superior transformation capability over common Bennett linkage; and can change its form between planar geometries to various hypars. In the paper, first, use of hypars in architecture is introduced briefly. Then, main principles and deficiencies of the Bennett linkage are presented. Finally, geometric principles, shape limitations and potential uses of the proposed novel mechanism are explained.

Keywords: Deployable, Bennett Linkage, Hypar, Transformation, Kinetic Architecture

1. Introduction

Parallel to the development at construction technologies and materials, non-orthogonal forms have become the demand of contemporary architecture. Architects design double-curved geometries as different building components, mostly roof or façade elements. As one of these double-curved geometries, a hyperbolic paraboloid (hypar) surface is obtained by sweeping a straight line over a straight path at one end and another non-parallel straight path. Hypar is a ruled surface which has convex one way along the surface and concave along the other. When the potential use of such surfaces in architecture is investigated, it is seen that many static examples have been constructed as shell structures. Being as spatial lightweight ruled surfaces, these shell structures are capable of carrying their own weights and additional loads due to their curvature and twist. Constructed from masonry, concrete, a grid of steel or timber members, they

are assembled to large-span buildings in which a large space is realized without columns. A concrete shell example of hypar which is designed by Felix Candela can be seen in Figure 1.



Fig. 1: Gas Station Building by Felix Candela

Although the hypars offer non-traditional architectural forms, constructed structures don't change shape and form of the buildings. However, from the demand for today's dynamic, flexible and constantly changing activities, a need for the adaptive buildings and building components has emerged in architecture. Today, the most impressive examples which meet this need are the deployable structures that are capable of large geometric transformations. When present solutions of such structures are investigated, it is seen that many concepts have been proposed by varying in size, geometry, retraction methods and structural systems in terms of their morphological and kinematic characteristics. However, most of the deployable structures do not offer real flexible alternatives and have only two configurations; transformation from a closed compact configuration to a predetermined, expanded form in which they are stable and can carry loads. Moreover, only few have been constructed at full-scale for architectural applications due to the mechanical complexity of their systems during the deployment and folding process [1].

It is possible to generate deployable hypar surfaces



with Bennett linkage which is a 4R spatial linkage. 4R closed chains can be classified into two types: the axes of rotation are all parallel to one another or they intersect at a point, leading to planar 4R or spherical 4R linkages. Any disposition of the axes different from these two special arrangements is known rigid chain and so furnishes no mechanism at all. But there is an exception, which is the Bennett linkage.

Bennett linkage is one type of spatial overconstrained mechanisms consisting of four straight rods. Discovered by G.T. Bennett in 1903, Bennett linkage is a spatial 4R closed chain whose four rigid links are connected by four revolute joints (Figure 2). It has the simplest geometric form and is the only 4R spatial linkage with revolute joints among all overconstrained linkages. The axes of revolute joints are neither parallel nor concurrent while they are either parallel or concurrent in common 4R linkages. This special characteristic of Bennett linkage has attracted the attention of many researchers and engineers. Most research has focused on kinematic characteristics, mathematical descriptions, geometric configurations and combination methods of Bennett linkage to generate new mechanisms for further applications.

In his “skew isogram mechanism,” Bennett [2] proved that all hinge axes of Bennett linkage can be regarded as the same regulus on a certain hyperboloid at any configuration of the linkage. Yu [3] found that Bennett linkage is directly related to the hyperboloid defined by its joint axes. He set up the Plucker coordinates of its four hinge axes and derived the equation of hyperboloid. Later, Yu [4] and Baker [5] investigated quadric surfaces associated with the Bennett linkage. While Yu studied sphere which pass through the vertices of the Bennett linkage and generated a spherical 4R linkage, Baker scrutinized J-hyperboloid defined by the joint axes of the Bennett linkage and L-hyperboloid defined by the links of the Bennett linkage. In his later works, Baker focused on the relative motion [6] and the axodes of the motion of the Bennett linkage [7]. He found that relative motion could be neither purely rotational nor purely translational at any time. Moreover, he demonstrated that the fixed axode of the linkage is ruled surface.

On the other hand, Huang [8] explored finite kinematic geometry of Bennett linkage based on the intersection of two basis screws associated with two RR dyads. Because the combination of two screws forms a cylindroid that is one type of ruled surface, the axis of cylindroid coincides with the line symmetry of the Bennett linkage. Further, Perez and McCarthy [9] established that the cylindroids can be generated directly from the three position synthesis of a spatial RR chain. In addition, by using the Bennett linkage as the basic element, Chen and You [10] developed large mobile assemblies for aerospace applications. They offered many

alternative forms of the linkage to obtain the most compact folding and maximum expansion for large structures [11]. For this purpose, they introduced and verified simple methods to build the linkage in its alternative form [12]. Furthermore, Y Yu [13] proposed a deployable membrane structure based on the alternative form of the Bennett linkage. Besides, many other structural mechanisms associated with Bennett linkage have been developed by combining two or three linkages in such a way that common link is removed and adjacent links are attached to each other, but this paper does not cover the studies about 5R and 6R linkages based on Bennett linkage.

To understand the main principles and superiority of the proposed novel mechanism, its ancestor Bennett linkage should be thoroughly investigated.

2. Geometric and Kinematic Principles of Bennett Linkage

It is known that the mobility M of a spatial linkage can be determined by Grübler mobility criterion.

$$M = 6(n-1) - \sum_{i=1}^5 (6-i)p_i$$

where n is number of links and $\{p_i\}_1^5$ is number of degree of freedom (DOF) of joints. According to the above equation, mobility of Bennett linkage can be calculated as follows.

$$M = 6(4-1) - 5.4 = -2$$

It must be rigid chain. Even though Bennett linkage does not meet the mobility criterion, it has full-range mobility. Bennett is an exception like all other overconstrained mechanisms because of their special geometry conditions among the links and joint axes.

The dimension of active motion of rigid body for planar mechanisms is RPP, for spherical mechanism is RRR, and for Bennett is RRP. So the dimension of subspace is $\lambda=3$ and all mechanisms moving in this subspace are called overconstrained mechanisms. All the kinematic joints will have constraint $d=6-\lambda$, or $d=3$. The Grübler formula for subspace $\lambda=3$ gives:

$$M = 3(n-1) - 2p_1 - p_2 = 3(4-1) - 2.4 = 1$$

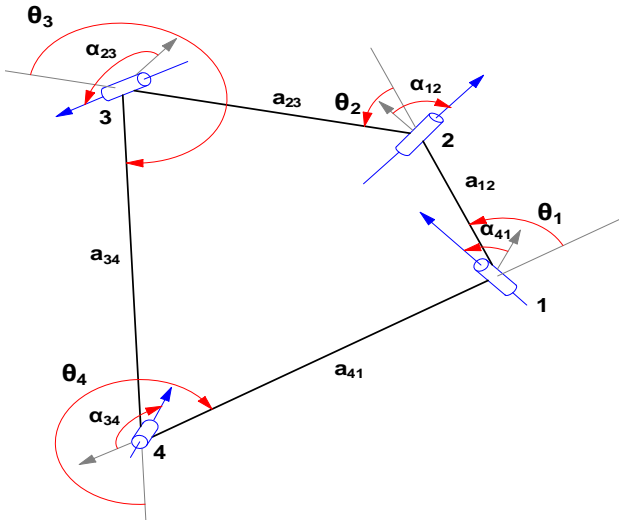


Fig. 2: Abstraction of Bennett Linkage

The movement of Bennett is allowed due to its special configurations. The conditions defined by Bennett are as following:

- a) The twists that are the skewed angles between the axes of two revolute at the ends of links and the lengths of the bars on opposite sides are equal.

$$\begin{aligned} a_{12} &= a_{34} = a \\ a_{23} &= a_{41} = b \\ \alpha_{12} &= \alpha_{34} = \alpha \\ \alpha_{23} &= \alpha_{41} = \beta \end{aligned} \quad (1)$$

- b) The twists and the lengths must satisfy the condition of

$$\frac{a}{\sin \alpha} = \frac{b}{\sin \beta} \quad (2)$$

- c) Because the skewed angles α and β are restricted to the range $(0, \pi)$, the displacement closure equations based on the four variable joint angles θ_i can be written as:

$$\theta_1 + \theta_3 = 2\pi = \theta_2 + \theta_4 \quad (3)$$

$$\tan \frac{\theta_1}{2} \tan \frac{\theta_2}{2} = \frac{\sin \frac{1}{2}(\beta + \alpha)}{\sin \frac{1}{2}(\beta - \alpha)} \quad (4)$$

These closure equations are only in use when one of the revolute variables θ_i is independent. In addition to above conditions, there is a special case in which a different type of Bennett linkage is generated. When $\alpha + \beta = \pi$ and $a = b$, an equilateral linkage is obtained (Figure 2). Therefore, Eq. (4) becomes

$$\tan \frac{\theta_1}{2} \tan \frac{\theta_2}{2} = \frac{1}{\cos \alpha} \quad (5)$$

2.1. Deficiencies of Bennett Linkage

The revolute joints used in the Bennett linkage are mechanically simple but their placement along each link and angle between the pin axes are complicated. There is a need to determine the link cross-sections or design new joints for architectural applications.

On the other hand, the geometry of the Bennett linkage defines a hyper surface, intermediate links are necessary to attach the cover plates. However, it is impossible to cover its surface with straight rods whose lengths are identical to the linkage, because the connection points of the intermediate links on opposite sides of the linkage which subdivide the surface into equal parts come closer during the deployment. Therefore, during the deployment process each intermediate link must extend or shorten. This argument can easily be proved by Denavit-Hartenberg (DH) convention. The transformation matrix of D-H is:

$$T_{i-1}^i = \begin{bmatrix} \cos \theta_i & -\sin \theta_i \cos \alpha_i & \sin \theta_i \sin \alpha_i & a_i \cos \theta_i \\ \sin \theta_i & \cos \theta_i \cos \alpha_i & -\cos \theta_i \sin \alpha_i & a_i \sin \theta_i \\ 0 & \sin \alpha_i & \cos \alpha_i & d_{12} \\ 0 & 0 & 0 & 1 \end{bmatrix} \quad (6)$$

where θ_i is joint angle, α_i is link twist, a_i is link length and d_i is link offset. By using Eq. (6) for equilateral Bennett linkage in Figure 3:

$$T_1^2 = \begin{bmatrix} \cos \theta_1 & -\sin \theta_1 \cos \alpha_{12} & \sin \theta_1 \sin \alpha_{12} & a_{12} \cos \theta_1 \\ \sin \theta_1 & \cos \theta_1 \cos \alpha_{12} & -\cos \theta_1 \sin \alpha_{12} & a_{12} \sin \theta_1 \\ 0 & \sin \alpha_{12} & \cos \alpha_{12} & d_{12} \\ 0 & 0 & 0 & 1 \end{bmatrix} \quad (7)$$

$$T_2^3 = \begin{bmatrix} \cos \theta_2 & -\sin \theta_2 \cos \alpha_{23} & \sin \theta_2 \sin \alpha_{23} & a_{23} \cos \theta_2 \\ \sin \theta_2 & \cos \theta_2 \cos \alpha_{23} & -\cos \theta_2 \sin \alpha_{23} & a_{23} \sin \theta_2 \\ 0 & \sin \alpha_{23} & \cos \alpha_{23} & d_{23} \\ 0 & 0 & 0 & 1 \end{bmatrix} \quad (8)$$

$$T_1^3 = T_1^2 \cdot T_2^3 \quad (9)$$

Because $a_{12} = a_{23} = a_{34} = a_{41}$ and $\alpha_{12} = \alpha_{23} = \alpha_{34} = \alpha_{41}$, θ_1 is variable. By using Eq. (5), θ_2 can be found as:

$$\theta_2 = 2 \tan^{-1} \left(\frac{1}{\cos \alpha \cdot \tan(\theta_1 / 2)} \right) \quad (10)$$

The distance between midpoints of a_{23} and a_{41} can be calculated as follows:

$$D = \sqrt{(x-a)^2 + (y-b)^2 + (z-c)^2} \quad (11)$$

By using Eqs. (9), (10) and (11), a numerical example can be solved. Let take $a_{12}=a_{23}=a_{34}=a_{41}=100\text{cm}$, $\alpha_{12}=\alpha_{23}=\alpha_{34}=\alpha_{41}=45^\circ$ and $\theta_1=90^\circ$.

$$\theta_2 = 2 \tan^{-1} \left(\frac{1}{\cos 45 \cdot \tan 45} \right) = 109.4712^\circ \quad (12)$$

$$T_1^3 = \begin{bmatrix} 0 & -0.7071 & 0.7071 & 0 \\ 1 & 0 & 0 & 100 \\ 0 & 0.7071 & 0.7071 & 0 \\ 0 & 0 & 0 & 1 \end{bmatrix} \quad (13)$$

$$T_2^3 = \begin{bmatrix} -0.3333 & 0.6667 & 0.6667 & -33.3333 \\ 0.9428 & 0.2357 & 0.2357 & 94.2809 \\ 0 & 0.7071 & -0.7071 & 0 \\ 0 & 0 & 0 & 1 \end{bmatrix} \quad (14)$$

$$T_1^3 = T_1^2 \cdot T_2^3 = \begin{bmatrix} -0.6667 & 0.3333 & -0.6667 & -66.6667 \\ -0.3333 & 0.6667 & 0.6667 & 66.6667 \\ 0.6667 & 0.6667 & -0.3333 & 66.6667 \\ 0 & 0 & 0 & 1 \end{bmatrix} \quad (15)$$

According to aforementioned solution, the coordinates of midpoints a_{23} is found as $(-33.3, 83.3, 33.3)$ while the midpoint of a_{41} is $(-50, 0, 0)$. Therefore, $D=91.25\text{cm}$. When $\theta_1=45^\circ$, the coordinates of midpoints a_{23} is $(27.5, 54.4, 19.1)$ and the midpoint of a_{41} is $(-50, 0, 0)$. Therefore, $D=96.59\text{cm}$. The results show that the dimensions of intermediate links between a_{23} and a_{41} will change when the linkage deploy, therefore intermediate links require prismatic joints which allow translation during deployment.

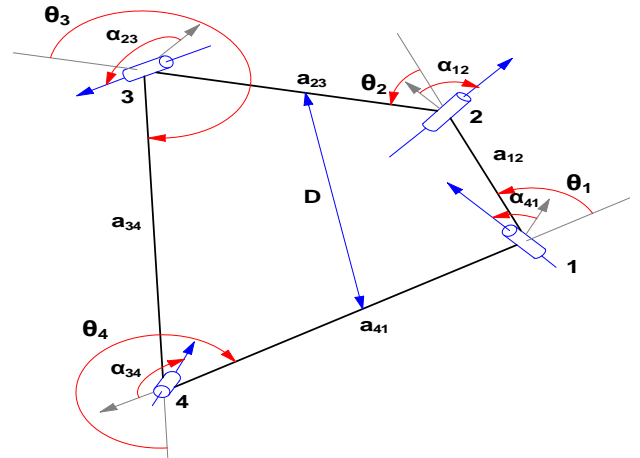


Fig.3. Equilateral Bennett linkage

As it is seen, Bennett linkage has many limitations to offer flexible solutions. Due to the restrictions of the linkage, researchers have sought for alternative forms of Bennett linkage. For instance, Chen[14] explores the possibilities of constructing large structural mechanisms using Bennett linkage as the basic element. For this purpose, first of all Chen identifies basic element from Bennett linkage with skew square cross-section bars to obtain compact folding and maximum expansion (Figure 4). With this particular example Chen shows that construction of a Bennett linkage with compact folding and maximum expansion is not only mathematically feasible, but also practically possible. Secondly she develops a way by which the basic element can be connected to form a large deployable structure while retaining the single degree of freedom.

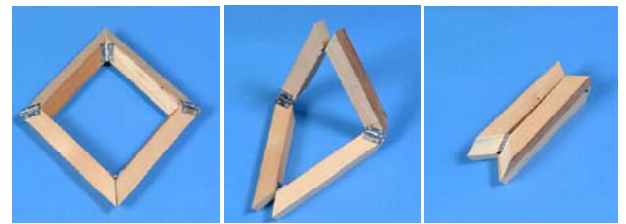


Fig.4. Chen's Bennett linkage

Basic element based on the alternative forms of Bennett linkage provide the most efficient compact folding with a maximum expansion, but it limited to deployable mechanism whose DoF is one. Basic element transforms from a closed compact configuration to a predetermined, expanded form. Therefore it is not possible to change its form between planar geometries to various hypars. To obtain real flexible solutions for transformable structures, there is a need to develop novel mechanism whose DoF is more than one.

3. Proposed Novel Structural Mechanism

Figure 5 shows three equilateral Bennett linkages with same joint angle θ_1 . Even though these three linkages have same lengths and same joint angle, their configuration is different because of the different skewed angles α_{12} and α_{23} for each Bennett linkage. Consequently, skewed angles are different but constant for each linkage, so any linkage cannot transform to another one.

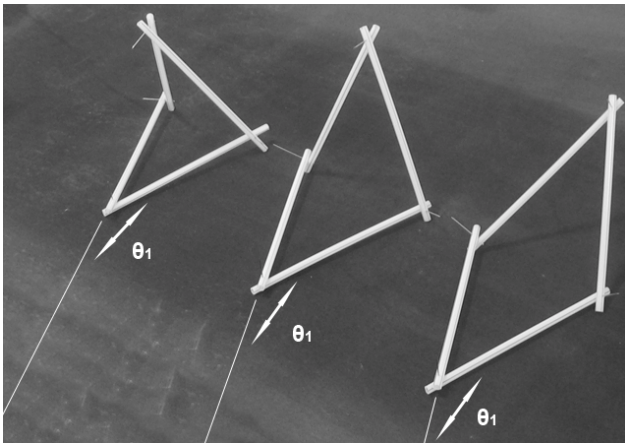


Fig.5. Equilateral Bennett Linkages with same θ_1 .

Main idea is to develop an equilateral mechanism with variable α_{12} , α_{23} , α_{34} , α_{41} so that it can take form of any equilateral Bennett linkage. Proposed mechanism is an 8R closed chain system with eight cylindrical link cross-sections (Figure 6). Revolute joints between links 1 and 2, 3 and 4, 5 and 6, 7 and 8 let rotations around the links' axes. This rotation makes skewed angles α_{12} , α_{23} , α_{34} , α_{41} variables. By its additional links and joints this novel mechanism has a superior transformation capability over common Bennett linkage.

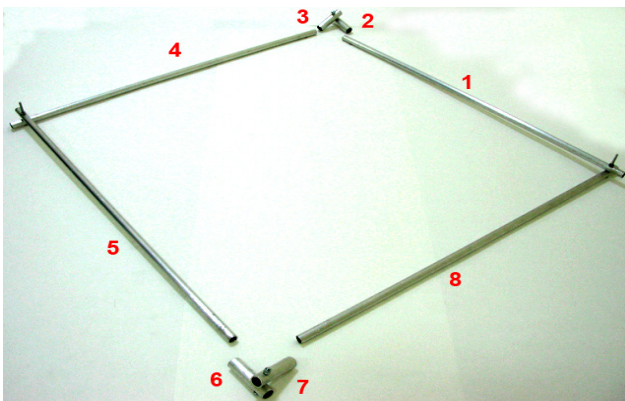


Fig.6. Proposed Novel Mechanism

Kinematic diagram of this novel mechanism is represented in Figure 7.

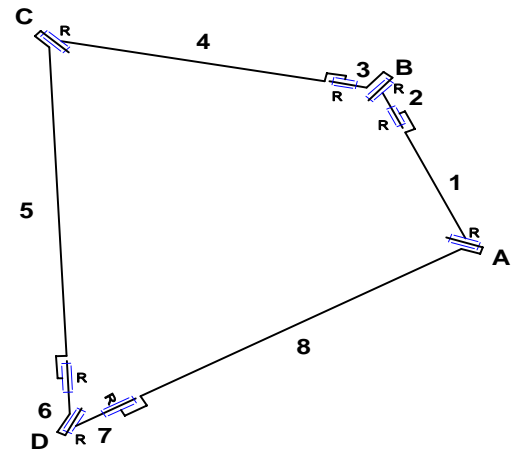


Fig.7. Kinematic Diagram of the Proposed Novel Mechanism

According to Grübler's criterion, the mobility of this novel mechanism is:

$$M = 6(n - 1) - 5p_1 = 6(8 - 1) - 5 \cdot 8 = 2$$

As one of the most important superiority of this novel system over classical Bennett linkage, the system can physically move with overlapped links. This property increases the transformation capability of the original Bennett linkage and the novel mechanism can stow and deploy completely. Furthermore, both side of the mechanism can move individually, and the system can achieve both planar geometries and various hypars. Figure 8 shows example shape alternatives of the proposed novel system.



Fig.8. Transformation Capability of the Proposed Novel Mechanism

As it is mentioned above, the proposed structural mechanism can constitute various hypars and the geometry of these hypars can change according to the needs. Thus, this mechanism can be used as an adaptive building component (such as a roof, façade system, or furniture, etc.) which can change its shape according to the expectations of the users or the exterior conditions.

As an example architectural application, the proposed mechanism has been developed as an adaptive roof. In order to use this system as a roof structure, some additional struts which are needed to fix the cover material are necessary. Kinematic diagram of this adaptive roof system with these additional elements can be seen in Figure 9. Mobility of this system can be found by Freudenstein-Alizade Formula [15] as;

$$M = \sum_{i=1}^j f_i - \sum_{K=1}^L \lambda_K = 26 - (4 \times 6) = 2$$

where f_i is degree of freedom of i -kinematic pair, λ_K is number of space or subspace of k -closure loop, L is number of independent loops.

According to Grübler's equation:

$$M = 6(n-1) - 5p_1 - 4p_2$$

$$M = 6(14-1) - 5 \cdot 8 - 4 \cdot 9 = 2$$

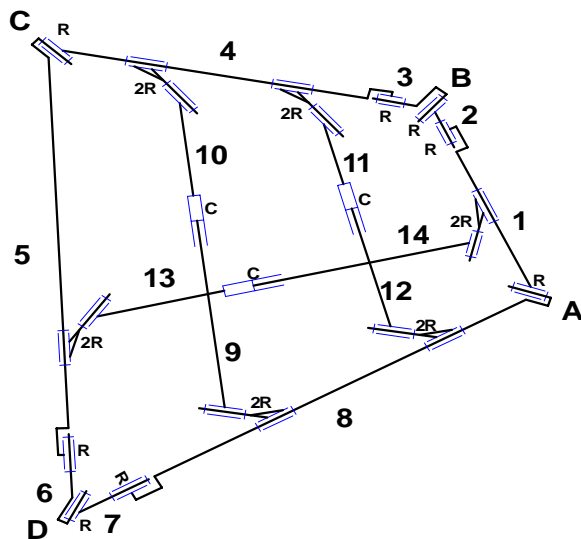


Fig.9. Kinematic Diagram of the Proposed Novel Mechanism with additional struts

By multiplying the intermediate links which connect the main frame of the proposed structural mechanism, an adaptive roof structure has been obtained. This structure can change its form with additional struts on it which is needed to assemble cover material (Figure 10).

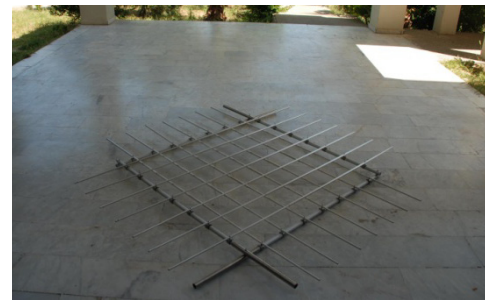
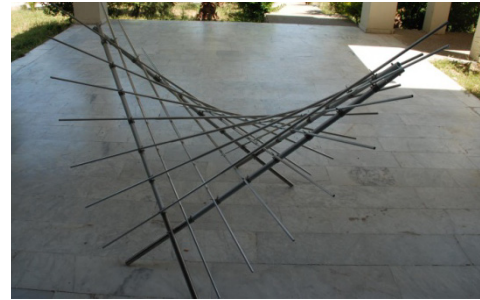


Fig.10. Deployed and Stowed Forms of the Proposed Novel Mechanism as an Adaptive Roof

4. Conclusions

This paper has exposed a novel structural mechanism which is based on Bennett linkage. General principles, superiority over original Bennett linkage have been thoroughly explained. Finally, application of this novel structural mechanism as an adaptive roof structure has been presented.

This study shows that well-known mechanisms, especially overconstrained mechanisms can be used as a building component with some small modifications.



References

- [1]. Asefi, M. "An Architectural Evaluation of Transformable Roof Structures." Adaptables 2006, Proceedings of the International Conference on Adaptability in Design and Construction, vol 2 (2006): 85-89.
- [2]. Bennett, G. T. "The Skew Isogram Mechanism." Proceedings of the London Mathematical Society, vol. 13 (1914): 151-173.
- [3]. Yu, H. C. "The Bennett Linkage, its Associated Tetrahedron and the Hyperboloid of its Axes." Mechanism and Machine Theory 16:2 (1981):105-114.
- [4]. Yu, H. C. "Geometry of the Bennett Linkage via its Circumscribed Sphere." Proc. 7th World Congress on the Theory of Machines and Mechanisms, Sep. 17-22, Seville, Spain, vol. 1 (1987): 227-229.
- [5]. Baker, E. J. "The Bennett Linkage and its Associated Quadric Surfaces." Mechanism and Machine Theory 23 (1988): 147-156.
- [6]. Baker, E. J. "On the Motion Geometry of the Bennett Linkage." Mechanism and Machine Theory 35 (2000): 1641-1649.
- [7]. Baker, E. J. "The Axodes of the Bennett Linkage." Mechanism and Machine Theory 36 (2001): 105-116.
- [8]. Huang, C. "The Cylindroid Associated with Finite Motions of the Bennett Mechanism." Trans. ASME, J. Eng. Ind. 119 (1997): 521-524.
- [9]. Perez, A. and McCarthy, J. M. "Dimensional Synthesis of Bennett Linkages." Transactions of the ASME, Journal of Mechanical Design 125:3 (2003): 98-104.
- [10]. Chen, Y. and You, Z. "Mobile Assemblies based on the Bennett Linkage." Proceedings of the Royal Society A 461 (2005): 1229-1245.
- [11]. Chen, Y. and You, Z. "Square Deployable Frames for Space Applications. Part 1: Theory." Proc. IMechE, Part G: J. Aerospace Engineering, 220 (2006): 347-354.
- [12]. Chen, Y. and You, Z. "Square Deployable Frames for Space Applications. Part 2: Realization." Proc. IMechE, Part G: J. Aerospace Engineering, 221 (2007): 37-45.
- [13]. Yu, Y. "Deployable Membrane Structure Based on the Bennett Linkage." Proc. IMechE, Part G: J. Aerospace Engineering, 221 (2007): 775-783.
- [14]. Chen, Y. "Design of Structural Mechanisms." PhD thesis, University of Oxford, 2003.
- [15]. Freudenstein, F., and R. Alizade. "On the Degree of Freedom of Mechanisms with Variable General Constraint." IV. World IFTtoMM Congress. England, 1975. 51-56.



Designing a Bricard Linkage Module to Stabilize Unstable Spherical Space Frames

Melodi Simay ACAR^{1*}, Koray KORKMAZ¹

Department of Architecture, Izmir Institute of Technology, Turkey
melodiacar@gmail.com

Abstract:

The nodes are the main component of the space structures, but standardize the form of the structures. The target of this paper is to propose a single module which gives capability to maintain spherical space structures with variable volumes. As the natural structures always form in minimum energy shapes, the proposed three armed node is inspired by the structural behaviour of the natural structures. The assembly of the proposed node has only one degree of freedom obtained by trihedral case of Bricard linkage which has capability of forming from tetrahedron to hexahedron and dodecahedron and further provides stability to the unstable ones.

Keywords: structural mechanism, Bricard linkage, space frames, minimum energy structures, modular three-arm node

1. Introduction

Structure is the skeleton which carries the whole load and the main component for defining space with variable geometric forms. Architects and engineers usually think of parts such as beams, trusses and frames when defining a closed space. However, the structural behaviour of these planar beams and trusses are two-dimensional. On the other hand, the space structures such as space grids, trusses and geodesic dome, etc. is concerned by their three dimensional behaviour as they spread the loads in three axes. In that case, the understanding of the three-dimensional behaviour of the structures is significant in the design process of space structures [1].

In nature, every structure tends to be in the configuration of minimum potential energy. One of the fundamental geometric principles that nature solve repeatedly is packing the objects close together in minimal ways [2, 3]. Even we can see these structures in natural environment, such as in bee's honeycombs, basalt blocks and in our muscles etc, the efficiency of minimal ways is not considered deeply while building the manmade environment. The analysis of close-

packing in minimum energy configuration can give benefits on architecting variety and diversity on forms, saving material and energy and maintaining long-time structures.

Therefore, in this research, the natural structures configurations will be examined in the light of the books of Keith Critchlow "Order in Space", Peter Pearce "Structure in Nature is a Strategy for Design" and Siegfried Gass, Frei Otto and Wolfgang Weidlich, "Experimente = Experiments IL 25" in which the significance of minimal energy structures are highlighted [4, 5, 6]. The natural structures lead to the significance of the three arm node which has three-dimensional behaviour with minimum potential energy.

The nodes are the most important consideration point for space structures. The nodes are mainly solved by rigid components for gaining stability. As this approach limits the form of the structures, the mobility of linkage mechanisms gives possibilities to verify the forms of space structures. Therefore, analyzing the space frames and linkage mechanisms are significant.

The node design has always been the most particular unit for defining the space structures. When triangulation which provides stability, applied to the space frames, the node becomes complex. Therefore, in this research, a Bricard linkage module is proposed for stabilizing the unstable polyhedrons; hexahedron/cube and dodecahedron and maintaining 3 different stabilized volumes by just adding the same module; from tetrahedron, to hexahedron and further dodecahedron.



2. Background

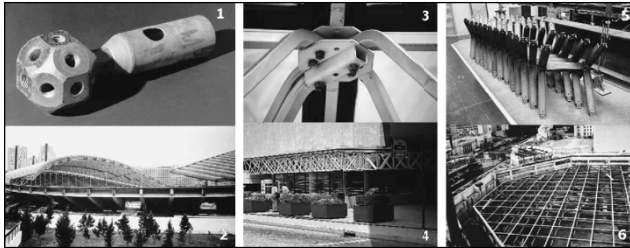


Fig. 1. The nodes that has been applied in several space structures [1]

1-2. Standart Mero KK, used in stadium, Split
 3-4. Typical Moduspan, applied in entrance canopy in Georgia Dome,
 5-6. CUBIC Space Frame modules applied in International Convention Center in Birmingham, UK

The nodal points of the space structures which generate the form by integrating the bars, are the transmitting points of the forces affecting on the structure in three dimension. That is the reason, in the study of space structures, the main focus points of the engineers and architects are mostly the nodal points as the applications of the nodes are shown in Figure 1.

2.1. Importance of Nodal Point

Basically, point is the origin for defining a plane or a solid. Point describes unlimited possibilities of axis for defining line, plane and solid. The economic unfolding of the dimensions of space starts firstly by defining a point in the space. Positioning the second point limits one of the axes spreading from one point and defines a line. Then, by adding the third point on the same axis with the first and second point defines the plane. Lastly, by adding the fourth point on the axis of the other three points, the plane turns into solid, tetrahedron [4]. The tetrahedral shape is a repeating motif in molecules such as in water molecules and methane molecules, as the molecules form in most efficient bonding [7]. This approach as visualized in Fig. 2 shows the importance of nodal points for defining the space through three-dimension in the economic unfolding of the space.

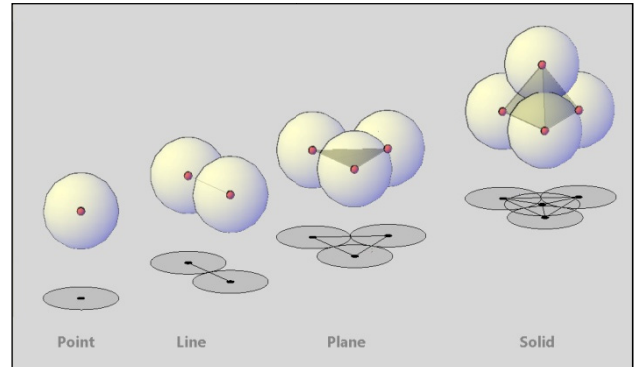


Fig. 2. Presenting the economic unfolding of the dimensions of space regarding to “Order in Space” [4]

The node of a structure determines the area of the plane and further the volume of the space. In space structures, as they enable the architects and engineers new forms and wide diversity and flexibility, the node design gains its significance. The node design is mainly solved by rigid and determined angles [1]. In general, rigidity and no internal mobility are accepted in the components of a structure [8].

However, in natural forms, such as cyclohexane molecule has a capability of changing forms from one rigid phase to another in minimum potential energy configurations [9] (Fig. 3).

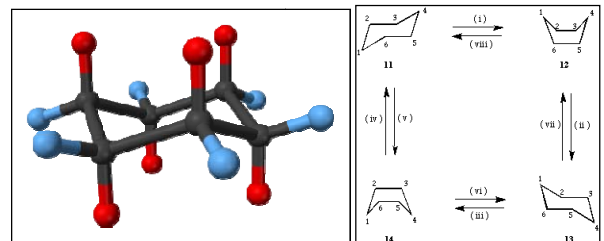


Fig. 3. The formation of cyclohexane molecule
 (<http://tr.wikipedia.org/wiki/Dosya:Cyclohexane-chair-colour-coded-3D-balls.png>, <http://ce.t.soka.ac.jp/stereo/ch4/ch4.materials.html>)

In that case, it is advantageous to analyze the minimum energy configurations in natural forms in the process of designing space structures.

2.2. Minimum Energy Shape

The bubble foam is used for experiments in many disciplines on analyzing the geometric principles for minimal energy configurations. A single soap bubble which floats in space freely is in the form of a sphere. All forms in nature are occurred by the interaction of the forces. That is the reason that the soap bubble configures the sphere as it is the state of minimum potential energy.

2.2.2. Three-arm node

When associate with other equal size bubbles, the more economical configurations occur [5]. When two or three bubble foams get together, the three angles are all equal [10]. The bubbles tend to form triangle as their tendency is to arrange themselves in triangulation for minimum energy shape as triangle is the only stable polygon even with flexible joints [2,3,5,6]. The characteristic feature of all minimal way systems is the three arm node with the constant angle of 120° [6,10] (Fig. 4).

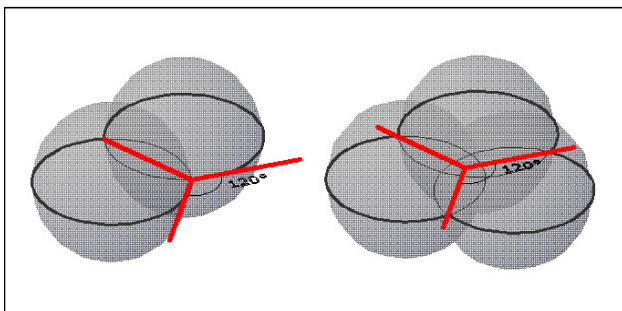


Fig. 4. Two and three bubbles joining with an external angle 120° [3, 6]

The invisible forces which form the three arm node in 120° appear when the bubbles get together. Three-arm node consists of three arms and one nodal/junction point is the main module in the formation of minimum potential energy shape.

After locating three bubbles on a glass surface, the fourth bubble directly locates on top of them forming tetrahedron [2]. Tetrahedron is the simplest and most stable arrangement of spheres in three dimensions, as triangulation is the natural structural behaviour [3, 11]. In nature, even in the early embryo the four cells arrange as tetrahedron which is one of the platonic solids.

2.2.3. Platonic solids

Plato was one of the people who attempted to describe the geometry in natural structures. While analyzing the natural structures, he explored the basic geometric shapes, five regular polyhedrons. These are called Platonic solids, which are the only the three dimensional figure defined by a closed set of same polygon faces, defining a sphere. Briefly, polyhedron is a volume which occurs from plane surfaces in which all vertices are equal. [5].

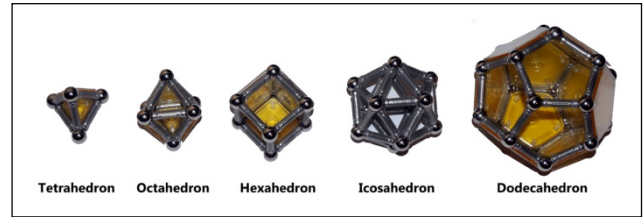


Fig. 5. The platonic solids
*tetrahedron (4 faced) octahedron (8 faced) hexahedron (6 faced),
icosahedron(20 faced) dodecahedron (12 faced)*

As defined before, tetrahedron is the prime solid, which is the first and most economical configuration. After tetrahedron, the next most economic regular grouping of spheres is octahedron which is possible to be seen in the bones of birds [3,10]. In octahedron all spheres touch the other four in triangulated configuration. By adding eight spheres to octahedron, the hexahedron, cube occurs. The cube is the dual of the octahedron. The icosahedron is the third regular grouping of sphere which is in triangulated configuration. By adding spheres, dodecahedron occurs [4] (Fig. 5).

3. Space frames and Structural Mechanism

It is advantageous to study simple, regular, polyhedral shapes for understanding the structural behaviour stability of the space frames, either lattice or plate structures [1]. The formation of the regular polyhedral shapes has always been a research field in mathematics, physics, chemistry, mechanics, architecture and engineering. In this study, platonic solids are chosen because of their minimum energy shape configurations and obtained by the same modules; bars, joints and plates.

3.1. Unstable spherical space frames

In space frames, the bar structures are especially used. The type of the node used for construction qualifies the identity of the structure [1]. However, when these five figures are constructed by bars, the cube and dodecahedron will collapse as not being triangulated at their nodes, differently from the other three (Fig. 6). Triangulation gives strength to the structures even before the physics of materials is taken into account. On the other hand, the complexity of the junction points is one of the merits of triangulated systems [5]. As triangulation gives rigidity to living and nonliving structures, this paper is searching a triangulated system for the nodes for the unstable space frames.

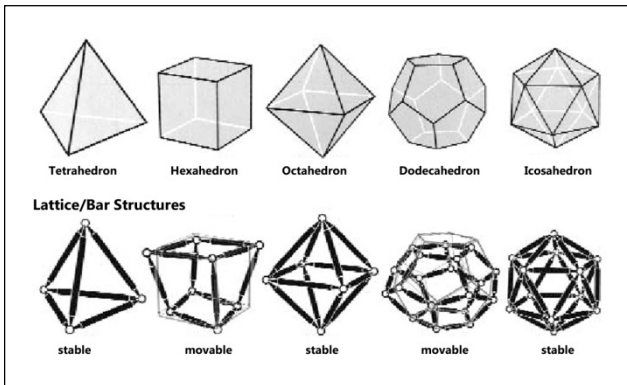


Fig. 6. The lattice structures of platonic solids, *Tetrahedron, octahedron, icosahedron are stable but hexahedron and dodecahedron are unstable, movable.* [1]

As the cube and dodecahedron let more efficient volume to use, this study considers a linkage method for obtaining stability by different triangulation system. In that case, the design of the node becomes more critical in the design process.

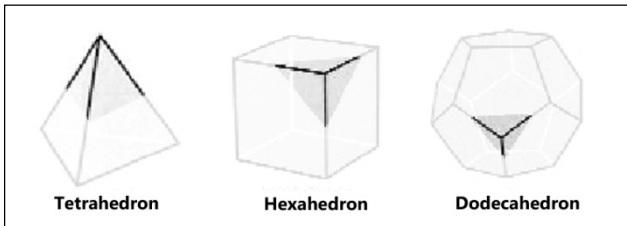


Fig. 7. Three arm nodes in stable tetrahedron and unstable hexahedron and dodecahedron

As seen in figure 7, the forms of tetrahedron, hexahedron and dodecahedron are generated by the three arm nodes. The three-armed node, as described before, is a key issue in economic packing of the structures. Therefore, a module design with multiple parallel axis with right angles give advantages for obtaining three-dimensional structural behaviour in bar structures. The angular relationships, dihedral angles, the angles between the adjacent faces and vertex angles, the angles between the edges are significant while designing the three arm node module.

Polyhedron	vertices, nodal points	edges	faces	dihedral angle	vertex angle
tetrahedron	4	6	4	70.53	60
hexahedron	8	12	6	90	90
dodecahedron	20	30	12	116.57	108

Fig. 8. The angular properties of tetrahedron, hexahedron and dodecahedron

The angular relationship is shown in Figure 9. The angles between blue lines are all 60°, the oranges 90°, and the grey 108°. The red lines refer to the minimum energy configuration that was pointed in Fig. 4. When one of the edges, X1, X2, X3, X4 is fixed as shown in the Fig. 9, the other two legs of the node is changing its angle on the same circular axes. In this perspective, a module which has three dimensional motion from planar to spherical is needed for the node design.

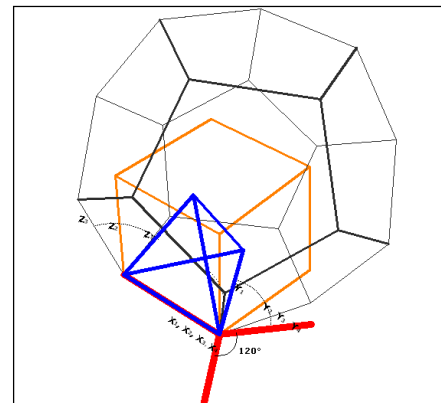


Fig. 9. The angular relationship between tetrahedron, hexahedron and dodecahedron

In the research for stabilizing cube and dodecahedron, a structural mechanism which can deploy from planar to spherical will be the main considering path for achieving the target.

3.2. Structural Mechanism

The structural synthesis of over-constrained mechanisms is a geometrical methodology for generating the dedicated structural design [12]. Over-constrained geometry is mostly chosen in mechanisms which offer a preference for extra stiffness [13]. The structural rigidity is one of the main requirements in space structures. Although, the structures are mostly designed by rigid



connections, alternate structures which are capable of geometrical transformation also exist [8]. These structures are mainly classified as deployable structures. Especially, closed loop linkage mechanisms had its place in literature with its ultra lightweight applications of solar arrays, radar structures by Dr. J.M. Hedgepeth [14].

The closed loop mechanism with 6 Revolute joints, trihedral case of Bricard linkage in which all three axis meet at a point and generating 120o in its planar form is chosen for generating the right angles.

In trihedral case of the Bricard linkage, the full cycle mobility of the chain is achieved [15]. The geometrical configuration of this type of Bricard linkage is

$$a^2_{12} + a^2_{34} + a^2_{56} = a^2_{23} + a^2_{45} + a^2_{61}$$

$$\alpha_{12} = \alpha_{34} = \alpha_{56} = \frac{\pi}{2}, \quad \alpha_{23} = \alpha_{45} = \alpha_{61} = \frac{3\pi}{2}$$

$Ri=0$ for all i

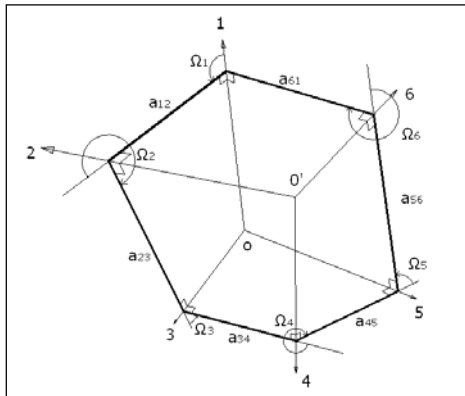


Fig. 10. The trihedral case of Bricard Linkage

In platonic solids as all the edges are equal, this geometrical configuration can easily be applied as using the same distances between the rotational axes,

$$a_{12} = a_{34} = a_{56} = a_{23} = a_{45} = a_{61} = a$$

$$\alpha_{12} = \alpha_{34} = \alpha_{56} = \frac{\pi}{2}, \quad \alpha_{23} = \alpha_{45} = \alpha_{61} = \frac{3\pi}{2}$$

$Ri=0$ for all i

In this form of the trihedral Bricard linkage, the closed loop can be continuously turned through its centre [13]. For determination of the lengths of the faces and their relations among joint angles, the following equations are applied [15].

$$s\Omega_1(a_{61} + a_{12}c\Omega_1) = s\Omega_1(a_{34} + a_{23}c\Omega_1)$$

$$s\Omega_4(a_{12} + a_{23}c\Omega_2) = s\Omega_2(a_{45} + a_{34}c\Omega_2)$$

$$s\Omega_5(a_{23} + a_{34}c\Omega_3) = s\Omega_3(a_{56} + a_{45}c\Omega_3)$$

$$s\Omega_6(a_{34} + a_{45}c\Omega_4) = s\Omega_4(a_{61} + a_{56}c\Omega_4)$$

$$s\Omega_5 s\Omega_6 = s\Omega_2 s\Omega_3$$

The number of independent parameters which are gained from the particular positioned of the structure can be defined as the mobility of a mechanism [8]. From these independent equations, as the lengths are all equal, we can determine that all the angles that meet in one point are all equal.

$$\Omega_1 = \Omega_3 = \Omega_5$$

$$\Omega_2 = \Omega_4 = \Omega_6$$

In the planar case, this structural mechanism form in triangle, and the three rotation axes form 120o. That means the desired three dimensional behaviour of the three arm node can be achieved as all the angles change dependently to each other.

4. Application

The design process of the joints and the structural components need appropriate considerations for gaining performance of the structure in order to provide flexibility and interchangeability of spaces that extends the lifecycle of built structure [16]. In that case, considering a three-dimensional module give more benefits than approaching partially for designing the space.

Therefore, an object which has capabilities of portability, reusability, easy to construct, minimizing the cost and material usage and reducing application time is passing through designing a three-dimensional module which can be used as joint in many space frames.

4.1. Proposed Bricard Linkage Module

In trihedral case of the Bricard Linkage, three rotation axes meet in one point at a constant angle 120o as shown in Fig. 11. However, for obtaining three arm node, the design of the structural mechanism should be modified.

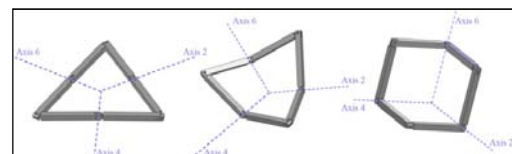


Fig. 11. The formation of trihedral case of Bricard Linkage from planar 120° to 3D



The design of the linkages can be obtained by taking the axes into consideration. Each rod has two joint axes which are perpendicular to each other. At the axes which intersect at one point, a leg is fixed to the rod to obtain three arm node module.

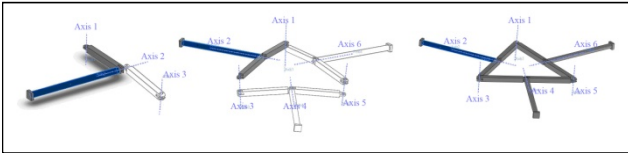


Fig. 12. The linkage designs in the process of making the three arm node.

The mobility of the mechanism enables to obtain the angular relationships that the three armed platonic solids have, regarding to the independent parameters that trihedral Bricard linkage has.

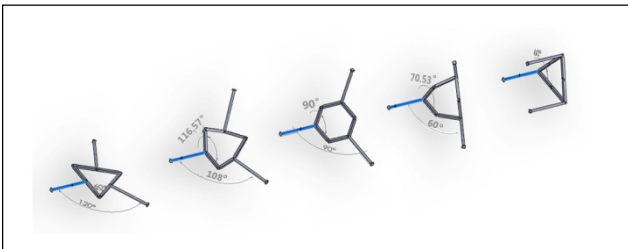


Fig. 13. The dihedral and vertex angles of tetrahedron, hexahedron and dodecahedron.

4.2. Case Studies

The main consideration of this research was to obtain a single module which provides diversity in space structures. By analyzing deeply the structural behaviour of the three arm nodes, obtaining stable cube form without triangulation in between the bar structures is also possible. The three arm node module gives more opportunities than it was expected.

4.2.1. Tetrahedron



Fig. 14. The formation of tetrahedron by using four three arm node modules

When three of the module added in the form of triangle, the third arms of the Bricard linkages enables the fourth module easy to construct. In this case, even if triangle and tetrahedron are stable even with flexible joints, the structural mechanism loses its mobility and gain stability.

4.2.2. Hexahedron (cube)

When four of the module added in the form of a square the structure directly gains stability. In this case, it is possible to say that this Bricard linkage module discarded the needs for triangulating the bar structures.

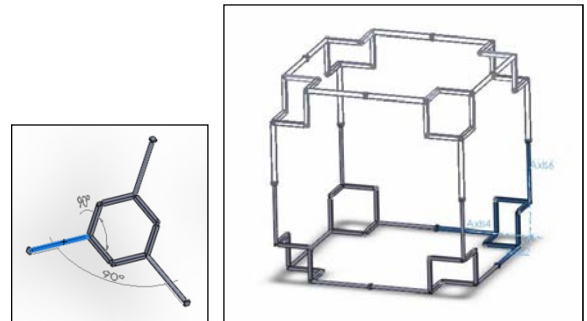


Fig. 15. The formation of stable hexahedron by using eight three arm node modules.

4.2.3. Dodecahedron

When five of the module added in the form of a pentagon the structure gains stability. By adding the left modules, the stable spherical space is obtained with huge openings with no need of triangulation.

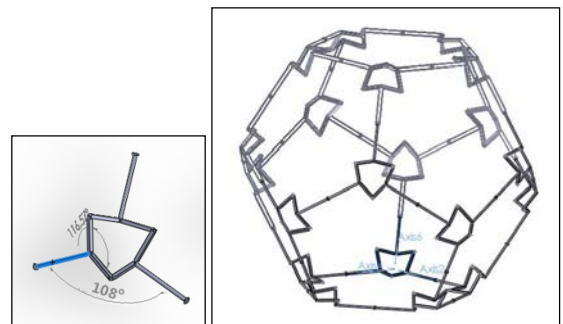


Fig. 16. The formation of stable dodecahedron by using four twenty arm node modules.

This structural difference also provides variety in volumes of the spaces.

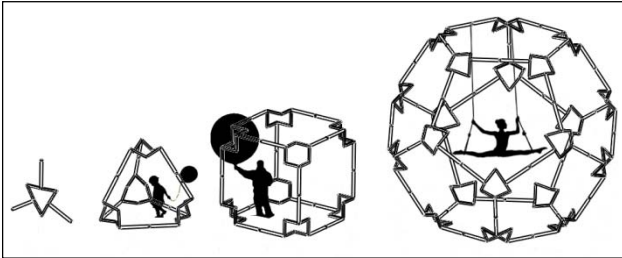


Fig. 17. The variety of spaces defined by the same three arm node module

4.3. Future Works

This study shows the significance of analyzing the structural behaviour in three dimensions give benefits for variety of forms and stationary. The Archimedean solids are the further research field for different node analysis, with other over-constrained mechanisms. The other types of Bricard linkages have potential for deep analysis on space filling and obtaining multiform. The modular foldable covering plates or membranes are the further research fields in the demand of designing the whole concept for space frames. However, the stability which is gained by this over-constrained mechanism needs calculations to understand if it is efficiency to use in applications.

5. Conclusion

“One could almost redefine biology as the natural history of deployable structures. An organism is successful partly because it uses minimum amount of material to make its structure and partly because it can then optimize its use of that material so that it can influence as much of its local environment as possible.”

The three dimensional behaviour of the structures and the minimum way of close-packing property in natural structures is a treasure to focus on maintaining space structures. The clues from nature provide richness and efficiency in the design process. The three arm node obtained by the minimum energy configuration from natural structures is modified into Bricard linkage mechanism for a modular node design. This module enables variable forms for space structures and also maintains stability for the unstable hexahedron and dodecahedron by triangulating ability of the node. This study shows the huge possibilities of space structures by analyzing the three dimensional behaviour

of structural mechanisms.

Acknowledgements

I am grateful to Prof. Dr. Rasim Alizade, Aylin Gazi and Erkin Gezgin for their great motivations by heart and supports with their knowledge and Dr. Koray Korkmaz who always gives a wide freedom for choosing the research field that I wanted to focus on and Erman Aytaç who always supported me technically.

References

- [1] John Chilton, *Space Grid Structures*, Architectural Press, Oxford, 2000
- [2] Edgar Stach, *Form-Optimizing Processes in Biological Structures. Self-generating structures in nature based on pneumatics*, Textile Composites and Inflatable Structures, 2005
- [3] Graham Scarr, *Simple geometry in complex organisms*, Journal of Bodywork & Movement Therapies, 2009
- [4] Keith Critchlow, *Order in Space*, Thames&Hudson Inc., New York, 1969
- [5] Peter Pearce, *Structure in Nature is a Strategy for Design*, Synestructics Inc. Chatsworth, California, 1978
- [6] Siegfried Gass, Frei Otto and Wolfgang Weidlich, *Experimente = Experiments IL 25*, University of Stuttgart Press, 1990
- [7] Campbell, Reece, *Biology*, Pearson International Edition, Eight Edition, 2008
- [8] Zhong You, *Motion Structures extend their reach*, Materials Today, December 2010
- [9] J. Eddie Baker, *Limiting Positions of a Bricard Linkage and Their Possible Relevance to the Cyclohexane Molecule*, Mechanism and Machine Theory Vol. 21, 1985
- [10] D'Arcy Thompson, *On Growth and Form*, Cambridge University Press, UK, 1961
- [11] Richard Buckminster Fuller, *Synergetics, Explorations in the Geometry of Thinking*, 1975
- [12] Rasim Alizade, Ozgun Selvi, Erkin Gezgin, *Structural design of parallel manipulators with general constraint one*, Mechanism and Machine Theory 45, 2010
- [13] Yan Chen, *Design of Structural Mechanisms*, A dissertation submitted for the degree of Doctor of Philosophy in the Department of Engineering Science at the University of Oxford, 2003
- [14] W. W. Gan, S. Pellegrino, *Closed-Loop Deployable Structures*, 44th AIAA/ASME/ASCE/AHS/ASC Structures, Structural Dynamics, and Material Conference, 2003
- [15] J. Eddie Baker, *An Analysis of the Bricard Linkages*, Mechanism and Machine Theory Vol. 15, 1980
- [16] Dr Sergio Altomonte, and Dr Mark B Luther, *A Roadmap to Renewable Adaptive Recyclable Environment (R. A. R. E.) Architecture PLEA2006 - The 23rd Conference on Passive and Low Energy Architecture*, Geneva, Switzerland, 2006
- [17] Julian F.V. Vincent, *Deployable Structures in Nature*, Deployable Structures, CSIM Courses and Lectures, 2001

Obtaining New Linkages From Jitterbug-Like Polyhedral Linkages

Gökhan KİPER^{1*}, Eres SÖYLEMEZ¹

^{1*}Mechanical Engineering Department, Middle East Technical University, 06531, Ankara, Turkey
kiper@metu.edu.tr

Abstract

Jitterbug-like linkages are polyhedral linkages with single link for each face and edge. They comprise revolute joints only. When proper geometric conditions are satisfied, more links can be added to these assemblies without any change in the motion of original links. Cardan motion is used in making these additions. Then, further new linkages can be obtained by removing certain links/joints.

Keywords: Polyhedral Linkages, Jitterbug, Cardan Motion

1. Introduction

The *Jitterbug* is discovered and entitled by R. Buckminster Fuller. As described by Fuller, it consists of 24 struts which constitute 8 triangles able to move with respect to each other [1]. The connections are such that the assembly goes through a single degree-of-freedom (dof) transformation. Originally introduced as a conceptual system, the motion of the Jitterbug described in Fig. 460.08 of [1] was brought to life as a mobile sculpture in a research exhibition in Zürich and became to known as the *Heureka Octahedron* [2].

The Heureka Octahedron comprises 8 ternary, 12 binary links and 24 revolute joints. Although such an assembly generally has $6(20 - 24 - 1) + 24 = -6$ dofs, this assembly is mobile with single dof. The 3 revolute joint axes of a ternary link are parallel and equidistant while the 2 joint axes of a binary link are intersecting. When the linkage is in its most compact form, it resembles a regular octahedron and during the motion the centers of the triangular links remain on the three-fold symmetry axes of a regular octahedron (Fig. 1). At any configuration, the planes of the triangular faces bound an octahedral region, hence as the linkage expands/contracts, a dilation of an octahedron is realized. The binary links are used to preserve the dihedral angle along the edges of the bounded octahedron.

Although became famous in the Zürich expo in 1991, use of dihedral angle preserving (dap) links was proposed by Verheyen in 1989 [3]. In [3], Verheyen explores many Jitterbug-like linkages, which he calls as dipolygonids.

Dipolygonids consist of equilateral polygonal links sliding along and rotating about fixed axes in space, just like the Jitterbug. These axes all intersect at a common point.

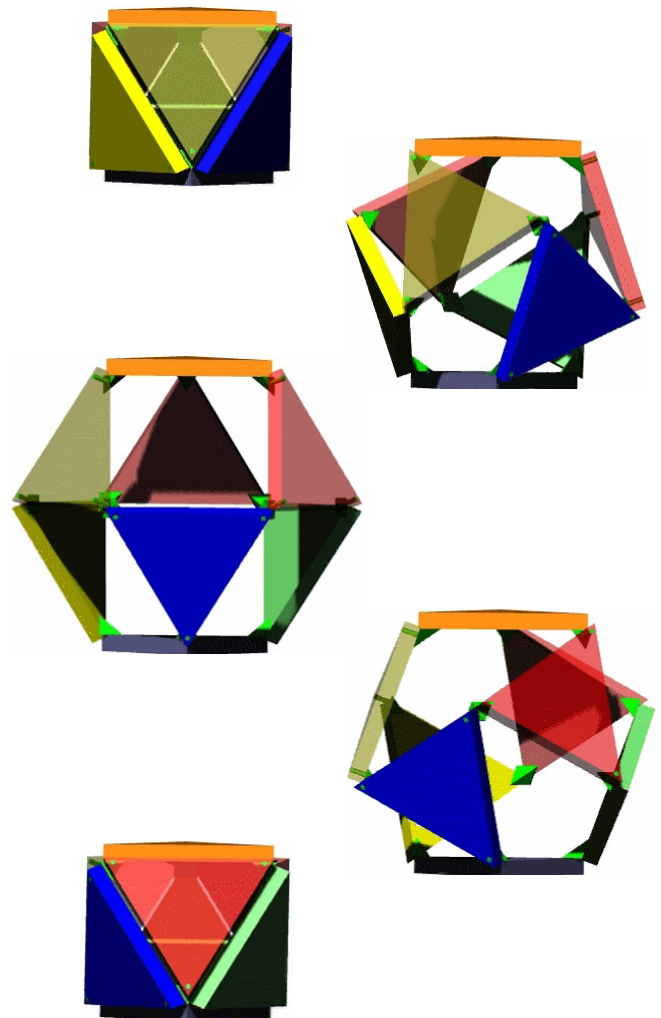


Fig. 1: The Jitterbug motion



Next attempt to generalize these linkages was by Röschel, who coupled Darboux motions to synthesize not necessarily regular Jitterbug-like assemblies [4-7].

More recently, a definition for Jitterbug-like linkages is given by Kiper [8], for which it is shown that the polygonal links have Schönflies motion. This study makes use of this definition and shows that Jitterbug-like linkages may further be constrained with addition of several links and joints without changing the original motion. Cardan motion plays the key role in this procedure (See ex. [9] for the details of the Cardan motion). Then some more new linkages are obtained by removal of certain links and joints.

The organization of the paper is as follows: Next section is devoted to the introduction of Jitterbug-like linkages. Section 3 issues the Cardan motion of the polygonal links. In Section 4, linkages with additional links are presented. In Section 5 are some new linkages obtained by removing some link groups. Last section is for conclusions.

2. Jitterbug-Like Linkages

First of all, Jitterbug-like linkages are a special class of polyhedral linkages. Roughly speaking, a polyhedral linkage is a spatial linkage which resembles a polyhedral shape at any configuration. They may be used for transformation between different polyhedral shapes as studied by Bricard [10], Bennett [11] and Goldberg [12]. In this type of polyhedral linkages, the revolute joint axes are along edges of polyhedra and polyhedral faces are invariant. Alternatively, there are angle preserving polyhedral linkages for which dihedral and planar angles are invariant throughout the motion. Jitterbug-like linkages are of the latter type.

In Jitterbug-like linkages, there are two type of links: polygonal links and dap links. All joints are revolute type. All the joint axes of a polygonal link are parallel to each other while the two joint axes of a dap link should intersect. No polygonal link is directly connected to another one as this is also true for dap links. The joint intersections of the dap links around a polygonal link should be coplanar. The intersection points define a plane for each polygonal link and all such planes should bound a finite volume. That finite volume with planar boundaries defines a supporting polyhedron at every instant of the motion of the linkage. If the assembly is mobile with single dof, planes/lines associated with the supporting polyhedra map to parallel planes/lines, i.e. the transformation is conformal.

How much the Jitterbug-like linkage represents its supporting polyhedra depends on the type of transformation that the supporting polyhedron goes through. It is easier to visualize the transformation when it

is a dilative one, i.e. all the supporting polyhedra at all instances are similar to each other. On the other hand, when the planar boundaries move at different rates, the variation of the edge lengths is hard to follow. An example is given by both Verheyen [3] and Röschel [5] as a linkage comprising 6 square and 8 equilateral triangular links (Fig. 2). In this linkage, the triangular and square links translate at different rates, hence the side length ratios of the hexagons on which the triangular links sit vary as the assembly expands/contracts.

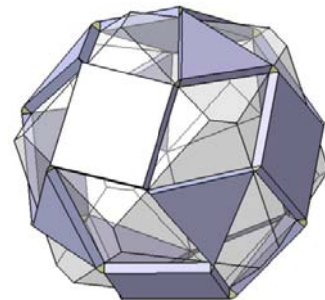


Fig. 2: Dipolygonid $8\{3\} + 6\{4\}|54^\circ44'08''$

Even if the transformation of the supporting polyhedron is a dilative one, some edges may not be represented by any part of the linkage. An example is given as an irregular tetrahedron by Röschel [6] (Fig. 3). In this linkage, two sides of the pentagons are left open since there are just triangles on these faces.

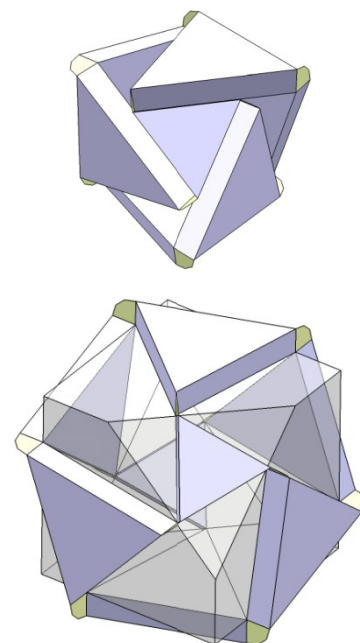


Fig. 3: An irregular octahedral linkage – in compact form and intermediate form with its supporting polyhedron

Whether the transformation is a dilative one or some less special conformal transformation depends on the geometry of the supporting polyhedron. For example, if a supporting polyhedron has an inscribing sphere, it is a sufficient condition for the associated linkage to result in a dilative transformation. This case was investigated by Röschel in [6] and Wolhart in [13]. Which geometries result in which cases is not discussed in this study.

A much more special case can be obtained when there is a one-to-one correspondence between the faces, edges, and vertices of the supporting polyhedra and polygonal links, dap links and spatial loops of the linkage. To formulate this, let E, F, V, n_i denote the number of edges, faces, vertices and valency of i^{th} vertex ($i = 1, \dots, V$) for a polyhedral shape P . Then the corresponding linkage has E many binary (dap) links, F many polygonal links and V many loops comprising $2n_i$ revolute joints. Some properties of such linkages were extracted in [8] as:

- i. The valencies of vertices of a polyhedral shape to be dilated should be even.
- ii. Polyhedral geometries that obey Euler's formula contain at least one 8R (revolute) loop.
- iii. The spherical indicatrix (See [14]) of a spatial loop is immobile and the dimensions of the spherical indicatrix of a loop around a vertex are uniquely given by the dihedral angles associated with the edges and planar angles of the faces meeting at this vertex. The immobility of the spherical indicatrix demands that the polygonal links go through a Schoenflies motion and the dap links are in pure translation.
- iv. If a $2nR$ loop is constrained such that the spherical indicatrix is immobile, the loop is in general overconstrained.
- v. The assembly of spherical indicatrices associated with the vertex figures results in a spherical polyhedron, which is a spherical projection of the supporting polyhedron.

How such assemblies are constructed is not the subject of this study. In the following sections the linkages are assumed to be given and modifications are performed on them.

3. The Cardan Motion Associated with the Polygonal Links

Consider a spatial loop around a vertex according to the definition in §2, like the one in Fig. 4. The corners of a side AB of a polygonal link will be constrained to move on two adjacent edges. Since $\angle VAB$ remains constant during the motion of a Jitterbug-like linkage, the motion of the segment AB on the associated face is equivalent to the coupler link of a double slide mechanism (Fig. 5). The

motion of the coupler link with respect to the fixed frame in Fig. 5 is a Cardan motion, hence a coupler point, in general, traces an ellipse (See ex. [15]). In Cardan motion, the moving and fixed centrodes are circles and the fixed centrode radius is twice as the moving centrode radius. The trajectories of the points on the moving centrode degenerate into straight lines, so Cardan motion is widely used for exact straight line motion generation.

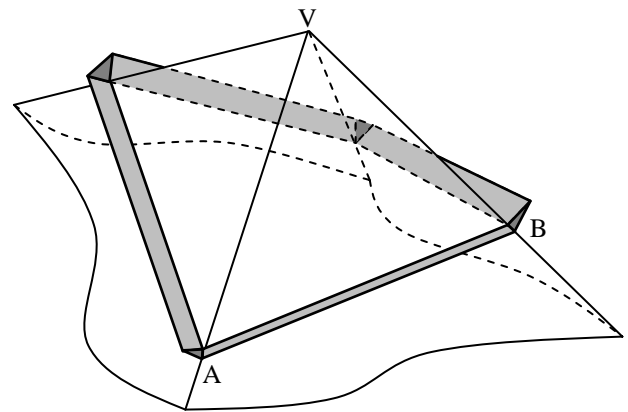


Fig. 4: An 8R loop around a 4-valent vertex

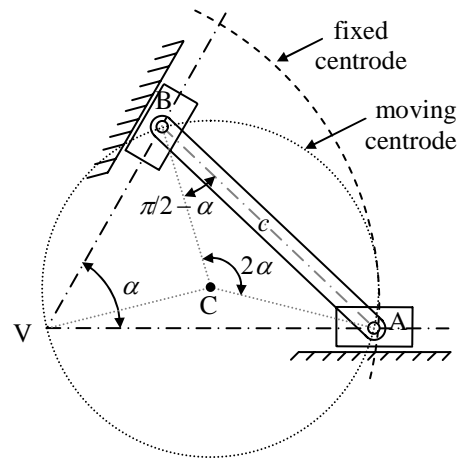


Fig. 5: A double slide mechanism

There is a special point C on the moving plane, the center of the moving centrode, the trajectory of which is a circle. Given the planar angle α and the length $c = |AB|$, this point is located easily. Since points A and B have straight line trajectories, they are on the moving centrode. Also the center of the fixed centrode (point V in Fig. 4) is on the moving centrode at all times, so the moving centrode is uniquely given by points V, A and B . Then by inscribed angle theorem $\angle BCA = 2\alpha$ and hence $|CA| = |CB| = c/2\sin\alpha$. This uniquely locates point C .

How is this information useful for the Jitterbug-like linkages? If for every side AB, a link VC is attached at the proper point C, then all such attached links around a vertex can be connected to a common link without disturbing the original motion. In the next section, examples of such linkages are presented.

4. Attaching Links to Jitterbug-Like Linkages - Examples

The first example shall be the Jitterbug. By addition of the extra joints to the triangular links, the polygonal links of the jitterbug become regular hexagons. Some snapshots of the obtained mechanism is given in Fig. 6.

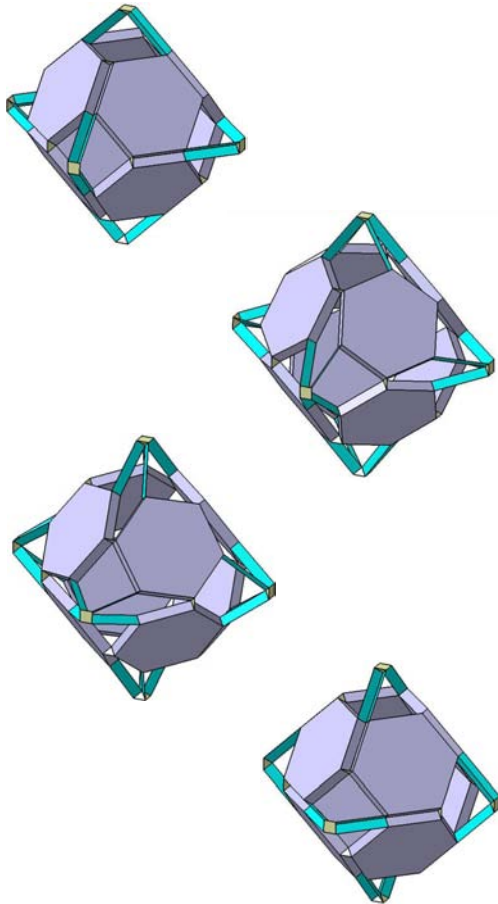


Fig. 6: The Jitterbug with extra links

Remember that the supporting polyhedron of the jitterbug is a regular octahedron. In the following two examples, the supporting polyhedra are the regular tetrahedron and the cube (Figs. 7-8). Note that for the tetrahedron and the cube the vertex valencies are 3, so they cannot directly be used as supporting polyhedra for a Jitterbug-like linkage. The trick is considering a double

tetrahedron/cube instead of a single one and double the number of faces, edges and vertices (See [Kiper1]).

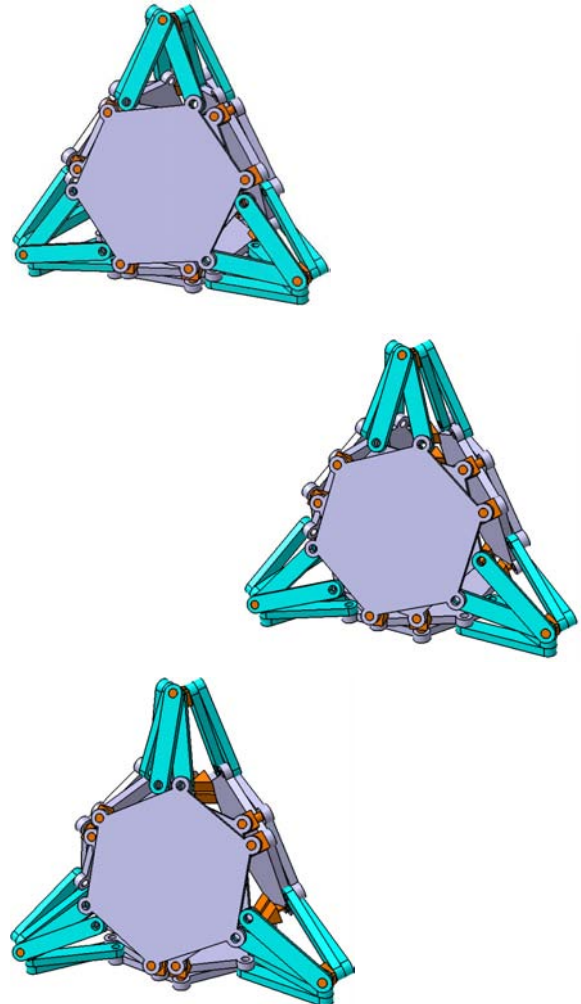


Fig. 7: Tetrahedral dipolygonid with extra links

Similarly, links can be added to the remaining two Platonic solids, i.e. the dodecahedron and the icosahedron (See, ex. [16] for classification of polyhedra). Among the polyhedra with regular faces, the non-Platonic deltahedra (triangular dipyramid, pentagonal dipyramid, snub disphenoid, triaugmented triangular prism and gyroelongated square dipyramid) can also be used as supporting polyhedra. However, Archimedean solids are not suitable for the purpose; an example is already presented in Fig. 2.

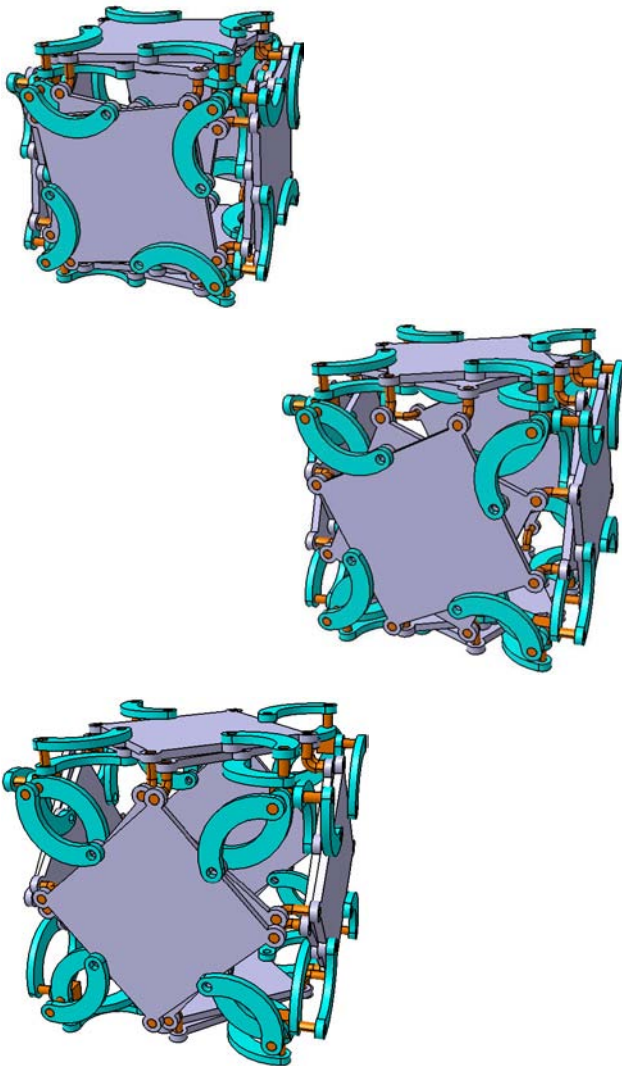


Fig. 8: Cubic dipolygonid with extra links

The Archimedean duals, i.e. Catalan solids have an insphere, so they can be used here. As an example, the linkage obtained from a tetrakis hexahedron is given in Fig. 9. The tetrakis hexahedron is the only Catalan solid all vertices of which are of even valency, so the double polyhedra of remaining 12 should be used to obtain a linkage - just like the tetrahedron and the cube.

The examples given in Figs. 6-8 turn out to be some special cases of linkages presented in [17], where some polygonal linkages are introduced and used in the faces of polyhedral linkages. The cubic linkage in Fig. 8 is also the subject of [18]. What is not in [17] are issued in the next section.

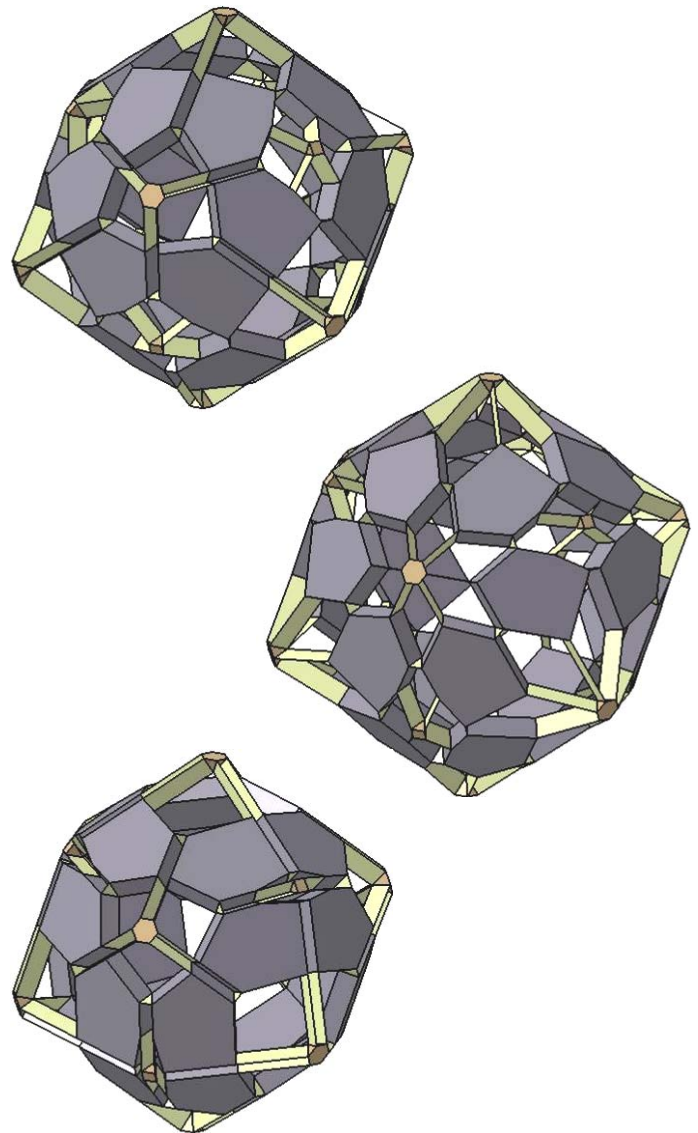


Fig. 9: Linkage obtained from a Tetrakis hexahedron

5. Obtaining New Linkages by Removing Some Links and Joints

Again the first example comes out of the Jitterbug. Moving out two hexagonal links and the twelve binary links connected to these two polygonal links of the linkage in Fig. 6, the linkage in Fig. 10 is obtained. The supporting polyhedron of this linkage is a hexahedron with equilateral rhombic faces.

Another linkage can be obtained by keeping 4 adjacent hexagonal links meeting at a vertex and deleting the remaining four (Fig. 11). In this case, a pyramidal cap like geometry is obtained: the planes of the polygonal links do not bound a finite volume.

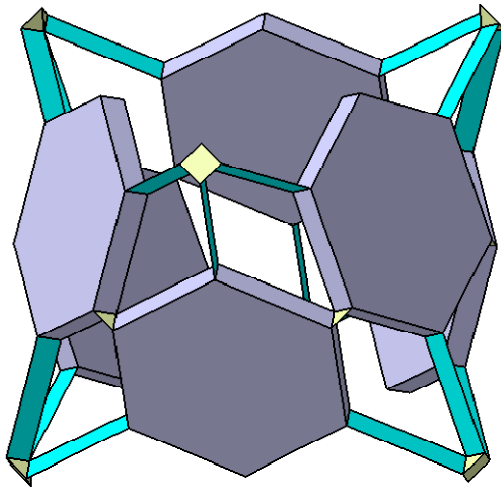


Fig. 10

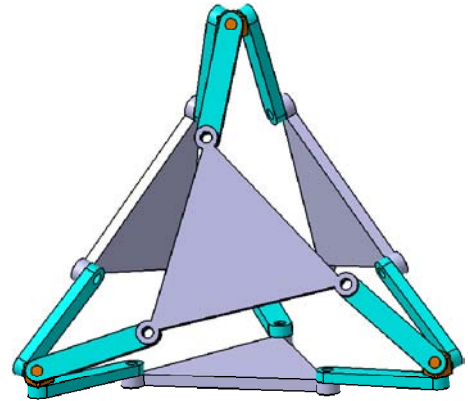


Fig. 12

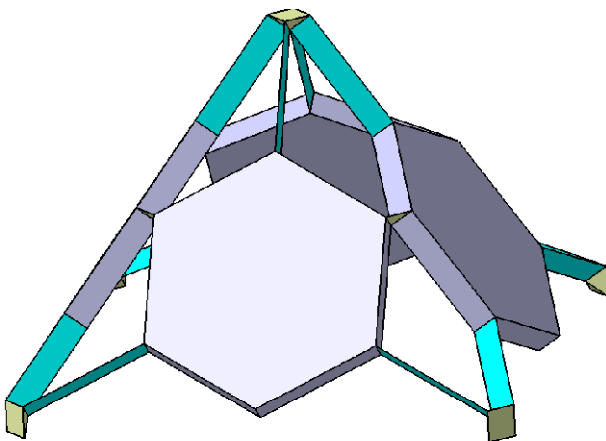


Fig.11

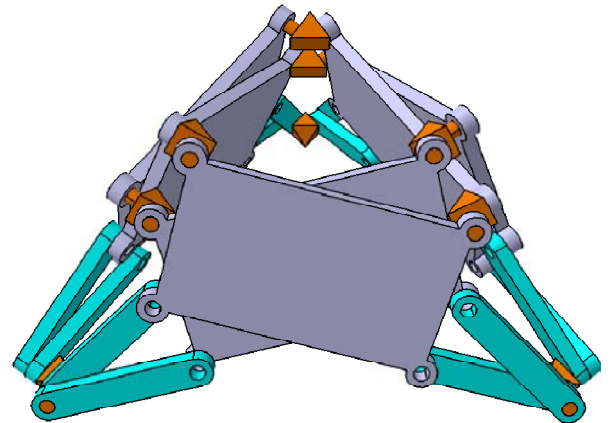


Fig. 13

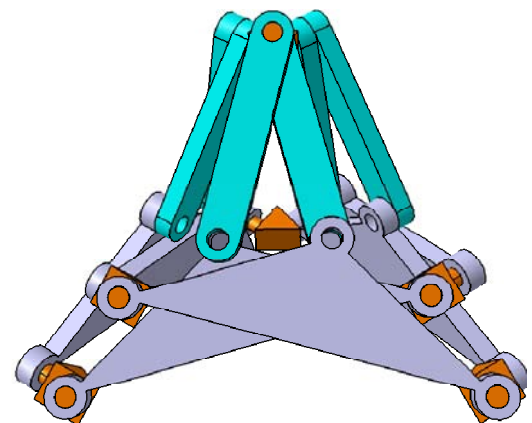


Fig. 14

Next, consider the tetrahedral linkage of Fig. 7. Deleting one of the polygonal links on each face one obtains the linkage in Fig. 12. Note that there is no dup link in this linkage. This type of linkages was synthesized by Wohlhart [19].

Alternatively one can remove a pair of polygonal links of a face. Furthermore, the binary links opposite to the removed polygonal links may be removed. The resulting linkage has still single dof (Fig. 13).

As another alternative, the three vertices of the tetrahedron may be chopped off to get a pyramid cap like in Fig. 14.

Similar linkages can be obtained from other linkages. When the links to be removed are chosen properly, the new linkage still possesses the single dof, basically because the remaining links are still constrained to move exactly as in the original linkage.



6. Conclusions

In this study, a method is presented to obtain polyhedral linkages by addition of links to Jitterbug-like linkages using Cardan motion. The obtained linkages better represent their supporting polyhedra visually than the associated Jitterbug-like linkages.

By removal of proper link groups new linkages are obtained. The new linkages have single dof thanks to the overconstrainedness of the original linkages.

This “First (further) overconstrain a linkage and the remove some links/joints to obtain new linkages” is a quite handy trick in obtaining new linkages. This idea is used for example in synthesizing planar six bar linkages with translator coupler link [20]. The idea can be used whenever it is possible to add links to a linkage without disturbing the motion of the remaining links.

Acknowledgments

The first author acknowledges the financial support of The Scientific and Technological Research Council of Turkey (TÜBİTAK) during this study.

References

- [1]. R.B. Fuller, *Synergetics*. Macmillan; New York, 1979, Section 460.
- [2]. H. Stachel, *The Heureka Polyhedron*. In: G., Fejes Tóth (ed.): *Intuitive Geometry*, Coll. Math. Soc. J. Bolyai 63. North-Holland, pages 447-459, 1994.
- [3]. H.F. Verheyen, *The Complete Set of Jitterbug Transformers and the Analysis of Their Motion*, Int. J. Comput. Math. Appl. 17, pages 203-250, 1989.
- [4]. O. Röschel, *Linked Darboux Motions*, Math. Pannonica 7, pages 291-301, 1996.
- [5]. O. Röschel, *Zwangläufig Bewegliche Polyedermodelle I*. Math. Pannonica 6, pages 267-284, 1995.
- [6]. O. Röschel, *Zwangläufig Bewegliche Polyedermodelle II*. Studia Sci. Math. Hung. 32, pages 383-393, 1996.
- [7]. O. Röschel, *Zwangläufig Bewegliche Polyedermodelle III*. Math. Pannonica 12, pages 55-68, 2001.
- [8]. G. Kiper, *Some Properties of Jitterbug-Like Linkages*, to be published.
- [9]. O. Bottema & B. Roth, *Theoretical Kinematics*. North-Holland; New York, pages 346-349, 1979.
- [10]. R. Bricard, *Mémoire sur la théorie de l'octaèdre articulé*. J. Math. Pures Appl. 3, pages 113-150, 1897.
- [11]. G.T. Bennett, *Deformable Octahedra*. Proc. Lond. Math. Soc. 2, pages 309-343, 1911.
- [12]. M. Goldberg, *Polyhedral Linkages*. Nat. Math. Mag. 16, pages 323-332, 1942.
- [13]. K. Wohlhart, *The Kinematics of Röschel Polyhedra*, In: J. Lenarcic & M. Husty (ed.): *Advances in Robot Kinematics: Analysis and Control*, Kluwer Acad. Pub.; Netherlands, pages 447-459, 1998.
- [14]. K. H. Hunt, *Kinematic Geometry of Mechanisms*. Clarendon Press, page 287, 1978.
- [15]. E.A. Dijkman, *Motion Geometry of Mechanisms*. Cambridge University Press, pages 16-18, 1976.
- [16]. P.R. Cromwell, *Polyhedra*, Cambridge University Press; Cambridge, 1997.
- [17]. G. Kiper, E. Söylemez & A.U.Ö. Kişisel, *A Family of Deployable Polygons and Polyhedra*, Mech. Mach. Theory 43, pages 627-640, 2008.
- [18]. X.Z. Wei, Y.A. Yao, Y.B. Tian & R. Fang, *A New Method of Creating Expandable Structure for Spatial Objects*, Proc. Inst. Mech. Eng. C Mech. Eng. Sci. 220, pages 1813-1818, 2006.
- [19]. K. Wohlhart, *Regular Polyhedral Linkages*. Proc. 2nd Workshop on Computational Kinematics, Bucharest, Rumania, pages 239-248, 2001.
- [20]. E. Söylemez, *Four-Bar and Slider-Crank Cognates Roberts Chebychev Theorem*. In: *Mechanisms*. Middle East Technical University Press; Ankara, Section 4.5, 2009.



Proceedings of the International Symposium of Mechanism and Machine Science, 2010
AzCIFTtoMM – Izmir Institute of Technology
5-8 October 2010, Izmir, TURKEY



Session 2:

Control Systems (Cs) Mechanisms of Flying and Space Machinery (MfSm)



Proceedings of the International Symposium of Mechanism and Machine Science, 2010
AzCIFTtoMM – Izmir Institute of Technology
5-8 October 2010, Izmir, TURKEY



Structure of a Complex Diagnosis System for Aviation Engines

Arif M. PASHAYEV^{1*}, Ramiz A. SADIQOV¹, Parviz Sh. ABDULLAYEV¹, Ajdar H.SADIQOV¹,
 Azer J. MIRZOYEV¹

^{1*}Azerbaijan National Academy of Aviation
 AZ1045, Azerbaijan, Baku, Bina, 25th km
 Phone: (994 12) 4972829; Fax: (994 12) 497-28-29
 Email: a_parviz@azeronline.com

Abstract

In this paper, demonstrated the efficiency of Soft Computing technology combined with the fuzzy logic and neural network methods. Specifically, we diagnose the technical condition over time of an aviation Gas Turbine Engine (GTE) when the flight information is fuzzy, limited and uncertain. Multiple fuzzy linear and non-linear models are trained with high accuracy, using fuzzy regression equations on fuzzy statistical data. Further, we propose additional models of GTE technical condition that analyse the dynamics of the skewness and kurtosis coefficients. Research into the changes in skewness and kurtosis coefficients suggests that the distributions of the GTE work parameters are fuzzy. Hence, we conclude that fuzzy skewness and kurtosis coefficients should be taken into account. Investigating the dynamics of GTE work parameters allows us to use Fuzzy Statistical Analysis for preliminary assessments of an engine's technical condition. For a more comprehensive overview of GTE technical condition diagnosis, we also explore Fuzzy Thermodynamic Models in this paper. We use the outlet gas temperature of the gas turbine (turbine exhaust gas temperature or EGT) expediency as the output parameter of our model. Semi-empirical models are also used, in an effort to address the limitations associated with controllable parameters.

Keywords:

Nomenclature

H	=	flight altitude [m]
M	=	Mach number
T_H^*	=	atmosphere temperature [°C]
p_H	=	atmosphere pressure [Pa]
n_{LP}	=	low pressure compressor speed (rotate per minute - RPM) [%]
T_4^*	=	exhaust gas temperature [°C]
G_T	=	fuel flow [kg/h]
p_T	=	fuel pressure [kg/cm ²]
p_M	=	oil pressure [kg/cm ²]
T_M	=	oil temperature [°C]
V_{BS}	=	back support vibration [mm/s]
V_{FS}	=	forward support vibration [mm/s]

a_1, a_2, a_3, \dots	regression coefficients in the initial linear multiple regression equation of the GTE condition model
a_1', a_2', a_3', \dots	regression coefficients in the actual linear multiple regression equation of the GTE condition model
$\tilde{a}_1, \tilde{a}_2, \tilde{a}_3, \dots$	fuzzy regression coefficients in the linear multiple regression equation of the GTE condition model
\tilde{X}, \tilde{Y}	measured fuzzy input and output parameters of the GTE condition model
$r_{X,Y}$	correlation coefficients between the GTE work parameters
$\tilde{r}_{X,Y}$	fuzzy correlation coefficients between the GTE work parameters
\otimes	fuzzy multiplier
$\tilde{+}$	fuzzy summation of results that are output by various methods
ini	initial
act	actual
cor	corrected

1. Introduction

One of the important requirements for conditional maintenance of the modern aviation gas turbine engine (GTE) is the availability and proper operation of an efficient parametric technical diagnostics system. The difficulty of GTE diagnosis for certain aircraft models lies



primarily in the fact that the onboard objective control systems may fail to register all engine work parameters. This circumstance requires the additional manual registration of other GTE work parameters. Consequently, it is necessary to create a diagnostic system that can monitor GTE conditions and thereby output a precise recommendation regarding further GTE maintenance procedures, using data recorded either manually or from onboard systems.

Today, airlines around the world operate with a variety of automatic diagnostic systems (ADS) that monitor the technical condition of the GTE [1-10]. The ADS outputs flexible ranges for the recorded parameters. It takes into account the engine operating time and compares it with other parameters, through point or interval estimations.

We feel that statistical data processing using the aforementioned method generally assumes that the recorded parameters follow normal distributions, impacting the reliability of the GTE technical condition monitoring process. It may also lead to can cause errors in GTE diagnosis and operation. [1-13]. In addition, sometimes identical combinations of changes in various GTE work parameters can be caused by different malfunctions. Finally, this method complicates the definition of the defect address.

Other aviation GTE diagnosis methods are not universal and are applied, as a rule, only to concrete cases [1-10]. Research has shown that with accessible computing power it is possible to create a complex GTE diagnosing system based on a combination of methods. The kernel unit in the complex analysis system may operate on the basis of fuzzy logic. The development of modern information technologies facilitates the creation of an effective GTE condition monitoring system.

Our condition monitoring system is grounded in comprehensive analysis (CA) of GTE thermo-gas-dynamic and mechanical parameters, and incorporates the methods shown in Fig. 1 (see Appendix):

- M0 - GTE Condition Monitoring Technique (CMT), using Non-Destructive Testing Methods, oil analysis, etc.,
- M1 - GTE CMT using Mathematical Models,
- M2 - GTE CMT using Classical Statistics methods,
- M3 - GTE CMT using Kalman type filters,
- M4 - GTE CMT using Fourier and Wavelet analyses,
- M5 - GTE CMT using Soft Computing methods,
- M6 - GTE CMT using Hybrid Methods.

Thus, soft computing methods are applied separately and in combination with other methods (for example, the $M1 \tilde{M}2 @ CA$ subsystem, etc., see Fig.1), allowing for a stage-by-stage estimation of the GTE technical condition (TC).

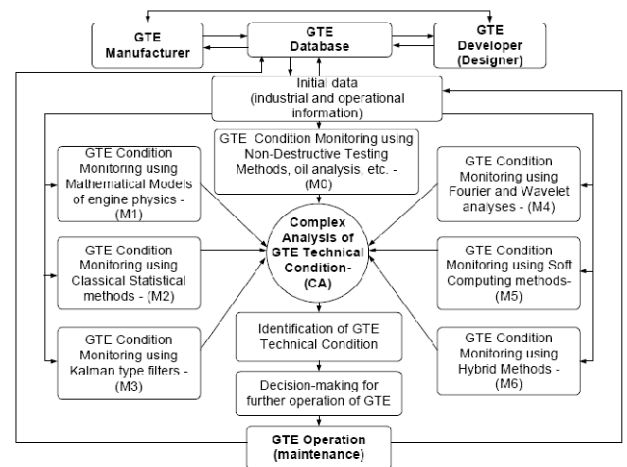


Fig.1. Structure of Aviation GTE Complex Condition Monitoring System

Let us consider a GTE diagnosing process using a $M2 \tilde{M}5 \rightarrow CA$ subsystem. At the first stage of diagnosis (after the start of maintenance operations), when the incoming information is insufficient and fuzzy, the GTE Technical Condition (TC) is estimated using fuzzy logic and neural network methods (Fig. 2). The preliminary estimation of the fuzzy performance of the GTE work parameters is carried out using Fuzzy Statistics. Furthermore, by using fuzzy correlation and fuzzy regression analyses, fuzzy relations between work parameters and identified fuzzy models of the GTE can be determined. The advantage of this monitoring stage is that we may identify initial patterns on the basis of fuzzy information. Once certain information is accumulated (second stage), the GTE technical condition can be estimated with mathematical statistics (MS). Furthermore, by means of the Least Squares Method (LSM), multiple linear regression equations for modeling changes in the GTE technical condition can be identified during the initial maintenance stage of each checked and working engine. On the basis of regression analysis (influence monitoring), we can evaluate how certain coefficients may change the dynamics and we may then use this information to further estimate the GTE technical condition. In the third stage, ridge-regression is used with the LSM to compile actual models of the GTE technical condition and compare the actual values of regression (influence) coefficients with their known base or tolerance ranges.

The $M1 \tilde{M}2 \tilde{M}5 \rightarrow CA$ subsystem of stage-by-stage diagnosis deals with the analysis of thermodynamic parameters such as G_T , T_4^* and n_{LP} . The $M0 \tilde{M}2 \tilde{M}4 \tilde{M}5 \rightarrow CA$ subsystem identifies the GTE technical condition on the basis of analyzing parameters' such as the concentration of metals in the scavenged oil and the vibration rate.



The final estimation of the GTE technical condition is carried out through a complex comparison of all diagnostic subsystems outputs by means of fuzzy logic. Thus, separate diagnostic subsystems are used to compare and make decisions based on the GTE work parameters.

2. Fuzzy-Neural Identification of GTE Technical Condition (Preliminary Stage)

A combined GTE monitoring and diagnosis method, based on the evaluation of engine parameters by soft computing methods, mathematical statistics (high order statistics), and regression analysis, is suggested. The method provides stage-by-stage (3-step) evaluation of GTE technical conditions (Fig.2). Experimental investigations using manual records confirm that, at the beginning of monitoring, 40 to 60 accumulated parameter measurements from a GTE in good working order fail to follow a normal distribution.

Consequently, in the first stage of the diagnostic process (at the preliminary stage of GTE operation), when initial data is insufficient and fuzzy, the GTE condition is estimated by soft computing methods – namely fuzzy logic (FL) and neural networks (NN). In spite of the rough parameter estimations, this stage presents the advantage of the possible creation of an initial image (initial condition) of the engine, based on uncertain information.

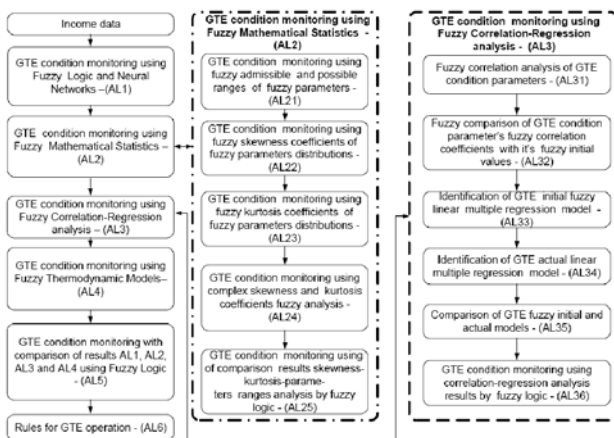


Fig. 2. Flow chart for the aircraft gas turbine engine fuzzy-parametric diagnostic algorithm

One method of GTE technical condition estimation used in practice is the exhaust gas temperature control, together with analysis of the changes in temperature during operation. Applications of various mathematical models described by the regression equations for aviation GTE condition estimation are presented in [14, 15].

Let us consider the following linear and non-linear models of the aviation GTE temperature described by

fuzzy regression equations:

$$\tilde{Y}_i = \sum_{j=1}^n \tilde{a}_{ij} \otimes \tilde{x}_j, i = \overline{1, m} \quad (1)$$

$$\tilde{Y}_i = \sum_{r,s} \tilde{a}_{rs} \otimes \tilde{x}_r^s \otimes \tilde{x}_s^s, r = \overline{1, l}; s = \overline{1, l}; r+s \leq l \quad (2)$$

where \tilde{Y}_i is the fuzzy output parameter (e.g., GTE exhaust gas temperature T_4^*), \tilde{x}_j or \tilde{x}_1, \tilde{x}_2 are the input parameters ($H, M, T_H^*, p_H^*, n_{LP}, G_T, p_T, p_M, T_M, V_{BS}, V_{FS}$), and \tilde{a}_{ij} and \tilde{a}_{rs} are the calculated fuzzy parameters (fuzzy regression coefficients).

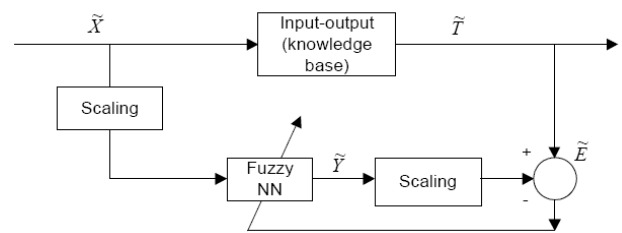


Fig. 3. Neural identification system

The general task is to define the fuzzy values \tilde{a}_{ij} and \tilde{a}_{rs} in equations (1) and (2) on the basis of the input coordinates \tilde{x}_j or \tilde{x}_1, \tilde{x}_2 and the output co-ordinate \tilde{Y} of the model.

Let us consider using FL and NN [16-18] to approach this task. NN consists of interconnected fuzzy neuron sets, with input signals composed of the fuzzy values of the variables ($\tilde{X} = \tilde{x}_1, \tilde{x}_2, \dots, \tilde{x}_n$) $\tilde{X} = (\tilde{x}_1, \tilde{x}_2)$ and \tilde{Y} .

The parameters of the network are the fuzzy values of the parameters \tilde{a}_{ij} and \tilde{a}_{rs} . We shall present fuzzy variables in the triangular form, in which membership functions are calculated using the formula:

$$\mu(x) = \begin{cases} 1 - (\bar{x} - x) / \alpha, & \text{if } \bar{x} - \alpha < x < \bar{x}; \\ 1 - (x - \bar{x}) / \beta, & \text{if } \bar{x} < x < \bar{x} + \beta; \\ 0, & \text{otherwise.} \end{cases}$$



The basic problem in using the NN method is training the parameters \tilde{a}_{ij} and \tilde{a}_{rs} . To train the parameters, we shall take advantage of an α -cut [18]. Imagine that statistical fuzzy data are received from the experiments. Training pairs (\tilde{X}, \tilde{T}) are constructed on the basis of these input and output data. To construct a model using the NN input, input signals \tilde{X} are provided and the outputs are compared with the reference output signals \tilde{T} (Fig. 3).

After comparison, the deviation value is calculated

$$\tilde{E} = \frac{1}{2} \sum_{j=1}^k (\tilde{V}_j - \tilde{T}_j)^2$$

With application of an α -cut, the left and right parts of the deviation value are calculated using the formulas

$$E_1 - \frac{1}{2} \sum_{j=1}^k [v_{j1}(\alpha) - t_{j1}(\alpha)]^2, \quad E_2 - \frac{1}{2} \sum_{j=1}^k [v_{j2}(\alpha) - t_{j2}(\alpha)]^2, \quad E = E_1 + E_2,$$

where, $\tilde{V}_j(\alpha) = [v_{j1}(\alpha), v_{j2}(\alpha)]$; $\tilde{T}_j(\alpha) = [t_{j1}(\alpha), t_{j2}(\alpha)]$.

If the deviation value E is less than some maximum value for all training pairs, then training (correction) of the parameters of the network ceases (Fig. 4). Otherwise, training continues until the value of E reaches a minimum.

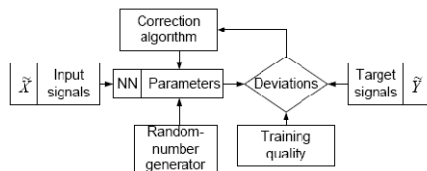


Fig. 4. System for network parameter (weights, threshold) training (with feedback)

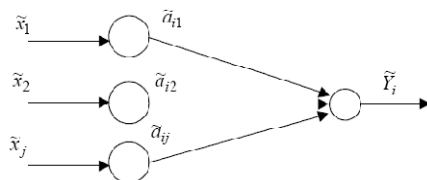


Fig.5. Neural network structure for multiple linear regression equation

Correction of network parameters for the left and right parts is carried out as follows:

$$a_{rs1}^n = a_{rs1}^o - \gamma \frac{\partial E}{\partial a_{rs}}, \quad a_{rs2}^n = a_{rs2}^o + \gamma \frac{\partial E}{\partial a_{rs}},$$

Where $a_{rs1}^o, a_{rs1}^n, a_{rs2}^o, a_{rs2}^n$ are the old and new values of the left and right parts of the NN parameters $\tilde{a}_{rs} = [a_{rs1}, a_{rs2}]$, and γ is the training speed.

The structure of the NN that identifies the parameters of equation (1) is shown in Fig. 5. For equation (2), we shall consider a concrete special case of the second-order regression equation:

$$\tilde{Y} = \tilde{a}_{00} + \tilde{a}_{10}\tilde{x}_1 + \tilde{a}_{01}\tilde{x}_2 + \tilde{a}_{11}\tilde{x}_1\tilde{x}_2 + \tilde{a}_{20}\tilde{x}_1^2 + \tilde{a}_{02}\tilde{x}_2^2$$

Construction of a neural structure (Fig. 6) for decision of equation (2), where the parameters of the network are the coefficients $\tilde{a}_{00}, \tilde{a}_{10}, \tilde{a}_{01}, \tilde{a}_{11}, \tilde{a}_{20}, \tilde{a}_{02}$ is shown in [11-13].

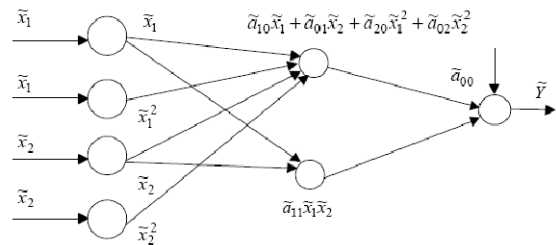


Fig. 6. Structure of neural network for second-order regression equation

From training on receiving equations we find network parameters that agree with the data satisfy to the required training quality.

3. GTE Condition Monitoring using Fuzzy Statistical Analysis (First Stage)

Research results show that certain fuzzy relations exist between the fuzzy thermodynamic and mechanical GTE parameters, which describe how the dynamics change during operation and diagnosis. These relations can be characterized by fuzzy correlation coefficients and ratios.

The choice of a GTE technical condition model (linear or nonlinear) may be aided by a complex comparison analysis of the fuzzy correlation coefficients \tilde{r}_{xy} and fuzzy correlation ratios $\tilde{p}_{y/x}$ [11-13].

However previous research has shown that the distributions of GTE work parameters are unstable (fuzzy) [11-13]. Therefore, we note that a correct application of the fuzzy correlation-regression approach demands the analysis of the fuzzy characteristics of GTE work parameter distributions. Fuzzy analysis of the distributions of GTE work parameters should be carried out on the basis of the fuzzy skewness and kurtosis coefficients



according to formulas, which are shown in [11-13].

4. GTE Condition Monitoring using Regression Analysis and a Kalman-type Filter (Second Stage)

The analysis shows that the individual GTE parameters approach a normal distribution after 60-120 measurements. Therefore, at the second stage after accumulating the certain information, GTE conditions can be estimated with the help of mathematical statistics. Here, the GTE work mode and standard atmospheric parameters are controlled to conform to the calculated admissible ranges. Furthermore, multiple linear regression models of GTE condition dynamics are identified using the Least Squares Method (LSM). These models are created for each correct subcontrol engine of the fleet during the initial operation period. Base levels and admissible ranges of the coefficients are determined by analyzing the values of the regression coefficients (coefficients of influence) for all of the engine's multiple regression models, with the help of mathematical statistics [13,19].

GTE Condition Monitoring using Regression Analysis and a Kalman type Filter (Second Stage) is presented in [11].

5. GTE Condition Monitoring using Fuzzy Thermodynamic Models

One of the methods for detecting faults at an early stage involves examining the control of changes in the thermodynamic and gas-dynamic parameters of the GTE. This approach is based on registered parameters' individual deviations in certain GTE work modes during operation.

The following GTE parameters are measurable: low and high rotor rotation frequencies (n_{LP} and n_{HP}), ratio of rotor frequencies or rotor sliding ($\delta = n_{HP} / n_{LP}$), turbine inlet gas temperature (T_3^*), turbine exhaust gas temperature (T_4^*), fuel flow (G_T), and power lever angle (α_{PLA}).

For the simultaneous processing of parameter measurements results received under various flight conditions, it is necessary to correct the measurement values to International Standard Atmosphere (ISA, or Standard Day) baselines and to adjust for the engine operation mode. ISA corrections are carried out with the help of similarity theory. If parameters are registered in cruise flight mode at identical engine power settings, then there is no need to correct for a given engine operational mode. For turbojets, the following correction formulas are used:

$$G_{T.cor} = G_T \frac{P_{H,ISA}}{P_H^*} \sqrt{\frac{T_{H,ISA}}{T_H^*}}, \quad n_{cor} = n \sqrt{\frac{T_{H,ISA}}{T_H^*}}, \quad T_{4.cor} = T_4^* \frac{T_{H,ISA}}{T_H^*}$$

However, even if GTE thermodynamic and gas-dynamic parameters are registered only in the cruise flight stage and at established power settings, changes in n_{LP} (henceforth designated as n), T_4^* and G_T have a fuzzy character. A principal reason for this involves the fuzzy values of total air pressure P_H^* and total air temperature T_H^* at the engine entrance for the considered flight mode. Hence, the correction formulas stated above should be applied in view of the fuzzy values of the basic parameters (\tilde{P}_H^* , \tilde{T}_H^* , \tilde{n}_{LP} , \tilde{T}_4^* , \tilde{G}_T). The correction formulas take the forms

$$\tilde{G}_{T.cor} = \tilde{G}_T \frac{P_{H,ISA}}{\tilde{P}_H^*} \sqrt{\frac{T_{H,ISA}}{\tilde{T}_H^*}}, \quad \tilde{n}_{cor} = \tilde{n} \sqrt{\frac{T_{H,ISA}}{\tilde{T}_H^*}}, \quad \tilde{T}_{4.cor} = \tilde{T}_4^* \frac{T_{H,ISA}}{\tilde{T}_H^*}$$

Where \tilde{P}_H^* , \tilde{T}_H^* , \tilde{n}_{LP} , \tilde{T}_4^* , and \tilde{G}_T are the measured fuzzy values of the parameters P_H^* , T_H^* , n_{LP} , T_4^* and G_T in the considered flight mode. Finding \tilde{n} , \tilde{T}_4^* , and \tilde{G}_T requires the appropriate estimation of membership function cores

$$d_n = 1, \quad d_{T_4^*} = 1, \quad d_{G_T} = 1$$

where

$$d_n = \max_{n \in \{n\}} \mu_n(n), \quad d_{T_4^*} = \max_{T_4^* \in \{T_4^*\}} \mu_{T_4^*}(T_4^*), \quad d_{G_T} = \max_{G_T \in \{G_T\}} \mu_{G_T}(G_T)$$

The values of the parameters n , T_4^* , and G_T are elements of the fuzzy sets (n) , (T_4^*) and (G_T) respectively,

μ_n , $\mu_{T_4^*}$, and μ_{G_T} are the membership functions of fuzzy sets relating (n) , (T_4^*) and (G_T) to general sets $\{n\}$, $\{T_4^*\}$ and $\{G_T\}$. The application described above is shown in p.VI.

6. GTE Condition Monitoring using Complex Analysis of First and Second Stage results (Third Stage)

In the third stage (for more than 120 measurements), a detailed analysis of GTE conditions is conducted using the LSM. This procedure creates an actual model (multiple linear regression equation) of GTE conditions and compares the actual coefficients of influence (regression coefficients) with their base admissible ranges. The reliability of the diagnostic results for this stage is high, in the range 0.95-0.99. If the coefficient values exit the allowed ranges, we draw conclusions about the influence



of changes in the physical parameters on the concrete GTE work parameters. One or several coefficient's influences going beyond the admissible range confirms any additional features of the incorrectness and allows us to determine the address and possible reason for any faults. LSM and ridge-regression analysis is used to produce stable estimations.

7. GTE Condition Monitoring using Complex Analysis involving the Fuzzy Logic Basis (Final Stage)

The elementary construction of membership functions assumes the input of several experts. Imagine we have m available experts (experts on methods M1... M7; see Fig. 7), of whom several answer positively to questions regarding the membership of element $x \in X$ (where x is one of the GTE parameters $n_{LP}, G_T, p_T, p_M, T_M, T_4^*, V_{BS},$ or V_{FS} ; in this case $x = T_4^*$) within fuzzy set A_x . Assume there are n_1 such experts. The rest of the experts ($n_2 = m - n_1$) answer the question in the negative. Then, the membership function becomes $\mu_{A_x}(x) = n_1 / (n_1 + n_2)$.

We note that this scheme of defining the membership function is the most simple. The membership function can be constructed more precisely on the basis of quantitative conjugate comparisons of membership degrees. Such a scheme also assumes that there is only one expert. The result of questioning the experts is the matrix $M = \parallel m_{ij} \parallel, i, j = 1, \dots, n$, where n is the number of points for which membership function values are compared. The number m_{ij} reflects by what multiple the membership degree $\mu_{A_i}(x_i)$ is more than $\mu_{A_j}(x_j)$ in the judgment of the experts. For example, the expert operates with the concepts presented in Table 1.

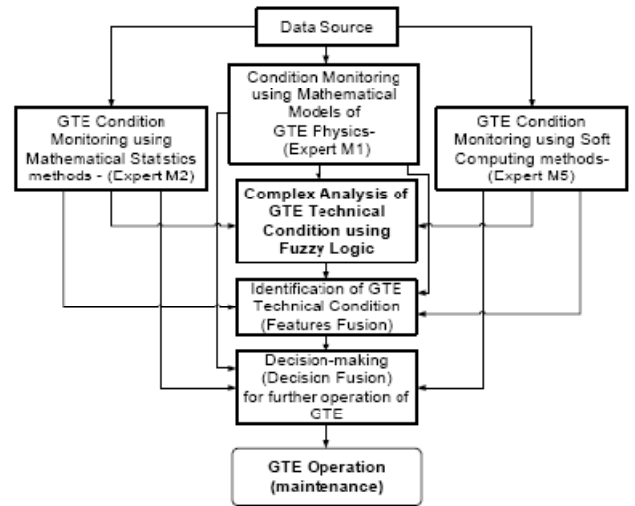


Fig. 7. Structure of Aviation GTE Complex Condition Monitoring System using Experts M1, M2, and M5

Table 1. Operations for Complex Condition Monitoring System using Experts M1, M2, and M5

Sense	m_{ij}
$\mu_{A_i}(x_i)$ is equal to $\mu_{A_j}(x_j)$	1
$\mu_{A_i}(x_i)$ is slightly more than $\mu_{A_j}(x_j)$	3
$\mu_{A_i}(x_i)$ is more than $\mu_{A_j}(x_j)$	5
$\mu_{A_i}(x_i)$ is noticeably more than $\mu_{A_j}(x_j)$	7
$\mu_{A_i}(x_i)$ is much more than $\mu_{A_j}(x_j)$	9
Values intermediate between the enumerated degrees above	2,4,6,8

The membership function values $\mu_{A_i}(x_i)$ at the points x_1, x_2, \dots, x_n can be defined using the formula

$$\mu_{A_i}(x_i) = \frac{m_{ij}}{\sum_{i=1}^n m_{ij}}$$

where j is an arbitrary column of the matrix $M = \parallel m_{ij} \parallel$

8. Example of GTE Condition Monitoring using Complex Analysis

As an example application of the method described herein, changes in a GTE's (aviation engine D-30KU-154) temperature conditions have been investigated. In the preliminary stage, when $N \leq 60$, the GTE technical condition is described by the fuzzy linear regression



equation (1). The fuzzy linear model of the GTE is identified with a NN, the structure of which is given in Fig. 3. The output parameters of the GTE model are accepted as the GTE exhaust gas temperature

$$(\tilde{T}_4^*)_{ini} = \tilde{a}_1 \tilde{H} + \tilde{a}_2 \tilde{M} + \tilde{a}_3 \tilde{T}_H^* + \tilde{a}_4 \tilde{n}_{LP} + \tilde{a}_5 \tilde{P}_T + \tilde{a}_6 \tilde{P}_M + \tilde{a}_7 \tilde{T}_M + \tilde{a}_8 \tilde{G}_T + \tilde{a}_9 \tilde{V}_{FS} + \tilde{a}_{10} \tilde{V}_{BS} + \tilde{a}_{11} \tilde{P}_H^* \quad (6)$$

In the subsequent stage, when $N > 60$, the engine work parameters are observed to follow normal distributions, the GTE temperature is described by the linear regression equation (6), the parameters of which are estimated by a recurrent algorithm [11]

$$D = (T_4^*)_{act} = a'_1 H + a'_2 M + a'_3 T_H^* + a'_4 n_{LP} + a'_5 P_T + a'_6 P_M + a'_7 T_M + a'_8 G_T + a'_9 V_{FS} + a'_{10} V_{BS} + a'_{11} P_H^* \quad (7)$$

Given the results of research into the technical conditions of the considered engine, we uncover certain dynamics of the correlation and regression coefficients values, which are given in [19].

The basic characteristics of the correlation coefficients [19] demonstrate the necessity of applying the fuzzy NN during flight information processing. In that case, a correct application of this approach to describe the changes in GTE technical conditions is possible using a fuzzy linear or non-linear model [11, 13].

For the third stage, the following regression coefficients (influence coefficients for various parameters) describing the effects of various parameters on GTE exhaust gas temperature are admitted into the linear multiple regression equation (1): engine rotation frequency (RPM of low pressure (LP) compressor)- 0.596-0.622; fuel pressure- 1.16-1.25; fuel flow- 0.0240-0.0252; oil pressure- 11.75-12.45; oil temperature- 1.1-1.2; vibration of the forward support- 3.0-5.4; vibration of the back support- 1.2-1.9; atmosphere pressure- 112-128; atmosphere temperature- (-0.84)-(-0.64); flight speed (Mach number)- 57.8-60.6; and flight altitude- 0.00456-0.00496. Within the specified limits, the current values of the regression coefficients are approximated by polynomials of the second and third degree, with the help of the LSM and cubic splines [19].

In estimating the GTE technical condition, we also consider the fuzzy parameter T_4^* , which is included in the correction formulas. To do this, we present this parameter in triangular form. Our tentative estimation of \tilde{T}_4^* allows $\tilde{T}_{4.cor}^*$ (corrected to ISA) to be defined more precisely. Apparently, using fuzzy values of $\tilde{T}_4^* (d_{T_4^*} = 1)$ for a

more flexible estimation of the GTE technical condition than average values. It is necessary to note that the dynamics of the \tilde{T}_4^* show that significant changes are not occurring under given GTE technical conditions. For example, the abnormal phenomena associated with the GTE technical condition are observed in the measurement intervals of $N = 115-120, 125-130, 150-155, 195-200, 335-345$. This circumstance proves to also be true with the dynamics of the influence coefficients (regression coefficients) included in the regression equation $D = (T_4^*)_{act}$ (Fig 8).

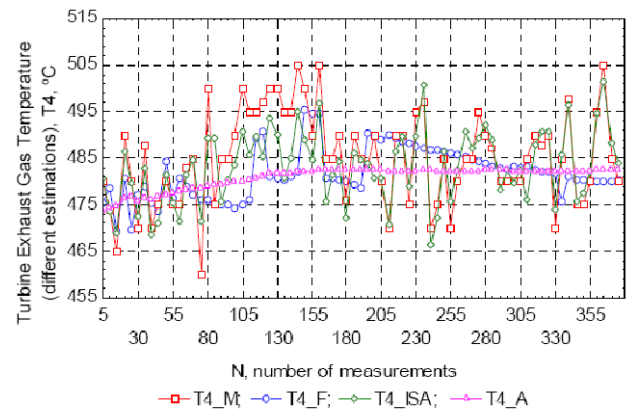


Fig. 8. Estimation of engine exhaust gas temperature T_4^* (°C) changes during GTE operation: T4_M- measured exhaust gas temperature values, T4_F- exhaust gas temperature fuzzy values, T4_ISA- exhaust gas temperature values corrected to ISA, T4_A- exhaust gas temperature average values, N - number of measurements

We note that accounting for the parameters' fuzziness in the correction formulas allows for a more precise estimation of the GTE technical condition. Our application of Fuzzy Logic improves the complex GTE diagnosis system. Such a system allows for more effective decision-making regarding further maintenance of the GTE. Our conclusions are based on the comparative analysis of results from Mathematical Statistics, Correlation-Regression Analysis, Neural Networks, and Fuzzy Analysis.

9. Conclusions

- 1) A combined GTE technical condition diagnosis approach is presented. The method is based on fuzzy and nonfuzzy engine work parameter estimation, with the help of Soft Computing methods.
- 2) Through complex analysis, we have established that:
 - a) There are certain fuzzy relations between the fuzzy



thermodynamic and mechanical GTE parameters, which describe how the dynamics change during fuzzy diagnostic situations. Changes in the fuzzy connections (correlation coefficients) between engine work fuzzy parameters are observed during the development of various malfunctions during operation, caused by the occurrence or disappearance of factors that impact the GTE technical condition,

b) to improve the accuracy of decisions that impact the GTE technical conditions, it is expedient to apply Fuzzy Statistics and Fuzzy Thermodynamic Modelling using the presented Condition Monitoring System,

c) the research shows that, to make more exact decisions about GTE operation, it is necessary to develop models and methods on the basis of observed features and fuzzy decision-making algorithms. The suggested methods make it possible to diagnose and predict the safe engine runtime. This method outputs tangible results and may be useful for practical application as an automatic engine diagnostic system, where the handle record is used as the initial information, and for an onboard system for engine work control.

References

- [1]. Brotherton, T, and Johnson, T, Anomaly Detection for Advance Military Aircraft Using Neural Networks, Proceeding of. The 2001 IEEE Aerospace Conference, Big Sky, MT, March 2001.
- [2]. Volponi, A, and Urban, L, Mathematical Methods of Relative Engine Performance Diagnostics, SAE 1992, Transactions, Vol.101, Journal of Aerospace, Paper # 922048.
- [3]. Volponi, A, Foundations of Gas Path Analysis I & II, Von Karman Institute for Fluid Dynamics Lecture Notes 2003-01, Jan. 2003.
- [4]. Doel, D. L., An Assessment of Weighted-Least-Squares Based Gas Path Analysis, ASME Paper 93-GT- 119, 1993.
- [5]. Merrington, G.L., Fault Diagnosis in Gas Turbines Using a Model Based Technique, ASME Paper 93-GT-13, 1993.
- [6]. Mathioudakis K., Turbofan Performance Deterioration Tracking Using Non-Linear Models And Optimization Techniques, ASME GT-2002-30026, June 2003.
- [7]. Kobayashi, T., and, Simon, D., A Hybrid Neural Network –Genetic Algorithm Technique for Aircraft Engine Performance Diagnostics, 37th AIAA/ASME/SAE/ASEE Joint Propulsion Conference, July 2001.
- [8]. Ganguli, R, Application of Fuzzy Logic for Fault Isolation of Jet Engines, ASME 2001-GT-13, June 2001.
- [9]. Lu, P.J., An Evaluation of Engine Fault Diagnostics Using Artificial Neural Networks, ASME 2000-GT-0029, May 2000.
- [10]. Brotherton, T, Volponi, A, Luppold, R, and Simon, D, eSTORM: Enhanced Self Tuning On-board Realtime Engine Model, Proceedings of the 2003 IEEE Aerospace Conference. Big Sky, MT, March 2003.
- [11]. Pashayev A.M., Askerov D.D., Sadiqov R.A., Abdullayev P.S. "Fuzzy-Neural Approach for Aircraft Gas Turbine Engines Diagnosing", AIAA 1st Intelligent Systems Technical Conference (Chicago, Illinois, Sep. 20-22, 2004), AIAA-2004-6222, 2004
- [12]. Pashayev A.M., Sadiqov R.A., Abdullayev P.S., "Complex identification technique of aircraft gas turbine engine's health", ASME TURBO EXPO 2003: Power for Land, Sea and Air Conference, June 16–19, 2003, Atlanta, Georgia, USA, Paper GT2003-38704, 2003
- [13]. Abdullayev P.S., Pashayev A.M., Askerov D.D., Sadiqov R.A. "Aircraft Gas Turbine Engines' Technical Condition Identification system", ASME TURBO EXPO 2005: Power for Land, Sea and Air Conference, June 6–9, 2005, Reno-Tahoe, Nevada, USA, Paper GT2005-69072, 2005
- [14]. Ivanov L.A. and etc., "The technique of civil aircraft GTE technical condition diagnosing and forecasting on registered rotor vibrations parameters changes in service", GosNII GA, Moscow, 1984, 88p.
- [15]. Doroshko S.M., "The control and diagnosing of GTE technical condition on vibration parameters", Transport, Moscow, 1984, 128
- [16]. Abasov M.T., Sadiqov A.H., Aliyarov R.Y., "Fuzzy neural networks in the system of oil and gas geology and geophysics", Third International Conference on Application of Fuzzy Systems and Soft Computing, Wiesbaden, Germany, 1998, pp.108-117.
- [17]. Yager R.R., Zadeh L.A. (Eds.), "Fuzzy sets, neural networks and soft computing", VAN Nostrand Reinhold, N.-Y. - № 4, 1994.
- [18]. Mohamad H. Hassoun., "Fundamentals of artificial neural networks", A Bradford Book, The MIT press Cambridge, Massachusetts, London, England, 1995
- [19]. P.Abdullayev, Identification System of Aviation Gas Turbine Engines' Technical Condition, 43rd AIAA/ASME/SAE/ASEE Joint Propulsion Conference and Exhibit, Cincinnati, OH, USA, July 8-11, 2007, Paper AIAA-2007-5111, 2007



Vibrations Control of Rail Vehicle Body using Parameters Adaptive PID Controller

Muzaffer METIN¹, Rahmi GUCLU^{1*}, Fatih DUMAN¹

^{1*} Yildiz Technical University
Mechanical Eng. Dept. Besiktas, Istanbul
Email*: guclu@yildiz.edu.tr

Abstract

In this study, vertical rail vehicle vibrations are controlled by the use of conventional and parameters adaptive PID controllers. A quarter rail vehicle model is designed as 5 degrees of freedom using Manchester Benchmark dynamic parameters. Rail vehicle consists of a vehicle body, a bogie, primary and secondary suspensions and two wheels. A type of rail irregularity is used for disturbance input of the rail vehicle system. A sinusoidal irregularity is applied to the system, which symbolizes collapses of railway superstructure. A parameters adaptive PID controller is designed to obtain a comfortable travel and minimize vertical vibrations of rail vehicle body. Genetic algorithm toolbox is used to achieve new parameters of adaptive controller. Simulations are performed for 30 km/h, 60 km/h and 90 km/h rail vehicle speeds and $\pm 5\%$ load changes of rail vehicle body to test the robustness of controllers. Simulations are carried out in time and frequency domains.

Keywords: Active suspensions, parameters adaptive PID controller, vibrations, rail vehicle.

1. Introduction

Guided rail systems cause vibrations that affect passenger comfort significantly. Essentially with development of technology, the expected comfort level is increased by passengers. Nowadays, during the travel with rail vehicles passengers want to drink beverages and at the same time they want to work with their computers. This approach has been the concept of comfort by passengers. In this regards, rail vehicle vibrations that negatively affect passenger comfort, has become a serious engineering problem to control vibrations actively.

In this study, active control will be implemented through the secondary suspension system which is located between vehicle body and bogie. For this aim, rail vehicle is modeled as 5 degrees of freedom and consist of vehicle body, bogie, primary and secondary suspensions and wheels. In this study and many other studies quarter vehicle model is used due to its simplicity and convenience. In rail vehicle model, the interaction

between wheel and rail is not linear, but the interaction model is going to a simplified linear solution using Hertz spring [1, 2]. For a different approach, Dukkipati and Dong modeled wheel and rail interaction as multiple springs' interaction [3]. Vibrations that cause distortions, was applied as a real rail irregularity. In recent years, many researchers have applied linear and nonlinear controls to minimize vertical rail vehicle vibrations. Stribersky et al. have worked on semi-active vibration damping system for rail vehicle systems [4]. In this way, they have improved ride comfort in rail vehicles carried a variety of applications. Foo and Goodall applied active controller to the rail vehicle secondary suspensions to minimize vehicle body vertical accelerations [5]. X. Lei and N.-A. Noda modeled and analyzed rail vehicle and rail dynamics using finite element method [6]. Guclu examined dynamic behavior of 8 degrees of freedom full vehicle model having passenger seat with an active suspension using PID controller [7]. Guclu examined with dynamic behavior of the same model having passenger seat with an active suspension using fuzzy logic controller [8]. In another study, Rao and Prahlad carried out a study on rail vehicles adjustable fuzzy logic controller application [9]. Yagiz and Gursel applied sliding mod type controller for improving ride comfort of a flexible modeled rail vehicle wagon [10]. Metin and Guclu controlled vibrations of a high speed train moving on a corrugated rail with fuzzy logic controller [11]. Vibrations of a rail vehicle modeled as 6 degrees of freedom was controlled a designed fuzzy logic controller [12]. In another study, fuzzy logic controller and conventional PID controller performances were compared using 11 degrees of freedom half rail vehicle model with sinusoidal rail disturbance [13]. Then, on 6 degrees of freedom rail vehicle model to control vibrations were used conventional PID, fuzzy logic PID and parameters adaptive PID controllers and compared their performances [14].

In this study, vertical rail vehicle vibrations are controlled by the use of conventional and parameters

adaptive PID controllers. A quarter rail vehicle model is designed as 5 degrees of freedom using Manchester Benchmark dynamic parameters. Rail vehicle consists of a vehicle body, a bogie, primary and secondary suspensions and two wheels. A combination of varying loading conditions and robustness of controllers were examined under varying speeds and sinusoidal rail irregularity. In addition, time and frequency domain responses were investigated under varying loading conditions.

2. Dynamic Model of Rail Vehicle

The quarter rail vehicle model as designed 5 degrees of freedom used in this study is shown in Fig. 1. Uncontrolled system inputs are load changes and rail irregularities which can make the system unstable. System outputs are displacement and acceleration of vehicle body. Passive system response depends on parameters such as mass, spring, damping ratio and suspension geometry. Active suspension structure is a more complex dynamic system than passive suspension. Performance of the active suspension depends on sensors, actuators and hardware and software of controller.

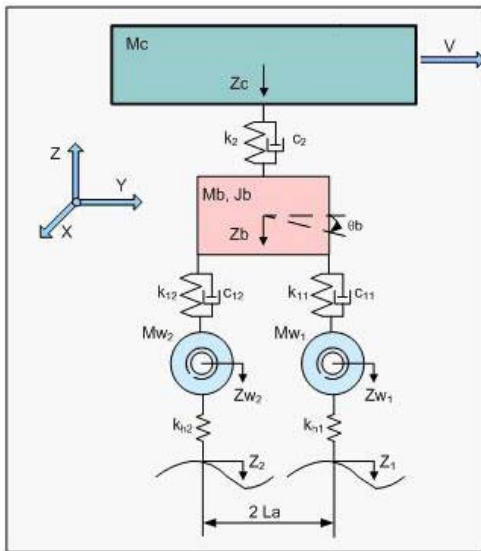


Fig. 1. The quarter rail vehicle model

Quarter vehicle model contains M_c mass of rail vehicle body, M_b mass of bogie, J_b inertia moment of bogie, M_{w1}, M_{w2} masses of wheels which are located under bogie. K_2 and C_2 are secondary suspension stiffness and damping coefficients, respectively. K_{11}, K_{12} and C_{11}, C_{12} are stiffness and damping coefficients of primary suspension. K_{h1} and K_{h2} are expressions of the wheel-rail linear contact form of Hertz spring stiffness. U is control force which generated by actuators. All these parameter values are given in the Appendix.

This model has five degrees of freedom. These are $Z_c, Z_b, \theta_b, Z_{w1}$ and Z_{w2} . Z_c is vertical displacement of vehicle body, Z_b is vertical displacement of bogie, θ_b is pitch motion of bogie, Z_{w1} and Z_{w2} are vertical displacements of front and rear wheels.

Differential equations of rail vehicle obtained using Lagrange Equation.

Differential equation of the system:

$$[M] \ddot{Z} + [C] \dot{Z} + [K] Z = F_z + F_u \quad (1)$$

here,

$$Z = [Z_c, Z_b, \theta_b, Z_{w1}, Z_{w2}]^T, \quad F_z = [0 \ 0 \ 0 \ K_{h1} Z_1 \ K_{h2} Z_2]^T \quad \text{and} \\ F_u = [u \ -u \ 0 \ 0 \ 0]^T.$$

F_z is rail disturbance that causes vibrations. These disturbances act on rail vehicle via rigid wheels. F_u is a force that is applied by an actuator. $[M], [C], [K]$ are mass, damping and stiffness matrices, respectively which are given in the Appendix.

$Z_1(t)$ and $Z_2(t)$ are rail irregularity inputs applied to wheel masses.

During the interaction of rail-wheel produced forces are transmitted by rail-wheel contact area. Due to the geometry of contact area between rail and wheel, for the wheel-rail dynamic interaction, the relation between the force and deflection is defined by the Hertz contact spring. Hertz contact spring is not linear contact and depends on the relationship between contact force and deflection of wheel-rail contact surface (y). This expression [1] is given below;

$$F = C_h \cdot y^{3/2} [N] \quad (2)$$

In this equation $C_h [Nm^{-3/2}]$ is Hertz spring coefficient which depends on wheel radius, rail radius and material, F represents static wheel load. All components have to be linear to express the relationship between wheel and rail. Therefore Hertz contact spring has to be defined as a linear spring. Rigidity of Hertz contact linear value can be obtained from static wheel load depending on the force-displacement relationship. This is represented by the following equation [2];

$$K_h = dF/dy = \frac{3}{2} (C_h^{2/3} \cdot F^{1/3}) [N/m] \quad (3)$$

3. Controllers Design

To suppress the vibrations on rail vehicle, first a conventional PID controller designed. Then, in order to increase performance of this controller, the parameters adaptive method is used.

3.1. Conventional PID Controller

Because of the widespread use in industry and its simplicity if not optional in many applications, PID controllers are used in more than 95% of closed-loop industrial processes [15].

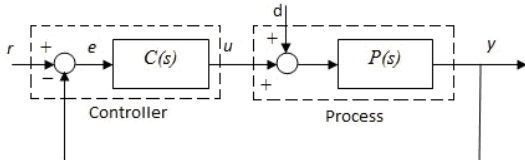


Fig. 2. Conventional feedback control system

According to Fig. 2, the PID controller is used as the compensator $C(s)$. When used in this way, three elements of the PID controller produce outputs with the following nature;

- P element: Proportional to the error at the instant t , which is the “present” error. By tuning proportional gain K_p , rise time can be decreased.
- I element: Proportional to the integral of the error up to the instant t , which can be interpreted as the accumulation of the “past” error. By tuning integration gain K_i , the steady-state error can be eliminated.
- D element: Proportional to the derivative of the error at the instant t , which can be interpreted as the prediction of the “future” error. By tuning derivative gain K_D , the over shoot and settling time can be reduced [16].

Feedback has had a revolutionary influence in practically all areas where it has been used and will continue to do so. PID controller is perhaps the most basic form of feedback [17]. Well known PID algorithm is described as below;

$$u(t) = K_p \left(e(t) + \frac{1}{K_i} \int_0^t e(\tau) d\tau + K_d \frac{de(t)}{dt} \right) \quad (4)$$

where;

$e(t)$ is the control error and the controller parameters K_p , K_i and K_d are proportional gain, integral gain and derivative gain, respectively.

$$C(s) = K_p + \frac{K_i}{s} + K_d s \quad (5)$$

$C(s)$ is the transfer function of controller describes the feedback from process output y to control signal u .

3.2. PID Controller with Parameters Adaptive Method

Sometimes using only simple PID controller does not presents enough effective response on system which has

random disturbances. Thus, some specific structured hybrid controllers used that involved PID. In this study, a parameters adaptive method is used for tuning the PID parameters (K_p , K_i and K_d) in system model. It is well known that the proportional component of the PID has an important role on the performance of PID system to control vertical vibrations of vehicles. If the proportional control is too weak, the response will be slow and if the integration component is too strong, the response will become unstable. So it is desirable to make further improvement on it can be let take a larger value and reduce it gradually with time so as to increase the damping of the system and make the system more stable. By this way, it can be imagined an effective suppression for the system’s displacement responses and a short settling time acceleration responses. Figure 3 shows the block diagram of the parameters adaptive PID controller.

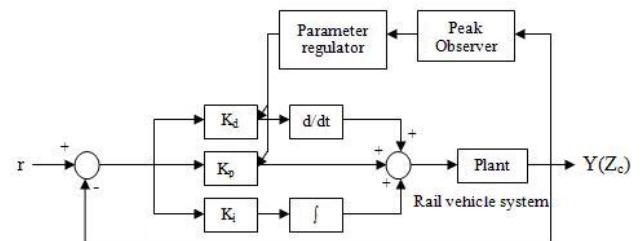


Fig. 3. Block diagram of parameters adaptive PID controller

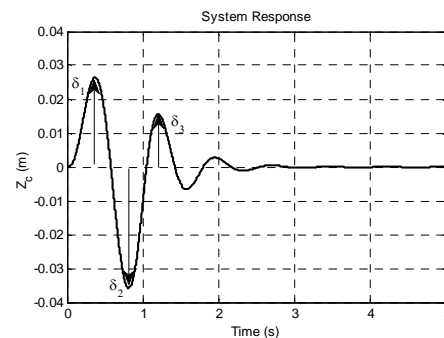


Fig. 4. Peaks of the system response

Mizumoto describes broadly how to use parameters adaptive method for PID type fuzzy controller structure [18]. It is known that displacement level of rail vehicle body vibrations occur as near disturbance level. In this study, effect of a sinusoidal rail irregularity is used to obtain disturbance effect. Amplitude of sinusoidal rail irregularity is $|a_{sin}|=0.02$ m. So disturbance effect is smaller than 1 m. Peak observer detects peak values of rail vehicle vibrations and sends values to parameters regulator, G_p and G_d . G_p and G_d are new parameters which regulate K_p and K_d online, respectively. While increasing the value of K_p and K_d will increase the proportional



control component; thus the reaction of the control system against the error will be speed up and vibrations will be suppressed effectively.

Motivated by this idea, a parameters adaptive PID controller is designed. The parameters adaptive PID controller is composed of a PID controller, a peak observer and parameter regulators (Fig. 3). The peak observer keeps watching on the system's output and transmits a signal at each peak time and measures the absolute peak value. The parameter regulator tunes the controller parameters K_p and K_d simultaneously at each peak time signal and according to the peak value at that time. The algorithm of tuning the scaling constants and the derivative gain as follows;

$$K_p = \frac{K_{ps}}{\delta_k G_p}, \quad K_d = \frac{K_{ds}}{\delta_k G_d} \quad (6)$$

Where, K_{ps} and K_{ds} are the initial values of K_p and K_d , respectively. δ_k is the absolute peak value (Fig. 4) at the peak time t_k ($k=1, 2, 3, \dots$). G_p and G_d are additional scaling factors of peak values for parameters adaptive PID controller. K_p , K_i and K_d values are fixed for the both controllers. These values are established by trial and error in this study. G_p and G_d scaling factor values are determined with ISE performance index by the use of genetic algorithm toolbox in Matlab.

4. Simulations

The assessment of the driving performance should be examined on the comfort level of passengers. Looking for driving safety value depends on displacement responses. Looking for comfort level value depends on accelerations. Controller was designed to take into account both two responses. Parameters of adaptive PID controller were defined using Genetic Algorithm Toolbox according to the formula ISE (Integral of Square Error). These parameter values of controllers are given in appendix.

$$S_{ISE} = \int_0^{10} e^2(t) dt \quad (7)$$

ISE value of controller is $2,486 \cdot 10^{-11}$.

In simulations, passive responses of rail vehicle, responses of conventional PID controller and responses of parameters adaptive PID controller were compared. In these simulations, to compare controller performances, three different speeds were used and these are 30 km/h, 60 km/h and 90 km/h. Performances of controllers according to sinusoidal rail irregularity was compared. Sinusoidal rail irregularity is shown in Fig. 5. A combination of varying loading conditions and robustness of controllers were examined under varying speeds. In addition to the

time domain responses, frequency responses were investigated under varying loading conditions.

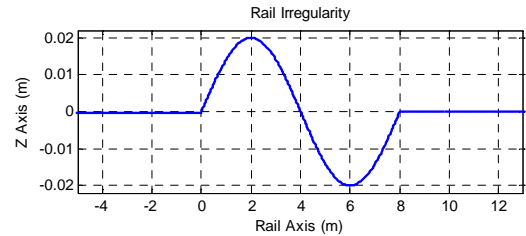


Fig. 5. Sinusoidal rail irregularity

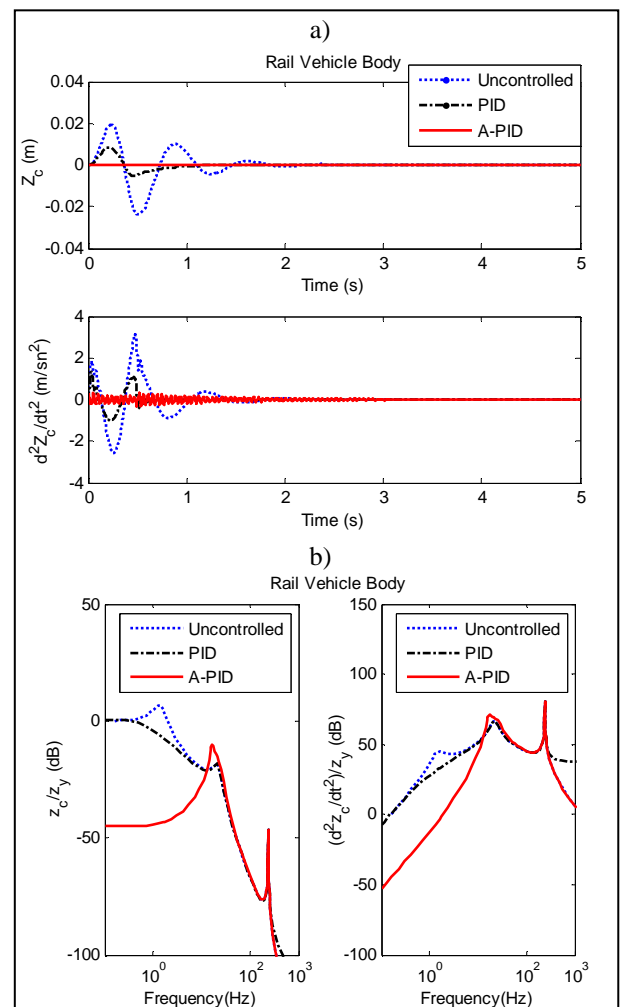


Fig. 6. Uncontrolled and controlled rail vehicle body responses in time and frequency domain ($V=60$ km/h, $M_c=8400$ kg)

In Fig. 5, a sinusoidal rail irregularity is shown that describes the collapse of the railway substructures with time. In these simulations, to compare controller performances, three different operation speeds were used and these are 30 km/h, 60 km/h and 90 km/h. To test

robustness of controllers for uncertainty of rail vehicle body mass ($\pm 5\%$) because of passengers, simulations are carried out at 60 km/h rail vehicle speed.

Fig. 6 (a) demonstrates rail vehicle body displacements and accelerations for passive system, PID and adaptive PID controlled systems at 60 km/h and for 8400 kg body mass. Fig. 6 (b) represents the rail vehicle body displacement and acceleration responses in frequency domain for 8400 kg body mass.

4.1 Examination of performances of controllers under varying rail vehicle speed ($V=30$ km/h and $V=90$ km/h)

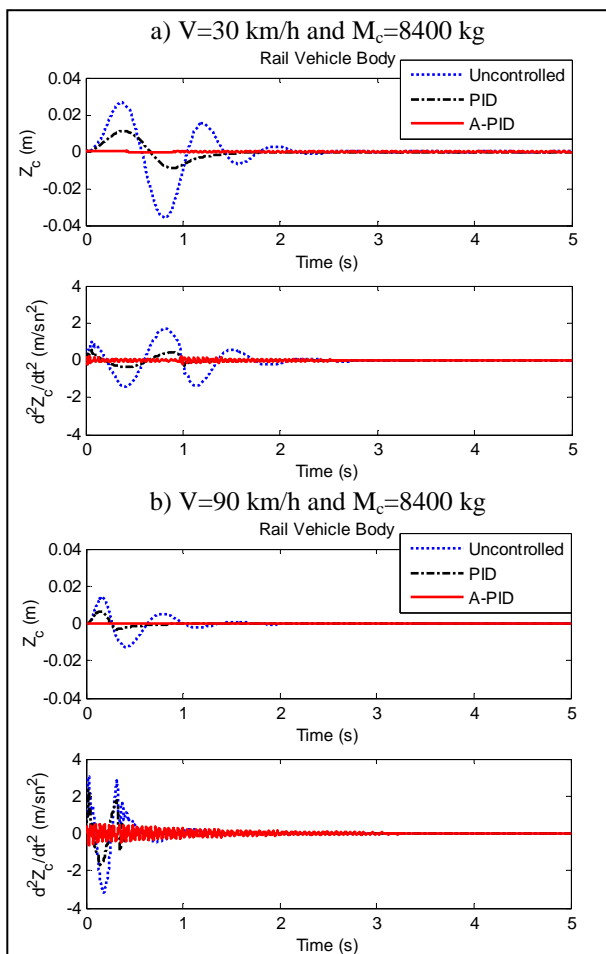


Fig. 7. Uncontrolled and controlled rail vehicle body vibrations at different operation speeds

To compare controller performances and examine robustness of controllers, two different operation speeds from mainly used speed (60km/h) of rail vehicle were used and these are 30 km/h and 90 km/h. Fig. 7 (a) and (b) demonstrate responses of rail vehicle body vibrations at 30 km/h and 60 km/h operation speeds, respectively.

4.2 Examination of robustness of controllers under rail vehicle body mass uncertainty ($\pm 5\% M_c$)

To test robustness of controllers for uncertainty of rail vehicle body mass ($\pm 5\%$) because of passengers, simulations are carried out at 60 km/h rail vehicle speed. Fig. 8 (a) and (b) represent responses of rail vehicle body vibrations at fixed operation speed (60 km/h) for 7980 kg and 8820 kg rail vehicle body mass, respectively. 80 kg is determined per person in rail vehicle.

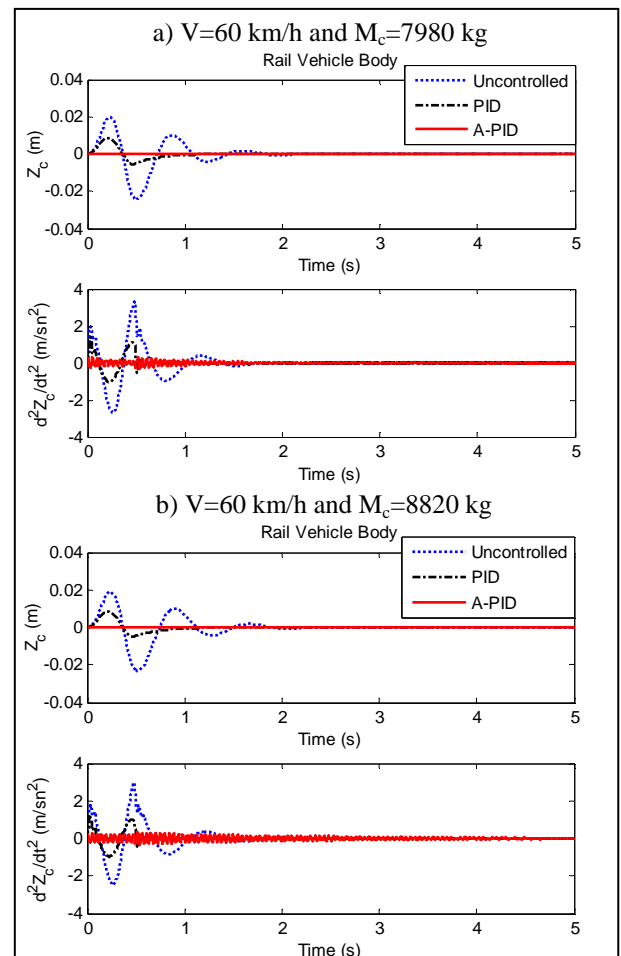


Fig. 8. Uncontrolled and controlled rail vehicle body vibrations for body mass uncertainty ($\pm 5\% M_c$)

Frequency responses of rail vehicle body for rail vehicle body mass uncertainty ($\pm 5\% M_c$) are shown in Fig. 9.

This quarter rail vehicle system has 5 degrees of freedom. Thus, this system has 5 eigenvalues. In this study, 3 different rail vehicle body masses ($M_c=7980, 8400, 8820$ kg) which represent varying loading conditions of body are used to examine robustness of



controllers. In case of $M_c=7980$ kg, eigenvalue matrix of system is $[1 \ 21 \ 30.8 \ 239.7 \ 239.7]^T$. For second case of simulations ($M_c=8400$ kg), eigenvalue matrix of system is $[0.98 \ 21 \ 30.8 \ 239.7 \ 239.7]^T$. For the last simulation case ($M_c=8820$ kg), eigenvalue matrix of system is $[0.95 \ 21 \ 30.8 \ 239.7 \ 239.7]^T$. Eigenvalue analysis show that the first eigenvalue belongs to rail vehicle body mass, predominantly. In Fig. 6 and 9, the first peak of uncontrolled system is suppressed successfully by the both controllers. By using parameters adaptive method on PID controller demonstrate the fine performance to control vibrations of rail vehicle body in time and frequency domain.

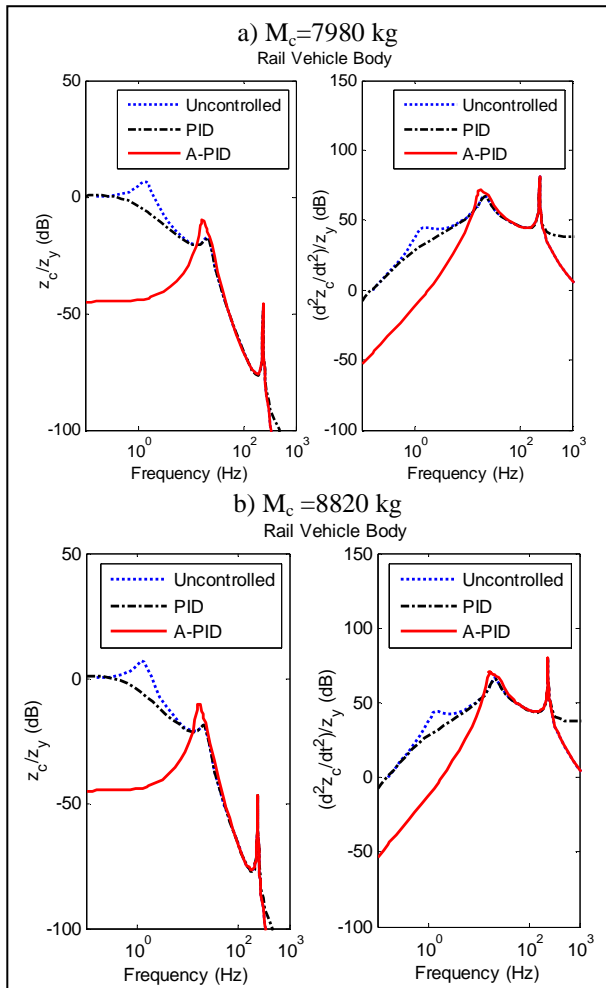


Fig. 9. Frequency responses of rail vehicle body for body mass uncertainty ($\pm 5\% M_c$)

5. Conclusions

In this study, a quarter rail vehicle model as designed 5 degrees of freedom examined under combinations of varying loading conditions, varying speeds and a

sinusoidal rail irregularity. To control rail vehicle body vertical vibrations, a conventional PID and parameters adaptive PID controller performances are compared. For controlled and uncontrolled cases, displacement and acceleration responses of rail vehicle body in time and frequency domains are shown. In the case of parameters adaptive PID controller, K_p , K_i and K_d parameters are tuned online under a sinusoidal rail irregularity. Controllers protect their robustness for different operation speeds and varying loading conditions. Generally speaking, the simulation results demonstrate that the adaptive PID substantially improves the performance of the control system. It has presented the simulation results to demonstrate the fine performance of the proposed PID controller with parameters adaptive method.

6. Appendix

Parameters of the five degrees of freedom rail vehicle model [19];

Mass Parameters	Stiffness Parameters	Damping Parameters
$M_c = 8400$ kg	$k_{11} = 12200000$ N/m	$c_{11} = 4000$ Ns/m
$M_b = 653,75$ kg	$k_{12} = 12200000$ N/m	$c_{12} = 4000$ Ns/m
$J_{b1} = 1121$ kgm ²	$k_2 = 320000$ N/m	$c_2 = 20000$ Ns/m
$M_{w1} = 453,25$ kg	$k_{h1} = 1015549000$ N/m	
$M_{w2} = 453,25$ kg	$k_{h2} = 1015549000$ N/m	
Other Parameters	PID Controller Parameters	Adaptive PID Parameters
$L_a = 0,9$ m	$K_p = 6,27 \cdot 10^5$	$G_p = 0,55$
$V = 140$ km/h	$K_i = 100$	$G_d = 52,8$
$a = 0,02$ m	$K_d = 120$	
$y = 8$ m		
$F = 85$ kN		
$c_h = 1.10^{11}$ N/m ^{3/2}		

Mass, damping and stiffness matrices of the system:

$$M = \begin{bmatrix} M_c & 0 & 0 & 0 & 0 \\ 0 & M_b & 0 & 0 & 0 \\ 0 & 0 & J_b & 0 & 0 \\ 0 & 0 & 0 & M_{w1} & 0 \\ 0 & 0 & 0 & 0 & M_{w2} \end{bmatrix},$$

$$C = \begin{bmatrix} c_2 & -c_2 & 0 & 0 & 0 \\ -c_2 & (c_2 + c_{11} + c_{12}) & (c_{11} - c_{12})L_a & -c_{11} & -c_{12} \\ 0 & (c_{11} - c_{12})L_a & (c_{11} + c_{12})L_a^2 & -L_a c_{11} & L_a c_{12} \\ 0 & -c_{11} & -L_a c_{11} & c_{11} & 0 \\ 0 & -c_{12} & L_a c_{12} & 0 & c_{12} \end{bmatrix},$$



$$K = \begin{bmatrix} k_2 & -k_2 & 0 & 0 & 0 \\ -k_2 & (k_2 + k_{11} + k_{12}) & (k_{11} - k_{12})L_a & -k_{11} & -k_{12} \\ 0 & (k_{11} - k_{12})L_a & (k_{11} + k_{12})L_a^2 & -L_a k_{11} & L_a k_{12} \\ 0 & -k_{11} & -L_a k_{11} & (k_{11} + k_{h1}) & 0 \\ 0 & -k_{12} & L_a k_{12} & 0 & (k_{12} + k_{h2}) \end{bmatrix}$$

- [18]. M. Qiao, M. Mizumoto, *PID Type Fuzzy Controller and Parameters Adaptive Method*, Fuzzy Sets and Systems, 78, 23-25, 1996.
- [19]. Rail Technology Unit, *The Manchester Benchmarks for Rail Vehicle Simulation*, Manchester Metropolitan University, 1998.

7. References

- [1]. H. Jenkins, J. Stephenson, G.A. Clayton, G.W. Morland and D. Lyon, *The Effect of Track and Vehicle Parameters on Wheel/Rail Vertical Dynamic Forces*, Railway Engineering Journal, January, 2-16, 1974.
- [2]. C. Esveld, *Modern Railway Track*, MRT Productions, Netherlands 2001.
- [3]. R.V. Dukkipati and R. Dong, *The Dynamic Effects of Conventional Freight Car Running Over A Dipped-Joint*, Vehicle System Dynamics, 31, 95-111, 1999.
- [4]. Stribersky, A. Kienberger and H. Muller, *Design and Evaluation of a Semi-Active Damping System for Rail Vehicles*, Vehicle System Dynamics Supplement, 28, 669-681, 1998.
- [5]. E. Foo and R.M. Goodall, *Active Suspension Control of Flexible-Bodied Railway Vehicles Using Electro-Hydraulic and Electro-Magnetic Actuators*, Control Eng. Practice, 8, 507-518, 2000.
- [6]. X. Lei, N.-A. Noda, *Analyses of Dynamic Response of Vehicle and Track Coupling System with Random Irregularity of Track Vertical Profile*, Journal of Sound and Vibration, 258(1), 147-165, 2002.
- [7]. R. Guclu, *Active Control of Seat Vibrations of a Vehicle Model Using Various Suspension Alternatives*, Turkish J. Eng. Env. Sci., 27, 361- 373, 2003.
- [8]. R. Guclu, *Fuzzy Logic Control of Seat Vibrations of a Non-Linear Full Vehicle Model*, Nonlinear Dynamics, 40, 21-34, 2005.
- [9]. M.V.C. Rao, and V. Prahlad, *A Tunable Fuzzy Logic Controller for Vehicle-Active Suspension Systems*, Fuzzy Sets and Systems, 85, 11-21, 1997.
- [10]. N. Yagiz, A. Gursel, *Active Suspension Control of a Railway Vehicle with a Flexible Body*, Int. J. Vehicle Autonomous Systems, 3(1), 80-94, 2005.
- [11]. M. Metin, R. Guclu, H. Yazici and N.S. Yalcin, *Fuzzy Logic Control of High Speed Rail Vehicle Vibrations on Corrugated Rail*, The 36th International Congress & Exhibition on Noise Control Engineering, Inter-noise 2007, Istanbul, Turkey, 37, Aug. 28-31, 2007.
- [12]. M. Metin, R. Guclu, H. Yazici and N.S. Yalcin, *Rayli Tasit Titresimlerinin Bulanik PID Kontrolor ile Kontrolu*, TOK'07 Otomatik Kontrol Ulusal Toplantisi, 4-7 September, Sabanci Universitesi, Istanbul, 312-317, 2007.
- [13]. M. Metin, R. Guclu, H. Yazici and N.S. Yalcin, *A Comparison of Control Algorithms for a Half Rail Vehicle Model under Track Irregularity Effect*, Mechanics Conference and 100th Anniversary of Engineering of Science and Mechanics Department, Virginia Polytechnic and State University, Blacksburg-VA, USA, Jun. 29-30 2008.
- [14]. M. Metin and R. Guclu, *Olcekleme Carpanlarini Kendiliginden Ayarlayabilen PID Tipli Bulanik Kontrolor ile Bir Hafif Metro Aracina Ait Dusey Titresimlerin Aktif Kontrolu*, TOK'08 Otomatik Kontrol Ulusal Toplantisi, ITU, S.551-556, Istanbul, 13-15 November, 2008.
- [15]. K.J. Astrom and T.H. Hagglund, *New tuning methods for PID controller*, Proceeding of the 3rd European Control Conference, Rome, Italy, 1995.
- [16]. M. Araki, *PID Control*, Control Systems, Robotics, and Automation, Vol 2, 1992.
- [17]. K.J. Astrom, T.H. Hagglund, *The Future of PID Control*, Control Engineering Practice 9, 1163-1175, 2001.



An Electro-Hydraulic Spherical Manipulator Dynamic Modelling and Simulation: A Case Study

Mehmet TOPALBEKİROĞLU^{1*}, L. Canan DÜLGER², Ali KİREÇCİ¹

^{1*} Department of Textile Engineering, Faculty of Engineering,
University of Gaziantep, 27310 Gaziantep,
tbekir@gantep.edu.tr

² Department of Mechanical Engineering, Faculty of Engineering,
University of Gaziantep, 27310 Gaziantep,
dulger@gantep.edu.tr

¹ Department of Textile Engineering, Faculty of Engineering,
University of Gaziantep, 27310 Gaziantep,
kirecci@gantep.edu.tr

Abstract

The dynamic modelling and experimental implementation of a PID controller on a spherical hydraulic robot are studied in the present paper. The mathematical model of the manipulator and its drive system is developed by applying Lagrange's equations. The mathematical model and the real system under the applied controller are tested for tracking of several example trajectories, and it is observed that the tracking performance of both systems are quite close to each others. The graphical results of the simulations and experimental applications are presented with comment.

Keywords: Dynamic modelling, numerical simulation, spherical manipulator, electro-hydraulic servo valve.

1. Introduction

Industrial manipulators can perform a variety of different tasks in factories; the loading and unloading of a work piece, welding, raw or partly processed material handling, and assembly of processed parts forming a product can be given as examples. Manipulators can be classified according to their kinematics structures as Cartesian (rectangular), cylindrical, spherical (polar), revolute (articulated) and Scara manipulator. Another classification can be done on the basis of power systems as electric, hydraulic or pneumatic. An electro-hydraulic servo-valve connects the electronic and hydro-mechanical parts of the system. Knowledge of mechanics, magnetism, hydraulics and electronics needed to understand the dynamics of these systems. [1-3].

A previously designed and manufactured hydraulic spherical manipulator named as ARTISAN (a project

supported by State Planning Organization of Turkey) is used for the experimental study. The manipulator has two revolute and one prismatic joint, and the moves of this manipulator are the base rotation, the elevation angle and the reach by occupying a large volume. Many different research studies were carried on this manipulator. Gültekin [4] has performed design and testing of a control software for a RRP robot manipulator. Kapucu [5] has considered adaptive control of this manipulator by using visual data. Doğan [6] has performed vocal control of an industrial manipulator, and ARTISAN was used for this purpose. Topalbekiroğlu [7] has then considered control of this manipulator by using adaptive control and learning methods. Kapucu et al [8] have addressed a hybrid input shaping method to reduce the residual swing of a simply suspended object moved by ARTISAN. Kirecci et al [9] have presented a study with self tuning control on the manipulator referred. Kirecci et al [10] have recently performed a case study on experimental evaluation of model reference adaptive control for hydraulic robot, ARTISAN. Kapucu et al [11] have presented an approach to determine the geometric parameters of a robot manipulator by visual data. Same robot is used in the study.

Many other research studies on similar hydraulic servo systems may be found in literature. For example, Borovaç et al [12] have considered the mathematical model of actuators on control synthesis and simulation. In this study, manipulator configurations powered by electromechanical and hydraulic actuators were included. Bayseç and Jones [13] have performed an improved



mathematical model of an electro-hydraulic servo valve together with the experimental work. Yun and Cho [14] have then applied an adaptive model control technique to a hydraulic servo system subjected to unknown disturbances. Kim and Cho [15] have done suboptimal PID control for a load sensing hydraulic servo system. Fitzsimons and Palazzolo [16] have presented a study on a model of the hydraulic system dynamics together with its state space model. Liu and Handroos [17] have discussed on sliding mode control for a class of hydraulic position servo and the experimental results were given.

In the study presented, dynamics of the manipulator, ARTISAN is combined with the hydraulic actuator characteristics which are not included in previous studies. Lagrange equations are applied; the systems equations of motion are derived. Based on the mathematical model, simulation studies are carried out, and the dynamic system equations are solved numerically by using an integration routine. So the effect of each parameter is easily examined with the model. Two trajectory examples are presented together with the experimental system and simulation studies. Initially torques and forces to be applied to the actuating system of the manipulator are calculated. The movements of the end-effector on the desired trajectory are then performed. Iterative tuning (for PID controllers) is applied during simulation. Experimental and simulation tracking results are included.

2. The experimental system

The experimental system is available at the Laboratory of Dynamic systems in University of Gaziantep, Department of Mechanical Engineering. Fig.1 represents a view of the experimental system. The system consists of a hydraulically driven spherical manipulator, a PC, an interface card for required communications between the manipulator and computer, hydraulic actuators and servo amplifiers and position transducers fitted to each joint.

Joint actuator drives are produced by Bosch NG6 Regenventils and servo amplifiers are available on the manipulator. The joints are actuated by electro-hydraulic servo valves controlled by analog control signals by a PC. The supply of hydraulic pressure and flow to the servo valves are provided by 22 kW hydraulic power unit which can supply up to 95 lit/min at 0.12 MPa. The feedback is performed by position potentiometers connected to each joint. The range of movement of each joint can be given as

Joint 1 (revolute)	$-160^{\circ} \leq \theta_0 \leq 163^{\circ}$
Joint 2 (revolute)	$-39^{\circ} \leq \theta_1 \leq 15^{\circ}$
Joint 3 (prismatic)	$42.95 \text{ cm} \leq r_2 \leq 142.75 \text{ cm}$



Fig.1. A view from the experimental system

3. Manipulator dynamics

The mathematical model of manipulation system consists of the manipulator configuration and the actuator model. The degree of the complexity of the model is quite important to get a better representation of the real system. However, some simplifying assumptions are taken while deriving a mathematical model of the manipulator. For example; no friction in the joints, fluid friction, nonlinear effects, and transmission losses etc. are neglected.

The configuration of RRP manipulator is given in Fig.2. It is described by moving two revolute joints and one prismatic link. Initially the kinematics relations between coordinate variables are defined. The position, velocity and acceleration relationships between the joint and the coordinate variables are then established. Details of the kinematics analysis are included in Appendix 1. Here the first two joints from the ground are revolute joints (θ_0 - the base rotation, θ_1 - the elevation angle) and the last joint is prismatic (r_2 -the reach).

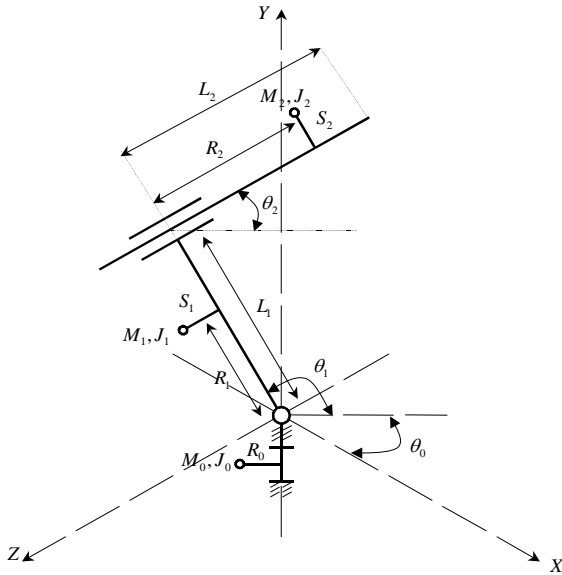


Fig.2. RRP manipulator configuration

M_0, M_1, M_2 the link masses (kg)
 J_0, J_1, J_2 the link moment of inertias (kg/m²)
 L_1, L_2 the link lengths (m)
 R_0, R_1, S_1, S_2 distances to the links centre of gravities (m)

$\theta_0, \dot{\theta}_0, \ddot{\theta}_0$ The angular displacement, velocity and acceleration of the base rotation

$\theta_1, \dot{\theta}_1, \ddot{\theta}_1$ The angular displacement, velocity and acceleration of the elevation angle

$r_2, \dot{r}_2, \ddot{r}_2$ The linear displacement, velocity and acceleration for the output link

The equations of motion are derived by using Lagrange's equation [19, 20]. The generalized coordinates are θ_0, θ_1 , and r_2 . The dynamic equations of spherical manipulator are a set of highly nonlinear coupled equations. Torques are developed by joint motors, and determined by using the electro-hydraulic servo valve dynamics which is included in the next section.

The equations of motion for the manipulator are

$$TORQUE0 = [J_0 + M_0 r_0^2 + J_1 \cos^2 \theta_1 + J_2 \sin^2 \theta_1] \ddot{\theta}_0 + \frac{d}{dt} \left[M_1 \frac{\partial v_1}{\partial \dot{\theta}_0} \right] + \frac{d}{dt} \left[M_2 \frac{\partial v_2}{\partial \dot{\theta}_0} \right] \quad (1)$$

$$TORQUE1 = [J_1 + J_2] \ddot{\theta}_1 + \frac{d}{dt} \left[M_1 \frac{\partial v_1}{\partial \dot{\theta}_1} \right] + \frac{d}{dt} \left[M_2 \frac{\partial v_2}{\partial \dot{\theta}_1} \right] + \frac{1}{2} [J_1 + J_2] \dot{\theta}_0^2 \left[\frac{\partial \cos^2 \theta_1}{\partial \theta_1} + \frac{\partial \sin^2 \theta_1}{\partial \theta_1} \right] + \frac{\partial V_{1g}}{\partial \theta_1} + \frac{\partial V_{2g}}{\partial \theta_1} \quad (2)$$

$$FORCE = \frac{d}{dt} \left[M_1 \frac{\partial v_1}{\partial \dot{r}_2} \right] + \frac{d}{dt} \left[M_2 \frac{\partial v_2}{\partial \dot{r}_2} \right] - \frac{\partial V_{2g}}{\partial r_2} \quad (3)$$

4. Electro-hydraulic servo valve dynamics

This section covers a mathematical model for the hydraulic actuator in which its schematic representation is given in Fig.3. The actuator cylinder lies in a follower configuration to a critically centred three-land four-way spool servo valve with matched and symmetric orifices. The hydraulic power unit delivers a constant supply pressure P_s irrespective of the oil flow rate. Arrows at the ports indicate the assumed directions of flows, and the numbers at ports refer to the subscripts of the flow and the area at the ports. Before beginning the theoretical analysis we make the following assumptions; Hydraulic oil is incompressible. Only the inertial load system is taken into consideration. The servo valve has zero-lap construction and the discharge coefficients of its metering orifices are constant. [21-22]

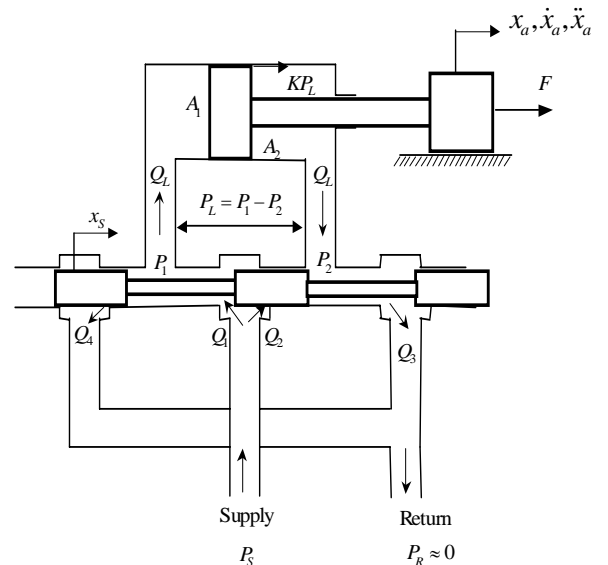


Fig.3. Schematic representation for the hydraulic actuator

Positioning of the spool x_s directs high pressure fluid flow to either one of the cylinder chambers and



connects the other chamber to the pump reservoir. This flow creates a pressure difference PL across the piston. This pressure difference multiplied by the piston area A_1 is what provides the active force F for the manipulator system. The change in force is proportional to the position of the spool with respect to centre, the relative velocity of the piston, and the leakage through the piston seals. In

reality, spool valve position x_s is controlled by a current-position feedback loop. The essential dynamics of the spool have been shown to resemble a first order system forced by a voltage. Here a PID (proportional-integral-derivative) controller is used to control spool valves in ARTISAN manipulator.

Referring to Fig. 3, for steady-state flow analyses, assume that the compressibility flows are zero, then

$$\begin{aligned} Q_L &= Q_1 - Q_4 \\ Q_L &= Q_3 - Q_2 \end{aligned} \quad (4)$$

Where Q_L is the flow rate through the load. Flow rates Q_1 , Q_2 , Q_3 , and Q_4 through the valve orifices are described by the orifice equation (Assuming the return line pressure P_R is neglected because it is usually much smaller than the other pressures involved). Therefore;

$$Q_1 = C_d A_{o1} \sqrt{\frac{2}{\rho} (P_s - P_1)} \quad (5)$$

$$Q_2 = C_d A_{o2} \sqrt{\frac{2}{\rho} (P_s - P_2)} \quad (6)$$

$$Q_3 = C_d A_{o3} \sqrt{\frac{2}{\rho} P_2} \quad (7)$$

$$Q_4 = C_d A_{o4} \sqrt{\frac{2}{\rho} P_1} \quad (8)$$

Where C_d is the discharge coefficient of the metering orifice of the servo valve. A_{o1} , A_{o2} , A_{o3} and A_{o4} are servo valve orifice areas. P_1 and P_2 represents actuator pressures. P_s is supply pressure and ρ is density of the hydraulic oil. Assume that the valve orifices are matched and symmetrical, which is the case for most of the spool valves manufactured. Matched orifices mean that

$$A_{o1} = A_{o3} \quad A_{o2} = A_{o4}$$

and symmetrical orifices mean that

$$A_{o1}(x_s) = A_{o2}(-x_s) \quad A_{o3}(x_s) = A_{o4}(-x_s)$$

Matched and symmetrical orifices indicate that

$$A_{o1}(x_s) = A_{o2}(-x_s) = A_{o3}(x_s) = A_{o4}(-x_s) = A_o(x_s) \quad (9)$$

Only one orifice area A needs to be defined. If the orifice areas are linear with valve stroke, only one defining parameter is required: the width of the slot in the valve sleeve w . w is the rate of change of orifice area with stroke, and is called the *area gradient*. The relationship between w and A is given by

$$A_o(x_s) = wx_s \quad (10)$$

If the orifices are matched and symmetrical, then

$$Q_2 = Q_4 \quad \text{and} \quad Q_1 = Q_3 \quad (11)$$

Substituting equations (5) and (7) into (11) yields

$$P_s = P_1 + P_2 \quad (12)$$

Which together with the definition of P_L

$$P_L = P_1 - P_2 \quad (13)$$

$$P_1 = (P_s + P_L)/2 \quad \text{and} \quad P_2 = (P_s - P_L)/2 \quad (14)$$

The leakage flows (Q_2 and Q_4 when x_s is positive; Q_1 and Q_3 when x_s is negative) for such a valve are zero because the geometry is assumed ideal. Therefore by substituting equations (7) and (14) into equation (4) yields;

$$Q_L = C_d wx_s \sqrt{\frac{P_s - P_L}{\rho}} \quad x_s > 0 \quad (15)$$

$$Q_L = -C_d wx_s \sqrt{\frac{(P_s + P_L)}{\rho}} \quad x_s < 0 \quad (16)$$

The flow-pressure equations (15) and (16) are obtained if the orifice area of slide valve is matching and symmetric. The pressure and direction of flow change with loading condition. An analytical form describing such relationship can be obtained by setting up the flow equations through the spool port and clearance restrictors and the equations of continuity of flow [21-22]. They are included in Appendix B as the spool valve and the actuator section.

4.1. Conventional Controller Action

Hydraulic systems can be applied as position, speed and pressure control systems. The controllers can be based on conventional PD, PID or advanced control techniques [9, 10]. In this study, a PID controller is applied for the hydraulic robot model. Fig. 4 shows block diagram for RRP manipulator with PID controller.

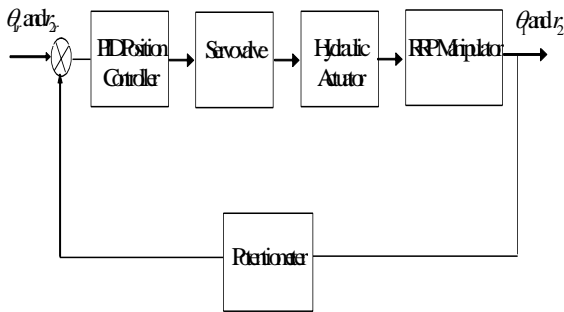


Fig.4. Block diagram for RRP Manipulator with PID controller

Since the base is fixed, the configuration has been a RP model, and the spool valve displacements (given in Appendix B) are written for two robot joints as

$$x_{s1} = K_{p1}(\theta_{1r} - \theta_1) + K_{d1}(\dot{\theta}_{1r} - \dot{\theta}_1) + K_{i1} \int_0^t (\theta_{1r} - \theta_1) dt \quad (17)$$

$$x_{s2} = K_{p2}(r_{2r} - r_2) + K_{d2}(\dot{r}_{2r} - \dot{r}_2) + K_{i2} \int_0^t (r_{2r} - r_2) dt \quad (18)$$

Where K_{p1} , K_{p2} , K_{d1} , K_{d2} , K_{i1} and K_{i2} are the proportional, derivative and integral gains for the controller. Here θ_{1r} and r_{2r} represent the reference data for the revolute and prismatic joints. Optimal gains values can be found by using Ziegler and Nichols PID controller tuning methods.

5. Structure Configuration

The relationships between pressure and torque or force are obtained by using the structure configuration of the robot given in Fig. 5

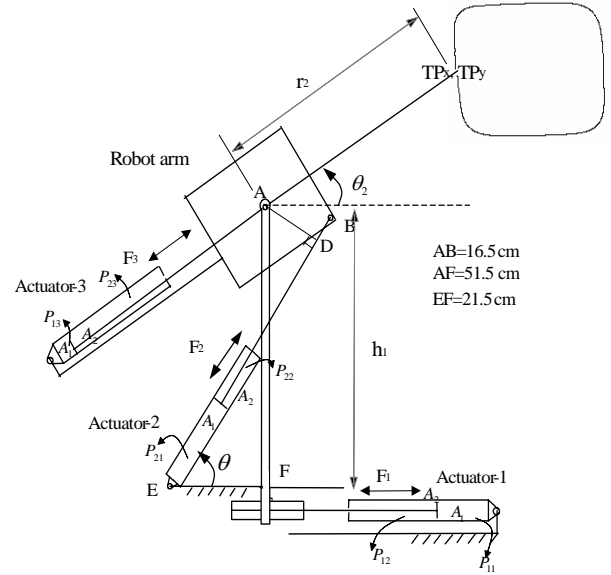


Fig.5. Structure configuration

$$|AD| = \frac{(|AF| + |EF| \tan \theta)}{\sqrt{1 + \tan^2 \theta}} \quad (19)$$

$$\tan \theta = \frac{(|AF| \cos(58^\circ + \theta_2) + |AF|)}{(|AB| \sin(58^\circ + \theta_2) + |EF|)} \quad (20)$$

The resulting torque and force equations used in equations (1), (2) and (3) are given as.

$$TORQUE_0 = F_1 R \text{ and } F_1 = P_{11} A_1 - P_{21} A_2 \quad (21)$$

$$TORQUE_1 = F_2 |AD| \text{ and } F_2 = P_{12} A_1 - P_{22} A_2 \quad (22)$$

$$FORCE = F_3 = P_{13} A_1 - P_{23} A_2 \quad (23)$$

Where A_1 and A_2 represent actuator cross-sectional areas. The unknown pressure values P_{11} , P_{21} , P_{12} , P_{22} , P_{13} , and P_{23} in equations (21) to (23) for each joint can be calculated by using equations (B.4), (B.6), (B.8) and (B.10) given in Appendix B together with controller equations (17) and (18).

5.1. Trajectory Planning and Inverse Kinematics

A motion design software MOTDES[18] is applied for planning of example trajectories. These trajectories are initially designed at the end-effectors level and then they are converted into joint angles of the manipulator by inverse kinematics solution as shown in Fig. 6 and Fig. 7. The software uses polynomial functions to produce motion curves, since it is the most suitable mathematical function to generate motion curves which are continuous



up to the desired derivative, such as that velocity, acceleration and jerk. However, high order polynomial functions may produce unexpected oscillations between the boundary points, therefore, the power of the polynomial functions are restricted by 5th order to eliminate the unexpected oscillations in the motion curves. Consequently, each trajectory is divided into segments then the motion curves of each segment are produced by polynomial functions and finally the whole trajectory can be obtained by combining the motion segments. Designing of a trajectory in computer graphic environment gives the choice of inspection of motion curves and correction option if there are some undesirable circumstances by changing the boundary conditions in position, velocity or acceleration level.

The joint motions of the manipulator are obtained by inverse kinematics solution. Therefore, each trajectory at the end-effectors level is stored as a data file consisting of 180 data points. The joint coordinates of the manipulator are then calculated using the link lengths and the initial geometry as given in Fig. 5.

$$TP_x = r_2 * \cos\theta_2 \quad \text{and} \quad TP_y = h_1 + r_2 * \sin\theta_2$$

Where TP_x and TP_y correspond to the trajectory point at the end-effectors level. The corresponding joint positions r_2 and θ_2 are obtained for each data point to be used as control inputs for the manipulator. Here h_1 Indicates $|AF|$ distance given in Fig.5.

6. Computer simulation

Equations (1) to (3), and (21) to (23) represent the mathematical model which include the manipulator and the servo valve dynamics. The manipulator and the actuator equations are coupled together. The assumption is that there is single-input single-output independent joint control structure (SISO). The base is taken as stationary, not moving and the coordinates θ_1 and r_2 are used in simulation. The system equations (2) and (3) are taken together with equations (22) and (23) during integration, like a 2 dof system. Equations (2) and (3) are represented as 1st order differential equations. Four 1st order differential equations are resulted for integration. They are used together with equations (22) and (23) which are included in Appendix B.

To obtain solutions for ODEs, a numerical integration scheme, fourth order Runge-Kutta is implemented. The manipulator equations are converted into 1st order ones, a time increment (integration step size) $\Delta h=t$ is defined, and taken as 0.0925 seconds.

A computer program is written in Pascal. Many of the system parameters have been determined by measuring and calculations. The manipulator and the

hydraulic actuator parameters are listed in Table 1 and Table 2. The manipulator parameters; link lengths, moment of inertias, masses, hydraulic actuator constants, controller tuning gains, and the initial conditions for the positions and velocities of joints are to be specified first.

A conventional PID controller is introduced to the control architecture. The tuning of the gains in the controller is performed by many independent runs. So the movement of the arm in a desired position is obtained by simultaneous solutions of the actuator and the manipulator equations for each simulation interval. The output of simulation then gives a description of the response as joint displacements, velocities and accelerations.

Table 1 Mechanical Parameters for ARTISAN Manipulator

$R_0 = 0.0$ mm	$R_1 = 280$ mm	$S_1 = 7$ mm	$S_2 = 400$ mm
$L_1 = 0.0$ mm	$L_2 = 752$ mm		
$M_0 = 79$ kg	$M_1 = 49$ kg	$M_2 = 50$ kg	
$J_0 = 1.198$ kg m ²	$J_1 = 1.95$ kg m ²	$J_2 = 6.8$ kg m ²	

Table 2 Parameters for Hydraulic Actuators

$A_1 = 1.963 \times 10^{-3}$ m ²	$A_2 = 1.348 \times 10^{-3}$ m ²	$C_d = 0.6$	$w = 0.018$ mm
$\rho = 860$ kg/m ³	$P_s = 6.9$ MPa	$R_a = 60$ mm	$K = 9 \times 10^{-7}$ m ⁵ / l

7. Simulated and Experimental results

A series of experiments and simulations are performed. Based on the system model derived, the proportional and the derivative gains and the pressure settings are obtained. The tracking trajectories for joint 2 and 3 are presented in Figs. 6 and 7 respectively. Motion profiles include 180 points which are performed in 16.65 seconds in both examples.

Figs. 6a and 6b represent the simulated, reference and experimental points for the revolute and the prismatic joint tracking of the first motion. In Figs. 6a and 6b, the vertical axes are given in radians and centimetres, and the horizontal axes in seconds. In Fig. 6c, the output is represented in centimetres as the coordinates of the end effector x, y. Experimental, reference and simulated points are shown by thick, thin and dotted lines respectively. The controller proportional, derivative and integral gains are $K_{p1}=0.3$, $K_{d1}=0.02$ and $K_{i1}=0.01$ for the elevation angle.

Figs.7a and 7b represent the simulated, reference and experimental points for the revolute and the prismatic joint tracking of the second motion. In Figs. 7a and 7b, the vertical axes are given in radians and centimetres, and the horizontal axes in seconds. In Fig.7c, the output is represented in centimetres as the coordinates of the end effector x, y. Experimental, reference and simulated points are shown by thick, thin and dotted lines respectively. The



controller proportional, derivative and integral gains are $K_{p2}=0.28$, $K_{d2}=0.016$ and $K_{i2}=0.008$ for the reach.

Simulated and experimental responses are compared and the accuracy of the model is examined. Although similar following characteristics are obtained, throughout the motion, small variances are seen between the experimental and simulated results. It can be noticed in both results that since a conventional PID controller is introduced. However, in recent studies performed with ARTISAN [9, 10], model reference adaptive control (MRAC) and self tuning control (STC) are applied to the manipulator, better trajectory tracking are obtained experimentally. Here since the modelling is performed with a conventional PID controller available, the experimental results are presented under PID controller for consistency. There are also many simplifying assumptions taken during the modelling procedure. Satisfactory response characteristics are produced in both examples. So the mathematical model can be regarded as completely sufficient for the system.

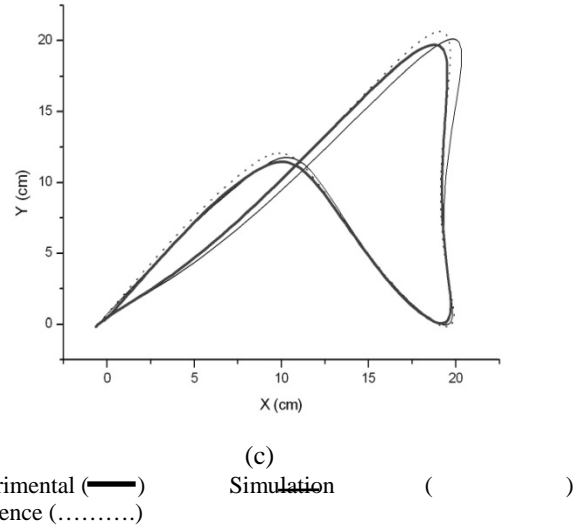
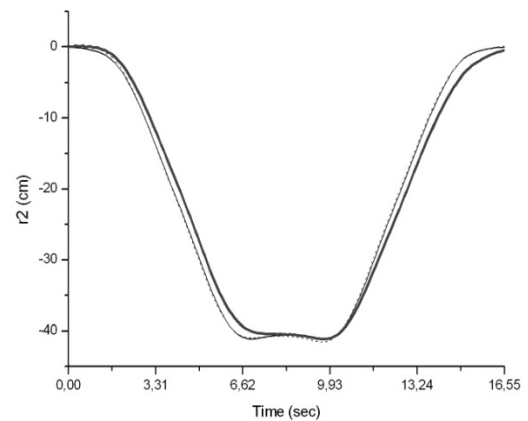
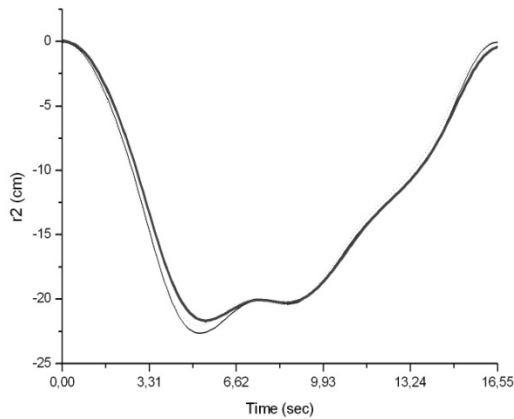
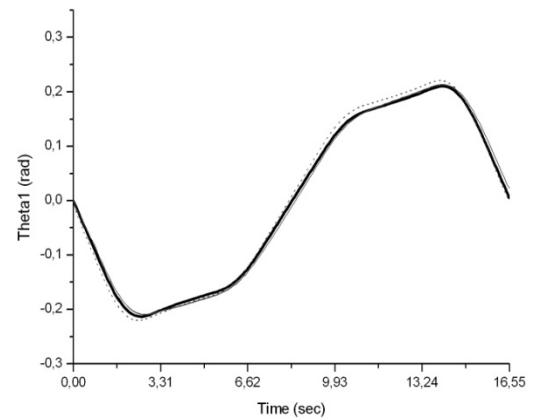
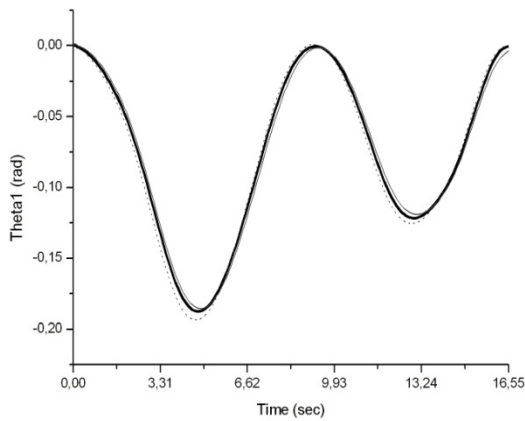


Fig.6. Results for 1st motion



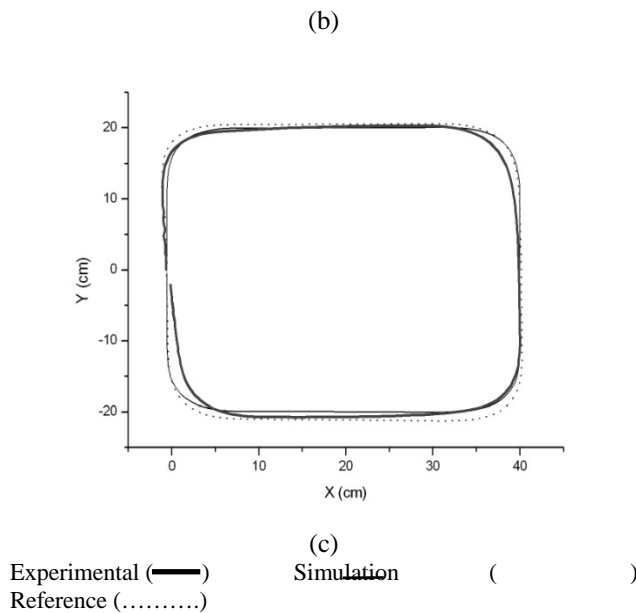


Fig.7. Results for 2nd motion

8. Conclusions

The dynamical model of the spherical manipulator-hydraulic actuator was obtained. Lagrangian mechanics was applied while deriving equations of motion of the spherical manipulator. The manipulator was considered with two moving axes as RP configuration, since the base was taken as fixed. The manipulator-actuator equations were solved numerically. Two characteristically different trajectory examples were designed and tested. The general form of the model has contained lengthy expressions, and they were given in closed form. A conventional PID controller was applied to the actual system of manipulator-actuator; the simulated and experimental results were obtained by implementing the motion profiles and compared.

The simulated and experimental results have shown that good tracking performances with designed trajectories were obtained. No oscillatory behaviour was seen in both results. Difference in the simulated results was simply caused by assumptions taken while deriving the mathematical model of the manipulator-actuator system. Some parameters for the servo valve were calculated or taken as the actuator data. Link masses and inertias of the manipulator were also calculated by measuring the link dimensions on the available manipulator. For the first trajectory (Fig. 6), a working space of 20 cm x 20 cm was taken. Tracking error of 0.55° at maximum was obtained for the first axis corresponding to 0.7 cm on total trajectory in the experimental results. For the second trajectory, a working space of 40 cm x 40 cm was taken

giving a big working space. Tracking error at maximum 0.6° was obtained causing nearly 0.9 cm error on total trajectory. Satisfaction on the model was simply provided. However the experimental system [9,10] has already been studied by using advanced control techniques, and better results on tracking were presented.

Acknowledgements:

The authors wish to thank for the advices and comments taken by Prof. Dr. S. Kapucu, Gaziantep University, Mech. Eng. Dept. for the electro hydraulic servo valves.

References

- [1]. A.J. Koivo, *Fundamentals for control of robotic manipulators*, John Wiley and Sons Inc., 1989.
- [2]. E.I. Rivin, *Mechanical design of robots*, McGraw Hill, 1988.
- [3]. W. Stadler, *Analytical robotics and mechatronics*, Mc Graw Hill, 1995.
- [4]. H.M. Gültekin, *Design and testing of a control software for a RRP robot manipulators*, M.Sc.Thesis, University of Gaziantep, 1994.
- [5]. S. Kapucu, *Adaptive control of a robot manipulator by visual data*, Ph.D.Thesis, University of Gaziantep, 1994.
- [6]. H.S. Doğan, *Vocal control of an industrial robot manipulator*, M.Sc.Thesis, University of Gaziantep, 1995.
- [7]. M. Topalbekiroğlu, *Control of robotic systems by using adaptive control and learning methods*, M.Sc.Thesis, University of Gaziantep, 1996.
- [8]. S. Kapucu, G. Alici, S. Bayseç, *Residual swing vibration reduction using a hybrid input shaping method*, Mechanism and Machine Theory, 36, pages 311-326, 2001.
- [9]. A. Kirecci, İ. Eker, L.C. Dülger, *Self-tuning as conventional method*, Electrical Eng., Springer-Verlag, 85, pages 101-107, 2003.
- [10]. A. Kirecci, M. Topalbekiroğlu, İ. Eker, *Experimental evaluation of a model reference adaptive control for a hydraulic robot: a case study*, Robotica, Vol.21-01, pages 71-78, 2003.
- [11]. S. Kapucu, S. Bayseç, 'Determination of the geometric parameters of a robot manipulator by visual data', Strojnický Casopis, Journal of Mech. Eng., pages 143-162, 2005.
- [12]. B. Borovaç, M. Vukobratovic, D. Stokic, *Analysis of the influence of actuator model complexity on manipulator control synthesis*, Mechanism and Machine Theory, Vol.18, No.2, pages 113-122, 1983.
- [13]. S. Bayseç, J.R. Jones, *An improved model of an electro-hydraulic servo-valve*, 7th IFToMM Congress-Sevilla, pages 118-124, 1987.
- [14]. J.S. Yun, H.S. Cho, *Application of an adaptive model following control technique to a hydraulic servo system subjected to unknown disturbances*, J. of Dynamic Systems Measurement And Control, Vol.113, pages 479-486, 1991.
- [15]. Kim S.D., Cho H.S., *A Suboptimal controller design method for the energy efficiency of a load sensing hydraulic servo system*, Journal of Dyn. Sys. Meas. And Control, Vol. 113, pages 487-493, 1991.
- [16]. P.M. Fitzsimons, J.J. Palazzolo., *Part I: Modelling of a one-degree-of-freedom active hydraulic mount*, Journal of Dynamic. Systems Measurement and Control, Vol. 118, pages 439-442, 1996.
- [17]. Y. Liu, H. Handroos, *Technical note sliding model control for a class of hydraulic position servo*, Mechatronics, 9, (1999), 113-123.
- [18]. A. Kirecci, M.J. Gilmartin, *Improved trajectory planning using arbitrary power polynomials*, Proceedings of IMechE Part I: Journal of System and Control Engineering, Vol.208, pages 3-13, 1994.



- [19]. T.D. Burton, *Introduction to Dynamic Systems Analysis*, McGraw Hill, 1994.
[20]. V. H. Vu, R.S. Esfandiari, *Dynamic systems-modelling and analysis*, McGraw Hill, 1997.
[21]. Merritt, H. E., *Hydraulic Control Systems*, Wiley, New York, 1967.
[22]. John S. Cundiff, CRC Press, *Fluid Power Circuits and controls: Fundamentals and Applications*, 2002.

Appendices

Appendix A-Manipulator Kinematics

Referring to manipulator configuration given in Fig. 2, the geometric relation between θ_1 and θ_2 can be given as

$$\theta_1 = \theta_2 + 90^\circ$$

The positions to the centre of gravity of link1;

$$\begin{aligned} x_1 &= (R_1 \cos \theta_1 - S_1 \sin \theta_1) \cos \theta_0 \\ y_1 &= (R_1 \cos \theta_1 - S_1 \sin \theta_1) \sin \theta_0 \\ z_1 &= (R_1 \sin \theta_1 + S_1 \cos \theta_1) \end{aligned} \quad (A.1)$$

and the positions to the centre of gravity of link2,

$$\begin{aligned} x_2 &= (L_1 \cos \theta_1 + r_2 \sin \theta_1 + S_2 \cos \theta_1) \cos \theta_0 \\ y_2 &= (L_1 \cos \theta_1 + r_2 \sin \theta_1 + S_2 \sin \theta_1) \sin \theta_0 \\ z_2 &= (L_1 \sin \theta_1 - r_2 \cos \theta_1 + S_2 \cos \theta_1) \end{aligned} \quad (A.2)$$

By taking derivatives of the positions, the velocities at the centre of gravities (v_1 and v_2) are found. Relative link velocities are then derived and substituted into the kinetic energy equations for each link. Kinetic and potential energies for each link are then found as:

$$\begin{aligned} T_0 &= \frac{1}{2} J_0 \dot{\theta}_0^2 + \frac{1}{2} M_0 v_0^2 \\ T_1 &= \frac{1}{2} J_1 \dot{\theta}_1^2 + \frac{1}{2} M_1 v_1^2 \\ T_2 &= \frac{1}{2} J_2 \dot{\theta}_2^2 + \frac{1}{2} M_2 v_2^2 \end{aligned} \quad (A.3)$$

$$\text{where } v_1^2 = \dot{x}_1^2 + \dot{y}_1^2 + \dot{z}_1^2 \quad \text{and} \quad v_2^2 = \dot{x}_2^2 + \dot{y}_2^2 + \dot{z}_2^2$$

$$\begin{aligned} V_{0g} &= M_0 g h_0 \\ V_{1g} &= M_1 g (R_1 \sin \theta_1 + S_1 \cos \theta_1) \\ V_{2g} &= M_2 g (L_1 \sin \theta_1 - r_2 \cos \theta_1 + S_2 \sin \theta_1) \end{aligned} \quad (A.4)$$

where h_0 is a constant.

Appendix B- Spool Valve and Actuator Equations

Referring to Fig. 3 given in text, assume fluid compressibility at the actuator is neglected and the relation between the effects of piston motion, leakage and load flow rates is written as;

$$Q_L = A_i \dot{x}_{aj} \mp KP_{ij} \quad (B.1)$$

Sign \mp in equation (B.1) is changed with respect to positive or negative spool displacement, and the actuator speed. Here, j represents number of each actuator $j=1,2$ and 3. i indicates number of subscription of actuator cross-sectional area $i = 1,2$. K is the coefficient of leakages flow and \dot{x}_{aj} is the actuator speed. [21-22] Positive spool displacement ($x_{sj} > 0$) for each actuator and $\dot{x}_{aj} \geq -KP_s / A_1$, the quadratic in P_{1j} is obtained by substituting equations (B.1) into (15) in the text given (Section 4):

$$Q_L = C_d w x_s \sqrt{\frac{2}{\rho} (P_s - P_{1j})} = A_1 \dot{x}_{aj} + KP_{1j} \quad (B.2)$$

$$\begin{aligned} 0 &= P_{1j}^2 (K^2 P_s) + P_{1j} (2A_1 \dot{x}_{aj} KP_s + 2K_3^2 x_{sj}^2) \\ &+ P_s A_1^2 \dot{x}_{aj}^2 - 2K_3^2 x_{sj}^2 P_s \\ a &= K^2 P_s, \quad b = 2A_1 \dot{x}_{aj} KP_s + 2K_3^2 x_{sj}^2 \quad \text{and} \\ c &= P_s A_1^2 \dot{x}_{aj}^2 - 2K_3^2 x_{sj}^2 P_s \end{aligned}$$

$$\text{and } P_{1j} = (-b + \sqrt{b^2 - 4ac}) / 2a \quad (B.3)$$

Where K_3 is the flow gain of spool ($K_3 = C_d w \sqrt{\frac{P_s}{\rho}}$,

w is the port width of the servo valve).

$$\text{for } \dot{x}_{aj} \leq -KP_s / A_1$$

$$\begin{aligned} 0 &= P_{1j}^2 (K^2 P_s) + P_{1j} (2A_1 \dot{x}_{aj} KP_s - 2K_3^2 x_{sj}^2) \\ &+ P_s A_1^2 \dot{x}_{aj}^2 + 2K_3^2 x_{sj}^2 P_s \\ a &= K^2 P_s, \quad b = 2A_1 \dot{x}_{aj} KP_s - 2K_3^2 x_{sj}^2, \quad \text{and} \\ c &= P_s A_1^2 \dot{x}_{aj}^2 + 2K_3^2 x_{sj}^2 P_s \end{aligned}$$

$$\text{and } P_{1j} = (-b - \sqrt{b^2 - 4ac}) / 2a \quad (B.4)$$

For $x_{sj} > 0$, the quadratic in P_{2j} is obtained by substituting equations (B.1) into (16) in the text given (Section 4):

$$Q_L = C_d w x_s \sqrt{\frac{2}{\rho} P_2} = A_2 \dot{x}_{aj} - KP_{2j} \quad (B.5)$$

$$\begin{aligned} 0 &= P_{2j}^2 (K^2 P_s) + P_{2j} (-2A_2 \dot{x}_{aj} KP_s - \text{sign}(\dot{x}_{aj}) 2K_3^2 x_{sj}^2) \\ &+ P_s A_2^2 \dot{x}_{aj}^2 \\ a &= K^2 P_s, \quad b = -2A_2 \dot{x}_{aj} KP_s - \text{sign}(\dot{x}_{aj}) 2K_3^2 x_{sj}^2, \\ c &= P_s A_2^2 \dot{x}_{aj}^2 \end{aligned}$$



$$P_{2j} = (-b - \text{sign}(\dot{x}_{aj})\sqrt{b^2 - 4ac})/2a \quad (\text{B.6})$$

For negative spool displacement ($x_{sj} < 0$), the quadratic in P_{1j} is :

$$Q_L = C_d w x_s \sqrt{\frac{2}{\rho}} P_1 = A_1 \dot{x}_{aj} + K P_{1j} \quad (\text{B.7})$$

$$0 = P_{1j}^2 (K^2 P_s) + P_{1j} (2A_1 \dot{x}_{aj} K P_s + \text{sign}(\dot{x}_{aj}) 2K_3^2 x_{sj}^2) + P_s A_1^2 \dot{x}_{aj}^2$$

$$a = K^2 P_s, b = 2A_1 \dot{x}_{aj} K P_s + \text{sign}(\dot{x}_{aj}) 2K_3^2 x_{sj}^2, c = P_s A_1^2 \dot{x}_{aj}^2$$

$$\text{and } P_{1j} = (-b + \text{sign}(\dot{x}_{aj})\sqrt{b^2 - 4ac})/2a \quad (\text{B.8})$$

Condition $\dot{x}_{aj} \leq -K P_s / A_2$ expression for P_{2j} ;

$$0 = P_{2j}^2 (K^2 P_s) + P_{2j} (-2A_2 \dot{x}_{aj} K P_s + 2K_3^2 x_{sj}^2) + P_s A_2^2 \dot{x}_{aj}^2 - 2K_3^2 x_{sj}^2 P_s$$

$$a = K^2 P_s, b = -2A_2 \dot{x}_{aj} K P_s + 2K_3^2 x_{sj}^2, \text{ and}$$

$$c = P_s A_2^2 \dot{x}_{aj}^2 - 2K_3^2 x_{sj}^2 P_s$$

$$\text{and } P_{2j} = (-b + \sqrt{b^2 - 4ac})/2a \quad (\text{B.9})$$

Condition $\dot{x}_{aj} \geq K P_s / A_2$ expression for P_{2j} ;

$$0 = P_{2j}^2 (K^2 P_s) + P_{2j} (-2A_2 \dot{x}_{aj} K P_s - 2K_3^2 x_{sj}^2) + P_s A_2^2 \dot{x}_{aj}^2 + 2K_3^2 x_{sj}^2 P_s$$

$$a = K^2 P_s, b = -2A_2 \dot{x}_{aj} K P_s - 2K_3^2 x_{sj}^2, \text{ and}$$

$$c = P_s A_2^2 \dot{x}_{aj}^2 + 2K_3^2 x_{sj}^2 P_s$$

$$\text{and } P_{2j} = (-b - \sqrt{b^2 - 4ac})/2a \quad (\text{B.10})$$



Neural Network-based Nonlinear Control Design for Twin Rotor MIMO Systems

Alper BAYRAK^{1*}, Mohammad SALAH², Nitendra NATH³, and Enver TATLICIOGLU⁴

^{1*,4} Department of Electrical &
Electronics Engineering, Izmir Institute of Technology, Urla, Izmir, 35430 Turkey
alperbayrak@iyte.edu.tr

²Department of Mechatronics Engineering, Hashemite
University, Zarqa 13115, Jordan.

³Department of Electrical & Computer Engineering,
Clemson University, Clemson, SC 29634-0915, USA.

Abstract

In this paper, a robust tracking control law for twin rotor multi-input multi-output systems (TRMSs) is presented. The controller is developed by fusing a continuous nonlinear feedback component with a nonlinear neural network feedforward term. The controller is designed based on the assumption that the TRMS dynamic model is unknown. Numerical simulation results are provided to illustrate that the addition of the neural network feedforward component to the continuous nonlinear feedback component provides improved tracking performance.

1. Introduction

The twin rotor multi-input multi-output system (TRMS) is a laboratory set-up [1] which resembles main and tail rotors of a simplified helicopter model (see Figure 1). The TRMS is a highly nonlinear and complex system with significant cross-coupling which makes it rather difficult to derive accurate dynamic models to be utilized in the design of control algorithms. There has been some previous research in dynamic modeling of the TRMS where various analytical and artificial intelligence-based empirical approaches were utilized. In [2], Lagrangian approach was utilized to derive a dynamic model for the TRMS and the characteristics of the proposed model were analyzed. Rahideh and Shaheed [3] presented two dynamic models for the TRMS by utilizing Newtonian and Lagrangian approaches. Artificial intelligence-based empirical approaches such as genetic algorithms and neural networks were also utilized to develop dynamic models for the TRMS. These empirical approaches were usually used by adding an auxiliary term to the analytical model [4]. Ahmad et al. utilized system identification

techniques to derive dynamic models for one degree of freedom [5], [6] and two degrees-of-freedom [7], [8] TRMSs. In [4], Rahideh et al. derived dynamic models for a one degree-of freedom TRMS by using analytical approaches and neural networks. Ahmad et al. [9] utilized radial basis function based neural networks to model the dynamic behavior of the TRMS. In [10], Rahideh and Shaheed derived a dynamic model by utilizing Newtonian approach along with genetic algorithms. Shaheed [11] developed a dynamic model of the TRMS by utilizing feedforward neural networks with a resilient propagation algorithm. Toha and Tokhi [12] derived a dynamic model by utilizing system identification techniques fused with artificial neural networks. Review of relevant past research highlights the fact that the dynamic modeling of TRMS is difficult and remains an active research topic.

Classical control techniques such as proportional-integral derivative (PID) controllers were preferred commonly to control TRMSs. Liu et al. [13] proposed a PID controller with a method to obtain optimal parameters and then designed a fuzzy PID controller. In [14] and [15], Juang et al. utilized a switching grey prediction PID controller with genetic algorithms. Shih et al. [2] proposed two nonlinear controllers, namely a PD controller and a fuzzy PID controller, for set-point control of TRMSs. In [16], Rahideh and Shaheed proposed a hybrid fuzzy PID based controller for the one degree-of-freedom TRMS model that they derived. Lopez-Martinez et al. [17] designed an H^∞ controller which can be seen as a combination of a PID controller with time-varying gains and a computed-torque linearization controller. Robust, open-loop, adaptive, and feedback linearization control techniques were also investigated. In [18], Lu and Wen proposed an optimal

robust controller where the dynamic model of the TRMS was decomposed into two single-input single-output systems and the cross-coupling effects were treated as disturbance or parametric uncertainty. Karimi and Motlagh [19] proposed a robust controller based on a feedback linearization scheme to cope with the model uncertainties and unmeasured disturbances. Ahmad et al. [6] proposed a robust optimal controller. Su et al. [20] proposed a robust control scheme for a class of uncertain nonlinear systems which was applied to TRMSs. Rahideh et al. [21] developed an adaptive model inversion controller utilizing an artificial neural network compensator to reduce the inversion errors fused with genetic algorithms that tune the control parameters. In [5], [7], [22], Ahmad et al. investigated open-loop control strategies using input shaping control techniques. Mustafa and Iqbal [23] presented a feedback linearization controller for TRMS which relied on exact model knowledge.

In this paper, we aimed to develop a robust tracking control law for TRMSs. The lack of accurate TRMS dynamic models motivates us to design a robust tracking control law that can deal with a high level of dynamic uncertainty. Inspired by the results in neural network based control strategies for robot manipulators [24], [25], the proposed control law consists of a nonlinear feedback component fused with a nonlinear neural network feedforward term. The nonlinear feedback component is based on [26] and provides semi-global asymptotic tracking and does not require any dynamic model knowledge. The design of the nonlinear neural network feedforward term is based on the universal approximation properties of the neural network as a feedforward compensator [24] that can be utilized to compensate for the uncertain dynamics of the TRMS. Numerical simulations are conducted to show the performance of the proposed robust tracking controller.

The rest of the paper is organized as follows; the model of the TRMS is presented in Section II. The robust tracking control development and the neural network feedforward design are presented in Sections III and IV, respectively. Numerical simulation results are given in Section V. Finally, concluding remarks are provided in Section VI.

2. TRMS Model

The twin rotor multi-input multi-output system serves as a model of a helicopter as shown in Figure 1. The TRMS mechanical unit consists of two rotors placed on a beam together with a counterbalance as seen in Figure 2. The whole unit is attached to the tower allowing for safe helicopter control experiment. The

state of the beam is described by vertical and horizontal angles,



Fig. 1. The twin rotor MIMO system 33-220 at Mechatronics Laboratory, Hashemite University [1].

and angular velocities may be measured by sensors on the system. The position and velocity of the modeled helicopter are controlled through the rotor velocity variation whereas in a real helicopter, the rotor velocity is slowly time-varying and the propulsion is varied through the rotor blades angle modification. The electrical unit (placed under the tower) allows for the measured signals to be transferred to the PC and control signal application via an input/output card [1].

The dynamic model for a twin rotor multi-input multi-output (MIMO) system is described as [3]

$$f \ddot{\theta}_h + f_1 \ddot{\theta}_v + f_2 + f_3 = \tau_h \quad (1)$$

$$J \ddot{\theta}_v + f_1 \ddot{\theta}_h + f_4 + f_5 = \tau_v \quad (2)$$

where $f(\theta_v)$, $f_1(\theta_v)$, $f_2(\theta_v, \dot{\theta}_v)$, $f_3(\theta_v, \dot{\theta}_v, \dot{\theta}_h)$, $f_4(\theta_v, \dot{\theta}_h)$, $f_5(\theta_v) \in \mathbb{R}$ are nonlinear functions, $J \in \mathbb{R}$ is equal to the sum of the moment of inertia of the free-free beam and counterbalance beam, $\theta_v(t)$, $\dot{\theta}_v(t)$, $\ddot{\theta}_v(t) \in \mathbb{R}$ are

the angular position, velocity, and acceleration of the beam in the vertical plane, respectively, and $\theta_h(t)$, $\dot{\theta}_h(t)$, $\ddot{\theta}_h(t) \in \mathbb{R}$ are the angular position, velocity, and acceleration of the beam in the horizontal plane, respectively. The dynamic model in (1) and (2) can be combined in a compact form as

$$M\ddot{\theta} + N = \tau \quad (3)$$

in which

$$M \triangleq \begin{bmatrix} f & f_1 \\ f_1 & J \end{bmatrix} \quad \theta \triangleq \begin{bmatrix} \theta_h \\ \theta_v \end{bmatrix} \quad (4)$$

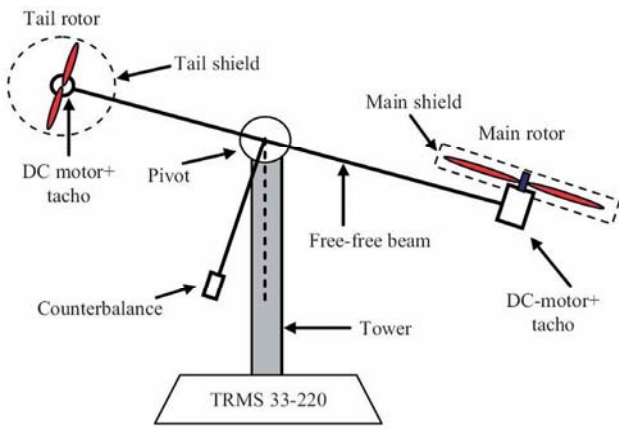


Fig. 2. The complete assembly of the twin rotor MIMO system [3].

$$N \triangleq \begin{bmatrix} f_2 + f_3 \\ f_4 + f_5 \end{bmatrix} \quad \tau \triangleq \begin{bmatrix} \tau_h \\ \tau_v \end{bmatrix} \quad (5)$$

where $M(\theta) \in \mathbb{R}^{2 \times 2}$ represents the inertia matrix, $\theta(t) \in \mathbb{R}^2$ is the combined angular position vector, $N(\theta, \dot{\theta}) \in \mathbb{R}^2$ represents other dynamic effects such as coriolis and centrifugal forces, and $\tau(t) \in \mathbb{R}^2$ is the combined control vector. The subsequent control development assumes the nonlinear function $f(\cdot)$, $f_1(\cdot)$, $f_2(\cdot)$, $f_3(\cdot)$, $f_4(\cdot)$, $f_5(\cdot)$ and the moment of inertia J are unknown; hence the nonlinear functions $M(\cdot)$ and $N(\cdot)$ are unknown. To facilitate the control design, the following assumptions are imposed on system dynamics.

Assumption 1: The dynamic terms $M(\cdot)$ and $N(\cdot)$ are continuously differentiable up to their second order derivatives, and $M(\cdot)$, $\dot{M}(\cdot)$, $\ddot{M}(\cdot)$, $N(\cdot)$, $\dot{N}(\cdot)$, $\ddot{N}(\cdot)$ are bounded provided that their arguments are bounded.

Assumption 2: The inertia matrix $M(\cdot)$ is symmetric, positive definite, and satisfies the following

$$m_1 \|\xi\|^2 \leq \xi^T M(\theta) \xi \leq m_2 \|\xi\|^2, \forall \xi \in \mathbb{R}^2$$

inequalities

(6)

where $m_1, m_2 \in \mathbb{R}$ are positive bounding constants, and $\|\cdot\|$ denotes the standard Euclidean norm. The control objective is to design a continuous controller that guarantees asymptotic tracking of a desired angular position, denoted by $\theta_d(t) \in \mathbb{R}^2$, in the sense that

$$\theta(t) \rightarrow \theta_d(t) \text{ as } t \rightarrow +\infty. \quad (7)$$

The desired trajectory is assumed to satisfy the following standard boundedness assumption

$$\theta_d^{(i)}(t) \in L_\infty, \forall i = 0, 1, 2, 3 \quad (8)$$

where the superscript i denotes the i th time derivative. In the controller design, the combined angular position $\theta(t)$ and angular velocity $\dot{\theta}(t)$ are assumed to be measurable.

3. Robust Control Development

To quantify the control objective, a tracking error, denoted by $e_1(t) \in \mathbb{R}^2$, is defined as

$$e_1 \triangleq \theta_d - \theta. \quad (9)$$

From (9), it is clear that as $\|e_1(t)\| \rightarrow 0$ then $\theta(t) \rightarrow \theta_d(t)$, thus meeting the control objective. To facilitate the control development, filtered tracking error signals, denoted by $e_2(t), r(t) \in \mathbb{R}^2$, are defined as

$$e_2 \triangleq \dot{e}_1 + \lambda_1 e_1 \quad (10)$$

$$r \triangleq \dot{e}_2 + \lambda_2 e_2 \quad (11)$$

where $\lambda_1, \lambda_2 \in \mathbb{R}$ are positive control gains. In order to meet the tracking control objective the control input $\tau(t)$ is designed as [26]

$$\tau = (K_s + I) \left[e_2(t) - e_2(t_0) + \lambda_2 \int_{t_0}^t e_2(\rho) d\rho \right] + \int_{t_0}^t [\hat{f}(\rho) + \beta \text{Sgn}(e_2(\rho))] d\rho \quad (12)$$

where $K_s, \beta \in \mathbb{R}^{2 \times 2}$ are positive definite, diagonal, control gain matrices, $I \in \mathbb{R}^{2 \times 2}$ denotes a standard 2-by-2 identity matrix, $\hat{f}(t) \in \mathbb{R}^2$ is a neural network feedforward term that is yet to be designed, and $\text{Sgn}(\cdot) : \mathbb{R}^2 \rightarrow \mathbb{R}^2$ is a vector signum function defined as $\text{Sgn}(\xi) = [\text{sgn}(\xi_1) \text{sgn}(\xi_2)]^T$ where $\forall \xi, [\xi_1 \xi_2]^T \in \mathbb{R}^2$.

As mentioned previously, the dynamic model of



the twin rotor MIMO system is assumed to be unknown. To compensate for the uncertainties in the dynamics, the controller in (12) was utilized, for the following reasons: i) it is continuous, ii) it does not require the dynamic model to be known (i.e., robust), and iii) it provides semi-global asymptotic tracking. For more information regarding the controller and its detailed analysis, the reader is referred to [26].

Remark 1: It should be noted that the only restriction imposed on the neural network feedforward term $\hat{f}(t)$ in (12) is that it should remain bounded throughout the closed-loop operation.

4. Neural Network Feedforward Design

The neural network feedforward term is computed by using a two layer network with n neurons and defined as [24]

$$\hat{f} \triangleq \hat{W}^T \bar{\sigma}(\hat{V}^T x) \quad (13)$$

where $\hat{W}(t) \in R^{n \times 2}$ and $\hat{V}(t) \in R^{8 \times n}$ are estimated weight matrices, and $x(t) \in R^8$ is the input vector to the neural network which is defined as

$$x \triangleq \begin{bmatrix} \theta_d^T & \dot{\theta}_d^T & \ddot{\theta}_d^T & \dots^T \end{bmatrix}^T. \quad (14)$$

In (13), $\bar{\sigma}(\cdot) : R^n \rightarrow R^n$ denotes the vector activation function and is defined as

$$\bar{\sigma}(w) \triangleq \begin{bmatrix} \sigma(w_1) & \dots & \sigma(w_n) \end{bmatrix} \quad (15)$$

where $w = [w_1 \dots w_n]^T \in R^n$ and $\sigma(s) : R \rightarrow R$ is the sigmoid activation function defined as

$$\sigma(s) \triangleq \frac{1}{1 + \exp(-s)}. \quad (16)$$

The gradient of the vector activation function, denoted by $\bar{\sigma}_\nabla(w) \in R^{n \times n}$, can be obtained as

$$\bar{\sigma}_\nabla(w) = \text{diag}\{\bar{\sigma}(w)\} [I - \text{diag}\{\bar{\sigma}(w)\}]. \quad (17)$$

The estimated weight matrices are updated according to the following expressions [27]

$$\dot{\hat{W}} = -\alpha_w \hat{W} + \gamma_1 \bar{\sigma}(\hat{V}^T x) \text{Sat}(\lambda_2 e_2 + \zeta)^T \quad (18)$$

$$\dot{\hat{V}} = -\alpha_v \hat{V} + \gamma_2 x \left[\bar{\sigma}_\nabla(\hat{V}^T x) \hat{W} \text{Sat}(\lambda_2 e_2 + \zeta) \right]^T \quad (19)$$

where $\alpha_v, \alpha_w, \gamma_1, \gamma_2 \in R$ are positive constants, $\text{Sat}(\cdot) : R^n \rightarrow R^n$ is the vector saturation function, and the auxiliary signal $\zeta(t) \in R^2$ is developed to approximate the time derivative of $e_2(t)$ and is defined as

$$\dot{\zeta} \triangleq \frac{1}{\varepsilon} (e_2 - \eta) \quad (20)$$

where $\varepsilon \in R$ is a small positive constant, and the auxiliary filter signal $\eta(t) \in R^2$ is updated according to the following expression

$$\dot{\eta} = \frac{1}{\varepsilon} (e_2 - \eta). \quad (21)$$

Similar to [27], the standard boundedness assumption in (8) can be utilized along with the expressions in (13)-(19) to prove that $\hat{f}(t)$ remains bounded for all time; thus, the only constraint imposed on the neural network feedforward term is satisfied.

5. Numerical Simulation Results

The performance of the proposed robust controller in (12) and (13) was evaluated by conducting numerical simulations using Matlab Simulink program. The nonlinear functions of the system model in (1) and (2) are given below [3], [4]

$$\begin{aligned} f &= \phi_1 \cos(2\theta_v) + \phi_2 \sin^2(\theta_v) + \phi_3 \\ f_1 &= \phi_4 \sin(\theta_v) - \phi_5 \cos(\theta_v) \\ f_2 &= \phi_4 \cos(\theta_v) + \phi_5 \sin(\theta_v) \dot{\theta}_v^2 \\ f_3 &= 2 \phi_6 \sin(\theta_v) \cos(\theta_v) \dot{\theta}_v \dot{\theta}_h \\ f_4 &= -\phi_6 \sin(\theta_v) \cos(\theta_v) \dot{\theta}_v^2 \\ f_5 &= \phi_7 \cos(\theta_v) + \phi_8 \sin(\theta_v) \end{aligned}$$

where $\phi_1 = 0.0591$, $\phi_2 = 0.0058$, $\phi_3 = 0.0132$, $\phi_4 = 0.0019$, $\phi_5 = 0.022$, $\phi_6 = -0.0533$, $\phi_7 = 0.1535$, and $J = 0.0649$ are model parameters. It should be noted that the functions above were used only to simulate the dynamics of the TRMS and were not utilized anywhere else in the numerical simulation.

In the simulation study, different number of neurons (ranging from 4 to 15) were tried by comparing angular position tracking error in (9) and the best performance was achieved using 10 neurons. During these simulations, the update laws in (18) and (19) were utilized with gains $\gamma_1 = 100$, $\gamma_2 = 10$, $\alpha_v = 0.01$, $\alpha_w = 0.01$, and $\varepsilon = 0.001$. The lower and upper limits of saturation function were chosen as -1 and 1 , respectively. The initial value of the angular positions was chosen as $\theta(0) = [0.5, 0.5]^T$ in radians, while the control gains were set to $\lambda_1 = 1$, $\lambda_2 = 1$, $K_s = I$, $\beta = I$. The desired angular position was $\theta_d(t) = [0.2 \sin(0.2\pi t), 0.6 \sin(0.2\pi t)]^T$ in radians. The controller gains were selected via a trial-error method until a good tracking performance was obtained. Two



different cases were considered in the simulation study without changing the above mentioned parameters: Case I was without any noise injected into the angular velocities whereas in Case II, additive white Gaussian noise with a constant signal to noise ratio of 20 dB was injected into the angular velocities. It should be noted that the noise was injected to the angular velocities to model the noise in the sensor readings to simulate real measurements.

In Figures 3 and 4, the tracking error $e_1(t)$ (in degrees) and the controller $\tau(t)$ are presented, respectively, for case I. In Figures 5 and 6, the tracking error $e_1(t)$ (in degrees) and the controller $\tau(t)$ are presented, respectively, for case II. It is clear from Figures 3 and 5 that the control objective was achieved in both cases, thus robustness of our controller to noise in angular velocity measurements was also demonstrated. To quantify the effect of the neural network feedforward component, the following measures were computed as a measure of controller's performance

$$M_e \triangleq \int_{t_0}^t \|e_1(\rho)\|^2 d\rho \quad (22)$$

$$M_\tau \triangleq \int_{t_0}^t \|\tau(\rho)\|^2 d\rho \quad (23)$$

where $M_e(t)$ is a measure of magnitude of the tracking error (in degrees) and $M_\tau(t)$ is a measure of the energy expended by the controller. The performance of the controller was tested with and without neural network feedforward component for both cases as shown in Table I. Apparently, after adding the neural network feedforward term to the control law, improved tracking performances for both cases were achieved.

Case	Measure	$\tau(t)$ without $\hat{f}(t)$	$\tau(t)$ with $\hat{f}(t)$
I	M_e	919.68	829.31
	M_τ	0.56	0.56
II	M_e	932.52	834.07
	M_τ	0.56	0.56

Table I. Comparison Of Performance Measures For The Controller With And Without Neural Network Feedforward Term For Cases I And II

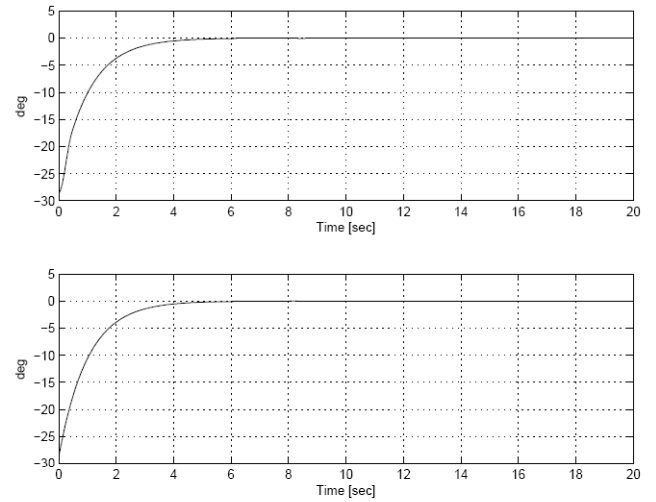


Fig. 3. The tracking error $e_1(t)$ for Case I (i.e., without noise). Top and bottom plots indicate the tracking error $e_1(t)$ in horizontal and vertical planes, respectively.

When presenting Figures 3 and 5, and when computing $M_e(t)$ the tracking error was evaluated in degrees to better demonstrate the differences between the “with” and “without” the neural network feedforward cases.

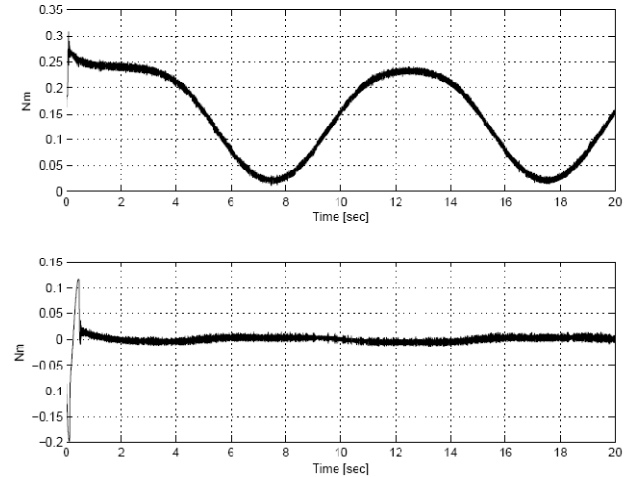


Fig. 4. The control input $\tau(t)$ for Case I (i.e., without noise). Top and bottom plots indicate the control input in horizontal ($\tau_h(t)$) and vertical ($\tau_v(t)$) planes, respectively.

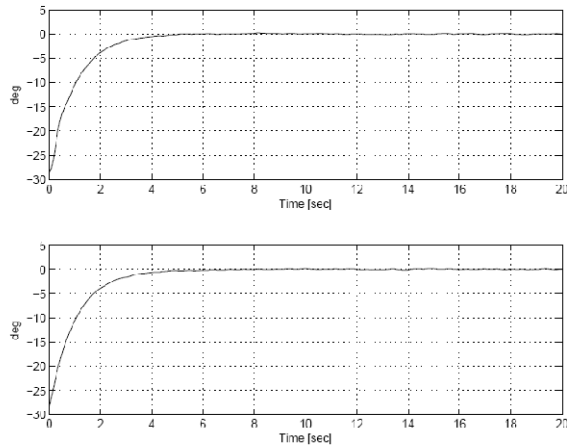


Fig. 5. The tracking error $e_1(t)$ for Case II (i.e., with noise). Top and bottom plots indicate the tracking error $e_1(t)$ in horizontal and vertical planes, respectively.

6. Conclusions

In this paper, a robust tracking controller was designed for twin rotor multi-input multi-output systems. The controller was developed based on the assumption that the dynamic model of the TRMS is unknown. In the design of the controller, a continuous nonlinear feedback component was fused with a nonlinear neural network feedforward term. The nonlinear feedback component provided semi-global asymptotic tracking and the nonlinear neural network feedforward term was utilized to employ the universal approximation properties of the neural networks to compensate for the uncertain dynamic model of the TRMS. Numerical simulation results were presented which demonstrated that the addition of the neural network feedforward component to the continuous nonlinear feedback term improved the tracking performance. In the numerical simulation study, the robustness of the proposed controller to noise was validated by injecting additive white Gaussian noise into the angular velocity measurements to model the sensor noise in real systems. Future efforts will focus on implementation of the proposed controller in a laboratory TRMS setup.

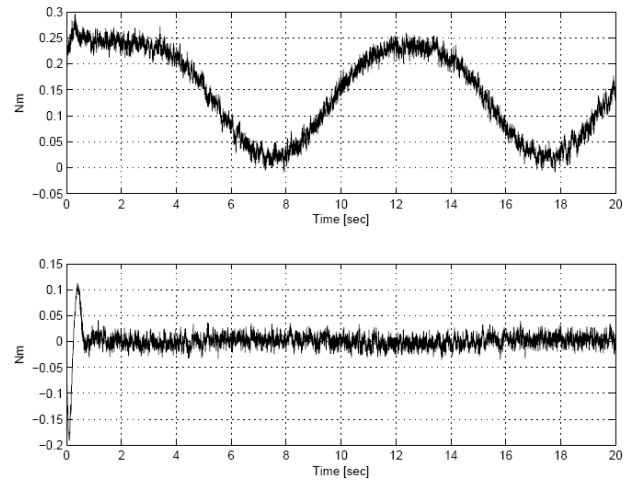


Fig. 6. The control input $\tau(t)$ for Case II (i.e., with noise). Top and bottom plots indicate the control input in horizontal ($\tau_h(t)$) and vertical ($\tau_v(t)$) planes, respectively.

References

- [1]. Twin Rotor MIMO System 33-220 User Manual, Crowborough, UK, 1998.
- [2]. C. L. Shih, M. L. Chen, and J. Y. Wang, "Mathematical model and set-point stabilizing controller design of a twin rotor MIMO system," *Asian J. Control*, vol. 10, pp. 107–114, 2008.
- [3]. A. Rahideh and M. H. Shaheed, "Mathematical dynamic modeling of a twin-rotor multiple input multiple output system," *Proc. of Ins. of Mechanical Engineers Part I: J. Systems and Control Engineering*, vol. 221, pp. 89–101, 2007.
- [4]. A. Rahideh, M. H. Shaheed, and H. J. C. Huijberts, "Dynamic modelling of a TRMS using analytical and empirical approaches," *Control Engineering Practice*, vol. 16, pp. 241–259, 2008.
- [5]. S. M. Ahmad, A. J. Chipperfield, and M. O. Tokhi, "Dynamic modelling and open-loop control of a twin rotor multi-input multioutput system," *Proc. of Ins. of Mechanical Engineers Part I: J. Systems and Control Engineering*, vol. 216, pp. 477–496, 2002.
- [6]. "Dynamic modelling and linear quadratic Gaussian control of a twin-rotor multi-input multi-output system," *Proc. of Ins. Of Mechanical Engineers Part I: J. Systems and Control Engineering*, vol. 217, pp. 203–227, 2003.
- [7]. "Dynamic modelling and control of a 2 dof twin rotor multiinput multi-output system," in *Proc. of Conf. of IEEE Industrial Electronics Society*, Nagoya, Japan, 2000, pp. 1451–1456.
- [8]. "Parametric modelling and dynamic characterization of a twodegree- of-freedom twin-rotor multi-input multi-output system," *Proc. of Ins. of Mechanical Engineers Part I: J. Systems and Control Engineering*, vol. 215, pp. 63–78, 2001.
- [9]. S. M. Ahmad, M. H. Shaheed, A. J. Chipperfield, and M. O. Tokhi, "Nonlinear modelling of a twin rotor MIMO system using radial basis function networks," in *Proc. of IEEE National Aerospace and Electronics Conf.*, Dayton, OH, USA, 2000, pp. 313–320.
- [10]. A. Rahideh and M. H. Shaheed, "Dynamic modelling of a twin rotor MIMO system using grey box," in *Proc. of Int. Symposium onMechatronics and its Applications*, Amman, Jordan, 2008, pp. 237–242.



- [11]. M. H. Shaheed, "Feedforward neural network based non-linear dynamic modelling of a TRMS using RPROP algorithm," *Aircraft Engineering and Aerospace Technology*, vol. 77, no. 1, pp. 13–22, 2005.
- [12]. S. F. Toha and M. O. Tokhi, "MLP and Elman recurrent neural network modelling for the TRMS," in *Proc. of IEEE Int. Conf. on Cybernetic Intelligent Systems*, London, UK, 2008, pp. 391–396.
- [13]. C. S. Liu, L. R. Chen, B. Z. Li, S. K. Chen, and Z. S. Zeng, "Improvement of the twin rotor MIMO system tracking and transient response using fuzzy control technology," in *IEEE Conference on Industrial Electronics and Applications*, Singapore, Singapore, 2006, pp. 1411–1416.
- [14]. J. G. Juang, M. T. Huang, and W. K. Liu, "PID control using presearched genetic algorithms for a MIMO system," *IEEE Trans. Syst., Man, Cybern. C*, vol. 38, pp. 716–727, 2008.
- [15]. J. G. Juang, K. T. Tu, and W. K. Liu, "Hybrid intelligent PID control for MIMO system," in *Proc. of Int. Conf. on Neural Information Processing*, Hong Kong, China, 2006, pp. 654–663.
- [16]. A. Rahideh and M. H. Shaheed, "Hybrid fuzzy-PID-based control of a twin rotor MIMO system," in *Proc. of Conf. of IEEE Industrial Electronics Society*, Paris, France, 2006, pp. 1258–1263.
- [17]. M. Lopez-Martinez, C. Vivas, and M. G. Ortega, "A multivariable nonlinear h-infinity controller for a laboratory helicopter," in *Proc. IEEE Int. Conf. Decision and Control*, Seville, Spain, 2005, pp. 4065–4070.
- [18]. T. W. Lu and P. Wen, "Time optimal and robust control of twin rotor system," in *Proc. of 4th Int. Conf. on Control and Automation*, Guangzhou, China, 2007, pp. 1435–1439.
- [19]. H. R. Karimi and M. R. J. Motlagh, "Robust feedback linearization control for a non linearizable MIMO nonlinear system in the presence of model uncertainties," in *Proc. of IEEE Int. Conf. on Service Operations, Logistics and Informatics*, Shanghai, China, 2006, pp. 965–970.
- [20]. J. P. Su, C. Y. Liang, and H. M. Chen, "Robust control of a class of nonlinear systems and its application to a twin rotor MIMO system," in *Proc. of IEEE Int. Conf. on Industrial Technology*, Bangkok, Thailand, 2002, pp. 1272–1277.
- [21]. A. Rahideh, M. H. Shaheed, and A. H. Bajodah, "Adaptive nonlinear model inversion control of a twin rotor multi-input multi-output system using artificial intelligence," *Proc. of Ins. of Mechanical Engineers Part I: J. Systems and Control Engineering*, vol. 221, pp. 343–351, 2007.
- [22]. S. M. Ahmad, A. J. Chipperfield, and M. O. Tokhi, "Dynamic modelling and open-loop control of a two-degree-of-freedom twin rotor multi-input multi-output system," *Proc. of Ins. of Mechanical Engineers Part I: J. Systems and Control Engineering*, vol. 218, pp. 451–463, 2004.
- [23]. G. Mustafa and N. Iqbal, "Controller design for a twin rotor helicopter model via exact state feedback linearization," in *Int. Multi-Topic Conference*, Lahore, Pakistan, 2004, pp. 706–711.
- [24]. F. L. Lewis, S. Jagannathan, and A. Yesildirek, *Neural Network Control of Robot Manipulators and Nonlinear Systems*. London, UK: Taylor and Francis, 1999.
- [25]. S. S. Ge, T. H. Lee, and C. J. Harris, *Adaptive Neural Network Control of Robotic Manipulators*. Singapore: World Scientific, 1999.
- [26]. B. Xian, D. M. Dawson, M. S. de Queiroz, and J. Chen, "A continuous asymptotic tracking control strategy for uncertain nonlinear systems," *IEEE Trans. Automat. Contr.*, vol. 49, no. 7, pp. 1206–1211, 2004.
- [27]. D. Braganza, D. M. Dawson, I. D. Walker, and N. Nath, "A neural network controller for continuum robots," *IEEE Trans. Robot.*, vol. 23, no. 5, pp. 1270–1277, 2007.



Adaptive Identification of Tire Cornering Stiffness and Vehicle Center of Gravity

Alper Bayrak¹, Enver Tatlicioglu^{1*}, Michael L. McIntyre²

¹Izmir Institute of Technology, Department of Electrical & Electronics Engineering
Gulbahce Koyu, Urla, Izmir, 35430, Turkey.
envertatlicioglu@iyte.edu.tr

²Western Kentucky University, Department of Engineering
Bowling Green, KY 42101 USA.

Abstract

In this paper, a filtering technique augmented with a least-square estimator is developed to estimate the moment of inertia, cornering stiffness of the wheels, and location of center of gravity for a vehicle. The proposed technique utilizes standard signals that may be readily available through the vehicle's control area network and removes the requirement to measure accelerations. Thus, any numerical difficulties that may arise due to the noise present in the acceleration measurements is avoided. Numerical simulation results are presented to demonstrate that the unknown parameters are identified successfully.

Keywords: ...

1. Introduction

In the automotive industry, exact knowledge of vehicle parameters such as moment of inertia, cornering stiffness of the wheels, and location of center of gravity, is very important when controlling the vehicle safely. For example, in the literature, it is widely mentioned that vehicle center of gravity is important for vehicle dynamics and especially for the road handling behavior of the vehicle [1]. In some vehicle control applications [2], [3], [4], these parameters were assumed to be known via the information provided by the manufacturer. However, the difficulty is that most of these parameters are not directly measurable and they can vary significantly with changing loading conditions or by some other effects such as peripheral effects or modifications on the vehicle. Thus, identification techniques are usually required to identify vehicle parameters accurately.

In vehicle control systems, there are two common parameter estimation methods: i) sensor-based, ii) model-based. Modelbased parameter estimation techniques utilize standard signals that are readily available through the vehicle control area network and

are cheaper when compared to sensor-based parameter estimation [5].

In [6], Gaspar et. al. investigated a gray-box identification method to estimate the center of gravity for heavy-duty vehicles. In [1] and [7], Solmaz et. al. presented a methodology based on multiple models and switching for real-time estimation of center of gravity, center of gravity height, and the suspension parameters of the vehicle, respectively. However, the multiple models and switching methodology utilized in [1] and [7] are computationally inefficient. In [8], Sivaramakrishnan developed a method to estimate vehicle center of gravity location and tire cornering stiffness through INS and GPS measurements using simple vehicle maneuvers. In [9], Wesemeier and Isermann estimated the combinations of parameters like cornering stiffness and center of gravity by using the velocity dependent static gains of a track model. In [10], Rajamani et. al. focused on algorithms to estimate roll angle and center of gravity height.

In this paper, the bicycle model of lateral dynamics in [10] is utilized and an adaptive least-squares estimator is designed to estimate the moment of inertia, cornering stiffness of the wheels, and location of center of gravity. The main motivation of our work is to remove the requirement for acceleration measurements. In an attempt to remove the need for acceleration measurements, inspired by the work in [5], a filtering technique augmented with a least-square estimator based on the model is developed. Upon satisfaction of a persistent excitation condition by the filtered regression matrix, the parameter estimation error is proven to go to zero. The technique presented in this paper reduces the numerical difficulties that may arise due to the noise present in the acceleration measurements and is an improvement over the similar methods in the literature (e.g. [8]). Numerical simulations are conducted to



demonstrate the proof of concept. The rest of the paper is organized as follows. In Section II, the system model is given, while the adaptive identification algorithm is presented in Section III. The numerical simulation results are given in Section IV. Finally, concluding remarks are provided in Section V.

2. System Model

The bicycle model of lateral vehicle dynamics utilized in this paper is as follows [10]

$$m(\ddot{y} + V_x \dot{\psi}) = 2C_f \left(\delta - \frac{\dot{y} + l_f \dot{\psi}}{V_x} \right) + 2C_r \left(-\frac{\dot{y} - l_r \dot{\psi}}{V_x} \right) \quad (1)$$

$$I_z \ddot{\psi} = 2C_f \left(\delta - \frac{\dot{y} + l_f \dot{\psi}}{V_x} \right) l_f - 2C_r \left(-\frac{\dot{y} - l_r \dot{\psi}}{V_x} \right) l_r \quad (2)$$

where $\dot{y}(t)$, $\dot{\psi}(t)$ are the lateral velocity and acceleration, $\ddot{y}(t)$, $\ddot{\psi}(t)$ are the yaw velocity and acceleration, V_x is the longitudinal velocity, I_z is the moment of inertia of the vehicle about the vertical axis, l_f and l_r are the distances of the front and the rear tire from center of gravity of the vehicle, C_f and C_r are the tire cornering stiffness of the front and rear wheels, m is the mass of vehicle, and $\delta(t)$ is the front wheel steering angle. In (1) and (2), the constant parameters which need to be identified are $2C_f/m$, l_f , $2C_r/m$, l_r , $2C_f/I_z$, $2C_r/I_z$.

The system model in (1) and (2) can be represented in a compact form as follows

(3)

where $a(t) \in \mathbb{R}^2$ is an auxiliary unmeasurable signal, $W(t) \in \mathbb{R}^{2 \times 6}$ is the regression matrix and $\theta \in \mathbb{R}^6$ is the unknown system parameters, and are defined as follows

$$a \triangleq \begin{bmatrix} \ddot{y} + V_x \dot{\psi} \\ \dot{\psi} \end{bmatrix} \quad (4)$$

$$W \triangleq \begin{bmatrix} \delta & \frac{\dot{y}}{V_x} & \frac{\dot{\psi}}{V_x} & 0 & 0 & 0 \\ 0 & 0 & 0 & \delta & \frac{\dot{y}}{V_x} & \frac{\dot{\psi}}{V_x} \end{bmatrix} \quad (5)$$

$$\theta \triangleq [\theta_1 \ \theta_2 \ \theta_3 \ \theta_4 \ \theta_5 \ \theta_6]^T \quad (6)$$

The unknown parameter vector can also be represented as follows

$$\begin{bmatrix} \theta_1 \\ \theta_2 \\ \theta_3 \\ \theta_4 \\ \theta_5 \\ \theta_6 \end{bmatrix} \triangleq \begin{bmatrix} \xi_1 \\ -\xi_1 - \xi_3 \\ \xi_3 \xi_4 - \xi_1 \xi_2 \\ \xi_5 \\ \xi_2 \\ \xi_6 \xi_4 - \xi_5 \xi_2 \\ -\xi_5 \xi_2^2 - \xi_6 \xi_4^2 \end{bmatrix} \quad (7)$$

where $\theta_1 = 2C_f/m$, $\theta_2 = l_f$, $\theta_3 = 2C_r/m$, $\theta_4 = l_r$, $\theta_5 = 2C_f/I_z$, $\theta_6 = 2C_r/I_z$ denote the parameters which need to be identified. It should be noted that, the definitions in (7) can be utilized to find θ_i , where $i=1, \dots, 6$ uniquely in terms of ξ_i , $i = 1, \dots, 6$. The subsequent adaptive identification development requires $\dot{y}(t)$, $\dot{\psi}(t)$ and $\delta(t)$ to be measurable, and V_x is assumed to be a known constant. It is also noted that lateral acceleration and yaw rate are assumed to be continuous functions of time.

3. ADAPTIVE IDENTIFICATION

To facilitate the design of adaptive identification strategy, a prediction error, denoted by $\varepsilon(t) \in \mathbb{R}^2$, is defined as follows

$$\varepsilon \triangleq a_f - \hat{a}_f \quad (8)$$

where $a_f(t) \in \mathbb{R}^2$ is an auxiliary filter signal obtained as follows¹

$$\dot{a}_f = -\beta_0 a_f + \beta_0 a; \quad a_f(t_0) = 0_{2 \times 1}, \quad \beta_0 \in \mathbb{R}^+ \quad (9)$$

and $\hat{a}_f(t) \in \mathbb{R}^2$ is the estimate form of $a_f(t)$. It is to be noted that, since $a(t)$ is unmeasurable, an implementable form of $a_f(t)$ can be obtained as follows

$$a_f = P + \beta_0 A \quad (10)$$

¹Throughout the paper, $0_{p \times q}$ and I_n will be utilized to denote a $p \times q$ zero matrix, and a standard $n \times n$ identity matrix, respectively.

$$\dot{P} = -\beta_0 P + \beta_0 V_x B; \quad P(t_0) = 0_{2 \times 1} \quad (11)$$

where β_0 , V_x , B and $A \in \mathbb{R}^2$ are auxiliary measurable signals, and $P(t) \in \mathbb{R}^2$ is an auxiliary filter signal. By using the time derivative of (10) and (11), $\dot{a}_f(t)$ can be written as seen in (9). It should be noted that the expression in (9) is utilized in the design and analysis of the identification law, while



the expressions in (10) and (11) represents an implementable form of (9).

To facilitate the adaptive identification design, the filtered regression matrix, denoted by $W_f(t) \in \mathbb{R}^{2 \times 6}$, is designed as follows

$$\dot{W}_f = -\beta_o W_f + \beta_o W \quad (12)$$

where $W_f(t_0) = 0_{2 \times 6}$. After utilizing (9) along with (3) and (12), it is possible to write the following expression

$$\dot{a}_f + \beta_o a_f = \dot{W}_f \theta + \beta_o W_f \theta. \quad (13)$$

Since $a_f(t_0) = W_f(t_0) \theta = 0_{2 \times 1}$, from (13), it is easy to see that

$$a_f = W_f \theta. \quad (14)$$

Based on (14), the estimate form of $a_f(t)$ is designed as follows

$$\hat{a}_f = W_f \hat{\theta} \quad (15)$$

where $\hat{\theta}(t) \in \mathbb{R}^6$ denotes the estimate of θ that is yet to be designed. After taking the time derivative of (15), and utilizing (12), it is possible to write the following expression

$$\dot{\hat{a}}_f + \beta_o \hat{a}_f = \frac{d}{dt} (W_f \hat{\theta}) + \beta_o W_f \hat{\theta}. \quad (16)$$

After subtracting (16) from (13), and utilizing (8) the following expression can be obtained

$$\dot{\varepsilon} + \beta_o \varepsilon = \frac{d}{dt} (W_f \tilde{\theta}) + \beta_o W_f \tilde{\theta} \quad (17)$$

where $\tilde{\theta}(t) \in \mathbb{R}^6$ is the parameter estimation error defined as

$$\tilde{\theta} \triangleq \hat{\theta} - \theta. \quad (18)$$

Since $\varepsilon(t_0) = a_f(t_0) - \hat{a}_f(t_0) = 0_{2 \times 1}$ and $W_f(t_0) \tilde{\theta}(t_0) = 0_{2 \times 1}$, from (17), it is clear that an unmeasurable form of the prediction error $\varepsilon(t) \in \mathbb{R}^2$ can be written as follows

$$\varepsilon = W_f \tilde{\theta}. \quad (19)$$

A least-squares update law is selected as the preferred approach to estimate the unknown parameters, which is designed as follows [11]

$$\dot{\hat{\theta}} = -K_{ls} P_{ls} W_f^T \varepsilon \quad (20)$$

where $K_{ls} \in \mathbb{R}^{6 \times 6}$ is a constant, diagonal gain matrix, and $P_{ls}(t) \in \mathbb{R}^{6 \times 6}$ is the covariance matrix. The covariance matrix $P_{ls}(t)$ is generated by the covariance propagation equation, which is described as follows [11]

$$\dot{P}_{ls}^{-1} \triangleq K_{ls} (-\lambda P_{ls}^{-1} + W_f^T W_f) \quad (21)$$

where $P_{ls}(t_0) = k_0 I_6$ and $k_0, \lambda \in \mathbb{R}$ are positive constant gains.

Theorem 1: The least-squares update law as described by (20) and (21) ensures that $\|\tilde{\theta}(t)\| \rightarrow 0$ as $t \rightarrow \infty$ provided the following sufficient conditions are met: (i) the plant of estimation is strictly proper, (ii) the input is piecewise continuous and bounded, (iii) the output of the plant of estimation is bounded, and the following persistence of excitation condition [11] holds

$$\alpha_1 I_6 \leq \int_t^{t+T} W_f^T(\tau) W_f(\tau) d\tau \leq \alpha_2 I_6 \quad (22)$$

where $\alpha_1, \alpha_2, T \in \mathbb{R}$ are positive constants.

Proof: To prove $\|\tilde{\theta}(t)\| \rightarrow 0$ as $t \rightarrow \infty$, The proof of Theorem 2.5.3 from [11] is followed directly. To prove that sufficient condition (i) is valid; the plant of estimation as described in (9) can be as follows

$$\frac{a_f(s)}{a(s)} = \frac{\beta_o}{s + \beta_o} \quad (23)$$

where the vehicle's longitudinal acceleration $a(t)$ is the input of the plant of estimation. From (23), the plant is shown to be strictly proper. To prove that sufficient condition (ii) is valid; after utilizing the expression in (3) along with the assumption that lateral acceleration and yaw rate are being to be continuous functions of time, it can be proven that $a(t)$ is piecewise continuous and bounded. To prove that sufficient condition (iii) is valid; from (10) and standard linear analysis tools are utilized to show that (10), (11); therefore, proving that the output of the plant of estimation is bounded. Following the proof in [11], the convergence result follows.

Remark 1: The persistent excitation condition given by (22) is essential for the proof of Theorem 1. As explained

thoroughly in [12], despite its technical nature, the persistent excitation condition in (22) has an intuitively appealing practical interpretation as well. Before proceeding, we should note that, Lemma 4.8.3 from [13] can be utilized along with (12) to prove that the filtered regression matrix $W_f(t)$ satisfying a persistent excitation condition is equivalent to $W(t)$ satisfying a persistent excitation condition (similar to the one in (22)). The regression matrix $W(t)$ depends on lateral velocity, yaw rate, steering angle, and the regression matrix being persistently exciting is satisfied if these signals are varied. Specifically, the persistent excitation condition will be satisfied if there is variation in lateral velocity, yaw rate, and steering angle. It should be noted that a certain amount of change in steering angle will cause variation in lateral velocity and yaw rate as well. On the



other hand, this change should not necessarily happen all the time as after choosing a large enough T (see (22)), it will be possible to obtain some variation within any time interval in [12]. It should also be noted that, if there is no variation in $W(t)$ (i.e., if lateral velocity, yaw rate, and steering angle are constant functions with respect to time), then the persistent excitation condition will not be satisfied; thus, it will be impossible to identify the model parameters.

4. Simulation Results

The performance of the identification law in (20) and (21) was evaluated by conducting numerical simulations using Matlab Simulink. The parameter values used for the vehicle model are taken from [8] and are presented in Table I.

TABLE I
 PARAMETERS FOR VEHICLE MODEL

Parameter Name	Symbol	Value
Mass	m	1573 kg
Moment of inertia	I_z	1873 Nm^2
Front wheel distance from CG	l_f	1.1 m
Rear wheel distance from CG	l_r	1.58 m
Front tire cornering stiffness	C_f	80000 N/rad
Rear tire cornering stiffness	C_r	80000 N/rad

The longitudinal velocity, V_x , was chosen 10 m/s. A commonly used steering angle input was used as shown in Figure 1. Gaussian noise was added to the steering angle with 20 dB SNR for a more realistic steering angle input. Resulting yaw rate and lateral velocity are given in Figures 2 and 3. The simulation was ran for 100 seconds. The gains were

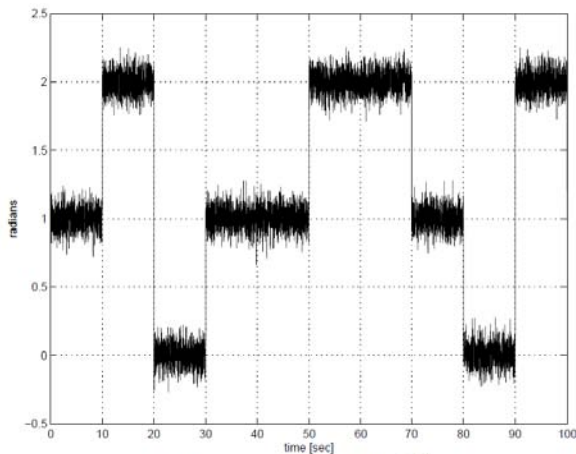


Fig. 1. Steering angle $\delta(t)$.

selected as $\lambda = 9 \times 10^{-6}$, $K_{ls} = 5.5 \times 10^6 I_6$, and $k_0 = 50$. The initial value of parameter estimate vector was set to $\hat{\theta}(t_0) = [70 \ -218 \ 38 \ 51 \ 20 \ -220]^T$. The identification of the unknown parameters was achieved in 0.68 seconds with a precision of six digits after the decimal point. The comparison of the real and estimated values can be seen in Table II. The parameter estimation error $\tilde{\theta}(t)$ is given in Figure 4, while the estimated parameters, $\hat{\xi}(t)$, are given in Figures 5-10. From Figure 4, it is clear that parameter estimation error is driven to zero, and from Figures 5-10, it is clear that the unknown model parameters are estimated accurately.

5. Conclusions

In this paper, the bicycle model of lateral dynamics in [8] and [10] was utilized with an adaptive least-squares estimator to identify the cornering stiffness of the wheels, moment of inertia, and location of center of gravity for a vehicle. Upon satisfaction of a persistent excitation condition, the parameter estimation error was proven to go to zero. The main advantage of our work when compared to the literature is the removal of the requirement of acceleration measurements. Numerical simulation results were presented to demonstrate proof of concept. In the numerical simulations, the parameter estimation errors were driven to zero in less than one second with a precision of six digits after the decimal point.

Future research efforts will focus on: i) testing the proposed method with experimental data, ii) developing estimation techniques to identify center of gravity height which is very important for rollover prevention.

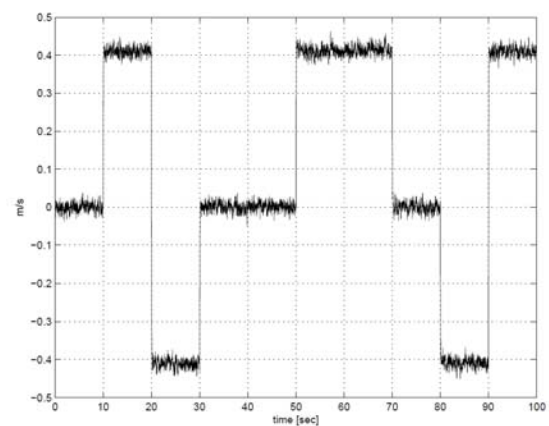


Fig. 2. Yaw rate $\dot{\psi}(t)$.

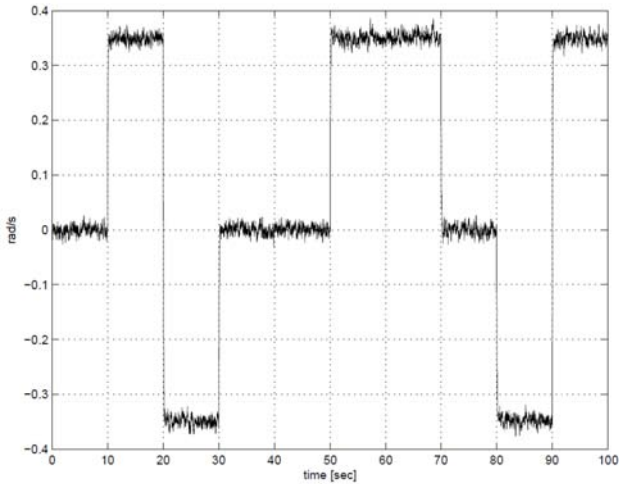


Fig. 3. Lateral velocity $\dot{y}(t)$.

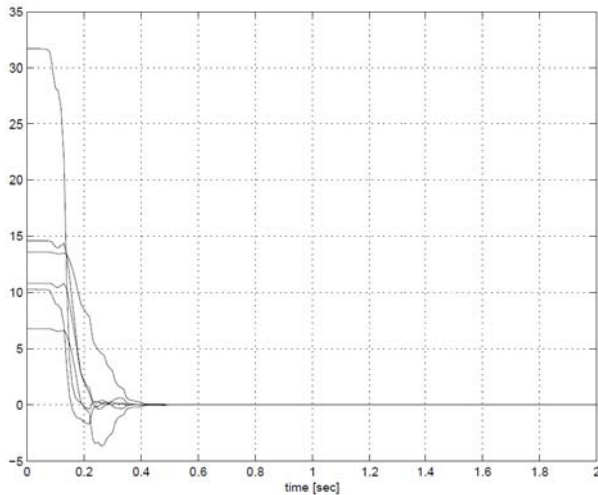


Fig. 4. Parameter estimation error $\tilde{\theta}(t)$.

TABLE II
COMPARISON OF REAL AND ESTIMATED VALUES

Parameter Name	Real value	Estimated value
l_f (m)	1.1000	1.1000
l_r (m)	1.5800	1.5800
C_f/m ($\text{rad}^{-1}\text{s}^{-2}\text{m}$)	50.8582	50.8582
C_r/m ($\text{rad}^{-1}\text{s}^{-2}\text{m}$)	50.8582	50.8582
C_f/I_z ($\text{m}^{-1}\text{rad}^{-1}\text{s}^{-2}$)	27.8455	27.8455
C_r/I_z ($\text{m}^{-1}\text{rad}^{-1}\text{s}^{-2}$)	27.8455	27.8455

References

- [1]. S. Solmaz, M. Akar, and R. Shorten, "Adaptive rollover prevention for automotive vehicles with differential braking," in Proc. of the 17th IFAC World Congress, COEX, South Korea, 2008.
- [2]. D. Odenthal, T. Bunte, and J. Ackermann, "Nonlinear steering and braking control for vehicle rollover avoidance," in Proc. European Control Conf., Karlsruhe, Germany, 1999.
- [3]. B.-C. Chen and H. Peng, "Differential-braking-based rollover prevention for sport utility vehicles with human-in-the-loop evaluations," *Vehicle System Dynamics*, vol. 36, no. 4-5, pp. 359–389, 2001.
- [4]. C. Ning, C. Nan, and C. YanDong, "On fractional control method for four-wheel-steering vehicle," *Science in China Series E-Technological Sciences*, vol. 52, no. 3, pp. 603–609, 2009.
- [5]. M. L. McIntyre, T. J. Ghotikar, A. Vahidi, X. Song, and D. M. Dawson, "A two-stage lyapunov-based estimator for estimation of vehicle mass and road grade," *IEEE Transactions on Vehicular Technology*, vol. 58, pp. 3177–3185, 2009.
- [6]. P. Gaspar, Z. Szabo, and J. Bokor, "Gray-box continuous-time parameter identification for lpv models with vehicle dynamics applications," in Proceedings of the 13th Mediterranean Conference on Control and Automation, Limassol, Cyprus, 2005, pp. 393–398.
- [7]. S. Solmaz, M. Akar, and R. Shorten, "Online center of gravity estimation in automotive vehicles using multiple models and switching," in Control, Automation, Robotics and Vision, Singapore, 2006, pp. 1–7.
- [8]. S. Sivaramakrishnan, "Simultaneous identification of tire cornering stiffnesses and vehicle center of gravity," in Proc. American Control Conf., Seattle, WA, USA, 2008, pp. 2846–2851.
- [9]. D. Wesemeier and R. Isermann, "Identification of vehicle parameters using stationary driving maneuvers," *Control Engineering Practice*, vol. 17, no. 12, pp. 1426–1431, 2009.
- [10]. R. Rajamani, D. Piyabongkarn, V. Tsourapas, and J. Lew, "Real-time estimation of roll angle and cg height for active rollover prevention applications," in Proc. American Control Conf., Minneapolis, MN, USA, 2009, pp. 433–438.
- [11]. S. Sastry and M. Bodson, *Adaptive Control: Stability, Convergence and Robustness*. Englewood Cliffs, NJ, USA: Prentice-Hall, 1989.
- [12]. H. F. Grip, L. Imsland, T. A. Johansen, T. I. Fossen, J. C. Kalkkuhl, and A. Suissa, "Nonlinear vehicle side-slip estimation with friction adaptation," *Automatica*, vol. 44, no. 3, pp. 611–622, 2008.
- [13]. P. Ioannou and J. Sun, *Robust Adaptive Control*. Englewood Cliffs, NJ, USA: Prentice-Hall, 1996.



State Space Smoothing through Singular Value Decomposition (SVD)

Hakki Erhan SEVIL^{1*}, Serhan OZDEMIR², Tunc BILGINCAN³

^{1*} Izmir Institute of Technology
Department of Mechanical Engineering, Artificial Intelligence & Design Laboratory,
Gulbahce 35430, Urla / Izmir TURKEY
erhansevil@iyte.edu.tr

² Izmir Institute of Technology
Department of Mechanical Engineering, Artificial Intelligence & Design Laboratory

³ Izmir Institute of Technology
Department of Mechanical Engineering, Robotics Laboratory

Abstract

The focus of this paper is the application of singular value decomposition (SVD) to the state space smoothing. State space smoothing in the analysis of nonlinear dynamics has been traditionally carried out by a smoothing operator on the constructed attractor. Smoothing this way eliminates outliers as well as the noise itself. However, smoothing haphazardly removes part of the information carrying part of the signal, elimination of which causes computation of spurious invariants on the manifold. SVDs, on the other hand, separate the signal into active and passive modes, i.e. information carrying part of the signal and the noise. SVDs have been in use for decades not just for noise removal, but also for dimension reduction. On a USV structure, a proper threshold blocks the noise and reveals the true dimensionality of the signal. This is applied to a one dimensional Van der Pol oscillator. 20 dB and 6 dB noise levels are added successively, where not only the attractor dimensionality is exposed but also noise is removed via an iterative algorithm. Noise-free and cleaned signal singular values are compared for a clear picture. Furthermore, in the comparison of retrieval signals by SVD and smoothing in means of nonlinear invariants, noise reduction through SVD accomplished relatively better results over smoothing.

Keywords: Noise Filtering, Singular Value Decomposition, Signal Processing.

1. Introduction

Although the differential geometers exposed the singular value decomposition the decomposition technique's history goes back to 1870s based on the Gauss with his well known algorithm [1]. Eugenio Beltrami (1835-1899), Camille Jordan (1838-1921), James Joseph

(1814-1897), Erhard Schmidt (1876-1959) and Hermann Weyl (1885-1955) were the owners of the singular value decomposition technique. Eugenio Beltrami and Camille Jordan discovered the bilinear forms of the singular values in 1970's. The singular value decomposition for real square matrices founded in 1880's and singular values of the matrix were named canonical multipliers by James Joseph Sylvester. In 1880s, Erhard Schmidt defined the infinite dimensional analogue for singular value decomposition in 1900s [1].

In the last century the theory was developed and became practical by many mathematicians, and it took its basic form which we generally use today.

The concept of understanding dynamics of a system, represented in the form of matrix, is an important and challenging issue. In linear algebra, matrix decomposition techniques which define the original matrix with several distinct matrixes are the considerable keys for this challenging issue.

Of the many worthwhile decompositions techniques, in this paper, Singular value decomposition (SVD), a very simple and useful technique is discussed and emphasized for eigenvalue related concepts. Singular value decomposition that is the factorization of an m by n matrix X into the product form $U*S*V^T$ is basically defines matrix X with distinct matrices. In this formulation, U and V are unitary matrices. S is the diagonal matrix and the diagonal elements of S are called the eigenvalues or the singular values of X . The most recognizable specification of singular value decomposition is the appropriateness of the technique to any type of matrix, both square and rectangular matrix.



Singular value decomposition has wide range of applications in general data processing procedures. For the signal processing it is basically used for noise and dimension reduction.

As a property of the singular value decomposition technique, we can easily see and separate the original signal so; it is really effective tool to separate the noise from the signal itself. There are several works about noise reducing with singular value decomposition. Hamid Hassanpour used singular value decomposition in his work [2], to reduce noise from a signal's time series. The noise reduction results for stationary and non stationary signals were promising in both time-frequency and time domains. Per Christian Hansen et al. worked with singular value decomposition due to the same reason, they used it as tool to separate a clean signal from a noisy signal for speech signals [3]. S.H. Jensen P et al. used singular value decomposition as a noise filter but they were emphasized the possible type of the noise. According to them SVD can be only applied to white noise for filtering, for the non-white cases, pre-whitening process is necessary [4]. In magnetic resonance imaging, singular Value decomposition is applied in multiple-echo data sets by Mark Bydder et al. [5], the results determined that the singular value decomposition purifies the magnetic resonance image, increases the signal-to-noise ratio with minimal loss in the image contrast and resolution. Again it is pointed out the necessity of pre-whitening of the noise. K. Shin et al. [6] used singular value decomposition iteratively to clean the noise from low dimensional chaotic signal. According to the paper the technique is really effective and applicable under certain conditions.

Singular value decomposition also has applications in overlapped signal separation. Al-Zaben et al. used singular value decomposition to separate electrocardiographic (ECG) signal which includes both foetal and maternal rhythms. The technique is based on Singular value decomposition and neuro-fuzzy system. The results show that the algorithm is working successful [7]. Another similar practice of SVD is applied by J. S. Paul et al. [8] to extract muscle noise artifacts in ECG signal while exercising. The unique advantage of removing noise with singular value decomposition is that it does not need any prior information about the system. M. Wevers et al. filtered the noise from processing of transient signals from damage data of carbon fiber reinforced plastic. Singular value decomposition applied and the results were compared with different several techniques [12].

Data compression is a challenging subject for data processing issues especially for real time applications. Singular value decomposition is truly suitable for data compression due to its capability to identify the considerable part and relatively unnecessary part of the

signal by removing the low singular values and keeping the high singular values of the singular value vector matrix (S) which means reduction of dimension. In reference [9] Ping Bai et al. used singular value decomposition for independent component analysis of Functional Magnetic Resonance analysis as a data reduction step. In this case SVD is an effective tool to find out the spatio temporal features of FMRI. In mechanical engineering applications high spatial resolution frequency response function measurements are required. However processing of this high spatial resolution results is a time consuming process so as a robust dimension reducing technique singular value decomposition was used by S. Vanlanduit et al. [10]. The technique's computation time is acceptable and more accurate than others. Another application of singular value decomposition is applied to Intrusion detection systems by Sanjay Rawat et al. [11] as a pre-processing step to reduce dimension, noise and shorten the computation time.

An unexpected application of singular value decomposition is described by M. M. Škorić et al. and M. R. Rajković in their work [13]. They used SVD as clustering technique to find out locally linear regions in a data set. In other words they used SVD as a sort of linearization technique.

Milan Rajkovic also used singular value decomposition in his work [14] for noise reduction and calculation of the probabilities.

Although several decomposition techniques exist, singular value decomposition is the most commonly used which is unique in many area of science for many applications.

In this study, the main goal is to find an alternative way for nonlinear noise reduction, a better approach than existing one which is called state space smoothing (a.k.a. phase space averaging), introduced by Thomas Schreiber [17]. Readers can refer to [17-18] for further information about state space smoothing.

2. Van der Pol oscillator

State space smoothing via SVD is shown to be effective on a one dimensional Van der Pol oscillator (VdP). This oscillator originally devised by Balthasar Van der Pol during the 1920s to describe the dynamics of a triode electronic oscillator [15]. Oscillator describes the time variation of the triode charge. The damping is the key point in a VdP oscillator, as it changes with respect to the amount of a charge at a given time.

Van der Pol intended to study heart dynamics through electronic oscillators. When these oscillators are driven by an external signal whose frequency is close to that of the circuit, synchronization occurs. It is then said that the



circuit is entrained to the driving signal. This phenomena has the essence of driving the human heart with the desired frequency so that heart beat becomes regular. This regularity is lost during arrhythmias, this is when a pacemaker may help get the heart entrained [16].

Van der Pol equation has thus been used to model heartbeats, sunspot cycles, pulsating stars, as well as many others. VdP oscillators are autocatalytic oscillators since they release the energy to the same environment that they gathered the energy from.

The general forced form of one dimensional Van der Pol equation is

$$\ddot{x} - \varepsilon(1 - x^2)\dot{x} + x = A \sin wt$$

and in terms of first order state equations

$$\begin{aligned} \dot{x}_1 &= x_2 \\ \dot{x}_2 &= -x_1 + \varepsilon(1 - x_1^2)x_2 + A \sin wt \end{aligned}$$

3. Original and noisy time series

One dimensional driven Van der Pol eq is solved from the above state equations where $\varepsilon = 3$, $A = 5$, and finally $w = 1.788$, for which values the system is chaotic (Fig 1.a). VdP time series is used to construct and embedding space of 10 using the Taken's theorem. To test the effectiveness of the method, Gaussian white noise is added at signal to noise ratio (SNR) equals to 20 dB, fig 1.b, and 6 dB, fig 1.c, respectively. In each case, it is seen that the energy of the eigenvalues are concentrated mainly in the first one. Employing the algorithm in [6], only the first singular value is used in all cases to retrieve the signal from noise.

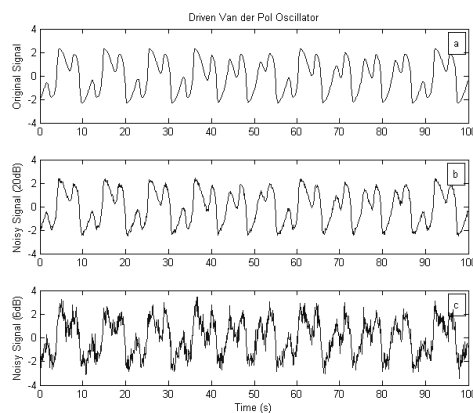


Fig. 1.a: Original time series **b.** Noisy time series (20 dB) **c.** Noisy time series (6 dB)

The clean time series is obtained once the SVD analysis is made on the reconstructed data matrix.

$$X = U S V^T$$

where matrix S contains all the singular values, and U and V are left and right singular matrices, respectively.

4. Noise reduction

Singular values (SVs) are the square roots of the eigenvalues. While a square matrix is formed in the computation the eigenvalues, $A A^T$, which is rather cumbersome when very long time series is involved, only the A matrix itself is used in the computation of the SVs.

As mentioned before, only the largest SV is used to retrieve the noise-free time series. In doing so, a new embedded data matrix is computed by

$$X_n = s(1)*u(1)*v^T(1)$$

where $s(1)$ is the first SV, $u(1)$ is the first left singular vector, $v^T(1)$ is the transpose of the first right singular vector. Then the resulting matrix X_n has the same dimension as the original one, X . Any of the columns are representative of the cleaned signal. After reconstructing the attractor, using any of the columns to the same embedding dimension removes noise, when compared to the original signal in fig 2.

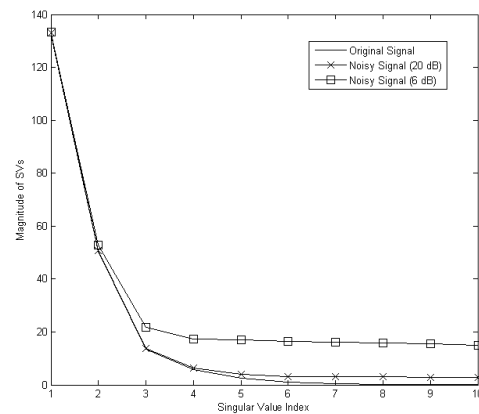


Fig. 2: — SVs of original signal, -x- SVs of noisy signal (20 dB), -□- SVs of noisy signal (6 dB)

As easily noticed, noise causes noise floor magnitude to go up. Retrieval of the signal in 20 dB noise case requires simply one iteration, whereas 6 dB noise requires the algorithm be applied at least twice.



Figure 3.a shows the signal with 20 dB noise after only one iteration. Please note the effectiveness this technique, when compared to figure 1.a, even when only the first SV is considered.

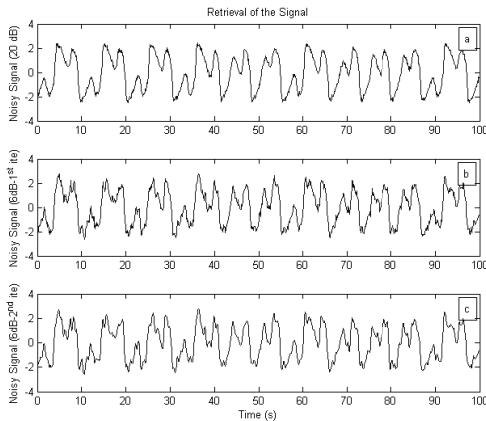


Fig. 3.a: Retrieval of the signal (20 dB)
 b. Retrieval of the signal (6 dB) after the first iteration
 c. Retrieval of the signal (6 dB) after the second iteration

Figures 3.b and 3.c show the successive steps of noise reduction on the signal contaminated with considerable noise power. Recovered signal seems to be still a little deformed, but SVs tell a different story.

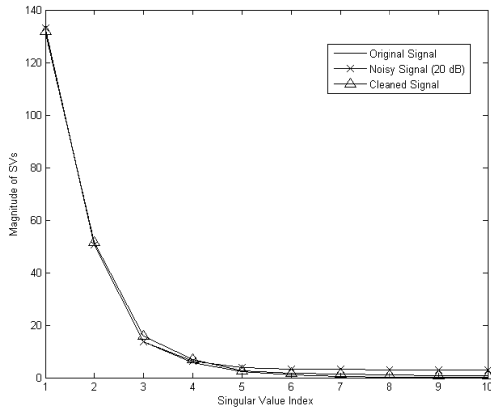


Fig. 4: — SVs of original signal, \times SVs of noisy signal (20 dB), Δ SVs of cleaned signal (20 dB)

20 dB noise is removed after just one, and the 6 dB noise is removed after 2 iterations. In either case, dominant SVs and their original magnitudes are recovered, as seen in figures 4 and 5.

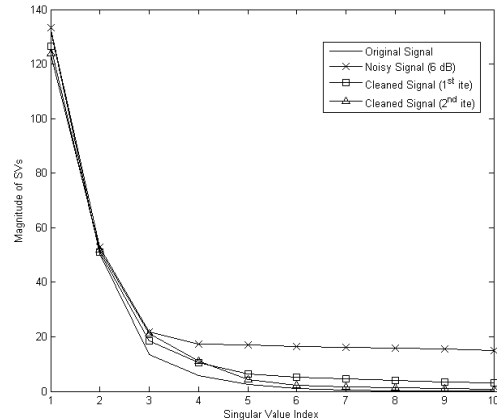


Fig. 5: — SVs of original signal, \times SVs of noisy signal (6 dB), \square SVs of cleaned signal (6 dB – 1st ite), Δ SVs of cleaned signal (6 dB – 2nd ite)

Finally, the signals are compared via nonlinear analysis. Nonlinear analyses, which consist of calculation of nonlinear invariants, i.e. Correlation Dimension (CD) and Kolmogorov-Sinai Entropy (KSE) in this study, are extremely sensitive to noise. The effect of noise in a signal can be seen more clearly in multi dimensional phase space than in one dimensional time series, as shown in Fig 6a-b and Fig. 7a-b. One important detail in the process of signal retrieval is worth to mention here, after noise reduction by SVD, the phase space of the signal still keeps its frame, on the other hand, smoothing causes crooked phase portrait (Fig. 6c-d and Fig. 7c-d).

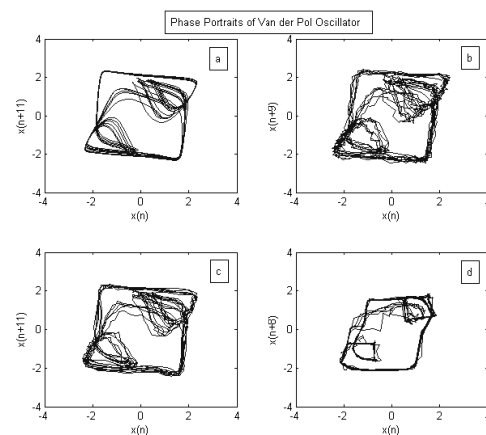


Fig. 6.a: Phase Portrait of original signal
 b. Phase Portrait of noisy signal (20 dB) c. Retrieval of the signal (20 dB) using SVD d. Retrieval of the signal (20 dB) using state space smoothing

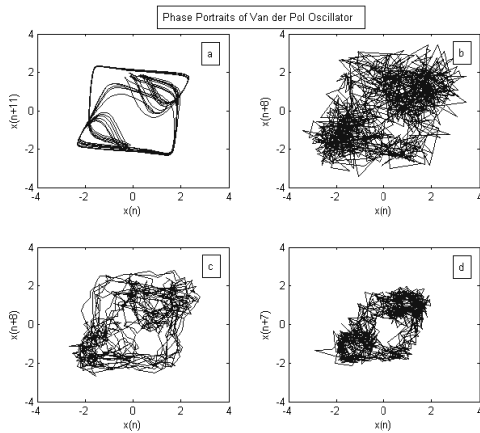


Fig. 7: a. Phase Portrait of original signal
 b. Phase Portrait of noisy signal (6 dB) c. Retrieval of the signal (6 dB) using SVD d. Retrieval of the signal (6 dB) using state space smoothing

Table 1: Comparison of nonlinear invariants, Correlation Dimension (CD) and Kolmogorov-Sinai Entropy (KSE).

	CD	KSE
Original Signal	1.5450	0.1494
Noisy Signal (20 dB)	1.6773	0.1581
Retrieval signal by SVD (20 dB)	1.5655	0.1482
Retrieval signal by Smoothing (20 dB)	1.6014	0.1546
Noisy Signal (6 dB)	2.8379	0.1908
Retrieval signal by SVD (6 dB)	2.0412	0.1606
Retrieval signal by Smoothing (6dB)	2.1118	0.1771

5. Conclusions

The noise reduction capability of singular value decomposition technique is presented on a one dimensional driven Van der Pol oscillator. The attractor is reconstructed deliberately to a larger embedding dimension to accentuate the signal mode against the noise floor. An iterative process is carried out on contaminated signal to regain the signal. As noise power goes up, more iterations are needed. But when noise is 20 dB and below, one iteration suffices to reduce any possible effects of the noise.

One problem may arise when the signal power is not concentrated at the top eigenvalues. If this is the case, then

if the noise floor level is roughly known, more eigenvalues may be processed in the computation of the noise-free signal. There are, however, other techniques that drive the percent energy of the first eigenvalue further up, which is beyond the scope of this current work.

Nonlinear time series analysis is highly affected from noise. Noise brings on additional complexity to original signal which actually does not exist. This leads an increase in nonlinear invariants' values (Table I). It's essential to remove as much noise with retaining the original signal. Elshorbagy et al. [19] showed that the use of smoothing for noise reduction might remove significant part of the original signal and introduce nonexisting chaotic behavior. Although SVD also cause an additional complexity to the signal, it fulfills relatively better results than smoothing (Table I). Still yet, it is believed that this method will prove useful in many cases.

References

- [1]. G.W. Stewart, *On the early history of the singular value decomposition*, SIAM REV, Vol.35 Issue 4, December 1993, pages 551–566.
- [2]. H. Hassanpour, *A time-frequency approach for noise reduction*, *Digital Signal Processing*, Elsevier Science, Volume 18, Issue 5, pages 728-738, 2008.
- [3]. P. C. Hansen, S. H. Jensen, *Subspace-Based Noise Reduction for Speech Signals via Diagonal and Triangular Matrix Decompositions*, EURASIP Journal on Advances in Signal Processing, Hindawi Publishing Corporation, Volume 2007, pages 24, 2007.
- [4]. S.H. Jensen, P.C. Hansen Esat, S.D. Hansen, J.A. Sorensen, "Reduction of General Broad-Band Noise in Speech by Truncated QSVD: Implementation Aspects, *Speech and Audio Processing*, Elsevier Science, Volume 3 Issue 6, pages 439-448, 1995.
- [5]. M. Bydder, J. Du, *Noise reduction in multiple-echo data sets using singular value decomposition*, *Magnetic Resonance Imaging*, Elsevier Science, Vol.24, pages849–856, 2006.
- [6]. K. Shin, J. K. Hammand, P. R. White, *Iterative SVD Method for Noise Reduction of Low-Dimensional Chaotic Time Series*, *Mechanical Systems and Signal Processing*, Academic Press, Volume 13 No: 1, pages 115-124, 1999.
- [7]. A Al-Zaben and A Al-Smadi, *Extraction of foetal ECG combination of singular value decomposition and neuro-fuzzy inference system*, *Physics in Medicine and Biology*, Institute of Physics Publishing , Phys. Med. Biol. 51 (2006), pages 137-143, 2005.
- [8]. J. S. Paul, M. R. Reddy, V. J. Kumar, *A Transform Domain SVD Filter for Suppression of Muscle Noise Artifacts in Exercise ECG's*, *IEEE Transactions on Biomedical Engineering*, Volume 47 No:5, pages 654-663, 2000.
- [9]. P. Bail, H. Shen, X. Huang, Y. Truong, *A Supevised Singular Value Decomposition for Independent Component Analysis of fMRI*, *Statistica Sinica*, Statistica Sinica 18, pages 1233-1252, 2008
- [10]. S. Vanlanduit, B. Cauberghe, P. Guillaume, P. Verboven, E. Parloo, *Reduction of large frequency response function data sets using a robust singular value decomposition* *Computers & structures*, Elsevier Science, Volume 84, pages 808-822, 2006
- [11]. S. Rawat, A. K. Pujari, V. P. Gulati, *On the Use of Singular Value Decomposition for a Fast Intrusion Detection System*, *Electronic*



- Notes in Theoretical Computer Science, Elsevier Science, Volume 142, pages 215-228, 2006.
- [12]. M. Wevers, L. Ripperta, J. M. Papy, S. V. Huffel, *Processing of transient signals from damage in CFRP composite materials monitored with embedded intensity-modulated fiber optic sensors*, NDT & E international, Elsevier Science, Volume 39, pages 229-235, 2003.
- [13]. M. S. Jovanović, M. R. Rajković, *Transition to turbulence via spatiotemporal intermittency in stimulated Raman backscattering*, Physical Review E, Volume 53 No 4, pages 4057-4066, 1996.
- [14]. M. Rajkovic, *Entropic nonextensivity as a measure of time series complexity*, Physica A, Elsevier Science, Volume 304, pages 327-333, 2004.
- [15]. R. C. Hilborn, *Chaos and Nonlinear Dynamics*, Oxford University Press, USA, 2000.
- [16]. J. C. Sprott, *Chaos and Time Series Analysis*, Oxford University Press, USA, 2003.
- [17]. T. Schreiber, *Extremely Simple Nonlinear Noise Reduction Method*, Phys. Rev. E 47, 1993.
- [18]. Kantz, H., Schreiber, T., 1997. *Nonlinear Time Series Analysis*, (Cambridge University Press).
- [19]. A. Elshorbagy, S. P. Simonovic and U. S. Panuc, *Noise Reduction in Chaotic Hydrologic Time Series: Facts and Doubts*, Journal of Hydrology 256, pages 147-165, 2002



Moving Sliding Mode Control of a DC Motor Driven Four-Bar Mechanism

Alper Kadir TANYILDIZI¹ and Orhan ÇAKAR²

¹Firat University, Faculty of Engineering, Department of Mechatronic Engineering, Elazığ, Turkey

²Firat University, Faculty of Engineering, Department of Mechanical Engineering, Elazığ, Turkey

atanyildizi@firat.edu.tr, cakaro@firat.edu.tr

Abstract

In this study, the crank velocity control of a four-bar mechanism driven by a DC motor is considered. The mathematical model of the motor-mechanism system is developed and the equations are solved numerically. Then the system is controlled by moving sliding mode control (MSMC) method. The results of the MSMC and the conventional sliding mode control (SMC) methods were compared. The numerical results show that MSMC is more effective than the SMC method and has smaller reaching time.

Keywords: Moving Sliding Mode Control, Four-bar linkage, Speed Control

1. Introduction

Single degree of freedom (SDOF) mechanisms driven by a DC motor are widely used and preferred in industry. One of the problems about the motor driven mechanism is that; the mechanism is designed and analyzed such that the angular velocity of the crank of mechanism is constant during its rotation. But the reaction torque of crank varies due to the external forces and inertia of links of the mechanism and as a result the velocity of the crank is fluctuated. So the expected behavior of the mechanism such as timing requirement can be altered and its performance is reduced [1-3]. Sadler et al. [1-2] presented a pair of study in which an analytical model was developed for a four-bar mechanism driven by a DC motor. Later, Liou et al. [3] investigated a motor-gear-mechanism system. Tao and Sadler [4] developed some control strategies based on PID control theory to reduce the crank angular velocity fluctuations of a four-bar mechanism driven by a DC motor and coupled a gear box. A complete mathematical model for the controller-motor-mechanism system was developed using state space representation. It was shown by numerical simulations that crank speed fluctuations can be reduced substantially adjusting the DC motor voltage by using feedback control. PID control gains were selected by trial-error firstly and

then were tuned by the pattern search optimization algorithm. After optimization, it was shown that the performance of the method is increased.

Gündoğdu and Erentürk [5] used a fuzzy logic controller (FLC) to regulate crank speed fluctuations of the the four-bar mechanism driven a DC motor. Performance of the proposed method was compared with optimum PID control method suggested in Ref.[4]. It was shown that the FLC method more efficient and more robust than PID control. In their study it was observed that the rise time to steady-state condition was very fast without a large overshoot and the percentage of speed fluctuations were very low compared to open-loop responses and PID controller cases.

Since PID controller is very sensitive to the nonlinearities, the tuning of the PID gains properly is quite difficult. During the past decades, to increase the capabilities of PID controllers, many artificial intelligence (AI) techniques such as neural networks (NN), fuzzy systems and neural-fuzzy logic have been employed. A self-tuning PID control based on particle swarm optimization (PSO) was adapted to the position control of a crank-slider mechanism actuated a PM synchronous motor by Kao et al. [6], a few years ago. In the proposed method, once the upper and the lower bounds of PID gains are determined by PSO algorithm, then the optimum values of which are determined by fuzzy rules. In order to demonstrate the efficiency of the proposed method, its sensitivity to the mass of the slider and to the external force was examined both the numerical simulations and the experiments.

Lin et. al. [7] used a novel adaptive controller to control the position of the slider of a crank-slider mechanism driven by a permanent magnet (PM) synchronous motor. In their study, the robustness of the controller was examined with regard to the parametric variations and external forces. However, all the gains in the adaptive controller must be chosen according to the requirement of stability, and complex mathematical model

of the mechanism. On the other hand, an FNN controller can be designed without using a complex mathematical model. Therefore, Wai et. al. [8] applied an FNN controller with adaptive learning rates to the position control of the slider-crank mechanism. The adaptive learning rates of the FNN were derived based on the analysis of a discrete-type Lyapunov function to guarantee convergence and stability in the sense of Lyapunov. A good tracking performance was achieved without the knowledge of the dynamics of the nonlinear system which require heavy computations. Lin et. al. [9] also applied the computed torque technique to control the coupled motor-crank-slider mechanism. Computed torque, or the inverse dynamics technique is a special application of feedback linearization of nonlinear systems. In addition, an adaptive computed torque controller, in which the gains are tuned using adaptive scheme, was proposed to control the coupled mechanism considering the existence of uncertainties.

Recently, the sliding mode control (SMC) has been used effectively in many control areas. This method is fewer sensitive to the plant parameter variations and the external load disturbance. SMC design is constitute to choose the sliding surface and determine the control law for the state variables to move on sliding surface. The performance of the SMC strictly depends on the control gain. When the control gain is large, the reaching time to the sliding surface from the initial state is minimized. But, the chattering phenomenon, which is undesirable for practical applications, occurs for the large values of the control gain. Şevkat and Telli [10] applied the SMC to the four bar mechanism driven by DC motor and the results compared with those of refs.[4] and [5]. It is concluded that the performance of the SMC is better than non-linear PID and FNN. They adopted a filter in order to alleviate the chattering phenomenon.

One way to alleviate the chattering phenomenon is to employ a boundary layer, which includes the uncertainties around the sliding surface. However, the bound of the uncertainties is difficult to obtain beforehand for practical applications. Fung et. al. [11] applied the SMC for the position control of a crank-slider mechanism driven by a PM synchronous servo motor. They utilized a simple fuzzy inference mechanism to estimate the upper bound of uncertainties for the SMC. It was shown that the proposed method has robust control performance to parametric variations and external disturbances. Lin et. al. [12] added a supervisory controller to FNN-SMC controller presented in [8] in order to stabilize the system states around bounded region. Lin and Wai [13] adopted an online-trained FNN to estimate the bound of uncertainties in real time. Also, Fung and Shaw [14] presented a method named as region-wise linear fuzzy

sliding mode control in order to increase the performance of the controller by minimizing the number of fuzzy rules.

Although chattering phenomenon can be alleviated with the insertion of a boundary layer, this approach is known to degrade robustness. Another way in order to improve the robustness of SMC is to rotate and/or shift the sliding surface during control action which called as moving sliding mode control (MSMC) proposed by Choi and et.al. [15, 16]. Sliding mode control with a moving sliding surface (MSS) has a robust and fast response. The MSS was designed to pass the initial conditions at first and subsequently moved towards a predetermined sliding surface by rotating and/or shifting. Employing the MSS, it is possible to lessen the sensitivity of the system to extraneous disturbances by means of shortening the reaching phase without increasing undesirable chattering of the control signals. Furthermore, the reaching phase can be almost eliminated by increasing the dwelling time of the surface, hence guaranteeing system robustness during whole intervals of control action. Alli and Yakut [17] adopted the MSS in conjunction with fuzzy tuning for a seismic isolation of earthquake-excited structure.

In the present paper MSS is applied to a four-bar mechanism driven by a DC motor to control the velocity of the input link. The upper voltage limit is also applied to the system in order to avoid the saturation of the motor in start-up duration which is not considered in refs.[4,5,10]. The results are compared with conventional SMC presented in [10]. The comparisons show that MSMC has smaller reaching time and it controls the system much robust than SMC, PID control and FNN.

2. Equation of Motion

A four-bar linkage is shown in Figure-1. Link 2 is driven by a DC motor with the torque T_2 . The lengths of the links are given by r_i ($i=1-4$). Angular position of the input link 2 is described by q and the angular positions of the other moving links are described by ϕ_1 and ϕ_2 . G_2 , G_3 and G_4 are the mass centers of the links.

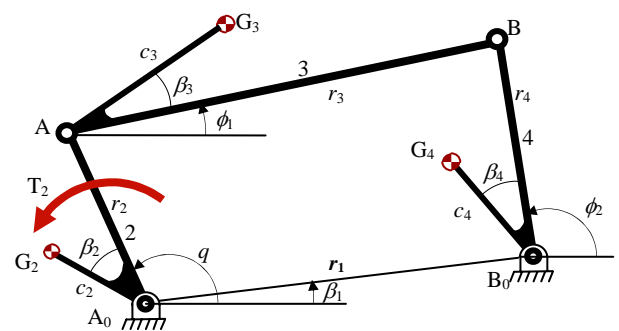


Fig.1. A four-bar mechanism

The generalized equation of motion of a single degree-of-freedom system is given by [18]:

$$\mathfrak{I}(q)\ddot{q} + \frac{1}{2} \frac{d\mathfrak{I}(q)}{dq} \dot{q}^2 = Q(q, \dot{q}, t) \quad (1)$$

where q, \dot{q} and \ddot{q} are independent displacement, velocity and acceleration; \mathfrak{I} and Q are the equivalent inertia and equivalent force, respectively and these are given by,

$$\mathfrak{I} = \sum_i [m_i (u_i^2 + v_i^2) + I_i h_i^2] \quad (2)$$

$$Q = \sum_i [F_i^x u_i + F_i^y v_i + M_i h_i] \quad (3)$$

where m_i and I_i are the mass and the mass moment of inertia of the link i , respectively; u_i and v_i are the components of the velocity influence coefficients of the mass center of the link i or of the point at which the force F acts and h_i is the velocity coefficient of the link i or of the link on which the torque M_j acts. Note that, the conservative or the dissipative forces can be included in Eq.(3) when they are presented.

The derivative of the equivalent inertia with respect to q is

$$\frac{d\mathfrak{I}}{dq} = 2 \sum_i [m_i (u_i u_i' + v_i v_i') + I_i h_i h_i'] \quad (4)$$

where the prime ($'$) defines the acceleration influence coefficient which is the derivative of the velocity coefficient with respect to independent variable q .

For the four-bar linkage given in Fig.(1) the equivalent inertia, the equivalent force and the velocity and the acceleration influence coefficients are given Appendix.

3. Mathematical Model of the DC Motor

The motor and the reduction gear which drive the mechanism are shown in Fig.(2).[4, 5, 10]

The ratio of the reduction gear is

$$n = \frac{T_b}{T_a} = \frac{\omega_a}{\omega_b} \quad (5)$$

where ω_a and ω_b are the angular velocities of the shafts a and b respectively. The input to the system is the voltage V and the output is the torque T_b which is the torque applied to the input link, i_f , R_f and L_f are called the field

current, resistance and inductance, respectively. R , L and i are the resistance, the inductance and the current of the rotor. J is the mass moment of inertia of the rotor and B is the viscous damping at the bearings. T_l is a constant mechanical load due to the brush friction, the gear friction or the dry bearing friction, etc...

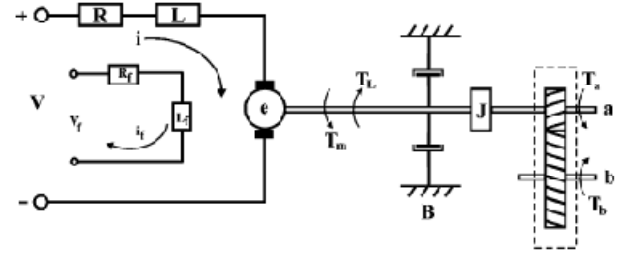


Fig.2. The motor and reduction gear.

Applying Kirchhoff's voltage law gives

$$V = Ri(t) + L \frac{di}{dt} + e \quad (6)$$

where e is the generated electromotive force of the motor. On the other hand, from the torque equilibrium on the rotor and the speed-reducer is obtained as

$$T_b = n(T_m - T_l - B\omega_a - J\dot{\omega}_a) \quad (7)$$

T_m represents the magnetic motor torque, and n is the gear ratio defined in Eq. (5). The magnetic torque and the generated electromotive force for a given constant field current i_f are defined as

$$T_m = K_m i(t) \quad (8)$$

and

$$e = K_g \omega_a \quad (9)$$

where K_m and K_g are the constants of motor torque and the motor voltage, respectively. Since shaft b drives the crank of the mechanism, Eq. (10) can be written as

$$\omega_a = n\omega_b = n\dot{q}_2 \quad (10)$$

When Eqs. (8) and (10) are substituted into Eqs. (6) and (7), the mathematical model of the motor can be obtained as



$$\frac{di}{dt} = \frac{1}{L}(V - Ri(t) - nK_g \dot{q}_2) \quad (11)$$

and

$$T = nK_m i - nT_L - n^2 B \dot{q}_2 - n^2 J \ddot{q}_2. \quad (12)$$

4. State-Space Representation

The equation of the system involving DC motor-gear-mechanism is the second order, the non-linear and the variable coefficients. For the solution of this equation the fourth order Runge-Kutta method is used in this study. First, the new variables \mathbf{x} (x_1 , x_2 and x_3) are described as

$$\begin{aligned} x_1 &= q \\ x_2 &= \dot{x}_1 = \dot{q} \\ x_3 &= i \end{aligned} \quad (13)$$

and then the state-space equations can be written as:

$$\begin{aligned} \dot{x}_1 &= x_2 \\ \dot{x}_2 &= \frac{1}{\mathfrak{I} + n^2 J} [-0.5 \mathfrak{I}' x_2^2 - n^2 B x_2 + nK_m x_3 - nT_L] \\ \dot{x}_3 &= \frac{1}{L} (V - R x_3 - nK_g x_2) \end{aligned} \quad (14)$$

5. Sliding Mode Control Design

Sliding mode control is known as variable structural control method controlling complex high-order non-linear systems robustly. The most important advantage of SMC is the insensitivity to the parametric variations and the external factors. In SMC, user chooses the sliding surface and forces the state variables to get close to the sliding surface. When the system approaches to the surface, the control signal is determined for dragging the system to the origin. SMC design is consist of deciding sliding surface and determining the control law for moving on sliding surface. Sliding surface is designed as not to contain the control parameter. Controller has to contain the control parameters getting the system closer to sliding surface and holding the system on surface.

Consider an n^{th} -order single-input non-linear controllable canonical form system given by

$$\begin{aligned} \dot{x}_1(t) &= x_2(t) \\ \dot{x}_2(t) &= x_3(t) \\ &\dots \\ \dot{x}_n(t) &= \sum_{i=1}^a f_i(x, t) + b(x, t)u(t) + d(t) \end{aligned} \quad (15)$$

where $x(t)$ is the state vector and $u(t)$ is the control input, $f(x, t)$ and $b(x, t)$ are the characteristics of the system and $d(t)$ denotes the external disturbances. The user has to choose sliding surface as the same number of inputs. When considering a second-order system there will be a sliding surface

$$s(x, t) = ce_1(t) + e_2(t) \quad (16)$$

where c is a strictly positive real constant which determines the slope of the sliding surface and e_1 and e_2 are tracking errors defined as

$$e(t) = [e_1(t) \quad e_2(t)] = [x_1(t) - x_{d1}(t) \quad x_2(t) - x_{d2}(t)] \quad (17)$$

where x_d is the desired trajectory.

A homogenous differential equation that has a unique solution $e=0$ could be obtained by setting $s=0$. Thus, the error will asymptotically reach to zero with an appropriate control law that could keep the trajectory on the sliding surface. Lyapunov's direct method, could be used to obtain the control law that maintains the goal and a candidate function, is defined as

$$V(s) = \frac{1}{2} s^2 \quad (18)$$

with $V(0)=0$ and $V(s)>0$ for $s>0$. Therefore, an efficient condition for the stability of the system can be given as

$$\dot{V} = \frac{1}{2} \frac{d}{dt} s^2 \leq 0 \quad (19)$$

Obtaining the inequality above means that, the system is stable and controlled in such a way that the state always moves towards the sliding surface and hits it. Therefore, Eq.(19) is called as the reaching condition for the sliding surface. Differentiating Eq.(16) with respect to time

$$\dot{s} = ce_1 + \dot{e}_2 = (f + bu - \ddot{x}_d + c\dot{e}) \quad (20)$$

and substituting Eq.(20) into the reaching condition given in Eq.(19)

$$s(f + bu - \ddot{x}d + c\dot{e}) \leq 0 \quad (21)$$

is obtained. Therefore, a control input satisfying the reaching condition can be chosen as

$$u = \frac{-\hat{f} + \ddot{x}d + c\dot{e}}{b} - K \text{sign}(s) = u_{eq} + u_{dis} \quad (22)$$

where \hat{f} is the estimated state equation, K is a strictly positive real constant with a lower bound depending on the estimated system parameters. The control input in Eq. (22) consists of two terms. The first term abbreviated as u_{eq} is the continuous term that is known as equivalent control based on estimated system parameters and it compensates the estimated undesirable dynamics of the system. The second term with the signum function is the discontinuous control law, u_{dis} that requires infinite switching on the part of the control signal and actuator at the intersection of error state trajectory and sliding surface. In this way, the trajectory is forced to move always towards the sliding surface.

The significant disadvantage of sliding mode control is discontinuity and changing the direction of input signal. This phenomenon is known as chattering and it is not desired. To eliminate chattering, the sign function in control law is changed by saturation function which can be defined as

$$\text{sat}(s) = \begin{cases} s > \varepsilon & 1 \\ s < -\varepsilon & -1 \\ s = \varepsilon & s/\varepsilon \end{cases} \quad (23)$$

The input signal is hold in specified values therefore it obstructs the chattering. For the considered system the equivalent control and the discontinuous control given as

$$u_{eq} = -2 \frac{d\mathfrak{S}}{dq} \ddot{q} (J + n^2 J_m) - \frac{n^2 B(Q - \frac{d\mathfrak{S}}{dq} \ddot{q}^2) L}{(J + n^2 J_m) n K_m} + R\dot{q} - n K_g \ddot{q} \quad (24)$$

and

$$u_{dis} = K \text{sat}(s, \varepsilon) \quad (25)$$

respectively.

6. Moving Sliding Mode Control

In conventional SMC, the sliding surface is fixed with constant slope of non-optimal or optimal value of c_k in the error state space. Hence, if the representative point (RP) lies in the stable zone (the second and fourth

quadrants) the absolute value of $e_2(t)$ becomes small for a fixed gain of K when large values were chosen for c . This will yield longer reaching time of the RP to the surface $s(t)$. On the other hand, if we choose small values for c , we know that the convergence speed on the surface itself will be slow, leading to a longer tracking time. Therefore, if an appropriate small value for time-varying slope c according to the trajectories of the RP is chosen, fast tracking is achieved without increasing the gain K . This is the key feature of the moving sliding surface. The surface is initially chosen to pass arbitrary initial conditions, and the surface is subsequently moved towards the predetermined sliding surface. The movement can be executed by rotating or/and shifting as shown in Fig.(4a-b). In the present paper MSMC is adopted to velocity control of the four-bar linkage.

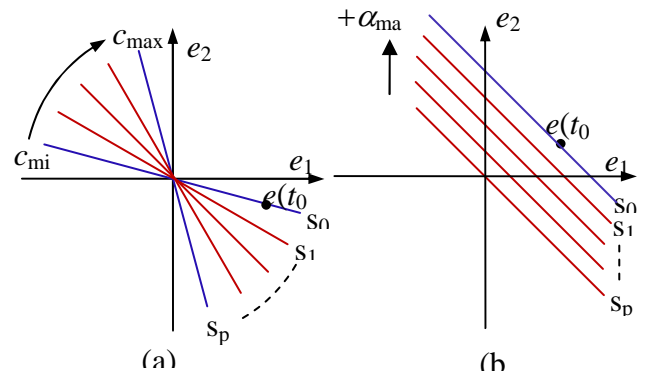


Fig.3. Illustration of moving sliding surface: a) Rotating sliding surface b) Shifting sliding surface.

7. Simulation Results

The steady-space representation of the four-bar mechanism and motor system is simulated by using Runge-Kutta method for open-loop step responses for the case tabulated in Table-1 and Table-2. The velocity of the crank reaches to 30 rad/s in 0.148 sec. But it crosses the desired value and fluctuates between 38.89 and 34.86 rad/s as shown in Fig.5.

Table 1. Mechanism Parameters

	Link 1	Link 2	Link 3	Link 4
L (m)	0.5593	0.102	0.610	0.406
r (m)		0.0	0.305	0.203
m (kg)		1.362	1.362	0.2041
J (kgm ²)		0.00071	0.0173	0.00509
β (rad)		0.0	0.0	0.0



Table 2. Motor Parameters

R (Ω)	L (H)	K _m (Nm/a)	K _g (Vs)	J (kgm ²)	T _L (Nm)	B (Nms)
0.4	0.050	0.678	0.678	0.056	0.00	0.226

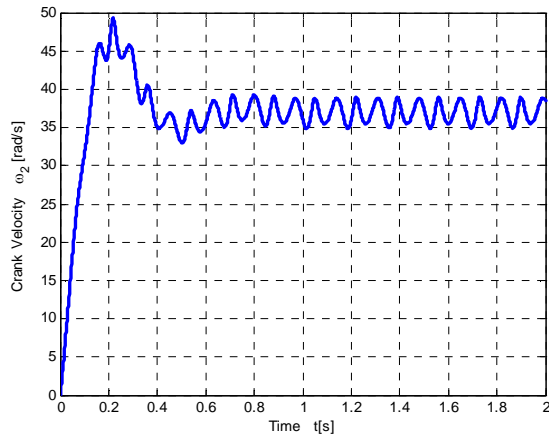


Fig.4. Crank Velocity without Control

8. Closed-Loop Control Results

The state-space representation of the four-bar mechanism and the motor driving system are integrated with the MSMC. For MSMC, the errors are calculated at first. Then the specific c values are calculated for each error satisfying $s(t)=0$. These different c values also give the specific sliding surfaces with variable slope. Hence the sliding surface moves during simulation.

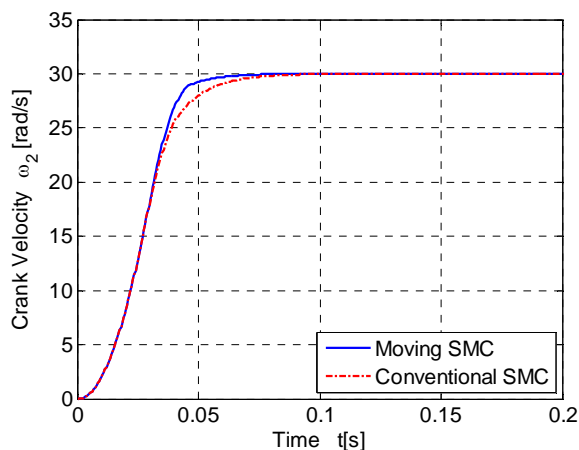


Fig.6. Comparison of crank velocities for MSMC and conventional SMC

In Fig.6 the comparison of MSMC and conventional SMC for the same values of k is given. The conventional SMC parameter c is taken from Şevkat and Telli [10] to show performance of the MSMC. MSMC has

smaller rise time because the slope of the sliding surface is set during simulation according to the error state.

It should be noted that a high level of voltage is applied to the system in start-up duration in order to reach the desired velocity. Therefore a voltage limiter should be adapted to the system to avoid motor saturation in the start-up duration, however it is not considered in refs. [5, 10]. When the control voltage is limited to 80 V, the rise time for this case takes long time compared to the unlimited case as shown in Fig.7.

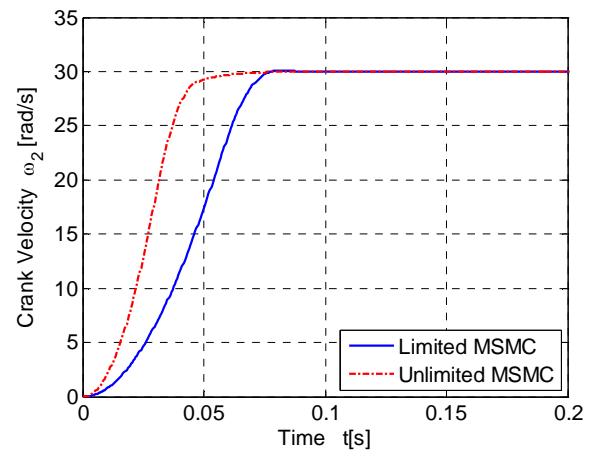


Fig.7. Comparison of the crank velocities for both the limited and unlimited MSMC cases

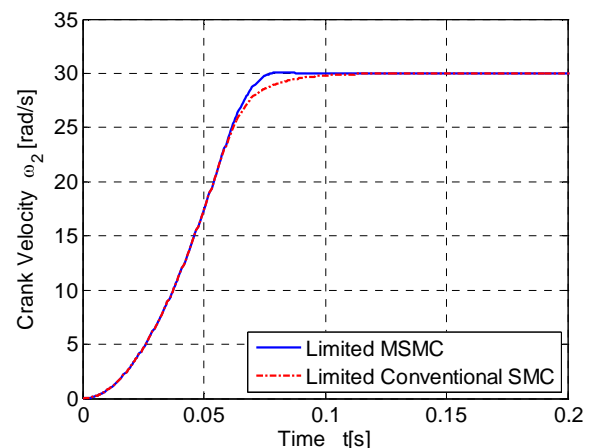


Fig.8. Comparison of the crank velocities at limited MSMC and limited conventional SMC

Also the comparison between MSMC and conventional SMC is given in Fig. 8. It is seen that MSMC is more robust than conventional SMC after limiting the motor voltage. The simulations are carried out for different c , k and voltage limit values and the obtained results such as average speed, rise time, overshoot and



speed fluctuations are given in Table 3. As seen, MSMC is effective than the control with constant sliding surface.

Table 3. Simulation Results

	Average Speed	Rise Time (s)	Overshoot (%)	Speed Fluctuations (%)
c=80 k=1300 Limit=220	29,9997	0,033	0,087	0,167
c=80 k=220 Limit=80	30,0077	0,031	0,087	0,966
c=Moving k=1300 Limit=220	30,0011	0,028	0,093	0,167
c=Moving k=1300 Limit=80	30,0017	0,046	0,093	0,167
c=Moving k=220 Limit=220	30,0088	0,028	0,290	1,033

9. Conclusion

In the present study, MSMC is adopted to control of a four bar mechanism driven by a DC motor. The results are compared with conventional SMC; it is shown that MSMC has smaller reaching time and robust control with respect to conventional sliding mode control.

From the simulations, it is shown that when the larger k value is chosen, the reaching time increases but the speed fluctuation decreases. That means, the optimum k value must be selected to have the robust control with small reaching time.

On the other hand, in this study a voltage limiter has been adopted to the system for avoiding the motor saturation in start-up time period unlike from the references and the results are concluded.

References

- [1] J.P. Sadler, R.W. Mayne and K.C. Fan, Generalized study of crank-rocker mechanisms driven by a dc motor – Part I Mathematical Model, *Mechanisms and Machine Theory*, 15, 435-445, 1980.
- [2] J.P. Sadler, R.W. Mayne and K.C. Fan, Generalized study of crank-rocker mechanisms driven by a dc motor – Part II Applications, *Mechanisms and Machine Theory*, 15, 447-461, 1980.
- [3] F.W. Liou, A.G. Erdman and K.C. Fan, Dynamic analysis of a motor-gear-mechanism system, *Mechanisms and Machine Theory*, 26, 2399-252, 1991.
- [4] J. Tao and J.P. Sadler, Constant speed control of a motor driven mechanism system, *Mechanisms and Machine Theory*, 30(5), 737-748, 1995.

- [5] Ö. Gündoğdu, K. Erentürk, Fuzzy Control of a dc motor driven four-bar mechanism, *Mechatronics*, 15,423-438, 2005.
- [6] C.C. Kao, C.W. Chuang, R.F. Fung, The self-tuning PID control in a slider-crank mechanism system by applying particle swarm optimization approach, *Mechatronics*, 16, 513-522, 2006.
- [7] F.J. Lin, R.F. Fung and Y.S. Lin, Adaptive control of slider-crank mechanism motion: simulations and experiments, *International Journal of Systems Science*, 28(12),1227 - 1238, 1997.
- [8] R. J. Wai and F.J. Lin, A fuzzy neural network controller with adaptive learning rates for nonlinear slider-crank mechanism, *Neurocomputing*, 20, 295-320, 1998.
- [9] F.J. Lin, Y.S. Lin and S.L. Chiu, Slider-crank mechanism control using adaptive computed torque technique, *IEE Proc. Control Theory Application* 145(3), 364-376, 1998.
- [10] G. Şevkat and S. Telli, Sliding Mode Speed Control of an Electric Motor Driven Four-Bar Linkage Mechanism, (Elektrik Motor Tahrikli Bir Dört-Çubuk Mekanizmasının Kayan Kip Hız Kontrolü)(In Turkish) Uludağ Üniversitesi Mühendislik-Mimarlık Dergisi, 13 (2), pages 15-26, 2008.
- [11] R.F. Fung, K.W. Chen and J.Y. Yen, Fuzzy sliding mode controlled mechanism using PM synchronous servo motor drive, *International Journal of Mechanical Science*, 41, 337-355, 1999.
- [12] F.J. Lin, R.F. Fung, H.H. Lin, C.M. Hong, A supervisory fuzzy neural network controller for slider-crank mechanism. *Mechatronics*, 11, 227-250, 2001.
- [13] F.J. Lin and R.J. Wai, Sliding-Mode-Controlled Slider-Crank Mechanism with Fuzzy Neural Network, *IEEE Transactions On Industrial Electronics*, 48(1), 60-70, 2001.
- [14] R.F. Fung and C.C. Shaw, Region-wise linear fuzzy sliding mode control of the motor-mechanism system, *Journal of Sound and Vibration* (2000) 234(3), 471-489.
- [15] S.B. Choi and D.W. Park, Moving sliding surface for fast tracking control of second-order dynamic systems, *ASME Journal of Dynamic Systems Measurement and Control*, 116, 154-158, 1994.
- [16] S.B. Choi and D.W. Park and S. Jayasuriya, A time-varying sliding surface for fast tracking control of second-order dynamic systems, *Automatica*, 30, 894-904, 1994.
- [17] H. Alli and Yakut O., Application of robust fuzzy sliding-mode controller with fuzzy moving sliding surfaces for earthquake-excited structures, *Structural Engineering and Mechanics*, 26 (5),517-544, 2007.
- [18] B. Paul, *Kinematics and Dynamics of Planar Machinery*, Prentice-Hall, 1979.

APPENDIX

The vector loop closure equation of the four-bar linkage given in Fig.(1) is

$$\mathbf{A}_0\mathbf{A} + \mathbf{AB} = \mathbf{A}_0\mathbf{B}_0 + \mathbf{B}_0\mathbf{B} \quad (\text{A1})$$

and two explicit constraint equations can be written as:

$$\begin{aligned} f_1(q, \phi_1, \phi_2) &= r_2 \cos q + r_3 \cos \phi_1 - r_1 \cos \beta_1 - r_4 \cos \phi_2 = 0 \\ f_2(q, \phi_1, \phi_2) &= r_2 \sin q + r_3 \sin \phi_1 - r_1 \sin \beta_1 - r_4 \sin \phi_2 = 0 \end{aligned} \quad (\text{A2})$$

where q is the independent coordinate; ϕ_1 and ϕ_2 are the dependent ones. The constraint equations are non-linear and can be solved by the numerical methods.

The velocity coefficient can be calculated as:



$$\mathbf{g} = -\mathbf{J}^{-1}\mathbf{f}' \quad (\text{A3})$$

where

$$\mathbf{g} = \{g_1 \quad g_2\}^T, \quad \mathbf{f}' = \left\{ \frac{\partial f_1}{\partial q} \quad \frac{\partial f_2}{\partial q} \right\}^T \quad (\text{A4a-b})$$

and \mathbf{J} is the Jacobian matrix and the elements of which are given by;

$$J_{ij} = \frac{\partial f_i}{\partial \phi_j}, \quad (i, j = 1, 2) \quad (\text{A5})$$

For the four-bar linkage:

$$\mathbf{J} = \begin{bmatrix} -r_3 \sin \phi_1 & r_4 \sin \phi_2 \\ r_3 \cos \phi_1 & -r_4 \cos \phi_2 \end{bmatrix}, \quad \mathbf{f}' = \begin{bmatrix} -r_2 \sin q \\ r_2 \cos q \end{bmatrix} \quad (\text{A6})$$

and the velocity coefficients are determined as:

$$g_1 = -\frac{r_2 \sin(q - \phi_2)}{r_3 \sin(\phi_1 - \phi_2)} \quad (\text{A7a-b})$$

$$g_2 = -\frac{r_2 \sin(q - \phi_1)}{r_4 \sin(\phi_1 - \phi_2)}$$

The components of the velocity influence coefficient of the mass center of the link i can be determined by differentiating the position variables with respect to input variable:

$$u_i = \frac{dx_i}{dq} = \frac{\partial x_i}{\partial q} + \sum_{j=1}^2 \frac{\partial x_i}{\partial \phi_j} g_j \quad (\text{A8})$$

$$v_i = \frac{dy_i}{dq} = \frac{\partial y_i}{\partial q} + \sum_{j=1}^2 \frac{\partial y_i}{\partial \phi_j} g_j$$

$$\begin{aligned} u_2 &= -a \sin(q) \\ v_2 &= a \cos(q) \\ u_3 &= -r_2 \sin(q) - b \sin(\phi_3) g_1 \\ v_3 &= r_2 \cos(q) + b \cos(\phi_3) g_1 \\ u_4 &= -c \sin(\phi_4) g_2 \\ v_4 &= c \cos(\phi_4) g_2 \end{aligned} \quad (\text{A9})$$

The acceleration influence coefficient or the second order influence coefficient is the derivative of the velocity influence coefficient with respect to independent variable, and can be written as:

$$g'_i = \frac{dg_i}{dq} = \frac{d^2 \phi_i}{dq^2} = \frac{\partial g_i}{\partial q} + \sum_{j=1}^2 \frac{\partial g_i}{\partial \phi_j} g_j; \quad i=1, 2 \quad (\text{A10})$$

The acceleration influence coefficients of the four-bar linkage are determined as:

$$g'_1 = -\frac{r_2 \cos(q - \phi_2)}{r_3 \sin(\phi_1 - \phi_2)} + \frac{r_2 \cos(\phi_1 - \phi_2) \sin(q - \phi_2)}{r_3 \sin^2(\phi_1 - \phi_2)} g_1 \quad (\text{A11a})$$

$$+ \frac{r_2 \sin(\phi_1 - q)}{r_3 \sin^2(\phi_1 - \phi_2)} g_2$$

$$g'_2 = -\frac{r_2 \cos(q - \phi_1)}{r_4 \sin(\phi_1 - \phi_2)} + \frac{r_2 \sin(q - \phi_2)}{r_4 \sin^2(\phi_1 - \phi_2)} g_1 \quad (\text{A11b})$$

$$- \frac{r_2 \cos(\phi_1 - \phi_2) \sin(q - \phi_1)}{r_4 \sin^2(\phi_1 - \phi_2)} g_2$$

Similarly the components of the accelerations coefficients of the mass center of the link i can be written as:

$$u'_i = \frac{\partial u_i}{\partial q} + \sum_{j=1}^2 \frac{\partial u_i}{\partial s_j} g_j \quad (\text{A12})$$

$$v'_i = \frac{\partial v_i}{\partial q} + \sum_{j=1}^2 \frac{\partial v_i}{\partial s_j} g_j$$

$$\begin{aligned} u'_2 &= -a \cos(q) \\ v'_2 &= -a \sin(q) \\ u'_3 &= -r_2 \cos(q) - b \cos(\phi_3) g_1^2 \\ &\quad - b \sin(\phi_3) g_1' \\ v'_3 &= -r_2 \sin(q) - b \sin(\phi_3) g_1^2 \\ &\quad + b \cos(\phi_3) g_1' \\ u'_4 &= -c \cos(\phi_4) g_2^2 - c \sin(\phi_4) g_2' \\ v'_4 &= -c \sin(\phi_4) g_2^2 + c \cos(\phi_4) g_2' \end{aligned} \quad (\text{A13})$$



Space Vector Modeling and Control of a Three-Pole Magnetic Bearing

Barış Oğuz GÜRSES^{1*}, Aysun BALTACI¹, Mutlu BOZTEPE², Mehmet SARIKANAT¹

^{1*} Ege Üniversitesi, Makina Mühendisliği Bölümü
Ege Üniversitesi, Makina Mühendisliği Bölümü, 35100 Bornova/İZMİR
oguz.gurses@ege.edu.tr

² Ege Üniversitesi, Elektrik - Elektronik Mühendisliği Bölümü

Abstract

The high speeds that rotordynamic systems operate at are pushing the conventional bearing systems to their limits. Active magnetic bearing systems can answer the needs that occur at these high speeds and extreme conditions like extreme low or high temperature, vacuum or in contaminant processing units. Thus the researchers that work on alternative bearing systems focus on this subject.

In this study, force – current – displacement relationship of three pole heteropolar active magnetic bearing is defined and position control is made by two feedback loops in which inverse dq transformation is used as a nonlinear transformation block.

Keywords: Heteropolar Magnetic Bearing, Space Vector, Y Connection, inverse dq Transformation

1. Introduction

In the last decades; advances in turbomachinery technology defined new requirements for bearing systems, thus researches are focused on new bearing technologies. Especially one of these new bearing systems which is active magnetic bearing technology is drawn much more attention due to its non-contact, wear and contamination free nature. At first glance, their unstable characteristics could be seen as a disadvantage but with closed loop control, they can have superior dynamic performances and can be used for active vibration control. If they are properly designed, they have low power loss compared to thin film bearings at high speed. Even though they have superior characteristics against convention bearing systems, because of requirements for sensors and active control elements they are not popular in the market. Researchers are especially focused on reducing manufacturing costs of active magnetic bearings to increase their usage. One of the ways to reduce costs is reduce the number of sensors and switching elements in AMB system. Three pole magnetic bearings have the minimum number of poles to stabilize a rotor in two axis which is a great advantage to magnetic bearings which

have more poles but due to highly coupled magnetic forces they are neglected until the last years.

Several researches are done in modeling, control and analysis of three pole magnetic bearings. Chen and Hsu worked on optimal design of magnetic bearings with analytical methods. They are considered bias currents, pole areas, winding schemes and number of turns in coils. They have concluded that the optimal orientation angle is $\pi/6$ and with that orientation angle only two power amplifiers are needed because upper poles can share the same control current but in opposite directions[1] [2].

Yang and his friends studied on control of a three pole magnetic bearing which is driven by a three phase inverter. They have used hysteresis control as current controller and PID control scheme as position controller. In their study, they have analyzed force magnitude dependence on relative motion of rotor on x-axis by numerical methods[3].

Hoffman studied a inverted-Y type three pole magnetic bearing and made a comparison between heteropolar and homopolar magnetic bearing with different pole numbers[4].

In this study, force – current – displacement relationship of three pole heteropolar active magnetic bearing is defined and position control is made by two feedback loops in which inverse dq transformation is used as a nonlinear transformation block.

2. Modeling of Three Pole Magnetic Bearing

2.1. Space Vector Modeling(SVM)

Space vector control technique depends on the instantaneous position of current or flux vectors in d-q plane. Fluxes in a Y connected three pole magnetic bearing can be defined by two independent flux vectors because current in the one of the poles is equal to the sum of other currents (Figure 1)

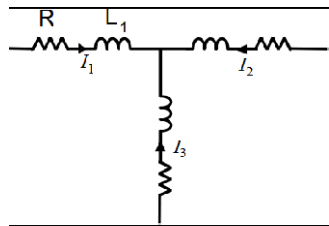


Fig. 1. Currents in Y Connected Coils

$$\sum_{n=1}^k i_n = 0 \quad (1)$$

where i_n is the current in coils of pole n and k is the number of poles. As magnetic flux depends on current, a flux conservation equation can be defined like the equation above.

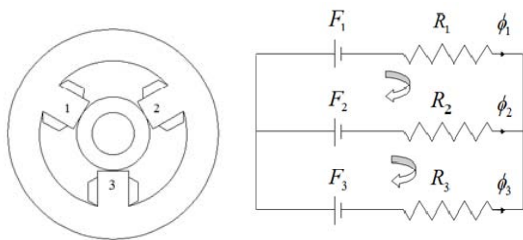


Fig 2. a) Location of Poles b) Magnetic Circuit of Magnetic Bearing

$$\sum_{n=1}^k \phi_n = 0 \quad (2)$$

where ϕ is magnetic flux and k is the number of poles.

There can be defined a transformation vector that compress three variable information into one complex variable in which magnitude and direction of the force can be stored.

$$B = k\mathbf{B} \quad (3)$$

where b is a complex number, k is complex transformation and B is the magnetic field vector. In literature, complex transformation vector k is suggested as equation below for three phase Y connected systems in which the first phase has not any phase shift [2].

$$k = \sqrt{\frac{4}{3}} \begin{bmatrix} 1 \\ e^{i\frac{2\pi}{3}} \\ e^{i\frac{4\pi}{3}} \end{bmatrix} \quad (4)$$

2.2. SVM of Three Pole Bearing at Center Position

If it is assumed that rotor is centered and magnetic material is linear and its magnetic permeability does not depend on magnetic intensity; there is a simple and linear relationship between magnetic flux in poles and coil currents.

$$\begin{bmatrix} \bar{R}_1 & -\bar{R}_2 & 0 \\ 0 & \bar{R}_2 & -\bar{R}_3 \\ 1 & 1 & 1 \end{bmatrix} \begin{bmatrix} B_1 \\ B_2 \\ B_3 \end{bmatrix} = N \begin{bmatrix} 1 & -1 & 0 \\ 0 & 1 & -1 \\ 0 & 0 & 0 \end{bmatrix} \begin{bmatrix} i_1 \\ i_2 \\ i_3 \end{bmatrix} \quad (5)$$

where B_n is magnetic flux, i_n is coil current, \bar{R}_n is normalized reluctance in the n th pole. \bar{R}_n is defined as;

$$\bar{R}_n = \frac{x}{\mu_0} \quad (6)$$

where x is airgap and μ_0 is magnetic permeability of air. It is reported in literature that one that can use the transformation vector k to transform magnetic flux vector into flux phasor [2]. A model of magnetic bearing and phasor transformer is simulated in SIMULINK (Figure 3 and 4).

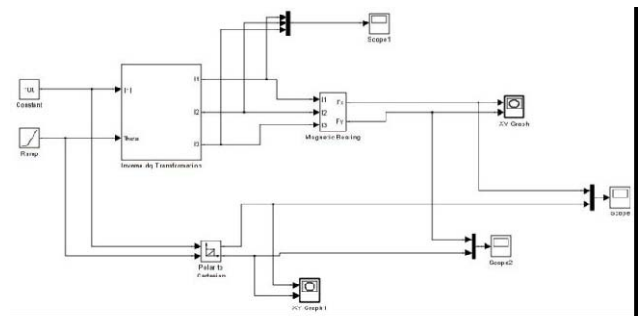


Fig 3. SIMULINK model of Three Pole Magnetic Bearing

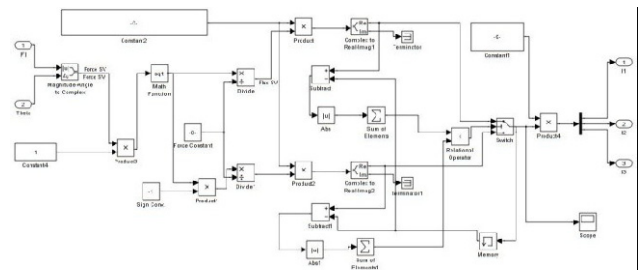


Fig 4. Inverse Phasor Transformation

System is simulated with a force phasor that is rotating from 0 to 2π rad.

As it is seen in the simulation results, there is a phase shift of $\pi/2$ in system output(Figures 5 and 6).

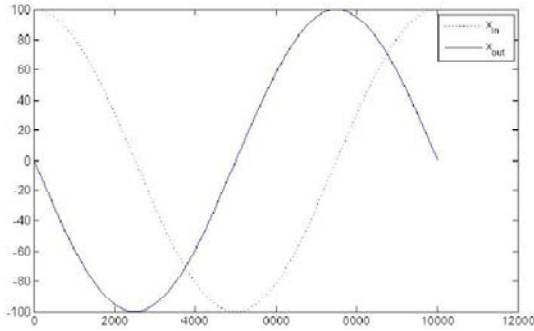


Fig 5. Output and Input Force in x Axis

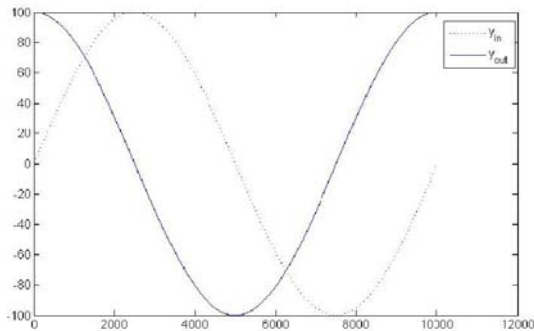


Fig 6. Output and Input Force in y Axis

To cancel this delay, a rotation of $-\pi/2$ is added in inverse dq transformation algorithm.

3. Generalized SVM of Three Pole Bearing

In the previous section location of rotor is considered that it is fixed in the center of workplane, so reluctances between pole faces and rotor are assumed to be equal and magnetic fluxes are only dependent on currents. But when rotor is moved in the plane, reluctances change so fluxes start to depend on position. If magnetic circuit of the three pole magnetic bearing is analyzed, the relation between fluxes, positions and currents can be defined as in equation below.

$$\frac{1}{A\mu_0} \begin{bmatrix} x_1 & -x_2 & 0 \\ 0 & x_2 & -x_3 \\ 1 & 1 & 1 \end{bmatrix} \begin{bmatrix} B_1 \\ B_2 \\ B_3 \end{bmatrix} = N \begin{bmatrix} 1 & -1 & 0 \\ 0 & 1 & -1 \\ 0 & 0 & 0 \end{bmatrix} \begin{bmatrix} i_1 \\ i_2 \\ i_3 \end{bmatrix} \quad (7)$$

3.1. Nonlinear Control of Three Pole Bearing

3.1.1 Mathematical Modeling of Rotor

In this study, rotor is assumed as a 2 DOF non-rotating disc which has a circular cross-section(Figure 7).

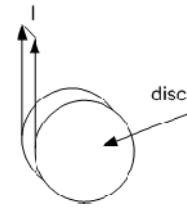


Fig 7. Zero - length Beam

Rotor has no length in z axis, so there can be no bending vibration in x or y axis due to the stiffness of rotor.

Transfer function of rotor is given in equation below.

$$\frac{X(s)}{F(s)} = \frac{1}{ms^2} \quad (8)$$

where m equals to unit mass per length of rotor.

3.1.2 Controller Design

Magnetic force on a pole is a quadratic function of both coil current and airgap. If the magnetic structure of system is homopolar, conventional linearization methods (Taylor series expansion etc.) can be used at operating points because magnetic coupling is minimal in the system. But in the case of heteropolar magnetic structure with three poles, magnetic fluxes in the poles are highly coupled and linearization methods are not effective. Hence alternative nonlinear control algorithms should be used.

In this paper, inverse dq transformation was proposed as a nonlinear transformation algorithm to transform whole magnetic bearing system into a double integrator (Figure 8).

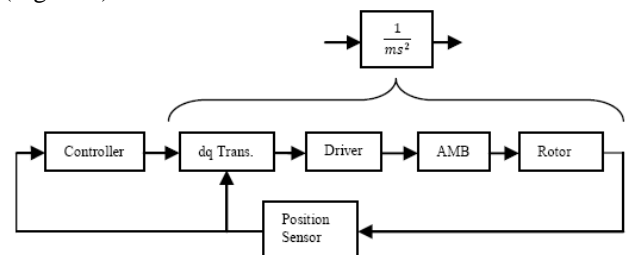


Fig 8. Active Magnetic Bearing System with Nonlinear Transformation

Nonlinear Transformation Algorithm

Nonlinear transformation algorithm contains two blocks which are calculation of required magnetic flux and current allocation.

Required magnetic fluxes are calculated equations number 8 and 9.

$$b = \sqrt{\frac{f_{req}}{k_{mag}}} \quad (9)$$

$$B = \text{Re}\{k*b\} \quad (10)$$

Magnet coefficient (k_{mag}) is defined in equation in number 10.

$$k_{mag} = \frac{A}{\mu_0} \quad (11)$$

Coil currents are calculated from fluxes by equation number 6.

PD controller is chosen as the linear controller because proportional controller is not capable of injecting damping characteristics into the dynamic response of rotor which is a double integrator. Transfer function of a PD controller is given in equation below.

$$G_c(s) = K_p + K_D s \quad (12)$$

SIMULINK model of the controller is given in figure 9.

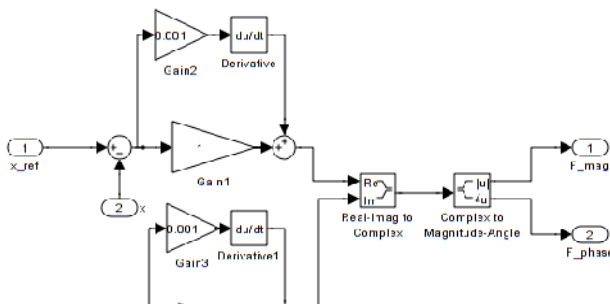


Fig 9. SIMULINK Model of PD Controller

Simulations

SIMULINK model of AMB system is given in figure 11.

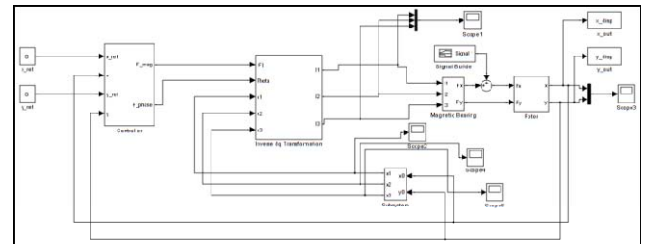


Fig 10. SIMULINK Model of AMB System

Controller block is responsible for generating required force magnitude and phase for displacement of rotor from the origin. Control force and magnitude is the input of inverse dq transformation. Inverse dq transformation block calculates required coil currents for given force and location data (Figure 10).

K_D and K_P parameters are varied between 0-0.1 and 0.1-25, respectively. Simulation was run for 0.05s and ode5 (Dormand - Prince algorithm) was selected as the solver with fixed time step of $10\mu s$. Disturbance force is a step function which has a magnitude of 100N and duration of 1ms.

RMS and maximum values of output signals are calculated and listed in table 1 and table 2.

Table 1. RMS values of displacement (μm) in the x axis (Disturbance force = 100 N in x axis)

$K_p \backslash K_d$	0.001	0.01	0.1
0.1	30.38	9.60	1.40
1	8.82	3.22	0.97
10	1.48	0.89	0.32
25	0.62	0.47	0.20

Table 2. Maximum values of displacement (μm) in the x axis (Disturbance force = 100 N in x axis)

$K_p \backslash K_d$	0.001	0.01	0.1
0.1	128.56	14.56	1.48
1	89.29	13.91	1.47
10	18.00	9.27	1.41
25	8.36	5.42	1.31

Table 3. RMS values of displacement (μm) in the y axis (Disturbance force = 100 N in y axis)

$K_p \backslash K_d$	0.001	0.01	0.1
0.1	30.42	9.60	1.40
1	8.82	3.22	0.97
10	1.48	0.89	0.32
25	0.62	0.47	0.20



Table 4. Maximum values of displacement (μm) in the y axis (Disturbance force = 100 N in y axis)

$K_p \backslash K_d$	0.001	0.01	0.1
0.1	128.71	14.56	1.48
1	89.36	13.91	1.47
10	18.00	9.27	1.41
25	8.36	5.42	1.31

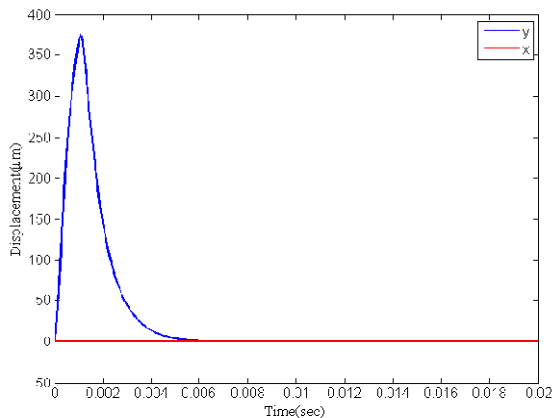


Fig 11. System Response to F=500 N in y direction

In figure 11, system response to 100N impulse input in the y axis direction is given.

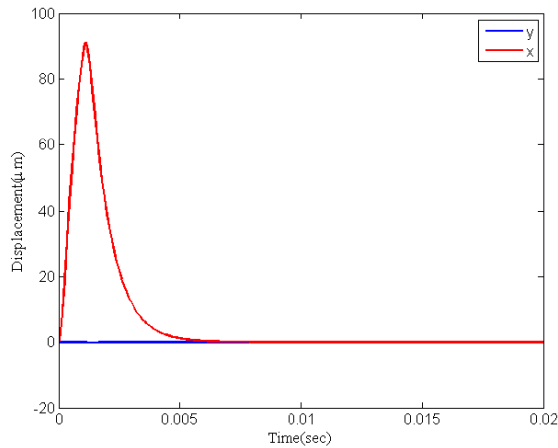


Fig 12. System Response to F=100 N in x direction

System response to 100N and 500N in the x axis is given in figures 12 and 13.

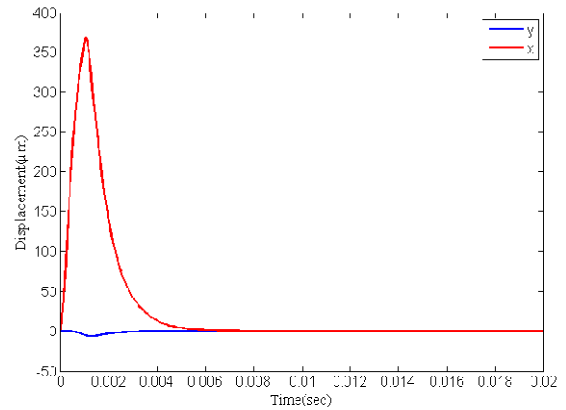


Fig 13. System Response to F=500 N in x direction

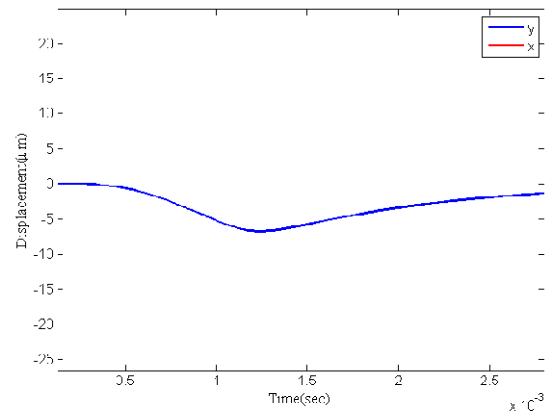


Fig 14. Parasitic motion in y direction

The response is overdamped but there is a parasitic motion in y direction (Figure 14).

4. Conclusion

Simulation results show that one can design a linear controller to a three pole heteropolar magnetic bearing with dq transformation as a nonlinear transformation block. As it is seen in tables 1 to 4, one can achieve a desired performance with changing K_p and K_d parameters. Response to disturbance in y direction is as expected but when a disturbance in x direction is applied, there is parasitic motion in y direction with 1.84% of displacement magnitude in x direction ($-6.77\mu\text{m}$) (for a disturbance force with magnitude of 500N). Thus special attention should be given in dq transformation when applying to precision motion control and further investigation is required to define the root of coupling problem in nonlinear transformation algorithm.



5. Acknowledgment

Financial support for this study was provided by TUBITAK-The Scientific and Technological Research Council of Turkey, Project Number: 108M267.

References

- [1]. C.-T. H. Shyh-Leh Chen, "Optimal design of a three pole active magnetic bearing," *IEEE Transactions on Magnetics*, vol. 38, no. 5, pp. 3458–3466, September 2002.
- [2]. D. Meeker and E. Maslen, "Analysis and control of a three pole radial magnetic bearing," in *Tenth International Symposium on Magnetic Bearings*, Switzerland, August 2006.
- [3]. H. Z. Yang and Q. R. Tang, "Study on inverter-fed three-pole active magnetic bearing," in *Applied Power Electronics Conference and Exposition, 2006. APEC '06. Twenty-First Annual IEEE*, 2006.
- [4]. W. Hoffman, "Behaviour and control of an inverter-fed three-pole active radial magnetic bearing," in *Industrial Electronics, 2003. ISIE '03. 2003 IEEE International Symposium on*, 2003.



Vibration Control of Beams Via Electromagnetic Fields

Barış Oğuz GÜRSES^{1*}, Aysun BALTACI¹, Mutlu BOZTEPE², Mehmet SARIKANAT¹

^{1*} Ege Üniversitesi, Makina Mühendisliği Bölümü
Ege Üniversitesi, Makina Mühendisliği Bölümü, 35100 Bornova/İZMİR
oguz.gurses@ege.edu.tr

² Ege Üniversitesi, Elektrik - Elektronik Mühendisliği Bölümü

Abstract

It is known that, time-varying magnetic fields create eddy currents on conductive materials. These eddy currents which are affected by magnetic field, producing a time-varying electromechanical force. This force, which acts as a contactless external factor, has a viscous damping characteristic. In many metal working machines vibration control is used for increasing surface quality and reducing chips (for example; circular saws, grinding machines). So that, the quality of manufactured product has increased and the total costs of the facility has decreased.

In this study, vibration behaviour of a cantilevered aluminium beam under the DC electromagnetic field, is examined experimentally. A current source, which drives the electromagnet, is designed and produced. On this current source, two different control algorithms are applied, named proportional-integral and Hysteresis.

Keywords: vibration control, time-varying magnetic fields

1. Introduction

Machines are usually affected by a force which is characterized by a certain frequency. If the frequency of this force is equal or close to any of natural frequency of this machine, machine structure vibrates at resonance which vibrations occur in great magnitude. This phenomenon may cause catastrophic failures and noise[1].

Portability and energy efficiency become key design factors by advances in technology. One of the factors that affect these design criteria is machine mass. Designers reduce mass to reach higher technology levels and to get more ratios in competitive market.

When a time varying magnetic field acts on a conductive material, eddy currents are formed. The electrical energy of eddy currents is transformed into thermal energy according to the Ohm Law and dissipated from the system by heat transfer. This transformation

causes a time varying force that acts on the structure which effects in the opposite direction.

Eddy currents have various application fields in engineering like energy conversion, magnetic breaking, vibration damping and damage detection in structures.

Vibration damping due to eddy currents have many advantages compared to conventional damping methods like constraint layer damping. The most important advantage is the characteristic properties of damping force which acts on the damped structure without any contact. Hence mass and stiffness variations in structure do not occur in this method. Also non-contact behavior of damping force prevents any wear and damper may function without any performance loss for a long time without any maintenance. It is known that there is a performance change in viscous dampers due to oil leak.

In literature, there are many applications of eddy current dampers (ECD). Bae et al. study vibration damping of cantilevered beams with eddy current dampers. They used a permanent magnet as magnetic field source. Their theoretical model and experimental results are matched. They found out that when magnetic field density is greater than 0.275Tesla, vibration characteristic of EDC - beam system becomes overdamped [2].

Sodano et al. studied vibration reduction of cantilevered beams which on they fixed a conductive plate with eddy currents. In their experiments, they made a reduction of 42.4 dB at the magnitude of first bending mode [3]. In their next study, Sodano and his colleagues expand their passive eddy current damper with active control. They improved the damping characteristic of EDS with active control algorithm which they used the location of permanent magnet as output and the velocity of beam as input [4]. Sodano et al. used two magnets instead of one in another their study. They reported that if the magnets are placed across as their same pole faces see each other; the damping ability of EDC would be improved [5].

Gerber, studied on vibrations in a hot dip galvanizing process produces variations in zinc coating weight and tried to solve the problem with EDC systems. As a result of his study, he found that EDC systems are suitable for such a problem [7].

In this study, vibration behavior of cantilevered beam under DC electromagnetic field is investigated experimentally. A switching converter to drive electromagnet is designed and manufactured. Proportional-integral (PI) control algorithm is chosen as current control algorithm.

2. Experimental Methods

2.1. Design of Electromagnet Driver

Magnetic field density depends on coil currents on electromagnets. Design of current control has great importance.

In this study, a switching converter is designed that drives electromagnet at desired current values for usage in vibration experiments. Designed converter is in full bridge topology that operates in four quadrants (Figure 1).

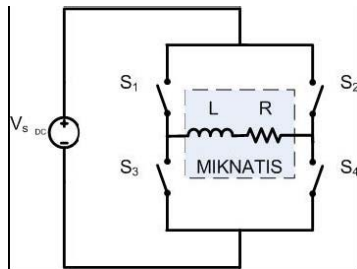


Fig 1. Full Bridge Circuit

Subparts of driver are shown in figure 2 schematically. IRFP460 Power Mosfets that has drain current limit of 10 A are chosen as switching components. IR2112 ICs are selected as MOSFET gate drivers. 6N137 optocouplers are used as optical isolators between control board and power board. LEM - LTS25NP Closed loop hall effect current sensor is used in feedback loop.

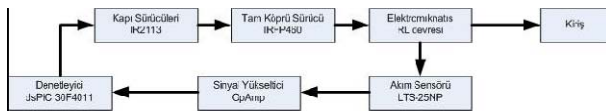


Fig 2. Subparts of Driving Circuit

Current control algorithm is run on dsPIC 30F4011A. MOSFETs are driven by MPWM module of microcontroller and 20 kHz is chosen as PWM frequency.

2.2. Experiments on Aluminum Beam

In this study, performance of eddy current damper

used to reduce vibrations of a conductive beam is investigated. Conductive beam is cantilevered at a point, and an electromagnet is located perpendicular to XZ plane of beam (Figure 3).

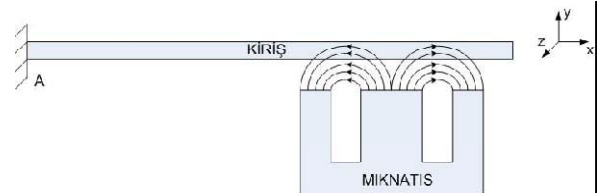


Fig 3. Experimental Setup

When beam moves in y axis, magnetic field that acts on beam will be varied thus eddy currents will be formed in cantilevered beam (Figure 4).



Fig 4. Magnetic Field that Acts on Beam

Eddy currents will interact with magnetic field and a time varying, velocity dependent force will be created.

Experimental setup is shown in Figure 5. Coil current is measured by Breymen BM – 812 CF model multimeter.

TT-T-ECHNI-C MCH – 303D – II is used as power supply and magnetic field density of electromagnet poles are measured by F.W. Bell 5180.

Displacement of vibrating beam is measured by KEYENCE LK-G517 contactless laser displacement sensor.

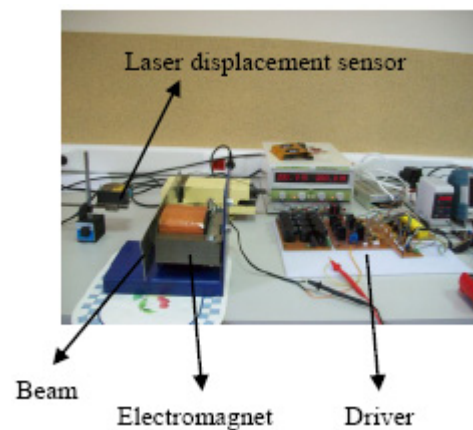


Fig 5. Experimental Setup



3. Results

Experiments, in which an aluminum beam that has dimensions of 80x450x1mm is used, are conducted at 4 different current values. Frequency spectrums of measured displacement signals are calculated in MATLAB by Fast Fourier transform (FFT). Displacement signals and their corresponding frequency spectrums are listed below. Free vibration of aluminum beam is shown in Figure 6.

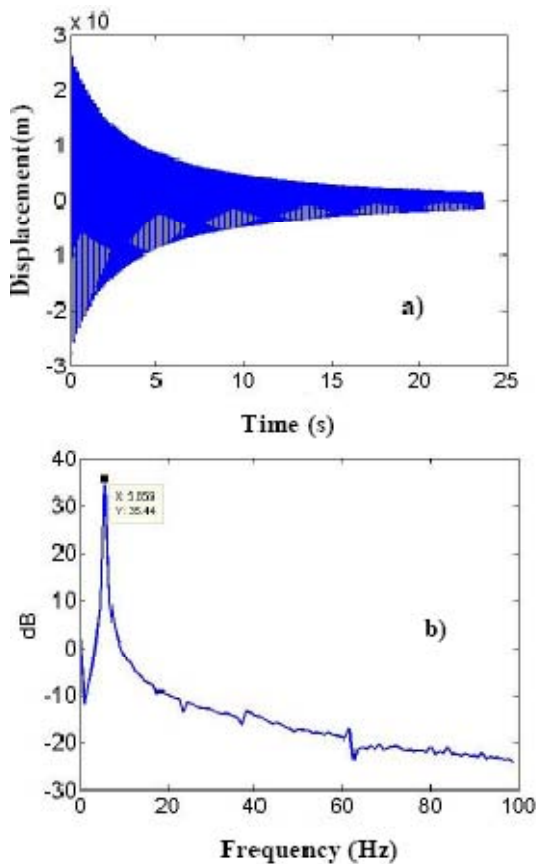
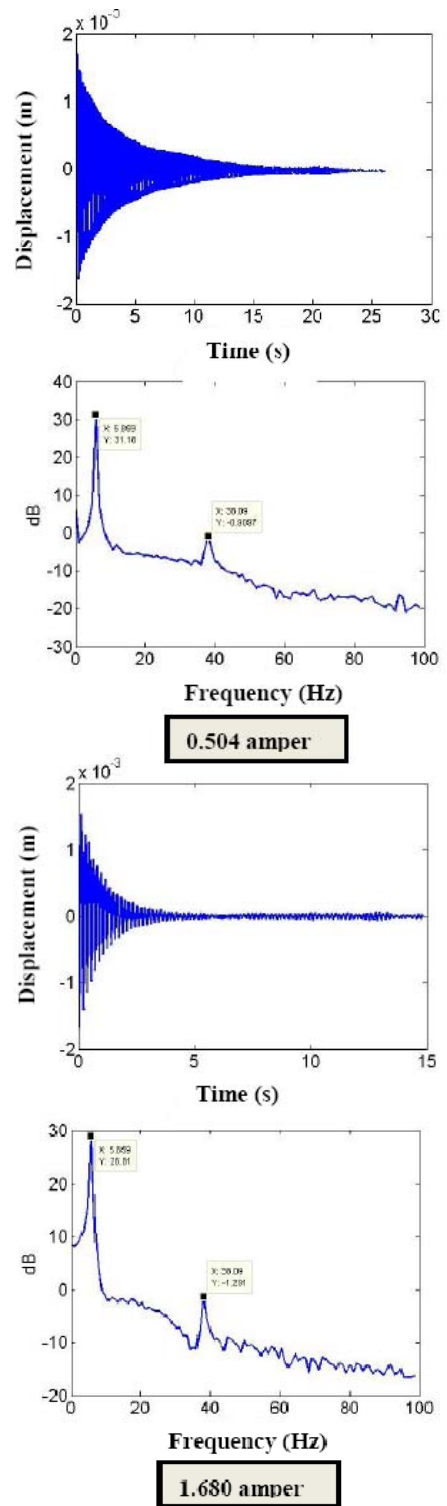


Fig 6. a) Free vibration of aluminum beam b) Frequency spectrums

Measured displacement signals and their corresponding FFTs of eddy current damper system are given in Figure 7 for various current levels.



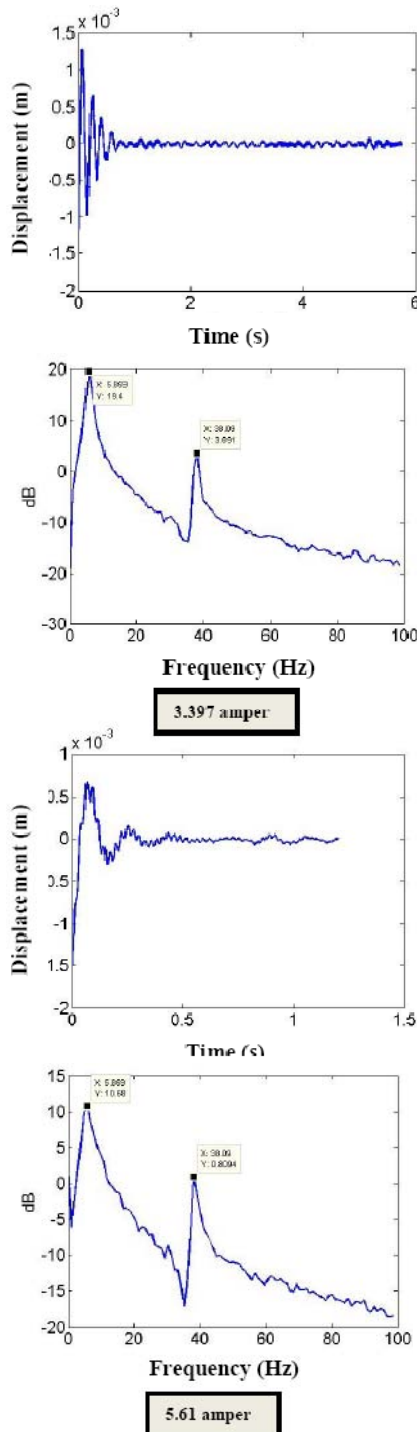


Fig 7. Vibration responses of aluminum beam for various current levels

As it is seen, damping coefficient depends on coil current proportionally which is an expected result.

Experiments could be conducted with a maximum current of 5.61A because of limited power capacity of

power supply. If current value is increased beyond this limit, an overdamped vibration behavior could be reached.

The change of magnitude at first bending mode, coil current and corresponding magnetic field density is listed in Table 1.

Table 1. The Variance of Vibration Amplitude of First Bending Mode of Beam due to Coil Current and Magnetic Field Density

Current (A)	Amplitude (dB)	Magnetic Field Density (mT)
0.50	31.18	16.9
1.68	28.81	61.30
3.39	19.40	134.90
5.61	10.68	223.10

The relation between coil current and damping coefficient which is calculated by logarithmic decrement method is shown in Figure 8.

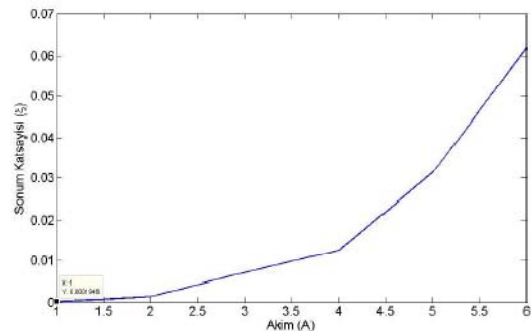


Fig 8. Variation of damping coefficient at different current values

As it is shown in figure, there is nonlinear relationship between magnetic field density and damping coefficient.

4. Conclusion

There is a second order nonlinear relation between coil current and damping coefficient of ECD system.

5. Acknowledgement

The authors gratefully acknowledge to Research Foundation of Ege University (Project No:2008/MUH/037) for financial support.



References

- [1]. A.E. Fitzgerald, C. Kingsley, *Electric Machinery*, Mc-Graw Hill Companies, New York, 1990.
- [2]. [2]. J.S. Bae, M.K. Kwak, D.J. Inman, *Vibration suppression of a cantilever beam using eddy current damper*, Journal of Sound and Vibration 284, pages 805-824, 2005.
- [3]. [3]. H.A. Sodano, J.S. Bae, D.J. Inman, W.K. Belvin, *Concept and model of eddy current damper for vibration suppression of a beam*, Journal of Sound and Vibration 288, pages 1177–1196, 2005.
- [4]. [4]. H.A. Sodano, J.S. Bae, D.J. Inman, W.K. Belvin, *Improved concept and model of eddy current damper*, Trans. of the ASME Journal of Vibration and Acoustics 128, pages 294–302, 2006.
- [5]. [5]. H.A. Sodano, D.J. Inman, W.K. Belvin, *Development of a new passive-active magnetic damper for vibration suppression*, Trans. of the ASME Journal of Vibration and Acoustics 128, pages 318–327, 2006.
- [6]. [6]. H.L. Gerber, *Magnetic damping of steel sheet*, IEEE Transactions on Industry Applications 39(5), pages 1448–1453, 2003.



Numerical Modelling of Protection of Gas Turbine Blades From Influence of High Temperature

A. PASHAYEV¹, R. SADIQOV^{1*}, A. SAMADOV¹, R. MAMMADOV¹

Azerbaijan National Academy of Aviation,
 AZ-1045, Bina, 25th km, Baku, Azerbaijan
 Phone: (99450) 385-35-11; Fax:(99412) 497-28-29
 e-mail: sadixov@mail.ru

Abstract

At the present the heat protection of high-temperature gas turbine blades is mainly provided at the expense of efficient cooling systems development. The task of turbine cascades streamlining comes to boundary integral equation (BIE) Fredholm II with a peculiarity. Stationary and quasistationary temperature fields of blades are calculated with application of new mathematical models represented in BIE in multi connected fields of complex configuration. For solving proper equations discrete operators have been investigated, converging quadrature and cubature processes have been developed and values in terms of A. Zigmound's modules of continuity have been received. Approximate BIE solutions are mathematically proved by appropriate theorems and lemmas. Methods of turbine profile approximation have been developed (method of least square with automatic joint, smoothing splines, smooth replenishment and neural nets have been used). In basis of potential flow theory, boundary integral equations had been received for components of flow complex potential – velocity potential and stream function differing from existence of the effectiveness of numerical realization (Complex Boundary Integral Equation Method). The corresponding algorithms and softwares in object-oriented programming language DELPHI 7 were created for the solution of equations. The reliability of the methods was proved by numerical and experimental investigations heat and hydraulic characteristics of the first stage of cooled nozzle blade of high pressure turbine. Geometric model, equivalent hydraulic schemes of cooling tracks have been obtained, cooler parameters and temperature field of gas turbine nozzle blade have been determined. Methods have demonstrated high efficiency at repeated and polivariant calculations, on the basis of which the way of blade cooling system modernization has been offered.

Nomenclature

T_g	gas temperature	K
T	required temperature	K
T_0	temperature of environment at $i = 0$;	K
T_{z_0}	temperature on the outline z_i at $i = 0$ (outside outline of blade);	K
T_i	field temperature at $i = 1, M$ (temperature of the cooler)	K

T_{z_i}	temperature on the outline z_i at $i = 1, M$ (outline of cooling channels)	K
T_k	temperature in the point k	K
ρ	material density;	kg/m ³
	density of a logarithmic potential	-
c_v	thermal capacity	J/kg·K
λ	heat conduction coefficient of material; thermal conductivity of the blade material	W/m·K
q_v	internal heat source or drain	W/m ²
α_0	heat transfer coefficient from gas to a surface of blade (at $i = 0$)	W/m ² ·K
α_g	gas local heat exchange coefficient	W/m ² ·K
α_c	air convective heat exchange local coefficient	W/m ² ·K
M	outline quantity	-
x, y	segment coordinates	mm
n	external normal to outline	-
	the quantity of outline segments	-
m	quantity of inline segments of all cooling channels	-
R	variable at an integration of the distance between fixed and "running" points	-
ΔS	mean on sections of the partition	-
$(L_{\tau, \varepsilon, f})(z)$	two-parameter quadrature formula for logarithmic double layer potential	-
$\sim f(z)$	double layer logarithmic potential operator	-
$(I_{\tau, \varepsilon, f})(z)$	two-parameter quadrature formula for simple layer logarithmic potential	-
$\&f\&\&(z)$	simple layer logarithmic potential operator	-
$\omega_f(x)$	module of a continuity	-
Γ	curve outline; velocity circulation	-
φ	velocity potential	m ² /s
ψ	stream function	m ² /s
V_∞	gas velocity of main inlet flow	m/s
α_∞	angle between the velocity vector and the profile cascade axis	deg
θ_{out}	angle that corresponds to the exit edge of the airfoil	deg
G_c	air flow	kg/s



Ψ_g, Ψ_c	gas and air temperature coefficients	-
κ_f	form coefficient	-
$^c \mu, \lambda_c$	cooler dynamic viscosity, heat conductivity coefficient	poise W/m·K
Bi	Bio criterion	-
ρ_{ij}	density of coolant flow	kg/m ³
ξ_{ij}	coefficient of hydraulic resistance	-
Nu	Nusselt criterion	-
Re	Reynolds criterion	-

1. Introduction

One of the main directions for the performance efficiency improvement of the power system in the modern aviation engines include increasing of the work flow conditions, and most of all it's come to the temperature increasing in the gas turbine inlet. In this case the most complicated problem is the design reliability assurance of the nozzle and rotating blades of the gas turbine, which falls under the direct effect of the high potential gas flow and significant loads. Therefore improvement and defining the ways for thermal protection, the lifetime and reliability increasing of the turbine details have a great scientific and practical importance. The activities for the temperature increasing can be compared to several directions. However assimilation of high T_{gin} AGTE mainly reached by refinement of the cooling systems for turbine blades. It is especially necessary to note, that with T_g increase the requirement to accuracy of results will increase. In other words, at allowed values of AGTE metal temperature T_{lim} = (1100...1300K), the absolute error of temperature calculation should be in limits (20 - 30K), that is no more than 2-3%. This is difficult to achieve (multiconnected fields with various cooling channels, variables in time and coordinates boundary conditions). Such problem solving requires application of modern and perfect mathematical device.

2. Problem formulation

In classical statement a heat conduction differential equation in common case for non-stationary process with heat distribution in multi-dimensional area (Fourier-Kirchhoff equation) has a kind [1,2]:

$$\frac{\partial(\rho C_v T)}{\partial t} = \text{div}(\lambda \text{grad} T) + q_v, \quad (1)$$

where ρ , c_v and λ - accordingly material density, thermal capacity, and heat conduction; q_v - internal source or drain of heat, and T - is required temperature.

Research has established that the temperature condition of the airfoil with radial cooling channels can be determined as two-dimensional [1,2]. Besides, if to suppose constancy of physical properties and absence of internal sources (drains) of heat, then the temperature field under fixed conditions will depend only on the skew shape and on the temperature distribution on the skew boundaries. In this case, equation (1) will look like:

$$\Delta T = \frac{\partial^2 T}{\partial x^2} + \frac{\partial^2 T}{\partial y^2} = 0 \quad (2)$$

When determining particular temperature fields in gas turbine elements are used boundary conditions of the third kind, describing heat exchange between the skew field and the environment (on the basis of a hypothesis of a Newton-Riemann). In that case, these boundary conditions will be recorded as follows;

$$\alpha_o(T_o - T_{\gamma o}) = \lambda \frac{\partial T_{\gamma o}}{\partial n} \quad (3)$$

This following equation characterizes the quantity of heat transmitted by convection from gas to unit of a surface of a blade and assigned by heat conduction in a skew field of a blade.

$$-\lambda \frac{\partial T_{\gamma i}}{\partial n} = \alpha_i(T_{\gamma i} - T_i) \quad (4)$$

Equation (4) characterizes the heat quantity assigned by convection of the cooler, which is transmitted by heat conduction of the blade material to the surface of cooling channels: where T_0 - temperature of environment at $i = 0$; T_i - field temperature at $i = 1, M$ (temperature of the cooler), where M - quantity of outlines; $r_0 T$ - temperature on an outline r_i at $i = 0$ (outside outline of blade); $r_i T$ - temperature on an r_i at $i = 1, M$ (outline of cooling channels); $0 a$ - heat transfer factor from gas to a surface of a blade (at $0 i =$); $I a$ - heat transfer factor from a blade to the cooling air at $i = 1, M$; l - thermal conductivity of the material of a blade; n - external normal on an outline of researched area.



3. Application of boundary integrated equations method for definition of AGTE elements' temperature fields

For the solution of this boundary problem (2)-(4) four numerical methods are used: Methods of Finite Differences (MFD), Finite Element Method (FEM), probabilistic method (Monte-Carlo method), and Boundary Integral Equations Method (BIEM) (or its discrete analog — Boundary Element Method (BEM)). Let us consider BIEM application for the solution of

problem (2)-(4) [1-3]. The function $T = T(x, y)$, continuous with the derivatives up to the second order, satisfying the Laplace equation in considered area, including and its outline $\Gamma = \bigcup_{i=0}^M \zeta_i$, is harmonic. Consequence of the Grin integral formula for theresearched harmonic function $T = T(x, y)$ is the ratio:

$$T(x, y) = \frac{1}{2p} \int_{\Gamma} [T_{\Gamma} \frac{\partial(\ell n R)}{\partial n} - \ell n R \frac{\partial T_{\Gamma}}{\partial n}] ds \quad (5)$$

where R - variable at an integration of the distance between point K(x, y) and “running” on the outline k - point; T_{Γ} - temperature on the outline Γ . The temperature value in some point k lying on the boundary is determined (as limiting at approach of point K(x, y) to the boundary)

Any equations or formulae should be centered; and there should be one blank between the texts and the formulas.

$$T_k = \frac{1}{2p} \left[\int_{\Gamma} T_{\Gamma} \frac{\partial(\ell n R_k)}{\partial n} ds - \int_{\Gamma} \frac{\partial T_{\Gamma}}{\partial n} \ell n R_k ds \right] \quad (6)$$

With allowance of the boundary conditions (2)-(3), after collecting terms of terms and input of new factors, the ratio (6) can be presented as a linear algebraic equation, computed for the point R :

$$\varphi_{k1} T_{\zeta_{01}} + \varphi_{k2} T_{\zeta_{02}} + \dots + \varphi_{kn} T_{\zeta_{0m}} - \varphi_{k\zeta_0} T_0 - \varphi_{k\zeta_i} T_i - 2p T_k = 0 \quad (7)$$

where, n is the quantity of sites of a partition of an outside outline of a blade $l_{\gamma 0}$ ($l_{\gamma i}$ on $i = 0$) on small sections

S_0 (S_i at $i = 0$) $\Delta \Delta =$, m is the quantity of sites of a partition of outside outlines of all cooling channels $l_{\gamma i}$ ($i = 1, M$) on small sections ΔS_i .

Let us note, that unknowns in the equation (7) except the unknown of true value T_k in the k point are also mean onsections of the outlines partition ΔS_0 and ΔS_i temperatures $T_{\gamma 01}, T_{\gamma 02}, \dots, T_{\gamma 0m}$ and $T_{\gamma i1}, T_{\gamma i2}, \dots, T_{\gamma im}$ (total number $n + m$). From a ratio (7), we shall receive the required temperature for any point, using the formula (5):

$$T(x, y) = \frac{1}{2\pi} [\varphi_{k1} T_{\gamma 01} + \varphi_{k2} T_{\gamma 02} + \dots + \varphi_{kn} T_{\gamma 0n} + \dots + \varphi_{km} T_{\gamma im} - \varphi_{k\gamma 0} T_{c\gamma 0} - \varphi_{k\gamma i} T_{c\gamma i}] \quad (8)$$

$$\varphi_{k1} = \int_{\Delta S_{01}} \frac{\partial(\ell n R_k)}{\partial n} ds - \frac{\delta_{01}}{r_1} \int_{\Delta S_{01}} \ell n R_k ds$$

$$\varphi_{kn} = \int_{\Delta S_{0n}} \frac{\partial(\ell n R_k)}{\partial n} ds - \frac{\delta_{0n}}{r_n} \int_{\Delta S_{0n}} \ell n R_k ds$$

$$\varphi_{k\zeta_0} = \frac{\delta_{01}}{r_1} \int_{\Delta S_{01}} \ell n R_k ds + \dots + \frac{\delta_{0m}}{r_m} \int_{\Delta S_{0m}} \ell n R_k ds$$

$$\varphi_{k\zeta_i} = \frac{\delta_{01}}{r_1} \int_{\Delta S_{i1}} \ell n R_k ds + \dots + \frac{\delta_{im}}{r_m} \int_{\Delta S_{im}} \ell n R_k ds$$

In activities [2] the discretization of a line $\Gamma = \bigcup_{i=0}^M \zeta_i$ by a many discrete point and integrals that are included in the equations as logarithmic potentials, was calculated approximately with the following ratios:

$$\int_{\Delta S_{\zeta_i}} \frac{\partial(\ell n R_k)}{\partial n} ds \approx \frac{\partial(\ell n R_k)}{\partial n} \Delta S_{\zeta_i} \quad (9)$$

$$\int_{\Delta S_{\zeta_i}} \ell n R_k ds \approx \ell n R_k \Delta S_{\zeta_i} \quad (10)$$

(where $\Delta S_{\zeta_i} \in L = \bigcup_{i=0}^M l_i$; $l_i = \int_{\gamma_i} ds$)



4. New interpretation of the BIEM

In contrast to [2], we offer to decide the given boundary value problem (2)-(4) as follows. We locate the distribution of temperature $T = T(x, y)$ as follows:

$$T(x, y) = \int_{\Gamma} c \ln R^{-1} ds, \quad (11)$$

where $\Gamma = \bigcup_{i=1}^M \zeta_i$ smooth closed Jordan curve; M - quantity of cooled channels; $\rho = \bigcup_{i=1}^M \rho_i$ density of a logarithmic potential uniformly distributed on ζ_i ; $S = \bigcup_{i=1}^M S_i$. Thus curve Γ are positively oriented and are given in a parametric kind:

$$x = x(s); y = y(s); s \in [0, L]; L = \int_{\Gamma} ds$$

Using BIEM and expression (11) we shall put problem (2)-(4) to the following system of boundary integral equations:

$$\rho(s) - \frac{1}{2\pi} \int_{\Gamma} (\rho(s) - \rho(\xi)) \frac{\partial}{\partial n} \ln R(s, \xi) d\xi = \frac{\alpha_i}{2\pi\lambda} (T - \int_{\Gamma} \rho(s) \ln R^{-1} ds), \quad (12)$$

where $R(s, \xi) = ((x(s) - x(\xi))^2 + (y(s) - y(\xi))^2)^{1/2}$.

For the singular integral operator's evaluation, which are included in (12) the discrete operators of the logarithmic potential with simple and double layer are investigated. Their connection and the evaluations in modules term of the continuity (evaluation such as assessments by A. Zigmund are obtained) is shown Theorem (main)

Let

$$\int_0^{\infty} \frac{\omega_{\xi}(x)}{x} < +\infty$$

And let the equation (12) have the solution $f \in C$ (the set of continuous functions on Γ). Then $\exists N_0 \in \mathbb{N} = \{1, 2, \dots\}$ such that the discrete system $\forall N > N_0$, obtained from (12) by using the discrete double layer potential operator (its properties has been studied), has unique solution $\{f_{jk}^{(N)}\}, k = \overline{1, m}; j = \overline{1, n}$;

$$|f_{jk}^* - \widehat{f}_{jk}^{(N)}| \leq C(\Gamma) \left(\int_0^{\varepsilon_N} \frac{\omega_{\xi}(x) \omega_{f^*}(x)}{x} dx + \right.$$

$$\left. \varepsilon_N \int \frac{\omega_{\xi}(x) \omega_{f^*}(x)}{x} dx + \omega_{f^*}(\|\tau_N\|) \int_0^{\varepsilon_N} \frac{\omega_{f^*}(x)}{x} dx + \|\tau_N\| \int \frac{\omega_{f^*}(x)}{x} dx \right),$$

where $C(\Gamma)$ is constant, depending only on $\|\tau_N\|_{N=1}^{\infty}$ the sequence of partitions of Γ ; $\{\varepsilon_N\}_{N=1}^{\infty}$ the sequence of positive numbers such that the pair $(\|\tau_N\|, \varepsilon_N)$, satisfies the condition $2 \leq \varepsilon_N \|\tau_N\| \leq p$.

Let $\delta \in (0, d/2)$, where d is diameter Γ , and the splitting τ is that, which is satisfied the condition $p' \geq \delta / \|\tau\| \geq 2$.

Then for all $f \in C(\Gamma)$ - space of all functions continuous on Γ and $z \in \Gamma$, ($z = x + iy$).

$$|(L_{\tau, \delta} f)(z) - \widetilde{f}(z)| \leq C(\Gamma)$$

$$\left(\|f\|_C \delta \ln \frac{2d}{\delta} + \omega_f(\|\tau\|) + \|\tau\| \ln \frac{2d}{\delta} + \|f\|_C \omega_z(\|\tau\|) \right);$$

$$|(L_{\Omega, \Gamma} f)(z) - \widetilde{f}(z)| \leq \left(C(\Gamma) \int_0^{\Gamma} \frac{\omega_f(x) \omega_l(x)}{x^2} dx + \right.$$

$$\left. \omega_f(\|\tau\|) \int_{\Delta} \frac{\omega_l(x)}{x} dx + \|\tau\| \int_{\Delta} \frac{\omega_f(x)}{x^2} dx \right),$$

where

$$(L_{\tau, \varepsilon} f)(z) = \sum_{z_m, \varepsilon \in \tau(z)} \left(\frac{f(z_{k, e+1}) + f(z_{k, e})}{2} - f(z) \right)$$

$$\frac{(y_{k, e+1} - y_{k, e})(x_{k, e} - x) - (x_{k, e+1} - x_{k, e})(y_{k, e} - y)}{|z - z_{k, e}|^2} + \pi f(z)$$

$(L_{\tau, \varepsilon} f)(z)$ - two-parameter quadrature formula (depending on τ and δ parameters) for logarithmic double layer potential; $\widetilde{f}(z)$ - double layer logarithmic potential operator; $C(\Gamma)$ - constant, dependent only from a curve Γ ;



$f(x) \in \mathcal{O}$ is a module of a continuity of functions f ;

$$(I_{\tau, \varepsilon} f)(z) = \sum_{z_{m, \in \tau(z)}} \frac{f(z_{k, j+1}) + f(z_{k, j})}{2}$$

$$\ln \left| \frac{1}{z_{k, j} - z} \right| \left| z_{k, j+1} - z_{k, j} \right|$$

$(I_{\tau, \varepsilon} f)(z)$ - two-parameter quadrature formula (depending on τ and δ parameters) for logarithmic potential simple layer; $f(z)$ - simple layer logarithmic potential operator;

$$z_{k, e} \in \tau; z_{k, e} = x_{k, e} + iy_{k, e}$$

$$\tau(z) = \{z_{k, e} \mid |z_{k, e} - z| > \varepsilon\}; \tau_k = \{z_{k, 1}, \dots, z_{k, m_k}\},$$

$$z_{k, 1} \leq z_{k, 2} \leq \dots \leq z_{k, m_k}; \|\tau\| = \max_{j=1, m_k} |z_{k, j+1} - z_{k, j}|$$

Thus are developed effective from the point of view of realization on computers the numerical methods basing on constructed two-parametric quadrature processes for the discrete operators logarithmic potential of the double and simple layer. Their systematic errors are estimated, the methods quadratures mathematically are proved for the approximate solution Fredholm I and II boundary integral equations using Tikhonov regularization and are proved by appropriate theorems [3,4].

6. Solution technique of direct and Inverse problems of heat conductivity

The given calculating technique of the blade temperature field can be applied also to blades with the plug-in deflector. On consideration blades with deflectors in addition to boundary condition of the III kind adjoin also interfaces conditions between segments of the outline partition as equalities of temperatures and heat flows.

$$T_v(x, y) = T_{v+1}(x, y), \quad (13)$$

$$\frac{\partial T_v(x, y)}{\partial n} = \frac{\partial T_{v+1}(x, y)}{\partial n}, \quad (14)$$

where v - number of segments of the outline partition of the blade cross-section; x, y - coordinates of segments. At finding of cooler T best values, is necessary to solve the inverse problem of heat conduction. For it is necessary at first to find solution of the heat conduction direct problem with boundary condition of the III kind from a gas leg and

boundary conditions I kinds from a cooling air leg

$$T_v(x, y)|_{z_0} = T_{i_0} \quad (15)$$

Where T_{i_0} - the unknown optimum temperature of a wall of a blade from a leg of a cooling air.

6. Application of BIEM to quasistationary problems of heat conductivity

The developed technique for the numerical solution of stationary task of the heat conduction in cooled blades can be distributed also to quasistationary case.

Let us consider a third boundary-value problem for the heat conduction quasilinear equation:

$$\frac{\partial}{\partial x} \left(\lambda(T) \frac{\partial T}{\partial x} \right) + \frac{\partial}{\partial y} \left(\lambda(T) \frac{\partial T}{\partial y} \right) = 0 \quad (16)$$

$$\alpha_i (T_{ci} - T_{yi}) - \lambda(T) \frac{\partial T_{yi}}{\partial n} = 0 \quad (17)$$

For linearization of tasks (16) - (17) we shall use the Kirchhoff permutation:

$$A = \int_0^T \lambda(\xi) d\xi \quad (18)$$

Then equation (16) is transformed into the following Laplace equation:

$$\frac{\partial^2 A}{\partial x^2} + \frac{\partial^2 A}{\partial y^2} = 0 \quad (19)$$

For preserving convection additives in boundary-value condition (17), we shall accept in initial approximation $\lambda(T) = \lambda_c$. Then from (18) we have;

$$T = A / \lambda_c. \quad (20)$$

$$\alpha_i (T_{ci} - A_{yi} / \lambda_c) - \frac{\partial A_{yi}}{\partial n} = 0 \quad (21)$$

So, the stationary problem (19) with (21) is solved by boundary integrated equations method.

7. Calculation of the gas flow velocity distribution around the airflow

The most important role in the blade raw analysis and improvement belongs to the aerodynamic estimation methods, which proceed to the gas-dynamic efficiency estimation and for the heat exchange problem research.



On the basis of potential flow theory, the velocity distribution of gas flow around the airfoil has been defined by solving the following integral equations for the complex potential flow $W(z)$ [5] (alternate to existing [6] by effective realization):

$$W(z) = \varphi(z) + i\psi(z);$$

integral equations for the velocity potential:

$$\varphi(x_k, y_k) = V_\infty (x_k \cos \alpha_\infty + y_k \sin \alpha_\infty) \pm \frac{1}{2\pi} \Gamma \theta_{out} \mp \frac{1}{2\pi} \oint_{S+} \varphi(S) d\theta, \quad (22)$$

and integral equation for the stream function ψ :

$$\psi = V_\infty (y \cos \alpha_\infty - x \sin \alpha_\infty) \mp \frac{1}{2\pi} \oint_{S+} V \ln \sqrt{\sin^2 \frac{\pi}{l} (x - x_k) + \sin^2 \frac{\pi}{l} (y - y_k)} ds,$$

Which based on the theory of the zero stream function on airfoil contour. In this: φ - (x_k, y_k) the value of velocity potential; V_∞ - the main flow velocity; α_∞ - the angle between the velocity vector V_∞ and the blade raw axis; Γ - the velocity circulation; θ_{out} - the angle that corresponds to the outlet edge of the airfoil. The integral equation (22) solved by the following received approximating equation:

$$\varphi_j \pm \sum_{i=1}^n \varphi_i (\theta_{j,i+1} - \theta_{j,i-1}) = V_\infty (x_{k_j} \cos \alpha_\infty + y_{k_j} \sin \alpha_\infty) \pm \frac{1}{2\pi} \Gamma \theta_{j,B},$$

where, $i = 2n - 1$, $j = 2n$, n is the number of divided parts of the airfoil. The velocity potential φ distribution along the airfoil has been received by solving the system of the linear algebraic equations. The flow velocity magnitude determined using velocity potential differentiation along the airfoil contour s , i.e.

$V(s) = d\varphi/ds$. As opposite to potential flow, the heat-conducted viscous turbulent flow in the turbine blade channel is explored based on Navier-Stokes equations. As a turbulence models the standard $k-\varepsilon$ [7] and Spalart-Allmaras models used [8]. The Navier-Stokes equations solved by ANSYS CFX10© [9] (based on finite element method) and Fluent© [10] (based on control volume method) software's. As the meshing tool Gambit© software, and for 3D modeling – Solid Works10© have been used.

8. Solution of problem of the cooling systems' internal heat exchange and hydrodynamics

The velocity distribution data along the airfoil are incoming for determining outer boundary heat exchange conditions. In case of potential flow, the heat transfer coefficient of gas flow defined by using integral equation for the energy of heat boundary layer [2,11,12]. Correction to the base values of heat coefficient was made by using the recommendations, that was approved by experiment-calculated way [2,11,12]. For the internal heat exchange boundary conditions determination the correlation between inner geometry and hydrodynamic with heat models are used.

At known geometry of the cooling scheme, for the convective heat exchange local coefficients α_c definition of the cooler by the standard empirical formulas it is necessary to have the basic data's of the air flow distribution in cooling channels. For example, for blades with deflector and with cross current, the value of the airflow G_c for blade cooling can be defined with the following:

$$G_c = \frac{\mu_c F_c}{d_c} \left(\frac{d_c}{\lambda_c \cdot C} \right)^{\frac{1}{n}} \left[\frac{\alpha_g (\psi_g - 1)^{\kappa_f}}{1 - \frac{2Bi(\psi_g - 1)^{\kappa_f}}{1 + \kappa_f} - \psi_c} \right]^{\frac{1}{n}},$$

Where g ψ , c ψ - the gas and air temperature coefficients; f κ - coefficient of the form; d_c - the characteristic size in the formula c **Re**; c μ , c λ - cooler dynamic viscosity and heat conductivity coefficients; Bi - the Bio criterion for the blade wall; F_c - the total area of passage for air; C and n - coefficient and exponent ratio in criteria formulas for convective heat exchange n

$Nu_c = C$ **Re** c for considered cooling parts. To determine the distribution of flow in the blade cooling system, an equivalent hydraulic scheme is built. The construction of the equivalent hydraulic tract circuit of the vane cooling is connected with the description of the cooled vane design. The whole passage of coolant flow is divided in some definite interconnected sections, the so-called typical elements, and every one has the possibility of identical definition of hydraulic resistance. The points of connection of typical elements are changed by node points, in which the streams, merger or division of cooler flows istaking places proposal without pressure change. All the typical elements and node points are connected in the same sequence and order as the tract



sites of the cooled vane. To describe the coolant flow at every inner node the 1st law by Kirchhoff is used [11-13]:

$$f_i = \sum_{j=1}^m G_{ij} = \sum_{j=1}^m \text{sign}(\Delta p_{ij}) k_{ij} \sqrt{\Delta p_{ij}}; \quad i = 1, 2, 3, \dots, n \quad (23)$$

where G_{ij} is the discharge of coolant on the element, $i - j$, m are the number of typical elements connected to i node of the circuit, n is the number of inner nodes of hydraulic circuit, Δp_{ij} - losses of total pressure of the coolant on element $i - j$. In this formula the coefficient of hydraulic conductivity of the circuit element ($i - j$) is defined as:

$$k_{ij} = \sqrt{2 f_{ij}^2 \cdot p_{ij} / \xi_{ij}}, \quad (24)$$

where f_{ij} , p_{ij} , ξ_{ij} are the mean area of the cross-section passage of elements ($i - j$), density of coolant flow in the element, and coefficient of hydraulic resistance of this element. The system of nonlinear algebraic equations (23) is solved by the Zeidel method with acceleration, taken from:

$$p_i^{k+1} = p_i^k - f_i^k / (\partial f / \partial p)^k,$$

where k is the iteration number, p_i^k is the coolant pressure in i node of the hydraulic circuit. The coefficients of hydraulic resistance ξ_{ij} used in (24) are defined by analytical dependencies, which are in the literature available at present [12,13]. For example, to calculate a part of the cooling tract that includes the area of deflector perforation coefficients of hydraulic resistance in spray [13]:

$$\xi_{c\sigma} = \frac{(G_r / G_k)^m}{2(f_c / f_k) - 0.1}, \quad m = \frac{1}{2(f_c / f_k) - 0.23}$$

and in general channel:

$$\xi_{c\sigma} = 1.1(G_r / G_k)^n, \quad n = 0.381 \ln(f_c / f_k) - 0.3$$

In these formulas, G_r , G_k are cooling air consumption in the spray stream through the perforation deflector holes and slot channel between the deflector and vanes wall, and f_r , f_k - the flow areas.

9. Results

For the verification of described methods the computational data's of the first stage nozzle blades of high pressure turbine are used. The nozzle array of test experiment was analytically formed for transonic speed.

The blade profile has the following geometrical parameters: blade chord $b = 60\text{mm}$; array spacing $t = 41.5\text{mm}$; throat section width $a_2 = 11.26\text{mm}$; the exit edge depth $d_2 = 1.8\text{mm}$; bend angle of the exit edge $= 12^\circ 48' \delta$. The computing experiment based on the following gas flow parameters: blade raw inlet velocity $V_1 = 156\text{m/s}$; outlet velocity $V_2 = 512\text{m/s}$; outlet angle $216^\circ 6' \alpha$; inlet stagnation temperature and pressure $T_g^* = 1193\text{K}$, $p_g^* = 1.2095\text{MPa}$; outlet conditions $T_{e1} = 1142\text{K}$, $p_{e1} = 0.75\text{MPa}$; relative outlet velocity $\lambda_{1ad} = 0.89$. The fig.2 represents the velocity distribution along the airfoil. In case of potential flow the results was obtained by the solution of boundary integral equation (\diamond) [5]. On the same figure the Navier-Stokes differential equations system's solution is displayed (\blacksquare), which obtained by ANSYS for the viscous turbulent flow using the $k - \varepsilon$ turbulence model.

On the fig.3 the computational domain represents, which received by the Gambit meshing tool. The 2D gas flow with the $k - \varepsilon$ turbulence model is displayed on fig.4. The fig.5 describes the velocity distribution along the airfoil for the same flow conditions by using of the Spalart-Allmaras turbulence model with Fluent solver. Fig.6 and fig.7 shows the temperature distribution of the gas flow in the blade channel, which determined with $k - \varepsilon$ and Spalart-Allmaras turbulence model accordingly. By using these results the cooling tract equivalent scheme is developed (fig.8) and temperature field of blade cross section (fig.9) are determined.

The calculations reproduce good flow structure as well as local characteristics of the velocity and temperature distribution. Received results approve the accuracy of described methods and their validity the temperature field researches in gas-turbine engines. On basis of acquired calculations the 3D geometrical model of the cooled nozzle blade is developed, and expressed on fig.10.

9. Conclusions

The multiples computing experiments with the using BIEM for calculation the temperature fields of nozzle and working blades with various amount and disposition of cooling channels, having a complex configuration, is showed, that for practical calculations in this approach, offered by us, the discretization of the integrations areas can be conducted with smaller quantity



of discrete points. Thus the reactivity of the algorithms developed and accuracy of evaluations is increased. The accuracy of temperatures calculation, required consumption of the cooling air, heat flows, losses from cooling margins essentially depends on reliability of boundary conditions, included in calculation of heat exchange. The reliability of the methods was proved by experimental investigations for the heat and hydraulic characteristics of blades. Geometric model, equivalent hydraulic schemes of cooling tracks have been obtained, cooler parameters and temperature field of gas 1st stage turbine nozzle blade of the have been determined. Methods have demonstrated high efficiency at repeated and polivariant calculations on the basis of which was offered as the way of blade cooling system modernization.

References

- [1]. Leontiev, A.I., Osipov, M.I., Ivanov, V.L., Manushin, E.A., (2004), «Heat exchange apparatus and cooling systems of gas turbine and combined arrangements », Moscow, MGTU nam. N.E. Bauman, 592 p.
- [2]. Zisina-Molojen, L.N. and etc. (1974), «Heat exchange in turbomachines», Leningrad, Mashinostroeniye, 1974, 336 p.
- [3]. Pashayev, A.M., Askerov, D.D., Sadiqov, R.A., Samedov, A.S. (2005), «Numerical modeling of gas turbine cooled blades», International Journal of Aviation of Vilnius Gediminas, Technical University., vol. 9, No. 3, 2005, pp.9-18.
- [4]. A.M.Pashaev, R.A.Sadiqov, C.M.Hajiev, (2002), «The BEM Application in development of Effective Cooling Schemes of Gas Turbine Blades». 6th Biennial Conference on Engineering Systems Design and Analysis, Istanbul, Turkey, (July, 8-11, 2002).
- [5]. Pashayev, A.M., Sadiqov, R.A., Samadov, A.S., Mammadov, R.N., (2004), «The solution of fluid dynamics direct problem of turbomachines cascades with integral equations method», Baku, proceed. NAA, vol. 3, pp. 28-56
- [6]. Beknev, V.S., Epifanov, V.M., Leontiev, A.I., Osipov, M.I. and etc., (1997), «Fluid dynamics. A mechanics of a fluid and gas», Moscow, MGTU nam. N.E. Bauman, 671 p.
- [7]. Launder, B.E., Spalding, D.B., (1974), «The Numerical Computation of Turbulent Flows», Journal of Computational Methods in Applied Mechanics and Engineering, vol. 3, pp. 269-289
- [8]. Spalart, P. and Allmaras, S., (1992), «A one-equation turbulence model for aerodynamic flows», Technical Report AIAA-92-0439, American Institute of Aeronautics and Astronautics, 1992.
- [9]. Imgrund, M.C. (1992), ANSYS® Verification Manual, Swanson Analysis Systems, Inc.
- [10]. Fluent. Fluent Inc., (2001), Centerra Resource Park, Cavendish Court, Lebanon, NH 03766, USA.
- [11]. Galitsevskiy, G. and etc., (1996), «A thermal guard of blades», Moscow, Moscow Aviation Institute, 356 p.
- [12]. Kopelev, S.Z., Shtenko, A.F., (1994), «Construction and calculation of GTE cooling systems», Ukraina, Kharkov, Osnova, 240 p.
- [13]. Arseniev, L.V., Mitryayev, I.B., Sokolov, N.P., (1985), «The flat channels hydraulic resistances with a system of jets in a main stream», Journal of Energetic, 1985, No. 5, pp.85-89

APPENDIX

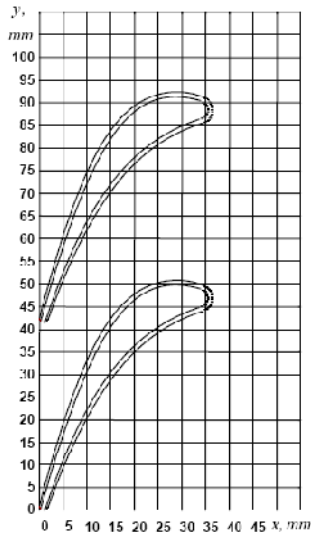


Fig.1. The cascade of the nozzle cooled blade's profiles

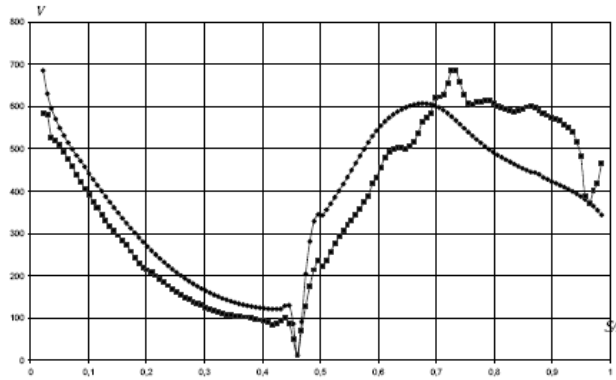


Fig.2. Velocity distribution along the airfoil: ♦ - solution of boundary integral equation for the potential flow; ■ - solution of Navier-Stokes differential equations system; V - gas velocity, m/s; S/l - relative length.

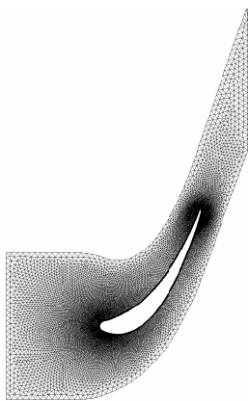


Fig.3. Computation domain

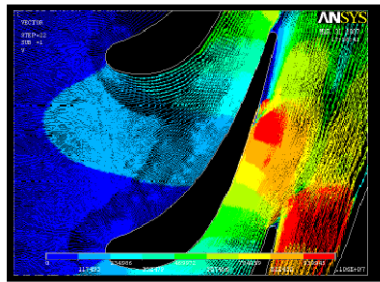


Fig.4. 2D viscous compressible gas flow with $k-\epsilon$ turbulence model by ANSYS

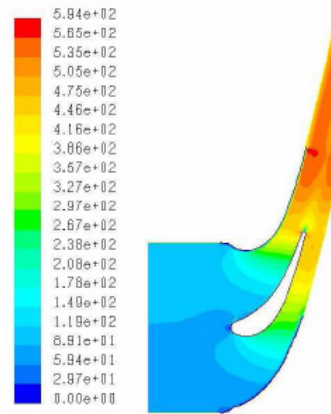


Fig.5. Velocity distribution along the airfoil (m/s), Spalart-Allmaras turbulence model, Fluent.

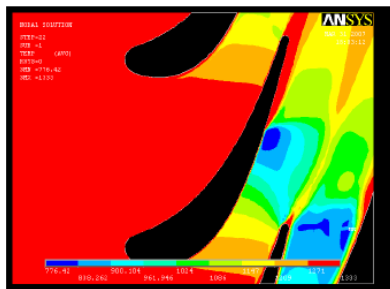


Fig.6. Static temperature field around the airfoil, ANSYS, $k-\epsilon$ turbulence model.

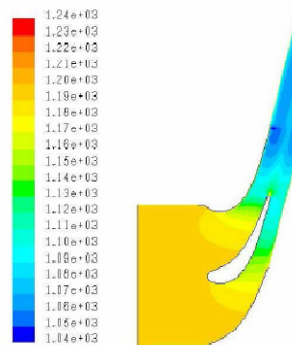


Fig.7. Static temperature field around the airfoil (K), Fluent, Spalart-Allmaras turbulence model

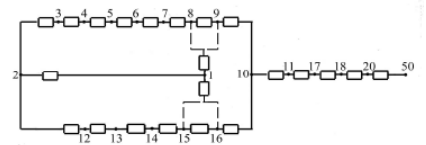


Fig.8. The equivalent hydraulic scheme of experimental nozzle blade cooling system

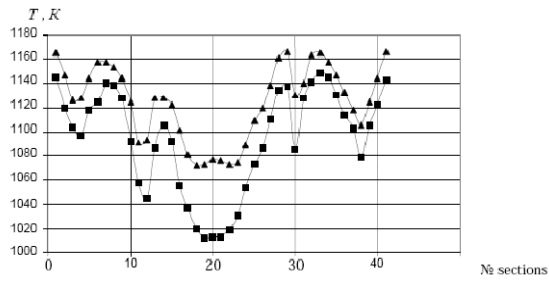


Fig. 9. Distribution of temperature along outside (▲) and internal (■) contours of the cooled nozzle blade

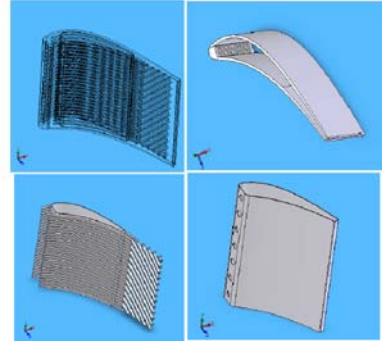


Fig. 10. 3D model of the 1st stage nozzle blade of the high pressure gas turbine



Single and Multi-objective Genetic Algorithm Optimizations of the Laminated Composites used in Satellite Structures

Levent AYDIN^{1*}, H. Secil ARTEM²

^{1*} Department of Mechanical Engineering, Izmir Institute of Technology
Gulbahce Koyu, 35430-Urla, Izmir, Turkey
leventaydinn@gmail.com

² Department of Mechanical Engineering, Izmir Institute of Technology

Abstract

Fiber reinforced composites are widely used in many space structures such as antennas, optical platforms and satellites. Especially, in satellite applications, carbon fiber composites are preferred because of low coefficient of thermal expansion (CTE) and high stiffness features of them. The aim of the present study is to design the stacking sequence of the laminated composites having low CTE and high elastic moduli. In design process, multi-objective genetic algorithm optimization of the carbon fiber symmetric-balanced laminated composite plates are verified by single objective optimization approach. MATLAB Optimization Toolbox is used to obtain Pareto-optimal designs and global optimum points for six different model problems. Simplified micro-mechanics equations, classical lamination theory and MATLAB Symbolic Math toolbox are used in order to obtain the fitness functions of the problems. Stress and strain distributions are presented through the thickness of the laminates subjected to mechanical, thermal, and hygral loadings.

Keywords: Carbon fiber composites—Genetic Algorithms—Single and multi objective optimization—Satellites—Hygro-thermo-mechanical loading

1. Introduction

Fiber reinforced laminated composites are widely used in aerospace engineering applications. In satellite structures, the materials should exhibit the features low density, high stiffness, low coefficients of thermal and moisture expansions. Carbon fiber reinforced polymer composites can match these requirements with an appropriate stacking sequence. The deformation induced by non-uniform moisture/ temperature is an important feature in the design of composites. This kind of deformation is named as hygro-thermal deformation [1]. The varying environmental conditions such as moisture absorption and temperature change, affect the stiffness and strength of the structures severely.

Optimum design of fiber composite plates is one of the most interesting problem of structural mechanics. In

order to obtain an optimal design for such a plate, the number of layers and fiber orientations together with their required thicknesses must be decided on. In order to achieve this objective, designers and scientists have developed some procedure for laminated composites subjected to various loading types.

Optimization of laminated composite materials have been studied by several researchers. The problem of the multi-objective optimal design of laminated composite structures has been studied by [2]. Two examples are presented, referring to different structural layout and loading. A methodology for the multi-objective optimization of laminated composite materials based on an integer-coded genetic algorithm has presented by [3]. The fiber orientations and fiber volume fractions of the lamina are chosen as the primary optimization variables. Simplified micromechanics equations are used to estimate the stiffness and strength of each lamina using the fiber volume fraction and material properties of the matrix and fibers. In reference [4], authors have presented two examples of multi-objective optimization problem for composite laminate plates using GA and FEM. Minimization of two objectives, such as weight-deflection or weight-cost, are simultaneously performed and a Pareto-optimal set is obtained by shifting the optimization emphasis using a weighting factor.

Usage of fiber reinforced composites in space and robotics applications are also available in literature. Wood *et. al.*[5] have presented a new framework for creating micro-robots which makes the use of composite materials. In their paper, composite microstructure fabrication and process details are given as well as calculation of mechanical and flexural properties. Le Rich and Gaudin [1] have interested in the dimensional stability concept which is crucial feature of space structures. To design composite laminates accounting for thermal, hygral and mechanical constraints are main objective of their study. Another example of composites in aerospace applications



is given in the paper by [6] which consider investigation of variations in thermal expansion coefficient of the composite as an aerospace structural material. The longitudinal and transverse CTEs of unidirectional composites were determined over the temperature range -101°C to 120°C . The CTEs of cross-ply laminates have been predicted by using classical lamination theory and verified experimentally.

All the problems considered here have been focused on in-plane design of $(\pm\theta_1/\pm\theta_2)_s$ eight-layered carbon/epoxy symmetric and balanced laminated composites satisfying the conditions, low CTE on longitudinal and high elastic moduli on longitudinal and/or transverse directions. In design process, the problems are firstly formulated as multi-objective optimization problems. An alternative single objective formulations including the nonlinear constraints are utilized for verification of the multiobjective approach. Multi-objective optimization problems aim to minimize the CTE while maximizing the elastic moduli, simultaneously. In the single objective representation of the problem, CTE obtained from the multiobjective formulations, are used to define the nonlinear constraints of the single optimization. This study consists of three main parts: In the first part, simplified micromechanics expressions [1] are used to predict the stiffness, thermal and moisture expansion coefficients of a lamina using constituent material properties. The classical lamination theory [7] is utilized to determine the effective elastic modulus, thermal and moisture expansion coefficients for composite laminates. The effective elastic properties obtained from the first part of the study defining the fitness functions have been used to obtain the optimum fiber orientation angles of each layer by a stochastic search technique called genetic algorithms (GAs). MATLAB *Optimization Toolbox* and *Symbolic Math Toolbox* [8-10] are used to obtain Pareto-optimal and best designs for six (1a, 1b, 2a, 2b, 3a, 3b) different model problems. In the last part, through the thickness stresses have been calculated for each layer of the optimized (obtained from multi-objective formulations) composites subjected to the hygral, thermal and mechanical loadings.

2. Formulation

2.1. Macro-Mechanical Analysis

The geometric mid-plane of the laminate contains the x - y axes and z axis defines the thickness direction. The total thickness of the laminate is h . The total number of laminae is n . Laminate strains are linearly related to the distance from the mid-plane as

$$\varepsilon_{xx} = \varepsilon_{xx}^o + z\kappa_{xx}, \quad (1)$$

$$\varepsilon_{yy} = \varepsilon_{yy}^o + z\kappa_{yy}, \quad (2)$$

$$\gamma_{xy} = \gamma_{xy}^o + z\kappa_{xy} \quad (3)$$

where ε_{xx}^o , ε_{yy}^o are midplane normal and γ_{xy}^o is midplane shear strains, κ_{xx} , κ_{yy} are bending and κ_{xy} is twisting curvatures in the laminate.

Applied normal force resultants (per unit width) N_x , N_y , shear force resultant N_{xy} on a laminate are related to the mid-plane strains and curvatures by the following equations in matrix notation

$$\begin{bmatrix} N_x \\ N_y \\ N_{xy} \end{bmatrix} = \begin{bmatrix} A_{11} & A_{12} & A_{16} \\ A_{12} & A_{22} & A_{26} \\ A_{16} & A_{26} & A_{66} \end{bmatrix} \begin{bmatrix} \varepsilon_x^o \\ \varepsilon_y^o \\ \gamma_{xy}^o \end{bmatrix} + \begin{bmatrix} B_{11} & B_{12} & B_{16} \\ B_{12} & B_{22} & B_{26} \\ B_{16} & B_{26} & B_{66} \end{bmatrix} \begin{bmatrix} \kappa_x \\ \kappa_y \\ \kappa_{xy} \end{bmatrix} - \begin{bmatrix} N_x^T \\ N_y^T \\ N_{xy}^T \end{bmatrix} - \begin{bmatrix} N_x^C \\ N_y^C \\ N_{xy}^C \end{bmatrix} \quad (4)$$

The matrices $[A]$ and $[B]$ appearing in Eq.(4) can be defined as

$$A_{ij} = \sum_{k=1}^n (\bar{Q}_{ij})_k (h_k - h_{k-1}) \quad (5)$$

$$B_{ij} = \frac{1}{2} \sum_{k=1}^n (\bar{Q}_{ij})_k (h_k^2 - h_{k-1}^2) \quad (6)$$

$i, j = 1, 2, 6$

where \bar{Q}_{ij} are the elements of the transformed reduced stiffness matrix [7]; $[N^T]$ and $[N^C]$ given in Eq.(4) are the resultant thermal and hygral forces, respectively:

$$\begin{bmatrix} N_x^T \\ N_y^T \\ N_{xy}^T \end{bmatrix} = \Delta T \sum_{k=1}^n \begin{bmatrix} \bar{Q}_{11} & \bar{Q}_{12} & \bar{Q}_{16} \\ \bar{Q}_{12} & \bar{Q}_{22} & \bar{Q}_{26} \\ \bar{Q}_{16} & \bar{Q}_{26} & \bar{Q}_{66} \end{bmatrix}_k \begin{bmatrix} \alpha_x \\ \alpha_y \\ \alpha_{xy} \end{bmatrix}_k (h_k - h_{k-1}) \quad (7)$$

$$\begin{bmatrix} N_x^C \\ N_y^C \\ N_{xy}^C \end{bmatrix} = \Delta C \sum_{k=1}^n \begin{bmatrix} \bar{Q}_{11} & \bar{Q}_{12} & \bar{Q}_{16} \\ \bar{Q}_{12} & \bar{Q}_{22} & \bar{Q}_{26} \\ \bar{Q}_{16} & \bar{Q}_{26} & \bar{Q}_{66} \end{bmatrix}_k \begin{bmatrix} \beta_x \\ \beta_y \\ \beta_{xy} \end{bmatrix}_k (h_k - h_{k-1}) \quad (8)$$

Here, the effective coefficients of thermal and moisture expansions $[\alpha]$, $[\beta]$ are defined as



$$\begin{Bmatrix} \alpha_x \\ \alpha_y \\ \alpha_{xy} \end{Bmatrix} = \begin{Bmatrix} \varepsilon_x^0 \\ \varepsilon_y^0 \\ \gamma_{xy}^0 \end{Bmatrix} \Big|_{\substack{AC=0 \\ AT=1}} = \begin{bmatrix} A_{11}^* & A_{12}^* & A_{16}^* \\ A_{12}^* & A_{22}^* & A_{26}^* \\ A_{16}^* & A_{26}^* & A_{66}^* \end{bmatrix} \begin{bmatrix} N_x^T \\ N_y^T \\ N_{xy}^T \end{bmatrix} \quad (9)$$

$$\begin{Bmatrix} \beta_x \\ \beta_y \\ \beta_{xy} \end{Bmatrix} = \begin{Bmatrix} \varepsilon_x^0 \\ \varepsilon_y^0 \\ \gamma_{xy}^0 \end{Bmatrix} \Big|_{\substack{AC=1 \\ AT=0}} = \begin{bmatrix} A_{11}^* & A_{12}^* & A_{16}^* \\ A_{12}^* & A_{22}^* & A_{26}^* \\ A_{16}^* & A_{26}^* & A_{66}^* \end{bmatrix} \begin{bmatrix} N_x^C \\ N_y^C \\ N_{xy}^C \end{bmatrix} \quad (10)$$

where $[A^*] = [A]^{-1}$.

In macro-mechanical analysis, it is also convenient to introduce the effective elastic properties for symmetric balanced or symmetric cross-ply laminated plates subjected to in-plane loading the effective in-plane moduli, E_x and E_y are as follows [3, 11]

$$E_x = \frac{1}{hA_{11}^*} \quad (11)$$

$$E_y = \frac{1}{hA_{22}^*} \quad (12)$$

2.1. Micro-mechanical Analysis

Simplified micro-mechanical expressions used to predict the stiffness and CTE of a lamina using constituent material properties are given as [1,12]

$$E_1 = V_f E_{1f} + (1 - V_f) E_m \quad (13)$$

$$E_2 = \frac{E_m}{1 - \sqrt{V_f} (1 - E_m / E_{2f})} \quad (14)$$

$$G_{12} = \frac{G_m}{1 - \sqrt{V_f} (1 - G_m / G_{12f})} \quad (15)$$

$$\nu_{12} = V_f \nu_{12f} + (1 - V_f) \nu_m \quad (16)$$

$$\alpha_1 = \frac{V_f \alpha_{1f} E_{1f} + (1 - V_f) \alpha_m E_m}{E_1} \quad (17)$$

$$\alpha_2 = \alpha_{2f} \sqrt{V_f} + (1 - \sqrt{V_f}) (1 - V_f \nu_m E_{1f} / E_1) \alpha_m \quad (18)$$

where indices 1 and 2, f and m appearing above equations denote the longitudinal and transverse directions, fiber and matrix properties, respectively. V_f represents the fiber volume fraction of the lamina.

3. Optimization

Essentially, optimization of a structure can be defined as finding the best design or elite designs for the structure by minimizing the specified single or multi-objectives satisfying all the constraints. In the optimization formulations, there are two approaches: single and multi-objective optimizations. In single objective approach, an optimization problem consists of a single objective function and some constraints and bounds. However, design of practical composite structures often require the maximization or minimization of multiple, often conflicting, two or more objectives, simultaneously. In such a case, multi-objective formulation is used and a set of solutions are obtained with different trade-off called Pareto optimal. Finding a set of solutions as diverse as possible and as close as possible to Pareto front are crucial. Only one solution is to be chosen from the set of solutions for practical engineering usage. There is not a solution that is best with respect to all objectives in multi-objective optimization. One solution can be better in one objective while worse in another. [3, 13-15]. Many engineering design problems are very complex and non-solvable by the traditional optimization techniques. In this cases, utilizing stochastic optimization methods such as Genetic algorithms and simulated annealing, are appropriate.

3.1. Genetic Algorithm

The genetic algorithm (GA) is a numerical optimization and search technique which allows to obtain alternative solutions some of the complex engineering problems. GA method based on the principles of genetics and natural selection. This method is simple to understand and uses three simple operators: selection, crossover and mutation.

3.2. MATLAB Optimization Toolbox

MATLAB Optimization Toolbox includes a few routines for solving optimization problems using Direct search (DS), Genetic algorithm (GA) and simulated annealing (SA). All of these methods have been used in design of composite materials by many researchers [3,16,17]. Direct Search functions include two direct search algorithms called the generalized pattern search (GPS) algorithm and the mesh adaptive search (MADS) algorithm. GA mode of the toolbox consists of two main part : (i)problem definition (fitness function, bounds and constraints, number of variables), (ii) Options (Population, Fitness scaling, Selection, Reproduction, Mutation, Crossover, Migration). The Toolbox has some optimization solvers such as *ga*, *gamultiobj*, *simulannealbnd*, *patternsearch* and these solvers can be selected as an optimization algorithm. In this study,



two of the solvers (*ga* and *gamultiobj*) are utilized for the optimization problems. *Selection* option uses *Tournament* selection function. The selection function chooses parents for the next generation based on their scaled values from the fitness functions. An ideal selection strategy should be such that it is able to adjust its selective pressure and population diversity so as to fine-tune GA search performance. *Reproduction* options determine how the genetic algorithm creates children at each new generation. In the toolbox *Crossover* fraction is used as a sub-option. This property specifies the fraction of the next generation that crossover produces. *Mutation* produces the remaining individuals in the next generation. *Crossover fraction* must be a fraction between 0 and 1. *Mutation* option has four different mutation functions such as *Constraint dependent*, *Gaussian*, *Uniform* and *Adaptive feasible*. If there are no constraints or bounds in the specified problem *Gaussian* can be selected, otherwise *Adaptive feasible* sub-option should be used. In the *Crossover* option, it should be specified the function that performs the crossover in the sub-option *Crossover function*. There exist following six different crossover functions in the toolbox: *Scattered*, *Single point*, *Two point*, *Intermediate*, *Heuristic* and *Arithmetic*.

4. Model Problems

In this study, all the problems consider the design of stacking sequences of $(\pm\theta_1/\pm\theta_2)_s$ eight-layered carbon/epoxy symmetric and balanced laminated composites satisfying the conditions, low CTE on longitudinal and high elastic moduli on longitudinal and/or transverse directions. Design variables are the fiber orientation angles θ_1 and θ_2 . In all model problems, the fiber volume fraction is taken as 0.50, thickness of each layer is $150 \cdot 10^{-6} m$. Laminates are subjected to loading case 1 : (mechanical+thermal) $F_x = 20kN$, $F_y = 20kN$, $F_{xy} = 0kN$, $\Delta T = -150^\circ C$, width=0.3 m or loading case 2 : (mechanical+thermal+ hygral) $F_x = 50kN$, $F_y = 1kN$, $F_{xy} = 0kN$, $\Delta T = -150^\circ C$, $\Delta C = 2\%$, width = 0.1 m [1]. Temperature change leads to thermal loads and moisture change leads to hygral load for the composites. Table 1 shows the details of model problems in terms of loading types and optimization formulations.

In design process, the problems are firstly formulated as multi-objective optimization problems. An alternative single objective formulations including the nonlinear constraints are utilized for verification of the multi-objective approach. Multi-objective optimization problems (1a, 2a, 3a) aim to minimize the CTE while maximizing the elastic moduli, simultaneously. In the single objective representation of the problems(1b, 2b,

3b), CTE obtained from the multi-objective formulations, are used to define the nonlinear constraints of the single optimization. This study consists of three main parts: In the first part, simplified micromechanics expressions are used to predict the stiffness, thermal and moisture expansion coefficients of a lamina using constituent material properties. The classical lamination theory is utilized to determine the effective elastic modulus, the effective thermal and moisture expansion coefficients for composite laminates [4]. The effective elastic properties define the fitness functions have been used to obtain the optimum fiber orientation angles of each layer by a stochastic search technique called genetic algorithms. MATLAB *Optimization Toolbox* solvers *ga* and *gamultiobj* are used to obtain best design and Pareto-optimal designs[6] for six(1a, 1b, 2a, 2b, 3a, 3b) different model problems. In the last part, through the thickness stresses have been calculated for each layer of the optimized composites subjected to the mechanical, thermal and hygral loadings.

5. Results and Discussion

In this section, results of optimal design studies based on multi and single objective optimizations are presented for coefficient of thermal expansion and elastic moduli. In genetic algorithm optimization, selection of optimization parameters are very important since the change of the parameters affect the efficiency of the algorithm. Table 2 shows the genetic algorithm parameter selection of *gamultiobj* solver options for multi-objective approach used in the model problems. The set of solutions(Pareto-optimal) have been obtained as the maximum number of generations has reached to 51. Table 3 shows Pareto-optimal designs and corresponding CMEs for multi-objective optimization of the model problems (1a and 3a). If the fiber orientation angles are selected as 0° for all lamina as expected the Young's modulus in x direction is maximum ($E_x = 277.3$ GPa). However, this design is not suitable for minimum coefficient of thermal expansion ($\alpha_x = -1.0 \cdot 10^{-6} / ^\circ C$). Similarly, if all of the fiber orientation angles are selected as 32° , the CTE becomes minimum ($\alpha_x = -5.24 \cdot 10^{-6} / ^\circ C$) but this is again not an appropriate design for Young's modulus of the composite ($E_x = 40.8$ GPa)[14]. Regarding this fact, more reliable solutions, obtained after the optimization process, are given in Table 3 as designs 1-9. For practical engineering use, only one of these solutions is to be chosen. For example, if one assumes the constraints as $E_x \geq 188$ GPa and $\alpha_x \leq -2.63 \cdot 10^{-6} / ^\circ C$, design 5 is to be an appropriate solution and therefore the stacking



Table 1. Definition of the model problems in terms of loading, optimization algorithms, objective functions and constraints-bounds

Problem	Loading	Optimization Type	Objective Functions	Constraints-Bounds
1a	$F_x = 20kN$ $F_y = 20kN$ $F_{xy} = 0$ $\Delta T = -150^\circ C$ $\Delta C = 0\%$	Multi Objective	E_x, α_x	$-90^\circ \leq \theta_1 \leq 90^\circ$ $-90^\circ \leq \theta_2 \leq 90^\circ$
	$F_x = 20kN$ $F_y = 20kN$ $F_{xy} = 0$ $\Delta T = -150^\circ C$ $\Delta C = 0\%$			Single Objective
2a	$F_x = 20kN$ $F_y = 20kN$ $F_{xy} = 0$ $\Delta T = -150^\circ C$ $\Delta C = 0\%$	Multi Objective	E_x, E_y, α_x	$-90^\circ \leq \theta_1 \leq 90^\circ$ $-90^\circ \leq \theta_2 \leq 90^\circ$
	$F_x = 20kN$ $F_y = 20kN$ $F_{xy} = 0$ $\Delta T = -150^\circ C$ $\Delta C = 0\%$			Single Objective
3a	$F_x = 50kN$ $F_y = 1kN$ $F_{xy} = 0$ $\Delta T = -150^\circ C$ $\Delta C = 2\%$	Multi Objective	E_x, α_x	$-90^\circ \leq \theta_1 \leq 90^\circ$ $-90^\circ \leq \theta_2 \leq 90^\circ$
	$F_x = 50kN$ $F_y = 1kN$ $F_{xy} = 0$ $\Delta T = -150^\circ C$ $\Delta C = 2\%$			Single Objective

sequence becomes $[\pm 13.8 / \mp 18.5]_S$. MATLAB Optimization Toolbox have produced 14 Pareto-optimal design for model problem 2a because of more than two objective functions. This Pareto optimal design is listed in Table 4. In model problem 2a, design 8 is to be chosen with the constraint assumptions $E_x \geq 180 GPa$, $E_y \geq 9.5 GPa$ $\alpha_x \leq -2.30.10^{-6} / ^\circ C$ and therefore, the corresponding stacking sequence for the 8 layered composite becomes

$[\pm 5.7 / \pm 25.5]_S$.

Table 2. Genetic algorithm parameters for multi objective approach used in the model problems (1a, 2a and 3a)

Population Type	Double vector
Population size	40
Initial range	[-90 -90 ; 90 90]
Selection function	Tournament
Crossover fraction	0.8
Mutation function	Adaptive feasible
Crossover function	Intermediate Ratio=1.0
Migration direction	Both Fraction=0.2, Interval=20
Initial penalty	10
Penalty factor	100
Hybrid Function	None
Stopping criteria	generation=100, Stall generation=50 Function tolerance= 10^{-6}

Table 3. Pareto-optimal designs for the model problems (1a and 3a) and the corresponding CMEs.

Design	E_x (GPa)	α_x ($10^{-6}/^\circ C$)	β_x ($10^{-6}/\%M$)	θ_1 ($^\circ$)	θ_2 ($^\circ$)
1	115.9	-3.66	-58.8	25.9	-19
2	127.6	-3.49	-54.1	24.6	-18
3	152.7	-3.21	-46.1	20	-18
4	169.4	-2.89	-37.3	14.9	-20.5
5	188.0	-2.63	-29.9	13.8	-18.5
6	194.2	-2.44	-24.7	20.6	-10.2
7	206.9	-2.16	-17.0	4.7	-21.6
8	222.1	-1.99	-12.2	19.5	-2.6
9	239.9	-1.80	-6.8	8.1	-13.7

Genetic algorithm parameters used in single objective optimization of the model problems (1b, 2b, 3b) are tabulated in Table 5. Evolutions of the fitness function (E_x) value for those problems are illustrated in Fig.5.

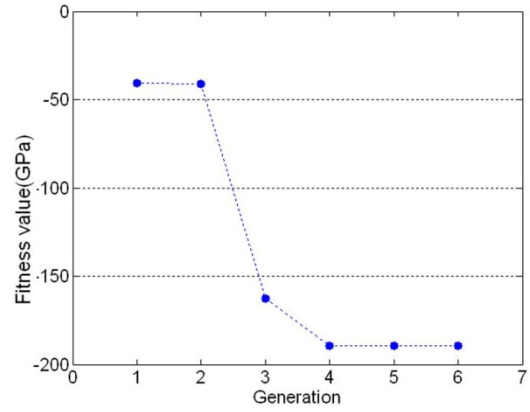


Table 4. Pareto optimal designs of the model problem 2a and the corresponding CMEs.

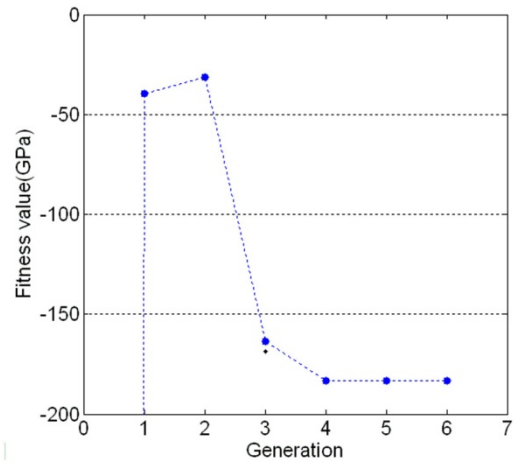
Design	E_x (GPa)	E_y (GPa)	α_x ($10^{-6}/^{\circ}\text{C}$)	β_x ($10^{-6}/\%M$)	θ_1 ($^{\circ}$)	θ_2 ($^{\circ}$)
1	149,5	9,1	-2,90	-36,3	13	26,5
2	159,5	16,9	-1,90	-9,7	1,2	34,7
3	159,8	13,0	-2,21	-18,3	6,5	31,2
4	161,3	7,4	-3,00	-40,5	15,5	21,2
5	170,2	8,4	-2,69	-31,8	11,6	23,7
6	172,4	11,8	-2,20	-17,9	3,9	29,2
7	181,9	8,0	-2,57	-28,4	10,9	22,1
8	184,1	9,7	-2,31	-21,0	5,7	25,5
9	190,2	7,2	-2,60	-29,2	13,7	18,3
10	193,2	8,5	-2,34	-21,8	7,4	22,7
11	202,6	9,0	-2,15	-16,5	1,2	23,3
12	217,8	8,1	-2,04	-13,4	2,5	20,3
13	234,0	7,6	-1,85	-8,1	2,1	17,4
14	245,9	7,4	-1,67	-3,3	0,3	15,2

Table 5 Genetic algorithm parameters for single objective approach used in model problems (1b, 2b and 3b)

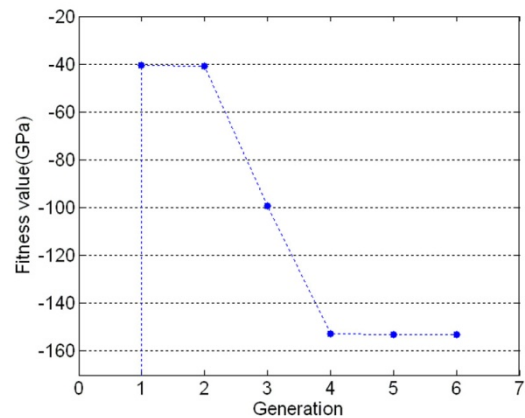
Population Type	Double vector
Population size	20
Creation function	Use constraint dependent
Initial population	[]
Initial scores	[]
Initial range	[-300;-100]
Scalling function	Top, Quantity=12
Selection function	Tournament Tournament size=7
Elite count	2
Crossover fraction	0.6
Mutation function	Use constraint dependent
Crossover function	Scattered
Migration direction	Both Fraction=0.2, Interval=20
Initial penalty	10
Penalty factor	100
Hybrid Function	None
Stopping criteria	Generation=100, Stall generation=50 Function tolerance= 10^{-6}



(a)



(b)



(c)

Fig.5. Evolution of fitness function value in each generation



It is observed from the figure, this value converges only after 4 generations as a result of relatively small feasible solution space obtained from the multi-objective solutions. The single and multi-objective optimization results of the model problems are given in Table 6. It is seen that similar results have been obtained in both (multi and single objective) approach for E_x, E_y, α_x and β_x with different stacking sequences.

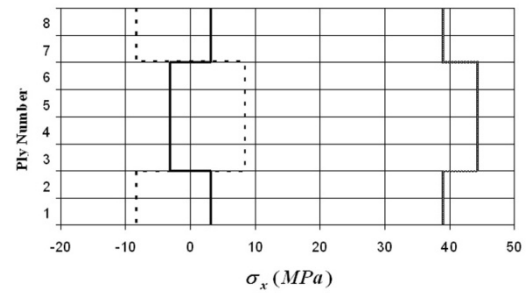
Table 6. Genetic Algorithm optimization results of the model problems for two optimization approaches

Problem	Optimization Type	E_x (GPa)	E_y (GPa)	α_x ($10^{-6}/^{\circ}\text{C}$)	β_x ($10^{-6}/\%M$)	Stacking Sequence
1a	Multi Objective	188.0	7.3	-2.63	-29.9	($\pm 13.8/\mp 18.5$) _s
1b	Single Objective	189.5	7.1	-2.63	-30.0	(± 16.1) _{2s}
2a	Multi Objective	184.1	9.7	-2.31	-21.0	($\pm 5.7/\pm 25.5$) _s
2b	Single Objective	183.4	9.7	-2.31	-21.1	($\mp 5.8/\pm 25.6$) _s
3a	Multi Objective	152.7	7.2	-3.21	-46.1	($\pm 20/\mp 18$) _s
3b	Single Objective	152.7	7.1	-3.22	-46.4	($\mp 19.3/\mp 18.7$) _s

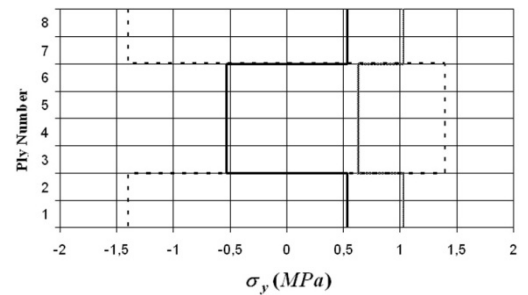
Investigation of stresses for optimized problems under combined loading give some additional information about composite design. This type of information provides production of safer structures [18]. The state of stress through the thickness of a composite plate can be determined by using the relation given in Eq. (19).

$$\begin{Bmatrix} \sigma_x \\ \sigma_y \\ \tau_{xy} \end{Bmatrix} = \begin{bmatrix} \bar{Q}_{11} & \bar{Q}_{12} & \bar{Q}_{16} \\ \bar{Q}_{12} & \bar{Q}_{22} & \bar{Q}_{26} \\ \bar{Q}_{16} & \bar{Q}_{26} & \bar{Q}_{66} \end{bmatrix} \begin{Bmatrix} \varepsilon_x - \alpha_x \Delta T - \beta_x \Delta C \\ \varepsilon_y - \alpha_y \Delta T - \beta_y \Delta C \\ 2(\varepsilon_{xy} - \alpha_{xy} \Delta T - \beta_{xy} \Delta C) \end{Bmatrix} \quad (19)$$

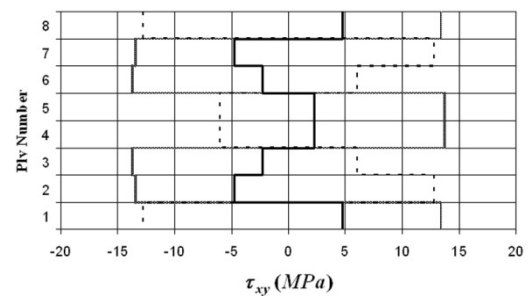
For model problem 3a, the through the thickness normal and shear stresses distributions of the optimized (using multiobjective approach) composite plate under the mechanical, thermal and hygral loads are given in Fig. 6. It is observed that normal stresses σ_x and σ_y become



(a)



(b)



(c)

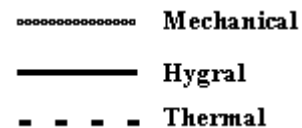


Fig.6. Stresses distribution of optimized composite plates under the thermal, hygral and mechanical loads in model problem 3a



maximum in plies 3-6. Another observation is that the mechanical load is very effective compared to hygral and thermal loads for normal stress σ_x . However, thermal load dominates for σ_y . It would be so due to relatively low mechanical load in y direction ($F_y = 1kN$). Considering the negative hygral stresses in plies 3-6, a question can be asked that, is it advantageous to absorb moisture? Unfortunately moisture degrades the strength of laminates [18]. Therefore, it is not really an advantage to use the stress relieving tendencies of moisture absorption. Unlike normal stresses, relatively more complicated through the thickness stress distribution have been obtained for shear stress τ_{xy} .

6. Conclusion

In the present study, two different optimization approaches are proposed to design the carbon fiber reinforced epoxy laminated composites. All of the model problems consider minimization of the CTE and maximization of elastic moduli simultaneously. The resulting fiber orientation angles automatically minimize the CME and this provides some advantages for the materials used in satellite structures. Therefore, it is sufficient to minimize the CTE only and not necessary to solve a new optimization problem in order to minimize the CME of the laminated composites. Simplified micro-mechanical equations and classical lamination theory combined with MATLAB Symbolic Math Toolbox have been utilized in order to obtain objective functions and constraints in terms of design variables θ_1 and θ_2 for single and multi-objective optimization problems. The optimization solutions have been achieved after 6 and 51 generations for single and multi-objective approaches, respectively. Both approaches give similar results with different stacking sequences. Regarding mechanical analysis, shear and normal stress distributions of the optimized composite plate(model problem 3a) are presented and results show that mechanical loads dominate to thermal and hygral effects.

References

- [1]. R. Le Rich and J. Gaudin, *Design of dimensionally stable composites by evolutionary optimization*, Composite Structures 41, pages 97–111, 1998.
- [2]. R. Spallino, S. Rizzo, *Multiobjective Discrete Optimization of Laminated Structures*, Mechanics Research Communications 29, pages 17–25, 2002.
- [3]. J. L. Pelletier, S. S. Vel, *Multiobjective optimization of fiber reinforced composite laminates for strength, stiffness and minimal mass*, Computers and Structures 84, pages 2065–2080, 2006.
- [4]. F. S. Almeida, A. M. Awruch, *Design optimization of composite laminated structures using genetic algorithms and finite element analysis*, Composite Structures 88, pages.443–454, 2009
- [5]. R.J. Wood, S. Avadhanula, R.Sahai, E. Steltz, R.S. Fearing, *Mikrorobot design using fiber reinforced composites*, Journal of Mechanical Design 130, 052304-1, May 2008.
- [6]. R.Y. Kim, A.S. Crasto, G.A. Schoeppner, *Dimensional stability of composite in a space thermal environment*, Composites Science and Technology 60, pages 2601-2608, 2000.
- [7]. A. K. Kaw, *Mechanics of Composite Materials*. Taylor & Francis Group; LLC, 2006
- [8]. The Mathworks, Inc, MATLAB Optimization Toolbox in version R2008b
- [9]. The Mathworks, Inc, MATLAB Genetic Algorithm and Direct Search Toolbox in version R2008b
- [10]. The Mathworks, Inc, MATLAB Symbolic Math Toolbox in version R2008b
- [11]. G. Z. Voyiadjis, P. I. Kattan, *Mechanics of Composite Materials with MATLAB*, Springer-Verlag; Berlin Heidelberg, 2005.
- [12]. C. C. Chamis, *Simplified Composite Micromechanics Equations for Hygral, Thermal and Mechanical properties*, SAMPE Quarterly, pages 14–23, April 1984.
- [13]. J. Branke, K. Deb, K. Miettinen, R. Slowinski, *Multiobjective Optimization Interactive and Evolutionary Approaches*, Springer-Verlag; Berlin, 2008.
- [14]. L. Aydin, H.S. Artem, *Multiobjective Genetic Algorithm Optimization Of The Composite Laminates As A Satellite Structure Material For Coefficient Of Thermal Expansion And Elastic Modulus*, 4th International Conference on Recent Advances in Space Technologies, RAST '09, pages 114-119, 2009.
- [15]. M.Gen, R. Cheng, *Genetic Algorithms and Engineering Optimization* John Wiley & Sons, Inc., 2000.
- [16]. S. Karakaya, O. Soykasap, *Buckling optimization of laminated composite plates using genetic algorithm and generalized pattern search algorithm*, Structural and Multidisciplinary Optimization 39, pages 477-486, 2009
- [17]. M. Akbulut, F. O. Sonmez, *Optimum design of composite laminates for minimum thickness*, Computers and Structures 86, pages 1974-1982, 2008.
- [18]. M. W. Hyer, *Stress Analysis of Fiber Reinforced Composite Materials*, McGraw-Hill, 1998.



The Influence of the Spring Rate on the Dynamics of the Special Centrifugal Regulator

Jafar AGALAROV¹, Vugar JAVADOV¹

¹ National Academy of Aviation
AZ1045, Bina 25-ci km, Baku, AZERBAIJAN,
samedov@naa.edu.az; Vugar.Javadov@swhs.az

Abstract

The special centrifugal regulator (SCR) is an epicycle mechanism. According to the mechanical connection between the crankshafts of engine the regulator which fixed to the end of the one of the crankshafts. The kinetic and potential energy of the SCR defined, consequently defined motion equation in accordance with the II type of Lagrangian's equations in order to research the influence of spring rate to the internal vibration of the SCR. The equation of motion brought to the algebraical equations and solved by using the finite difference method. Researched the influence of spring rate to the internal vibration of the SCR and the dependence graphs has been plotted.

Keywords: Special Centrifugal Regulator, Variable Compression engine, Finite Difference Method

1. Introduction

The special centrifugal regulator which regulated the compression ratio of the variable compression engine [1] is a epicycle mechanism as demonstrated [2,3,4,5,6]. As the epicycle mechanism is consist of the sun gear, two satellites in which fixed eccentric weights, spring and two valve are mounted on the eccentric weights and the crown wheel. The SCR allows to be filled with liquid for damping oscillations. The mechanism that actuated by centrifugal force creates relative angle shift of shafts in accordance with depending on revolutions per minute (RPM).

The regulating of crankshafts provides engine with low compression degree in the low RPM and with high compression degree in the high RPM. Procedure is carried out by shifting between the angle of turn of the shafts. Regarding the influence of centrifugal force the satellites with the eccentric weights is actuated. Consequently the sun and crown wheels sections is actuated, too. It creates double effect. Also in presence of the damping liquid supports to canceling the the vibration and hence it helps for providing quiet regulating. Efficiency of regulating are increased by the relief valve.

2. Problem Formulation

During starting of SCR the springs will be cause vibrations. It means that the vibration influences to the regulating procedure. That is why it is necessary to research the influence of the spring rate to the vibration.

The aim of this paper is to define the influence of the spring rate to internal vibration of the regulator in accordance with the depend on RPM. There are two motion freedom of the mechanism. Therefore the system of motion equation consists of two equations. In order to define the system of motion equation firstly must be defined the kinetic and potential energy of the system (adjuster).

3. Definition Kinetic and Potential Energy

The kinetic energy of the system is defined as follow (Figure 1.):

$$T_{SYS} = T_1 + T_2 + T_3 \quad (1)$$

where, T_{SYS} - the kinetic energy, T_1, T_2, T_3 the kinetic energy of the cog-wheels regarding the indexes:

$$\begin{cases} T_1 = \frac{1}{2} J_1 \omega_1^2 \\ T_2 = \sum_i \frac{1}{2} m_{p_i} v_{p_i}^2 \\ T_3 = \frac{1}{2} J_3 \omega_3^2 \end{cases} \quad (2)$$

where, J_1, J_3 - the inertia moments of the members regarding the indexes, ω_1, ω_3 the angular velocities of the cog-wheels regarding the indexes, m_{p_i} the weights of the elementary parts of the eksentric fixed satellite,

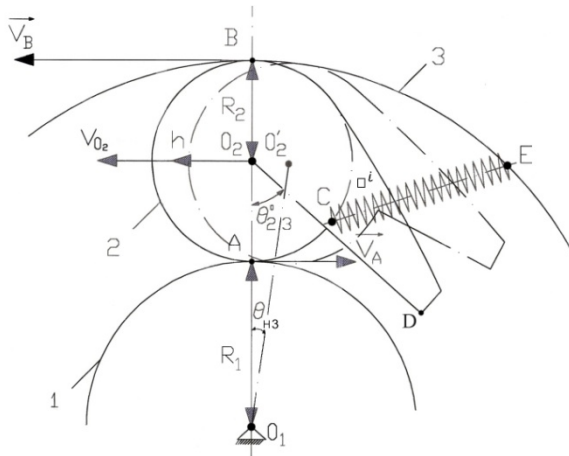


Fig. 1: The kinematical scheme of the adjuster

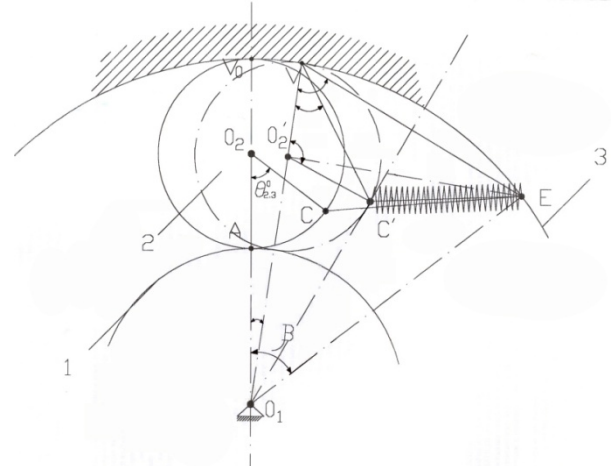


Fig. 2: The geometrical scheme of the adjuster.

\vec{v}_{p_i} - the velocity of the elementary parts of the eksentric fixed satellite which is define as follow (Fig.1):

$$\vec{v}_{p_i} = \vec{v}_{O_2} + \vec{v}_{p_i O_2} \quad (2.3)$$

where, \vec{v}_{O_2} - the velocity of the O_2 point, ($v_{O_2} = \omega_H (R_1 + R_2)$), the ω_H - is the angular velocity of the point O_2 , R_1, R_2 - the radiuses of the cog-wheels regarding the indexes; $v_{p_i O_2} = \omega_2 R_{p_i}$; $\vec{v}_{p_i O_2}$ - the velocity of the elementary part in relation to the O_2 point, ω_2 - the angular velocity of the eccentric fixed satellite eccentric, R_{p_i} - the distance from arbor O_2 to the elementary part P_i ; if taken into account the (2), (3) and aforementioned in the formula (1) consequently the equation of kinetic energy could be written:

$$T_{SYS} = \frac{1}{2} J_1 \omega_1^2 + \frac{1}{2} J_3 \omega_3^2 + \frac{1}{8} M_2 [\omega_3 (R_1 + 2R_2) + \omega_1 R_1]^2 - \frac{1}{4R_2} M_2 r_C [\omega_3^2 (R_1 + 2R_2)^2 - \omega_1^2 R_1^2] \cdot \cos \left[\frac{R_1 (\theta_3 - \theta_1) + 2R_2 \theta_{2,3}^0}{2R_2} \right] + \frac{1}{8R_2^2} J_S [\omega_3 (R_1 + 2R_2) - \omega_1 R_1]^2 \quad (4)$$

where, M_2 - is the weight of satellite, r_c - the distance from the O_2 point to center of gravity of the satellite eccentric, $\theta_3 - \theta_1 = \Delta\theta$ - the relative turning angle of the shafts, $\theta_{2,3}^0$ - the angle between the line in relation to the vertical symmetrical axes which of the eksentric fixed satellite and between center of gravity, θ_1, θ_3 - absolute turning angles of the cog-wheels regarding the indexes, J_s - the inertia moment of the satellite in relation to the O_2 point.

The potential energy of system is equal to the energy of the spring is defined as follow (Figure2.):

$$V_{sis} = \frac{1}{2} \cdot k \cdot \left\{ L_0 - \left[4R_2^2 \cos^2 \left[\frac{(\theta_3 - \theta_1)R_1 + 2R_2 \theta_{2,3}^0}{4R_2} \right] + 4(R_1 + 2R_2) \sin^2 \left[\frac{\beta}{2} - \frac{R_1(\theta_3 - \theta_1)}{4(R_1 + R_2)} \right] - 8R_2(R_1 + 2R_2) \cdot \cos \left[\frac{(\theta_3 - \theta_1)R_1 + 2R_2 \theta_{2,3}^0}{4R_2} \right] \cdot \sin \left[\frac{\beta}{2} - \frac{R_1(\theta_3 - \theta_1)}{4(R_1 + R_2)} \right] \cdot \sin \left[\frac{\beta}{2} - \frac{R_1(\theta_3 - \theta_1)}{4(R_1 + R_2)} \right] + \frac{(\theta_3 - \theta_1)R_1 + 2R_2 \theta_{2,3}^0}{4R_2} \right]^2 \right\} \quad (5)$$

where, V_{SYS} - the potential energy of the system, k - spring constant, L_0 - the initial length of the spring, β - the angle of setting of the spring.

4. Differential Motion Equation of the Special Centrifugal Regulator

The differential motion equation of the special centrifugal regulator could be written as follow if the (4) and (5) expression be taken into account in the formula [7,8] the Langranj's equation referring to [9,10]:

$$\begin{cases} \ddot{\theta}_1 \cdot \phi_1(\theta_3 - \theta_1) + f_1(\dot{\theta}_1, \dot{\theta}_3, \theta_3 - \theta_1) = Q_1 \\ \ddot{\theta}_3 \cdot \phi_2(\theta_3 - \theta_1) + f_2(\dot{\theta}_1, \dot{\theta}_3, \theta_3 - \theta_1) = Q_2 \end{cases} \quad (6)$$



where, $\ddot{\theta}_1$ - is the double the in relation to the time of angular velocity of the sun cog-wheel, $\ddot{\theta}_3$ - is the double the in relation to the time of angular velocity of the crown cog-wheel, $\dot{\theta}_1, \dot{\theta}_3$ - the derivative in relation to the time of angular velocity of the cog-wheels regarding the indexes,

$$\xi = k\Delta L \frac{1}{2L},$$

$$\phi_1(\theta_3 - \theta_1) = J_1 + \frac{1}{4}M_2R_1^2 + \frac{1}{2R_2}M_2r_C R_1^2$$

$$\cos\left[\frac{R_1(\theta_3 - \theta_1) + 2R_2\theta_{2.3}^0}{2R_2}\right] + \frac{J_2R_1^2}{4R_2^2}$$

$$\phi_2(\theta_3 - \theta_1) = J_3 + \frac{1}{4}M_2(R_1 + 2R_2)^2 - \frac{1}{2R_2}M_2r_C(R_1 + 2R_2)^2$$

$$\cos\left[\frac{R_1(\theta_3 - \theta_1) + 2R_2\theta_{2.3}^0}{2R_2}\right] + \frac{1}{4R_2^2}J_2(R_1 + 2R_2)^2$$

$$\begin{cases} f_1(\dot{\theta}_1, \dot{\theta}_3, \theta_3 - \theta_1) = A_1 + B_1 - \xi(\Gamma + E - Z - H + N) \\ f_2(\dot{\theta}_1, \dot{\theta}_3, \theta_3 - \theta_1) = A_2 - B_1 - \xi(-\Gamma - E + Z + H - N) \end{cases}$$

$$A_1 = -\frac{R_1}{4R_2^2}M_2r_C R_1^2 \sin\left[\frac{R_1(\theta_3 - \theta_1) + 2\theta_{2.3}^0 R_2}{2R_2}\right] (\dot{\theta}_3 - \dot{\theta}_1)$$

$$B = \frac{R_1}{8R_2^2}M_2r_C \left[(R_1 + 2R_2)^2 \dot{\theta}_3^2 - R_1^2 \dot{\theta}_1^2 \right]$$

$$\sin\left[\frac{R_1(\theta_3 - \theta_1) + 2\theta_{2.3}^0 R_2}{2R_2}\right]$$

$$A_2 = \frac{R_1}{4R_2^2}M_2r_C (R_1 + 2R_2)^2$$

$$\sin\left[\frac{R_1(\theta_3 - \theta_1) + 2\theta_{2.3}^0 R_2}{2R_2}\right] (\dot{\theta}_3 - \dot{\theta}_1),$$

$$\Gamma = 2R_2 \cos\left[\frac{R_1(\theta_3 - \theta_1) + 2\theta_{2.3}^0 R_2}{4R_2}\right].$$

$$\sin\left[\frac{R_1(\theta_3 - \theta_1) + 2\theta_{2.3}^0 R_2}{4R_2}\right] R_1$$

$$E = \frac{1}{2}(R_1 + 2R_2)^2 \sin\left[\frac{\beta}{2} - \frac{R_1(\theta_3 - \theta_1)}{4(R_1 + R_2)}\right].$$

$$\cos\left[\frac{\beta}{2} - \frac{R_1(\theta_3 - \theta_1)}{4(R_1 + R_2)}\right] \frac{R_1}{R_1 + R_2},$$

$$Z = 2(R_1 + 2R_2) \sin\left[\frac{R_1(\theta_3 - \theta_1) + 2\theta_{2.3}^0 R_2}{4R_2}\right] R_1.$$

$$\sin\left[\frac{\beta}{2} - \frac{R_1(\theta_3 - \theta_1)}{4(R_1 + R_2)}\right] \cdot \sin\left[\frac{\frac{\beta}{2} - \frac{R_1(\theta_3 - \theta_1)}{4(R_1 + R_2)} + \frac{R_1(\theta_3 - \theta_1) + 2\theta_{2.3}^0 R_2}{4R_2}}{R_1(\theta_3 - \theta_1) + 2\theta_{2.3}^0 R_2}\right],$$

$$H = 2R_2(R_1 + 2R_2) \cos\left[\frac{R_1(\theta_3 - \theta_1) + 2\theta_{2.3}^0 R_2}{4R_2}\right].$$

$$\cos\left[\frac{\beta}{2} - \frac{R_1(\theta_3 - \theta_1)}{4(R_1 + R_2)}\right] \frac{R_1}{R_1 + R_2}.$$

$$\cdot \sin\left[\frac{\beta}{2} - \frac{R_1(\theta_3 - \theta_1)}{4(R_1 + R_2)} + \frac{R_1(\theta_3 - \theta_1) + 2\theta_{2.3}^0 R_2}{4R_2}\right]$$



$$N = 2R_2(R_1 + 2R_2) \cos \left[\frac{R_1(\theta_3 - \theta_1) + 2\theta_{2,3}^0 R_2}{4R_2} \right]$$

$$\cos \left[\frac{\beta}{2} - \frac{R_1(\theta_3 - \theta_1)}{4(R_1 + R_2)} \right] \cdot \cos \left[\frac{\beta}{2} - \frac{R_1(\theta_3 - \theta_1)}{4(R_1 + R_2)} + \frac{R_1(\theta_3 - \theta_1) + 2\theta_{2,3}^0 R_2}{4R_2} \right]$$

$$\frac{R_1^2}{(R_1 + R_2)R_2}$$

$$Q_1 = M_K \left[\frac{\alpha_1}{1 + \dot{\theta}_1} + \left(\gamma_2 + \frac{\gamma_1}{\dot{\theta}_1} \right) \sin(\dot{\theta}_1 \cdot t) \right]$$

$$Q_2 = M_K \left[\frac{\alpha_1}{1 + \dot{\theta}_3} + \gamma_2 \sin(\dot{\theta}_3 \cdot t) \right]$$

where, Q_1 and Q_2 - the general external oscillatory forces applied in the engine, which in practically could affect to the mechanism, $\alpha_1, \alpha_2, \gamma_1, \gamma_2, M_K$ - the constants which characterize force, t - is time.

The following formula could be written from the system of equation (3.1):

5. Solving of Differential Motion Equation

The system of equation can be written as follow if is substituted the derivatives for the finite differences as demonstrated [11]:

$$\begin{cases} \theta_{1i+1} = \frac{Q_{1i} - f_{1i}(\dot{\theta}_1, \dot{\theta}_3, \theta_3 - \theta_1)}{\phi_{1i}(\theta_3 - \theta_1)} \cdot \Delta t^2 + 2\theta_{1i} - \theta_{1i-1} \\ \theta_{3i+1} = \frac{Q_{2i} - f_{2i}(\dot{\theta}_1, \dot{\theta}_3, \theta_3 - \theta_1)}{\phi_{4i}(\theta_3 - \theta_1)} \cdot \Delta t^2 + 2\theta_{3i} - \theta_{3i-1} \end{cases} \quad (7)$$

The system of equation Eq. (7) could be solved by using the appropriate program if the system of equation Eq. (6) is show as algebraical equation. So, in accordance with Cauchy problem by given initial values to the absolute turning angles (θ_1 and θ_3), the relative turning angle ($\Delta\theta$)

and the absolute spring rate and obtained satisfactory result.

6. The Influence of the Spring Rate on Vibrations

After solving the motion equation is researched the influence of the spring rate on vibration of the SCR. Several springs are chosen with various of their rates for researching the influence of the spring rate on vibration. Three cases have been considered. spring rates are accepted: 1) $k_1=k$; 2) $k_2=1.5k$; 3) $k_3=2/3k$; the other value of the parameters of the regulator is taken as: $R_1=a$; $R_2=1.2a$; $M_2=b$; $M_1=3.3b$; $M_3=6.6b$; $\beta=54^\circ$ are remained constant, and as the initial value of absolute turning angles (θ_1, θ_3) are given $\theta_{10} = 0, \theta_{1i} = -0.5, \theta_{30} = 0, \theta_{3i} = -0.1$. other parameters' values are remained constant. As a result is plotted the dependence graphs. The dependence graphs of the absolute turning angles (θ_1 and θ_3), the relative turning angle ($\Delta\theta$) and the absolute spring rate relative turning angle ($\Delta\theta$) and the absolute spring rate will be as follow:

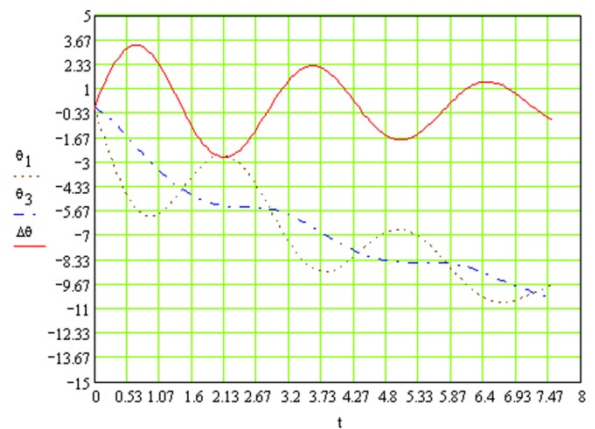


Fig. 3: The dependence on time of the absolute and relative angles

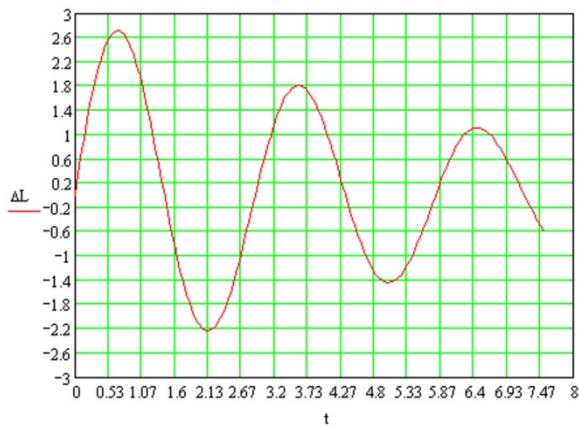


Fig. 4: The dependence on time of the absolute spring rate

- [11]. G. Korn, T. Korn, "Spravochnik po matematike" M., 1968 q., 720 pages (G. Korn, T. Korn, "Handbook for Mathematics" M., 1968 q., 720 pages).

7. Conclusion

The finite difference method used in this article for solving the differential motion equation of the system. The appropriate graphs has been built which characterize the dynamics of system. It seems that from the Fig. 3 and Fig. 4 that the fluctuation is harmonical damping oscillation. It is possible to built other graphs by given different initial values to the absolute turning angles (θ_1 and θ_3). The damping applying is necessary if the amplitude of oscillation is out margine. It has been taken into account on construction. The oscillation damping is performed by the damping liquid or by the applying the opposite spring.

References

- [1]. Agalarov et al., Internal combustion engine with opposed pistons, U.S. Patent № 6,039,011., 03/2001
- [2]. Mallory, Ignition governor, U.S. Patent № 1,967,445., 06/1934
- [3]. Mallory, Inertia governor, U.S. Patent № 2,009,934., 12/1935
- [4]. Lucien Trappo, Centrifugal Regulator, U.S. Patent № 4,144,725., 07/1977
- [5]. Hartman et al., Centrifugal governor for internal combustion engines, U.S. Patent № 5,131,361., 07/1992
- [6]. Hubert Wehr, Eccentric mechanism with adjustable stroke, U.S. Patent № 6,250,178., 06/2001
- [7]. V.S. Naumov "Mashinovedenie" chast vtoraya, Moskva-1932 (V.S. Naumov "Science of machines" second part, Moskva-1932)
- [8]. S.M. Targ "Kratkiy kurs teoreticheskoy mekhaniki", uchebnik dlya vtuzov, Baku-1983, str. 512 (S.M. Targ "Brief course theoretical mechanic", textbook for the technical college Baku-1983, pages. 512)
- [9]. N.S.Piskunov "Differensialnoe i integralnoe ischislenie" uchebnik dlya vtuzov, vtoroy chast M.,1976 q., str. 576 (N.S.Piskunov "Differential and integral calculation" textbook for the technical college, second part M.,1976 year., page. 576)
- [10]. Parnaby J., Porterr B., Non-linear vibration of a centrifugal governor, International Journal of Non linear Mechanics, № 3, 187-200 (1968).



Fault Detection and Isolation using Redundant Sensors for a Wind Turbine with Doubly-Fed Induction Generator (DFIG)

Hakki Erhan Sevil^{1*}

^{1*} Izmir Institute of Technology
Department of Mechanical Engineering, Artificial Intelligence & Design Laboratory,
Gulbahce 35430, Urla / Izmir TURKEY
erhansevil@iyte.edu.tr

Abstract

Modern wind turbines increase in size, megawatt capacities and their power production to overcome their financial disadvantage. This leads a necessity of more reliable power plants and much effort to enhance the reliability of the wind turbines. That's where Fault Detection and Isolation (FDI) systems become important. The aim of this study is to create a system that detects sensor faults in a redundant speed sensor system which is used on wind turbine with doubly-fed induction generator (DFIG). Fault detection and isolation simulations were performed via Simulink for a linear model of a 2MW wind turbine. Two kinds of faults are considered, fixed value (bias type) and gain factor faults. These faults are assumed to affect the redundant sensor system which measures the angular speed of the generator shaft. The generated residuals were controlled using a statistical approach. A chi-square hypothesis test was performed to achieve the fault detection, and angle comparison was taken into account for isolation. The designed system achieves fault detection and isolation with a prespecified false alarm probability.

Keywords: Fault Detection and Isolation (FDI), Wind Turbine with DFIG, Hardware Redundancy.

1. Introduction

In our world today, the topic of energy becomes more and more critical. Renewable energy resources and their sustainability gain serious importance in the last two decades, because of decreasing production the fossil energy. Energy acquired from fossil fuels, that is approximately amounting to an 86% share for primary energy production in the world in 2006, mainly from oil, is expected to be expended, almost totally, in the next five or six decades. Therefore, renewable energies, such as wind energy, have a major role in the future energy market.

A wind turbine converts wind energy to electrical energy. Although world's power production is more and

more contributed by wind energy every day, it cannot compete with traditional energies due to the fact that it is more expensive than others. To overcome this, size of modern wind turbines increases, the megawatt capacities of turbines and their power production keep improving. All these conclude as raise in construction expense, and necessity of more reliable power plants. Considering the economy of their installation and maintenance, wind turbines should be able to continue working as much time as possible. However the main element of a turbine, that is wind, performs as a source of stress and causes failures on some components of wind turbines. Consequently, much effort is needed to enhance the reliability of the wind turbines. That's where Fault Detection and Isolation (FDI) systems become important. Basically FDI can be described as a system for identifying the occurrence a fault which causes of changes in the system structure or parameters leading lowered system performance or loss of function, and also for pinpointing the type of fault and its location.

In the literature, there are some works on fault detection and isolation on wind turbines. One of these studies which are worth to mention belongs to Wei et al. [1]. Wei and his colleagues presented their work about blade root moment sensor fault detection and isolation by investigating residual which are generated by Kalman filter. Meanwhile, an unknown input observer based scheme for detecting faults in a wind turbine converter is proposed in [2]. Odgaard and Stoustrup tried to estimate the faults in the converter and isolate them either to be an actuator fault or a sensor fault. Furthermore, two feasible fault detection and identification algorithms that are based on the Kalman filter are presented by [3] where pitch-to-vane controlled horizontal axis wind turbines are taken into consideration to examine the usability of time-domain model based FDI. From a sensor fault detection point of view, two more studies are worth to mention here. Rothenhagen and Fuchs [4] presented a work on advanced

sensor fault detection of wind power plants with doubly fed induction generators (DFIG). Moreover, the fault detection on current sensor of DFIG was investigated by [5].

The aim of this study is to create a system that detects sensor faults in a redundant speed sensor system which is used on wind turbine with doubly-fed induction generator (DFIG). This paper is organized as follows. In the first part, linear modeling of wind turbine is described. Then, in the second part sensor fault detection and isolation is presented. In part 3, simulations results are presented. And finally, this paper ends with a conclusion.

2. Wind Turbine Modeling

In this study, a linear model of a 2MW wind turbine which was presented by [6] is used. In that model, the considered wind turbine was as variable-speed, variable pitch wind turbine with doubly-fed induction generator. The working principle of a wind turbine is simple; the wind moves the blades of turbine therefore it rotates the rotor shaft which is connected to the generator shaft. A gear box between two shafts is used to change the speed ratio.

The general model consists of subsystems, i.e. wind model, aerodynamic model, drive train model. Each subsystem was described using a state-space model in [6]. This study mainly focuses on mechanical model of wind turbines, which is described in next section.

In this report, details on modeling of wind turbines and its subsystems will not be introduced. Readers can refer to [6] for more information.

2.1. Mechanical Model

Wind turbines transform the available power of the wind into mechanical power. The wind causes a torque on the wind turbine rotor. This torque is applied to an electrical unit via a mechanical system, namely the drive train. The drive train dynamics of a wind turbine consist of rotor, gearbox and generator dynamics.

The rotor and gearbox are connected through a low speed shaft. On the other hand, a high speed shaft connects the gearbox and the generator. Commonly, a two-mass model is used in simulations of wind turbines, instead of three-mass model which is thought to be the representation of complete dynamics.

The reasons of selecting a two-mass model are the simplification of the model and the relatively small inertia of the gearbox compared to the wind turbine rotor and the generator inertia. So, in a two-mass model, the gearbox is considered as lossless. A scheme of two-mass model is given in figure 1.

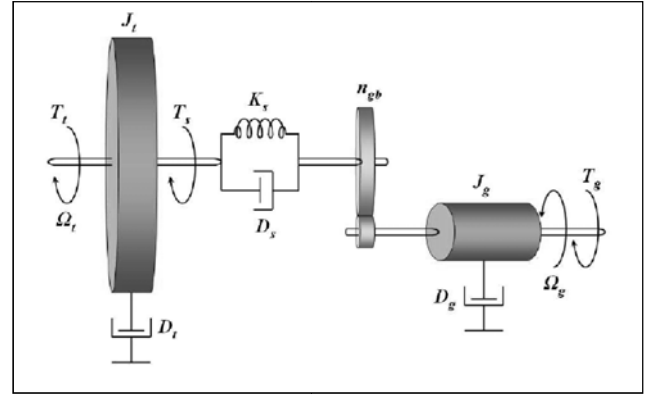


Fig. 1: Two-mass Drive Train Model for Wind Turbines

As can be seen in the figure, the gearbox is taken into account as lossless. The mechanical equations of the two-mass model are presented in equation 1 and 2,

$$J_t \dot{\Omega}_t(t) + D_t \Omega_t(t) = T_t(t) - T_s(t) \quad (1)$$

$$J_g \dot{\Omega}_g(t) + D_g \Omega_g(t) = T_s(t) / n_{gb} - T_g(t) \quad (2)$$

where the torque of the shaft, T_s , is equal to

$$T_s(t) = K_s \theta_s(t) + D_s (\Omega_t(t) - \Omega_g(t) / n_{gb}) \quad (3)$$

In equation 1, 2 and 3, Ω is the rotational speed, T is the torque, J represents the inertia and D and K are coefficients of damping and stiffness, respectively. Additionally, sub-indices t , s and g stand for rotor, shaft and generator. Also, n_{gb} represents the ratio between high speed shaft and low speed shaft. The resulting state space model in terms of states Ω_t , Ω_g and T_s is given in equations 4 and 5.

$$\begin{bmatrix} \dot{\tilde{\Omega}}_t(t) \\ \dot{\tilde{\Omega}}_g(t) \\ \dot{\tilde{T}}_s(t) \end{bmatrix} = \begin{bmatrix} -\frac{D_t}{J_t} & 0 & \frac{1}{J_t} \\ 0 & -\frac{D_g}{J_g} & \frac{1}{n_{gb} J_g} \\ K_s - \frac{D_s D_t}{J_t} & n_{gb} (\frac{D_s D_g}{J_g} - K_s) & -D (\frac{1}{J_t} + \frac{1}{n_{gb} J_g}) \end{bmatrix} \begin{bmatrix} \tilde{\Omega}_t(t) \\ \tilde{\Omega}_g(t) \\ \tilde{T}_s(t) \end{bmatrix} + \begin{bmatrix} \frac{1}{J_t} & 0 \\ 0 & -\frac{1}{J_g} \\ \frac{D_s}{J_t} & \frac{D_s}{n_{gb} J_g} \end{bmatrix} \begin{bmatrix} \tilde{T}_t(t) \\ \tilde{T}_g(t) \end{bmatrix} \quad (4)$$



$$\Omega_g(t) = \begin{bmatrix} 0 & 1 & 0 \end{bmatrix} \begin{bmatrix} \tilde{\Omega}_i(t) \\ \tilde{\Omega}_g(t) \\ \tilde{T}_s(t) \end{bmatrix} \quad (5)$$

The character tilde on the variables means that these equations are written around a given operation point. It should be noted that the used simulator contains all systems and sub-systems of a wind turbine. What is done in this study is, taking the measurement of angular speed of the generator with a redundant sensor system, and trying to detect sensor faults by tracking the residuals via a statistical approach, explained in the next section.

3. Sensor Fault Detection and Isolation

As mentioned in the introduction, the reliability of wind turbines gains importance increasingly day-by-day due to the fact that they should keep running as much as possible to overcome the economical drawbacks. To ensure this, one possible way is to get help from advanced methods, i.e. fault detection and isolation (FDI) systems. Basically, there exists some FDI system embedded in industrial wind turbines. However they are often conservative and do not exploit systematically the correlation between the different measurements. The concern of this study is to create advance systems for detection of sensor faults in redundant measurement system.

3.1. Generation of Residuals

Consider the measurement equation as follows,

$$\begin{bmatrix} y_1(k) \\ y_2(k) \\ y_3(k) \end{bmatrix} = \begin{bmatrix} 1 \\ 1 \\ 1 \end{bmatrix} x(k) + \begin{bmatrix} \xi_1(k) \\ \xi_2(k) \\ \xi_3(k) \end{bmatrix} + \begin{bmatrix} f_1(k) \\ f_2(k) \\ f_3(k) \end{bmatrix} \quad (6)$$

where $\xi_i(k)$ are normally distributed random sequences and they are independent from each other. They have zero mean and covariance R ; $\Xi(k) \sim N(0,R)$. Moreover, $f_i(k)$ are corresponding fault values and $x(k)$ represents the measured state. Equation 6 can be written in matrix form as,

$$Y(k) = A_s x(k) + \Xi(k) + F(k) \quad (7)$$

In order to eliminate the state variable, equation 7 can be multiplied on the left by a row vector v^T such that;

$$v^T [1;1;1]^T = 0 \quad (8)$$

In our particular case, the left null space of A_s has dimension 2. Hence, one can introduce a matrix V made of two independent vectors v_i that span this left null space

$$V = \begin{bmatrix} v_1^T \\ v_2^T \end{bmatrix} \quad (9)$$

If both sides are multiplied by matrix V , equation 6 becomes,

$$V \begin{bmatrix} y_1(k) \\ y_2(k) \\ y_3(k) \end{bmatrix} = V \begin{bmatrix} \xi_1(k) \\ \xi_2(k) \\ \xi_3(k) \end{bmatrix} + V \begin{bmatrix} f_1(k) \\ f_2(k) \\ f_3(k) \end{bmatrix} \quad (10)$$

Let us defined $\tau(k)$ as,

$$\tau(k) = V \begin{bmatrix} y_1(k) \\ y_2(k) \\ y_3(k) \end{bmatrix} = V \begin{bmatrix} \xi_1(k) \\ \xi_2(k) \\ \xi_3(k) \end{bmatrix} + V \begin{bmatrix} f_1(k) \\ f_2(k) \\ f_3(k) \end{bmatrix} \quad (11)$$

This variable is called residual, and it indicates the inconsistency exhibited in the signals $y_i(k)$, $i=1, 2, 3$. In summary, residual is generation described by,

$$\tau(k) = V Y(k), \quad \tau(k) = V \begin{bmatrix} y_1(k) \\ y_2(k) \\ y_3(k) \end{bmatrix} \quad \text{where } V = \begin{bmatrix} v_1^T \\ v_2^T \end{bmatrix},$$

$$v_i^T \begin{bmatrix} 1 \\ 1 \\ 1 \end{bmatrix} = 0, \quad \text{and } v_1 \text{ is independent of } v_2$$

In the no-fault case, where $F=0$ in equation 7, the residual becomes,

$$\tau(k) = V \begin{bmatrix} y_1(k) \\ y_2(k) \\ y_3(k) \end{bmatrix} = V \begin{bmatrix} \xi_1(k) \\ \xi_2(k) \\ \xi_3(k) \end{bmatrix} = \begin{bmatrix} \tau_1(k) \\ \tau_2(k) \end{bmatrix} \quad (12)$$



in this case the expected value of the residuals is equal to,

$$E [\tau(k) \tau^T(k)] = E [V \Xi(k) \Xi^T(k) V^T] = V R V^T \quad (13)$$

where R is the covariance vector of $\Xi(k)$. In here one more parameter, Γ , can be introduced as,

$$E [\tau(k) \tau^T(k)] = V R V^T = \Gamma^T \Gamma \quad (14)$$

If one transforms the residuals, the normalized residuals are equal to,

$$\tilde{\tau}(k) = (VRV^T)^{-1/2} \tau(k)$$

$$\tilde{\tau}(k) = (VRV^T)^{-1/2} V \begin{bmatrix} y_1(k) \\ y_2(k) \\ y_3(k) \end{bmatrix} \quad (15)$$

Again in the non-faulty case the expected value of $\tilde{\tau}(k)$ is equal to,

$$E [\tilde{\tau}(k) \tilde{\tau}^T(k)] = \Gamma^{-T} E [\tau(k) \tau^T(k)] \Gamma^{-1} \quad (16)$$

Inserting equation 14 into equation 16, the expected value of $\tilde{\tau}(k)$ in the non-faulty case becomes,

$$E [E[\tilde{\tau}(k) \tilde{\tau}^T(k)]] = I = I \quad (17)$$

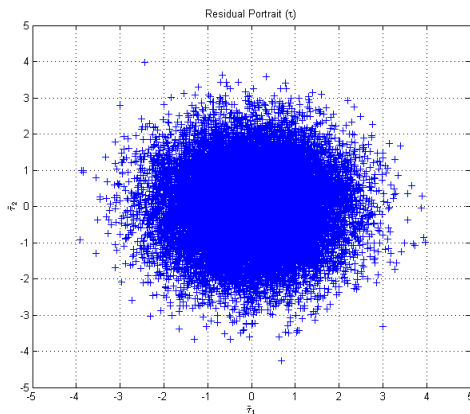


Fig. 2: The residual portrait in non-faulty case

where I is the identity matrix of proper size. As a result the plot of the residuals in non-faulty case would be as in figure 2. It can be easily seen that the realizations of the residual samples lie within in a disc.

Now consider that there is a fault in one of the sensors. The residual equation becomes,

$$\tau(k) = V \begin{bmatrix} \xi_1(k) \\ \xi_2(k) \\ \xi_3(k) \end{bmatrix} + V \begin{bmatrix} f_1(k) \\ f_2(k) \\ f_3(k) \end{bmatrix} = \begin{bmatrix} \tau_1(k) \\ \tau_2(k) \end{bmatrix} \quad (18)$$

Letting $V_{\bullet 1}$, $V_{\bullet 2}$ and $V_{\bullet 3}$ denote the three columns of matrix V , the residual equation can be written as follows when F is non-zero

$$\tau(k) = V \begin{bmatrix} \xi_1(k) \\ \xi_2(k) \\ \xi_3(k) \end{bmatrix} + V_{\bullet 1} f_1 + V_{\bullet 2} f_2 + V_{\bullet 3} f_3 \quad (19)$$

Thus if only the i^{th} sensor has a fault, the residuals are located in the direction vector $V_{\bullet i}$, instead of locating in the center (Fig. 3).

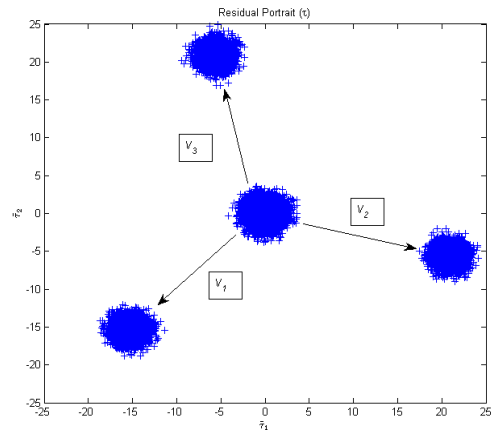


Fig. 3: The residual portrait in faulty case

3.2. Detection

In order to detect faults in the redundant sensor system, a statistical approach is used. Consider that initially a test of hypotheses is introduced as

$$H_0: E[\tilde{\tau}(k)] = 0$$

$$H_1: E[\tilde{r}(k)] \neq 0$$

Acceptance of the hypothesis depends on the second degree chi-square test as

$$\chi^2(2) = \tilde{r}_1^2 + \tilde{r}_2^2 = \gamma \quad (20)$$

The chi-square test is based on the look-up table giving the threshold h corresponding to the false alarm probability α as

$$\Pr(\gamma \leq h) = 1 - \alpha \quad (21)$$

In order to detect faults, the χ^2 random variable γ is compared to h . If γ is equal or smaller than that value, this results of a acceptance of H_0 , contrary to this if γ is bigger than h , this results in the acceptance of H_1 . It should be noted that these evaluation includes a false alarm probability, that is α .

3.3. Isolation

As mentioned in previous sections, if there is a single fault in the system and the χ^2 test leads to hypothesis H_1 , the residual vector is located in the direction of corresponding vector $V_{\bullet i}$, $i=1, 2, 3$ up to the disturbance due to the noise. By checking the angle between residual vector and the column vectors of vector V , the origin of the fault can be indicated.

$$\mathcal{G}_i \approx \left\| \frac{\tilde{r}}{\|\tilde{r}\|} - \frac{\mu_i}{\|\mu_i\|} \right\| \quad (22)$$

where $\mu_i = (VRV)^{-1/2} V_{\bullet i}$.

Mainly if the angle \mathcal{G} between the direction of the residual and μ_i is minimal, one decides that the more likely fault is affecting the sensor i .

4. Simulations

Simulations were performed by using Simulink. The Simulink model of FDI system is shown in figure 4. In the implementation of the FDI system, the significant parameters that are used as follows; the mean speed of the wind is taken as 16 m/s, the turbulence intensity is set to

15%, the simulation time and sampling time are equal to 600 sec and 0.025 sec, respectively.

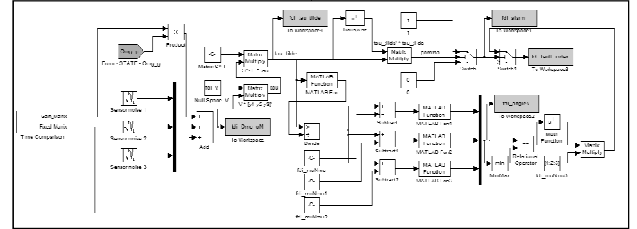


Fig. 4: Simulink model of FDI system

In the absence of fault, the sensor system with 3 different sensors gives the measurement of angular speed of the generator shaft as shown in the figure 5.

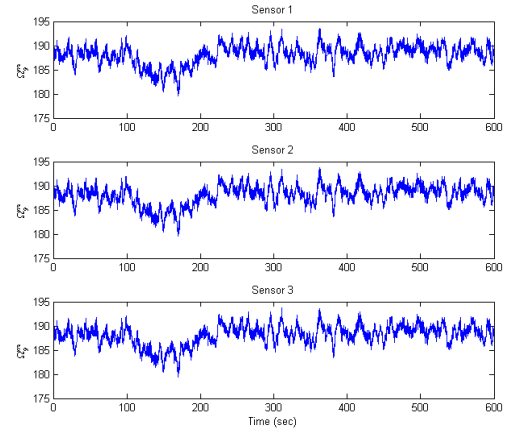


Fig. 5: Sensor measurements in absence of fault

4.1. Types of faults

In this study, two kinds of faults are considered, fixed value (a bias) and gain factor faults. These faults are assumed to affect the redundant sensor system which measures the angular speed of the generator shaft. In general, the measurements are acquired using encoders, thus the faults can be due to both electrical and mechanical faults. However this issue is not the concern of this study. Various fault types, in different appearance time can be constructed in the simulations. Two examples of implementation of FDI system are shown below. Figures 6 and 7 correspond to a fault in sensor 2, between the 200 and 300 seconds with a fixed value of 1% of the nominal wind speed value. Meanwhile, figures 8 and 9 correspond to a fault of 1% in the gain factor in sensor 1 which occurs between 350 and 500 seconds. Addition to these, the false alarm probability α was specified in advance as 1% where the resulting false alarms in the simulations were computed as 0.8% and 0.74% respectively.

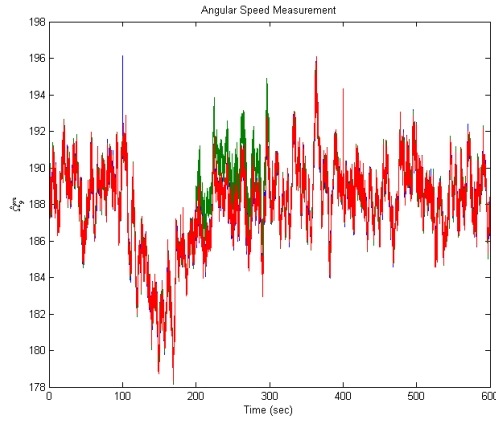


Fig. 6: Sensor measurements with fixed fault in sensor two between 200-300 sec

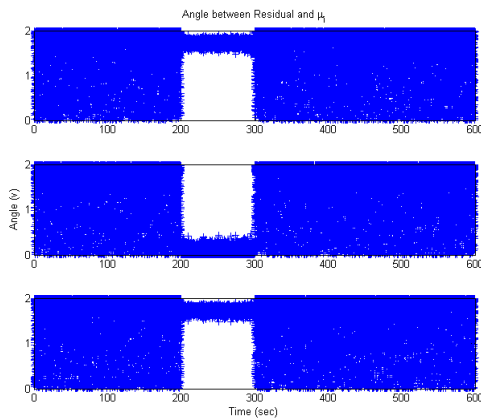


Fig. 7: Angle between residual and corresponding μ_i

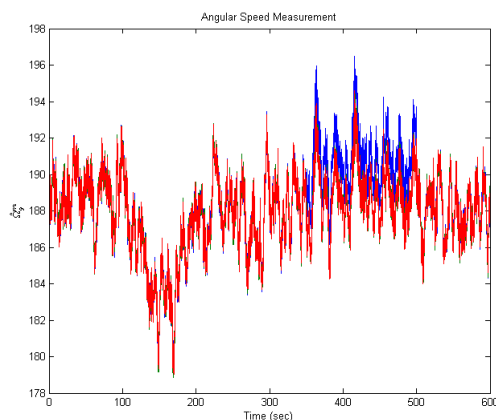


Fig. 8: Sensor measurements with gain type fault in sensor one between 350-500 sec

As can be seen from the figures, the angle between the residual and the corresponding μ_i is minimum in comparison with the others during the fault occurrence. In figure 7, throughout the fault duration, the angle of the second sensor remains smallest. Besides this, in absence of fault, there is no clear difference observed between the angles. Similarly, in figure 9, except during the fault occurrence, there is no obvious difference between the angles. Thus, it can be indicated that the FDI system successively achieve to detect and isolate the given faults.

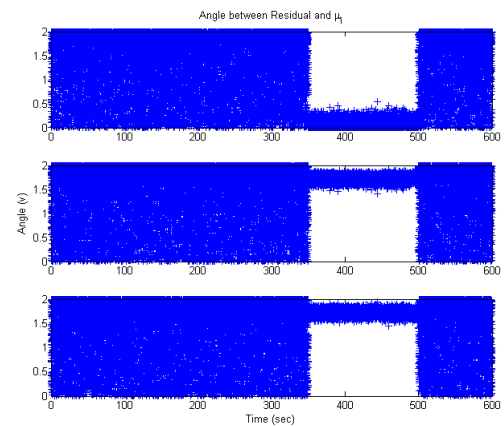


Fig. 9: Angle between residual and corresponding μ_i

5. Conclusions

The major purpose of this study is to create a system that detects sensor faults in a redundant sensor system on a wind turbine with doubly-fed induction generator (DFIG). In this manner, using previously completed wind turbine model, a statistical approach based FDI system was introduced. The mechanical system of wind turbine with DFIG was taken into consideration for simulations performed in Simulink. In a redundant sensor system with three sensors that are measuring the speed of the generator shaft, two kinds of faults were created, i.e. fixed type (bias like) and gain type faults. In the simulations, the generated residuals were controlled using a statistical approach. A chi-square hypothesis test was performed to achieve the fault detection, and angle comparison was taken into account for isolation. The designed system achieves fault detection and isolation with a prespecified false alarm probability. The latter can be decreased by considering residual samples over a finite time window, but the resulting detection delay will increase. Combining this FDI system with a software sensor is a possible extension of this work.



Acknowledgement

The author gratefully acknowledges Fonds de la Recherche Scientifique (FNRS) grant 2.4.553.08 FRFC that supported this work. Also, the author would like thank to M. Galvez Carrilo, for his support, and especially thank to Prof. Michel Kinnaert for making this study possible.

References

- [1]. X. Wei, M. Verhaegen, T. van der Engelen, *Sensor Fault Diagnosis of Wind Turbines for Fault Tolerant*, Proc. 17th World Congress, IFAC, Seoul, Korea, July 6-11, 2008, pages 3222-3227.
- [2]. P.F. Odgaard, J. Stoustrup, *Unknown Input Observer Based Scheme for Detecting Faults in a Wind Turbine Converter*, Proc. 7th IFAC SAFEPROCESS, Barcelona, Spain, June 30- July 03 2009.
- [3]. S. Donders, *Fault Detection and Identification for Wind Turbine Systems: A closed-loop analysis*, Master's Thesis, University of Twente, 2002.
- [4]. K. Rothenhagen, F.W. Fuchs, *Advanced Sensor Fault Detection and Control Reconfiguration of Wind Power Plants using Doubly Fed Induction Generators*, IEEE Power Electronics Specialists Conference, Rhodes, June 15-19, 2008, pages 913-919.
- [5]. K. Rothenhagen, F.W. Fuchs, *Current Sensor Fault Detection and Reconfiguration for a Doubly Fed Induction Generator*, IEEE Power Electronics Specialists Conference, Orlando, FL, June 17-21, 2007, pages 2732-2738.
- [6]. M. Galvez Carrilo, *Wind Turbine Modeling, Linear Models for Multivariable Control*, Internal Report for ARC Project, 2008.
- [7]. M. Kinnaert, *Fault diagnosis based on analytical models for linear and nonlinear systems - A tutorial*, Proc. 5th IFAC SAFEPROCESS, Washington, USA, June 9-11, 2003, pages 37-50.



Session 3:

Mechatronics (Mc)

Robotics (Rb)



Proceedings of the International Symposium of Mechanism and Machine Science, 2010
AzCIFTtoMM – Izmir Institute of Technology
5-8 October 2010, Izmir, TURKEY



Dexterity of a Welding Industrial Robot

Karl GOTLIH^{1*}, Tomaž VUHERER², Denis KOVAČ³, Andrejka ZVER², Simon BREZOVNIK²

^{1*}University of Maribor, Faculty of Mechanical Engineering,
Smetanova 17, SI-2000 Maribor, Slovenia
gotlih@uni-mb.si

²University of Maribor, Faculty of Mechanical Engineering,
Smetanova 17, SI-2000 Maribor, Slovenia

³Varstroj d.d.,
Industrijska ulica 4, SI-9220 Lendava

Abstract

Industrial robots are part of production systems and it is important to place them into the system according to their properties - behaviour and requirements. The information, obtained from the technical sheets of robots, about workspace (its dimensions and shape) is insufficient for designing the production system. The information about dexterity is missing. To represent the behaviour of the robot in the workspace, velocity anisotropy of the robot is introduced and defined as the normalised length of the shortest velocity ellipsoid axes which can be constructed in the tool centre point for any position of robot. A graphical representation of the 3D workspace with included velocity anisotropy is then performed and an example for a design of a robotised welding production system is given. In this example the benefits of the graphical representation of the workspace with included velocity anisotropy are presented and discussed.

Keywords: robot, workspace, velocity anisotropy

1. Introduction

Robots are used in variety of industrial applications. The use of robots is dictated from the market requirements and the competitiveness between producers in different branches. The majority of industrial robots are used in the motor vehicles industry, followed by the production of automotive parts, [1]. And most of them are used for welding operations. The introduction of robotised welding systems is important particularly when the technological and quality requirements on the product are higher than it can be done with conventional or manual welding methods. The robotisation of production systems is not important just for the humanisation of the working process but also for increasing the quality and the continuity of products in particular welding and the decreasing of production costs. The welding robot is almost an

indispensable part of the production chain where pretentious structures are welded. This is possible because of the wide selection of industrial robots in the world's market. Especially for welding operations new robotic structures, welding equipment and peripheral devices are designed. The peripheral devices increase the applicability of welding robots for different welding technologies. But only the use of high quality robots and equipment cannot guarantee top-level quality of the products if the technological set-up of the robotised technological system is not optimal. The proper design of robotised technological systems is therefore very important for high quality realization of the technological processes and because of this, high quality products [2].

In the literature we can find some contributions where authors try to show the manipulability distribution in the workspace of the robot. Zacharias, Borst and Hirzinger [3] show the use of capability maps. Using this map, a manipulator is able to deduce places that are easy to reach. Ottaviano, Ceccarelli and Husty [4] use mathematical analysis to characterize workspace topologies of 3R manipulators. Industrial 3R manipulators are classified as functions of workspace kinematic properties. The manipulability is a very often discussed property of manipulators. In the literature we can find a lot of interesting papers which deal with this problem, so Lee [5-6] introduces in his work polytopes instead of velocity ellipsoids. The ellipsoid always inscribed into the polytope, and Doty [7] demonstrates some fundamental problems with dexterity measures. A new algorithm for measuring and optimizing the manipulability index is shown in [8].

The aim of the present paper is to show the development and the 3D representation of the velocity anisotropy of the industrial robot in the workspace. The anisotropy measure is defined with the so-called

“Condition number” which is the quotient between the length of the shortest and the longest velocity ellipsoid axes for the defined point in the workspace.

The development is shown on the example of a real industrial robot which is specially designed for spot and MAG (Metal Arc Gas) welding applications. The graphic representation of the 3D workspace with included velocity anisotropy field is generated with an auxiliary software package on the basis of Autocad Mechanical Desktop [9]. The graphical presentation enables the visualization of the velocity anisotropy in a three dimensional space and it is specially designed for the use with production system design software. The presented approach can be also used for creating 3D maps for families of industrial robots which differ in dimensions or even in the structure. These maps can be integrated into CAD programs for designing robotised production systems and for off-line programming purposes of industrial robots and simulations.

2. Trajectories in the workspace

The TCP trajectories of industrial robots can be divided into two main groups:

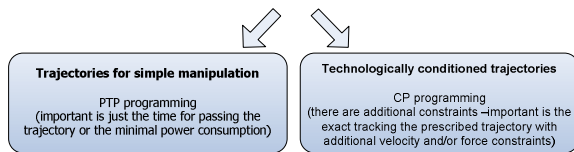


Fig. 1: Trajectories for simple manipulation / technologically conditioned trajectories (PTP – point to point, CP continuous path)

In this work we are interested in technologically conditioned trajectories, where not just the correct passing through is important, but also the velocity profile on it, Fig. 1.

The parameter for determining the velocity anisotropy in each point in the robot’s workspace depends on the momentary robot’s position in the space. To overcome the difficulties which result from the description of the position and the orientation of the TCP [10-12] and because the transmission of kinematic and kinetic quantities from the actuators to the TCP depends in general on the first three “positional” degrees of freedom, the wrist degrees of freedom which are responsible for the orientation of the TCP are not taken into consideration.

3. Manipulability of the mechanism

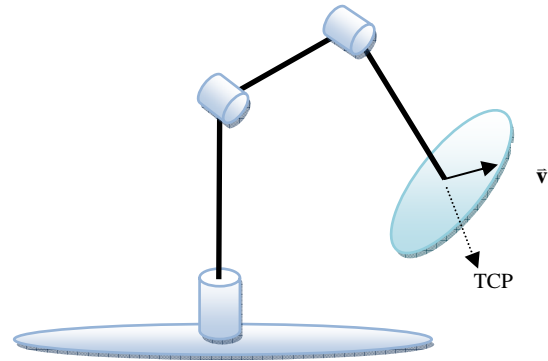


Fig. 2 : Manipulability and the velocity ellipsoid

In all positions in the workspace the robot has not got equal dexterity. The transmission of motions, from each actuator to the TCP, will not guarantee equal velocities of the TCP in all points in the space, Fig. 2. The TCP point on the robot is identical with the point in the workspace. For each point in the workspace we can find a position of the robot mechanism and to this position the corresponding manipulability.

The velocities which the robot’s TCP can produce in an arbitrary point of the workspace are different not just from point to point in the workspace, but also differ in different directions in a point. So the velocity is anisotropic in robot’s workspace. This can be clear represented with a velocity ellipsoid [10-11]. The velocity ellipsoid in the workspace of the robot can be constructed in the TCP as the result of transformation of velocity hyper-sphere from configuration space into an ellipsoid in the task space, Fig. 3.

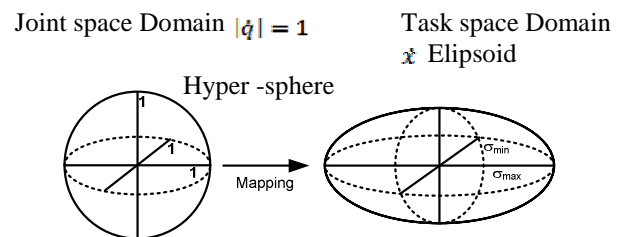


Fig. 3: Hyper-sphere / Velocity ellipsoid

The lengths of the axes of the ellipsoid are proportional to the singular values of J . Singular values of the Jacobian matrix are calculated for each robot position numerically. Singular values of matrix J , if the matrix is regular, corresponds with the eigenvalues of the matrix [10-11] with

$$\sigma_i = \sqrt{\lambda_i} \quad , \quad i = 1, 2, \dots, m \quad (1)$$

The number of non-zero singular values σ_i of the matrix defines the range of the Jacobian matrix. If just one singular value is zero, the Jacobian matrix is singular and the mechanism is in a singular position. The product of singular values defines the volume of the velocity ellipsoid and through this the manipulability index of the serial mechanism.

$$M = \sigma_1 \sigma_2 \dots \sigma_m \quad (2)$$

The relation between the minimal and the maximal singular value is the “condition number”

$$K = \frac{\sigma_{\min}}{\sigma_{\max}} \quad (3)$$

it is a normalized quantity which defines the roundness of the velocity ellipsoid. The ellipsoid is close to a sphere when K is near to 1 and flat, when K is near to zero. If $K=0$, the Jacobian matrix is singular, and if $K=1$ it is far from a singular position, the mechanism is in a velocity isotropic position.

4. Industrial robot IR

For calculation of the condition number we need the robot’s kinematic structure and its geometrical data. From the structure and the geometrical data the Jacobian matrix can be calculated in symbolic form. The eigenvalues are then calculated numerically. If the matrix is regular, the eigenvalues represent the lengths of all three axes of the velocity ellipsoid and therefore our parameter of velocity anisotropy is given according to (3).

5. Example of the OTC AX-V4 IR

The robot AX-V4 is one from the new generation of OTC [13] robots specially designed for MAG arc welding purposes. The speciality of this robot structure is a hollow arm, which is used to carry through the required installations and so enables better flexibility for welding because no wires and pipes are installed outside the robot structure. The payload of the robot is 4 kg and in fig.4 two layouts of the workspace are given. Both are from the data sheets of the robot.

With the introduced procedure for developing the workspace with included parameter of velocity anisotropy we get fig.5, where isometric projection of the workspace is given. Additional to this isometric projection two cross

sections in the x-y and x-z direction through the robots base coordinate origin are shown in fig.6 and fig.7.

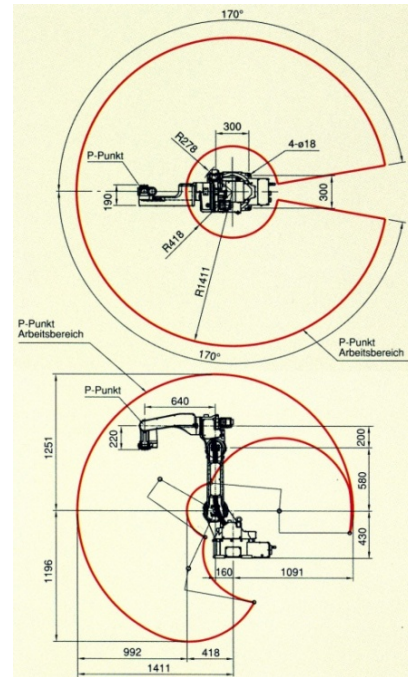


Fig. 4: Layouts of the workspace

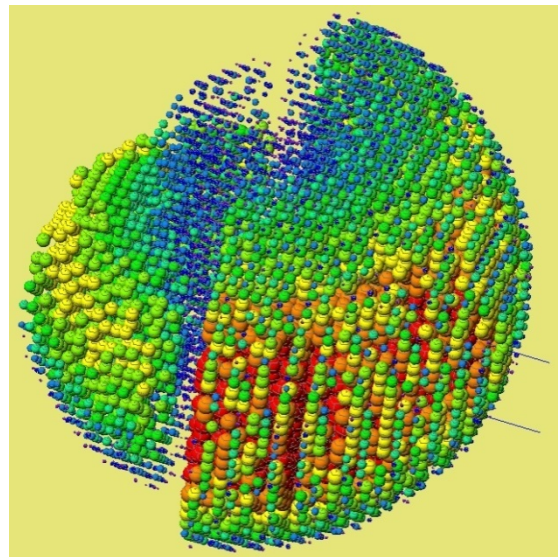


Fig. 5. Isometric projection of the workspace

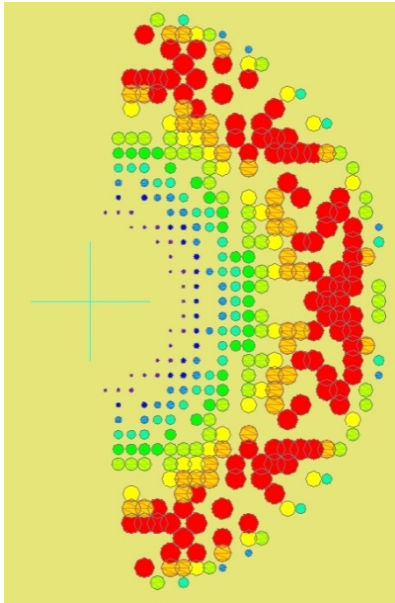


Fig. 6. X-Y cross section of the workspace

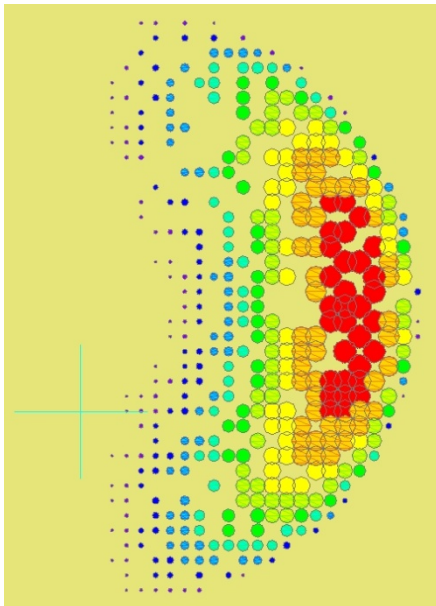
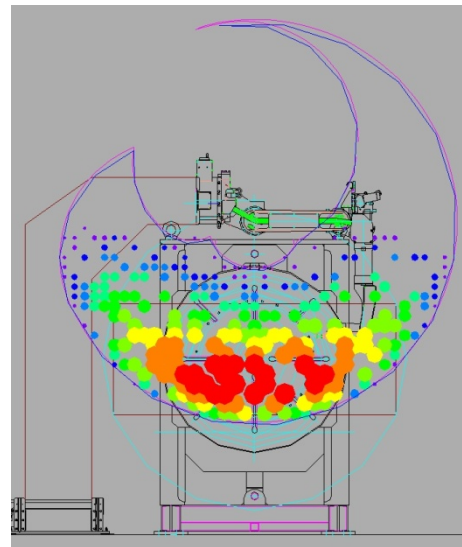


Fig. 7. X-Z cross section of the workspace

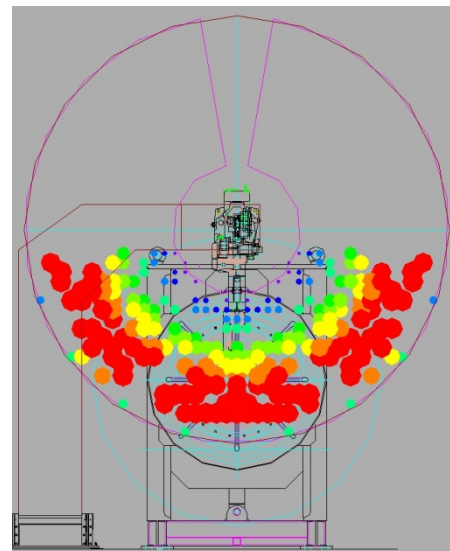
6. Discussion and conclusions

The graphical presentation of velocity anisotropy in fig. 5-7 is very useful for designing robotic systems for welding operations. Two shown layouts (fig. 6 and fig. 7) can be perfectly used for embedding the welded part into the workspace when the welds are positioned on the edges of the part. In fig. 8a the welded part is set into the

workspace perpendicularly to the robot. The robot can move parallel to the part. The area of high manipulability is too small according to the dimensions of the part and the robot cannot completely cover it with sufficiently high manipulability. If we rotate the robot's axes for 90° , fig. 8b, so that the robot is parallel to the welded part, then the workspace area of higher manipulability covers the welded part much better and we can expect better quality of welding on it.



a



b

Fig. 8. Production system for arc spot and MAG welding



In the preset paper a procedure for analyzing and 3D representation of robot's workspace is given. Additionally a parameter for velocity anisotropy in each point of the workspace is introduced. The velocity anisotropy is defined with the condition number.

To show the benefits of the presented procedure a realized robotised production system for MAG welding is presented in fig. 8a and b. In given figures it is clearly shown that the correct positioning of the work part can guarantee better covering of all welding operations on the part (fig. 8b). The benefit of the introduced graphical representation of the anisotropy is the recognition of difficulties with welding in the edges of the part during the design of the robotic system. The position of the robot could be displaced before the production system is finished and put into work.

From the designer's point of view the visualization of the velocity anisotropy is an important and useful tool, because it gives the possibility of over-viewing the robot's behaviour in the production system in the phase of designing and virtual simulations before the system is really produced.

The introduced tool helps the designer of production systems with additional data, which are not available from the producer's data sheets. With the given tool it becomes possible to avoid difficulties which appear when the robot is not properly positioned into the production system.

Today it is impossible to think about design without software tools which do not support 3D representation. The presentation of the velocity anisotropy of the robot's workspace is in 3D with the possibility of making arbitrary cross sections through it to get better insight into the behaviour of the velocity anisotropy inside the workspace.

References

- [1] Web, <http://www.ifr.org/industrial-robots/statistics/>
- [2] D. Botturi, S. Martelli, P. Fiorini, *A Geometric Method for Robot Workspace Computation*, Proceedings of "International Conference on Autonomous Robots and System (ICAR)", 2003.
- [3] F. Zacharias, C. Borst, G. Hirzinger, *Capturing Robot Workspace Structure: Representing Robot Capabilities*, Proceedings of the 2007 IEEE/RSJ International Conference on Intelligent Robots and Systems, San Diego, CA, USA, 2007.
- [4] E. Ottaviano, M. Ceccarelli, M. Husty, *Workspace Topologies of Industrial 3R Manipulators*, International Journal of Advanced Robotic Systems, Vol. 5, No. 2, 2008.
- [5] J. Lee, *A Study on the Manipulability Measures for Robot Manipulators*, Proceedings of the IROS, 1997.
- [6] J. Lee, *Velocity workspace analysis for multiple arm robot systems*, Robotica, Vol. 19, 2001.
- [7] K. L. Doty, C. Melchiorri, E. M. Schwartz, C. Bonivento, *Robot Manipulability*, IEEE Transactions on Robotics and Automata, Vol. 11, No. 3, 1995.
- [8] A.Y. Elkady, M. Mohammed, T. Sobh, *A New Algorithm for Measuring and Optimizing the Manipulability Index*, J. Intelligent Robot Systems, Springer, 2009.
- [9] Autodesk Inventor Suite 2008 EE License, 52712-091462-9540, C4645079, 2008.
- [10] T. Yoshikawa, *Manipulability of robotic mechanisms*, The Int. J. Robotics Res., 4, No. 2, pp. 3-9, 1985.
- [11] J. Angeles, *Fundamentals of robotic mechanical systems: theory, methods, and algorithms*, 2nd ed., New York, Springer, cop. 2003.
- [12] D. Kovač, *Hitrostna anizotropija delovnih prostorov industrijskih robotov*, University of Maribor, Faculty of Mech. Engineering, Master degree Thesis, 2008.
- [13] Almega AX Series, Daihen Corporation, CAT.NO.R20503, Osaka 566-0021, 2006.

Design, Kinematic Solution and Control of a 3-PUU Translational Parallel Manipulator

Erol UYAR^{1*}, Lyutvi Yusein YUMER¹, İsmet ATEŞ¹

^{1*} Dokuz Eylül Üniversitesi Mekatronik Mühendisliği
Fen Bilimleri Enstitüsü, Bornova, 35100, İZMİR
erol.uyar@deu.edu.tr, lutfi@live.com, iismetates@gmail.com

Abstract

In this paper mechanical design, and kinematic solution of a 3-PUU translational parallel manipulator (TPM) with its position control, is presented. A SolidWorks based design and simulation is used for further analysis and a MATLAB based iterative algorithm for the forward and inverse kinematics solutions is developed. The inverse kinematic solutions of limbs, which are activated through screw rails driven by encoded DC motors, are then used to control the end effector position.

After the general mechanical design of the manipulator all parts are drawn and modelled in SolidWorks, and a simulation of the motion in three dimensional space is made. For the kinematic analysis relevant equations are derived from the geometrical vector relations, which are then solved with MATLAB iteration. The calculated results of kinematic solutions by using MATLAB iteration are then compared with the SolidWorks simulation model.

Finally the accuracy of position control is tested with the calculated values and very satisfactory results are obtained.

Keywords: kinematics, manipulator, workspace, control, simulation

1. Introduction

In recent years parallel mechanical manipulators have become very popular in various industrial applications. Their main advantages can be expressed as high accuracy, velocity, stiffness, and load carrying capability. Compared with their serial counterparts, parallel manipulators suffer a main disadvantage of relatively small workspace [15].

Parallel manipulators with less than six DOF, which maintain the inherent advantages of parallel mechanisms [16] and possess several other advantages such as reduction of the total cost of the device in manufactures and operations, are attracting attentions of various researchers.

A parallel manipulator typically consists of a moving platform that is connected to a fixed base by several

kinematic chains in parallel [5]. Rather exhaustive and versatile applications of parallel robots are described in [14, 4]. Many 3-DOF parallel manipulators have been designed and investigated for relevant applications, such as the famous DELTA robot with three translational DOF [2, 3] whose concept then has been realized in many different configurations [11, 15].

Y-Star like and Orthoglide parallel robots with pure translational motions [1, 8], spherical 3-DOF manipulators with pure rotational DOF [6,7,10,11,13] and 3-RPS and 3-PRS parallel mechanisms with combined translational and rotary motions [9, 12] etc.

Among them, translational parallel manipulators (TPMs) have potential wide applications (as seen in Fig.1 and Fig.2), where a pure translational motion is needed in cases of a motion simulator, a positioning tool of an assembly line and others.



Fig. 1: Tripod manipulator



Fig. 2: Application in food industry

2. General Description of TPM

A parallel manipulator is a closed-loop kinematic chain mechanism whose end effector is linked to the base by several independent kinematic chains a parallel manipulator, also called a parallel robot, consists of a fixed "base" platform, connected to an end effector platform by means of a number of "limbs". These limbs (legs) often consist of an actuated prismatic joint, connected to the platforms through passive (i.e. not actuated) spherical and/or universal joints. The actuators for the prismatic joints can be placed in the motionless base platform, so that their mass does not have to be moved, which makes the construction lighter. Parallel manipulators have generally high structural stiffness, since the end effectors are supported in several places at the same time. All these features result in manipulators with a wide range of motion capability

The schematic diagram of TPM is represented in Figure 3. It consists of a moving platform, a fixed base, and three limbs of identical kinematic structure. Each limb connects the fixed base to the moving platform by a prismatic (P) joint followed by two universal (U) joints in sequence, where the P joint is driven by a linear actuator. (In our designed model they are screwed rails)

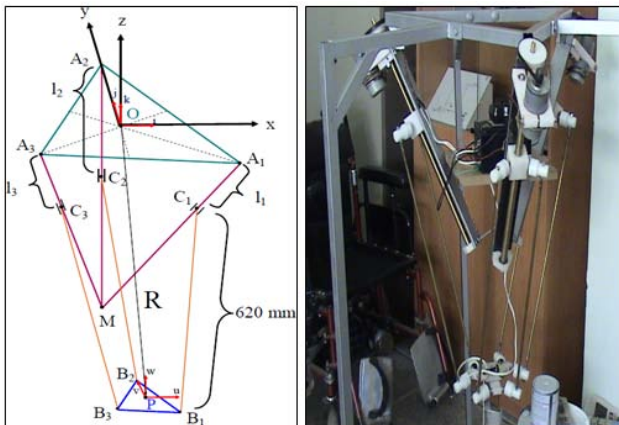


Fig. 3: Schematic of a general 3-PUU TPM

Since each U joint consists of two intersecting revolute joints, each limb is kinematically equivalent to a PRRRR chain. It is shown that in order to keep the moving platform from changing its orientation, it is sufficient for the four revolute joint axes within the same limb to satisfy some certain geometric conditions [3, 20]. That is, the first revolute joint axis is parallel to the last revolute joint axis; the two intermediate joint axes are parallel to one another. Since the geometric conditions stated above do not require the U joint axes to intersect at a point, any 3-PRRRR parallel manipulator whose revolute joint axes satisfy the above conditions will result in a manipulator with a pure translational motion.

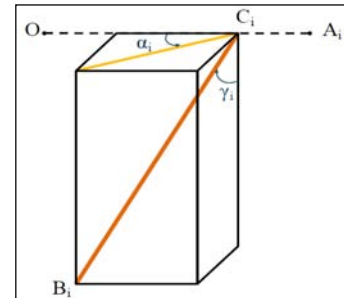


Fig. 4: Schematic of limb angles

Some parts of the manipulator, which are designed in SolidWorks are shown in Fig.5. These drawings are then used to evaluate the general assembling and motion simulation of the manipulator.

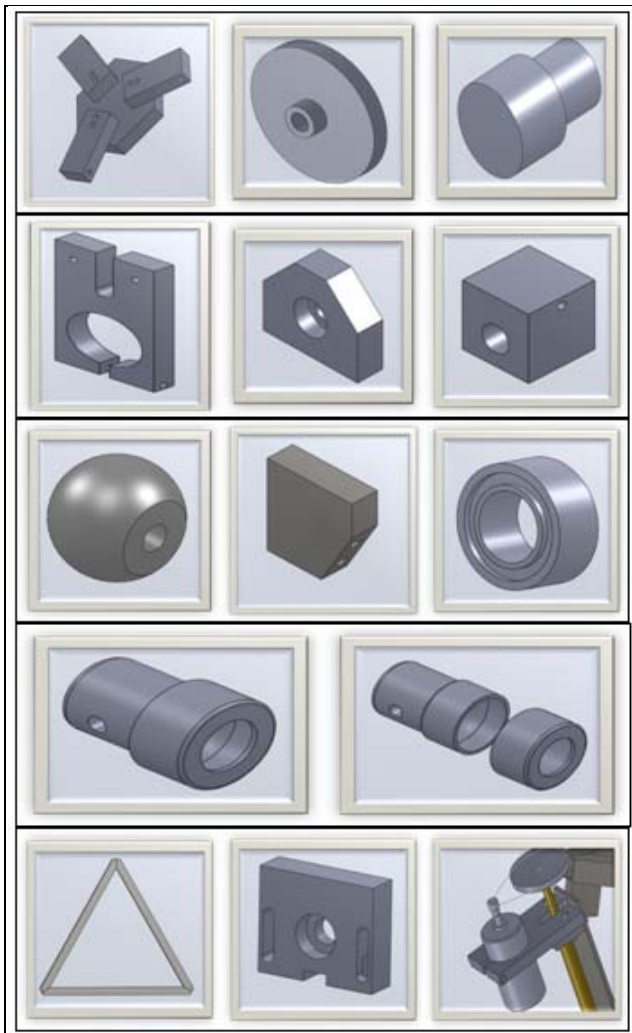


Fig. 5: SolidWorks design of parts

For the purpose of analysis, as represented in Fig. 3 and Figure 4, a fixed Cartesian coordinate system $O\{x, y, z\}$ is assigned at the centered point O of the fixed base platform A_1, A_2, A_3 and a moving Cartesian frame $P\{u, v, w\}$ at the centered point P of triangle B_1, B_2 and B_3 on the moving platform.

During the motion the moving platform keep its parallelism to base platform. In Fig. 4 one of the kinematic chains of TPM is shown.

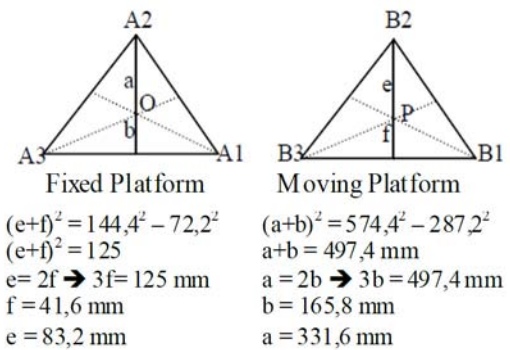
The one ends of screwed rails are connected to the fixed platform with a lay out angle of 60 degrees and intersect the x - y plane at points A_1, A_2 , and A_3 . The intersected ends are fixed with each other at the point M . The three limbs $C_i B_i$ ($i = 1, 2, 3$) with the length of l intersect the u - v plane at points B_1, B_2 and B_3 .

Angle γ_i is measured from the z -axis to limb vector $C_i B_i$, and angle α_i is measured from the limb projection on base frame with OA_i vector.

The sizes of Fixed and moving platforms in form of equilateral triangles and following measured datas are given as main construction parameters below;

Table 1: Rail and Screw sizes

Table 1	Rail and Screw Sizes
The length of rail	$l = 600$ mm
The length of screw	$l_s = 490$ mm
Screw diameter	$D = 50$ mm
Pitch of screw	$p = 6$ mm
Speed of screw	$n = 740$ rpm



3. Vector Analysis

An analytic method referring to Figure 3, by using a vector-loop equation can be applied to solve the nonlinear kinematic relations. For this purpose the vectorial relations according to the predefined coordinate frames are used. The position vectors of points A_i and B_i with respect to frames O and P can be written as below:

For the i -th limb following vector - loop equations:

$$OP = OA_i + A_i C_i + C_i B_i + B_i P \quad (1)$$

So as first vector equation, $OP = OA_1 + A_1 C_1 + C_1 B_1 + B_1 P$ and followings can be written from the geometry of Fig. 3:

$$\begin{aligned} OA_1 &= +331.6 \cdot \cos(30)i - 331.6 \cdot \sin(30)j \\ A_1 C_1 &= -l_1 \cdot \cos(60) \cdot \cos(30)i + l_1 \cdot \cos(60) \cdot \sin(30)j \\ &\quad - l_1 \cdot \sin(60)k \\ C_1 B_1 &= -620 \cdot \sin(\gamma_1) \cdot \cos(30 + \alpha_1)i + 620 \cdot \sin(\gamma_1) \cdot \sin(30 + \alpha_1)j \\ &\quad - 620 \cdot \cos(\gamma_1)k \\ B_1 P &= -83.2 \cdot \cos(30)i + 83.2 \cdot \sin(30)j \\ OP &= +x \cdot i + y \cdot j + z \cdot k \end{aligned}$$

where i, j and k represents the relevant unit vectors in directions x, y and z . The limb rates are expressed as l_1, l_2 and l_3 and relevant angles α_i and γ_i are shown in Fig.5



$$\begin{aligned} i &\rightarrow 331.6 \cdot \cos(30) - l_1 \cdot \cos(60) \cdot \cos(30) - 620 \cdot \sin(\gamma_1) \cdot \cos(30 + \alpha_1) - 83.2 \cdot \cos(30) - x = 0 \\ j &\rightarrow -331.6 \cdot \sin(30) + l_1 \cdot \cos(60) \cdot \sin(30) + 620 \cdot \sin(\gamma_1) \cdot \sin(30 + \alpha_1) + 83.2 \cdot \sin(30) - y = 0 \\ k &\rightarrow -l_1 \cdot \sin(60) - 620 \cdot \cos(\gamma_1) - z = 0 \end{aligned}$$

As second vector equation $OP = OA_2 + A_2C_2 + C_2B_2 + B_2P$ and following statements:

$$\begin{aligned} OA_2 &= +331.6j \\ A_2C_2 &= -l_2 \cdot \cos(60)j - l_2 \cdot \sin(60)k \\ C_2B_2 &= -620 \cdot \sin(\gamma_2) \cdot \cos(\alpha_2)i - 620 \cdot \sin(\gamma_2) \cdot \sin(\alpha_2)j - 620 \cdot \cos(\gamma_2)k \\ B_2P &= -83.2j \\ OP &= +x \cdot i + y \cdot j + z \cdot k \end{aligned}$$

$$\begin{aligned} i &\rightarrow -620 \cdot \sin(\gamma_2) \cdot \cos(\alpha_2) - x = 0 \\ j &\rightarrow -331.6 + l_2 \cdot \cos(60) + 620 \cdot \sin(\gamma_2) \cdot \sin(\alpha_2) + 83.2 + y = 0 \\ k &\rightarrow -l_2 \cdot \sin(60) - 620 \cdot \cos(\gamma_2) - z = 0 \end{aligned}$$

As last vector equation $OP = OA_3 + A_3C_3 + C_3B_3 + B_3P$ and following statements:

$$\begin{aligned} OA_3 &= -331.6 \cdot \cos(30)i - 331.6 \cdot \sin(30)j \\ A_3C_3 &= +l_3 \cdot \cos(60) \cdot \cos(30)i + l_3 \cdot \cos(60) \cdot \sin(30)j - l_3 \cdot \sin(60)k \\ C_3B_3 &= +620 \cdot \sin(\gamma_3) \cdot \cos(30 + \alpha_3)i + 620 \cdot \sin(\gamma_3) \cdot \sin(30 + \alpha_3)j - 620 \cdot \cos(\gamma_3)k \\ B_3P &= +83.2 \cdot \cos(30)i + 83.2 \cdot \sin(30)j \\ OP &= +x \cdot i + y \cdot j + z \cdot k \end{aligned}$$

where i , j and k represents the relevant unit vectors in directions x , y and z .

$$\begin{aligned} i &\rightarrow 331.6 \cdot \cos(30) - l_3 \cdot \cos(60) \cdot \cos(30) - 620 \cdot \sin(\gamma_3) \cdot \cos(30 + \alpha_3) - 83.2 \cdot \cos(30) + x = 0 \\ j &\rightarrow -331.6 \cdot \sin(30) + l_3 \cdot \cos(60) \cdot \sin(30) + 620 \cdot \sin(\gamma_3) \cdot \sin(30 + \alpha_3) + 83.2 \cdot \sin(30) - y = 0 \\ k &\rightarrow -l_3 \cdot \sin(60) - 620 \cdot \cos(\gamma_3) - z = 0 \end{aligned}$$

Solving the 9 final nonlinear equations above with iteration in MATLAB, the 9 unknown parameters can be investigated.

4. Kinematic Analysis

The schematic and assembled view of the manipulator is given in Fig.3. A MATLAB iterative method is used to obtain both the forward and inverse the kinematic solutions.

4.1. Inverse Kinematics Solution

Using the non-linear MATLAB Solution Method, limb motion rates (l_1 , l_2 and l_3) can be calculated from given the location (center point coordinates x , y , z) of moving platform as given in the following MATLAB (inverse.m) file:

```
function var=bul(X,Y,Z)
var0=[0,0,0,0,0,0,0,0,0]; %Initial values
var=fsolve(@(var0) myfun(var0, X,Y,Z),var0).';
for i=4:9
var(i)=rad2deg(var(i)); %Convert angles radian to degree
end

function F=myfun(var, X,Y,Z)
l1=var(1); %Length_1
l2=var(2); %Length_2
l3=var(3); %Length_3
g1=var(4); %Gama_1
g2=var(5); %Gama_2
g3=var(6); %Gama_3
a1=var(7); %Alfa_1
a2=var(8); %Alfa_2
a3=var(9); %Alfa_3

f1= +331.6*cos(pi/6) - l1*cos(pi/3)*cos(pi/6)
- 620*sin(g1)*cos(pi/6-a1) - 83.2*cos(pi/6) - X;
f2= -331.6*sin(pi/6) + l1*cos(pi/3)*sin(pi/6)
+ 620*sin(g1)*sin(pi/6-a1) + 83.2*sin(pi/6) - Y;
f3= +568.0646 - l1*sin(pi/3) - 620*cos(g1) - Z;

f4= -620*sin(g2)*sin(a2) + X;
f5= -331.6 + l2*cos(pi/3) + 620*sin(g2)*cos(a2) + 83.2
+ Y;
f6= +568.0646 - l2*sin(pi/3) - 620*cos(g2) - Z;

f7= +331.6*cos(pi/6) - l3*cos(pi/3)*cos(pi/6)
- 620*sin(g3)*cos(pi/6+a3) - 83.2*cos(pi/6) + X;
f8= -331.6*sin(pi/6) + l3*cos(pi/3)*sin(pi/6)
+ 620*sin(g3)*sin(pi/6+a3) + 83.2*sin(pi/6) - Y;
f9= +568.0646 - l3*sin(pi/3) - 620*cos(g3) - Z;

F=[f1;f2;f3;f4;f5;f6;f7;f8;f9]; %Nonlinear Equation Set
```



4.2. Forward Kinematics Solution

Using the same non-linear MATLAB Solution model given above, the location (center point coordinates x, y, z) of moving platform can be calculated from given limb motion rates (l_1 , l_2 and l_3) with following MATLAB (forward.m) file:

```
function var=bul(l1,l2,l3)
var0=[0,0,0,0,0,0,0,0,0]; %Initial values
var=fsolve(@(var0) myfun(var0,l1,l2,l3),var0).';
for i=4:9
var(i)=rad2deg(var(i)); %Convert angles radian to degree
end

function F=myfun(var,l1,l2,l3)
X=var(1); %Gripper Position X
Y=var(2); %Gripper Position Y
Z=var(3); %Gripper Position Z
g1=var(4); %Gama_1
g2=var(5); %Gama_2
g3=var(6); %Gama_3
a1=var(7); %Alfa_1
a2=var(8); %Alfa_2
a3=var(9); %Alfa_3

f1= + 331.6*cos(pi/6) - 11*cos(pi/3)*cos(pi/6)
- 620*sin(g1)*cos(pi/6-a1) - 83.2*cos(pi/6) - X;
f2= - 331.6*sin(pi/6) + 11*cos(pi/3)*sin(pi/6)
+ 620*sin(g1)*sin(pi/6-a1) + 83.2*sin(pi/6) - Y;
f3= + 568.0646 - 11*sin(pi/3) - 620*cos(g1) - Z;

f4= - 620*sin(g2)*sin(a2) + X;
f5= - 331.6 + 12*cos(pi/3) + 620*sin(g2)*cos(a2) + 83.2
+ Y;
f6= + 568.0646 - 12*sin(pi/3) - 620*cos(g2) - Z;

f7= + 331.6*cos(pi/6) - 13*cos(pi/3)*cos(pi/6)
- 620*sin(g3)*cos(pi/6+a3) - 83.2 * cos(pi/6) + X;
f8= -331.6*sin(pi/6) + 13*cos(pi/3)*sin(pi/6)
+ 620*sin(g3)*sin(pi/6+a3) + 83.2*sin(pi/6) - Y;
f9= + 568.0646 - 13*sin(pi/3) - 620*cos(g3) - Z;

F=[f1;f2;f3;f4;f5;f6;f7;f8;f9]; %Nonlinear Equation Set
```

5. Comparison of MATLAB Results with SolidWorks Model

By using the values of SolidWorks animation model in Fig.6, a comparison of the calculated results with iterative method in MATLAB are given in Table 2 for forward kinematics and Table 3 for inverse kinematics.

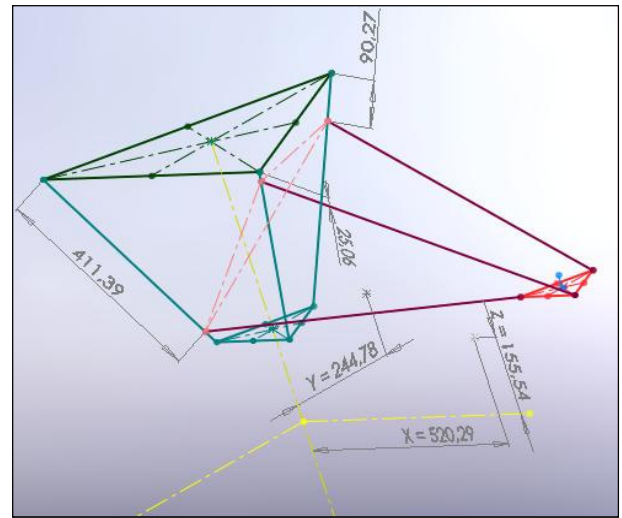


Fig. 6. SolidWorks Animation Model

Table 2::Results for $l_1=25.06$, $l_2=90.27$, $l_3=411.39$

Table 2	Forward Kinematic Example		
	i (mm)	j (mm)	k (mm)
$P_{obtained}(x,y,z)$	520.1605	244.6751	155.0479
$P_{real}(x,y,z)$	520.29	244.78	155.54
Errors	+ 0.13	+ 0.10	+ 0.49

Table 2: Results for $x=520.29$, $y=244.78$, $z=155.54$

Table 3	Inverse Kinematic Example		
	l_1 (mm)	l_2 (mm)	l_3 (mm)
Obtained values	24.6720	89.9244	411.5927
Real values	25.06	90.27	411.39
Errors	+ 0.39	+ 0.35	- 0.20

The top and side views of the investigated workspace by using MATLAB simulation and the real (effective) workspace are given in Fig.7 and Fig.8. With given X, Y, Z coordinates in space, special trajectories and time dependent functions can be simulated in the same way.

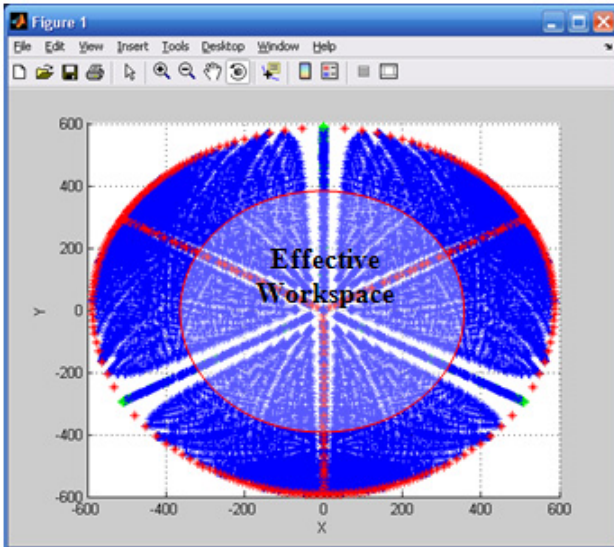


Fig. 7: Top view of theoretical and effective Workspace

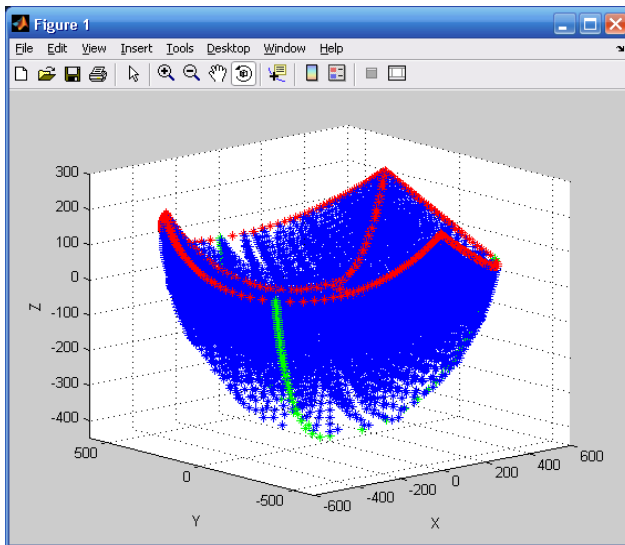


Fig. 8: Side view of Workspace

6. Trajectory Planning

As can be seen from Table 2 the position errors for X, Y and Z values in case of forward kinematics are less than half millimeter. Also inverse kinematics errors are similar to forward kinematics errors as shown in Table 3.

To demonstrate the trajectory following of the manipulator in three dimensional space, a given time dependent trajectory function $F(t)$ as in the following can be used:

$$\begin{aligned} &\text{For } 0 < t < 6\pi \text{ time interval} \\ &F(t) = X(t) \cdot i + Y(t) \cdot j + Z(t) \cdot k \\ &F = [10t \cdot \cos(t)] i + [10t \cdot \sin(t)] j + [10t - 200] k \end{aligned}$$

The time dependent limb values l_i 's can be calculated from X, Y and Z values through iterative method in MATLAB and the manipulator can be let to follow the trajectory in workspace boundary as shown in Fig.9 and Fig.10.

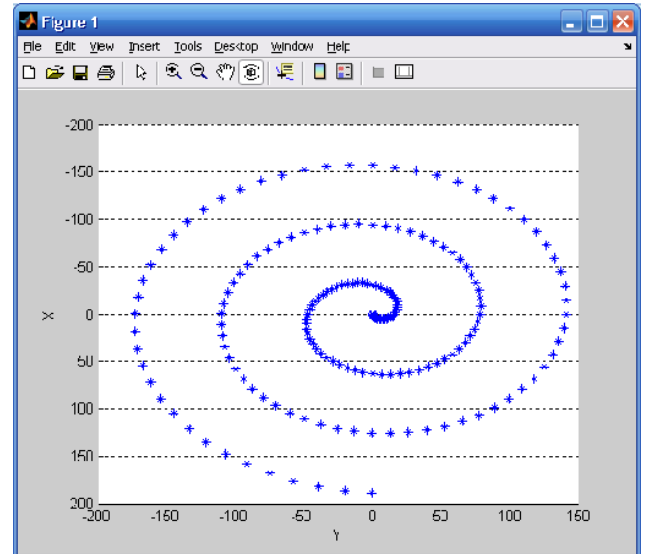


Fig. 9: Trajectory planning (Top view)

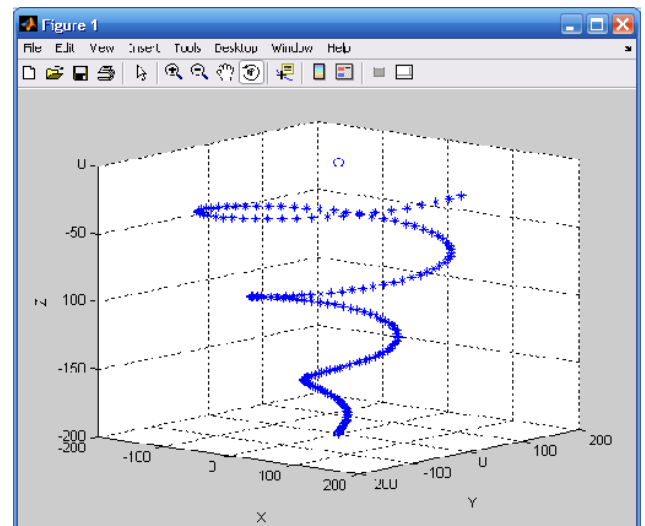


Fig. 10: Trajectory following (3-dimensional)

7. Control of Limbs

To control the limb motions screwed rails which are driven by encoded DC motors as seen in Fig.11 are used. The reference motion rates given through hyper terminal of a PC and the feedback values of limbs are transmitted and received from RS-232 serial port of PC



via an interface circuit by using PIC 16F877. According to the screw datas given in Table 1 relevant motion rates are then evaluated through measured pulses from the encoders. The very simple position control algorithm involves the comparison of measured pulses coming from the encoders with the given reference motion rates. The serial interface unit and animation model in PROTEUS ISIS to test the control unit are shown in Fig.12 and Fig.13.

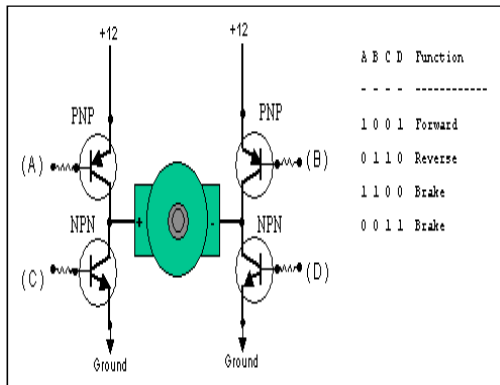


Fig. 11: Connection of DC Motors and motor drive electronic circuit diagram



Fig. 12: The serial Interface Unit

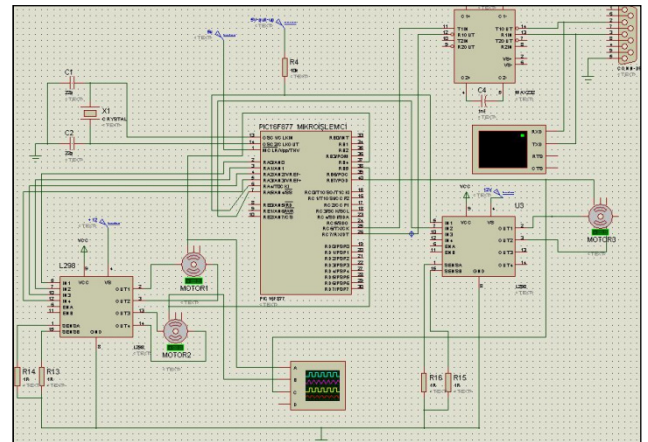


Fig. 13: PROTEUS ISIS Animation Model

As motor drive L298 Transistorised H Bridge devices are used. Through these a probable speed control for trajectory planning can be realised easily. As future work different control algorithms like P, PI and PD can be applied and for trajectory planning time dependent applications by synchronous driving motors will be tested. A simple trajectory following test by using an equivalent time synchronous motion of limbs delivered satisfactory results.

8. Conclusions

By using MATLAB iterative method both the inverse kinematics and forward kinematics solutions are evaluated and theoretical workspace of the manipulator is generated. However the real (effective) workspace can be expressed in the same way under physical constraints (like collision of limbs, limitation of rail screw motions because of the screw nut lengths etc.) taken into consideration Fig. 6.

In a future work this general disadvantage of parallel manipulators will be investigated by using the dexterity analysis of workspace.

In case of forward kinematic application and within effective workspace, the calculated values both by using MATLAB iteration and evaluated values from SolidWorks simulation are compared in Table 2 and Table 3. From the comparison of the calculated and simulated results given in tables it can be seen that both confirm each other with a great accuracy.

The calculated results can further be used for trajectory planning and control of manipulator in three dimensional space. Because of the simplicity and accuracy of created equations, these can also be used for further dynamic analysis.



References

- [1]. Merlet, J.-P.: *Parallel Robots*. Kluwer, London (2000)
- [2]. Clavel, R.: DELTA, a fast robot with parallel geometry. In: *Proc. of 18th Int. Symp. Industrial Robots*, Lausanne, pp. 91–100 (1988)
- [3]. Li, Y., Xu, Q.: Dynamic analysis of a modified DELTA parallel robot for cardiopulmonary resuscitation. In: *Proc. of IEEE/RSJ Int. Conf. on Intelligent Robots and Systems*, Edmonton, Canada, pp. 3371–3376 (2005)
- [4]. Miller, K.: Synthesis of a manipulator of the new UWA robot. In: *Proc. of Australian Conf. on Robotics and Automation*, Brisbane, Australian, pp. 228–233 (1999)
- [5]. Tsai, L.W., Walsh, G.C., Stamper, R.E.: Kinematics of a novel three DOF translational platform. In: *Proc. of IEEE Int. Conf. on Robotics and Automation*, Minneapolis, Minnesota, pp. 3446–3451 (1996)
- [6]. Chablat, D., Wenger, P.: Architecture optimization of a 3-DOF translational parallel mechanism for machining applications, the Orthoglide. *IEEE Trans. Robot. Autom.* 19(3), 403–410 (2003)
- [7]. Herve, J.M., Sparacino, F.: Star, a new concept in robotics. In: *Proc. of Advances in Robot Kinematics*. Ferrara, Italy, pp. 176–183 (1992)
- [8]. Gosselin, C., Angeles, J.: The optimum kinematic design of a spherical three-degree-of-freedom parallel manipulator. *ASME J. Mech. Transm. Autom. Des.* 111(2), 202–207 (1989)
- [9]. Vischer, P., Clavel, R.: Argos: A novel 3-DOF parallel wrist mechanism. *Int. J. Rob. Res.* 19(1), 5–11 (2000)
- [10]. Lee, K.M., Arjunan, S.: A three-degrees-of-freedom micromotion in-parallel actuated manipulator. *IEEE Trans. Robot. Autom.* 7(5), 634–641 (1991)
- [11]. Li, Y., Xu, Q.: Kinematics and inverse dynamics analysis for a general 3-PRS spatial parallel mechanism. *Robotica* 23(2), 219–229 (2005)
- [12]. Di Gregorio, R. and Parenti-Castelli, V.: A translational 3-DOF parallel manipulator. In: Lenarcic, J., Husty, M.L. (eds.) *Advances in Robot Kinematics: Analysis and Control*, pp. 49–58 (1998)
- [13]. Tsai, L.W.: Kinematics of a three-DOF platform with three extensible limbs. In: Lenarcic, J., Parenti-Castelli, V. (eds.) *Recent Advances in Robot Kinematics*, pp. 401–410 (1996)
- [14]. Giberti, H., Righettini, P., Tasora, A.: Design and experimental test of a pneumatic translational 3DOF parallel manipulator. In: *Proc. of 10th Int. Work. Rob. in RAAD*. Vienna, Austria (2001)
- [15]. Merlet, J.-P.: Workspace-oriented methodology for designing a parallel manipulator. In: *Proc. Of IEEE Int. Conf. Robotics and Automation*, Minneapolis, Minnesota, pp. 3726–3731 (1996)
- [16]. Tsai, L.W., Joshi, S.: Kinematics analysis of 3-DOF position mechanisms for use in hybrid



Morphology of a Single Actuator Tetrapod Walking Spider Robot

Servet SOYGUDER^{1*}, Hasan ALLI²

^{1*}Tennessee State University, Department of Computer Science Engineering, Nashville, USA
servetsoyguder@yahoo.com

²Firat University, Department of Mechanical Engineering, Elazig, Turkey

Abstract

The This study describes design and control of a eight-legged single actuator walking ROBOTÜRK SA-2 spider robot based on the features of a creatural spider. The tetrapod walking robot is formed by being mounted spider-like leg structure. Since a creatural spider walks in a style of 4 legged support (R1 the first and R3 the third leg of the right side and L2 the second and L4 the forth leg of the left side) and the others moves forward, ROBOTÜRK SA-2 eight-legged walking robot has been developed by designing a novel motion mechanism to realize this walking motion using one only actuator. In the second step, the roles of legs change vice versa. First, the single actuator eight-legged tetrapod walking spider robot was modeled on Solid Works and then the animation of the model was realized to ensure the accurate walking patterns and more stable walking. Based on this model, the novel prototype of the single actuator eight-legged walking spider robot was constructed. In order to give more flexibility to the legs and mimic muscles, two springs were mounted to each leg. The control of the system was realized by using PLC(Programmable Logic Controller). To verify to walking performance, the experimental results were obtained. Consequently, the single actuator eight-legged tetrapod walking spider robot proposed in this paper is believed to be the first design specifically for having novel motion mechanism and minimum number of actuators in the knowledge of the authors.

Keywords: ROBOTURK-SA2 Spider Robot, Robotics, Tetrapod Walking, A Single Actuator, Motion Mechanism Concept.

1. Introduction

In last years, a lot of studies on legged robots have been published [1-10]. People have considered in manufacturing legged robots whose designs one based at least in part an biological principles [6]. The basic advantage of legged robots is to be capable of going where wheeled robots are not capable of.

Formerly, H. ALLI and S. SOYGUDER designed six-legged robot using only two actuators [1]. In this study, ROBOTÜRK SA-2 with eight-legged and only one actuator has been realized for the aim of defense industry and natural disasters (Fig.2). The design of this robot has

been made both low energy consumption and weight minimum and its control ease by decreasing the number of the used actuators. The most important feature of the designed robot is to realize walking like spiders in nature using only one dc motor (with planetary gear; 28:1) actuating all legs and joints of the robot. The kinematics chain of the legs actuated by the cam mechanism and transmission bar is six-bar Watt's chain. The springs are mounted to the legs to mimic important muscle characteristics. PLC is used for controlling the motion mechanisms.

This article has six sections. The next section presents the steps of motion mechanism concept and morphology of a single actuator walking spider robot. The prototype model and innovations are investigated in section 3. Workspace and walking plan of the ROBOTURK SA-2 spider robot is given in section 4 and section 5 presents the experimental works. Finally, the last section includes some conclusion remarks and future works.

2. Motion Mechanism Concept and Morphology

In this study, a different morphology for the designed robot from those of animals, including many insects, to superior to the current legged robots, has been formed. The used motion mechanism couples the robot joints for the aim of reducing the number of actuators and simplifying the control problem since actuators are generally heavy and reducing the number of actuators are also able to save energy consumption. Autonomy, a critical component of our aspiration toward real-world tasks in unstructured environments outside the laboratory, imposes very strict design constraints on the hardware and software components. It is often impossible to achieve with simple modifications to a system otherwise designed for non-autonomous operation. These constraints also justify our preference for overall simplicity, in particular the minimum amount of actuation and energy. The mobility of the legged robot is one degree of freedom (DOF) and it has identical legs. The main target in this study is for the legged robot to walk on smooth ground

and verify the tetrapod gait pattern similar to that observed in the spider. For more information, Fig.1 shows body size of the single actuator eight-legged walking spider robot.

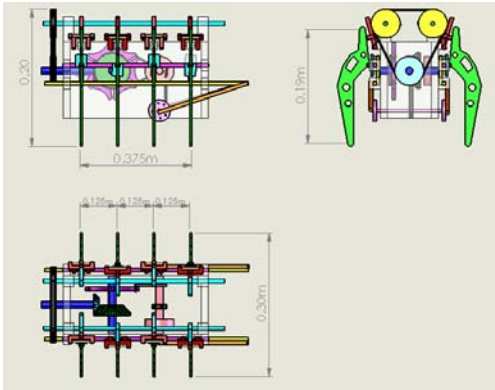


Fig. 1: Body size of the single actuator eight-legged tetrapod walking spider robot

3. ROBOTÜRK SA-2 and Innovations

ROBOTÜRK SA-2 is name of the eight-legged tetrapod walking robot with a single actuator, owning many innovations (Fig.2). The innovations of ROBOTÜRK SA-2 as follows;

- * The number of actuators,
- * The cam mechanism mounted in the back of the eight-legged spider robot,
- * Mounting springs to mimic muscles,
- * The characteristics of gait are similar to those in nature.



Fig. 2 : ROBOTÜRK SA-2

3.1. Design of Motion Mechanism

3.1.1 The Actuator of The Robot

The main feature of the spider robot owning the tetrapod gait like spiders in nature (Fig. 6.) by using only single dc motor is to be one degree of freedom. The motions of the all legs and joints are provided by geneva, cam mechanisms and springs driven by single dc motor.

Providing to contact with the ground for the marked legs in Fig.6 and lifting up/down motions of the other legs have been realized by means of cam and geneva mechanisms driven by a dc motor. It is seen in Figure 3 that each of the links mounted on the cam mechanisms provides the legs to contact with the ground. Furthermore, the geneva mechanism rotates only 120° and then waits 240° while the dc motor rotates one revolution. Hence, the motion of the geneva mechanism transmits to the cam mechanism so that the legs simultaneously contact with the ground. At the same time, the same dc motor in each revolution performs the walking of the spider robot by the belt-pulley mechanism making the legs leaving from the ground translate forward by the means of the transmission-bar and connecting rod.

The obtained results of the minimizing of the number of actuators:

- The energy consumption has been minimized by decreasing the number of actuators. (The designed spider robot uses only single dc motor in this study while the similar robots in the literature use at least six or eight dc motors.
- Increasing the number of actuators would make the control difficult.
- The structure of the robot has been made more flexible.
- The cost has been minimized.

3.1.2. Function of The Transmission bar and Connecting rod

The transmission bar and the connecting rod is used for swinging motion of the legs, as illustrated in Fig.3. The left and right side transmission bar and connecting rod group of the spider robot are simultaneously actuated by the same dc-motor. Furthermore, each leg of the spider robot is placed on the fixed bar. The right tetrapod and left tetrapod legs, oscillating through the rotating-axis, pace forward by the forward/backward motion of the transmission bar. This motion is realised by only one dc-motor which drives the connecting rod (Fig.3). That is, the lifting legs go forward one step by means of the connecting rod and transmission bar when the dc-motor rotates one revolution. It is seen in Figure 8 that the legs are connected to the fixed bar while the leg joints are connected to the transmission bar by means of the connecting links. The swing angle (θ) limits $\pm 15^\circ$ while the transmission bar translates 0.02m when the connecting rod moves one period, as in the previous study of the authors [1].

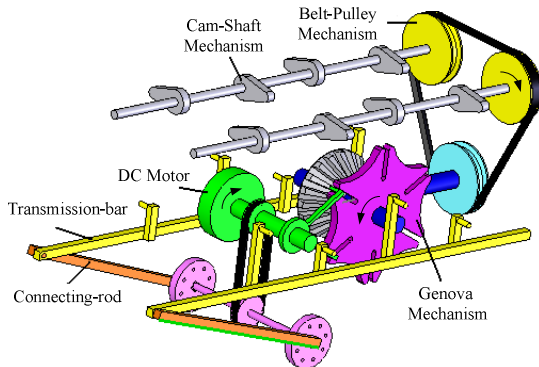


Fig.3: The transmission-bar, the connecting-rod and the genova mechanism group

3.2. The Cam Mechanism Mounted to The Back of The Spider Robot

The cam mechanism provides that the legs forming the gait of the robot contact with the ground as shown in Fig.4. In the each step of the gait, the cam mechanism makes the some legs contact with the ground while the some legs stop contacting with the ground depending upon the character of the gait. The innovations because of using the cam mechanism are followings:

- It is no need to use different actuators for each leg because the cam mechanism realizes to contact the each leg with the ground.
- The period of service needs and technical defaults decreases because of using the cam mechanism instead of using many number of dc-motors.

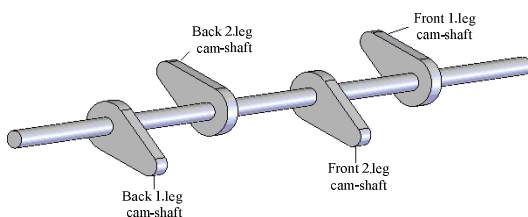


Fig. 4. The cam-shaft

3.3. The Springs To Mimic Muscles

The springs transmit the motion obtained by the cam mechanism to the joints (Fig.5). The existence of the cam mechanism and springs cause the easy control of the spider robot and minimizing the number of actuators used. The innovations because of using the springs are followings:

- Using the springs in the leg joints makes the legs gain the features of muscles like those in nature.

- The motion is transmitted to the joints by the extension and compression of the springs like the flexion and laxation of muscles in living being.

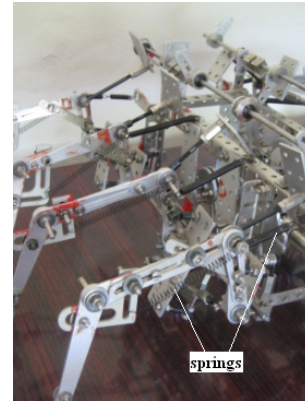


Fig 5: The springs to the prototype to give more flexibility to the legs and mimic muscles.

4. Workspace and Walking plan of the ROBOTÜRK SA-2

The walking stability of the eight-legged robot is provided by the four legs becoming support legs in each walking step [11]. It is also seen in Fig.6 that L1 and L3 on the left-side and R2 and R4 on the right-side become support legs in the first step while L2 and L4 on the left-side and R1 and R3 on the right-side become support legs in the second step.

These situations are also presented in Table I that the leg supporting the body are represented by a solid black circle and the ones floating are represented by an open circle. The walking is realized by repeating this cycle. The most important feature in this design is that the legs are connected to the clippers on the fixed bar as shown in Fig.3. The leg clippers are connected to the transmission-bar by means of a connecting-rod. Transmission-bar translates forward 0.02 m from the reference point in one cycle of the motion of the connecting-rod. Then, this motion provides the translation of the spider robot by means of the $\pm 15^\circ$ (θ) angular displacement of the legs depending on walking patterns. Besides, the up/down motion of the legs is realized by the cam mechanism. By the way, the motion of the cam mechanism is provided by 120° angular displacement of genava mechanism transmitting to the cam-shaft by the bevel gears. After that, the support legs stop touching with ground as they rotate between 0° and $+60^\circ$ (φ) from the ground to the up-position whereas the other legs touch with the ground by moving from up to down. Furthermore, Fig.7 and Fig.8 show the trajectory of

each leg in the workspace of the spider robot.

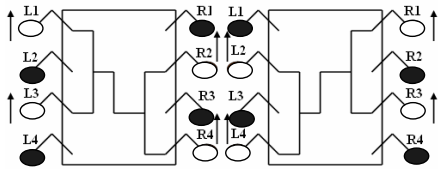


Fig. 6: The structure of walking pattern [1,4,5]

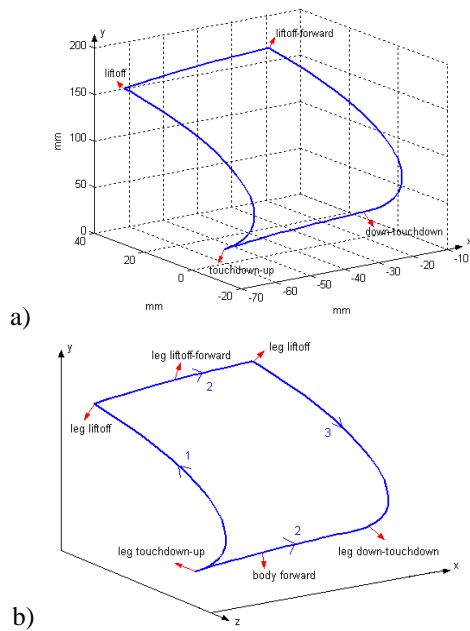


Fig.7(a-b): Body and right-side legs of ROBOTÜRK SA-2 workspace [18,19]

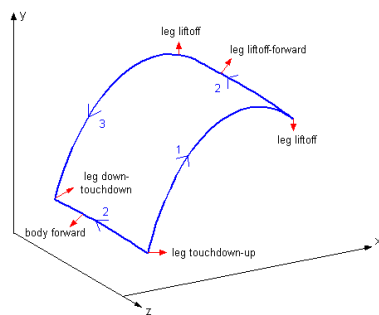


Figure 8. Body and left-side legs of ROBOTÜRK SA-2 workspace [18,19]

Table 1: Walking-Pattern [5]

leg no walking cycle	Left				Right			
	L1	L2	L3	L4	R1	R2	R3	R4
1. step	●	○	●	○	○	●	○	●
2. step	○	●	○	●	●	○	●	○

5. Experimental Results

The bottom half of Fig.9 illustrates the typical sequence of leg contact conditions. To make more understandable, this part of the figure consists of top view and side view of the conceptual diagram. The tetrapod legs start to liftoff in the first interval. Then, the legs perform floating and followed by an interval of touching down. At the end, the interval of the fixed tetrapod stance of the next step occurs. The top half of the figure shows the relation between these four phases and leg positions, obtained the gathered data from the potentiometers located to the legs. At the end of measuring at 1 KHz averaged over 25 experimental runs, Table II indicates the average times of four phases and the total time in one complete stride. Table II [8-12] has been motivated and obtained by using Figure 9.

Table 2: Experimental phase relations in insect robot tetrapod gait

Phases	Phases in one complete stride	
	Average time(sec)	Percentage of time (%)
Quadruped Stance (touchdown transient to wait)	0.82	45.05
Liftoff Transient	0.18	9.89
Quadruped Stance Forward	0.64	35.16
Touchdown Transient	0.18	9.89
Total	1.82	100.0

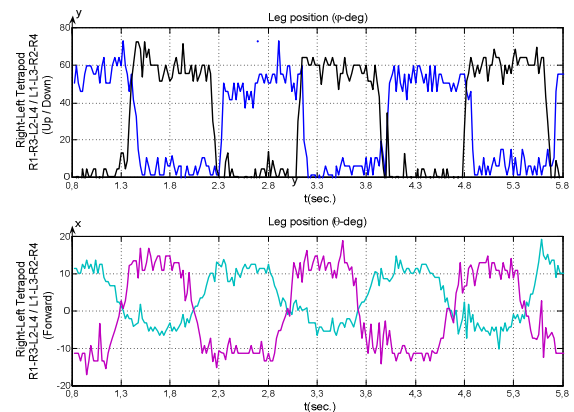


Fig.9: The four following intervals during the i th tetrapod stride $S(i)$, with data plotted in the upper figure showing the relation between leg angular positions. ($0^\circ = (\varphi)$ vertically downward, $+60^\circ (\varphi) =$ vertically upward and $\pm 15^\circ (\theta) =$ forward) and four intervals gathered from the physical insect robot experimental data.

6. Conclusion

The developed legged robot in this study is based on resembling much or less spider leg mechanism. One DC gear motor has only been used to get the tetrapod gait. Using the minimum number of actuators makes the light



structure possible and simplify the control problem. Increasing power consumption and complexity of the control systems depending on number of the used actuators are well known. To disappear the mentioned problems, special mechanisms can be used. The Geneva mechanism, the cam mechanisms, the connecting rods, and springs used in our design made the number of actuators decrease thus the control of the spider robot eased and its cost also decreased. It is indicated and compared to number of actuator, leg number and speed of the presented insect and spider robot and a few leg robots in the literature in Table III. This table concludes that the speed of the presented robot is reasonable in the existing leg robots in the literature. In order to save trial-error time and faults, first, the design was modelled on Solid Works and the animation was realized on COSMOSMotion. Based on the developed model, the prototype of the single actuator eight-legged tetrapod walking spider-like robot was built. The control of the systems was realized by using PLC. As a result, using intelligent biologically inspired walking robots have great potential for in inaccessible and dangerous places to humans and currently available equipments. Studies on biologically inspired robots will increase to improve the actual performance of the designed walking robots in the near future.

Table 3: Actuator number, leg number and speed of some leg robots [1,20,21,10,18]

Robots	Number of Actuator	Number of Leg	Speed(centimeter/sec)
Our insect Robot	2	6	5.40
Our spider Robot (ROBOTÜRK SA-2)	1	8	5.40
Rhex	6	6	45.0
Robug III	16	8	10.0
Dante II	6	6	1.70
Genghis	6	6	3.80
Commet	6	6	5.00
Rimbo-2	6	6	5.00
Whigs	6	6	20.0

References

- [1]. Soygüder, S., Alli, H., "Design and prototype of a six-legged walking insect robot", *Industrial Robot –An International Journal*, Vol: 34(5), pp: 412-42, 2007.
- [2]. Delcomyn, F. and Nelson, M.E. "Architectures for a biomimetic hexapod robot", *Robotics and Autonomous Systems*, Vol. 30, pp.5-15, 2000.
- [3]. Huang, Q.J. and Nonami, K. "Humanitarian mine detecting six-legged walking robot and hybrid neuronal walking control with position/force control", *Mechatronics*,13, pp. 773-790, 2003.
- [4]. Ohnishi, T. and Asakura, T. "Walking Behaviour of Spider-robot with Adaptation for Environment Information", *SICE Annual Conference in Sapporo*, August 4-6, Hokkaido Institute of Technology, Japan, 2004.
- [5]. Ohnishi, T. and Asakura, T. "On walking Behavior Strategy for Spider-robot Based on Environmental Information", *Proceedings of 2004 IEEE/RSJ International Conference on Intelligent Robots and Systems*, September 28- October 2, Sendai, Japan, 2004.
- [6]. Quinn, R.D. Nelson, G.M. Bachmann, R.J. Kingsleg, D.A. Offi, J. and Ritzmann, R.E. "Insect Design for Improved Robot Mobility" , *Proc. 4th Int. Conf. On Climbing and Walking Robots*, Berns and Dillmann eds, Prof. Eng. Pub, pp. 69-76, 2001.
- [7]. Siegwart, R. and Nourbakhsh, I.R., *Autonomous Mobile Robots*, The MIT Press. USA, 2004.
- [8]. Saranli, U. and Buehler, M. and Koditschek, D.E. "Rhex-A simple and highly mobile hexapod robot", *Int. J. Robot. Res.*, 20, pp. 616-631, 2001.
- [9]. Berns, K. and Kepplin, V. Ilg, W. and Dillmann, R. "Experiments with a stereo camera head for the local navigation of LAURON II", *Forschungszentrum Informatik Karlsruhe*, Germany, 1993.
- [10]. Lin, P.C. and Komşuoğlu, H. and Koditschek, D.E. "Sensor Data Fusion for Body State Estimation in a Hexapod Robot with Dynamical Gaits" , *IEEE Transaction on Robotics*, Vol.22, No.5, October, 2006.
- [11]. Roy E. Ritzmann*, Roger D. Quinn, Martin S. Fischer, *Convergent evolution and locomotion through complex terrain by insects, vertebrates and robots. Arthropod Structure & Development* 33, 361–379, 2006.
- [12]. Daniel E. Koditschek*, Robert J. Full, Martin Buehler, "Mechanical aspects of legged locomotion control", *Arthropod Structure & Development* 33, 251–272, 2004.
- [13]. Barfoot, T.D. and Earon, E.J.P. and Eleuterio, G.M.T.D. "Experiment in learning distributed control for a hexapod robot" *Robotics and Autonomous Systems*, Vol. 54, pp. 864-872, 2006.
- [14]. Ranjit Kumar Barai *, Kenzo Nonami, " Optimal two-degree-of-freedom fuzzy control for locomotion control of a hydraulically actuated hexapod robot", *Information Sciences* 177, 1892–1915, 2007.
- [15]. Laurent Thiry*, Jean-Marc Perronne, Bernard Thirion, "Patterns for behavior modeling and integration", *Computers in Industry* 55, 225–237, 2004.
- [16]. Volker Durr*, Josef Schmitz, Holk Cruse, "Behaviour-based modelling of hexapod locomotion: linking biology and technical application", *Arthropod Structure & Development* 33, 237–250, 2004.
- [17]. J.M. Porta, E. Celaya, *Reactive free-gait generation to follow arbitrary trajectories with a hexapod robot. Robotics and Autonomous Systems* 47, 187–201, 2004.
- [18]. Luk, B.L. and Cooke, D.S. and Galt, S. and Collie, A.A. and Chen, S. "Intelligent legged climbing service robot for remote maintenance applications in hazardous environments" *Robotics and Autonomous Systems*, Vol. 53, pp. 142-152, 2005.
- [19]. Shinkichi Inagakia,_, Hideo Yuasab, Takanori Suzukid, Tamio Araic, *Wave CPG model for autonomous decentralized multi-legged robot: Gait generation and walking speed control. Robotics and Autonomous Systems* 54, 118–126, 2006.
- [20]. P. Gonzalez de Santos *, J.A. Cobano, E. Garcia, J. Estremera, M.A. Armada, "A six-legged robot-based system for humanitarian demining missions", *Mechatronics* 17, 417–430, 2007.
- [21]. Angle, C. "A six-legged autonomous walking robot", Ph.D. thesis, Massachusetts Institute of Technology, 1989.

Gaits and Trajectory Planning with Optimal Hip-Mass Positioning Strategies for 4-DOF Parallelogram Bipedal Robot

Nazim MIR-NASIRI^{1*} and Hudyjaya SISWOYO JO²

^{1*}School of Engineering, Computing and Science
Swinburne University of Technology (Sarawak Campus)
93350 Kuching, Malaysia
mnasiri@swinburne.edu.my

Abstract

This paper presents joint space trajectory planning strategy for the legs of 4-DOF parallelogram bipedal robot. The use of two sets of pulley-based parallelogram mechanisms in each leg allows to reduce the number of joint actuators by one in each leg and to keep legs feet parallel to the horizontal walking surface. By reducing some actuators in the legs design the overall weight, energy consumption of the robot and complexity of the robot controller can be reduced. The walk patterns presented in the paper allows the major body mass located at the robot hip to be always vertically aligned with the center of the foot area during the single-leg supporting phase of the robot. The hip mass is then transferred from one leg foot area to another leg foot area only during two-legged supporting phase when both legs are firmly in touch with the ground. The idea is to force the hip mass gravity force constantly generate the reverse torque with respect to the front edge of the stationary foot while other forward perturbation torques generated by various gravity and inertia forces tend to overturn the robot in forward direction when the robot takes a step forward. The two-dimensional spatial trajectories are planned also to reduce the ground impact during the legs motion. The legs desired Cartesian motion trajectories are derived in joint space coordinates form and can be used directly to control actuators motion. Although the paper does not discuss any issues related to the dynamic walk and dynamic properties of robot it however provides a logic precondition for its successful dynamic balancing in vertical forward motion plane in terms of proper positioning of the major (hip) mass on the robot structure and using this mass as a counter mass for the balancing.

Keywords: Parallelogram bipedal robot, Hip mass, Single- and Two- legged supporting phases, Joint -space trajectory

1. Introduction

Nowadays the development of robotics system to assist and replace human in various tasks is continuously growing. Most of the existing robots work in a restricted environment such as assembly lines and product inspection. In order for a robot to be able to replace

human completely, one of the criteria is to have a similar physical structure with human. This will enable the robot to work and directly adapt into human environment. However, realizing human like walking in a robot is a big challenge due to the complexity of motion and the number of human's limbs involved in the walking. Over the years, researchers are looking into many different issues related to bipedal walking i.e. stability, walking style, energy efficiency etc [1][2][3]. One of the problems commonly faced by conventional bipedal that utilize compass-like walking gait is it will suffer from impact with the ground at the end of every single support phase and all the forces tend to overturn the robot in forward direction over the foot edge e (Fig. 1a). This impact will cause an impulsive force to occur at the contact point which will disturb the stability of the robot. Furthermore, the effect of impact in bipedal walking is difficult to predict by a dynamic model, as a result various alternative approach are proposed to tackle this problem. Huang et al. [4] proposed the method to minimize the impact force by using heel-to-toe landing instead of landing the whole sole at once. Wongsuwarn and Laowattana [5] proposed a learning method to correct the planned trajectory in order to minimize the impact. Also, many are opting for the traditional way of using deformable sole or absorbing mechanisms to absorb the force caused by the impact [6][7][8][9][10].

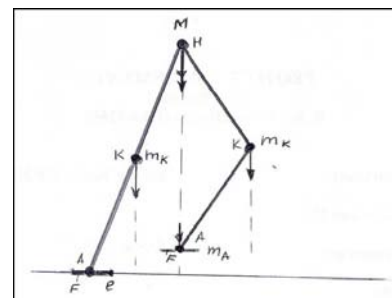


Fig. 1a: Impact occurs during foot landing (gravitational force of body hip mass contributes to the impact)

This paper proposes a method to minimize the impact force during the foot landing by carefully planning the walking gait of the robot in forward direction of motion at the first stage of the robot design and design of special balancing mechanism to prevent sideway motions of the robot in the following stage of the research. The spatial leg trajectory is design in such a way that in the single-legged supporting phase, the robot main body mass (the hip mass) held stationary on the stationary leg and it is always vertically aligned with the center of the stationary foot area (Fig 2a). The other leg is swinging around the stationary hip when the robot is taking a step. Since the main body mass is within the area of stationary foot (i.e. at its center), it should not contribute to the impacting forces and to the landing velocity as in the case of compass-like gait (Fig. 1a). Meantime mass M acts as a counter mass preventing the robot from overturning in forward direction about the foot edge e . The robot has to advance its body mass in forward direction for successful walk. For the designed walk pattern it occurs only when both legs are in touch with the ground, i.e. when there is a bigger supporting area for the body mass transfer. The paper also introduces traditional parallelogram mechanism for the legs design. It reduces the number of actuators required to achieve human like leg design and allows keeping the robot feet always parallel to the ground surface. In addition, space joint trajectory planning strategy developed in this work would simplify the control of the legs actuators to implement the designed walk patterns. One of the key design objectives is also to avoid an excessive inertial forces (accelerations) applied on the actuator shafts during the implementation for the joint space trajectories.

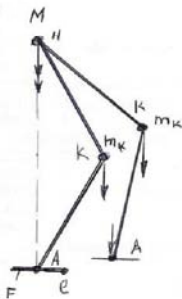


Fig. 1b: Impact occurs during foot landing (gravitational force of body hip mass does not contribute to the impact)

Details of the design are presented as follows. Section II discusses the mechanical components and structure, section III discusses trajectory planning strategy. In section IV, computer simulation results are presented followed by the conclusion of work in section V.

2. Mechanical Structures of Robot Legs

This paper describes only the basic structure of the robot legs. Mechanical system of the robot has been divided into two separate subsystems:

- Robot locomotion subsystem (robot legs)
- Robot balancing mechanism (additional balancers)

This paper describes only the robot leg structure, optimal hip-mass carry walk patterns, joint space legs trajectory planning and its computer simulation in terms of the legs successive positions and actuators time-based angular position, velocities and accelerations. Robot real time balancing strategies will be developed at the later stages of the research

The robot leg structure is shown in Fig. 2.

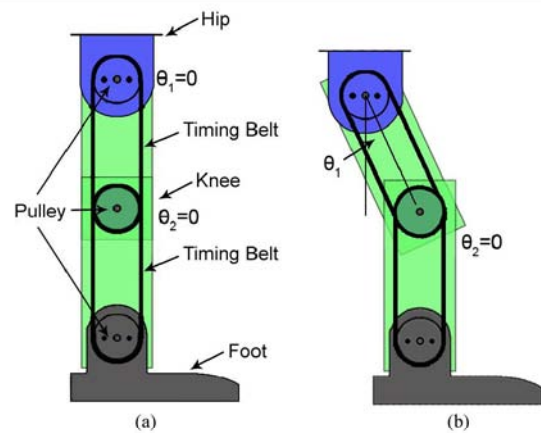


Fig. 2: Simplified structure of the leg

The main components of the legs are timing belts and pulley system that work as a parallelogram mechanism. The main advantages of the parallelogram mechanisms leg structure are that they are able (Fig. 1):

- To decouple the motion of the upper leg from the lower leg
- To maintain the foot plane level always parallel to the ground while the robot moves

Fig. 1(a) shows that when the upper and lower sections of the leg are both vertical, the actuation angles are initialized to zero. Fig. 1(b) shows the upper section of the leg after it has been actuated. However, lower section of the leg still maintains its vertical position ($\theta_2=0$) and foot plane always remains horizontal. The other advantage of the structure is that the joint angles are always counted from to the vertical axis of the stationary world coordinate frame regardless of the leg postures. This structure also allows either removing the ankle actuator from the structure if the walk is intended on the horizontal ground surface, or just keeping it if the walk on the sloped

surface is an option. For the design without the ankle actuator, the irregularities of the ground can be absorbed by adding some controllable degree of freedom to the ankle structure alone.

3. Trajectory Planning

A. Classification of angular boundary conditions for single- and two-legged supporting phases of robot walk

The basic requirement for the trajectory planning is to achieve smooth walking pattern of bipedal robot with less stresses the actuators and minimum impact at the end of the walking phase. In addition, the trajectory is deliberately planned to keep the hip height at a constant level above the ground as it walks. This feature of the robot can be used if the robot is employed as a service robot that carries items not to be shaken up and down. The main body mass (hip mass) is planned to be advanced forward only when both legs are in touch with the ground for the sake of static stability condition. The dynamic stability will be designed at the later stage of research by implementing of special balancing mass and related mechanical system (it is not a topic for this paper).

The entire trajectory planning for the robot legs motion is achieved only by controlling the motors in joint space coordinates without referring to the legs 3D Cartesian space coordinates. Matching of the parameters in joint and Cartesian spaces is achieved by carefully selecting the boundary conditions for the joint space control and proper timing. This will provide smooth transition from one controlled interval of the time into another one.

The joint space trajectories are designed to fulfill the following boundary conditions for a joint motion during interval $0 < t < t_f$

$$\text{when } t = 0, \theta(0) = \theta_i; \dot{\theta}(0) = 0; \ddot{\theta}(0) = 0$$

$$\text{when } t = t_f, \theta(t_f) = \theta_f; \dot{\theta}(t_f) = 0; \ddot{\theta}(t_f) = 0$$

θ_i - initial position of the joint angle when $t = 0$

θ_f - final position of the joint angle when $t = t_f$

$\dot{\theta}(0)$ - initial speed of the joint angle when $t = 0$

$\dot{\theta}(t_f)$ - initial speed of the joint angle when $t = t_f$

$\ddot{\theta}(0)$ - initial acceleration of the joint angle when $t = 0$

$\ddot{\theta}(t_f)$ - initial acceleration of the joint angle when $t = t_f$

A complete walking cycle consists of single-legged and two-legged supporting phases. In single legged supporting phase only one foot is in contact with the ground while the other is swinging to make a step

forward. During this phase, the position of the hip is kept stationary and aligned vertically with the supporting foot in order to maintain static stability for the main hip mass. In two-legged supporting phase, while two feet are in contact with the ground, the hip is transported forward horizontally. Moving the hip only during the two-legged supporting phase will help to widen the static stability condition since the area of support polygon is larger.

The boundary conditions of the joint are selected based on the designed walking gait as mentioned above. A complete walking cycle is formed by executing three different sets of movement in specific sequence, i.e. thigh movement, shank movement and hip movement. Thigh and shank movement are executed in single-legged supporting phase whereas the hip movement is executed in two-legged supporting phase.

1) Single Support Phase

In Fig. 3, $\theta_{1,1}$ and $\theta_{1,2}$ are the joint angles for hip and knee joints of the supporting leg respectively, whereas $\theta_{2,1}$ and $\theta_{2,2}$ are the joint angles for hip and knee joints of the swinging leg respectively. l is the equal length for both upper and lower legs. It is clear from the drawing that during thigh movement, the hip joint for the swinging leg moves from its initial to final angular position while the knee joint stays at the same angular position. During the shank movement, the hip joint remains at its final angular position while the knee joint move from its initial to final angular position.

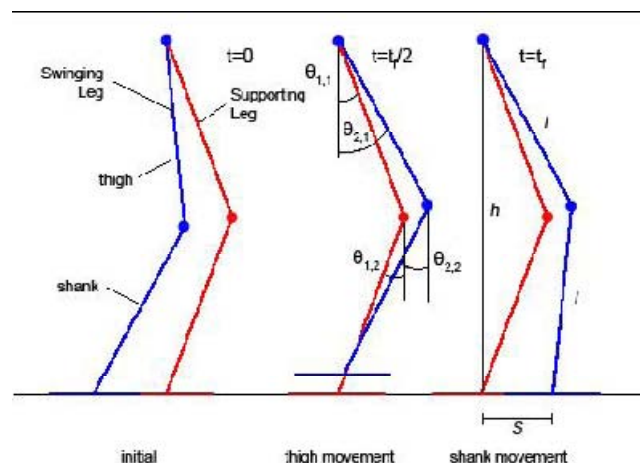


Fig. 3: Leg posture of single-leg supporting phase

The reason for moving the hip joint before the knee joint is to provide some clearance for the foot above the ground in order to prevent the foot from dragging along the ground surface. The angular boundary conditions for $\theta_{2,1}$ and $\theta_{2,2}$ can be calculated from the geometry of the leg postures shown in Fig. 3. The duration for the single-leg

supporting phase is assumed to be t_f and the step size is s .

The angular boundary conditions for hip joint are as follows:

for $0 < t < t_f$

$$\theta_{2,1}(0) = \cos^{-1}\left(\frac{h}{2l}\right)$$

$$\theta_{2,1}\left(\frac{t_f}{2}\right) = \cos^{-1}\left(\frac{\sqrt{h^2 + s^2}}{2l}\right) + \tan^{-1}\left(\frac{s}{h}\right)$$

The angular boundary conditions for knee joint are as follows:

for $\frac{t_f}{2} < t < t_f$

$$\theta_{2,2}\left(\frac{t_f}{2}\right) = -\cos^{-1}\left(\frac{h}{2l}\right)$$

$$\theta_{2,2}(t_f) = -\cos^{-1}\left(\frac{\sqrt{h^2 + s^2}}{2l}\right) + \tan^{-1}\left(\frac{s}{h}\right)$$

2) Double Support Phase

In Fig. 4, $\theta_{1,1}$ and $\theta_{1,2}$ are joint angles for hip and knee joints of the supporting leg respectively, whereas $\theta_{2,1}$ and $\theta_{2,2}$ are the joint angles for hip and knee joints of the swinging leg respectively. In this phase, both feet are in contact with the ground and the hip is moving forward horizontally. In order to keep the hip at constant height, the horizontal trajectory of the hip and the trajectory of the joint angle $\theta_{1,1}$ are predefined and the remaining joint angles are calculated to follow the hip trajectory.

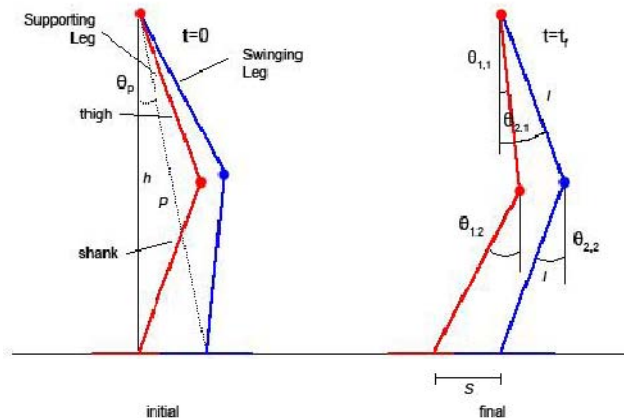


Fig. 4: Leg posture of double support phase

The angular boundary conditions for $\theta_{1,1}$ and the joint angle for $\theta_{1,2}$, $\theta_{2,1}$ and $\theta_{2,2}$ can be calculated from the

geometry of the leg postures according to Fig. 3. The duration for the two-leg supporting phase is assumed to be t_f and the hip advances by the distance s .

The angular boundary conditions for $\theta_{1,1}$

for $0 < t < t_f$

$$\theta_{1,1}(0) = \cos^{-1}\left(\frac{h}{2l}\right)$$

$$\theta_{1,1}(t_f) = \cos^{-1}\left(\frac{\sqrt{h^2 + s^2}}{2l}\right) - \tan^{-1}\left(\frac{s}{h}\right)$$

The joint angle for $\theta_{1,2}$

$$\theta_{1,2}(t) = \cos^{-1}\left(\frac{h - l \cos \theta_{1,1}(t)}{l}\right)$$

The joint angle for $\theta_{2,1}$ and $\theta_{2,2}$

$$\theta_{2,1}(t) = \cos^{-1}\left(\frac{P(t)}{2l}\right) - \theta_p(t)$$

$$\theta_{2,2}(t) = -\cos^{-1}\left(\frac{P(t)}{2l}\right) - \theta_p(t)$$

Where $P(t)$ and $\theta_p(t)$ can be calculated as follows:

$$P(t) = \sqrt{\left((-l \sin \theta_{1,1}(t) - l \sin \theta_{1,2}(t)) - s\right)^2 + h^2}$$

$$\theta_p(t) = \left(\frac{-l \sin \theta_{1,1}(t) - l \sin \theta_{1,2}(t) - s}{h}\right)$$

B. Joint space trajectory planning

Trajectory planning for the postures shown in Fig. 3 and 4 are designed based on linear segment blended with polynomial sections. This type of planning will produce less tension on the actuators because they will run with nominal constant speed most of the time. Moreover, the order of the trajectory curve will be less as compared to the choice of single polynomial function for the entire segment of the trajectory which will result in less complex controller.

Selection of linear segments blended with fourth order polynomial sections will smooth the transition between the trajectory intervals at points A and B (Fig 5) at least to the acceleration level.

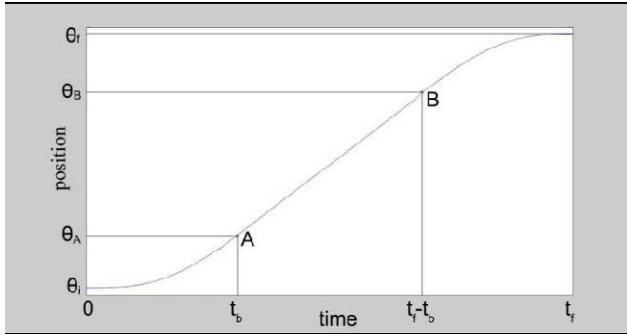


Fig. 5: Linear segment with parabolic blends

The angular boundary conditions for the actuator shaft are:

$$\begin{aligned}\theta(0) &= \theta_i ; \theta(t_f) = \theta_f \\ \dot{\theta}(0) &= 0 ; \dot{\theta}(t_f) = 0 \\ \ddot{\theta}(0) &= 0 ; \ddot{\theta}(t_f) = 0\end{aligned}$$

The fourth order polynomial and derivatives are as follow:

$$\begin{aligned}\theta(t) &= c_1 t + \frac{1}{2} c_2 t^2 + \frac{1}{3} c_3 t^3 + \frac{1}{4} c_4 t^4 \\ \dot{\theta}(t) &= c_1 + c_2 t + c_3 t^2 + c_4 t^3 \\ \ddot{\theta}(t) &= c_2 + 2c_3 t + 3c_4 t^2\end{aligned}$$

Substituting the initial boundary condition (1) to the polynomial gives:

$$\begin{aligned}\theta(t) &= \theta_i + \frac{1}{3} c_3 t^3 + \frac{1}{4} c_4 t^4 \\ \dot{\theta}(t) &= c_3 t^2 + c_4 t^3 \\ \ddot{\theta}(t) &= 2c_3 t + 3c_4 t^2\end{aligned}$$

Fig. 5 shows angular motion of the actuator designed as linear segment blended with polynomial sections at the beginning and the end of the motion period.

Matching the first and second derivatives of the polynomial with constant speed ω and zero acceleration to the linear segment of the trajectory yields the following expression:

$$\begin{aligned}\dot{\theta}_A &= c_3 t_b^2 + c_4 t_b^3 = \omega \\ \ddot{\theta}_A &= 2c_3 t_b + 3c_4 t_b^2 = 0\end{aligned}$$

Solving equations (2) simultaneously yields:

$$c_3 = \frac{3\omega}{t_b^2} ; c_4 = -\frac{2\omega}{t_b^3}$$

Matching the boundary angular values for polynomial and linear segments yields:

$$\theta_A = \theta_i + \frac{1}{3} c_3 t_b^3 + \frac{1}{4} c_4 t_b^4 ; \theta_B = \theta_A + \omega(t_f - 2t_b)$$

$$\theta_f = \theta_B + (\theta_A - \theta_i)$$

$$\theta_f = \theta_A + \omega(t_f - 2t_b) + (\theta_A - \theta_i)$$

$$\theta_f = 2\theta_A - \theta_i + \omega(t_f - 2t_b)$$

$$\theta_f = 2\left(\theta_i + \frac{1}{3} c_3 t_b^3 + \frac{1}{4} c_4 t_b^4\right) - \theta_i + \omega t_f - 2\omega t_b$$

$$\theta_f = 2\theta_i + \frac{2}{3} c_3 t_b^3 + \frac{1}{2} c_4 t_b^4 - \theta_i + \omega t_f - 2\omega t_b$$

$$\theta_f = 2\theta_i + \frac{2}{3} \left(\frac{3\omega}{t_b^2}\right) t_b^3 + \frac{1}{2} \left(-\frac{2\omega}{t_b^3}\right) t_b^4 - \theta_i + \omega t_f - 2\omega t_b$$

$$\theta_f = 2\theta_i + 2\omega t_b + \omega t_b - \theta_i + \omega t_f - 2\omega t_b$$

$$t_b = \frac{\theta_i - \theta_f + \omega t_f}{\omega}$$

The motion of the actuator for three separate time segments can be expressed as:

for $0 < t \leq t_b$

$$\theta(t) = \theta_i + \left(\frac{\omega}{t_b^2}\right) t^3 + \frac{1}{2} \left(\frac{\omega}{t_b^3}\right) t^4$$

$$\dot{\theta}(t) = \left(\frac{3\omega}{t_b^2}\right) t^2 - \left(\frac{2\omega}{t_b^3}\right) t^3$$

$$\ddot{\theta}(t) = \left(\frac{6\omega}{t_b^2}\right) t - \left(\frac{6\omega}{t_b^3}\right) t^2$$

for $t_A < t \leq t_B$

$$\theta(t) = \theta_A + \omega t$$

$$\dot{\theta}(t) = \omega$$

$$\ddot{\theta}(t) = 0$$

for $t_B < t \leq t_f$

$$\theta(t) = \theta_f - \left(\frac{\omega}{t_b^2}\right) (t_f - t)^3 + \frac{1}{2} \left(\frac{\omega}{t_b^3}\right) (t_f - t)^4$$

$$\dot{\theta}(t) = \left(\frac{3\omega}{t_b^2}\right) (t_f - t)^2 - \left(\frac{2\omega}{t_b^3}\right) (t_f - t)^3$$

$$\ddot{\theta}(t) = -\left(\frac{6\omega}{t_b^2}\right) (t_f - t) + \left(\frac{6\omega}{t_b^3}\right) (t_f - t)^2$$

4. Simulation Of The Bipedal Motion Trajectory

To simulate the bipedal motion, arbitrary step size s , leg length l and time interval for full step t_f are selected. The simulation of the above algorithms was done using MATLAB programming environment. Plotting of random positions or postures of both legs during the simulation is shown in Fig. 6.

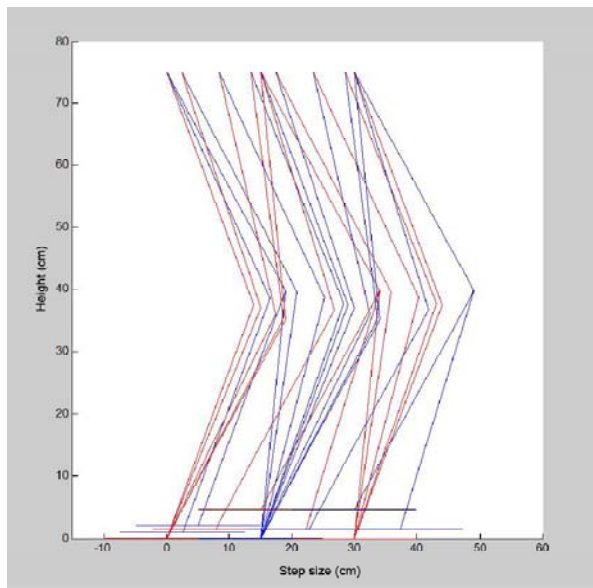


Fig. 6: Stick diagram for walking pattern

Fig. 7, 8 and 9 show the position, velocity and acceleration for each joint of the leg 1 and 2 respectively during the simulated walk. From the figures it is clear that the objective of providing a smooth transition between the strides has been achieved up to the second order derivatives of the motion curves. All the picks of motion characteristics curves are within the controlled limits.

5. Conclusion

The paper presents 4-DOF parallelogram bipedal walking robot which requires less number of actuations and thus less energy consumption than the traditional leg structure. The single-legged and two-legged walk patterns and trajectory planning are deliberately designed to keep the main body mass (hip mass) within the center of static stability region, i.e. vertically aligned with the center of the stationary robot foot area. It will eliminate unnecessary stability disturbance torque (by setting moment arm to zero) generated by the largest mass at the hip of the robot and helps to stabilize the remaining forces by designing additional counter masses for the dynamic balancing and selecting proper control strategies. A trajectory planning method developed in the work

potentially minimizes the impact force between robot feet and the ground because of the minimum acceleration and velocity of the foot when it approaches the ground. The effectiveness of joint space trajectory planning is verified by the results of real time computer simulation. The stick diagram of the computer animation is presented in Fig 5. The graphs of legs motion characteristics (Fig. 7, 8, 9) show that the planned trajectories are within an applicable range for all four actuators limits while the walking robot demonstrates smooth legs motion in the animation test (Fig. 5). The work will be continued towards the development of dynamic algorithms for the structure using controlled motion a specially designed balancers and building a working prototype of real size robot.

References

- [1]. J. Yamaguchi, A. Takanishi, and I. Kato, "Development of a biped walking robot compensating for three-axis moment by trunk motion," IEEE Int. Conf. on Intelligent Robots and Systems, pp. 561-566, 1993.
- [2]. H. Siswoyo Jo, N. Mir-Nasiri, and E. Jayamani, "Design and Trajectory Planning of Bipedal Walking Robot with Minimum Sufficient Actuation System," WASET Int. Conf. on Control, Automation, Robotics and Vision Engineering, pp. 65-71, 2009.
- [3]. R. Kurazume, S. Tanaka, M. Yamashita, T. Hasegawa, and K. Yoneda, "Straight legged walking of a biped robot," IEEE/RSJ Int. Conf. on Intelligent Robots and Systems, pp. 3095-3101, 2005.
- [4]. Q. Huang et al., "A high stability, smooth walking pattern for a biped robot," IEEE Int. Conf. on Robotics and Automation, pp. 66-71, 1999.
- [5]. H. Wongsuwarn and D. Laowattana, "Experimental study for a FIBO humanoid robot," IEEE Conf. on Robotics, Automation and Mechatronics, pp. 1-6, 2006.
- [6]. G. Kinoshita, C. Oota, H. Osumi and M. Shimojo, "Acquisition of reaction force distributions for a walking humanoid robot," IEEE/RSJ Int. Conf. on Intelligent Robots and Systems, pp. 3859-3864, 2004.
- [7]. N. Oda, T. Nagaki and M. Takighira, "An approach of hip motion compensation using laser range sensor for biped walking robot," The 30th Annual Conf. of the IEEE Industrial Electronics Society, pp. 1064-1069, 2004.
- [8]. K. Hirai, M. Hirose, Y. Haikawa and T. Takenaka, "The development of Honda humanoid robot," IEEE Int. Conf. on Robotics and Automation, pp. 1321-1326, 1998.
- [9]. K. Kaneko et al., "Humanoid robot HRP-2," IEEE Int. Conf. on Robotics and Automation, pp. 1083-1090, 2004.
- [10]. J. Yamaguchi, A. Takanishi and I. Kato, "Experimental development of a foot mechanism with shock absorbing material for acquisition of landing surface position information and stabilization of dynamic biped walking," IEEE Int. Conf. on Robotics and Automation, pp. 2892-2899, 1995.

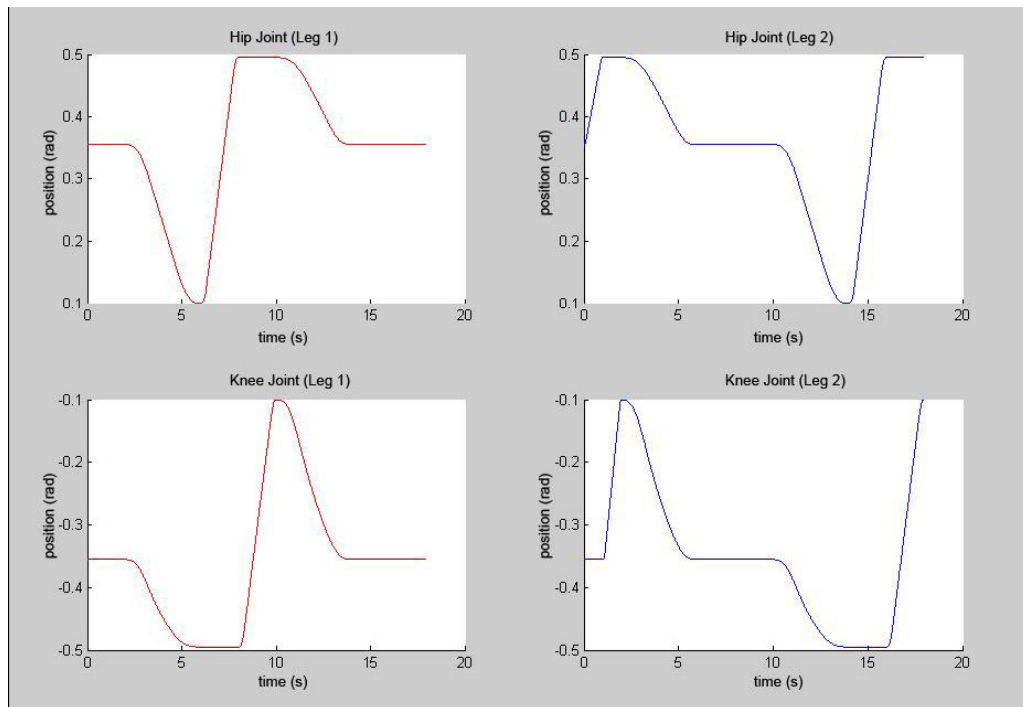


Fig. 7: Joint positions for simulated walk

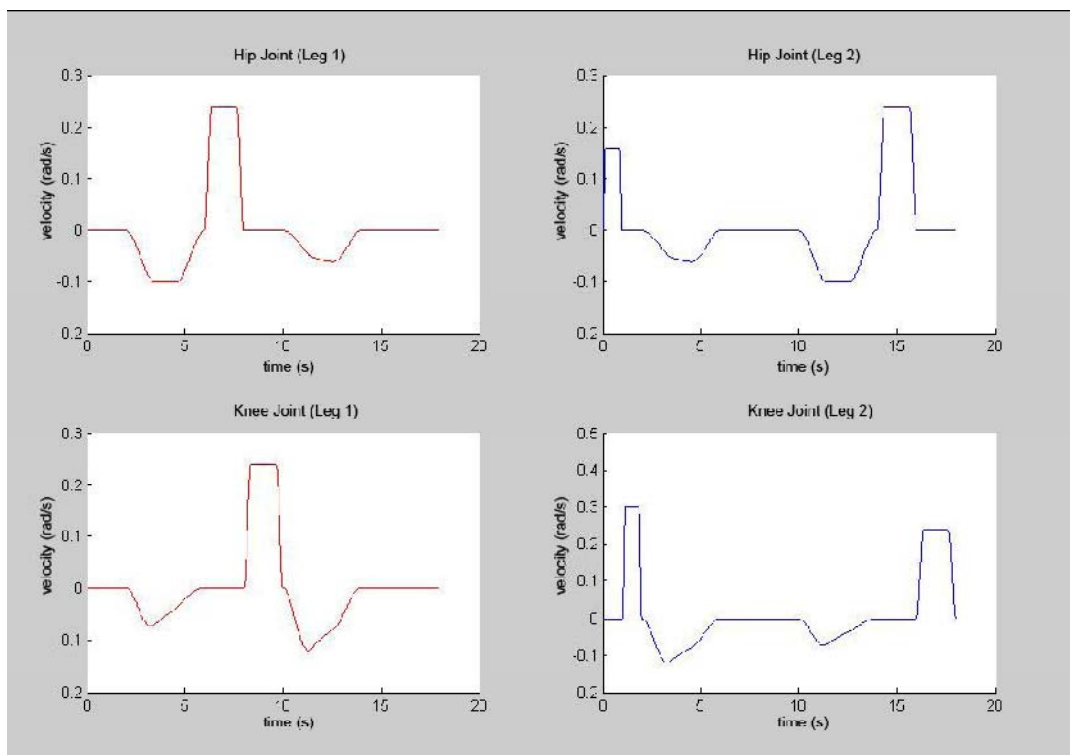


Fig. 8: Joint velocities for simulated walk

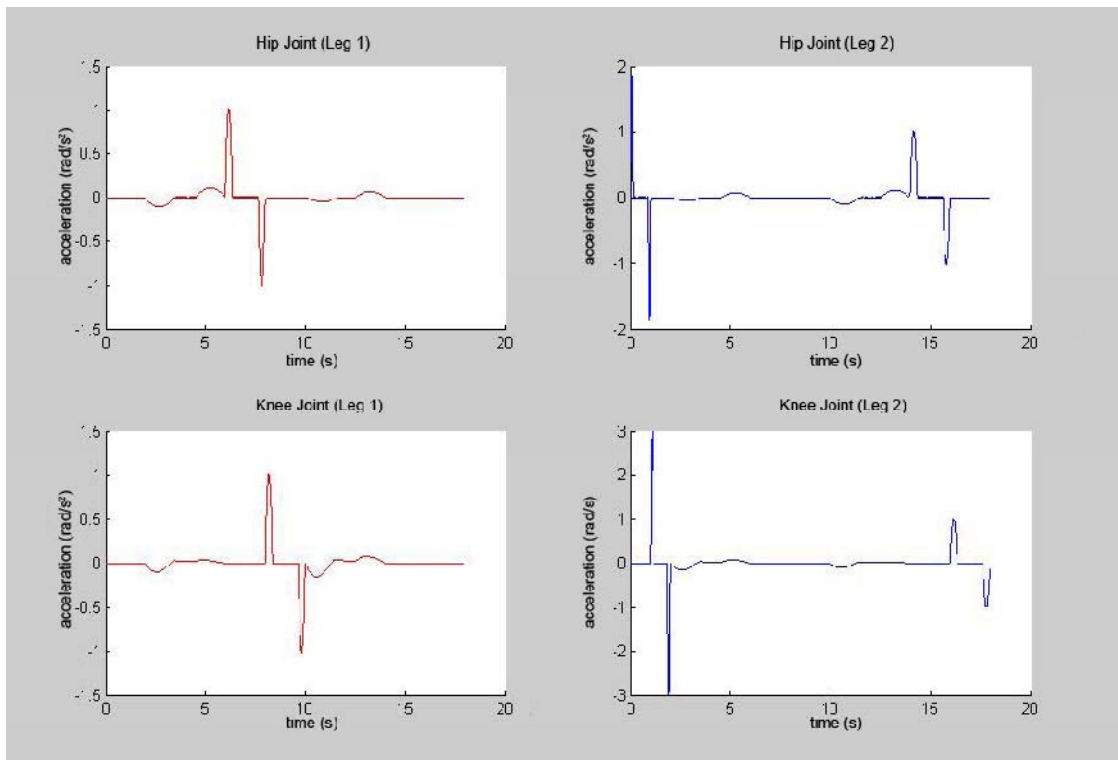


Fig. 9: Joint accelerations for simulated walk



Integration of the Hybrid-Structure Haptic Interface: HIPHAD v1.0

Tunç Bilginçan¹, Erkin Gezgin¹, Mehmet İsmet Can Dede^{1*}

^{1*} Izmir Institute of Technology, Department of Mechanical Engineering, Robotics Laboratory
Gülbahçe, Urla, Izmir, Turkey 35430
candede@iyte.edu.tr

Abstract

Design, manufacturing, integration and initial test results of the 6-DoF haptic interface, HIPHAD v1.0, are presented in this paper. The hybrid haptic robot mechanism is composed of a 3-DoF parallel platform manipulator, R-Cube, for translational motions and a 3-DoF serial wrist mechanism for monitoring the rotational motions of the handle. The device is capable of displaying point-type of contact since only the R-Cube mechanism is actuated. The dimensions and the orientation of the R-Cube mechanism are reconfigured to comply with the requirements of the haptic system design criteria. The system has several advantages such as relatively trivial kinematical analysis, compactness and high stiffness. The integration of the system along with its mechanism, data acquisition card (DAQ), motor drivers, motors, position sensors, and computer control interface are outlined.

Keywords: Haptic interface, Parallel manipulators, R-Cube

1. Introduction

Among all senses, touch sense is the most amazing and necessary one. In embryos, it develops and activates before all other senses. It provides information about texture, shape, temperature, weight, etc. of an object or environment. Touch sense is the most durable sense organ because it employs many connections to nervous system from every single part of the body. This complexity also provides reliable sensory inputs to cerebral cortex of the brain. Basically, the mechanoreceptors can be classified into two groups based on the location in the body. Kinaesthetic receptors are located in muscles, tendons and joints of the body and cutaneous receptors located in the skin. Nowadays, haptics technology is developing to stimulate both of these systems.

The word Haptic, based on an ancient Greek word called haptios, means related with touch. As an area of robotics, haptics technology provides the sense of touch for robotic applications that involve interaction with human operator and the environment. The sense of touch accompanied with the visual feedback is enough to gather most of the information about a certain environment. It

increases the precision of teleoperation and sensation levels of the virtual reality (VR) applications by exerting physical properties of the environment such as forces, motions, textures. Currently, haptic devices find use in many VR and teleoperation applications such as computer aided design, entertainment, education, training, rehabilitation, nano-manipulation, virtual prototyping and virtual sculpturing.

Various types of haptic devices are developed, and they are employed in different types of tasks. Especially for accurate teleoperation and precision required VR applications, high precision haptic systems are required with respect to the current commercially available haptic devices. In order to meet this precision criterion, in this work, the aim is to design and manufacture a 6-DOF high precision desktop haptic device.

This paper focuses on the integration of a general purpose 6-DoF haptic desktop interface along with its mechanical, electromechanical and electronics components. The design criteria of the system are listed as high stiffness, high precision and high loading capacity (high force-feedback capability). The design process of the device is outlined in [1]. The system is selected to have hybrid structure that is composed of a 3-DoF parallel mechanism for translational motions and a 3-DoF serial mechanism for rotational motion.

The parallel mechanism is a modified R-Cube mechanism and it is actuated with direct driven brushless DC motors to simulate point-type of contact. The mechanism for rotational motions is a passive mechanism with only position sensors to monitor the motion of the handle.

The next section provides a brief summary on the haptic devices. Haptic devices are classified by their haptic sensation types, and mechanism types. The fundamentals and basic components of a haptic device design are also described in the following section. The next section is dedicated to design, analysis and simulations of the mechanism. Also, in this section, the design criteria are listed and discussed, the design procedure is presented both for translation and orientation

mechanism along with the kinematics analysis for the mechanism. The manufacturing processes of the mechanism are explained in Section 5. Finally, in the last section, the integration of the mechanical, electro-mechanical and electronic components are presented, part selection and integration of the complete system is described and experimental results are provided and discussed.

2. Background

Wide variety of types and sizes of haptic devices are utilized in various state-of-the-art applications for both scientific and commercial purposes. Haptics technology is usually used for complex tasks such as controlling a manipulator in hazardous environments, minimal invasive surgery, robotic rehabilitation, nano-manipulation task, 3D design, education, and training applications.

In this section, the aim is to describe previous haptic applications and clarify the concept of haptics. In order to achieve this objective haptics technology is investigated in three separate groups by their: (1) feedback types, and (2) mechanical structures.

2.1. Kinaesthetic and Cutaneous Haptic Devices

Kinaesthetic receptors are located in muscles, tendons and joints of the body as shown in Fig. 1(a). The kinaesthetic system refers to the awareness of force, motion, position and low frequency vibration. Cutaneous receptors are located in the dermis and epidermis layer of skin as shown in Fig. 1(b). Cutaneous system refers to the awareness of touch, pressure, stretch, texture and high frequency vibration.

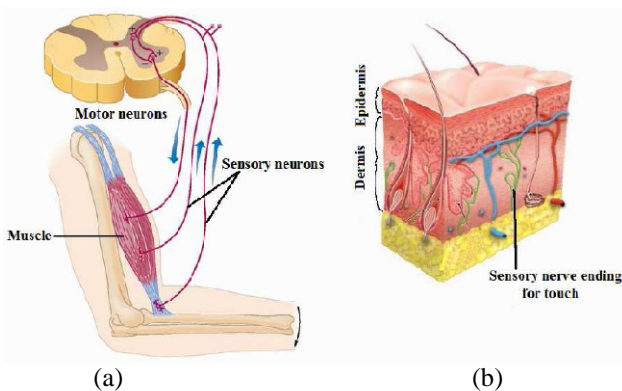


Fig. 1. Types of mechanoreceptors receptors: (a) Kinaesthetic, (b) Cutaneous [2]

Kinaesthetic display devices are human-computer interfaces that can simulate kinaesthetic parameters of an environment or an object, such as motion, location, weight and rigidity. Recently, kinaesthetic haptic devices are the most common type of haptic interfaces. Several types of

robot arm mechanisms have already been configured as kinaesthetic haptic devices. However, it is still an active field of research and development. Wearable haptic devices [3 & 4] and desktop haptic devices [5 & 6] are the most common device types of this class. An example of a haptic desktop device is shown in Fig. 2.



Fig. 2. Prototype of 3-DOF parallel-type haptic device [6]

Cutaneous display devices are human-computer interfaces that can copy tactile parameters of a surface such as texture, shape, roughness and temperature. Cutaneous device technology has been developed making use of several technologies such as mechanical needles actuated by electro-magnetics, piezoelectric materials, shape memory alloys and pneumatics. Various types of tactile display devices and tactile actuation systems are still an active research area. A tactile display device called VITAL1 is shown in Fig. 3. It has an 8x8 arranged pin matrix that is actuated by electro-magnetic actuators [7].



Fig. 3. VITAL1: vibrotactile display [7]

Combination of kinaesthetic and cutaneous sensation in one haptic device improves realistic hand and object interaction between user and computer. Currently most of the developed haptic interfaces are separated as, force feedback devices and tactile devices. Nevertheless some combined haptic systems that have the capability to stimulate both kinaesthetic and cutaneous receptors.

A pen-like haptic interface is shown in Fig. 4. The system is based on a tactile display and a vibrating

module. It is also combined with PHANTOM™ haptic system in order to add kinaesthetic feedback capabilities to the pen-like haptic interface [8].

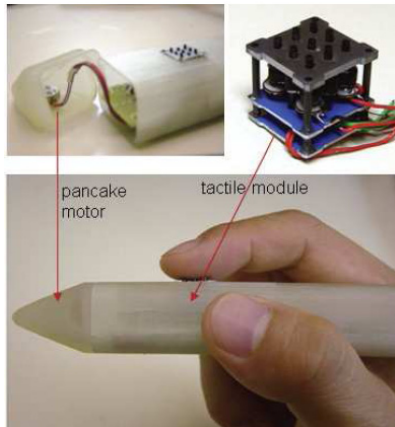


Fig. 4. Prototype of a pen-like Haptic Interface [8]

2.2. Haptic Device Mechanisms

Serial manipulators are the most common industrial robots that have been widely used variety of applications. They have serial mechanical arm structure, which is a composition of serial chain of links and joints. The main advantage of the serial manipulators is their large workspace with respect to their footprint. However their low stiffness, amplified errors from link to link due to their open kinematic structure are their main disadvantages. The serial structure has to carry and move the large weights of links and the actuators; hence it has limited loading capacities.

A parallel manipulator is a closed-loop mechanism with an end-effector placed on the moving platform that is connected to the ground with kinematic chains. Parallel manipulators have some structural advantages with respect to serial manipulators such as their higher precision, robustness and stiffness. The mechanism has to carry relatively low mass due to its ground fixed actuators. Therefore, parallel manipulators have higher loading capacity with respect to the serial manipulators. Their major disadvantage is their limited workspace, and low stiffness in singular positions.

A Hybrid manipulator is a combination of parallel and serial manipulators. They embrace the advantages of both serial and parallel manipulators.

Serial structures have been used in many haptic interface designs. Serial structure haptic devices are commercially available and probably the most well known devices are the products of Sensable Technologies [9]. The PHANTOM haptic device (Fig. 5) is currently used in various types of applications that range from commercial to scientific purposes.



Fig. 5. PHANTOM® Desktop™ Haptic Device [9]

Wearable haptic interfaces are usually designed in serial structure in order to fit the mechanism to human body. These haptic interfaces are frequently used as rehabilitation systems. An example for such an application is the wearable haptic interface shown in Fig. 6. The Maryland-Georgetown-Army (MGA) Exoskeleton has 6-DOF and it is designed and developed for shoulder rehabilitation applications [10].



Fig. 6. The MGA Exoskeleton [10]

Various researchers have recently designed several types of parallel structure haptic interfaces. Most of the published designs in the literature are based on Delta structure [6].

In Fig. 7, a modified version of Gough–Stewart platform is configured as 6-DOF parallel haptic device. The system has cable-driven pantographs and rotational electrical actuators for improved workspace and output bandwidth [11].

Hybrid manipulators have the advantages of a parallel structure and serial manipulators such as high loading capacity, manipulability, stiffness, high precision, robustness and relatively large workspace. Commercial hybrid haptic devices are also available in the market for various types of applications such as Force Dimension's Delta-based haptic devices [12]. The Delta-based hybrid haptic device, Omega 6, from Force Dimension is shown in Fig. 8.



Fig. 7. 6 URS Haptic Device [11]



Fig.8. Omega 6 haptic device [12]

3. Haptic Desktop Device Components

Towards developing a new haptic desktop device, a designer has to identify the task that the haptic device will be employed. According to the task requirements, the design criteria of the haptic device have to be formed and the components should be selected. Although the components of a haptic device vary depending on the outlined types of the devices, basically all haptic systems are composed of mechanical, electro-mechanical, electronics and software parts. In this section, the commonly used components of the haptic desktop devices are investigated and discussed.

3.1. Mechanical Components

Mechanical components of a haptic device can be listed as the mechanism, material and drive system. Mechanism selection is probably the most important phase in developing a haptic device. Therefore the selection procedure is outlined in the next section. In this section, only the materials and drive systems of the haptic devices are explained and discussed.

3.1.1. Materials for the mechanism

In haptic devices the specifications of the selected material for the mechanism are directly related with the quality of the haptic perception. The weight of the mechanical components must be minimized and the

device has to have low inertia and high stiffness. Hence the most important specifications for the design haptic device material are;

- i) Low density
- ii) High strength and rigidity

In order to minimize the gravitational effects, haptic devices are manufactured from light weight materials such as aluminum, nickel, titanium alloys and plastics. Haptic devices transmit the forces that are applied by the user. Hence, the rigidity and the strength of the mechanism are important for precision and perception of the system. As a consequence strength to weight ratio is an important factor, which has to be considered in haptic device development.

Among the other alloys, aluminum alloys is the most remarkable material in haptic devices. In general aluminum alloys have reasonable price, good machinability, high corrosion resistance and vital specifications outlined above.

Non-metallic material plastics also provide good strength to weight ratio and very low cost which are used in many haptic devices. In mass production of the haptic devices, plastic injection molding is an easy manufacturing process that is used for the manufacturing of the least important parts. Hence in general, the commercial haptic devices are composed of plastic and aluminum alloy parts and the custom haptic devices include only aluminum alloy components.

3.1.2. Drive systems

In haptics, drive systems are used for the transmission of the torques from actuators to the operator and the performance of the actuation system is more important with respect to the other robotic systems. Hence selection of the appropriate drive systems considering the type of the haptic device is important. The appropriate drive systems for a haptic device can be selected depending on the two broad classes;

- i) Admittance type devices
- ii) Impedance type devices

Admittance haptic devices include force sensors that sense the applied force by the operator and adjust the operator's position according to the manipulated virtual or real object. Hence the traditional transmission mechanisms such as gears can be employed in admittance type haptic devices. Nevertheless, the precision loss due to the use of transmission mechanisms is an important fact, which has to be considered in haptic device design. Therefore, high efficient and precise gearing transmission technology such as harmonic drive is currently used in haptic devices. Harmonic drives provide nearly zero backlash, light weight and high torque reduction ratios. An example for an admittance type haptic interface is VISHARD7 which can be seen in Fig. 9. VISHARD7 is a 6-DOF mobile haptic interface for large remote

environments. The haptic interface is built by using brushless DC motors coupled with harmonic drive gears that provide relatively high force feedback capacity [13].



Fig. 9. Mobile haptic interface VISHARD7 [13]

In contrast to the admittance haptic devices, in an impedance haptic device, position sensors sense the position of the operator, and then the computed forces are applied to the user. Therefore, impedance type haptic devices have to be back-drivable which is possible with low inertial and low frictional drive systems. Today most of the commercially available haptic desktop devices such as Phantom, Omega and Falcon are impedance type haptic systems. They are back-drivable and have a common mechanical transmission system called Capstan drive mechanism (Fig. 10). The capstan drive mechanism consists of tendon wrapped around pulley that actuates a semi-circular link. The ratio between the pulley's and the semi-circular link's diameters provides reduction that increases the force feedback capacity of the haptic systems. Capstan drive mechanism of a 1-DOF haptic paddle can be seen in Fig. 10 [14].

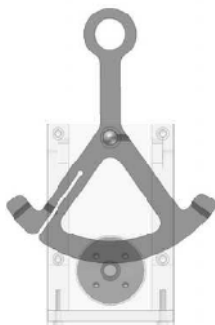


Fig. 10. Capstan drive mechanism of a haptic paddle [14]

3.2. Electro-Mechanical Components

Electro-mechanical components of a haptic desktop

device can be listed as the brakes, sensors and actuators. In haptics usually two types of sensors are used; position and force/torque sensors. Position sensors measure the angles or positions of the links and this sensory input is transmitted to the computers. Depending on the type of the haptic system, force/torque sensors are also used especially in admittance type haptic devices. Moreover brakes and motors are used for the actuation of the mechanism and the properties of the actuation system are directly related with performance of the haptic device. In this section, electro-mechanical components of a haptic device is presented and discussed.

3.2.1. Brake systems

Haptic interfaces can also be categorized as active or passive interfaces depending on the employed actuators. Active haptic interfaces employ active motors, to provide active feedback to the user. On the other hand, passive haptic interfaces use dampers or brakes that dissipate the energy of the motion. In contrast to the active actuators, passive actuators such as brakes, dampers and clutches are actually stable components that they can only absorb the energy of the system. Therefore they can provide relatively larger forces without risking the user's safety. Furthermore it can improve the stability of the system. However passive actuators can only simulate some models such as high stiff wall or any rigid surface but they cannot simulate a model of an elastic surface or moving object. Nevertheless, due to the outlined advantages, dissipative components are recently employed in some haptic devices for better force-feedback capabilities and higher perception levels. Currently mechanic friction, electro-magnetic, magneto-rheological, electro-rheological brake systems are employed and tested in haptic devices.

Mechanical brake system of the previously presented, 4-DOF wearable passive haptic interface is shown in Figure 3.7. The brake system of the device is located at the top of the exoskeleton and the mechanism consists of separate transmission cables for actuation with brake mechanism. In this example, the requirements of an exoskeleton haptic device such as simplicity, lightweight, high safety and hard-contact simulation are provided by passive actuation [15].

An example for hybrid actuation is the 2-DOF haptic interface that is used for medical purposes has rotational and translational axes actuated by both active and passive actuators. The combination of active motors and passive brakes improves sensation levels by reflecting the natural friction and high level force feedback of the haptic colonoscopy [16].

Electromagnetic brakes such as eddy current brakes (ECB) are also employed in haptic systems. Some of the specifications of the ECBs such as programmable damping rates, applicability to the linear motion, high

frequency responses make them very appropriate for passive haptic interfaces. The development and implementation of an ECB to a haptic interface is proposed in [17].

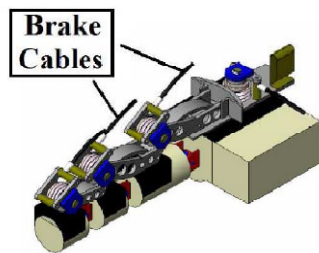


Fig. 11. Wearable passive haptic interface [15]

Magneto-rheological (MR) fluids and electro-rheological (ER) fluids are types of smart materials. They are both capable to change their viscosity reversibly within milliseconds by controlling the applied magnetic or electric field. This feature can be applied to wide range of applications such as variable damping systems. Especially in haptics due to the short response time and damping abilities of both MR and ER fluids are used as braking systems. An example of MR fluid brake system in haptic devices is presented in [18].

3.2.2. Actuators

Motors are the active actuation components in haptic devices. The performance of an active haptic device is directly related with the characteristics of the actuators. In order to provide high level sensations in a haptic interface, the actuators of the system must have low inertia, low friction, low torque ripple, high back-driveability, low backlash and high torque ratings. The selection of the appropriate actuators to meet the requirements of the haptic device is important. Currently various types of active actuators are employed in haptic desktop devices such as pneumatic, hydraulic, shape memory alloys (SMA), piezoelectric, pneumatic muscle, ultrasonic, magnetic and electrostatic actuators.

Currently, DC motors are the most common actuation systems utilized in haptic devices. Most of the haptic devices in literature, including the commercial ones are configured with DC motors. DC motors are the pioneer electrical actuation method with respect to the other actuation methods. The performance, limitations, dynamics and control methods of the DC motors are well known. Moreover, DC motors have low cost, high reliability, and simple structure. Hence in robotics, actuation with brushed or brushless DC motors is the most preferred method. However, in haptic devices other actuation systems can provide better results.

Shape memory alloys (SMA) are smart materials that have the ability to change its dimension via heat

variations. Recently SMAs are employed in various types of applications including haptics. Although it seems that the SMA actuators are only employed in tactile haptic devices, SMA actuators have the potential to be used in SMA actuated haptic devices.

Pneumatics converts air pressure to rotational or linear motion. The main advantage of the pneumatic actuation is the flexibility of the actuators which is necessary in a device that interacts with human. Due to the difficulties of position and force control, the pneumatics is not common in haptic devices. An example for pneumatic parallel haptic interface is proposed by Masahiro Takaiwa et al. The proposed device is a parallel mechanism that includes 6 pneumatic actuators and potentiometers [19].

Similar to the human muscles, pneumatic muscle actuators (PMA) are contractile components work with pressurized liquid or gas. The specifications of the PMAs are similar to the conventional pneumatic actuators, but the power/weight ratios of the PMAs are relatively greater. Due to the presented advantage, PMA actuators are suitable for exoskeleton haptic devices. A 7-DOF PMA actuated exoskeleton haptic device is presented in [20].

Ultrasonic motors are piezoelectric motors that are actuated by ultrasonic vibrations. Similar to the DC motors, they consist of a rotor and a stator which is produced by piezoelectric materials. The ultrasonic motors are driven by two sinusoidal signals with a different phase. Associated with the phases of the signals the ultrasonic actuator has three phases; free, active and fixed phase. Thus, ultrasonic sensors are capable to actuate a haptic device as a hybrid (passive/active) system without using brakes or clutches. An example of such a mechanism is actuated with only four ultrasonic actuators that reflect bi-directional forces [21].

Magnetic levitation actuators are probably the most interesting ones among the other actuators. The theory is based on suspending a handle object in magnetic field. A study on developing a magnetic haptic device is presented by Berkelman et al. 6-DOF device has motion ranges of ± 5 mm and ± 3.5 degrees in all directions and can generate 20N force, 1.7 Nm torque [22]. A commercial magnetic levitation haptic is the product of Butterfly Haptic Inc.

3.2.2. Sensors

In haptic device design, appropriate sensor selection is important for the electro-mechanical precision of the mechanism. Essential sensors of a haptic device are force/torque and position sensors. Position sensors can be categorized in two groups; analog and digital sensors. In general, hall-effect and resistive sensors are frequently employed in haptic devices due to their high resolution and low cost.



However the noisy nature of the analog signals needs extra care during transfer and conversion to the digital signals. Besides potentiometers have various technical specifications that have to be evaluated carefully for use in haptic devices, such as mechanical resolution, linearity errors and resistance tolerance. On the other hand, digital encoders provide more accurate and noise free signal therefore digital encoders are more convenient for haptic applications. Nevertheless today, the cost of the digital encoders is relatively high and supplied resolution is limited.

Currently commercially available haptic devices are composed of both optical encoders and potentiometers. 6-DoF PHANTOM haptic device includes optical encoders and potentiometers on its active and passive joints respectively.

A variety of sensors are designed to measure forces/torques for different applications. The components of a force/torque sensor can be categorized in two groups as; the construction of the sensor and the sensing element. The construction of force sensors has to be designed considering the requirements of the application and the sensing element. Currently, strain gauges and piezoresistive sensing elements are the most common sensing elements in the force/torque sensor design. In admittance type haptic devices, both custom and commercial type force/torque sensors can be used. Although the commercial type sensors have relatively high cost, they can provide more accurate and reliable measurements.

3.3. Electronics

Data acquisition (DAQ) cards and motor amplifiers can be listed as electronic components of a haptic device. DAQ cards are the systems that measure, process, convert and transmit real world data to computers. Although the components of a DAQ system vary, depending on the specified tasks, DAQ systems may include, analog to digital converters (ADC), digital to analog converters (DAC), encoder decoders, counters, timers, digital inputs and outputs. In this section, appropriate DAQ systems for a haptic device are reviewed.

During the development of a robotic system, commercial DAQ systems provide fast and reliable environment for initial tests of the integrated mechanism. Various DAQ cards are available for haptic device development with varying low prices. The primary specification of a DAQ system in haptic device design is the sampling rate requirement of the system. The selected commercial DAQ acquisition system has to support at least 1 KHz sampling rate [23]. Moreover the supported software environments such as Simulink and LabVIEW are also important for easy programming phases and initial test of the device. Some of the commercial DAQ

system providers can be listed as National Instruments (NI), Labjack, Quanser, Sensoray, Diamond Systems, dSpace, IOTech, Servo2go.

Towards developing an end product, custom designed and manufactured data acquisition cards and drives for the developed system are a necessity. As a result of the literature survey, it is observed that PIC© (Programmable Interface Controller) based DAQ cards via serial port (RS-232) is commonly used in most haptic device designs. PIC is a popular microcontroller that is developed by Microchip Technology Inc. It is used in many digital control applications due to their low cost, easy development process, wide availability and high ability.

4. Mechanism Design

This paper outlines the design of a general purpose haptic device for fine VR and teleoperation applications that require higher level of precision. In order to develop a general purpose haptic device, a kinaesthetic desktop device is selected since it supports a wide variety of applications. The hybrid mechanisms have both the advantages of serial and parallel structures as discussed in Section 2.2. Therefore, the structure of the mechanism is selected to be configured as a hybrid structure.

Table 1. Design criteria of the haptic device

Sensation	Kinaesthetic
Structure	Hybrid
Concept of Structure	Desktop Device
Footprint	<150-200 mm ²
DOF	≥6
Force feedback	Translation $\vec{u}_1, \vec{u}_2, \vec{u}_3$
Workspace	>100 W x 100 H x 100 D mm
Continuous exertable force	> 0.8 N
Nominal Resolution	< 0.1 mm

The device is designated to provide feedback signals to determine the pose of the rigid body in space, therefore it should be configured as a 6-DOF mechanism. Only point type contact is considered for this work, so the DOF can be grouped as 3-DOF active translational and 3-DOF passive rotation. Considering the task requirements the design criteria of the mechanism are listed in Table 1. The workspace, continuous exertable force and the resolution of the system are selected to be compatible with the commercial haptic desktop devices.

4.1. Conceptual Designs

According to the specified design criteria, the possible mechanism types for the hybrid structure reviewed in two groups, translation and orientation mechanisms. For translational mechanism, Delta, Cartesian Parallel, and R-Cube manipulators are considered and for orientation mechanism Agile Eye, Hybrid-Spherical and Serial-Spherical manipulators are considered in conceptual designs [1].

4.1.1. Translation mechanisms

Delta robot is a 3-DOF parallel manipulator with 3RRNR structure that is used for translational motions for various haptic device designs (Fig. 12(a)). It has seventeen links connected with twenty-one joints that are actuated by three ground fixed rotary motors. It has coupled motion and its structure provides high resolution, manipulability and high loading capacity with relatively limited workspace.

Cartesian manipulator is a 3-DOF parallel manipulator with 3PRRR structure. It can generate only translational motions (Fig. 12(b)). It has three legs that consists eleven links connected with twelve joints including base and platform. The actuation is provided by three prismatic joints with linear actuators. The motion of the manipulator is de-coupled in the direction of the prismatic axes.

R-CUBE manipulator is a 3-DOF parallel manipulator with 3NRRR structure (Fig. 12(c)). It can generate translational motions with only revolute joints. It has three legs and seventeen links connected with twenty-one revolute joints. The motion of the moving platform is directly related with the input of the first links, therefore the structure has decoupled motion making use of rotary actuators. Its kinematics analysis is simple with respect to other manipulators due to the de-coupled motion. The singularities of the manipulator only exist at the limits of the workspace which is easy to avoid [24].

4.1.2. Orientation mechanisms

Agile Eye is a 3-DOF parallel manipulator with 3RRR structure (Fig. 13(a)). Its workspace is a 140° cone with ±30° in torsion. It has eight links connected with nine joints. As a constructional advantage, it has ground fixed sensors. The structure has coupled motion.

Hybrid-Spherical is a 3-DOF hybrid manipulator with 2RE+R structure (Fig. 13(b)). Its workspace is a spherical surface with ±90°(x) ±90°(y) ±120°(z). It has four links connected with six joints. It has 2 ground fixed and 1 moving sensors.

Serial Spherical Manipulator is a 3-DOF serial manipulator with RRR structure (Fig. 13(c)). As a consequence of its serial structure, it has large workspace with a range about ±120° around all directions, but it has

two moving sensors.

The comparison tables of the conceptual designs for translation and orientation mechanisms are shown in Tables 2 and 3 respectively. These two tables are used to select the configuration for the prototype of the hybrid mechanism.

Table 2. Comparison of translation mechanisms

Mechanism	Delta	Cartesian	R-CUBE
Number of Joints	21	12	24
Number of Links	17	11	17
Kinematic analysis	Complex	Simple	Simple
De-coupled motion	No	Yes	Yes
Actuation	Revolute	Prismatic	Revolute
Ground fixed motors	Yes	Yes	Yes
Types of joints	R	R-P	R

Table 3. Comparison of the orientation mechanisms

Mechanism	Agile eye	Hybrid - Spherical	Serial-Spherical
Number of Joints	9	6	3
Number of Links	8	4	4
Kinematic analysis	Easy	Partially Complex	Complex
De-coupled motion	No	Yes	No
Workspace	Cone 140° with ±30° torsion	±90° ±90° ±120°	±120° ±120° ±120°
Sensation	Revolute	Revolute	Revolute
Ground fixed sensors	Yes	Partially	No
Types of joints	R	R-S-SI	R

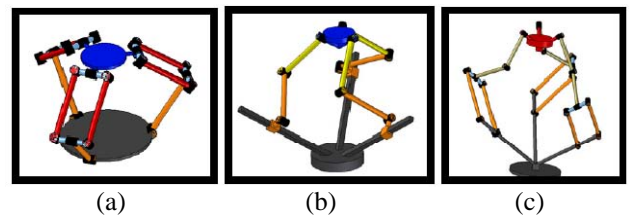


Fig. 12. (a) Delta, (b) Cartesian, (c) R-Cube parallel mechanism

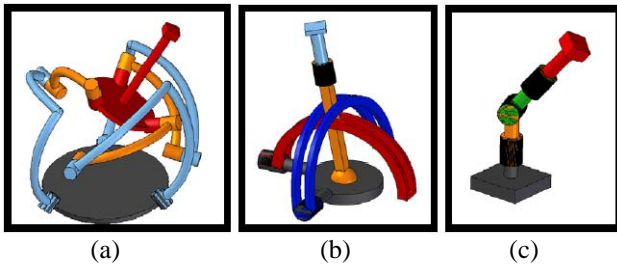


Fig. 13. (a) Agile Eye, (b) Hybrid-Spherical, (c) Serial-Spherical

4.2. Design of the Final Translation Mechanism

Design of the translational mechanism is presented into three sections (1) Structural design parameters, (2) Mechanical part designs and (3) Link parameter determination. In the first subsection, the design criteria of the mechanism are identified. The necessary mechanical component designs are developed in the second subsection and finally, in the third subsection the dimensions of the links are determined.

4.2.1. Structural design criteria

In the prototype mechanism, the original structure of R-CUBE had some actuation problems due to the unequally distributed gravitational effects. Hence, the original structure of R-CUBE is reoriented and the effect of gravity is distributed equally to all actuators. Apart from that, such an oriented configuration also facilitates the controller design and gravity cancellation algorithms.

The original structure configuration and the proposed configuration are shown respectively in Fig. 14(a) and 14(b). The rotation of the structure is based on isometric projection problem, which is explained in the following section [25].

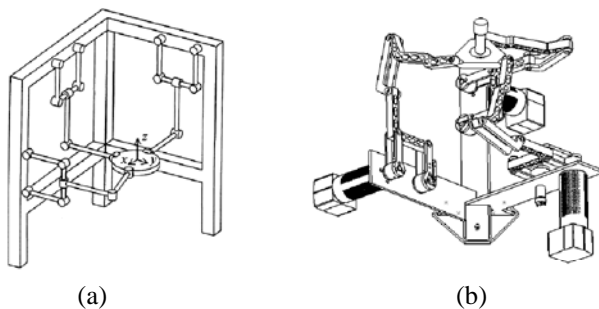


Fig. 14. R-CUBE designs: (a) Original design [24], (b) Rotated design

In haptics, due to the random motion of the operator, motion through singular positions must be restricted. During the design procedure two singularity conditions

are encountered which are important to avoid mechanically. One of them is already discussed in the work in [24] and presented as avoidable with a proper design. The reported singularity is at $\theta_i = \pm 90$ of the first link of the mechanism which is shown in Fig. 15(a). Although the four-bar mechanisms are reported as possible engineering trouble in [24], the problem is resolved by precise manufacturing technologies and the redundant constraint structures are used in order to avoid the singularity position mechanically (Fig. 15(b)).

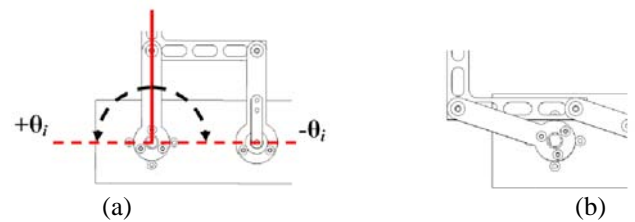


Fig. 15. Singularity in the first link: (a) Singularity if $\theta_i = \pm 90$, (b) Singularity avoidance

In Fig. 16, the link lengths of the j^{th} link is denoted by l_{ij} for $j=1, 2, 3, 4$. The singularity at $\theta_{i4}=0$ may cause trouble at the boundaries of the workspace. Hence the link lengths of the link, l_{ij} for $j=2, 3, 4$ are configured to avoid any link collisions and possible singularity positions. The link length determination process is based on the iterative simulations of the mechanism that were carried out in CosmosMotion[®].

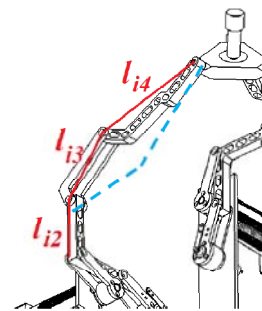


Fig. 16. Length of the second, third and fourth links

The location of the workspace is important for the compactness of the design and it is limited with the footprint of the haptic device which is specified in the design criteria table (Table 1). The graphical representations of the workspace and S_i parameter which defines the distance of the actuation axis from the origin of the base frame are shown in Fig. 17. The location of the workspace is determined with S_i parameter by identification of the dimensional limitations of the mechanism.

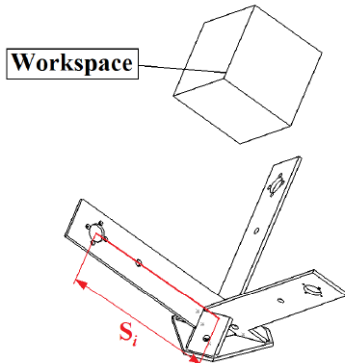


Fig. 17. The workspace and the S_i parameter of the mechanism

Lengths of the first links (Fig. 18) determine the volume of the workspace. According to the design criteria the first link length of the mechanism is calculated by direct kinematics analysis formula which is shown in detail in the following section on mechanism analysis in order to meet the 120x120x120mm workspace specification.

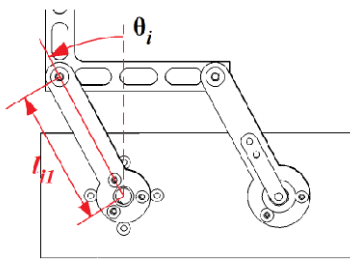


Fig. 18. Joint variables and length of the first links

4.2.2. Component design criteria

The main criterion of the parallel mechanism is to develop a universal design that is appropriate for different types of orientation mechanisms, so the moving platform of the mechanism (Fig. 19) is designed complying with this criterion. An example of this is presented in Fig. 20(a), where instead of the orientation mechanism a simple handle mechanism is mounted on the platform thus the hybrid mechanism's total DOF is decreased to 3-DOF. Similarly, mounting a 4-DOF mechanism can result in a total 7-DOF hybrid structure.

During the design of haptic desktop devices, one of the most important design specifications is the handle space that is required for operator's hand to fit ergonomically, especially when converting a standard manipulator design into a haptic device. Therefore during the design of the final mechanism, the ergonomics of the handle space is also conceived in the design phase.

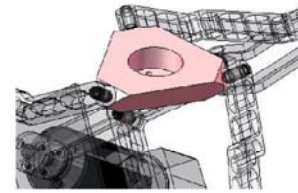


Fig. 19. Platform of the mechanism

In the design, the locations of the sensors are selected for aesthetic considerations and to have a universal design for incorporating various sensor types. The three position sensors of the mechanism mounted at the base frame on the free rocker of the four-bar mechanisms as shown in Fig. 20(a) denoted as 1, 2, 3. The position sensors of the mechanism can be replaced with various types of sensors only by remanufacturing the sensor housings. In Fig. 20(b), the sensor mechanism is shown with the sensor housing denoted as 1, the sensor as 2, the bearings as 3, and the shaft of the sensor as 4.

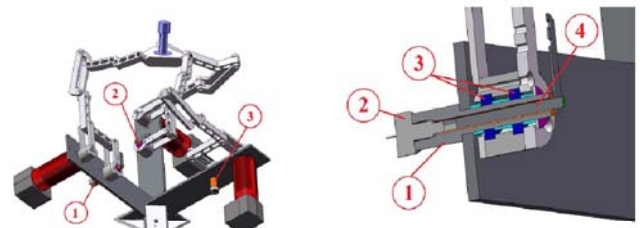


Fig. 20. Sensor locations and sensor housing designs: (a) Location of the sensors, (b) The design of the sensor housings

The CAD representation of the joint structure is shown in Fig. 21. The structure has a shaft (4), bearings (3), screws (1) and the bearing plates (2). The outer bearing plates at the left and right hand side of the image are shown in the Fig. 21. They provides leaning surface for the screws while fastening the joints. The inner bearing plate shown in the middle of the image prevents the outer races of bearings against getting stuck. The main objective in this design is to improve the mechanical precision of the joints. Besides it is also aimed to design a compact structure which has easy disassembling procedure.

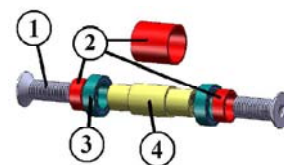


Fig. 21. CAD representation of joint components M4 screw, bearings and bearing plates

4.2.3. Link dimensioning and shape identification

Link dimensioning and shape identification of the translation mechanism are results of the structural and mechanical criteria outlined previously. The determination criteria can be listed as;

- i) Dimensions of the workspace
- ii) Location of the workspace
- iii) Universal design
- iv) Structure of the joints
- v) User's handle space requirements
- vi) Singularity avoidance

The lengths of the first links are determined to meet the workspace dimension specification. Previously defined 100x100x100mm workspace criterion is extended to 120x120x120mm, in order to avoid the motions in the close-range of the singular positions. The location of the workspace, which is important for the general dimensions of the mechanism, is identified with the max footprint criterion (Table 1). The universal design criterion sets the dimensions of the moving platform (Fig. 19); therefore the dimensions are determined by the size of the possible upper mechanisms. Volumes of the links are minimized to decrease the weight of mechanism. The cross-sectional area of the links is determined through the dimensions of the joint structure (Fig. 21). The second, third and the fourth link length and shape determination process is based on the iterative simulations carried out in SolidWorks[®] CosmosMotion[®] utilizing the singularity positions, link collisions and handle space ergonomics.

4.3. Design of the Final Orientation Mechanism

The serial structure proposed for the final design does not have any structural criteria. Therefore, link dimensioning and shape identification of the orientation mechanism's links is the result of criteria;

- i) Sensation levels
- ii) Ergonomic design
- iii) Available sensors

Due to the manufacturing limitations and precision requirements, previously employed orientation mechanism of the prototype system is replaced with the serial-spherical manipulator in the final design. The orientation mechanism, serial-spherical manipulator is a 3-DOF-RRR spatial serial mechanism shown in Fig. 22.

The mechanism is designed for monitoring the rotational motions of the user's hand, so it is designed in consideration with handle ergonomics. The design is manufactured in rapid prototyping machine in our laboratories and the ergonomics of the design are evaluated.



Fig. 22. Orientation mechanism

The primary challenge in the design of this mechanism is adjusting the size of the mechanism with huge amount of components, such as position sensors, bearings, cables and A/D converters. 3-DOF rotational motions of the end-effector are monitored through three miniature sensors as shown in Fig. 23(b). The A/D converters are mounted inside the mechanism (Fig. 23(a)) in order to reduce the noise level by converting the analog outputs of the position sensors to digital signals.



Fig. 23. Position sensors: (a) Location of the sensors, (b) Dimensions

The design procedure of the mechanism is finished with necessary modifications to facilitate the manufacturing process. Finally, the model is designed in CAD environment and blue-prints are prepared for the test of the ergonomics of the mechanism. The CAD design of the new configuration of the hybrid mechanism with motors, sensors, bearings is shown in Fig. 24.

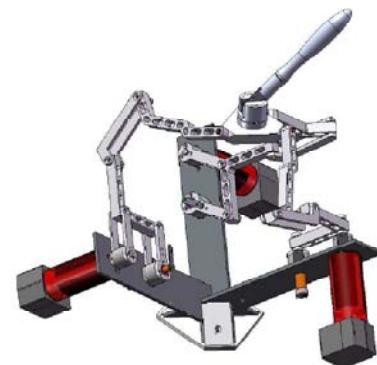


Fig. 24. The CAD representation of the final design

4.4. Kinematics and Static Force Analysis

Haptic devices are the systems that are used to manipulate virtual or real systems that may be a virtual or a robotic arm. In order to control a virtual or real system by a haptic interface, the position of the handle point has to be measured then measured or calculated forces from the VR system or the slave side of the teleoperation must be reflected back to the operator. The position of the tip point, W_r , (Fig. 25) must be calculated with direct kinematic analysis of the parallel mechanism (R-Cube) making use of the joint sensor readings. Forces on the VR system or teleoperation slave system must be calculated or measured to restrain the operator's motion with calculated forces. In this section the position and torque calculation formulas of the developed haptic device are presented and discussed.

In Fig. 25, position of the tip point, W_r , is defined as the intersection point of the last link connection surfaces on the moving platform. The origin of the base coordinate frame, O , is located at the intersection point of the unit vectors of the coordinate frame that is originated from the respective actuator axes. The mechanism parameters, variables and the rotated coordinate axes as shown in Fig. 25 that are used in the direct and inverse kinematics analysis, and in the static torque calculations.

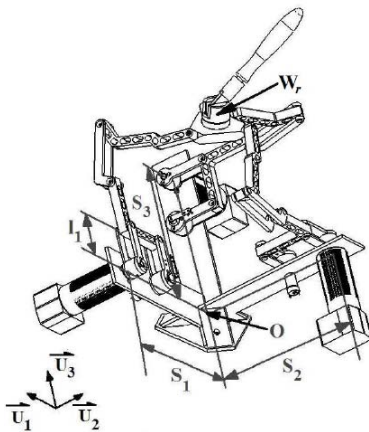


Fig. 25. Mechanism parameters

In the parallel mechanism, the translational motion of the platform is regulated by the orientation of the actuators. Due to the decoupled motion of the mechanism, the motion along \vec{u}_1 , \vec{u}_2 , and \vec{u}_3 axes is only dependent on the motors placed on the same axes which have rotations about \vec{u}_2 , \vec{u}_3 , and \vec{u}_1 axes, respectively. Therefore, the mechanism's direct and inverse kinematics analysis is relatively trivial. Nevertheless, the mechanism is only decoupled in rotated coordinate frame as shown in Fig. 25, hence the torque and position analysis of the system is

carried out in rotated coordinate frame. For VR or teleoperation applications coordinate frame is reoriented with rotation sequence presented in Eq. (1), (2) and (3). The reorientation angles, α and β , are calculated by using the isometric projection representation (Fig. 26) [25].

$$\hat{C}^{(R,W)} = e^{\tilde{u}_1\alpha} e^{\tilde{u}_2\beta} \quad (1)$$

$$\alpha = \arcsin(\tan 30^\circ) \cong 35.26^\circ \quad (2)$$

$$\beta = -45^\circ \quad (3)$$

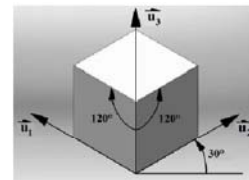


Fig. 26. Isometric projection

The control scheme of the slave system is based on the calculation of the W_r point by utilizing the measurements from the positions sensors. This procedure is generally called direct kinematics. In Eq. 4, the calculation of the position vector of the tip point, W_r , with respect to the origin point, O , in the ground reference frame which is presented in Fig. 25, is described.

$$\vec{W}_r = \sum_{i=1}^3 W_{r_i} \vec{u}_i \quad (4)$$

Components of the W_r vector are a function of the rotation amounts of the actuators, θ_i , as shown in Eq. 5. The zero position of the angle, θ_i , is represented with dotted line in Fig. 27. In Eq. 5, S_i is the distance between motor axes and origin point and l_i is the link length of the first link which is previously presented in Fig. 25.

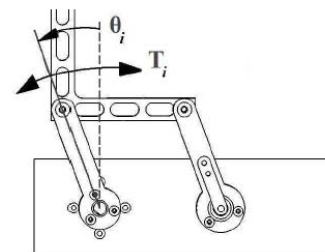


Fig. 27. Joint variable (θ_i) and torque (T_i) directions

$$W_{r_i} = S_i + l_i \sin(\theta_i); \quad i = 1,2,3 \quad (5)$$

The inverse kinematics solution is given in Eq. 6, 7 and 8. In inverse kinematics solution, the mechanical structure of the four-bar mechanism limits the motion of the first link to about $\pm 65^\circ$. Therefore, it is not possible to pass to the region where the cosines of the joint variables become negative. As a result of this, the sign ambiguity denoted with σ in Eq. 7 can be neglected and σ can be taken as +1 without the loss of generality.

$$\sin(\theta_i) = \frac{Wr_i - S_i}{l_i} \quad i = 1, 2, 3 \quad (6)$$

$$\cos(\theta_i) = \sigma \sqrt{1 - \sin^2(\theta_i)}; \quad \sigma = \pm 1 \quad (7)$$

$$\theta_i = \arctan_2(\sin(\theta_i), \cos(\theta_i)) \quad (8)$$

The components of the applied force, F , are calculated in the ground reference frame in Eq. 9.

$$\vec{F} = \sum_{i=1}^3 F_i \vec{u}_i \quad (9)$$

Torque demands for a specified force that has to be applied to the operator's hand can be formulated by Eq. 10. In Eq. 10, T is the torque required to be applied by the actuators about their respective axis of rotation as shown in Fig. 27, and F is the desired force to be applied to the operator's hand. Torque values for each actuator are calculated by taking cross product of the moment arm vector, Wr , and the force vector, F , and then taking the dot product with the respective actuator's rotation axis. The torque element in all axes that has the moment arm along its respective axis is neglected because the forces will not be transferred as a consequence of the rotation axis arrangement of links 2, 3, and 4. T is the torque applied by the actuator about each axis as shown in Fig. 25, and F is desired force to be applied to the operator's hand.

$$\begin{aligned} T_1 &= F_1(Wr_3) \\ T_2 &= F_2(Wr_1) \\ T_3 &= F_3(Wr_2) \end{aligned} \quad (10)$$

In Figure 4.23, the tip point of the parallel mechanism is denoted with Wr . The orientation mechanism is in the form of a spherical wrist configuration. Thus, its forward kinematics analysis is provided as a series of pure rotations as in Eq. 11. The orientation mechanism is a passive mechanism. The inverse kinematics solution is not required since the motion of the mechanism is not controlled by any actuation system. The measured angles from this mechanism are used only for the control of the

rotation motion in VR or teleoperation applications.

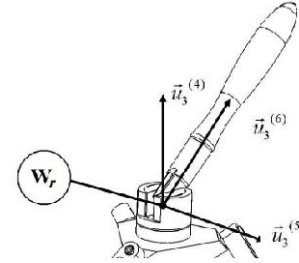


Fig. 28. Wr point of the mechanism

$$\hat{C}^{(3,6)} = e^{\vec{u}_3 \theta_4} e^{\vec{u}_2 \theta_5} e^{\vec{u}_3 \theta_6} \quad (11)$$

Three rotational sequences of the spherical orientation mechanism can be carried out by simple quaternion operations (Eq. 12-16) as any quaternion operator $q(\)^{-1}$ will rotate any vector around any axis by the desired amount of angle, provided that they are passing from a common point.

$$\begin{aligned} r_2 &= q_1(r_1)q_1^{-1} \quad ; \quad q_1 = \cos \frac{\theta_4}{2} + \vec{u}_3 \sin \frac{\theta_4}{2}, \\ q_1^{-1} &= \cos \frac{\theta_4}{2} - \vec{u}_3 \sin \frac{\theta_4}{2} \end{aligned} \quad (12)$$

$$\vec{u}_2^{(1)} = q_1(\vec{u}_2)q_1^{-1}, \quad \vec{u}_3^{(1)} = \vec{u}_3 \quad (13)$$

$$\begin{aligned} r_3 &= q_2(r_2)q_2^{-1} \quad ; \quad q_2 = \cos \frac{\theta_5}{2} + \vec{u}_2^{(1)} \sin \frac{\theta_5}{2}, \\ q_2^{-1} &= \cos \frac{\theta_5}{2} - \vec{u}_2^{(1)} \sin \frac{\theta_5}{2} \end{aligned} \quad (14)$$

$$\vec{u}_3^{(2)} = q_2(\vec{u}_3^{(1)})q_2^{-1} \quad (15)$$

$$\begin{aligned} r_f &= q_3(r_3)q_3^{-1} \quad ; \quad q_3 = \cos \frac{\theta_6}{2} + \vec{u}_3^{(2)} \sin \frac{\theta_6}{2}, \\ q_3^{-1} &= \cos \frac{\theta_6}{2} - \vec{u}_3^{(2)} \sin \frac{\theta_6}{2} \end{aligned} \quad (16)$$

Consider that the global axes are carried to the Wr point of the mechanism, and r_i shows the initial position of the tool point. Eq. 12 represents the first rotation of r_i around \vec{u}_3 by angle θ_4 . After calculating the new $\vec{u}_2^{(1)}$ (Eq. 13.), the second rotation θ_5 can be carried out around $\vec{u}_2^{(1)}$ to obtain r_3 (Eq. 14.). The final rotation will be performed around the precalculated $\vec{u}_3^{(2)}$ by rotation

amount of θ_6 (Eq. 15, and 16). The whole rotation sequence can be represented by Eq. 17.

$$r_f = q_3 q_2 q_1 (r_i) q_1^{-1} q_2^{-1} q_3^{-1} \quad (17)$$

Although θ_4 , θ_5 and θ_6 can easily be obtained from the acquired potentiometers signals, as it is required for the VR representation they should be converted into a single rotation ψ around a single rotational axis \vec{m} (Eq. 18).

$$r_f = q(r_i)q^{-1} \quad ; \quad q = \cos \frac{\psi}{2} + \vec{m} \sin \frac{\psi}{2}, \quad (18)$$

$$q^{-1} = \cos \frac{\psi}{2} - \vec{m} \sin \frac{\psi}{2}$$

Using Eq. 17 and 18, and recalling that the quaternions have four components including one scalar and three vectoral parts, Eq. 19 and 20 can be developed to find the desired parameters ψ and m .

$$q = q_3 q_2 q_1 = a + b\vec{u}_1 + c\vec{u}_2 + d\vec{u}_3 = \cos \frac{\psi}{2} + \vec{m} \sin \frac{\psi}{2} \quad (19)$$

$$\vec{m} = \frac{b}{\sin \frac{\psi}{2}} \vec{u}_1 + \frac{c}{\sin \frac{\psi}{2}} \vec{u}_2 + \frac{d}{\sin \frac{\psi}{2}} \vec{u}_3 \quad (20)$$

$$\psi = 2 \cos^{-1}(a);$$

It should be noted that multiplications between the quaternions should be carried out by using the rules of quaternion multiplications.

5. Manufacturing Process

The designed device is manufactured by utilizing various types of manufacturing processes, such as wire erosion, laser cutting, milling and turning for both translation and orientation mechanism. In general the manufacturing process of the entire mechanism is challenging due to;

- i) Small scale parts
- ii) High precision parts
- iii) Parallel structure
- iv) Irregular part shapes
- v) Non-magnetic materials
- vi) Average machinability materials

The design of the mechanism includes small bearings, bearing housings, bearing shafts, wiring and electronic component houses which are difficult to manufacture with conventional manufacturing processes. All moving parts

of the mechanism are manufactured with high precision in order to detain possible backlashes and develop high precision mechanism. Non-identical and less precise parts in a parallel mechanism can also block the motion of the mechanism. As a result of the link length and shape determination process outlined in the previous section, the manufacturing of the irregular shaped parts result in a difficult and long manufacturing process. Especially, the platform of the mechanism is manufactured in several manufacturing phases. The presented materials which are discussed in the next section have average machinability and non-magnetic atomic configuration. In general magnetic materials can be clutched with magnetic clutches to the milling and turning machines, however non-magnetic materials require custom manufactured fixture in order to fix the workpiece to the machines. Manufacturing the parts of the mechanism with custom gages and fixtures increases the cost and time of the manufacturing process.

In material selection for translational mechanism, the primary objectives are to manufacture the mechanism with a material that is light, non-corrosive, and rigid. Therefore, non-ferrous metal alloys based on aluminum, zinc, nickel, copper, titanium, tungsten and cobalt are investigated and among the other non-ferrous alloys aluminum alloy 7075 is used to manufacture of the parallel mechanism. 7075 aluminum alloy includes 5.1-6.1% zinc, 2.1-2.9% magnesium, 1.2-2.0% copper, maximum 0.4% iron, less than 0.4% silicon and other metals. Its density is 0.0028 g/mm³ and it has wide application in highly stressed structural parts that range from various commercial aircraft components, aerospace to defense equipments. The material combines high strength with moderate toughness and corrosion resistance. Alloy 7075 offers reasonable price and good machinability when machined with carbide machining tools.



Fig. 29. Assembled (a) translation mechanism, (b) orientation mechanism

The primary objective during the material selection of the orientation mechanism is to use ultra light materials, in order to reduce the payload amount of the platform of the mechanism. An engineering plastic, cast polyamide

commonly known as Kestamid[®] can provide low densities with reasonable rigidity and price. Delrin material has density of 0.0014 g/mm³ and it has wide application for general purposes especially in chemical and food industries. It is resistant to corrosion and it has average machinability.

Both mechanisms, translation and orientation, are manufactured by using different materials and machining processes as discussed in this section. The assembled representations of both mechanisms are shown in Fig. 29.

6. System Integration

Haptic systems are composed of mechanical, electro-mechanical and electronics components. The mechanical component of the system is presented and manufacturing processes are explained in the previous sections. The electronics and electromechanical components such as actuators, sensors, data acquisition cards and motor amplifiers of the system are required to be selected and integrated to the system. In this section, the selection of the outlined components of the system is discussed and selected components are presented.

The basic components and the data flow among these components are shown in Fig. 30. This flow chart facilitates the identification of the correlation and data transfer between the system and the components. The control scheme of impedance type haptic system starts with the measurement of the positions of the mechanism's degrees of freedom from potentiometers via data acquisition card. The analog signals from the potentiometer are converted to digital signals by ADCs in the DAQ card. Through the reserved communication port of the PC, digital signals are transferred to the computer control software and the forces are calculated as a result of the interaction between the object and the environment in VR or teleoperation application. Afterwards, the resultant forces are transmitted back through the same way, back to the actuators of the mechanism. In a VR application, acquired signals from the motion sensors through the DAQ card are used to move a virtual object in VR screen.

The only difference in teleoperation integration of this haptic device would be that actual forces has to be measured on the slave side of teleoperation instead of calculating virtual forces in the VR environment. The slave system is usually at a distant site. Therefore, the signals between the master and the slave robot must have a communication system such as the Internet, cables or wireless technology in teleoperation systems.

Among the other actuation methods presented in the Chapter 2, DC motors are the most frequently used actuator types in the design of the robotic applications owing to their simple structure, low cost, high reliability and wide availability for various applications. DC motors

are also used in the design of the haptic devices. In this thesis due to their advantages outlined above, Brushless DC motors are employed in the system. Basically DC motors can be grouped in two categories as brushed and brushless DC motors. Brushed DC motors are composed of brushes, commutator, stator and rotor. Because of the switching mechanism, motor and the maintenance cost of the actuator is high and the structure of the motor is sensitive to dust and abrasion. In contrast brushless DC (BLDC) motors include only a permanent magnet rotor and a stator. In BLDCs, the switching is generated with electronic switching circuits, instead of any mechanical switching.

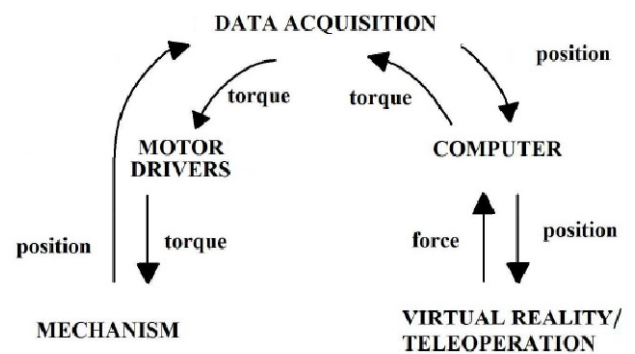


Fig. 30. Data flow

The actuators are selected as a result of the force analysis performed in the simulation studies. The applied force specification of the haptic device is to apply at least 0.8 N of force in all directions. This specification is consistent with the similar haptic devices in the market [9]. The initial selection of the actuator is a Maxon brushless DC motor that provides 310 mNm of continuous torque according to its datasheet to comply with the force requirements of the device.

In impedance type haptic devices, usually DC motors with capstan drives are used. However, it is foreseen that in time, the cables of the capstan drives loosen and results in loss of precision since the mechanism is driven without any transmission mechanism. Brushless DC (BLDC) motors are used in direct drive formation.

The system requires motor amplifiers that drive the three BLDC motors through current mode requiring +/- 10 V analogue signals as inputs. Maxon BLDC motor amplifiers (drivers) are selected to be compatible with the current requirements of the motors. These amplifiers are used to drive the actuators in current mode, which enables to drive the actuators by torque inputs that originated from the haptic controller system. The amplifiers are selected to have a response rate of at least 1 kHz.

The design of the mechanism allows using separate

sensors to measure the rotation amount of each actuator. Thus, it is not required to have an encoder system at the rear end of the actuator which usually has 9-bit of resolution. The four-bar structure placed as the first link has identical nominal lengths, which permits the same motion on each link.

A potentiometer or a higher bit resolution encoder (12-bit) can be aligned with the free link of the four-bar system and measure the same motion with more precision. In the initial system, six potentiometers that provide analogue signals, three on the parallel mechanism and three on the orientation mechanism, are used due to their low cost and simplicity. The selected potentiometer for the links of translation mechanism has linear track taper, approximately 270° mechanical angle, $\pm 5\%$ resistance tolerance and 1% linearity error. In order to design a compact handle mechanism, it is required to use miniaturize potentiometers.

The potentiometers of the rotational mechanism have small dimensions about 10x11x4 mm. Although the presented components, called trimpot, are not designed for position sensing, due to the availability limitations of miniaturize size position sensors, these trimpots are used as sensors.

In order to minimize noise in the analog signal it is required to convert to digital signals directly. Therefore 16-Bit, High-Speed, ADC ADS8331 and the passive filtering components are mounted on the back of the trimpots. Finally, the integrated sensor modules are placed into the links of the mechanism. Located sensor of the second link can be seen in Fig. 31.



Fig. 31. Integration of the miniaturize position sensors

Due to the noise effects in high speed digital signals, cased ribbon cables are used for the power and data transmission between the integrated sensors and DAQ card. The array of the signal cables are composed of data, clock, positive supply, ground and enable signal cables.

A data acquisition (DAQ) card developed to convert analogue inputs from the potentiometers to digital signals to be fed into the computer and digital outputs from the computer to analogue signals to be fed into the motor amplifiers. The developed data acquisition card is a

Microchip[®] PIC based system that has six 16-bit A/D converters and three 16-bit D/A converters. The developed data acquisition system includes three analog to digital converter, micro processor, three digital to analog converters and RS-232 communication ports.

Although various types of commercial data acquisition systems are available, due to the performance ratings, Quanser Q8 Hardware in the Loop (HIL) Board from Quanser Consulting Inc. is selected. Q8 has eight 12-bit D/A converters, eight 14-bit A/D converters which is enough for 6-DOF mechanism. Furthermore, it also has eight quadrature encoder inputs is for future modifications on the system's sensors. The system currently occupies three D/A converters for motor amplifiers and six A/D converters for the potentiometers of the Q8. While human motion is limited to 10 Hz, forces that are up to 1 kHz is important for the perception of the outer media. Therefore, in general, haptic devices are required to have at least 1 kHz of sampling rate in order to accurately provide the sense of touch [26]. Quanser Q8 DAO card can operate at 100 kHz sampling rates even in simultaneous acquisition.

Due to the sampling rate limitations of the developed custom data acquisition card, the initial tests of the mechanism are performed with the purchased commercial DAQ system. Nevertheless the small dimensions and wire houses transmitting the analog sensory outputs from the mechanism are impossible. Therefore, the digital signals from the embedded DAQ components (Figure 6.6) are converted by developed ADC to DAC converter circuit.

Integrated mechanism can be seen in Figure 6.14. The VR application, computer control scheme, DAQ components and the mechanism is denoted by 1, 2, 3, 4 in Fig. 32, respectively.

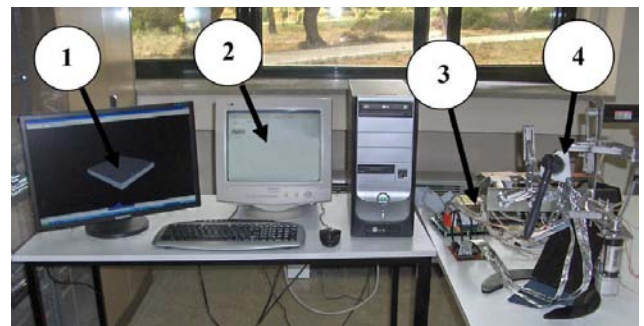


Fig. 32. The 6-DOF haptic system

7. Initial Tests and Modifications

The integrated system is tested and necessary design modifications are identified and some of them are applied system. According to the integrated system test results, necessary modifications are addressed in;

- i) Rotation of the mechanism

- ii) Motor selection
- iii) Sensor selection
- iv) Second link of the orientation mechanism

The initial test results revealed that the reoriented mechanism increased power consumption with respect to the original configuration due to the gravitational effects as shown in Table 4. Hence the orientation of the translation mechanism is changed back to the previous configuration (Fig. 33).

Table 4. Power Consumptions due to Gravitational Effects

	Motor No	Ampere
Reoriented Configuration	1	4.2
	2	4.21
	3	4.35
Original Configuration	1	0
	2	4.81
	3	0.8



Fig. 33. Modified 6-DOF mechanism

Although the technical specification sheet of the selected rate presents the motor's stall torque at 310 mNm, it is measured that the actuator can apply one third of the rated stall torque. Furthermore, changing back the orientation of the mechanism decreased the force feedback capability. Nevertheless this configuration can still provides enough torque rates to the mechanism. In order to achieve the required the feedback capacity more powerful brushed dc motors are planned to be used.

A closed-loop position control is used for gravity compensation. Fig. 34 shows the variation between torque demands for actuator 1 and different positions for actuators 1 and 2 while 3 is kept at a constant position. The torque is given in the unit of current, A, and it is

experimentally measured that 1 A can be converted as about 90 mNm of torque for all actuators. It is clearly observed that gravitational effects vary as the manipulator travels. Therefore, at each instant the center of mass information should be recalculated to compensate for gravity.

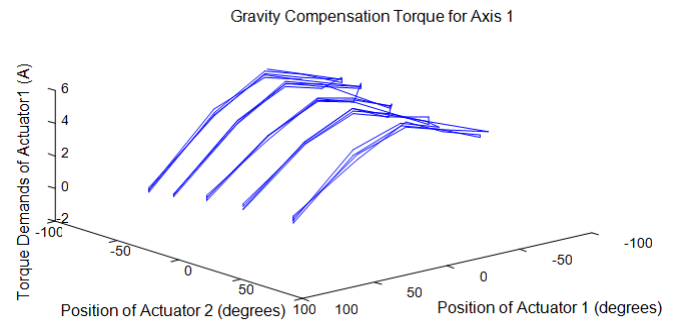


Fig. 34. Torque supplied to actuator 1 at different positions of the axes 1&2 (@ axis3: -65°)

Initially selected analog position sensors (potentiometers) provide noisy data which can results in precision loss. Therefore 12-bit three-channel incremental optical sensors can be replaced far the potentiometers.

8. Conclusions

The aim of this work is to develop a general purpose haptic device that provides higher precision ratings. Hence, previous haptic device designs are investigated, current haptic systems' sensation types are reviewed, mechanisms and their structural advantages are identified. Afterwards, the general haptic device components are listed and previously employed materials are reviewed. The difference of the admittance and impedance haptic devices is described, and drive systems are investigated according to the type of the haptic device.

Design criteria are identified and the conceptual designs are formed. Evaluating the literature survey results and the developed conceptual designs, R-CUBE mechanism is selected for reflecting three-dimensional forces and 3R serial spatial mechanism is selected for monitoring the orientation of the operator's hand. The selected mechanisms are configured as a haptic device and the dimensions and shapes of the links are determined to meet the specified design criteria. The designed mechanism is modified according to the manufacturing abilities, and then the mechanism is manufactured utilizing various manufacturing processes.

The mechanical, electro-mechanical, electronics and software parts of the device are integrated. Considering the force feedback requirements, motors are selected along with the appropriate motor amplifiers. In order to improve the precision of the actuation system, the driving



type is determined as direct drive. The sensors of the system are identified and the orientation mechanism is integrated with its DAQ modules. Then, the commercial DAQ system is integrated with the other components of the mechanism. Finally initial tests are performed, necessary design changes are offered and some of them are applied to the system.

In the future the mechanism can be remanufactured with composite material in order to improve the weight/strength ratio. The electro-mechanical components such as sensors and actuators can be replaced for better accuracy and force ratings. Hence, the potentiometers can be replaced with optical encoders and the motors of the system can be changed with other types of actuators such as coreless DC motors. Furthermore, passive actuators can be integrated to the existing device; the four-bar mechanism provides unique advantage for such an implementation. The developed custom DAQ card's sampling rate can be improved with the use of more advanced technologies such as DSPs and FPGAs. VR application can be enhanced with better VR modules or custom programming. Moreover, the system can be configured as the master system of a teleoperation application.

References

- [1]. M.I.C. Dede, O. Selvi, T. Bilginca & Y. Kant, *Design of a haptic device for teleoperation and virtual reality systems*, IEEE International Conference on Systems, Man and Cybernetics, pages 3623 – 3628, 2009.
- [2]. Web, www.medical-look.com
- [3]. J. Sone, R. Inoue, K. Yamada, T. Nagae, K. Fujita & M. Sato, *Development of a Wearable Exoskeleton Haptic Interface Device*, Journal of Computing and Information Science in Engineering, vol. 8, is. 4, pages 041009-1:12, 2008.
- [4]. A. Frisoli, F. Simoncini, M. Bergamasco & F. Salsedo, *Kinematic Design of a Two Contact Points Haptic Interface for the Thumb and Index Fingers of the Hand*, Journal of Mechanical Design vol. 129, is. 5, pages 520-1:10, 2007.
- [5]. P. Gallina & G. Rosati, *Manipulability of a planar wire driven haptic device*, Mechanism and Machine Theory, vol. 37, is. 2, pages 215-228, 2002.
- [6]. J.W. Kim, D.H. Park, H.S. Kim & S.H. Han, *Design of a Novel 3-DOF Parallel-type Haptic Device with Redundant Actuation*, International Conference on Control, Automation and Systems, Seoul, Korea, Oct. 17-20, 2007.
- [7]. M. Benali-Khoudja, M. Hafez & A. Kheddar, *VITAL: An electromagnetic integrated tactile display*, Displays, vol. 28, is. 3, pages 133–144, 2007.
- [8]. K.U. Kyung, J.Y. Lee & J. Park, *Design and Applications of a Pen-Like Haptic Interface with Texture and Vibrotactile Display*, Frontiers in the Convergence of Bioscience and Information Technologies, 2007.
- [9]. Web, www.sensable.com
- [10]. C. Carignan, J. Tang & S. Roderick, *Development of an Exoskeleton Haptic Interface for Virtual Task Training*, The 2009 IEEE/RSJ International Conference on Intelligent Robots and Systems, St. Louis, USA, October 11-15, 2009.
- [11]. J.M. Sabater, R.J. Saltařn & R. Aracil, *Design, Modelling and Implementation of a 6 URS Parallel Haptic Device*, Robotics and Autonomous Systems, vol. 47, is. 1, pages 1–10, 2004.
- [12]. Web, www.forcedimension.com
- [13]. A. Peer & M. Buss, *A New Admittance-Type Haptic Interface for Bimanual Manipulations*, IEEE/ASME Transactions On Mechatronics vol. 13, is. 4, pages 416–428, 2008.
- [14]. K. Bowen & M. K. O'Malley, *Adaptation of Haptic Interfaces for a LabVIEW-based System Dynamics Course*, Symposium on Haptic Interfaces for Virtual Environment and Teleoperator Systems, Alexandria, Virginia, USA, March 25 – 26, 2006.
- [15]. M.J. Lelieveld & T. Maeno, *Design and Development of a 4 DOF Portable Haptic Interface with Multi-Point Passive Force Feedback for the Index Finger*, IEEE International Conference on Robotics and Automation, Orlando, Florida, USA, May 2006.
- [16]. E., Samur, L. Flaction, U. Spaelter & H. Bleuler, *A Haptic Interface with Motor/Brake System for Colonoscopy Simulation Symposium on Haptic Interfaces for Virtual Environment and Teleoperator Systems*, Reno, Nevada, USA, 13-14 March, 2008.
- [17]. A.H.C. Gosline & V. Hayward, *Eddy Current Brakes for Haptic Interfaces: Design, Identification, and Control*, IEEE/ASME Transactions On Mechatronics, vol. 13, is. 6, pages 669–677, 2008.
- [18]. W.H. Li, B. Liu, P.B. Kosasih & X.Z. Zhang, *A 2-DOF MR Actuator Joystick for Virtual Reality Applications*, Sensors and Actuators, vol. 137, is. 2, pages 308–320, 2007.
- [19]. M. Takaiwa & T. Noritsugu, *Application of Pneumatic Parallel Manipulator as Haptic Human Interface*, IEEE/ASME International Conference on Advanced Intelligent Mechatronics, Atlanta, GA, USA, September 19-23, 1999.
- [20]. N. Tsagarakis, D.G.Caldwell & G.A.M. Cerda, *A 7 DOF Pneumatic Muscle Actuator (pMA) Powered Exoskeleton*, IEEE International Workshop on Robot and Human Interaction Pisa, Italy, September 1999.
- [21]. B.H. Choi. & H. R. Choi, *A Semi-direct Drive Hand Exoskeleton Using Ultrasonic Motor*, IEEE International Workshop on Robot and Human Interaction Pisa, Italy, September 1999.
- [22]. P.J. Berkelman, R.L. Hollis & S.E. Salcudean, *Interacting with Virtual Environments using a Magnetic Levitation Haptic Interface*, IEEE/RSJ International Conference on Intelligent Robots and Systems, Pittsburgh, PA , USA, pages 117–122, August 1995.
- [23]. N.A. Tanner & G. Niemeyer, *High-Frequency Acceleration Feedback in Wave Variable Telerobotics*, IEEE/ASME Transactions on Mechatronics vol. 11, is. 2, pages 119-127, 2006.
- [24]. W. Li, F. Gao & J. Zhang, *R-CUBE, a decoupled parallel manipulator only with revolute joints*, Mechanism and Machine Theory, Elsevier, vol. 40, is. 4, pages 467-473, 2005.
- [25]. I. Carlbomand & J. Paciorek, *Planar Geometric Projections and Viewing Transformations*, ACM Computing Surveys, vol. 10, is. 4, pages 465–502, 1978.
- [26]. K. Akahane, S. Hasegawa, Y. Koike & M. Sato, *A Development of High Definition Haptic Controller*, First Joint Eurohaptics Conference and Symposium on Haptic Interfaces for Virtual Environment and Teleoperator Systems, pages 576-577, March 2005.



Navigation of a Hydraulically Actuated Mobile Robot Using Stereo Vision

Ali KILIÇ^{1*}, Sadettin KAPUCU¹

^{1*}Gaziantep University

Faculty of Engineering, Mechanical Engineering Department, 27310 Gaziantep/TURKEY

akilic@gantep.edu.tr, kapucu@gantep.edu.tr

Abstract

Mobile robots may be able to navigate in an unknown environment acquiring visual information of their surroundings with the aim of estimating the position and orientation of an obstacle which is in front of it. In this study, a robust stereo depth perception and obstacle detection algorithms are proposed for collision free navigation of a hydraulically actuated experimental crawling mobile robot in an unknown indoor environment. For safely navigation of the mobile robot within its environments and reliably move from start point to destination point, a navigation algorithm, obstacle avoidance strategy and motion planning algorithms are implemented on the robot and the behavior of robot was observed. Experimental results were presented to show how the robot is able to reach destination point without collision with any obstacle.

Keywords: Stereo vision, Mobile robot navigation, Stereo vision obstacle detection, Depth perception via stereo vision.

1. Introduction

Mobile robots are a kind of robots which have the capability to navigate around their environment and are not fixed to one physical location in contrast with industrial robots. Mobile robot which is placed in an unknown environment must discover unaided and collect sufficient information about its surroundings to be able to accomplish its task. For such a robot, the most important requirement is adequate sensing. Visual information is widely used for navigation and obstacle detection of mobile robots. In order to navigate a mobile robot in unknown environment, the obstacle, which is in front of the robot, must be detected and depth information of the obstacle must be calculated. However, in order to avoid obstacles, when there is enough information about obstacles and their distance from the robot, complete information about the object in front of the robot is not required. Obstacle avoiding is an essential task for mobile robots. This problem has been investigated to solve for many years by researchers and a lot of obstacle detections and avoiding systems have been proposed so far. Nevertheless designing an accurate and totally robust and reliable system remains a challenging task, in the real

environments.

In the mobile robot navigation, there are two important requirements: perception and navigation. In this study, stereo vision has been used as a perception sensor. Due to large number of available literature on the concept of mobile robot navigation, there is small number of studies closely related with mobile robot navigation using stereo vision.

Real time or nearly real time stereo images are available from different stereo hardware systems. But raw stereo images are useless for robot obstacle avoidance and navigation tasks. These images require significant post-processing operation to extract three dimensional, range information. For example, researchers generally have applied some image processing and image enhancement techniques. Additionally researchers have applied various navigation and obstacle avoidance techniques which are developed for different sensors.

Don Murray et al. [1, 2] studied stereo vision based mapping and mobile robot navigation. They used occupancy grid mapping and potential field path planning techniques to form a robust cohesive robotic system for robotic mapping and navigation in both Spinoza [1] and Jose robots [2]. In these projects, trinocular, which is described as three camera stereo vision system, was used. Researchers used some techniques to improve the quality of stereo vision results on a working system and several example implementation results are given in related references.

Kumano and Ohya [3] proposed a new obstacle detection method. This method was based on stereo depth measurement but there was no corresponding point matching. Proposed method was fast enough for mobile robot navigation, but, not suitable robust for obstacle detection. For example, some ghost objects could not be detected during navigation.

Chin et al. [4] proposed an approach for robot navigation using distance transform methodology (DT). DT can be used in path planning for indoor robot navigation and also in performing obstacle avoidance simultaneously. But DT method is inefficient when performing both the tasks of path planning and obstacle

avoidance. Usually, both have to be coupled and DT is normally only used for path planning. The DT methodology developed in that paper [5] can solve the navigation problem by optimizing the DT algorithm and reducing the processing area. Finally, the researchers performed simulation and actual tests on their autonomous mobile robot to verify the algorithm.

Sabe et al. [6] performed stereo vision system on a humanoid robot QRIO and also they developed a method for path planning and obstacle avoidance allowing the robot autonomously walk around in a home environment. Researchers' approach was based on floor extraction using Hough transform from image captured by stereo vision camera.

Stereo vision system also has been used for small mobile robot. It is a very challenging work and it requires small computing system instead of computer. Mingxiang and Yunde [7] studied on stereo vision system on programmable chip (SVSoC) which can be implemented by one Field Programmable Gates Array (FPGA). The researchers used three miniature CMOS cameras that are trinocular stereo systems with triangular configuration and all these systems were mounted on small hexapod robot for obstacle avoidance and navigation.

Recently stereo vision system has been tried to use on a passenger car as a driver assistant systems to perform with reliability to avoid any potential collision with the front vehicle. The feasibility of these systems in passenger car requires accurate and robust sensing performance. Huh et al. [8] developed an obstacle detection system using stereo vision sensors. Proposed method utilized stereo vision feature matching, epipolar constraint and feature collection in order to robustly detect initial corresponding pairs. After initial detection the system executed the tracking algorithm for the obstacles. After this operation system could detect a front obstacle, a leading vehicle then the position parameters of the obstacles and leading vehicles could be obtained. Researchers also implemented this system on a passenger car and their performances were verified experimentally on a Korean highway.

The main concentration of this study is to have an autonomous robot that will be able to visually navigate an unknown environment and be able to keep away from the obstacles during navigation. Obstacles detection and avoidance have been performed by our robot using computer stereo vision system.

A navigation algorithm for a mobile robot has been developed using stereo vision by MATLAB programming language. In the navigation algorithm, the starting and destination coordinates are specified and robot travels from the starting point to the destination point without having any prior knowledge of the environment. Thus, robot has been able to avoid static obstacle in this manner. Consequently, this study describes obstacle avoidance, in

other words, collision free navigation using stereo vision perception system has been implemented on a hydraulically actuated crawling mobile robot.

2. Stereo Vision

Stereo vision is a widespread technique for inferring the three dimensional position of objects from two or more simultaneous views of a scene. Mobile robots can take advantages of a stereo vision system as a reliable and an effective way to extract range information from the surroundings. Accuracy of the results is generally adequate for applications such as depth perception and obstacle avoidance. Figure 1 shows overall stereo vision system and all operations which are used in this study.

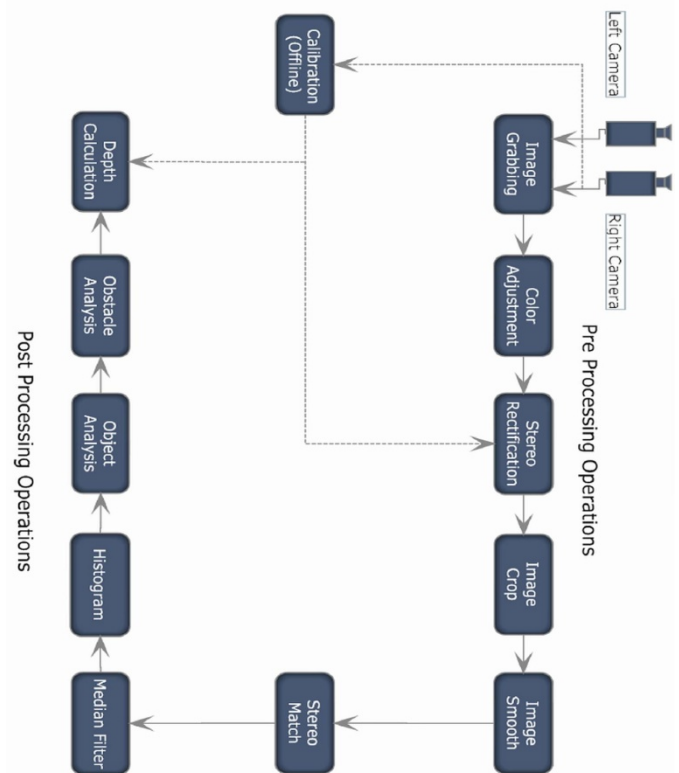


Fig.1: Stereo vision system and all operations

2.1 Pre Processing Operations

Pre processing operations are all the operations that are done before stereo matching. These operations have crucial role in stereo vision depth perception, because raw images are not adequate enough for depth perception and images should be prepared for matching operation. In this study five different pre processing operations are used which are;

Image Grabbing: In stereo vision image grabbing is

performed via stereo rig in which two cheap USB web camera are used although, there are a lot of professional stereo rig in the market. Today most webcams are of a reasonable quality and have a sufficiently high frame rate to be practical on slow moving robots

Color Adjustment: Color adjustment operation is the second operation of the pre processing operations. This function is used for making contrast or brightness adjustment of stereo image pair. Contrast is the difference in brightness between two adjacent pixels. On the other hand, brightness refers to the overall lightness or darkness of an image. This operation is necessary in order to improve the match quality, so stereo image pair should be set same contrast and same brightness level.

Stereo Rectification: In order to improve stereo correspondence in other words in order to get correct depth map, images require some pre-processing operations for example reduction of noise, adjustment of illuminations or a white balance of each cameras. But the most effective pre-processing operation is the calibration of the cameras [9] and rectification of images to use of the epipolar constraint. Meaning of epipolar constraint is pixel in the left image the corresponding point in the right image lies on the same horizontal line (i.e. epipolar line). This constraint is used to reduce the searching area of the correspondence algorithms that calculates depth maps.

Image Cropping: After rectification operation some useless areas appear on both left and right images as seen in Figure 2. For reducing computation time of stereo match, useless areas which are on the images are cut out by using image crop operation.

Image Smoothing: Image smoothing operation (i.e. image blurring) is the last operation of pre processing operation and is used to make blur stereo image pair because image blurring reduces the sharp color changes. According to experimental results sharp color changes reduce stereo match quality. Because of that reason image smoothing operation were added into pre processing operations.



Fig. 2: After rectification operation some useless areas appear on both left and right images

2.2 Stereo Match

Stereo vision correspondence analysis tries to solve the problem of finding which pixels or objects in one image correspond to a pixels or objects in the other image. This is stereo correspondence and also called as stereo matching. Stereo corresponding algorithms require a measure of similarity in order to find correspondences between the left and right image. The stereo correspondence algorithms can roughly be divided into feature based and area based, also known as region based or intensity based [10].

Feature based algorithms extract features (e.g. edges, angles, curves, etc.) from images and tries to match them in two or more views. They are very efficient but as drawback they produce poor depth maps.

Area based algorithms solve the correspondence problem for every single pixel in the image. Therefore they take color values and / or intensities into account as well as a certain pixel neighborhood. A block consisting of the middle pixel and its surrounding neighbors will then be matched to the best corresponding block in the second image.

In a robotic application generally an area based stereo algorithm has been used. Because feature based ones do not generate dense depth map and have difficulty to match smooth surfaces. Also the area based algorithm is faster than feature based. The main challenge of adopting an area based correspondence algorithm is its computational cost. An area based algorithm produces a dense depth map, which means that for each pixel of an image the algorithm tries to find its mutual pixel on the other view. This process is quite computationally expensive, but profiting on optimization techniques and by preprocessing operation such as image calibration and rectification. Finally we can reach a good compromise between the depth map density and its computation time.

In recent studies Sum of Absolute Differences (SAD) and Sum of Squared Differences (SSD) are the most widespread area or region based stereo correspondence algorithms in robotic and real time applications. Because they are faster than other algorithms and they give dense depth map (i.e. disparity map). According to these reasons, SSD type stereo matching algorithm is used in this study [10, 11].

$$SSD_x(x, y) = \sum_j \sum_i [I_L(x + i, y + j) - I_R(x + d_x + i, y + d_y + j)]^2$$

Where;

I_L = Left image (Reference image)

I_R = Right image



x = Image Coordinate in x direction
 y = Image Coordinate in y direction
 i = Enumerator in x direction
 j = Enumerator in y direction
 dx = Disparity in x direction
 dy = disparity in y direction

In this study, during calculation of disparity between two stereo image pair, epipolar line constraint has been used. In other words stereo images are rectified with horizontal epipolar line. Because of that reason disparity in y direction is zero disparity only exist in x direction.

Disparity Map: A disparity map is a method for storing depth of each pixel in an image. Each pixel in the disparity map corresponds to the same pixel in a reference image. Determine the disparity of a physical point in multiple point of view projections. By repeating this process for all points of the 3D scene the correspondence phase computes a disparity map. Figure 3 shows how disparity estimation works from any world scene.

In Figure 4 are shown left and right pictures, which are taken from our stereo hardware, and in Figure 5 histogram equalized disparity map are shown. In disparity map objects which are on red pixels are close to cameras and objects which are on blue pixels farther away from cameras.

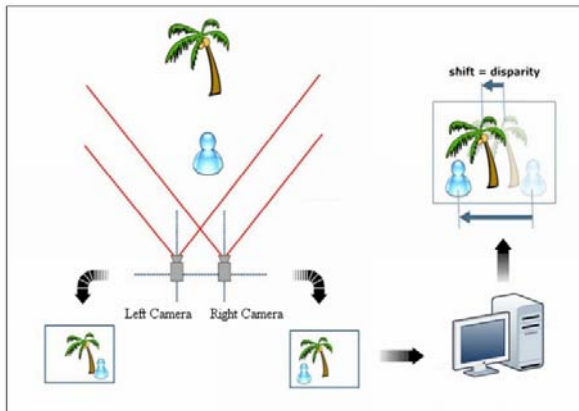


Fig. 3: Disparity Estimation



Fig. 4: Stereo Image Pair

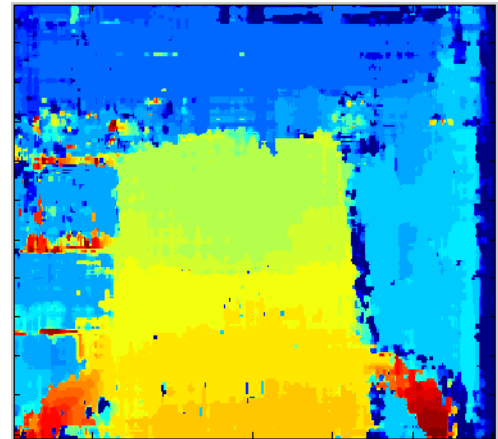


Fig. 5: Disparity Map

2.3 Post Processing Operations

Post processing operations are all the operations that are done after stereo matching. These operations have crucial role in stereo vision depth perception because raw disparity map are not adequate enough and it is meaningless for depth perception and obstacle avoidance. Because of that reason disparity map should be passed through the following operations. In this study five different operations are developed which are;

Median Filter: The median filter is a non-linear digital filtering technique, often used to remove noise from images or other signals. Median filtering is a common step in image processing. It is particularly useful to reduce speckle noise and salt and pepper noise [12]. After stereo matching produced, disparity map includes some noise due to mismatching. In order to remove this noise after stereo matching, median filter has been used. Figure 6 shows median filtered left disparity map.

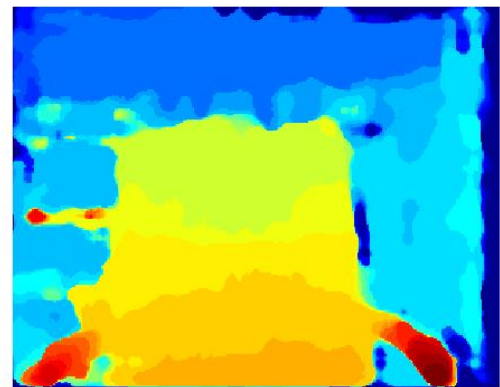


Fig. 6: Median Filtered Disparity Map

Histogram: An image histogram is type of histogram which acts as a graphical representation of the tonal distribution in a digital image. It plots the number of pixels for each tonal value. By looking at the histogram for a specific image a viewer will be able to judge the entire tonal distribution quickly. [13]

In disparity map each color represents a disparity level. Hence histogram of disparity map gives information about object or objects positions and by using this information an object is recognizable. In Figure 7 histogram of the median filtered disparity map shown in Figure 8 and Histogram of it after ghost object removed. In the figure horizontal axis indicates disparity value 0 to 32 and vertical axis shows number of pixels.

In this study our stereo matching algorithm searches disparity at 5 bit level. In other words the closest object has a disparity value 32 and most far object has a 0 disparity value. If we look at the full histogram of the disparity map we can see two different groups. Of course the number of groups can be changed. But the important group is last one in every time because robot navigation calculations are done for closest object. So the other objects can be canceled as seen histogram plot which can be seen in Figure 8.

The interpretation of histogram is main important operation for object detection and its disparity. After finding the closest object disparity level and physical parameters of the objects can be found easily.

Object Analysis: This function has been enhanced for finding the object position and object size from disparity map. Because object position and size are important parameters for collision free robot navigation. This function firstly takes closest object disparity information from histogram and then according to disparity level function combines neighbor disparity level and construct the near shape of the real objects.

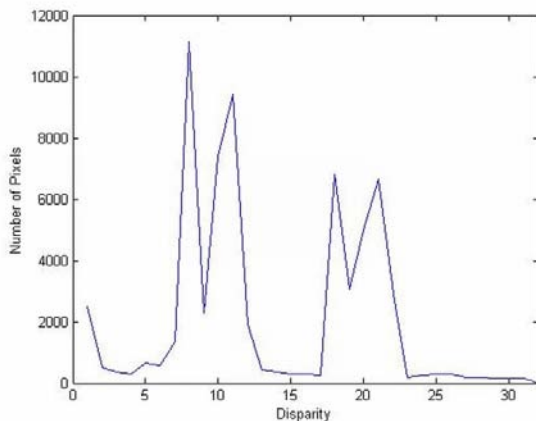


Fig. 7: Histogram of the Median Filtered Disparity Map

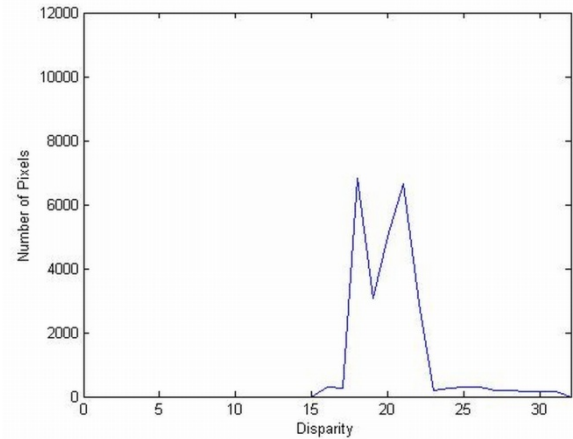


Fig. 8: Histogram of the Median Filtered Disparity Map after Ghost Objects Removed

Obstacle Analysis: Object analysis function is used to calculate area and centroid of the object which is found in object analysis step. Area of the object helps to get an idea about the obstacle size. Centroid of the object is used to calculate depth of obstacle instead of calculation of each pixel of the obstacle and also is used to determine position of the obstacle in the image.

Figure 9 shows calculated obstacle centroid and contour of the object. Also in the figure there is a blue box which shows the obstacle centroid.



Fig. 9: Closest Obstacle Found by Stereo Vision

Depth Calculation: In depth calculation step, real depth of the obstacle centroid is calculated. Disparity value of obstacle centroid has been calculated in stereo match step. Using disparity value of centroid, depth of the obstacle can be calculated via triangulation method and previously calculated parameters, which are internal and external camera parameters, in the stereo camera calibration step.

3. Robot Navigation

For any mobile robotic system, the ability to navigate in its environment is one of the most important capabilities. Mobile Robots, which are equipped with computer vision, may be able to navigate around an unknown environment acquiring visual information of their surroundings with the aim of estimating the position of obstacles which stay in front of it. Actually mobile robot navigation consists of two main tasks. Firstly remaining operational that is avoiding dangerous situations such as, collisions, secondly going through the start point to destination point. In other words, robot navigation is an ability to determine its own position in its frame of reference and then to plan a path towards some goal location while avoiding collisions. Navigation of mobile robots can be defined as the combination of the three fundamental abilities which are Perception, Localization and Motion control.

Perception is the interpreting its sensor data (i.e. stereo image data) to meaningful depth data. Localization denotes the robot's ability to establish its own position and orientation within the start point or any reference. Also in that it requires the determination of the robot's current position and a position of a goal location, both within the same reference or coordinates frame. Motion control is the modulating of motor outputs to achieve the desired trajectory. Furthermore, interrelation between perception, localization and motion control can be seen in Figure 10 [14, 15]

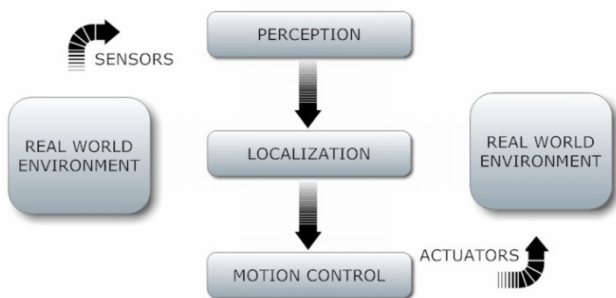


Fig. 10: Mobile Robot Navigation

3.1 Perception

One of the most important tasks of an autonomous mobile robot of any kind is to acquire some useful information about its environment. This is done by taking measurements using various sensors and then extracting meaningful information from those measurements.

In previous part, mobile robot stereo vision perception system has been discussed. However, only depth

perception is not adequate for mobile robot navigation. In order to safely navigation obstacle detection must be done by the robot perception system. Actually, not only obstacle detection but also position measurement of the robot has a crucial role during navigation. Because of that reason, odometry sub system has been developed for safe navigation. Perception system of our mobile robots can be easily divided into two main groups;

- Depth Perception and Obstacle Detection
- Position Estimation of Robot

In this study obstacle detection of the robot includes a lot of calculations. The prepared stereo vision perception system gives high quality depth map, which is 240x320 pixels with 32 disparities, using two calibrated cameras with an algorithm named Sum of Squared Differences (SSD). But unfortunately using only depth map, accomplishing of mobile robot navigation is impossible. Hence an obstacle detection system has been developed and reported at the post processing part. So in this part, only position measurement and position estimation of the robot are going to be discussed.

In order to perform robust and accurate robot localization, mobile robotic systems need some odometry sensors. There are a wide variety of odometry sensors used in mobile robots such as servo potentiometer or encoder for position measurement of wheels or tracks, tachometer for velocity measurement of wheels or tracks or GPS (Global Positioning System). GPS can give latitude, longitude and altitude of the robot but unfortunately for indoor applications GPS is useless. The mobile robot used in this experiment is equipped with two servo potentiometers, two encoders and two tachometers.

During the experimental studies an experimental crawling robot, which is hydraulically actuated small scale tank, has been used. The research robot was developed and constructed at University of Gaziantep, Mechanical Engineering Department, Robotics Laboratory.

Our robot employs two servo potentiometers for position measurement of the tracks. They are enough for robust localization. Potentiometer has a capability to infinite turn. During linear movement each potentiometer gives a signal like a saw tooth. But unfortunately these signals are meaningless and due to the analog signal drawbacks they contain noise. In order to convert these analog voltage signals into the meaningful distance value, an odometry algorithm was developed. This algorithm is combination of some linear filter like mean filter, low pass filter, and also counting and summing algorithms. This algorithm calculates position of each track, turned angles and walked distances. Finally, measured and calculated



parameters are sent to navigation algorithm and they are used for accurate localization.

3.2 Localization

Autonomous mobile robots need localization ability to move and to get to any goal location. During mobile robot navigation, both location and pose information of the mobile robot in its surroundings are very important. So robot current location, walked distance and distance between goal (destination) location and current location must be known by the robot navigation algorithm for accurate localization. Actually in order to sense robot current location, there are three methods. The first one is landmark sensing which can be usable with computer vision but it requires extra computation time and it needs landmarks. The second one is GPS (Global Positioning System). It is easy to use but it is useless for indoor applications. Third one is dead reckoning (i.e. odometry). It is very easy to use and of course it needs some calculations as it was discussed in previous section. But it is the most applicable method for our applications.

With the help of odometry algorithm, mentioned in previous section robot is able to estimate its own position at any time and also it is able to calculate the distance between current location and goal location. Figure 11 shows data flow of obstacle avoidance algorithm operated during robot navigational motion. The prepared robot navigation algorithm contains four different sub algorithms which are;

- Stereo Vision Depth Perception and Obstacle Detection Algorithm
- Odometry Algorithm
- Motion Planning Algorithm
- Motion Control Algorithm

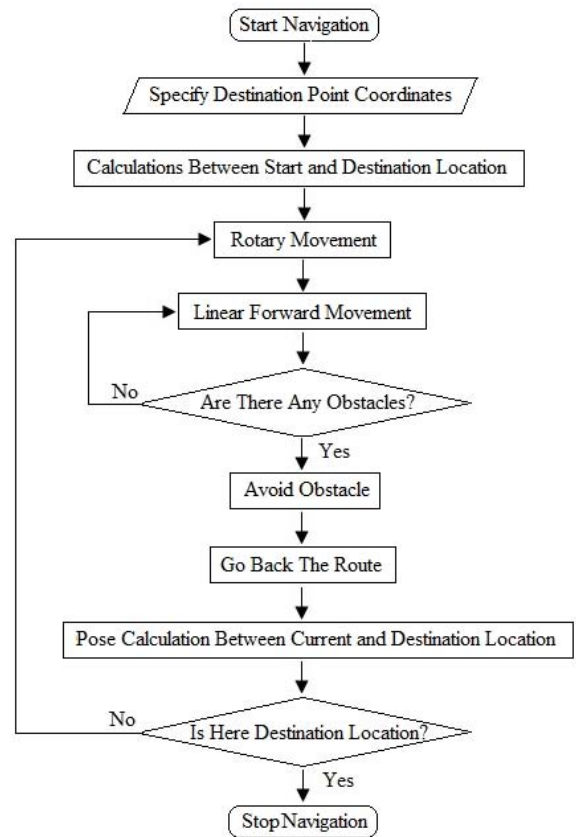


Fig. 11: The Proposed Robot Navigation Algorithm

Navigation algorithm of robot starts with specifying destination location coordinates. Navigation area of the robot is a two dimensional plane and it can be thought like a two dimensional Cartesian coordinate system. Goal location coordinates has to be entered to the algorithm by the user both in x and y directions. In the next step navigation algorithm calculates the shortest distance between start point and destination point and turning angle. During this calculation the start point coordinates are taken into account as a zero in both x and y directions. After the shortest distance and the turning angle calculated, by the help of robot motion control algorithm, the robot will turn up to calculated the turning angle and then robot starts to move in forward direction. During movement, stereo vision and depth perception algorithm checks the existence of obstacles. In the navigation algorithm “Are there any obstacles?” question is completely related with stereo vision depth perception and obstacle detection algorithm and detail of the algorithm can be seen in Figure 1. If the obstacle detection algorithm detects any obstacle, the robot tries to escape from collision and after escaping it tries to go back to the target route by the help of motion planning algorithm as shown

in Figure 12. If there aren't any obstacles on the route then the robot keeps itself on the route and it keeps on linear movement. Finally at each position robot motion planning algorithm checks rest distance between current location and goal location by the helps of odometry algorithm. If the robot reaches the destination point then the navigation algorithm stops the navigation.

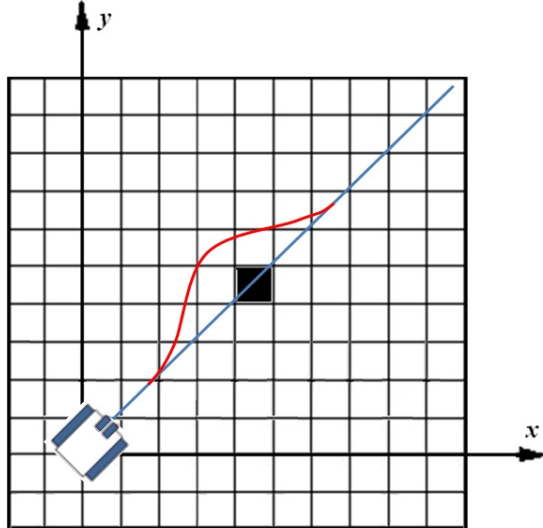


Fig. 12: Obstacle Avoidance Strategy

3.3 Motion Control

Motion control of the robot is interconnection between perception algorithm and robot locomotion system. A basic motion planning problem is to produce a motion that connects a start position and a goal position, while avoiding collision with detected obstacles. Prepared stereo vision depth perception and obstacle avoidance algorithm (i.e. perception algorithm) gives depth map of the robot's current scene, and also if the algorithm detects any object, it is able to recognize as an obstacle, it is able to calculate the distance between robot and object and it is able to calculate centroid, occupied area and position of the obstacle. However, to escape the obstacle which is detected by the perception algorithm robot must have a motion control mechanism. Motion control of robot contains two sub algorithms which are;

- Motion Planning Algorithm
- Locomotion Control Algorithm

At the beginning of the motion, motion planning algorithm calculates shortest distance and turning angle. During navigation if perception algorithm detects any obstacle, it sends the position information of obstacle to

the motion planning algorithm. According to the obstacle information motion planning algorithm plans proper obstacle avoidance motion.

Motion Control Algorithm arranges track driving voltages according to the information which comes from the motion planning algorithm. In other words, the motion planning algorithm sends only distance and angle information to the motion control algorithm and then the motion control algorithm converts the distance and the angle information into voltage values by help of the odometry algorithm. Finally the motion control algorithm sends to voltage value to the robot locomotion system and also speed of the tracks are decided by this algorithm.

4. Robot Locomotion System

During the experimental studies an experimental crawling robot, which is hydraulically actuated, has been used. The robot is powered by four stroke air cooled single internal combustion engine motor. The IC engine drives the pump shaft of hydraulic power pack unit with a time belt reduction. Robot has two independent hydraulic motors and each hydraulic motor is connected to tracks separately. Hence velocities of the tracks can be changed separately. Hydraulic motor can be defined as a motor which is able to convert to hydraulic power into mechanical power. Rotation speed of the hydraulic motor is proportionally dependent on flow rate of the fluid (i.e. oil). The torque which is produced by the hydraulic motor is proportionally dependent on the operating pressure. In our robot operating pressure of the hydraulic system is set manually by helps of pressure relief valve. But the flow rate, which is sent to hydraulic motor, is changed by direct operated servo solenoid valves. Basically, servo valve is a type valve that produces an output that is proportional to the electronic control signal. For the any type of application there are many type of servo valve which are able to control direction, flow and pressure. In our robot flow rate and direction of the hydraulic motor are controlled by servo valves. Each hydraulic motor is controlled with one servo valve and flow rate passing through the hydraulic motor is proportional with the signal sent to the servo valve and it is also proportional to rotational speed of the motor. In order to operate the servo valve, the servo valve requires a power amplifier. To control the robot by computer, an interface is necessary between computer and hydraulic amplifiers. Our robot is equipped with data acquisition and motion control card for that purposes. This card is also used for getting potentiometer and tachometer information to the control computer.

An interconnection between all electronic mechanic and hydraulic hardware, which are constructed on the



In this study, a navigation task is defined which is collision free navigation from start point to any destination point which is defined by the user. To accomplish this task robot need some algorithms which are motion planning, obstacle avoidance and motion control algorithms and combination of all these algorithms is called as robot navigation algorithm. Motion planning algorithm is used for planning of robot motion, it calculates shortest distance between current position and destination position and required turning angle. By helps of obstacle avoidance algorithm, robot tries to escape obstacles according to the position and size of the obstacle. Motion control algorithm is interconnection software between robot locomotion system and navigation algorithm. In other words, motion control algorithm changes distance and angle value into track voltages and it does communication between control card and computer. In order to succeed position control of the mobile robot, kinematics of the robot is taken into account during writing codes of locomotion control algorithm.

To execute developed stereo perception algorithm and navigation algorithm an experimental crawling vehicle are modified and improved to build up a real autonomous robot. In order to control the robot easily and to combine all algorithms which are developed during this study. After optimization and combining all algorithms and codes, behavior of robot is observed, by use of developed algorithms, the robot is able to reach destination point without collision any obstacles.

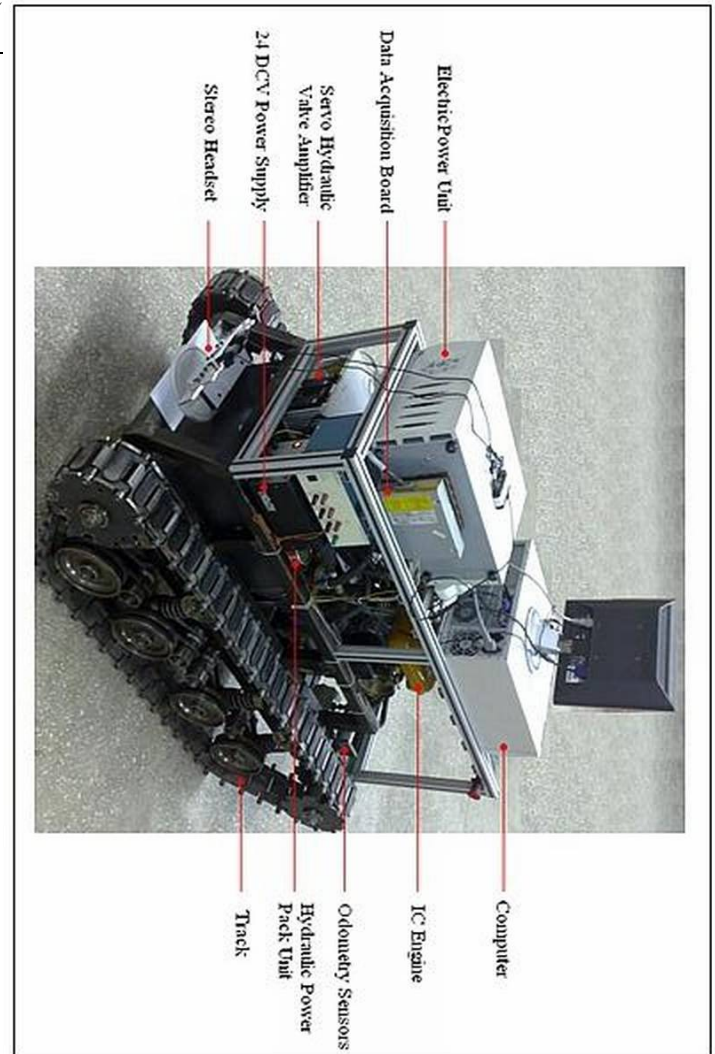


Fig. 14: General Appearance of Robot

6. References

- [1]. Murray, D. and Jennings, C.; *Stereo Vision Based Mapping and Navigation for Mobile Robots*. In Proceedings of the IEEE International Conference on Robotics and Automation (ICRA '97), 1694-1699, 1997
- [2]. Murray D. and Little J.J. *Using real-time stereo vision for mobile robot navigation*. *Autonomous Robots*, **8** 161-171, 2000
- [3]. Kumano, M., Ohya, A. and Yuta, S. *Obstacle Avoidance of Autonomous Mobile Robot using Stereo Vision Sensor*, in Proc. of 2nd International Symposium on Robotics and Automation, ISRA2000, 2000
- [4]. Chin, Y. T., Wang, H., Tay, L.P., Wang, H. and Soh, W. Y. C. *Vision Guided AGV Using Distance Transform*. Proc. of 32nd International Symposium on Robotics, 2001
- [5]. Scharstein, D. and Szeliski, R. *A Taxonomy and Evaluation of Dense Two-Frame Stereo Correspondence Algorithms*. *International Journal of Computer Vision*, **47** 7-42, 2004
- [6]. Sabe, K., Fukuchi, M., Gutmann, J.-S., Ohashi, T., Kawamoto, K., and Yoshigahara, T. *Obstacle Avoidance and Path Planning for Humanoid Robots Using Stereo Vision*. *Int. Conf. on Robotics and Automation (ICRA, 2004)*
- [7]. Mingxiang, L. and Yunde, J. "Stereo Vision System on Programmable Chip (SVSoC) for Small Robot Navigation," Proceedings of IEEE/RSJ International Conference on Intelligent Robots and Systems (IROS '06), 1359-1365,
- [8]. Huh, K., Park, J., Hwang, J Daegun Hong, D. "A Stereo Vision-Based Obstacle Detection System in Vehicles", *Optics and Lasers in Engineering*, **46**, 168-17, 2008
- [9]. KILIÇ A.; *Navigation of A Mobile Robot Using Stereo Vision*, Msc Thesis, University of Gaziantep, 2010
- [10]. Trucco E & Verri A; *Introductory Techniques for 3-D Computer Vision* (1998) Prentice Hall PTR
- [11]. Hannah M J; *Computer Matching of Areas on Stereo Images*, PhD Thesis, Stanford University (1974)
- [12]. Matlab Image Processing Toolbox Release Notes Version 6 (R2009a)
- [13]. http://en.wikipedia.org/wiki/Image_histogram
- [14]. http://en.wikipedia.org/wiki/Mobile_robot_navigation
- [15]. Siegwart R and Nourbakhsh I R; *Introduction to Autonomous Mobile Robots* MIT Press, 2004



Decoding Processes and Characterization Studies of a 2-D Laser Scanning Range Finder

Gökhan BAYAR¹, A. Buğra KOKU¹, E. İlhan KONUKSEVEN¹

¹Mechanical Engineering Department,
Middle East Technical University
İnönü Bulvarı, 06531, Ankara / TURKEY
 {bayar, kbugra, konuk}@metu.edu.tr

Abstract

This paper presents a characterization study conducted on a laser scanning range finder, Hokuyo URG-04LX. The working principle and the technical specifications of the laser scanner are represented. The effects of working environment and distance measured are investigated. The characteristics of the laser scanning range finder are searched by doing measurements on the surfaces clothed with different colours. The set-up, which is used during the experiments, is also introduced. The developed programming algorithm for the real time communication of the laser scanner is presented. The results of the measurement experiments are given in order to give a user guideline for the researchers who utilize a laser range finder into their works.

Keywords: Laser scanning, Distance measurement, Range Finder, Characterization.

1. Introduction

While an unmanned ground vehicle or a mobile robot is traversing over an area, scanning of the environment is very important to recognize for the obstacles. In order to scan the work space and notice the obstacles on the travel path, a variety of sensors can be used. Among these sensors, 2D and 3D scanners are mostly preferred by the researchers. 2D laser range finders may scan a planar surface whereas a 3-dimension surface can be scanned by a 3D laser scanning range finders [1, 2].

The most appropriate choice for scanning obstacles with which an unmanned ground vehicle may come upon is the 3D laser scanning range finder. However this type of range finder is highly expensive for mobile robotic applications. In addition 3D laser scanning range finders are slow for the real time objectives [2].

2D laser scanning range finders are used in robotic applications for pursuing, recognizing and avoiding obstacles. Moreover, robots can position themselves by using these range finders. The work space of a robot can also be mapped using a 2D range finder [3]. Sick LMS [4], Zoller-Fröhlich [5] and Hokuyo [6] are the laser scanning range finders commonly preferred by the

researchers and engineers.

In the literature many different works have been proposed related to the characterization studies of the laser scanning range finders. Hoffman has used a 3D laser scanner for making a terrain mapping. He has investigated the effects of the surface and temperature changes on the measurements [7]. Adams has investigated the performance of a laser scanner on the surfaces with different colors [8]. Hebert has explored the effects of the noise on the measurements of a laser scanning range finder. He has also conducted a theoretical modeling study for this characterization [9]. Reina has developed a measurement model for a 2D laser scanning range finder (Schwartz Electro-Optic) [10]. Langer has searched the measurement characteristics of a Zoller laser range finder that is located on a rail-way of a tunnel. He has observed the errors happened by the noise changes [11]. Kneip has been worked with Hokuyo URG-04LX. He has investigated the effects of time drift, distance, target properties (such as color, brightness and material) and incidence angle on the measurement. He has also compared the sensor characteristics with those of the Sick LMS 200 [12].

In this paper characterization studies conducted for Hokuyo URG-04LX laser scanning range finder is presented. The organization of the paper can be given as follows. After the introduction section, the working principles and the technical specifications of the used laser scanning range finder are given. The programming algorithm steps for performing real time studies and the developed experimental set-up are given in section 3. The experiment results and the characterization studies are represented in section 4. The discussion on the results is provided in the last section of the paper.



2. HOKUYO URG-04LX Laser Scanning Range Finder

During the characterization studies, Hokuyo URG-04LX laser scanning range finder [6], which is shown in Figure 1, is used.



Fig. 1. Hokuyo URG-04LX laser scanning range finder [6].

The baud rate speed of the range finder can be set to 19.2, 57.6, 115.2, 250 and 500 Kbps. In our experiments it is set to 19.2 Kbps. This sensor has two communication alternatives: RS232 serial or USB port. The angular resolution of the range finder is 0.3515625° ($360^{\circ} / 1024$).



Fig. 2. The angular measurement range of Hokuyo range finder.

The angular measurement scope of the range finder, which is used in this study, is shown in Figure 2. The sensor divides this scope (240°) into 683 equal intervals. The minimum and the maximum measurement distance for which the range finder can be effectively used are 60 mm and 4095 mm, respectively. However, It should be noted that the minimum distance that range finder can measure is 70 mm on a white surface.

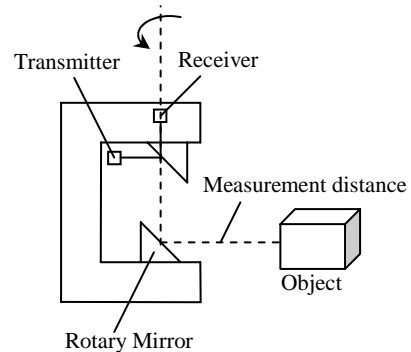


Fig. 3. The working principle of the range finder.

It has been seen from the experiments that Hokuyo URG-04LX laser scanning range finder has a sensitivity of ± 10 mm in the measurement range of 1000 mm. It takes 0.1 s to scan a 240° scope. The sensor works with 5 Volt DC power. It has been also recognized during the experiments that it draws 800 mA, and 500 mA at the start-up and steady state working conditions, respectively. The working principle of the range finder is shown in Figure 3. It has a transmitter, a receiver and a rotary mirror.

3. Working with the Sensor

The laser scanning range finder used in this study scans a 240° scope in a 0.1 s and it sends this scanning information in a data packet that contains 1435 bytes. In order to convert this data into meaningful distance information in real time, a PC is used. The data packet content sent by the range finder is given in Table 1.

Table 1. Data packet sent by the range finder.

S_1	S_2	D_A^1	D_B^1	D_A^{683}	D_B^{683}
-------	-------	---------	---------	-------	-------------	-------------

As seen in Table 1, a distance value is represented by two parts specified as D_A and D_B and each distance value has 12 bytes length. An example related to shown the conversion process is given in Table 2.

Table 2. An example to a conversion process.

$(A,B) = (0x41,0x42)$
↓ $(0x30)$ Subtraction
$(0x11,0x12) = (00010001,00010010)_2$
↓ Parse
$(010001,010010)_2$
↓ Concatenate
$(010001010010)_2 = 1106$ mm



Table 2 shows an example for the conversion process. The character A and B that are sent by the sensor are concatenated and a distance value is obtained.

In this study, in order to work with the laser scanning range finder in real time, Matlab Real Time WorkShop toolbox is utilized. As given in Figure 4, the data packets sent by the sensor are converted into Matlab environment. The conversion algorithm is developed by using C language. In addition, in order to show the distance values on a polar plot, Embedded Matlab Function is used.

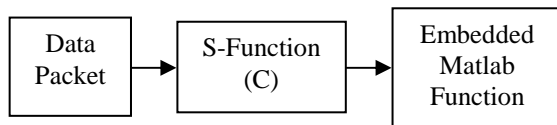


Fig. 4. Conversion process.

An experimental set-up shown in Figure 5 is constructed for calibration and characterization studies. The surface which is used for the distance measurement tests is covered with 5 different clothes. These clothes are white, green, purple, orange, and black colors. In the experiments, the surface is scanned by the laser scanning range finder from a known distance. All the experiments conducted with the range finder are performed in indoor environment and with the room temperature of 23° . The laser scanning range finder is connected to a PC having Windows XP operating system.



Fig. 5. Test set-up.

4. Characterization Studies

A sample polar plot drawn by using distance information of the laser scanning range finder is shown in Figure 6.

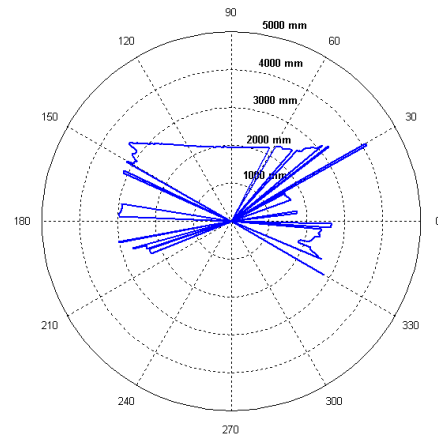


Fig. 6. A sample polar plot.

As given in Figure 7, three points that are on the scanned range are selected for the distance measurement experiments. Point B represents the middle of the scanning range of the laser scanning range finder. In other words it indicates the angle of 0° . Point A and B show $+15^{\circ}$ and -15° , respectively according to point B.

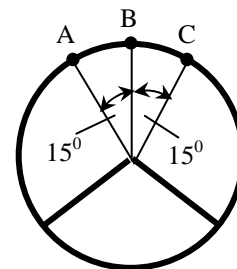


Fig. 7. Test points of the laser scanning range finder.

The angular resolution of the range finder is $360^{\circ} / 1024$. The distance gotten from the points of A, B, and C are obtained by the intervals of 385, 342, and 299, respectively. The measurement experiments are conducted for three different distances. The laser scanning range finder is located on a distance of 450 mm, 1570 mm, and 1980 mm from the set-up.

In the first experiment, the range finder is located on a distance of 450 mm from the experimental set-up cloth covered with white surface. The results are given in Figure 8. In this experiment, 1000 values for three points are taken for 100 seconds. Actually, in all experiments distance data is taken from the sensor for over 10000 seconds. After observing the results, it is seen the characteristics do not change. Therefore the experiments have been conducted for 100 seconds.

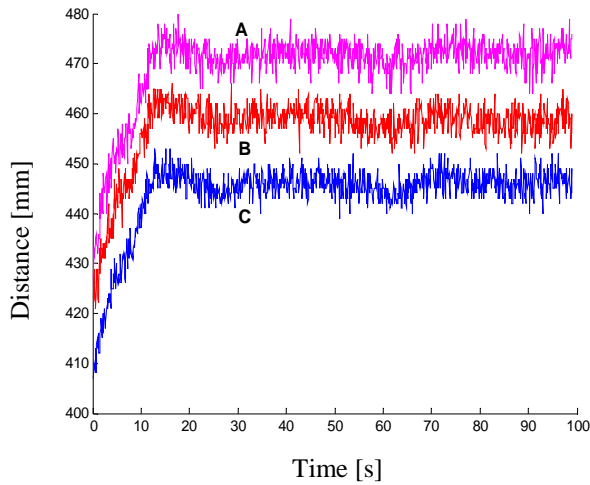


Fig. 8. Results obtained from a white surface located on a 450 mm distance from the range finder.

The laser scanning range finder stabilizes itself into 15-20 seconds time period (Figure 8). It is a clear observation that in order to increase the reliability of the results, the distance information, which is obtained after 15-20 seconds from the start-up of the sensor, should be used.

The distance measurement studies mentioned above have also been performed for the surfaces covered with green, purple, orange and black colored clothes. The measurement results taken from the green and black colored surface are given in Figure 9 and Figure 10, respectively.

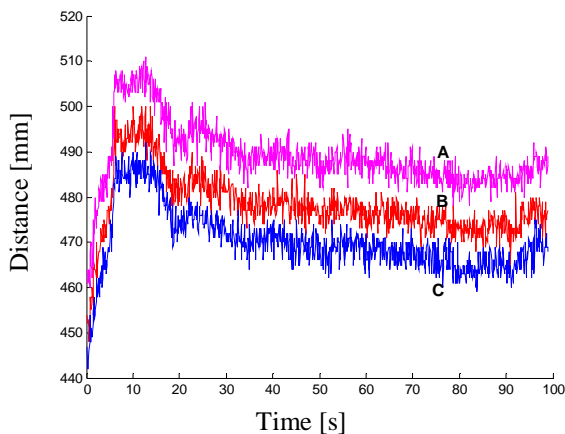


Fig. 9. Results obtained from a green surface located on a 450 mm distance from the range finder.

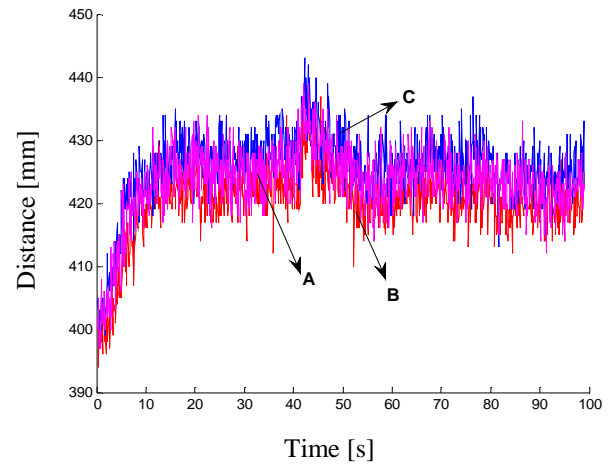


Fig. 10. Results obtained from a black surface located on a 450 mm distance from the range finder.

In Figure 8, 9, and 10, the measurement values for points A, B, and C are given. In Figure 9, the experiment results conducted on a green surface is given. As seen in Figure 10, results obtained from a black surface located on a 450 mm distance from the range finder show that it is not easy to recognize the measurement values of the points A, B, and C. It can be seen from these plots that the absorption of the laser lights are increased from white surface to black surface. The quality of the measurement is also declined in this color range.

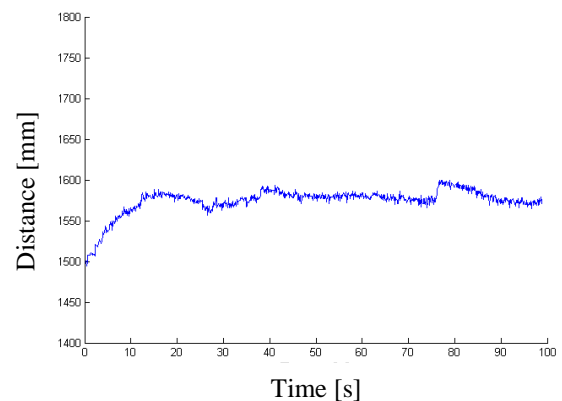


Fig. 11. Results obtained from a white surface located on a 1570 mm distance from the range finder.

As seen in Figure 11 and 12, results obtained from a surface located on a 1570 mm and 1980 mm distances from the range finder are given, respectively. Both experiments are conducted on a white colored surface. The results given in Figure 11 and 12 indicate that the measurement characteristics show a similar attitude with



the results given above. The sensor stabilizes itself into 15-20 seconds time period. After this time period it shows a linear and stable behavior.

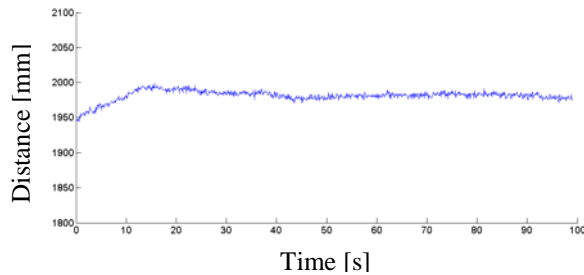


Fig. 12. Results obtained from a white surface located on a 1980 mm distance from the range finder.

The results obtained from a surface located on a 1570 mm distance from the range finder are given in Table 3. The measurements are taken from the point B, which is located at the middle of the sensor. This table indicates the effects of the colors on the reliability and the quality of measurements.

Table 3. Results taken from the point located at the middle of the laser scanner.

	White	Green	Purple	Orange	Black
Minimum (mm)	1543	1540	1550	1546	1544
Maximum (mm)	1566	1563	1569	1569	1564
Average (mm)	1555	1552	1559	1557	1555
Standard Deviation	3,09	3,265	2,991	3,317	2,868

In the experiment studies, it is also seen that if the Hokuyo URG-04LX laser scanning range finder is used for an unmanned ground vehicle or a mobile robot, it should be located 60-70 mm inside from the outer surface of the vehicle. Since the minimum measurement capability of the sensor is about 60 mm.

5. Conclusion

In this study, the characterization of Hokuyo URG-04LX laser scanning range finder is investigated. The experiments have indicated the following results. Laser scanning range finder stabilizes itself in 15-20 seconds. Therefore it can be advised that for getting high measurement quality, the sensor data should be collected after 15-20 seconds from the start-up. The measurement characteristics show differences for the different colored surfaces. The absorption of the laser lights declines from

black to white color.

References

- [1]. M. Hebert, (2000), *Active and Passive Range Sensing for Robotics*, Proc. Int. Conf. On Robotics and Automation, San Francisco, CA, pp 102-110, 2000.
- [2]. C. Ye, J. Borenstein, *Characterization of a 2-D Laser Scanner for Mobile Robot Obstacle Negotiation*, Proc. Int. Conf. on Robotics and Automation, Washington, DC, pp 2512-2518, 2002.
- [3]. J. L. Martinez, et al, *Object Following and Obstacle Avoidance Using a Laser Scanner in Outdoor Mobile Robot Auriga-a*, Proc. Int. Conf. on Intelligent Robots and Systems, Victoria, B.C., Canada, pp 204-209, 1998.
- [4]. SICK Laser Scanner Web site, <http://www.sick.com>, Last visit, April 2010.
- [5]. Zoller-Fröhlich Laser Scanner Web site, <http://www.zf-laser.com>, Last visit, April 2010.
- [6]. Hokuyo Laser Scanner Web site, <http://www.hokuyo-aut.jp>, Last visit, April 2010.
- [7]. R. Hoffman, E. Krotkov, *Perception of Rugged Terrain for a Walking Robot: True Confession and New Directions*, Proc. Int. Conf. on Intelligent Robots and Systems, Osaka, Japan, pp 1505-1510, 1991.
- [8]. M. D. Adams, A. J. Kerstens, *The Interpretation of Phase and Intensity Data from AMCW Light Detection Sensors for Reliable Ranging*, International Journal of Robotics Research, Vol. 15, No. 5, pp 441-458, 1996.
- [9]. M. Hebert, E. Krotkov, *3D Measurements from Imaging Laser Radars: How Good are They?*, Image and Vision Computing, Vol. 10, No. 3, pp 170-178, 1992.
- [10]. A. Reina, J. Gozalez, *Characterization of a Radial Laser Scanner for Mobile Robotic Navigation*, Proc. Int. Conf. on Intelligent Robots and Systems, Grenoble, France, pp 579-585, 1997.
- [11]. D. Langer, et al, *Imaging Laser Scanner for 3-D Modeling and Surveying Applications*, Proc. Int. Conf. on Intelligent Robots and Systems, San Francisco, CA, USA, pp 116-121, 2000.
- [12]. L. Kneip, F. Tache, R. Siegwart, *Characterization of the Compact Hokuyo URG-04LX 2D Laser Range Scanner*, IEEE Int. Conf. on Robotics and Auto., Kobe, Japan, 2009.



Design and Control of an Inserting Mechanism for PP (Polypropylene) and PE (Polyethylene) Sacks

Gökhan BAKIR¹, L. Canan DÜLGER²

¹ M.Sc.

Gaziantep University, Faculty of Engineering, Dept. of Mech.Eng.

gokhanbakir@yahoo.com

^{2*} M.Sc., Ph.D.

dulger@gantep.edu.tr

Abstract

PP and PE sacks are used to store various items in industry. PE and PP sacks are separately produced and inserted together to form a strong sack for storing artificial fertilizers. Inserting of sacks are performed manually by human operators using different inserting and storing platforms. An inserting mechanism is proposed in this study by considering motion requirements during sack insertion. The proposed mechanism is presented with construction details. A mathematical model is given for horizontal sack inserting mechanism with turret configuration. Simulation results are seen for actuator and load given with action of different controllers.

Keywords: PP (Polypropylene) sack, PE (Polyethylene) sack, Conceptual design, inserting mechanism, control of an inserting mechanism.

1. Introduction

The installed production capacity of Turkey is about 912 million sacks per year [1]. The purpose of this study is related with fertilizer packaging. The PP sacks with PE are used for protecting the fertilizer from moisture. The PE sack is placed into that of PP manually. This labor-intensive process is not only difficult but also causes many problems in practice. There is a necessity of an improvement in inserting procedure.

The aim of this study is to design and control an inserting mechanism for PP and PE sacks. This study involves three important parts: design of an inserting mechanism with its auxiliary parts, synchronization with other units during the inserting procedure and the control of sensors and actuators properly in real time. Thus, the sack inserting rate will definitely be increased and faults caused by human operators will be overcome. The plastic packaging plant will be able to deliver more sacks while consuming less labor and time by using this mechanism. So a design procedure and its feasibility for further

application will be presented with real figures taken from a Fertilizer Company. Referred sack dimensions are 550 mm x 950 mm. This proposed design when used in future development will certainly provide a considerable contribution to reducing plant expenses [2-5]

The inserting steps of a sack are also explained with concept design and evaluation for final design is given. The information on control issues on inserting of the PP and PE sacks mechanism is presented. Some design requirements on the placing mechanism are determined. They are taken from a fertilizer company. Here, the inserting operation of the sacks is explained. Design requirements of the placing mechanism used in the manual inserting platform are determined. Finally, the actuators drive systems and synchronization with other systems and automation of the system are given. A mathematical model is built for a brushless DC motor driven horizontal sack turret with a belt drive herein.

2. Manual Inserting Procedure for PP and PE Sacks

The PP and PE sacks are inserted manually in the sub-suppliers' workshop. The sack inserting speed is 6 sacks / min in average and the production output is 3200 sacks/10hr per operator. The final sack means PE sack inserted into that of PP. The sack inserting workbench consists of four parts as PE sack storing table, PP sack storing table, the final sack storing table and the sack inserting platform. Manual inserting platform is seen in Fig. 1. The PE and PP sacks are separately stored on storing tables. They are put on the left and right side of the inserting platform. The PE sack storing table is 700x700x1000 mm, and the PP sack 600x700x1000 mm, and the sack inserting platform 460x1050 mm in dimensions for placing the sack [2].

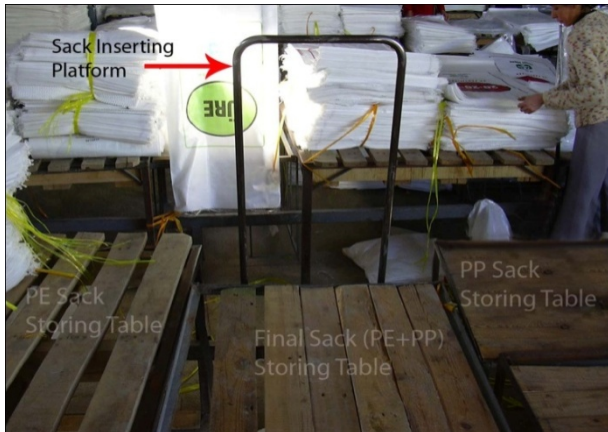


Fig.1. Manual Inserting Platform

The manual sack inserting procedure is summarized as (i) The PE sack is initially taken from the storing table. (ii) The PE sack is placed on the sack inserting platform. (iii) The PE sack is pulled down up to the sealed side of its reach the sack inserting platform (iv) The PP sack is taken from the storing table. (v) The PP sack slides down on that of PE which is already placed on the sack inserting platform. (vi) The PP sack is pulled down up to its stitched side to reach the sack inserting platform. Since PE sack is 7 cm longer than PP, it is then folded outside to form the cuff. (vii) The PE sack inserted PP sack is moved to outside of the sack inserting platform. (viii) Finally, the PE sack inserted into PP, the final sack is stored on the finish table.

3. Concept Design

The manual sack inserting procedure is given in above section. Because of several movements of the operator, it is seen that sack inserting looks simple but the procedure involves many problems in practice. A cycle should be completed in as short of time as possible. Many observations are made, and many independent measurements are also taken, and a final sack is completed in 10 seconds [6-8].

The PE sack inserting system consists of (i) PE sack storing tables (2) and PP sack storing tables (2), (ii) the sack-turret, (iii) the sack-turret stand, (iv) horizontal and vertical pneumatic cylinders and a vacuum system, (v) final sack storing tables (2)

(i) PE and PP Sack Storing Table

The PE and PP sacks are separately stored on storing tables. These tables are necessary for starting the inserting procedure. They are made of steel profile with dimensions of 560 mm width, 800 mm height and 1000 mm length.

(ii) The Horizontal Sack-Turret

The horizontal sack-turret consists of 6 sack inserting platforms and a chassis. Every three inserting platforms are used for a sack inserting cycle, shortly in a cycle. On the front of every third inserting platform, there is a final sack storing table. On top of every inserting platform, there is a Horizontal-Vertical Pneumatic Cylinder, and a Vacuum System.

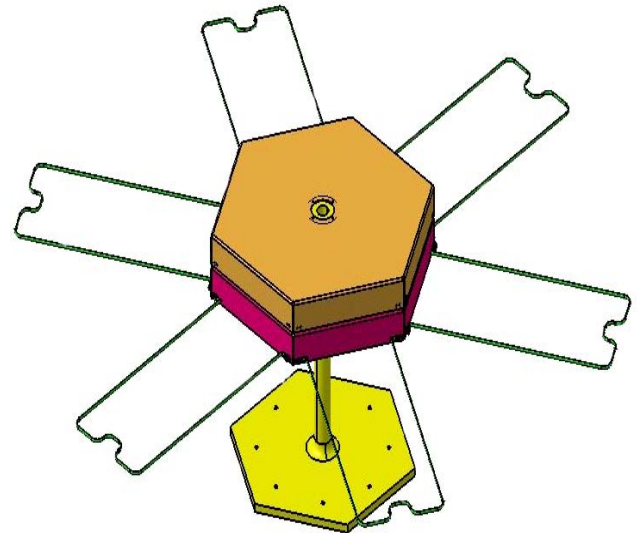


Fig.2. The horizontal sack turret

(iii) The Horizontal Sack-Turret Stand

In the proposed design, the horizontal sack-turret is actuated by a BLDC motor via belt. Its stand has an overall height of 1300 mm. It can carry the motor and transmission system of interest. Here a belt driven system is considered. The sack-turret is fixed to the floor via a hollow shaft and a circular support which are made of steel for stability.

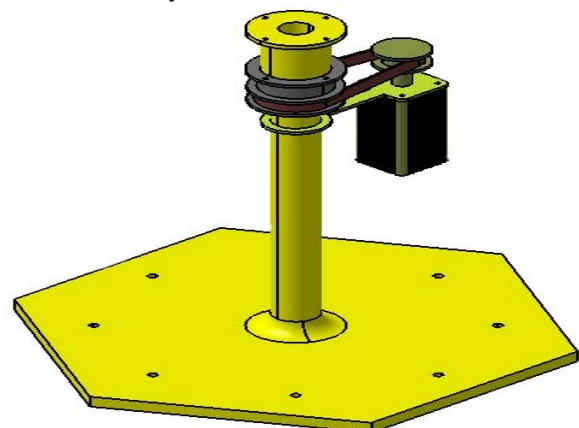


Fig.3. Turret Stand

(iv) Horizontal and Vertical Pneumatic Cylinders and Vacuum System

The PE and PP sacks will be held and placed via Horizontal and Vertical Pneumatic Cylinders, and a Vacuum System. It is shown in Fig.4. It is designed by a rod less pneumatic cylinder, two horizontal mechanical supports, a profile pneumatic cylinder, two vertical mechanical supports, twelve bellow suction pads [9-11].

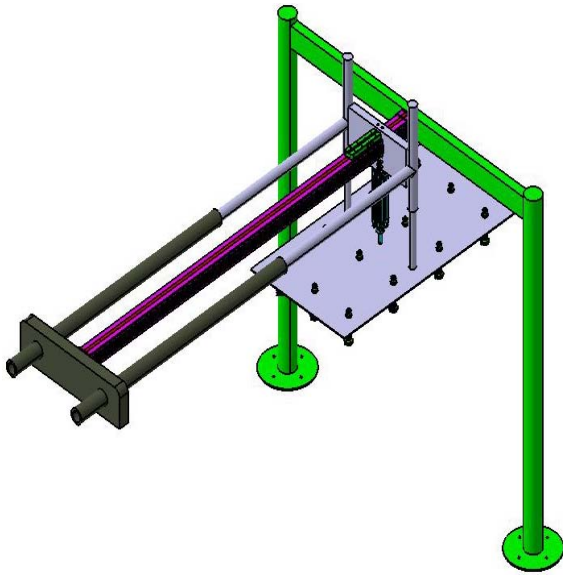


Fig.4 Horizontal-vertical pneumatic cylinders, and vacuum system

(v) Final Sack Storing Tables

Final sack storing tables are necessary for completing the inserting procedure. They are made of steel profiles with dimensions of 1160 mm width, 800 mm height and 1990 mm length.

All parts are assembled together using Figures 1, 2, 3 and 4. It is given in assembly in Fig.5. Fig.6 (a) and (b) show details in suction pads and installed sensors as well. The sensors (Sensors 1, 2 and 3) placed on the vacuum system of the sack inserting mechanism are shown in Fig. 6. The sensors of the other vacuum systems (2nd, 3rd, 4th, 5th and 6th) are placed in the same manner. A proximity sensor is one to detect the presence of nearby objects without any physical contact. Different sensors are used on the sack inserting system, a capacitive sensor for the plastic target, and inductive one for the metal target [12-13].

3.1 Design Criteria

The mechanism for the inserting operation of PE and PP sacks must satisfy the following design requirements:

- i. Each Horizontal and Vertical Pneumatic Cylinders, and Vacuum System must transport PE and PP sack horizontally.

- ii. The sack inserting turret mechanism must work in sequence. When the Horizontal and Vertical Pneumatic Cylinders, and Vacuum System that works on the PE sack inserting platform has completed its task, which of PP sack has also completed its task too. In the same time interval, PE inserted PP sack is withdrawn by that of the final sack.
- iii. The mechanism must be in optimum geometry to allow sack placing and pulling and must not cause high tension on the sacks.
- iv. The sack inserting turret mechanism must be simple with a compact structure. The mechanism must not use a large space for operation.
- v. The mechanism must be simple to control and must be easily manufactured [2, 13-15].

4. Drive Systems and Control Structure of Inserting Mechanism

The motion coordination and the control of the mechanisms are explained here. The inserting system consists of four different mechanisms; the sack-turret, the sack-turret actuator, the horizontal and vertical pneumatic cylinders and the vacuum system. Each mechanism has a different function and the structure which makes the system difficult to control. The above mechanisms can be controlled by using an electrical actuator, servo motor, vertical and horizontal pneumatic cylinders, sensors or vacuum systems [16-20]. Fig 7 shows the mechanism of the sack inserting system with a block diagram. A DC servo motor is used to control the sack-turret. A vacuum system is used to hold the sack. The Horizontal and Vertical Pneumatic Cylinders are used to transport the vacuum system which holds the sack and to place the sack on the sack-turret inserting platform and finally, to transport the final sack to the storing table.

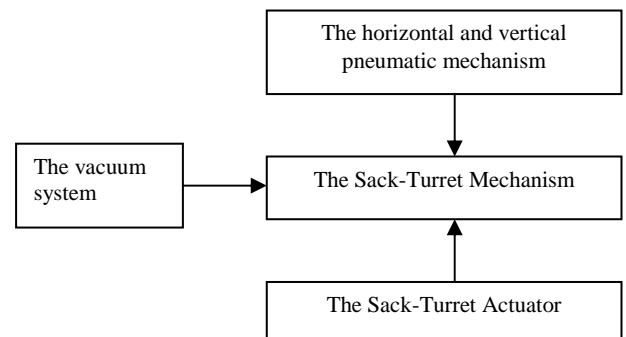


Fig.7. The sack turret inserting system

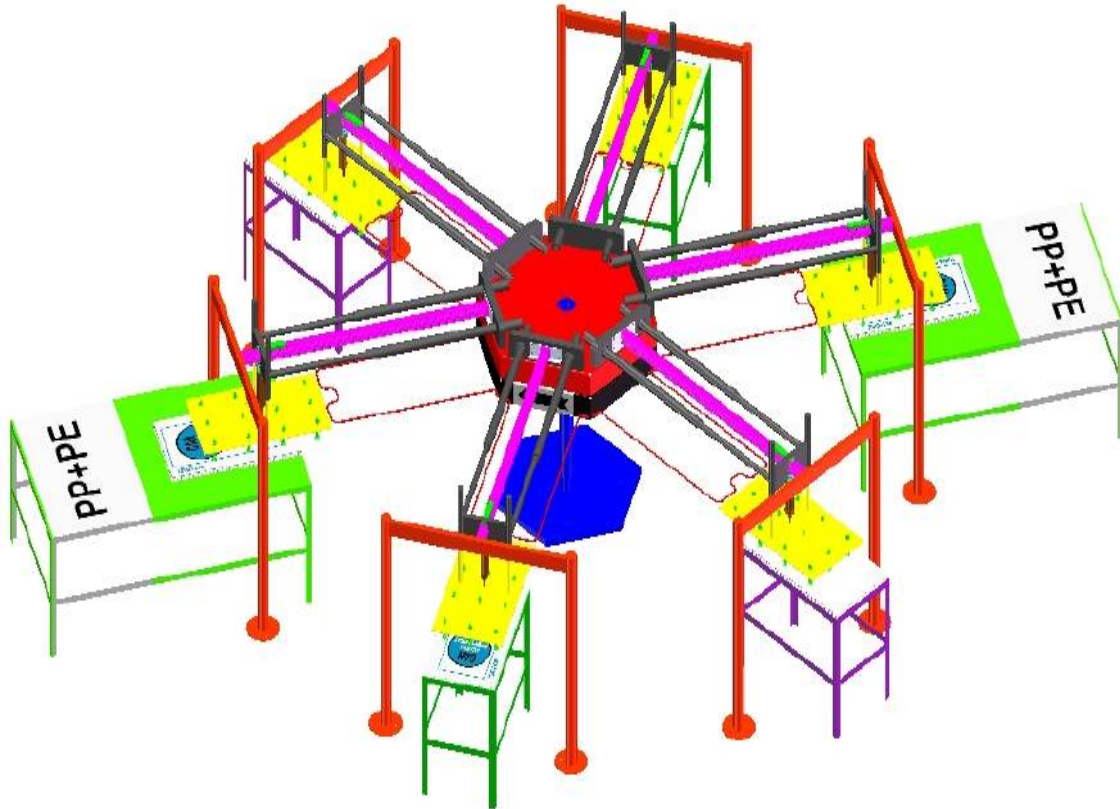
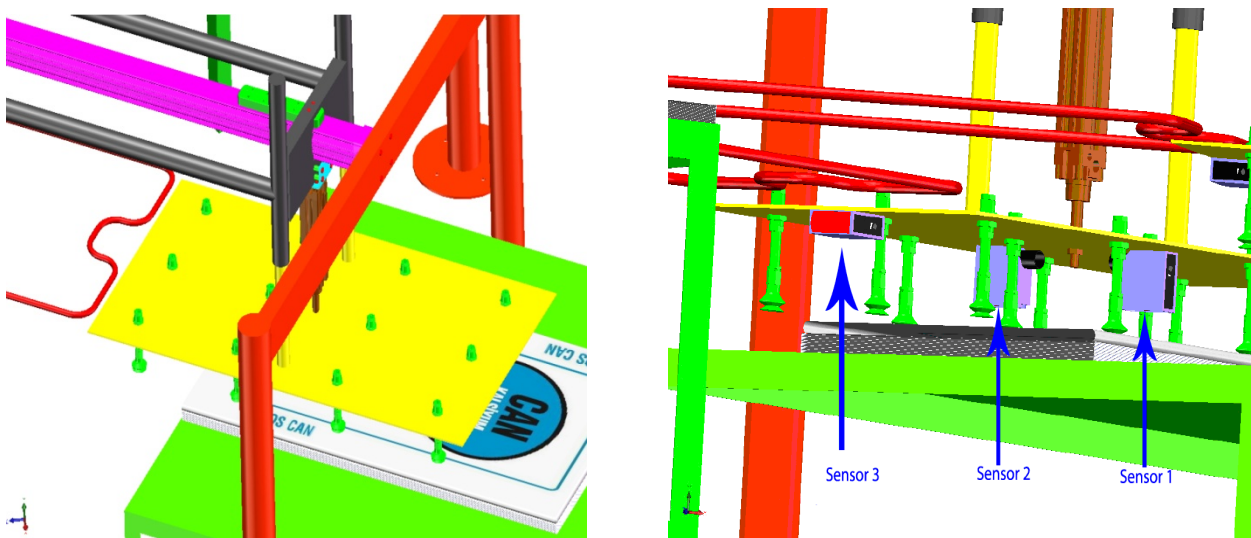


Fig.5. An isometric view of sack inserting mechanism.



(a) A view of vacuum system with suction pads

(b) A view of vacuum system with sensors

Fig.6. Different views on the assembly

As the first part of the motion cycle, the motor adjusts the location of the positioning mechanism, which can carry all the mechanisms to place the sack. The motion profile of the servo motor is designed using the trajectory available to the location of the PE sack, PP sack and the final sack. Here the servo motor operates at a 60o angle, and stops to perform the required operation.

5. Synchronization Issues on Inserting Mechanism

This section describes the synchronization all of the actuators in the system to insert PE sack into the PP. The operation steps of actuators are sequential, in a defined order for the purpose of synchronization. Twenty-one (21) operations (18 independent and 3 dependent) are needed to perform a sack insertion. Three dependent operations are performed by the servo motor. Eighteen independent operations are carried out by three horizontal and vertical pneumatic cylinders and a vacuum system. The six of them are performed by horizontal and vertical pneumatic cylinders and a vacuum system. The initiations of the operations are carried out by vertical pneumatic cylinders whereas the terminations are performed by that of the horizontal.

The total time of all the operations is accepted as a specified unit of time to get the final sack – or when the PE sack is inserted into the PP. All the operations are explained as the following in Table 1.

Table 1. Sequence of Operations

Step-1 Positioning of Vertical Pneumatic Cylinders for PE
Step-2 Vacuum On
Step-3 Positioning of Vacuum
Step-4 Placing PE Sack
Step-5 Vacuum Off
Step-6 Positioning of Horizontal Pneumatic Cylinders for PE
Step-7 Positioning of Sack-Turret Inserting Platform of the PE
Step-8 Positioning of Vertical Pneumatic Cylinder for PP
Step-9 Vacuum On
Step-10 Positioning of Vacuum
Step-11 Placing PP Sack
Step-12 Vacuum Off
Step-13 Positioning of Horizontal Pneumatic Cylinders for PP
Step-14 Positioning of Sack-Turret Inserting Platform of PE Sack Inserted that of PP
Step-15 Positioning of Vertical Pneumatic Cylinder for Final
Step-16 Vacuum On
Step-17 Positioning of Vacuum
Step-18 Vacuum Off
Step-19 Positioning of Vertical Pneumatic Cylinder
Step-20 Positioning of Horizontal Pneumatic Cylinder
Step-21 Positioning of Sack-Turret Inserting Platform

6. Trajectories on Inserting Mechanism

The manual sack inserting mechanism has a trajectory like Fig. 8. The first step of the manual sack inserting process is to place the PE sack. The trajectory of the PE sack is drawn by the green line and arrow (Number 1). After placing the PE sack, the PP is placed on it and the trajectory of the PP sack is drawn by the blue line and arrow (Number 2). The final sack, which is the PE sack inserted into the PP sack, is removed outside of the sack inserting platform. Its trajectory is drawn by the red line and arrow (Number 3). Trajectory is also represented in X-Y coordinate in Fig.9.

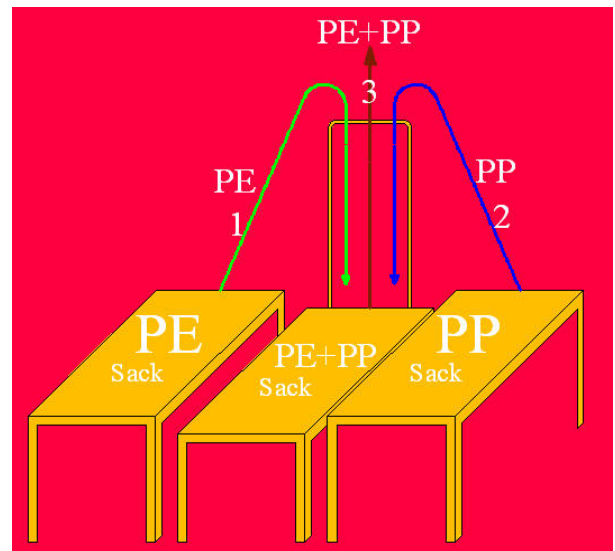


Fig. 8 Manual sack inserting mechanism trajectory

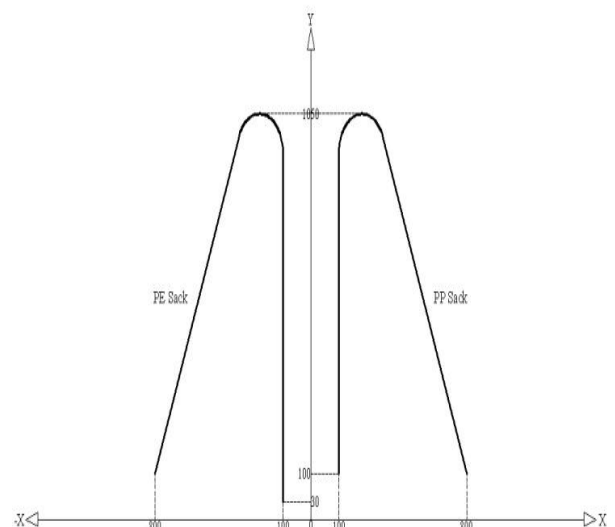


Fig.9 Representation of trajectory in X-Y coordinates

7. Mathematical Model of Horizontal Sack Inserting Mechanism

This section presents a mathematical model for a horizontal sack inserting mechanism given. The dynamic characteristic of the actuator is studied by using the mathematical model available. Here an inserting turret is used; an inserting is performed by 60° indexing at the output. This is provided by a servo motor as a servo mechanism in the application. The system consists of a BLDC motor with an incremental encoder for positional feedback. A horizontal turret is attached indirectly to the motor via a belt drive. System representation is schematically given in Fig. 10.

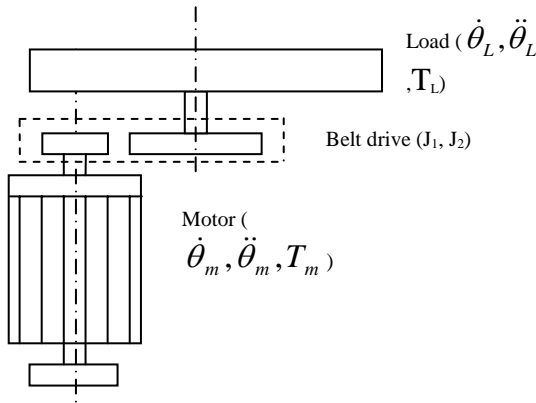


Fig.10 Schematic representation of motor-load system

Since a Brushless DC motor is chosen, the equations can be written by looking at a representative system as [20-21]

$$L \frac{di(t)}{dt} + Ri(t) + V_{emf}(t) = V_{app}(t) \quad (1)$$

$$J \frac{dw(t)}{dt} + Dw(t) - T(t) = T_L \quad (2)$$

Where $V_{app}(t)$ is the applied voltage, $w(t)$ is the motor angular velocity, $i(t)$ is the motor circuit current, R is the motor resistance, L is the motor inductance, and D is the motor viscous coefficient. J refers the total inertia referred to motor shaft and the rotary actuator, motor as

$$J = J_m + J_1 + \frac{J_2}{N^2} + \frac{J_L}{N^2} \quad (3)$$

J_m is the motor inertia, J_1 and J_2 are the inertias of pulley 1 and 2, J_L is the load inertia, calculated from the horizontal turret configuration. A belt drive model

contains the belt ratio (ratio of pulley diameters), the efficiency (η). Thus

$$N = \frac{\theta_m}{\theta_L} = \frac{w_m}{w_L} = \frac{d_2}{d_1} \quad (4)$$

The applied voltage in equation (1) is calculated using PID control which combines P (Proportional), I (Integral) and D (Derivative) control action producing the necessary voltage from the amplifier. This control takes the past, current and future error [19-20]. It can be represented as

$$V_{app}(t) = K_p e(t) + K_v \dot{e}(t) + K_i \int_0^t e(t) dt \quad (5)$$

Here P control is the simplest type of control and always tried first in a control system. Other types of control are considered to improve the system performance. The damping action is introduced by D control providing stability. Finally integral control reduces the steady state error. In the application $e(t)$ refers to the positional error. It is fed back to the system to get proper indexing after reduction. In equations (1) and (2); $V_{emf}(t) = K_e w(t)$ and $T(t) = K_t i(t)$ representing K_e is the motor back emf constant, K_t is the motor torque constant. These equations can be represented as first order ones as

$$\begin{bmatrix} L_a & 0 \\ 0 & J \end{bmatrix} \begin{bmatrix} \dot{i}_a \\ \dot{w} \end{bmatrix} + \begin{bmatrix} R_a & K_e \\ -K_t & D \end{bmatrix} \begin{bmatrix} i_a \\ w \end{bmatrix} = \begin{bmatrix} V_{app}(t) \\ T_L \end{bmatrix} \quad (6)$$

The electro mechanical characteristics of the motor are given in Table 2.

Table 2. Motor parameters [22]

Parameter Description	Value
Motor inertia	$J_m=0.000813 \text{ kg.m}^2$
Motor torque constant	$K_t=0.745 \text{ Nm/A}$
Motor back emf constant	$K_e=86 \text{ (V/krpm)}$
Motor resistance	$R=1.35 \text{ } \Omega$
Motor inductance	$L=7.3 \text{ mH}$
Electrical time constant	$t_e=5.92 \text{ ms}$
Mechanical time constant	$t_m=1.80 \text{ ms}$
Maximum speed (no load)	$w=3000 \text{ rpm}$
Static friction torque	$T_f=0.113 \text{ Nm}$

7.1. Numerical Simulation

There are different packages to solve equations of interest. Having obtained equations for the inserting



mechanism and the horizontal turret, the 4th order Runge Kutta method is applied for solutions. The time interval taken for integration is $\Delta t=0.01$ sec. The system equations (1) and (2) are linear in character. They are represented in state space for and solved with initial conditions given as motor current, motor displacement and motor velocity. For optimum performance, K_p , K_v and K_i must be tuned properly by looking at the closed loop performance of the system [23-25].

The dynamic model equations; (1) and (2) are solved to simulate system behavior. The response of the horizontal sack inserting mechanism is dependent on specified inputs. Here a step input is given, with $N=6$ belt-pulley ratio. The motor is required to turn 360° , resulting 60° angular indexing at the end. Load inertia is calculated using the figures given in Chapter 2, horizontal turret configuration as $J_L=2.52$ kg/m². Many observations are taken by running simulations independently. Three basic observations are given here corresponding to P, PD and PID control system performance.

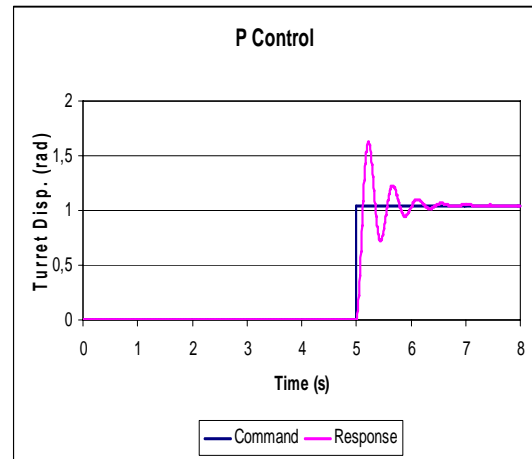
Step responses of BLDC motor are given below with PID controller in this system, Figs. 11 (a),(b) and (c). The period of motion is taken as 8 seconds. The dwell motion is 5 seconds where the pneumatic action for holding the sack is performed. Rotation of turret for proper positioning is performed in 3 seconds to stay ready, in front of other table for sacks. Here the load is taken as a hexagonal turret made of galvanized steel. During different successive runs, P action is performed $K_p=30$, PD action is applied using $K_p=30.0$ and $K_d=2.0$ and finally, $K_p=30.0$, $K_d=2.0$ and $K_i=1.0$ with PID.

8. Conclusions

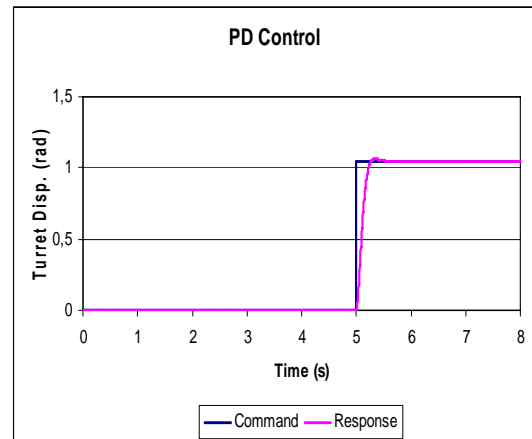
This work presents a study for inserting PE sack into that of PP, the basic sack placing type used in the manual sack inserting procedure by means of an electromechanical system. The system referred to as the sack inserting system was designed and controlled by benefiting from technological developments of computers, actuators, etc. During the design of the whole system the function of the sack inserting system and its decomposition were firstly considered. The function was broken down into the sub-mechanisms and components, and then assemblies were developed to provide these functions.

The sack inserting system involves different mechanisms: the sack-turret, the sack-turret actuator, the horizontal-vertical pneumatic cylinders and the vacuum system. The main mechanism was the sack inserting mechanism. The others were accepted as auxiliary mechanisms to be developed and designed referring to the sack inserting mechanism. The design studies on

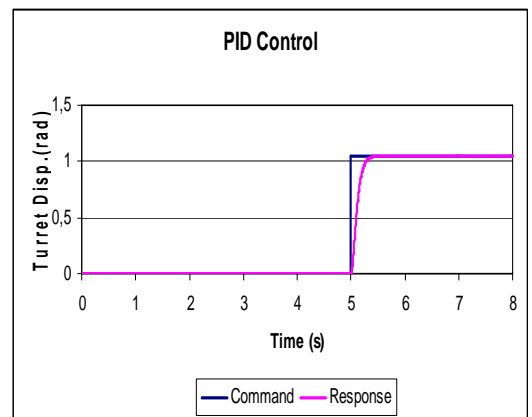
each mechanism, which depended on the functional requirements, design criteria, assumptions and general properties of the sacks, were realized. In this study; rod less and profile pneumatic cylinders, solenoid valves, vacuum equipments, photoelectric proximity switches, brushless DC motor and servo driver were used.



(a)



(b)



(c)

Fig. 11 Step responses for the horizontal turret



Having completed simulation of the system with real system data with an available fertilizer filling procedure, there will be a chance of applying this design in the future. This will eliminate the need for individual human effort as the process will be done automatically. Of course, production and integration of parts will take some time. Inserting procedure will be quicker and no time loss will happen in the operating system.

References

- [1]. http://sanayi.tob.org.tr/kitap_son2.php?kodu=32120116
- [2]. Bakir G., 'Design and Analysis of Placing (Inserting) Mechanism for Polypropylene (PP) and Polyethylene (PE) Sacks', Ms. Thesis, Gaziantep University, April 2010.
- [3]. Soroka, W., *Fundamentals of Packaging Technology*. Institute of Packaging Professionals. ISBN 1-930268-25-4, 2002.
- [4]. Bix, L., Rafon, Lockhart, Fuente. *The Packaging Matrix. IDSPackaging*. http://www.idspackaging.com/Common/Paper/Paper_47/PdfImage.pdf, 2003
- [5]. Choi, S. J., and Burgess. 'Practical mathematical model to predict the performance of insulating packages'. *Packaging Technology and Science*, 20 (6),. DOI: 10.1002/pts.747, pages 369-380, 2007.
- [6]. Courtesy of Hao Yu Precision Machinery Industry Co., Ltd. , Taiwan (Catalogue)
- [7]. Pons, D. J., and Raine, J. K. 'Design Mechanisms and Constraints'. *Research in Engineering Design*, 16, pages 73-85, 2005.
- [8]. Bateson, R.N. *Introduction to Control System Technology*. New York: Macmillan Pub. Com. 1991.
- [9]. Basic Training Motors, Gears and Drives Industrial-Duty and Commercial- Duty Leeson Electric Corporation, Canada 1999
- [10]. Pinches, M. J., and Callear, B. J. (Eds.). *Power Pneumatics*. Prentice-Hall Europa, 1996.
- [11]. Wee, H. W. N. G. *Iterative Learning Control and Bumpless Transfer for an Electro-Pneumatic Servo System*. Ph.D. Thesis. University of Illinois at Urbana-Champaign. <http://mr-roboto.me.uiuc.edu/hanthesis.PDF>, 2000.
- [12]. Festo Didactic GmbH & Co., 06/2001
- [13]. http://en.wikipedia.org/wiki/Proximity_sensor
- [14]. Jewery, K. C., and Jeffcoat, W. (Eds.). *The PLC Workbook: Programmable Logic Controllers Made Easy*. England: Prentice-Hall Europa, 1996.
- [15]. Norton, R. L. *Design Of Machinery: An Introduction to the Synthesis and Analysis of Mechanisms and Machines*. Singapore: McGraw-Hill International Editions, 1992.
- [16]. Söylemez, E. *Mechanisms*. (3rd ed.). Ankara-Middle East Technical University Publication Number: 64, 2009.
- [17]. Shigley, J. E., and Uicker, J. J. JR. (Eds.). *Theory of Machines and Mechanisms*. (2nd ed.). Singapore: McGraw-Hill International Editions, 1995.
- [18]. Vu, H.V., and Esfandiari, R. S. (Eds.), *Dynamic Systems- Modeling and Analysis*. McGraw Hill., 1998.
- [19]. Ong, C. M., *Dynamic Simulation of Electric Machinery*. New Jersey: Prentice Hall, 1998.
- [20]. Dorf, R.C., and Bishop, R. H. (Eds.). *Modern Control Systems*. (10th ed.). Pearson: Prentice Hall, 2005.
- [21]. Cetinkunt, S., *Mechatronics*. Wiley., 2007.
- [22]. Roos, F., Johansson, H., and Wikander, J. Eds., 'Optimal selection of motor and gearhead in mechatronic applications'. *Mechatronics*, 16, pages 63-72, 2006.
- [23]. Electro-Craft, Brushless Servo Systems (ACE120X-ACE130X) User's Manual, <http://www.electrocraft.com>
- [24]. Cuminos, P., and Munro, N. (Eds.). PID Controllers: Recent Tuning Methods and design to specification. *IEEE Proc. Control Theory Applications*, 49, 1, pages 46-56, 2002.
- [25]. Li, Y., Ang, K. H., and Chang, G. C. Y. (Eds.). 'PID Control System Analysis and Design', *IEEE Control Systems Magazine*, pages 32-41, 2006.
- [26]. Babuska, R., and Stramigioli, S. (Eds.). *Matlab and Simulink for Modeling and Control*. Delf University of Technology, Control Laboratory. 1999.



Multiaxis Three Dimensional (3D) Circular Weaving: Concept to Prototype Design Methodology and Preliminary Investigation of Feasibility of Weaving Method

Kadir BİLİSİK*

Erciyes University, Engineering Faculty, Department of Textile Engineering, 38039, Kayseri, Turkey
kadirbilisik@gmail.com

Abstract

The aim of the study is to develop new preform structures and process in use for the technical textile and composite industries. Multiaxis and orthogonal 3D circular woven preforms and methods have been developed. The multiaxis structure has five yarn sets as \pm bias, axial, circumferential and radial yarns whereas the orthogonal structure has three yarn sets as axial, circumferential and radial yarns. The weaving method, which is called "Radial crossing", was introduced to form the structures. The developed experimental weaving prototype was constructed to evaluate the methods. Basic process and structure parameters have been identified. The preliminary studies showed that it seemed feasible.

Keywords: Multiaxis and orthogonal 3D circular woven preforms, Multiaxis 3D circular weaving machine, Weaving method, Radial crossing, \pm Bias yarns.

1. Introduction

At the beginning of twenty first century, textile structural composite has become attractive to various industrial sections as defense, energy and civilian areas. It is indicated that textile structural composites have superior specific properties compared to the basic materials as metal and ceramics [1, 2, 3, 4, 5, 6 and 7]. The researchers who studied on textile structural composites indicated that it could be considered alternative materials due to the delamination free and damage tolerance material [3, 8 and 9]. In textile processing standpoint, it is explained that they are readily available, cheap and not labor intensive [1, 10]. Fabrication of textile preform is made by weaving, braiding, knitting, stitching and nonwoven techniques and they can be chosen generally based on the end use requirements. Originally 3D preforms can be classified as fiber interlacement types. Simple 3D preform consists of 2D fabrics and is stitched depending on stack sequence. More sophisticated 3D preforms can be fabricated by specially designed automated loom and made near -net shape to reduce scrap rate. However, it is mentioned that they are low in-plane properties [1, 11].

Multiaxis 3D flat weaving is a relatively new concept, since they include also bias yarn sets introduced to the orthogonally structured preform. Bilisik and Mohamed pointed out that Multiaxis 3D preforms enhance in-plane properties. However, there is no one process to make multiaxis 3D woven preform with complex shape and various fiber orientations in the structure cross-section with large dimensions [12, 13 and 14]. To make circular preform, traditional filament winding and pultrusion techniques were used to make one or multi-directional preforms. However, there is no radial reinforcement in the thickness direction. 2D Triaxial and 3D braiding are employed to make multi directional preforms but there is no circumferential and true radial reinforcement. A few special processes have also been developed to make multiaxis preforms. They are sleeve wrapping and fiber placement. But there is no radial reinforcement in the preform [15]. A thick walled circular woven preforms were developed in which integrally woven preform has four yarn sets. These are axial, circumferential and only bias(+) yarn. They are woven upon the surface of a mandrel with resulting shape being determined by the action of the jacquard [16]. Another type of 3D circular woven preform was developed in where three yarn sets have been used as axial, circumferential and radial yarns. All yarn sets are cylindrically orthogonal inside the structure except outer and inner surfaces in where yarn sets are interlaced to provide structural integrity [17]. Stitching-winding based 3D circular preform was introduced in where axial and circumferential yarns were wound on the mold and later stage, the preform was stitched to put some fiber in the radial direction. But, stitching could be damaged yarn sets [18]. 3D preform technology called Autoweave which was transferred to the Textron Inc. in where the 3D preform structures were developed to be used in exit cone for aerospace application. The preform has axial, circumferential yarn and pultruded radial rod and is suitable for only the part manufacturing. Winding principle was employed to form the structure. But, preparing the radial rod skeleton in the mandrel is labor intensive and not suitable to make continuous circular preform [19]. Yasui and co-workers



have been developed 3D circular preform where axial, circumferential and radial yarns were used. Axial yarns were stationary but, winding principal was employed to insert the circumferential yarns and radial yarn bobbins were exchanged between each adjacent radial row in order to insert the radial yarn. This is also suitable part manufacturing and can not make continuous circular preform fabrication [20].

Recently, Bilisik developed the multiaxis 3D circular weaving to make 3D circular woven preform under the various unit cells [21, 22]. Bhatnagar and Parrish modified the existing weaving machine to make non crimp preform for ballistic applications [23]. Also, Kostar and his co-worker developed new method to make complex shaped multi directionally oriented orthogonal woven preforms for composite applications [24].

The objective of the paper is to describe newly developed multiaxis 3D circular weaving and method in terms of concept and machine design perspective and, woven preform which could lead to enhance torsional properties of the woven composite. The preliminary research results showed that it looked feasible.

Woven Preform

Circular unit cells of the multiaxis 3D circular woven preforms have been developed. They were based on radial crossing weaving principle. One of the multiaxis three dimensional circular woven perform has five yarn sets as \pm bias, axial, circumferential and radial yarns. Axial yarns are arranged in a matrix of circular rows and radial columns within the required circular cross section. It looks a spares network for laying the fibers in between adjacent axial fibers. Circumferential fibers are laid down between each adjacent axial fiber row. They are single end and deposited through the preform length. \pm Bias yarns have two sets. They are positioned on both surfaces of the preform. First pair of bias yarns are placed on outer surface and second pair of bias yarns are placed on inner surface of the circular preform but there is a circumferential yarn between bias(+) and bias(-) yarns. They are oriented preform surface at an angle. Radial ends are positioned between each axial row through the preform thickness. They lock all other yarn sets to provide structural integrity of the preform where odd number radial yarns are crossing the structure to the inner diameter but even number are crossing the structure to the outer diameter. The preform is seen in figure 1(a).

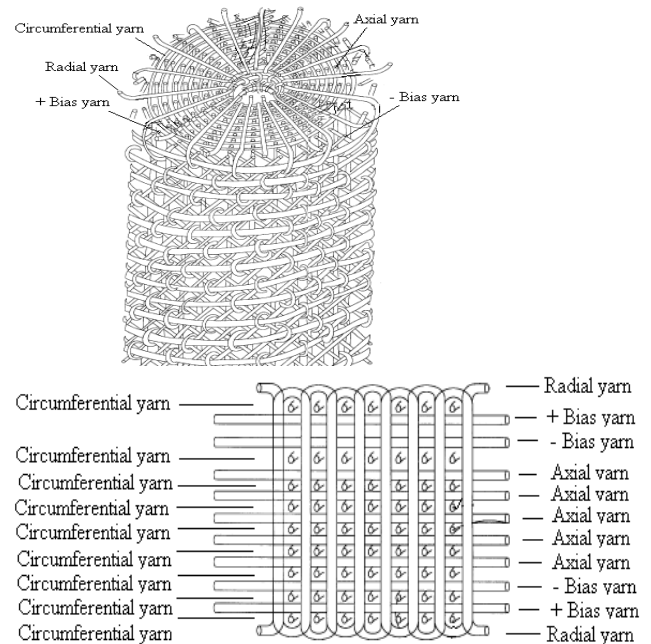


Fig. 1(a): Perspective and side views of the unit cell of the multiaxis 3D circular woven preform.

In side view, circumferential yarns are secured by radial yarns and just beneath both surface of the circumferential fibers, bias yarns are laid. Although, one circumferential layer corresponds to each axial layer, there is no circumferential fiber between bias(+) and bias(-) fibers at outer surface but one circumferential fiber lays down between bias(+) and bias(-) fibers on the inner surface of the circular preform. It can be realized that preform has an interlacement surrounding outer and inner surfaces, but inside the preform \pm bias and circumferential fiber sets are helical path, whereas axial and radial are almost straight. Again, circumferential fiber has made single end to the unit cell diameter. A small diameter polyethylene tube is used in order to visually understand the multiaxis 3D circular woven preform unit cells and radial yarn path in the unit cell in the radial crossing principles. Figure 1(b) shows the radial yarn path at “crossing” principle on the multiaxis 3D circular woven preform unit cell.

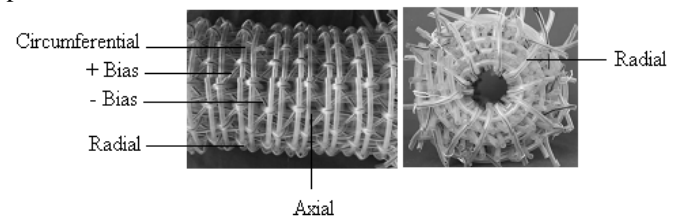


Fig. 1(b): Radial tube path in the preform unit cells as “crossing” principle where unit cell has \pm bias, axial, circumferential and radial tubes.



3D orthogonal circular woven preform unit cell has basically three yarn sets as axial, circumferential and radial yarns. Axial yarns are arranged in a matrix of circular rows and radial columns within the required circular cross section. It looks a sparse network for laying the fibers in between adjacent axial fibers. Circumferential fibers are laid down between each adjacent axial fiber row. They are single end and deposited through the preform length. Radial ends are positioned between each axial row through the preform thickness based on radial crossing and in-out principals. They lock all other yarn sets to provide structural integrity of the preform based on radial crossing principal as it is seen schematically in figure 1(c). In side view, circumferential yarns are secured with axial fiber layers by radial yarns. It can be realized that preform has an interlacement surrounding outer and inner surfaces but inside the preform circumferential fiber sets are helical path, whereas axial and radial are almost straight. Again, circumferential fiber has made single end to the unit cell diameter.

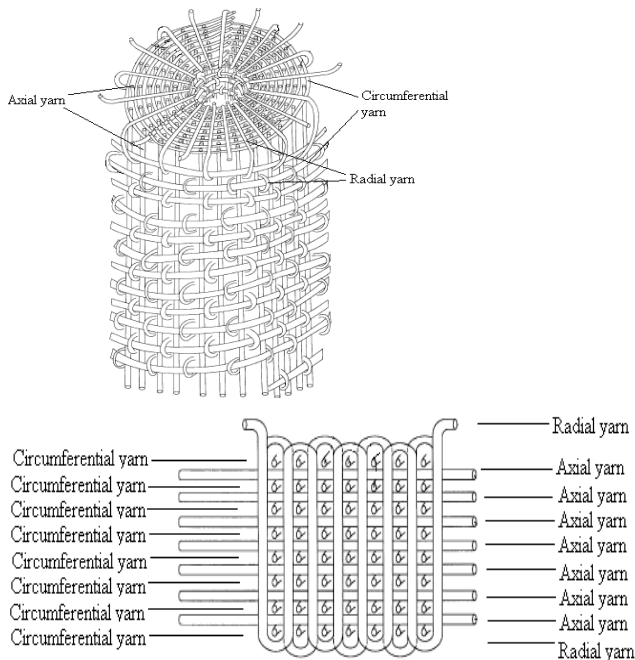


Fig. 1(c): Perspective and side views of the unit cell of the 3D orthogonal circular woven preforms.

A small diameter polyethylene tube is used in order to visually understand the orthogonal 3D circular woven preform unit cells and radial yarn path in the unit cell as radial crossing principles. Figure 1(d) shows the radial yarn path “crossing” principles on the 3D orthogonal circular woven preform unit cell.

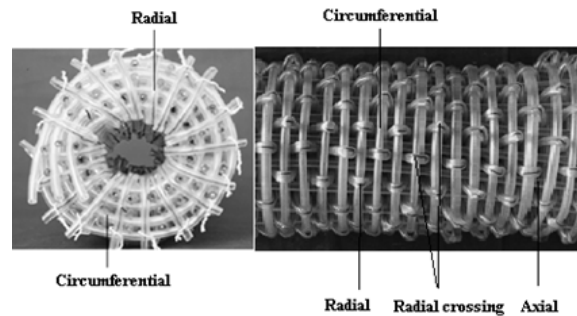


Fig. 1(d): 3D orthogonal circular woven preform unit cell cross-section and radial tube path in the cell show as “crossing” principles.

Method to Weave

Starting position of the multiaxis 3D circular weaving is seen in figure 2(a) where \pm bias yarns, circumferential and radial yarn sets have on the carriers. Warp yarn sets pass through the guide tube and fed by bobbins. As seen in weaving cross section, bias(+) yarns are denoted as b_{+1} , b_{+2} , b_{+3} , b_{+4} , b_{+5} , b_{+6} and bias(-) yarns are denoted as b_{-1} , b_{-2} , b_{-3} , b_{-4} , b_{-5} , b_{-6} . The circumferential yarns are denoted as c_1 , c_2 , c_3 , c_4 , c_5 , c_6 . The axial yarn sets are denoted ‘o’ on the cross section of the weaving bed. The radial yarns are denoted as r_1 , r_2 , r_3 , r_4 , r_5 , r_6 . The \pm bias and circumferential are mounted on the each individually rotated ring. The radial carriers can reciprocate linearly to the radial corridor of the machine bed.

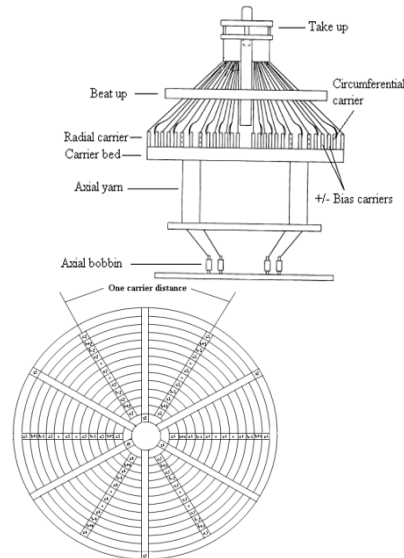


Fig. 2(a): Starting position of side (left) and cross section (right) view for multiaxis 3D circular weaving based on radial crossing principals.

For the first half weaving cycle, after the two pair of \pm bias carrier rings rotates anticlockwise and clockwise

directions according to yarn orientation direction, bias yarns become at an angle compared to the axial yarns as seen in figure 2(b). Rotation of the \pm bias carrier rings is equal to one carrier distance for every weaving cycle. Two axial layers remain in their original positions. The fiber position in the structure is seen in the left corner of schematic side view of the weaving.

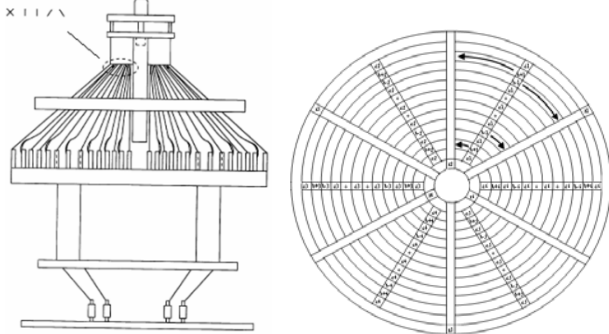


Fig. 2(b): \pm Bias carrier ring rotation based on radial crossing principals.

Circumferential carrier rings rotate one complete rotation around the machine bed to anticlockwise direction and lay the circumferential yarns in the structure seen in the left corner of the side view of the weaving. This is also seen in figure 2(c).

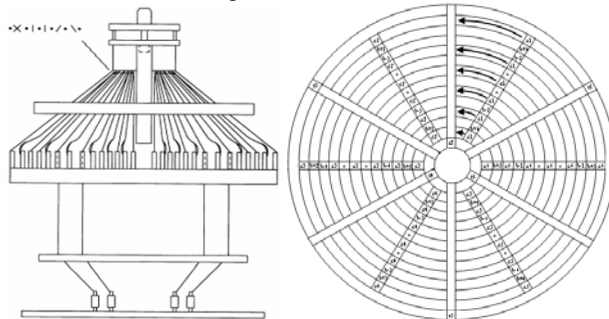


Fig. 2(c): Circumferential carrier ring rotation based on radial crossing principals.

In radial crossing principal, odd number radial carriers move from outer diameter to inner diameter to the radial corridor whereas even number radial carriers move from inner to outer diameter to the radial corridor. They are crossing and lock all the previously inserted yarn sets to provide structural integrity as seen in the top of the left corner of side view of the weaving. Figure 2(d) shows the radial insertion cycle.

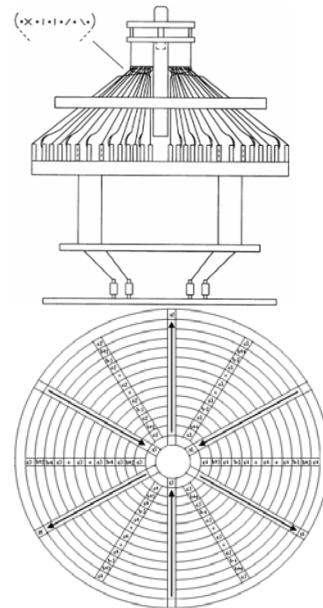


Fig. 2(d): Radial insertion based on radial crossing principals.

Circular open reed moves linearly toward the woven formation line and slides the inserted circumferential yarns. Then it beats the inserted fibers to provide dense fabric structure. During beat up action, excessive lengths on circumferential and radial yarns are compensated for by carriers, and the radial yarn formation in the preform structure is seen in the left corner of the side view of the weaving. It is seen in figure 2(e). After beat up is completed, reed is returned to the original position and take up unit removes the inserted yarns from the weaving formation line to provide the space for next weaving cycle. Fabric volume fraction can be controlled by take up.

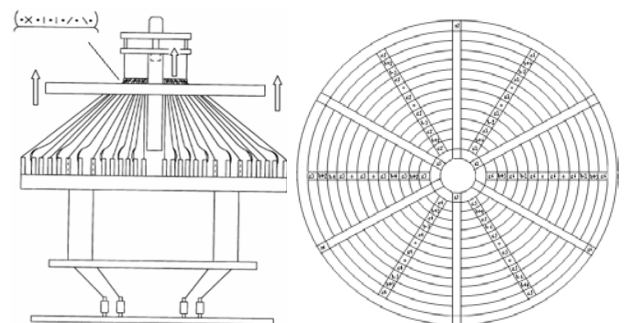


Fig. 2(e): Beat-up movements based on radial crossing principals.

For second half cycle of the weaving, after the weaving action has been completed as described in figure 2(b) and (c), odd number radial carriers move from inner diameter to outer diameter to the radial corridor whereas



even number radial carriers move from outer to inner diameter to the radial corridor. They are crossing and lock all the previously inserted yarn sets to provide structural integrity as seen in the left corner of side view of the weaving. Beat-up unit packs the previously inserted yarns to the weaving formation line. After beat up is completed, reed is returned to the original position and take-up unit removes the inserted yarns from the weaving formation line to provide the space for next weaving cycle. Therefore one weaving cycle is completed and it is repeated according to required preform length.

3D orthogonal circular woven preform unit cell is made by following weaving method in which the circumferential yarns are denoted as $c_1, c_2, c_3, c_4, c_5, c_6$. The axial yarn sets are denoted 'o' on the cross-section of the weaving bed. The radial yarns are denoted as $r_1, r_2, r_3, r_4, r_5, r_6$. The circumferential are mounted on the each individually rotated ring. The radial carriers can reciprocate linearly to the radial corridor of the machine bed. In the first half of the weaving cycle, circumferential carrier rings rotate one complete rotation around the machine bed to the anticlockwise direction and lay the circumferential yarns in the structure as it is seen in the top of the left corner side view of the weaving. This is also seen in figure 3(a).

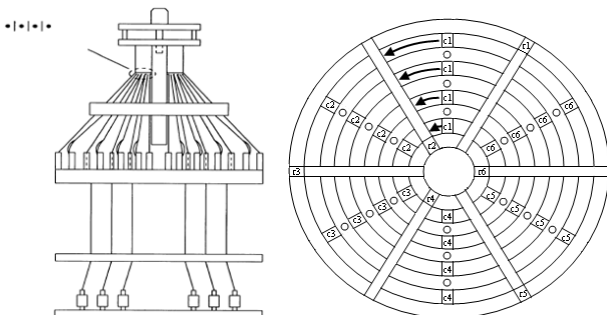


Fig. 3(a): Circumferential carrier rings rotations based on radial crossing principal.

In the radial crossing principal, odd number radial carriers move from outer diameter to inner diameter to the radial corridor whereas even number radial carriers move from inner to outer diameter to the radial corridor. They are crossing and lock all the inserted circumferential yarn sets to provide structural integrity as seen in the top of the left corner side view of the weaving. Figure 3(b) shows the radial insertion cycle.

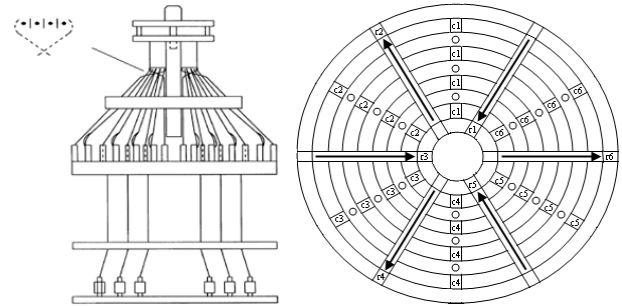


Fig. 3(b): Radial insertion cycle based on radial crossing principal.

Circular open reed moves linearly toward the woven formation line and slides the inserted circumferential yarns. Then it beats the inserted yarns to provide dense fabric structure. During beat up action, excessive lengths on circumferential and radial yarns are compensated for by carriers, and the radial yarn formation in the preform structure is seen in the left corner of the side view of the weaving. It is seen in figure 3(c). After beat up is completed, reed is returned to its original position and take-up unit removes the inserted yarns from the weaving formation line to provide the space for next weaving cycle. Fabric volume fraction can be controlled by take-up.

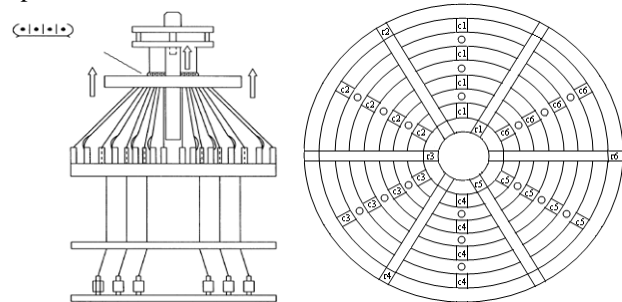


Fig. 3(c): Beat-up movements based on radial crossing principal.

In the second half of the weaving cycle, after the circumferential yarns inserted in the preforms as described in figure 3(a), odd number radial carriers move from inner diameter to outer diameter to the radial corridor whereas even number radial carriers move from outer to inner diameter to the radial corridor. They are crossing and lock all the previously inserted yarn sets to provide structural integrity as it is seen in the top of the left corner side view of the weaving. Beat-up unit packs the previously inserted yarns to the weaving formation line. After beat up is completed, reed is returned to its original position and take-up unit removes the inserted yarns from the weaving formation line to provide the space for next weaving cycle. Therefore one weaving cycle is completed and it is repeated according to required preform length.



Bias Angle

Bias fiber sets can be arranged between 15° to 85° through the in plane of both outer surface and inner surface of the preform. In bias carrier ring when they are rotated to each other just for one carrier distance, each carrier distance is equivalent to the 15° . This is seen in figure 2(a). If the carrier ring is rotated two, three or four carrier distance, the preform surface has 30° , 45° , and 60° bias angle orientations, respectively.

Weaving Machine

Multiaxis 3D circular weaving machine has been designed and constructed to make multiaxis 3D circular woven preform to test the necessary units. The multiaxis 3D circular weaving is an experimental concept prototype and manually driven to make multiaxis circular structure. It has mainly six units as \pm bias carriers and bias carrier rings, axial fiber feeding, circumferential carriers and circumferential carrier rings, radial carriers, beat-up and take-up. The weaving prototype has basement for axial bobbins. All axial fiber ends are fed to the weaving zone through the guiding tube in the machine bed via whole plate to provide proper alignment and prevent any entanglement. The braider type carrier can be used for yarn sets except axial yarn set to maintain the yarn feeding and tension functions. In the machine bed there are concentric rings in which the number of the rings depend on the number of layers in the preform unit cell. Two pairs of bias carrier ring move in reverse directions to align the bias yarns both on the inner surface and outer surface of the preform. However, any carrier ring in the machine bed can be used as \pm bias or circumferential or axial feeding depending upon preform unit cell. All radial carriers are positioned in outermost position of the machine bed, and the number of the radial carriers depends upon the radial row. The beat-up is a circular open reed which has many finger rods corresponding to each radial row. They beat the circumferential yarns against the preform formation zone. Take-up unit consists of a pair of cylinders to deliver the inserted circumferential and radial from the weaving zone. If single part multiaxis 3D circular woven preform with complex contour is fabricated, mandrel is used depending upon part geometry. The multiaxis 3D weaving concept prototype is seen schematically in figure 4(a).

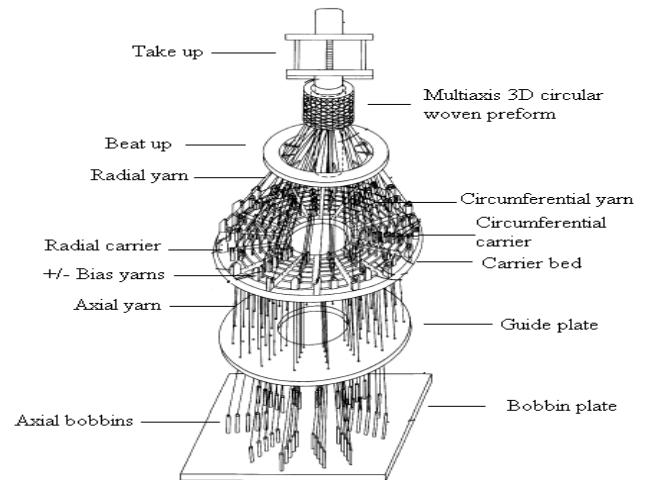


Fig. 4(a): Schematic views of the multiaxis 3D circular weaving concept prototype.

Multiaxis 3D circular weaving fabricates basically two types of preform with multiaxis or orthogonal unit cells. The first type is continuous uniform volume fractional preform, and the second is complex part preform as conical or cylinder-conical shapes in which volume fraction in the preform section is variable and depends on preform location. Figure 4(b) shows example of multiaxis 3D cylindrical Kevlar™ (Kevlar is an Aramid base fibers and sold under the trade name of Kevlar by DuPont fiber producer) fiber preform, and it is weaving zone during fabrication. Figure 4(c) shows multiaxis 3D cylinder-conical carbon fiber preform on the developed weaving concept prototype.



Figure 4(b). Weaving zone and multiaxis cylindrical 3D woven Kevlar™ preform which has five yarn sets as \pm bias, axial, circumferential and radial.

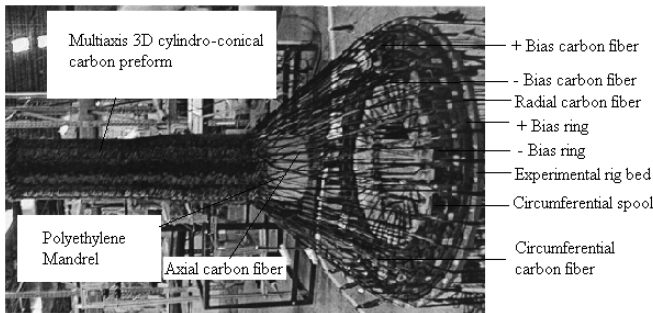


Fig. 4(c): Multiaxis 3D cylindro conical carbon fiber preform and weaving zone in the manually drive concept prototype.

2. Results and Discussion

Multiaxis 3D woven preforms

Multiaxis 3D cylindrical woven preforms were fabricated by the developed concept prototype. The specifications of the multiaxis 3D cylindrical and cylinder-conical Kevlar™ woven preforms were presented in table 1. In Kevlar™ cylindrical preforms which is denoted as PI-A and PII-A, all yarns are 1100 dtex for PI-A and 1600 dtex for PII-A. PI-A has five yarn sets as 2 bias(+) and 2 bias(-) layers, and 7 axial layers, 6

circumferential layers and each radial yarn corresponds for each axial row, whereas PII-A has four yarn sets and half yarn ends compared to that of the PI-A as 2 bias(-) layers, 7 axial layers, 6 circumferential layers and 6 radial yarns correspond for each axial row. It is observed that both preform surfaces were not equal. PI-A has smooth surface and has a few local yarn undulations, whereas PII-A has uneven surface and has many local yarn undulations. PIII-A is conical shape and has five yarn sets which are 1600 dtex Kevlar™ fiber. PIII-A has half yarn ends for all yarn sets compared to that of the PI-A and has 2 bias(+) and 2 bias(-) layers, and 7 axial layers, 6 circumferential layers and each radial yarn corresponds for each axial row in the preform. The basic differences in conical shape compared to the cylindrical preforms is the local fiber fraction. When the preform profile was changed from small to large surface, all yarn fiber fractions were reduced. The solution of the problem can be considered as either adding the fiber end to the weaving area when the profile was changed or using the yarn ends based on maximum preform surface area in where high volume fraction must be achieved in large surface area.

Table 1. Specifications of the multiaxis 3D circular woven Aramid preforms.

Preform unit cells	Multiaxis 3D woven		
	PI-A	PII-A	PIII-A
Material			
Axial fiber	1100 dtex -Kevlar™ 29	1600 dtex-Kevlar™ 49	1600 dtex -Kevlar™ 49
Circumferential fiber	1100 dtex -Kevlar™ 29	1600 dtex-Kevlar™ 49	1600 dtex -Kevlar™ 49
Radial fiber	1100 dtex -Kevlar™ 129	1600 dtex-Kevlar™ 49	1600 dtex -Kevlar™ 49
± Bias fiber	1100 dtex -Kevlar™ 29	1600 dtex-Kevlar™ 49	1600 dtex -Kevlar™ 49
Preform structure			
Axial	7 layers x 36 rows	7 layers x 36 rows	7 layers x 36 rows
Circumferential	6 layers	6 layers	6 layers
Radial fiber	36 ends (single end)	36 ends (6 plied)	36 ends (single end)
+Bias fiber	2 layers x 36 rows	-----	2 layers x 18 rows
-Bias fiber	2 layers x 36 rows	2 layers x 18 rows	2 layers x 18 rows
Cross section	Cylindrical section	Cylindrical section	Conical section
Dimensions (Outside diameter x wall thickness, mm.)	100 x 5	55 x 5	150(bottom) x 70(top) x 5
Preform tightness	Very high	Medium	Low
Diameter ratio	7	12.7	4.7 - 10

Multiaxis 3D cylinder-conical carbon preform was also produced and specification of the preform was given in table 2. Preform has five yarn sets and 2 layers ± bias which have 12 K, 2 layers axial which has 12 K, 1 layer circumferential which has 6 K and has 6 ends and each

radial yarn, which has 1K corresponds for each axial row in the preform. The surface of the multiaxis 3D carbon preform was smooth and no inconsistency was observed through out the preform length as it is seen in figure 4(c).

Table 2. Multiaxis 3D circular carbon preform specification from radial crossing weaving.



Preform unit cells	Multiaxis 3D woven perform- PI-C
Material	Thornel T-300 Carbon fiber
Axial fiber	12 K ²
Circumferential fiber	6 K
Radial fiber	1 K
± Bias fiber	12 K
Preform structure	
Axial	2 layers x 36 rows, Layer 1 (1 end), Layer 2 (2 ends)
Circumferential	1 layer (6 ends per layer)
Circumferential density	6 ends/ 10 cm
Radial fiber	36 ends (one radial for every axial row)
+ Bias fiber	1 layer x 36 rows
-Bias fiber	1 layer x 36 rows
Bias angle (measured)	60°
One carrier movement	15°-20°
Cross section	Cylinder - conical
Dimensions (top diameter x bottom diameter x wall thick x length, mm.)	130 x 150 x 1 x 610
Diameter ratio	1 / 5
Mold	Polyethylene
Weave unit cell in section	Radial, +Bias, Axial, Circumferential, Axial, -Bias, Radial

Bias Orientation

Bias orientation is made by means of concentric rings movement in clockwise direction for bias(-) and anticlockwise direction for bias(+). Any ring can be used as bias orientation around the machine bed. This provides a versatile preform unit cell, and any layer in the structure can be assigned as bias(+) or bias(-). The bias angle can be arranged between 15° to 85°. On the experimental concept prototype, it is found out that bias yarns on the outer and inner surfaces of the structure form helical paths and there is a slight difference of angle between them especially making the thick wall preforms. As it is seen in figure 4(b), PI-A which is high density woven preform has around 60° angle between bias and axial to the machine direction, whereas PII-A which is medium density woven preform has around 45° angle between bias and axial to the machine direction. It is observed that there is a certain relation between preform density (fiber volume fraction) and bias yarn orientation and take –up rate. More research may be required to understand relations between those processing parameters and preform structural parameters on the concept prototype.

Circumferential Yarn Insertion

After circumferential fiber insertion was completed, excessive length was retracted by carrier. The excessive yarn length occurred because of diameter (**preform outer diameter / Outermost ring diameter**) ratio is not 1. The amount of diameter ratio depends on the number of the rings. When the excessive circumferential yarn is not retracted, this causes waviness in the structure for some local yarn undulations. However, there must be adequate

tension applied on the circumferential yarns to get proper packing during beat-up. Circumferential yarn ends in each layer, which is the equivalent filling in the flat weaving, were six during insertion as seen in table 1 and table 2. This is resulted high insertion rate.

Radial yarn insertion

Radial fibers are inserted by carrier movement in the radial corridors. They make cross movement in the radial crossing weaving. It is realized that there is a relation between number of layers and radial yarn retraction. If the number of layer in the preform is increased, yarn retraction in the radial carrier is increased. The retraction must be kept within the capacity of the radial carrier. It is also observed that tension level in the radial yarn is kept high compared to that of the circumferential yarns because of easy packing and applying tensioning force to the bias crossing points which resist the radial fibers movement during structure formation at weaving zone. However, there is a certain relation between radial yarn tension and beat-up force. There must be an optimum tension level and beat-up force between them and applied during weaving for proper structural formation. It is observed that radial fiber in the structure is at a slight angle. This depends partly on structure wall thickness and partly on weaving zone length during structure formation. In this point, take-up rate is a crucially important processing parameter.

Beat-up

Inserted circumferential yarns locked with radial fibers must be beaten firmly against woven formation line to



have a high volume fraction and a consistent preform. For this purpose, small finger type rods connected to the inside wall of the circular ring were used. Each finger is moveable towards the machine bed. During beat-up action, each finger moves forward to the machine bed, and circular open beat-up reed moves vertically towards the weaving formation zone to beat the circumferential yarns. After the beat-up is completed, each finger moves backward to the original position in the circular open reed and clears the weaving zone for the next action. It performs the function. However weaving formation line must be kept short to get effective beat up. On the other hand, beat-up rods were sometimes entangled to radial fibers. This was eliminated by applying proper tension on the radial yarns. Also, it was observed that high beat-up force caused local fiber distortion in the structure. It is understood that beat-up unit in the experimental prototype must be modified to get consistent volume fraction, especially when the brittle fibers are used.

Take-up

From experimental weaving prototype, it is understood that two types of take-up are necessary. Part fabrication needs mandrel and is adapted to the take-up unit. Continuous fabrication needs a pair of coated cylinders. It is realized that for both take-up units, the important processing parameter is take-up rate during delivering the fabric from the weaving zone. The rate affects fabric volume fraction and bias angle and there must be found certain relation between preform structural parameters and processing parameters. This is addressed future analytical research in take-up rate.

3. Conclusion

Multiaxis 3D circular woven preform unit cells and methods have been developed. The preforms were basically orthogonal and multiaxis unit cells. The method was radial crossing weaving principals. The method has been trailed and tested on the experimentally developed weaving prototype. The method has been worked successfully to make multiaxis and orthogonal unit cell based preforms.

The simple multiaxis and orthogonal 3D circular cylindrical woven preforms have been fabricated. The preforms were analyzed and basic structural parameters and processing parameters were identified. The important structural parameters are straight fiber path during preform formation, constant bias angles and tight packing which relates directional and total fiber volume fraction. The important processing parameters are tension in each yarn sets, ring rotation for bias, applied force in the yarn sets during beat-up and take-up rate. These parameters

must be achieved all together based on end-use requirements.

The complex shape preforms have been fabricated. These are conical and cylinder-conical shapes. It is found out that the volume fraction and bias angle are changed based on preform profile. This must be solved by proper modification in the developed weaving prototype.

These preliminary results show that various preform structures can be made thin and thick wall simple cylinders and circular complex shapes. Process is one step, versatile and simple. The method, called “radial crossing” weaving is feasible. On the other hand, the automation of the multiaxis 3D circular weaving is the future challenges for the benefit of especially technical textile and composite industries for defense and space applications.

Acknowledgments

Author would like to acknowledge to useful discussion and encouragement to Mansour H. Mohamed (Emeritus Professor) in NCSU at Raleigh/USA and Mr. Brad Lienhart who was former CEO in 3TEX Inc./NC/USA.

References

- [1]. M.B. Dow, & H.B. Dexter, *Development of stitched, braided and woven composite structures in the ACT program and at Langley Research Center (1985 to 1997)*, NASA/TP-97-206234, 1997.
- [2]. J.W.S. Hearle, *Textiles for composites*, Textile Horizons, pages 11-14, 1994.
- [3]. R. Kamiya, B.A. Cheeseman, P. Popper & T.W. Chou, *Some recent advances in the fabrication and design of three dimensional textile preforms: A review*, Composite Science and Technology 60, pages 33-47, 2000.
- [4]. M.H. Mohamed, *Three dimensional textiles*, American Scientist 78, pages 530-541, 1990.
- [5]. N.F. Dow, *Triaxial fabric*, USP 3446251, May 27, 1969.
- [6]. N.F. Dow, & G. Tranfield, *Preliminary investigations of feasibility of weaving triaxial fabrics (Doweave)*, Textile Research Journal 40, pages 986-998, 1970.
- [7]. J. Skelton, *Triaxially woven fabrics: Their structure and properties*, Textile Research Journal 41, pages 637-647, 1971.
- [8]. B.N. Cox, M.S. Dadkhah, W.L. Morris, & J.G. Flintoff, *Failure mechanisms of 3D woven composites in tension, compression and bending*, ACTA Metallurgica et Materialia 42, pages 3967-3984, 1993.
- [9]. Web, H. Uchida, T. Yamamoto, & H. Takashima, *Development of low cost damage resistant composites*, 2000, <http://www.muratec.net/jp>.
- [10]. N. Khokar, *Noobing: A nonwoven 3D fabric-forming process explained*, Journal of the Textile Institute 93(1), pages 52-74, 2002.
- [11]. A. Bilisik, & M.H. Mohamed, *Multiaxis 3D weaving machine and properties of Multiaxial 3D woven carbon/epoxy composites*, The 39th International SAMPE Symposium, Anaheim, USA, April 11-14, 1994.
- [12]. K. Bilisik, & M.H. Mohamed, *Multiaxis three dimensional (3D) flat woven preform (tube rapier weaving) and circular woven preform (radial crossing weaving)*, Textile Research Journal 79(12), pages 1067-1084, 2009.



-
- [13]. K. Bilisik, & M.H. Mohamed, *Multiaxis three dimensional (3D) flat woven preform-tube carrier weaving*, Textile Research Journal 80(8), pages 696-711, 2010.
 - [14]. M.H. Mohamed, & A. Bilisik, *Multilayered 3D fabric and method for producing*, USP 5465760, Nov. 1995.
 - [15]. F.K. Ko, & T.W. Chou, *Textile structural composites*. Elsevier Publication; USA, 1989.
 - [16]. P.D. Emerson, J. Davis, J.C. Oakfield, F.H Engleman, C.H. Barter, *Circular weaving apparatus, products and process*, US P 3719210, 1973.
 - [17]. J. Banos, J.C. Cantagre, G. Cahuzac, & J.L Darrieux, *Method and machine for 3D weaving for obtaining woven hollow reinforcements of revolution*, US P 4183232, 1980.
 - [18]. B. Bompard, J. Brochier, A. Bruyere, *Method of and apparatus for the production of bodies of parts of 3D fabric*, US P 4080915, 1978.
 - [19]. P.G. Rolincik, *Autoweave - a unique automated 3D weaving technology*, SAMPE Quarterly 32, 1987.
 - [20]. Y. Yasui, M. Anahara & H. Omori, *3D fabric and method for making the same*, USP 5091246, 1992.
 - [21]. A.K. Bilisik, *Multiaxial three dimensional (3D) circular woven fabric*, USP 6129122, Oct. 10, 2000.
 - [22]. A.K. Bilisik, *Multiaxial three dimensional (3D) circular weaving and multiaxial 3D circular woven preforms for composites*, Proceeding of NATO Advanced Research Workshop Series, Ed: Y.M. Haddad and M. Firstov, Advanced multilayered and fiber reinforced composites, Kluwer academic publisher, June, 1998.
 - [23]. A. Bhatnagar, E.S. Parrish, *Bidirectional and multiaxial fabric and fabric composites*, USP 7073538, July 11, 2006.
 - [24]. T.D. Kostar, D.M. Carper, & S. Subramanian, *Orthogonal weaving for complex shape preforms*, USP 7247212, July 24, 2007.



Robust Optimal Design of a Micro Series Elastic Actuator (μ SEA)

Ozan TOKATLI¹, Volkan PATOGLU¹

Mechatronics Engineering, Sabanci University
{otokatli,vpatoglu}@sabanciuniv.edu

Abstract

We propose using series elastic actuation (SEA) in micro mechanical devices to achieve precise control of the interaction forces. Using μ SEA for force control removes the need for high-precision force sensors/actuators and allows for accurate force control through simple position control of the deflection of a compliant coupling element. Since the performance of a μ SEA is highly dependent on the design of this compliant coupling element, we employ a design optimization framework to design this element. The proposed design framework deals with the robustness of the design while optimizing the objective functions. The robust design optimization method relies on sensitivity region concept which minimizes the change of the objective function with respect to the small changes in the design variables. The design of the compliant coupling element is chosen among the Pareto set of the optimal solutions by considering some secondary design criteria that are not included in the optimization problem.

Keywords: Series elastic actuator, robust design, micro manipulation.

1. Introduction

Micro mechanical devices are becoming ubiquitous as they find increasing uses in applications such as micro-fabrication, micro-surgery and micro-probing. Use of micro-electromechanical systems not only offer compactness and precision, but also increases the efficiency of processes. Whenever mechanical devices are used to interact with the environment, accurate control of the forces arising at the interaction surfaces arise as an important challenge. The situation is not any different at the micro scale; for instance, during *in vitro* cell indentation--- a process where a living cell is nudged with a micro-probe to observe the flexibility of the cell membrane--- it is critical to prevent damaging the cell by ensuring that the force threshold dictated by the strength of the membrane is not exceeded.

We propose using series elastic actuation (SEA) in micro mechanical devices to achieve precise control of the interaction forces at the device end-effector. Since the performance of any SEA is highly dependent on the design of its compliant coupling element, after selecting a

compliant, under-actuated half-pantograph mechanism as an appropriate kinematic structure to implement the compliant coupling element, we optimize the performance of this compliant element over multiple design objectives through dimensional synthesis. Then, the optimal mechanism can be utilized in a μ SEA which requires it be instrumented with a position sensor and an actuator, and a typical position controller for controlling its deflection to control the force exerted at the device end-effector.

Although the type selection increases the reliability of the system due to external disturbances and noises, robustness is not guaranteed. Robustness guaranteed design framework should be adopted instead of a pure optimal dimensional synthesis. The proposed design framework combines the multi-objective optimal dimensioning with reliability based design technique. Therefore, the obtained solutions will not only satisfy the performance considerations but also have a promised reliability.

The use of μ SEA for force control at micro scale is advantageous, since it alleviates the need for high-precision force sensors/actuators and allows precise control of the force exerted by the actuator through typical position control of the deflection of the compliant coupling element. In particular, SEA introduces a compliant element between the actuator and the environment, then measures and controls the deflection of this element.

That is, an SEA transforms the force control problem into a position control problem [21] that can be addressed using well established motion control strategies. Even though all force measurement techniques depend on measuring deflection of some compliant element by different means (capacitive, resistive, optical, etc.) and mapping this data to relevant forces, an SEA is different in terms of its compliance which is orders of magnitude lower than typical force sensors: At the macro scale, a typical force sensor has a stiffness on the order of 10^7 N/m, while for example the SEA in [21] have a stiffness on the order of 10^3 N/m.

For every non-collocated sensor actuator system, there is an upper limit on the loop gain which is a combination of the controller gains and the plant. Within



this limit, the controller gains for the system with a very stiff force sensor should be kept low. However, introducing a series elastic actuator to the system, instead of a force sensor, gives the ability to use higher controller gains since the stiffness of the SEA is significantly lower than a force sensor. Hence, using SEA offers implicit superiority such that the accuracy of the force control is not limited by the actuator itself while the closed loop system enjoys better disturbance rejection characteristics.

Another benefit of SEAs, include low overall the impedance of the system at the frequencies above the control bandwidth which avoids hard impacts with environment [22]. The main disadvantage of SEAs is their low bandwidth due to the intentional introduction of the soft coupling element [16]. The force resolution of an SEA improves as the coupling is made more compliant; however, increasing compliance decreases bandwidth of the control system, trading off response time for force accuracy.

Advantages of SEAs, such as the ones presented in the previous paragraphs, have been well-recognized at macro scale since early 1990s [16] and these devices have been utilized in various applications, including exoskeletons [17,31], prosthetic devices [8], and legged robots [15,19]. Design challenges of SEAs have been studied in [14,20,23], while control challenges of these devices have been addressed in [16,22,30,32].

Some of the existing micro manipulation technologies based on micro cantilever beams, such as AFMs, are similar to SEAs in that they measure the deflection of an elastic cantilever beam to estimate reaction forces and actuate the base of the beam to achieve force tracking. However, designs of these devices have not carefully considered the performance trade-offs that exist during the design. Those trade-offs can be studied by various multi-criteria optimization methods.

In general, introducing one more objective function into an optimization problem increases the complexity. Most of the time, the optimal solution of one objective function will not be an optimal solution with respect to another objective function, especially if those optimization metrics are conflicting with each other. Therefore, instead of optimizing the objective functions independent of each other, a solution procedure that can handle multiple objective functions simultaneously should be used.

The optimization problem, which includes more than one objective function, can be attacked using two different approaches, namely scalarization and Pareto methods. Scalarization methods transform multiple objective functions into a single performance metric by aggregating/prioritizing these functions. The fundamental disadvantage of scalarization approaches is that, the weight/priority of each objective needs to be assigned a

priori, in other words, the best choice of the weights/priorities, which can only be determined after the optimization procedure is complete, is demanded before the optimization procedure is initialized. An improper choice of the weights/priorities may yield to an unsatisfactory optimal solution.

Unlike scalarization approaches, Pareto methods do not require a priori information about the design trade-offs, instead they try to characterize these trade-offs among multiple objective functions. In this study, the multi-criteria optimization problem is solved using Pareto methods, in particular, utilizing the framework introduced in [25,28,29]. The framework proposes using the Normal Boundary Intersection (NBI) method to obtain efficient solutions for the multi-criteria optimization of parallel mechanisms.

The NBI method is one of the robust methods to obtain the design trade-offs (the boundary of the feasible domain) of multi-objective optimization problems [3]. The NBI method uses a geometric approach to solve for the optima of the multi-objective problems. In particular, the NBI method performs a sequence of gradient-based searches on the feasible domain defined by the problem. The method is computationally efficient, since it attacks the geometric problem directly and solves for single-objective constrained subproblems using fast, reliable gradient-based optimizers. Because the geometric problem is only affected by the properties of the feasible domain, the single-objective subproblems can be addressed using gradient based optimization techniques, even when the objective functions are non-smooth and non-convex. Moreover, the method is applicable to a general set of performance indices and results in exceptionally uniform distributed points on the Pareto-front hyper-surface without requiring any tuning of the core algorithm.

Limitations of the technique exist since the NBI method relies on an equality constraint. It is possible for the NBI method not to find a solution on the Pareto-front hyper-surface or converge to local optima. In such a case, the solutions of NBI subproblems can be post-processed to filter out undesired dominated solutions. Moreover, NBI method assumes sufficient smoothness of the boundary of the feasible domain so that gradient techniques can be employed. However, it has also been demonstrated in the literature that the method performs remarkably well even for non-smooth geometries of the objective space [18].

The goal of the design is to come up with an optimal design that is also “robust” to manufacturing tolerances, alignment errors, changes in the operating conditions and uncontrollable parameters of the off-the-shelf items. The choices in the type selection aim to minimize the adverse effects of these disturbances; however, these choices can not ensure performance guarantees under uncertainties of



the design variables or parameters. Such uncertainties are unavoidable and if these uncertainties are not explicitly handled during the design process, the actual performance of the mechanism may fall short of the performance estimated by using the nominal values. The aim of robust optimal design is to find the optimum of the performance metric, while the variables and parameters in the problem definition are allowed to have certain uncertainties.

The robust design techniques proposed in the literature can be loosely grouped as stochastic and deterministic methods. Taguchi, [24], developed one of the first robust design techniques, which also formed a basis to latter stochastic approaches. He analyzed the sensitivity of a function by not using the partial derivatives that are tedious and computationally time consuming, but instead utilizing the orthogonal array method. However, the technique of Taguchi requires careful experiments conducted with different combinations of design variables. Yu *et. al.*, [34], analyzed *manufacturing variation patterns*, the pattern of manufacturing errors that frequently occur. In this method, the robustness of the design is improved for correlating manufacturing errors. This method, like Taguchi method, requires experiments and statistical data for defining the correlation between the manufacturing error patterns. Jung and Lee, [10], developed a stochastic approach which constrains the original optimization problem with a robustness index. The robustness index is a probability constraint which is solved using advanced first-order second moment. Their method is advantageous since it eliminates the need of second order derivatives. A comparison of various robust design methods can be found in [4]. The main disadvantage of stochastic methods is that they generally require a priori information of distribution of the possible errors be known. This information may require many costly experiments be performed.

The other approach to robust design is the deterministic methods. Belegundu and Zhang [2] proposed increasing the robustness of a design by minimizing the sensitivity of the objective function by selecting appropriate design variables. Their formulation works even for large variations for linear systems and is limited to small variations for nonlinear systems. Although this method does not require a priori information on probability distributions of design variables and parameters, it requires computation of the first derivative for minimization. In a similar approach, Balling *et. al.* [1] used the first derivatives to linearize the optimization problem around the nominal optimum and used a worst-case analysis to find conservative robust design. Calculation of derivatives is not trivial for many problems and can be computationally infeasible. For optimization problems, in which the derivative

information may not be available, Gunawan and Azarm developed a non-gradient based sensitivity region method for robust optimization [6,7]. In this study, this robust optimization method is incorporated into our optimal dimensional synthesis framework, details of which are discussed in Section 2.2.

This paper extends the optimal design framework for μ SEA first introduced by the authors in [26] by introducing robustness considerations. The robustness based design framework utilized in this paper has also been proposed by the authors in [27].

The paper is organized as follows: The design of the μ SEA is introduced in Section 2. In this section the optimization problem is formulated in 2.1.1, the kinematic analysis of the pantograph mechanism that is used as the compliant coupling element of the μ SEA is performed in 2.1.2. In Section 2.2, the robust optimal design framework is introduced for both single and multi objective optimization problems. The solution of the robust optimal design problem and the configuration selection for the μ SEA is introduced in 2.3. Finally Section 3 concludes the paper.

2. Overall Mechanical Design of μ SEA

SEAs in macro level are generally implemented using high precision helical springs between the motor and the load. Since such springs are not available or easy to implement at the micro scale, we propose using a planar compliant mechanism which is to be designed for required characteristics. Planar compliant mechanisms are easy to manufacture at micro scales and are, in general, free of parasitic effects such as friction, backlash [3].

To implement the compliant element of the μ SEA, we choose a parallel mechanism based design, since parallel mechanisms are more robust against manufacturing errors and dimensional changes due to thermal noise [12]. The errors at the joint level are averaged at the end effector; therefore, parallel mechanisms can achieve more precise motion than their serial mechanism counterparts. Moreover, parallel mechanisms can be designed to be more compact with higher stiffness, compared to serial mechanisms [12].

In particular, a half pantograph mechanism with 3 degrees of freedom (DoF) is selected as the underlying kinematic structure of the compliant element.

The half-pantograph is driven by a single actuator; therefore, the μ SEA is under-actuated. The under-actuation is intentionally built into the μ SEA design, since it introduces reliability and robustness by passively compensating the alignment errors of the actuator and the end effector. The under-actuation also helps with the impact-resistance of the device.

Figure 1 depicts a schematic representation of the

mechanical design of the μ SEA with compliant half-pantograph based elastic elements where the solid line represents the initial configuration of the μ SEA and the dash line is the configuration due to actuation. In the figure, the actuator is located in between two half-pantograph mechanisms. This configuration is especially suitable for use with low cost piezoelectric actuators with screw motions, since the actuator can simply be placed in position and kept there by pre-loading the elastic elements. In the figure, the end effector is assumed to be a microprobe suitable for cell manipulation.

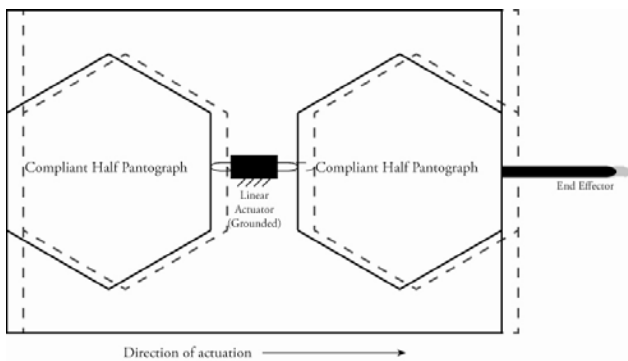


Fig. 1: Schematic representation of μ SEA

2.1. Optimal Dimensional Synthesis of μ SEA

2.1.1. Optimization Problem

As motivated in the Introduction, the performance trade-offs that exist during the design of μ SEA s need to be handled systematically so that the best possible force tracking performance can be achieved. In this section, given the half-pantograph mechanism as the underlying kinematics of the compliant element, an optimal dimensional synthesis problem is formulated. The dimensional synthesis problem is critical especially for parallel mechanism, since small changes in these parameters can have crucial effects on the overall performance of the mechanism [12].

The most important aspect of the compliant mechanism is its stiffness, which lets it act as a spring. In general, compliant mechanisms have configuration dependent task-space stiffness at their end-effectors. While designing a μ SEA, the task stiffness of the mechanism needs to be optimized for the accuracy and reliability of force control. Hence, task space stiffness is the first metric to be included in the optimization problem.

The compliant mechanism used in the μ SEA is implemented as a flexure joint mechanism, in which deflections can only occur at the corners of the mechanism where two rigid links articulate. Since the deflection of these joints is limited, the dexterous workspace of the mechanism is drastically reduced

compared to a traditional rigid body mechanism of the same kinematics. One of the important design goals for the μ SEA is increasing the dexterous workspace of the device so that a wider range of operation becomes feasible. In order to characterize the size of the dexterous workspace, manipulability [33] is used as the second metric for the optimization problem.

Two metrics (stiffness and manipulability) need to be optimized for the half-pantograph mechanism while implementing the μ SEA. However, the half-pantograph possesses 3DoF in plane and it is more proper to conduct the analysis along different directions, in other words, consider the directional manipulability and stiffness of the mechanism. The analysis considers two mutually perpendicular directions: direction of actuation (y -direction), and the direction that is perpendicular to it (x -direction). Along the direction of actuation, the end effector of the μ SEA contacts with the environment, *ie* it is the active direction; while no motion is desired along the perpendicular direction.

In particular, we analyze the manipulability and the stiffness of the mechanism along the direction of actuation and along the direction perpendicular to this motion as follows: We increase the manipulability and decrease the stiffness of the mechanism along the movement direction of actuation to achieve high stroke with high force resolution, while we decrease the manipulability and increase the stiffness of the mechanism along the direction perpendicular to the actuator motion to achieve good disturbance rejection characteristics.

The manipulability and the stiffness metrics are equivalent for the half-pantograph mechanism, that is, both performance criteria converge to the same optimal dimensions for the mechanism. Decreasing stiffness and increasing manipulability yields a long mechanism with the link lengths at their upper limits, while increasing the stiffness and decreasing the manipulability converges to a short mechanism with the link lengths at their lower limits.

Due to this equivalence, it is unnecessary to distinctly analyze the stiffness and the manipulability metrics; hence, only the stiffness along the x - and y -directions is examined during optimization.

The negative null form of the optimization problem can be formulated as,

$$\begin{aligned} \arg \max_{\alpha} \quad & F(\alpha, \beta) && \text{subject to} \\ & G(\alpha, \beta) \leq 0 && \text{and} \\ & \alpha_L \leq \alpha \leq \alpha_U \end{aligned}$$

where α represents the vector of design variables - the link

lengths and the pose of the mechanism $\alpha = [\ell_1 \ \theta]^T$ - and β denotes the design parameters - not available in this problem. In this negative null form, $F(\alpha, \beta)$ is the vector of performance metrics. For this optimal design problem: $F(\alpha, \beta) = [\mu_{S_x} \ \mu_{S_y}]^T$, where μ_s represents the task space stiffness. $G(\alpha, \beta)$ is the vector of inequality constraints. The inequality constraints are imposed during the kinematic analysis to ensure a closed kinematic chain and elbow out posture of the half-pantograph mechanism.

The calculation of the stiffness metric μ_s requires derivation of the Jacobian matrix of the compliant half-pantograph mechanism. The next subsection describes this kinematic analysis.

2.1.1. Kinematic Analysis of the Compliant Half-Pantograph Mechanism

The analysis of compliant mechanisms is significantly harder than the analysis of their rigid body counterparts, since the study of these mechanisms requires the determination of their deformations under externally applied forces. In this paper, an approximate model, namely the pseudo-rigid body model [13], is used to study the kinematics of the compliant half-pantograph mechanism. Pseudo-rigid body model is preferred due to its computational efficiency and ease of use.

A pseudo-rigid body approximates the motion of a compliant mechanism by replacing its flexible links with rigid links and introducing torsional springs at both ends of these rigid links. The torsional springs mimic the flexibility of the system while the introduction of rigid links enables the use of rigid body mechanics. Link lengths and spring constants in the model are selected such that the kinematics of the model closely approximates the solution of elliptic integrals that arise from the exact solution of the compliant link deformations. While the accuracy of the pseudo-rigid body method depends on many parameters, such as the length of the flexible members, for small pivot movements with relatively long link lengths, as studied in this paper, the approximate solution lies within 0.5% percent of the exact solution [9].

Figure 2 depicts the pseudo-rigid body model of the half-pantograph mechanism. The joint angles are chosen to be the generalized coordinates of the system. The generalized coordinates q are categorized as active, q_a , and passive, q_p , ones: an active generalized coordinate corresponds to the orientation of a joints that is actuated, while a passive generalized coordinate pertains to the orientation of an hindered joint.

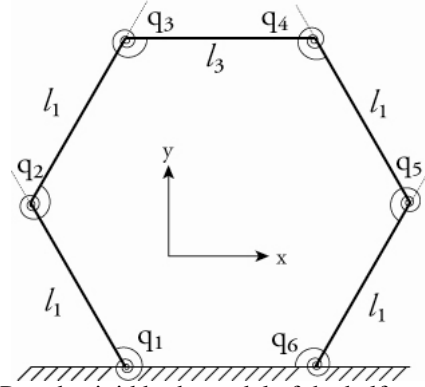


Fig. 2: Pseudo-rigid body model of the half-pantograph mechanism

$$q = \begin{bmatrix} q_a \\ q_p \end{bmatrix} = [q_1 \ q_6 \ q_2 \ q_3 \ q_4 \ q_5]^T$$

The Jacobian matrix of the system is also partitioned into a kinematic Jacobian J_T , which gives the relation between the joint space and task space velocities, and a constraint Jacobian J_C , which imposes the motion constraints to the system.

$$\begin{aligned} \dot{x} &= J_T(q)\dot{q} \\ 0 &= J_C(q)\dot{q} \end{aligned}$$

The kinematic and constraint Jacobian matrices are then grouped by the type of the joint. This new form of the Jacobian matrix provides more insight about the system, since the sub-blocks of the matrix clearly reflects the contributions of the active and passive joints.

$$\begin{bmatrix} \dot{x} \\ 0 \end{bmatrix} = \begin{bmatrix} J_{T_a} & J_{T_p} \\ J_{C_a} & J_{C_p} \end{bmatrix} \begin{bmatrix} \dot{q}_a \\ \dot{q}_p \end{bmatrix}$$

The compliant half-pantograph is under-actuated since the number of driven joints is less than the degrees of freedom of the system. The under-actuated nature of the mechanism increases the complexity of the kinematic analysis. Since the under-actuated compliant half pantograph mechanism obeys the Hamilton's principle, it can be stated that, the motion of the pantograph will minimize the strain energy in its passive joints. Such an approach is also adopted in [11]. This new optimization problem can be formulated as,

$$\arg \min_{q_p} \frac{1}{2} \dot{q}_p^T K \dot{q}_p \quad \text{subject to} \quad J_{C_a} \dot{q}_a + J_{C_p} \dot{q}_p = 0$$



where K_{q_p} is the stiffness matrix of the passive joints. This optimization problem can be solved using the method of Lagrange multipliers and the relation between the active joint velocities to passive joint velocities can be obtained as (see [11] for details).

$$\dot{q}_p = -\left(K_{\dot{q}_p} + K_{\dot{q}_p}^T\right) J_{C_p}^T \left[J_{C_p} \left(K_{\dot{q}_p} + K_{\dot{q}_p}^T\right)^{-1} J_{C_p}^T \right]^{-1} J_{C_a} \dot{q}_a$$

Substituting this equation into the Jacobian of the system yields to the mapping between the task space velocities and the active joint velocities. This mapping can be uniquely derived as,

$$\dot{x} = \left(J_{T_a} - J_{T_p} J_{C_p}^* J_{C_a} \right) \dot{q}_a = \bar{J}_T \dot{q}_a$$

where $J_{C_p}^* = \left(K_{\dot{q}_p} + K_{\dot{q}_p}^T \right)^{-1} J_{C_p}^T \left[J_{C_p} \left(K_{\dot{q}_p} + K_{\dot{q}_p}^T \right)^{-1} J_{C_p}^T \right]^{-1} J_{C_a}$. As a result task space stiffness of the mechanism can be calculated as,

$$K_T = \bar{J}_T^{-1} \left(K_{q_a} + J_{C_a}^T J_{C_p}^{-T} K_{q_p} J_{C_p}^{-1} J_{C_a} \right) \bar{J}_T$$

In the optimization problem, directional stiffness is analyzed along two different directions: x- and y- directions (refer to Figure 2). Stiffness of the compliant half-pantograph mechanism; hence; the optimization metrics can be calculated as,

$$\begin{aligned} \mu_{S_x} &= u^T K_T u \\ \mu_{S_y} &= v^T K_T v \end{aligned}$$

where u and v represent the unit vectors in the x- and y- directions, respectively.

In this section, the robust optimization method proposed by Gunawan and Azarm [6] is utilized to extend the optimal dimensional synthesis framework introduced in [28,29] to incorporate robustness into the design. The aim of the robust optimization is to find design variables for the mechanism such that the objective function value is less sensitive to the deviations in the design variables.

2.2. Robust Optimal Design

2.2.1. Single Objective Robust Optimal Design

The NBI method used to solve the multi-criteria optimization problem requires to be initialized with the solutions, called shadow points that minimize each objective function individually. To determine the optimum of each objective function, a single objective optimization problem needs to be solved for each criterion. Since we are interested in robust designs,

robustness criteria should be added to this optimization problem so that performance can be guaranteed under variations of the design variables.

To ensure robustness, the key concept of the sensitivity region is defined as,

$$S(x_0) = \left\{ \Delta x \in \mathbb{R}^N \mid [f(x_0 + \Delta x) - f(x_0)]^2 \leq [\Delta f_0]^2 \right\}$$

where Δx is an N dimensional vector of variations of design variables and Δf_0 is the maximum allowed change in the objective function to be determined by the designer. The sensitivity region represents a set, where the changes in the function value due to the deviations from the nominal values of the design variables by an amount of Δx remains less than or equal to Δf_0 . In general, the sensitivity regions have an arbitrary shape rendering its computation ineffective. Moreover, the combination of deviations in the design variables cannot be foreseen during the design step. To address these challenges, a conservative and simple approximation to the sensitivity region is proposed in [6]. In particular, the largest hyper-sphere that tightly fits inside the sensitivity region is considered and the radius of this hyper-sphere, that is also the closest point on to boundary of the sensitivity region to the origin of the variation space, is proposed as a measure of robustness. This radius can be calculated as the solution of the following optimization problem.

$$\begin{aligned} \arg \min_{\Delta x} R(\Delta x) &= \|\Delta x\|_2 \\ \text{subject to} & \frac{\Delta f_0^2}{(f(x_0 + \Delta x) + f(x_0))^2} - 1 = 0 \end{aligned}$$

In this new optimization problem, the constraint imposes that the solutions lie on the boundary of the sensitivity region.

Introducing the robustness criteria into the single optimization problem to calculate the shadow points transforms this problem into a multi-objective optimization, where the objective function and the robustness of the system have to be optimized simultaneously. However, in order to simplify the analysis, it is convenient to consider the robustness condition as a constraint to the single optimization problem. In particular, the optimization problem can be constrained to have solutions that satisfy some predetermined robustness index, R_0 . The negative null form of the single optimization problem with robustness constraint is formulated as,



$$\begin{aligned} \arg \max_{\alpha} f(\alpha, \beta) \quad \text{subject to} \\ g(\alpha, \beta) \leq 0 \\ h(\alpha, \beta) = 0 \\ \alpha_L \leq \alpha \leq \alpha_U \\ R_0 - R < 0 \end{aligned}$$

Even though considering the robustness condition as a constraint avoids a multi objective problem, choosing a proper value for R_0 is not trivial. In [6] using $R_0 = N^{1/2}$, where N is the number of design variables in the optimization problem, is suggested as a proper choice for R_0 . For further details of this choice and the theory behind the robust optimization technique, readers can refer to [6].

2.2.2. Multi Objective Robust Optimal Design

In [7], the robustness criteria based on sensitivity region is extended to multi-criteria optimization problems. In particular, it is shown that the concept can be incorporated into Multi-Objective Genetic Algorithm (MOGA) [5] after some minor tuning. In this study, we follow a similar formulation but utilize the NBI method to solve the multi-criteria optimization problem, since it is one of the most efficient methods to solve for the design trade-offs [5]. Compared to MOGA [5] that requires problem dependent fitness search related tuning and several steps to reach convergence, a standard NBI approach can map the Pareto front hyper-surface with higher accuracy and uniformity, while also inheriting the efficiency of gradient-based methods. Benefits of NBI method over MOGA has been observed in many studies, including [18].

The multi-criteria optimization problem with robustness constraint can be formed as,

$$\begin{aligned} \arg \max_{\alpha} F(\alpha, \beta) \quad \text{subject to} \\ g(\alpha, \beta) \leq 0 \\ h(\alpha, \beta) = 0 \\ \alpha_L \leq \alpha \leq \alpha_U \\ R_0 - R < 0 \end{aligned}$$

where R is determined as the solution of the following optimization problem,

$$\begin{aligned} \arg \min_{\Delta x} R(\Delta x) = \|\Delta x\|_2 \\ \text{subject to} \max_{i=1 \dots M} \left(\frac{\Delta f_0^2}{(f(x_0 + \Delta x) + f(x_0))^2} \right) - 1 = 0 \end{aligned}$$

where $F(x) = [f_1(x) \dots f_M(x)]^T$ is the vector of objective functions and $\Delta f_{i,0}$ is the maximum allowed variation in each objective function.

2.3 Design Selection from the Pareto Front

In this design problem, the performance and the reliability is being achieved by changing the link length ℓ_1 and the initial posture of the mechanism, θ . The design variables can be seen in Figure 2.

$$x = [\ell_1 \ \theta]^T$$

Due to the constraints on the raw material that can be used in the manufacturing, the design variables have lower and upper bounds:

$$\begin{aligned} 10 \text{ mm} \leq \ell_1 \leq 60 \text{ mm} \\ 10^\circ \leq \theta \leq 60^\circ \end{aligned}$$

The design of the elastic element is conducted using the design framework which is introduced in the previous sections. In this analysis, Δx represents the variation on the variables. For 4 different variations, the Pareto front is calculated.

$$\begin{aligned} \Delta x_1 &= [0.1 \text{ mm} \ 0.1^\circ]^T \\ \Delta x_2 &= [0.5 \text{ mm} \ 0.5^\circ]^T \\ \Delta x_3 &= [0.75 \text{ mm} \ 0.75^\circ]^T \\ \Delta x_4 &= [1 \text{ mm} \ 1^\circ]^T \end{aligned}$$

In order to observe the shift in the Pareto, in other words view the trade-off between the performance and reliability, the nominal Pareto front, which does not have any robustness constraint, and the robust Pareto fronts are given in the same figure (refer to Figure 3). It is clear from the figure that, as the variations in the design variables increases (in this case they vary from $[0.1 \text{ mm} \ 0.1^\circ]^T$ to $[1 \text{ mm} \ 1^\circ]^T$) the Pareto front curve shifts towards into the feasible region by becoming a dominated solution.

In Figure 3, the Pareto curve of Δx_4 is clearly distinct from others. However, it can be observed that, the Nominal Pareto front and the robust Pareto fronts of Δx_1 , Δx_2 , Δx_3 are overlapping. This is due to the inherent

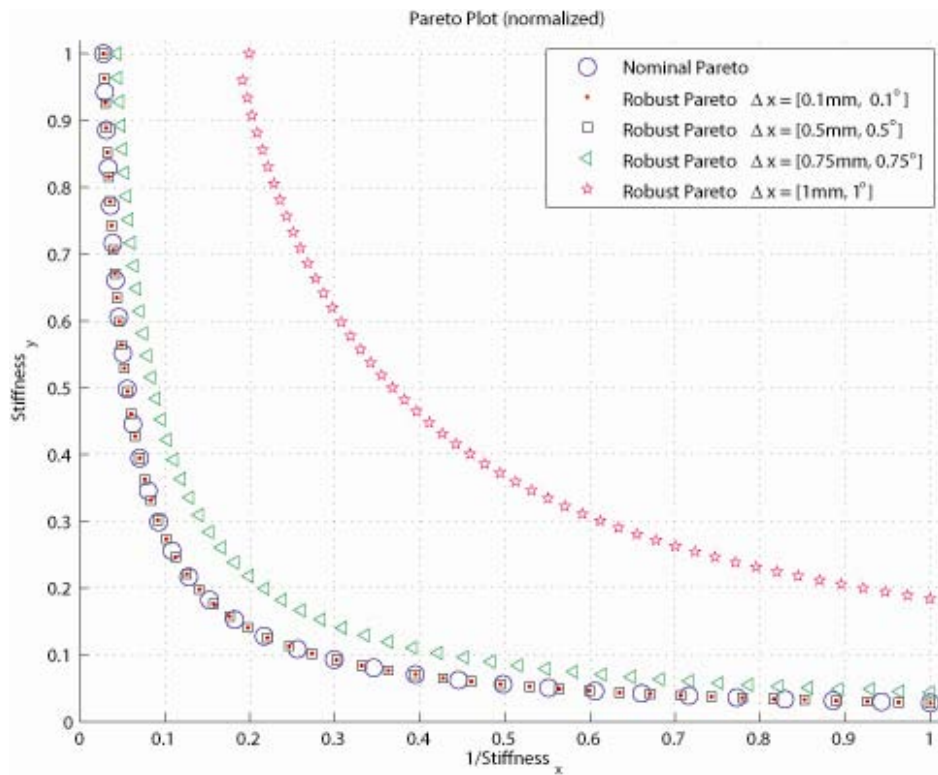
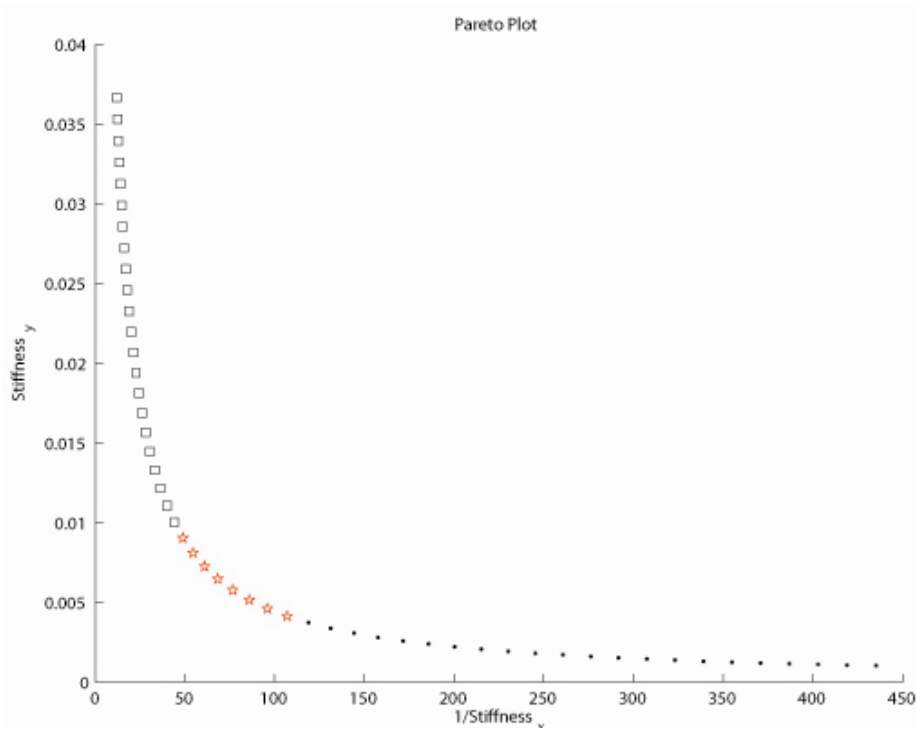


Fig. 3: Normalized Pareto front curves for nominal and robust designs





robustness of parallel mechanisms. As it is stated in the “Type Selection” step, parallel mechanisms can compensate errors such as the ones occur in manufacturing or thermal noise. Due to this inherent reliability of the system, the first three variations do not significantly degrade the performance of the design, *ie* the Pareto curve does not shift.

This pantograph mechanism will be manufactured using wire-EDM method. In this method the raw material is cut using a wire with a diameter of 0.25mm. The manufacturing tolerance of wire erosion is 1 μ m. Therefore, the rest of the analysis will be conducted using the first robust Pareto curve (the one with the variation Δx_1). The denormalized Pareto front can be seen in Figure 4.

On the Pareto curve there are many solutions which minimize the objective functions, stiffness in the x- and y- directions, simultaneously. In this set of solutions one final configuration should be chosen as the elastic element. This choice can be made by considering many criteria not restricted by the optimization metrics. In this design problem, the election of the final design is made by considering the footprint and the y-direction stiffness of the mechanism. Before going into the details of the selection one thing should be emphasized. The footprint constraint is not as important as the optimization metrics; hence it is not included in the optimization problem. Doing so leads to a broader perspective of solutions where the optimality is due to the criteria that are crucial according to the quality of the design. Once the solution set is obtained, a final configuration is chosen using the criteria including the less crucial ones.

In this design problem, the footprint of the criteria is a second degree criterion therefore it is embedded into the analysis after obtaining the Pareto front. The footprint criterion is identified according to the raw material that is available to manufacturing. This criterion states that the maximum area of the mechanism should be less than 2000mm². The points with black dots in Figure 4 do not satisfy this condition.

On the other hand, since this elastic element will serve as the spring of the μ SEA, it is important to have low stiffness along the actuation direction so that the force resolution of the μ SEA will be better. The second elimination criteria is the stiffness of the compliant element which is desired to be lower than 0.01Nmm/rad. This criteria eliminates the points marked with black boxes in Figure 4. The rest of the points, shown in red pentagram in Figure 4 satisfy not only the performance issues imposed into the optimization problem, but also satisfy the less important criteria like the footprint. Among those points, the one with the lower y-direction stiffness is chosen as the final configuration for the elastic element of μ SEA.

3. Conclusion

Robust optimal design of a μ SEA is presented. The design is performed in two steps: type selection and dimensional synthesis. In type selection, an under-actuated compliant half pantograph is selected as the underlying kinematics of the μ SEA. After the type selection, optimal dimensional synthesis is performed considering the directional manipulability and the directional stiffness metrics with robustness constraints. The manipulability of the system is increased along the direction of actuation and decreased along the perpendicular direction of actuation. During the optimal dimensional synthesis, the robustness of the design with respect to the variations in the design variables is considered using the sensitivity region approach. In particular, the sensitivity of the objective functions with respect to design variations are bounded while performing the optimal dimensional synthesis. The multi-criteria optimization problem is solved using NBI method which simultaneously minimizes the objective functions while satisfying the robustness constraint. The final design is chosen from the Pareto set by imposing footprint constraint and the task space stiffness along the direction of actuation as the secondary performance metrics. The chosen configuration has $\ell_1 = 29.774$ and $\theta = 60^\circ$ with the performance metrics $\mu_{S_x} = 107.14$ (Nmm/rad)⁻¹, $\mu_{S_y} = 0.0041362$ Nmm/rad. The footprint of the mechanism is 1833.2 mm². The variation in the performance of the mechanism is guaranteed to stay within the 10% of the nominal values under arbitrary variations of link lengths up to $\Delta x = [0.1\text{mm } 0.1^\circ]$.

References

- [1]. R. J. Balling, J.C. Free and A. R. Parkinson, *Consideration of worst-case manufacturing tolerances in design optimization*, Transactions of ASME **108** (1986), 438 -441.
- [2]. A. D. Belegundu and S. Zhang, *Robustness of design through minimum sensitivity*, Journal of Mechanical Design **114** (1992), 213-217.
- [3]. I. Das and J. E. Dennis, *Normal-boundary intersection: a new method for generating pareto surface in the nonlinear multi-criteria optimization* **8** (1996), no. 3, 631-665.
- [4]. X. Du and W. Chen, *Towards a better understanding of model feasibility robustness in engineering design*, Journal of Mechanical Design **122** (2000), 385-394.
- [5]. C. M. Fonseca and P. J. Fleming, *Generic algorithms for multiobjective optimization: formulation, discussion and generalization*, Multiobjective Evolution Algorithms: Empirical Genetic Algorithms (1993), 416-423.
- [6]. S. Gunawan and S. Azarm, *Non-gradient based parameter sensitivity estimation for single objective robust design optimization*, Journal of Mechanical Design **126** (2004), 395-402.
- [7]. _____, *Multi-objective robust optimization using a sensitivity region concept*, Structural Multidisciplinary Optimization **29**



- (2005), 50-60.
- [8]. H. Herr and A. Wilkenfeld, *User-adaptive control of a manotorheological prosthetic knee*, Industrial Robot: An International Journal **30** (2003), no. 1, 42-55.
- [9]. L. L. Howell, *Compliant Mechanisms*, John Wiley and Sons, 2001.
- [10]. D. Hung and B. C. Lee, *Development of a simple and efficient method for robust optimization*, International Journal of Numerical Methods in Engineering **53** (2002), no. 6, 2201-2215.
- [11]. B. H. Kang, J. T. Y. Wen, N. G. Dagalakis and J. J. Gorman, *Analysis and design of parallel mechanisms with flexure joints*, IEEE Transactions on Robotics **21** (2005), no. 6, 1179-1185.
- [12]. J. P. Merlet, *Parallel Mechanisms*, Springer-Verlag, 2006.
- [13]. A. J. Nielson and L. L. Howell, *An investigation of compliant micro half pantographs using the pseudorigid body model*, Mechanics Based Design of Structures and Machines **29** (2001), 317-330.
- [14]. D. Paluska and H. Herr, *The effect of series elasticity on actuator power and work output: implications for robotic and prosthetic joint design*, Robotics and Autonomous Systems **54** (2006), 667-673.
- [15]. G. A. Pratt, *Low impedance walking robots*, Iterative and Comparative Biology **42** (2002), no. 1, 174-181.
- [16]. G. A. Pratt and M. M. Williamson, *Series elastic actuators*, IEEE International Conference on Intelligent Systems, 1995.
- [17]. J. E. Pratt, B. T. Krupp, C. J. Morse and S. H. Collins, *The RoboKnee: an exoskeleton for enhancing strength and endurance during walking*, IEEE International Conference on Robotics & Automation, 2004.
- [18]. E. Rigoni and S. Poles, *NBI and MOGA-II, two complementary algorithms for multi-objective optimizations*, Practical Approaches to Multi-Criteria Optimization, 2005.
- [19]. D. W. Robinson, J. E. Pratt, D. J. Paluska and G. A. Pratt, *Series elastic actuator development for biomimetic walking robot*, IEEE/ASME International Conference on Advance Intelligent Mechatronics, 1999.
- [20]. J. W. Sensinger and R. F. Wier, *Design and analysis of a non-backdrivable series elastic actuator*, IEEE 9th International Conference on Rehabilitation Robotics, 2005.
- [21]. _____, *Improvements to series elastic actuators*, IEEE/ASME International Conference on Mechatronic and Embedded Systems and Applications, 2006.
- [22]. _____, *Unconstraint impedance control using a compact series elastic actuator*, IEEE/ASME International Conference on Mechatronic and Embedded Systems and Applications, 2006.
- [23]. J. S. Sulzer, M. A. Peshkin and J. L. Patton, *Pulling your strings*, IEEE Robotics & Automation Magazine **15** (2008), no. 3, 70-78.
- [24]. G. Taguchi, *Performance analysis design*, Int. J. Prod. Res. **16** (1978), no. 6, 521-530.
- [25]. O. Tokatli and V. Patoglu, *Multi-criteria design optimization of a compliant micro half-pantograph*, ECCOMAS Thematic Conferences on Multibody Dynamics, 2009.
- [26]. _____, *Optimal design of a micro series elastic actuator*, International Design Engineering Technical Conferences and Computers & Information in Engineering Conferences (IDETC/CIE), 2010.
- [27]. _____, *Robust optimal design of a micro gripper*, 1st Joint International Conference on Multibody System Dynamics, 2010.
- [28]. R. Unal, G. Kiziltas and V. Patoglu, *A multi-criteria design optimization framework for Haptic interfaces*, IEEE International Symposium on Haptic Interfaces for Virtual Environments and Teleoperator Systems, 2008.
- [29]. R. Unal and V. Patoglu, *Optimal dimensional synthesis of a dual purpose Haptic exoskeleton*, Springer in the Lecture Notes in Computer Science, EuroHaptics, 2008.
- [30]. H. Vallery, J. Veneman, E. van Asseldonk, R. Ekkelenkamp, M. Buss and H. van der Kooij, *Compliant actuation of rehabilitation robots*, IEEE Robotics & Automation Magazine **15** (2008), no. 3, 60-69.
- [31]. J. F. Veneman, R. Ekkelenkamp, R. Kuidhof, F. C. T. van der Helm and H. van der Kooij, *A series elastic and Bowden cable based actuation system for use as torque actuator in exoskeleton-type robots*, The International Journal of Robotics Research **25** (2006), no. 3, 261-281.
- [32]. G. Wyeth, *Demonstrating the safety and performance of a velocity source series elastic actuator*, IEEE International Conference on Robotics and Automation, 2008.
- [33]. T. Yoshikawa, *Manipulability of robotic mechanisms*, International Journal of Robotics Research **4** (1985), 3-9.
- [34]. J. C. Yu and K. Ishii, *Design for robustness based on manufacturing variation patterns*, Transactions of ASME **120** (1998), 196-22.



Design and Multi-criteria Optimization of a Haptic Interface

Aykut Cihan SATICI¹, Alper Mehmet ERGIN¹, Volkan PATOGLU^{1*}

^{1*}Faculty of Engineering and Natural Sciences

Sabancı University

Istanbul, 34956, Turkey

{acsatici, aergin, vpatoglu}@sabanciuniv.edu

Abstract

This paper presents the design and the optimal dimensional synthesis of a common haptic interface with closed kinematic chains: The Modified Delta Robot. Optimization of the device is performed with respect to multiple design objectives, namely kinematic and dynamic criteria. Both performance measures are discussed in detail and optimization problems for a haptic interface with best worst-case kinematic and dynamic performance are formulated. Normal Boundary Intersection method is applied to efficiently obtain the Pareto-front hypersurface characterizing the trade-off between these multiple design criteria. An “optimal” design is selected studying the Pareto-front curve and considering the primary and secondary design criteria. Once the dimensions of the device are decided, the haptic interface is implemented utilizing an optimized capstan ratio driven by double DC motors per shaft. The final design possesses good transparency and high bandwidth thanks to the optimal dimensioning of the parallel kinematic structure.

Keywords: haptic interface, dimensional synthesis, multi-criteria design optimization, Modified Delta Mechanism.

1. Introduction

A haptic interface is a computer-controlled motorized device that physically interacts with a human operator to render presence of computationally mediated environments. Haptic devices are expected to resist forces that a human can apply. Besides they should be able to display a large spectrum of impedances. Performances of haptic devices are measured through their *transparency*. Transparency of a haptic interface can be described as the difference between the desired impedance and the actual impedance the device can display. The actual impedance rendered by the haptic device is deteriorated due to parasitic effects of the system. As a result perfect mapping of the actual impedance cannot be guaranteed. Independent of the control algorithm used, both kinematic and dynamic performance of the haptic device have an impact on the overall performance of the haptic display.

Mechanisms with parallel kinematic chains are commonly preferred as haptic interfaces due to their inherent advantages.

As opposed to serial ones, the actuators of parallel mechanisms can be grounded. Therefore, these mechanisms can have low weight and still be rigid, ensuring a high bandwidth. In addition to high rigidity and large position/force bandwidths, fast and precise movements, low inertia and compact design are among the inherent properties of parallel mechanisms.

Even though parallel mechanisms have certain advantages that make them favorable among haptic devices, the design optimization of these mechanisms is challenging due to their prominent structure. As a result of being closed kinematic chains, parallel mechanisms may possess singularities in their workspace. Moreover, kinematic, dynamic and singularity analysis of parallel mechanisms are more challenging than the analysis of serial manipulators. Because of their indispensable complexities, the dimensional synthesis of parallel mechanisms is an active research area.

Optimum design of parallel mechanisms, even for a single objective function, is challenging due to the nonlinear, large scale nature of such mechanisms [14] and non-convex properties of performance indices with respect to the design variables [25]. Many different optimization approaches are applicable to nonlinear, non-convex design optimization problems such as genetic algorithms [13][14][33][39], simulated annealing [27], Bayesian techniques [33][34], Monte-Carlo simulations [33], controlled randomized searches [17], performance charts [17], workspace atlases [16], and branch and bound methods [32]. In general, deterministic methods can get stuck at a local optimum, heuristic methods cannot guarantee optimality of the converged solution, while branch and bound type methods are only as accurate as the discretization selected.

Design of haptic interfaces considers various performance criteria such as kinematic and dynamic isotropy, singularity-free workspace, sensitivity, and transmission capability simultaneously. In fact non of these measures can be optimized without deteriorating others; therefore there are trade-offs between design performances. Determination of optimal dimensions with



respect to many design criteria is a difficult problem and should be handled with multi-objective optimization methods so that trade-offs can be assigned in a systematic manner.

Optimal design of a haptic interface can only be achieved by handling many competing objectives together. There are many studies which focus on multiple design criteria optimization. The studies that can be categorized under *scalarization* methods approach the problem by first transforming the problem into several single objective problems. Among these approaches, Hayward et al. define the relationship between multiple criteria and utilize sensitivities of these criteria to conduct a hierarchical optimization study [5]. Multiple objectives are considered sequentially [9][27][32] by searching for parameter sets resulting in near optimal kinematic performance and then selecting the design exhibiting the best dynamic performance from this reduced parameter space. Task-priority, probabilistic weighting, composite index [13], and tabular methods are among the other scalarization approaches that consider multiple criteria. Scalarization methods possess the inherent disadvantage of their aggregate objective functions requiring preferences or weights to be determined *a priori*, i.e. before the results of the optimization process are actually known. Since assigning proper weights or prioritizing different criteria is a problem dependent, non-trivial task, these techniques fall short of providing a general framework to the design of the parallel mechanisms. The alternative approach for scalarization methods is *Pareto* methods. Pareto methods incorporate all optimization criteria within the optimization process and address them simultaneously to find a set of non-dominated designs in the objective space. Pareto methods allow the designer to make an informed decision by studying a wide range of options; therefore they contain solutions that are optimum from an overall standpoint. Unlike scalarization techniques, Pareto methods always consider design trade-offs. In literature Krefft et al. applied a modified genetic algorithm (GA) based Pareto method to design of parallel mechanisms [11][9]. Similarly, GA is applied to multi criteria optimization of a 2-DoF parallel robot in another study [31]. Finally, in [36][37] authors proposed a multi-objective design framework for optimization of parallel mechanisms based on Normal Boundary Intersection (NBI) method [3]. The proposed framework has been applied to design of rehabilitation robots [4][37], robotic exoskeletons [29][36], and compliant micro mechanisms [35]. The approach is computational efficient, applicable to other performance indices, and easily extendable to include further design criteria that may be required by the application.

In this study, the multi-criteria optimization methods for parallel mechanisms [36][37] is applied to the

dimensional synthesis of a Modified Delta Robot. Modified Delta Robots are popular parallel mechanisms among haptic device designs and even commercial versions of them are available [21]. This study extends authors work in [23] by including the capstan ratio as a design variable and implementing the final design as a haptic interface, where the device is driven by double DC motors per shaft through the optimal capstan ratio.

The paper is organized as follows: In Section 2, the design objectives and performance measures are presented. Section 3 introduces the kinematics of the Modified Delta Robot. In Section 4, the multi-criteria design optimization problem is formulated and solved. Section 5 presents the implementation of the haptic interface, while Section 6 concludes the paper.

2. Design Objectives and Performance Measures

In this section, the design objectives are detailed and the performance measures appropriate for the specified design objectives are introduced.

2.1 Design Objectives

Following the terminology of Merlet [18], one can categorize the performance requirements of a mechanism into four distinct groups: Imperative requirements that must be satisfied for any design solution, optimal requirements for which an extremal value of the index is required, primary requirements which take place in the specifications but can be modified to some extent to ensure a design solution, and secondary requirements which do not appear in the specifications but can be utilized to choose between multiple design solutions. Ensuring the safety and complying with the ergonomic needs of the human operator are two imperative design requirements every haptic interface must satisfy. Safety is typically assured by the selection of back-drivable actuation and power transmission with force/torque limits implemented in software, while predetermined ergonomic workspace volumes are imposed at the kinematic synthesis level. The absence of singularities in the workspace is another imperative design requirement that ensures the forward and inverse kinematics of the robot is solved uniquely at each point within the workspace. Both kinematic and dynamic performances of parallel mechanisms are to be optimized to achieve haptic devices with low parasitic effects. Specifically, to achieve high force bandwidths and a uniform “feel”, kinematic/dynamic isotropy and stiffness of the device have to be maximized while its apparent inertia is being minimized. To quantify performance, several design matrices, including Jacobian and inertia matrices, are studied and to date many scalar performance indices have been



proposed. These indices either quantify the directional independence (uniformity) of configuration dependent design matrices or represent a distance to a singular configuration. Since singular values of a matrix provide a versatile metric to quantify its properties, most of the indices are derived as a function of these values.

A common primary requirement for haptic interfaces is the workspace volume index [18], the ratio between the workspace volume and the volume of the robot. Even though predetermined workspace volumes are generally imposed as imperative requirements, a large workspace volume index is still desired to reduce the collisions of the device with the operator or the environment. The footprint area is yet another primary requirement commonly imposed during design. Finally, the secondary requirements include low backlash, low-friction, high back-driveability, and low manufacturing costs. Friction, backlash, and back-driveability are mainly influenced by the selection of the actuators and the transmission, while choice of link lengths may have an influence on manufacturing costs.

2.2 Measuring the Kinematic and Dynamic Performance

To measure kinematic performance, properties of the Jacobian matrix (J) are studied thoroughly. Condition number, proposed by Salisbury and Craig [28], describing the worst-case behavior at a given configuration is one of the most commonly used kinematic performance measures. Given as the ratio of the minimum and maximum singular values of the Jacobian matrix, this measure locally characterizes directional isotropy for both force/motion transmission accuracy and actuator utilization of a manipulator. Another popular index, manipulability, measures the ease of arbitrarily changing the position and orientation of the end-effector and is calculated by taking the product of singular values of the Jacobian matrix [38]. Sensitivity characterizes the precision of a manipulator by measuring the change in end-effector configuration with respect to small perturbations of joint angles and is given by the Sum of the absolute values of the Jacobian matrix elements in a single row [7]. Finally, minimum singular value of the Jacobian matrix is also proposed as a kinematic performance measure [10] quantifying the skewness of the velocity response. All of the mentioned indices are local measures of kinematic performance; therefore, are not constant over the entire workspace. Extensions of these indices have been proposed to characterize the performance of a manipulator over the entire workspace. Gosselin and Angeles proposed global condition indices based on the integral of local kinematic performance measures over the workspace [6]. However, being average

values, these indices fail to capture possible low performance configurations (near singular points) within the workspace. Moreover, integrating a local measure can be computationally expensive. Mean of the minimum singular value has also been proposed as global measure in order to characterize the path velocity of parallel robots [9]. Since mean values are not sufficient to guarantee homogeneity of performance, standard deviation of the minimum singular value has also been introduced as a measure [11]. Other global indices include global payload index that measures the force transmission capability [22]. Finally, the global isotropy index (GII), which is introduced by Stocco et al. [32], is a workspace inclusive worst-case kinematic performance measure that is intolerant of poor performance over the entire workspace. GII is calculated as the ratio of the minimum of the smallest singular value and the maximum of the largest singular value of the Jacobian matrix over the workspace.

In this study, a global performance index is chosen to quantify the kinematic isotropy of the haptic interface since the objective of the design problem is to minimize the parasitic effects of the manipulator over the workspace. Even though any global index can be utilized within the framework presented, the conservative workspace inclusive worst-case performance measure that is intolerant of poor performance over the entire workspace, GII, is preferred. As a global worst case performance measure, maximizing GII corresponds to designing a mechanism with best worst-case kinematic performance. Moreover, an optimal GII results in a uniform optimal design of haptic interfaces Jacobian matrix for the sake of precision, while also increasing the efficiency of utilization of the actuators. GII can be mathematically expressed as

$$GII = \min_{\gamma_0, \gamma_1} \in W \frac{\underline{\sigma}(J(\alpha, \gamma_0))}{\overline{\sigma}(J(\alpha, \gamma_1))}$$

where J represents the Jacobian of the manipulator, $\underline{\sigma}$ and $\overline{\sigma}$ are the minimum and maximum singular values of the Jacobian matrix, γ_0 and γ_1 are the configurations in the workspace that result in the extreme singular values, α is the column matrix of design variables, and W represents the workspace.

Dynamic performance is measured in a similar manner to the kinematic performance, but properties of the inertia matrix (M) capturing the relation between actuator force/torque and end-effector acceleration, take place in optimization. The goal for improving dynamic performance is to minimize inertial effects that conflict with high acceleration demands. To characterize *local* dynamic performance Asada defined the effective inertia



matrix expressing the homogeneity of the moment of inertia of the non-redundant manipulators and introduced the concept of generalized inertia ellipsoid [1]. Yoshikawa proposed a dynamic manipulability measure [38], which is an extension of manipulability concept and measures the degree of arbitrariness in changing end-effector accelerations. Dynamic manipulability is calculated as the product of singular values of M^{-1} matrix. Angeles et al. defined the dynamical conditioning index which measures dynamical coupling and numerical stability of the generalized inertia matrix of manipulators [6]. Finally, swiftness, a measure to characterize the attitude of the manipulator to produce high end-effector accelerations, is proposed by Di Gregorio et al. which can also be applied to planar manipulators with non-homogeneous generalized coordinates [8].

Similar to the case of local kinematic performance indices, extensions to local dynamic indices have been proposed to characterize the performance of a manipulator over the entire workspace. Calculating the mean value and standard deviation of the local dynamic indices are among the most commonly used approaches to achieve a global dynamic performance index. A global dynamic index (GDI) is introduced in [32] to quantify the global worst-case performance of a manipulator. GDI measures the largest effect of mass on the dynamic performance by calculating the maximum largest singular value over the workspace of the effective mass matrix at the end-effector and is computed as inverse of this maximum of largest singular value. To be consistent with the metric chosen for the kinematic performance, the workspace inclusive best worst-case performance measure (GDI) is used to quantify dynamic performance. As mentioned earlier, any dynamic index could be utilized in the framework introduced, but this decision is conservative and intolerant of poor performance over the entire workspace. As a global worst-case performance measure, minimizing GDI results in reduced maximum largest singular value of the effective mass matrix, decreasing the inertial interference by the system. GDI can be mathematically expressed as

$$GDI = \min_{\gamma \in W} \frac{1}{1 + \bar{\sigma}(M(\alpha, \beta, \gamma))}$$

where M represents effective inertia matrix of the manipulator as seen at the end effector, $\bar{\sigma}$ is the maximum singular value of the effective inertia matrix, γ is the configuration in the workspace that results in the maximum singular value, α is the column matrix of design variables, and W represents the workspace. In general, since Entries of the Jacobian and the inertia matrices may not be homogenous in units, proper

normalization is necessary such that the measures defined on these matrices are meaningful. Among several approaches proposed in literature, normalization with a characteristic length [9] or a nominal link length [13], and partitioning the matrices into translational and rotational parts [9] [14] are the most popular choices. Normalization is not necessary for the introduced study, as the Modified Delta Robot possesses only a translational workspace.

Another performance metric is the force output of the system at the end effector. Given the well known force and torque relation

$$\begin{aligned} F_e &= J^{-T} \tau_l \\ &= J^T \mu \tau_m \end{aligned}$$

where F_e is the force exerted to the end-effector, J is the Jacobian matrix, τ_l is the torque on the actuated link of the robot, τ_m is the motor torque and μ is the transmission ratio, the average static force output of a mechanism can be determined by calculating the Jacobian matrix of the system on the entire workspace.

In order to measure the force output performance, "Global Force Transmission Index" (GFTI) is proposed. GFTI needs to be minimized to optimize the force rendering performance of the mechanism. GFTI is formulated as

$$GFTI = \max_{\gamma \in W} \|J\|_F$$

where $\| \cdot \|_F$ denotes the Frobenius norm, W represents the workspace and J is the Jacobian matrix.

3. The Modified Delta Mechanism

The Modified Delta Mechanism, first introduced by Clavel [26], and further analyzed in [24], consists of eight bodies: a base platform N , three lower links A, B, C , three upper links R, S, T and a moving platform W . The end-effector held by the operator is rigidly attached to the moving platform W . The three lower links are connected to the base platform via revolute joints whose axes of rotation are oriented along the tangents of N . The upper three links are coupled to the lower links via revolute joints. Each of them is a planar four-bar parallelogram, which can perform one DoF motion constrained in its plane. The moving platform is connected to these three upper links by means of revolute joints whose axes of rotation are again oriented along the tangents of W . In this paper, the analysis is limited to a symmetric Modified Delta Mechanism where the revolute joints at the base and

at the moving platform are spaced at 120° along the circumference of each platform whose radii ratio is 0.375. Moreover, the lengths of each of the lower links and similarly that of each of the upper links are considered to be the same. The Modified Delta Mechanism has three translational DoF (x, y, z) of the moving platform W with respect to the Newtonian reference frame N . The controlled DoF are the three revolute joints, with which the lower three links are connected.

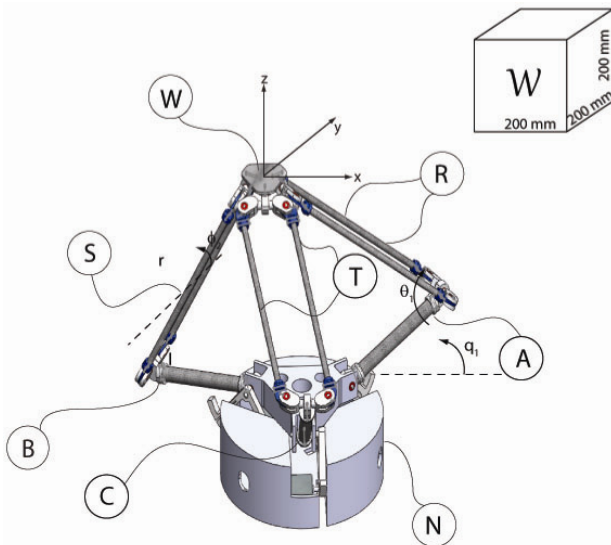


Fig. 1. The modified delta mechanism

Unlike the traditional Delta Mechanism, the Modified Delta Mechanism possesses a series of revolute joints instead of the spherical ones, that is, the motion of the spherical joints on Delta Mechanism are realized via a series of revolute joints. Revolute joints are advantageous over spherical joints, since they allow for larger range of rotations than the spherical joints. Therefore, using same link lengths, a Modified Delta Mechanism can achieve a much larger workspace than a traditional Delta Mechanism. Moreover, the revolute joints have simpler design than spherical joints, hence, are more durable with lower cost.

Design optimization of Modified Delta Robot mechanisms has received attention in the literature. Many of these studies concentrated on workspace optimization [12][19][30]. In addition to the studies on workspace, optimizations of kinematic performance [14], stiffness [2] and velocity [20] of Modified Delta Robots have also been studied. However, neither of the studied mentioned have pursued optimization of multiple objective functions simultaneously; hence, they have neglected the trade-offs between design criteria. In this study, Modified Delta Robot is optimized with respect to multiple design objectives and the trade-offs between different design

criteria are carefully studied.

4. Design Optimization

In this section design optimization of the Modified Delta Mechanism is presented. First, the design parameters and variables are determined, then the optimization problem is introduced. Next, the optimization methods are explained. Finally, the results of the optimization are discussed.

4.1 Design Parameters and Variables

In order to formulate an optimization problem, the design parameters and variables should be identified for the Modified Delta Mechanism. The optimization of the mechanism will be performed to increase GII, GDI and GFTI indices of the robot. Being global indices, GII, GDI and GFTI varies with the workspace of the mechanism. The link lengths of the mechanism also affect these indices, since they are change the weight and the Jacobian of the robot. Therefore, both upper and lower link lengths are chosen as design variables. Moreover, the capstan ratio affects how the rotor inertia of the DC motors are transferred to the end-effector. GDI minimizes the capstan ratio since it adds increases the mass matrix, on the other hand GFTI increases the capstan ratio; therefore GDI and GFTI acts in contrast to each other for the capstan ratio and emerges a design trade-off between these two indices.

Parameter set of the optimization problem encapsulates the values which do not change with the optimization solution. Therefore, parameters are set as the prescribed workspace of the mechanism. Since the delta robot has three translational degrees of freedom, the parameter space of the optimization is selected as the x, y and z coordinates of the predefined workspace. The parameter and variable sets used in the optimization problem are listed in Table 1.

Table. 1. Parameter and Variable Sets

Symbol	Variable/Parameter	Range
α_1	x-coordinate	0-200 mm
α_2	y-coordinate	0-200 mm
α_3	z-coordinate	200-400 mm
β_1	Lower arm	150-250 mm
β_2	Upper arm	250-350 mm
β_3	Capstan ratio	1:12 – 1:25

4.2 Problem Definition

In the optimization problem three objective functions characterize the kinematic and dynamic performance of the mechanism. The objective of optimization is to



maximize the worst kinematic isotropy (GII) of the mechanism while simultaneously minimizing the maximum singular value of the effective mass matrix (GDI) and global force transmission index (GFTI). In this study, it is assumed that the inertia of the mechanism is due to those of each link, DC motors and capstans; thus, other inertial factors such as inertia of the connecting members and the bearings are neglected. The negative null form of the multi-objective optimization problem can be stated as

$$\begin{aligned} \max F(\alpha, \beta, \gamma) \\ G(\alpha, \beta) < 0 \\ \alpha_l < \alpha < \alpha_u \end{aligned}$$

where F represents the column matrix of objective functions that depend on the design variables α , parameters β , and workspace positions γ . Symbol G represents the inequality constraint function that also depends on design variables and parameters. Finally, α_l and α_u correspond to the lower and upper bounds of the design variables, respectively. For the Modified Delta Mechanism, the column matrix F is simply given as

$$F = \begin{bmatrix} GDI \\ GII \\ GFTI \end{bmatrix}$$

The constraints on the other hand, are implicitly imposed during the kinematic analysis of the parallel mechanism, which is carried out using numerical integration.

4.3 Optimization Method

Before addressing the multi-criteria optimization problem, the nature of the problem with respect to the selected performance criteria is to be studied. Inspecting the performance criteria, one can conclude that GII, GFTI and GDI are non-convex with respect to the design variables. Moreover, as workspace inclusive measures, their calculation requires searches over the workspace. As discussed in the introduction, several methods have been proposed to solve for the single criteria optimization problem of parallel manipulators. In general, descent methods suffer from getting trapped at local optima while heuristic methods cannot guarantee optimality of their solution. Feasibility and efficiency of a branch-and-bound type method, called culling algorithm, is advocated in the literature to address single objective min-max problems [32].

In this study, a modified version of the culling algorithm is used to independently solve for the optimum designs with respect to GII, GDI and GFTI. The culling algorithm improves the computational efficiency of a brute-force method by reducing (culling) the amount of searches required through effective performance comparisons. The algorithm capitalizes on the fact that as a worst-case measure, once the global performance index for certain reference parameters is calculated conducting a search over the entire workspace, reduction of the feasible parameter set can be performed without performing any other searches over the workspace. Specifically, after a global index value is calculated for the reference parameters, comparisons with local indices at only a single configuration in the workspace can be overtaken. Hence, searches over workspace are significantly reduced as they are conducted only when it is necessary to calculate new reference global index values. Comparing all set of design variables to find the best worst-case index, the algorithm will converge to an optimum solution within the discretization accuracy. As the culling method substantially reduces the amount of workspace searches required by a brute-force method, it is a fast and efficient algorithm to address min-max type problems.

As it is mentioned earlier, GII aims to minimize the difference between maximum and minimum singular values of the Jacobian of the mechanism in the defined workspace. Calculation of GII requires numerical evaluation of the Jacobian matrix of the system. In this study, analytic solutions of the inverse/forward position and velocity level kinematics are formulated utilizing a symbolic software package and numerical values are evaluated as demanded by the optimization algorithm.

Similar to GII, GFTI is also calculated using the singular values of the Jacobian matrix for each transmission ratio calculated on the entire workspace. GFTI is also derived easily using numerical techniques.

In order to calculate GDI, the apparent inertia matrix of the mechanism at the end-effector is required. This inertia matrix is also derived using a symbolic software package. Symbolic calculation of the inertia matrix requires analytic parametric formulation of the inertia of each part of the mechanism. The inertia values of the links can be formulated easily since they can be modeled as hollow tubes. However, the capstan does not have a simple geometry and its inertia cannot be derived analytically. To derive a parametric inertia formula for the capstan, numeric evaluations for inertia of the capstan is calculated using computer aided design techniques for radii starting from 65mm to 300mm. The inertia of the capstan is calculated for every 0.5mm, which is a fine discretization. Then, a least squares curve fit using a 3rd degree polynomial is employed as shown in Figure 2 to estimate an inertia formula for the capstan. The



performance of curve fit is measured by *r-square*, which is coefficient of determination, as 0.999999999999351.

Since the performance of the culling algorithm is highly dependent on the initial reference values assigned, a fast gradient-based optimization method, sequential quadratic programming (SQP), is used to solve for a local extremum that will serve as a good initialization value. This modification increases the efficiency of the algorithm by resulting in a higher culling rate at the first iteration. Once a solution is obtained, another SQP is invoked to converge to a guaranteed optimum within the discretization region.

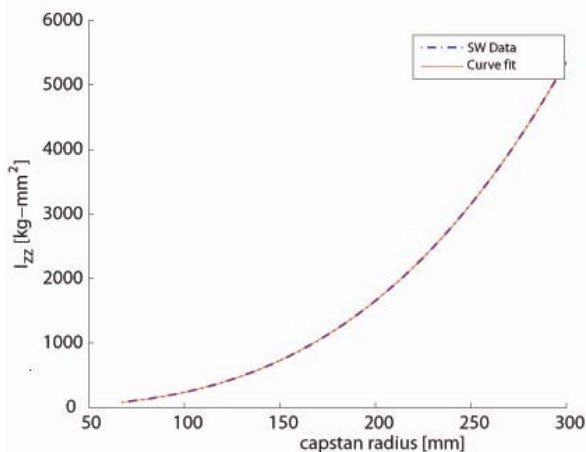


Fig. 2. Least-Squares Fit to Estimate Capstan Inertia

In order to construct a multi-criteria optimization problem the trade-offs between objectives should be clarified. Otherwise if the multi-criteria optimization problem is treated as many single objective problems, solution of the problems can be inconsistent with each other. In this study Pareto methods are used to solve the problem, because unlike scalarization methods, Pareto methods do not require any *a priori* knowledge about the design trade-offs and solve for the locus of all dominant solutions with respect to multiple objective functions, constituting the so-called the Pareto-front hyper-surface. Hence, designers can make a more realistic choice between multiple “best” solutions and avoid the challenge of synthetically ranking their preferences.

There exist several methods to obtain the Pareto-front hyper-surface, among which Normal Boundary Intersection (NBI) method is one of the most featured. As the Pareto-front hyper-surface is a geometric entity in the objective space forming the boundary of feasible region, NBI approach attacks the geometric problem directly by solving for single-objective constrained subproblems to obtain uniformly distributed points on the hyper-surface. NBI solves for subproblems which only depend on the

defined optimization model, that is, chosen objective functions and design constraints since these equations map the feasible design space onto the attainable objective space. Given independent optimal solutions for each objective function, called shadow points, NBI first constructs a hyper-plane in the objective space by connecting these shadow points with straight lines. Then, this hyper-plane is divided into grids. For each point on the grid, a geometric subproblem is solved to find the furthest point on the line that extends along the surface normal passing through the grid point. Hence, NBI obtains the Pareto-front with reducing the problem to many single-objective constrained subproblems.

4.4 Optimization Results

The single optima for GII, GFTI and GDI, that constitute the shadow points for the NBI method, are solved by using a modified version of culling algorithm. Since there are three objective functions to be optimized simultaneously, NBI yields a Pareto surface, $P \subset \mathcal{R}^3$, of non-dominated solutions. This surface is presented in Figure 3, where the objective functions GII, GDI and GFTI are all normalized.

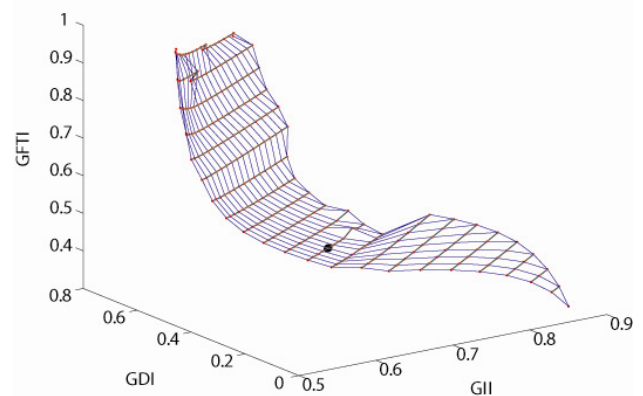


Fig. 3. Pareto Front Surface

Although a Pareto-front surface provides many non-dominated solutions, only one design shall actually be implemented. Therefore, the final design selection has to be made by imposing additional constraints on the set of non-dominated solutions. A number of sensible constraints may be imposed by inspecting the Pareto-front surface and invoking the design objectives presented in Section 2.1. As a primary requirement, the workspace volume index constraint is first employed to eliminate the non-dominated solutions on the Pareto surface with lower link length greater than 220 mm. In addition to this constraint, a minimum global force transmission value of

20 is imposed. On the Pareto surface this corresponds to eliminating points with normalized GFTI lower than 0.4647. Observing the projections of the Pareto surface onto the GII and GDI planes, it is deduced that trade-off between these objectives is quite low if GII and GDI values lower than about 0.31 are selected. That is, there exist points on the Pareto surface that yields high gains for at least one objective function while not losing significantly from the other. All of these considerations reduce a Pareto surface grid consisting of 253 points to mere 8 points. Finally, the minimum of minimum singular values of the Jacobian and maximum of maximum singular values of the mass matrix are calculated for these 8 points, and the design with best performance with respect to these values is selected, yielding the solution indicated with a black sphere on the Pareto surface in Figure 3. The design variables that yield this non-dominated solution are as follows: $\beta_1 = 216.2mm$, $\beta_2 = 258.2mm$ and $\beta_3 = 22.7$.

5. Implementation of the Modified Delta Mechanism

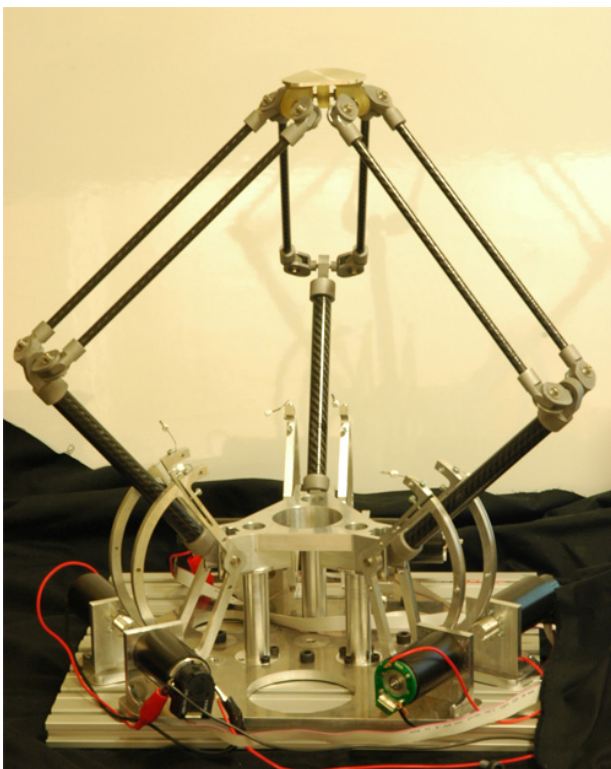


Fig. 4. Implementation of the Modified Delta Mechanism

The Modified Delta Mechanism is implemented as a haptic interface by using the results of the dimensional optimization.

To minimize the parasitic effects of dynamic forces acting on the haptic device, the weight of the links is minimized using carbon fiber tubes, while the connecting members are manufactured from aluminum, using rapid prototyping techniques. Rapid prototyping allows for construction of hollow (honey-comb like) structures, minimizing the weight of these connecting members.

High precision graphite-brushed direct-drive DC motors that can generate 150W power and 170mNm torque, are selected as the actuators. A capstan mechanism is used for power transmission since capstan transmission provides high back-driveability while ensuring smooth operation with negligible backlash and friction. Two actuators are used per link and a capstan transmission with the optimal radius is utilized to deliver power to the mechanism. By using two motors on one link, the delivered torque to the mechanism is doubled without increasing the capstan ratio, that is, without sacrificing speed and back-driveability. Each drive shaft is equipped with an encoder of 500 counts per turn resolution. Figure 4 depicts the final prototype of the Modified Delta Mechanism.

6. Conclusion and Future Work

Optimal design and implementation of a haptic interface is presented. A parallel mechanism, specifically a Modified Delta Mechanism, is selected as the underlying kinematics of the haptic interface to achieve a high bandwidth in three translational degrees of freedom. After the type selection, optimal dimensional synthesis is performed considering the global best-worst case kinematic and dynamic performance of the mechanism. The worst case isotropy of the mechanism is improved, while simultaneously decreasing its apparent inertia at the end-effector. The multi-criteria optimization problem is solved using NBI method which simultaneously optimizes the objective functions. The final design is chosen from the Pareto set by first imposing primary requirements and then selecting the configuration with the best performance among obtained solutions. The chosen configuration has lower links of 216.2mm, upper links of 258.8mm and a capstan ratio of 1:22.7. The final design is implemented using carbon fiber links, aluminum connecting members and direct drive motors driving the capstan transmission. Characterization of the device and experimental verification of the results are planned as future work.

References

- [1]. H. Asada, *A geometrical representation of manipulator dynamics and its application to arm design*, Journal of Dynamic Systems, Measurement, and Control **105** (1983), no. 3, 131–142.
- [2]. E. Courteille, D. Deblaise, and P. Maurine, *Design optimization of a delta-like parallel robot through global stiffness performance*



- evaluation, Intelligent Robots and Systems, 2009. IROS 2009. IEEE/RSJ International Conference on, 10-15 2009, pp. 5159 – 5166.
- [3]. Indraneel Das and J. E. Dennis, *Normal-boundary intersection: A new method for generating the pareto surface in nonlinear multicriteria optimization problems*, SIAM J. on Optimization **8** (1998), no. 3, 631–657.
- [4]. A. Erdogan, A.C. Satici, and V. Patoglu, *Design of a reconfigurable force feedback ankle exoskeleton for physical therapy*, Reconfigurable Mechanisms and Robots, 2009. ReMAR 2009. ASME/IFToMM International Conference on, 22-24 2009, pp. 400–408.
- [5]. Ferlay Fabien and Gosselin Florian, *A new cable-actuated haptic interface design*, Haptics: Perception, Devices and Scenarios, Springer Berlin / Heidelberg, 2008.
- [6]. C. Gosselin and J. Angeles, *A global performance index for the kinematic optimization of robotic manipulators*, Journal of Mechanical Design **113** (1991), no. 3, 220–226.
- [7]. K.W. Grace, J.E. Colgate, M.R. Glucksberg, and J.H. Chun, *A six degree of freedom micromanipulator for ophthalmic surgery*, Robotics and Automation, 1993. Proceedings., 1993 IEEE International Conference on, 2-6 1993, pp. 630–635 vol. 1.
- [8]. R. Di Gregorio and V. Parenti-Castelli, *On the characterization of the dynamic performances of planar manipulators*, Meccanica **40** (2005), no. 3, 267–279.
- [9]. J Hesselbach, M Krefft, and H Kerle, *The assessment of parallel mechanisms - it is not only kinematics*, Production Engineering **12** (2005), no. 12, 173–178.
- [10]. Charles A. Klein and Bruce E. Blaho, *Dexterity measures for the design and control of kinematically redundant manipulators*, Int. J. Rob. Res. **6** (1987), no. 2, 72–83.
- [11]. M. Krefft and J. Hesselbach, *Elastodynamic optimization of parallel kinematics*, Automation Science and Engineering, 2005. IEEE International Conference on, 1-2 2005, pp. 357 – 362.
- [12]. M.A. Laribi, L. Romdhane, and S. Zeghloul, *Analysis and dimensional synthesis of the delta robot for a prescribed workspace*, Mechanism and Machine Theory **42** (2007), 859 – 870.
- [13]. J.H. Lee, K.S. Eom, and H.I. Suh, *Design of a new 6-dof parallel haptic device*, Robotics and Automation, 2001. Proceedings 2001 ICRA. IEEE International Conference on, vol. 1, 2001, pp. 886 – 891.
- [14]. S.U. Lee and S. Kim, *Analysis and optimal design a new 6-dof parallel type haptic device*, IEEE/RSJ International Conference on Intelligent Robots and Systems (2006), 460–465.
- [15]. Xin-Jun Liu and Jinsong Wang, *A new methodology for optimal kinematic design of parallel mechanisms*, Mechanism and Machine Theory **42** (2007), no. 9, 1210 – 1224.
- [16]. Xin-Jun Liu, Jinsong Wang, and Hao-Jun Zheng, *Optimum design of the 5r symmetrical parallel manipulator with a surrounded and good-condition workspace*, Robotics and Autonomous Systems **54** (2006), no. 3, 221 – 233.
- [17]. Y. Lou, G. Liu, and Z. Li, *Randomized optimal design of parallel manipulators*, Automation Science and Engineering, IEEE Transactions on **5** (2008), no. 2, 223–233.
- [18]. J.-P. Merlet, *Parallel robots*, 2 ed., Springer, 2006.
- [19]. K. Miller, *Maximization of workspace volume of 3-dof spatial parallel manipulators*, Journal of Mechanical Design **124** (2002), 347-350.
- [20]. V. Nabat, M. de la O Rodriguez, O. Company, S. Krut, and F. Pierrot, *Par4: very high speed parallel robot for pick-and-place*, Intelligent Robots and Systems, 2005. (IROS 2005). 2005 IEEE/RSJ International Conference on, 2-6 2005, pp. 553 – 558.
- [21]. Novint, *Novint Falcon*, http://home.novint.com/products/novint_falcon.php.
- [22]. H. Ozaki, Hongrui Wang, Xinjun Liu, and Feng Gao, *The atlas of the payload capability for design of 2-dof planar parallel manipulators*, Systems, Man, and Cybernetics, 1996., IEEE International Conference on, vol. 2, 14-17 1996, pp. 1483 –1488 vol.2.
- [23]. V. Patoglu and A. C. Satici, *Advances in haptics: Optimal design of haptic interfaces*, 2 ed., IN-TECH, 2010.
- [24]. F. Pierrot, P. Dauchez, and Fournier A., *Fast parallel robots*, Journal of Robotic Systems **8** (1991), no. 6, 829 – 840.
- [25]. Liqun Qi and Rob S.Womersley, *On extreme singular values of matrix valued functions*, 1996.
- [26]. Clavel R., *Device for displacing and positioning an element in space.*, Patent EP0250470 B1, 01 1988, 07.
- [27]. A. Risoli, M. Prisco, F. Salsedo, and M. Bergamasco, *A two degrees-of-freedom planar haptic interface with high kinematic isotropy*, Robot and Human Interaction, 1999. RO-MAN '99. 8th IEEE International Workshop on, 1999, pp. 297–302.
- [28]. J. Kenneth Salisbury and John J. Craig, *Articulated Hands*, The International Journal of Robotics Research **1** (1982), no. 1, 4–17.
- [29]. A.C. Satici, A. Erdogan, and V. Patoglu, *Design of a reconfigurable ankle rehabilitation robot and its use for the estimation of the ankle impedance*, 11th International Conference on Rehabilitation Robotics, 2009.
- [30]. S.-D. Stan, V. Maties, R. Balan, and C. Lapusan, *Genetic algorithms to optimal design of a 3 dof parallel robot*, Automation, Quality and Testing, Robotics, 2008. AQTR 2008. IEEE International Conference on, vol. 2, 22-25 2008, pp. 365 –370.
- [31]. S. Dan Stan, Vistrian Maties, and Radu Balan, *Optimal design of 2 dof parallel kinematics machines*, PAMM **6** (2006), no. 1, 705-706.
- [32]. L. Stocco, S. E. Salcudean, and F. Sassani, *Fast constrained global minimax optimization of robot parameters*, Robotica **16** (1998), no. 6, 595–605.
- [33]. B.E. Stuckman and E.E. Easom, *A comparison of bayesian/sampling global optimization techniques*, Systems, Man and Cybernetics, IEEE Transactions on **22** (1992), no. 5, 1024–1032.
- [34]. B.E. Stuckman, G. Evans, and M. Mollaghasemi, *Comparison of global search methods for design optimization using simulation*, Simulation Conference, 1991. Proceedings., Winter, dec 1991, pp. 937–944.
- [35]. O. Tokatli and V. Patoglu, *Multicriteria design optimization of a compliant micro half-pantograph*, ECCOMAS Multibody Dynamics, 2009.
- [36]. R. Unal, G. Kiziltas, and V. Patoglu, *A multi-criteria design optimization framework for haptic interfaces*, Haptic Interfaces for Virtual Environment and Teleoperator Systems, 2008. Haptics 2008. Symposium on, march 2008, pp. 231–238.
- [37]. *Multi-criteria design optimization of parallel robots*, Robotics, Automation and Mechatronics, 2008 IEEE Conference on, sept. 2008, pp. 112–118.
- [38]. Tsuneo Yoshikawa, *Manipulability of Robotic Mechanisms*, The International Journal of Robotics Research **4** (1985), no. 2, 3–9.
- [39]. Yao Zheng and Roland W. Lewis, *Several algorithms of global optimal search*, Adv. Eng. Softw. **21** (1994), no. 2, 87–98.



Kinematic Analysis of the Cam-Lever Mechanisms of the Cotton-Cleaning Machines

Fazil VELIYEV^{1*}, Mazakhir FARZALIEV

^{1*} Azerbaijan International Institute

veliyev-fazil@mail.ru

^{2*} Azerbaijan State Economic University

Abstract

Cam-lever mechanisms widely adapt in the drives the cotton-folding, cleaning and drying mechanisms, etc. Mechanism for the formation of cotton riot at the cotton-cleaning plants is the same.

1. Introduction

With the kinematic analysis of cam-lever mechanisms the traditional method of constructing the substituting mechanism and the method of conversion of motion is for a number of reasons inconvenient for applying THE COMPUTER(S). The possibility of the automations of the kinematic analysis of flat lever systems on the basis of equations of state previously is shown. The development of algorithm on the basis of this method and the implementation it in the form of program in the algorithmic language for the computer allowed to automated carry out the analysis of different mechanisms of cotton-cleaning machines. Let us examine the application of this method for the kinematic analysis of cam-lever actuator of the riot of shaper functional diagram of which it is given in the figure 1.

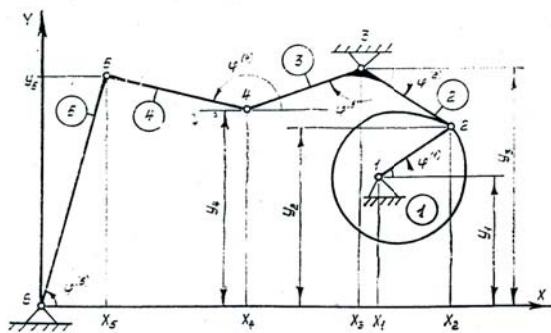


Fig. 1:

Information about the structure of mechanism is introduced into the program in the form of special

characteristic massifs, for example $n=5$ the number of mobile it is sectional; $k=6$ the number of kinematic pairs (subsequently - units); $T(2,n)$ the matrix of topology.

Motion rods can have the variable length (link gears, mechanisms with the sliders). In our case the first component, which represents the radius-vector of theoretical cam profile, is similar. The changeability of length it is sectional it is described by the massif $L(n)$, whose elements $l_i=1$, if i -e component has variable length, and $l_i=0$ with a constant length of this component. Furthermore, into the computer are introduced the numerical values of the coordinates of fixed units, length it is sectional, and also the parameters of the motion of the fist, which is been the leading component. The law of the motion of cam-lever mechanism is determined by cam profile, which is assigned in the form the tabular function of the radius-vector of fist from the angle of its turning. This function is introduced into the computer in the form of massif $R(N,2)$.

In this case $R(i,1)=\varphi_i$ the angle of rotation of fist i -m position, $R(i,2)$ the corresponding value of the radius-vector of theoretical cam profile. The equation of state of the positions of mechanism takes the form:

$$Y = AZ \quad (1)$$

Where $Y(2n)$ -the column vector, which contains the components of the projections of length is sectional:

$$y_{2i-1} = l^{(i)} \cos \varphi^{(i)}; \quad y_{2i} = l^{(i)} \sin \varphi^{(i)}; \quad i = 1, 2, \dots, n;$$

$Z(2k)$ - the column vector, which contains the coordinates of the units of the mechanism:

$$z_{2j-1} = x_j; \quad z_{2j} = y_j; \quad j = 1, 2, \dots, k;$$

$A(2n,2k)$ - the matrix, whose nontrivial elements take values when $p=2i-1$ and $q=2j-1$, where i and j the number of component and the number of unit respectively, $a_{pq}=-1$,



$$B_1^T = [b_1, b_2, \dots, b_{2i-1}, b_{2i}, \dots, b_{2n}];$$

$$b_1 = -l^{(1)} \cos \varphi^{(1)} (\omega^{(1)})^2 - 2l^{(1)} \dot{\varphi}^{(1)} \sin \varphi^{(1)} \omega^{(1)} + l^{(1)} \ddot{\varphi}^{(1)} \cos \varphi^{(1)};$$

$$b_2 = -l^{(1)} \sin \varphi^{(1)} (\omega^{(1)})^2 + 2l^{(1)} \dot{\varphi}^{(1)} \cos \varphi^{(1)} \omega^{(1)} + l^{(1)} \ddot{\varphi}^{(1)} \sin \varphi^{(1)};$$

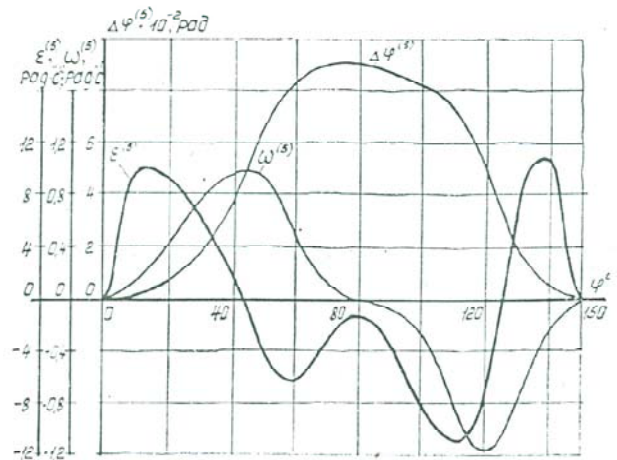
$$b_{2i-1} = -l^{(i)} \cos^{(i)}(\omega^{(i)})^2;$$

\ddot{x}_j, \ddot{y}_j the components of linear acceleration j of unit;
 $\varepsilon^{(i)}$ - the angular acceleration i of component.

Matrix A_0 in (8) has form (7); and B^T and V^T in (7) and B_1^T and W^T in (8) - there are the transposed column vectors respectively B, V in (7) and B_1, W in (8).

Thus, speed and acceleration of all elements with any of cam-lever mechanism it is determined by the method of solution of the systems of linear algebraic equations (6) and (8) for the standard program.

The calculation of inclined panel-riot by that forming of mechanism is carried out according to this program. Kinematic parameters of inclined panel (component 5 to fig.1.) for the angle of rotation fists from 0 to 150° it cam in the form graphs to fig.2.



2. Conclusion

1. The proposed method of the kinematic analysis of cam-lever mechanisms makes it possible to fully automate the process of obtaining and solving the equations for determining the kinematic parameters of all elements of mechanism with the assigned law of the motion of the leading component, which the fist is.

2. The given algorithm is realized in the form the program, according to which is executed the analysis of the inclined panel-riot of the forming mechanism. With a change in the kinematic parameters of inclined panel (5) it is possible to change the form of the upper part of the riot, and so the value of the density of the added raw cotton.



Proceedings of the International Symposium of Mechanism and Machine Science, 2010
AzCIFTtoMM – Izmir Institute of Technology
5-8 October 2010, Izmir, TURKEY



Session 4:

**Dynamics and Vibrations of Machinery (DvM)
Computational Kinematic Synthesis and Analysis (CkSa)**



Proceedings of the International Symposium of Mechanism and Machine Science, 2010
AzCIFTtoMM – Izmir Institute of Technology
5-8 October 2010, Izmir, TURKEY



Dynamics and stability of large turbine generators

Jan DUPAL^{1*}, Tomas KURUC²

^{1*}University of West Bohemia
Univerzitni 22, 30614 Pilsen, Czech Republic
dupal@kme.zcu.cz

² BRUSH SEM s.r.o.

Abstract

The goal of the submitted paper is to bring an approach to modelling of turbine generators whose bodies have primarily non-symmetrical geometry and stiffnesses in two perpendicular planes. The Floquet theory in combination with modal synthesis method is used for stability assessment. The attention is payed to the depth determination of the so called Lafoon's slits. This structure arrangement serves to eliminate parametric resonanse possibility. .

Keywords: vibration, Laffoon's slits, rotor dynamics, stability

1. Introduction

Before some structural arrangement the turbine generators have non-symmetrical stiffnesses in two perpendicular planes parallel to the rotor axis. The first goal of this paper is modelling presentation and motion stability assessment of the generator model. The second one will be proposal of the rotor operational adjustment. The equation of motion of such rotor can be written in form

$$\mathbf{T}^T(t)\mathbf{M}\mathbf{T}(t)\ddot{\mathbf{q}}(t) + [\mathbf{G} + \mathbf{T}^T(t)\eta_V\mathbf{K}\mathbf{T}(t) + \mathbf{B}_S]\dot{\mathbf{q}}(t) + [\mathbf{K}_S + \mathbf{T}^T(t)(\eta_V\mathbf{K}\boldsymbol{\Omega} + \mathbf{K})\mathbf{T}(t)]\mathbf{q}(t) = \mathbf{f}(t). \quad (1)$$

Individual matrices have meaning as follows:

$\mathbf{T}(t) \in \mathbf{R}^{n,n}$ -transformation matrix,

$\mathbf{T}^T(t)\mathbf{M}\mathbf{T}(t) \in \mathbf{R}^{n,n}$ -mass matrix,

$\mathbf{M} \in \mathbf{R}^{n,n}$ -constant mass matrix expressed in rotating coordinate system,

$\mathbf{G} \in \mathbf{R}^{n,n}$ -gyroscopic matrix,

$\mathbf{T}^T(t)\eta_V\mathbf{K}\mathbf{T}(t) \in \mathbf{R}^{n,n}$ -matrix of proportal radial damping,

$\mathbf{T}^T(t)\eta_V\mathbf{K}\boldsymbol{\Omega}\mathbf{T}(t) \in \mathbf{R}^{n,n}$ -matrix of proportional tangential damping,

$\mathbf{K}_S, \mathbf{B}_S \in \mathbf{R}^{n,n}$ -stationary part of stiffness matrix and damping matrix, respectively,

$\mathbf{T}^T(t)\mathbf{K}\mathbf{T}(t) \in \mathbf{R}^{n,n}$ -stiffness matrix.

Most of these matrices are periodically time dependent with time period

$$T = \frac{2\pi}{\omega}, \quad (2)$$

where ω is angular speed of the rotor. The equation of motion (1) can be briefly rewritten into form

$$\tilde{\mathbf{M}}(t)\ddot{\mathbf{q}}(t) + \tilde{\mathbf{B}}(t)\dot{\mathbf{q}}(t) + \tilde{\mathbf{K}}(t)\mathbf{q}(t) = \mathbf{0}, \quad (3)$$

where meaning of matrices in (3) follows from the comparison (1) and (3).

2. Floquet theory

Adding the identity

$$\tilde{\mathbf{M}}(t)\dot{\mathbf{q}}(t) - \tilde{\mathbf{M}}(t)\dot{\mathbf{q}}(t) = \mathbf{0} \quad (4)$$

to (3) we can transfer the original system of the ordinary differential equations (ODE) of the second order to the system of the first order in form

$$\dot{\mathbf{x}}(t) = \mathbf{A}(t)\mathbf{x}(t), \quad (5)$$

where

$$\mathbf{A}(t) = \begin{bmatrix} \mathbf{0}, & \mathbf{I}_n \\ -\tilde{\mathbf{M}}^{-1}(t)\tilde{\mathbf{K}}(t) & -\tilde{\mathbf{M}}^{-1}(t)\tilde{\mathbf{B}}(t) \end{bmatrix}, \quad \mathbf{x}(t) = \begin{bmatrix} \mathbf{q}(t) \\ \dot{\mathbf{q}}(t) \end{bmatrix}. \quad (6)$$

and $\mathbf{I}_n \in \mathbf{R}^{n,n}$ is identity matrix. A significant quantity for stability assessment is monodromy matrix whose eigenvalues are deciding on stability or instability of the system [2]. In case all the eigenvalues lie inside the unit circle in complex plane (included boundary) the system is



stable and vice versa. In case of at least one of eigenvalues lying outside this circle, the system is unstable. Monodromy matrix can be determined as a solution to the equation

$$\dot{\mathbf{X}}(t) = \mathbf{A}(t)\mathbf{X}(t), \quad \mathbf{X}(0) = \mathbf{I}_{2n}, \quad (7)$$

in time $t = T$. The $\mathbf{X}(t) \in \mathbf{R}^{2n, 2n}$ is fundamental matrix and

$$\mathbf{Z} = \mathbf{X}(T) \quad (8)$$

is monodromy matrix. The solution to the eq. (7) is very time expensive and the elapsed time for many structural variants and parameter changing is inadmissible. This problem is very unpleasant especially for use of FEM.

3. Modal reduction

For this reason some DOF reduction is necessary. One of the possibilities is modal reduction using modal and spectral matrices corresponding to the associated symmetrical conservative non-rotating mathematical model expressed in the initial time

$$\mathbf{M}_0 \ddot{\mathbf{q}}(t) + \mathbf{K}_0 \mathbf{q}(t) = \mathbf{0}, \quad (9)$$

where

$$\mathbf{M}_0 = \mathbf{T}^T(0)\mathbf{M}\mathbf{T}(0) = \mathbf{M}, \quad (10)$$

$$\mathbf{K}_0 = \mathbf{K}_s + \mathbf{T}^T(0)\mathbf{K}\mathbf{T}(0) = \mathbf{K}_s + \mathbf{K}, \quad (11)$$

because of $\mathbf{T}(0) = \mathbf{I}$. Solving the eigenvalue problem

$$(\mathbf{K}_0 - \Omega^2 \mathbf{M}_0) \mathbf{v} = \mathbf{0} \quad (12)$$

we can come to the modal matrix

$$\mathbf{V} = [\mathbf{v}_1, \mathbf{v}_2, \dots, \mathbf{v}_n] \in \mathbf{R}^{n, n} \quad (13)$$

and spectral matrix

$$\mathbf{\Lambda} = \begin{bmatrix} \Omega_1^2 & & & \\ & \Omega_2^2 & & \\ & & \ddots & \\ & & & \Omega_n^2 \end{bmatrix} \in \mathbf{R}^{n, n}. \quad (14)$$

There is no modal transformation of the coupled system of the differential equations (1) to the uncoupled one because of time dependence. The main meaning of modal transformation is modal reduction. Let us introduce the reduced modal and spectral matrices

$$\mathbf{V}_R \in \mathbf{R}^{n, m}, \quad \mathbf{\Lambda}_R \in \mathbf{R}^{m, m}, \quad m \ll n, \quad (15)$$

respectively. The choice of the modal matrix columns and columns and rows of the spectral matrix can be performed according to the fig. 1

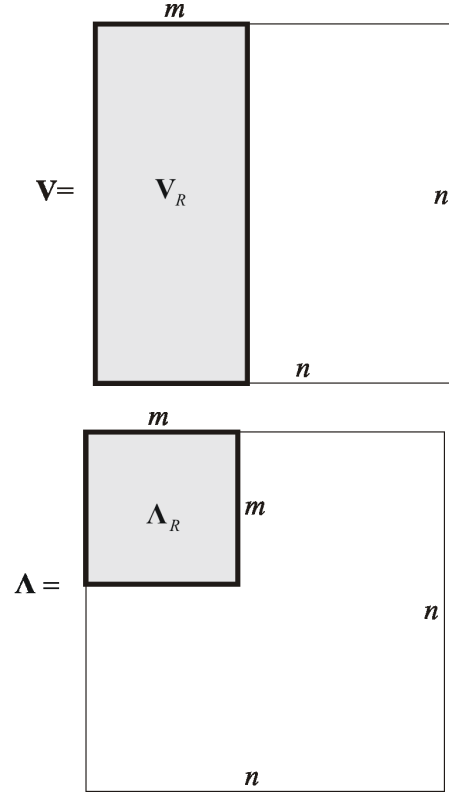


Fig. 1: Reduction of modal and spectral matrices

Let us introduce modal transformation

$$\mathbf{q}(t) = \mathbf{V}_R \mathbf{y}(t), \quad \mathbf{y}(t) \in \mathbf{R}^{m, 1} \quad (16)$$

substitute into (3) and pre-multiply (3) by \mathbf{V}_R^T . Now we can write

$$\mathbf{V}_R^T \tilde{\mathbf{M}}(t) \mathbf{V}_R \ddot{\mathbf{y}}(t) + \mathbf{V}_R^T \tilde{\mathbf{B}}(t) \mathbf{V}_R \dot{\mathbf{y}}(t) + \mathbf{V}_R^T \tilde{\mathbf{K}}(t) \mathbf{V}_R \mathbf{y}(t) = \mathbf{0}. \quad (17)$$

The relation (17) represents system of $m \ll n$ differential equations. It means that number of equations was significantly reduced. The thesis [1] brings a numerical comparison of the stability analysis performed by means of the reduced and full mathematical model, respectively. Adding the identity

$$\mathbf{V}_R^T \tilde{\mathbf{M}}(t) \mathbf{V}_R \dot{\mathbf{y}}(t) - \mathbf{V}_R^T \tilde{\mathbf{M}}(t) \mathbf{V}_R \dot{\mathbf{y}}(t) = \mathbf{0} \quad (18)$$

to the eq. (17) we can write similar relation to (5) in form

$$\dot{\mathbf{x}}(t) = \tilde{\mathbf{A}}(t) \mathbf{x}(t), \quad (19)$$

where

$$\tilde{\mathbf{A}}(t) = \begin{bmatrix} \mathbf{0}, & \mathbf{I}_n \\ -\mathbf{M}^{*-1}(t)\mathbf{K}^*(t), & -\mathbf{M}^{*-1}(t)\mathbf{B}^*(t) \end{bmatrix}, \quad (16)$$

$$\mathbf{M}^*(t) = \mathbf{V}_R^T \tilde{\mathbf{M}}(t) \mathbf{V}_R, \quad \mathbf{K}^*(t) = \mathbf{V}_R^T \tilde{\mathbf{K}}(t) \mathbf{V}_R \in \mathbf{R}^{m,m},$$

$$\mathbf{B}^*(t) = \mathbf{V}_R^T \tilde{\mathbf{B}}(t) \mathbf{V}_R \in \mathbf{R}^{m,m} \quad (17)$$

and

$$\mathbf{x}(t) = \begin{bmatrix} \mathbf{y}(t) \\ \dot{\mathbf{y}}(t) \end{bmatrix} \in \mathbf{R}^{m,1}. \quad (18)$$

Testing of the modelling methodology was performed on the turbine rotor RIGA (generator of the power plant in Riga-Latvia). The simplified physical model of the generator is depicted in fig. 2

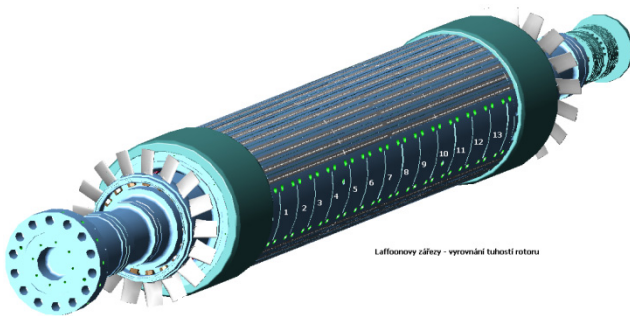


Fig. 2: Generator of Riga power plant

The cross section of the main part of generator is depicted in fig 3

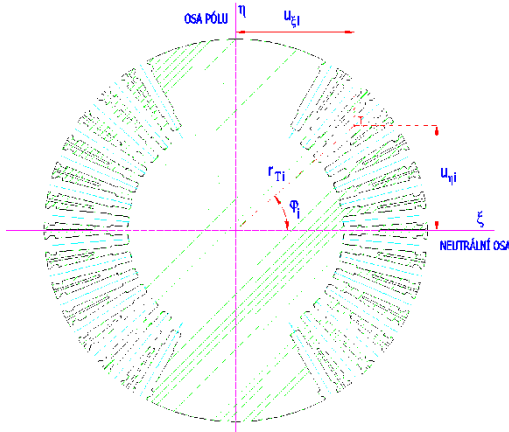


Fig. 3: Cross section of the part of generator

As one can see, the cross section has different second moments of inertia with respect to two axes perpendicular

to the rotor axis.

The generator stability assessment was performed in the region of $\langle 1000, 9000 \rangle$ rpm. The dependence of maximal eigenvalue of monodromy matrix (absolute value) on the angular speed of the rotor is depicted in fig. 4

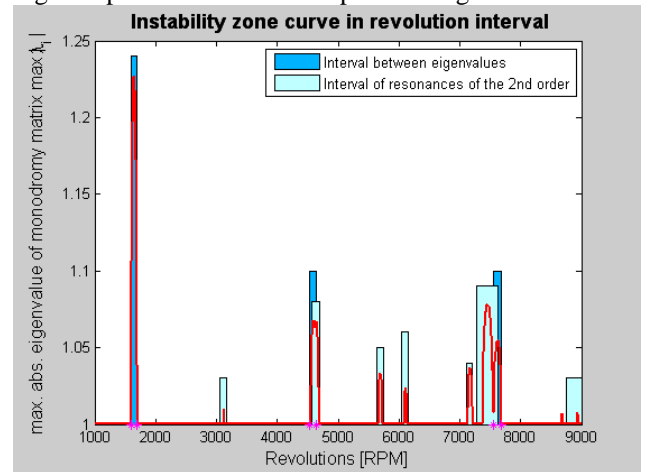


Fig. 4 : Absolute value of maximal eigenvalue

Zoom of this dependence is depicted in fig. 5. and 6. Let us remind that the monodromy matrix eigenvalues was calculated for rotor with no arrangements

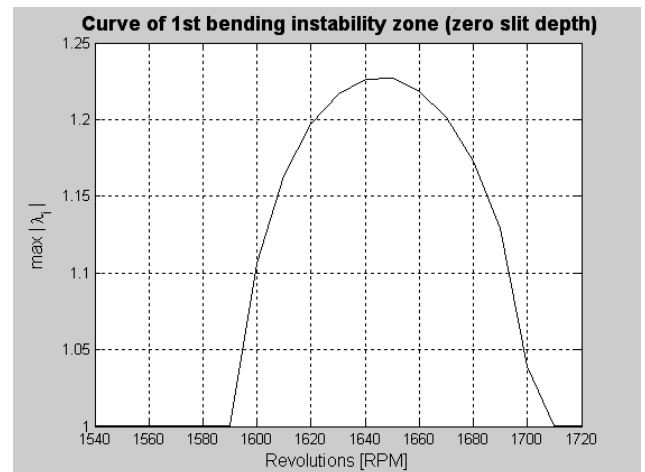


Fig. 5: Zoom of eigenvalue dependence

Fig. 4., 5., 6 show the regions of instability where the absolute value of the maximal eigenvalue of the monodromy matrix overgrows unit level. The regions of instability correspond to the parametric resonances which can be expressed by means of relation

$$\omega_s = \frac{\Omega_i \pm \Omega_j}{2p}, \quad (19)$$

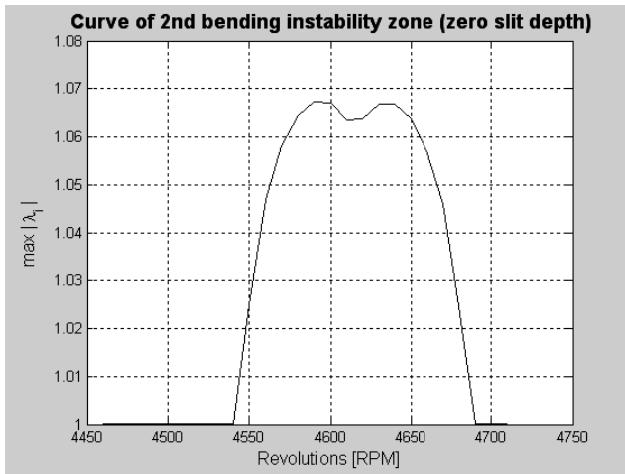


Fig. 6: Zoom of eigenvalue dependence

where p is order of resonance.

4. Structural arrangements

One of ways leading to the equalization of the rotor stiffnesses in two perpendicular planes is the use of Laffoon's slits into the generator body. The generator cross section after cutting off is depicted in fig. 7.

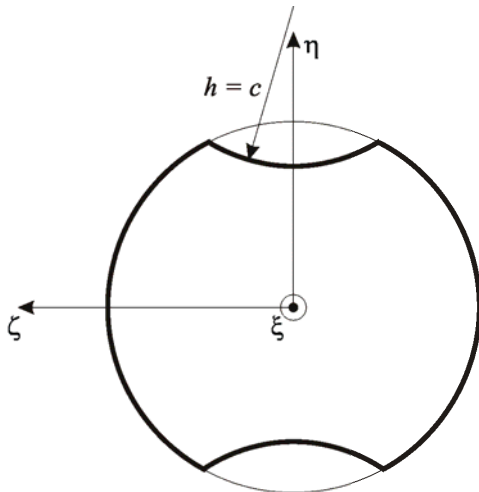


Fig. 7: Shape of the Laffoon's slits

The depth and the distance from each to other slit is the same for all slits. The slits have circle shape whose radius is equal to the saw radius.

4.1 Slit modelling

Fracture mechanics experience can be used for modelling of slits as permanently open cracks. The energy

necessary for crack rise can be added to the potential energy of deformation and than apply the Castigliano's principle to obtain the influence stiffness coefficients. The scheme of the cracked finite element is depicted in fig. 8

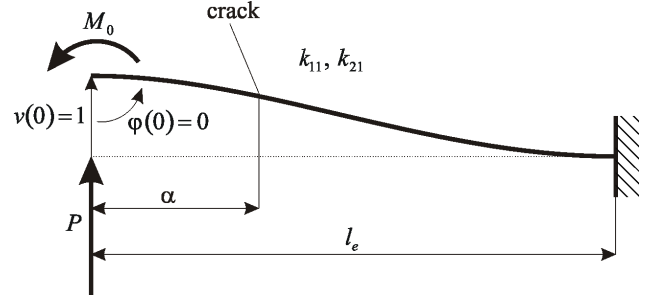


Fig. 8: The scheme of crack finite element

The i, j -th element of the crack element stiffness matrix can be expressed as a generalized force acting in position j caused by unit displacement in position i while the other generalized nodal displacements are equal to zero. Deformation potential energy of the intact element can be expressed in form

$$U_0 = \frac{1}{2E_0} \int_0^l \frac{M^2(\xi)}{I_c(\xi)} d\xi, \quad (20)$$

where E is Young's modulus, $M(\xi)$ is bending moment and $I_c(\xi)$ cross section moment of inertia. The crack energy density can be expressed in form

$$J(\eta) = \frac{1}{E} K_I^2, \quad (21)$$

where K_I is position dependent stress intensity factor. The relation (21) takes into account only the first strength mode. The other modes were neglected. For the circular crack this factor takes a form

$$K_I = \frac{2}{\pi} \sigma(\eta) \sqrt{\pi h} = \frac{2}{\pi} \sqrt{\pi h} \frac{M}{S_\zeta^2 - AI_\zeta} (S_\zeta - \eta A). \quad (22)$$

The individual symbols in (22) mark as follows: M - bending moment acting in the crack, S_ζ - cross sectional static moment (in case of symmetrical slits this static moment is equal to zero), I_ζ - cross sectional moment of inertia-both with respect to the axis ζ , A - cross sectional area. Respecting (22) the relation (21) can be rewritten into form

$$J(\eta) = \frac{1}{E} K_I^2 = \frac{4h}{E\pi} \frac{M^2}{(S_\zeta^2 - AI_\zeta)^2} (S_\zeta - \eta A)^2. \quad (23)$$



The whole crack energy can be expressed as an integral over the crack surface in form

$$U_{add} = \frac{4h}{E\pi} \frac{M^2(\alpha)}{(S_\zeta^2 - AI_\zeta)^2} \int_{\tilde{A}} (S_\zeta - \eta A)^2 d\tilde{A} \quad (24)$$

and after integration

$$U_{add} = \frac{4h}{E\pi} \frac{M^2(\alpha)}{(S_\zeta^2 - AI_\zeta)^2} (S_\zeta^2 \tilde{A} - 2S_\zeta \tilde{S}_\zeta A + \tilde{I}_\zeta A^2), \quad (25)$$

where tilda marks quantities concerning to the crack area. Now we can write the individual displacements necessary for stiffness matrix assessment e.g. in form

$$v_i = \frac{\partial U_0}{\partial P_i} + \frac{\partial U_{add}}{\partial P_i} = \frac{1}{EI_\zeta} \int_0^l M(\xi) \frac{\partial M(\xi)}{\partial P_i} d\xi + 2kM(\alpha) \frac{\partial M(\alpha)}{\partial P_i}. \quad (26)$$

Applying (26) we can come to time dependent stiffness matrix of the cracked finite element

$$\mathbf{K}_e^{CR}(t) = \mathbf{T}^T(t) \begin{bmatrix} \mathbf{K}_\zeta & \mathbf{0} & \mathbf{0} & \mathbf{0} \\ \mathbf{0} & \mathbf{PK}_\eta\mathbf{P} & \mathbf{0} & \mathbf{0} \\ \mathbf{0} & \mathbf{0} & \mathbf{0} & \mathbf{0} \\ \mathbf{0} & \mathbf{0} & \mathbf{0} & \mathbf{0} \end{bmatrix} \mathbf{T}(t) + \mathbf{K}_T, \quad (27)$$

where

$$\mathbf{T}(t) = \begin{bmatrix} \mathbf{c}(t) & \mathbf{s}(t) & \mathbf{0} & \mathbf{0} \\ -\mathbf{s}(t) & \mathbf{c}(t) & \mathbf{0} & \mathbf{0} \\ \mathbf{0} & \mathbf{0} & \mathbf{I}_2 & \mathbf{0} \\ \mathbf{0} & \mathbf{0} & \mathbf{0} & \mathbf{I}_2 \end{bmatrix} \in \mathbf{R}^{12,12}, \quad \mathbf{c}(t) = \cos \omega t \mathbf{I}_4,$$

$$\mathbf{s}(t) = \sin \omega t \mathbf{P}, \quad \mathbf{P} = \begin{bmatrix} 1 & & & \\ & -1 & & \\ & & 1 & \\ & & & -1 \end{bmatrix}$$

and $\mathbf{K}_\eta \in \mathbf{R}^{4,4}$ and $\mathbf{K}_\zeta \in \mathbf{R}^{4,4}$ are stiffness matrices of the element expressed in rotating coordinate system corresponding to the bending in planes $\xi\eta$ and $\xi\zeta$, respectively.

The matrix $\mathbf{K}_T \in \mathbf{R}^{12,12}$ is coordinate invariant part corresponding to longitudinal and torsional deformations. The matrix $\mathbf{K}_e^{CR}(t)$ corresponds to the order of generalized coordinates as follows:

$$\mathbf{q}_e(t) = \begin{bmatrix} \mathbf{q}_1(t) \\ \mathbf{q}_2(t) \\ \mathbf{q}_3(t) \\ \mathbf{q}_4(t) \end{bmatrix}, \quad \mathbf{q}_1(t) = \begin{bmatrix} v_1(t) \\ \psi_1(t) \\ v_2(t) \\ \psi_2(t) \end{bmatrix}, \quad \mathbf{q}_2(t) = \begin{bmatrix} w_1(t) \\ \vartheta_1(t) \\ w_2(t) \\ \vartheta_2(t) \end{bmatrix},$$

$$\mathbf{q}_3(t) = \begin{bmatrix} u_1(t) \\ u_2(t) \end{bmatrix}, \quad \mathbf{q}_4(t) = \begin{bmatrix} \varphi_1(t) \\ \varphi_2(t) \end{bmatrix}. \quad (28)$$

The order of element displacements should be finally rearranged. Meaning of the individual symbols follows from the fig. 9

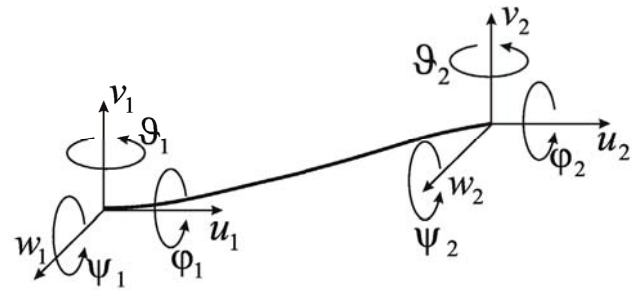


Fig. 9: Generalized displacements of the element

The other matrices (mass, damping and gyroscopic) continue to be the same as those ones for intact element.

4.2 Generator modelling

Generators modified by Lafoon's slits can be modelled by means of combination of crack and intact rotor finite elements. As an example we can show model of the above mentioned RIGA generator which is depicted in fig. 10

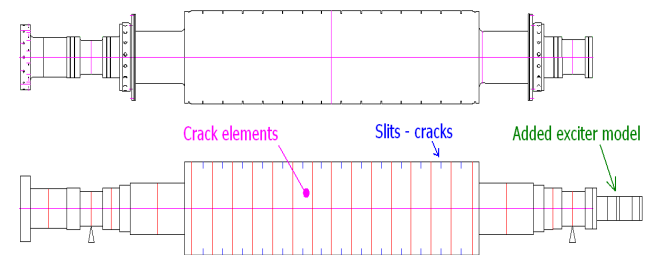


Fig. 10: Model of the RIGA generator

The mathematical model of this generator takes form (3). The change of the graph depicted in fig. 4 with respect to depth of slits is shown in fig. 11. As one can see, absolute value of the largest monodromy matrix eigenvalue is decreasing as slit depth is increasing until some critical value. This critical value is optimal value of slit depth.

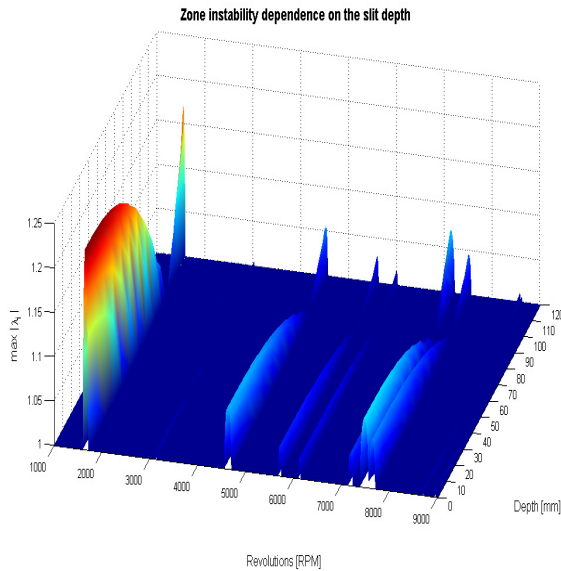


Fig. 11: Dependence of the bands and measure of instability on the depth of slits

5. Slit depth determination

The slit depth determination could be understood as an optimization process whose objective function will express measure of the difference between eigenfrequencies corresponding to the mode shapes of vibration in two perpendicular planes. The objective function can have form

$$\psi(s) = \mathbf{\Delta}^T \boldsymbol{\lambda} \mathbf{G} \boldsymbol{\Delta} \boldsymbol{\lambda}, \quad (29)$$

where $\mathbf{G} = \text{diag}\{g_1, g_2, g_3\}$, diagonal matrix of non-negative weighting coefficients,

$$\boldsymbol{\Delta} \boldsymbol{\lambda} = \begin{bmatrix} \text{Im}\{\lambda_{1\eta}\} - \text{Im}\{\lambda_{1\zeta}\} \\ \text{Im}\{\lambda_{2\eta}\} - \text{Im}\{\lambda_{2\zeta}\} \\ \text{Im}\{\lambda_{3\eta}\} - \text{Im}\{\lambda_{3\zeta}\} \end{bmatrix} \quad (30)$$

and $\lambda_{i\eta}$ and $\lambda_{i\zeta}$ are eigenvalues obtained from the eq. (3) corresponding to the time level

$$t = 0 \text{ and } t = \frac{T}{4} = \frac{\pi}{2\omega}, \quad (31)$$

respectively. The trivial inequality constraint was imposed on one optimization parameter-slit depth. To solve the optimization problem a standard MATLAB procedure was used. Especially for RIGA generator the optimal slit depth was determined 96.9 mm. Because of production demands all slits have to be equally deep. For this reason the optimization problem is from the

mathematical point of view very simple because the objective function is dependent only on one optimization parameter

This optimization approach was applied retrospectively to the five already made up generators by company BRUSH SEM. Our results were written down to the last column of the tab. 1.

Table 1. Experimentally and computationally obtained depths of slits

Rotor	Slit depth [mm]				
	Exp.	M. Balda	C. Hoschl I.	C. Hoschl II.	New
RIGA	104	134,5	114,4	112,6	96,9
BDAX98	95	129,7	109,1	112,6	92,8
DAX7	67,95	99,2	86,6	98,7	63,0
GE9A5	111,5	114,2	86,1	87,8	87,6
GE7A6	82,6	109,9	85,1	97,8	76,7

6. Conclusion

As reader can see our results lie more closely to the experimentally determined depths than the results obtained by the application of three approaches used by two Czech notable experts. In addition these results lie always on the safe side of values. The method of stability assessment was very simplified and accelerated by the modal reduction. Despite of the fact that the system matrices are time dependent the reduction successfully came through by means of modal matrix calculated in the initial time $t = 0$.

7. Acknowledgement

This work was supported by the research project MSM 4977751303 of the Ministry of Education, Youth and Sports of the Czech Republic.

References

- [1]. T. Kuruc, *Analysis of the generator rotors*, PhD. thesis, Pilsen 2008. (In Czech)
- [2]. J. Dupal, *Stability of non-symmetrical rotating continuum with non-isotropic supports*. Proceedings University of West Bohemia, Pilsen 1998.
- [3]. J. Dupal, *FEM model of cracked rotor*, Zeszyty naukowe KMS, no. 16, Gliwice, pp. 25-28.

An adaptive tuned vibration absorber using a string-mass system with quasi-zero stiffness string tension adjustment mechanism

Mustafa Ali ACAR^{1*}, Çetin YILMAZ²

^{1*} Mechanical Engineering Department, Bogazici University
34342 Bebek, Istanbul
ali.acar@boun.edu.tr

² Mechanical Engineering Department, Bogazici University

Abstract

This research introduces a new self-tunable Tuned Vibration Absorber (TVA) design employing a stiff string under tension with a mass attached at its midpoint. The major tuning parameter of the design is the string tension. This approach allows varying the natural frequency of the TVA over a wide range with relatively small displacement inputs to the string tip. Dynamic behavior of this system is analyzed both analytically and numerically. A leaf-spring having negative-stiffness behavior is designed using finite element method to be used together with the string to achieve a quasi-zero stiffness (QZS) structure. The force required to vary the string tension is significantly reduced with this combination.

Keywords: Tuned Vibration Absorber, Quasi-zero Stiffness Mechanism, Mass-String, Negative Stiffness Spring

1. Introduction

1.1. Tuned vibration absorbers

A tuned vibration absorber (TVA) can generally be viewed as a system attached to a structure with the intention of suppression of its vibration. There are various TVA designs reported in the literature. Each design either directly use a mass-spring system or continuous systems that can be reduced to an equivalent mass-spring system. TVAs have been widely used to suppress structural vibrations. The simplest TVA that can be realized is an absorber having one resonant frequency. A schematic of such a system is shown in Fig. (1) and its equation of motion is given in Eqns. (1) and (2). [1]

In this case, if the natural frequency of the TVA coincides with the frequency of excitation, $F(t)$, the response of the primary structure, x_s , can be suppressed. [1] This vibration attenuation is achieved by the counteraction to the excitation force with the force applied by the TVA.

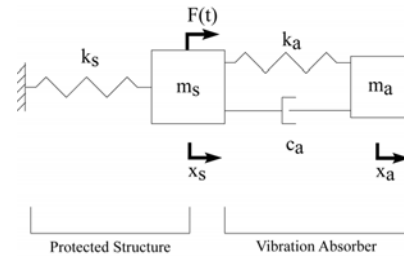


Fig. 5. Schematic of a basic one degree of freedom TVA is applied to a protected structure

$$m_s \ddot{x}_s + c_a (\dot{x}_a + \dot{x}_s) + (k_a + k_s)x_s - k_a x_a = F(t) \quad (1)$$

$$m_a \ddot{x}_a + c_a (\dot{x}_a + \dot{x}_s) + k_a (x_a - x_s) = 0 \quad (2)$$

Although, the idea of a TVA is simply attachment of an additional vibratory system to a structure, the designs and the intentions of the applications vary. [2] [3] [4] Depending on the requirements of the application, TVAs can be constructed as passive, adaptive (or adaptive-passive) and active devices. While a passive absorber is generally effective at a single frequency of vibration, adaptive-passive and active TVAs can be constructed so that a range of frequencies can be attenuated. The operation principle behind the active vibration absorbers is that by using a force actuator, they emulate the action of a passive TVA as if it is tuned to every frequency of its range. Thus, they are quite effective in many cases. However, using an actuator as a counteracting mechanism to vibration is an energy consuming method and is not always feasible. The adaptive-passive vibration absorbers can be thought of a hybrid version of both passive and active vibration absorbers. They generally consist of a passive TVA and a parameter tuning system employing feedback control.

Rather than counteracting to the vibration of the protected structure, this type of TVAs only consume energy to vary the parameters, usually the stiffness, that govern their dynamic behavior. [5]

1.2. Quasi-zero stiffness structures

The quasi-zero stiffness concept is widely used in vibration isolation systems. The idea behind the vibration isolation theory can be defined as effectively “separating” the source of vibration and the system subjected to vibration. This isolation can be achieved by connecting the two interacting systems with a very low stiffness element, or by increasing the mass of the system subjected to vibration. However, both of the methods are limited in practice. Employing a low stiffness connection between two systems or increasing the mass of the system causes large static deflections in the assembly, which may not be a feasible situation.

Structures exhibiting quasi-zero stiffness (QZS) behavior can support a certain static load, while allowing displacements within a certain range without much difference in the reaction force. In other words, systems equipped with these structures have almost zero stiffness. Using such a system in vibration isolation applications, therefore, is a common method. [6]

There are many different QZS mechanism designs reported in the literature. Generally QZS mechanisms are created by combining linear positive stiffness springs with non-linear, negative-stiffness spring elements. Force-displacement behavior of negative-stiffness springs have negative slope. In other words, unlike regular positive stiffness springs, the more a negative-stiffness spring is deformed the less reaction force is observed. [6] [7]

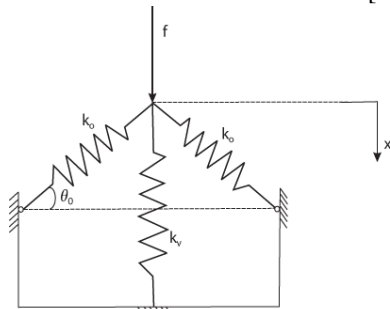


Fig. 6. Schematic of a simple mechanism that can exhibit QZS behavior [8]

In Fig. (2), the vertical spring is a positive stiffness element and it is combined with the inclined springs to create a QZS structure. A simplified characteristic force-displacement plot having QZS is shown in Fig. (3).

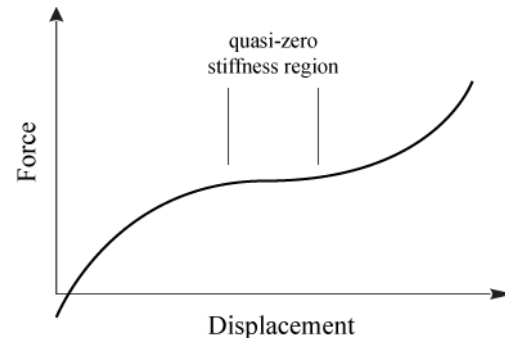


Fig. 7. A characteristic force-displacement curve for QZS systems [8]

2. Vibration of a string with concentrated mass attachment

As stated before, TVA's can consist of continuous vibratory systems. Although, these systems will have more than one resonant frequency, generally their first mode will be the most dominant one. Therefore, we can generalize the operation principle of TVA's to continuous systems. [1]

The present research is based on the usage of a stiff string under tension with a concentrated mass as a TVA. A schematic of this system is shown in Fig. (4).

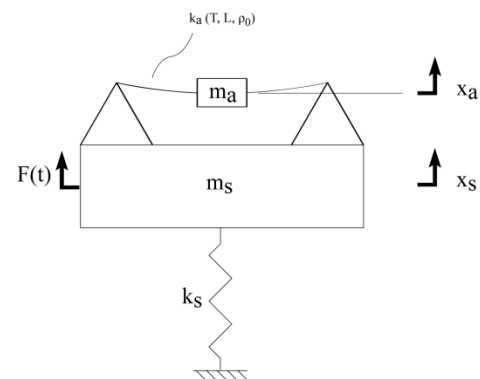


Fig. 8. Schematic design of the TVA system studied

The dynamical behavior of this TVA configuration is governed by the mass attached to the string, m_a , mass per length of the string, ρ_0 , length of the string, L and lastly the string tension, T . Thus, by varying T , a variable stiffness TVA can be achieved. The outcome of this method is that the required displacement input to the string tip is quite small compared to the achieved variation on the natural frequencies.



2.1. Analytic solution of vibration of a string with concentrated mass attachment

Solution of dynamical behavior of strings is considered among simple problems of vibration analysis. Addition of a concentrated mass to the system, however, requires some modifications in the solution procedure of vibration of homogenous strings.

The differential equation of the vibration of strings is given by

$$\frac{\partial}{\partial x} \left(T \frac{\partial u}{\partial x} \right) = \rho(x) \frac{\partial^2 u}{\partial t^2} \quad (3)$$

where x is the coordinate axis along the string, T is the string tension, $\rho(x)$ is the mass per length of the string and $u(x, t)$ is the transverse deflection of the string.

In [9], the concentrated mass on the string is treated as a sudden jump in the mass density of the string. Delta Dirac function is used to express this mathematically.

$$\rho(x) = \rho_0 + m\delta(x - x_1) \quad (4)$$

where ρ_0 is the constant mass per length of the string, m is the attached mass and x_1 is the position of the attached mass.

Solving the equation of motion yields that; eigenfunctions of the system are given by

$$\Phi(x) = \begin{cases} A \sin\left(\frac{\omega}{c}x\right) & 0 \leq x \leq L/2 \\ B \sin\left(k\left(\frac{\omega}{c} - L\right)\right) & L/2 \leq x \leq L \end{cases} \quad (5)$$

where $c = \sqrt{T/\rho_0}$, and the corresponding eigenvalues are given by

$$\left(\sin\left(\frac{\omega L}{2c}\right) \right) \left(p \sin\left(\frac{\omega L}{2c}\right) - 2 \cos\left(\frac{\omega L}{2c}\right) \right) = 0 \quad (6)$$

where $p = m\omega c/T$.

Equation (6) is satisfied when either part of the equation is zero. This yields that two sets of eigenvalues are obtained. By using a graphical method, zero crossings of the parts of the equation can be found.

If these eigenvalues are interpreted physically, it can be said that one set of eigenvalues are not affected by the existence of the concentrated mass. The reason is that the corresponding eigenfunctions have a zero value, i.e. a node, at the midpoint of the string. The other set of eigenvalues are determined by the mass.

Although the accuracy of these results is verified in [9] experimentally, the prediction of dynamical behavior of the system is done using finite element method with a more realistic model. Results of this analytical solution are only used to check the validity of the FEM model.

2.2. Natural frequency determination of vibration of a string with concentrated mass attachment using ABAQUS

The Abaqus finite element package offers a natural frequency extraction module to determine the dynamical behavior of flexible structures. The module is a linear perturbation analysis and therefore should be preceded by a static analysis, in which the string tension is applied. How many modes of vibration is requested and which algorithm should be used are set beforehand the analysis. [10]

The modeling of the string is done using linear 1D beam elements with circular profile. The concentrated mass attachment is modeled by using point mass definition in the "inertia" module of the Abaqus package on certain nodes at the middle of the string.

The initial model is constructed to verify the model by comparing the results with that of analytical solution. The concentrated mass is created only at a single node, in order to ensure that the "point mass" behavior in the analytical model is reflected to the finite element model. A system having the following parameters are analyzed using both analytical and numerical methods. Subspace Iteration eigensolver with five requested modes is used. A system with parameters shown in Table (1) is analyzed using both methods.

Table 1. Vibrating string with concentrated mass attachment configuration parameters

Parameter	Value	Unit
E	200	GPa
ν	0.28	
L	300	mm
ρ_0	$4.962 * 10^{-6}$	kg/mm
m	200	g
T	10-200	N

A second model is built with the intention of more realistic mass attachment modeling. In a real application, an attached mass will not have a single point behavior. To reflect this fact into the model, the point mass definitions in the model are distributed along several nodes which are kinematically tied together. The system

with same parameters in Table (1) is analyzed using this new model.

First natural frequencies of the system with respect to string tension obtained using the above mentioned models are plotted in Fig.(5). As shown in the figure, the methods give quite similar results. The slight difference in the frequencies between different methods stems from the way the concentrated mass is treated in analytical and numerical methods. Although, the mass is defined at a single node in the initial finite element model, it does not exactly reflect the behavior of the point mass defined in the analytical solution. Similarly, the mass definition used in the second finite element further diverges from the point mass behavior, thus, the frequencies obtained using this model gave the highest frequencies. However, it can be expected that the mass definitions used in the numerical methods are more realistic.

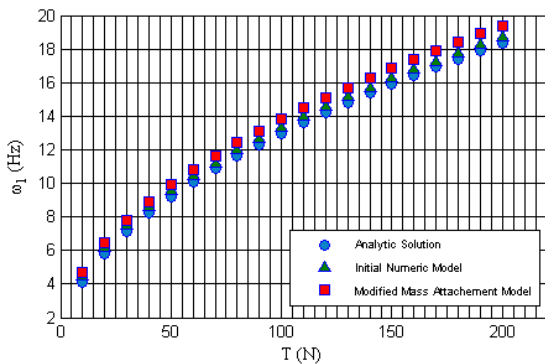


Fig. 9. First natural frequency of the system vs. string tension obtained by different methods

3. String tension adjustment using quasi-zero stiffness mechanism

As mentioned above, the adaptive-passive TVA studied in this research utilizes a stiff string under tension with a concentrated mass. The string tension is the major parameter that allows the device to tune itself to varying excitation conditions. Therefore, a mechanism that allows automatically varying the string tension is required. If a linear actuator was directly connected to the string with the intention of changing its tension, the actuator would have to apply at least the same tension every time a variation of the tension is required.

To overcome this problem, the idea of quasi-zero stiffness mechanisms, which are generally used in vibration isolation applications, is adapted to the string tension adjustment mechanism of the system. In the elastic region a string will have a linear tension-strain relationship. Therefore, in the design of the QZS mechanism, the string

is treated as a linear spring that will be deformed within its elastic region. Then a leaf spring that exhibits negative-stiffness behavior can be employed to “compensate” the stiffness of the string. [6]

3.1. Design of the negative stiffness leaf spring

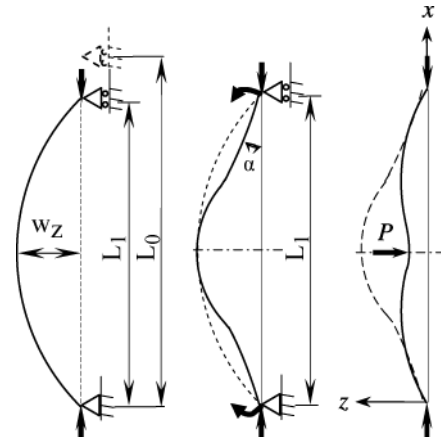


Fig. 10. Obtaining a negative-stiffness leaf spring [11]

The procedure of converting a beam into a spring having negative-stiffness behavior is schematically shown in Fig. (6). The method consists of a number of different steps. First the leaf spring is allowed to buckle in a controlled manner by pre-compression in the longitudinal direction. This operation causes the leaf spring bend in an arc shape. Following this step, the both ends of the leaf spring is held fixed at an angle with the longitudinal axis. From this point, any transverse deflection at the spring’s mid-point will cause a reaction force. However, the reaction force is not linearly dependent to the deflection. For a certain region, unit deflection on the midpoint of the leaf spring will increase the reaction force, thus, it has a positive stiffness region. After passing the maximum reaction force point in the positive stiffness region, any further deflection will require less and less force until the reaction force is reduced to zero. After crossing this zero-force point the reaction force will start to increase in the opposite direction, i.e. the spring will still negative-stiffness but this time force is applied to prevent the spring from further deflection. After a certain point the negative-stiffness behavior ends and the force required to hold the spring will decrease to zero again.

If the behavior of the leaf spring is physically interpreted, it can be said that the spring has three equilibrium states. One is the initial pre-compressed state; the second one is where the internal forces in the spring are horizontally balanced. The last equilibrium of the spring is the state at which the spring has entirely passed to the opposite side of the longitudinal axis.

Static force-displacement behavior of the leaf spring was studied in Abaqus finite element package. 1D, quadratic beam elements with rectangular profile is used to model the structure. Loading scenario of the model is divided into several steps.

At the first step of the analysis, the midpoint of the spring is slightly deflected in the transverse direction with the intention of eliminating any possible problems related with buckling. Afterwards, the leaf spring is compressed along the longitudinal direction and the endpoints are rotated to a certain angle. In the last step of the analysis, the force-displacement behavior of the transverse deflection of the spring midpoint is analyzed by gradually increasing the deflection.

The parameters that influence the force-displacement behavior of the leaf spring are elastic material properties (E , ν), thickness (t), width (w), and the length (L_0) of the beam used and the preloading parameters, namely the initial precompression (L_0-L_1) and the angle (α) at which the spring endpoints are held fixed.

Several configurations are analyzed to predict the effects of these parameters on the spring behavior. The configurations examined and the corresponding force-displacement plots are shown in Table (2) and (3); and Fig. (7), respectively.

Table 2. Fixed parameters in the negative-stiffness leaf spring analysis

Parameter	Value	Unit
E	200	GPa
ν	0.28	
L_0	150	mm
t	1	mm

Table 3. Leaf spring configurations examined in negative-stiffness spring design

Configuration #	L_0-L_1 (mm)	w (mm)	A (deg)
1	4	20	20
2	6	20	20
3	8	20	20
4	4	40	20
5	4	20	15

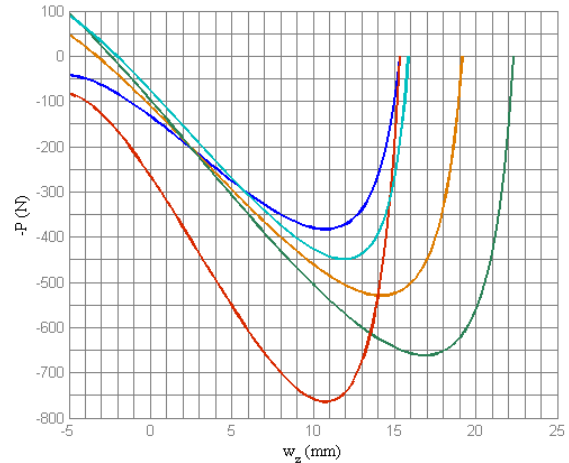


Fig. 11. Force-deflection behavior of the leaf spring configurations at Table (3)

The analysis results clearly show the effects of different parameters on the range and the slope of the negative-stiffness zone of the leaf spring.

3.2. Combination of the string and the negative stiffness element to obtain QZS

Figure (8), shows a schematic combination of the string, the resilient element of the TVA, and the negative stiffness spring designed. The procedure carried out to connect the two elements consists of two operations. First, the leaf spring should be deflected so that the positive stiffness region of the spring is passed. Further deflection of the spring will cause the reaction force to decrease until a second zero-force point is reached. At any point between the end of the positive stiffness region and the second zero-force point, the string is connected to the leaf spring.

After the connection is completed, any deflection in the positive z direction will increase the string tension. However, while the string becomes tenser, the restoring force applied to the string by the leaf spring is also increases. Similarly, by deflecting the system in the negative z direction will decrease both the string tension and the restoring force of the leaf spring. This cooperation of the two elements allows significantly reducing the resultant external force, required to vary the tension. If the parameters of the leaf spring are arranged so that, within the working range of the system the force-deflection slopes of the two elements match in magnitude, the variation in the tension can be carried out with almost zero external force.

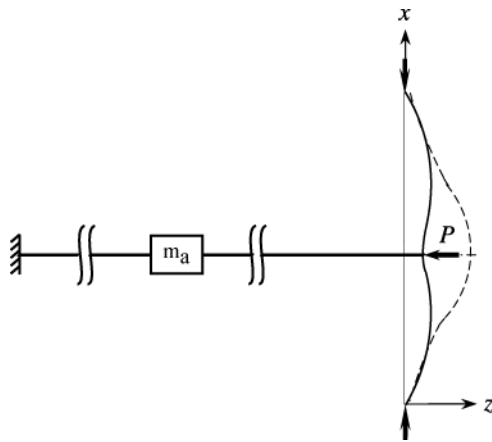


Fig. 12. Schematic combination of the string and the leaf spring (string illustration is truncated to save space)

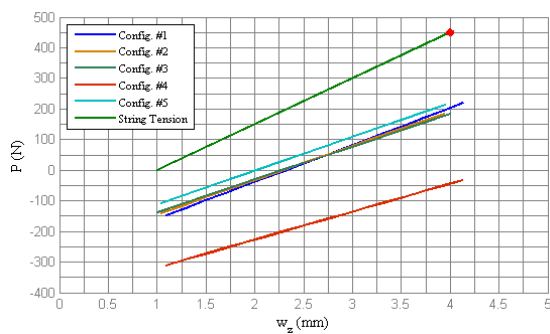


Fig. 13. Effect of the leaf spring on the combined force-deflection behavior

Figure (9) shows force-deflection curves of the string alone and the combined the leaf spring-string configurations. The leaf springs examined in 3.1 can reduce the force required. However, the result can easily be improved with a better match in the force-deflection curve slopes of the leaf spring and string.

4. Conclusion

First objective of the work presented in this paper is to introduce a new adaptive tuned vibration absorber system. A vibratory system that could be reduced to an equivalent mass-spring system with the ability of changing its stiffness was designed. A stiff-string under tension with a concentrated mass attached at its midpoint is selected as the TVA. The string tension is chosen to be the tuning parameter of the system. Analytical solution obtained by Gomez et. al. [9] are compatible with the finite element dynamic analysis results. The solutions revealed that small displacement inputs given to the string tip results in significant natural frequency variations. Another design objective of the research is to develop a

system that reduces the force required to vary the string tension. A non-linear negative-stiffness leaf spring is designed to be coupled with the string. The finite element model of the combined leaf spring – string system showed that with properly selected leaf spring parameters, the force required to change the string tension could almost reduced to zero. To conclude, the variable stiffness TVA have two major outcomes; wide frequency range variation with relatively small control inputs and dramatically reduced control effort. Thus, a future controller implementation to this mechanical framework will have promising performance results.

References

- [1]. B.G. Korenev, L.M. Reznikov, *Dynamic Vibration Absorbers Theory and Technical Applications*. Wiley; West Sussex, 1993.
- [2]. C. Yong, D.G. Zimcik, V.K. Wickramasinghe, F. Nitzsche, *Development of the smart spring for active vibration control of helicopter blades*, *Journal of Intelligent Material Systems and Structures* 15, pages 37-47, 2004.
- [3]. R.G. Jacquot, *Suppression of random vibrations in plates using vibration absorbers*, *Journal of Sound and Vibration* 248(4), pages 585-596, 2001.
- [4]. R.I. Wright and M.R.F. Kidner, *Vibration Absorbers: A review of applications in interior noise control of propeller aircraft*, *Journal of Sound and Vibration* 10, pages 1221-1237, 2004.
- [5]. J. Sun, M.R. Jolly, M.A. Norris, *Passive, adaptive and active tuned vibration absorbers - a survey*, *Transactions of the American Society of Mechanical Engineers* 117, pages 234-242, 1995.
- [6]. P. Alabuzhev, A. Gritchin, L. Kim, G. Migirenko, V. Chon, P. Stepanov, *Vibration Protecting and Measuring Systems with Quasi-zero Stiffness*. Hemisphere Publishing Corporation; USA, 1989.
- [7]. W. Robertson, R. Wood, B. Cazzolato, A. Zander, *Zero-stiffness magnetic springs for active vibration isolation*, *Active 2006 Adelaide Australia*, 2006.
- [8]. A. Carrella, M.J. Brennan, T.P. Waters, *Static analysis of a passive vibration isolator with quasi-zero-stiffness characteristic*, *Journal of Sound and Vibration* 301, pages 678-689, 2007.
- [9]. B.J. Gomez, C.E. Repetto, C.R. Stia, R. Welti, *Oscillations of a string with concentrated masses*, *European Journal of Physics* 28, pages 961-975, 2007.
- [10]. *Abaqus Analysis User's Manual* (v6.9.3).
- [11]. C.M. Lee, V.N. Goverdovskiy, A.I. Temnikov, *Design of springs with "negative" stiffness to improve vehicle driver vibration isolation*, *Journal of Sound and Vibration* 302, pages 865-874, 2007.



Vibration Characteristics of a Vertical Roller Mill

Engin H. ÇOPUR^{1*}, Metin U. SALAMCI² Tuncay KARAÇAY² Emine TOKA³

^{1*}Gazi University, Mechanical Engineering Department
Celal Bayar Bulvarı, 06570 Maltepe/Ankara- TURKEY
engincopur@gazi.edu.tr

² Gazi University, Mechanical Engineering Department

³ ERSEL Heavy Machinery Industry Inc.

Abstract

The main aim of this study is to determine vibration characteristics of a vertical roller mill for a range of variables. A vertical roller mill which is manufactured by Ersel Heavy Machinery Inc. is analyzed to investigate stable and unstable vibration characteristics. First, a mathematical model of the vertical roller mill is derived and by using the mathematical model the parameters are determined. Then for a range of variables (which are angular velocity of the table, compressive force, raw material feed rate) the vibration characteristics of the mill is obtained through simulations. It is observed that, some of these variables can be used as a control input to decrease the amplitude of vibrations of the roller.

Keywords: Vertical Roller Mills, Modeling, Unstable Vibration, Stable Vibration.

1. Introduction

In mining industry, grinding is widely used as a production technique in order to reduce particle sizes of raw materials to desired values [1]. Huge amount of coal, cement raw materials, clinker, metallic or non-metallic materials are grinded every year by using mills for industrial processes, such as combustion, cement production etc. [2]. Mills have different structures, capacity and performance values, advantages and disadvantages over each other and are divided into four main types; (i) air jet mills, (ii) ball mills, (iii) roller mills and (iv) impact mills [3, 4]. The selection of a mill is dominated by operating conditions, operating principles, physical properties of the material and grinding capacity.

In terms of energy efficiency, operating cost, fine grinding features, high capacity and compactness, Vertical Roller Mills (VRM) are widely preferred mill types which are manufactured in different countries with different design approaches [4]. Nevertheless, the working principle is more or less the same; maximize the grinding

by using both compression and shear forces. Therefore a VRM contains a grinding table on which the raw material (to be grinded) are hold and bulky rollers on the grinding table to create compression forces. Raw materials are crushed by the rollers by using compression forces and meanwhile the grinding table turns with a constant angular speed which creates shear forces. The raw materials fall down the centre of the grinding table from the feeder and move to the edge of the grinding table from the centre. The materials are crushed by the rollers until taken away by using airstreams. Then the bigger size materials fall down the grinding table and the process of crushing continues.

Although there are many advantages of VRMs as listed above, vibration problem is one of the undesirable properties of them. The problem occurs especially during the initial start up the mill. During this phase vibrations may cause unavoidable frequent stops which decrease the efficiency of the grinding process.

In this study, a VRM which is manufactured by Ersel Heavy Machinery Inc. is analyzed to investigate stable and unstable vibration characteristics. A mathematical model is obtained and simulated for various operational parameters. These operational parameters are selected as angular velocity of the grinding table, compressive load applied by hydraulic cylinder to the rollers and the material feed rate of the mills. With simulations, the operational parameters which have the most influence on these vibrations are investigated. The results are in good correlation with the literature [7, 13-14] and show that the unstable vibrations occur when the system resonates at the characteristic mill frequency due to stick-slip effect between the rollers and table.

2. Mathematical Model

A vertical roller mill can be modeled as roller-table as shown in Fig. 1 [7]. In this model, table and roller are modeled as masses and inertia. The grinding material shows viscoelastic characteristic, so it is modeled as two Kelvin-Voight models, a spring and damper system connected in parallel [16], one is for the vertical direction and the other is for the horizontal. There is also a friction force between the table-roller pair due to rolling over the grinding material. This has the nature of self-excitation due to stick-slip phenomena and affects only along the horizontal direction as shown in Fig. 1.

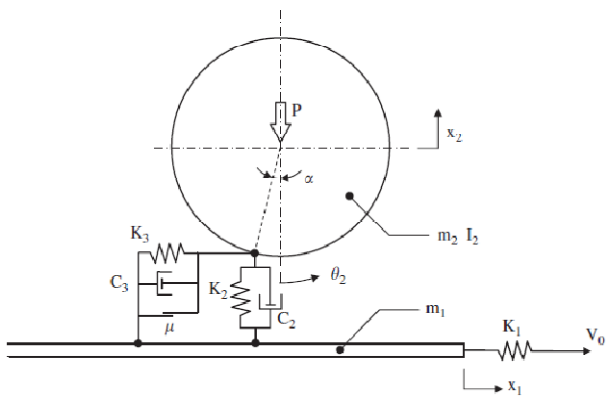


Fig 1. Model of Roller Mill [7]

Fujita and Saito [7] showed that the vibrations of the vertical roller mills depend on to the stiffness of the driving system of the table. The spring coefficient K_1 represents the equivalent spring coefficient of the driving system which contains motor, coupling, gearbox and individual shafts of the system.

The equations of motion is derived applying Newton's Second Law of Motion and given in Eq.1 to 3. for the horizontal motion of the table, x_1 , vertical motion of the roller, x_2 , and rotation of the roller θ respectively. In the equations, α is the internal friction angle of the grinding materials, H is the height of the grinding material over the table, P is the force applied to the roller and V_0 is the driving velocity of the table. Unlike the modeling approach of Fujita and Saito [7], the elasticity of the material is modeled as discontinues (such as mode) functions in order to represent the discontinuity of the raw material, i.e., they are not like a linear spring, they show elastic behavior for some certain time, then another elastic behavior starts. This approach is much more realistic then the model of [7]. In the equations, the height of the grinding material over the table, H , the force applied to the roller P , and the driving velocity of the table, V_0 are inputs which may be changed by the operating unit.

$$m_1 \ddot{x}_1 = \{K_2(H + r\theta_2 \sin \alpha - x_2) + C_2(r\dot{\theta}_2 \sin \alpha - \dot{x}_2) + (P + m_2 g)\} \tan \alpha - \mu \{K_2(H + r\theta_2 \sin \alpha - x_2) + C_2(r\dot{\theta}_2 \sin \alpha - \dot{x}_2) + (P + m_2 g)\} + K_1(V_0 t - x_1) - K_3(x_1 - r\theta_2) - C_3(\dot{x}_1 - r\dot{\theta}_2) \quad 1$$

$$m_2 \ddot{x}_2 = K_2(H + r\theta_2 \sin \alpha - x_2) + C_2(r\dot{\theta}_2 \sin \alpha - \dot{x}_2) - (P + m_2 g) \quad 2$$

$$\frac{I_2}{r} \ddot{\theta}_2 = \mu \{K_2(H + r\theta_2 \sin \alpha - x_2) + C_2(r\dot{\theta}_2 \sin \alpha - \dot{x}_2) + (P + m_2 g)\} \cos \alpha - \{K_2(H + r\theta_2 \sin \alpha - x_2) + C_2(r\dot{\theta}_2 \sin \alpha - \dot{x}_2) + (P + m_2 g)\} \sin \alpha + \{K_3(x_1 - r\theta_2) + C_3(\dot{x}_1 - r\dot{\theta}_2)\} \cos \alpha \quad 3$$

3. Simulation Results

In this study, an existing VRM parameters are used in order to analyze vibration characteristics. For this purpose, the EC-160 type vertical roller mills manufactured by Ersel Heavy Industry Inc., is utilized. The physical and geometrical properties of the components are calculated with the help of CAD programs. These are given in Table 1. The equivalent stiffness of the driving system of the EC-160 mill is also calculated and given in Table 1 as K_1 . The equations of motion given in Eq. 1 to 3 are simultaneously solved using a fixed-step fourth order Runge-Kutta algorithm. In order to compare the results of the simulations, similar grinding material characteristics studied in the Ref. [7] is used as given in Table 2.

Table 1. Parameters of the vertical roller mill

m_1	10000 kg
m_2	3258.23 kg
I_2	520.682 kg
r	0.596 m
K_1	4.9612×10^5 N/m

Similar to the results of Ref. [7], the characteristic mill frequency of the VRM is computed as 11.6 Hz. This frequency is measured and monitored in the existing EC-160 VRM plant and used as an alerting frequency to stop the plant in case of high level amplitudes.

Table 2. Constants of the grinding material (from Ref. [7])

K_2	1.7330×10^7 N/m
K_3	1.4141×10^6 N/m
C_2	125 N.s/m
C_3	4×10^4 N.s/m
α	0.1016 rad

Figure 1.a. represents the time response of the table. The position of the table is continuously increasing, with some fluctuations. The frequency of the fluctuation is around 1 Hz as seen from the spectrum given in Fig 1.b.

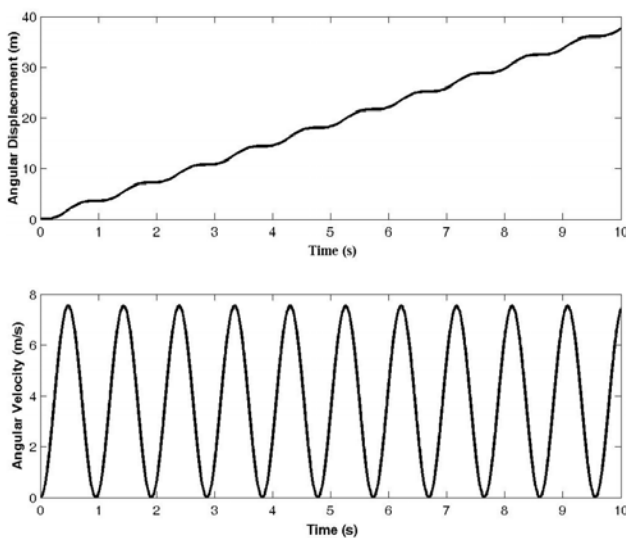


Fig. 1. Time response of angular displacement and velocity of the roller

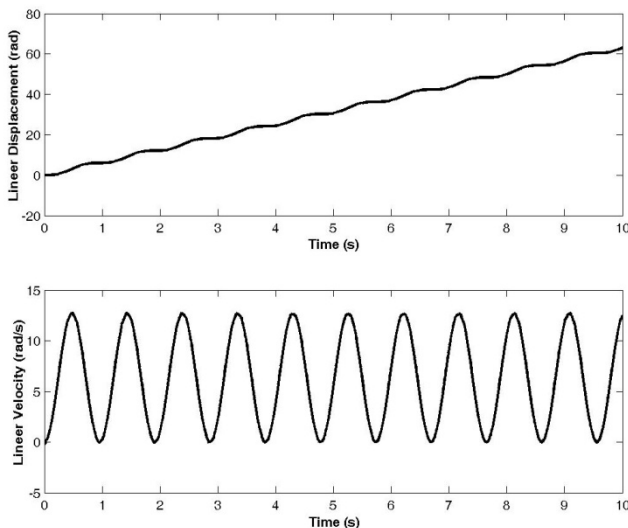


Fig. 2. Time response of linear displacement and velocity of the table

The rolling motion of the roller given in Fig. 2 is very similar to the table motion. This behavior is an expected one as the roller rolls over the table, i.e. they are mating bodies. On the other hand, there is grinding material between the roller and the table and it has the nature of dry slip. Fig. 3 shows the change of friction force between the roller-table pair. It is a typical fluctuating behavior for a stick-slip phenomena and the frequency of the fluctuation is same as the vibrations of the table and the rolling motion of the roller.

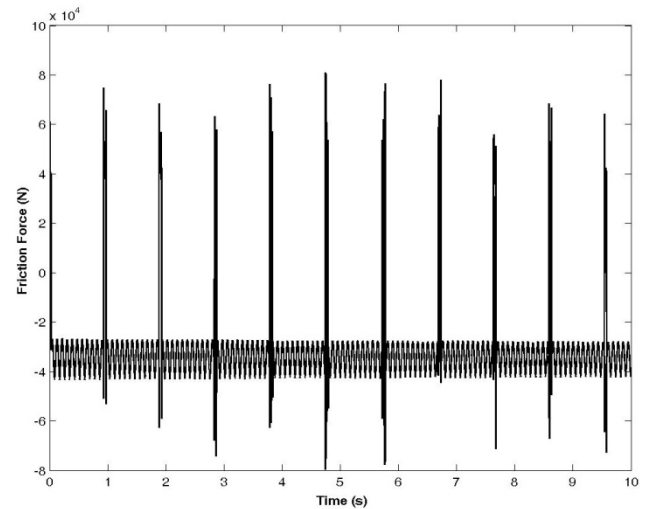


Fig. 3. Friction force versus time

Figure 4.a shows the motion of the roller along vertical direction. The roller is starting from the initial height of the grinding materials over the table and vibrating around the compressed equilibrium level. Fig. 4.b shows the spectrum of the time response. It shows periodic vibrations at 11.6 Hz which is known as the characteristic mill frequency of a vertical roller mill [7].

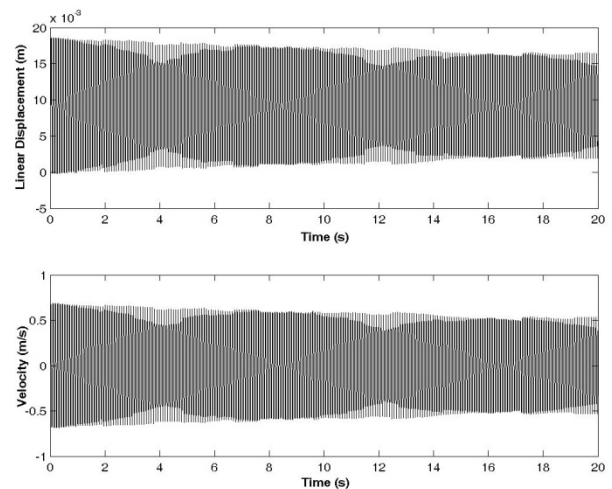


Fig. 4. Time response of vertical displacement and velocity of the roller

Simulations are repeated for various operational values of material height H , compressive force on the roller P and driving velocity of the table V_0 . In order to obtain vibrations behavior due to parameter change, spectrum of each individual simulation is calculated. Then these spectrums are put one after another and are given as waterfall diagram. Fig. 5-8 represent waterfall diagram when table rotate at 45 rpm. This angular velocity is the design and operating value which still in use in the existing EC-160 model mill.

Fig. 5 shows the vibrations of the table when the compressive force over the roller is changing. When the force is relatively light, spectra show unstable vibrations. However, the effect of compressive force is not significantly above 100 kN. The rolling motion vibrations of the roller have also similar behavior with the table as shown in Fig. 6.

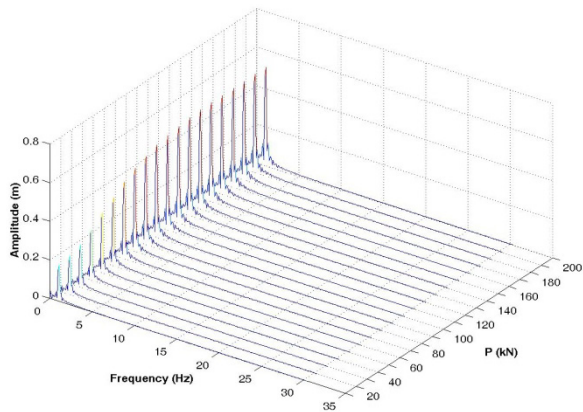


Fig. 5. Waterfall diagrams of vibrations of the table w.r.t. variation of P ($H=20\text{mm}$)

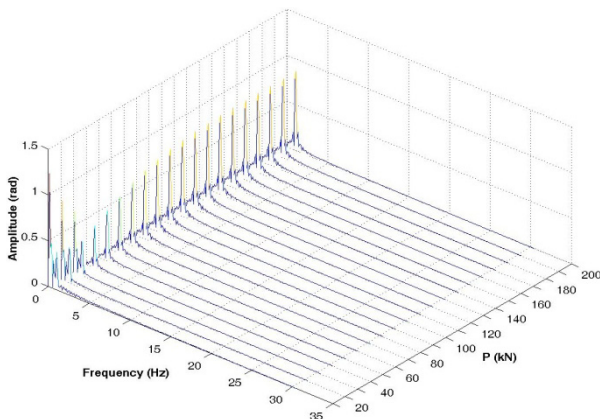


Fig. 6. Waterfall diagrams of torsional vibrations of the roller w.r.t. variation of P ($H=20\text{mm}$)

Fig. 7 shows the waterfall diagram of the vertical vibrations of the roller. The spectra show frequency bifurcations below the certain compressive force. Simulations are run for 10 kN increment from 10 kN to 200 kN. So, the resolution of the figure may not be

sufficient to give the end of bifurcation behavior. But from the Fig. 7 it is possible to say that if the compressive force on the roller is not sufficient (here, below 120 kN), the vertical vibrations of the roller is unstable.

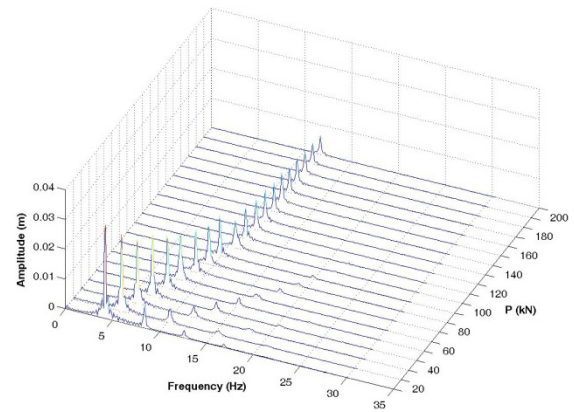


Fig. 7. Waterfall diagrams of vibrations of the roller in vertical direction w.r.t. variation of P ($H=20\text{mm}$)

Material height over the table H can be interpreted as the material feed rate of the mills. In order to obtain the effect of feed rate a set of simulations run for $H = 20$ to 36 mm which are the typical values for a EC-160 model Ersel Heavy Industry vertical roller mill. Only the vertical vibrations of the roller are analyzed because it is obvious that unstable vibrations occur along the vertical vibrations of roller. Fig. 8 shows the waterfall diagram of the vibrations of the roller. Spectra shows when the material height is increased vibrations tend to show frequency bifurcations. In other words, vibrations of the vertical mills under constant compressive force are unstable when the material feed rate is high.

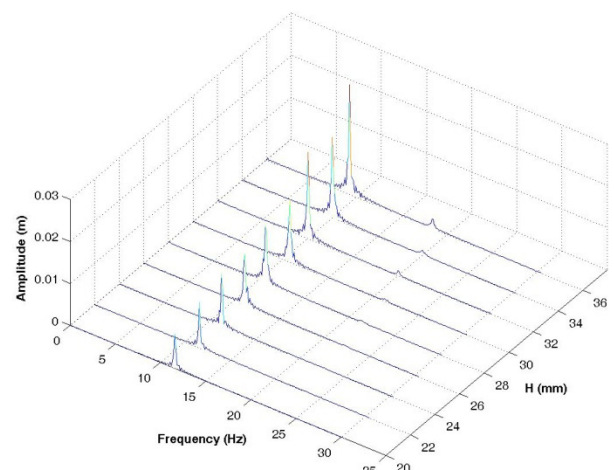


Fig. 8. Waterfall diagrams of vibrations of the roller in vertical direction w.r.t. variation of H ($P=160\text{kN}$)

Up to here, the influences of P or H variations on the vibrations are investigated at a constant table speed (45

rpm) and the following simulations are to investigate how the table speed affects the vibrations.

Fig. 9 shows the waterfall diagram of the vertical vibrations of the roller. The diagram is plotted for 10 rpm table speed and 36 mm material height. At lower compressive forces, bifurcations can be easily seen at Fig. 9.

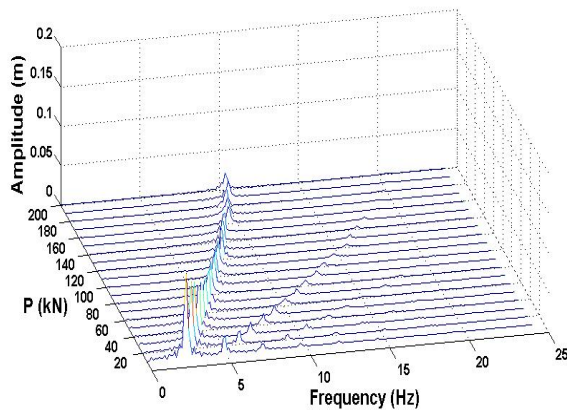


Fig. 9. Waterfall diagrams of vibrations of the roller in vertical direction w.r.t. variation of P (H=36mm)

Fig. 10 shows the influence of change of material height on vibrations of roller in vertical direction when compressive force is constant and has a value 160 kN. From Fig. 10, it may be possible to say that the unstable vibrations occur when material height exceeds 28 mm.

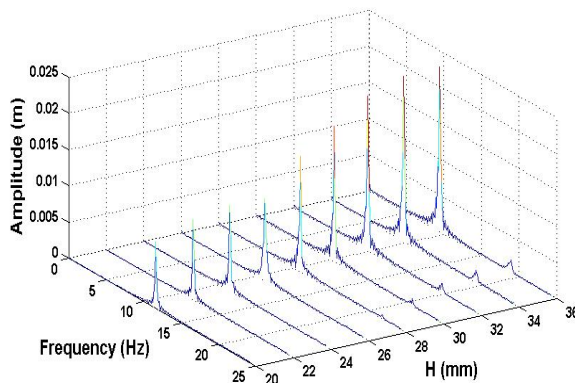


Fig. 10. Waterfall diagrams of vibrations of the roller in vertical direction w.r.t. variation of P (P=160kN)

Now, it can be researched how to decrease the amplitudes of vibrations and which operational parameters can be selected as control parameters. To answer these questions, Fig. 11-13 may be helpful. Fig. 11-13 represent the peak-to-peak amplitudes of vibrations of the roller in vertical direction.

Fig. 11 shows peak-to-peak amplitudes w.r.t. variations of P and H and simulation are run at a constant table speed 50 rpm. From Fig. 11, it may be deduced that amplitude of vibration can be reduced when material feed rate H is decreased and compressive force P is increased.

In Fig. 12, the investigation is steered how to affect both variations of material height and table speed the peak-to-peak amplitude. The compressive force P does not change during simulation and has a value of 160 kN. From Fig. 12, it can be seen that there is no influence of variation of table speed on amplitude of vibration and low material height is helpful for reducing the amplitudes.

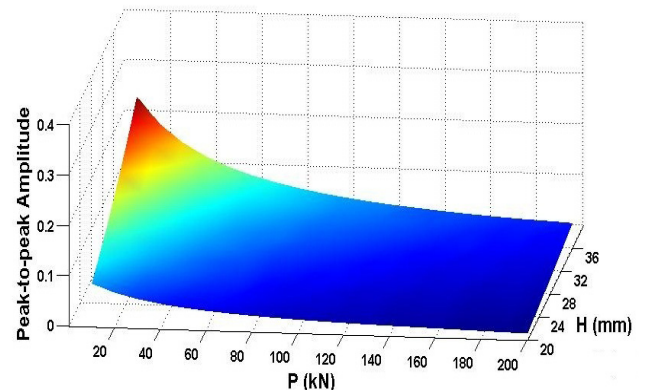


Fig. 11. The surface graph of peak-to-peak amplitudes of vibrations of the roller in vertical direction w.r.t. variations of P and H ($V_0=50$ rpm)

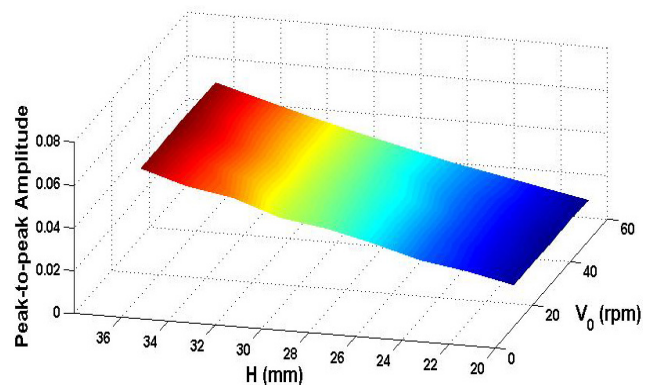


Fig. 12. The surface graph of peak-to-peak amplitudes of vibrations of the roller in vertical direction w.r.t. variations of V_0 and H (P=160 kN)

The result from Fig 12 is similar to the result from Fig. 13. In Fig. 13, compressive force is used as an operational parameter instead of material height in Fig. 12. Fig. 13 shows that if compressive force is increased, the amplitudes are decreased and table speed has no influence on amplitude of vibration.

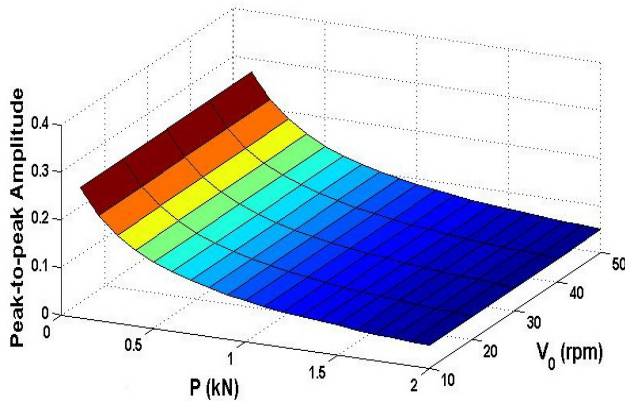


Fig. 13. The surface graph of peak-to-peak amplitudes of vibrations of the roller in vertical direction w.r.t. variations of V_0 and H ($H=36$ mm)

4. Conclusions

In this study, some simulations are run for determining the influences of some variables (input variables) on the amplitude of vibrations. The results are listed below:

- i. A stick-slip mechanism occurs when material are ground between table and roller.
- ii. Higher material feed rate obtains higher amplitude of vibration.
- iii. Higher compressive force obtains lower amplitude of vibration.
- iv. At low table speed, bifurcations can be seen.

By using some of the variables as control parameter, the vibration level, amplitude of vibration may be decreased. It is seen from Fig. 12 and 13, table speed has almost no influence on the amplitude of vibrations. Also, the table is very heavy and if table speed is selected as a control parameter, the response of table speed is not fast due to weight of table. For this reason, in the implementation, it can be never realized. As a result, compressive force and material feed rate can be used as control parameters in order to reduce the amplitudes of vibrations.

Acknowledgement: This study is supported by TUBİTAK/TEYDEB under the project number 3080674.

References

- [1]. P. Toneva & W. Peukert, *Modelling of Mills and Milling Circuit*, Handbook of Powder Technology, Vol. 12, Elsevier B.V.; 873-911, 2007.
- [2]. Jian-huai Wang, Qing-ru Chen, Ya-li Kuang, A. J. Lynch & Jin-wu Zhuo, *Grinding process within vertical roller mills: experiment and simulation*, Mining Science and Technology 19, pages 97-101, 2009.
- [3]. T. Yokoyama & Y. Inoue, *Selection of Fine Grinding Mills*, Handbook of Powder Technology, Vol. 12, Elsevier B.V.; 487-508, 2007.

- [4]. İ. Yıldırım & Y. Kaytaç, *Boyut Küçültme Teknolojisindeki Gelişmeler*, I. Ulusal Kırmataş Sempozyumu'96, İstanbul, pages 287-302, 1996.
- [5]. W. Donghui & K. C. Ian, *Grinding mill circuits — A survey of control and economic concerns*, Int. J. Miner. Process. 90, pages 56-66, 2009.
- [6]. R. Junga, S. Mateuszuk & J. Pospolita, *Investigations into the movement of milled medium in the bowl of a ring-roller mill*, Powder Technology 191, pages 61-71, 2009.
- [7]. K. Fujita & T. Saito, *Unstable vibration of roller mills*, Journal of Sound and Vibration 297, 329-350, 2006.
- [8]. Lucas R.D. Jensen, H. Friis, E. Fundal, P. Møller, Per B. Brockhoff & M. Jespersen, *Influence of quartz particles on wear in vertical roller mills. Part I: Quartz concentration*, Minerals Engineering, accepted for publication.
- [9]. F.-J. Elmer, *Nonlinear dynamics of dry friction*, J. Phys. A: Math. Gen 30, pages 6057-6063, 1997.
- [10]. J. J. Thomsen, *Using Fast Vibrations to Quench Friction-Induced Oscillations*, Journal of Sound and Vibration 228, No. 5, pages 1079-1102, 1999.
- [11]. R. I. Leine, D. H. Van Campen, A. De Kraker & L. Van Den Steen, *Stick-Slip Vibrations Induced by Alternate Friction Models*, Nonlinear Dynamics 16, pages 41-54, 1998.
- [12]. B. Armstrong-Helouvry, P. Dupont & C. C. De Witt, *A survey of Models, Analysis Tools and Compensation Methods for the Control of Machines with Friction*, Automatica. 30, No. 7, pages 1083-1138, 1994.
- [13]. J. J. Thomsen & A. Fidlin, *Analytical approximations for stick-slip vibration amplitudes*, Non-Linear Mechanics 38, pages 389-403, 2003.
- [14]. H.-K. Hong & C.-S. Liu, *Coloumb Friction Oscillator: Modelling and Response to Harmonic Loads and Base Excitations*, Journal Sound and Vibration 229, No. 5, pages 1171-192, 2000.
- [15]. U. Andreaus & P. Casini, *Dynamics of Friction Oscillators Excited by a Moving Base and/or Driving Force*, Journal of Sound and Vibration 245, No. 4, pages 685-699, 2001.
- [16]. David I. G. Jones, *Handbook of Viscoelastic Vibration Damping*. John Wiley & Sons; Chichester, England, 2001.



Vibrations of Crank Slider Mechanisms with Multi Cracks and Micromechanisms' Size Effects

Vedat KARADAG^{1*}

^{1*} Istanbul Technical University,
Department of Mechanical Engineering, 34437, Gumussuyu-Istanbul-Turkey
E-mail: karadagv@itu.edu.tr

Abstract

The present work has been carried out by using the finite element method considering three dimensional motion of multi cracked crank slider mechanisms, and micromechanisms, namely, for inplane, and out of plane bending, longitudinal and torsional frequencies, respectively, as new research aspects in the literature. The critically shaped, point masses added crank sliders, robot arms and frames as beams were analyzed on clamped- simple-simple and clamped-simple-free supported conditions. The cracks were put only on one side of the beam and several types of cracks were modelled by massless rotational and longitudinal springs. The present analytical and experimental results were compared with each other and with the results available in the literature, satisfactorily. Determining crack positions have been discussed for the related cases using point masses and vibration characteristics including, also, the response characteristics and random analysis. In the present analysis, it has been also, shown that, using undimensional crack ratios of at most 0.8 and 0.9; crack positions can be found satisfactorily by making use of the spatial mass added natural frequencies, frequency derivatives up to three derivatives and vibration characteristics, response characteristics of the cracked crank slider mechanisms and robot arms and micro robots currently used in industry. Effects of smaller sizes of one thousandths have been discussed for micromechanisms.

Keywords: Crank slider mechanisms, and micromechanisms, robot arms and microrobots, multi cracks' positions, random analysis

1. Introduction

In the current researches, one of the applied research subject is the vibrations of cracked crank slider mechanisms, robot arms which are used mainly in space antennas, reflectors, automotive vehicles and robot arms [1], [2]- [13], and controlling crack influence effectively. The theoretical relationships are developed between eigenfrequency changes and magnitudes, and locations of crack induced damage for beam structures [1]. The crack is modeled as a local flexibility computed with

fracture mechanics and measured experimentally [2-3]. Perturbation method, transfer matrix approach and finite element method are the known methods used on the area. One of the mostly used crack modelled as a massless rotational spring, is the widely used in theoretical and practical experimental analysis [4], [12]. In the literature, composed finite element and component mode synthesis as in [14], and an energy based numerical model developed to investigate the vibration of beams with open cracks as in [15], have been used in the recent analysis. In the most recent works of [13], [14]- [19], detection of crack positions using roving masses, analytical spectral centre correction method, using moving masses, response characteristics have been made. Recently, the newly emerged technology and vibrations of micro structures has become necessary and important for several major objectives as in [18], [19], [20], [21]. In the present work, method of representing a crack by a rotational, torsional and extensional spring has been combined with finite element method to find crack effects for 12 dof thin beam and applied to crank slider mechanisms and micromechanisms, and robot arms and microrobots. The crack modeled is in the middle of the clamped beam component and coupler, and the related spring constants of rotational, torsional and extensional springs, which will be used, are added to the global matrix in the process, respectively. The results obtained from the analytical and experimental studies are, also presented by showing in tables and in graphics, and their importance of the identification of multi cracks using point masses and vibration characteristics, and random analysis in design, is discussed as new aspects of research.

2. Equations of Motion

Cracked crank slider mechanisms, and micromechanisms, robot arms which cantilevered from one end, are considered and shown as in Fig.1, and Fig. 2



respectively. The beams have rectangular cross sections with area A , length L , and density ρ . The crack is in the middle of the beam and only on one side of the beam having a form of open crack. The depth of the crack is represented by (a). Differential equations of motion of a crank slider mechanisms and robot arms, have been obtained by making use of potential and kinetic energy equations of the conservative system, respectively, for each of the beams (I, II ,Fig.1, Fig. 2.), [3],

$$\begin{aligned}
 V = & \frac{1}{2} \int_0^L EI_{Gx} v''^2 dz + \frac{1}{2} \int_0^L EI_{Gy} u''^2 dz \\
 & + \frac{1}{2} \int_0^L EA w^2 dz + \frac{1}{2} \int_0^L GI_T \Phi^2 dz + \frac{1}{2} K_r (w_2 - w_1)^2 \\
 & + \frac{1}{2} K_T (\Phi_2 - \Phi_1)^2 + \frac{1}{2} K_L (w_2 - w_1)^2 \\
 & + \frac{1}{2} \int_0^L F_C (v^2 + u^2) dz \\
 & + \frac{1}{2} K_r (\dot{u}_2 - \dot{u}_1)^2 + \frac{1}{2} K_r (\dot{v}_2 - \dot{v}_1)^2
 \end{aligned} \quad (1)$$

here, 1 and 2, respectively, are the points before and after the crack. K_r is explained in eq. (4)

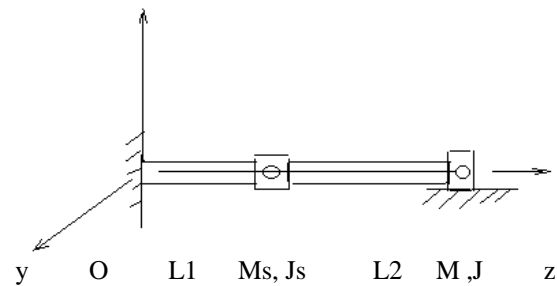
$$\begin{aligned}
 T = & \frac{1}{2} \int_0^L \rho A (\dot{u}^2 + \dot{v}^2 + \dot{w}^2) dz + \frac{1}{2} \int_0^L \rho I_{TP} \dot{\Phi}^2 dz \\
 & + \frac{1}{2} M_i (\dot{u}^2 + \dot{v}^2)_i + \frac{1}{2} J_i (\dot{u}^2 + \dot{v}^2)_i
 \end{aligned} \quad (2)$$

where, $F_C = P_i$ are axial forces as in Fig. 1. (·) is derivative with respect to time, (') is derivative with respect to z . The additional kinetic energy due to point masses (M_i) and rotary inertias (J_i) at the (x_i, y_i) coordinates ($i=1,2$), is the last terms in eq.(2). v and u are used as transverse bending displacements along x and y axes respectively (Fig. 1,2), in the thin beam analysis. The related geometric boundary conditions are; $u(0)=v(0)=0, u'(0)=v'(0)=0$ for clamped end, $u'(L)=v'(L)=0$ for free end, and at crank slider mechanisms, crank coupler connecting pins cases; the displacements and rotations such as, $w_I=w_{II}, v_I=v_{II}, v'_I=v'_{II}$ for inplane motion, and $w_I=w_{II}, u_I=u_{II}, u'_I=u'_{II}$ for out of plane motion at the beam connections (see, also, Fig. 1). For the case, (II) terms are connected as in (I) connection cases. 12 dof classical thin beam finite elements as in [15], have been used throughout in the numerical analysis. Degrees of freedom per node are; bending displacements and slopes on both x and y axes, respectively, torsional and longitudinal displacements. In

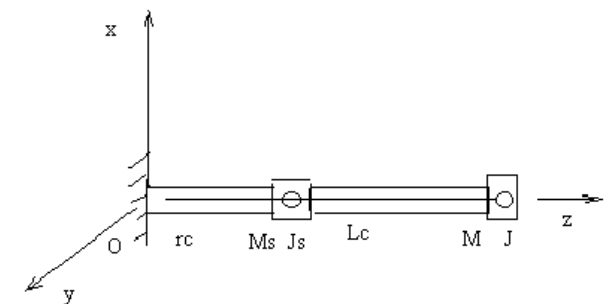
the equations; I_{Gx}, I_{Gy} are beam cross section second moments of inertias, E elasticity, G shear modulus, A cross section area, ρ density, I_T torsional constant, ρI_{TP} rotatory inertia of cross section. By using eqs. (1) and (2) for each beam element of beam system links and assembling according to Fig. 1. configurations, and applying standard finite element formulation as in [3] for each of the (I),(II) beam sections, equations of motion, have been obtained in matrix notation for the global system as ([3]):

$$[M]\{\ddot{q}\} + [K]\{q\} = 0 \quad (3)$$

where, $[M]$ is global mass matrix and $[K]$ is stiffness matrix. This equation, has been solved as an eigenvalue problem using double precision mathematics.



crack:(I) | — $rc/2$ → |, (II) | — $Lc/2$ → |
 Figure 1. Coordinate axes (crank-slider).



crack:(I) | — $rc/2$ → |, (II) | — $Lc/2$ → |
 Figure 2. Coordinate axes (robot mechanism).
 $rc=L1$ crank radius, $Lc=L2$ coupler length

The crack is in the middle of the beam and on one side of the beam having a form of open crack. In the analytical analysis, the spring coefficients of the crack are calculated in the computer programmes using eq.(4) and then directly added to the stiffness matrix. The physical

model of the beam having a crack only on its one side is shown in Fig. 3. In this model, local rigidities are shown by a massless rotational spring constant represented K_r for bending and extensional spring constant represented K_L for tension and K_T torsional spring for torsional displacements, respectively(Fig. 2.) [5]-[8].

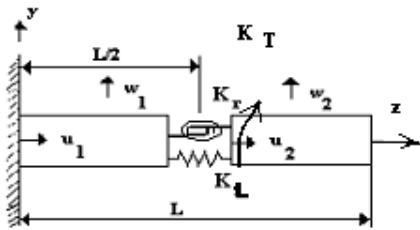


Figure 3. Physical model of the open crack.

In the industrial applications, this model gives very good results as pointed out in [5], [8]. For a crack, the local compliance D can be computed as in [5]-[8], using the local compliance function as,

$$D = \frac{5.346h}{EI} I\left(\frac{a}{h}\right) \quad (4)$$

where a = crack depth; $h = t$, beam thickness; and the $I(a/h)$ = dimensionless local compliance function. Then the dimensionless rotational stiffness for a given crack depth a can be computed via $K_r = K_r L/EI$, where $K_r = 1/D$. The extensional spring coefficient for a given crack depth a can be computed via $K_L = A_c E/L_c$, where A_c = the crack cross-section and L_c = the crack length. The torsional rotational stiffness is $K_T = G I_{Tc} /L_{Tc}$, where L_{Tc} is torsional constant of the cracked cross section, G is shear modulus.

In this study, the spring coefficients of the cracks are calculated in the computer program and then directly added to the stiffness matrix. The crack modeled is in the middle of the beam(I) and the effects of the related spring constants of rotational and extensional springs, which will be used, are added to the global matrix (Fig. 1.,2.).

3. Numerical values evaluation

First, the results obtained from the finite element program written in Fortran in the present work, were compared with the available results from the literature in Table 1 and Table 1.1,[5],[6],[13],[17]. Excellent agreements have been found between the presently obtained numerical values using thin beam finite elements and the exact analytical values for cracked and uncracked crank slider and robot arm with free end. In tables 2, 3, 4, 5 ; the numerical values have been given

obtained by the present work, exact analytical values, for the crack and uncracked crank slider and robot arm with free end beams. In Tables 1, 2 and 4; the in plane and out of plane vibration frequencies have been shown (see ,also, Fig. 1,2,3,4.1-4.7). Oxy plane is typically called as inplane, Oyz is called as out of plane frequencies. In Table 1.1 and 1.2, point tip mass added cases for M1 paint robot arm, have been shown and compared with each other and with the available experimental values. In Table 3 and 4 the numerical values obtained for the same examples for cracked and mass added cases with ank.-simple-free boundary conditions, have been shown. In Tables 1-4 , the results obtained for cracked, mass added robot arms with ank.-simple-free boundary conditions for different coupler lengths of $L1$ (Fig. 1, Fig. 2.), have been shown. The new aspects as different from the Works in [15-17], have been shown in Figures 4.1-4.7, in identification of crack positions in terms of frequencies and vibration mode shapes. The crack positions have been obtained with 4 % accuracy using the related values (Fig. 4.1.1,4.1.2,4.1.3, 4.2). The crack positions, have been more distinguished in the diagrams of cross section rotations as shown in Fig. 4.2, although 4 % accuracy is the same. The diagrams of numerical values obtained for spatial masses using 20 different points along the mechanisms, have been shown in Figures 4.13-4.14 for pinned and ank.-simple-free boundary conditions, and in Figures 4.15-4.16 for ank.-simple-simple boundary conditions. For these related cases; first derivatives of the first frequency, have been shown in Figures 4.7-4.8, and the second derivatives of the first frequency, have been shown in Figures 4.7-4.10 , and the third derivative of the first frequency, have been shown in Figures 4.11-4.12. Using Sandors' crank slider example data in [1], the presently calculated first derivatives of the first frequency, and the related spatial mass added frequency diagrams have been shown in Figures 4.13-4.16, and for the first frequency, and for the second frequency case. In the Figures 4.15-4.16, and for the related cross section rotations in Figure 4.16. In the analysis, the accuracy of determining the crack positions, is 4% for the first and second frequency derivatives.

The size of micromechanisms are changed from meters to millimeters for demonstration purposes(see, also the Tables). The effect of cracks have become more important , especially, at the first two frequencies with almost 90-98%.

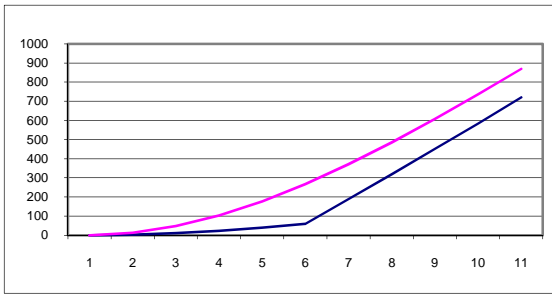


Figure 4.1.1. First vibration mode shape(normalized case),
 ____: m=10kg case,(1-10el., along L1 ,Fig.1). ____:m=10
 case,(1-10el.,along L1,Fig.1),midpoint cracks at both crank and
 coupler (a/t=0.9).

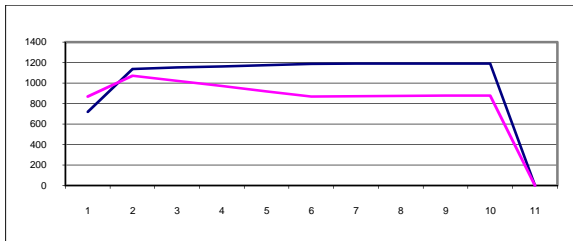


Figure 4.1.2. First vibration mode shape of Paint
 Robot(normalized case), ____: m=10kg case,(1-10el., along
 L2,Fig.1). ____:m=10 case,(1-10el.,along L2 ,Fig.1),
 midpoint cracks at both crank and coupler (a/t=0.9).

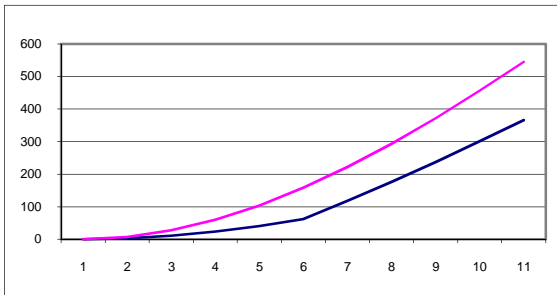


Figure 4.1.3. First vibration mode shape of Paint
 Robot(normalized case), ____: m=10kg case,(1-10el., along
 L1,Şek.2). ____:m=10 case,(1-10el.,along L1 ,Fig.2),
 midpoint cracks at both crank and
 coupler(a/t=0.9,L1=L/2,L2=L).

Table 1. M1 Paint Robot Arm Vibrations.

Circular cross section, mm,
 $E=2.10^{11}N/m^2, G=7.955510^{10}N/m^2, \rho=7850kg/m^3,$
 $L1=L2=L=1200mm, v=0.3, k=1.2, 10+10el., ank.-simple,$
 $M= 10 kg, crank+coupler , the similar midpoint cracks$

freq.	aa/t=0 10+10el.	aa/t=0.9	aa/t=0.0 10kg 10+10el.	aa/t=0.9 coupler
ω_1	13.800	6.654	7.806	9.832
ω_2	83.391	14.311	60.894	18.590
ω_3	150.775	73.360	184.050	83.429
ω_4	337.535	219.556	375.955	232.662
ω_5	830.564	252.571		338.791

Tablo1.1. M1 Paint Robot Arm Vibrations.

Circular cross section, mm,
 Continued Table 1 . ank.-free case

freq.	aa/t=0 present	aa/t=0.9 crank+ coupler crack	aa/t=0.9 cracked crank	aa/t=0.9 cracked coupler
ω_1	0.024	0.001	0.001	0.008
ω_2	14.626	7.360	7.572	12.638
ω_3	84.381	18.638	74.328	20.793
ω_4	336.315	75.586	237.812	86.624
ω_5	600.131	238.085	599.705	336.316

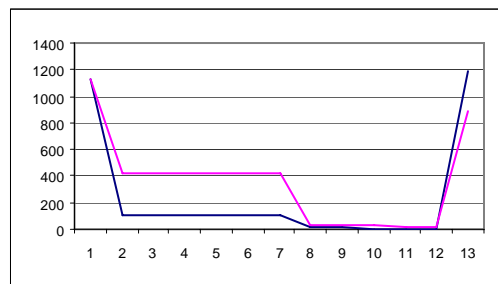


Figure 4.2. Vibration mode shape 1 of Paint Robot.
 cross section rotation along L2 ,Fig.1-4.1.
 crack on the midpoint of L2 ,Fig.1.



Table 1.2. M1 Paint Robot Arm Vibrations.

Circular cross section, mm,
 $E=2.10^{11}N/m^2, G=7.955510^{10}N/m^2, \rho=7850kg/m^3,$
 $L1=L2=L=1200mm, v=0.3, k=1.2, 10+10el., ank.-simple,$
 $M= 10 kg, crank+coupler , the similar midpoint cracks$

freq.	aa/t=0 [Hz]	aa/t=0.9 crank+ slider	aa/t=0.9 crank 10+10el.	aa/t=0.9 coupler
ω_1	41.3350	11.0356	19.6559	11.1782
ω_2	2460.85	20.6798	2460.64	42.9366
ω_3	4775.47	4162.27	4769.24	4166.97
ω_4	23551.0	22703.8	22713.3	23244.4
ω_5	33634.2	23244.8	23553.3	33625.7

Table1.3. M1 Paint Robot Arm Vibrations.

Circular cross section, mm,
 Continued Table 1 . ank.-free case

freq.	aa/t=0 [Hz]	aa/t=0.9 crank+ coupler crack	aa/t=0.9 cracked crank	aa/t=0.9 cracked coupler
ω_1	1.0277	-1.122	-0.13665	-1.986
ω_2	2.9751	1.48901	1.49002	2.6992
ω_3	82.9212	15.8091	74.5053	15.8129
ω_4	4167.87	79.8570	4167.84	88.8371
ω_5	30938.1	21209.1	21209.15	30937.9

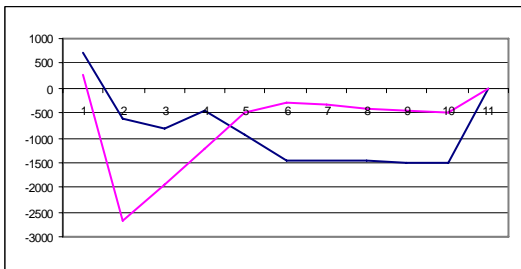


Figure 4.3 Vibration mode shape 2 of Paint Robot (normalized case).Along L2 (cont.from Fig.4.6.),on crank and coupler, a=0.9, midpoint crack case.

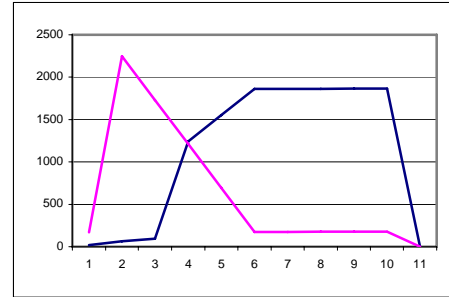


Figure 4.4. Crank-coupler vibration mode shape 1 (Sandor[1]),(normalized case).Along L2 (cont. from Fig. 4.8 .)

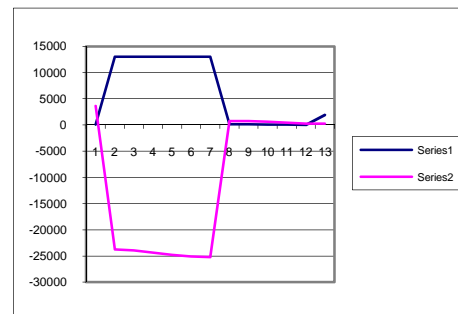


Figure 4.5. Crank-coupler vibration mode shape 1 (Sandor[1]),(normalized case).along L1(cont.from Fig. 4.8 .). a=0.9, midpoint crank and coupler .

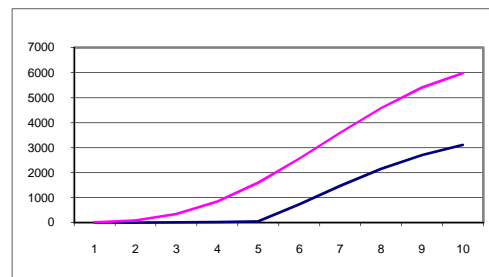


Figure 4.6. Paint robot spatial mass added frequencies, —: m=10kg case,(1-10el., L1 ,along Fig.1). —: m=10 case,(1-10el.,along L1 ,Fig.1),on crank and coupler midpoint crack case (a/t=0.9),1st freq. case(Fig.4.13), ank.-free case ,1st freq. derivative.

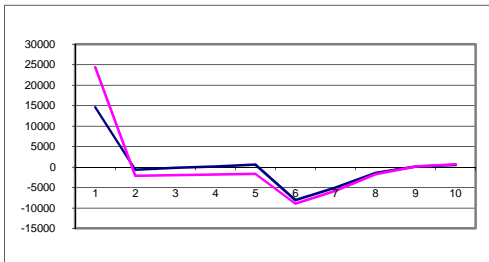


Figure 4.7. Paint robot spatial mass added frequencies,
 ____: m=10kg case,(1-10el., along L2 ,Fig.1). ____:m=10 case,(1-10el.,along L2 ,Fig.1),on crank and coupler midpoint crack case (a/t=0.9),1st freq. case(Fig.4.13), ank.-free case, 1st freq. derivative.

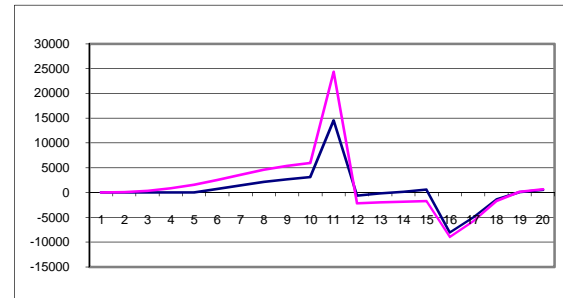


Figure 4.10. Paint robot spatial mass added frequencies,
 ____: m=10kg case(1-10el.,along L1-L2 ,Fig.1). ____:m=10 case,(1-10el.,along L1-L2 ,Fig.1),on crank and coupler midpoint crack case (a/t=0.9),1st freq. case(Fig.4.18), ank.-free case 1st freq. 1st derivative.

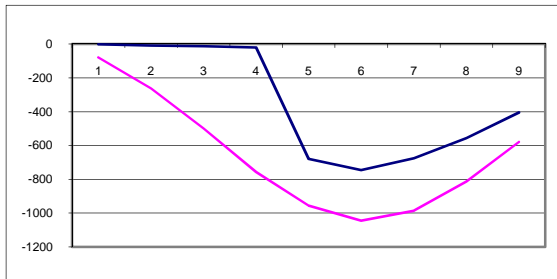


Figure 4.8. Paint robot spatial mass added frequencies,
 ____: m=10kg case(1-10el., along L1 ,Fig.1). ____:m=10 case,(1-10el.,along L1 ,Fig.1),crank and coupler midpoint crack case (a/t=0.9),1.frekans case(Fig.4.17), ank.-free case 1st freq 2nd derivative.

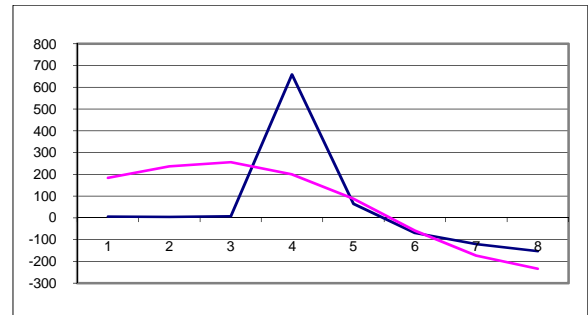


Figure 4.11. Paint robot spatial mass added frequencies,
 ____: m=10kg case,(1-10el., along L1 ,Fig.1). ____:m=10 case,(1-10el.,along L1 ,Fig.1),on crank and coupler midpoint crack case (a/t=0.9),1st freq. case(Fig.4.18), ank.-free case 1st freq. 3rd derivative.

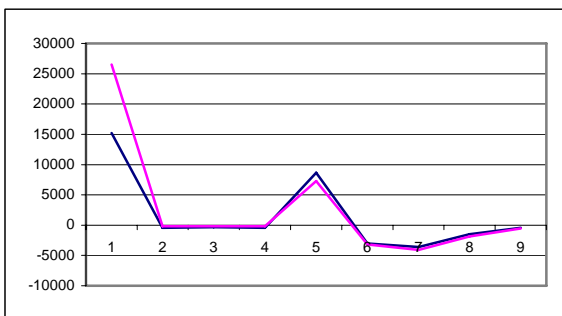


Figure 4.9. Paint robot spatial mass added frequencies,
 ____: m=10kg case(1-10el., along L2 ,Fig.1). ____:m=10 case,(1-10el.,along L2 ,Fig.1),on crank and coupler midpoint crack case (a/t=0.9),1st freq. case(Şek.4.18), ank.-free case,1st freq. 2nd derivative.

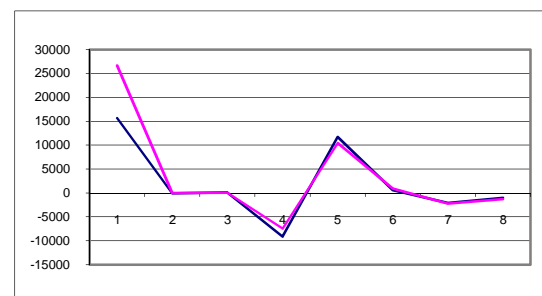


Figure 4.12. Paint robot spatial mass added frequencies,
 ____: m=10kg case,(1-10el., along L2 ,Fig.1). ____:m=10 case,(1-10el.,along L2 ,Fig.1),on crank and coupler midpoint crack case (a/t=0.9),1st freq. case(Fig.4.18), ank.-free case 1st freq. 3rd derivative.

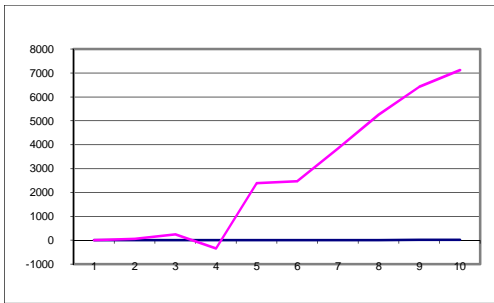


Figure 4.13. Paint robot spatial mass added frequencies,
 —: m=1kg case,(1-10el.,along L1 ,Fig.1). —:m=1 kg case,(1-10el.,along L1 ,Fig.1),on crank coupler midpoint crack case (a/t=0.9),1st freq. case(Fig.4.18), ank.-simple case 1st freq. 1st derivative. See Fig. 4.13. (Sandor[1]),(normalized case). Along L1(cont. from Fig. 4.8) .a=0.9 crank and coupler .

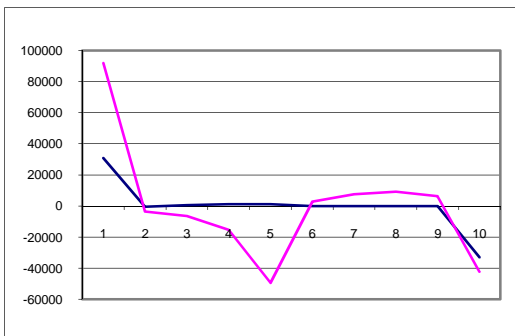


Figure 4.14. Paint robot spatial mass added frequencies, 1-10el.,along L2,Fig.1), crank and coupler midpoint crack case (a/t=0.9),1st freq. case(Fig.4.18), ank.-simple case 1st freq. 1st derivative,see Fig.4.23. Sandor[1]),(normalized case). Along L1(cont. from Fig. 4.8) .a=0.9 crank and coupler midpoint.

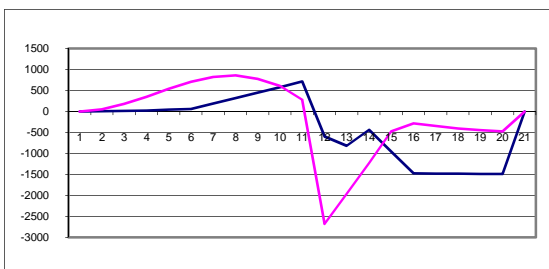


Figure 4.15. Paint robot spatial mass added frequencies, 1-10el., along L1-L2,Fig.1), crank and coupler midpoint crack case (a/t=0.9),2nd freq. case(Fig.4.25), ank.-simple case 2nd freq., see Fig.4.23. Sandor[1]),(normalized case).(cont. from Fig. 4.8) .a=0.9 crank and coupler midpoint.

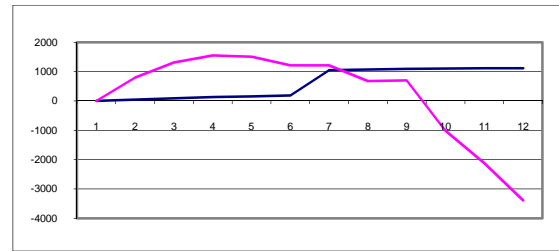


Figure 4.16. Paint robot mode shape of cross section rotations,

1-10el., along L1-L2,Fig.1), krank ve biyelde midpoint crack case (a/t=0.9),2nd freq. case(Fig.4.25), ank.-simple case 2nd freq., see Fig.4.23. Sandor[1]),(normalized case).(cont. from Fig. 4.8) .a=0.9 crank and coupler midpoint.

Table 2.Crank-slider vibration frequencies.

(Sandor[1] , out of plane vibrations.

$E=0.71^{11}N/m^2, G=7.955510^{10}N/m^2, \rho=2709.72kg/m^3,$
 $L1=10.8cm, L2=27.94cm, 10+10el., ank.-simple, m=1kg$
 $b=2.54cm, crank+coupler , the same rate midpoint crack$

freq. [Hz]	aa/t=0 10+10el.	aa/t=0.6 10kg 10+10el.	aa/t=0.6 10kg 10+10el.	aa/t=0.6 coupler
ω_1	102.941	124.317	38.602	9.832
ω_2	347.500	318.056	75.554	18.590
ω_3	754.661	337.144	341.690	83.429
ω_4	3657.761	1263.347	1264.821	232.662
ω_5	4824.048	3830.175	3864.977	338.791

Table 2.1. Crank-slider vibration frequencies.

(Sandor[1]), inplane vibrations.

$E=0.71^{11}N/m^2, G=7.955510^{10}N/m^2, \rho=2709.72kg/m^3,$
 $L1=10.8cm, L2=27.94cm, 10+10el., ank.-simple, m=1kg$
 $b=2.54cm, crank+coupler , the same rate midpoint crack$

freq. [Hz]	aa/t=0 10+10el.	aa/t=0.6 1kg 10+10el.	aa/t=0.6 1kg 10+10el.	aa/t=0.6 coupler
ω_1	21.850	3.130	9.559	3.138
ω_2	47.526	13.777	21.565	23.208
ω_3	243.645	79.634	80.965	79.956
ω_4	304.285	253.810	253.990	254.012
ω_5	4343ç375	344.461	345.189	345.311



Table 3. Vibration response averages, the mean values of M1 Paint robot. Properties in Fig.4.1. Ank.-simple-simple support ,First vibration frequency.L1=L/2

	crank		coupler	
	a/t=0.0	a/t=0.9	a/t=0.0	a/t=0.9
crank+coupler	333.9	218.0	839.5	1028.5
crack			crnk+cpler 573.3	crnk+cpler 618.6
crck on cpler	333.9	133.4	839.5	1209.1
crnk+cp L1=L/2	204.2	121.7	688.0	843.6
coupler L1=L/2	204.2	96.1	688	878.5

Table 4. Vibration response averages, the standart deviation values of M1 Paint robot.(Cont. from Table3)

	crank		coupler	
	a/t=0.0	a/t=0.9	a/t=0.0	a/t=0.9
crank+coupler	.333.9	218.0	839.5	1028.5
crack			crnk+c.pler 573.3	crnk+c.pler 618.6
on cpler	333.9	133.4	839.5	1209.1
crnk+cplr L1=L/2	204.2	121.7	688.0	843.6
crk on coupler L1=L/2	204.2	96.1	688	878.5

Table 5. Vibration response averages, skewness values of M1 Paint robot.(cont. from Table 4)

	crank		coupler	
	a/t=0.0	a/t=0.9	a/t=0.0	a/t=0.9
crank+coupler	0.571	0.980	-2.943	-2.663
crack			crnk+c.pler -0.380	crnk+c.pler -0.018
crck on coupler	0.571	0.577	-2.943	-0.929
crnk+cpler crk L1=L/2	0.630	0.865	0.108	-2.118
coupler L1=L/2	0.630	0.615	0.108	-1.596

Table 6. Vibration response averages Kurtosis values of M1 Paint robot.(Cont.from Table 3).

	crank		coupler	
	a/t=0.0	a/t=0.9	a/t=0.0	a/t=0.9
crank+coupler			7.149	9.359
crack	-1.110	-0.474	crnk+c.pler -1.596	crnk+c.pler -1.952
coupler	-1.011	-0.995	9.359	-0.430
crank+coupler L1=L/2	-0.904	-0.635	1.047	3.691
coupler L1=L/2	-0.904	-0.926	1.047	1.584

Table 7. Vibration response averages, the mean values of crank slider(Sandor).(Cont.from Table3).

	crank		coupler	
	a/t=0.0	a/t=0.9	a/t=0.0	a/t=0.9
crank+coupler	70.545	1.273	830.636	1122.727
crack			crnk+c.pler 462.524	crnk+c.pler 5888.571
crank+coupler	70.545	0.545	830.636	1186.455

Table 8. Vibration response averages, the standart deviation values of crank slider(Sandor).(cont.from Table 3).

First vibration frequency.L1=L

	crank		coupler	
	a/t=0.0	a/t=0.9	a/t=0.0	a/t=0.9
crank+coupler	68.841	1.679	1006.052	893.287
crack			crnk+coupler 814.880	crnk+coupler 853.539
crank+coupler crack	68.841	1.688	1006.052	838.240

In Tables 5-10, The numerical values obtained for M1 paint robot arm response averages obtained for the first frequency in the random analysis, have been shown in known averages such as the mean value, rms value, standart deviation, skewness and Kurtosis values. Using random vibration analysis, and experimental recordings,the positions of cracks occurred on cranks and



Table 9. Vibration response averages, the skewness values of crank slider(Sandor),(Cont. from Table 8).

	crank		coupler	
	a/t=0.0	a/t=0.9	a/t=0.0	a/t=0.9
crank+coupler crack	0.765	0.871	1.363 crnk+c.pler 2.286	-0.472 crank+c.pler 0.861
coupler	0.765	1.363	1.363	-0.617

Table 10. Vibration response averages, the Kurtosis values of crank slider(Sandor),(Cont. from Table 9).

	crank		coupler	
	a/t=0.0	a/t=0.9	a/t=0.0	a/t=0.9
crank+coupler crack	-0.620	-1.037	0.623 crnk+c.pler 4.489	-1.986 crank+c.pler -1.289
coupler	-0.620	0.081	-0.623	-1.535

Table 1.2. M1 Paint Robot Arm Vibrations.

Circular cross section, mm,
 $E=2.10^{11}N/m^2, G=7.955510^{10}N/m^2, \rho=7850kg/m^3,$
 $L1=L2=L=1200mm, v=0.3, k=1.2, 10+10el.,$ ank.-simple,
 $M= 10$ kg, crank+coupler, the similar midpoint cracks

freq. [Hz]	aa/t=0 10+10el.	aa/t=0.9 crank+ slider	aa/t=0.9 crank 10+10el.	aa/t=0.9 coupler
ω_1	41.3350	11.0356	19.6559	11.1782
ω_2	2460.85	20.6798	2460.64	42.9366
ω_3	4775.47	4162.27	4769.24	4166.97
ω_4	23551.0	22703.8	22713.3	23244.4
ω_5	33634.2	23244.8	23553.3	33625.7

Table1.3. M1 Paint Robot Arm Vibrations.

Continued Table 1 . ank.-free case

freq. [Hz]	aa/t=0 present	aa/t=0.9 crnk+cpler	aa/t=0.9 crked crank	aa/t=0.9 crckedcpler
ω_1	1.0277	-1.122	-0.13665	-1.986
ω_2	2.9751	1.48901	1.49002	2.6992
ω_3	82.9212	15.8091	74.5053	15.8129
ω_4	4167.87	79.8570	4167.84	88.8371
ω_5	30938.1	21209.1	21209.15	30937.9

Table13.Crank slider micromechanism Vibrations.

Continued Table 1 . ank.-simple case, L1=L2=1.2mm

freq. [Hz]	aa/t=0 present	aa/t=0.9 crnk+cpler	aa/t=0.9 crked crank	aa/t=0.9 crckedcpler
ω_1	41.450	11.054	19.712	11.195
ω_2	2848.928	20.646	2848.912	42.931
ω_3	41708.543	41617.386	41661.655	41664.121
ω_4	232473.98	227040.51	227041.66	232443.72
ω_5	336256.73	232443.76	232473.99	336255.90

Table14. MicroRobot Arm Vibrations.

Continued Table 1 . ank.-free case, L1=L2=1.2mm

freq. [Hz]	aa/t=0 present	aa/t=0.9 crnk+cpler	aa/t=0.9 crked crank	aa/t=0.9 crckedcpler
ω_1	0.693	0.000	0.000	1.058
ω_2	22.0364	0.5606	0.4754	11.9965
ω_3	82.792	15.8042	74.3249	16.1086
ω_4	4174.21	79.6888	4174.184	88.7222
ω_5	309377.56	212089.25	212089.25	309377.54

Table15. Crank slider micromechanism Vibrations.

Continued Table 1 . ank.-simple, L1=1.08cm, L2=2.794cm
 $m=0.001$ kg, $b=2.54$ cm

freq. [Hz]	aa/t=0 present	aa/t=0.6 crnk+cpler	aa/t=0.6 crked crank	aa/t=0.6 crckedcpler
ω_1	48.0668	0.174	47.640	1.112
ω_2	141.8395	96.2279	97.3822	141.1679
ω_3	2652.5752	2652.5487	2652.5534	2652.5712
ω_4	12608.088	12607.859	12608.030	12607.918
ω_5	39081.457	38649.320	38649.328	39081.448

Table16. Crank slider micromechanism Vibrations.

Continued Table 1 . ank.-simple, L1=1.08mm, L2=2.794mm
 $m=0.000001$ kg, $b=2.54$ mm

freq. [Hz]	aa/t=0 present	aa/t=0.6 crnk+cpler	aa/t=0.6 crked crank	aa/t=0.6 crckedcpler
ω_1	50.068	0.00	47.823	0.00
ω_2	142.1215	96.2809	97.3434	140.8544
ω_3	26444.169	26444.153	26444.153	26444.131
ω_4	126075.81	126075.79	126075.80	126075.77
ω_5	390814.55	386493.23	386493.23	390814.55



coupler, can be satisfactorily and reliably determined. In similar manner, using the numerical values obtained for the crank slider example properties of ref. [1], have been shown in Tables 8-10. In addition, the same analysis can be made for ank.-simple-free boundary cases. Microsize dimensions are generally effective at the higher number of modes and longitudinal, and torsional frequencies in the kHz range not MHz range (Table 11-Table 14, also, Table 1.2-1.3). First two or three frequencies are in the lower frequency range. Multicrack effects and positions can be analysed reliably using current finite element approach with the same accuracy for micromechanisms.

4. Conclusions

In determination of crack positions; first, the vibrations of crank slider mechanisms and cracked robot arms, have been analysed by using the finite element method considering three dimensional motion of cracked beams, namely, for inplane, and out of plane bending, coupled bending-longitudinal and bending-torsional frequencies, respectively, as new research aspects in the literature. The end point masses added crank slider mechanism and industrial robot arms as beams were analyzed on clamped-simple-free or simple supported conditions. The cracks were put only one side of the beam in span. The present analytical and experimental results were compared with each other and with the results available in the literature, satisfactorily. Estimation ways of crack positions have been established and demonstrated for the related cases, and in the related Figures. In the present analysis, it has been also, shown that, using undimensional crack ratios of about 0.8 and 0.9; substantially exact determination of satisfactory (4%) levels, have been obtained of the cracked robot arms and crank slider mechanisms and frames currently used in industry.

For the robot arms cases; the ratios of crack effects for clamped-clamped case (% 18), are usually lower than the case for clamped-free case (% 48.1). Additions of spatial masses cases, increase substantially, the determination of cracks along the arms. The detection becomes more pronounced for the mode shapes for the rotation of the bending cross sections. The edgewise vibration frequencies and first and second, and even third frequencies for the related cases, can be used for more accurate detection models. It has been shown that in the spatial mass added cases, the determination of crack positions, can, also, made with 4% accuracy in the first, second, and third derivatives of frequencies cases. Microsize dimensions (up to one thousandths) are

generally effective at the higher number of modes and longitudinal, and torsional frequencies in the kHz range.

References

- [1]. Sandor, G.N., and Erdman, A.G., *Advanced mechanism design: Analysis and synthesis*, Vol. 2, Prentice Hall, Inc., Englewood Cliffs, 1984.
- [2]. Amirouch, F.M.L., *Computational methods in multibody dynamics*, Prentice-Hall, Englewood Cliffs, 1992.
- [3]. Karadag, V., 1999, *Vibrations and dynamic stability of thick flexible new material composite mechanisms with heavy masses*, Proc. Tenth World Congress on the Theory of Machines and Mechanisms, Vol. 5, Vibrations, Oulu, Finland, June 20-24, s. 2156-2161.
- [4]. Liang, R., Hu, J., Choy, F., 1992, *Analytical study of crack-induced eigenfrequency changes on beam structures*, Journal of Eng. Mech., 118, pp. 384-396.
- [5]. Dimarogonas, A.D., 1996, *Vibration of cracked structures: A state of the art review*, Engineering Fracture Mechanics, 55(5), pp. 831-857.
- [6]. Dimarogonas, A.D., Chondros, T.G., Yao, J., 1998, *A continuous cracked beam vibration theory*, Journal of Sound and Vibration, 215(1), pp. 17-34.
- [7]. Dimarogonas, A.D., Paipetis, S.A., 1983, *Analytical Methods in Rotor Dynamics*, Applied Science Publishers, London.
- [8]. Chondros, T.G., Dimarogonas, A.D., 1980, *Identification of cracks in welded joints of complex structures*, Journal of Sound and Vibration, 69(4), pp. 531-538.
- [9]. Rizos, P.F., Aspragathos, N., 1990, *Identification of crack location and magnitude in a cantilever beam from the vibration modes*, Journal of Sound and Vibration, 138(3), pp. 381-388.
- [10]. Masoud, S., Jarrah, M.A., Al-Maamory, A., 1997, *Effect of crack depth on the natural frequency of a prestressed fixed-fixed beam*, Journal of Sound and Vibration, 214(2), pp. 201-212.
- [11]. Kisa, M., Brandon, J., Topçu, M., 1998, "Free vibration analysis of cracked beams by a combination of finite elements and component mode synthesis methods", Computers and Structures, 67, pp. 215-223.
- [12]. Yang, X.F., Swamidass, A.S.J., Seshadri, R., 2001, "Crack identification in vibrating beams using the energy method", Journal of Sound and Vibration, 244(2), pp. 339-357.
- [13]. Altay, Kaan, and Karadag V., 2002, "Vibration analysis of generally cracked beams with spring and masses and axial load", Proc. of ESDA2002, 6th Biennial Conf. on Eng. Systems Design and Analysis, Istanbul, Turkey, July 8-11, pp. 1-6.
- [14]. Cacciola, P., Impollonia, N., and Martin H.R., "Crack detection and location in damaged beam vibrating under white noise", Comp. and Structures, 81, 2003, 1773-1782.
- [15]. Zhong S., Oyadji O.S., (2008), "Analytical predictions of natural frequencies of cracked simply supported beams with a stationary roving mass", J. of sound and vibration, v. 311, n1-2, March 18, s. 328-352.
- [16]. Zhong S., Oyadji O.S., Ding, K., (2008), "Response-only method for damage detection of beam-like structures using high accuracy frequencies with auxiliary mass spatial probing", J. of sound and vibration, v311, n3-5, Apr. 8, s.1075-1099, 2008.
- [17]. Yang, J., Chen Y., Xiang Y., Jia, X.L., (2008), "Free and forced vibration of cracked inhomogeneous beams under an axial force and moving load", J. of sound and vibration, v 311, n1-2, Apr. 22, 2008, pp. 166-184.
- [18]. Lin, R.M. and Wang, W.J., 2006, "Structural dynamics of microsystems-current state of research and future directions", Mechanical systems and signal processing, 20, 1015-1043.
- [19]. Hayashi, Teru, 1999, "Research and development of



- micromechanisms*", 10th World Congress IFToMM, Oulu, Finland, June 20-24, pp. 18-23.
- [20]. Zhang, Y.Z. and Liu, G., 2009, "Wireless swimming microrobot design, analysis and experiments", J. of dynamic systems, measurement and control, Jan., Vol. 131, pp. 011004-1-8.
- [21]. Pasqueale, G. De, Veijola, T., and Soma, A., 2010, "Modelling and validation of air damping in perforated gold and silicon MEMS plates", 20(2010), 015010.



The Free Vibration of Symmetrically Laminated Conical Shells with Freely Supported Edges

A. H. SOFIYEV^{1*}, E. SCHNACK², A. DENIZ³, M. AVCAR⁴

^{1*}Suleyman Demirel University, Department of Civil Engineering, Isparta, Turkey

E-mail: asofiyev@mmf.sdu.edu.tr

²Karlsruhe University, Institute of Solid Mechanics, Karlsruhe, Germany

³Usak University, Department of Mathematics, Usak, Turkey

⁴Suleyman Demirel University, Department of Civil Engineering, Isparta, Turkey

Abstract

In this study an analytical procedure is given to study the free vibration characteristics of symmetrically laminated orthotropic truncated and complete conical shells with freely supported edges. Applying Galerkin methods to the modified Donnell type stability and compatibility equations, the expression for the fundamental frequency parameters of laminated orthotropic conical shells are obtained. The appropriate formulas for single-layer and laminated cylindrical shells made of orthotropic and isotropic materials are found as a special case. Furthermore, parameter λ which is included in the obtained formulas is get from the minimum conditions of frequencies. Finally, the influences of the number and ordering of layers and the variations of conical shells characteristics on the dimensionless frequency parameters are investigated.

Keywords: Laminated conical shells, Orthotropic materials, Freely supported edges, Vibration, Frequency parameters

1. Introduction

The laminated composite conical shells are being widely used in construction of engineering structures is an important field of current area of research. The conical shells made up of composite materials are one of the important structural elements in a variety of high performance engineering systems including aircraft, submarine, and space structures. Considerable efforts have been made in the past by researchers and investigators on the predictions of the dynamic response of laminated composite shells [1-7].

In all the above studies, the boundary conditions of the conical shells are in variety such as free, clamped, and simply supported or their combinations. Studies on vibration analyses of shells with freely supported (held

circular but unrestrained axially) edges are limited in the literature, comparatively to the other types of edge restraints. Most of these works have been done for the vibration analyses of cylindrical shells [8-11]. However, there are some studies on the vibration and stability of freely supported single-layer homogeneous and FGM isotropic conical shells in the open literature [12-14].

It is evident from the available literature that the studies on the free vibration of freely supported symmetrically laminated composite conical shells are not dealt by the researchers due to complexity associated with the conical shells. In the present work, an attempt is made to address this problem.

2. Basic relations and equations

Consider a circular conical shell as shown in Fig.1a, which is assumed to be thin, laminated and composed of N layers of orthotropic materials. The thickness of the layers is equal, i.e. is $\delta = 2h / N$. Here $2h$ is the total thickness, L is the length and γ is the semi-vertex angle of the conical shell. R_1 and R_2 indicate the radii of the cone at its small and large ends, respectively. S_1 and S_2 are the distances from the vertex to the small and large bases, respectively. A set of curvilinear coordinates (z, θ, S) is located on the middle surface. The z -axis is always normal to the moving S -axis, lies in the plane generated by the S -axis and the axis of the cone, and points inwards. The θ -axis is in the direction perpendicular to the $S - z$ plane. Fig. 1b shows a cross-sectional configuration of the laminated composite conical shell in thickness direction. The middle surface $z = 0$ is located at a layer interface for even values of N , whereas for odd values of N the middle surface is located at the center of the middle layer.

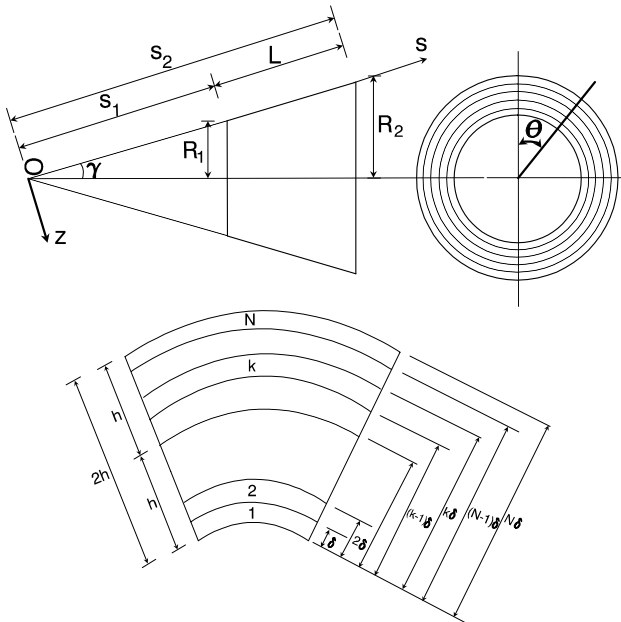


Fig. 1 (a)Geometry and b) cross sectional view of thickness of the laminated conical shell

The stress-strain relations for thin orthotropic layers are given as follows [6]:

$$\begin{pmatrix} \sigma_S^{(k+1)} \\ \sigma_\theta^{(k+1)} \\ \sigma_{S\theta}^{(k+1)} \end{pmatrix} = \begin{bmatrix} Q_{11}^{(k+1)} & Q_{12}^{(k+1)} & 0 \\ Q_{12}^{(k+1)} & Q_{22}^{(k+1)} & 0 \\ 0 & 0 & Q_{66}^{(k+1)} \end{bmatrix} \begin{bmatrix} \varepsilon_S^0 - z \frac{\partial^2 w}{\partial S^2} \\ \varepsilon_\theta^0 - z \left(\frac{1}{S^2} \frac{\partial^2 w}{\partial \theta_1^2} + \frac{1}{S} \frac{\partial w}{\partial S} \right) \\ \varepsilon_{S\theta}^0 - z \left(\frac{1}{S} \frac{\partial^2 w}{\partial S \partial \theta_1} - \frac{1}{S^2} \frac{\partial w}{\partial \theta_1} \right) \end{bmatrix} \quad (1)$$

where $\sigma_S^{(k+1)}, \sigma_\theta^{(k+1)}$ and $\sigma_{S\theta}^{(k+1)}$ are the stresses in the layers, ε_S^0 and ε_θ^0 are the normal strains in the curvilinear coordinate directions S and θ on the middle surface, respectively, whereas $\varepsilon_{S\theta}^0$ is the corresponding shear strain; $\theta_1 = \theta \sin \gamma$, w is the displacement of the middle surface in the normal direction, positive towards the axis of the cone and assumed to be much smaller than the thickness. The quantities $Q_{ij}^{(k+1)}$, $i, j = 1, 2, 3$, for orthotropic lamina are

$$\begin{aligned} Q_{11}^{(k+1)} &= \frac{E_{0S}^{(k+1)}}{1 - \nu_{S\theta}^{(k+1)} \nu_{\theta S}^{(k+1)}}, & Q_{22}^{(k+1)} &= \frac{E_{0\theta}^{(k+1)}}{1 - \nu_{S\theta}^{(k+1)} \nu_{\theta S}^{(k+1)}}, \\ Q_{12}^{(k+1)} &= \nu_{\theta S}^{(k+1)} Q_{11}^{(k+1)} = \nu_{S\theta}^{(k+1)} Q_{22}^{(k+1)}, \\ Q_{66}^{(k+1)} &= 2G_0^{(k+1)}, \quad k = 0, 1, 2, \dots, (N-1) \end{aligned} \quad (2)$$

in which $\nu_{S\theta}^{(k+1)}$ and $\nu_{\theta S}^{(k+1)}$ are the Poisson's ratios of the layer $k+1$.

The force and moment resultants are expressed by [6]

$$\begin{aligned} &[(N_S, N_\theta, N_{S\theta}), (M_S, M_\theta, M_{S\theta})] \\ &= \sum_{k=0}^{N-1} \int_{-h+k\delta}^{-h+(k+1)\delta} (I, z) [\sigma_S^{(k+1)}, \sigma_\theta^{(k+1)}, \sigma_{S\theta}^{(k+1)}] dz \end{aligned} \quad (3)$$

The relations between the forces N_S, N_θ and $N_{S\theta}$ and the stress function Ψ are given by

$$\begin{aligned} &(N_S, N_\theta, N_{S\theta}) \\ &= \left(\frac{1}{S^2} \frac{\partial^2 \Psi}{\partial \theta_1^2} + \frac{1}{S} \frac{\partial \Psi}{\partial S}, \frac{\partial^2 \Psi}{\partial S^2}, -\frac{1}{S} \frac{\partial^2 \Psi}{\partial S \partial \theta_1} + \frac{1}{S^2} \frac{\partial \Psi}{\partial \theta_1} \right) \end{aligned} \quad (4)$$

Substituting expressions (1) in (3) after some rearrangements, the relations found for moments and strains, being substituted into the modified Donnell type dynamic stability and strain compatibility equations of laminated orthotropic truncated conical shells [5], together with relation (4), and then considering the new variable $S = S_2 e^x$, after lengthy computations, can be written in the following matrix form:

$$\begin{bmatrix} L_{11} & L_{12} \\ L_{21} & L_{22} \end{bmatrix} \begin{bmatrix} \Psi \\ w \end{bmatrix} = 0 \quad (5)$$

where $L_{ij} (i, j = 1, 2)$ are differential operators and defined by follows:



$$\begin{aligned}
 L_{11} &= S_2 e^{-3x} \left[\frac{\partial^2}{\partial x^2} - \frac{\partial}{\partial x} \right] \cot \gamma \\
 L_{12} &= -A_{32} e^{-4x} \frac{\partial^4}{\partial \theta_1^4} - 2(A_{22} + A_{42}) e^{-4x} \frac{\partial^4}{\partial x^2 \partial \theta_1^2} \\
 &+ 4(A_{22} + A_{42}) e^{-4x} \frac{\partial^3}{\partial x \partial \theta_1^2} \\
 &- 2(A_{22} + A_{32} + A_{42}) e^{-4x} \frac{\partial^2}{\partial \theta_1^2} - A_{12} e^{-4x} \frac{\partial^4}{\partial x^4} \\
 &+ 4A_{12} e^{-4x} \frac{\partial^3}{\partial x^3} + (5A_{12} - A_{32}) e^{-4x} \frac{\partial^2}{\partial x^2} \\
 &+ 2(A_{12} - A_{32}) e^{-4x} \frac{\partial}{\partial x} - \rho_1 S_2^4 \frac{\partial^2}{\partial t^2} \\
 L_{21} &= A_{30} e^{-4x} \frac{\partial^4}{\partial \theta_1^4} + 2(L_0 / A_{40}) e^{-4x} \frac{\partial^4}{\partial x^2 \partial \theta_1^2} \\
 &- 4(L_0 / A_{40} - A_{10}) e^{-4x} \frac{\partial^3}{\partial x \partial \theta_1^2} \\
 &+ 2(L_0 / A_{40} - A_{20} + A_{30}) e^{-4x} \frac{\partial^2}{\partial \theta_1^2} + A_{10} e^{-4x} \frac{\partial^4}{\partial x^4} \\
 &- 4A_{10} e^{-4x} \frac{\partial^3}{\partial x^3} + 4A_{10} e^{-4x} \frac{\partial^2}{\partial x^2} + 2(A_{30} - A_{10}) e^{-4x} \frac{\partial}{\partial x} \quad (6) \\
 L_{22} &= L_0 S_2 e^{-3x} \left(\frac{\partial^2}{\partial x^2} - \frac{\partial}{\partial x} \right) \cot \gamma
 \end{aligned}$$

in which

$$\begin{aligned}
 A_{1k_1} &= h^{k_1+1} \sum_{k=0}^{N-1} \frac{E_{0S}^{(k+1)} \bar{h}^{(k+1)}}{1 - \nu_{S\theta}^{(k+1)} \nu_{\theta S}^{(k+1)}}, \\
 A_{2k_1} &= h^{k_1+1} \sum_{k=0}^{N-1} \frac{\nu_{\theta S}^{(k+1)} E_{0S}^{(k+1)} \bar{h}^{(k+1)}}{1 - \nu_{S\theta}^{(k+1)} \nu_{\theta S}^{(k+1)}}, \\
 A_{3k_1} &= h^{k_1+1} \sum_{k=0}^{N-1} \frac{E_{0\theta}^{(k+1)} \bar{h}^{(k+1)}}{1 - \nu_{S\theta}^{(k+1)} \nu_{\theta S}^{(k+1)}}, \\
 A_{4k_1} &= 2h^{k_1+1} \sum_{k=0}^{N-1} G_0^{(k+1)} \bar{h}^{(k+1)}, \\
 \bar{h}^{(k+1)} &= \int_{-1+2k/N}^{-1+2(k+1)/N} \bar{z}^{k_1} d\bar{z}, \rho_1 = 2h \sum_{k=0}^{N-1} \rho_0^{(k+1)} \\
 L_0 &= A_{10} A_{30} - (A_{20})^2, \quad k_1 = 0, 1, 2
 \end{aligned} \quad (7)$$

3. Solution of basic equations

For the present laminated conical shell, the freely supported (held circular but unrestrained axially) boundary conditions at both ends are considered and expressed as [14]

$$\begin{aligned}
 v = w = M_S = T_S = 0 \quad \text{at } S = S_1 (x = -x_0) \text{ and at} \\
 S = S_2 (x = 0)
 \end{aligned} \quad (8)$$

where v is displacement in the circumferential direction. The solution of the dynamic stability and compatibility equations (5) is sought in the following form [14]:

$$\begin{aligned}
 w &= \xi(t) e^{\lambda x} \sin(\beta_1 x) \cos(\beta_2 \theta_1) \\
 \Psi &= \zeta(t) S_2 e^{(\lambda+1)x} \sin(\beta_1 x) \cos(\beta_2 \theta_1)
 \end{aligned} \quad (9)$$

where λ is a parameter which is found from minimum conditions of frequencies, $\xi(t)$ and $\zeta(t)$ are time dependent amplitudes and the following definitions apply:

$$\beta_1 = \frac{\pi}{x_0}, \quad \beta_2 = \frac{n}{\sin \gamma}, \quad x_0 = \ln \frac{S_2}{S_1} \quad (10)$$

Multiplying the first equation of (5) by $w S_2^2 e^{2x} dx d\theta_1$ and the second equation of (5) by $\Psi S_2^2 e^{2x} dx d\theta_1$, for $0 \leq \theta_1 \leq 2\pi \sin \gamma$ and $-x_0 \leq x \leq 0$, applying the Galerkin method to equations (5), thus obtained, one gets

$$\int_0^{2\pi \sin \gamma} \int_{-x_0}^0 (L_{11} \Psi + L_{12} w) w S_2^2 e^{2x} dx d\theta_1 = 0 \quad (11)$$

$$\int_0^{2\pi \sin \gamma} \int_{-x_0}^0 (L_{21} \Psi + L_{22} w) \Psi S_2^2 e^{2x} dx d\theta_1 = 0 \quad (12)$$

Substituting Eqs. (9) into Eqs. (11) and (12) after some rearrangements, for the frequency of the free vibration, the following expression is obtained:

$$\omega_{TC} = \sqrt{\frac{1}{Q_4} \left(\frac{Q_1 Q_6}{Q_5} + Q_2 \right)} \quad (13)$$



where ω_{TC} is the frequency of laminated orthotropic truncated conical shells in radians per second, Q_i , ($i=1\div 6$) are depending on the materials and shell characteristics, see Ref. [14].

The dimensionless frequency parameter ω_{1TC} for the laminated orthotropic truncated conical shells with freely supported edges is defined as

$$\omega_{1TC} = \omega_{TC} R_2 \sqrt{(1 - \nu_{0S}^{(k+1)} \nu_{S0}^{(k+1)}) \rho_0^{(k+1)} / (E_{0S}^{(k+1)} E_{00}^{(k+1)})^{0.5}} \quad (14)$$

$k = 0, 1, 2, \dots, N-1$

The expressions (13) and (14) can be used for the study of laminated orthotropic complete conical and cylindrical shells with freely supported edges. The truncated conical shell is transformed into the complete conical shell when $R_1 \rightarrow 0$. In limiting case of zero cone half-angle ($\gamma \rightarrow 0$), the truncated conical shell is transformed into the cylindrical shell. When $k=0$, the laminated shells are transformed into single layer shells.

4. Numerical computations and results

To check the accuracy of the present work, a comparison with the results in open literature is made. The values of the fundamental frequency $f_{cyl} = \omega_{cyl} / (2\pi)$ (Hz) of freely supported laminated cylindrical shells are compared in Table 1 with solutions of Lam and Loy [10]. The laminated cylindrical shell considered in the present study is constructed of three isotropic layers of which the outer and inner layer are of the same material and the middle layer is of a different material. The layer dimensions and material properties for the laminated cylindrical shell are as follows: here L_1 is length of the cylindrical shell, h_i ($i=1,2,3$) thickness of the layers in m, E_i ($i=1,2,3$) Young's moduli of the layers in Pa, ν_i ($i=1,2,3$) Poisson ratio's of the layers, and ρ_i ($i=1,2,3$) mass densities of the layers in kg/m^3 . For both the inner and outer layers $h_1 = h_3 = 0.0008\text{m}$, $E_1 = E_3 = 4.8265 \times 10^9$ Pa, $\nu_1 = \nu_3 = 0.3$ and $\rho_1 = \rho_3 = 1314$ kg/m^3 ; for the middle layer, $h_2 = 0.0004\text{m}$, $E_2 = 2.0685 \times 10^{11}$ Pa, $\nu_2 = 0.3$ and $\rho_2 = 8053$ kg/m^3 . The comparisons show that the present results agree well with solutions of Lam and Loy [10].

Table 1. Comparison of values f_{cyl} (Hz) of a laminated cylindrical shell with different L_1/R ratios ($R/h=500$; $\gamma = \pi / 180000$)

L_1/R	Lam and Loy [10]	Present study
0.5	87.986(19)	88.195(19)
1.0	43.830(14)	44.066(14)
2.0	21.812(10)	22.029(10)
5.0	8.7522(6)	8.9658(6)

Numerical computations, for symmetric cross-ply laminated truncated conical shells with freely supported edges have been carried out using the expression (14). The material of lamina is assumed to be graphite/epoxy, with the following properties [2]

$$E_{0S}^{(k+1)} = 1.496 \times 10^{11} \text{ Pa}; E_{00}^{(k+1)} = 9.929 \times 10^9 \text{ Pa};$$

$$G_0^{(k+1)} = 4.482 \times 10^9 \text{ Pa}; \nu_{S0}^{(k+1)} = 0.28; k = 0, 3, 5, 7$$

After the various numerical computations and analyses for the fundamental frequency of freely supported cylindrical shells, truncated and complete conical shells, the following generalized values are obtained for the λ parameter: $\lambda=0$, $\lambda=1.2$, $\lambda=2.4$ respectively.

In Table 2, variations of dimensionless frequency parameters and corresponding circumferential wave numbers for symmetric cross-ply laminated orthotropic conical shells with four, six and eight layers are presented. It is easily observed that, as the number and ordering of the layers change, the effect of the values of the dimensionless frequency parameters are changed importantly. It is seen that the values of ω_{1CC} is lower than the values of ω_{1TC} . When laminated orthotropic truncated and complete conical shells are compared with single layer orthotropic truncated and complete conical shells, respectively; the highest effect of the arrangement of the layers on ω_{1TC} and ω_{1CC} , are (-21.6%) and (-31%), respectively, in the conical shells with laminations $(90/0)_S$ and $(90_2/0_2)_S$, whereas, the lowest effect on ω_{1TC} and ω_{1CC} is 0.7% in the conical shells with laminations $(0/90)_S$ and $(0/90_2)_S$.



Table 2. Variations of ω_{1TC} , ω_{1CC} and n_{cr} for orthotropic laminated truncated and complete conical shells with different number and ordering of layers ($R_1=1m$ and $R_1=10^{-50}\approx 0$; $R_2=2m$; $h=0.005m$; $\gamma=30^\circ$)

Stacking sequence	ω_{1TC} (n_{cr});	ω_{1CC} (n_{cr});
	$\lambda = 1.2$	$\lambda = 2.4$
Single layer(0)	0.171(5)	0.140(3)
(0/90) _S	0.160(6)	0.139(4)
(90/0) _S	0.208(5)	0.195(3)
(0 ₂ /90) _S	0.146(7)	0.125(5)
(0/90/0) _S	0.176(6)	0.156(4)
(0/90) _{2S}	0.172(6)	0.148(4)
(90/0) _{2S}	0.204(5)	0.191(4)
(90/0/90) _S	0.198(5)	0.184(4)
(90 ₂ /0) _S	0.206(5)	0.190(3)
(0 ₂ /90) _{2S}	0.160(6)	0.139(4)
(0/90) _{2S}	0.178(6)	0.156(4)
(0/90 ₂ /0) _S	0.186(6)	0.164(4)
(90/0 ₂ /90) _S	0.197(5)	0.179(4)
(90/0) _{2S}	0.201(5)	0.186(4)
(90 ₂ /0) _{2S}	0.208(5)	0.195(3)

The values in parentheses are the wave numbers

In Fig. 2, variations of dimensionless frequency parameters for symmetric cross-ply laminated orthotropic truncated conical shells with the semi vertex angle γ for different ordering of layers are presented. It can be seen that the values of ω_{1TC} increase for $10^\circ \leq \gamma \leq 50^\circ$ and decrease for $50^\circ < \gamma \leq 70^\circ$.

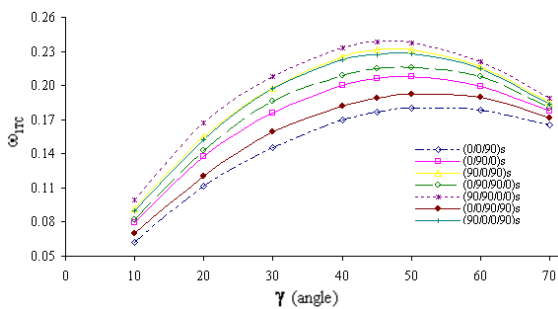


Fig. 2. Variations of ω_{1TC} for orthotropic laminated truncated conical shells with semi vertex angle γ for different ordering of layers ($R_1=1m$; $R_2=2m$; $h=0.005m$)

5. Conclusions

In this study, an analytical procedure is given to study the free vibration characteristics of symmetrically laminated orthotropic truncated conical shells with freely

supported edges. Applying Galerkin methods to the modified Donnell type stability and compatibility equations, the expression for the fundamental frequency parameters of laminated orthotropic conical shells are obtained. The appropriate formulas for single-layer and laminated cylindrical shells made of orthotropic and isotropic materials are found as a special case. Furthermore, parameter λ which is included in the obtained formulas is get from the minimum conditions of frequencies. Finally, the influences of the number and ordering of layers and the variations of the conical shells characteristics on the dimensionless frequency parameters are investigated.

Acknowledgement

First and fourth authors thank to TUBITAK for the support of the project with No: 108M322.

References

- [1] A. Kayran, & J.R. Vinson, *Free Vibration analysis of laminated composite truncated circular conical shells*, AIAA J 28, 1259-1269, 1990.
- [2] B. Han, & G.J. Simitses, *Analysis of anisotropic laminated cylindrical shells subjected to destabilizing loads Part II: Numerical results*, Compos Struct 19,183-205, 1991.
- [3] L. Tong, *Free vibration of composite laminated conical shells*, Int J Mech Sci 35, 47-61, 1993.
- [4] K.Y. Lam, & C.T. Loy, *Analysis of rotating laminated cylindrical shells by different thin shell theories*, J Sound Vibr 186, 23-35, 1995a.
- [5] A.H. Sofiyev, & E. Schnack, *The buckling of cross-ply laminated non-homogeneous orthotropic composite conical thin shells under a dynamic external pressure*. Acta Mech 162, 29-40, 2003.
- [6] J.N. Reddy, *Mechanics of laminated composite plates and shells: Theory and Analysis*, Second Ed, CRC Press, 2004.
- [7] S. Liang, H.L. Chen, T. Chen, Yu Michael, & M.Y. Wang, *The natural vibration of a symmetric cross-ply laminated composite conical-plate shell*, Compos Struct 80, 265-278, 2007.
- [8] W. Soedel, *A new frequency formula for closed circular cylindrical shells for a large variety of boundary conditions*, J Sound Vibr, 70:209-17, 1980.
- [9] T. Koga, *Effects of boundary conditions on the free vibrations of circular cylindrical shells*, AIAA J 26, 1387-1394, 1988.
- [10] K.Y. Lam, & C.T. Loy, *Effect of boundary conditions on frequencies of a multi-layered cylindrical shell*, J Sound Vibr 188, 363-384, 1995b.
- [11] M. El-Mously, *Fundamental natural frequencies of thin cylindrical shells: a comparative study*, J Sound Vibr 264:1167-1186, 2003.



- [12] E.I. Grigolyuk, *On small vibrations of thin elastic conical shells*, Communication of the Academy of Science of USSR, Section of Technical Science (OTN) 6, 35-44, 1956.
- [13] L.G. Aganesov, & A.V. Sachenkov, *The stability and vibration of circular conical and cylindrical shells at different boundary conditions*. Research on the Theory of Plates and Shells, Kazan State University, Kazan, 2, 111-126, 1964 [in Russian].
- [14] A.H. Sofiyev, *The vibration and stability behavior of freely supported FGM conical shells subjected to external pressure*, Compos Struct, 89, 3, 6-66, 2009.



About Some Methods of Calculation Nonlinear Oscillations in Machines

A.A.ALIFOV^{1*}

^{1*} Mechanical Engineering Research Institute, Russian Academy Sciences
(Russia, 101990, Moscow, Malij Haritonjevskij pereulok, 4)
alishir@mail.ru

Abstract

In overwhelming majority of methods of research of nonlinear oscillatory systems character (law) of required movement with which use the further analysis of the initial equations is carried out is usually set. Along with them there are also the methods which have been not based on character of required movement: method of straight linearization nonlinear forces of elasticity and resistance. They are effective enough because demand much less volume of calculations.

Keywords: Method, Nonlinear Oscillations, Linearization

1. Method of straight linearization nonlinear forces

Nonlinear force of elasticity can be linearized method of a straight linearization, described in work [1]. According to it is possible to replace nonlinear force of elasticity $f(x)$ linear $f_9(x) = \omega^2 x$. The method of a straight linearization nonlinear force of resistance is offered in work [2]. On this method, force of resistance, which is approximated usually a kind of polynomial

$$F(\dot{x}) = \sum_p b_p \dot{x} |\dot{x}|^{p-1}, \quad b_p = \text{const}, \quad (1)$$

it is possible to replace with linear force equivalent to it

$$F_9(\dot{x}) = k \dot{x}, \quad (2)$$

where \dot{x} – speed of movement.

The factor linearization k is defined under the formula

$$k = \sum_p b_p N_p v^{p-1}, \quad (3)$$

$$N_p = (2n+3)/(2n+2+p),$$

where v – the maximum value $|\dot{x}|$.

As shown in [2], the size n can be chosen from an interval $(0, 2)$ as N_p quickly enough changes approximately to $n = 2$. In the elementary case corresponding to identical importance of deviations irrespective of size \dot{x} , we have $n = 0$. If deviations are more essential at great values \dot{x} it is necessary to choose great values n .

On the basis of noted methods of a straight linearization it is possible to offer following simple and effective methods of calculation of nonlinear systems.

Let's consider these methods on an example of nonlinear system with one degree of freedom described by the equation of a general view

$$\ddot{x} + F(\dot{x}) + f(x) = H(t, x). \quad (4)$$

Here function (force) $H(t, x)$ can describe as excitation types (external, parametrical), and a class of mixed excitations [3], including external and parametrical excitation. Function $F(\dot{x})$ can possess properties of positive (damping) and negative (causing self-oscillation) friction. If function $F(\dot{x})$ possesses property of a negative friction the equation (4) can describe classes of mixed oscillations «the forced oscillations and self-oscillations», «parametrical oscillations and self-oscillations», «the forced oscillations, parametrical oscillations and self-oscillations». Thus, the equation of a general view (4) can describe, in particular, types of oscillations and all classes of the mixed oscillations.

Replacing nonlinear force of resistance $F(\dot{x})$ linear (2), and nonlinear force of elasticity $f(x)$ linear $\omega^2 x$, we will have the linearized equation

$$\ddot{x} + k \dot{x} + \omega^2 x = H(t, x), \quad (5)$$

where $k = k(v)$, $\omega = \omega(a)$, a – the maximum value $|x|$.



2. Method of the Linear Form

Such name of a method is connected by that for the decision of the equation (5) it is possible to use results of the analysis of the linear equation having the form (5). We will consider it on the basis of some special cases.

1) *Self-oscillations.* Let $H(t, x) \equiv 0$ that is

$$\ddot{x} + k \dot{x} + \omega^2 x = 0. \quad (6)$$

If to consider that the same kind the linear equation

$$\ddot{z} + k_0 \dot{z} + \omega_0^2 z = 0 \quad (7)$$

has the decision

$$z = A e^{-0.5k_0 t} \cos(p_0 t + \xi), \quad p_0 = \sqrt{\omega_0^2 - 0.25 k_0^2}$$

that decision linearized equation (6) can be written down the formally (proceeding from its "linear" form) so:

$$x = B e^{-0.5k(\nu)t} \cos(p_{\square} t + \xi),$$

$$p_{\square} = \sqrt{\omega^2(a) - 0.25 k^2(\nu)}. \quad (8)$$

From (8) at $k(\nu) = 0$ the boundary case of fading and not fading decisions follows. If function $F(\dot{x})$ possesses property of a negative friction the equation $k(\nu) = 0$ allows to define size ν at self-oscillations. Frequency of self-oscillations $p_{\square} = \omega(a)$ that follows from (8) at $k(\nu) = 0$.

The decision at self-oscillations taking into account (8) and that, as $\max |x| = a$, $\max |\dot{x}| = \nu$ looks like

$$x = a \cos \psi, \quad \dot{x} = -\nu \sin \psi,$$

$$\psi = p_{\square} t + \xi. \quad (9)$$

Differentiating the first expression (9) and comparing to the second, we will receive $\nu = a p_{\square}$ or

$$a \omega(a) = \nu. \quad (10)$$

Having defined ν from the equation $k(\nu) = 0$ and having substituted in (10), it is possible to find amplitude a . In particular, if force $f(x)$ linear frequency ω does not depend on amplitude, i.e., $\omega(a) = \omega_0$ whence follows $a = \nu / \omega_0$.

Thus, from (3) at $k(\nu) = 0$ we will receive a following equation for definition of the maximum value of speed ν at self-oscillations:

$$\sum_p b_p N_p \nu^{p-1} = 0. \quad (11)$$

Let's compare now the resulted results to the results received by other methods. With that end in view we use results of the analysis of self-oscillations by known methods. Let force of a friction is described by [3] function

$$T(U) = q(\operatorname{sgn} U - \alpha_1 U + \alpha_3 U^3), \quad U = V - \dot{x},$$

$$\operatorname{sgn} U = 1 (U > 0), \quad \operatorname{sgn} U = -1 (U < 0),$$

which at $V > \dot{x}$ it is possible to present in a kind

$$T(U) = T(V) + q(\alpha_1 - 3\alpha_3 V^2) \dot{x} + 3\alpha_3 q V \dot{x}^2 - \alpha_3 q \dot{x}^3.$$

From comparison (1) and the given expression follows $b_1 = q(\alpha_1 - 3\alpha_3 V^2)$, $b_3 = -\alpha_3 q$, $p = 1, 3$. Taking into account these expressions from (11) for $n = 1.5$ the formula

$$\nu^2 = 4(V_0^2 - V^2), \quad V_0^2 = \alpha_1 / 3\alpha_3, \quad (12)$$

which at $\nu = a\omega_0$ completely coincides received by methods of harmonious balance or averaging.

For $n = 1$ and $n = 2$ from the equation (11) formulas follow accordingly $\nu^2 = 21(V_0^2 - V^2)/5$, $\nu^2 = 27(V_0^2 - V^2)/7$, the relative mismatch of numerical factors (21/5 and 27/7) which with factor in the first formula (12) makes $\sim 4.7\%$ ($n=1$) and $\sim 3.6\%$ ($n=2$) that is not too great.

2) *The forced oscillations.* Let $H(t, x) \rightarrow H(t) = \lambda \sin \Omega t$ then the equation (5) will become

$$\ddot{x} + k \dot{x} + \omega^2 x = \lambda \sin \Omega t. \quad (13)$$

As well as above, we will remind that a similar kind linear system

$$\ddot{z} + k_0 \dot{z} + \omega_0^2 z = \lambda \sin \Omega t \quad (14)$$

has, as it is known, the following private decision for the forced oscillations:



$$z = A \sin(\Omega t + \xi),$$

$$A = \lambda / \sqrt{(\omega_0^2 - \Omega^2) + k_0^2 \Omega^2}. \quad (15)$$

The solution (13) on the basis of its "linear" form and that, as $\max|x| = a$, $\max|\dot{x}| = v$ it is possible to write down the decision in a kind

$$\begin{aligned} x &= a \sin \psi, & \dot{x} &= v \cos \psi, \\ \psi &= \Omega t + \xi, \end{aligned} \quad (16)$$

whence by analogy to a case for self-oscillations follows $v = a\Omega$.

From (13) with the account $v = a\Omega$ and (16) we will receive defining amplitude the formula

$$a = \lambda / \sqrt{(\omega^2 - \Omega^2)^2 + \Omega^2 k^2}, \quad (17)$$

coinciding under the form with expression for amplitude A in (15). Apparently, if functions $F(\dot{x})$ and $f(x)$ linear from expression (17) follows expressions for A .

If nonlinear function $F(\dot{x})$ describes a negative friction (a class of the mixed forced oscillations and self-oscillations) the formula (17) allows to define amplitude of grasped oscillations. It is easy to be convinced of it if, for example, to take function $F(\dot{x})$ in a kind leading (12). Then to define $k(v)$ on (3) and to substitute in (17). The parity deduced by such way coincides with received on a method of averaging and harmonious balance. In a case when force $F(\dot{x})$ dissipative, the formula (17) gives the chance to define amplitude of the nonlinear forced oscillations.

Similarly it is possible to define characteristics of parametrical oscillations and other classes of the mixed oscillations.

3. Method of replacement of variables with averaging

On the basis of the assumption of small forces we will enter into the equation (5) formally small parameter ε (such assumption is necessary for averaging carrying out) and we will present it in a kind

$$\ddot{x} + \omega^2 x = \varepsilon [H(t, x) - k \dot{x}] \equiv \varepsilon \bar{H}(t, x, \dot{x}). \quad (18)$$

Let's make in system (18) replacement of variables

$$x = v p_0^{-1} \cos \psi, \quad \dot{x} = -v \sin \psi,$$

$$\psi = p_0 t + \xi. \quad (19)$$

Differentiating the first expression (19) and considering the second, we will receive

$$\dot{\psi} \cos \psi = v \dot{\xi} \sin \psi. \quad (20)$$

Differentiating the second expression (19) and substituting in (18) we will receive taking into account (20) parities

$$\begin{aligned} \frac{dv}{dt} &= \frac{v(\omega^2 - p_0^2)}{p_0} \sin \psi \cos \psi - \varepsilon \bar{H}(\dots) \sin \psi, \\ \frac{d\xi}{dt} &= \frac{\omega^2 - p_0^2}{p_0} \cos^2 \psi - \frac{\varepsilon}{v} \bar{H}(\dots) \cos \psi. \end{aligned} \quad (21)$$

Assuming a difference of frequencies $|\omega^2 - p_0^2|$ of order ε it is possible to average (21) therefore (it is rejected ε) it is had

$$\frac{dv}{dt} = -\frac{kv}{2} - H_s(v, \xi), \quad (22)$$

$$\frac{d\xi}{dt} = \frac{\omega^2 - p_0^2}{2p_0} - \frac{1}{v} H_c(v, \xi),$$

$$H_s(v, \xi) = \frac{1}{2\pi} \int_0^{2\pi} H(\dots) \sin \psi d\psi,$$

$$H_c(v, \xi) = \frac{1}{2\pi} \int_0^{2\pi} H(\dots) \cos \psi d\psi.$$

Stationary movements are defined by the equations

$$0.5kv + H_s(v, \xi) = 0, \quad (23)$$

$$0.5v(\omega^2 - p_0^2)p_0^{-1} - H_c(v, \xi) = 0.$$

The equations (22) allow to study non-stationary processes, and the equations (23) to define characteristics of stationary oscillations. We will consider the cases again resulted above.

1) In a case $H(t, x) \equiv 0$ the first equation (22) at dissipative to force $F(\dot{x})$ defines bending around fading oscillations, at negative friction process of an establishment of self-oscillations. Parameters of stationary self-oscillations are from (23) at $H_s \equiv 0$, $H_c \equiv 0$, i.e. from parities $k(v) = 0$, $p_0 = \omega$ which coincide with received above for self-oscillations.



2) In a case $H(t, x) \rightarrow H(t) = \lambda \sin \Omega t$ it is had
 $H_s = 0.5 \lambda \cos \xi$, $H_c = -0.5 \lambda \sin \xi$ at $p_* = \Omega$.
From the equations (23) taking into account these expressions we will receive a parity for definition ν which at $\nu = a \Omega$ coincides with (17). We will notice that equality $\nu = a \Omega$ follows from (19) on the basis of that $\max |x| = a$.

Operating it is similarly possible to consider by means of (22) both (23) parametrical oscillations and classes of the mixed oscillations.

The stated methods as shows the analysis, can be used for calculation of nonlinear systems with several degrees of freedom, with shock influences, etc. Their basic difference from known that factors linearization are defined before search of the form of the decision, instead of after.

References

- [1]. Пановко Я.Г. *Введение в теорию механических колебаний*. – М.: Наука, 1971.
- [2]. Алифов А.А. *Действие вибраций на системы с нелинейным трением*. // «Техника», Баку, 2001, №4, с.47-51.
- [3]. A.A.Alifov, K.V. Frolov. *Interaction of nonlinear oscillatory systems with energy sources*. – Hemisphere Publishing Corporation; New York, Washington, Philadelphia, London. 1990.



On Function Generation of Watt I Mechanisms for Finger Design

John Q. SHEN^{1*}, Kevin RUSSELL², Raj S. SODHI³

^{1*}Power Control System Engineering,
ASCO Power Technologies,
Florham Park, NJ 07932, U.S.A,
john.shen@emerson.com

²Armaments Engineering and Technology Center,
U.S. Army Research, Development and Engineering Center,
Picatinny, NJ 07806, U.S.A

³New Jersey Institute of Technology,
Department of Mechanical Engineering,
Newark, NJ 07102, U.S.A

Abstract

This work includes a function generation model for the synthesis of a particular type of planar six-bar mechanism commonly used in mechanical finger design-the Watt I mechanism. Using the function generation method presented in this work, Watt I mechanical finger mechanisms are synthesized to approximate prescribed angular displacements of the human finger Metacarpophalangeal (MCP), Proximal Interphalangeal (PIP) and Distal Interphalangeal (DIP) joints. The examples included in this work demonstrate the synthesis of mechanical hands to achieve limited and expanded prescribed grasping sequences.

Keywords: Planar Mechanism, Six-Bar Linkage, Watt I Mechanism, Mechanical Finger, Function Generation

1. Introduction

Six Bar and multi-loop mechanism design includes the work of Simionescu and Smith [1] who presented a proof of the existence of function cognates of Stephenson II and Stephenson III mechanisms. Xiaohong and Ting [2] developed an approach for the branch identification of a variety of multi-loop linkages (including Watt and Stephenson chains). Todorov [3] presented a method for dimensional synthesis of symmetrical six-bar Watt mechanisms. Shiakolas, et al. [4] presented a methodology for the synthesis of six-bar mechanisms that combines differential evolution, an evolutionary optimization scheme and the geometric centroid of precision position technique. Watanabe and Katoh [5] considered every relationship between the input and output displacement (the domain of motion of the driving

link and the circuit) of the Stephenson III mechanism. Pramanik [6] synthesized a six-bar mechanism to achieve five precision points of an automotive steering mechanism. Baker [7, 8] investigated two specific groups of six-bar mechanisms and demonstrated a method for generating a family of six-bar folding mechanisms. Foster and Cipra [9] examined the problem of identifying assembly configurations of planar multi-loop mechanisms with joint limits, link interference, link collision and constraint regions. Kim, et al. [10] extended the matrix approach developed by Suh and Radcliffe [11] for the synthesis of six-bar mechanisms for path point generation.

When classifying published works on planar six-bar multi-loop mechanisms into those dedicated to **mechanism analysis** and those dedicated to **mechanism synthesis** (specifically for function generation) it becomes clear that far more work has been dedicated to the former as opposed to the latter. Two methods to synthesize a particular type of planar six-bar mechanism-the Watt I mechanism to approximate limited and expanded groups of prescribed MCP, PIP and DIP joint displacement angles are presented in this work. The methods and mechanism are effective in the design of finger mechanisms for robotic hands [12, 13, 15]. The Watt I mechanism has two closed loops, one degree of freedom, four binary links (and two ternary links) and is essentially a “stacked” arrangement of two planar four-bar mechanisms. The structure of this six-bar multi-loop mechanism is similar to the structure of the Belgrade/USC robotic hand [14, 15]. Unlike the works of Rodriguez, et al. [16] which consider force transmission and Gruver, et al. [17] which consider joint friction and transmission

efficiency for opening and grasping Watt I mechanical finger poses, this work considers an entire prescribed grasping sequence for the Watt I mechanical finger. Also, in this work, the finger dimensions are among the unknown parameters to be calculated unlike [16]. Unlike the works of Shen et al. [18, 19] on mechanical finger synthesis which consider prescribed *finger displacements* as input, this latest work considers *joint rotations* as input—a more easily measured and commonly applied parameter for mechanical finger design. Finally, this work extends the conventional function motion generation method of Suh and Radcliffe [11] to consider function generation of Watt I mechanisms unlike [16] and [17].

2. Watt I Finger Mechanism and Function Generation Model

Watt I Finger Mechanism

Figure 1 illustrates a mechanical finger incorporating the Watt I mechanism. For decades, empirical design methods have been used for this mechanism [12, 13, 14, 15]. Like the human finger, the mechanical finger has a proximal, middle and distal phalanx (and associated joints \mathbf{a}_0 , \mathbf{a}_1 and \mathbf{c}_1 respectively) and is capable of achieving extended and grasping positions (Fig. 2). By affixing several mechanical fingers to a rigid palm and thumb, a mechanical hand can be produced.

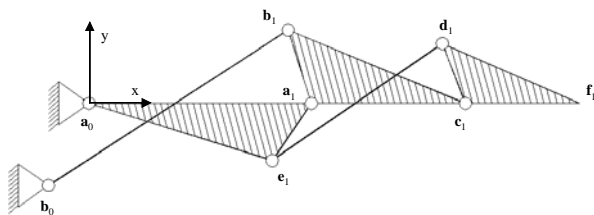


Fig. 1: The Watt I finger mechanism

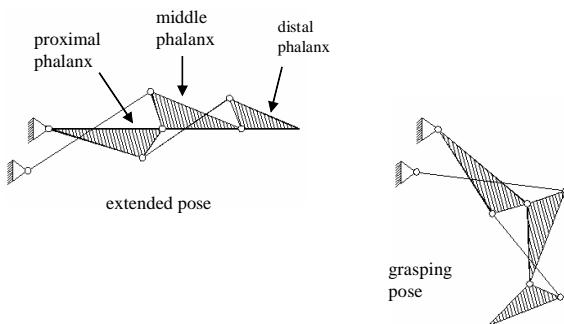


Fig. 2: Extended and arbitrary grasping poses

Synthesis Model for Watt I Function Generator-Limited Prescribed Displacement Angles

It is important that the Watt I finger mechanism be synthesized by way of prescribed rotation angles of finger joints [12] because a “data glove” (a motion tracking device that fits over the hand like a glove) typically measures PIP, MCP and DIP rotation angles. For the four-bar linkage $\mathbf{a}_0\text{-}\mathbf{a}_1\text{-}\mathbf{b}_1\text{-}\mathbf{b}_0$ in Fig. 1, the rotation angle of joint \mathbf{a}_0 is the rotation angle of link $\mathbf{a}_0\text{-}\mathbf{a}_1$ relative to ground (link $\mathbf{a}_0\text{-}\mathbf{b}_0$) and the rotation angle of joint \mathbf{a}_1 is the rotation angle of link $\mathbf{a}_1\text{-}\mathbf{b}_1$ relative to link $\mathbf{a}_0\text{-}\mathbf{a}_1$. Likewise, for the four-bar linkage $\mathbf{a}_1\text{-}\mathbf{c}_1\text{-}\mathbf{d}_1\text{-}\mathbf{e}_1$ in Fig. 1, the rotation angle of joint \mathbf{a}_1 is the rotation angle of link $\mathbf{a}_1\text{-}\mathbf{c}_1$ relative to link $\mathbf{a}_0\text{-}\mathbf{a}_1\text{-}\mathbf{e}_1$ and the rotation angle of joint \mathbf{c}_1 is the rotation angle of link $\mathbf{c}_1\text{-}\mathbf{d}_1$ relative to link $\mathbf{a}_1\text{-}\mathbf{c}_1$.

For the function generator illustrated in Fig. 3a, Eqns. (1) and (2) [11] are used to calculate four of the five unknown mechanism variables \mathbf{a}_1 , \mathbf{b}_1 and $L_{a_1b_1}$ where $\mathbf{a}_1=(a_{1x}, a_{1y})$, $\mathbf{b}_1=(b_{1x}, b_{1y})$ and $L_{a_1b_1}$ is the scalar link length. The remaining parameters of this function generator are $\mathbf{a}_0=(0, 0)$ and $\mathbf{b}_0=(1, 0)$. The prescribed rotation angles of the input crank $\mathbf{a}_0\mathbf{a}_1$ and output crank $\mathbf{b}_0\mathbf{b}_1$ are denoted by variables θ_{1j} and ϕ_{1j} respectively.

$$(\mathbf{a}_1 - \mathbf{b}_1)^T (\mathbf{a}_1 - \mathbf{b}_1) - L_{a_1b_1}^2 = 0 \quad (1)$$

$$([\mathbf{D}_{1j}] \mathbf{a}_1 - \mathbf{b}_1)^T ([\mathbf{D}_{1j}] \mathbf{a}_1 - \mathbf{b}_1) - L_{a_1b_1}^2 = 0 \quad j = 2, 3, 4 \quad (2)$$

where

$$[\mathbf{D}_{1j}] = \begin{bmatrix} \cos(\theta_{1j} - \phi_{1j}) & -\sin(\theta_{1j} - \phi_{1j}) & (1 - \cos \phi_{1j}) \\ \sin(\theta_{1j} - \phi_{1j}) & \cos(\theta_{1j} - \phi_{1j}) & \sin \phi_{1j} \\ 0 & 0 & 1 \end{bmatrix}$$

To utilize Eqns. (1) and (2) for synthesizing a Watt I finger mechanism, a modified four-bar function generator model is required where a new $\mathbf{X}'\mathbf{Y}'$ coordinate system is fixed on the input crank $\mathbf{a}_0\text{-}\mathbf{a}_1$ and the mechanism is inverted as shown in Fig. 3b. In the $\mathbf{X}'\mathbf{Y}'$ coordinate system, the four-bar linkage becomes a function generator where link $\mathbf{a}_0\text{-}\mathbf{b}_0$ is the input crank, link $\mathbf{a}_0\text{-}\mathbf{a}_1$ is the ground, link $\mathbf{b}_0\text{-}\mathbf{b}_1$ is the coupler, and link $\mathbf{a}_1\text{-}\mathbf{b}_1$ is the output crank. Equations (3) and (4) are used with respect to the $\mathbf{X}'\mathbf{Y}'$ coordinate system to calculate four of the five unknown variables \mathbf{b}_0 , \mathbf{b}_1 and $L_{b_0b_1}$ (see Fig. 4) given prescribed values for joint rotation angles θ^{a_0} and θ^{a_1} . In Eqns. (3) and (4), $\mathbf{b}_0=(b'_{0x}, b'_{0y})$, $\mathbf{b}_1=(b'_{1x}, b'_{1y})$, $\mathbf{a}_0=(0, 0)$

and $\mathbf{a}_1=(1, 0)$. Variable $L_{b_0b_1}$ in Eqns. (3) and (4) is the scalar link length.

$$(\mathbf{b}_0 - \mathbf{b}_1)^T (\mathbf{b}_0 - \mathbf{b}_1) - L_{b_0b_1}^2 = 0 \quad (3)$$

$$([\mathbf{D}_{1j}] \mathbf{b}_0 - \mathbf{b}_1)^T ([\mathbf{D}_{1j}] \mathbf{b}_0 - \mathbf{b}_1) - L_{b_0b_1}^2 = 0 \quad j = 2, 3, 4 \quad (4)$$

where

$$[\mathbf{D}_{1j}] = \begin{bmatrix} \cos(\theta_{1j}^{a_0} - \theta_{1j}^{a_1}) & -\sin(\theta_{1j}^{a_0} - \theta_{1j}^{a_1}) & (1 - \cos \theta_{1j}^{a_1}) \\ \sin(\theta_{1j}^{a_0} - \theta_{1j}^{a_1}) & \cos(\theta_{1j}^{a_0} - \theta_{1j}^{a_1}) & \sin \theta_{1j}^{a_1} \\ 0 & 0 & 1 \end{bmatrix}$$

Equations (5) and (6) are used to calculate four of the five unknown parameters \mathbf{e}_1 , \mathbf{d}_1 , and $L_{e_1d_1}$ (see Fig. 6) given prescribed values for rotation angles θ^{a_1} and θ^{c_1} . In Eqns. (5) and (6), $\mathbf{e}_1=(e_{1x}, e_{1y})$, $\mathbf{d}_1=(d_{1x}, d_{1y})$, $\mathbf{a}'_1=(0, 0)$, and $\mathbf{c}_1=(1, 0)$. Variable $L_{e_1d_1}$ in Eqns. (5) and (6) is the scalar link length.

$$(\mathbf{e}_1 - \mathbf{d}_1)^T (\mathbf{e}_1 - \mathbf{d}_1) - L_{e_1d_1}^2 = 0 \quad (5)$$

$$([\mathbf{S}_{1j}] \mathbf{e}_1 - \mathbf{d}_1)^T ([\mathbf{S}_{1j}] \mathbf{e}_1 - \mathbf{d}_1) - L_{e_1d_1}^2 = 0 \quad j = 2, 3, 4 \quad (6)$$

where

$$[\mathbf{S}_{1j}] = \begin{bmatrix} \cos(\theta_{1j}^{a_1} - \theta_{1j}^{c_1}) & -\sin(\theta_{1j}^{a_1} - \theta_{1j}^{c_1}) & (1 - \cos \theta_{1j}^{c_1}) \\ \sin(\theta_{1j}^{a_1} - \theta_{1j}^{c_1}) & \cos(\theta_{1j}^{a_1} - \theta_{1j}^{c_1}) & \sin \theta_{1j}^{c_1} \\ 0 & 0 & 1 \end{bmatrix}$$

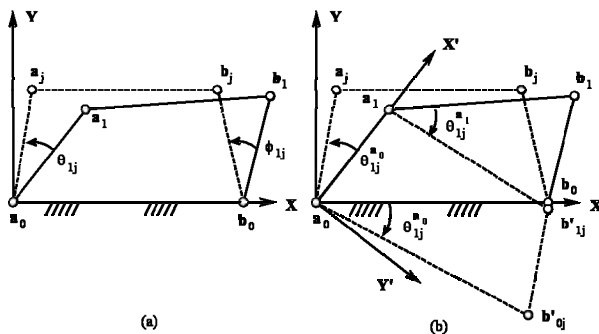


Fig. 3 : Conventional (a) and inverted (b) four-bar function generators

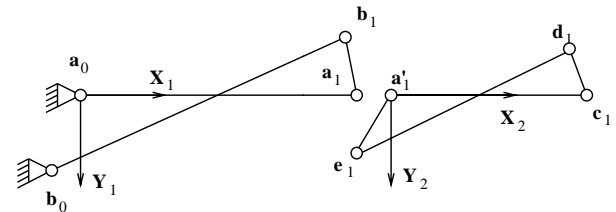


Fig. 4 : Modified function generation layout for Watt I finger mechanism

To synthesize the Watt I finger mechanism, two four-bar function generators are synthesized in the established $\mathbf{X}_1\mathbf{Y}_1$ and $\mathbf{X}_2\mathbf{Y}_2$ coordinate systems as illustrated in Fig. 4 using Eqns. (3)~(6). The user has the option to uniformly scale the calculated four-bar mechanism solution to satisfy any finger size or proportionality requirements. To assemble the two four-bar mechanism solutions into a single Watt I finger mechanism, joint \mathbf{a}'_1 is merged to joint \mathbf{a}_1 and ternary links $\mathbf{a}_0\text{-}\mathbf{a}_1\text{-}\mathbf{e}_1$ and $\mathbf{a}_1\text{-}\mathbf{b}_1\text{-}\mathbf{c}_1$ are formed. Equations (3)~(6) constitute a model to synthesize a Watt I finger mechanism to approximate a set of three prescribed displacement angles for the PIP, MCP DIP joints.

Synthesis Model for Watt I Function Generator-Expanded Prescribed Displacement Angles

With Eqns. (3)~(6), the user is limited to a maximum of three prescribed angular displacements per joint for synthesis. The equation sets included in this section are applicable for an indefinite number of prescribed angular displacements (and subsequent grasping poses) beyond three.

Equation (7) is the objective function (to be minimized) incorporating Eqns. (3) and (4). The form of this objective function resembles the “best fit” criteria from the method of least squares [18] and can theoretically accommodate an indefinite number of prescribed joint displacement angles. When Eqn. (7) is minimized, its constant link length constraints are satisfied. Eqn. (8) is the minimization condition for the objective function. Equations (9)~(12) are the matrix cells in Eqn. (8). These equations will be used to calculate four of the five unknowns for the link defined by parameters \mathbf{b}_0 , \mathbf{b}_1 and $L_{b_0b_1}$ (see Fig. 6) given the parameters for N prescribed joint displacement angle groups defined by variables θ^{a_0} and θ^{a_1} .



$$f(\mathbf{x}) = \sum_{j=1}^N \left(([\mathbf{D}_{1j}] \mathbf{b}_0 - \mathbf{b}_1)^T ([\mathbf{D}_{1j}] \mathbf{b}_0 - \mathbf{b}_1) - L_{b_0b_1}^2 \right)^2, \quad (7)$$

$$\mathbf{x} = \begin{pmatrix} x_1 \\ x_2 \\ x_3 \\ x_4 \\ x_5 \end{pmatrix} = \begin{pmatrix} b_{0x} \\ b_{0y} \\ b_{1x} \\ b_{1y} \\ L_{b_0b_1} \end{pmatrix}$$

$$f(\mathbf{x}) = \sum_{j=1}^N \left(([\mathbf{S}_{1j}] \mathbf{e}_1 - \mathbf{d}_1)^T ([\mathbf{S}_{1j}] \mathbf{e}_1 - \mathbf{d}_1) - L_{e_1d_1}^2 \right)^2, \quad (13)$$

$$\mathbf{x} = \begin{pmatrix} x_1 \\ x_2 \\ x_3 \\ x_4 \\ x_5 \end{pmatrix} = \begin{pmatrix} e_{1x} \\ e_{1y} \\ d_{1x} \\ d_{1y} \\ L_{e_1d_1} \end{pmatrix}$$

$$\nabla f(\mathbf{x}) = \begin{pmatrix} \frac{\partial f(\mathbf{x})}{\partial x_1} \\ \vdots \\ \frac{\partial f(\mathbf{x})}{\partial x_4} \end{pmatrix} = 0 \quad (8)$$

$$\nabla f(\mathbf{x}) = \begin{pmatrix} \frac{\partial f(\mathbf{x})}{\partial x_1} \\ \vdots \\ \frac{\partial f(\mathbf{x})}{\partial x_4} \end{pmatrix} = 0 \quad (14)$$

$$\frac{\partial}{\partial b_{0x}} \sum_{j=1}^N \left(([\mathbf{D}_{1j}] \mathbf{b}_0 - \mathbf{b}_1)^T ([\mathbf{D}_{1j}] \mathbf{b}_0 - \mathbf{b}_1) - L_{b_0b_1}^2 \right)^2 = 0 \quad (9)$$

$$\frac{\partial}{\partial e_{1x}} \sum_{j=1}^N \left(([\mathbf{S}_{1j}] \mathbf{e}_1 - \mathbf{d}_1)^T ([\mathbf{S}_{1j}] \mathbf{e}_1 - \mathbf{d}_1) - L_{e_1d_1}^2 \right)^2 = 0 \quad (15)$$

$$\frac{\partial}{\partial b_{0y}} \sum_{j=1}^N \left(([\mathbf{D}_{1j}] \mathbf{b}_0 - \mathbf{b}_1)^T ([\mathbf{D}_{1j}] \mathbf{b}_0 - \mathbf{b}_1) - L_{b_0b_1}^2 \right)^2 = 0 \quad (10)$$

$$\frac{\partial}{\partial e_{1y}} \sum_{j=1}^N \left(([\mathbf{S}_{1j}] \mathbf{e}_1 - \mathbf{d}_1)^T ([\mathbf{S}_{1j}] \mathbf{e}_1 - \mathbf{d}_1) - L_{e_1d_1}^2 \right)^2 = 0 \quad (16)$$

$$\frac{\partial}{\partial b_{1x}} \sum_{j=1}^N \left(([\mathbf{D}_{1j}] \mathbf{b}_0 - \mathbf{b}_1)^T ([\mathbf{D}_{1j}] \mathbf{b}_0 - \mathbf{b}_1) - L_{b_0b_1}^2 \right)^2 = 0 \quad (11)$$

$$\frac{\partial}{\partial d_{1x}} \sum_{j=1}^N \left(([\mathbf{S}_{1j}] \mathbf{e}_1 - \mathbf{d}_1)^T ([\mathbf{S}_{1j}] \mathbf{e}_1 - \mathbf{d}_1) - L_{e_1d_1}^2 \right)^2 = 0 \quad (17)$$

$$\frac{\partial}{\partial b_{1y}} \sum_{j=1}^N \left(([\mathbf{D}_{1j}] \mathbf{b}_0 - \mathbf{b}_1)^T ([\mathbf{D}_{1j}] \mathbf{b}_0 - \mathbf{b}_1) - L_{b_0b_1}^2 \right)^2 = 0 \quad (12)$$

$$\frac{\partial}{\partial d_{1y}} \sum_{j=1}^N \left(([\mathbf{S}_{1j}] \mathbf{e}_1 - \mathbf{d}_1)^T ([\mathbf{S}_{1j}] \mathbf{e}_1 - \mathbf{d}_1) - L_{e_1d_1}^2 \right)^2 = 0 \quad (18)$$

Equation (13) is the objective function (to be minimized) incorporating Eqns. (5) and (6) and is identical in formulation as Eqn. (7). When Eqn. (13) is minimized, its constant link length constraints are satisfied. Equation (14) is the minimization condition for the objective function. Equations (15)~(18) are the matrix cells in Eqn. (14). These equations will be used to calculate four of the five unknowns for the link defined by parameters \mathbf{e}_1 , \mathbf{d}_1 , and $L_{e_1d_1}$ (see Fig. 6) given the parameters for N prescribed joint displacement angle groups defined by variables θ^{a_1} and θ^{c_1} .

3. Function Generation Examples

Limited Prescribed Displacement Angles

Table 1 includes the three prescribed MCP, PIP and DIP joint displacement angles. These rotation angles represent the prescribed finger grasping sequence. The design objective here is to synthesize a Watt I finger mechanism to approximate the prescribed grasping sequence.

Using Eqns. (3) and (4) with the initial guesses $\mathbf{b}_0 = (-0.1, 0.1)$, $\mathbf{b}_1 = (0.6, -0.1)$ and the specified value of $L_{b_0b_1} = 1.3$, the calculated values are $\mathbf{b}_0 = (-0.2754, 0.1138)$ and $\mathbf{b}_1 = (1.0040, -0.1167)$. Using Eqns. (5) and (6) with the prescribed values $\mathbf{e}_1 = (-0.1, 0.1)$, $\mathbf{d}_1 = (0.6, -0.1)$ and the



specified value of $L_{e1d1} = 1.4$, the calculated values are $e_1 = (-0.1864, 0.0669)$, $d_1 = (1.1919, -0.1785)$.

To make a more proportional Watt I finger mechanism, results of the first four-bar mechanism solution are uniformly scaled by a factor of 3.1257 and the second solution by a factor of 2.3687. Mechanism assembly consists of merging pivot a_1' to a_1 , connecting pivot e_1 to a_0 and pivot b_1 to c_1 to produce a Watt I finger mechanism in the extended position. After mechanism scaling and assembly, the calculated values are $a_0=(0, 0)$, $a_1=(3.1257, 0)$, $b_0=(-0.8608, -0.3558)$, $b_1=(3.1382, 0.3649)$, $c_1=(5.4944, 0)$, $e_1=(2.6842, -0.1585)$, $d_1=(5.9490, 0.4229)$, and $f_1=(6.8625, 0)$ in the **XY** coordinate system. The approximated grasping poses (Fig. 5) and corresponding joint rotation angles (Fig. 6, Table 2) were measured using a virtual model of the synthesized finger mechanism developed in MATLAB's SimMechanics module.

By affixing several Watt I finger mechanisms to a rigid palm and thumb, a mechanical hand is produced. Fig. 7 illustrates a mechanical hand (comprised of the synthesized mechanical finger) in the extended and final grasping pose.

Table 1. Prescribed joint rotation angles (in degrees)

	θ^{a_0} (MCP)	θ^{a_1} (PIP)	θ^{c_1} (DIP)
Pos 2	16	14	6
Pos 3	21	21	12
Pos 4	26	30	33

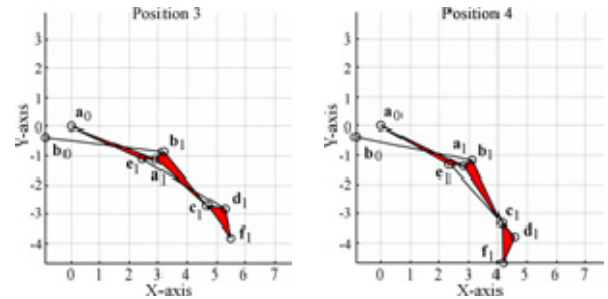
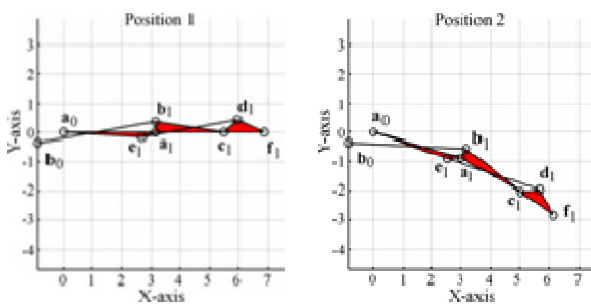


Fig. 5: Synthesized finger mechanism grasping poses (in MATLAB SimMechanics)

Fig. 6: Synthesized finger mechanism joint rotation angles (in MATLAB SimMechanics)

Table 2. Joint rotation angles achieved by the synthesized Watt I finger mechanism (in degrees).

	θ^{a_0} (MCP)	θ^{a_1} (PIP)	θ^{c_1} (DIP)
Pos 2	16	13.9999	5.9999
Pos 3	21	20.9999	11.9999
Pos 4	26	29.9999	32.9999

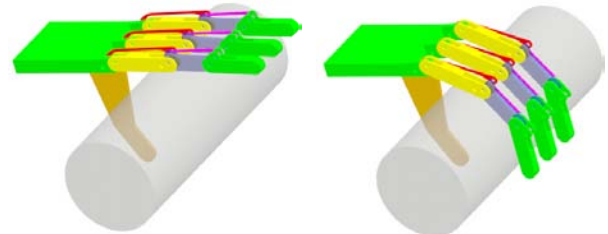


Fig. 7: Synthesized mechanical hand in extended (left) and grasping (right) positions

Expanded Prescribed Displacement Angles

Table 3 includes six prescribed MCP, PIP and DIP displacement angles. This is twice the number of

displacement angles used in the previous example. The design objective here is to synthesize a Watt I finger mechanism to approximate the expanded prescribed grasping sequence.

Using Eqns. (9)~(12) with the initial guesses $\mathbf{b}_0 = (-0.1, 0.6)$, $\mathbf{b}_1 = (0.9, -0.1)$ and $L_{bob1} = 1.3$, the calculated values are $\mathbf{b}_0 = (-0.1693, 0.3572)$, $\mathbf{b}_1 = (0.9656, -0.1102)$, and $L_{bob1} = 1.2273$. Using Eqns. (15)~(18) with the prescribed values $\mathbf{e}_1 = (-0.4, 0.4)$, $\mathbf{d}_1 = (0.8, -0.3)$ and $L_{eld1} = 1.4$, the calculated values are $\mathbf{e}_1 = (-0.4648, 0.1021)$, $\mathbf{d}_1 = (0.8751, -0.1098)$, and $L_{eld1} = 1.3571$.

To make a more proportional Watt I finger mechanism, results of the first four-bar mechanism solution are uniformly scaled by a factor of 4.4498 and the second solution by a factor of 2.7452. Mechanism assembly consists of merging pivot \mathbf{a}_1' to \mathbf{a}_1 , connecting pivot \mathbf{e}_1 to \mathbf{a}_0 and pivot \mathbf{b}_1 to \mathbf{c}_1 to produce a Watt I finger mechanism in the extended position. After mechanism scaling and assembly, the calculated values are $\mathbf{a}_0 = (0, 0)$, $\mathbf{a}_1 = (4.4498, 0)$, $\mathbf{b}_0 = (-0.7532, -1.5893)$, $\mathbf{b}_1 = (4.2966, 0.4905)$, $\mathbf{c}_1 = (7.1950, 0)$, $\mathbf{e}_1 = (3.1738, -0.2802)$, $\mathbf{d}_1 = (6.8522, 0.3015)$, and $\mathbf{f}_1 = (8.7, 0)$ in the XY coordinate system. The approximated grasping poses (Fig. 8) and corresponding joint rotation angles (Fig. 9, Table 4) were measured using a virtual model of the synthesized finger mechanism developed in MATLAB's SimMechanics module.

By affixing several Watt I finger mechanisms to a rigid palm and thumb, a mechanical hand is produced. Fig. 10 illustrates a mechanical hand (comprised of the synthesized mechanical finger) in the extended and grasping poses.

Table 3. Prescribed joint rotation angles (in degrees)

	θ^{a_0} (MCP)	θ^{a_1} (DIP)	θ^{c_1} (DIP)
Pos 2	2.5	6	2.5
Pos 3	5	12	5
Pos 4	7.5	19	11
Pos 5	10	26.5	17.5
Pos 6	12.5	35	26
Pos 7	15	45	41

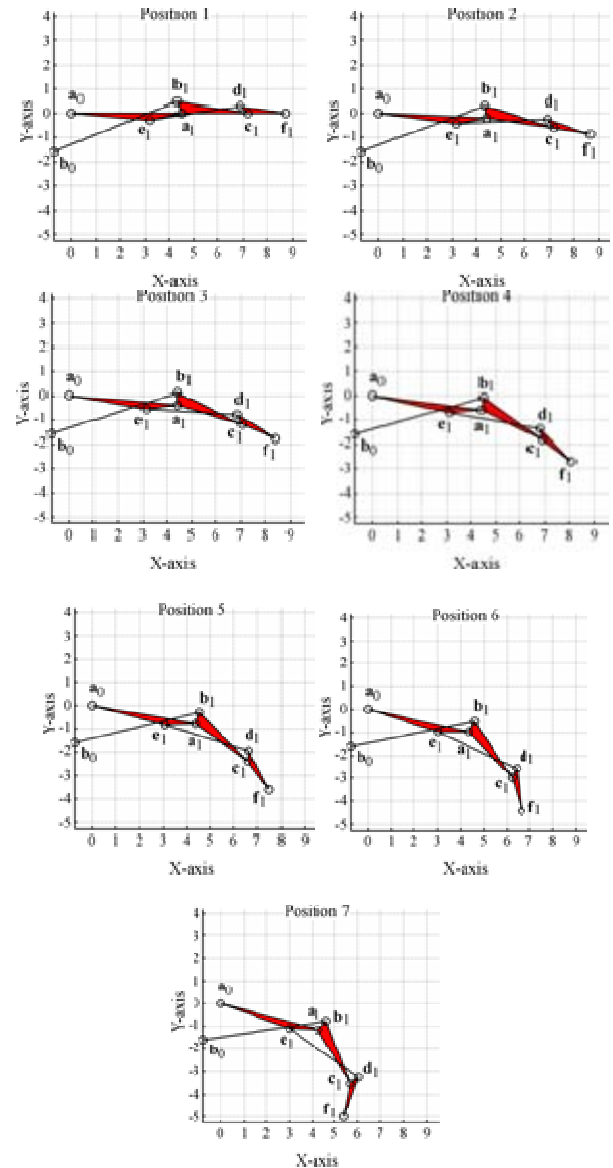


Fig. 8: Synthesized finger mechanism grasping poses (in MATLAB SimMechanics)

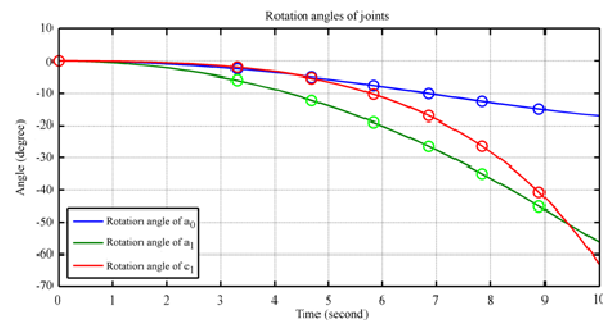


Fig. 9: Synthesized finger mechanism joint rotation angles (in MATLAB SimMechanics)



Table 4. Joint rotation angles achieved by the synthesized finger mechanism (in degrees).

	θ^{a_0} (MCP)	θ^{a_1} (PIP)	θ^{c_1} (DIP)
Pos 2	2.5	5.9263	1.9591
Pos 3	5	12.2191	5.3227
Pos 4	7.5	19.0055	10.2195
Pos 5	10	26.4766	16.9849
Pos 6	12.5	34.9551	26.4244
Pos 7	15	45.0867	40.7187

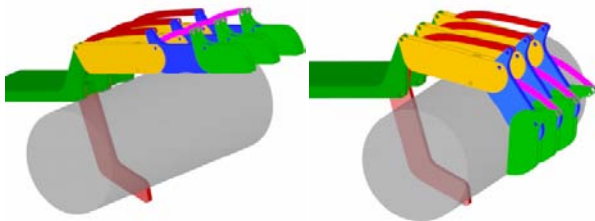


Fig. 10: Synthesized mechanical hand in extended (left) and grasping (right) positions

4. Discussion

The solution data in the Example section were calculated using the mathematical analysis software MATLAB and were expressed to four decimal places. The SimMechanics module in MATLAB was used to independently confirm the achieved grasping poses, driver displacement angles and check for singularity throughout the grasping poses of the synthesized Watt I finger mechanisms. Although the authors limited the number of prescribed grasping poses in Example 3.2 to six (twice the number of poses in Example 3.1), Eqns. (9)~(12) and (15)~(18) can theoretically incorporate an indefinite number of prescribed grasping poses.

5. Conclusion

Two models to synthesize Watt I function generators to approximate limited and expanded groups of prescribed finger joint displacement angles are formulated in this work. These two models were demonstrated to be effective in the synthesis of mechanical hands to approximate sets of limited and expanded grasping poses.

References

[1]. P.A. Simionescu and M.R. Smith, *Four and six bar function cognates and overconstrained mechanism*, Mechanism and Machine Theory 36, pages 913–924, 2001.

[2]. D. Xiaohong and K. Ting, *Module approach for branch analysis of multi-loop linkages/manipulator*, Mechanism and Machine Theory 33, pages 565–582, 1998.

[3]. T.S. Todorov, *Synthesis of Watt's six link mechanism for manipulation action in relative space*, Mechanism and Machine Theory 32, pages 559–568, 1997.

[4]. P.S. Shiakolas, D. Koladiya and J. Kebrle, *On the optimum synthesis of six bar linkages using differential evolution and the geometric centroid of precision positions technique*, Mechanism and Machine Theory 40, pages 319–335, 2005.

[5]. K. Watanabe and H. Katoh, *Identification of motion domains of planar six link mechanisms of Stephenson type*, Mechanism and Machine Theory 39, pages 1081–1099, 2004.

[6]. S. Pramanik, *Kinematic synthesis of a six member mechanism for automotive steering*, Journal of Mechanical Design 124, pages 642–645, 2002.

[7]. J.E. Baker, *A curious new family of overconstrained six bars*, Journal of Mechanical Design 127, pages 602–606, 2005.

[8]. J.E. Baker, *On generating a class of foldable six-bar spatial linkages*, Journal of Mechanical Design 128, pages 374–383, 2006.

[9]. D.E. Foster and R.J. Cipra, *Assembly configurations of planar multi-loop mechanisms with kinematic limitations*, Journal of Mechanical Design 128, pages 747–754, 2006.

[10]. H.S. Kim, S. Hamid and A.H. Soni, *Synthesis of six-link mechanisms for path point generation*, Journal of Mechanisms 6, pages 447–461, 1971.

[11]. C.H. Suh and C.W. Radcliffe, *Kinematics and Mechanism Design*. John Wiley and Sons; New York, 1978.

[12]. R. Vinet, Y. Lozac'h, N. Beaudry and G. Drouin, *Design methodology for a multifunctional hand prosthesis*, Journal of Rehabilitation Research and Development 32, pages 316–324, 1995.

[13]. N. Dechev, W.L. Cleghorn and S. Naumann, *Thumb design of an experimental prosthetic hand*, Proceedings of the 2nd International Symposium of Robotics and Automation, Monterrey, N.L., Mexico, 2008.

[14]. G.A. Bekey, R. Tomovic and I. Zeljkovic, *Control architecture for the Belgrade/USC hand, Dextrous Robot Hands*, Springer-Verlag; New York, pages 136–149, 1990.

[15]. J.K. Salisbury and J.J. Craig, *Articulated hands: force control and kinematic issue*, International Journal of Robotic Research 1, pages 4–17, 1982.

[16]. N.E.N. Rodriguez, G. Carbone and M. Ceccarelli, *Optimal design of driving mechanism in a 1 dof anthropomorphic finger*, Mechanism and Machine Theory 41, pages 879–911, 2006.

[17]. J. Zhang, G. Guo and W.A. Gruver, *Optimal design of a six-bar linkage for an anthropomorphic three-jointed finger mechanism*, Proceedings of the ASME Mechanisms Conference, Phoenix, Arizona, 1992.

[18]. Q. Shen, K. Russell, W. Lee and R.S. Sodhi, *On mechanical finger design for expanded prescribed grasping poses*, Journal of Advanced Mechanical Design Systems and Manufacturing 2, pages 903–914, 2008.

[19]. Q. Shen, K. Russell, W. Lee and R.S. Sodhi, *On motion generation of Watt I mechanisms for mechanical finger design*, Transactions of the Canadian Society for Mechanical Engineering 32, pages 411–421, 2008.

[20]. S. C. Chapra and R. P. Canale, *Numerical Methods for Engineers*. McGraw-Hill; New York, 1998.



A New Geometric Algorithm for Workspace Analysis in Planar 3-RRR Manipulator

Özgür KİLİT^{1*}, Sedat SAVAŞ²

^{1*} Mechanical Engineering Department,
Ege University, Bornova 35100, Izmir, Turkey

ozgurkilit@gmail.com

² Graduate Student, Graduate School of Natural and Applied Science,
Ege University, Bornova 35100, Izmir, Turkey

savasedat@yahoo.com

Abstract

Workspace analysis plays an important role in the inverse kinematics of the robots, especially in path programming of the parallel robots. This paper presents a methodology for the determination of the workspace of 3-RRR type PPM (Planar Parallel Manipulator) with revolute joints based on sweep operations in solid modeling tools. In this method, workspace volume is simply derived by a pure geometrical way without need for objective function derivation or any code for numerical calculation.

Keywords: PPM (Planar Parallel Manipulator), Workspace, Sweep Operation, Intersection.

1. Introduction

Workspace analysis is a very important issue in inverse kinematic analysis, especially for emphasizing the reaching capabilities of the mechanism's end-effector. There are several methods used for workspace analysis. Gosselin *et. al.* [1] investigated workspace of closed loop kinematic chains with the method of singularity analysis and this method was also expanded to workspace problems of platform type 6-DOF mechanisms. Bonev *et. al.* [2] worked on singularity analysis 3-DOF planar parallel mechanisms via screw theory in all working modes. In other study, Glozman *et. al.*[3] reported a workspace comparison of his newly promoted 6-DOF mechanism with Eclipse [4], Alizade [5], Delta [6] and Hexa [7] robots. These comparisons were only made as translational (constant orientation) workspace.

Paternell *et. al.* [8] reported an approximation of the boundary surface of the solid volume as a smooth one-parameter swept surface. Merlet [9], on the other hand, recommended using a numerical solution method of interval analysis in workspace analysis. This method is a guaranteed method in equation solving procedure without

risk of local minima problem. But the main drawbacks are pixel-based (non-smooth) workspace volume and exhaustive CPU time.

([†]) Corresponding author

Although there are many methods, e.g., vector loop equations, numerical calculations, Jacobian matrix and singularity methods, to determine the workspace of 3-RRR planar manipulators, we, in this study, propose a new geometric approach for workspace analysis completely depends on the simple solid modelling routines in any standard CAD (Computer Aided Design) software. This method is based on swept volume approach. Workspace of the platform has three independent degrees of freedom (two translational and one rotational). In order to show these three parameters on the same graphics, it is assumed, in this study, that one of the axes shows the rotation angle of the platform. In this way, it becomes possible to present the completely planar workspace of the platform as a solid body. Once a mathematically defined solid workspace is gained, any workspace scenarios, such as, an obstacle-free workspace, path planning or P&P (pick and place) applications can be reached by simple Boolean (union, subtraction and intersection) operations in solid modelling. The main contribution of this study is to provide an intuitive and very simple geometrical way to the designer, requiring what-if scenarios of 3-RRR PPMs without having mathematical background.

2. 3-RRR PPMs (Planar Parallel Manipulators)

A planar manipulator is a system of rigid bodies assembled so that the end-effector moves on a plane and rotates about a vector perpendicular to this plane. The 3-RRR all revolute joint planar parallel manipulator is a three legged platform manipulator that is constructed so

that the all joint axes are parallel (Fig. 1). A_i joints are active joints and connected to the fixed frame, B_i s are passive joints and C_i s are the joints connected to the moving platform. $\{F\}$ is fixed and $\{M\}$ is moving frames.

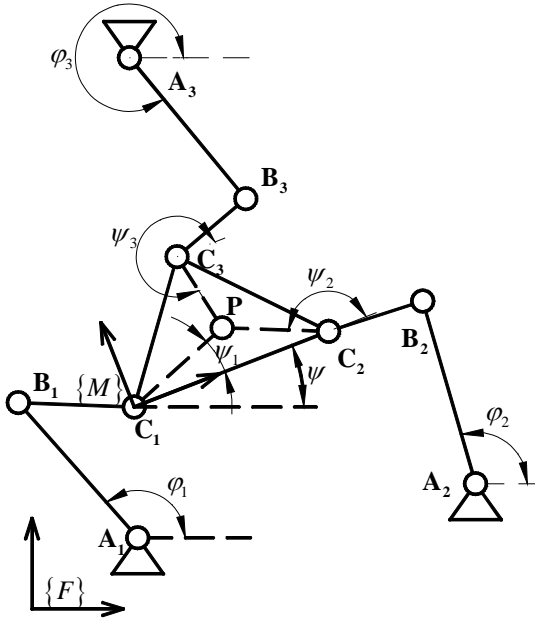


Fig. 1. A 3-RRR Planar Parallel Manipulator

Constant parameters are: (A_{1x}, A_{1y}) , (A_{2x}, A_{2y}) , (A_{3x}, A_{3y}) , $d_1 = \|C_2 - C_1\|$, $d_2 = \|C_3 - C_2\|$, $d_3 = \|C_3 - C_1\|$, $a_i = \|B_i - A_i\|$, $b_i = \|C_i - B_i\|$, $c_i = \|P - C_i\|$ ($i=1,2,3$), Platform constant angles, ψ_i , are the angles of $P - C_i$ vectors with respect to $\{M\}$. Output parameters, $\{P_x, P_y, \psi\}$, are controlled by input parameters, φ_i . This 3-RRR PPM can be seen as a combination of three serial chains, $A_i B_i C_i$, which are constrained by the constant distances of the platform sides, $C_1 C_2$, $C_2 C_3$ and $C_1 C_3$.

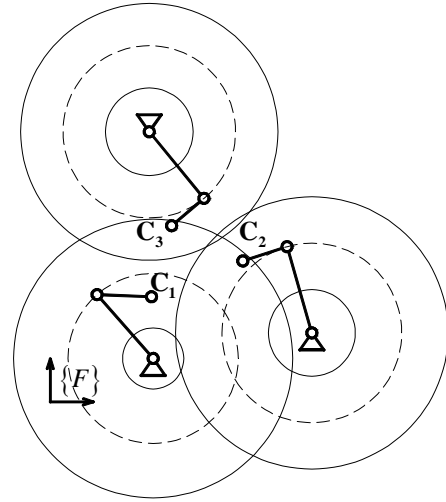


Fig. 2. Workspaces of C_i joints as serial chains

3. Workspace

3.1 Workspace of Joints

Let $A_i B_i C_i$ be two hinged serial chains. $\overline{A_i B_i}$ links can only rotate about A_i joints so, workspace of B_i joints is a circle centered at (A_{ix}, A_{iy}) points with a radius of a_i and can be formulated in set theory terms as

$$W_{B_i, A_i} = \left\{ (x, y) \in \square^2 \mid (x - A_{ix})^2 + (y - A_{iy})^2 = a_i^2 \right\}. \quad (1)$$

Similarly, C_i points can only be rotated with respect to B_i joints and so workspaces of C_i s with respect to B_i s are,

$$W_{C_i, B_i} = \left\{ (x, y) \in \square^2 \mid (x - B_{ix})^2 + (y - B_{iy})^2 = b_i^2 \right\}. \quad (2)$$

Since W_{C_i, B_i} is a circle which is rotating about (A_{ix}, A_{iy}) points, then using Eq.s (1) and (2), W_{C_i, A_i} becomes,

$$W_{C_i, A_i} = \left\{ (x, y) \in \square^2 \mid (x - A_{ix})^2 + (y - A_{iy})^2 = e_i^2 \right\} \quad (3)$$

where $e_i = [a_i - b_i, a_i + b_i]$. Workspace W_{C_i, A_i} in Eq. (3) represents a collection of points falling inside an area bounded by two concentric circles, by radii $a_i - b_i$ and $a_i + b_i$ (Fig. 2).

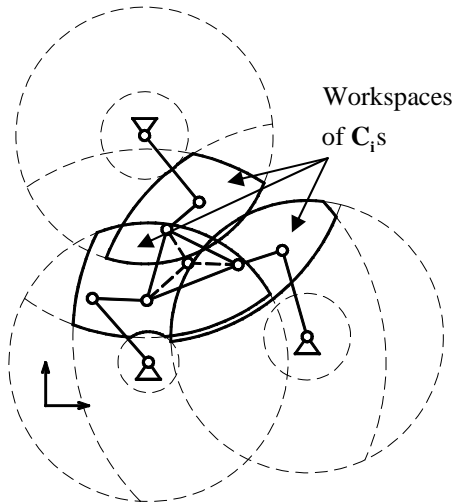


Fig. 3. Workspaces of joints with additional constraints
3.2. Constrained Workspace of C_i joints

Once $A_i B_i C_i$ serial chains are connected to a platform, distance between end joints, d_1 , d_2 and d_3 , becomes constant. This means that W_{C_i, A_i} in Eq. (3) are bounded by two additional constraints.

$$\begin{aligned} W_{C_{i+1}, A_i} &= \left\{ (x, y) \in \square^2 \mid (x - A_{ix})^2 + (y - A_{iy})^2 = f_i^2 \right\}; \\ W_{C_{i+2}, A_i} &= \left\{ (x, y) \in \square^2 \mid (x - A_{ix})^2 + (y - A_{iy})^2 = g_i^2 \right\}. \end{aligned} \quad (4)$$

where $f_i = [a_i - b_i - d_i, a_i + b_i + d_i]$ and $g_i = [a_i - b_i - d_{i+2}, a_i + b_i + d_{i+2}]$. Using additional constraints given in Eq. (4), C_i workspaces are found as,

$$W_{C_i}^P = W_{C_i, A_i} \cap W_{C_i, A_{i+1}} \cap W_{C_i, A_{i+2}} \quad (i = 1, 2, 3 \text{ MOD } 3) \quad (5)$$

Where $(^P)$ superscript is for parallel platform. Note that i index in Eq. (5) is a MOD 3 number, so $i = 4$ and $i = 5$

becomes $i = 1$ and $i = 2$ respectively. Workspace of each C_i joint with additional constraints coming from other two legs is depicted in Fig. 3.

3.3. Reachable Workspace of the End-effector, P

P is a point on which the end-effector is attached on platform. This point is in c_i distances from C_i corners respectively. So, locus of P point, W_P , is inside a region that is bounded by upper bound of $W_{C_i}^P + c_i$ and lower

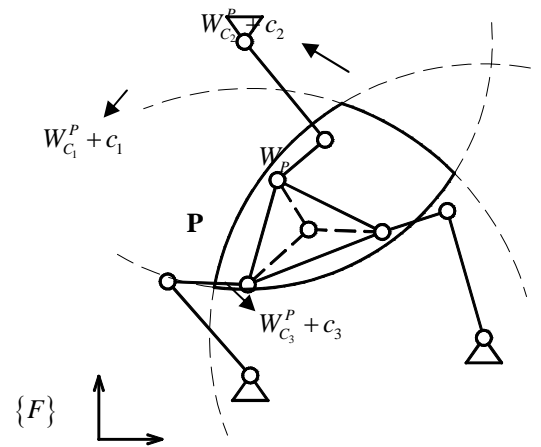


Fig. 4. Reachable (maximal) workspace of P .
 bound of $W_{C_i}^P - c_i$. It should be noticed that the workspace of P point is affected by orientation of the platform. But *reachable workspace* for parallel manipulators is defined as the collection of reachable points with at least one orientation of the platform [9]. This definition points out that the workspace is a function of orientation of the platform and any *constant orientation workspace* is a subset of this *reachable* or *maximal workspace*.

3.4. Constant Orientation Workspace of Platform

This kind of workspace is the collection of the end-effector's reaching points when a specific orientation is given. Moving bodies of any planar mechanism can at most have two translational and one rotational degree-of-freedom. Once it is assumed that the orientational angle, ψ , of the platform is fixed then the platform can only translate on a plane.

In chapter 3.2, constrained workspace of C_i joints was given. Translational and angular distances of P point relative to C_i points are given as constant parameters, c_i and ψ_i in $\{M\}$. So the orientation of $P - C_i$ vectors are

$\psi + \psi_i$ in $\{F\}$. Finally, constant orientation workspace of \mathbf{P} can be calculated by moving constrained workspaces of $W_{C_i}^P$ along $\mathbf{C}_i \rightarrow \mathbf{P}$ direction. Intersection of these three moved workspaces gives constant orientation workspace of \mathbf{P} for given ψ orientation angle.

$$W_{P,\psi} = W_{C_1 \rightarrow P}^P \cap W_{C_2 \rightarrow P}^P \cap W_{C_3 \rightarrow P}^P \quad (6)$$

As stated above, constant orientation workspace of \mathbf{P} , $W_{P,\psi}$, for any given orientation angle must be a subset of reachable workspace, W_P . It is shown, in Fig. 5, in detail.

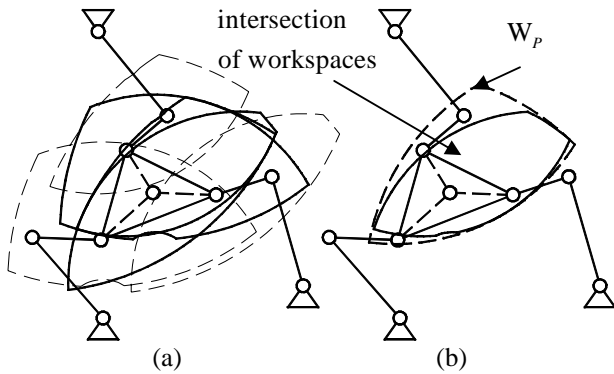


Fig. 5. (a) Moving $W_{C_i}^P$ s along $\mathbf{P} - \mathbf{C}_i$ vector and intersect and (b) comparison with maximal workspace

4. Swept Volume Approach to Workspace

3-RRR PPMs are 3 degree-of-freedom manipulators and 3 inputs, φ_i , controls three outputs, $\{P_x, P_y, \psi\}$. In representing the output link (platform) workspace, to show these two translational (P_x, P_y) and one rotational (ψ) output parameters on the same workspace graphics is not a straightforward issue. Some researchers prefer to construct voxel based workspace representation [11]. This type of representation depends on to check the output link's pose for every possible input variable. Software creates a database with voxels (volumetric pixels) satisfying the conditions and depicts in a 3D graphics. The main drawback of this method is that it is impossible to get a mathematically smooth solid. Some other researchers prefer to draw a serial of cut-sections to represent the workspace of planar robots in 3D [9]. Although this method is useful in path planning tasks, again, it's impossible to apply Boolean algebraic

operations onto this set of section curves.

In computer graphics, sweeping is to trace a 2D closed section through a 3D path [10]. In this way a very complex 3D solid body can be represented by using only a section and its path. Sweeping is a very common and well known solid modeling tool and built in most commercial CAD systems.

In this study, we investigate whether it is possible to use swept volume approach alone in representing the workspace of a 3-RRR PPM.

In chapter 3.4, workspace of end-effector was shown for a given orientation angle, ψ .

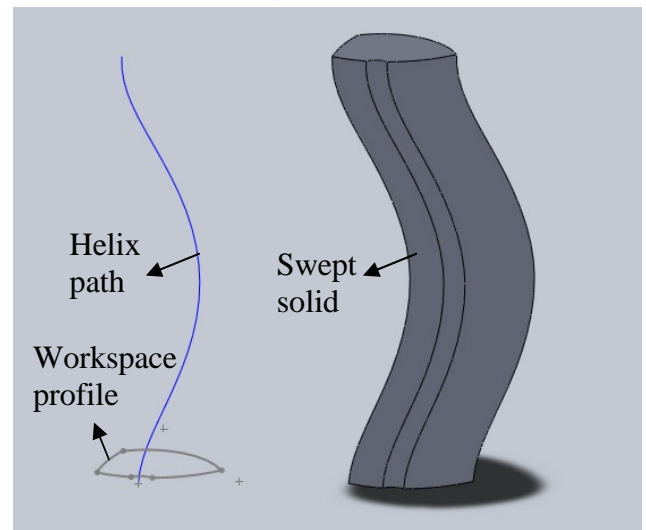


Fig. 6. Workspace profile, path and swept solid model of one of the branch

So, the problem becomes how to model a sweep solid volume representing the workspace for any possible orientation angle, namely in $[-\pi, \pi]$ interval.

Firstly we will show the procedure for the first leg, $\mathbf{A}_1\mathbf{B}_1\mathbf{C}_1\mathbf{P}$. In Fig. 5, $W_{C_1}^P$ workspace was moved through \mathbf{P} point. $\angle \mathbf{C}_1\mathbf{P}$ angle in $\{F\}$ frame is the sum of two angles, constant angle, ψ_1 , and variable angle, ψ . So, if ψ angle is traced in $[-\pi, \pi]$ interval, then $W_{C_1 \rightarrow P}^P$ workspace is moved by c_1 distance in $[\psi_1 - \pi, \psi_1 + \pi]$ direction. A helix centered on the point \mathbf{A}_1 and with the radius c_1 is constructed. Starting angle is selected as $\psi_1 - \pi$. Height of helix can be chosen freely. But it should be a reasonable value relative to the mechanism size. The last step is to sweep $W_{C_1 \rightarrow P}^P$ workspace by accepting this helix as a path. It should be considered in sweep operations that there is an option whether to rotate the

profile by path normals. Since W_G^P profile moves through point P without rotating about itself, “without rotation” option should be selected in sweep command of CAD software.

Same procedure is applied to the other legs. For workspace of the end-effector, three conditions (volumes of the three swept solid models) must be satisfied simultaneously. This corresponds in set theory to the intersection of these three solid bodies. This intersection solid is shown in Fig. 7.

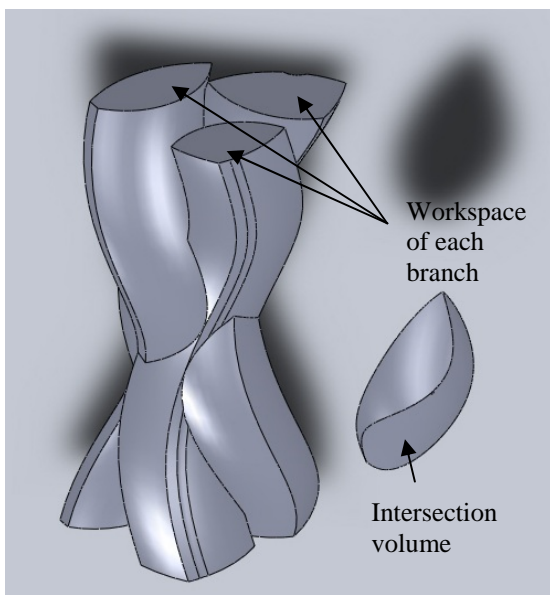


Fig. 7. Three workspaces in swept solid form and their intersection solid.

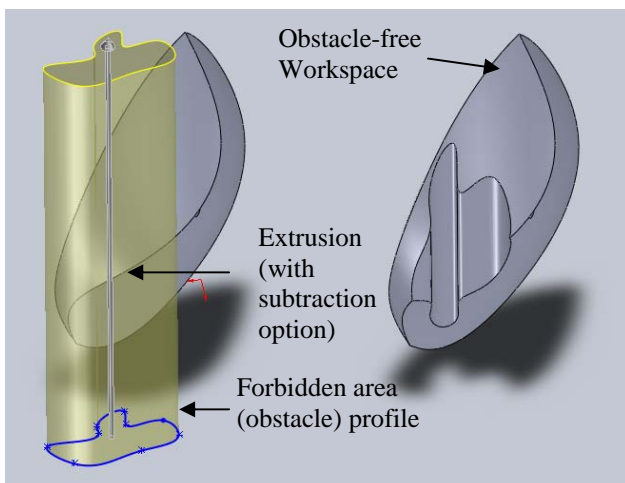


Fig. 8. An obstacle-free workspace creating by extruding (with subtraction option) of a forbidden area profile

Once the workspace is represented in swept solid

form, it becomes a solid which is bounded by analytically determined, i.e. ideally smooth surfaces. This makes possible to create a cut section of this solid using a cutting plane which falls inside this solid and oriented to any possible direction. This helps designer to analyze the workspace for a specific values, say, $x = x_0$, $y = y_0$, $\psi = \psi_0$ or even for a condition of $ax + by + c\psi + d = 0$.

5. Applications of Swept Solid Workspace

5.1. Island of Forbidden Area in Workspace

In the workspace of a robot manipulator, there may be one or more forbidden areas. These areas may be an obstacle in a P&P (pick-and-place) robot’s workspace,

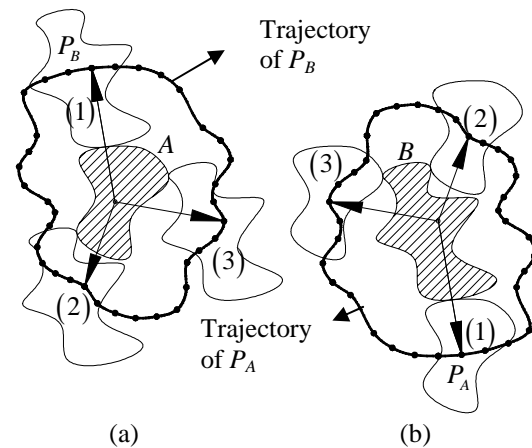


Fig. 9. Geometric proof of the theorem. (a) B moves around A and (b) A moves around B .

a secure area for a welding robot or any other forbidden area. By taking into consideration of these forbidden areas, the real workspace will become smaller. In set theory terms, real (or obstacle-free) workspace will be the difference of end-effector’s workspace and forbidden areas. Generally, these forbidden areas are independent from the platform orientation. So, in (x, y, ψ) graphics these forbidden areas can be shown as an extrusion along ψ direction without changing the orientation. In any CAD program with solid modeling tools, this can be done by extruding of the forbidden area profile and subtracting this from workspace solid. This operation is shown in Fig. 8.

5.2. Obstacle-free workspace in P&P applications

In P&P applications not only the workspace of the platform but also geometric shape of the object to be carried should be taken into consideration. In a workspace

with the obstacles, collision-free path generation of the end-effector should be recalculated when carrying different objects with different geometries. A related theorem is given below.

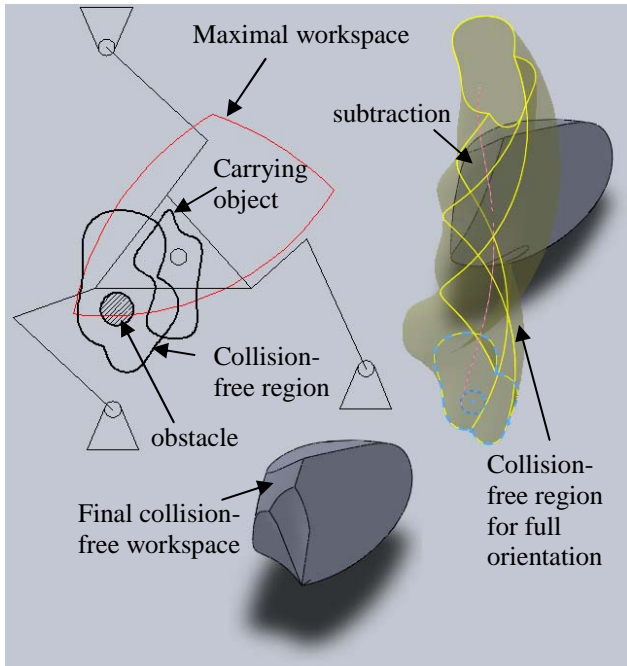


Fig. 10. Operations to derive a collision-free workspace for a given carrying part and circular obstacle.

Theorem: Let A and B are two coplanar closed shapes and P_A and P_B are two arbitrary points on these shapes respectively. Let these two shapes move around each other without overlapping, without detaching and without changing the orientation. Trajectory of P_A with respect to P_B and trajectory of P_B with respect to P_A are exactly the same shapes but rotated by 180° .

Proof: Assume that A and B are touching as in the Fig. 9 (a). $\mathbf{P}_{B/A}$ (position vector of P_B with respect to P_A) is in the same distance but in the opposite direction with $\mathbf{P}_{A/B}$ (position vector of P_A with respect to P_B). When A and B moves around each other in (1), (2), (3) positions and so on, $\mathbf{P}_{B/A}$ and $\mathbf{P}_{A/B}$ position vectors will exactly be in the same length but in the opposite direction.

Trajectories are the curves traced by the tip of $\mathbf{P}_{A/B}$ and $\mathbf{P}_{B/A}$ vectors. Hence the trajectories are the same curves but rotated by 180° .

Assume that an arbitrary shaped object is being carried by

a 3-RRR PPM and there is a circular obstacle inside the workspace of the end-effector.

To be able to determine the forbidden area for the end-effector we need to draw the trajectory of it with respect to the fixed obstacle as in Fig. 10.

In the point of view of theorem given in section 5.2, either we can draw end-effector's trajectory with respect to the circular obstacle's center or draw the circle's trajectory with respect to end-effector, then rotate it by 180° and move it to the center of the circle.

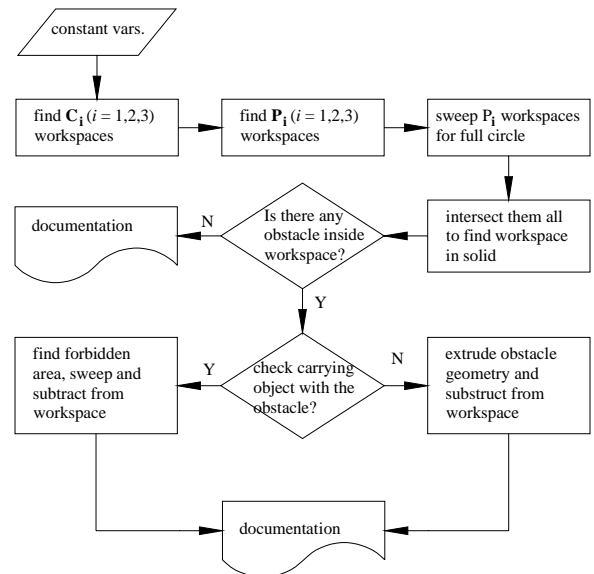


Fig. 11. Flowchart for workspace of 3RRR PPMs

The latter way is much easier than the former. The reason for that is that the trajectory of the center point of a circle which is moving around an object is always in a distance in radius from the original shape in normal direction. Actually, this is a definition of the “offset” command which is standard in any commercial CAD software. All procedure is summarised in a flowchart in Fig. 11.

6. Conclusion

This study presents a new strategy to create a swept solid representation for the workspace of 3-RRR PPMs. This method doesn't need any function derivation, jacobian matrix or any numerical calculations but relies only on standard solid modeling functions of any commercial CAD software package. Construction of swept solid volume of workspace is shown step by step in detail. An analysis example of this solid workspace in a pick-and-place application is presented. Interaction of carrying object and circular obstacle is also analyzed.



References

- [1]. C. Gosselin and J. Angeles, *Singularity Analysis of Closed-Loop Kinematic Chains*, IEEE Transactions of Robotics and Automation, vol. 6 no. 3, 1990.
- [2]. I. A. Bonev, D. Zlatanov and C. M. Gosselin, *Singularity Analysis of 3-DOF Planar Parallel Mechanisms via Screw Theory*, Journal of Mechanical Design, vol. 125 pp. 573-581, 2003.
- [3]. D. Glozman and M. Shoam, *Novel 6-DOF Parallel Manipulator with Large Workspace*, Robotica, vol. 27 pp. 891-895, 2009.
- [4]. M. Ceccarelli and E. Ottaviano, *A Workspace Evaluation of a Eclipse Robot*, Robotica, vol. 20(3) pp. 229-313, 2002.
- [5]. R. I. Alizade, N. R. Tagiyev and J. Duffey, *A Forward and Reverse Displacement Analysis of a 6-DOF In-parallel Manipulator*, Mechanism and Machine Theory, vol. 29(1) pp. 115-124, 1994.
- [6]. R. Clavel, *Delta: A Fast Robot with Parallel Geometry*, 18th International Symposium on Industrial Robots, Lausanne, Switzerland, pp. 91-100, 1988.
- [7]. F. Pierrot, P. Dauchez and A. Fournier, *Hexa: A Fast 6-DOF Fully Parallel Robot*, ICAR, Pise, pp. 1159-1163, 1991.
- [8]. M. Peternell, H. Pottmann, T. Steiner and H. Zhao, *Swept Volumes*, Computer-Aided Design and Appl., vol. 2 pp. 599-608, 2005.
- [9]. J. -P. Merlet, *Parallel Robots*, Springer, The Netherlands, 2006.
- [10]. Web, http://en.wikipedia.org/wiki/Solid_modeling#Sweeping
- [11]. F. Bulca, J. Angeles and P. J. Zsombor-Murray, *On the workspace determination of Spherical Serial and Platform Mechanisms*, Mechanism and Machine theory, vol. 34 pp. 497-512, 1999.



A New Geometric Algorithm for Direct Position Analysis of Planar 3-RRR Manipulator

Özgür KİLİT^{1*}

Mechanical Engineering Department,
Ege University, Bornova 35100, Izmir, Turkey.

ozgurkilit@gmail.com

Abstract

This paper presents a novel and intuitive geometric design methodology for the direct kinematic analysis of 3-RRR type PPM (Planar Parallel Manipulator). This method, which is based on CAGD (Computer Aided Geometric Design) operations, solves direct kinematic analysis problem of 3-RRR PPMs and uses a pure geometrical way without need for objective function derivation and any source code for numerical calculation.

Keywords: PPM (Planar Parallel Manipulator), Direct Kinematic Analysis, CAGD (Computer Aided Geometric Design), Sweep Operation, Intersection.

1. Introduction

Due to the increasing demand for accuracy, rigidity and ability to manipulate large loads in recent hi-tech industry, parallel mechanisms have become very popular. Parallel mechanisms typically consist of two platforms, which are connected by several legs. One of these platforms is rigidly connected to the fixed frame and the other one moves with a prescribed motion in its workspace [1-3].

Direct task has been defined in general manner in IFTtoMM (International Federation for the Promotion of Mechanism and Machine Science) terminology as: “Computation of the pose, motion and forces at the end-effector of a robot arm from given actuator forces, displacements, velocities and accelerations.” [4]. The particular aim in this study is to find the position and orientation of the end-effector platform of a 3-RRR mechanism with respect to given input parameters by using a novel geometric algorithm.

CAGD (Computer Aided Geometric Design) or more specifically CAD/CAM (Computer Aided Design and Manufacturing) systems are applications of *Computational Geometry* and has been used in manufacturing industry since 1971 [5]. Today’s commercial CAD softwares are capable of digital modelling of almost every type of complex parts or assemblies by their built-in 3D parametric solid and

surface modelling tools. With millions of installations world-wide, CAD packages are being extensively used in the area of machine design, but only a few researchers have applied these powerful CAD softwares to kinematic design and analysis problems of parallel robots. Kinzel et. al. used commercial CAD tools in solution of kinematic synthesis problems for their parametric functionality [6]. The advantages of using of parametric 3D modelling tools of commercial CAD softwares in kinematic problems of robotics are that they are user friendly, accurate, highly repeatable and highly accessible.

Due to their highly nonlinear behavior, solution of kinematic problems of most mechanisms need sophisticated mathematical background. Nevertheless, dedicated mathematical solvers are generally seen as a nonintuitive “black box” by the designers who have limited mathematical skills. So, intuitive geometric algorithm presented in this study, may help to those people who have an experience in mechanical part modelling and intends to expand their abilities to design and analysis of parallel robots.

2. Main Motivation: Symbolic Mathematics Approach vs. CAD Approach

To give an idea how the CAD approach simplify the process of solution in kinematics problems, a very simple example is given now. Let $A(x_1, y_1)$ and $B(x_2, y_2)$ are two points in \square^2 Cartesian space. Where are the points which are in a distance of r_1 from A and in a distance of r_2 from B ? It’s very clear that these points must satisfy two criteria: $(x-x_1)^2 + (y-y_1)^2 = r_1^2$ and $(x-x_2)^2 + (y-y_2)^2 = r_2^2$. Solving these equations simultaneously using symbolic mathematics approach gives two solutions: $\{x, y\}_i$ ($i = 1, 2$). But this approach needs numerous mathematical operations: 8 additions, 20 subtractions, 23 multiplications, 4 divisions, 16 powers and 2 square roots (totally 73 operations) (Fig. 1(a)).

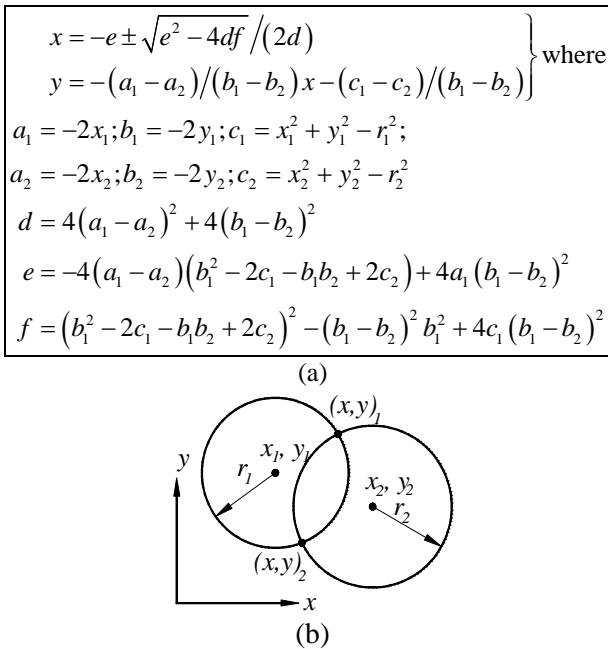


Fig. 1 (a) Symbolic Mathematics vs. (b) CAD Approach

Alternatively, the same solution can be achieved by drawing two circles and intersecting them in any standard CAD software (Fig. 1(b)). This CAD approach needs neither to derive the analytical expression nor any computation. It's very clear in this example that CAD approach is much easier and intuitive way than the other.

At this point a question arises: is it possible to find an equivalent geometric way for complex problems of parallel robotics like workspace, direct or inverse tasks and even synthesis? This idea is the main motivation of this study.

3. Direct Kinematic Analysis of 3-RRR PPMs

As shown in Fig. 2, the 3-RRR (3 revolute-revolute-revolute) mechanism consists of 8 links, 9 revolute joints, 3 branches and 2 independent loops. Every $A_i B_i C_i$ ($i=1,2,3$) chains are connected to fixed frame at A_i joints and to end-effector platform, P , at C_i joints. Underscore in 3-RRR type indicates the actuated joint. So, A_i joints are active joints while all others are passive. The joint angles, α_i , are input parameters, while the pose (position+orientation) of the end-effector platform, P , is assumed as output parameters. Direct task of a 3-RRR PPM has at most eight possible poses of the end-effector [1]. As shown in Fig. 2, once all constant parameters and α_i and β_i variable parameters are known, pose of the

platform is unique and can easily be calculated.

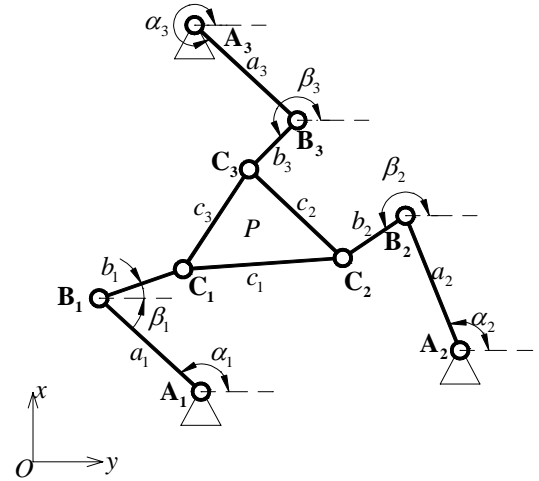


Fig. 2 The schematic representation of a 3-RRR PPM

So, the direct kinematic analysis problem simplified to a problem to find β_i angles with respect to given α_i input angles. In this study β_i angles are found using CAGD tools like: *extrude*, *sweep*, *intersection*, and *project*. This is a very short list of CAGD tools, a more complete list of these commands and their options are available in these references [8-10].

Our geometric algorithm has two phases. Firstly, an orthonormal basis with unit vectors $\hat{\beta}_i$ ($i=1,2,3$), is constructed for Euclidean space \mathbb{R}^3 . Unit vectors must satisfy these conditions: $\hat{\beta}_1 \times \hat{\beta}_2 = \hat{\beta}_3$, $\hat{\beta}_2 \times \hat{\beta}_3 = \hat{\beta}_1$ and $\hat{\beta}_3 \times \hat{\beta}_1 = \hat{\beta}_2$ because of the orthonormality condition. Then function curves of β_i angles, as $f_1(\beta_1, \beta_2)$, $f_2(\beta_2, \beta_3)$ and $f_3(\beta_1, \beta_3)$ are drawn. Secondly, surfaces are formed by extruding every curve along a normal direction (perpendicular to plane on which the curves are drawn). Then intersection curves are found by intersecting of these surfaces. These curves are constraints between β_i and β_{i+1} ($i=1,2,3 \pmod{3}$) angles. So, intersecting these curves leads to all real solutions of β_1 , β_2 and β_3 .

Second phase of our algorithm, i.e. extrusion of planar curves in normal direction and creating intersection curves between these surfaces, is relatively straightforward. But this is not the case in the first phase. Because there is no direct geometrical method for determination of the function between β_i and β_{i+1} ($i=1,2,3 \pmod{3}$), an indirect route is followed here.

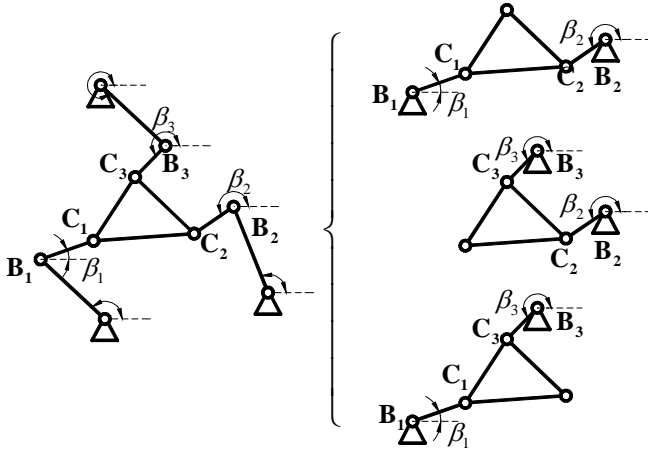


Fig. 3 3-RRR PPM and its three four-bar equivalent.

Since all α_i input angles are given in direct task, positions of \mathbf{B}_i joints are known. This makes possible to decompose the 3-RRR manipulator into three planar four-bar linkages, as, $\mathbf{B}_1\mathbf{B}_2\mathbf{C}_2\mathbf{C}_1$, $\mathbf{B}_2\mathbf{B}_3\mathbf{C}_3\mathbf{C}_2$ and $\mathbf{B}_3\mathbf{B}_1\mathbf{C}_1\mathbf{C}_3$ quadrilaterals where \mathbf{B}_i joints are fixed and \mathbf{C}_i joints are moving. Now the problem is simplified to find the relations between input and output angles, (β_i and β_{i+1} angles) of three planar four-bar linkages (Fig. 3).

3.1 Phase-I: Determination of (β_1, β_2) Curve

The relation between input and output angles of an all-revolute planar four-bar linkage is known as Freudenstein Equation and has been given by F. Freudenstein [7]. This equation is as follows,

$$R_1 c\varphi - R_2 c\psi + R_3 = c(\varphi - \psi) \quad (1)$$

where $R_1 = 1/d$, $R_2 = 1/b$ and $R_3 = (1+b^2-c^2+d^2)/(2bd)$. In this linkage, a (fixed link), b , c and d are link-lengths, φ and ψ are input and output angles respectively. Length of fixed link, a , is assumed as 1 for a scalable mechanism. Equation (5) use symbolic mathematics and gives output angle(s) for a given input value. Namely, if an input-output diagram is required, we need to calculate the output angle using constant parameters and a series of input angle values. This is true in most cases, hand-held drawing and even in case of using a mathematical package. In any such drawing, of course, the curve precision is affected by step size. On the other hand, in geometric approach given in this study, curves are generated without needing any step size. That is because curves are generated by intersecting

surfaces rather than plotting the curve point-by-point.

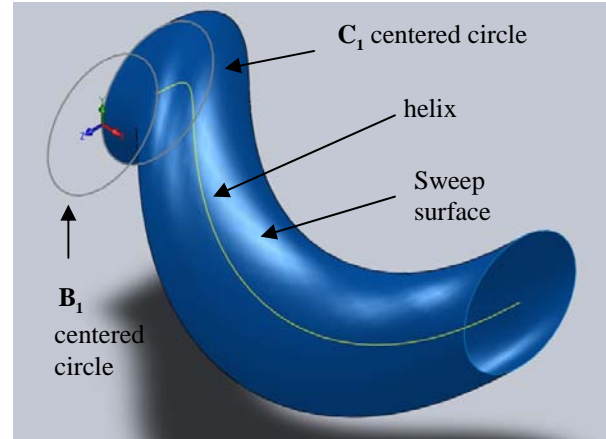


Fig. 4 Drawing of helix sweep surface

The algorithm starts at $\mathbf{B}_1\mathbf{C}_1\mathbf{C}_2$ serial chain of $\mathbf{B}_1\mathbf{B}_2\mathbf{C}_2\mathbf{C}_1$ quadrilateral as follows. An $Oxyz$ frame is located at \mathbf{B}_1 joint and a circle, centered at origin of Oyz plane with a radius of b_1 , is drawn (Fig. 4). This circle represents the locus of point, \mathbf{C}_1 , which is rotating about fixed point, \mathbf{B}_1 . A right-handed helix is then created by using this circle's center and radius, starting from $-z$ -axis (rightmost quadrant of the circle) and one full turn in ccw (counterclockwise) direction along x -axis. The height of helix, h , is calculated by $h = k\beta_1$ relation. Coefficient k in this formula can freely be chosen to obtain a graphics with a convenient aspect ratio. In this study, we assumed that k is 1. Thus, as \mathbf{C}_1 rotates about \mathbf{B}_1 by 1 degree in ccw direction, the projection of \mathbf{C}_1 on x -axis moves 1 unit in positive direction. We can think that revolute joint at \mathbf{B}_1 is replaced with a screw joint with vertical axis. By doing this, a rotational variable is transformed into a translational variable.

In the next step, a circle is drawn on the same plane, centered at the starting point of helix (\mathbf{C}_1) with radius c_1 . This circle represents the locus of \mathbf{C}_2 point. But because the center of this circle, \mathbf{C}_1 , is moving along a helix, locus of \mathbf{C}_2 becomes a collection of points in a specific distance from helix path on planes which are parallel to base (Oyz) plane. In CAGD terms, the locus of \mathbf{C}_2 is a *sweep surface* and can completely be defined by a *profile* (\mathbf{C}_1 centered circle), and a *path* (\mathbf{B}_1 centered helix). It should be noted that, sweep surface locus (workspace) of \mathbf{C}_2 is only possible when \mathbf{B}_1 point moves vertically with the function of $h = k\beta_1$.

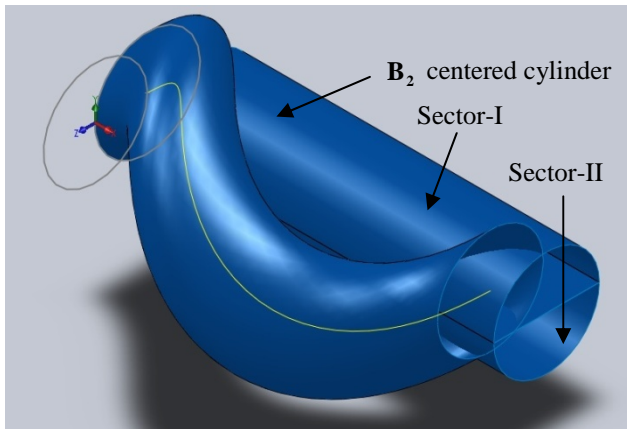


Fig. 5 Intersection of helical and cylindrical surfaces

In the B_2C_2 serial chain of $B_1B_2C_2C_1$ quadrilateral, on the other hand, the locus of C_2 is a circle centered at B_2 with radius b_2 (Fig. 5). To maintain the connection at C_2 , B_2 joint must freely move on x -axis. This kind of joint corresponds to a cylindrical joint. This makes locus of C_2 in B_2C_2 serial chain a *cylindrical surface*. In this way, two fixed revolute joints, B_1 and B_2 , are changed to screw and cylindrical joints respectively and hence an all-revolute four-bar linkage is transformed into a SCRR (screw-cylindrical-revolute-revolute) linkage. It should be noticed that, As β_1 angle is changed, all moving links of four-bar linkage moves vertically, but because all revolute, screw and cylindrical joint axes are parallel and aligned to x -axis direction, projections of all moving points onto Oyz plane are exactly the same with RRRR linkage. It is shown in Fig. 5 that extrusion of B_2 centered circle is divided into two semi-cylinders. The reason for this is that we need two separate intersection curve for sector-I ($\beta_2 = [0, 180^\circ]$) and sector-II ($\beta_2 = [180^\circ, 360^\circ]$). This will be explained later.

Both $B_1C_1C_2$ and B_2C_2 chains are connected at C_2 joint. So, C_2 joint must satisfy both, sweep and cylindrical surface workspaces. By intersecting these two surfaces we get a spatial curve representing the locus of C_2 . Since x -axis of this curve is a scale of β_1 , this graphics becomes a (β_1, y, z) graphics. This spatial curve is then projected onto Oxz plane and we get $z\beta_1$ graphics (Fig. 6). Projecting the curve onto Oxy plane and getting $y\beta_1$ graphics is a possible alternative way. But, in this study we preferred the former one.

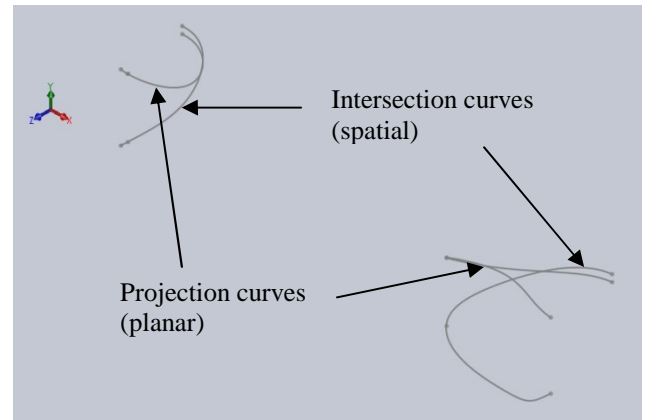


Fig. 6 Intersection curves of helical and cylindrical surfaces and their projection onto Oxz plane

In the next step, another circle is drawn on Oxz plane, centered at B_2 joint with radius of b_2 . We then draw a helix using this circle's center and radius, with a starting point at the intersection point with $-z$ -axis (rightmost quadrant of the circle) and one full turn in ccw direction along y -axis (Fig. 7). It should be noted here that, two helices, centered at B_1 and B_2 , have the same height and mutually perpendicular. B_2 centered helix is then projected onto Oyz plane and because y -axis of this curve is a scale of β_2 , we obtain (z, β_2) graphics. It's clear from Fig. 7 that, this is a sinusoidal curve, $z = B_{2z} - \cos \beta_2$, and divided into two parts: sector-I and sector-II.

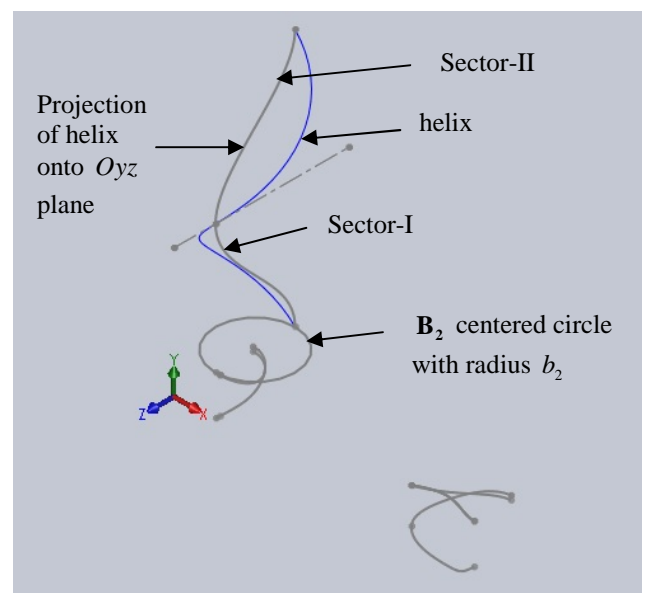


Fig. 7 Drawing of B_2 centered helix

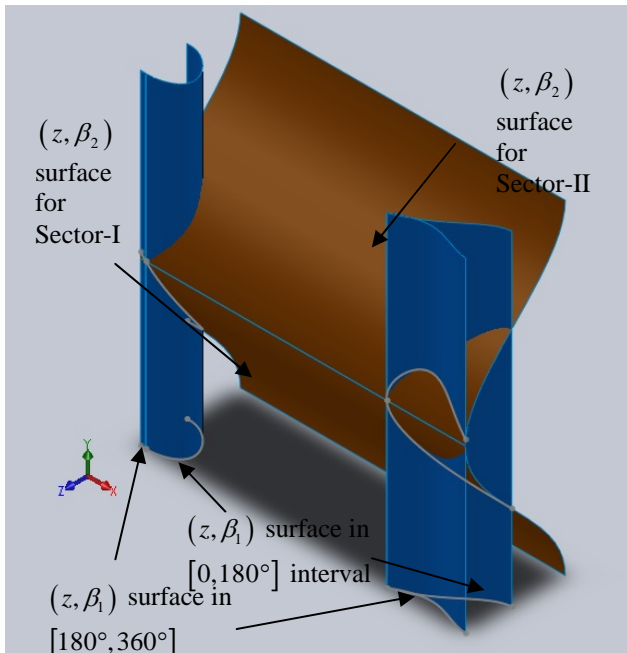


Fig. 8 Extrusion surfaces and their intersection curves

At this point, two mutually perpendicular graphics: (z, β_1) and (z, β_2) curves are achieved. Extruding (z, β_1) curve toward y -axis and (z, β_2) curve toward x -axis creates a set of two surfaces (Fig. 8).

Here, one important thing should be taken into consideration. Projecting a 3D (spatial) curve onto an orthonormal plane, i.e. Oxy , Oxz or Oyz , leads to lose one dimension and the curve becomes thus two dimensional (Fig. 9).

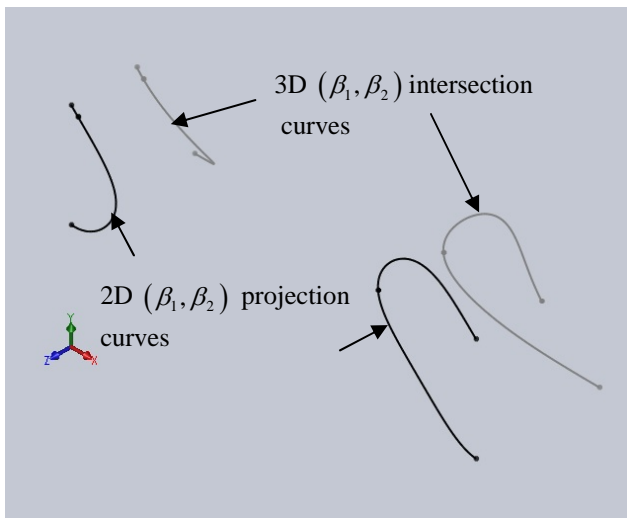


Fig. 9 (β_1, β_2) Intersection curves and their projection

For example, suppose that H is a helix centered at origin on Oxy plane with radius of r and height of h . Projecting H onto Oxz and Oyz planes will lead to two curves: $x = r \cos z$ and $y = r \sin z$ where $z = [0, h]$. Notice that y and x values are lost in former and latter equations respectively. Projection operation is one-directional, i.e. none of these two projection curves can be used alone to form the original helix again. Let the former curve extrude through y direction and latter curve through x direction. Intersection of these two surfaces will give helix curve again. Keeping this idea in mind, sector-I and sector-II parts of the extrusion surfaces of (z, β_1) and (z, β_2) curves are formed separately. Intersections of (z, β_1) and (z, β_2) surfaces for sector-I and then intersections of (z, β_1) and (z, β_2) surfaces for sector-II are created. If this did not happen some extraneous solutions would then be created.

Another example for one-directional operations is taking square. If we square a function, say, $y = x$, and take square root again, we get two equations as $y = \pm x$. One is original equation while the other is extraneous and should be eliminated.

These two surfaces, (z, β_1) and (z, β_2) , represent two constraints equations. Intersection of these surfaces gives a curve satisfying both constraints. Finally projecting this spatial curve onto Oxy plane gives a 2D curve. Since β_1 and β_2 are assumed as a scale of x and y respectively, this curve is accepted as a (β_1, β_2) function curve (Fig. 9). These operations are geometric equivalent of taking two trigonometric equations, $f_1(\beta_1, x)$ and $f_2(\beta_2, x)$, eliminating x between f_1 and f_2 and finally having an equation, $g(\beta_1, \beta_2)$.

3.2 Phase-II: Combining of Three Loop Curves

Geometric determination of the function curve of two angles, (β_1, β_2) , are given in the previous section. The other two function curves, (β_2, β_3) and (β_1, β_3) , for corresponding two loops, $B_2B_3C_3C_2$ and $B_3B_1C_1C_3$, can easily be derived following the same route. When deriving these function curves, it should be noted that, β_1 , β_2 and β_3 axes should be aligned to three orthonormal axes, say, x , y and z respectively. This is particularly important for later extrusion and intersection phases.

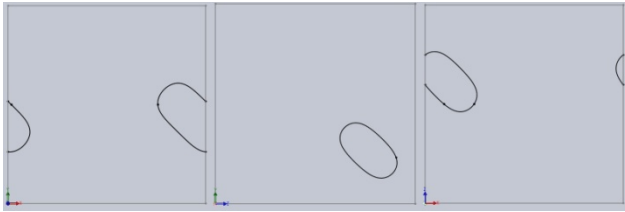


Fig. 10 (β_1, β_2) , (β_2, β_3) and (β_1, β_3) graphics

In Fig. 10, three graphics, (β_1, β_2) , (β_2, β_3) and (β_1, β_3) function curves are depicted separately. In the next figure, Fig. 11, all of the extrusions are shown: (β_1, β_2) curve through β_3 direction, (β_2, β_3) curve through β_1 direction, and (β_1, β_3) curve through β_2 direction. Intersection of these surfaces are corresponding to all of the constraint equations between β_1 , β_2 and β_3 output angles. Hence, to find the output angles, β_1 , β_2 and β_3 , we simply intersect these surfaces and find the intersection curves. Final step is to find the intersection points of these curves. This gives all of the real solution of the output angles. Examples of these curves are depicted in Fig. 12. In this figure, two real solutions of $\{\beta_1, \beta_2, \beta_3\}$ set are shown. To measure the curve intersection points precisely, it may be chosen to project the curves onto orthonormal planes. In this figure, spatial curves are shown as light (gray) lines while projection curves are shown as solid (black) lines.

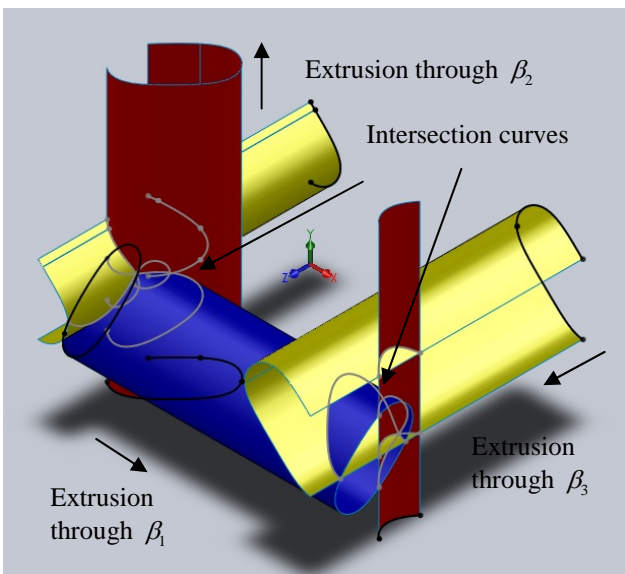


Fig. 11 Intersection of all surfaces

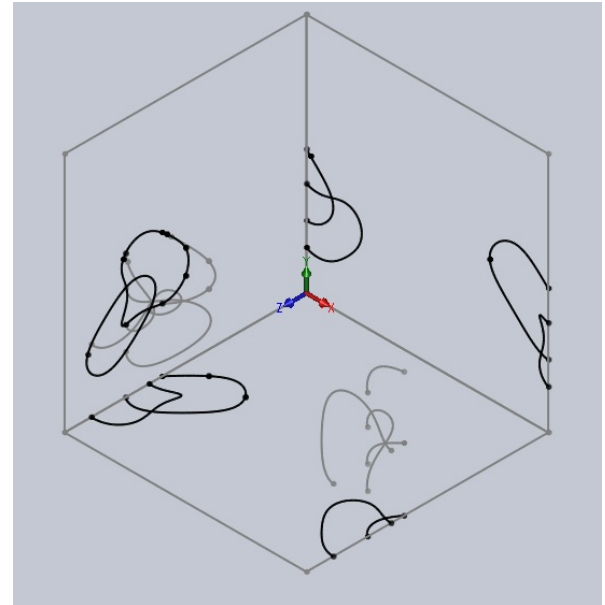


Fig. 12 Determination of $\{\beta_1, \beta_2, \beta_3\}$ solution set.
 (Intersection points are real solutions).

4. Algorithm Summary

All steps of the geometric algorithm presented in this study are summarized as follows.

1. Draw \mathbf{B}_1 centered circle on Oyz plane with radius b_1
2. Draw a helix using \mathbf{B}_1 centered circle with height h ($h = k\beta_1$), starting at $\beta_1 = 0$
3. Draw a circle at start point of helix with radius c_1
4. Sweep circle at step 3 along helix
5. Draw a circle centered at \mathbf{B}_2 with radius b_2
6. Divide this circle horizontally as sectors I and II
7. Extrude two semi-circles with height h
8. Intersect sweep surface and cylindrical surface
9. Project intersection curves onto Oxz plane. This is (z, β_1) curve
10. Draw a \mathbf{B}_2 centered circle on Oxz plane with radius b_2
11. Draw a helix using \mathbf{B}_2 centered circle with height h starting at $\beta_2 = 0$
12. Project this helix onto Oyz plane. This is (z, β_2) curve
13. Divide this projection into two equal parts horizontally as sectors I and II



14. Extrude two projections curves at steps 9 and 13 at normal directions
15. Intersect these surfaces (sector-I to sector-I, sector-II to sector-II) and find intersection curves
16. Project intersection curves to Oxy , i.e. $O\beta_1\beta_2$ plane.
This is $(\beta_1\beta_2)$ curve
17. Repeat steps 1 to 16 for (B_2, β_3) and (β_1, β_3) curves
18. Locate curves in step 17 onto $Oxzy$ orthonormal frame as $O\beta_1\beta_2\beta_3$ frame
19. Extrude curves at normal direction
20. Find intersection curves
21. Intersection points are real values of β_1 , β_2 and β_3
22. End of algorithm

5. Numerical Example

In this chapter an example of 3-RRR PPM is given. Solutions of symbolic mathematics and our new geometric algorithm are compared. Derived equations in symbolic calculations are not shown here.

Fixed joint coordinates:

$$\mathbf{A}_1 = \{0, 0\}; \mathbf{A}_2 = \{189.47984832, 4.68181258\};$$

$$\mathbf{A}_3 = \{69.43343935, 164.92131724\}$$

Link-lengths:

$$a_i = \{54.33090895, 57.31187516, 56.62564401\}$$

$$b_i = \{54.54511354, 55.42961639, 53.37896397\}$$

Platform sides:

$$c_i = \{55.45460812, 54.93874320, 54.64359803\}$$

Input angles:

$$\alpha_i = \{69.82673067^\circ, 183.21503093^\circ, 329.64333374^\circ\}$$

Symbolic mathematics solution of the output angles:
(software: MATLAB)

$$\begin{Bmatrix} \beta_{1i} \\ \beta_{2i} \\ \beta_{3i} \end{Bmatrix} = \begin{Bmatrix} 37.595447152133296 & 349.5363049912351 \\ 141.9167496035696 & 96.851869082010879 \\ 268.1608246503477 & 232.2260540089448 \end{Bmatrix}$$

Our novel geometric algorithm solutions (average values):
(software: SolidWorks)

First solution set:

$$\beta_i = \begin{Bmatrix} 37.59579624^\circ (\% \text{ error: } -9.29E-4) \\ 141.917084285^\circ (\% \text{ error: } -2.36E-4) \\ 268.160537305^\circ (\% \text{ error: } 1.07E-4) \end{Bmatrix}$$

Second solution set:

$$\beta_i = \begin{Bmatrix} 349.536282365^\circ (\% \text{ error: } 6.47E-6) \\ 96.85188306^\circ (\% \text{ error: } -1.44E-5) \\ 96.85188306^\circ (\% \text{ error: } 6.62E-5) \end{Bmatrix}$$

Note: error numbers inside parentheses are deviations from Matlab solutions.

All modern CAD softwares use spline in curve (and surface) modelling. Unlike algebraic functions, spline interpolations are determined piecewise by polynomials and therefore they have some unevitable errors.

6. Conclusion

The purpose of this paper is to solve direct task kinematic analysis problem of 3-RRR PPMs in a pure geometrical way. This novel algorithm needs no objective function derivation, no exhaustive symbolic mathematics manipulations or even no any calculations. It needs only some basic CAD modelling commands, e.g. extrude, sweep, intersect, etc., of a standard CAD modeller which is now very common in design offices. In Chapter 5, a numerical example is given, and the solutions show that there is a small deviation from Matlab solution. This difference comes from spline algorithms which are built-in in CAD software. But, these deviations are so small that, except extremely high precision industries, solutions are fairly enough for most applications. It is thought that this intuitive geometric method can play an important role in attracting the attention of some industrial/mechanical designers who have limited mathematical skills but willing to solve parallel robot kinematics problems.

References

- [1] Lung-Wen Tsai, *Robot Analysis-The Mechanics of Serial and Parallel Manipulators*, John Wiley & Sons, Inc., 1999.
- [2] J. -P. Merlet, *Parallel Robots*, Springer, 2006.
- [3] S. Staicu and D. Zhang, *A novel dynamic modelling approach for parallel mechanisms analysis*, Robotics and Computer-Integrated Manufacturing, v. 24(1), pp. 167-172.
- [4] T. G. Ionescu, *IFToMM terminology/English 5.1*, Mechanism and Machine Theory 38, pages 819–825, 2003.
- [5] A.R. Forrest, *Computational geometry*, Proc. Royal Society London, 321, series 4, 187-195, 1971.
- [6] E. C. Kinzel, J. P. Schmiedeler and G. R. Pennock, *Kinematic Synthesis for Finitely Separated Positions Using Geometric Constraint Programming*, Journal of Mechanical Design, v. 128, pp. 1070-1079, 2006.
- [7] F. Freudenstein, *Design of Four-link Mechanisms*, PhD Thesis, Columbia University, USA, 1954.
- [8] <http://www.catia.com/>.
- [9] <http://www.solidworks.com/>
- [10] <http://www.autodesk.com/>.

Interactive Least-Squares Synthesis of a Watt I Six-bar Path Generator

Andrew B. KIKIN^{1*}, Anton A. KIKIN²

^{1*}Prof. Dr. Sc., Saint-Petersburg State University of Technology and Design
18, Bolshaya Morskaya St., Saint-Petersburg, 191186, Russia
kikin@sutd.ru

²Post graduate, Saint-Petersburg State University of Technology and Design

Abstract

An original technique of interactive analytical and optimization synthesis of six-bar path generator is suggested. A Watt I six-bar path generator has sixteen constant parameters. The law of coupler point motion along some path is given. Four parameters of base four-bar kinematic chain are assigned arbitrary. The remaining twelve parameters of the synthesized linkage are calculated in two stages. Six unknown parameters are found analytically by equations. Other six parameters are scanned numerically by a special automated interactive computer technique. Synthesis process has visual interface with interactive control using color histograms for each stage of synthesis. Numerical examples of synthesis are presented – straight-line and circle arc path generators.

Keywords: six-bar linkage, path generator, least-squares synthesis, interactive computer program, arc path generator.

1. Introduction

This work studies a problem of analytical and optimization synthesis of a Watt I six-bar path generator in accordance with a given law of coupler point motion. The considered linkage has a working point on the coupler which is connected to the input link (crank). This six-bar linkage (Fig. 1) has an input link 1 (ABC) and an output link 4 (CGH) whose coupler point H reproduces the trajectory σ .

The kinematic diagram of a Watt I six-bar linkage has fifteen constant parameters: four coordinates of fixed pivots A and E : x_A and y_A , x_E and y_E ; eleven linear and angular dimensions of mechanism links: $h_1=AB$, $\lambda_1=\angle BAC$, $b_1=AC$, $h_2=BD$, $\lambda_2=\angle DBF$, $b_2=BF$, $h_3=DE$, $h_4=CG$, $\lambda_4=\angle GCH$, $b_4=CH$, $h_5=FG$.

Let's introduce the signs r_1 and r_2 for the assembly configurations of the first BDE and the second CGF dyads ($r_1, r_2 = +1$ or -1 , which depends on the signs of the vectors BD and CG moments relative to the points E and F , respectively). In addition, the following angles are shown (see Fig. 1): μ_1 and μ_2 – transmission angles in the

dyads BDE and CGF , respectively; α_0 – initial angular coordinate α of the input link AB ; φ – the angle of relative rotation of input link AB , measured from the initial position $\alpha = \alpha_0$. The value of the angle φ lies in the interval $0 \leq \varphi \leq \Phi$; for cyclic mechanisms $\Phi = 2\pi$, for non-cyclic $\Phi < 2\pi$.

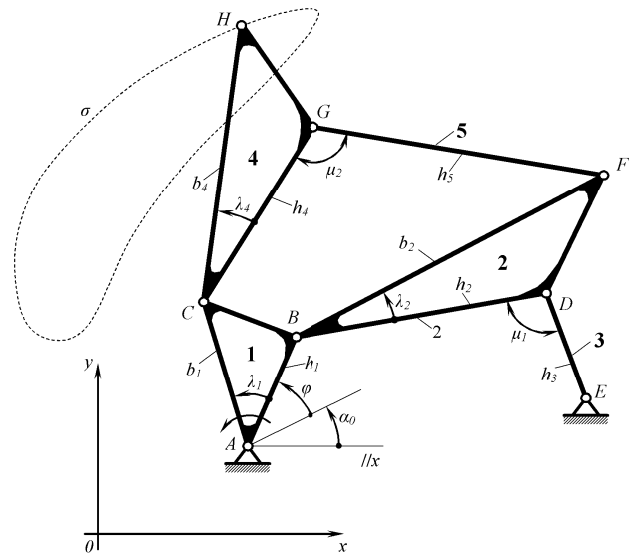


Fig. 1: Watt I six-bar linkage

When solving the problem of the path generator synthesis we also have a parameter α_0 among constant parameters of the linkage, with their total number increasing to sixteen. In case of non-cyclic linkage another parameter is added: the angle Φ specifying the working angle magnitude of the input link AB .

Parameters α , α_0 and φ are correlated by the following dependence: $\alpha = \alpha_0 + v_1 \cdot \varphi$, where v_1 is the sign of the input link AB rotation ($v_1 = +1$ or -1).

2. Statement of the synthesis task

It is required to synthesize a six-bar path generator, whose H coupler point would reproduce in the best way the given motion on curve σ . The problem of synthesis consists in defining all constant parameter values of the six-bar linkage kinematic diagram (see Fig. 1). All constant parameters of the linkage are divided into *fixed, calculated and free*.

Fixed parameters. In case of the general statement of synthesis problem, this group of parameters includes only four dimensions: h_1, h_2, h_3, AE and the r_1 sign of the first BDE dyad assembly configuration. These parameters set the base $ABDE$ four-bar linkage. In practical tasks often it happens that position of pivot A is fixed (e.g. it is irrational to change the main shaft arrangement within the machine frame) in this case x_A and y_A coordinates also can be added to fixed parameters. For non-cyclic mechanisms the value of Φ angle is an additional fixed parameter.

Calculated parameters. This group includes the following parameters: $x_A, y_A, xE, yE, \lambda_1, b_1, \lambda_2, b_2, h_4, \lambda_4, b_4, h_5$ and α_0 . Moreover, the synthesis provides for definition of a sign r_2 of the second CGF dyad assembly. Thus, the total number of calculated parameters for the general statement of the synthesis problem is twelve plus a sign r_2 . Calculated parameters are determined in two stages, six parameters – by formula, analytically, one – by numerical solving of the equation of the ninth order, and other required parameters are varied, i.e. they are scanned in accordance a special interactive computer technique.

Free parameters. These parameters only include a sign v_1 showing the direction of input link rotation.

The main condition of synthesis suggests that the H coupler point of the synthesized linkage should reproduce the required movement along path σ . We estimate the quality of the implemented main condition by maximum deviation δ_{\max} from the given curve:

$$\delta_{\max} = \max_{i=1,2,\dots,N} (|HH_i|). \quad (1)$$

In order to reduce the search zone to mechanisms of practical use, the maximum limit deviation $(\delta_{\max})_{\lim}$ is given and only those synthesized mechanisms are selected for which $\delta_{\max} \leq (\delta_{\max})_{\lim}$ is valid.

Additional conditions of synthesis are expressed by the following inequalities:

$$(b_1)_{\min} \leq b_1 \leq (b_1)_{\max}; \quad (2)$$

$$(b_2)_{\min} \leq b_2 \leq (b_2)_{\max}; \quad (3)$$

$$(x_A)_{\min} \leq x_A \leq (x_A)_{\max}; \quad (y_A)_{\min} \leq y_A \leq (y_A)_{\max}; \quad (4)$$

$$(x_{4H})_{\min} \leq x_{4H} \leq (x_{4H})_{\max}; \quad (y_{4H})_{\min} \leq y_{4H} \leq (y_{4H})_{\max}. \quad (5)$$

Here we can also add the condition of a favorable transfer of movement in the synthesized linkage. Let's accept that the extreme (least favorable) value of the transmission angle $\mu_2 = \mu_2(\varphi)$ in the second CGF dyad of the synthesized mechanism is supposed to be:

$$\mu_{2\text{ext}} \geq \mu_{\lim} \quad (0 \leq \varphi \leq \Phi), \quad (6)$$

where μ_{\lim} is the given limited value of the transmission angle in a synthesized linkage.

It should be noted, that the condition $\mu_1(\varphi) \geq \mu_{\lim}$ for the first dyad is to be performed due to a proper choice of base four-bar linkage parameters and it does not change during synthesis.

3. Algorithm of the first stage of synthesis

At this stage a two-link kinematic ACH chain of the mechanism is synthesized (Fig. 2). The initial data for synthesis are N number triplets: $\{(x_H)_i, (y_H)_i, \varphi_i\}$ ($i = 1, 2, \dots, N$) specifying the law of coupler point H motion along path σ . The purpose of six-bar linkage synthesis at the first stage is to find values of the following four parameters: x_A, y_A, b_1, b_4 and the sum of angles $(\alpha_0 + \lambda_1)$. This problem almost exactly coincides with the problem of the least-square synthesis studied in detail in the paper [1] and used earlier for the synthesis of both a four-bar path generator [2] and a Stephenson I six-bar path generator [3].

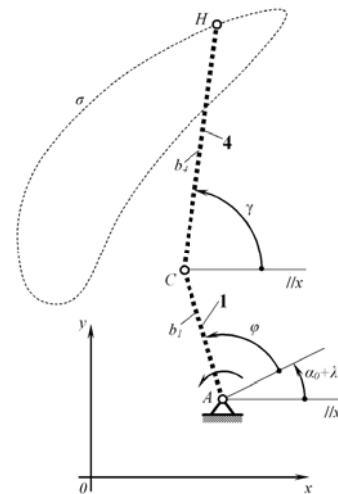


Fig. 2: The first stage of synthesis

The distance l_i between two synchronously moving points C and H is

$$l_i = C_iH_i = \sqrt{(x_A + b_1 \cdot \cos \alpha_i - (x_H)_i)^2 + (y_A + b_1 \cdot \sin \alpha_i - (y_H)_i)^2} \quad (i = 1, 2, \dots, N), \quad (7)$$

where $\alpha_i = (\alpha_0 + \lambda_1) + v_1 \cdot \varphi_i$. Assume that value of sum $(\alpha_0 + \lambda_1)$ is known. We introduce the sum $S = S(x_A, y_A, b_1, b_4)$:

$$S = \sum_{i=1}^N (l_i^2 - b_4^2)^2. \quad (8)$$

Then the unknowns x_A, y_A, b_1, b_4 are found from the condition of the sum (8) minimum:

$$\frac{\partial S}{\partial x_A} = 0; \quad \frac{\partial S}{\partial y_A} = 0; \quad \frac{\partial S}{\partial b_1} = 0; \quad \frac{\partial S}{\partial b_4^2} = 0. \quad (9)$$

The system (9) was reduced to one equation of the ninth order in parameter b_1 [1]. The parameter b_1 represents the length of an input link AC limited by the condition (2) that essentially facilitates numerical search of equation roots. Then the roots are found, the unknowns b_4, x_A and y_A are defined by formula unambiguously.

For numerical search of varied parameters values in a synthesis algorithm an original interactive technique «Automatic Scanning of Coordinates» (ASC) [2] is used. This technique is intended for automated scanning (searching) of one to three varied parameters and allows numerical search for the minimum of implicit functions with additional restrictions considered. The method provides both automatic narrowing of the scanning area and changing of the parameter scanning steps. The results of scanning are shown on the PC display as two-dimensional color histograms where the process of a synthesis problem solution is visually presented. Each histogram clearly shows the quality of the basic and additional conditions fulfilled.

To estimate the synthesis quality of a two-link chain ACH and to select the results at the first stage of synthesis we use the criterion $\Delta l_{\max} \leq \Delta l_{\lim}$, where

$$\Delta l_{\max} = \max_{i=1,2,\dots,N} (|CH_i - b_4|). \quad (10)$$

At this stage the ASC method is applied in various modes of computer scanning: a) one parameter $(\alpha_0 + \lambda_1)$, b) two parameters b_1 and $(\alpha_0 + \lambda_1)$, c) two parameters x_A and y_A . Thus, a color picture of conditional minimization of the criterion (10) considered the restriction (2) is displayed, for example, $\Delta l_{\max} = \Delta l_{\max}(x_A, y_A)$ or $\Delta l_{\max} = \Delta l_{\max}(b_1, (\alpha_0 + \lambda_1))$. The histogram is filled up dynamically, also being as an indicator of the first stage synthesis process.

When the scanning is over, i.e., when the whole field of the histogram is filled with cells of corresponding colors, the program automatically finds and marks on the screen all available local minima following the criterion

(10), or gives a message about their absence. For any of the local minima found by the program the user can:

- analyze and estimate the results of synthesis of the kinematic chain ACH , received at the first stage of synthesis;
- make a decision whether to reject this minimum or to start, for this local unit, ASC process automatically specifying the parameters being scanned down to the required accuracy.

Then it is possible to proceed to the second stage of synthesis for any of the found local minima.

For a local minimum chosen, i.e. for a specified set of values x_A, y_A, b_1, b_4 and $(\alpha_0 + \lambda_1)$ the parameters $\{(x_C)_i, (y_C)_i, \gamma_i\}$ of the CH coupler plane motion are found as functions of an input angle $\{\varphi_i\}$ for $i = 1, 2, \dots, N$, where angle $\gamma = \angle xCH$ (see fig. 2).

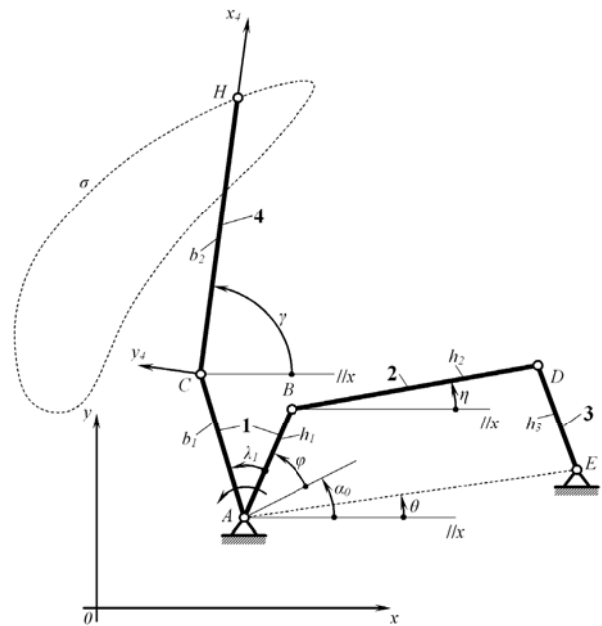


Fig. 3: Rotation of $ABDE$ around the point A

4. Algorithm of the second stage of synthesis

At the second stage of synthesis two varied parameters are scanned by the ASC method: the initial angle α_0 and the angle $\theta = \angle xAE$, determining coordinates x_E and y_E of pivot E (Fig. 3). The angle θ specifies rotation of the base four-bar $ABDE$ linkage around the point A . For each combination of α_0 and θ (unit of scanning) parameters of the BD coupler plane motion are found: coordinates $(x_B)_i$ and $(y_B)_i$ and the value of angle η_i for each value of angle $\varphi_i (i = 1, 2, \dots, N)$.

Thus, the synthesis problem for each unit of scanning at the second stage is to be solved as follows:



Given: plane motion $\{(x_C)_i, (y_C)_i, \gamma_i\}$ and $\{(x_B)_i, (y_B)_i, \eta_i\}$ ($i = 1, 2, \dots, N$) of two couplers CH and BD , accordingly (Fig. 4);

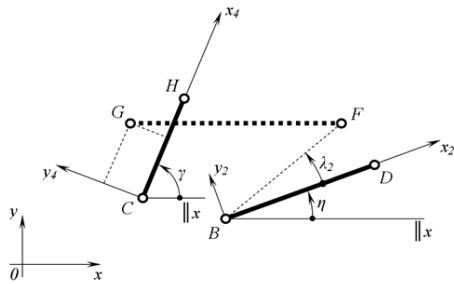


Fig. 4: Motion of couplers CH and BD

To find: parameters of a two-pair link 5 (FG), connecting moving couplers 4 (CH) and 2 (BD), i.e. values of unknown constant parameters $\lambda_2, b_2, \lambda_4, h_4$ and h_5 . Here instead of parameters λ_4 and h_4 it is more convenient to use the Cartesian coordinates x_{4G} and y_{4G} of point G .

The detailed description of a synthesis problem given above is presented in the paper [1].

The synthesis algorithm looks as follows. We assume that the values of parameters λ_2 and b_2 are known. We introduce the sum $S = S(x_{4G}, y_{4G}, h_5)$:

$$S = \sum_{i=1}^N (l_i^2 - h_5^2)^2. \quad (11)$$

Here $l_i^2 = ((x_B)_i + b_2 \cos(\eta_i + \lambda_2) - (x_G)_i)^2 + ((y_B)_i + b_2 \sin(\eta_i + \lambda_2) - (y_G)_i)^2$, where $(x_G)_i$ and $(y_G)_i$ are functions of $x_{4G}, y_{4G}, (x_C)_i, (y_C)_i$ and γ_i ($i = 1, 2, \dots, N$).

Then unknown values h_5, x_{4G} and y_{4G} can be found by solving a system of three equations:

$$\frac{\partial S}{\partial x_{4G}} = 0; \quad \frac{\partial S}{\partial y_{4G}} = 0; \quad \frac{\partial S}{\partial h_5} = 0. \quad (12)$$

The system (12) is reduced to a system of two linear equations in parameters x_{4G} and y_{4G} [4]. Hence three unknowns h_5, x_{4G} and y_{4G} are found using proper formula.

For numerical determination of parameters λ_2 and b_2 (previously assumed as known) we use the ASC technology in a fully automatic mode (without displaying any interactive histogram) with these parameters being scanned. At stage 2 the synthesis procedure automatically allows for constructive restrictions (3), (5) and (6). In addition, the value of a sign r_2 for CGF dyad assembly (Fig. 5) is defined.

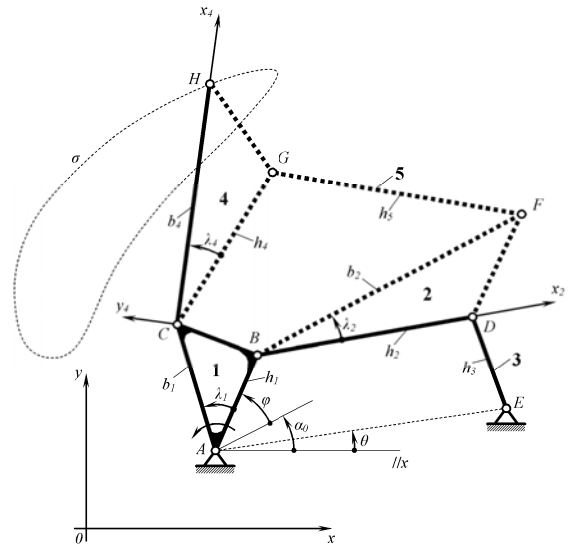


Fig. 5: The second stage of synthesis

The results of the synthesis are shown on the PC display as a 2-D histogram having a rectangular form (Fig. 6) and consisting of cells, each is the unit of scanning, i.e. a certain combination of two parameters being scanned. In fig. 6 these two parameters are angles α_0 and $\theta = \angle xAE$ which are scanning from 0 up to 360° with a 5° step. This approach supposes finding a global minimum of the function (1).

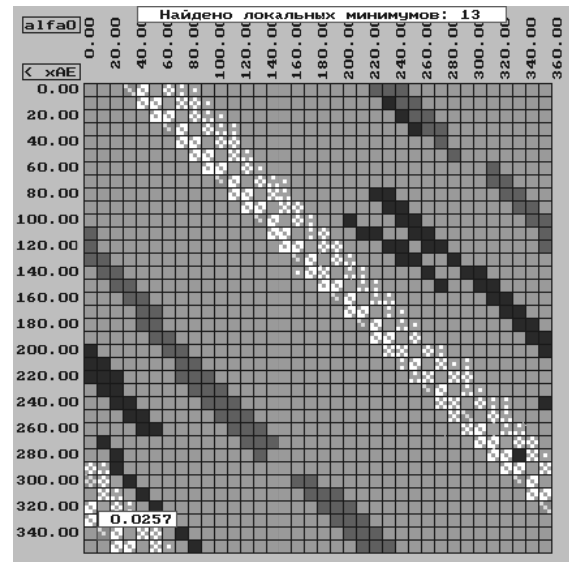


Fig. 6: A histogram for the second stage of synthesis

The color of each cell of the histogram depends on the quality of linkage synthesis according to all conditions. Thus, we can see on the display a color picture of conditional minimization of function $\delta_{max} = \delta_{max}(\alpha_0, \theta)$



with the following restrictions (3), (5) and (6) considered. A special color scale is used; dark shades show the restrictions failed while light zones show the availability of a synthesis problem solution. The histogram is filled up dynamically, also being an indicator of the second stage synthesis process.

When the scanning is over, i.e., when the whole field of the histogram is filled with cells of corresponding colors, the program automatically finds and marks on the screen all available local minima of the function $\delta_{max} = \delta_{max}(\alpha_0, \theta)$. For any of the local minima found by the program the user can interactively carry out the following actions:

- to start a new ASC process that on special algorithm narrows borders of scanning area and decreases the scanning step of parameters automatically. In result the solution is specified down to required accuracy for parameters α_0 and θ ;
- to compare the received trajectory of the H coupler point of the synthesized mechanism with the preset trajectory;
- to examine the animated kinematic diagram of the synthesized linkage, to estimate its configuration, dimensions, etc.;
- to save the successful solution in the database of the synthesized mechanisms or to exclude the unsuccessful solution found by the program.

5. Example of six-bar path generator synthesis

Example 1. The coupler point H is required to reproduce uniform straight-line motion, length is 300 mm; $\Phi = 120^\circ$; $N = 31$, $\nu_1 = 1$; $\mu_{lim} = 45^\circ$; $(\delta_{max})_{lim} = 0,5$ mm.

The base $ABDE$ four-bar linkage has the following parameters: $AB = h_1 = 150$ mm, $BD = h_2 = 450$ mm, $DE = h_3 = 300$ mm, $AE = 500$ mm. This linkage has $\mu_{1ext} = 50,98^\circ$.

The first stage of synthesis has yielded only one solution: $b_1 = AC = 75,4867$ mm; $b_4 = CH = 633,293$ mm; $x_A = 150$ mm; $y_A = 557,805$ mm. At the second stage of synthesis a number of solutions meeting given conditions have been received. The results of synthesis for two variants of mechanisms are presented in the Table.

Example 2. The working point of a thread-spreading mechanism of winding machine is required to uniformly trace a circular arc with radius $R = 236,01$ mm and the center at the origin of the coordinates (a real problem in textile industry). Angular stroke of this arc is 64° ; $\Phi = 128^\circ$; $N = 33$, $\nu_1 = 1$; $\mu_{lim} = 45^\circ$; $(\delta_{max})_{lim} = 0,5$ mm.

The base $ABDE$ four-bar linkage has the following parameters: $AB = h_1 = 150$ mm, $BD = h_2 = 600$

mm, $DE = h_3 = 300$ mm, $AE = 700$ mm. This linkage has $\mu_{1ext} = 54,12^\circ$.

Table 1: Parameters of synthesized linkages (mm)

Parameters	Straight-line generators		Arc generators	
	LINE1	LINE4	ARC06	ARC22
x_E	-171,39	619,846	1075,64	850,63
y_E	940,827	728,815	53,1694	1416,02
$\lambda_1 = \angle BAC$	380°	370°	56°	-2,75°
$\lambda_2 = \angle DBF$	345°	345°	300°	35°
$b_2 = BF$	490	490	590	320
$h_4 = CG$	186,794	170,097	411,256	181,408
$\lambda_4 = \angle GCH$	170,468°	-113,01°	-43,109°	139,036°
$h_5 = FG$	404,256	383,699	584,404	361,456
α_0	10°	51,32°	275°	333,75°
r_1	-1	+1	+1	-1
r_2	+1	-1	-1	+1
δ_{max}	0,4628	0,4487	0,3635	0,3737
μ_{2ext}	45,15°	47,25°	52,21°	45,74°

The first stage of synthesis has yielded only one solution: $b_1 = AC = 98,718$ mm; $b_4 = CH = 1175,83$ mm; $x_A = 1075,64$ mm; $y_A = 753,169$ mm. At the second stage of synthesis a number of solutions meeting given conditions have been received. Results of synthesis for two variants of mechanisms are presented in the Table. Kinematic diagram of one mechanism is shown in Fig. 7.

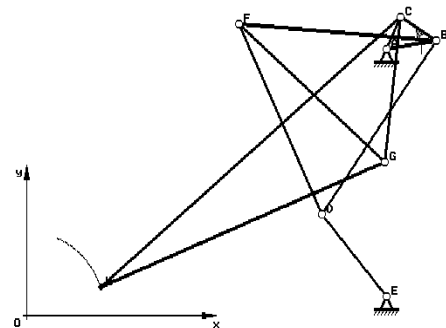


Fig. 7: Watt I circular arc generator ARC06

References

- [1] A.F. Al-Dwairy, A.B Kikin., *Multipurpose Technique for Least-Squares Synthesis of Linkages*, Proc. of the 11th World Congress in Mechanisms and Machines Science; Tianjin, China, pages 181-185, 2004.
- [2] A.B. Kikin, *Interactive Technique for Analytic-optimization Synthesis of Mechanisms*, Proc. of the 28th Summer school "Actual Problems in Mechanics"; St.-Petersburg, Russia., Vol.2, pages 416-423, 2000.
- [3] A.B Kikin., A.A. Kikin, *Least-squares Technique Synthesis of a Stephenson I Six-bar Path Generator*, Proc. of X. International Conference on the Theory of Machines and Mechanisms; Liberec, Czech Republic, pages 341-346 (in Russian), 2008.
- [4] E.E. Peisach, V.A Nesterov, *A system of Designing of Planar Linkages*. Publ. "Mashinostroenie", Moscow, Russia, 232p. (in Russian), 1988.



An Experimental Evaluation of Earthquake Effects on Mechanism Operation

Özgün SELVİ^{1*}, Marco CECCARELLI²

^{1*}Izmir Institute of Technology, Turkey
ozgunselvi@iyte.edu.tr

² LARM, Laboratory of Robotics and Mechatronics
University of Cassino, Italy

Abstract

In this paper the effects of earthquakes on the operation of mechanical systems has been investigated experimentally with the help of Capaman (Cassino Parallel Manipulator) which is a 3 DOF robot that can simulate 3D earthquake motion properly. The sensitivity of the operation characteristics of machinery to earthquake disturbance is identified and characterized. Experimental tests have been carried out by using a slider-crank linkage and LARM hand as a test-bed mechanisms. Results are reported and discussed to show characteristic seismic effects on mechanism operations.

Keywords: Experimental mechanics, simulation, mechanisms, earthquake effects

1. Introduction

In the last decade parallel manipulators have been proposed for new application areas because of their better characteristics such as higher stiffness, velocity and acceleration motion, and payload capacity, with respect to those of serial manipulators. In this work these properties of parallel manipulators have been used to investigate experimentally the effects of earthquakes on the operation of mechanical systems by the help of Capaman (Cassino Parallel Manipulator), which is a 3 DOF robot designed in 1997,[1].

For investigating the earthquake characteristics and earthquake resistant constructions, earthquake simulators are commonly used for experimental tests in the field of Civil Engineering. It is important to have earthquake simulators that can reproduce earthquakes with main and real characteristics. Generally, most of the earthquake simulators are shaking tables, which are actuated by hydraulic actuators fixed on the base. High payload capacity, high motion speeds, and high accelerations are the main characteristics of the shaking tables, but they refer to seismic translational motions only.

A new earthquake simulator is a suitable application of CaPaMan which can simulate not only translational

motion but also 3-D waving motions of earthquakes. Performances and suitable formulation for the operation of CaPaMan as earthquake simulator have been presented by theoretical investigations and experimental validations in [2- 5]. In fact, the operation of CaPaMan can be easily adjusted to obtain any kind of earthquake in terms of magnitude, frequency and duration by giving suitable input motion

. A novel field of interest can be recognized in investigating the effects of earthquake motion on the operation of machinery. Although vibrations and their isolations are well known as affecting the machinery operation, the specific characteristics of earthquake actions on machinery are not yet fully explored.

In this paper the effects of earthquake on the operation of mechanical systems have been investigated by an analysis and reproduction of an earthquake motion. This paper illustrates a specific activity that has been focused in determining experimentally the effects of earthquake motion on mechanism operation by looking at the changes in the motion (acceleration) or force outputs of the mechanisms. Experimental tests have been carried out by using a slider-crank linkage as a test-bed mechanism for standard machinery and LARM hand as representing robotic systems.

2. Earthquake Motion Characteristics

A sudden and sometimes catastrophic movement of a part of the surface of the Earth is called an earthquake which results from the dynamic release of elastic strain energy that radiates seismic waves. Large earthquakes can cause serious destruction and massive loss of life through a variety of types of damage such as fault rupture, vibratory ground motion, inundation, various kinds of permanent ground failure, and fire or a release of hazardous materials, but even buildings/constructions collapses and vehicles/machinery operation crashes. Ground motion is the dominant and most widespread

cause of damages. [6]

In Turkey seismic activities occurs due to the place of the country between continents. According to the earthquake regions map for Turkey in Fig.1 92 % of the country is in the risky region of earthquake, and 95% of the population in Turkey is under the danger of earthquake.

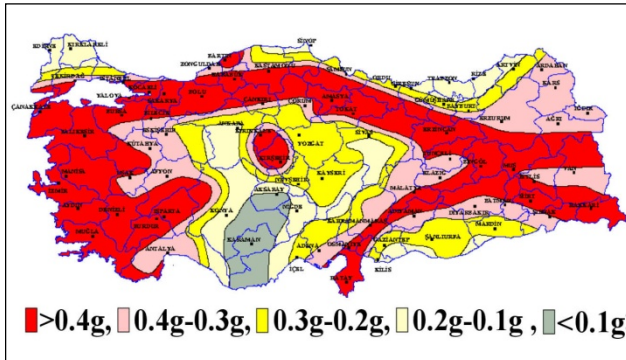


Fig.1. Earthquake Regions Map of Turkey. [8]

In general an earthquake has three phases such as an initial phase, which corresponds to the beginning of the seismic motion, an intermediate phase where the maximum acceleration peaks and displacements occur and a final phase representing the end of the earthquake. Main characteristics of an earthquake are frequency, amplitude and acceleration magnitude, since the resonance of a system is determined by frequency value, duration of the stress action due to a seismic motion, amplitude and acceleration magnitude of an earthquake

The period of a seismic cycle and characteristic length for each seismic wave must be identified to define the seismic motion. As mentioned in Fig.2, [5]; main types of seismic waves can be considered as: the compression expansion waves P, transversal waves S, and superficial waves M. They can be classified by referring to the spread speed and terrain movements. S waves are transversal waves and the usual period of the S waves are between 0.5 and 1 second. The P waves spread through a spring-like-motion with a typical period between 0.1 and 0.2 second. Both P and S waves occur close to the epicenter. Unlike P and S waves, M waves occur on the surface of the terrain at a considerable distance from the epicenter of the earthquake and usually they have a period from 20 second to 1 minute. In Fig. 2c main difference among the seismic waves is represented in terms of acceleration magnitude and characteristic period of oscillating motion which is responsible of a periodical excitation of structures that can be damaged when resonance situation occurs.

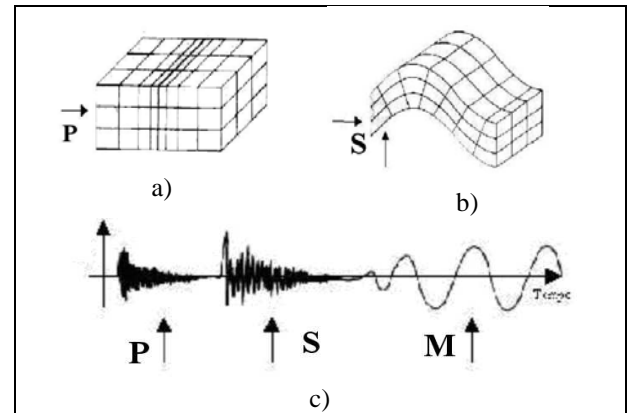


Fig. 2. Basic characteristics of seismic waves: a) compression and expansion waves; b) transversal waves; c) types of seismograms. [5]

Usually, critical resonant motion is analyzed in terms of translational seismic components, but even angular motion can strongly contribute to the resonant excitation. Thus unlike most of the simulators where the 3D motion of the terrain due to earthquake waves has not been taken into account in this paper 3D motion capability of CaPaMan parallel manipulator have been used to simulate earthquake motion with its full motion effects

3. Mechanism Operation

As mentioned in the terminology of IFToMM [9] a machine is a “mechanical system that performs a specific task, such as the forming of material, and the transference and transformation of motion and force.” and mechanism is defined as a “constrained system of bodies designed to convert motions of, and forces on, one or several bodies into motions of, and forces on, the remaining bodies”. Mechanisms, which can be considered the core parts for machines are combination of gears, cams, linkages, springs, and etc.

A sequence for the operation of mechanisms is input, task and output. Task and output of mechanisms can differ with respect to desired results. These desired results are task goals for mechanisms, which can be classified as function generation, point guidance and body guidance, [7]. Function generation is the coordination of positions of the input and output links, in which the output members need to rotate, oscillate or reciprocate to a specified function of time or input motion. Path generation is the design of mechanism for guiding a coupler point along a described path. Rigid body guidance is the problem of translation and/or orientation of a rigid body from one position to another.

Considerations in designing of the mechanisms for those and other tasks are related to characteristics of

operation such as, general operation performance, repeatability of operation frequency, efficiency, reliability, precision and accuracy. Also vibrations that can occur during the operation been considered and some isolation is applied to machine basements.

Machinery operations are usually aimed to perform motions and actions with the task performance that are related to the machinery aim and also interaction with users and environments. The machinery aim can be in general understand described by mechanical properties whose performance indices can be studied in term of motion characteristics and action transmission with efficiency features both from kinematical and energy view points. Machinery interactions can be understood as related to the effects toward the surrounding environment and mainly as from the viewpoint of human-machine interactions. Those last features will include issues on comfort and safety that can make strong constraints to machinery operations with limited range of feasible operations. Summarizing, machinery operations can be described and characterized by performance indices which can be formulated for general but specific aspects that permit both design procedures towards optimal solutions and experimental control/monitoring of successful operation. Special attention is today addressed to safety as interaction with human users, even when using a machine under critical, risky situations which can be characterized by impact, high accelerations or changed operation outputs. Also efficiency in force transmission and energy consumption is of great importance in modern machinery.

Unfortunately in general the effects of earthquakes are neglected during machine design. The difficulty to determine results of the effects of the earthquakes is due to the different types of totally random waves caused by them, as mentioned in section 2.

An illustrative example for machinery operation can be given as referring to the running of a train. Input for trains is the action of actuators for wheel motion. Task for the train is the body guidance of the train and the output is a stable motion with the features comfort, safety, efficiency and reliability. A general operation performance of the train is related to vibrations which effect also comfort. Characteristics of train motions are strongly affected by actions on machinery operations. Comfort in train task is felt by human users mainly in terms of acceleration of the train cars. But this task efficiency is a result from the transmission of motions and forces from the mechanism for the wheel actuation and car guidance in relative motion during the run. Those characteristics are demanded in more robust outputs in faster trains. And any disturbance can produce not only uncomfortable operation, but even risks of disasters in train run.

For a mechanism it is necessary to have a fixed reference for defining the motion. Usually ground is taken as the reference for machines and manipulators. When an earthquake occurs these fixed link starts to move and applies force acting on the machines or manipulators. The effect of these unexpected random forces and motions on machines must be investigated to see the unexpected changes of the outputs. This knowledge can give useful feedback for the design of machines that usually are not affected by earthquakes.

Bench-tests are made in this work by using a slider crank mechanism which can represent the work of industrial machinery and LARM to model the effect of earthquake to robotics and advanced systems. These systems are selected due to their easy-operation property and the output task goal can be clearly defined.

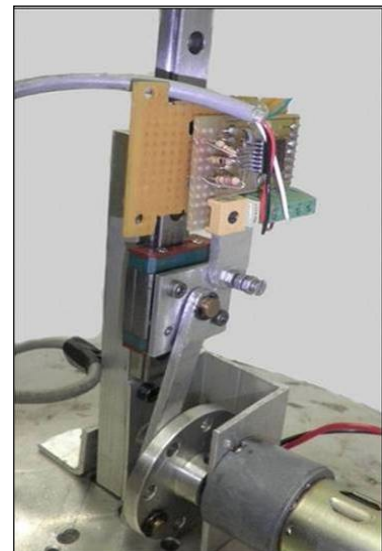


Fig. 3. A test-bed slider-crank mechanism at LARM: an experimental set up with accelerometer on the slider.

The slider-crank mechanism in Fig.3 is often used to convert rotary motion into alternating linear motion or vice versa. A slider-crank kinematic chain consists of four bodies that are linked with three revolute joints and one prismatic joint.

Four different mechanisms or inversions of this kinematic chain are possible depending on which body is grounded, namely the crank, connecting link, sliding link or slot link. One of the inversions is used in internal combustion engines (automobiles, trucks and small engines) with application of perhaps a billion engines making the slider-crank mechanism one of the most used mechanisms in the world today.

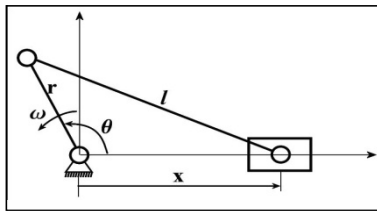


Fig. 4. Kinematic parameters for a test-bed slider-crank mechanism.

In Fig.4 kinematic parameters of slider crank are shown as referring to Fig.4 where the length of the coupler is 75 mm and length of the crank is 19 mm the angular velocity is 43 rpm. Using these parameters acceleration equation as output of the slider can be calculated as

$$\ddot{x} = -r\alpha \left(\sin\theta + \frac{r \sin 2\theta}{2l} \right) - r\omega^2 \left(\cos\theta + \frac{r \cos 2\theta}{l} \right) \quad (1)$$

A numerical computation is shown in Fig. 5 which shows a nearly harmonic motion.

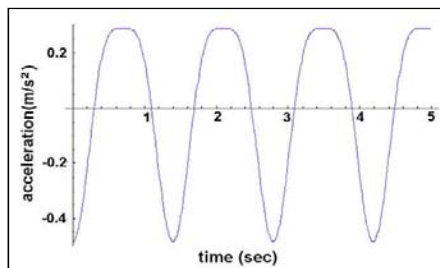


Fig. 5. Numerical accelerations of slider-crank mechanism.

Fig. 6 shows the experimental measure of the acceleration of the slider as from the case in Fig.3. The noise in the experimental measure is due to backlash of the components, flexibility of the links and design tolerances. Also some noise is caused by environmental waves into the frame link.

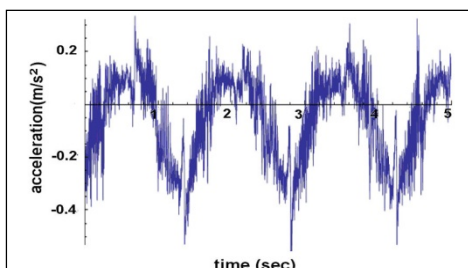


Fig. 6. An experimental measure of the typical accelerations of the slider-crank mechanism operation with crank rotating of 43 rpm.

Other peculiar mechanism operation can be considered from robotic systems. As test-bed mechanism the LARM Hand prototype has been used in this work. The LARM Hand shown in Fig.7 is composed of three fingers. In particular, a human-like grasping is obtained by each finger with one DoF motion by using a suitable mechanism, whose design has been obtained through cross four-bar linkages to be fitted in the finger body [11]. Consequently the grasp can be regulated through a simple control by using force sensor signals and an industrial small PLC for operation.

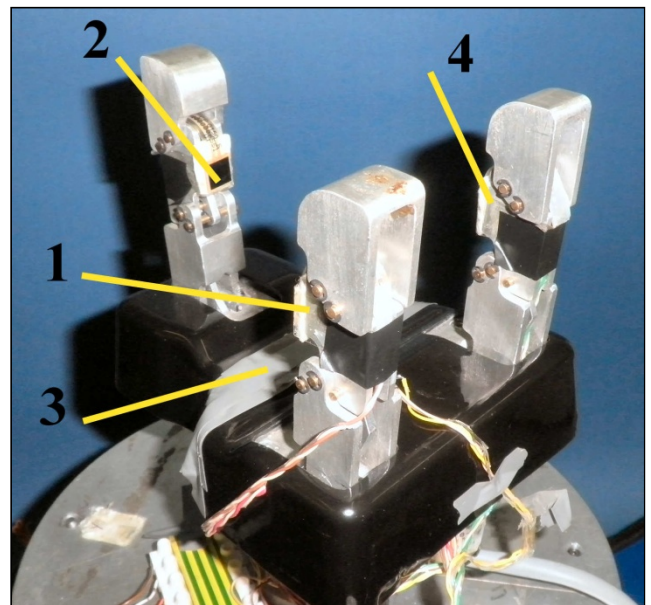


Fig. 7. LARM Hand.

The LARM Hand can be used as a grasping end-effector in robots and automatic systems. Each finger of LARM Hand has 3 joints and 1 actuator. The range of motion for the prototype in Fig.7 is 40 deg for finger inputs and 140 deg for fingertip links. LARM Hand is equipped with 4 force sensors whose sensitivities are from 1 to 100 N and with a resolution lower than 0.5% of its full scale. The dimensions of the finger are 1:1.2 of the human finger size and the hand is 110x240x120 mm and the size of objects that can be grasped is between 10 to 100 mm.

4. An Experimental Setup

The CaPaMan prototype is shown in Fig. 8. The laboratory test-bed prototype for earthquake simulator consists of CaPaMan prototype with sensors, a controller for its operation and an acquisition board connected to the computer, in order to acquire the components of the linear

accelerations occurring along the axes of the reference system belonging to the mobile platform.



Fig. 8. An experimental setup at LARM with the slider-crank mechanism.

Nine accelerometers have been properly installed on the faces of three cubes made of plastic at points H(Hx, Hy, Hz), P1(P1x, P1y, P1z) and P2(P2y, P2z) and another cube has been placed at point P3(P3z), as shown in Fig.9.

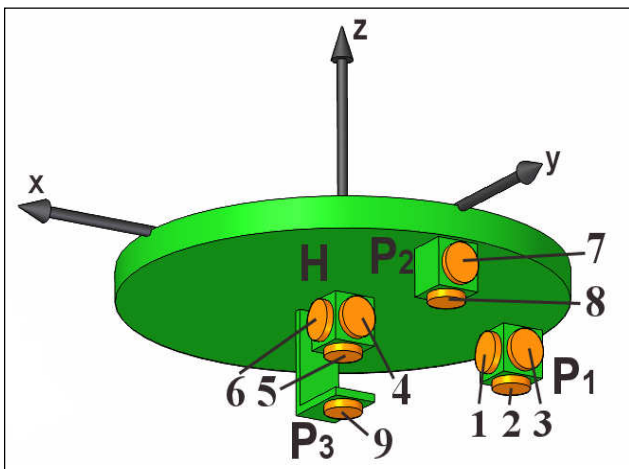


Fig. 9. A scheme of mobile platform for the accelerometers placement on points H, P1, P2, and P3.

The control system scheme layout for Capaman manipulator is shown in Fig.10. Data for simulating the earthquake is send to the servo motor controller (Scorbot-ER V) by using the ACL programming language. The motors move the mobile platform and by the help of accelerometers the acceleration information of the mobile platform through the CB-68 LP parallel Port is processed and visualized with the LabView software.

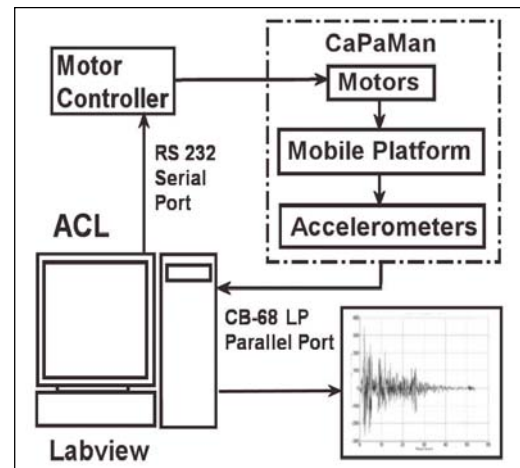


Fig. 10. Control system layout for CaPaMan as earthquake simulator.

The measured accelerations of the point H are the linear accelerations of the platform and the measured acceleration data from the other accelerometers are used to calculate angular accelerations and angular velocities of the rigid body by using equations

$$\begin{aligned}\omega_x &= \pm \sqrt{\frac{1}{2} \left(\frac{a_{HY} - a_{P2Y} + a_{HX} - a_{P1X} + a_{P3Z} - a_{HZ}}{r} \right)} \\ \omega_y &= \pm \sqrt{\frac{1}{2} \left(\frac{a_{P1X} - a_{HX} - a_{HY} - a_{P2Y} + a_{P3Z} - a_{HZ}}{r} \right)} \\ \omega_z &= \pm \sqrt{\frac{1}{2} \left(\frac{a_{HY} - a_{P2Y} - a_{HX} - a_{P1X} - a_{P3Z} - a_{HZ}}{r} \right)}\end{aligned}\quad (2)$$

and

$$\begin{aligned}\dot{\omega}_x &= \frac{a_{P2Z} - a_{HZ}}{r} \pm \frac{1}{2} \sqrt{\left(\frac{a_{P1X} - a_{HX}}{r} \right)^2 - \left(\frac{a_{HY} - a_{P2Y} - a_{P3Z} - a_{HZ}}{L} \right)^2} \\ \dot{\omega}_y &= \frac{a_{P1Z} - a_{HZ}}{r} \pm \frac{1}{2} \sqrt{\left(\frac{a_{HY} - a_{P2Y}}{r} \right)^2 - \left(\frac{a_{HX} - a_{P1X} - a_{P3Z} - a_{HZ}}{L} \right)^2} \\ \dot{\omega}_z &= \frac{a_{HY} - a_{P1Y}}{r} \pm \frac{1}{2} \sqrt{\left(\frac{a_{P3Z} - a_{HZ}}{r} \right)^2 - \left(\frac{a_{HY} - a_{HY} - a_{P1X} - a_{P2Y}}{L} \right)^2}\end{aligned}\quad (3)$$

These equations are derived from the theorem of the accelerations of the rigid body by three points [12]. By observing the first motion of the platform the sign of initial angular velocity is, determined and then following velocities are used with respect to that.

5. Experimental Tests and Effect Evaluation

Effects of seismic motion on mechanism operations and robotic applications have been investigated by using a slider-crank mechanism and LARM Hand. 3D earthquakes are applied to slider-crank mechanism when the slider of the mechanism is situated vertical, horizontal and inclined (45 deg) .The speed of the crank is set to 43 rpm and 26 rpm. The LARM Hand has been tested while handling of two different types of materials (wood, plastic) when subjected to seismic motion. The characteristic phases of the simulated earthquake whose frequency is 1.5 Hz is given is given in Table 1.

Table 1. The characteristics of simulated earthquake

Tmax	Tmin	Timax	Tfmax	No. of oscillations	Total time
60msec	60msec	30msec	30msec	20	13sec

An example of measured accelerations data of the platform during this earthquake is given in Fig. 11.

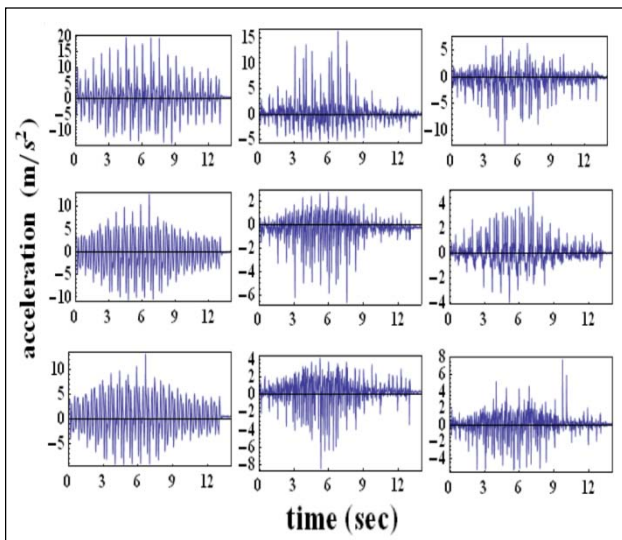


Fig 11. An example of the measured accelerations of CaPaMan during earthquake simulation.

Using the measurement data taken from the accelerometers, angular accelerations and angular velocities of the platform are calculated by using equation sets 2 and 3. Maximum values of linear acceleration

angular velocities and angular accelerations of the platform for three axes are listed in Table 2.

Table 2. Numerical characteristics of the simulated 3D earthquake

axis	a_{Hmax} [m/s ²]	ω_{max} [rad/s]	$\dot{\omega}_{max}$ [rad/s ²]
X	4.99	10.92	116.02
Y	12.85	7.96	253.60
Z	3.02	7.08	264.78

The static situation represents the case when the motor of the slider-crank linkage mechanism runs at constant speed, and there is no motion of CaPaMan. Results of the data acquisition from the sensor on the slider during static condition for crank velocity $w_{crank}=41$ rpm are reported in Fig 6 and for the case with 26. They are shown in Fig.12.

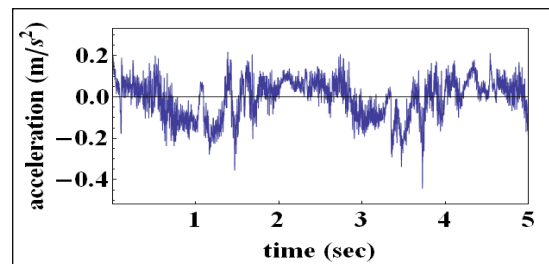


Fig. 12. The measured acceleration of the slider during static condition with crank rotating at 26 rpm.

When the slider-crank is subjected to an earthquake motion the acceleration of the slider is altered to the measured acceleration shown in Fig.13

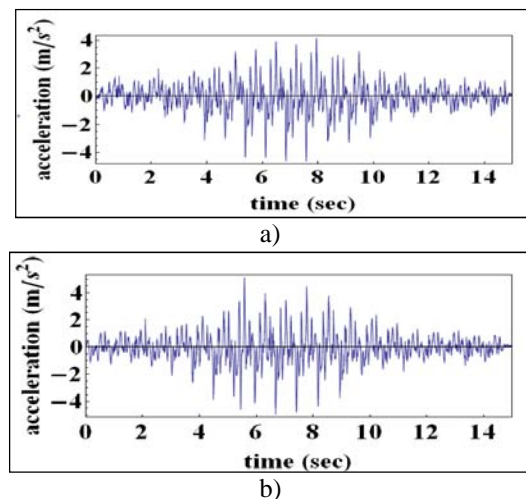
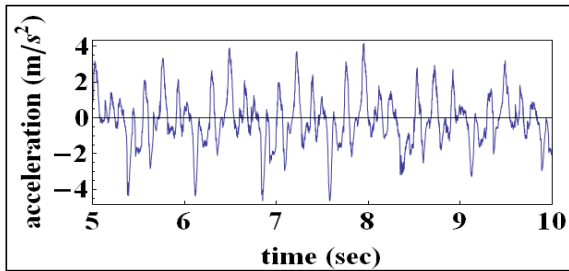
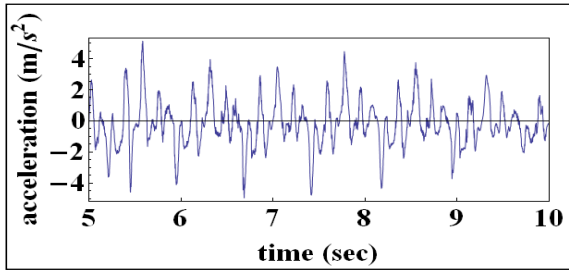


Fig.13. The measured acceleration of the slider moving vertical during a simulated earthquake: a) $w_{crank} = 43$ rpm; b) $w_{crank} = 26$ rpm.

From Fig.13 the slider acceleration is observed as it changed. Details of these changes are visible from Fig.14 to Fig 16 with views of slider acceleration between 5.0 and 10.0 seconds of earthquake motion when the seismic accelerations are at maximum.

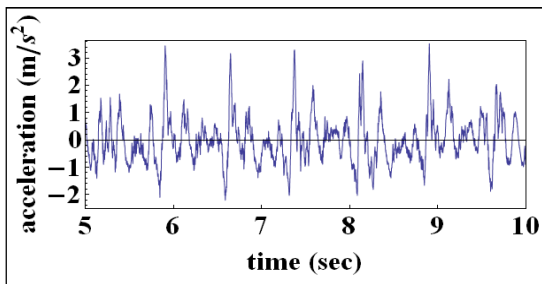


a)

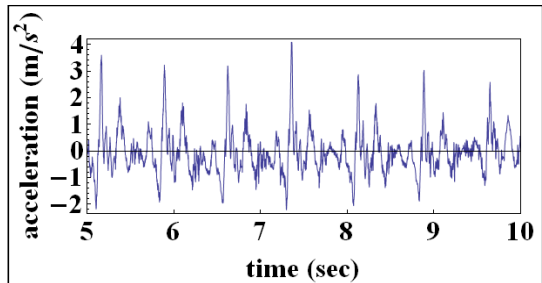


b)

Fig. 14. The measured acceleration of the slider while moving vertical during a simulated earthquake:
 a) $w_{crank}=43rpm$; b) $w_{crank}=26 rpm$.

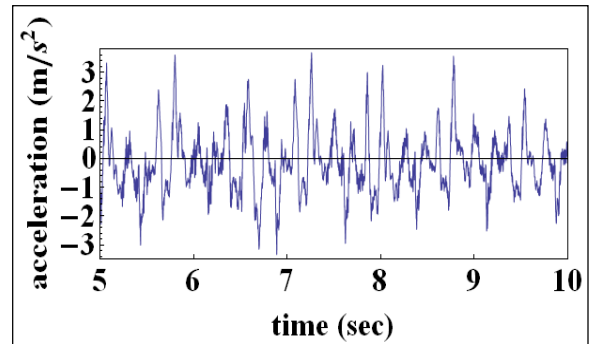


a)

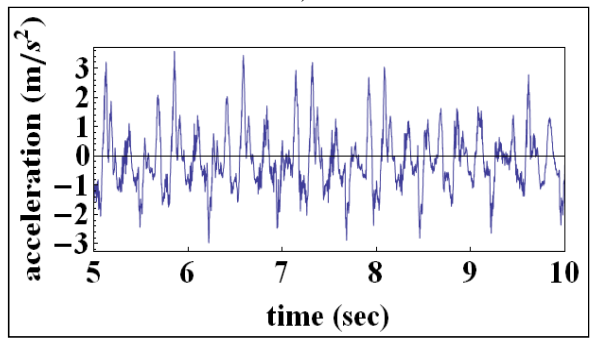


b)

Fig. 15. The measured acceleration of the slider while moving horizontal during a simulated earthquake:
 a) $w_{crank} =43rpm$; b) $w_{crank}= 26 rpm$.



a)



b)

Fig. 16. The acceleration of the slider while moving inclined during a simulated earthquake:
 a) $w_{crank} =43rpm$; b) $w_{crank}= 26 rpm$.

It is observed from the Figures 14-16 that the shape and amplitude of the acceleration of the slider during a simulated earthquake are strongly changed in addition oscillations of the slider acceleration are also vanished. Zoomed views with plot comparison are reported in Fig.17.

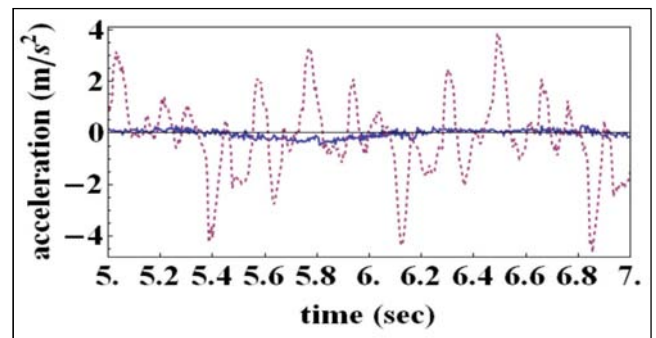


Fig.17. The measured accelerations of the slider while moving vertical: during static condition (plain line), during a simulated earthquake (dashed line),
 $w_{crank} =43rpm$

The numerical effects of the earthquake motion are shown in table 3. As referring to a_{Smax} which is the maximum

acceleration of the slider and a_{Smin} which is the minimum acceleration of the slider.

Table 3. Numerical results of slider acceleration during simulated earthquake in Fig.s 14-16

Position of the slider during earthquake	Speed of crank			
	43 rpm		26 rpm	
	a_{Smax} m/s ²	a_{Smin} m/s ²	a_{Smax} m/s ²	a_{Smax} m/s ²
Horizontal	4.17	-4.65	5.13	-4.96
Vertical	3.52	-2.38	4.08	-2.22
Inclined	3.68	-3.33	3.57	-3.11
Static	0.45	-0.71	0.31	-0.50

It seems the slider acceleration is fully disturbed by the earthquake effects. Considering the different speeds of the mechanism the slower one is more affected with respect to its lower static acceleration values.

Seismic disturbance on robotic applications has been investigated experimentally on the LARM hand.



Fig.18. An experimental setup with LARM Hand

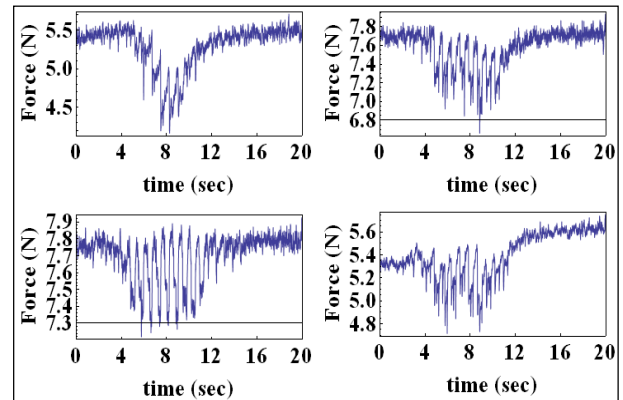
In Tables 3 and 4 the forces acting to the materials during static condition and during earthquake are given and in Fig.19 the force data of the grippers are shown during a simulated earthquake. From the Tables 3 and 4 and Fig.19. the force on the gripper fingers have an oscillatory motion during the earthquake and there is an obvious change at the end. These results show that during an earthquake characteristic for the manipulator such as output (force), repeatability of the operation frequency and efficiency, and the reliability of the process (precision accuracy) are affected. For the LARM Hand the holding force on the fingers decreases and if the force exceeds the force needed to handle the block it can cause to the slipping of material.

Table 4. The grasping forces of a wood cylinder of LARM Hand

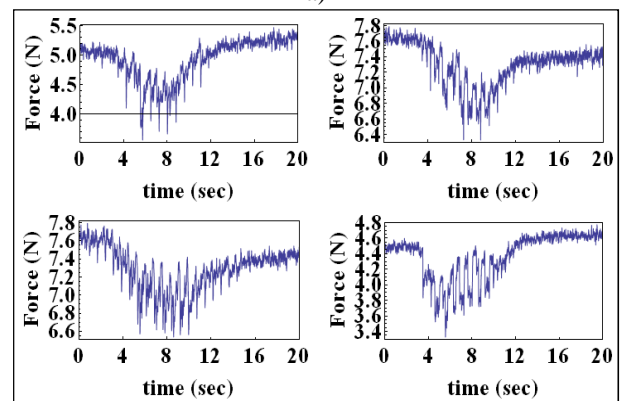
	F_1 [N]	F_2 [N]	F_3 [N]	F_4 [N]
Static	1.5	7.7	7.2	4.3
Initial	5.4	7.7	7.7	5.3
Final	5.5	7.7	7.8	5.6
Minimum	4.2	6.6	7.2	4.7

Table 5. The grasping forces of a wood cylinder of LARM Hand

	F_1 [N]	F_2 [N]	F_3 [N]	F_4 [N]
Static	2.9	7.1	5.7	2.2
Initial	5.1	7.6	7.6	4.5
Final	5.3	7.4	7.4	4.6
Minimum	3.6	6.3	6.5	3.3



a)



b)

Fig. 19. The grasping forces by LARM Hand during a simulated earthquake on: a) wood cylinder; b) plastic cylinder.



6. Conclusions

In this paper with the help of CaPaMan the effects of earthquakes on the operation of mechanical systems have been investigated experimentally. The sensitivity of the operation characteristics of machinery to earthquake disturbance is characterized in terms of acceleration response of output of machinery operation. Experimental tests have been carried out by using a slider-crank linkage with slider in horizontal, vertical and inclined positions with different crank speeds and by using the LARM hand while handling object of two types of materials such as wood and plastic. The results show that an earthquake will surely effect the acceleration of the mechanism operation both in shape and amplitude of the output motion of grasping. During a seismic disturbance applied to the LARM Hand the decreasing holding force on the fingers of the hand is observed towards to slipping of object.

Acknowledgements

Part of this work has been developed during a period of study of the first author at LARM within Socrates-Erasmus program in the year 2010. The Authors wish to acknowledge the support and help of Prof. Rasim Alizade from Izmir Institute of Technology.

References

- [1]. M. Ceccarelli, *A New 3 DOF Parallel Spatial Mechanism*, Mechanism and machine theory 1997, Vol.32,n.8, pp 895-902.
- [2]. M. Ceccarelli, F. Pugliese, C. Lanni., J.C.M. Carvalho, *CaPaMan (Casino Parallel Manipulator) As Sensored Earthquake Simulator*. Proceedings of the 1999 IEEE/RSJ International Conference on Intelligent Robots and Systems, Kyongiu 1999, pp 1501-1506.
- [3]. M. Ceccarelli, E. Ottaviano, M. Galvagno, *A 3-DOF Parallel Manipulator as a Earthquake Motion Simulator*, Seventh International Conference on Control, Automation, Robotics and Vision (ICARCV'02) Dec 2002, Signapore, 2002, p 1534.
- [4]. E. Ottaviano, M. Ceccarelli, *Application of a 3- DOF Parallel Manipulator for Earthquake Simulations*, IEEE Transactions on Mechatronics Vol. 11, No.2, 2006, pp. 140-146.
- [5]. M. Ceccarelli., E. Ottaviano, C. Florea, T.P. Itul, A. Pisla, *An Experimental Characterization of Earthquake Effects on Mechanism Operation*, IEEE-TTTC International Conference on Automation, Quality and testing, Robotics, AQTR 2008,Cluj-Napoca, 2008
- [6]. W.F. Chen, C. Scawthorn, *Earthquake engineering hand book*, CRC Press, Boca Raton , 2003
- [7]. J.J. Uicker, G.R. Pennock, J.E. Shigley, *Theory of machines and mechanisms* , Oxford University Press, Oxford, 2003
- [8]. General directorate of disaster, earthquake research department of Turkey, <http://www.deprem.gov.tr/>,2010
- [9]. IFToMM Terminology , <http://130.15.85.212/terminology/TerminologyWeb/index.html>,2010
- [10]. J.C.M. Carvalho, M. Ceccarelli. *Seismic motion simulation based on CaPaMan simulaton*, Journal of the Brazilian Society of Mechanical Sciences, Vol. 25, n. 3, July 2002, pp 213-219.
- [11]. G. Carbone, M. Ceccarelli, *Design of LARM Hand: Problems and Solutions*, Journal of Control Engineering and Applied Informatics, Vol.10, n.2, pp. 39-46,2008
- [12]. P. Field, A. Ziwet, *The accelerations of the points of a rigid body*, The American Mathematical Monthly, Vol. 23, No. 10 (Dec., 1916), pp. 371-381



Session 5:

Dynamics and Vibrations of Machinery (DvM) Nanotechnology and Micro: Manipulators, Robots, Mechanisms (NtMm)



Proceedings of the International Symposium of Mechanism and Machine Science, 2010
AzCIFTtoMM – Izmir Institute of Technology
5-8 October 2010, Izmir, TURKEY

The influence of the vibration frequency on the torsion stiffness of the driving coupling

Isa Ali oğlu KHALILOV^{1*}

^{1*} Azerbaijan Technical University, Cavid Ave. 25, AZ1073 Baku
 Fax : +994 12 438 32 80
 e-mail : khalilov@mail.az

Abstract

The article is about a mathematical model that takes into account the impact of the oscillation frequency driving the mechanical system for the torsion stiffness of the couplings. In the frame of this model, there got dependence of the definition of static and dynamic torsion stiffness of elastic couplings. It was found that coupling decreases with increasing oscillation frequency of the applied torque value of dynamic stiffness. This phenomenon is forming practical interest for the vibration frequencies of the load less than the natural frequencies of vibration couplings.

Keywords: coupling, dynamical torsion stiffness of coupling, dynamical vibration frequency, discontinuity.

1. Introduction

Reliability, productivity and quality of the work of machines and mechanisms are closely connected with dynamical properties of the driving system. In its turn, dynamical property of the driving system of machines and aggregates are characterized, first, in hardness of the composition elements, in particular, connecting couplings [2,3,4]. Such as the driving couplings work on the torsion, from the dynamical point of view, it presents interest to study the torsion stiffness of couplings.

In the available literature [2,4] and the standards [5] the static (C_M or C_{Mst} Nm/rad) and dynamical (C_{Mdin} , Nm/rad) stiffness on the torsion are distinguished. Hence, it is shown that dynamical hardness usually is more than static stiffness ($C_{Mdin} > C_M$). Static stiffness of couplings

on the torsion is determined depending on transmission moment (M) and from the relative twisting angle of half-coupling (φ) in the following form (Fig.1):

$$C_M = \frac{dM_{el}(\varphi)}{d\varphi} \quad (1)$$

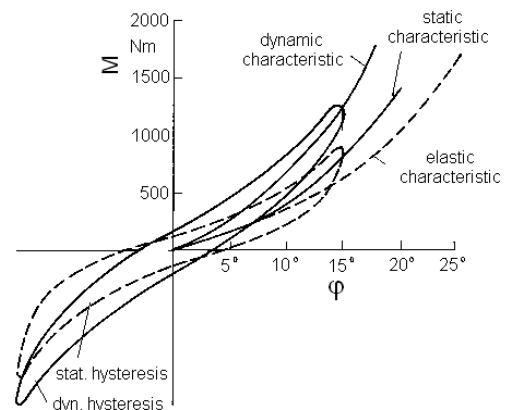


Figure1: Static and dynamical characteristic of the torsion stiffness of coupling with armoring.

It is known that joining shafts of the driving gears usually have different misalignment of assemblage (radial, axial and angle). In this case static stiffness cannot characterize completely dynamical characteristics of coupling. That's why, dynamical stiffness is determined by the following way:

$$C_{Mdin} = \frac{dM_{din}(\varphi)}{d\varphi} \quad (2)$$



We remark that for the small angles of turn this equation

$$\text{is accepted in the following form: } C_M = \frac{M}{\varphi}$$

$$\text{or in the common accepted form } M = C_M \varphi \quad (3)$$

As evident from equation (1) and (2) in the both cases torsion stiffness of couplings is expressed as function of the twisting angle of half-coupling. On the other hand, it is known us that on the torsion stiffness of couplings exerts essential influence on the character of loading, temperature, vibration frequency and so on. Among enumerating facts special interest present to the influence of vibration frequency of the transmitted loading on the dynamical stiffness of coupling.

2. Mathematical model.

For the researching of the influence of torsion vibration frequency on the dynamical vibration frequency we present the calculating model of coupling in two forms of hard disc (half- coupling),inter-joining by elastic rod (Fig.2) such as different constructions of elastic couplings (Fig.3) are accordingly aforesaid affirmation of principle work.

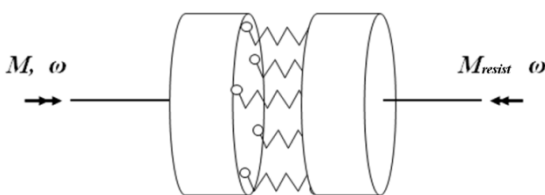
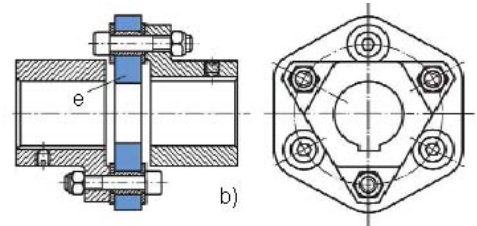


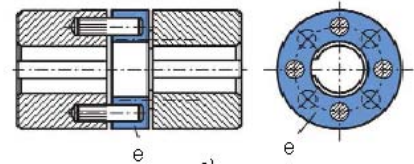
Fig.2. Calculation plan of the joint-coupling (M_{resist} -moment of resistance).



a)



b)



c)

Fig.3. The construction of elastic coupling (e-elastic element): a) pin flexible coupling, b) and c) bolt coupling with elastic intermediate disc.

In the common case elastic elements of couplings (rod, Fig. 2) work on the bend and twisting. However, in a small angle of turn of half-coupling of these rods will work on the bend density. The resultant of these bends of rods drive to the turn of half- coupling. This turn by itself is the twisting of coupling. Bend of rod coincides with the bend console under action of cutting strength. Taking into account of condition of the fastening to the disc (half-coupling) bend of rod has the following form

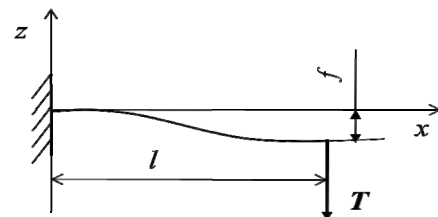


Fig.4. The deflection of elastic element of coupling.



The equation of the bend of elastic rod has a form

$$\varepsilon = z \frac{\partial \theta}{\partial x}; \quad \theta = -\frac{\partial f}{\partial x}; \quad \frac{\partial Q}{\partial x} = 0; \quad Q - \frac{\partial M}{\partial x} = 0;$$

$$M = EI \frac{\partial \theta}{\partial x} = -EI \frac{\partial^2 f}{\partial x^2} \quad (4)$$

With $x=0$; $f=0$ and $\frac{\partial f}{\partial x}=0$

With $x=l$; $\frac{\partial f}{\partial x}=0$ and $EI \frac{\partial^3 f}{\partial x^3} = -T$

Where ε - the deformation arbitrary point of rod along axial x , z – cross coordinate, θ - the turn corner of the rod on account of flexure, f - deflection, Q - the cutting force of rod, M - torque moment, I -moment mechanically section rod, E - coefficient of elasticity of the material of the elastic element of coupling (rod).

Let's determine the flexure of the rod $f|_{x=l} = f(l)$.

The equation (4) we change in the following way.

$$Q = T; \quad T + EI \frac{\partial^3 f}{\partial x^3} = 0;$$

$$f = -\frac{T}{EI} \left(\frac{1}{6}x^3 + \frac{1}{2}c_1x^2 + c_2x + c_3 \right) \quad (5)$$

From the limits condition follow that: $c_2 = 0$; $c_3 = 0$

$$\frac{1}{2}l^2 + c_1l = 0; \quad \text{from here } c_1 = -\frac{1}{2}l.$$

Then

$$f = -\frac{T}{EI} \left(\frac{1}{6}x^3 - \frac{1}{4}lx^2 \right); \quad f(l) = \frac{T}{EI} \cdot l^3 \cdot \frac{1}{12} \approx \varphi R$$

(6)

Found constant defines the turn corner of half- coupling or twisting corner of coupling such as $f(l) = \varphi R$ (where R - radius of circle in which is disposed the rods.

Let's determine the dependence of the cutting force T - from transmitted coupling of torque moment M_M . Let's present M_M in the following form $M_M = n \cdot R \cdot T$, where n -number of rods.

Then taking into account (3) we receive:

$$\varphi R = \frac{1}{12} \frac{1}{EI} l^3 \cdot \frac{M_M}{nR} = C_M^{-1} M_M R \quad \text{or}$$

$$C_M^{-1} = \frac{1}{EI} \cdot l^3 \cdot \frac{1}{12} \cdot \frac{1}{nR^2} \quad (7)$$

Thus, the offered model helps within the bounds determined the static stiffness of coupling.

For the determining of dynamical stiffness of coupling, by using the offered approach we consider the bending vibrations of elastic rod. Then instead of equation (4) we have

$$\varepsilon = z \frac{\partial \theta}{\partial x}; \quad \theta = -\frac{\partial f}{\partial x}; \quad \frac{\partial Q}{\partial x} - \rho \frac{\partial^2 f}{\partial t^2} - F = 0;$$

$$Q - \frac{\partial M}{\partial x} = 0; \quad M = -EI \frac{\partial^2 f}{\partial x^2} \quad (8)$$

Where ρ -the material density of elastic element of coupling (rod).

with $x=0$; $f=0$ and $\frac{\partial f}{\partial x}=0$

with $x=l$; $\frac{\partial f}{\partial x}=0$ and $Q=T$

Let's determine $f(l)$. In the majority of cases the torque moment of the driving system is changed from time to time according to the sinusoidal law, i.e. $M_M = \bar{M}_M \sin \omega t$ (for one harmony) [2];, where ω -the vibration frequency of the transmitted moment.

Then, accordingly torque moment in coupling the cutting force to the rod is determined with the following expression: $T = \bar{T} \sin \omega t$. Then

$$\frac{d\bar{Q}}{dx} - (-1)\rho F \bar{f} \omega^2 = 0; \quad \bar{Q} = \frac{dM}{dx}; \quad M = -EI \frac{d^2 \bar{f}}{dx^2} \quad (9)$$

with $x=0$ $f=0$; $\frac{d\bar{f}}{dx}=0$

with $x=l$ $\frac{d\bar{f}}{dx}=0$ $\bar{Q} = \bar{T}$

Where \bar{Q} , \bar{T} and \bar{f} - according to the amplitude of cross force, cutting force and the deflection of elastic rod. Such as the loading of coupling is changed for the sinusoidal



law, between enumerating parameters and their amplitude values have sinusoidal dependence, for $f = \bar{f} \sin \omega t$ and so on.

The equation for the determining of amplitude of deflection \bar{f} has the following form.

$$EI \frac{d^4 \bar{f}}{dx^4} - \rho F \bar{f} \omega^2 = 0 \quad \text{or} \quad \frac{d^4 \bar{f}}{dx^4} - \bar{f} \gamma^4 = 0 ;$$

Where $\gamma^4 = \frac{\rho F \omega^2}{EI}$ is given for the comfort of calculating designation,

$$\text{with } x=0; \quad \bar{f}=0 \quad \text{and} \quad \frac{d\bar{f}}{dx}=0$$

$$\text{with } x=l; \quad \frac{d\bar{f}}{dx}=0 \quad \text{and} \quad EI \frac{d^3 \bar{f}}{dx^3} = -\bar{T}$$

The decision of this equation we take in the following form [1]:

$$f = c_1 \cdot sh \gamma x + c_2 \cdot ch \gamma x + c_3 \cdot \sin \gamma x + c_4 \cdot \cos \gamma x \quad (10)$$

The equation received for the determining of amplitude of the deflection of elastic rod present the differential equation of fourth order with constant coefficient.

For determining of constant integration c_i ($i=1, 2, 3, 4$) we decide the following line of algebraic equation:

$$\begin{aligned} c_2 + c_4 &= 0; & c_1 + c_3 &= 0; \\ c_1 ch \gamma l + c_2 sh \gamma l + c_3 \cos \gamma l - c_4 \sin \gamma l &= 0 \\ c_1 ch \gamma l + c_2 sh \gamma l - c_3 \cos \gamma l + c_4 \sin \gamma l &= -\frac{\bar{T}}{EI} \cdot \frac{1}{\gamma^3} \end{aligned} \quad (11)$$

Thus

$$\bar{f} = -\frac{\bar{T}}{EI} \frac{1}{\gamma^3} \frac{1}{\Delta} [sh \gamma x (sh \gamma l + \sin \gamma l) + ch \gamma x (\cos \gamma l - ch \gamma l) - \sin \gamma x (sh \gamma l + \sin \gamma l) - \cos \gamma x (\cos \gamma l - ch \gamma l)] \quad (12)$$

where

$$\Delta = (ch \gamma l + \cos \gamma l)(sh \gamma l + \sin \gamma l) + (sh \gamma l - \sin \gamma l)(\cos \gamma l - ch \gamma l)$$

Then unknown quantity of constant amplitude of the deflection at the end of elastic rod after simplification is determined with equation:

$$\bar{f}(l) = \frac{\bar{T}}{EI} \frac{1}{\gamma^3} \frac{-ch \gamma l \cdot \cos \gamma l + 1}{ch \gamma l \cdot \sin \gamma l + sh \gamma l \cdot \cos \gamma l} \quad (13)$$

Taking into account that

$$\bar{f}(l) = \bar{\varphi} R; \quad \varphi = \bar{\varphi} \sin \omega t \quad \text{and}$$

$$M_M = \bar{M}_M \sin \omega t$$

We get:

$$\begin{aligned} \bar{f}(l) = \bar{\varphi} R &= \frac{1}{EI} \frac{1}{\gamma^3} \frac{1 - ch \gamma l \cdot \cos \gamma l}{ch \gamma l \cdot \sin \gamma l + sh \gamma l \cdot \cos \gamma l} \times \\ &\times \frac{1}{nR} \bar{M}_n = \frac{1}{C_{M_{din}}} \cdot \bar{M}_n R \end{aligned} \quad (14)$$

From this equation we determine the dynamical stiffness of coupling.

$$C_{M_{din}} = EI \gamma^3 n R^2 \frac{ch \gamma l \cdot \sin \gamma l + sh \gamma l \cdot \cos \gamma l}{1 - ch \gamma l \cdot \cos \gamma l} \quad (15)$$

$$C_M = EI n R^2 \frac{12}{l^3} \quad (16)$$

From the expression (14) follow that about $\Delta = 0$ it has peculiarity. In other words, in this case the value of the deflection of elastic rod for the own characteristic vibrations is growing sharply. From condition $\Delta = 0$ follow that

$$ch \gamma_0 l \cdot \sin \gamma_0 l + sh \gamma_0 l \cdot \cos \gamma_0 l = 0; \quad tg \gamma_0 l = -th \gamma_0 l$$

The last affirmative root of this equation we indicate by α .

Then

$$\frac{\rho F \omega^2}{EI} l^4 = \alpha^4; \quad \omega_0 = \frac{\alpha^2}{l^2} \sqrt{\frac{EI}{\rho F}}$$

where ω_0 – the frequency of characteristic vibrations of elastic element of coupling (rod).

$$\gamma^4 l^4 = \frac{\rho F \omega^2}{EI} l^4 = \omega^2 \alpha^4 \frac{1}{\omega_0^2}; \quad \gamma l = \alpha \cdot \sqrt{\frac{\omega}{\omega_0}}$$



We note that the constant C_{Mdin} has not got peculiarity, it presents the finite quantity, such as:

$$1 - ch\gamma l \cdot \cos \gamma l \neq 0 \quad \text{with} \quad \gamma l \neq 0$$

We change C_{Mdin} with a bit accounting γl . Then,

$$C_{Mdin} = EI\gamma^3 nR^2 \frac{2\gamma l - 2\gamma^5 l^5 \cdot 0,03}{\frac{1}{6}\gamma^4 l^4 - \frac{1}{6}\gamma^8 l^4 \cdot 0,002} \approx C_{Mst}$$

(17)

For the determining of stiffness by parameters of coupling (in particular the vibration frequency) we take the ratio of stiffness:

$$\begin{aligned} \frac{C_{Mdin}}{C_{Mst}} &= \frac{1}{12} \gamma^3 l^3 \frac{ch\gamma l \cdot \sin \gamma l + sh\gamma l \cdot \cos \gamma l}{1 - ch\gamma l \cdot \cos \gamma l} = \\ &= \frac{1}{12} \cdot \alpha^3 \left(\frac{\omega}{\omega_0} \right)^{\frac{3}{2}} \times \\ &\times \frac{ch\left(\alpha \cdot \sqrt{\frac{\omega}{\omega_0}}\right) \sin\left(\alpha \sqrt{\frac{\omega}{\omega_0}}\right) + sh\left(\alpha \sqrt{\frac{\omega}{\omega_0}}\right) \cos\left(\alpha \sqrt{\frac{\omega}{\omega_0}}\right)}{1 - ch\left(\alpha \sqrt{\frac{\omega}{\omega_0}}\right) \cdot \cos\left(\alpha \sqrt{\frac{\omega}{\omega_0}}\right)} \end{aligned} \quad (18)$$

In this equation the value α is determined from the following condition:

$$tg \alpha + th \alpha = 0 \quad \text{with} \quad \alpha > \frac{\pi}{2}.$$

Now, in accordance with equation (18) we can draw the graph dependence from the stretch coefficient $\frac{C_{Mdin}}{C_{Mst}}$ of

the correlation vibration frequency of system $\frac{\omega}{\omega_0}$ (Fig. 5).

With $\frac{\omega}{\omega_0} \Rightarrow 0$ coefficient of correlation dynamical and static stiffness of coupling approach to the unity:

$$\frac{C_{Mdin}}{C_{Mst}} \Rightarrow 1.$$

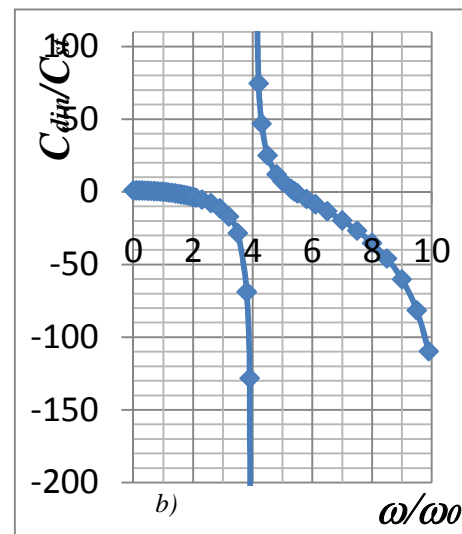
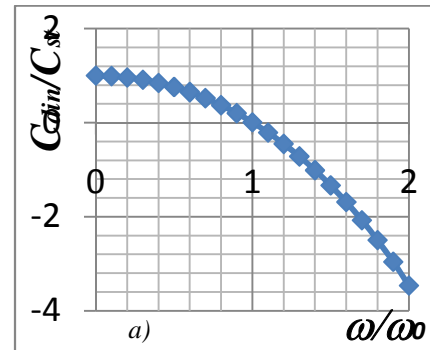


Figure 5: The dependence of the ratio of dynamic and static stiffness couplings $\frac{C_{Mdin}}{C_{Mst}}$ the dimensionless coefficient of the oscillation frequency $\frac{\omega}{\omega_0}$ system: a-in the range $0 \leq \frac{\omega}{\omega_0} \leq 2$ and b-in the range $0 \leq \frac{\omega}{\omega_0} \leq 10$.

3. Conclusions

Based on the results obtained for the linear elastic model couplings, we can draw the following conclusions:

1. With increasing frequency of the applied torque value of dynamic stiffness coupling decreases.
2. From the analysis of the dependence of the dynamic stiffness of the frequency of forced oscillations, it follows that it has a discontinuity.



3. To specify a dynamic stiffness to the static, you can find the frequency load on the coupling.
4. From a practical point of view of interest mainly to the resonant frequency of vibration load couplings, for example, interval $0 \leq \frac{\omega}{\omega_0} \leq 1$. Because after the resonant zone ($0 \leq \frac{\omega}{\omega_0} \leq \infty$) dynamic characteristics of the couplings have the discontinuities.

References

- [1] Корн Г., Корн Т.: Справочник по математике, М.: Наука, Издание 2-е перераб., 1973, 832с.
- [2] Khalilov I.A.: Mekanik kavramlarda ara boşlukların iletimin dinamik özelliklerine etkisini araştırmak için matematiksel modelin yapılması. // 14. Ulusal Makina Teorisi Sempozyumu – UMTS2009, 2-4 Temmuz 2009, ODTÜ Kuzey Kıbrıs Kampusu, S. 421-426.
- [3] Халилов И. А. Исследования динамических свойств геометрически замкнутых механических муфт. //Техника машиностроения. М.: 2009, №2, с. 25-31.
- [4] Peecken H., Troeder C.: Elastische Kupplungen: Ausführung, Eigenschaften, Berechnungen. Springer-Verlag, 1986, 211 S. ISBN 3-540-13933-8; ISBN 0-387-13933-8.



The Dynamics of Actuators of the Technological Machines in the Textile Industry

Mazakhir FARZALIEV^{1*}, Elman DJAFAROV

^{1*} Department of Technological machines and the equipment of the industrial sector

The Azerbaijan State Economic University Azerbaijan 370065,
Murtuza Mukhtarov Street 194, city Baku

Keywords: cloth formation, rigidity of the elastic system, vibration frequency, moment of friction

1. Introduction

One of the main branches of the textile industry is weaving where by the textile machinery is being produced the variety of cloth from various threads.

Nowadays has been created the weaving machines with continuous cloth formation which are the third stage in the development of design of weaving machines. In these machines the basic operations of cloth formation - the application of shot wives in the wavy pharynx of a basis and breaking of shot wives towards the edge of cloth is being carried out by the breaking plate that accumulated on the shaft in conformity with the certain regular and logical process, i.e. cloth formation mechanism. In the process of producing cloth it is necessary to push the basic threads regularly with a constant tension in the direction from wind to an edge of a cloth and at the same time the cloth formed in every cycle should be taken away from an edge and to wind on the commodity platen. The analysis shows that for producing a qualitative cloth the size of winding of cloth and size of pushing of basic threads in every cycle should be identical.

For maintaining of a constant tension and releasing of the basic threads in weaving machines are applied various mechanisms of a tension and releasing of basis but for tapping of cloth in each cycle are applied the commodities accepting mechanisms. Between these mechanisms there is a kinematic and power relation.

One of the basic power conditions is that the brake on a shaft of wind should create certain resistance so that at a certain tension of threads of the basis not exceeding previously specified size, the wind should turn and give a

necessary portion of a basis in a direction towards a cloth edge.

Various mechanisms of a tension and releasing of bases are applied for providing the constant value of tension of the basic threads and supplying the required length of the basic thread at various diameters of winding of a basis on the new one. The most advanced design of the mechanism of a tension and releasing of a basis is the regulator of a basis which is applied at continuous cloth formation, in a design of many gaped weaving machine of type TMM (fig. 1a). The mechanism works as follows.

In the process of work of the machine the movement from a cross shaft through chain drive is transferred to the platen 9 of the variator mechanism. The platen 3 is set in motion through the variator belt 2 from which through a replaceable gear wheels rotation is transferred to a worm 4 and to a worm wheel 5. At rotation it will lead through the casing satellite gear wheels. The pair of satellite gear wheels 6 and 7, connected with gear wheels 8 through a subwind gear wheel 9 and a winding gear wheel 10 will turn the first wind, and the pair of satellite gear wheels 11 and 12, connected to a gear wheel 13 through the platen 14 will turn a subwind gear wheel 15, a winding gear wheel 16 and the second wind.

During the work of the machine in the process of operating of a basis the tension increases. The shaft (is absent in drawing) on increasing the tension descends. By one lever system the mobile disk 17 moves to the right, pulling together disks, and simultaneously by the other lever system the mobile disk 18 moves to the right, disjointing disks and as a result the variator belt is dislocated upwards by the top disks and the speed of rotation of the bottom platen 18 increases. Hereupon the wind will turn to a certain corner, the supply of a basis will increase, and the increase of tension decreases. If in the process of work the tension of a basis decreases, the shaft rises and through the above-stated system the supply



of a basis will decrease, the tension increases. In this design the projecting pin of wind are installed on sliding bearings.

In the process of rotation of wind in the projecting pins arises the moment of force of a friction which leads to self-vibration of wind and therefore to the changes of a tension of the basic threads and accordingly to the production of a poor-quality cloth.

2. Drawing up of a dynamic model of movement of wind of bases and the equation of movement of wind

Let's provide the dynamic analysis of movement of wind of bases for definition of variable value of a tension of the basic threads. With this purpose let's draw up the dynamic model of wind of bases (fig. 16).

The carried out researches (1) have shown that non-uniform rotation of wind arises because of cyclic change of a tension at front - face fight along all charging width of the machine. In weaving *многосезвных* machines force of a break is absent (it is very small in comparison with machines of a front-face break) and fluctuations of tension of the basic threads are present.

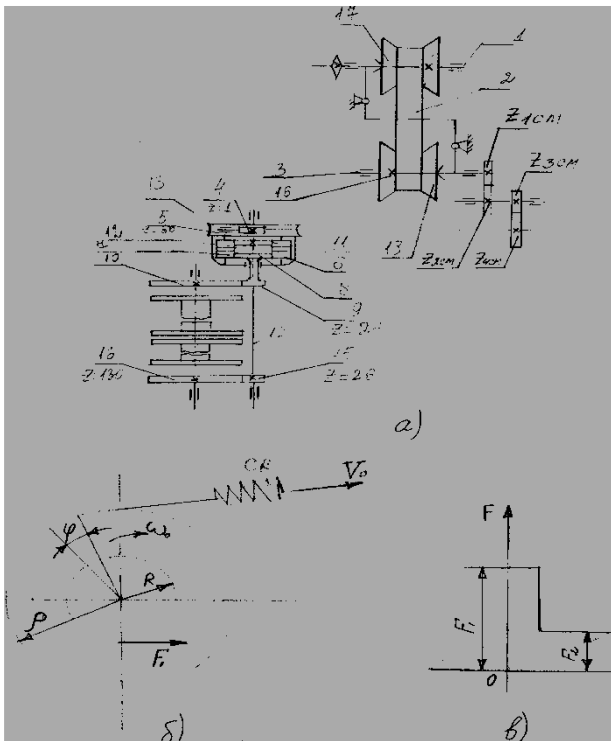


Fig.1:

Here v_0 - the speed of moving of elastic system of charging by *вальном*, i.e. speed of a leading link ; C_k - the unit rigidity of elastic system of charging and a drive of wind ; J - the equivalent moment of inertia of weight of wind and connected with it drive details; F_1 - limiting force of sleep; F_2 - force of a friction of movement (fig. 1).

Let's accept that the moment of force of elasticity of the basic threads of $M(t)$ is equal to the moment of forces of friction F_2R and the wind rotates with constant speed. Speed of leading link v_0 is rather small, the small casual obstacle can appear sufficient for stopping of wind. The wind continues movement until the moment of force of elasticity of the basic threads will not equate to the maximum moment of force of a friction of sleep F_1R . As, after that the further growth of force of a friction is impossible, there will occur "frustration" of wind. Along with, the moment of friction F_1R will instantly decrease to value F_2R , but the moment of force of elasticity of the basic threads cannot change instantly and at the first minute the begun movement will be equal to F_1R as before. And, consequently, balance of the moments influencing on the wind will be broken. Let's combine the break-away torque with the time report mark ($t=0$) and we will notice that, along with it they both a corner of turning of wind φ and angular velocity $\dot{\varphi} = 0$ are equal to zero

$$\varphi(0) = 0; \quad \dot{\varphi}(0) = 0 \quad (1)$$

It is evident, it is that the possible movement of system at which the speed of a point of reeling of a thread of wind is equal to $v_0 = \omega\rho$, as well. Along with, the elastic system is tensed by the constant moment $M(t)$, which is equal to the moment of force of a friction of movement on projecting pins of wind F_2R .

трения движения на цапфах навоя F_2R . This mode is unstable and under certain circumstances near it arise the self-vibrations.

3. Decision of the differential equation

Now let's consider the process of the subsequent movement of wind.

To some moments of time $t > 0$ the length of elastic system of charging will change on section $\rho\varphi - \rho\omega_0 t$ and accordingly the moment of elastic system of charging will decrease to value

$$M(t) = RF_1 - C\rho(\rho\varphi - \rho\omega_0 t) \quad (2)$$

Hereby, the differential equation of movement of wind looks like:



$$J\ddot{\varphi} = -C\rho(\rho\varphi - \rho\omega_0 t) + R(F_1 - F_2)$$

or

$$\ddot{\varphi} + p^2\varphi = p^2\omega_0 t + \frac{R}{J}(F_1 - F_2) \quad (3)$$

where $p^2 = \frac{C\rho^2}{J}$ - is a fundamental frequency of fluctuation of wind.

The decision of this equation, satisfying to initial conditions (1) looks like

$$\varphi = \omega_0 t - \frac{\omega_0}{p} \sin pt + \frac{pR(F_1 - F_2)}{\rho\omega_0 C} (1 - \cos pt) \quad (4)$$

The first summand of the right part expresses the uniform motion with speed of a leading link, and the other summands - are the additional fluctuations of wind.

The speed of the wind changes under the law

$$\dot{\varphi} = \omega_0 - \omega_0 \cos pt + \frac{pR(F_1 - F_2)}{\rho C \omega_0} \sin pt \quad (5)$$

and during some moment of time it will again turn into zero. The conditions for a new stopping of wind lead to the equation

$$\omega_0 - \omega_0 \cos pt_1 + \frac{pR(F_1 - F_2)}{\rho C \omega_0} \sin pt_1 = 0 \quad (6)$$

in which t_1 - is the time from the break-away torque till the moment of a new stopping.

Let's enter dimensionless parameter

$$\alpha = \frac{pR(F_1 - F_2)}{C\rho\omega_0} \quad (7)$$

Now the condition of stopping of wind will become

$$\alpha \sin pt_1 = \cos pt_1 - 1 \quad (8)$$

After the decision we will find

$$\sin pt_1 = -\frac{2\alpha}{1 + \alpha^2}; \quad \sin pt_1 = -\frac{2\alpha}{1 + \alpha^2} \quad (9)$$

Modules of the received expressions always are less than unit. So from (9) always follows real value t_1 . It is possible, having received this value t_1 , to define under the formula (5) coordinate position φ of the wind at the

moment of a new stopping, i.e. the way which has been passed by the wind during t_1 .

$$\begin{aligned} \varphi_1 &= \omega_0 t_1 - \frac{\omega_0}{p} \sin pt_1 + \frac{pR(F_1 - F_2)}{\rho C \omega_0} (1 - \cos Kt_1) \\ &= \omega_0 t_1 + \frac{2\alpha\omega_0}{k} \end{aligned} \quad (10)$$

Taking into account the expression (9) we will find in correlation (2) the moment of a stretching of elastic system of charging at the moment of stopping the wind.

$$M(t_1) = (2F_2 - F_1)R \quad (11)$$

From here it is visible, that $M(t_1) < F_1 R$ (as $RF_2 < RF_1$). Consequently, after stopping the wind will remain on a place some time, while the moment of a stretching for elastic system of charging will not reach again the value of the limiting torque of friction sleep.

After that there will be a new frustration of the wind and there will begin the following cycle completely coinciding with the previous one. Thereby, the considered process represents stationary fluctuations. Within the time the wind is sleeping, the moment of stretching gradually increases on size.

$$\Delta M = RF_1 - M(t_1) = 2F - (2F_2 - F_1)R = 2R(F_1 - F_2) \quad (12)$$

And the corresponding additional stretching of elastic system of charging will make

$$\Delta\varphi = \frac{\Delta M}{C\rho} = \frac{2R(F_1 - F_2)}{C\rho} \quad (13)$$

The way which has been passed by a leading link during a stopping of the wind is equal to the same size. Consequently, duration of a condition of the wind is equal to

$$t_2 = \frac{\varphi}{\omega_0} = \frac{2R(F_1 - F_2)}{C\rho\omega_0} = \frac{2\alpha}{p} \quad (14)$$

Thereby, the self-vibration period of the wind will be defined by the formula

$$T = t_1 + t_2 \quad (15)$$

for using it, at first it is necessary to find t_1 from expression (9) and then t_2 from the formula (14). Than the least angular velocity of the wind is, the process of self-vibrations is especially sharply expressed. Actually at small values ω_0 unitless parameter α becomes rather big and from expression (9) follows approximately.



$$\sin pt_1 \rightarrow 0, \quad t_1 = \frac{\pi}{p} \quad (16)$$

Accordingly (14) it leads to the following formula for the period of self-vibrations.

$$T = \frac{\pi + 2\alpha}{p} \quad (17)$$

Here it is clear, that the role of the second summand in numerator increases with reduction of angular velocity ω_0 .

For definition of numerical values of dynamic model of the wind is used the method specified in (2). Parameters of dynamic model have the following values. The equivalent moment of inertia of weight of the wind and the details of drive - $J=54494$, 35 kg.cm.second², the elastic system of charging the unit rigidity and a drive of the wind - $\text{Second}=900,074$ kg/cm, the radius of winding of a basis on the wind - $\rho_{\max}=40\text{cm}$, radius of projecting pin of the wind - $R=10\text{cm}$, force of a friction of sleeping - $F_1=18,0\text{kg}$, force of a - $F_2=14,4\text{kg}$.

At such values of parameters of dynamic model, the frequency of self-vibrations of the wind is $p=5,1\text{second}^{-1}$, dimensionless factor $\alpha=5,66$ and the period of self-vibrations $T=2,83\text{second}$.

The analysis shows, that provisions of the minimum value of dimensionless parameter α is possible also by the reduction of a differences of forces of a friction of

sleeping and. In the new designs of weaving machines the materials of the projecting pin of the wind and the support should be selected so that to provide the minimum difference of force of a friction of the wind and the friction of motion and to reduce the diameter of the projecting pin of the wind. Thus, the parameters of designs of actuating mechanisms of textile machines should be defined with the account of performing by them the technological operations.

4. Conclusions

1. The dynamic model of movement of the wind of bases has been developed.

2. In designs of weaving machines the materials of the projecting pins of the wind and their support should be selected so that to provide the minimum difference of forces of a friction of sleeping and friction of motion.

The parameters of a design of the actuating mechanisms should be defined taking into account the performance of technological processes by them.

References

- [1] A.Gordeev, «Dynamics of mechanisms of release and tension of a basis of weaving looms» M, the Light industry, 1965
- [2] E.I.Rivin, «Dynamics of a drive of weaving looms s», M, Mechanical engineering, 1966.
- [3] G.Farzaliev «The development of methods of calculation and designing cloth formation the mechanism and research of the process of a lining of shot wire in wavy pharynxes of a basis wide many gaped weaving machines of type TMM». The thesis for a doctor's degree, St.-Petersburg, 1990.



The Photoelectric Properties $\text{In}_2\text{O}_3\text{-SiO}_2\text{-Si-M}$ Structures

A.Z.BADALOV^{1*}, B.A.YUSIFOV¹, Sh. H. ZEYNALOVA¹

National Aviation Academy, Az -1045 Baku, Bina 25 km, Azerbaijan
arif.badalov@mail.ru

Abstract

The photoelectric properties of $\text{In}_2\text{O}_3\text{-SiO}_2\text{-Si-M}$ structures have been investigated. It is realized, that the photoelectric amplification of current is observed after switching at the application of the voltage to structure. It is also realized, that nonstationary photoelectric current goes through structure at the photovoltaic mode ($U < 0,25\text{V}$) and structure behaves itself as an ideal MDS structure, and the stationary photoelectric current goes through structure at $U \geq 0,25\text{V}$. It is proposed, that observation of amplification effect is connected with the formation of tunnel dielectric in the structure.

The investigation of the switching effect in $\text{In}_2\text{O}_3\text{-SiO}_2\text{-Si-M}$ structure is interesting from two points of view: the investigation of the influence of the different contacts on the switching effect and the probability of the control of the switching effect by the lightening. The samples were prepared in the common and planar version for the investigation of the switching effect and photoelectric properties [1]. The semi-transparent conducting layer $\text{In}_2\text{O}_3(\text{Sn})$, strongly doped by the tin, has been obtained by the cathode spraying. The Al ring was prepared with the inner diameter 150 μm and outside diameter 250 μm with the use of the photolithography. The semi-transparent conducting layer $\text{In}_2\text{O}_3(\text{Sn})$ is prepared with the around diameter 300 μm and orthogonal diameter 300' 500 μm . VAC structures are symmetrical in the initial state and dependence of the current on the voltage submits to the low $J \sim U^n$, where $n=1,5 \div 2$. The differential resistance in the initial closed state is defined by the SiO_2 resistance and changes in the interval $R \sim 10^{12}\text{-}10^{13}\ \Omega\text{m}$. The lightening of the structure by the white light in the initial state doesn't almost change its VAC. The structure transfers to the state with the low impedance at the defined value of applied voltage. In this state VAC is asymmetrical.

The photoelectric properties of such electroformed MDS structures have some peculiarities. The structure was lightening from the side of In_2O_3 by the modulated light with the frequency 300 Hz by monochrometer DMP-4. The silicon photodiode, calibrated by the power, is situated near MDS-structure. The signals from the photodiode and structure were measured by the

microvoltmeters Y2-8, the pulse photoresponse is registered by the oscillograph C1-16.

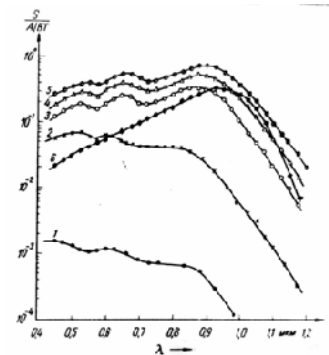


Fig.1. The spectral dependence of photosensitivity of $\text{In}_2\text{O}_3\text{-SiO}_2\text{-Si-M}$ structures after the switching at the different voltages: 1- $U=0$; 2- $U=1$; 3- $U=5$; 4- $U=19$; 5- $U=21\text{V}$; 6- photodiode; $\Phi=27\text{K}$ at $U=0$

From the spectrum dependence of photosensitivity (fig.1), investigated by the low resistance MDS-structure in the photovoltaic (fig.1. c.1) and photodiode modes (fig.1.c.2-5) is shown, that photosensitivity value and form of the spectral characteristic of MDS-structure change meaningfully with the applied constant electric field. The maximum of photosensitivity corresponds to $\lambda = 0,5\ \mu\text{m}$ and $S = 1,4 \cdot 10^{-3}\ \text{A/Vt}$ at the photovoltaic mode.

The photosensitivity increases and structure has the wide region of the practically spectral sensitivity at the application to the voltage structures in the direct direction (source pole to the semi-transparent electrode). $S = 0,35\ \text{A/Vt}$ at $U = 10\text{V}$ and $\lambda = 0,82\ \mu\text{m}$, i.e. the sensitivity of MDS-structures increases in 500 times.

As it is shown from fig. 1(c.6.), the character sensitivity range of silicon device with p-n junction has the range $0,4 \div 1,1\ \mu\text{m}$. As in MDS-structures the light absorption region in the region of the short length of waves agrees with the region of photoelectric current separation, so the influence of the surface recombination can be suppressed.

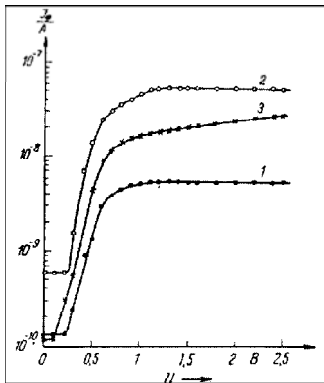


Fig.2. The dependence of photoelectric current of $\text{In}_2\text{O}_3\text{-SiO}_2\text{-Si-M}$ structures on the applied voltage after switching at the different wave lengths $0,56\text{mkm}$ $\lambda =$, $0,78\text{mkm}$ $\lambda =$, $0,90\text{mkm}$ $\lambda =$.

The value of the electric field of the Si surface, calculated by the formulae 5 of ref [2] for the given biases is $FS=106$ V/cm. That's way the condition of suppressing of surface recombination $\mu \cdot FS=S$, (where μ is mobility, S is velocity of surface recombination) at these electric fields for the silicon has already done, that is caused the absence of the decrease in the blue spectrum region. This should be lead to the sensitivity extension in the blue spectrum region. The long-length wave boundary of the photosensitivity is defined by the gathering depth of photocurrents, i.e. in our case by the diffusion length of holes.

In the fig.2 the dependence of photoelectric current on the applied constant bias at the different lengths of waves of incident light. The photocurrent doesn't depend on the applied constant voltage at small values $U<0,25\text{V}$. The value of photoelectric current strongly increases in 2-2,5 orders with the increase of the constant bias and leads to the saturation at $U \approx 1\text{V}$ at voltage $U \approx 0,25\text{V}$.

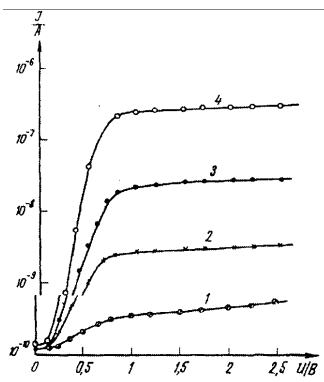


Fig.3. The dependence of current on voltage for $\text{In}_2\text{O}_3\text{-SiO}_2\text{-Si-M}$ structures at the different light intensities: 1-dark; 2-2Jn, 3-3Jn, 4-4Jn.

The current saturates through structure in the region of the voltage of biases that is caused by the surface concentration of the holes [2]. As it is shown from VAC (fig.3.), obtained at the different intensities of light, the photoelectric current amplification is observed. The value of the photoelectric increase in the structures was measured at room temperature on the change of saturate current at the different intensities of light, moreover internal amplification factor is calculated by the formulae:

$$M = \frac{\Delta J}{e \Delta \Delta_{ph}} \quad (1)$$

where ΔJ is the increment of the common current at the amplification of photons flux on ΔN_{ph} . The small value of amplification factor was 2,5-10. The value of increase coefficient is small in the comparison with the theoretical possible one is caused by the nonoptimal oxide layer thickness.

As it was shown in the ref [3], the electroformed MDS-structures can be used for the detection of theoptical signals. In this connection and the aim of the observation of photoelectric current character dependence on the photoresponse time and the different parameters: the voltage on the electrode, light intensity and e.t.c. investigated by the kinetics of photoresponse of such structures.

As it is known [4,5], in the dependence on the initial surface bands' bending ϕ_s in MTDS structures the amplification effect of photoelectric current can be observed [6] or the situation realized, in which their characteristics are identical to ones in observed in p-n junctions [7].

In the first case the current through structures is defined by the majority carrier, in the second case- by the minority carrier.

The MDS-structures was preparing on the base with $\rho \sim 10^1 \div 10^3 \text{ Ohm}\cdot\text{cm}$. the electro-treatment of MDS-structures was carrying out at $U=100 \div 150\text{V}$.

The thickness of the possible tunnel-transparent dielectric is $20 \div 40 \text{ \AA}$. The value of the initial surface bands' bending, measured by the method of saturated photoelectromotive force in the samples on n-Si was $\phi_s=0.05\text{eV}$ and corresponds to the weak enrichment of the subsurface region by the majority carries, on n-Si $0,2-0,3\text{eV}$, and corresponds to the depletion.

The photosensitivity in the samples on p-Si was higher on the several orders, than on n-Si correspondingly. This fact allows to propose, that in the behavior of structures on the base of n-Si is defined by

the minority carries and on the base of p-Si – by the majority carriers, and the amplification of photoelectric current can be released in last case.

The kinetics of photoresponse was studying at the room temperature at the lightening of the structures throw monochrometer from the source TPLII, and by the photodiode also. The value of the load resistance was $RH=1,6k\Omega$. The photoelectric current pulses were registered on the oscillograph C1-16.

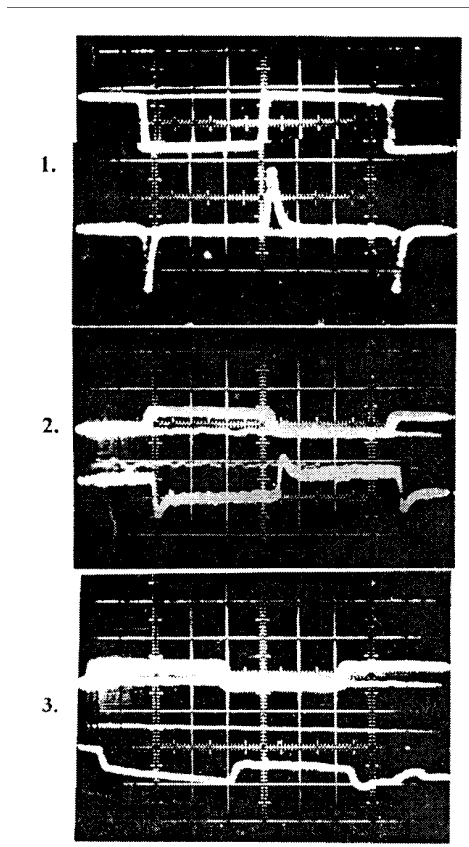


Fig.4. The oscillogramm of photoresponse of $In_2O_3-SiO_2-Si-M$ structures after switching at the lightening by the right-angled light pulse ($\lambda = 0,91\mu m$) at the different voltages of biases: 1- $U=0B$; 2- $U=0,25B$; 3- $U=1B$.

The oscillogramms of photolight pulses for the structures p-Si, obtained at the one lightening, but at the different voltage biases, are given in the fig.4; but the oscillogramms of photoresponse pulses for the structures p-Si, at the one voltage value, but at the different lightenings, are given on the fig.5. It is realized, that in the photovoltaic mode, i.e. at $U=0$, and $U<0,25V$ the only nonstationary photocapacity current goes throw electrotreated structure, i.e. the structure behaves

itself as an ideal MDS-structure (fig.4.a.), and at $U>0,25V$ the stationary photoelectric current goes throw structure (fig.4.b.).

For the discussion of the experimental data, we propose, that sing and value of the surface bands' bending are so, that photoelectric current of majority carriers is absent. In our case the such situation corresponds to the structures on n-Si, and the change storage on the surface state is the negligible small. The photoelectric current statement is defined by two processes this case: by the capacity charge of MTDS-structures and tunnel current of the photogenerated charge carries throw dielectric, i.e. expression for the photocurrent density can write in the following from [8]

$$j_p(t) = \frac{d\Delta Q_{SC}}{dt} + qS_{pe}\Delta P \quad (2)$$

where ΔQ_{SC} is the change of the density in the space charge region (SCR):

$$\Delta Q_{SC} = \frac{kT}{q} Cd\Delta\phi_s = q \frac{Cd}{Cd + C_{SC}} \Delta P_s \quad (3)$$

Cd and Cs are specific high-frequency densities of the dielectric and SCR,

$$H\phi_s = \frac{q\Delta\phi}{kT}$$

is the change of the dimension surface potential, S_{pe} is the effective velocity of the holes' flux from the semiconductor to the metal, P is the excess volume holes' concentration. The relaxation law is from the equation of the continuity for the holes' flux:

$$\frac{d\Delta P_s}{dt} = \begin{cases} J - (S_{pe} + S^*)\Delta P(t) & \text{at the switching on the lightening} \\ -(S_{pe} + S^*)\Delta P(t) & \text{at the switching off the lightening,} \end{cases}$$

Where S^* is the sum velocity of the recombination [8],

$$S^* = (S_{rv} + S_{rse} + S_{rs})$$

where J is the flux of generation of the electron-hole pair in the semiconductor volume.

In the line case by the lightening

$$\Delta\varphi_S^2 \ll 1, \frac{\Delta P}{P} < 1$$

at the depleting bended bands, the expression for ΔP_S has the form:

$$\Delta P_S = \frac{L_3}{\sqrt{-\varphi_S^0}} \Delta P(t) \exp(-\varphi_S^0) \quad (6)$$

and at the inversion bends of bands we have:

$$\Delta P_S = \frac{\frac{1}{2} P_S^0 \frac{\Delta P(t)}{P_0}}{1 + \frac{P_S^0 q^2}{2 kT C d^2}} \quad (7)$$

where L_S is the Debye screening length, L and O are indexes of the lightening and thermodynamical equilibrium.

Now, solving (4), taking into consideration (6) or (7), after substitution of (3), we can obtain the looking for the equation (2), solving for the kinetics of photoelectric current statement this equation has form:

$$j_p(t) = qJ \begin{cases} \frac{C_{de} \tau}{C_d + C_{SC}} + \frac{S_{pe}}{S_{pe} + S^*} \left(1 - e^{-\frac{t}{\tau}} \right) & \text{for the switching on in the moment } t=0 \\ \frac{S_{pe}}{S_{pe} + S^*} - \frac{C_d}{C_d + S_{ce}} e^{-\frac{t}{\tau}} & \text{for the switching off in the moment } t=0 \end{cases} \quad (8)$$

where time constants for the depleted and inversion of bends of bands, correspondingly:

$$\tau_{on} = \frac{L_3 \exp(-\varphi_S)}{(S_{pe} + S^*) \sqrt{-\varphi_S}} \quad (9)$$

$$\tau_{off} = \frac{L_3 \exp(\frac{\varphi_S}{2})}{(S_{pe} + S^*)} \frac{\left(\frac{n_0}{p_0}\right)^{\frac{1}{2}}}{1 + \frac{P_S^0 q^2}{2 C d k T}} \quad (10)$$

In the dependence on the ratio between S_{pe} , S^* , C_d , S_{ce} , as it follows from (8), the different character of relaxation is possible. If the emission velocity of the minority carries through dielectric is higher than recombination velocity $S_{pe} > S^*$ and if $C_d > C_{se}$, then the photoelectric current changes on the very small value C_{se} at the switching on, later it leads to qJ , that it is observed

experimentally (fig.4)

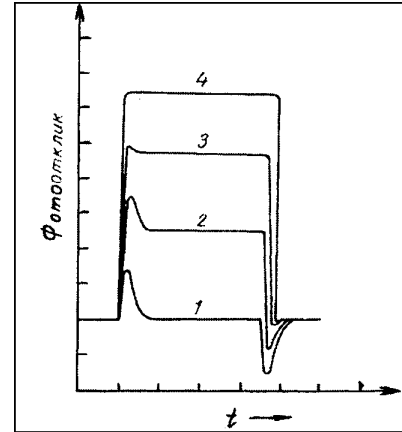


Fig.5. The oscillogramm of photoresponse of MTDS structures at the lightening by the right-angled light pulse ($\lambda = 0,92 \mu\text{m}$) at the different light intensities.

As

$$S_{pe} = \frac{1}{4 D_p V_p} \exp(-\varphi_S)$$

D_p is the effective tunnel transparentness, V_p is the thermal holes' velocity (4) and φ_S increases with the U_q increases, from (9)-(10) it follows, that time constant τ decreases with the U_q increase. The given dependences τ can realize in the experiments at $C_d \ll C_{se}$ and in our case they don't take place. At $C_d \gg C_{se}$, as in our case, it follows, that practically all photoelectric current states in the time is significantly smaller than τ and is defined by the biggest from such times, as transit time to RSC from the photoregeneration region or RH-C.

Thus, in the generation mode ($S_{pe} > S^*$) and $C_d > C_{se}$, factors, defining the time constant of photoresponse in MTDS-structures on the minority carries (n-type) don't differ from the analogical ones in p-n junctions.

The relaxation of photoelectric current, as follows from (8), is regular at the output from generation mode ($S_{pe} > S^*$) and at $C_d > C_{se}$. The photoelectric current strongly increases till the qJ value at the switching on, later it relaxes till the

$$qJ \frac{S_{pe}}{S^*}$$

with the time τ , and the symmetrical blip of the opposite polarity (the differentiation mode) takes place at the switching off. As the U_q increase leads to the S_{pe}



increase, and the lightening increase leads to the recombination loss increasing at the given U_q , so the experimental data, given on the fig.4, agree with the theoretical analysis [8]. The output from the differentiation mode was observed earlier [9, 10] at the switching on the opposite bias.

Let's stop on the photoelectric current relaxation at the presence of amplification factor.

At the amplification factor it is need to take into consideration in the equation (2) the presence of current of majority carries of charge, for the investigated structures (p-Si)-hole current.

$$j_p(t) = \frac{d\Delta Q_x}{dt} + qMS_{ne}\Delta n \quad (11)$$

where amplification factor $M=(j_n+j_p)/j_n$, a S_{ne} , but S_{ne} is emission velocity of minority carries of electrons (for the structures p-Si). The first term in (11) can be lost for the bigger amplification factors $M \gg 1$. Then, solving (11) analogically to (2), we obtain at the conduction inversion in the nonlinear case by the lightening $\Delta\phi_s^2 \gg 1$ and absence of the generation of minority electrons:

$$j_p(t) = MqJ \begin{cases} 1 - \frac{1}{\left(1 + \frac{t}{\tau_\delta}\right)^2} & \text{at the switching on} \\ \frac{1}{\left(1 + \frac{t}{\tau_\delta}\right)^2} & \text{at switching off} \end{cases} \quad (12)$$

where τ_δ is depend on light intensity in this case, as it

follows from the quality analysis and observes in the experiment. As in the big light intensive and in the structures with the amplification (p-Si) the differentiation doesn't observed, so, it is obvious, that condition $M \gg 1$ takes place. This gives possibility to propose, that in the given structures the values $D_p \gg D_n$.

Thus, all observable quality peculiarities of kinetics are well explained in the simple model [8], taking into consideration the respective deposit of photocurrents' recombination and throw dielectric.

References

- [11]. A.Z.Badalov, Doktorskaya dissert, 1992, Baku.(in Russian).
- [12]. C.M.Zi "Fizika poluprovodnikovix priborov" v 2-x kn.,kn.1, 1984, Moskva, Mir, s. 455.(in Russian).
- [13]. A.Z.Badalov, Z.A.Iskenderzade, E.A.Dzchafarova, A.Z.Masimov, G.M.Ismailov. Jurnal technicheskoy fiziki, 1984, t.54, N3, s. 645- 646.(in Russian).
- [14]. A.Ya.Vul, S.V.Kozirev, V.I.Fedorov. FTP, 1981, t.15, N1, s. 142-148. (in Russian).
- [15]. M.A.Green, Z.Sherohun. Solid St. Electron, 1974, v. 17, N19
- [16]. M.A.Green, V.A.Temple,Z.K.Mevchun. Solid St. Electron, 1975, 18, p.745-749.
- [17]. M.I.Abasov, A.A.Gutkin, A.L.Gerasimov, V.E.Sedov. FTP, 1979, t. 13, N4, s. 746-751. (in Russian).
- [18]. A.Ya.Vul, A.T.Dadeykin, Yu.S.Zinchik, K.B.Sanin, A.V.Sachenko. FTP, 1983, t. 17, v. 8, s. 1471-1477.(in Russian).
- [19]. A.L.Gerasimov, A.A.Gutkin, V.E.Sedov. FTP, 1980, v. 3, t.14, s. 550-552. (in Russian).
- [20]. A.Z.Badalov, R.Sh, Agayeva, X.A.Adigozalova, V.I.Sariyev. San- Marino BEA AM Azerbaycan filiali, " Elmi asarlari", b.3., Baku, Elm, 1999. (in Azerb.)



Process of growth and self organization on of nanofragment on TiGaSe₂ vicinal surfaces

A.M.PASHAEV¹, B.Y.TAGIYEV¹, F.K.ALESKEROV², K.Sh.KAHRAMANOV²

¹Azerbaijan National Aviation Academy, Bine 25 km, Baku, Azerbaijan

²Azerbaijan National Academy of Sciences “Selen” Scientific Production Association
Azerbaijan National Academy of Sciences, 29A, H.Cavid ave., Baku, Azerbaijan

Abstract

Keywords:

1. Introduction

Many problems of nanoelectronics are concerned not only with the creation pure content structures and homogeneous surface but with the formation of the structures of wanted sizes and forms of certain density without using special methods (for instance, lithography). Use of self organization process is promising for problems like these to be settled. Given process stands for the formation of ordered metal and semi conductive structures with distend density without using special methods. On this case nanostructure properties are revealed by surface morphology, effect of impurity atoms and growth condition. Method of self organization has been used for nanostructure creation on *Si* surface [1-2]. Experimental facetation has been observed for surfaces vicinal to (0001) on GaAs [3].

Interest to the given field of research is aroused in necessity of obtaining various nanostructures in sizes up to 100 nm. Spontaneous ordering of nanostructures allows the connection of narrow-band semiconductors to wide-band matrix to be produced and thereby localized potential for current carriers to be created. Periodical structures of such connections can form super lattices including quantum holes, hires and points, base for optoelectronic devises. Thus nanostructure ordering can be in various systems during crystal growth in TiGaSe₂ as well.

Considering physical mechanism of spontaneous appearance of ordered nanostructures and experimental detection of new classes of A^{III}B^V semiconductor nanostructures we put forward the tash on determining nano-graded interlayer structures in *TiGaSe₂*- typed layered crystals.

2. Subject of investigation and experimental method

The most suitable subject of study for self organization process of “parquet” structures of grade-layered growth is TiGaSe₃ crystals of rather distinct layered structure.

Investigations of layered crystal surface have been carried out on scanning probe microscope (SPM) of SOLVER NEKST model.

3. Experimental results

Roentgen diffraction picture of alloyed Dy *TiGaSe₂* is given in Fig.1 It is seen that on the crystal spall surface nanoparticles Dy and DyGa₂ are observed In Fig.2 there have been presented SPM image to 3D scale of TiGaSe₂; where vicinal surfaces of spall have been seen in Fig.3 the same surface only to 2D scale is given. In fig.4 there have been presented fragment of this surface with profilegram where height sizes (within 5-20 nm) and “flutes” in width 1 μm have been detected. From fig.5 repetition of “flute” – profiles in sizes 1 μm are seen as well. In fig.6 there has been visually demonstrated cross height of nanoobjects “flutes”; within the scan up to 5.10³ nm³ about 3 “normal” flutes have been arranged. From obtained experimental figures (1-6) appropriate conclusions have been made.

4. Conclusions

By scanning atomic-power microscopy initial stages of impurity growth on TiGaSe₂ (001) vicinal surfaces have been carried out. It is shown that on surfaces laid off in the direction of basic surface nanofragments in the regime of grade – layered growth have been formed. The height of grade is within 10-20nm. There like growth on microscopically ordered faced surfaces. By control of crystallization process, increase of rate, impurity introduction one can obtain vicinal surfaces including regular sets of steps (so called “parquet” structures).

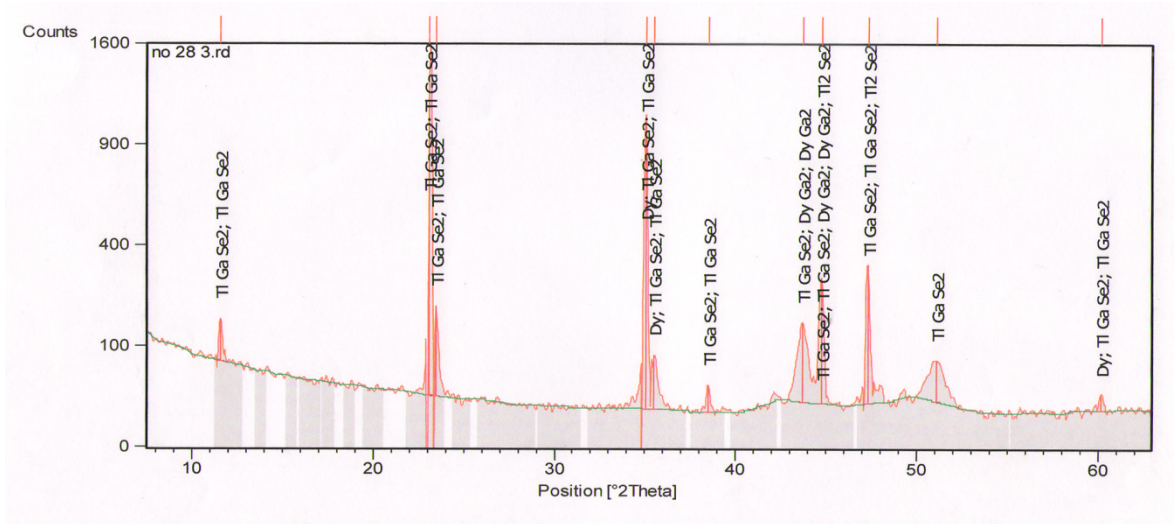


Fig.1

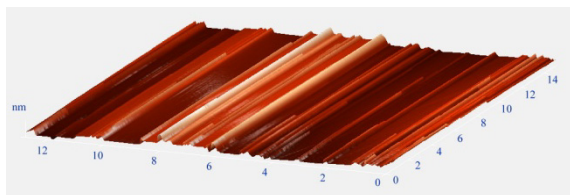


Fig.2

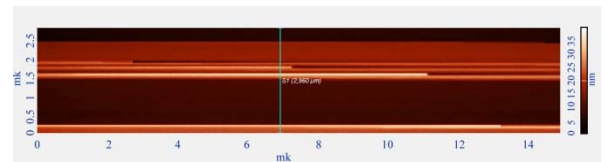


Fig.4

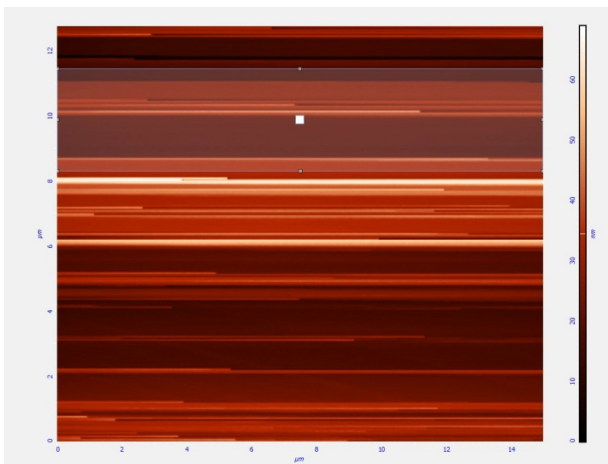


Fig.3

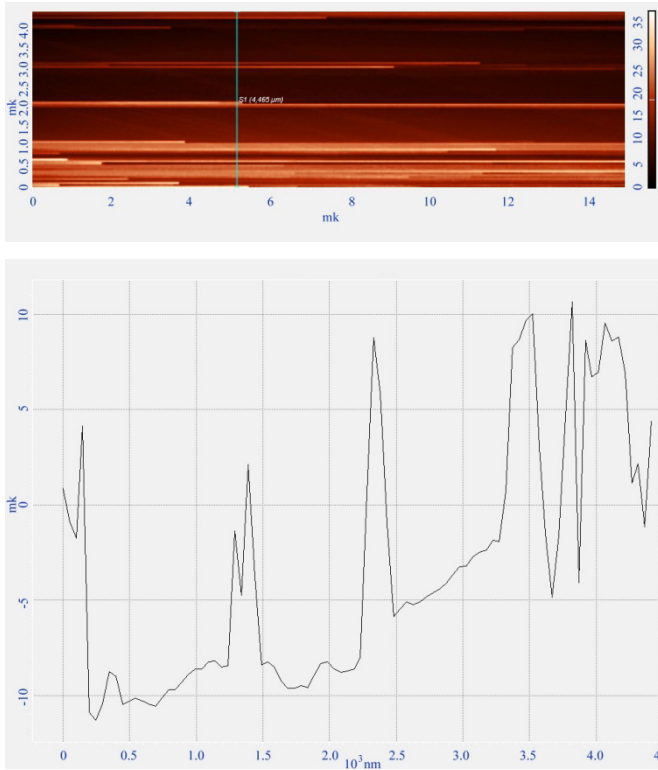


Fig.5

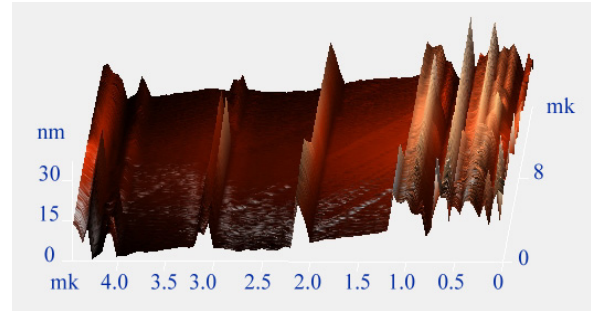


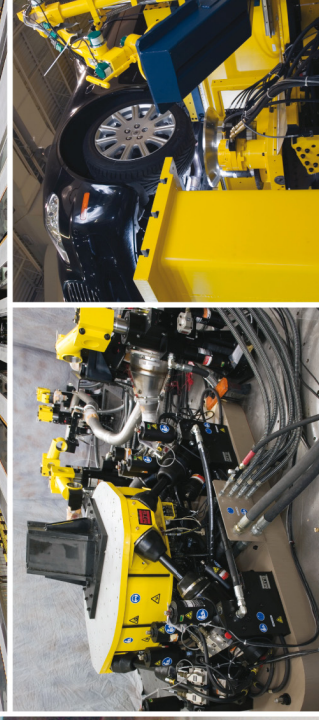
Fig.6

References

- [1]. O.P.Pchelnyakov, Yu.B.Bolokhovitynov, A.V.Dvurechenskii, L.V. Sokolov// *Physics and technique semiconductors (Russia)* 34, 11, 1281 (2000)
- [2]. Zhenyagh Zhong, A.Halilovic, M.Mühlberger, F.Schaffler, G.Bauer. *Appl. Phys. Lett.* 82, 445 (2003).
- [3]. M.Kasu, N.Kobayashi, *Appl. Phys. Lett.*, 62, 1262 (1993).



www.mts.com • www.megatr.com



MTS[®]

**MEGA
WECA**

be certain.

Kalitenizin Ölçüsü